

TRIBOLOGY SERIES, 32  
EDITOR: D. DOWSON

---

# ELASTOHYDRODYNAMICS - '96 FUNDAMENTALS AND APPLICATIONS IN LUBRICATION AND TRACTION

edited by

**D. Dowson\*, C.M. Taylor, T.H.C. Childs and  
G. Dalmaz, Y. Berthier, L. Flamand, J.-M. Georges, A.A. Lubrecht**

\* Principal Editor

*Proceedings of the 23rd Leeds-Lyon Symposium on Tribology  
held in the Institute of Tribology, Department of Mechanical Engineering,  
The University of Leeds, UK  
10th - 13th September, 1996.*



ELSEVIER  
Amsterdam • Lausanne • New York • Oxford • Shannon • Tokyo 1997  
For the Institute of Tribology, The University of Leeds  
and  
The Institut National des Sciences Appliquées de Lyon

ELSEVIER SCIENCE B.V.  
Sara Burgerhartstraat 25  
P.O. Box 211, 1000 AE Amsterdam, The Netherlands

ISBN 0 444 82809 5 (Vol. 32)  
ISBN 0 444 41677 3 (Series)

© 1997 ELSEVIER SCIENCE B.V. All rights reserved.

No part of this publication may be reproduced, stored in a retrieval system or transmitted in any form or by any means, electronic, mechanical, photocopying, recording or otherwise, without the prior written permission of the publisher, Elsevier Science B.V., Copyright & Permissions Department, P.O. Box 521, 1000 AM Amsterdam, The Netherlands.

Special regulations for readers in the U.S.A. – This publication has been registered with the Copyright Clearance Center Inc. (CCC), 222 Rosewood Drive, Danvers, MA 01923. Information can be obtained from the CCC about conditions under which photocopies of parts of this publication may be made in the U.S.A. All other copyright questions, including photocopying outside of the U.S.A., should be referred to the copyright owner, Elsevier Science B.V., unless otherwise specified.

No responsibility is assumed by the publisher for any injury and/or damage to persons or property as a matter of products liability, negligence or otherwise, or from any use or operation of any methods, products, instructions or ideas contained in the material herein.

pp. 37-48, 49-54, 81-90, 125-134, 175-182, 185-198, 261-268, 287-296, 511-522, 611-616:  
Copyright not transferred.

This book is printed on acid-free paper

Printed in The Netherlands

## INTRODUCTION

The 23rd Leeds-Lyon Symposium addressed the topic of “Elastohydrodynamics”. It was held at the regular UK venue, Bodington Hall, The University of Leeds from Tuesday September 10th to Friday September 13th 1996. The meeting was attended by 140 delegates from twenty countries and papers were presented in sixteen sessions with once again many parallel sessions in order to accommodate the large numbers of papers. The organisers from Leeds were magnificently supported by authors from the tribological community world-wide and we give our thanks to them, to other delegates and particularly to our colleagues from the Laboratoire de Mecanique des Contacts of the Institut National des Sciences Appliquées de Lyon who once again turned out in force.

There have been three previous international meetings addressing the general area of elastohydrodynamic lubrication.

- (a) “Elastohydrodynamic Lubrication” - A Symposium arranged by the Lubrication and Wear Group of the Institution of Mechanical Engineers from the 21st/23rd September 1965.
- (b) “Elastohydrodynamic Lubrication” a meeting arranged by the Tribology Group of the Institution of Mechanical Engineers from the 11-13th April 1972.
- (c) “Elastohydrodynamics and Related Topics” - The 5th Leeds-Lyon Symposium on Tribology held from the 19th to the 22nd September 1978.

All these meetings were at the University of Leeds and the Institute of Tribology within the Department of Mechanical Engineering and Leeds was particularly proud therefore to organise this fourth world-wide gathering of tribologists. Four authors at the first meeting in 1965 also presented papers at the 23rd Leeds-Lyon Symposium on Tribology - Alastair Cameron, Duncan Dowson, Chris Hooke and Jerry Kannel. It was a particular delight to have these colleagues with us thirty one years to the month after the first EHL Meeting.

Professor Stathis Ioannides presented the Keynote Address before the Symposium Dinner on the opening evening of the meeting. His paper “Tribology in Rolling Element Bearings, Recent Advances and the Wider Implications“ was a tour de force reflecting his wide experience of the influence of elastohydrodynamic lubrication studies on the development of rolling element bearing technology with particular reference to his experience at SKF Engineering and Research in the Netherlands. In addition to this Keynote Address there were fifteen other sessions covering the general areas, Analytical/Numerical, Experimental, Soft EHL, Lubricant Properties, Transmissions-Gears, Biotribology, Rolling Element Bearings,

Boundary Lubrication, Friction, Traction and Wear, Metal Forming, Transmissions - CVT's and Plain Bearings. Nine other invited technical papers supported these sessions and we are grateful to the Invited Authors for their carefully prepared papers and valuable contributions. Those who chaired sessions are recorded in this Volume of Proceedings and to them likewise we would like to express our thanks. Not only did those who chaired the sessions keep the busy programme to its time schedule but they also ensured valuable discussions which are recorded along with the Written Discussion in this Volume of Proceedings.

The Symposium Dinner was held at Nidd Hall Country House Hotel immediately after the Keynote Address of Professor Ioannides on the first evening. The dinner was graced by the presence of the Pro-Chancellor of the University of Leeds, Colonel A C Roberts, who has been a great supporter of the Department of Mechanical Engineering and the after dinner speech was made by Professor David A Parkes, Director of Shell Research Limited who entertained and informed delegates in a sparkling presentation. On the afternoon of Thursday 12th September 1996 the delegates repaired to the new Royal Armouries Museum in the City of Leeds. The visit had been prepared by a presentation the previous evening by Mr Chris O'Boyle, Chief Executive of the Royal Armouries, and the visit to this new £42 million development was much enjoyed by delegates and rounded off in the evening by an excellent meal. After the meeting many delegates remained in Leeds to enjoy a walk in the Yorkshire Dales on Saturday 14th September. Two years previously those who had undertaken a similar walk had scaled one of the three Yorkshire Peaks, Wharfedale. On this occasion walkers scaled the second of the three peaks, Ingleborough, enjoying a repast and drink or two in the same Public House, The Old Hill Inn, as previously. It was observed that at the next Leeds-Lyon Symposium to be held in Leeds there would be some sense in addressing the third of the three Yorkshire Peaks - Pen-y-ghent.

Yet again we are sincerely grateful to our colleagues at the University of Leeds who have joined us in the detailed planning and execution of the Symposium. These have included, Mrs Cath Goulborn, Mrs Sheila Moore, Dr Peter Dearnley, Mr Ron Harding, Mr David Hawkridge, Mr Brian Jobbins, Mr David Jones, and other academic colleagues, clerical staff, technical staff, research fellows and research students who have played their part. We would like in particular to note that David Jones retired from the Department of Mechanical Engineering on the 30th September 1996. His association with, and contribution to, the series of Leeds-Lyon Symposia since their inception has been exceptional including taking responsibility for all aspects surrounding the audio-visual presentations at Leeds. We should also like to record that one of our tribological colleagues Dr Chris Radcliffe has also left us but it is with pleasure that we wish to record that two new academic tribological colleagues have now joined us in Leeds, Dr Pascal Ehret on the 1st July 1996 and Dr Martin Priest on the 1st September 1996. Once again Elsevier Science Publishers BV, Amsterdam have supported our endeavours tremendously and we gratefully acknowledge them and the following organisations



who made financial contributions to the meeting. These financial contributions enabled us to achieve our goals and in particular to reduce the registration fee for many younger research workers.

BP International Ltd

Charities Aid Foundation - Unilever's Research and Engineering Division

DePuy International Ltd

Elsevier Science Publishers BV

FAG OEM und Handel AG

NSK Limited

Shell Research Ltd

SKF Engineering & Research Centre BV

The range of topics covered by the Leeds-Lyon series of meetings is now extensive as will be seen from the following list.

1. 'Cavitation and Related Phenomena in Lubrication'
2. 'Superlaminar Flow in Bearings'
3. 'The Wear of Non-Metallic Materials'
4. 'Surface Roughness Effects in Lubrication'
5. 'Elastohydrodynamic Lubrication and Related Topics'
6. 'Thermal Effects in Tribology'
7. 'Friction and Traction'
8. 'The Running-In Process in Tribology'
9. 'The Tribology of Reciprocating Engines'
10. 'Numerical and Experimental Methods Applied to Tribology'
11. 'Mixed Lubrication and Lubricated Wear'
12. 'Global Studies of Mechanisms and Local Analyses of Surface Distress Phenomena'
13. 'Fluid Film Lubrication - Osborne Reynolds Centenary'
14. 'Interface Dynamics'
15. 'Tribological Design of Machine Elements'
16. 'Mechanics of Coatings'

17. 'Vehicle Tribology'
18. 'Wear Particles : From the Cradle to the Grave'
19. 'Thin Films in Tribology'
20. 'Dissipative Processes in Tribology'
21. 'Lubricants and Lubrication'
22. 'The Third Body Concept: Interpretation of Tribological Phenomena'
23. 'Elastohydrodynamics - '96'

Over the years the organisers of the meeting and the editors of the Volume of Proceedings have taken great care to ensure the quality of the papers presented orally and included in the final Volume of Proceedings. A view on the quality of all material is taken at the presentations and all manuscripts are reviewed by international tribological authorities in Europe and occasionally from elsewhere. The editors would like to acknowledge the support of referees and to record their commitment to the continuation and improvements of the high quality of papers which appear in the Proceedings.

Exceptionally in 1997 there is to be a World Tribology Congress held from the 8th-12th September in London, the organisation being led by the Tribology Group of the Institution of Mechanical Engineers. All major tribological research societies have committed to the support of this World Tribology Congress in different ways. This includes the Leeds-Lyon Symposium which on this unusual occasion will be held at Imperial College of Science, Technology and Medicine from September 4th-6th immediately preceding the World Tribology Congress. We are grateful to our colleagues in the Department of Mechanical Engineering and the Department of Chemical Engineering at Imperial College - Professor Brian Briscoe, Dr Philippa Cann and Professor Hugh Spikes for their positive and energetic support of Leeds and Lyon on this occasion and we are already looking forward to this 24th Leeds-Lyon meeting which will be entitled "Tribology for Energy Conservation".

Duncan Dowson, Chris Taylor, Tom Childs

## **EHL in rolling element bearings, recent advances and the wider implications.**

E Ioannides

SKF Engineering & Research Centre, and  
Imperial College of Science, Technology and Medicine

Rolling element bearings were introduced industrially in the latter part of the nineteenth century and rapidly became the main machine element used in the support of rotating shafts and machinery, mainly because of their low frictional losses. Today's demands for increased reliability and downsizing, combined with the requirement for high speed development of equipment, have encouraged the development of predictive tools rather than following the usually more expensive and slower testing approach. This in turn has spurred the refinement of EHL predictions that model more realistic operational conditions in rolling bearing and other machine elements. In this paper, lubrication of real surfaces with roughness or damage from solid contaminants is discussed, together with frictional losses. The implications of treating a rolling element bearing as a full dynamic system are considered and the need for further research is identified.

### **1. INTRODUCTION**

The rolling element bearing is the most widespread machine element (after nuts and bolts) with some fifty billion bearings in operation throughout the world. The origin of rolling bearings can be traced in antiquity where bearings supporting platforms in Roman ships had rolling elements made of bronze and wood. Even earlier a Celtic cart was found with hubs, having spacing for supporting wooden elements, rolling or possibly sliding [1]. Despite these early origins rolling bearings were introduced industrially only during the latter part of the nineteenth century after a flurry of patents during the previous century. The chief reason for this is that low surface roughness of the rolling elements and the contacting raceways is needed to ensure satisfactory separation of these components by the very thin lubricant film formed during rotation of the bearing. This, together with the use of special steels of high cleanliness, is necessary to ensure long and trouble-free operation under the high contact pressures that develop in the minute contact areas between the relatively small rolling elements and the raceways, as may be seen in the photoelastic model of Fig. 1. Thus, commercialization of rolling element bearings had to await the capability of manufacturing smooth surfaces made of strong steel.

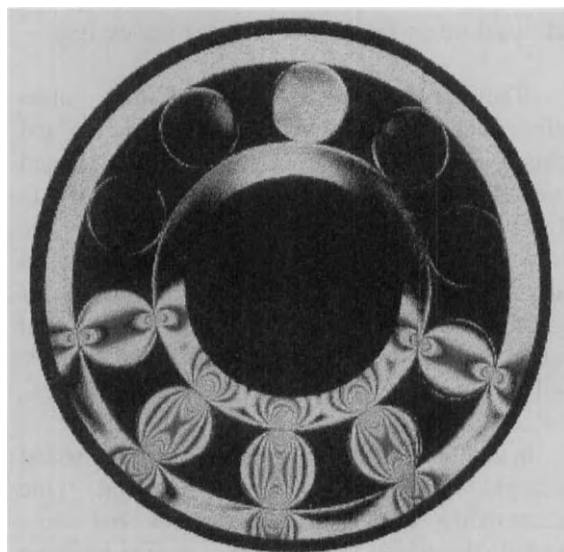


*Fig.1: Photoelastic model of a radially loaded bearing*

As a consequence the modern rolling element bearing is a precision machine element, usually mass produced at high speed with very demanding dimensional and working contact surface requirements. The high demand on dimensional accuracy of the different bearing components originates from the requirements for running accuracy of machinery whilst, as indicated above,

the need for low roughness originates from the need to build a separating lubricating film.

Optimising the selection of rolling bearings in machinery is an important issue, not only because of the large numbers of bearings involved, but also because of the critical role these components play in many applications, including safety, for example in transport systems. Today's high performance and reliability requirements are also a result of keen competition for all manufactured equipment combined with the need for high speed development from concept to finished product. This in turn implies that numerical modelling is usually preferable to testing because of both speed and cost. Considerable effort has therefore been put into modelling bearing performance in increasingly realistic terms by including, for example, effects of roughness and lubricant contamination. This is particularly important in modern machinery where the trends of higher speed and increased power density (downsizing) have been eroding the traditional safety factors built into earlier designs.

The paper discusses three of the main performance criteria of bearings, life, friction and dynamic behaviour, concentrating on EHL-related issues affecting these. The current issues of life calculation are addressed first, including the introduction of a fatigue limit for bearing steels and the representation of realistic rough or contaminated lubrication conditions. Some recent contributions to these topics may be found in Refs. [2-6].

In addition, advances in EHL calculations and rheology modelling, which extend the understanding of asperity interactions and more generally the effects of topography on film building and contact stresses, are also discussed. Some of the difficulties and the progress in understanding grease lubrication are also addressed, as sealed or greased-for-life bearing applications have been steadily increasing in past years. Recent work in this area is described in Refs. [6-9].

These broad issues of life, lubrication and contamination of rolling bearings, are also

dominant in field studies of causes of failure, Fig 2, see for example [10]. It should however be noted in this connection that the vast majority of bearings, 99.5%, are either scrapped with the equipment or replaced during maintenance without having failed.

#### CAUSES OF FAILURE FOR BEARING LIFE < L1 %

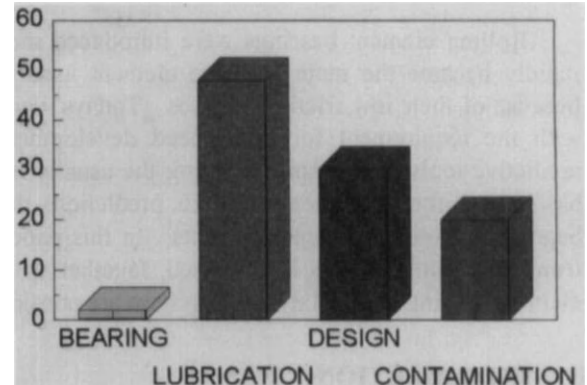


Fig. 2: Main Causes of Bearing Failure

The issue of rheology is also further discussed in the next section in relation to the friction torque of bearings. This aspect of bearing performance is gaining importance in the world of today with the keen interest in energy conservation.

Finally, in addressing the overall performance of bearings, the dynamic effects of the whole bearing operating as a system are discussed. Again, as forces are transmitted through EHL contacts, these contacts determine the dynamic behaviour of the rolling elements and the cage. A 'systems approach' to modelling the dynamics of the complete bearing therefore relies heavily on EHL simulation. Results from the dynamic modelling of complete bearings at various levels of complexity are reported in Refs. [11-12].

## 2. LIFE AND LUBRICATION

As indicated in the Introduction, the commercialization of rolling bearings had to wait until manufacturing practices could deliver surfaces smooth enough to be sufficiently separated by EHL

films. This is necessary to guarantee long life for rolling bearings which are expected to survive typically  $10^9$  contacts at each point of the contacting surface of the raceways, each at a high contact pressure between 1 to 4 GPa. With microslip present (Heathcote - i.e. curvature originated - slip, slip from manufacturing tolerances etc.) such separation is necessary since when a degree of metallic contact occurs, reduction of service life of the bearings has been observed. Empirically this has been introduced into bearing life calculations, [13], and into bearing manufacturers' catalogues.

Bearings are selected (type and size) such that the percentage probability ( $n$ ) to fail in an application within a prescribed number of Millions of revolutions  $L_{na}$ , i.e. the expected life of the bearings, is known. A number of conditions influence the bearing life  $L_{na}$  such as steel quality, contacting surface quality, lubricating conditions, load, operating temperature, internal stresses from fittings, bearing kinematics, etc. and an increasing number of these are taken into account in the prediction methodologies for  $L_{na}$  [14].

The lubricant in the bearing is the low shear strength "third body" which is used to separate the two otherwise contacting bodies. Thus shearing takes place in the lubricant and the shear stresses exerted on the metallic surfaces are reduced as the separation grows. Under a variety of operating conditions, the real engineering (rough) surfaces in rolling bearings experience different degrees of metallic contact. Traditionally this has been described by the ratio,  $\Lambda$ , of the film thickness to the composite roughness or by the viscosity ratio  $\kappa$  preferred by bearing manufacturers. Loss of bearing life has been empirically related to these parameters. In fact, this is the major cause of bearing failure as can be seen in Fig 2, showing the percentage share of the major causes of bearing failure. Efforts to model real surface lubrication have thus intensified in recent years. Three areas of this effort are discussed below.

## 2.1. EHL of rough surfaces

Lubricated rough contacts are characterised by pressure oscillations which describe the pressure increase at the top of the asperities and the pressure decrease in the intervening valleys compared to a smooth contact. The EHL solution for a rolling engineering rough surface must in most cases involve a simplified description of the surface or of the roughness, [15-18], as the solution must be time dependent to account for the varying amounts of entrained lubricant and its squeezing by the asperity approach velocities. In contrast, pure sliding of a rough surface against a smooth one produces a steady state, where there is no approach velocity. The problem is time independent and many solutions exist, [19-21].

Estimating the life of such real rough surfaces is of primary interest in the effort to predict the life of rolling bearings. The approach to this, given the present day calculation limitations described above, is to use expressions or design curves derived from test [13] or to utilise stress fields obtained from dry contact solutions to estimate the expected life. The latter approximation is valid for thin films where the pressure distribution approaches asymptotically the dry contact one as the film thickness diminishes. In the absence of pressure fluctuation attenuation by the lubricant film the dry contact pressure distributions provide a conservative limit for the purposes of life calculation. Such dry contact calculations have been reported by a number of authors, [22-23], and more recently the extension of the methods to layered contacts has been reported [24-25]. The dry contact subsurface stress fields were used in [26] to assess the relative effect of roughness parameters on life. In Fig. 3, from this reference, the computed surfaces show that averaged  $L_{10}$  values increase dramatically when the rms slope of the surface is reduced or when the skewness is made more negative. The benefit deriving from a reduction in the roughness amplitude  $R_q$  itself is, by contrast, more modest.

Moreover, in attempting to model the rough rolling and sliding lubricated contact present in rolling bearings the non-Newtonian rheology of the

lubricants must be addressed. At the typical pressures and temperatures of the contacts in these bearings such lubricants can solidify and react to the small amounts of sliding present in bearings by leaking sideways from the top of the asperities, allowing oil film collapse, [27-28]. This behaviour can also be modelled by treating the lubricant film as a perfectly plastic solid, [29]. Fig. 7 shows the calculated collapse of the oil film thickness with passage time through the contact for a smooth on rough surface combination with four different asperity wavelengths ( $\lambda$ ) in the direction transverse to the rolling/sliding [29].

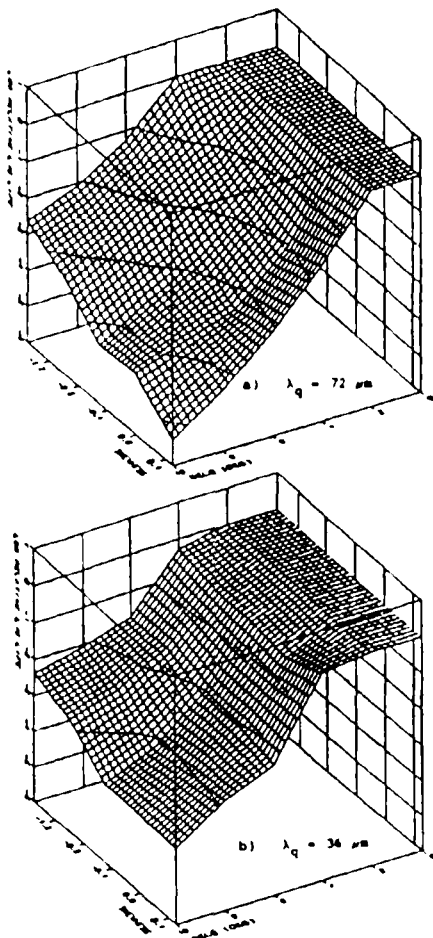


Fig.3: Relative life  $L_{10}$  variation versus roughness, slope and skewness

In general, the complexity of EHL calculations for real rough surfaces is prohibitive. However, in recent times progress in this direction has been greatly assisted by Multigrid techniques which have resulted in dramatically shorter computational times and smaller memory requirements. It is therefore expected that these computational techniques will further expand the ability to understand film formation and stress levels at the asperity contact level (micro EHL) within a rough lubricated contact, e.g. [30]. However, the true performance of rolling bearings under mixed or boundary lubrication conditions depends also on the chemical composition of the oil and any additives, which can have a profound effect on life. Thus, for the foreseeable future, additional experimental work will be needed to support life predictions.

## 2.2. EHL of damage

In the past, a considerable amount of experimental work has been reported in which contaminated lubricants were used in rolling element bearings and rolling contacts. An overview of this work is given in [3]. In general, such experimental work points to a wide range of life reductions, usually severe, indicating the need for a predictive model which can account for the effects of such realistic conditions. For this reason theoretical studies have recently been emerging in which an effort is made to systematize the many parameters that govern the effects of particulate contamination. These studies have concentrated on two main aspects: (a) the mechanisms and the prediction of damage by particles to the raceways and rolling elements [4-7], and (b) a theoretical confirmation of how such localised damage can reduce the fatigue life of a bearing [8-13]. For the latter, fatigue models such as the one reported in [14] have been used to predict the life reductions associated with damaged raceways and rolling elements. An alternative approach has been the use of Fracture Mechanics and Micromechanics modeling, e.g. [6].

Again in many cases the starting point for life predictions is the dry contact stress calculations.

These calculations themselves are quite complex and require large computer memory and time if sufficient detail of the real damaged surface is modelled during the passage of the rolling element over the damaged ring. Early examples are given in [31] where FE methods were used to simulate the effect of a certain level of filtration in helicopter gearboxes. Again with the advent of Multilevel-multintegration techniques it is now possible to calculate realistic contacts in bearings requiring many thousands of grid points. Fig 4a, shows the ball/raceway dry contact pressure distribution in a deep groove ball bearing with a large circular dent (600  $\mu\text{m}$  diameter) in the centre of the contact whilst Fig 4b, shows the fatigue criterion distribution of [14] in the subsurface region of the ring. The brighter colours in this figure signify higher values of the criterion and consequently higher risk of fatigue. It can further be seen in this figure that the risk of fatigue is higher in the rim area of the dent and the distribution is symmetric with respect to the centre of the dent. This implies that the risk for initiation of fatigue spalls is also evenly distributed around the rim of the dent. This contradicts the experimental evidence, that spalls invariably start near the trailing edge of the trailing side of the dent. With a full EHL calculation, however, it is possible to show that the film pressure and the corresponding value of the criterion are higher in the trailing edge of the dent and that therefore this is the predicted preferential site for fatigue spall initiation in agreement with the experimental evidence, [31].

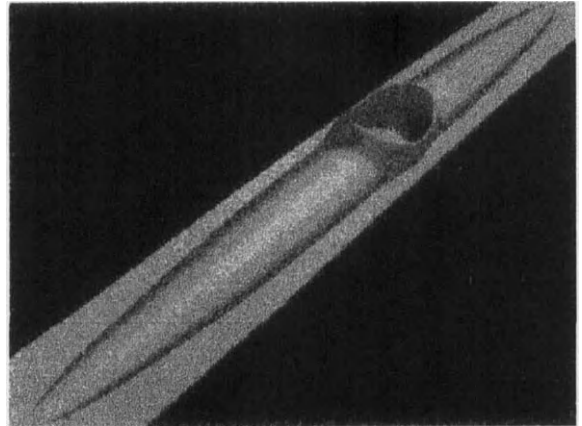


*Fig.4a: Pressure distribution in deep groove ball bearing with a dent of 600  $\mu$*

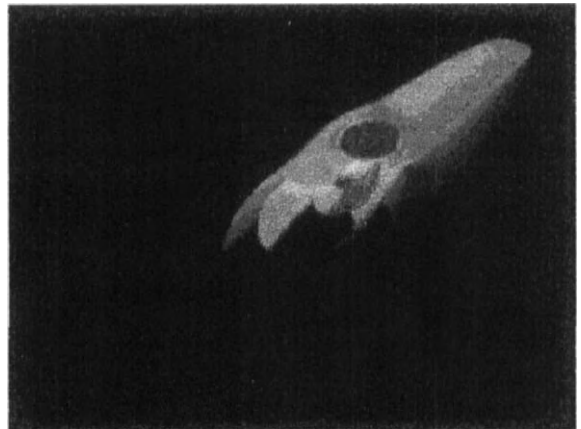


*Fig.4b: Subsurface fatigue criterion distribution*

The predicted contact pressures and the values of the fatigue criterion according to [14] are asymmetric, as shown in Fig 5. When effects of sliding are introduced, additional detrimental effects are suggested. [33]. Again further work is needed to integrate this with both thermal calculations and non-Newtonian rheology if the experimentally observed film thinning and raised temperatures are to be explained [34].

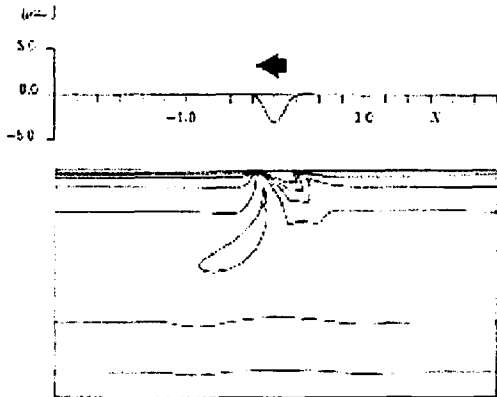


Fig.5: Predicted risk of fatigue in the neighbourhood of a dent using EHL calculations

### 2.3. Starvation and grease lubrication

The preceding discussion implies that EHD film thickness can be predicted with some confidence for cases of smooth surfaces with Newtonian rheology under isothermal conditions and also that by using modern calculation methods, these may be extended to include rough and damaged surfaces, thermal effects and non-Newtonian rheology. However, one further limitation still exists: such analyses generally assume a sufficient supply of lubricant to ensure that the inlet to the conjunction is fully flooded. If this condition is not met the contact becomes starved with significant reduction of the film thickness (50% of its fully flooded value under moderately starved conditions). This condition can occur even when excess oil is present if the combination of high oil viscosity and high rolling speed results in insufficient oil replenishing the raceway to sustain the inlet reservoir [35]. Grease-lubricated bearings operate almost exclusively in the starved regime.

The problem of starved lubrication was first recognised nearly 30 years ago. Early studies established that the degree of film depletion was determined by the position of the lubricant-air meniscus in the inlet. Both experimental [36] and numerical studies [37] have subsequently developed similar relationships for the critical inlet

boundary distance for starvation as a function of geometry and film thickness. An alternative approach was used by Chiu [35], who considered the starvation condition in terms of the balance between oil being pushed from the raceway due to passage of the ball and reflow into the raceway outside the contact. He thus derived a simple expression to predict the onset of starvation in real contacts. The regime of parched lubrication was first proposed by Kingsbury [38] to denote the fully starved condition where there is no inlet meniscus. In the parched regime no free oil is present and only a thin film of oil remains on the surface. It was shown that instrument hearings could run successfully for several hours with thin films of deposited oil only 80 - 200 nm thick as lubricant. This would certainly not be predicted by the  $\Lambda$  evaluation. More direct evidence of residual film separation in the parched regime has been obtained with thin film optical interferometry measurements of heavily starved contacts [39].

Grease lubrication similarly suffers from a lack of understanding, at a detailed level, of the mechanism of oil replenishment. It is still not possible to establish the nature of the separating film, to identify the film formation and lubricant supply mechanism, nor to predict bearing lubrication performance from fundamental grease properties. Experimental studies of film formation by greases in a single contact [40] have shown that the development of the EHL film is now governed by the supply of lubricant from the surrounding grease reservoir. This is seen in Fig. 6, where EHL film thickness is captured by thin film interferometry. The films shown are thicker at the sides of the track, next to the 'wall' of grease. This behaviour is characteristic of greases, although the starvation speed and the final film thickness level vary greatly with different grease types and operating conditions.



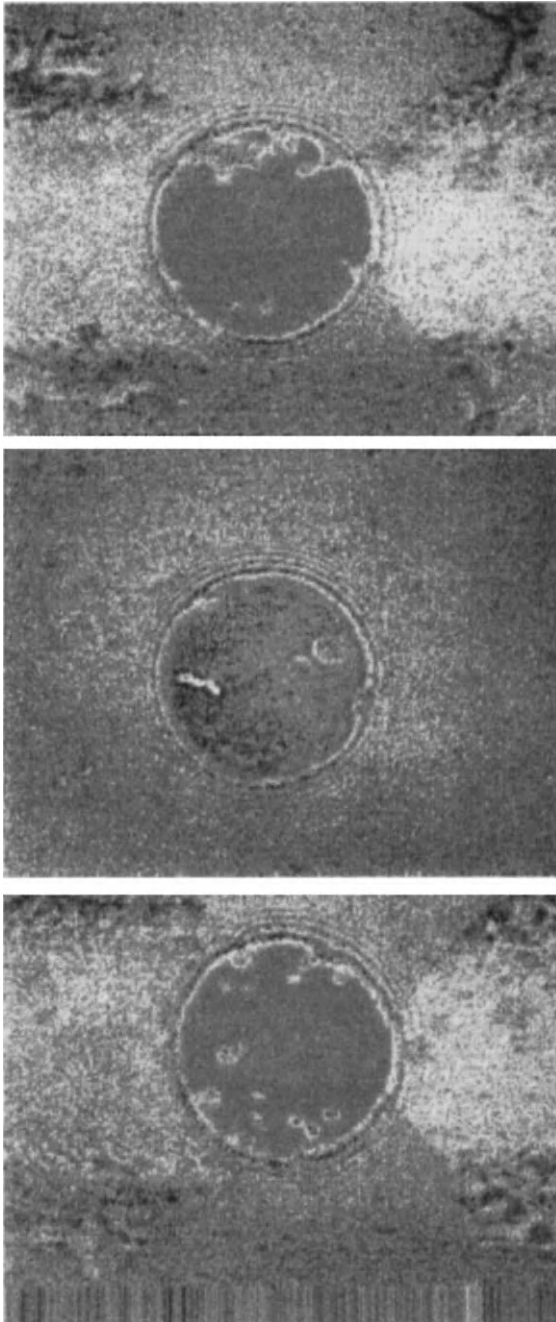


*Fig.6: Captured film images of grease lubrication*

Contrary to the above observations the ability of a grease to form an EHL film is often described only in relation to its base oil viscosity with no reference to starvation effects. Furthermore the

performance of rolling bearings is judged using a simple criterion based on the full film-to-roughness ratio  $\Lambda$ . The arguments presented above demonstrate some of the difficulties inherent in the use of  $\Lambda$  values for starved and grease-lubricated bearings. A more complete discussion of the limitations of the film-roughness ratio  $\Lambda$  can be found in [41].

### 3. FRICTION

As indicated above, the success of rolling bearings has been as a device that can support rotating shafts with a relatively small loss of power. The friction losses of rolling bearings are treated in an over-simplified manner in the bearing manufacturers' catalogues, where the friction torque of a bearing is calculated from both load-independent and load-dependent frictional moments using experimentally derived factors for the various bearing types and operating conditions.

EHL is one important issue in the generation of the frictional moment as, in most cases, the important contributions come from lubricated contacts where the film thicknesses attained and the rheology of the lubricant mainly determine the power loss (additional losses exist from hysteresis, churning etc). Progress in understanding and modelling the lubricant rheology are thus vital and importance advances in this area have been reported [42] and [43]. Non-Newtonian behaviour has significant implications not only for the frictional behaviour in the contact but also in the ability of the lubricant to maintain films without their collapse in the presence of some sliding, [27 - 29], Fig. 7.

Finally, because of the vast number of rolling bearings that are used world-wide any small reduction of their friction torque would have considerable total energy implications. Thus the downsizing of bearings in applications made possible through more accurate performance predictions in improvements and quality, design,

steel and manufacturing, can result in savings of many GWs of power.

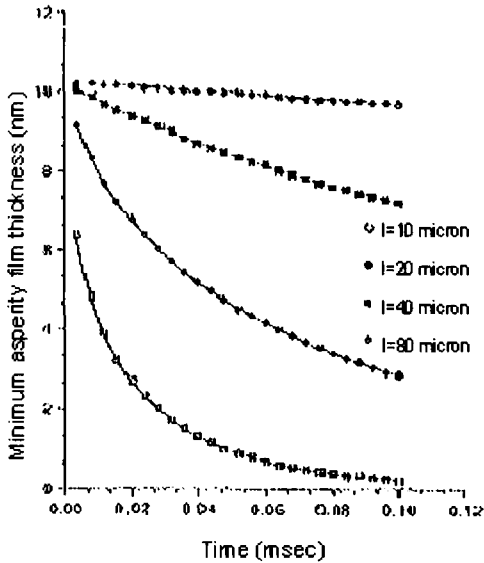


Fig.7: Oil film collapse versus time for different asperity wavelengths

**4. DYNAMIC BEHAVIOUR**

The discussion above pertains to a description of the bearing performance mainly in quasi-static terms. In reality the rolling bearing is a fully dynamic system with many moving parts, that is, the rolling elements, the cage and at least one of the rings. As the rotational speed of the application increases it becomes necessary to describe the bearing as a dynamic structure and more importantly as a 'system' where the interaction of its components, through EHL contacts, is responsible for the overall performance of the complete bearing. In this, the connection with the environment, i.e. the bearing housing, the shaft and rest of the machinery can also be important. Furthermore, while environmental trends require reduction of noise and vibration, rolling bearings can be both a source and a transmitter of vibration in rotating machinery. Thus description of the dynamic behaviour of a bearing fulfils two purposes: the understanding, modelling and optimisation of

vibration and noise, together with more accurate friction and life prediction.

A gradual approach to the dynamics of the bearing may be adopted, where the dynamic modelling is based, in the first instance, on dry contact, i.e. Hertzian spring characteristics of the rolling element and raceway contacts [44]. This can then be expanded to incorporate a simple description of local damping by the EHL film and the elastic contribution of the housing characterised from a FEM analysis in which the outer ring and the housing are modelled as single structure [45]. Fig. 8. There the displacement of the outer raceway originating from waviness in the raceways can be written in terms of a Fourier series. Fig. 9, [45], shows the effect of a measured outer ring waviness on the vibrational amplitude, for the ball pass frequency.

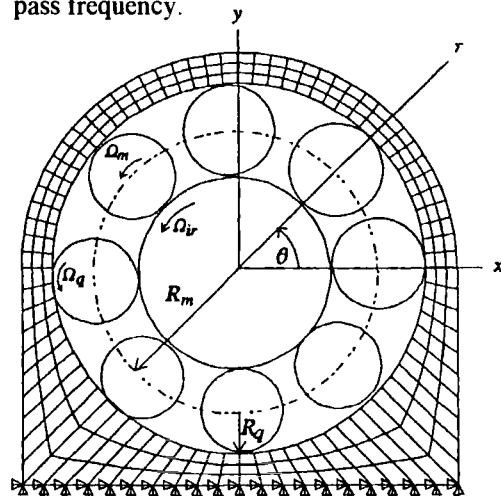


Fig.8: FEM model of a bearing in its housing

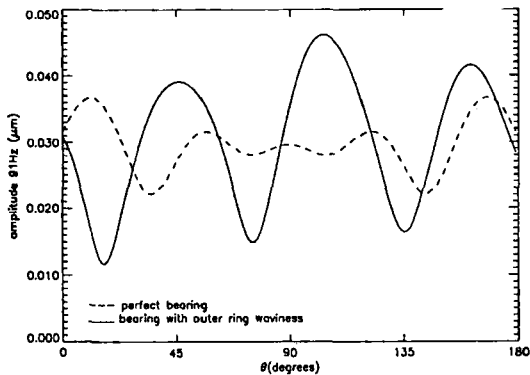


Fig.9: Contribution of the ball pass frequency in the circumferential direction on the outer surface of an application with a perfect bearing and a bearing with outer ring waviness

The simulation of complete bearing dynamics on parallel computers is discussed in [46], Fig.10. Here the contact forces and moments on the different elements of the bearing (rolling elements, cage, rings) are based on EHL theory. With complete 3-D motions allowed in this model for the moving elements as well as detailed geometrical description the model is computationally very intensive and requires high numerical accuracy. It does however produce extensive information describing in detail the forces on, and motions of, the elements of the bearing and as such can be used to shorten considerably the development cycle of bearings. This has been achieved in the design of a new type of bearing, the Compact Aligning Roller Bearing, (CARB™), [46].

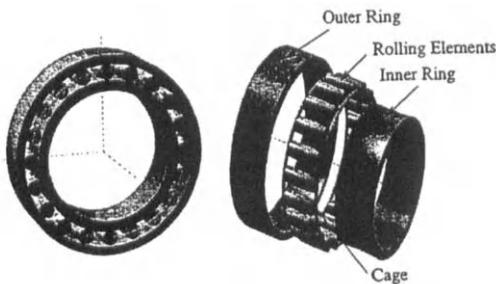


Fig.10: A Compact Aligning Roller Bearing (CARB™)

## 5. DISCUSSION AND CONCLUSION

The understanding and theory of EHL is inextricably related to rolling bearing technology. The design of rolling bearings, as explained above, is based on the transfer of forces from the shaft to the bearing housing through the small contacts between the rolling elements and the raceways. Consequently large pressures and local temperatures may develop creating a severe operating environment for the material of these elements of the bearing. As the longevity and the reliability of the bearing largely depend on the events in these small contacts, it is of paramount importance to extend knowledge in this area so that the rolling bearing, a machine element important to the economy of the society, can be designed (selected) for applications in an optimum way. For this, the bearing manufacturers who understand the application environment of bearings and their functioning as a mechanism, should work more closely with Universities and other Institutions which expend considerable effort in the understanding of the details of single EHL contacts. It is only through combining such elements of understanding that the performance of the bearing can be addressed properly in terms of a complete dynamic system. And it is only through this systems approach, assisted by such partnerships, that rapid progress can be made in optimising the performance and design of this very important, deceptively simple, though in reality rather complex, machine element, the rolling bearing.

### Acknowledgement

The author wishes to thank Dr. H.H. Wittmeyer, Managing Director of SKF Engineering and Research Centre B.V., for his kind permission to publish this paper.

## 6. REFERENCES

1. D. Dowson, History Of Tribology, Longman Group Ltd., London, 1979.
2. E. Ioannides, E. Beghini, G. Bergling, J. Goodall Wuttkowski and B. Jacobson, Cleanliness and its Importance to Bearing Performance, *Lubrication Engineering*, 49, 9 (1993) 657-662.
3. E. Beghini, R.S. Dwyer-Joyce, E. Ioannides, B. Jacobson, A.A. Lubrecht and J.H. Tripp, Elastic/Plastic Contact and Endurance Life Prediction. *J. Physics D: Appl. Phys.* 25 (1992) . 379-383
4. R.S. Sayles, J.C. Hamer and E. Ioannides, The Effects of Particulate Contamination In Rolling Bearings - A State of the Art Review, *The Proceedings of IMechE*, 204 (1990) 29-36.
5. R.S. Zhou, H.S. Cheng, and T. Mura, Micropitting in Rolling and Sliding Contact under Mixed Lubrication, *ASME J. Trib.*, 111 (1989) 605-613.
6. W. Cheng, and H.S. Cheng, T. Mura , and L. M. Keer, Micromechanics Modeling of Crack Initiation under Contact Fatigue, *ASME J. Trib.*, 116 (1994) 2-8.
7. X. Ai, H.S. Cheng, and L. Zheng, A Transient Model for Micro-Elastohydrodynamic Lubrication with Three- Dimensional Irregularities, *ASME J. Trib.*, 115 (1993) 102-110.
8. H. Astrom, J.O. Ostensson, and E. Hoglund, Lubricating Grease Replenishment in Elastohydrodynamic Point Contact, *ASME J. Trib.*, 115 (1993) 501-506.
9. F. Chevalier, A.A. Lubrecht, P.M.E. Cann, F. Colin, and G. Dalmaz, Starvation Phenomena in EHL Point Contacts, Influence of Inlet Flow Distribution , *Proc. 22nd Leeds-Lyon Symposium on Tribology, Lyon (1995)*, 213-223.
10. L. Engel, and H. Winter, Walzlagerschaden, *Antriebs Technik* 18, (1979) Nr. 3.
11. W.J. Crecelius, User's Manual for Steady State And Transient Thermal Analysis of a Shaft-Bearing System (Sharberth), Contract Report Arbrl-Cr-00386, Nov. 1978.
12. P.K. Gupta, Dynamics of Rolling-Element Bearings. Part 1: Cylindrical Roller Bearing Analysis, *ASME J. Lub. Technol.* 101 (1979) 293-304.
13. T.E.Tallian, On Competing Failure Modes In Rolling Contact, *Trans. ASLE*, 10 (1967) 418-439.
14. E. Ioannides, B. Jacobson and J. Tripp, Prediction of Rolling Bearing Life under Practical Operating Conditions, *Proc 15th Leeds-Lyon Symposium on Tribology, Leeds (1988)* 181-187.
15. X. Ai, and H. S. Cheng, A Transient EHL Analysis for Line Contacts with a Measured Surface Roughness using Multigrid Technique, *ASME J.Trib.*, 116 (1994), 549-558.
16. L. Chang, and M. N. Webster, A Study of Elastohydrodynamic Lubrication of Rough Surfaces, *ASME J. Trib.*, 113 (1991), 110-115.
17. L. Chang, Traction in Thermal Elastohydrodynamic Lubrication of Rough Surfaces, *ASME J. Trib.*, 114 (1992), 186-191.
18. K.F. Osborn, and F. Sadeghi, Time Dependent Line EHD Lubrication Using the Multigrid/Multilevel Technique, *ASME J.Trib*, 114 (1992) 68-74.
19. P.R. Goglia, C. Cusano, and T.F. Conry, The Effects of Surface Irregularities on the Elastohydrodynamic Lubrication of Sliding Line Contacts. Part I - Single Irregularities, *ASME J.Trib.*, 106 (1984), 104-112.

20. P.R. Goglia, C. Cusano, and T.F. Conry, The Effects of Surface Irregularities on the Elastohydrodynamic Lubrication of Sliding Line Contacts. Part II - Wavy Surfaces, *ASME J. Trib.*, 106 (1984), 113-119.
21. J.A. Greenwood and K.L. Johnson, The Behaviour of Transverse Roughness in Sliding Elastohydrodynamically Lubricated Contacts, *Wear*, 153, (1992) 107-117.
22. M.A. West and R.S. Sayles, A 3-dimensional method of studying 3-body contact geometry and stress on real rough surfaces. *Proc 14th Leeds-Lyon Symposium on Tribology, Lyon*, (1987) 195-200.
23. D.M. Bailey, and R.S. Sayles, Effect of roughness and sliding friction on contact stress. *ASME, J. Trib.*, 113 (1991), 729-738.
24. S.J. Cole, and R.S. Sayles, A numerical model for the contact of layered elastic bodies with real rough surfaces. *ASME, J. Trib.*, 114 (1992), 334-340.
25. A. V. Olver, S.J. Cole, and R.S. Sayles, Contact stresses in nitrided steels. *Proc 19th Leeds-Lyon Symposium on Tribology, Leeds*, (1992) 71-80.
26. J.H. Tripp and E. Ioannides, Effects of Surface Roughness on Rolling Bearing Life. *Proc. Japan International Tribology Conference, Nagoya*, (1990) 797-802.
27. B. Jacobson, E. Ioannides and J.H. Tripp, Redistribution of solidified films in rough Hertzian contacts, Part I: Theory, *Proc.14th Leeds-Lyon Symposium on Tribology, Lyon*, (1987) 51-57.
28. B. Jacobson, Redistribution of solidified films in rough Hertzian contacts, Part II: Experimental, *Proc. 14th Leeds-Lyon Symposium on Tribology, Lyon*, (1987), 59-63.
29. J.C. Hamer, R.S. Sayles and E. Ioannides, The collapse of sliding micro EHL films by plastic extrusion, *Proc. Joint ASME J. Trib.*, 113 (1991), 805-810
30. C.H. Venner, 1991, Multilevel Solution of the EHL Line and Point Contact Problems, Ph.D Thesis, University of Twente, Enschede, The Netherlands- ISBN 90-9003974-0.
31. M.N. Webster, E. Ioannides, and R.S. Sayles, The effects of topographical defects on the contact stress and fatigue life in rolling element bearings. *Proc. 12th Leeds-Lyon Symposium on Tribology, Lyon*, (1985) 207-221.
32. A.A. Lubrecht, C.H. Venner, S. Lane, B. Jacobson and E. Ioannides, Surface Damage - Comparison of Theoretical and Experimental Endurance Lives of Rolling Bearings. *Proc. Japan International Tribology Conference, Nagoya*, (1990) 185-190.
33. Ai, X., and H.S. Cheng, The Influence of Moving Dent on Point EHL Contacts, *STLE Trib. Trans.*, 37 (1994) 323-335.
34. L.D. Wedeven, and C. Cusano, Elastohydrodynamic Film Thickness Measurements of Artificially Produced Surface Dents and Grooves, *ASLE Trans.*, 22 (1979), 369-381.
35. Y.P. Chiu, An analysis and prediction of lubricant film starvation in rolling contact systems, *ASLE Trans.*, 17 (1974) 22-35.
36. L.D. Wedeven, D. Evans and A. Cameron, Optical analysis of ball bearing starvation, *J. Lubr. Technol.*, 93 (1971) 349-363.
37. B.J. Hamrock and D. Dowson, Isothermal elastohydrodynamic lubrication of point contacts, Part IV: Starvation results, *J. Lubr. Technol.*, 99, (1) (1977) 15-23.

38. E. Kingsbury, Parched Elastohydrodynamic Lubrication, ASME J. Trib., 107 (1985) 229-233.
39. G. Guangteng, P. Cann and H A Spikes, A study of parched lubrication, Wear, 153 (1992) 91-105.
40. P M. Cann and H.A. Spikes, Film thickness measurements of lubricating greases under normally starved conditions, NLGI Spokesman, 56 (1992) 21.
41. P.M. Cann, E. Ioannides, B. Jacobson, and A.A. Lubrecht, The lambda ratio - a critical re-examination. Wear, 1994, 175, 177-188.
42. E. Hoglund and B. Jacobson, Experimental investigation of the shear strength of lubricants subjected to high pressure and temperature, ASME J. Trib., 108 (1986) 571-578.
43. S. Bair, Recent Developments in High-Pressure Rheology of Lubricants, Proc. 21st Leeds-Lyon Symposium on Tribology, Lyon, (1994) 169-187.
44. F.P. Wardle, Vibration forces produced by waviness of the rolling surfaces of thrust loaded ball bearings, part 1 & 2, Proceedings I MECH E, Vol. 202, No C5, London. England, 1988
45. J.A. Wensing and G.C. van Nijen, 2D Computational Model for Vibration Analysis of Waviness in Rolling Bearing Applications, Proc. Sixth International Conference on Vibrations in Rotating Machinery, Oxford 1996, IMechE Conference Transactions (1996).
46. P. Nordling, 1996, The Simulation of Rolling Bearing Dynamics on Parallel Computers, Ph.D. Thesis, Linkoping University, S-581 83 Linkoping, Sweden.

## Influence of Local and Global Features in EHL Contacts

A.A. Lubrecht <sup>a</sup>

<sup>a</sup>Laboratoire de Mécanique des Contacts, UMR CNRS 5514, INSA de Lyon, France.

This paper re-groups some of the recent developments in the understanding of the ElastoHydrodynamic Lubrication (EHL) of non-smooth surfaces. The work is ordered according to the extent of the non-smoothness (local versus global). Single features like indentations fall into the local category and in general one is interested in features with amplitudes (depths) much larger than the oil film thickness. The influence of large amplitude features can be accurately approximated using a dry contact analysis. Both one- and two-dimensional results are discussed, and the influence of indentations on the pressure distribution, the subsurface stress field and finally on the contact life is outlined. Using a one-dimensional transient analysis, the asymmetrical failure position with respect to the dent is explained. An intermediate group is constituted by features like scratches and ridges, that are local in one dimension, and global in the second dimension. Generally, their study requires a transient two-dimensional analysis, unless the feature is longitudinal (aligned with the surface velocity) or if it is situated on a stationary surface. The numerical results obtained with a ridge agree surprisingly well with experimental data, for both pure rolling and rolling/sliding conditions. The global features are represented by waviness oriented with respect to the direction of entrainment. Compared with local features, waviness results in the interaction between subsequent minima and maxima, rendering its study delicate. Waviness is considered to be a first step towards the understanding of rough surface lubrication. In the general case of rolling and sliding two sets of perturbations in  $H$  and  $P$  can be observed in the solution, propagating with speeds  $\bar{u} = (u_1 + u_2)/2$  and  $u_2$  respectively and interacting. Finally, the amplitude reduction of the waviness in line contacts is discussed, together with the way this reduction depends on the wavelength and operating conditions.

### 1. INTRODUCTION

The classical problem of the fully flooded lubrication of smooth surfaces under stationary conditions was solved in the 60's by Dowson and Higginson [8] (line contact: 1d) and 70's by Hamrock and Dowson [12] (point contact: 2d). Their theoretical predictions correlated well with optical film thickness measurements [40].

However, these two successes mark only the start of the research into EHL. A topic that has received increasing attention over the last two decades is  $\mu$ EHL (micro-EHL), the lubrication of non-smooth surfaces, since technical surfaces are never perfectly smooth on the scale of the film thickness. Important contributions were made by Ai and Cheng [1-3], Chang et al. [5-7], and Kweh et al. [18].

Furthermore, the prediction of the film thickness is not a goal in itself, it is a first step towards the explanation of successful operation or failure of concentrated contacts. A classical example of a performance prediction parameter is  $\lambda$ : the ratio of film thickness to surface roughness  $h/\sigma$ . However, it is only a first order approximation, and

sometimes (or under some operating conditions) it turns out to be an unreliable one.

Experiments showed the dramatic performance reduction due to the influence of debris [19,20,31,32]. Theoretical work tried to relate the influence of the micro geometry on the pressure distribution, the stress distribution and consequently the performance (life) of bearings [9,14,20,21,39,41].

The influence of surface defects and surface roughness on the performance of concentrated contacts is increasing continuously, because of several reasons:

- \* The choice of grease as a lubricant generally results in film thicknesses much smaller than when using oil lubrication, because of insufficient lubricant supply.
- \* Weight reduction and higher power production result in smaller bearings (smaller safety factors) and higher power densities to be transmitted.
- \* Higher operating temperatures to obtain higher efficiencies result in thinner oil films.
- \* Reduction of viscous losses result in the choice of lubricants with lower viscosities, which in turn give thinner oil films.

The combined effect causes oil film thicknesses to decrease continuously and consequently causes  $h/\sigma$  to decrease. As a result the influence of surface roughness on concentrated contact performance becomes more and more important.

Therefore, it is vital to improve our understanding of the mechanisms of successful lubrication of concentrated contacts. Thus it is necessary to study the influence of surface defects and surface roughness more closely. This paper tries to give an overview of the work in this area performed in the last decade.

## 2. "ROUGH" EQUATIONS

The dimensionless Reynolds equation for the transient circular contact problem reads:

$$\frac{\partial}{\partial X} \left( \epsilon \frac{\partial P}{\partial X} \right) + \frac{\partial}{\partial Y} \left( \epsilon \frac{\partial P}{\partial Y} \right) - \frac{\partial(\bar{\rho}H)}{\partial X} - \frac{\partial(\bar{\rho}H)}{\partial T} = 0$$

The boundary conditions are  $P(X_a, Y, T) = 0$ ,  $P(X_b, Y, T) = 0$ ,  $P(X, Y_a, T) = 0$ ,  $P(X, Y_b, T) = 0$ ,  $\forall T$  where  $X_a$ ,  $X_b$ ,  $Y_a$  and  $Y_b$  denote the boundaries of the domain. Furthermore, the cavitation condition  $P(X, Y, T) \geq 0$ ,  $\forall X, Y, T$  must be satisfied.  $\epsilon$  and  $\lambda$  are defined according to:

$$\epsilon = \frac{\bar{\rho}H^3}{\bar{\eta}\bar{\lambda}} \quad \bar{\lambda} = \frac{6\eta_0 u_s R_x^2}{b^3 p_h}$$

The density  $\rho$  is assumed to depend on the pressure according to the Dowson and Higginson relation [8] and the Roelands viscosity pressure relation [30] is used.

The film thickness equation reads:

$$H(X, Y, T) = H_0(T) + \frac{X^2}{2} + \frac{Y^2}{2} - \mathcal{R}(X, Y, T) + \frac{2}{\pi^2} \int_{\Omega} \frac{P(X', Y', T) dX' dY'}{\sqrt{(X - X')^2 + (Y - Y')^2}}$$

where  $\mathcal{R}(X, Y, T)$  denotes the total undeformed geometry of the surface features ( $\mathcal{R} = \mathcal{R}_1 + \mathcal{R}_2$ ) at dimensionless time  $T$  and  $H_0(T)$  is an integration constant. At all times the force balance condition is imposed, i.e. the integral over the pressure must balance the externally applied contact load. This condition determines the value of the integration constant  $H_0(T)$  in the film thickness equation. Expressed in the dimensionless variables it reads:

$$\int_{\Omega} P(X, Y, T) dX dY - \frac{2\pi}{3} = 0, \quad \forall T$$

## 3. NUMERICAL METHOD

The nature of the lubricated contact; its transient character, high pressure, high shear rate, high heat generation and small dimensions, excludes almost every local experimental technique with one notable exception: interferometric film thickness measurement.

Consequently engineers have tried to understand the behaviour of rough concentrated contacts through mathematical models. Because of the statistical nature of the surface roughness, statistical approaches were utilized. However, because of the very non-linear nature of the Reynolds equation and even worse of the processes relating stress cycles to failure, this approach had only a limited success

A second approach tries to extend the successful numerical study of the global contact to the study of  $\mu$ EHL. There are, however, a number of complications. First of all, a study of the sub-contact size features requires a smaller length scale and thus many more discrete points. Secondly, the algorithms have to be more stable to cope with variations on sub-contact scales. Thirdly, with non-smooth surfaces the equations become generally time dependent, requiring a transient solution. These three factors lead to an important increase in complexity of the problem, resulting in a large increase in computing times. In order to study local features in a point contact problem one needs  $O(10^6)$  points ( $10^3 * 10^3$ ) and  $O(10^4)$  time steps.

Consequently one needs a very very fast computer or a fast solution algorithm. We have selected the second approach. A classical solver for the EHL problem requires a solution time which is proportional to  $n^3$  (where  $n$  is the number of discrete points). A modern solver such as the Multigrid solver requires a calculation time which is proportional to  $n \ln(n)$ . To achieve this efficiency, one needs to improve the speed of convergence of the fluid flow equation (Reynolds' equation [22,23,33]), and to speed up the deformation calculation (film thickness equation [4,26]).



## 4. RESULTS

In this section we will study the influence of (semi) local defects (dents and ridges) on film thickness, pressure and bearing fatigue life in line- and point contacts.

As a second step we will study the influence of sinusoidal waviness on the pressure and film thickness in line- and point contacts.

### 4.1. Dents

In order that its influence is noticeable, a local feature such as an indentation has to have an amplitude (depth) much larger than that of the global roughness. As a result, its amplitude is generally (much) larger than the lubricant film thickness. Consequently, the pressure distribution can be accurately approximated by the dry contact pressure distribution. In Figure 1 [24] the dry (top) contact pressure distribution is compared with the pressure distribution for the lubricated case (bottom). The differences are small and can only be perceived in the inlet and the pressure spike region. The stresses in the subsurface are consequently very similar. This confirms our hypothesis, that for features with amplitudes much larger than the film thickness, the dry contact simulation gives a good approximation of the subsurface stress field for the lubricated case and thus also a good approximation of the life expectancy, which is a function of the subsurface stress field.

This fact is used to study the influence of two dimensional (circular) dents on two dimensional (elliptical) contacts. Experimental measurements of this type are subject to statistical fluctuations. Consequently, to obtain meaningful results it is necessary to use average values, such as  $L_{10}$  defined as the life (or the number of stress cycles) surpassed by 90% of the population under test. This life can be related to an equivalent stress  $\sigma$  in the material according to [13,25] as:

$$\frac{1}{L_{10}} \sim \int_{V_r} (\sigma - \sigma_u)^c dV$$

where  $\sigma_u$  is the so-called fatigue limit of the material,  $c$  is an exponent close to 10, and  $V_r$  is the volume where  $\sigma$  exceeds  $\sigma_u$ . Note that  $L_{10} = \infty$  when  $\sigma \leq \sigma_u$  in the entire volume.

The life reduction of a contact was calculated as a function of the maximum smooth surface

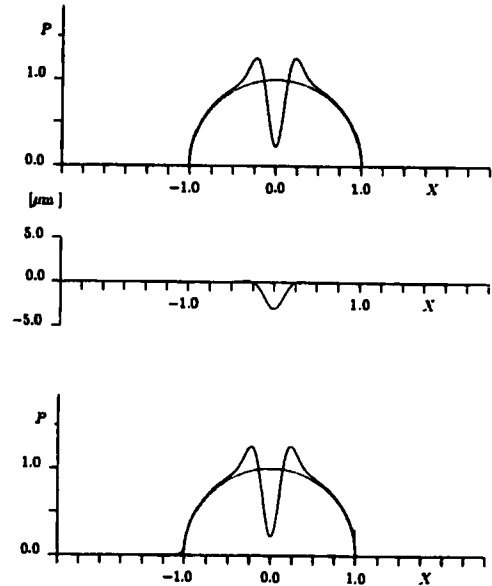


**Figure 1** Pressure distribution for a dry- and a lubricated contact (top and bottom) with a dent (middle).

contact pressure, the dent size (relative to the contact size) and the slope of the dent. Figure 2 [27] shows the life (reduction) as a function of the dent geometry. As the dent size increases, and as the slope increases, the life is reduced more and more.

Although the dry contact calculations accurately predict the life of the contact with a certain dent, they can not predict the failure posi-

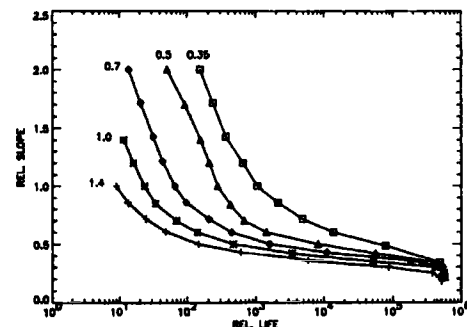


**Figure 2** Life reduction as a function of dent size and slope, for  $p_h = 2.5$  GPa.

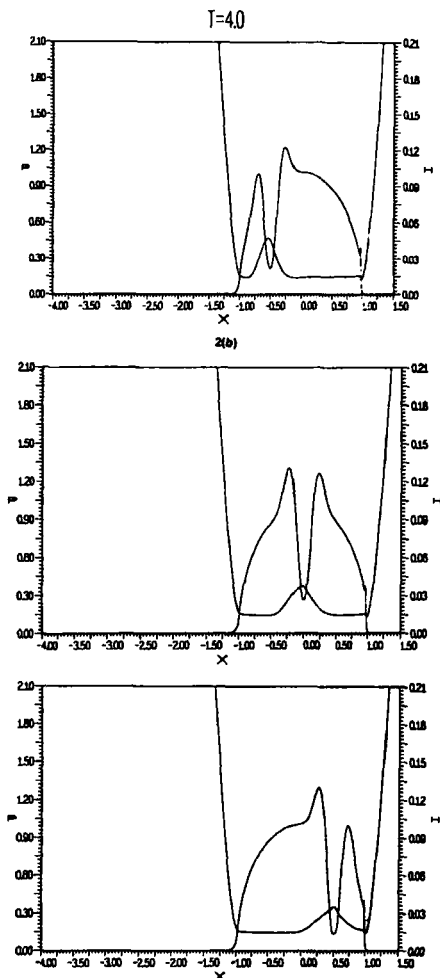


**Figure 3** Pressure distribution as a function of time.

tion, since the risk of failure is only a function of  $r$ , the distance from the centre of the dent. Practice, however, learns that the failure is always located on the trailing edge of the dent. In order to explain this preference it is necessary to perform transient lubricated calculations. The film thickness and the pressure distribution for such a transient overrolling of a dent are shown in Figure 3 [34]. Careful examination of the results shows that the pressure at the trailing edge is larger than at the leading edge. The resulting maximum stresses are displayed in Figure 4 [24], which clearly shows an asymmetry in the stresses between leading and trailing edge of the dent. Not only are the stresses below the trailing

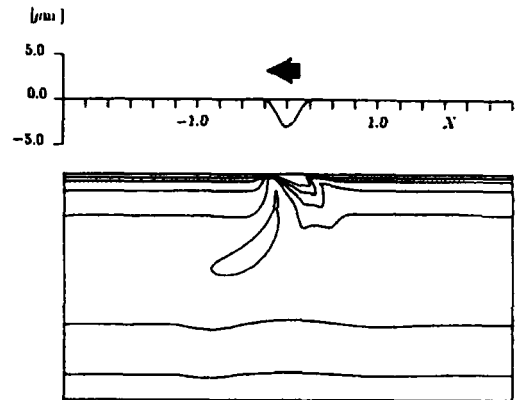


**Figure 4** Maximum subsurface stress over time, below a dent, overrolling from right to left.

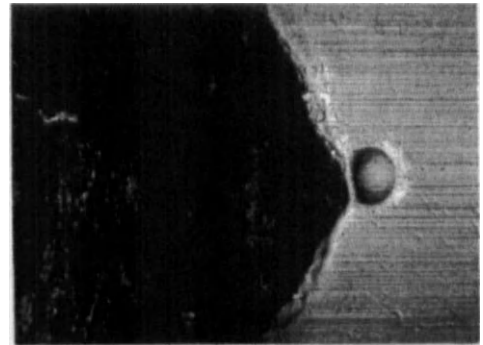


**Figure 5** Photograph of an artificially created dent and a spall originated below the trailing edge.

edge higher, they occur also at a much shallower depth. Consequently, the risk of failure is higher below the trailing edge of the dent. Figure 5 [24] shows a photograph of a spall generated below the trailing edge of an artificially produced dent.

In this section we have studied the influence of isolated sub-contact size features (dents) on the subsurface stress distribution and consequently on the life expectancy of the stressed component. In the next section we will study in detail the influence of waviness on the pressure and film thickness. In order to do this we will have to take a closer look at the Reynolds equation.

#### 4.2. Waviness in line contacts

As stated above, we will study the behaviour of the Reynolds equation more closely for the case that the surfaces are non-smooth. In the first part we will consider only one of the surfaces to be non-smooth (surface 2). First of all the Reynolds equation becomes intrinsically time dependent:

$$\frac{\partial}{\partial X} \left( \epsilon \frac{\partial P}{\partial X} \right) - \frac{\partial(\bar{\rho}H)}{\partial X} - \frac{\partial(\bar{\rho}H)}{\partial T} = 0$$

Because  $\epsilon \sim 1/\bar{\eta} = \exp(-\bar{\alpha}P) \ll 1$  the first term in the Reynolds equation vanishes for large values of  $p_h$  in the high pressure region, and the equation reduces to:

$$\frac{\partial(\bar{\rho}H)}{\partial X} + \frac{\partial(\bar{\rho}H)}{\partial T} = 0$$

where  $X = x/b$ ,  $T = \bar{u}t/b$ ,  $\bar{u} = (u_1 + u_2)/2$  is the average surface velocity and  $b$  is the radius of the Hertzian contact. Neglecting variations in  $\rho$  the solution for  $H$  in the high pressure region can be written as

$$H(X - T) = H(x - \bar{u}t) = \text{constant}$$

In other words: variations of the film thickness  $H$  are transported through the contact with a velocity  $\bar{u}$ , the mean surface velocity, independent of the velocity of the surfaces. As a result the pressure profile and the film thickness become largely decoupled. These numerical predictions have been verified semi-analytically (Greenwood and Morales Espejel [10,11,29]) and experimentally (Kaneta [15–17]). As a result the apparent wavelength  $\lambda^*$  in the contact depends on the surface speed ratio  $u_2/\bar{u} = 2u_2/(u_1 + u_2)$ :  $\lambda^* = \lambda\bar{u}/u_2$ , where  $\lambda$  is the wavelength of the undeformed surface with velocity  $u_2$ .

For a stationary wavy surface ( $u_2 = 0$ )  $\lambda^* = \infty$ , at pure rolling ( $u_1 = u_2$ )  $\lambda^* = \lambda$ , at rolling-sliding ( $u_2 = u_1/3 = \bar{u}/2$ )  $\lambda^* = 2\lambda$ , etc.

Figure 6 [35] shows the pressure profile and film thickness for the same contact conditions, while the surface speed ratio is varied. This Figure demonstrates the variation of the wavelength  $\lambda^*$  with the slide to roll ratio.

For the case that the waviness extends to both surfaces the effects become more difficult to interpret. Figure 7 [28] shows the pressure and film

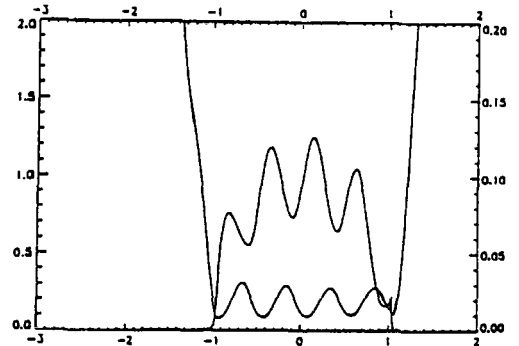


Figure 6a Pressure and film thickness for constant  $\bar{u}$ ;  $u_2/\bar{u} = 1$ .

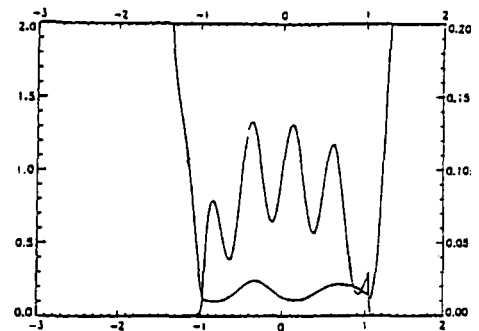
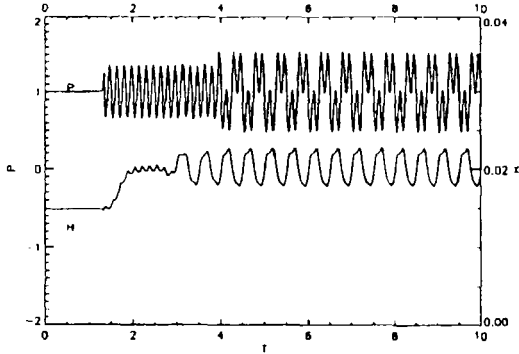


Figure 6b Pressure and film thickness for constant  $\bar{u}$ ;  $u_2/\bar{u} = 0.5$ .

thickness at one location ( $X = 0$ , contact centre) as a function of time  $T$ . The simulation starts with the waviness well outside the contact, so the conditions are identical to the stationary smooth surface case. As time progresses the waviness enters the contact, the time being determined by the actual surface velocities. The waviness of the fastest surface will arrive first at  $X = 0$ , giving rise to sinusoidal pressure and film thickness fluctuations. A little later the waviness of the second surface arrives causing harmonic fluctuations. Notice that the moment when the pressure and film thickness fluctuations arrive at  $X = 0$  is different for both cases. Also notice that the mean film thickness at  $X = 0$  increases significantly due to the waviness.



**Figure 7** Pressure and film thickness as a function of time for  $X = 0$  (two sided waviness).

#### 4.3. Ridge in point contacts

For the point contact case the transient Reynolds equation reads:

$$\frac{\partial}{\partial X} \left( \epsilon \frac{\partial P}{\partial X} \right) + \frac{\partial}{\partial Y} \left( \epsilon \frac{\partial P}{\partial Y} \right) - \frac{\partial(\bar{\rho}H)}{\partial X} - \frac{\partial(\bar{\rho}H)}{\partial T} = 0$$

and reduces similarly to the line contact case, for  $\bar{\eta} \gg 1$ , implying  $\epsilon \ll 1$  to:

$$\frac{\partial(\bar{\rho}H)}{\partial X} + \frac{\partial(\bar{\rho}H)}{\partial T} = 0$$

in the high pressure region. Since the pressure drops rapidly towards ambient values for  $\sqrt{X^2 + Y^2} \rightarrow 1$ , for instance  $X = 0, Y = \pm 1$  the pressure flow effects will remain significant in this region. Consequently the relation  $H(x - ut)$  is no longer valid in this region and film thickness variations follow the initial micro geometry.

Figure 8 shows a comparison of experimental and theoretical film thickness values (Kaneta [16], [36]) using interference techniques. In this experiment, a surface with a transverse ridge is passing through the contact area for different rolling/sliding speeds.

From these Figures it can be concluded that the theoretical predictions agree very well, both qualitatively and quantitatively, with the experimental results.

Consequently we believe that these experimental results validate the pressure and film thickness predicted by the theoretical models for  $\mu$ EHL conditions.

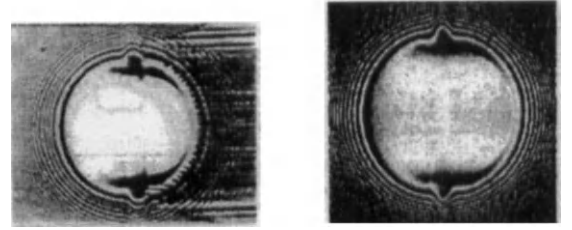


**Figure 8a** Experimental [16] and theoretical film thickness interference graphs, for  $u_2/\bar{u} = 0$ .

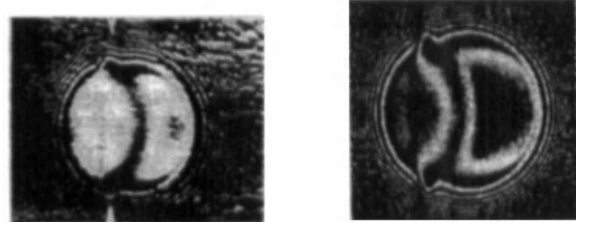


**Figure 8b** Experimental [16] and theoretical film thickness interference graphs, for  $u_2/\bar{u} = 0.5$ .

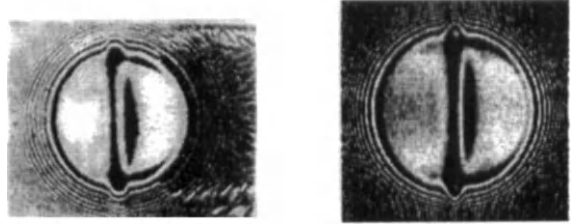


**Figure 8c** Experimental [16] and theoretical film thickness interference graphs, for  $u_2/\bar{u} = 1$ .

#### 4.4. Waviness in point contacts

As is the case for longitudinal ridges, longitudinal waviness results in a stationary lubrication problem. Here, however, the transient case of transverse waviness is studied.

The extension from a single feature (ridge) to a global feature (waviness) causes the same interaction problems as mentioned before. The problem of transient waviness was addressed in [37]. From this study a number of conclusions can be drawn. First of all, the location where the minimum film thickness occurs in case of a wavy surface is roughly the same as for smooth surfaces: the side lobe region. This is true for both pure rolling and rolling sliding conditions. For the case that the wavy surface has a velocity larger than the smooth surface ( $u_2 > \bar{u}$ ), the mean film thickness increases, see Figure 9. This increase is similar to the one observed for the line contact case

in Figure 7. However, it should be pointed out that the *minimum* film thickness decreases. Finally, this work shows that the places where the film thickness variations with time, are small or large, coincide with the location where the original waviness and its induced film variation interfere negatively or positively.

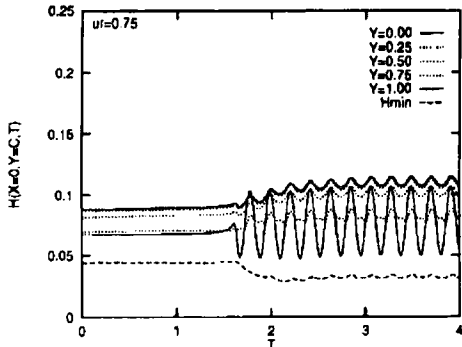


**Figure 9** Film thickness at  $X = 0$ ,  $Y = 0.0, 0.25, 0.5, 0.75, 1.0$  and  $H_{min}$  as a function of time for  $u_2 = 1.5 \bar{u}$ .

#### 4.5. Amplitude reduction in line contacts

The wavelength behaviour of the fluid in the high pressure zone being completely described by Greenwood et al., the major problem that remains to be solved is the amplitude of the deformed waviness  $A_d$ . In general, this amplitude will be a function of both the initial amplitude  $A_i$ , wavelength  $\lambda$ , and operating conditions ( $M$ ,  $L$ ), including slip. As shown in [38] it is possible to describe the relative amplitude reduction as a function of a dimensionless wavelength for all operating conditions, under pure rolling.

In Figure 10 the relative amplitude reduction is plotted as a function of a particular dimensionless wavelength  $\nabla = \lambda/(bH_c^{3/4})$ , for a variety of wavelengths and operating conditions. This Figure shows that the relative amplitude  $A_d/A_i$  can be described by a single curve, for different operating conditions. The relative amplitude reduces from 1 to 0, with increasing wavelength. Obviously, these theoretical line contact predictions need to be verified experimentally. Furthermore, the one dimensional analysis should be extended to a two dimensional one, in order to study the influence of two dimensional waviness as a function

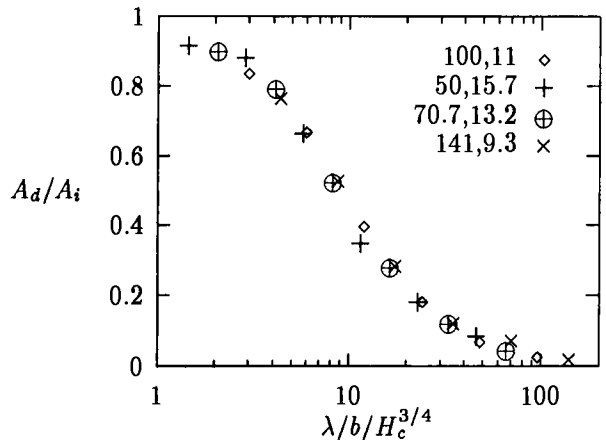


**Figure 10** Relative amplitude reduction as a function of  $\nabla$ , for different operating conditions ( $M$ ,  $L$ ) and pure rolling.

of wavelength, amplitude and operating conditions, but also aspect ratio and orientation. However, the generalization of the one dimensional results onto a single curve, represents a promising start.

## 5. CONCLUSIONS

The influence of three different categories of surface features has been studied in two different ways. First, the influence of indentations on pressure, stress and finally life was studied. Then the influence of waviness and single ridges on film thickness and pressure distribution was studied. Finally, the influence of operating conditions on the wavelength change and amplitude reduction of waviness was outlined. The numerical results have been compared with experimental and semi-numerical results, the agreement was both qualitatively and quantitatively good.

This good agreement between theoretical predictions and experimental results indicates that the models used are sufficiently accurate and the simplifications such as: newtonian lubricant and isothermal flow, do not have a large influence on film thickness and pressure distribution. Thus these models can be used to analyze and optimize the influence of waviness/roughness on contact performance, as a function of the contact operating conditions. A possible application of these results is the 'upgrade' of the classical parameter  $\lambda = h/\sigma$  by one containing  $A_d$ , for instance  $\lambda' = h/A_d(\nabla)$ . This parameter would yield a

maximum allowable amplitude as a function of the wavelength for a given set of operating conditions.

However, a more complete model should also include rolling/sliding, non-newtonian lubricant models, traction forces, heat generation, convection and conduction in a local way. This implies that the viscosity becomes a function of the temperature, which varies across the lubricant film. Consequently the assumptions which form the basis of the Reynolds equation are no longer valid. It is possible to integrate over the height of the film, but this now has only a limited advantage over the complete solution of the Stokes equations, without the use of the thin film approximation. The Stokes equation has other additional advantages: it allows for instance, the detailed study of the inlet meniscus, using realistic boundary conditions.

Finally, we are confident that such extensions of the models described in this overview will allow a more fundamental and detailed understanding of failure mechanisms in concentrated contacts, as surface induced spalling and scuffing.

## REFERENCES

1. Ai, X., Cheng, H.S., and Zheng, L., 1993, "A Transient Model for Micro-Elastohydrodynamic Lubrication with Three-Dimensional Irregularities," *ASME JOT*, **115**, pp. 102-110.
2. Ai, X., and Cheng, H.S., 1994a, "The Influence of Moving Dent on Point EHL Contacts," *STLE Trib. Trans.*, **37**, pp. 323-335.
3. Ai, X., and Cheng, H.S., 1994b, "A Transient EHL Analysis for Line Contacts with a Measured Surface Roughness using Multigrid Technique," *ASME JOT*, **116**, pp. 549-558.
4. Brandt, A. and Lubrecht, A.A. "Multilevel Matrix Multiplication and Fast Solution of Integral Equations", *Journal of Computational Physics*, **90**, No. 2, pp. 348-370, 1990.
5. Chang, L., Cusano, C. and Conry, T.F. "Effects of Lubrication Rheology and Kinematic Conditions on Micro-Elasto Hydrodynamic Lubrication", *ASME JOT*, **111**, pp. 344-351, 1989.
6. Chang, L. and Webster, M.N. "A Study of Elastohydrodynamic Lubrication of Rough Surfaces", *ASME JOT*, **113**, pp. 110-115, 1991.
7. Chang, L., "Traction in Thermal Elastohydrodynamic Lubrication of Rough Surfaces," *ASME JOT*, **114**, 186-191, 1992.
8. Dowson, D., and Higginson, G.R., "Elastohydrodynamic Lubrication, The Fundamentals of Roller and Gear Lubrication," Pergamon Press, Oxford, Great Britain, 1966.
9. Elsharkawy, A.A. and Hamrock, B.J. "Sub-surface Stresses in Micro-EHL Line Contacts", *ASME JOT*, **113**, pp. 645-655, 1991.
10. Greenwood, J.A., and Johnson, K.L., "The Behaviour of Transverse Roughness in Sliding Elastohydrodynamically Lubricated Contacts," *WEAR*, **153**, pp. 107-117, 1992.
11. Greenwood, J.A., and Morales Espejel, G.E., "The Behaviour of Transverse Roughness in EHL Contacts," *Proc. IMechE*, **208**, pp. 121-132, 1994.
12. Hamrock, B.J., and Dowson D., "Isothermal Elastohydrodynamic Lubrication of Point Contacts, part I, Theoretical Formulation," *ASME J. Lub. Tech.*, **98**, pp. 223-229, 1976.
13. Ioannides, E. and Harris, T.A. "A New Fatigue Life Model for Rolling Bearings", *ASME JOLT*, **107**, pp. 367-378, 1985.
14. Ioannides, E., Jacobson, B.O. and Tripp, J.H. "Prediction of Rolling Bearing Life under Practical Operating Conditions", *Proc. 15th Leeds-Lyon Symposium on Tribology*, pp. 181-187, 1989.
15. Kaneta, M., 1992, "Effects of Surface Roughness in Elastohydrodynamic Lubrication," *JSME*, III, **35**, 4, pp. 535-546.
16. Kaneta, M., Sakai, T., and Nishikawa, H., 1992, "Optical Interferometric Observations of the Effects of a Bump on Point Contact EHL," *ASME JOT*, **114**, pp. 779-784.
17. Kaneta, M., Sakai, T., and Nishikawa, H., 1993, "Effects of Surface Roughness on Point Contact EHL," *STLE Trib. Trans.*, **36**, 4, pp. 605-612.
18. Kweh, C.C., Evans, H.P. and Snidle, R.W. "Micro-Elastohydrodynamic Lubrication of an Elliptical Contact with Transverse and Three-dimensional Sinusoidal Roughness", *ASME JOT*, **111**, pp. 577-583, 1989.
19. Loewenthal, S.H. and Moyer, D.W. "Filtration Effects on Ball Bearing Life and Condition in a Contaminated Lubricant", *ASME JOLT*, **101**, pp. 171-179, 1979.

20. Lorösch, H.K. "Research on Longer Life for Rolling-Element Bearings", *ASLE*, **41**, pp. 37-43, 1985.
21. Lösche, T. "New Aspects in the Realistic Prediction of the Fatigue Life of Rolling Bearings", *WEAR*, **134**, pp. 357-375, 1989.
22. Lubrecht, A.A., "The Numerical Solution of the ElastoHydrodynamically Lubricated Line and Point Contacts, using MultiGrid Techniques", PhD thesis, Twente University, The Netherlands, 1987.
23. Lubrecht, A.A., ten Napel, W.E. and Bosma, R. "The Influence of Longitudinal and Transverse Roughness on the Elasto Hydrodynamic Lubrication of Circular Contacts", *ASME JOT*, **110**, pp. 421-426, 1988.
24. Lubrecht, A.A., Venner, C.H., Lane, S., Jacobson, B.O. and Ioannides, E. "Surface Damage - Comparison of Theoretical and Experimental Endurance Lives of Rolling Bearings", Proceedings of the Japan International Tribology Conference, Nagoya, I, pp. 185-190, 1990.
25. Lubrecht, A.A., Jacobson, B.O. and Ioannides, E. "Lundberg Palmgren Revisited", presented at the IMechE conference "Rolling element bearings - towards the 21st Century", pp. 17-20, 1990.
26. Lubrecht, A.A. and Ioannides, E. "A Fast Solution to the Dry Contact Problem and the Associated Sub-surface Stress Field, Using Multilevel Techniques", *ASME JOT*, **113**, pp. 128-133, 1991.
27. Lubrecht, A.A., Dwyer-Joyce, R.S. and Ioannides, E. "Analysis of the influence of Indentations on Contact Life", Proc. of 18 Leeds-Lyon Conference on Tribology, Lyon, pp. 173-181, 1991.
28. Lubrecht, A.A., and Venner, C.H., "Aspects of two-Sided Surface Waviness in an EHL Line Contact," Proc. of the 1992 Leeds-Lyon Symposium on Tribology, pp. 205-214.
29. Morales Espejel, G.E., "Elastohydrodynamic lubrication of smooth and rough surfaces," PhD. Thesis, University of Cambridge, Department of engineering, 1993.
30. Roelands, C.J.A., "Correlational Aspects of the Viscosity/Temperature-Pressure Relationship of Lubricating Oils" Ph.D. Thesis, Technical University Delft, Delft, The Netherlands, (V.R.B., Groningen, The Netherlands), 1966.
31. Sayles, R.S. and Macpherson, P.B. "Influence of Wear Debris on Rolling Contact Fatigue", in: "Rolling Contact Fatigue Testing of Bearing Steels", ed. Hoo, J.J.C., ASTM STP 551, pp. 255-274, 1982.
32. Sayles, R.S. and Ioannides, E. "Debris Damage in Rolling Bearings and its Effect on Fatigue Life", *ASME JOT*, **110**, pp. 26-31, 1988.
33. Venner, C.H. "Multilevel Solution of the EHL Line and Point Contact Problems", PhD thesis, University of Twente, Enschede, The Netherlands, 1991.
34. Venner, C.H., Lubrecht, A.A. and ten Napel, W.E. "Numerical Simulation of the Over-rolling of a surface Feature in an EHL Line Contact", *ASME JOT*, **113**, 777-783, 1991.
35. Venner, C.H., Lubrecht, A.A. "Transient Analysis of Surface Features in an EHL Line Contact in the case of Sliding", *ASME JOT*, **116**, 168-193, 1994.
36. Venner, C.H., Lubrecht, A.A. "Numerical Simulation of a Transverse Ridge in a Circular EHL Contact under Rolling/Sliding", *ASME JOT*, **116**, 751-761, 1994.
37. Venner, C.H., Lubrecht, A.A. "Numerical Analysis of the Influence of Waviness on the Film Thickness of a Circular EHL Contact", *ASME JOT*, **118**, 153-161, 1996.
38. Venner, C.H., Couhier, F., Lubrecht, A.A. and Greenwood, J.A. "Amplitude Reduction of Waviness in Transient EHL Line Contacts", presented at the 1996 Leeds-Lyon Symposium on Tribology.
39. Webster, M.N., Ioannides, E. and Sayles, R.S. "The Effect of Topographical Defects on the Contact Stress and Fatigue Life in Rolling Element Bearings", Proc. of 12 Leeds-Lyon Conference on Tribology, Lyon, 1985.
40. Wedeven, L.D., and Cusano, C., "Elastohydrodynamic Film Thickness Measurements of Artificially Produced Surface Dents and Grooves," *ASLE Trans.*, **22**, 369-381, 1971.
41. Zhou, R.S., Cheng, H.S. and Mura, T. "Micropitting in Rolling and Sliding Contact under Mixed Lubrication", *ASME JOT*, **111**, pp. 605-613, 1989.

## Fully Coupled Elastohydrodynamic Solution Techniques for the Analysis of Real Rough Line Contacts using Finite Element and Finite Difference Models

C D Elcoate, H P Evans and T G Hughes

School of Engineering, University of Wales Cardiff, Cardiff, CF2 1XH

This paper describes two computational models for the analysis of real roughness, line contact, elastohydrodynamic lubrication (EHL) problems assuming non-Newtonian lubricant behaviour. Models have been developed based on finite element and finite difference techniques. They are extremely robust with convergence of the numerical method assured irrespective of the starting conditions. Results are presented for a series of real roughness contacts. Of particular importance are the results where the lubricant film is considerably thinner than the roughness features of the surface finish. The results exhibit much less pressure rippling and asperity deformation than has been seen in equivalent Newtonian analyses.

### 1. Introduction

The engineering application which is the main driving force behind the numerical models presented in this paper is that of high speed, high temperature auxiliary gearboxes used in the aerospace industry. The contacting lubricated surfaces in such components have low geometric conformity resulting in high contact pressures. These high pressures produce elastic deformation of the contacting surfaces and in turn have significant effects on the viscosity and density of the lubricant. The behaviour of such contacts falls into the regime of EHL. Factors which affect the formation or otherwise of a lubricant film in such contacts include relative surface speeds, load, temperature, lubricant properties and component surface finish. Aerospace gear boxes often operate under extremely harsh conditions, for example, at high speeds, high temperatures and with low viscosity lubricants, and as a result tend to have relatively thin elastohydrodynamic lubricant films. In extreme cases the contact can suffer a drastic reduction in oil film leading to metal to metal contact and a condition known as scuffing. One of the main factors that needs to be accounted for when lubricant films are so thin is the surface finish of the contacting surfaces. A surface roughness  $R_a$  value of  $0.4 \mu\text{m}$  is typical for aerospace gear teeth, which becomes very significant when compared to typical predicted film thickness values of  $0.1 - 1.0 \mu\text{m}$ .

Numerical modelling of rough surface EHL contacts has been performed by numerous investigators in recent years. A number of models have been published involving various configurations of surface roughness. Sinusoidal roughness features have been considered by such authors as Goglia et al. (1984), Lubrecht et al. (1988) and Kweh et al. (1989). Real roughness features where the  $R_a$  value is significant compared to the film thickness have been considered by Kweh et al. (1992) and Patching (1994). Greenwood and Morales-Espejel (1994) extended the Newtonian steady state problem to include transient behaviour. They analysed sinusoidal roughness features and noted that the film thickness irregularities caused by the surface roughness travel at the mean velocity of the lubricant, and the pressure ripples travel at the velocity of the features that produced them. Ai and Cheng (1994) carried out transient analyses of measured surface roughness profiles with  $R_a$  values below  $0.1 \mu\text{m}$ . They concluded that for simple sliding where the rough surface was stationary the roughness asperities were almost completely flattened, and as the velocity of the rough surface increased then the degree of flattening reduced. When the velocity of the rough surface was equal to or greater than the rolling speed they noted that the resultant film shape was close to the initial undeformed profile. Chang et al. (1993) incorporated thermal, transient and non-Newtonian effects assuming sinusoidal roughness, and stated that "...misleading results of large pressure rippling and flattened surface roughness are obtained using



the Newtonian lubricant models under steady-state, isothermal conditions." They concluded that less asperity deformation is present due either to non-Newtonian and thermal effects or to transient effects.

The models presented in this paper stem from difficulties experienced in applying the model developed by Patching (1994) to the analysis of real rough contacts assuming Newtonian lubricant behaviour. The model he developed was based on a successful smooth surface numerical model which consisted of a forward/inverse hybrid formulation. Great difficulties were experienced however when applying the model to problems with real roughness profiles as the interchange between the forward and inverse methods was required for almost every individual roughness feature, of which there are many in a contact. Subsequently convergence was slow and required considerable user interaction.

The work reported in this paper follows on from an investigation into the benefits of coupling the elasticity and flow equations. This technique was described by Okamura (1982) who used a fully coupled Newton-Raphson model. This was subsequently extended by Houpert and Hamrock (1986) to enable analysis of heavily loaded, smooth line contacts assuming Newtonian lubricant behaviour. They achieved results up to maximum pressures of 4.8 GPa with the Reynolds equation formulated in its first order form. The models described in this paper include many of the features seen in these unified treatment, fully coupled models to overcome the difficulties experienced using a forward/inverse hybrid technique. However, the non-Newtonian Reynolds equation developed by Conry et al. (1987) is formulated in its second order form. This is the necessary form if the methods are to be extended to consider 2D problems.

## 2. Notation

|            |  |
|------------|--|
| b          | Hertzian semi-dimension                        |
| d          | elastic deflection                             |
| $E_1, E_2$ | Young's moduli of the two surfaces             |
| $E'$       | $2/E' = (1 - \nu_1^2)/E_1 + (1 - \nu_2^2)/E_2$ |
| h          | film thickness                                 |
| $h_{\min}$ | minimum film thickness                         |

|                        |  |
|------------------------|--|
| $h_{\text{effective}}$ | effective film thickness                               |
| p                      | pressure   |
| R                      | radius of relative curvature,<br>$1/R = 1/R_1 + 1/R_2$ |
| $R_1, R_2$             | radius of curvature of the surfaces                    |
| $R_a$                  | surface roughness parameter                            |
| s                      | dummy integration variable                             |
| U                      | mean entraining speed = $(u_1 + u_2)/2$                |
| $u_1, u_2$             | surface speeds relative to contact                     |
| $w'$                   | load per unit length                                   |
| x                      | co-ordinate in direction of rolling                    |
| $\alpha$               | pressure coefficient of viscosity                      |
| $\gamma, \kappa$       | parameters in density relationship                     |
| $\lambda$              | $h_{\text{effective}}/R_a$                             |
| $\eta$                 | viscosity  |
| $\eta_0$               | viscosity at zero pressure                             |
| $\rho$                 | density  |
| $\rho_0$               | density at zero pressure                               |
| $\tau_0$               | representative shear stress                            |
| $\nu_1, \nu_2$         | Poisson's ratios of the two surfaces                   |
| $\xi$                  | slide roll ratio = $2(u_1 - u_2)/(u_1 + u_2)$          |

Other symbols are defined in the text.

## 3. Formulation

This paper is concerned with one dimensional EHL line contacts. Both surfaces are treated as semi-infinite elastic solids so that the displacement normal to the surface is given by:

$$d(x) = -\frac{4}{\pi E'} \int_{-\infty}^{\infty} p(s) \ln \left| \frac{x-s}{r-s} \right| ds$$

where r is the co-ordinate of the point (usually 2b downstream of the contact), relative to which the displacement is established. The film thickness is given by:

$$h(x) = d(x) + \frac{x^2}{2R} + \varphi(x) + C$$

where  $\varphi(x)$  is the measured roughness at x. The constant C is made up of the undeformed separation and geometry at the point relative to which the displacement is established.

Isothermal conditions are assumed and the viscosity and density of the lubricant are taken to depend on pressure as follows:

$$\eta = \eta_0 \exp(\alpha p)$$

$$\rho = \rho_0 \frac{1 + \gamma p}{1 + \kappa p}$$

The non-Newtonian flow equation adopted is the second order, one dimensional, modified Reynolds equation developed by Conry et al. (1987).

$$\frac{d}{dx} \left( \frac{\rho h^3}{12 \eta} \frac{dp}{dx} S \right) = U \frac{d(\rho h)}{dx} \quad (1)$$

where:

$$S = \frac{3(\Sigma \cosh \Sigma - \sinh \Sigma)}{\Sigma^3} \sqrt{1 + \frac{\eta^2 (u_2 - u_1)^2}{\tau_0^2 h^2} \frac{\Sigma^2}{\sinh^2 \Sigma}}$$

and:

$$\Sigma = \frac{h}{2\tau_0} \frac{dp}{dx}$$

The representative stress,  $\tau_0$ , for the purpose of this work is taken as constant although it is known to be weakly dependent on the pressure.

The finite element method was adopted to solve equation (1). The finite element method used is the weak formulation of the Galerkin weighted residual approach. The domain is discretized using one dimensional quadratic elements and the numerical integration of the resultant equations is carried out on a local elemental level by 3 point Gauss quadrature.

The finite element method is formulated using an iterative Newton-Raphson technique which incorporates full coupling of the elastic and hydrodynamic equations. The full matrix is set up and solved for pressure by means of Gaussian elimination. The pressure is under relaxed as necessary and the process repeated until convergence is reached. A simple flow chart outlining the main steps involved in an analysis is shown in Figure 1. The boundary conditions imposed are  $p = 0$  at the upstream and downstream boundaries. The position of the upstream boundary is set at  $-3b$  but the position of the downstream boundary is initially unknown. The actual position of the downstream boundary is dealt with during the solution of the matrix. Whilst performing the back substitution, if a negative pressure is calculated in the exit region this pressure is set to zero and therefore eliminated from the remaining back substitution. This method allows the position

of the downstream boundary to be found automatically as long as sufficient downstream elements are provided.

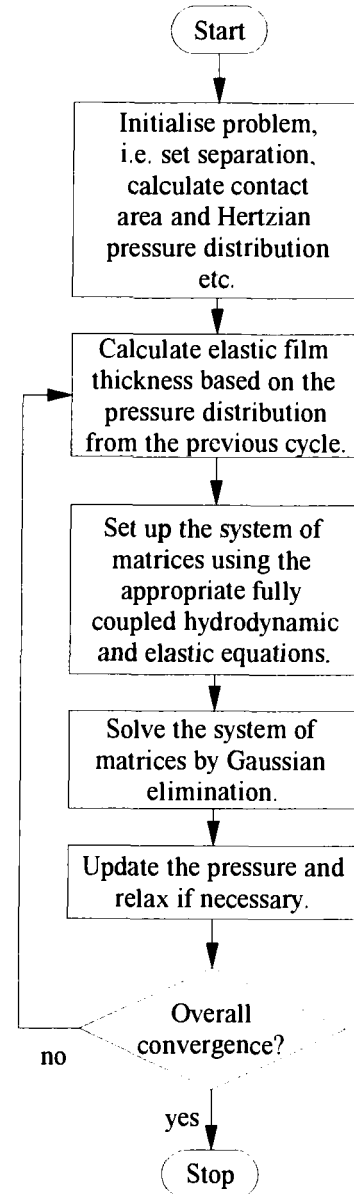


Figure 1 Flow chart for the fully coupled Newton-Raphson formulations.

An equivalent finite difference model was also developed using the same governing equations and assumptions as the finite element model. Full details of both the finite element and finite difference formulations will be presented in future publications.

#### 4. Roughness Model

The line contact model adopted for this work consists of a stationary, rough surface of parabolic shape loaded against a moving, smooth surface. The ground surface roughness is transverse to the direction of flow which is representative of the conditions present in most gear teeth contacts.

For the purpose of this work the ground surface analysed was that from a well run in but un-scuffed experimental disc. The disc measured was one used by Patching (1994) in a two disc scuffing rig. The disc was manufactured in such a way as to be representative of the finish found on gear teeth in aerospace auxiliary gearboxes. The surface was measured in a circumferential direction along the centre of the running track using a profilometer, the resultant profile is shown in Figure 2, where the rounding off of asperity tips caused by the running in process is apparent. The profile has an  $R_a$  value of  $0.32 \mu\text{m}$  with maximum peak to valley dimensions of approximately  $2 \mu\text{m}$ .

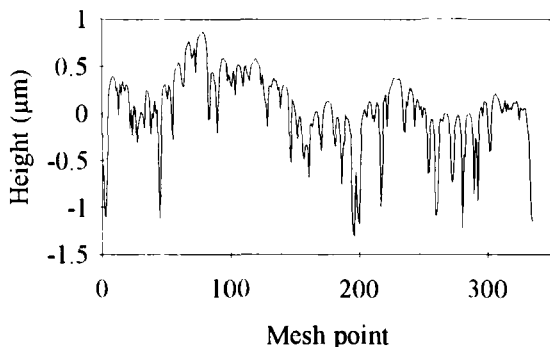


Figure 2 Real roughness profile.

The measured roughness data from the profilometer was taken at a sample spacing of  $3.5 \mu\text{m}$  which at the conditions analysed results in 96 measured points in the contact dimension b. To avoid individual roughness features being defined too coarsely, by only 3 points for example, the original measured data was interpolated to produce 288 points in b. The interpolation routine adopted is detailed in Patching (1994) but essentially fits a curve to the original data points so as to fit new

points between each original point without introducing new roughness features. Figure 3 shows an example section of the roughness profile with the interpolated data superimposed on the original measured data.

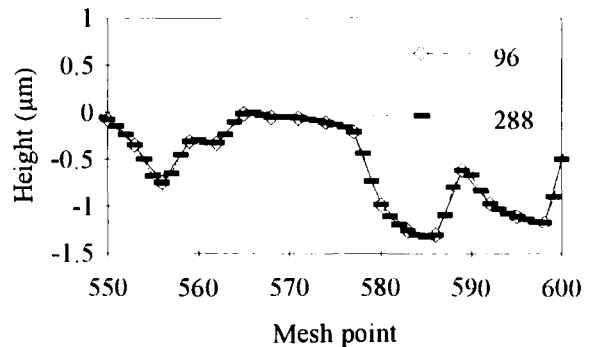


Figure 3 A section of the real roughness profile showing the original measured data (96 points in b) and the interpolated data (288 points in b).

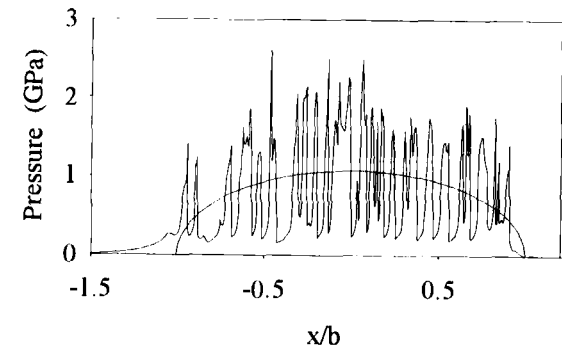
#### 5. Finite Element / Difference comparisons

Patching (1994) analysed the real roughness profile discussed above assuming Newtonian lubricant behaviour. Figure 4 which is taken from Patching (1994) shows the resultant pressure distribution and film shape from the analysis. To investigate the effect of non-Newtonian lubricant behaviour a comparison between the Patching (1994) result and those from the finite element and finite difference models was carried out. The conditions used are representative of Mobil Jet Oil at  $100^\circ\text{C}$  and are summarised in Table 1.

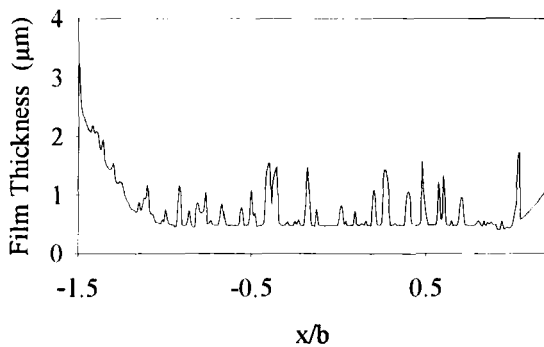
Table 1

Conditions assumed for comparison

|                     |                         |
|---------------------|-------------------------|
| $R_1$ and $R_2$     | 19.05 mm                |
| $\tau_0$            | 3.0 MPa                 |
| $\xi$               | 0.3                     |
| $w'$                | 600 KN/m                |
| $U$                 | 24.87 m/s               |
| $E_1$ and $E_2$     | 206.8 GPa               |
| $\nu_1$ and $\nu_2$ | 0.3                     |
| $\alpha$            | $11.1 \text{ GPa}^{-1}$ |
| $\eta_0$            | 0.0048 Pas              |



(a)



(b)

Figure 4 Results of Newtonian analysis (Patching (1994)). (a) Pressure distribution with Hertzian pressure shown for reference. (b) Film shape.

The value of  $\xi$  was chosen as a representative value for gear tooth contacts. The value of  $\tau_0$  used is discussed in section 6. Both models converged from an initial Hertzian pressure distribution, and corresponding film thickness with added roughness as shown in Figure 5. Both models converged within 50 cycles using a relaxation of 0.15 on the pressure. Figure 6 shows the resultant pressure distribution and film shape from the finite element model. (the results for the finite difference model are indistinguishable in this graphical form). Table 2 summarises the representative film thicknesses from Patching (1994) and the finite element and finite difference models. The central film thickness is not included in Table 2 because, at its fixed position, it does not give a true indication of the overall film thickness and can be misleading. Instead, the effective film thickness is given which represents an approximate value for the average

central film thickness obtained by drawing a line through the film shape asperities at the centre of the Hertzian contact region.

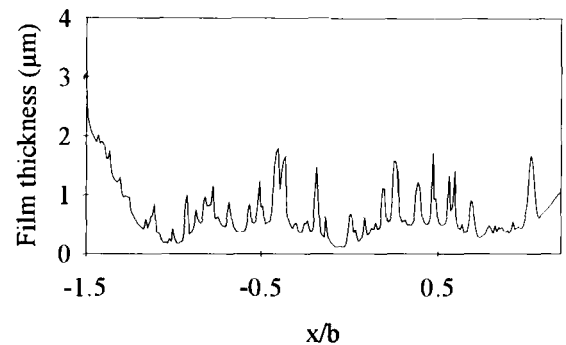
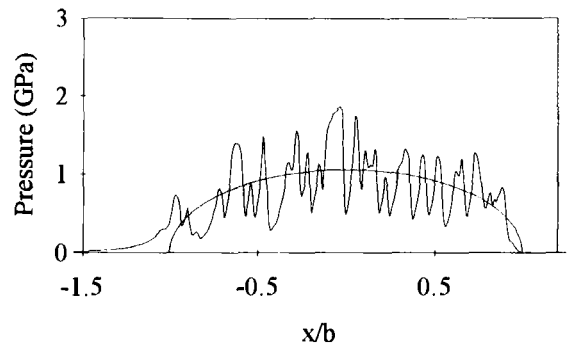
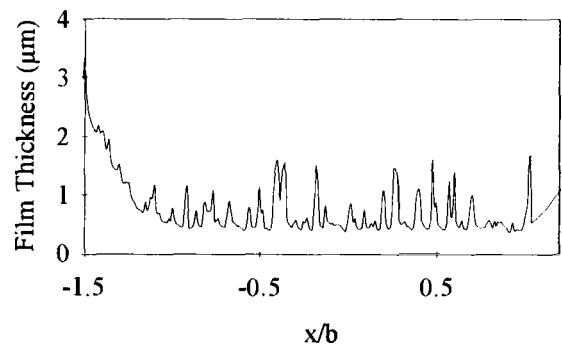


Figure 5 Initial film shape for non-Newtonian analyses.



(a)



(b)

Figure 6 Results of non-Newtonian analysis using finite element model. (a) Pressure distribution with Hertzian pressure shown for reference. (b) Film shape.

Table 2  
Film thicknesses from real rough comparison

| Method            | $h_{\min}$ ( $\mu\text{m}$ ) | $h_{\text{effective}}$ ( $\mu\text{m}$ ) |
|-------------------|------------------------------|--|
| Patching (1994)   | 0.389                        | 0.470                                    |
| Finite element    | 0.366                        | 0.450                                    |
| Finite difference | 0.373                        | 0.460                                    |

From Table 2 it can be seen that the agreement between the current finite difference and finite element models was very good, the difference being only 2 %. Comparing the minimum and effective film thicknesses of Patching's (1994) Newtonian analysis with those obtained from the non-Newtonian analyses shows a slight reduction in film thickness in the non-Newtonian case. This is in agreement with many results from Newtonian non-Newtonian comparisons where thinner films are seen when using a non-Newtonian formulation.

The most interesting features of these analyses though are seen in the plots of pressure distribution and film shape shown in Figures 4 and 6. Patching's (1994) Newtonian analysis, Figure 4, shows large ripples in the pressure distribution in the high pressure region and a corresponding film shape that has had the asperities almost completely flattened. The equivalent non-Newtonian analyses exhibit much smaller pressure ripples in the high pressure region and the corresponding film shapes still have prominent asperities although the valley features remain essentially the same. These findings are in agreement with those from Goglia et al. (1984) and Chang et al. (1989) albeit with simplified roughness models.

From this analysis it can be seen that the results from the finite element and finite difference models are essentially the same, and for the purposes of the investigation described in section 6 only the results from the finite element model will be presented, although the discussion will be relevant to both models.

## 6. Real Roughness Results

The finite element model has been used to investigate the effect on the pressure distribution and film shape of operating condition changes leading to different effective film thicknesses. The conditions selected for the comparison represent

severe scuffing conditions used during a two disc experiment forming one of a series reported by Patching et al. (1995). The actual conditions used are representative of Mobil Jet Oil at 192°C and are summarised in Table 3.

Table 3  
Conditions assumed for the real roughness analyses

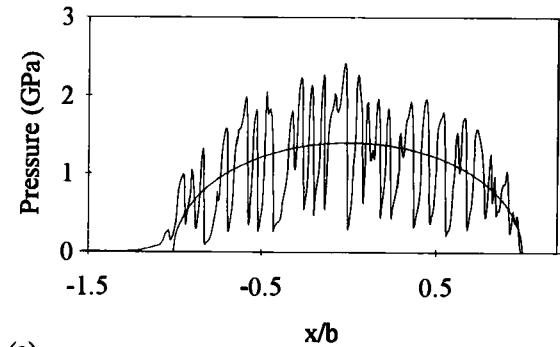
|                     |   |
|---------------------|---|
| $R_1$ and $R_2$     | 19.05 mm                                    |
| $\tau_0$            | 3.0 MPa                                     |
| $\xi^*$             | 1.24  |
| $w'$                | 1032 KN/m                                   |
| $\eta_0 U$          | 0.027, 0.064, 0.183,<br>0.342 and 0.660 N/m |
| $E_1$ and $E_2$     | 206.8 GPa                                   |
| $\nu_1$ and $\nu_2$ | 0.3   |
| $\alpha$            | 8.34 GPa <sup>-1</sup>                      |

Parameters particular to this analysis though are the assumed values of  $\eta_0 U$  and  $\tau_0$ .

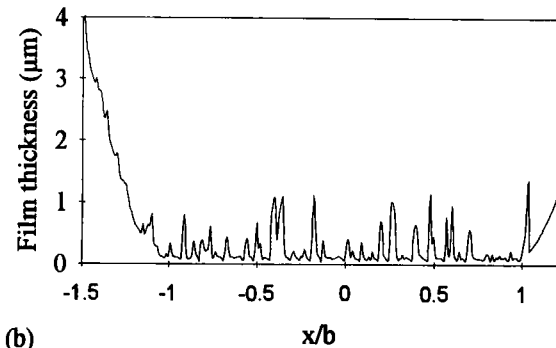
The value for  $\tau_0$  is the same value used by Conry et al. (1987). This value is at the lowest end of the range measured by Evans and Johnson (1986) and was selected to produce an analysis which exhibited non-Newtonian behaviour to the fullest possible extent.

In the modified Reynolds equation, equation 1, when using the Barus pressure viscosity law and for a specific slide roll ratio,  $U$  only appears as a product with  $\eta_0$ . To produce a full range of film thicknesses the product of  $\eta_0$  and  $U$  was adjusted. The actual values of  $\eta_0 U$  were increased from a minimum value of 0.027 N/m (case a) to 0.660 N/m (case e) in the five steps given in Table 3.

A converged solution for condition c was produced initially from a Hertz pressure distribution with corresponding rough surface similar to that shown in Figure 5. The solutions for the remaining conditions were produced from the converged solution of the previous condition, i.e. d and b from c, a from b and e from d. Condition c converged within 50 cycles using a relaxation factor of 0.15 on the pressure. The remaining conditions all converged within 30 cycles using a relaxation factor of 0.15 on the pressure. The pressure distributions and film shapes for cases a, c and e are shown in figures 7 to 9. The Hertzian pressure is included on the pressure distribution figures for reference.



(a)



(b)

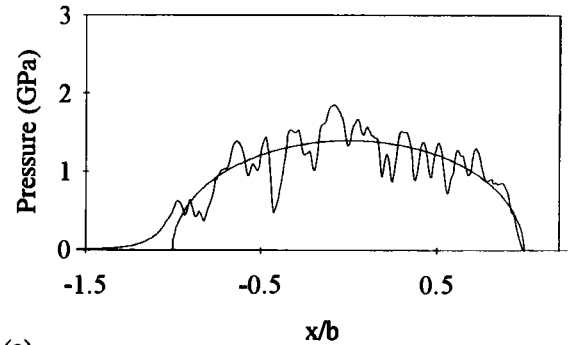
Figure 7 Results of non-Newtonian analysis using finite element model, case a. (a) Pressure distribution with Hertzian pressure shown for reference. (b) Film shape.

The resulting minimum and effective film thicknesses are given for each condition in Table 4.

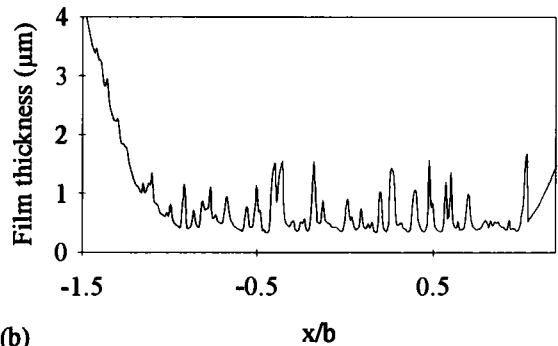
Table 4  
Minimum and effective film thicknesses from the real roughness analyses

| Case | $\eta_0 U$<br>(N/m) | $h_{\text{effective}}$<br>( $\mu\text{m}$ ) | $h_{\text{min}}$<br>( $\mu\text{m}$ ) |
|------|---------------------|---|---------------------------------------|
| a    | 0.027               | 0.10  | 0.047                                 |
| b    | 0.064               | 0.20  | 0.15                                  |
| c    | 0.183               | 0.45  | 0.33                                  |
| d    | 0.342               | 0.65  | 0.54                                  |
| e    | 0.660               | 1.00  | 0.86                                  |

Table 4 shows that by varying  $\eta_0 U$  from 0.027 to 0.660 N/m results in a change in the effective film thickness from 0.10 to 1.0  $\mu\text{m}$  and in minimum film thickness from 0.047 to 0.86  $\mu\text{m}$ . With the  $\lambda$  ratio varying from 0.31 to 3.1 this provides a full range of film thicknesses for discussion.



(a)

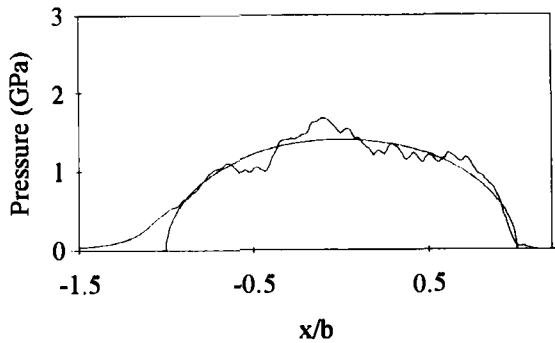


(b)

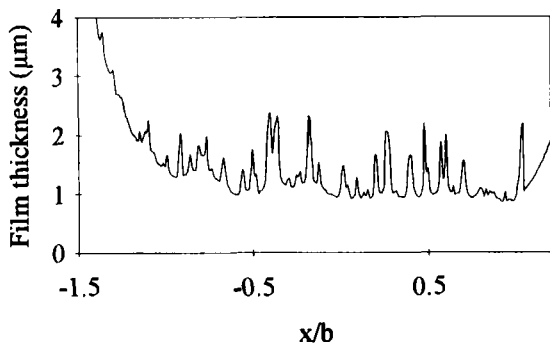
Figure 8 Results of non-Newtonian analysis using finite element model, case c. (a) Pressure distribution with Hertzian pressure shown for reference. (b) Film shape.

The general trend that can be seen in Figures 7 to 9 for the pressure distribution is that with increasing  $\eta_0 U$  the pressure distribution becomes less severely rippled. For example, Figure 7 shows the pressure distribution at condition a is severely rippled and exhibits large pressure gradients, whereas the pressure distribution in Figure 9 for condition e can be described as undulating with small pressure gradients. Conditions b, c and d represent gradual changes between the two extreme cases a and e, as can be seen for the intermediate case c shown in Figure 8.

The general trend that can be seen in Figures 7 to 9 for the film shapes is that with increasing  $\eta_0 U$  the film thickness increases and the basic film shape becomes less flat in the Hertzian region. For example Figure 7 shows that at condition a the effective film shape is almost completely flat and parallel in the Hertzian region with only the most



(a)



(b)

Figure 9 Results of non-Newtonian analysis using finite element model, case e. (a) Pressure distribution with Hertzian pressure shown for reference. (b) Film shape.

severe asperity features remaining. Figure 9 shows that at condition e the film shape is no longer flat or parallel, with both the large and small scale roughness still remaining and the film thickness reducing throughout the Hertzian contact region. Conditions b, c and d, as seen for the pressure distribution, represent a gradual change between the two extreme cases a and e, as can be seen for the intermediate case c shown in Figure 8. Figure 10 shows the series of film shapes together, and from this figure the gradual change as  $\eta_0 U$  increases can be clearly seen. Figure 10 also demonstrates that the valley features are essentially the same for each condition.

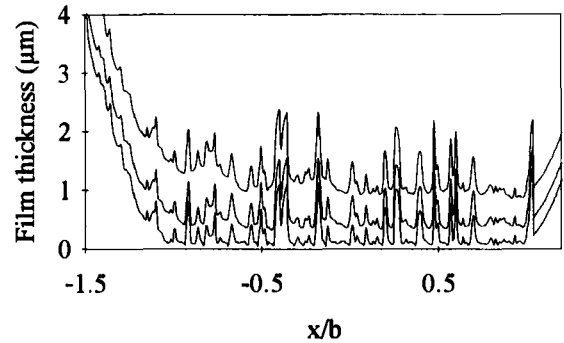


Figure 10 Comparison of film shapes from the non-Newtonian analyses using the finite element model, cases a, c and e.

The analyses presented so far were run at a minimum  $\eta_0 U$  value of 0.027 N/m, condition a. As stated earlier the conditions adopted for this analysis represent severe scuffing conditions from Patching et al. (1995) who experienced scuffing at an  $\eta_0 U$  value of approximately 0.01 N/m. To try and replicate this actual experimental condition analyses were carried out with decreasing values of  $\eta_0 U$  and results were obtained using a value of  $\eta_0 U = 0.015$  N/m. The effective and minimum film thicknesses from this analysis were 0.05  $\mu\text{m}$  and 0.007  $\mu\text{m}$  respectively with a  $\lambda$  ratio of 0.16. The results not presented show that the minimum oil film thickness is extremely low and is consistent with the experimental result where scuffing occurred at  $\eta_0 U = 0.01$  N/m, giving further confidence in the ability of the numerical models to predict pressure distributions and film shapes in real rough EHL problems.

## 7. Discussion and Conclusions

The theoretical results presented in this paper show that the fully coupled finite element and finite difference models can be used to obtain solutions to line contact EHL problems with real roughness and very thin films. The maximum Hertzian contact pressure analysed in this paper is 1.4 GPa although pressure peaks up to approximately 2.5 GPa are present. More heavily loaded contacts can be analysed using the models, which have been used to study smooth contacts with maximum Hertzian pressures of 4 GPa and above. The model has been

found to be extremely robust with convergence of the numerical method being assured irrespective of the starting conditions adopted. For example, the real roughness analyses presented in this paper can be converged from an initial Hertzian pressure profile which is far from the converged pressure profile. A number of analyses carried out have however been produced from a previous solution to reduce the number of cycles to convergence.

One of the most interesting features of the real roughness analyses are shown in the plots of pressure distribution and film shape. Patching (1994) in his Newtonian analyses of the same profile showed extreme rippling in the pressure distribution in the high pressure region and a corresponding film shape that had the roughness asperities almost completely flattened. The non-Newtonian analyses detailed here exhibit much smaller pressure ripples in the high pressure region and the corresponding film shapes still have prominent asperities, even at very thin films. In fact the authors have analysed contacts with very small slide roll ratios, as low as  $1.0 \times 10^{-4}$  i.e. approaching Newtonian behaviour, which still exhibited the asperity features seen at the higher slide roll ratios presented here. This suggests that the pure rolling Newtonian assumption when used in conjunction with a real roughness profile results in a very special case which is not realistic when considering actual engineering problems.

The analyses of a real roughness contact at different effective film thicknesses produced marked differences in the pressure distributions and film shapes. At thin film conditions the film shape, made up of the tips of contacting asperities, is almost completely flat and parallel in the Hertzian region with only the most severe asperity features remaining. The associated pressure distribution is sharply rippled and exhibits large pressure gradients. At thick film conditions the film shape converges towards the exit with asperity tip features largely unmodified. The associated pressure distribution can be described as undulating with small pressure gradients. The results presented here emphasise that even when the effective EHL film thickness is much smaller than the surface roughness the capability of maintaining separation of the contacting bodies still exists when analysing

the contact in one dimension. This observation supports the model proposed by Evans and Snidle (1996) that scuffing occurs due to leakage of the lubricant from the valley features in a transverse direction, i.e. side leakage.

It should be noted here that the results presented are obtained using an isothermal model. A thermal analysis is required to take the full effect of sliding at the contact into account. It has already been stated that aerospace auxiliary gearboxes operate at extreme conditions resulting in rapid shearing of the thin lubricant film. The heat generated by this shearing will cause further thinning of the lubricant and a thermal treatment will allow this aspect to be tackled.

## 8. Acknowledgements

The authors thank Dr R W Snidle for many helpful discussions. One of the authors (C D Elcoate) was supported by a studentship from the Engineering and Physical Science Research Council to whom we are most grateful.

## References

- Ai, X and Cheng, H S, 1994, "A transient EHL analysis for line contacts with measured surface roughness using multigrid technique", *Trans. ASME, Jn of Tribology*, Vol. 116, pp 549-556.
- Chang, L, Cusano, C and Conry, T F, 1989, "Effects of lubricant rheology and kinematic conditions on micro-elastohydrodynamic lubrication", *Trans. ASME, Jn of Tribology*, Vol. 111, pp 344-351.
- Chang, L, Webster, M N and Jackson, A, 1993, "On the pressure rippling and roughness deformation in elastohydrodynamic lubrication of rough surfaces", *Trans. ASME, Jn of Tribology*, Vol. 115, pp 439-444.
- Conry, T F, Wang, S and Cusano, C, 1987, "A Reynolds-Eyring equation for elastohydrodynamic lubrication in line contacts", *Trans. ASME, Jn of Tribology*, Vol. 109, pp 648-654.
- Evans, C R and Johnson, K L, 1986, "The rheological properties of elastohydrodynamic lubricants", *Proc. Instn Mech Engrs* Vol. 200, pp 303-312.



- Evans, H P and Snidle, R W, 1996, "A model for elastohydrodynamic film failure in contacts between rough surfaces having transverse finish", *Trans. ASME, Jn of Tribology*, Vol 118, in press.
- Goglia, P R, Cusano, C and Conry, T F, 1984, "The effects of surface irregularities on the elastohydrodynamic lubrication of sliding line contacts. Part I - single irregularities; Part II - wavy surfaces", *Trans. ASME, Jn of Tribology*, Vol. 106, pp 104-112, 113-119.
- Greenwood, J A and Morales-Espejel, G E, 1994, "The behaviour of transverse roughness in EHL contacts", *Proc. Instn Mech Engrs Vol. 208j*, pp 121-132.
- Houpert, L G and Hamrock, B J, 1986, "Fast approach for calculating film thicknesses and pressures in elastohydrodynamically lubricated contacts at high loads", *Trans. ASME, Jn of Tribology*, Vol. 108, pp 411-420.
- Kweh, C C, Evans, H P and Snidle, R W, 1989, "Micro-elastohydrodynamic lubrication of an elliptical contact with transverse and three-dimensional sinusoidal roughness", *Trans. ASME, Jn of Tribology*, Vol. 111, pp 577-584.
- Kweh, C C, Patching, M J, Evans, H P and Snidle, R W, 1992, "Simulation of elastohydrodynamic contacts between rough surfaces", *Trans. ASME, Jn of Tribology*, Vol. 114, pp 412-419.
- Lubrecht, A A, Ten Napel, W E and Bosma, R, 1988, "The influence of longitudinal and transverse roughness on the elastohydrodynamic lubrication of circular contacts", *Trans. ASME, Jn of Tribology*, Vol. 110, pp 421-426.
- Okamura, H, 1982, "A contribution to the numerical analysis of isothermal elastohydrodynamic lubrication" *Proc. of the 9th Leeds-Lyon Symp. on Tribology*, in *Tribology of Reciprocating engines*, Butterworths, London, pp 313-320.
- Patching, M J, 1994, "The effect of surface roughness on the micro-elastohydrodynamic lubrication and scuffing performance of aerospace gear tooth contacts", PhD Thesis, University of Wales.
- Patching, M J, Kweh, C C, Evans, H P and Snidle, R W, 1995, "Conditions for scuffing failure of ground and superfinished steel disks at high sliding speeds using a gas turbine engine oil", *Trans. ASME, Jn of Tribology*, Vol. 117, pp 482-489.

## **Fatigue and Brittle Fracture Analysis of Surface Engineered Materials in Rolling Contact**

T.H. Kim and A.V. Olver

Tribology section, Department of Mechanical Engineering, Imperial College, London SW7 2BX

An analysis is presented of the failure by fatigue and by brittle fracture of M50 tool steel surfaces subject to rolling sliding contact. The analysis includes the effects of roughness on both surfaces, of slide roll ratio and of the introduction of a shallow nitrided case such as has been previously investigated experimentally. Results suggest that the failure may be strongly influenced by the distribution of the magnitude and the cycle rate of stresses in a very shallow surface layer. The analysis agrees broadly with some published results but this may be fortuitous.

### **1. INTRODUCTION**

Application of surface engineering to rolling element bearings and gears is becoming commonplace as the search for higher performance continues. General surface treatment processes are described in Hutchings [1] and the use of nitriding and nitrocarburising for tool steel bearings by Vanes [2]. The stress distribution in loaded contact varies significantly with depth from the surface, as Olver [3] illustrates, and it is accepted that ideally engineered materials should possess an appropriate variation of hardness and residual stress to withstand these stress conditions.

So far, materials and processes have mostly been developed from experimental observations and trial and error approaches without relating to the mechanisms responsible for the failures. Studies to understand the stresses involved in rolling contact have been progressively developed from a smooth contact model by Smith & Liu [4] to real roughness and friction incorporating models by Sayles and co-workers [5,6].

In the present paper, we formulate an analysis method for surfaces whose properties vary with depth. The model is based on the fatigue life model developed by Ioannides and Harris [7]. Evaluation of full sub-surface stress distribution and the stress history of rolling-sliding contact between two rough surfaces under both normal and tangential loads is developed, with emphasis on the importance of

sliding effects on the stress cycles experienced. The profiles used in the analysis are measured from real rough surfaces, or generated artificially using a random staggering function. A similar stress criterion is also used in the model to assess the probability of brittle fracture, which often occurs when the hardness of the material is high. Analyses have been applied to a bearing steel (M50) with and without the surface treatment (nitriding). Mechanical property variations resulting from the surface treatment processes are accommodated in the analysis by means of a parameter which varies with depth from the surface.

### **2. BACKGROUND**

Rolling element bearings and gears in simplest terms can be described as moving components in nonconformal contact under transmitted load. As the area of contact is very small compared to the size of the components, dominant stresses are concentrated around the contact region and can be extremely high. The problem of the contact of elastic bodies under a normal load was first investigated by Hertz in 1881, who derived expressions for the load distribution over the contact area and the stresses in the bodies in the vicinity of the contact region. This classic theory of contact was solved for smooth frictionless contact. The contact area is elliptical in general, but when elongated bodies, such as a cylinder or a flat, are involved in the contact (the major axis of the contact area much greater than the minor one), the problem can be simplified as a two dimensional one by treating it as a line contact. This is a reasonable

assumption to apply to most roller bearings and gears to reduce the complexity of the analysis required. Definitions of different types of contact in general are described by Johnson [8].

Recent advances in numerical methods and computing powers have allowed more realistic features of the contact problem to be used in the analysis. The key features involved in rolling contact are the roughness of the contacting surfaces, lubrication and the friction, as well as the running conditions, such as the applied load, the rolling speed and the sliding induced. Each play a role in determining the nature of the contact conditions which consequently influences the stress and hence the failure mode. The models proposed in the past are described in the following section with regards to the above mentioned features of the rolling contact problem and their relevance in deducing more realistic account of the stresses experienced.

### 2.1. Surface and subsurface stress

The solution to the problem of the stresses in the smooth elastic body due to tangential and normal loads in line contact was presented by Smith and Liu in 1953, who showed that when the combination of loads considered are applied at the contact, the maximum shearing stress occurs at the surface instead of beneath the contact, as predicted by Hertz, and the magnitude is also larger. This emphasised the importance of friction in the contact which distorts the stress field significantly and shifts the location of the maximum stress of concern closer to the surface. They also showed the existence of some reversal of stress (tension behind the contact) due to friction and suggested how a crack may start and propagate when stresses are predominantly in compression. Such findings were important step towards explaining the cause of failures, such as pitting initiating from the surface in the rail heads, which appeared more severe in curved rails where contact stresses due to both tangential and normal forces occur. However, the model solved the contact problem on the basis of the Hertzian pressure distribution for both the tangential and normal loads and did not account for the

roughness which also induces critical stresses at the surface.

Webster and Sayles developed a numerical model to simulate the elastic frictionless contact of real rough surfaces by solving the classical two dimensional plane strain problem for the vertical displacements due to any applied pressure distribution. The numerical method used allows contact pressures and displacements to be solved simultaneously.

The pressure distributions of real measured rough surfaces in contact were shown to consist of a large number of pressure spikes existing across the contact, and in many places well above the corresponding hertzian pressure. A typical pressure distribution over a rough surface is shown in figure 1, which shows the pressure fluctuating rapidly with respect to each asperity contact and valleys within the contact area. The apparent area of contact is much less than that predicted by Hertz and the pressures are much higher.

Further development of the model is made by Cole and Sayles [9] who investigated the effects of a coating layer in the substrate on the contact pressure distribution. They varied the thickness and the ratio of elastic modulus of the coating and the substrate to examine the changes in the contact pressure. From their results, it can be seen that when the elastic modulus of the coating and the substrate are similar, the presence of the layer has little influence on the pressure distribution, but when the coating layer is stiffer than the substrate the pressure peaks generated become much more pronounced. However most of the surface engineering processes suitable for rolling contact are of the thermochemical process type which involves modification of the composition and microstructures of the surface locally, but the elastic moduli of the surfaces are very little affected. In this paper, we neglect variation of elastic modulus resulting from the surface treatments of interest, namely carburising and nitriding.

Using the pressure distribution of rough surfaces generated by Webster and Sayles' contact model, Bailey and Sayles developed a numerical model to

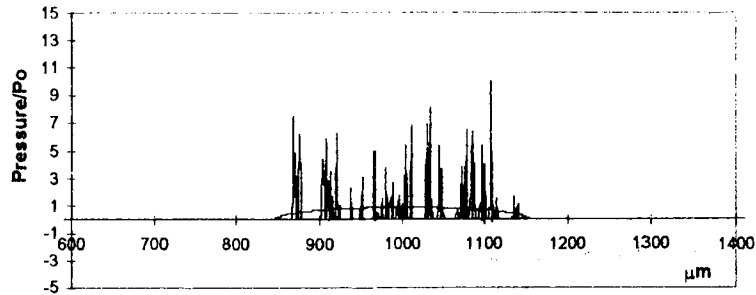


Figure 1. Pressure distribution over a rough surface loaded by a smooth cylinder. High pressures peaks many times greater than the hertzian pressure are evident throughout the contact area.

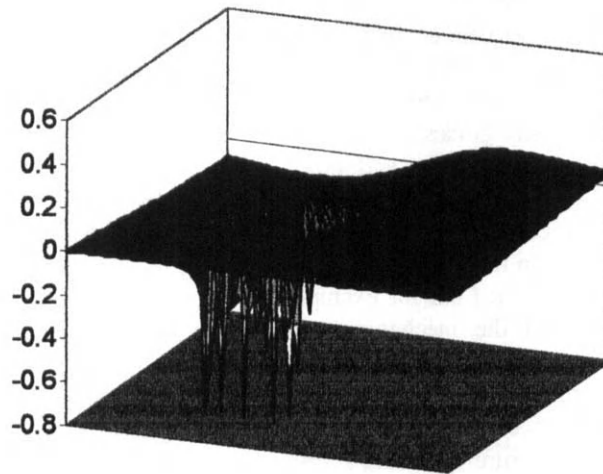


Figure 2. Orthogonal shear stress field beneath a rough contact. Concentration of high stresses at the surface due to individual asperity contacts decays rapidly with depth. The hertzian shear stress distribution is retained away from the surface.

evaluate the complete subsurface stress field of non-conforming rough bodies in elastic contact. Their model produced similar stress field to those shown by Smith and Liu when smooth flat profiles were used, but when measured rough profiles were used, the stresses near the surface were significantly large and concentrated locally. Figure 2 shows a typical stress field in the vicinity of the contact. The 'roughness stresses' concentrated near the surface are the result of localised asperity contacts which give rise to very high local contact pressures. Large pressure spikes dominate and influence the stress field at the surface and superimpose with the neighbouring stresses, but

these 'roughness stresses' are very local to the contact surface and the typical hertzian stress field is retained away from the contact.

They demonstrated the importance of surface finish (i.e. roughness) on the stress field by analysing several different surface finishes to illustrate how the maximum shear stress could occur very close to the surface, even when the frictional effect is ignored.

One of the most notable changes in bearing failures in recent years has been the origin of fatigue failures. At one time it was common to observe

failure at inclusions which was believed to have initiated by cycles of shear stress below the surface at depths given by Hertz. when these random defects were inside the stressed zone. However, as the quality of materials has improved, both as a result of improvements secondary steelmaking and in some sectors introduction of vacuum remelting, the number and size of internal defects acting as critical stress raisers have been reduced, so that when failures occur they are found to be surface originated, perhaps caused by the 'roughness stresses'.

## 2.2. Lubrication

In bearings and gears, the lubrication films generated are elasto-hydrodynamic lubrication (EHL) or micro- elasto-hydrodynamic. The contact stress and the operating temperature are often very high and relatively low viscosity grades of lubricant are often selected because of cold start and other equipment constraints. In these regimes of lubrication, there exist significant surface interactions on the asperity scale. Studies on the lubrication films in these regimes have been carried out for example by Chang [10] to understand the mechanisms of lubricated friction and wear, and Ai and Cheng [11] have studied the effect of roughness and the relative sliding speed between the contact surfaces to demonstrate fluctuations of pressure occurring across the contact. Although, these features of lubricant films are important in obtaining more precise picture of the pressure distribution in sliding contact of rough surfaces, results have not in the main been confirmed experimentally and there are considerable difficulties associated with the analysis. We will assume dry contact in this paper, corresponding to the lubricant films generated being thin compared to the roughness ( $0 < \lambda < 1$ ).

## 2.3. Failure modes and life calculations

The most common failure in rolling contact subject to cyclic loading is fatigue fracture. Lundberg and Palmgren [12] developed a theory to evaluate fatigue life of rolling bearings in the early 1940's. Their theory relates the survival probability  $S$  of the bearing subject to a number of cycles  $N$  of repeated

concentrated stress, in terms of the maximum orthogonal shear stress  $\tau_o$  and the depth  $Z_o$  at which it occurs, and the volume  $V$  of the stressed zone.

$$\ln \left( \frac{1}{S} \right) \approx \frac{N \tau_o^c V}{Z_o^a} \quad \text{eqn(1)}$$

$\tau_o$  and  $Z_o$  were deduced from Hertz theory for smooth elastic body contact subject to a normal load only. It predicted the failure to occur from the subsurface zone where the maximum orthogonal shear stress occurs. Although, the theory provided useful predictions, several life adjustment factors had to be introduced to the original model in order to justify new observations in modern bearings, such as longer lives and surface originated failures when the maximum stress was thought to occur below the surface.

A new fatigue life model developed by Ioannides and Harris in 1985 uses the complete subsurface stress field of the body, rather than a maximum value for the stressed volume. This is done by dividing the stressed volume in the region under the contact into small elements of  $\Delta V$  of uniform stress. This allows every point in the volume to be assessed individually for failure, whether it initiate at the surface, or from subsurface. They also implied a threshold fatigue stress limit to exist for rolling contact, below which no failure would occur, to explain the extended fatigue life of bearings. Ioannides, Jacobson and Tripp [13] employed the shear stress amplitude modified by the hydrostatic pressure, which influences the onset of yield, and the fatigue limit to achieve better predictions without the need for ambiguous life adjusting factors. Lubrecht, Jacobson and Ioannides [14] eliminated the use of the depth weighting parameter arguing that the survival of each volume elements should depend only on the stress experienced and not its relative position to the surface.

More recently, Hamer et al. [15] used the maximum shear stress amplitude, modified by the hydrostatic pressure component and the threshold shear stress, from a simulated rolling-sliding contact. They simulated rolling and sliding by moving one

body in relation to another and translating profiles relative to each other, respectively. A series of pressure distribution resulting from each discretized movements is used to determine the stress field variation of the subsurface region and the maximum value of each elements is used in the life calculation. They also investigated the importance of the asperity sliding completely over another and contributing greater fatigue risk due to the shear stress reversal. They expressed expected number of asperities overtaken in the contact in terms of the sliding speed and the average asperity spacing and showed the fatigue life to be inversely proportional to the sliding speed. This is an important feature of the model which is taken further in this paper by considering the stress history generated in more detail from a fatigue point of view by examining the cycles of shear stress experienced within the passage of contact, rather than the number of asperities expected to slide over one another, and using a special counting method to determine equivalent damaging cycles to be used in the fatigue model.

Brittle fracture is another important failure mode to consider as the materials of interest are becoming harder at the surface to be susceptible to fast fracture. Pearson [16] implemented rolling contact tests of several hard surfaces and showed longer lives from strengthened contact surfaces, but the failures appeared to be brittle in nature. Stanley, Fessler and Sivill [17] derived a general expression for the failure probability of a component subject to a non uniform, multi-axial stress system by means of the usual Weibull analysis. As with the fatigue analysis, the full stress distribution in the component is used by dividing the component into a number of elements small enough to warrant the assumption of constant stresses. There is a close similarity between the two analyses in that both use the localised stresses of individual elements where each one contributes to the overall assessment. The differences are the stress component used in the criterion, the maximum principal stress is used in brittle fracture analysis, and the omission of the number of cycles to failure term. The probability of failure term is used instead to describe their susceptibility, as there is an inherent variation involved with brittle materials behaviour.

The following section describes in detail the proposed model to assess rolling contact fatigue of rough surfaces and the significance of the sliding effects on the actual damaging cycles experienced and the probability of brittle fracture under the same stress conditions.

### 3. DESCRIPTION OF MODEL

The model proposed by Ioannides and Harris, given in equation (2), is used as the starting block where  $\sigma$  is any stress criterion integrated over the stressed volume.

$$\ln\left(\frac{1}{S}\right) = A N^c \int_V \frac{(\sigma - \sigma_u)^c}{z^h} dV \quad \text{eqn(2)}$$

In this paper, we have chosen to neglect the  $Z$  term, as discussed before, and use the shear stress range in the stress criterion as the shear stress variation is quite random in nature in rough contact and determining the amplitude of the cycles can be ambiguous as it depends on the mean value. The range is defined as the difference between the maximum and the minimum shear stresses modified by the hydrostatic pressure with a coefficient of 0.3. The fatigue limit  $\sigma_u$  is the minimum range that can be considered to contribute towards the accumulation of fatigue damage and is set to zero. The model simulates rolling-sliding contact, as described in [15], by moving two bodies relative to each other and shifting the profiles according to the rolling and the sliding speed, respectively. The radii of the curvature of two bodies is combined and the effective radius is assumed on one body while the other is treated as a half body plane. The profiles of two bodies are also superimposed at each simulated instances of the movements and the combined roughness is put on the half plane surface while keeping the other surface (curved one) smooth. For convenience of analysis, the half body with the combined rough profile is fixed while the curved body is moved across. From each instances of simulated rolling-sliding contact, a series of pressure distributions is obtained and the corresponding subsurface stress distributions of a small subsurface region below the contact is determined. The size of the region and the resolution

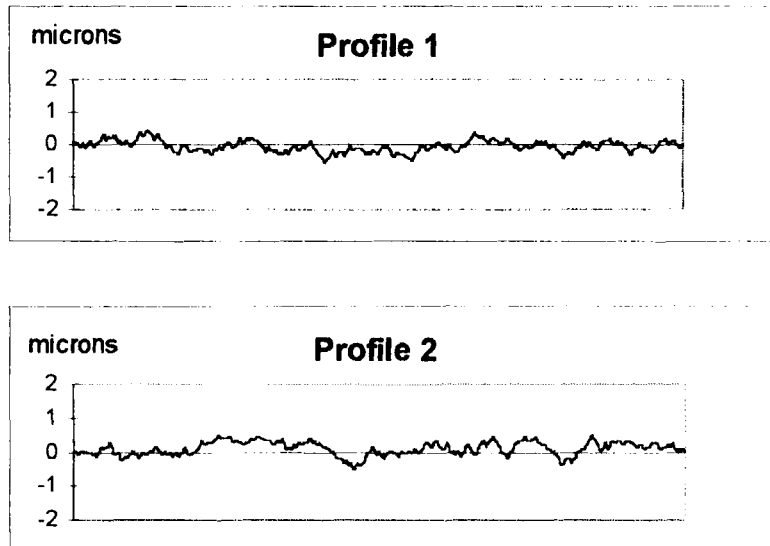


Figure 3. Two rough profiles used in the analysis (1mm long). A third smooth flat surface is used in combination with the above two to simulate different contact conditions.

(element size) depend on how large the stress field is and how significantly the stress varies near the surface due to the roughness effects. (The smaller the element the better it is in adopting finer changes of stress, but the element size is limited to that of the material's grain size ( $2-3\mu\text{m}$ ), since fatigue initiation appears to occur on this scale.) In the fatigue analysis, the complete stress history of each element in the stress field is used, and for the brittle analysis, the maximum principal stress determined of each element is used as being the most damaging stress.

### 3.1. Stress cycle counting methods

We have discussed so far in this paper the means of calculating the pressure distribution of any real surfaces in contact and subsequently the complete subsurface stress field and the stress history by simulating rolling-sliding contact. For fatigue analysis, however, it is necessary to assess the effect of the damaging stress cycles experienced during a passage of contact. Schijve[18] described several counting methods in detail and more recently Dowling[19] discussed the suitability of the range-pair and rain flow methods, which are identical, and assessed their importance.

The fatigue life model uses the range-pair method to assess the stress variation during contact to determine how they influence the life of the component under such stress conditions experienced in rolling-sliding contact.

## 4. RESULTS OF MODELLING

To illustrate the effect of roughness in rolling-sliding contact three profiles, two rough profiles and a smooth one, are used in combination to simulate different contact conditions by superimposing a smooth profile on a rough profile, a rough profile on a smooth one and a rough profile on another rough profile. Two rough profiles are generated artificially to represent typical fine ground finish surfaces (figure 3). To obtain a full stress history of the material in the region near the surface, the contact starts away from this region so that the stress experienced is zero initially and starts to register as the contact passes over and to zero again when the contact moves away. An orthogonal shear stress distribution for a 10 mm radius cylinder on flat with the nominal load of  $0.2 \text{ N}/\mu\text{m}$  shows the stress field to be about  $600 \mu\text{m}$  wide and  $400 \mu\text{m}$  deep, where outside this field the stress is negligibly small. A profile of  $2000 \mu\text{m}$  long with a

1  $\mu\text{m}$  sampling length is used and the contact position is moved from 700  $\mu\text{m}$  to 1300  $\mu\text{m}$  in rolling steps of 10  $\mu\text{m}$  to generate a series of subsurface stress distributions with respect to time during contact. The total rolling distance of 600  $\mu\text{m}$  is chosen to allow the stress field to sweep across the central region, 200  $\mu\text{m}$  wide and 400  $\mu\text{m}$  deep, to experience full stress variation.

The first case examined is pure rolling of a smooth body over a smooth surface. This is just a simple hertzian stress field passing over the region and the stress history of elements at 2  $\mu\text{m}$  below the surface (first element down) is plotted out in figure 4 which shows a sharp reversal of the orthogonal shear stress from maximum to minimum. Elements deeper at 120  $\mu\text{m}$  below the surface experience more gradual, but slightly larger stress variation as they lie close to the maximum shear stress zone. When the friction is added to the problem ( $\mu=0.1$ ), the elements near the surface sees a large part of its shear stress cycle in the direction of the applied traction (opposite the rolling direction), but this change gradually becomes unnoticeable below 50  $\mu\text{m}$ . When the hydrostatic pressure term is also introduced, the modified shear stress is now very much in one direction during most part of its cycle close to the surface and again, typical hertzian cycle is retained deeper below the surface.

When a smooth body is rolled over a rough surface without sliding, the elements that lie beyond 50  $\mu\text{m}$  from the surface are not influence by the roughness and shows stress variation identical to the smooth on smooth case, but the elements close to the surface exhibit different stress cycles, depending on where they lie in relation to the peaks or valleys of the rough profile. The stress range of the elements directly below asperity peaks are much larger than those found in the smooth case (2 or 3 times larger) and although, only a small number of them experience higher stresses than the smooth case, their damaging effect could be significant as the stress is the most dominant factor in determining the fatigue life. For a case of a smooth surface rolling-sliding over a rough one, in terms of the stresses experienced, it does not differ from pure rolling

(Sliding may influence wear mechanisms, lubricant film formation and heat generation, but these aspects are not considered in this paper). A rough surface rolling over a smooth surface without sliding exhibits the same stress variation as the smooth on rough case, but when sliding is induced, the stress variation is very different. The stress history of elements at the surface in a rough over a smooth case with a slide roll ratio,  $\frac{U_1 - U_2}{\frac{1}{2}(U_1 + U_2)}$ , of 0.33 is shown in figure 5. It

shows a large number of stress fluctuations during the time in contact. The number of cycles counted for each elements are plotted in figure 6 which shows high concentration close to the surface where the variation is most severe.

The stress variation encountered when *two* rough surfaces are made to roll with the slide roll ratio of 0.33 is similar to the rough over a smooth case, but larger number of elements are subject to higher number of stress cycles. There is more chance of asperities colliding into each other and the depth to which it is affected is deeper as the 'roughness' stresses involved are higher. The relative fatigue lives obtained from different contact conditions and the slide-roll ratios of two rough surfaces are given in table 1.

The maximum principal shear stress found at each depth below the contact is plotted out in figure 7a for a rough surface rolling-sliding on another rough one. It shows rapid attenuation of the stress to a depth of about 20  $\mu\text{m}$  where it starts to reduce much more gradually and, as with the number of shear stress cycles counted, the stress is concentrated in a shallow region close to the surface. To assess the damages incurred at each depth, the probability of failure  $P_f$  is determined for each layer of elements in a rough contact by setting the number of cycles,  $N$ , as 100,000,000 in equation (2), where  $P_f = 1 - S$ , and assuming the parameter  $A_i$  to be related to the hardness in the form given below,

$$A_i = \frac{1}{\langle \text{strength} \rangle^c V_{ref}} = \frac{1}{\langle 32 \times HR \rangle^c V_{ref}} \quad \text{Eqn(4)}$$

where *strength* is the tensile strength of the material and *HR* is the Rockwell Hardness of the



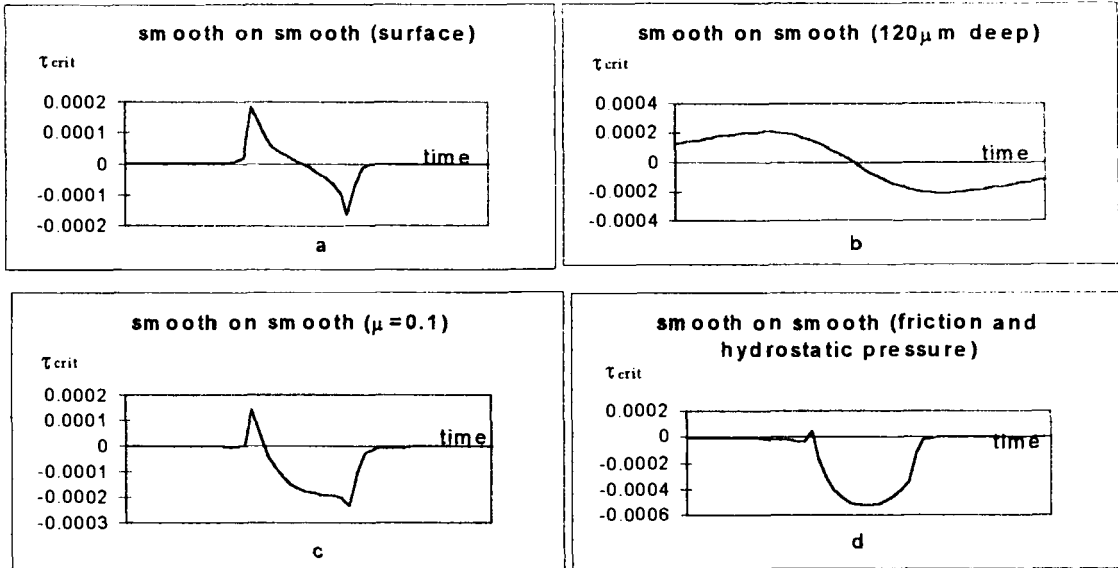


Figure 4. The stress criterion history plot of the elements in the stressed region in rolling contact. The stress criterion is in TPa and the time duration is over a distance of  $600\mu\text{m}$  with respect to the rolling speed (a,c and d at  $2\mu\text{m}$  below the surface).

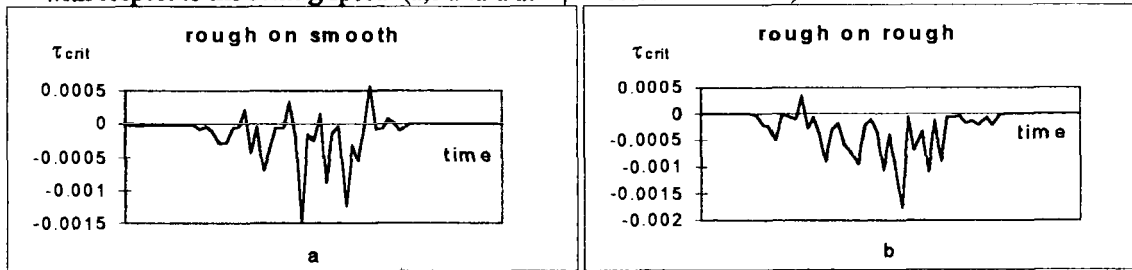


Figure 5. The stress criterion history of a rough profile rolling-sliding over a smooth one (a) and a rough profile rolling-sliding over another rough profile (b). The slide roll ratio in both cases is 0.33.

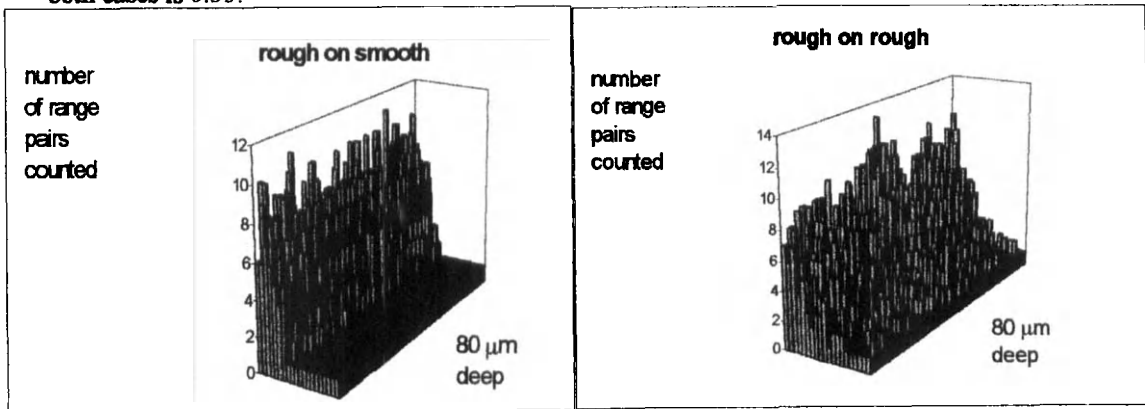


Figure 6. Number of stress variations counted as damaging cycles using a range-pair counting method is carried out for rolling-sliding contact.



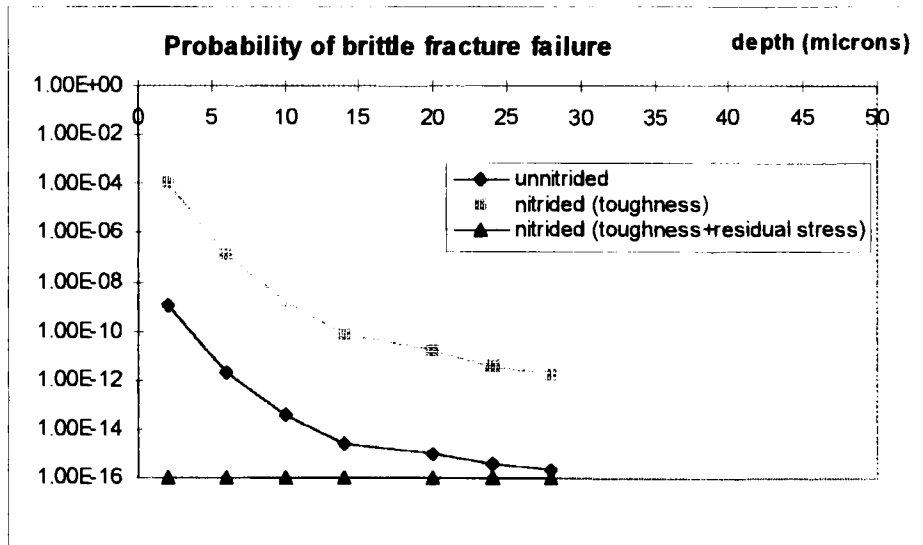


Figure 9. Comparison of the brittle fracture failure probability of the region close to the surface.

material. The hardness variation from nitriding is given in figure 7b.

The probability of fatigue failure for M50 steel with a uniform hardness of 62 HR and the nitrided M50 steel with a varying hardness profile are given in figure 8. For the uniform hardness case, the probability of failure is highest at the surface which drops fast to the quiescent zone where the roughness effect is no longer reached and increases again slightly in the maximum shear stress zone. It then approaches zero value further below. The same general variation of the probability of failure exists for the nitrided material, but the values are lower in the shallow region near the surface and the maximum shear stress zone compared to the uniform case. With the assumed hardness variation of a typical nitrided M50 steel, the chances of failure in the critical region has reduced by a factor, however, the surface is still much more susceptible to failure.

For the brittle analysis, we assumed the variable  $A_i$  to be related to the fracture toughness of the material, as suppose to the hardness in the fatigue analysis, and assumed a

simple linear variation of the value from the surface down to  $100\mu\text{m}$  deep (7 to  $20\text{ MPam}^{1/2}$ ). The probability of the brittle fracture failure with depth is given in figure 9.

## 5. DISCUSSION

### 5.1 Fatigue Analysis

The present analysis probably represents the simplest possible approach which can take into account the practically important features of roughness on both surfaces, sliding and case depth. The model is two-dimensional, perfectly elastic, and neglects lubricant film, wear - even when there is sliding present - and thermoelastic effects, all of which may have a significant role. It is probably best, therefore, to regard any apparent agreement with experiment as fortuitous.

Nevertheless, it is plain that the main features of the analytical results are indeed credible. Nakajima [19] has reported a similar reduction of life with slide roll ratio using finely ground discs and the observation that smooth surfaces show a lower reduction of life with sliding than

do rough ones has also been reported by the same author. The analysis of the nitrided M50 also shows an increase in life comparable, at least qualitatively, with those reported by Pearson [16].

The most significant finding from the point of view of surface engineering, is that the principal controlling parameter is the variation with depth of the stress field. This is highly dependent on the finishing method, and it is likely that shallow reinforcement of the type studied would perform very differently in situations where, for example the roughness was much greater, such as in typical gear teeth. It remains to be seen whether the present approach to rolling fatigue analysis can assist in this instance. Even in the present roughness, fatigue origination is still predicted at the surface, where the material is hardest.

### 5.2 Brittle Analysis

The observation that brittle fracture occurred in very high hardness surfaces subjected to rolling and the relative simplicity of the analysis, prompted its inclusion here. However, it is more likely that the observed brittle fractures were initiated from fatigue cracks so that a combined analysis is really necessary. This may be possible in due course but is beyond the scope of the present paper.

## 6. CONCLUSIONS

An analysis based upon the method of Ioannides and Harris has been carried out for the case of M50 steel in which both contacting surfaces were rough. The effect of a shallow nitrided case of the type tested by Pearson was investigated.

The results show that the distribution in depth of both the magnitude and the cycle rate of the stresses is strongly dependent upon the sliding regime.

The reduction in life associated with sliding and the improvement associated with nitriding were similar to those measured, but this could be fortuitous in view of the simplicity of the model.

## 7. ACKNOWLEDGEMENTS

The authors are grateful to the Engineering and Physical Sciences Research Council for financial support.

## REFERENCES

1. I.M. Hutchings. (1992) "Tribology: Friction and Wear of Engineered Materials" Publ. Edward Arnold.
2. S.E. Vanes. (1995) "Review of Process and Materials Developments for Aerospace Rolling Bearings", AeroTech 95, ImechE conference on Transmissions.
3. A.V. Olver, S.J. Cole & R.S. Sayles (1993) "Contact Stresses in Nitrided Steels", Proc. 19<sup>th</sup> Leeds-Lyon Symposium on Tribology, Leeds, publ. Elsevier
4. J.O. Smith and C.K. Liu (1953) "Stresses Due to a Tangential and Normal Loads on an Elastic Solids With Application to Some Contact Stress Problems", ASME Journal of Applied Mechanics, pp. 157-166.
5. M.N. Webster & R.S. Sayles (1986) "A Numerical Model for the Elastic Frictionless Contact of Real Rough Surfaces", ASME Journal of Tribology, Vol. 108, No.3, pp. 314-320.
6. D.M Bailey & R.S. Sayles (1991) "Effects of Roughness and Sliding Friction on Contact Stresses", ASME, Journal of Tribology, Vol. 113, pp. 729-738.
7. E. Ioannides & T.A. Harris (1985) "A New Fatigue Life Model for Rolling Bearings", ASME, Journal of Tribology, Vol. 107, pp.367-378.
8. K.L. Johnson, (1985) "Contact Mechanics", publ. Cambridge Univ. Press.
9. S.J. Cole & R.S. Sayles (1992) "A Numerical Model for the Contact of Layered

- Elastic Bodies With Real Rough Surfaces”, ASME, Journal of Tribology, vol. 114, pp.334-340.
10. L. Chang (1995) “Deterministic Modelling and Numerical Simulation of Lubrication Between Rough Surfaces”, Wear, vol. 184, pp155-160.
11. X. Ai & H.S. Cheng (1994) “A Transient EHL Analysis for Line Contact With Measured Surface Roughness Using Multigrid Technique”, ASME, Journal of Tribology, vol. 116, pp 549-558.
12. G. Lundberg and A. Palmgren (1947) “Dynamic Capacity of Rolling Bearings”, Acta Polytechnica, Mechanical Engineering Series, Royal Swedish Academy of Engineering Sciences, vol.1, No.3.
13. E. Ioannides, B. Jacobson and J.H. Tripp (1988) “Prediction of rolling bearing fatigue life under practical operating conditions” Proc. of 15<sup>th</sup> Leeds/Lyon symposium, vol. 14, pp 181-187.
14. A.A. Lubrecht, B.O. Jacobson and E. Ioannides “Lundberg and Palmgren Revisited”, SKF Engineering and Research Centre
15. J.C. Hamer, J.M. Hutchinson, A.V. Olver, R.S. Sayles & E. Ioannides (1991) “fatigue Life Modelling of Gear Contact”, British Gear Association, Annual Congress, Sheffield.
16. P.K. Pearson (1995) “Rolling Contact Behaviour of High Hardness Surfaces”, ASC Metal Symposium, 2<sup>nd</sup> International Bearing Steel Symposium.
16. P. Stanley, H. Fessler and A.D. Sivill (1973) “An Engineer’s Approach to the Prediction of Failure Probability of Brittle Components”, Proc. of the British Ceramic Society. Vol.22, pp453-487.
17. J. Schijve (1961) “The analysis of random load-time histories with relation to fatigue tests and life calculations”, Proc. of the symposium on Fatigue of Aircraft Structures, international series of monographs in Aeronautics and Astronautics, vol. 12, pp115-149.
18. N.E. Dowling (1972) “Fatigue failure prediction for complicated stress strain histories” Journal of Materials, JMLSA, vol. 7, No. 1, pp71-87.
19. A. Nakajima, “Effects of Surface Roughness and Oil Viscosity on Rolling Fatigue Strength of Case Hardened Rollers”, Proc. Japan International Tribology Conference, Nagoya, 1990, pp773-778.

## Elastohydrodynamic Effects in Piston Ring Lubrication in Modern Gasoline and Diesel Engines

J.E. Rycroft, R.I. Taylor & L.E. Scales

Shell Research & Technology Centre, Thornton, P.O. Box 1, Chester, CH1 3SH, UK

A study has been carried out to investigate the importance of elastohydrodynamic effects in the lubrication of piston rings of modern gasoline and diesel engines. It has been found that, in terms of frictional power losses, elastohydrodynamic effects are not significant in gasoline engines, but can be important in diesel engines. In terms of top ring/liner wear, however, elastohydrodynamic lubrication effects may be important for both types of engines.

### 1. INTRODUCTION

In 1983, Professor Dowson undertook a study<sup>1</sup> into the importance of elastohydrodynamic (EHD) effects in piston ring lubrication. More recently, other authors have also carried out such an analysis<sup>2,3</sup>. Since then, engine design has continued to evolve, and combustion chamber pressures have been pushed ever higher in attempts to squeeze more power from the engine. Therefore it was considered timely to repeat the investigation into the importance of EHD effects in the piston assembly, by considering two modern engines. The gasoline engine chosen for analysis was a Mercedes-Benz M111 2.0 litre, 4 cylinder gasoline, currently being considered as the engine for a European fuel economy engine test. The diesel engine chosen for analysis was an RVI 10.0 litre, 6 cylinder diesel engine, designed to meet modern (EURO-2) European emission limits. The peak combustion chamber pressure for the gasoline engine was approximately 35 bars (for conditions of 2500 rpm and 95.4 Nm load), whereas the peak combustion chamber pressure of the diesel engine was approximately 140 bars.

Initially, a hydrodynamic lubrication analysis of both engines was carried out,

using piston ring lubrication software that has been validated against experimental oil film thickness<sup>4</sup> and friction measurements<sup>5</sup> carried out in a running engine. The hydrodynamic lubrication analysis was used to identify conditions where EHD lubrication was most likely to occur. Unsurprisingly, the most likely place for EHD lubrication to occur was found to be around dead centre positions, with the most demanding conditions being found around top dead centre firing.

An EHD analysis was then performed for piston ring lubrication around both top and bottom dead centres, for both engines. It was found that the largest elastic deflections occurring in the gasoline engine were around top dead centre firing, and were approximately 0.3 microns in magnitude. No significant elastic deflections were found at any other crank angles. For the diesel engine, the elastic deflection around top dead centre firing was found to be approximately 2.0 microns, and significant elastic deflections were also observed around bottom dead centre positions.

Since the piston is stationary at dead centre positions, the conclusion of this work is that as far as frictional power losses are concerned, EHD effects are not significant in modern gasoline engines, but could be

significant in modern diesel engines. However, for reliable top ring/liner wear estimates, EHD conditions should be taken into account for both engines.

## 2. HYDRODYNAMIC LUBRICATION ANALYSIS

A hydrodynamic lubrication analysis of the Mercedes-Benz M111 gasoline engine, and the RVI diesel engine was carried out. The software for the hydrodynamic lubrication analysis allowed for viscosity/temperature and viscosity/shear rate effects<sup>4,5</sup>, and also took into account the starvation of the upper piston rings due to the scraping action of the lower rings. The model assumed axial symmetry, and so neglected any effects due to ring gaps. The model was based on a 1D solution of the Reynolds' equation, and the algorithm is similar to that used by a number of other researchers<sup>6-10</sup>.

Figure 1 shows the results for the top ring oil film thickness predicted by the hydrodynamic model for the Mercedes-Benz M111 2.0 litre gasoline engine, for engine conditions of 2500 rpm and 98.4 Nm load. In Figure 1, it can be seen that it is essential to take starvation effects into account, particularly for mid-stroke positions. However, close to dead centre positions, the assumption of fully flooded lubrication conditions was found to be justified. This result has also been found by other authors<sup>9</sup>. In Figure 1, the "squeeze" effect was ignored, so that the predicted oil film thickness was zero at dead centre positions. Figure 2 shows a fully flooded analysis of the M111 engine that takes the "squeeze" effect into account.

Figures 3 and 4 show corresponding results for the RVI 10 litre diesel engine. For this case, the engine speed was 1100 rpm, and the engine was operated at full load.

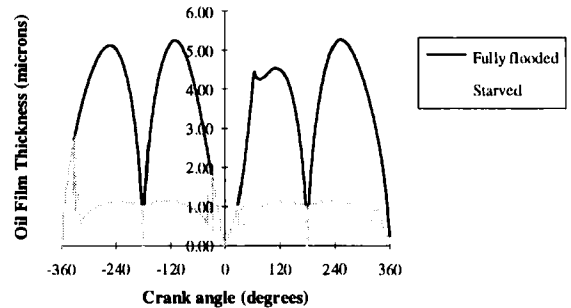


Figure 1 : Fully flooded and starved analysis of oil film thickness under the top ring of the Mercedes-Benz M111 2.0 litre gasoline engine

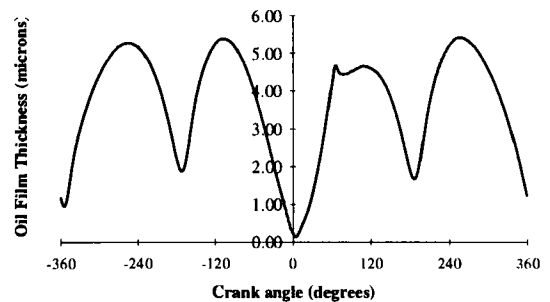


Figure 2 : Fully flooded top ring oil film thickness predictions for the Mercedes-Benz M111 2.0 litre gasoline engine, taking into account the "squeeze" effect

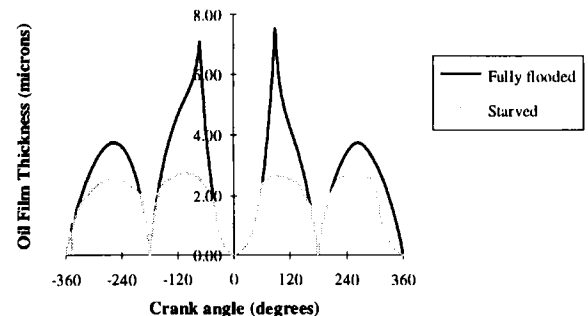


Figure 3 : Fully flooded and starved analysis of oil film thickness under the top ring of the RVI 10.0 litre diesel engine

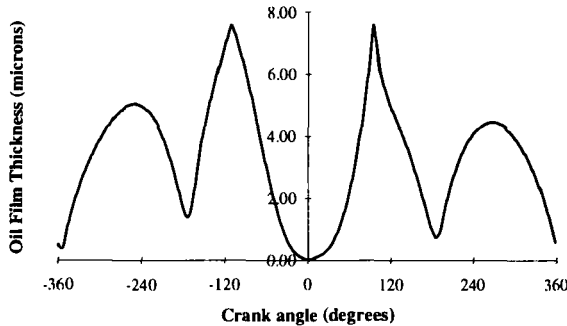


Figure 4 : Fully flooded top ring oil film thickness predictions for the RVI 10.0 litre diesel engine, taking into account the "squeeze" effect

The calculations above were carried out assuming that the piston assemblies were lubricated with an SAE-30 monograde oil, and the bottom dead centre (BDC) liner temperature was taken to be 100 °C, and the top dead centre liner temperature was taken to be 150 °C.

For the fully flooded analyses that incorporated the "squeeze" effect, the minimum oil film thicknesses were found, for both engines, close to top dead centre firing (0° crank angle on above graphs), as expected. For the Mercedes-Benz M111 2.0 litre gasoline engine, the minimum oil film thickness was 0.13 microns at a crank angle of 4°, and at this crank angle, the peak pressure under the top ring was estimated to be 124 bars. Similarly, for the RVI 10 litre diesel engine, the hydrodynamic calculations that included the "squeeze" effect found that the minimum oil film thickness was 0.006 microns, at a crank angle of 1°, and the peak pressure under the contact was predicted to be 2950 bars. Therefore, at first sight, it would appear that conditions in the gasoline engine are only marginally elastohydrodynamic, whereas in the diesel engine, around TDC firing, elastohydrodynamic effects will be highly significant. In the next Section, an EHD analysis is described, concentrating in particular on the TDC firing positions identified by the hydrodynamic analysis.

However, BDC positions were also studied, to compare the relative importance of EHD in the two engines at different crank angles.

### 3. ELASTOHYDRODYNAMIC ANALYSIS

To study the role of EHD lubrication in the lubrication of a single parabolic piston ring an EHD black-box solver was used. EHDLIB Version 1.0 is a library of functions and programs that performs various EHD lubrication modelling tasks. It was developed in-house and has been widely used particularly for the valve train and involute spur gears<sup>11</sup>. It calculates the pressure distribution in the oil film across the line contact by solving the Reynolds equation. This is used to calculate the oil film thickness across the contact and thus yields the minimum oil film thickness. This solver was modified to cope with the film reformation that is present in piston ring lubrication. Such a film reformation is not present in valve train and gear lubrication<sup>11</sup>. The version of EHDLIB used in this note includes the pressure effect on viscosity. Currently the approach is isothermal but thermal effects are to be included later this year. The solver can be run in either pseudo-static or dynamic mode. The pseudo-static mode is time independent and ignores the squeeze term in the Reynolds equation. The dynamic mode includes these transient effects. Including the transient effects gives more physically realistic results.

The viscosity values used in the EHD study were calculated from the input data used in the hydrodynamic lubrication study. For that analysis the viscosity varied with temperature according to Vogel's equation<sup>12</sup>. To obtain a viscosity value for the EHD calculations the temperature at TDC,  $T$ , was used in Vogel's equation as followings

$$\eta_o = \kappa \cdot \exp\left(\frac{\theta_1}{\theta_2 + T}\right) \quad \dots(1)$$



where  $\theta_1$ ,  $\theta_2$  and  $\kappa$  are constants for the lubricant. The values used were  $\kappa = 0.0348$  mPas,  $\theta_1 = 1295.59^\circ\text{C}$  and  $\theta_2 = 122.98^\circ\text{C}$ .

Figure 5 shows the transient minimum oil film thickness for the M111 gasoline. The transient effects are clearly visible around TDC and BDC i.e.  $-180^\circ, 0^\circ, 180^\circ, 360^\circ$ .

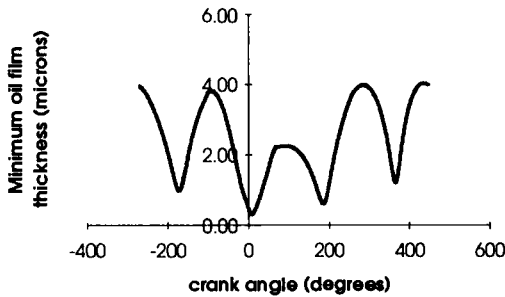


Figure 5: Minimum oil film thickness for M111 engine

The size of the elastic deflections around TDC can be seen from Figures 6 and 7. Figure 6 shows the undeflected shape (lower curve) and the film thickness distribution (upper curve) across the line contact for  $0^\circ$ . The difference between these curves gives the amount of elastic deflection. So the larger the difference the more elastohydrodynamic (and so the less hydrodynamic) the lubrication regime. For the M111 the elastic deflection is seen to be in the order of  $0.3\ \mu\text{m}$  at TDC firing position. The deflection at  $180^\circ$  is much reduced. Figure 7 is the analogous graph for  $180^\circ$ . Figure 8 shows the pressure distribution associated with Figure 6.

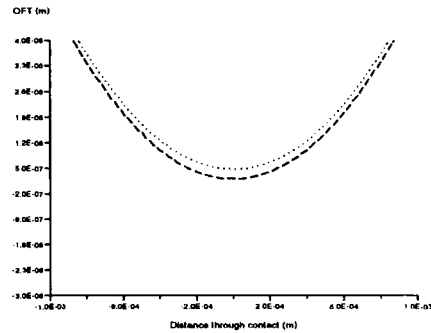


Figure 6: Film thickness across the line contact and undeflected shape at TDC ( $0^\circ$ ) M111 engine

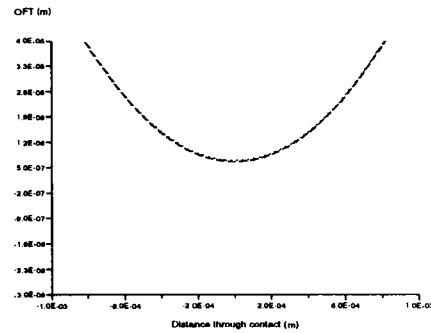


Figure 7: Film thickness across the line contact and undeflected shape at TDC ( $180^\circ$ ) - M111 engine

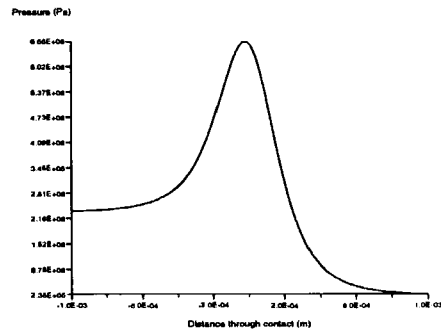


Figure 8: Pressure distribution across the line contact at TDC ( $0^\circ$ ) - M111 engine

Figures 9 to 11 are the corresponding graphs for the RVI. The elastic deflection for the RVI at TDC firing is approximately 2  $\mu\text{m}$  while at 180° it is negligible.

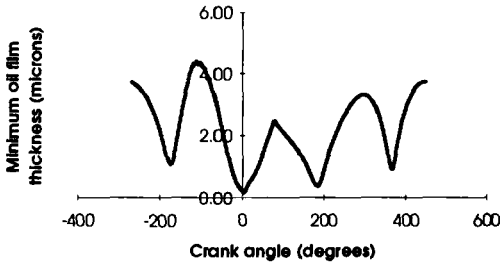


Figure 9: Minimum oil film thickness for RVI engine

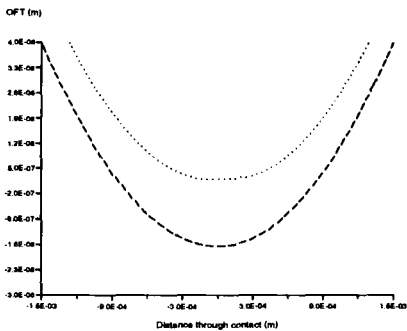


Figure 10: Film thickness across the line contact and undeflected shape at TDC (0°) - RVI engine

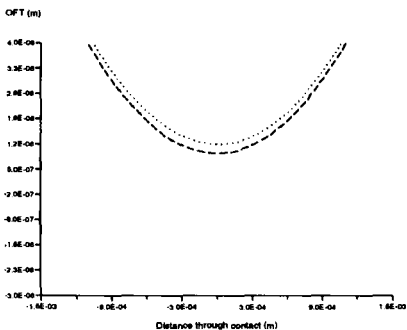


Figure 11: Film thickness across the line

contact and undeflected shape at TDC (180°) - RVI engine

Figure 12 shows the pressure distribution across the contact at 0°. The peak pressure is almost ten times that seen for the M111 engine.

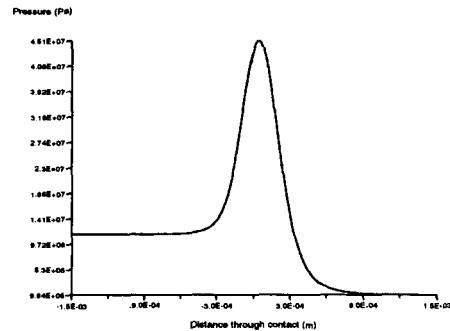


Figure 12: Pressure distribution across the line contact at TDC (0°) - RVI engine

These results are consistent with those obtained using hydrodynamic lubrication, e.g. the maximum squeeze effect is seen around BDC and TDC positions.

#### 4. DISCUSSION

The hydrodynamic and elastohydrodynamic calculations of OFT in the Mercedes-Benz M111 gasoline engine and the RVI diesel engine are in close agreement. Differences have been observed, however, around TDC firing (i.e. at a crank angle of 0°). At such dead centre positions, the piston is stationary, so the effect on frictional loss is not expected to be great. However, it is at such positions that wear is expected to be greatest. Therefore, it is expected that elastohydrodynamic effects would have to be taken into account if reliable predictions of top ring/liner wear were required. Also it is worth noting that, for the gasoline engine, EHD conditions only occur very close to the vicinity of TDC firing. For the diesel engine, EHD conditions are expected to occur within

10-20° of TDC, so that the frictional loss could be affected.

Hence, to summarise, we believe that EHD effects in gasoline engines are only significant for top ring/liner wear, and not for frictional power loss. On the other hand, for a diesel engine, EHD effects need to be taken into account both to predict top ring/liner wear, and also to predict frictional losses.

## 5. CONCLUSIONS

Models of piston assembly lubrication have been developed, using both hydrodynamic and elastohydrodynamic lubrication theories. The models have been applied to two modern engines, a Mercedes-Benz M111 2.0 litre gasoline engine and an RVI 10 litre heavy duty diesel engine, designed to meet modern European emission limits (EURO-2).

It was found that a hydrodynamic lubrication model was adequate to predict oil film thickness except in the vicinity of TDC firing, where an EHD model had to be used. For the gasoline engine, it was found that the EHD model was only required for the prediction of top ring/liner wear effects, whereas for the diesel engine, the EHD model was required to predict both top ring/liner war and frictional power losses.

## REFERENCES

1. D. Dowson, B.L. Ruddy & P.N. Economou, "The Elastohydrodynamic Lubrication of Piston Rings", Proc. R. Soc. Lond. A **386**, 409-430 (1983)
2. G. Wu & Z. Chen, "The Numerical Study of Piston Ring Elastohydrodynamic Lubrication by the Multigrid Method", Trib. Trans., **35**, pp 135-141, 1992
3. Q. Yang & T.G. Keith, "An Elastohydrodynamic Cavitation Algorithm for Piston Ring Lubrication", Trib. Trans., **38**, pp 97-107, 1995
4. R.I. Taylor, M.A. Brown, D.M. Thompson & J.C. Bell, "The Influence of Lubricant Rheology on Friction in the Piston Ring-Pack", SAE 941981
5. R.I. Taylor, T. Kitahara, T. Saito & R.C. Coy, "Piston Assembly Friction & Wear : The Influence of Lubricant Viscometry", Proceedings of the International Tribology Conference, Yokohama, 1995
6. S. Furuhashi, "A Dynamic Theory of Piston Ring Lubrication", Bull. JSME. First Report - Calculation, Vol. 2, 1960, p 423 ; Second Report - Experiment, Vol. 3, 1960, p 291 ; Third Report - Measurement of Oil Film Thickness, Vol. 4, 1961, p 744
7. L.L. Ting & J.E. Mayer, Jr., "Piston Ring Lubrication and Cylinder Bore Wear Analysis", ASME Journal of Lubrication Technology, Part 1 - Theory, Vol. 96, 1974, pp 305-314 ; Part 2 - Theory Verification, Vol. 96, 1974, pp 258-266
8. D. Dowson, P.N. Economou, B.L. Ruddy, P.J. Strachan & A.J.S. Baker, "Piston Ring Lubrication - Part II. Theoretical Analysis of a Single Ring and a Complete Ring-Pack", Energy Cons. through Fluid Film Lubr. Technology; Frontiers in Research & Design, edited by S.M. Rohde, D.F. Wilcock & H.S. Cheng, ASME Publication, 1979, pp 23-52
9. Y-R. Jeng, "Friction and Lubrication Analysis of a Piston Ring-Pack", SAE 920492
10. R. Keribar, Z. Dursunkaya & M.F. Fleming, "An Integrated Model of Ring-Pack Performance", Trans. ASME, Vol. 113, 1991, pp 382-389
11. L.E. Scales, J.E. Rycroft, N.R. Horswill and B.P. Williamson, "Simulation and Observation of Transient Effects in Elastohydrodynamic Lubrication", SAE 961143
12. A. Cameron, "Basic Lubrication Theory", Third Edition, (published by Ellis Horwood Ltd.)

## Nanometer Elastohydrodynamic Lubrication

A. J. Moore

BP Oil Technology Centre, Chertsey Road, Sunbury-on-Thames, Middlesex, TW16 7LN, UK

The ultra-thin film optical interferometry technique has extended the exploration of elastohydrodynamic (EHD) lubrication to a regime where film thickness is measured in nanometers. With the gap between the lubricated surfaces corresponding to the width of just a few molecules, investigations are now being made into the validity of classical EHD theory in a regime where it may no longer be appropriate to treat the lubricant as a continuum. Indications, so far, have been mixed. Some fluids appear to conform to EHD behaviour quite closely while others do not. Why this should be so has yet to be established.

This paper examines the behaviour of EHD oil films in the light of the knowledge of confined liquid films gained from surface force apparatus (SFA) studies. To allow comparisons be made with EHD behaviour, a new series of experiments are presented for a range of liquids of known molecular structure. Results support the view that some liquids form immobile molecular layers on rolling surfaces of the type identified by SFA experiments. This type of layer behaves as part of the surface for the time that it spends within the contact, supplementing the film formed by elastohydrodynamic action in a simple additive manner.

Somewhat different behaviour is seen for polar molecular species, for which a step change in effective viscosity is identified at a critical value of film thickness. Once again, though, elastohydrodynamic behaviour appears to remain quite normal once the change in viscosity has been completed.

### 1. INTRODUCTION

It has long been accepted that the thickness of the oil film in a conventional elastohydrodynamic (EHD) contact is determined by the effective viscosity of the lubricant in the inlet region. For Newtonian lubricants, the effective viscosity at any temperature is defined by the viscosity at atmospheric pressure and the response of viscosity to pressure within the inlet region. For non-Newtonian oils, the response of viscosity to shear must also be taken into account. The term "conventional" is used here to categorise conditions where the thickness of the oil film is comparable with, or greater than, the combined surface roughness and both are large in relation to the molecular dimensions of the lubricant. It

is then appropriate to treat the lubricant as a continuum, to assume that shear commences at the oil-surface interface and to either ignore the influence of surface roughness or treat it as a secondary consideration.

Such an approach has proved entirely satisfactory until recently since the regime of behaviour where it might not be valid could not be seen. This situation has changed with the development of the ultra-thin optical interferometry technique for measuring oil film thickness [1]. Films of molecular dimensions can now be measured with sub-nanometer accuracy. Not surprisingly, perhaps, the behaviour found in such a domain does not always follow the predictions of classical EHD theory. It does depend on the molecular structure of the lubricant but not according to an easily

identifiable set of rules. While structural features of both base oil and additive components influence behaviour in the thin film regime [2, 3, 4, 5, 6, 7], attention is devoted here to the more fundamental aspects on the lubrication phenomenon and hence on the behaviour of base oils.

The prospect of stable elasto-hydrodynamic oil films enduring at the nanometer level raises a number of questions that are not easily answered. At the more detailed level they include: what is the viscosity of the oil? where is the plane of zero slip? what is the influence of surface roughness? where does fluid film lubrication end and boundary lubrication begin?

In seeking answers to these question, resort will initially be made to the knowledge of confined liquid films gained from studies based on the surface force apparatus (SFA). Although the conditions of pressure and shear in SFA experiments are very mild compared with those of the EHD contact, a view of the molecular behaviour of liquids can be formed that can at least be tested against observed EHD behaviour. Since the body of work available for such purposes remains slender at present, additional experiments have been conducted on a range of fluids of known molecular structure.

## 2. THE BEHAVIOUR OF LIQUIDS IN THE SURFACE FORCE APPARATUS

Surface force apparatus studies involve determinations of the equilibrium forces between two very smooth surfaces as a film of liquid is squeezed between them [8, 9, 10]. Alternatively, a small oscillation may be applied to the film so that the response of the liquid to shear may be observed [11, 12]. The surfaces employed are usually molecularly smooth sheets of mica.

From the response of liquids to shear, three flow regimes have been identified [10, 13]. When film thickness is large, i.e. greater than about 10 molecular diameters, the liquid flows hydrodynamically from the contact with the viscosity of the bulk fluid.

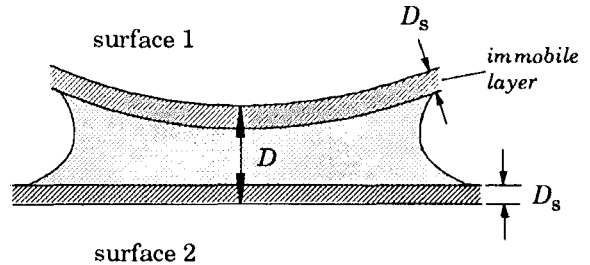


Figure 1. Confined liquid films in surface force apparatus experiments

However, an “immobile” layer, one or two molecular diameters thick, forms on each of the two surfaces and does not participate in the flow; these layers are represented by the films of thickness  $D_s$  in Figure 1. At a critical value,  $D_c$ , of film thickness, flow ceases to behave in a classical hydrodynamic manner and the liquid exhibits the behaviour of a “confined” film. Finally, hard wall behaviour is observed when the immobile layers ultimately make contact; the layers then follow the elastic deformation of the underlying surfaces.

It should be emphasised that, used in this context, the term “immobile” is not meant to imply that molecules are static, only that movement parallel to the surface is slow compared with the time-scale of experimental observations. Movement normal to the surface is not necessarily affected and molecules may continue to exchange rapidly with those adjacent to it.

In the “confined” regime, so-called because behaviour there is only found for liquids confined between two surfaces, fluids of relatively simple structure may form quasi-discrete molecular layers. This only occurs, however, if the bounding surfaces are themselves molecularly smooth [14]. As the film is compressed, a repulsive force must be overcome as each successive molecular layer is squeezed out of the contact and the force-distance relationship becomes oscillatory. The forces which give rise to this type of characteristic are known as structural or

solvation forces [15]. Films which behave in this way are found to be more solid-like than liquid-like in their response to shear [16, 17].

Simple molecular species, such as cyclohexane and the n-alkanes, give rise to particularly strong structural forces, reflecting the ease with which they form ordered molecular layers. The periodicity of the oscillatory force corresponds to the width or diameter of the species concerned, 0.6 nm for cyclohexane, and 0.4 nm for n-alkanes such as n-tetradecane and n-hexadecane [9, 17]. The figure for the n-alkanes, it will be noted, reflects a high degree of molecular alignment in the direction of shear.

Side-branching, even in the form of a single methyl group, destroys the capacity of higher molecular weight alkanes to form ordered structures [16]. 2-methyloctadecane, for example, exhibits a monotonic force-distance relationship in confined films and forms an immobile layer 1.2-1.5 nm in thickness. 2-methylundecane shows similar behaviour to 2-methyloctadecane, as does a white oil. However, the lower molecular weight compound 2-methyloctane shows one oscillation in the force-distance relationship, of period 0.4 nm.

Surface roughness has been shown to exert very little influence on the thickness of immobile layers [13]. For n-dodecane, a layer about one molecular width in thickness, i.e.

0.4 nm, has been found to form on surfaces ranging from 2 to 50 nm in peak-to-valley roughness. The elemental composition of the surface material also seems not to be important.

Molecular structure does exert a recognisable influence, as illustrated by the results of Georges et al [13] reproduced in Table 1. Immobile layer thicknesses for a range of fluids of similar molecular size varies by a factor of five and the thicknesses,  $D_c$ , of the confined film by a factor of four.  $D_s$  for the linear species n-dodecane again corresponds to its molecular width while that for the roughly spherical species octamethylcyclotetrasiloxane equates to its molecular diameter. Confined layer behaviour begins at a film thickness,  $D_c$ , of about five molecular diameters. In the tests involving cobalt surfaces represented in Table 1, n-hexadecane yields higher values of both  $D_s$  and  $D_c$  than n-dodecane, suggesting either a lower degree of molecular alignment or more than one molecular layer within the immobile layer.

For the semi-rigid molecule 2,4-dicyclohexyl-2-methylpentane (the traction fluid known commercially as Santotrac 40),  $D_s$  again corresponds to an immobile layer thickness of more than one molecular width or length. The behaviour of this fluid in the confined domain was elastic and suggested

Table 1  
Characteristics of liquids in drainage experiments between smooth cobalt surfaces [13]

| Liquid                           | Formula           | Behaviour  | $D_s$ / nm | $D_c$ / nm |
|----------------------------------|-------------------|------------|------------|------------|
| n-dodecane                       | $C_{12}H_{26}$    | flexible   | 0.4        | 2.4        |
| n-hexadecane                     | $C_{16}H_{34}$    | flexible   | 1.15       | 4.4        |
| 2,2,4,4,6,8,8-heptamethylnonane  | $C_{16}H_{34}$    | rigid      | 0.9        | 3.5        |
| 2,4-dicyclohexyl-2-methylpentane | $C_{18}H_{34}$    | semi-rigid | 2.0        | 9.5        |
| octamethylcyclotetrasiloxane     | $[(CH_3)_2SiO]_4$ | rigid      | 0.8        | 6.0        |

that molecules were both aligned and entangled.

### 3. THIN FILM EHD BEHAVIOUR

Pressures, shear rates and shear stresses in EHD contacts are orders of magnitude higher than those arising in SFA experiments. It is not obvious, therefore, that the attributes of liquids in SFA studies will persist in EHD oil films. Surface roughness considerations probably rule out the possibility of highly ordered films being formed but the prospects for immobile layers are more difficult to judge.

Evidence that low molecular weight polymers form immobile layers has been presented by Cann et al [18]. A series of polyisoprene fluids, ranging from 1180 to 62,800 in molecular weight, formed layers two radii of gyration thick, in total, corresponding to a single layer of coiled polymer on each surface. On halting the rolling motion, a residual film was observed which decreased in thickness at an approximately exponential rate.

If molecular influences go no further than the immobile layer, thin EHD contacts might take the form shown in Figure 2. This represents a contact of the usual shape with an immobile layer of aligned molecules superimposed on each of the rolling surfaces. The immobile layer effectively forms part of the surface and follows the deformation of the surface as it moves through the contact. Shear begins at the interface between the immobile layer and a fluid film conforming to classical EHD theory.

For such a situation, the total thickness of the oil film at the centre of the contact is given by

$$h = h' + h_c \quad (1)$$

where  $h' = 2D_s$  and  $h_c$  is the central film thickness defined by EHD theory.

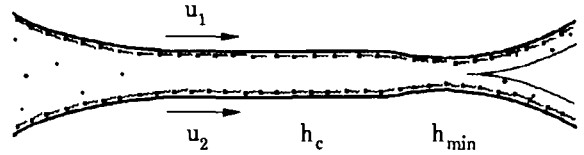


Figure 2. Elastohydrodynamic oil film with an immobile layer, of thickness  $D_s$ , on each surface

Although immobile layers have not been identified as such for lubricant base oils, departures from classical EHD behaviour have been observed in the film thickness regime below 10 nm [3, 4]. An "excess" film thickness occurs in this domain which has been interpreted in terms of a rise in effective viscosity with narrowing contact width [4]. Estimates of the film thickness,  $h'$ , below which such behaviour begins to become significant are given in Table 2. Comparison with molecular dimensions, also taken from [4], does not reveal an obvious relationship with molecular size.

Guangteng and Spikes [4] observed in their study of these fluids that film thickness rapidly fell to zero when the movement of the rolling surfaces was halted. No solid film thus remained to account for the anomalously high film thicknesses they had observed at low rolling speeds. They also noted that two fluids, n-hexadecane and 2,4-dicyclohexyl-2-methylpentane, continued to obey the linear relationship between  $\log(h_c)$  and  $\log(\text{speed})$  predicted by EHD theory. This allowed surface roughness effects to be ruled out as a possible source of the anomalies observed. Examination of their results suggests that the argument is strong when applied to 2,4-dicyclohexyl-2-methylpentane but less so for n-hexadecane. The speed exponent for this fluid, at about 0.5, is much lower than that predicted by theory and a symptom of a significant non-

Table 2

Estimates of  $h'$  based on the EHD film thickness measurements of Guangteng and Spikes [4].

| Fluid                            | Molecular dimensions / nm             | $h^\dagger$ / nm | $h'$ / nm |
|----------------------------------|---------------------------------------|------------------|-----------|
| n-hexadecane                     | 2.2 length, 0.4 width                 | ?                | ?         |
| di(2-ethylhexyl)sebacate         | 1.0 (ester group + alcohol chain)     | 4                | 1.0       |
| di(2-ethylhexyl)phthalate        | 1.0 (ester group + alcohol chain)     | 10               | 1.5       |
| silicone                         | 0.7 (2 units of chain, SiO-SiO-)      | 7                | 1.0       |
| synthetic hydrocarbon            | 2.3 length, 1.3 width, 0.25 thickness | 3                | 0.6       |
| 2,4-dicyclohexyl-2-methylpentane | 1.3 length, 0.6 width                 | <1               | -         |

$h^\dagger$  = thickness of non-linear region

conformance of some description.

Visual inspection of the film thickness data reported by Guangteng and Spikes suggests that the presence of immobile layers could equally well be invoked as an explanation for the trends observed. Estimates of  $h'$  are included in Table 2. Each is comparable with the dimensions of individual molecules and suggests that the immobile layer is no more than one or two molecules in width. Results for n-hexadecane are again considered uninterpretable while those for 2,4-dicyclohexyl-2-methylpentane do not support the presence of immobile layers.

Examples of the behaviour predicted by equation (1) when  $h'$  takes the values listed in Table 2 are illustrated for di(2-ethylhexyl)sebacate and di(2-ethylhexyl)phthalate in Figure 3. Theoretical values of central film thickness,  $h_c$ , are defined by the Hamrock and Dowson [19] expression:

$$h_c = 2.69\alpha^{0.53}(\mu\eta_0)^{0.67}KR^{0.46}W^{-0.067}E^{-0.073} \quad (2)$$

where  $\eta_0$  is the viscosity at atmospheric pressure,  $\alpha$  the pressure-viscosity coefficient,  $W$  the applied load,  $E$  the effective elastic modulus,  $R$  the effective radius and  $K$  a geometric parameter equal to 0.706 for circular point contacts. Predicted film thicknesses, in Figure 3, provide excellent representations of the behaviour observed for

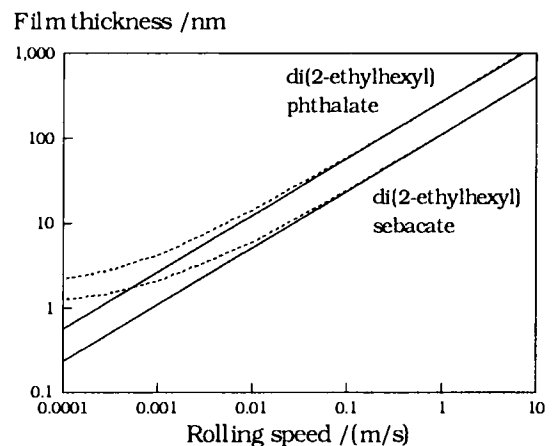


Figure 3. Predicted film thickness at 30 °C for di(2-ethylhexyl)sebacate (—  $h'=0$ , ----  $h'=1.0$  nm) and di(2-ethylhexyl)phthalate (—  $h'=0$ , ----  $h'=1.5$  nm).

the fluids concerned, di(2-ethylhexyl)phthalate revealing non-linearity in the  $\log(h_c)$  versus  $\log(u)$  relationship at about 10 nm film thickness and di(2-ethylhexyl)sebacate at about 4 nm.

#### 4. FILM THICKNESS STUDIES FOR MODEL LIQUIDS

Studies are reported here of the thin film EHD behaviour of a series of liquids of known molecular structure. Film thicknesses are determined for two simple and one



complex hydrocarbon and a single mono-ester. Comparison is finally made with the behaviour of a hydrocracked base oil, with and without a performance additive package.

#### 4.1. Experimental

Film thickness was determined by the ultra-thin film optical interferometry technique developed by Johnson et al [1]. Details of the experimental methods involved have been described elsewhere [2, 3, 6, 7].

The specimen configuration consists of a steel ball rotating against a coated glass disc at a condition close to pure rolling. The glass disc is coated first with chromium and then with a "spacer-layer" of silica, the purpose of the latter being to act as an artificial film of oil and allow constructive interference to occur at any real value of oil film thickness. Film thicknesses is deduced from shifts in the wavelength of constructive maxima, as determined by a diffraction grating spectrometer. The apparatus and computer system used to measure film thickness were supplied by the Imperial College Tribology Section and PCS Instruments Ltd., respectively.

Specimen properties and contact conditions between ball and disc were as summarised below.

Glass disc:

|                          |        |
|--------------------------|--------|
| Elastic Modulus          | 75 GPa |
| Poisson's Ratio          | 0.220  |
| R <sub>a</sub> roughness | 10 nm  |

Steel ball:

|                          |         |
|--------------------------|---------|
| Elastic Modulus          | 207 GPa |
| Poisson's Ratio          | 0.293   |
| Radius                   | 9.5 mm  |
| R <sub>a</sub> roughness | 10 nm   |

|                        |           |
|------------------------|-----------|
| Effective Modulus, $E$ | 116.9 GPa |
| Effective Radius, $R$  | 9.5 mm    |

|                     |          |
|---------------------|----------|
| Load, $W$           | 20 N     |
| Max. Hertz Pressure | 0.53 Gpa |

Each reported value of film thickness is

the mean of either 10 or 15 consecutive measurements taken at a set value of rolling speed. The standard deviation of data sets typically varied from 1 to 2.5 nm and the standard error of mean film thickness values from about 0.3 to 0.6 nm. Above 10 nm, the repeatability of film thickness measurements was generally better than  $\pm 10\%$ . Below 10 nm, behaviour tended to be more variable.

Experiments were carried out in an open lubrication laboratory with no control of ambient temperature or humidity. The purity of the liquids examined was typically 95%.

#### 4.2. Cyclohexane and n-tetradecane

These two liquids feature prominently in SFA studies because of the readiness with which they form structured films. Viscosities are very low even at room temperature, 1 mPa.s for cyclohexane and 2 mPa.s for n-tetradecane. Despite this, the fluids acted as good lubricants and could be examined without damage to the silica spacer layer.

Film thickness measurements, in Figure 4, show that classical EHD theory was not obeyed by either fluid. The relationship between  $\log(h)$  and  $\log(u)$  does not take the linear form predicted by equation (2).

If immobile layers are assumed to contribute to film thickness in the manner represented by equation (1), the total observed film thickness,  $h$ , consists of two immobile layers separated by a fluid film of the type predicted by EHD theory. For cyclohexane a single layer of molecules will be 0.6 nm thick, corresponding to a value of  $h'$  of 1.2 nm. Assuming this to be so, Figure 5 shows that a logarithmic plot of the fluid film component,  $h-h'$ , against rolling speed lies in good accord with classical EHD theory. The slope of the plot is 0.67.

A similar treatment of the results for n-tetradecane suggested that  $h'$  was about 2.3 nm. On this basis, the behaviour of the fluid film component,  $h-h'$ , is found to lie in fairly good accord with EHD theory, in Figure 6, yielding a speed exponent of 0.70.

The implied thickness,  $D_s$ , of the

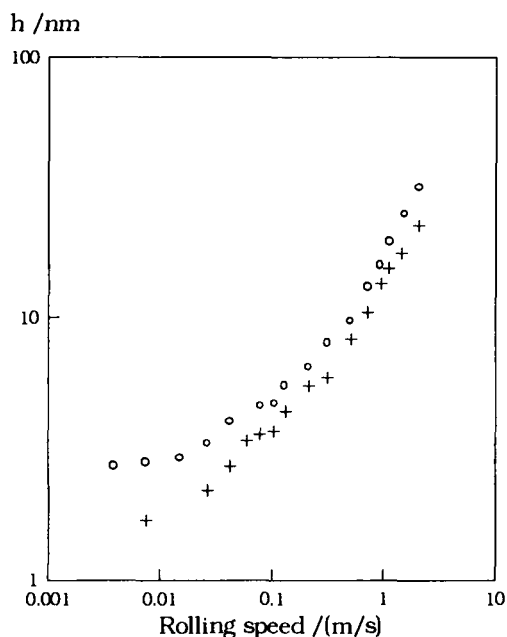


Figure 4. Film thickness at 30 °C for cyclohexane (+) and n-tetradecane (o)

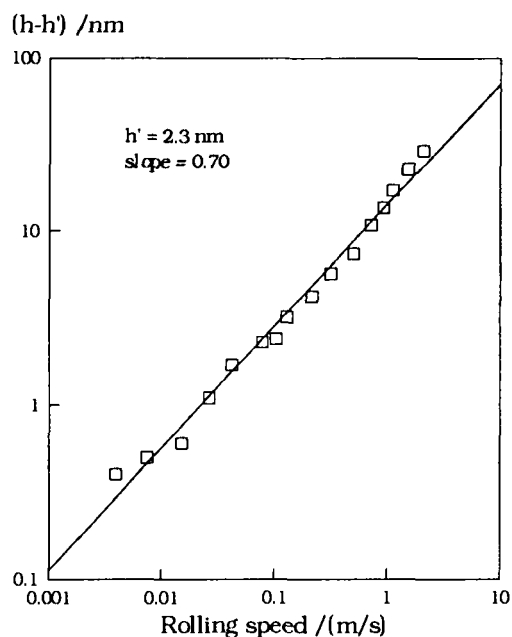


Figure 6. Fluid film component for n-tetradecane at 30 °C assuming  $h'=2.3$  nm

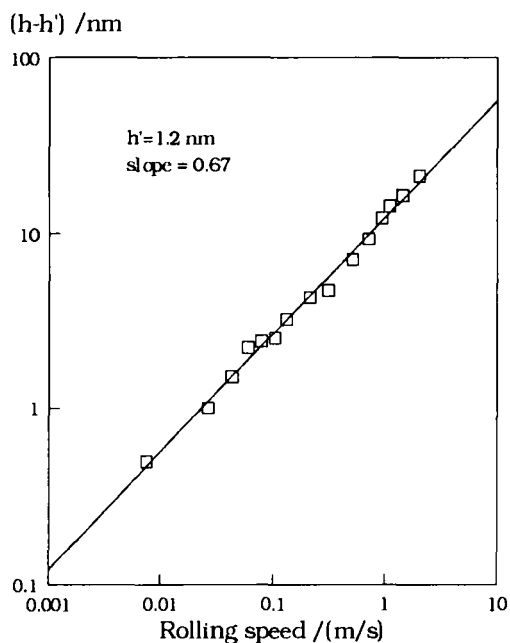


Figure 5. Fluid film component for cyclohexane at 30 °C assuming  $h'=1.2$  nm

immobile layer for n-tetradecane is 1.15 nm, or about three molecular widths. This compares with a value of 0.7 nm, or two molecular widths, for this fluid in SFA experiments carried out with mica surfaces [10] and a value of 1.15 nm for n-hexadecane when cobalt surfaces were used [13].

#### 4.3. 11,13-dioctyl-11-methyltricosane

11,13-dioctyl-11-methyltricosane is a much larger  $C_{40}$  hydrocarbon featuring two  $C_8$  side-chains near the centre of the molecule. It more closely represents the paraffinic content of mineral oils than do the n-alkanes.

No evidence of immobile layers can be deduced from the film thickness behaviour presented in Figure 7. Speed exponents listed in Table 3 lie close to the theoretical value of 0.67 at each temperature, again suggesting that behaviour remains in consistently good accord with EHD theory.

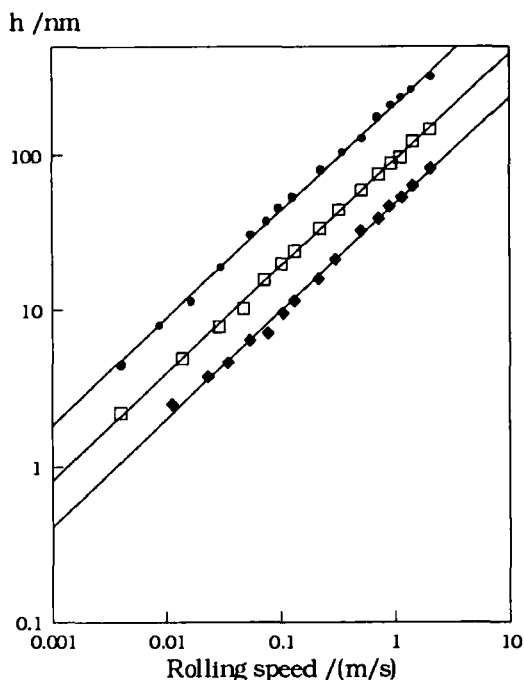


Figure 7. Film thickness for 11,13-dioctyl-11-methyl-tricosane at 30 °C (●), 60 °C (□) and 90 °C (◆)

Table 3.  
Speed exponents for 11,13-dioctyl-11-methyl-tricosane

| $\theta / ^\circ\text{C}$ | $d \log(h)/d \log(u)$ |
|---------------------------|-----------------------|
| 30                        | 0.687                 |
| 60                        | 0.687                 |
| 90                        | 0.689                 |

#### 4.4. Isopropyl palmitate

The mono-ester isopropyl palmitate,  $\text{CH}_3(\text{CH}_2)_{14}\text{CO}_2\text{CH}(\text{CH}_3)_2$ , is a more polar compound based on a straight chain,  $\text{C}_{16}$  carboxylic acid. Figure 8 shows that film thickness at 30 °C varies at a rate consistent with theory down to a separation of about 7 nm. Below that level, the behaviour observed may signify the presence of immobile layers

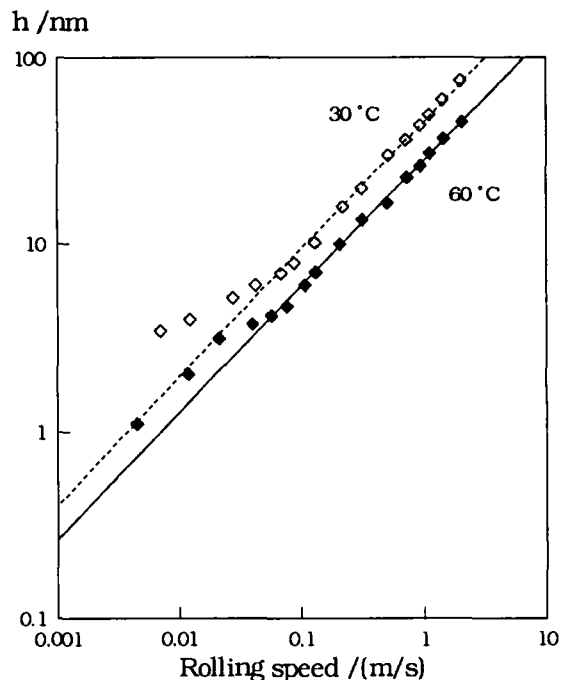


Figure 8. Film thickness for isopropyl palmitate at 30 °C and 60 °C

or it may represent an incomplete version of the behaviour seen at 60 °C.

At 60 °C the theoretical power law is observed down to a film thickness of about 4 nm but a step-change then appears to occur in effective viscosity. Thereafter, behaviour continues to follow the form expected of a conventional EHD oil film. No indication of immobile layer behaviour can be detected as film thicknesses varies down to 1 nm.

An explanation for the change in effective viscosity seen at 60 °C may be given by the micropolar theory of molecular (or granular) behaviour [20, 21]. The theory predicts changes in the viscosity of a liquid containing polar molecular species when film thickness falls to a level that restricts the range of movements available to the polar entities. In the present instance, the critical value of central film thickness is 4 nm and the important range of separations in the

inlet region about 4 to 8 nm. This corresponds to about two to four lengths of the isopropyl palmitate molecule.

#### 4.5. Commercial lubricants

In two respects, the behaviour reported in preceding sections for model fluids are reflected by the characteristics of more complex commercial lubricants [6]. Results for a hydrocracked base oil, with and without an additive system, are reproduced Figure 9. The base oil, like the  $C_{40}$  hydrocarbon in Figure 7, gives no evidence of immobile layers at the temperature 100 °C and yields a speed exponent very close to the theoretical value. The additive solution also gives no sign of immobile layers being present but does show an apparent transition in effective viscosity at the film thickness of 5 nm. This is clearly similar to the behaviour of isopropyl palmitate in Figure 8. More explicitly than in the case of isopropyl palmitate, however, a link is found between the introduction of polar molecules into a lubricant and a step change in viscosity that takes place at a critical value of film thickness.

### 5. CONCLUDING DISCUSSION

It is tempting, but possibly incorrect, to infer from the results presented here that molecular structure differentiates the tendency of liquids to form immobile layers. Unfortunately, variations in both structure and temperature occur together in this study. For practical reasons, fluids of simple molecular structure have, so far, only been examined at 30 °C. Fluids of more complex structure are also much more viscous at this temperature and yield a higher range of film thickness values. Immobile layers then become more difficult to identify. Film thickness can be reduced by raising the temperature but this introduces another potentially important variable.

A technical solution to the problem experienced here has already been described

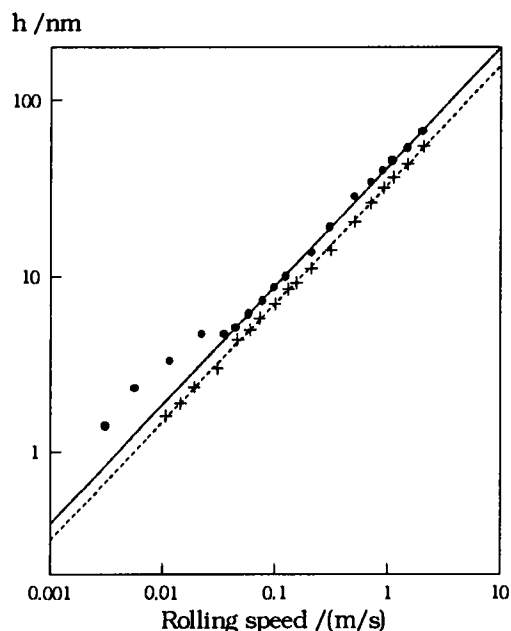


Figure 9. Film thickness at 100 °C for hydrocracked base oil (+) and hydrocracked base oil plus additive system (o)

in the literature [3]. It involves reducing the lower limit to the range of rolling speed to enable very thin films to be observed for the more viscous fluids. To do this, multiple samples of film thickness must be taken around the circumference of the disc in order to keep the time-scale of measurements within acceptable bounds.

Applied to 2,4-dicyclohexyl-2-methylpentane, this technique has allowed film thicknesses as low as 1.2 nm to be observed at 25 °C, with little evidence of the type of behaviour associated with immobile layers. This is in marked contrast to the behaviour seen in SFA experiments where the same fluid forms a layer about 2 nm thick (see Table 1). Studies of structural forces in confined liquids indicate that small compact molecules are more strongly attracted to surfaces than large complex ones. The possibility can hence be entertained that complex molecules form relatively weakly

bound immobile layers that are more easily removed by the shear forces encountered in the inlet region.

Of the questions posed at the start of this paper, answers to some seem clearer than others. The question regarding viscosity is difficult to answer in a general way since it depends on the composition of the lubricant and possibly on temperature. Instances have nevertheless been found where the bulk viscosity prevails even in films of nanometer thickness.

Surface roughness does not emerge as an especially important factor in thin film studies. SFA studies suggest that it has remarkably little impact on the thickness of immobile layers and this may prove to be true under EHD conditions as well. The influence of immobile layers may well reduce the impact of surface roughness on the potential for surface damage. Unless such layers can be removed from surfaces by shear forces, they are likely to form an important barrier between opposing asperities as they come into contact.

The question regarding the position of the plane of shear is more straightforward. If an immobile layer is present, slip begins at the interface between the immobile layer and the fluid film. Otherwise it remains at the interface between surface and oil.

Finally, the answer to the question of whether molecularly thin EHD films can be differentiated from boundary films seems to be becoming clearer. The behaviours discussed in this paper are entirely those of liquids and the films discussed are films of liquid. Their life-span does not extend significantly beyond the time the lubricant dwells within the contact. Boundary films generally have the attributes of solids and persist on surfaces for longer periods of time.

## 7. ACKNOWLEDGEMENTS

Permission to publish this paper has been given by the British Petroleum Company, plc. The author would also like to thank Miss F. M. Baskerville for assistance

with the film thickness studies.

## 8. REFERENCES

1. Johnson, G. J., Wayte, R. and Spikes, H. A., "The measurement and study of very thin lubricant films in concentrated contacts", *Tribology Trans.*, 1991, 34, 187-194.
2. Cooper, D. and Moore, A.J., "Applications of the ultra-thin elastohydrodynamic oil film thickness technique to the study of automotive engine oils", *Wear*, 1994, 175, 93-105.
3. Guangteng, G. and Spikes, H. A., "Behaviour of lubricants in the mixed elastohydrodynamic regime", *Lubricants and Lubrication, Proceedings of the 21st Leeds-Lyon Symposium on Tribology*, Elsevier, 1995.
4. Guangteng, G. and Spikes, H. A., "Boundary film formation by lubricant base fluids", to be published in *Trib. Trans.*
5. Smeeth, M., Gonsel, S. and Spikes, H. A., "Boundary film formation by viscosity index improvers", to be published in *Trib. Trans.*
6. Baskerville, F. M., and Moore, A. J., "Film thickness anomalies in very thin elastohydrodynamic oil films", *Elastohydrodynamics: Fundamentals and Applications in Lubrication and Traction*, 23rd Leeds-Lyon Symposium on Tribology, 1996.
7. Moore, A. J., Cooper, D. and Robinson, T. M., "Rheological properties of engine crankcase and gear oil components in elastohydrodynamic oil films", *SAE Trans.*, 1994, 103, Section 4, 1352-1364.
8. Horn, R. J. and Israelachvili, "Direct measurement of structural forces between two surfaces in a non-polar liquid", *J. Chem. Phys.*, 75, 1400-1411, 1981.
9. Christenson, H. K., Horn, R. G. and Israelachvili, J. N., "Measurement of forces due to structure in hydrocarbon

- liquids", *Journal of Colloid and Interface Science*, 88, 79-88, 1982.
10. Chan, D. Y. C. and Horn, R. G. J., "The drainage of thin liquid films between solid surfaces", *J. Chem. Phys.*, 83, 5311-5324, 1985.
  11. Israelchvili, J. N., "Measurements and relation between the dynamic and static interactions between surfaces separated by thin liquid and polymer films", *Pure and Appl. Chem.*, 60 (10), 1473-1478, 1988.
  12. Tonck, A., Georges, J. M. Loubet, J. L., J. "Measurements of intermolecular forces and the rheology of dodecane between alumina surfaces", *Colloid and Interface Science*, 126 (1), 1540-1563, 1988.
  13. Georges, J. M., Millot, S., Loubet, J. L. and Tonck, A., "Drainage of thin liquid films between relatively smooth surfaces", *J. Chem. Phys.*, 98, 7345-7360, 1993.
  14. Israelachvili, J. N., "Measurement of the viscosity of liquids in very thin films", *J. Colloid and Interface Science*, 110, 263-271, 1986.
  15. van Megen, W. and Snook, I., "Solvent structure and solvation forces between solid bodies", *J. Chem. Soc.*, 75, 1095-1102, 1978.
  16. Israelachvili, J. N., Kott, S. J., Gee, M. L. and Witten, T. A., "Forces between mica surfaces across hydrocarbon liquids: effects of branching and polydispersivity", *Macromolecules*, 22, 4247-4253, 1989.
  17. Gee, M. L., Mcguiggan, P. M. and Israelachvili, J. N., "Liquid to solid-like transitions of molecularly thin films under shear", *J. Chem. Phys.*, 93 (3), 1895-1906, 1990.
  18. Cann, P. M. and Spikes, H. A., "The behaviour of polymer solutions in concentrated contacts: immobile surface layer formation", *Trib. Trans.*, 37, 580-586, 1994.
  19. Hamrock, B. J. and Dowson, D., "Isothermal elastohydrodynamic lubrication of point contacts", *Trans. A.S.M.E.*, A99, 264-276, 1977.
  20. Prakash, J. and Sinha, P., "Lubrication theory for micropolar fluids and its application to a journal bearing", *Int. J. Engng. Sci.*, 13, 217-232, 1975.
  21. Prakash, J. and Christensen, H., "A microcontinuum theory for the elastohydrodynamic inlet zone", *Trans. ASME, J. Lub. Tech.*, 99, 24-29, 1977.

## Optical Interferometric Observations of the Effects of a Moving Dent on Point Contact EHL

M. KANETA, T. KANADA and H. NISHIKAWA

Department of Mechanical Engineering, Kyushu Institute of Technology,  
1 - 1, Sensuicho, Tobata, Kitakyushu 804, Japan

In 1979, Wedeven and Cusano [1] observed very interesting feature concerning EHL film which was influenced by a moving dent. That is, if the dent is on the faster moving surface, the film shape upstream of the dent is influenced by the dent. Ai and Cheng [2] solved numerically this problem using the multigrid method, and pointed out that the dent is extended in the direction of sliding with a rate approximately equal to the sliding velocity, resulting in the pressure increase at the edge of the dent in the direction of sliding. The present study offers more detail experimental results, by duochromatic optical interferometry, concerning the effects of a moving dent on EHL films.

### 1. INTRODUCTION

The calculated minimum film thickness based on the smooth surface EHL theory is of the same order as the surface roughness of the contacting bodies. Consequently, it is important to clarify the effects of the surface roughness on the behavior of EHL films in order to have a better understanding of the working performance and durability of many machine elements. The present authors have therefore discussed through optical interferometric observations why and how EHL films are influenced by the surface kinematic conditions and the orientation and shape of surface asperities. They have used artificially-produced latticed asperities [3][4], transverse and longitudinal bumps [5][6], a circular bump [7], and a groove [8] formed on highly polished steel balls, and have obtained numerous important findings. However, they have never conducted experiments using artificially-produced dents. This is because these experiments have already been carried out by Wedeven and Cusano [1, 9, 10, 11].

Recently, multigrid technique has enabled to simulate a transient behavior of EHL films induced by moving surface defects such as grooves, bumps, dents and real surface roughness [2, 12, 13, 14, 15]. Hence, it seems to be very necessary to accumulate detailed experimental results in order to have a deep understanding of the effects of surface roughness on

EHL contacts.

The purpose of this study is to investigate the influence of a moving dent on point EHL contacts in more detail by using duochromatic optical interferometry [16].

#### 1.1. Notation

- $a$  = Hertzian contact radius
- $d$  = diameter of dent measured at half the maximum depth
- $E'$  = reduced elastic modulus,  
 $2/E' = (1 - \nu_B^2)/E_B + (1 - \nu_D^2)/E_D$
- $E_B, E_D$  = elastic moduli of steel ball and glass disk
- $G$  = material parameter,  $\alpha E'$
- $h$  = film thickness
- $R$  = radius of steel ball
- $t$  = time
- $u_B, u_D$  = surface velocities of steel ball and glass disk
- $U$  = speed parameter,  $\eta_0(u_D + u_B)/2E'R$
- $w$  = load
- $W$  = load parameter,  $w/E'R^2$
- $x$  = distance from center of dent to that of Hertzian contact in the direction of motion
- $x_{thick}$  = length, in the direction of sliding, of thick film emitted from dent
- $X$  = dimensionless distance,  $x/a$

- $y$  = coordinate perpendicular to  $x$ -axis
- $\alpha$  = pressure coefficient of viscosity
- $\nu_B, \nu_D$  = Poisson's ratios of steel ball and transparent disk
- $\eta_o$  = viscosity at atmospheric pressure
- $\Sigma$  = slide-to-roll ratio,  $2(u_D - u_B)/(u_D + u_B)$

**2. EXPERIMENTAL PROCEDURE**

**2.1. Apparatus and specimens**

Figure 1 shows a schematic diagram of the apparatus used in this study. Contacting surfaces were composed of a precision 25.4mm diameter steel ball and a glass disk of 165mm diameter and 12mm thick, whose lower surface was sputtered with a semi-reflecting chromium layer. The reduced elastic modulus  $E'$  was 117GPa. A center-line average roughness and roundness of the steel ball were about  $0.005\mu\text{m}$  and  $0.13\mu\text{m}$ , respectively.

The ball and glass disk were separately driven by variable speed motors through toothed belts. The surface velocities of the ball and disk could be measured with a rotary encoder attached to the end of each shaft.

A dent was produced onto one part of the ball surface with a spherical cemented carbide tool. Five types of dent, three of which had similar shape and size, were used in experiments. Their styry traces through the deepest portion of each dent are shown in Fig.2.

The optical interferometry technique [16] was used to measure the film thickness distribution. The duochromatic interference fringe pattern obtained by a Xenon light source with a flash duration of  $20\mu\text{s}$  through red and green filters was recorded with a high speed VCR (200 frames per second) and a 35mm camera attached to a microscope. In photographing

with the 35mm camera, the flash of the Xenon lamp was triggered by a signal from the rotary encoder attached to the end of the shaft to which the ball was fastened. The exposure time was fixed by a single discharge from the Xenon lamp, which was short enough to freeze movement. As a result, we could take photographs of EHL films influenced by the dent passing through the contact region at a space of  $55\mu\text{m}$ , although their pictures were not continuous with time. Comparing a series of interferograms recorded with the high speed VCR with that with the 35mm camera, it has been clarified that the change of EHL film caused by a dent passing through the EHL conjunction can be evaluated using interferograms recorded with the 35mm camera. Consequently, in this paper, interferograms obtained with the 35mm camera were used, because of the good resolution.

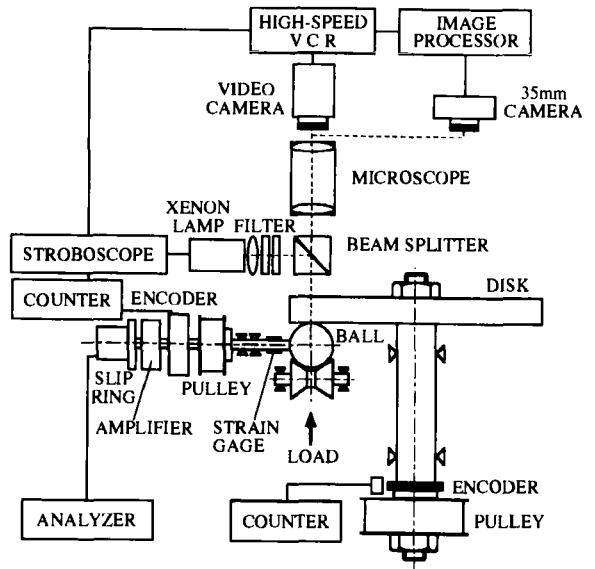


Figure 1. Schematic diagram of experimental apparatus

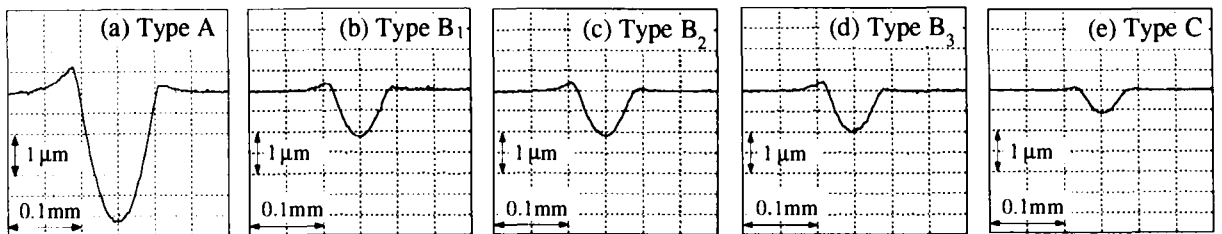


Figure 2. Stylus traces of dent used



## 2.2. Experimental conditions

The lubricating oil used in this investigation was a mineral bright stock having a kinematic viscosity of  $393\text{mm}^2/\text{s}$  at  $40^\circ\text{C}$  and  $30\text{mm}^2/\text{s}$  at  $100^\circ\text{C}$ , a specific gravity of 0.878 at  $5/4^\circ\text{C}$ , and a pressure-viscosity coefficient,  $\alpha$ , of  $22.5\text{GPa}^{-1}$  at  $21.5^\circ\text{C}$  and  $18\text{GPa}^{-1}$  at  $40^\circ\text{C}$ .

The experiments were performed by changing slide-to-roll ratio,  $\Sigma$ , under a constant dimensionless rolling velocity of  $U=9\times 10^{-12}$  or  $4\times 10^{-11}$ . A load of  $w=39.2\text{N}$ , which gave a maximum Hertzian pressure of  $0.54\text{GPa}$  and a Hertzian diameter of  $0.37\text{mm}$ , was applied to the ball against the glass disk by a spring system. The oil temperature in the inlet to the contact was  $21.5\pm 0.8^\circ\text{C}$ . These conditions gave the dimensionless load parameter  $W=2.1\times 10^6$  and the materials parameter  $G=2630$ .

Throughout the experiments, the directions of surface velocities of the steel ball and the glass disk at the contact point were the same; fluid flows from the left to right for all figures shown in this paper.

## 3. RESULTS AND DISCUSSION

### 3.1. Effects of slide-to-roll ratio

Figure 3 shows interferograms observed at various positions when the type  $B_1$  dent passes through the EHL conjunction under conditions of  $\Sigma=1, 0$  and  $-1$  with  $U=9\times 10^{-12}$ . The values in the interferograms indicate film thicknesses in  $\mu\text{m}$ . Venner [12] and Ai and Cheng [2] have pointed out through their numerical simulations that the flow in the EHL conjunction is mainly dominated by shear flow and pressure induced flow is almost absent due to the very high viscosity. If the pressure-induced flow is dominated by the shear flow, the film thickness in the EHL conjunction is expressible, from the Reynolds equation, in the form

$$h = h\left(x - \frac{u_D + u_B}{2}t, y\right)$$

This means that a local film shape moves through the EHL conjunction approximately at the average

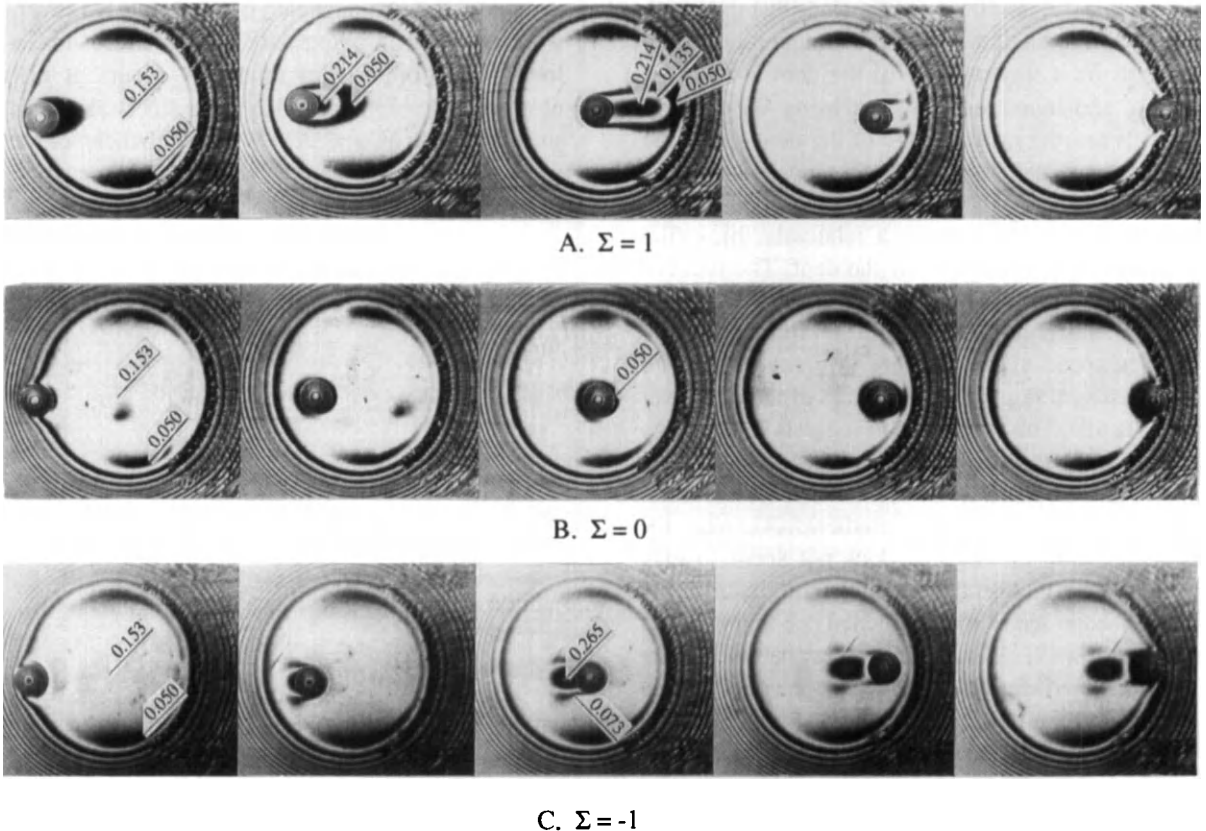


Figure 3. Interferograms with type  $B_1$  dent passing through contact area with  $U=9\times 10^{-12}$

speed of the contacting surfaces, while preserving its thickness and shape. The authors have proved this phenomenon experimentally using the optical interferometry technique [5][6][7], and pointed out that the film thickness distribution is significantly influenced by surface kinematic conditions.

Under condition of  $\Sigma > 0$  where the speed of the glass disk is faster than that of the ball with a dent, the average speed of fluid in the EHL conjunction is faster than the speed of the dent. Therefore, when the dent is in the inlet region of the EHL conjunction, a local reduction in film thickness takes place at a certain region just downstream of the dent as shown in Fig.3A, because of a notable side leakage of the entraining fluid as well as a fall of the hydrodynamic pressure generation by the wedge film action. The film thicknesses at the other region are the same as the smooth surface values. The length of the film reduction area in the direction of sliding was approximated by  $(d/u_b)(u_d + u_b)/2 - d$ , i.e.,  $d\Sigma/(2 - \Sigma)$ , where "d" is the diameter of the dent at half the maximum depth under no-loading condition. As a result, we can conclude that the length of the film reduction area in the direction of sliding depends on a staying time of the dent at the inlet region, and increases with increasing slide-to-roll ratio. When the trailing edge of the dent enters the contact area, the film thicknesses upstream of the dent recover almost completely to the smooth surface values, and the dent emits a relatively thick film into the downstream side of the dent. The reduced film formed at the inlet of the contact area travels through the contact area with approximately the average speed of the surfaces. Moreover, the film thicknesses along the trailing edge of the dent over  $180^\circ$  are thin. This phenomenon suggests that pressure gradients along this portion are very steep. Ai and Cheng [2] have shown by the numerical simulation that there are such pressure gradients. Although the dent has built-up edge, it does not seem to give substantial effect on this phenomenon, because the built-up edge seems to be flattened due to the effects of shear flow [7]. As a result, two very narrow beltlike film reduction areas are produced at the downstream side of the dent. A full recovery to an EHL film based on smooth surfaces is accomplished at the moment when the dent passes over the contact area.

Under pure rolling conditions ( $\Sigma = 0$ ), the influence of the dent is localized to a region around the dent as shown in Fig.3B. It should be noticed that film

thicknesses along the edge of the dent are thin as compared with film thickness observed using smooth surfaces and its reduction rate is slightly larger at the leading and trailing edges of the dent than at the side shoulders of the dent. This phenomenon seems to be closely related to the numerical result obtained by Ai and Cheng [2] that the pressure rises slightly at the side shoulders of the dent and drops at the leading and trailing edges of the dent.

Under conditions of  $\Sigma < 0$  where the average speed of the oil in the EHL conjunction is faster than the speed of the dent, the motion of the fluid in the contact area relative to the dent is opposite to the motion of the entraining fluid. Consequently, the film downstream of the dent is never influenced by the dent. Furthermore, the dent does not bring about noticeable side-leakage for the oil flowing into the upstream side of the dent across the dent when the dent is entering the contact region. Therefore, unlike cases of a groove where the side-leakage takes place along the groove [8], a local reduction in film thickness due to side-leakage does not occur at a certain region just upstream of the dent. However, when the dent is going out of the contact area, a local reduction in film thickness occurs at just upstream side of the dent due to the side-leakage, as shown in Figs.3C and 9C. When the whole of the dent enters the contact area, a thick film is emitted from the dent into the upstream side of the dent, as

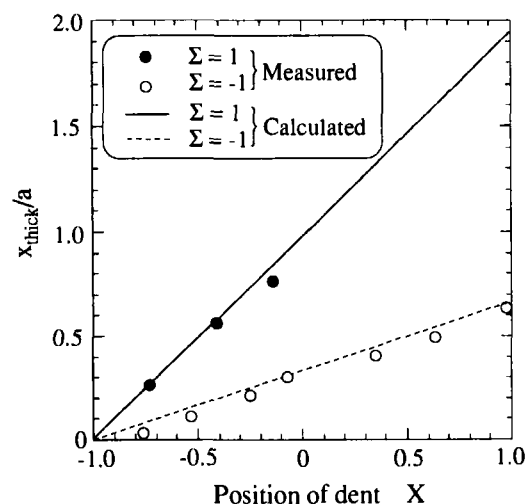


Figure 4. Length, in the direction of sliding, of thick film emitted from dent as a function of location of dent ( $U=9 \times 10^{-12}$ )

shown in Fig.3C. As the dent approaches the exit, its thick film is left within the contact area. Owing to the same phenomenon as the cases of  $\Sigma > 0$ , the film thicknesses along the leading front of the dent over  $180^\circ$  are thin as compared to the smooth surface value. As a result, two very narrow beltlike film reduction areas are produced at the upstream side of the dent shoulders and extend with a speed approximately equal to  $(u_d - u_b)/2$ . Consequently, a full recovery to an EHL film based on smooth surfaces is established after a while when the dent passes over the contact region.

Figure 4 shows the length, in the direction of sliding, of thick film emitted from the dent, i.e., the distance from the leading or trailing edge of the dent to the end of the thick film, as a function of the position of the center of the dent. The position of the dent is specified by  $X=x/a$ , where  $x$  is the distance from the center of the dent to that of the Hertzian contact and "a" is the Hertzian contact radius. The lines in Fig.4 were obtained by multiplying  $|u_d - u_b|/2$  by time after the whole of the dent entered the EHL conjunction. The calculated values almost agree with the observed results. That is, the speeds of the thick oil films being emitted from the dent into the downstream and upstream sides for cases of  $\Sigma > 0$  and  $\Sigma < 0$ , respectively, are  $|u_d - u_b|/2$ .

As has been described in above, the effects of a moving dent on point EHL contacts observed in this study, as a whole, agree well with numerical simulations carried out by Ai and Cheng [2]. A marked difference between numerical and experimental results is the film thicknesses downstream of the dent under conditions of  $\Sigma \leq 0$ . The numerical result shows that the overall film thickness downstream of the dent is increased as compared with the smooth surface value. However, such a phenomenon has never observed within the limits of present experiments. In cases of  $\Sigma \leq 0$ , it can be considered that the film downstream of the dent is never influenced by the dent.

### 3.2. Deformation of dent

Figure 5 shows film thicknesses at the center of the dent as a function of the location of the dent in the direction of motion for different side-to-roll ratios. The plots in Fig.5 were obtained with the type B<sub>1</sub> dent for  $\Sigma = 1.5, 1$  and  $-1$  and with the type B<sub>2</sub> dent, which was almost the same shape and size as the type B<sub>1</sub> dent, for  $\Sigma = 0$  and  $-1.5$ . In Fig.6, the

midplane film profiles in the direction of motion overlaid onto the undeformed dent profiles, where each dent locates near the central position of the EHL conjunction. The dotted line in each figure corresponds to the undeformed profile (stylus trace) of the dent. The position of the stylus trace was determined in conformity with the undeformed dent extending outside the Hertzian contact, and the horizontal line was positioned at the smooth-surface film thickness. Figure 7 shows their enlarged views.

As seen from Figs.5 to 7, under pure rolling conditions, the dent moves through the EHL conjunction while almost maintaining the undeformed shape. However, when sliding is introduced, film thickness within the dent is reduced substantially. That is, the depth of the dent decreases as the dent enters the contact area, and takes a minimum when the dent locates near the central region of the contact area. It should be noted that in cases of  $\Sigma > 0$  the amount of the film reduction is large and almost independent of the values of  $\Sigma$ . However, in cases of  $\Sigma < 0$ , the reduction rate seems to depend markedly on  $|\Sigma|$  and the amount of the film reduction seems to increase with the increase in  $|\Sigma|$ . In order to clarify the reason why such a difference occurs, a load of 39.2N was applied slowly so as not to make an oil entrapment to the ball with the dent against the glass disk, and then the ball and glass disk were moved under various slide-to-roll ratios. In cases of

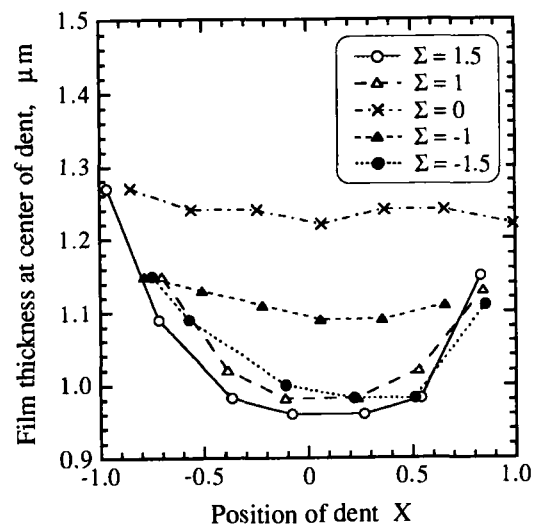


Figure 5. Film thickness at center of dent as a function of location of dent ( $U=9 \times 10^{-12}$ )

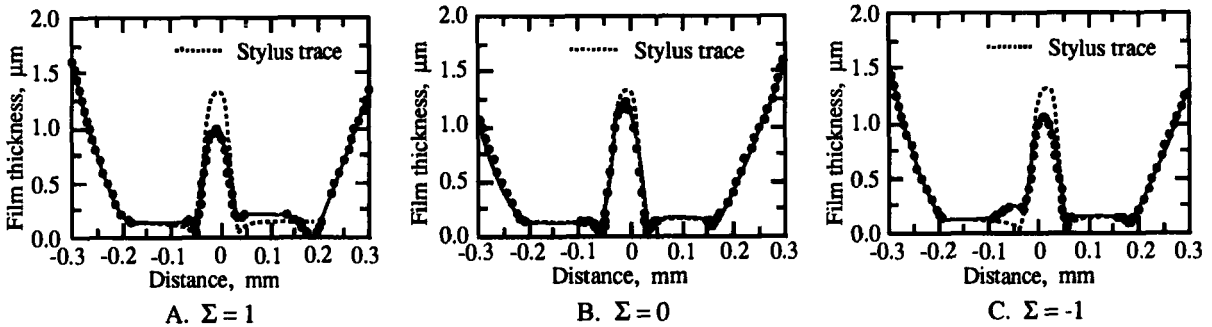


Figure 6. Midplane film profile in the direction of motion (type B, dent,  $U=9 \times 10^{-12}$ )

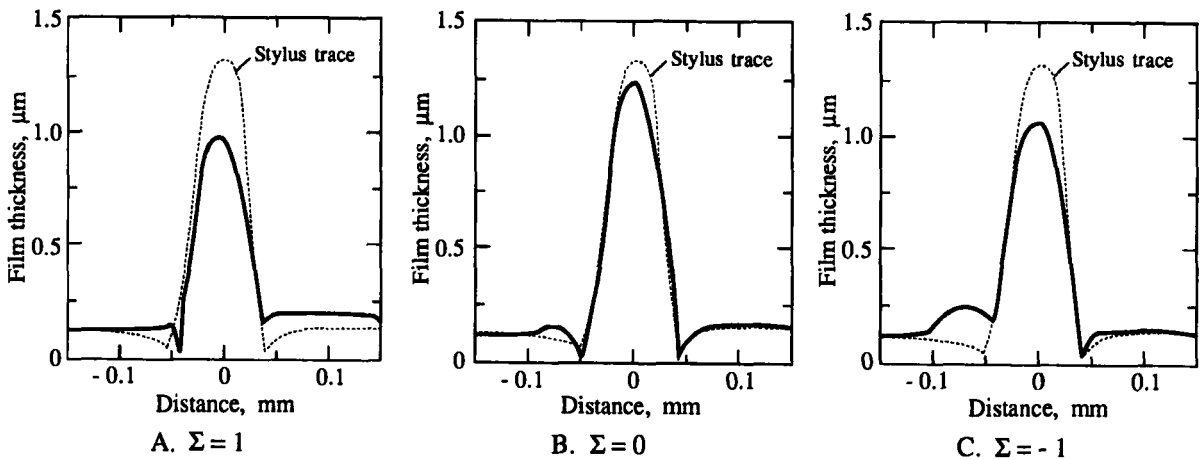


Figure 7. Enlarged views of midplane film profiles shown in Figure 6

$\Sigma > 0$ , a large amount of oil in the dent was discharged immediately after the motion was given. However, in cases of  $\Sigma < 0$ , the discharge of the oil from the dent depends on the slide-to-roll ratio and it is difficult to discharge the oil from the dent under low slide-to-roll ratios. Although further detail experiments may be necessary, these results suggest that the discharge of the oil in the dent due to shear force depends upon a sign of  $\Sigma$ .

It should also be noticed from Figs. 6 and 7 that when the dent exists at the central region of the EHL conjunction, a local reduction in film thickness at the midplane in the direction of motion is significant at the trailing edge of the dent in cases of  $\Sigma > 0$  and the leading edge of the dent in cases of  $\Sigma < 0$ . In cases of  $\Sigma = 0$ , the film reduction occurs at both the leading and trailing edges as has been described.

### 3.3. Effects of dent size

Figures 8 and 9 show typical interferograms obtained with the types A and C dents for  $\Sigma = 1$  and  $\Sigma = -1$  under the same conditions as those for Fig. 3, showing the effect of the size of the dent on EHL films. The amount of side-leakage, which may occur when the dent is entering and going out of the contact area, is controlled by the width and depth of the dent and the overall EHL film thickness; if the dent has a large depth and width, a large amount of side-leakage will be caused. As seen in Fig. 8, with the type A dent, which is the largest of dents used in these experiments, a part of the film downstream of the dent is almost completely collapsed when the dent stays at the edge of the inlet of the contact for  $\Sigma = 1$ , but for  $\Sigma = -1$  a part of the film upstream of the dent is almost completely collapsed when the

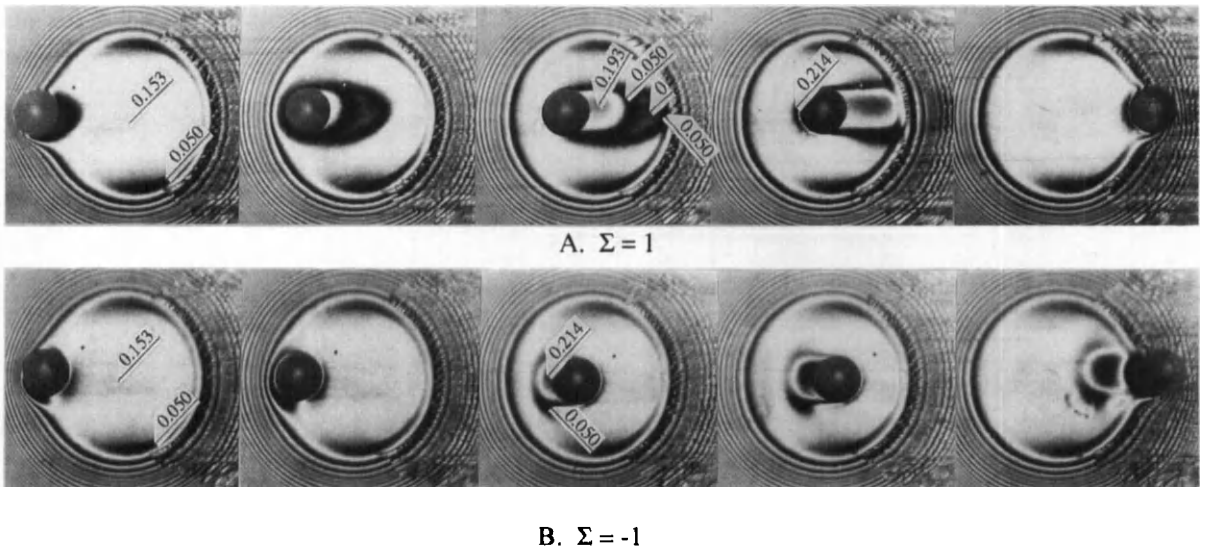


Figure 8. Interferograms with type A dent passing through contact area with  $U=9 \times 10^{-12}$

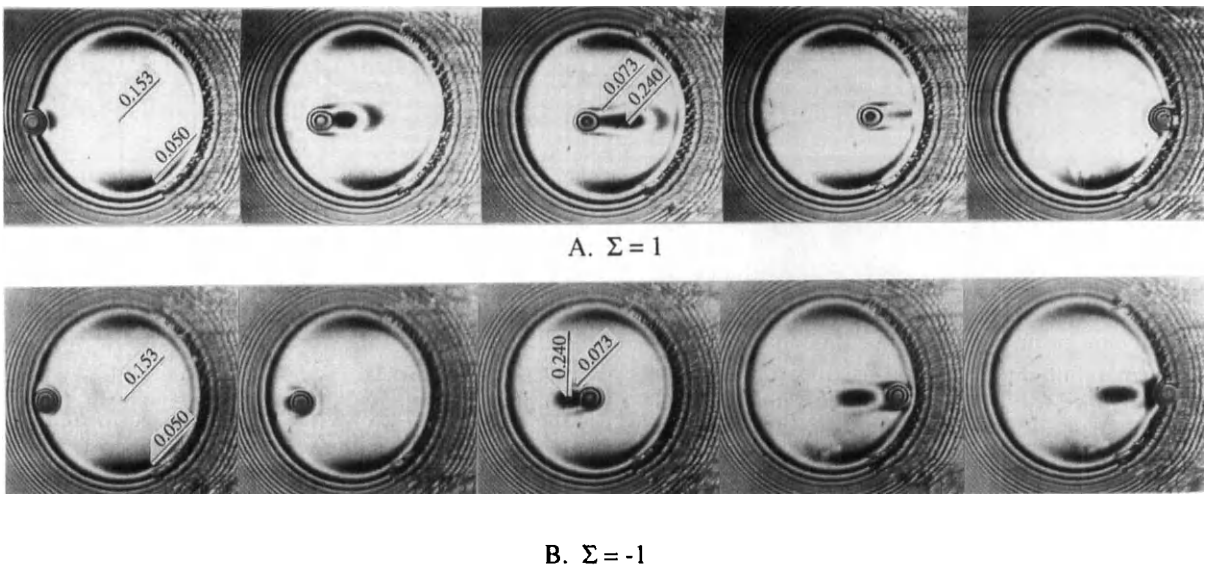


Figure 9. Interferograms with type C dent passing through contact area with  $U=9 \times 10^{-12}$

dent stays at the edge of the exit of the contact. On the other hand, with type C dent (see Fig.9), which is the smallest of the dents, the amount of local reduction in film thickness is small for both cases of  $\Sigma = 1$  and  $\Sigma = -1$ .

The thickness of the film being emitted from the dent into the film reduction area becomes almost independent of the size of the dent, as the dent moves through the EHL conjunction.

### 3.4. Effects of rolling speed

Figure 10 shows the results obtained using the type B<sub>3</sub> dent under conditions of  $\Sigma = 1.5$ , 0 and -1.5 with  $U=4 \times 10^{-11}$ . The overall features concerning EHL films which are influenced by the moving dent are the same as those described in section 3.1. However, it should be noted that film thicknesses in the region where there is no effect of the dent, i.e., film thicknesses based on the smooth surfaces, are

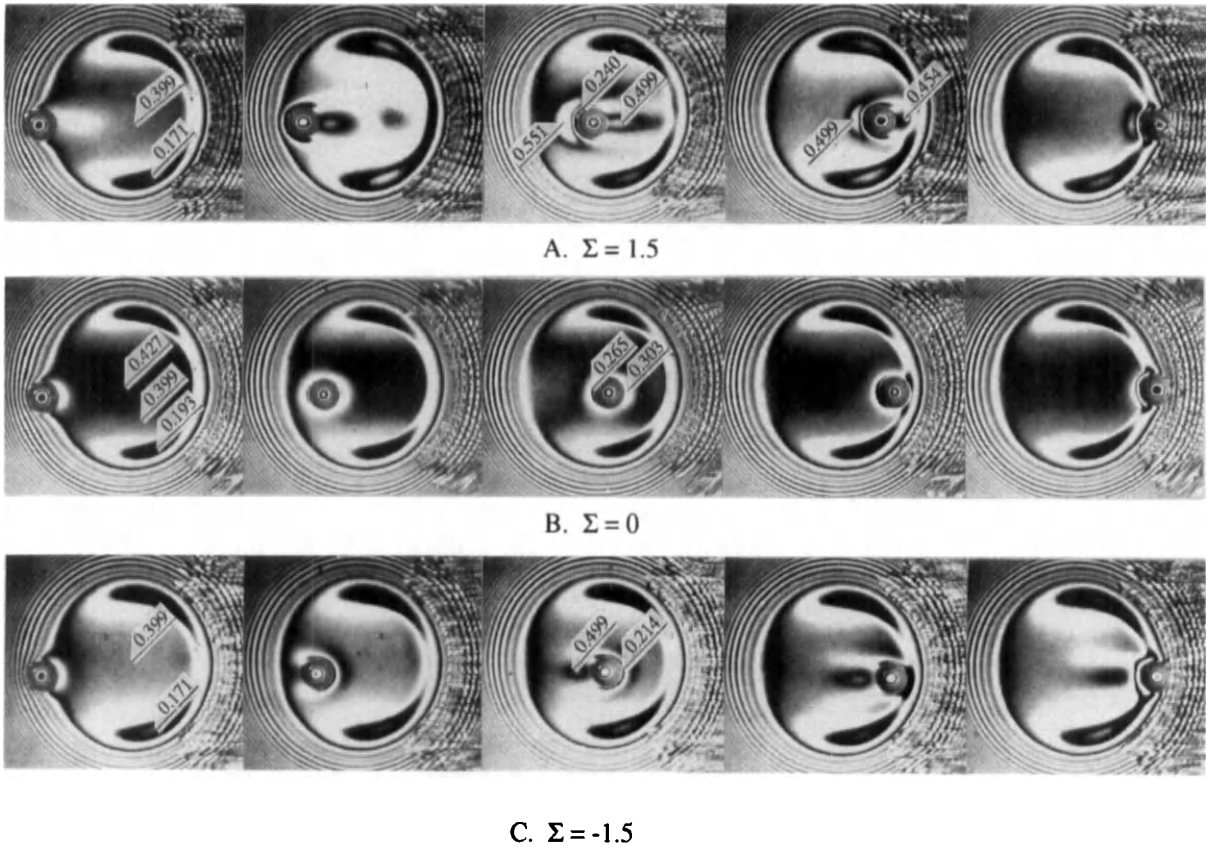


Figure 10. Interferograms with type  $B_3$  dent passing through contact area with  $U=4 \times 10^{-11}$

slightly thinner in cases of  $\Sigma = -1.5$  and  $\Sigma = -1.5$  than in pure rolling. This seems to be influenced by heat generation due to sliding friction, although the temperature rise could not be detected with the thermocouple placed at the entry side of the contact.

When the entraining or rolling speed increases and the overall film thickness increases, the effects of the dent on EHL film seem to be relatively reduced. Figure 11 shows film thicknesses at the center of the dent as a function of the location of the dent corresponding to Fig. 10. When sliding is introduced, film thickness within the dent or the depth of the dent is reduced. The amount of the film reduction is larger for  $\Sigma > 0$  than for  $\Sigma < 0$ . It can also be seen from the comparison of Fig. 10 with Fig. 5 that the reduction rate in the dent depth with  $U=4 \times 10^{-11}$  is lower than that with  $U=9 \times 10^{-12}$ .

Only difference from cases of  $U=9 \times 10^{-12}$  shown in Fig. 3 is that a slightly thick film is formed at a narrow region just up- and downstream of the dent

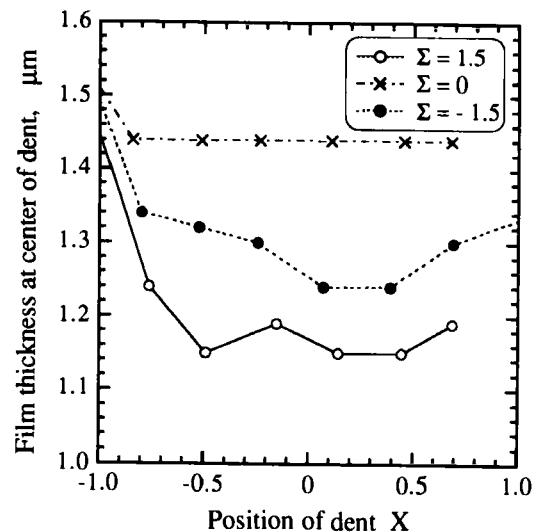


Figure 11. Film thickness at center of dent as a function of location of dent ( $U=4 \times 10^{-11}$ )

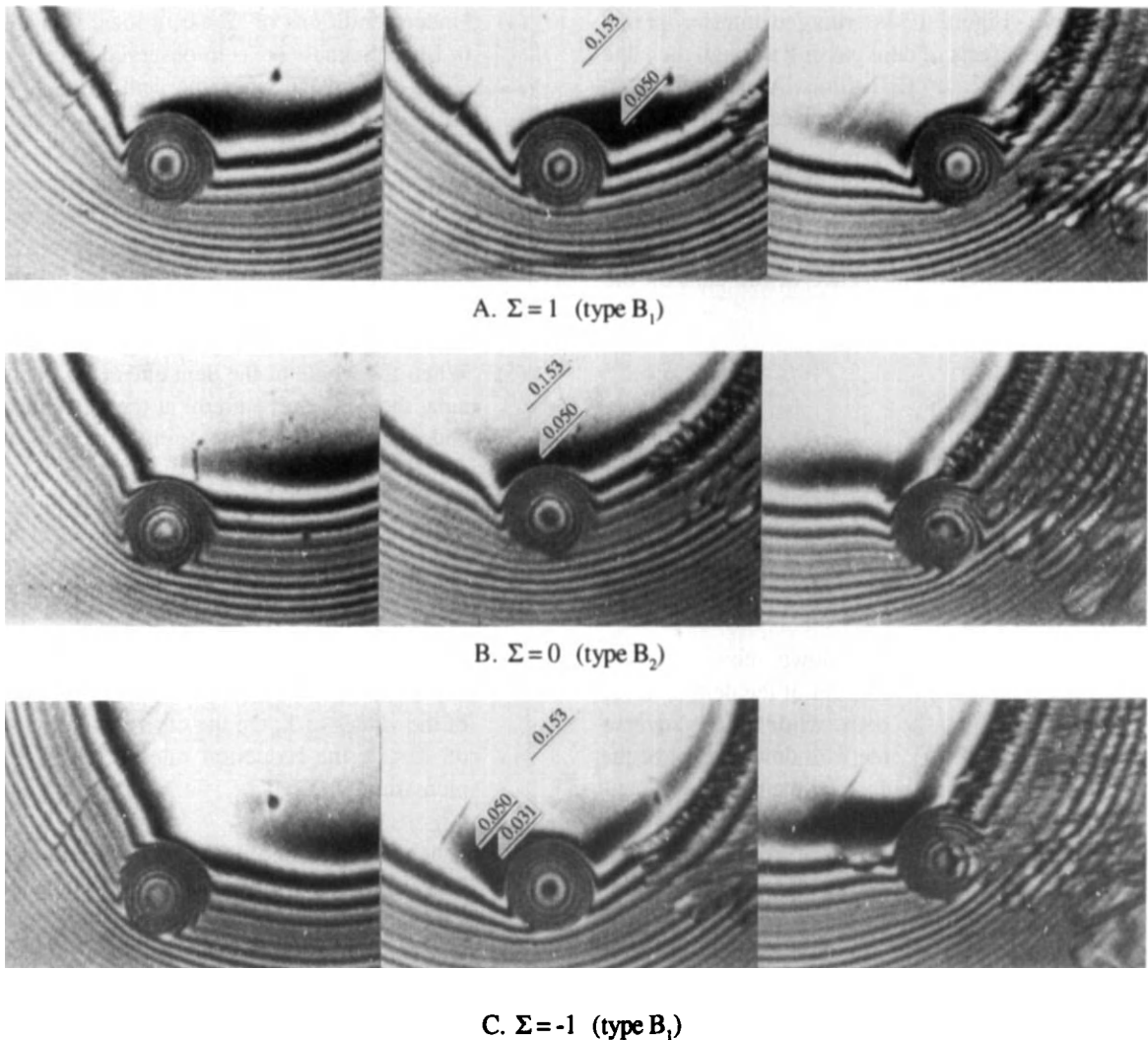


Figure 12. Interferograms with dent passing through edge of contact area with  $U=9 \times 10^{-12}$

according to  $\Sigma = 1.5$  and  $\Sigma = -1.5$ , respectively. The thickness for  $\Sigma = 1.5$  is thicker than that for  $\Sigma = -1.5$ . It should be noted from Fig. 2 that the height of built-up edge of the type B<sub>3</sub> dent is higher at the trailing edge than at the leading edge. Furthermore, the distance between the slightly thick film and the center of the dent does not change by the movement of the dent. These facts suggest that the occurrence of such a slightly thick film is caused by the squeeze film action acting parallel to the contact plane [17][18]. Such a thick film is also observed in Fig.8A. This is because the type A dent has a large built-up edge at the trailing side of the dent, although the rolling speed is lower than that

for Fig.10.

### 3.5. Effects of location of dent

In the previous paragraphs, the behavior of EHL films induced by a dent passing through the middle region of the EHL conjunction has been discussed.

It has been found that the effects of the dent on EHL films are almost the same wherever the dent passes through the contact area if the whole of the dent exists in the contact area. However, if a part of the dent passing through the EHL conjunction is always out of the contact area, there is a little discrepancy in the film behavior, because the EHL film is always influenced by the side leakage induced

by the dent. Figure 12 is enlarged interferograms showing the effects of dent passing through the edge of the contact area on EHL films. A local reduction in film thickness always takes place, while the dent exists in the EHL conjunction, at the down- and upstream sides in the direction of motion of the dent according to the positive and negative values of the side-to-roll ratio. Even in these cases, under pure rolling conditions the influence of the dent on the EHL film is moderate.

#### 4. CONCLUSIONS

The effects of a moving dent on point contact EHL have been examined by direct observations by means of optical interferometry. The main conclusions drawn from the present work are summarized as follows:

- (1) When the dent is on the slower moving surface ( $\Sigma > 0$ ), the film upstream of the dent is never influenced by the dent, while in the reverse situation ( $\Sigma < 0$ ), the film downstream of the dent is never influenced by the dent.
- (2) When the dent passing through the EHL conjunction exists at the inlet region under conditions of  $\Sigma > 0$ , a local reduction in film thickness occurs at a certain area downstream of the dent, because of side leakage induced by the dent. The length of the film reduction area in the direction of sliding increases with increasing  $\Sigma$ . The degree of a local reduction in film thickness depends on the relative size of the dent with respect to the overall film thickness. When the whole of the dent enters the contact area, the reduced film moves through the contact area with approximately the average speed of the contacting surfaces.
- (3) Under pure rolling conditions ( $\Sigma = 0$ ), the variation in film thickness associated with the dent is confined to the vicinity of the dent. Although a local reduction in film thickness occurs at the peripheral edge of the dent, the amount of the film reduction is slightly larger at the leading and trailing edges than at the shoulders of the dent.
- (4) Under conditions of  $\Sigma < 0$ , a local reduction in film thickness so as to observed in cases of  $\Sigma > 0$  takes place when the dent exists at the outlet region. When the dent passes through the contact area, very narrow beltlike film reduction areas are produced at the upstream side of both shoulders of the dent. In cases of  $\Sigma > 0$ , the similar film reduction areas are also produced at the downstream side of the dent shoulders.
- (5) When the whole of the dent enters the contact area, the dent emits the oil at the downstream and upstream sides according to  $\Sigma > 0$  and  $\Sigma < 0$ .
- (6) In cases of  $\Sigma \neq 0$ , the depth of the dent decreases as the dent enters the contact area, and takes a minimum when the dent locates near the central region of the contact. In cases of  $\Sigma > 0$ , the amount of the reduction in the depth of the dent is large and almost independent of the values of  $\Sigma$ . On the other hand, in cases of  $\Sigma < 0$ , the reduction rate increases with increasing  $|\Sigma|$ .
- (7) When a part of the dent passing through the EHL conjunction exists out of the contact area, a local film break down or a local film reduction takes place at the downstream and upstream sides according to  $\Sigma > 0$  and  $\Sigma < 0$ , respectively.

#### ACKNOWLEDGMENTS

The authors wish to offer their thanks to Messrs. T. Eto, H. Masuda and Y. Inoue for their help for this work. The oil was supplied by Idemitsu Kosan Co., Ltd., and the steel balls were supplied by Nippon Seiko K.K. This study was supported by Grant-in-Aid for Scientific Research (No.05452146) from the Ministry of Education, Science and Culture, Japan. The authors are grateful for their supports.

#### REFERENCES

1. Wedeven, L. D. and Cusano, C., Elastohydrodynamic Film Thickness Measurements of Artifi-



- cially Produced Surface Dents and Grooves, ASLE Trans., 22 (1979) 369-381.
2. Ai, X. and Cheng, H.S., The influence of Moving Dent on Point EHL Contacts, Tribology Trans., 37-2 (1994) 323-335.
  3. Kaneta, M. and Cameron, A., Effects of Asperities in Elastohydrodynamic Lubrication, J.Lub. Tech, Trans. ASME, 102 (1980) 374-379.
  4. Kaneta, M. and Kanzaki, Y., Effects of Surface Roughness on Squeeze Film Characteristics in EHL, Tribologist, 36 (1991) 319-326 (in Japanese).
  5. Kaneta, M., Sakai, T. and Nishikawa, H., Optical Interhemispheric Observations of the Effects of a Bump on Point Contact EHL, J. Tribology, Trans. ASME, 114 (1992) 779-784.
  6. Kaneta, M., Sakai, T. and Nishikawa, H., Effects of Surface Roughness on Point Contact EHL, Tribology Trans., 36, 4 (1993) 605-612.
  7. Kaneta, M., Effects of Surface Roughness in Elastohydrodynamic Lubrication, JSME Int. Journal, Series III, 35, 4 (1992) 535-546.
  8. Kaneta, M. and Nishikawa, H., Local Reduction in Thickness of Point Contact EHL Films Caused by a Transversely Oriented Moving Groove and Its Recovery, J. Tribology, Trans. ASME, 116 (1994) 635-639.
  9. Wedeven, L. D., Influence of Debris Dent on EHD Lubrication, ASLE Trans., 21 (1978) 41-52.
  10. Cusano, C. and Wedeven, L.D., Elastohydrodynamic Film Thickness Measurements of Artificially Produced Nonsmooth Surfaces, ASLE Trans., 24 (1981) 1-14.
  11. Cusano, C. and Wedeven, L.D., The effects of Artificially-produced Defects on the Film Thickness Distribution in Sliding EHD Point Contacts, J.Lub.Tech, Trans. ASME, 104 (1982) 365-375.
  12. Venner, C.H., Multilevel Solution of the EHL Line and Point Contact Problems, Ph.D. thesis, Twente University, The Netherlands (1991).
  13. Ai, X. and Cheng, H.S., A Transient EHL analysis for Line Contacts With Measured Surface Roughness Using Multigrid Technique, J. Tribology, Trans. ASME., 116 (1994) 549-558.
  14. Venner, C.H. and Lubrecht, A.A., Numerical Simulation of a Transverse Ridge in a Circular EHL Contact Under Rolling/Sliding, J. Tribology, Trans. ASME, 116 (1994) 751-761.
  15. Venner, C.H. and Lubrecht, A.A., Numerical Simulation of Waviness in a Circular Contact, under Rolling/Sliding, Proc. 21st Leeds-Lyon Symp., (1995) 259-272.
  16. Foord, C.A., Wedeven, L.D., Westlake, F.J. and Cameron, A., Optical elastohydrodynamics, Proc. I.Mech.E., 184, Pt.1, 28 (1969/1970) 487-505.
  17. Kaneta, M., Nishikawa, H., Kameishi, K., Sakai, T. and Ohno, N., Effects of Elastic Moduli of Contact Surfaces in Elastohydrodynamic Lubrication, J. Tribology, Trans. ASME, 114 (1992) 75-80.
  18. Kaneta, M., Nishikawa, H., Kanada, T. and Matsuda, K., Abnormal Phenomena Appearing in EHL Contacts, J. Tribology, Trans. ASME, (to be appeared).

## Lubricant film thickness and shape using interferometry and image processing

R. Bassani and E. Ciulli

Dipartimento di Costruzioni Meccaniche e Nucleari, Università degli Studi di Pisa  
Via Diotisalvi, 2 - 56126 Pisa - Italy

Optical interferometry is today one of the most used technique to determine the film thickness and shape in typical elastohydrodynamic lubrication (EHL) conditions, but unfortunately the interpretation of interference patterns is not very easy and often depends on the observer. In this work a method is presented to reduce the uncertainty due to the human factor and to make the process of interpreting interference patterns more automatic.

The used experimental apparatus is first described. The procedures developed for the elaboration of monochromatic interference images are then reported. The image processing method is based on the determination of maximum and minimum of light intensity along some directions; in these points the heights can be calculated. Computer programs for both static and dynamic test conditions are developed to automatically obtain the shape of the lubricant film in digital and graphical three-dimensional form too. Some first results are finally shown.

### 1. INTRODUCTION

Determination of film thickness is the most important measurement for lubricated contacts. Several methods have been used to evaluate in particular the minimum film thickness. They can be classified in four different main categories: electrical (resistance, capacitance and inductance measurements), X-ray, mechanical (using strain gauges or dynamometers) and optical (interferometry, laser diffraction, laser fluorescence) methods [1-3].

Optical interferometry is one of the most used techniques for its capacity to give high precision values and punctual evaluation of film thickness in the whole contact zone. In other words, not only the minimum film thickness but also the form of the lubricated meatus can be determined using interference images. First applications of this methodology go back to the 60's [4-7]. Till today, many researchers in several countries have developed their own test rigs

based on optical interferometry. Works of some research groups are reported in [8-16].

As well known, two different kinds of light can be used: the white one and the monochromatic one. Obtained pictures (photos or video camera images) have been normally investigated with the naked eye. Resolution is better using white light than with the monochromatic one. On the other hand it is not possible to use chromatic images to determine film thicknesses over about  $1\mu\text{m}$  and there are some uncertainties due to the human factor (colors can be perceived with a certain degree of inaccuracy; interpretation of calibration and test results must be performed by the same person, because someone else can have a different idea about what is a certain color). Monochromatic light, obtained using laser or white light filtered with interference filters, allows to measure thicknesses till several  $\mu\text{m}$ ; in addition to this, different wavelengths can be used and the relative results combined to have more

detailed information. The minimum film thickness that can be detected is about  $0.1\ \mu\text{m}$  for both cases. Particular methods to avoid this limitation have been developed allowing film thicknesses of less than  $0.01\ \mu\text{m}$  to be measured [17-18]. Another problem is that only discrete values of film thickness can be evaluated. Normally zones with difference of heights of the order of  $0.03\text{-}0.06\ \mu\text{m}$  can be detected with white light and of the order of  $\lambda/4n$  with monochromatic light ( $\lambda$  is the wavelength of the used light and  $n$  the refractive index of the lubricant; a mean value of this ratio, with green light and usual oils, is about  $0.1\ \mu\text{m}$ ).

Improvements to the interpretation of interference pictures are possible with image processing methods. A technique for elaboration of color interference images is reported in [19]. The method is shown to work well in the range  $0.095\text{-}0.7\ \mu\text{m}$ . Anyway there is the limitation of  $1\ \mu\text{m}$  for images obtained with white light that cannot be overcome: only elaboration of monochromatic images allows to do it.

In this paper an image processing method for elaboration of monochromatic pictures is presented. Using the experimental apparatus briefly described in this paper, images are obtained both in static and dynamic conditions and then elaborated. Computer programs to treat these images are developed. Some first results are presented and 3-D mesh surface plots of calculated heights are shown.

## 2. EXPERIMENTAL APPARATUS

The used experimental apparatus (Figure 1) is a test rig for interference film thickness and shape measurements.

The contacting bodies are a glass disc and an easy changeable specimen. They simulate a real contact between components of machine elements as rolling bearings. Tests with different rolling and sliding speed, load and oil are possible. Friction force developed in the contact can also be

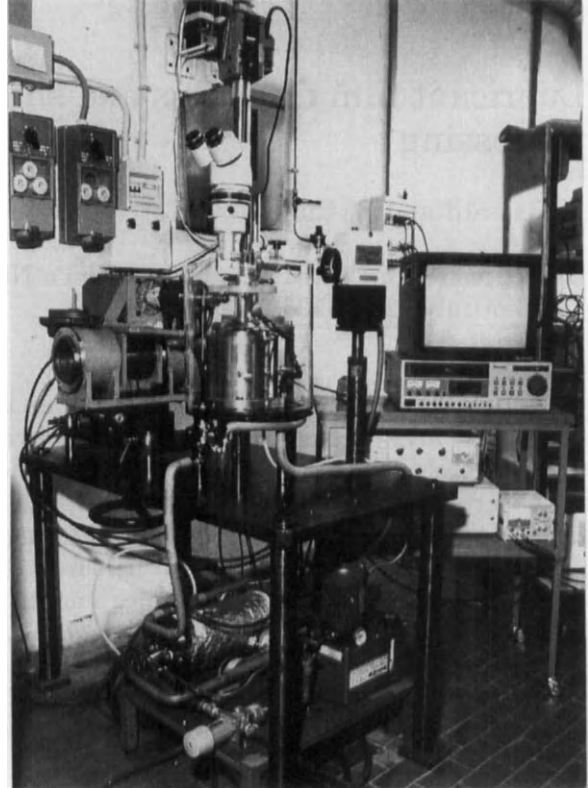


Figure 1. General view of the apparatus.

measured. The apparatus, built in the middle 80's, has never been presented in an international context. A brief description of it is here reported.

Both the disc and the specimen are driven by DC electric motors allowing continuous variation of rotating speed from 0 to 3000 rpm. The disc can also be easily disconnected from the motor for pure rolling tests in which it is moved directly by the specimen. This is possible thanks to an integral gas bearing supporting the disc itself. Many studies were necessary about externally pressurized gas bearings [20-22], mainly on pneumatic instability, a crucial problem for the integral aerostatic bearing. The bearing of the apparatus is today working as a "Yates" one, with axial jets' air supply turned off. Another gas bearing is used for supporting the group of the specimen and the connected motor and it is the

fulcrum of a first order lever system used for the application of the load. The use of this radial gas bearing, whose axis is perpendicular to the rotation axis of the specimen, also allows to measure the friction force with a suitable load cell. The whole structure supporting specimen and motor is placed on a cross table for micrometrical positioning of the specimen. The supply gas pressure for the two bearings is normally set to  $6 \cdot 10^5 \text{ N/m}^2$ .

The lubricant can be heated or cooled thanks to a suitable system visible at the bottom of Fig. 1. Then it is splashed into the contact zone whose detail is shown in Fig. 2.

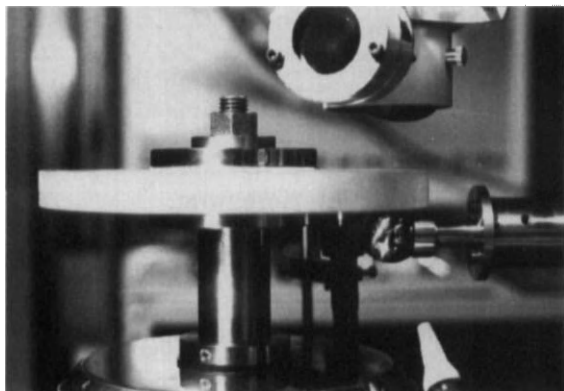


Figure 2. Detail of the contact zone.

Interference images are produced using the light of a xenon (for tests with white light) or mercury (for monochromatic light) arc lamp. In the second case interference filters are used, three different kinds of which are available to obtain lights of three wavelengths: 436 nm (blue), 546 nm (green) and 577 nm (yellow). A chromium layer for increasing reflectivity is deposited on the surface of the disc in contact with the specimens. The observation of interference images is made through a suitable microscope.

Many specimens have been made of different forms, dimensions and materials; some of these are completely machine-worked and some others have been made using bearing balls glued in a conical seat.

Also some discs with different glass and coatings are available (the thickness of chromium is varied and a further layer of silica can be used for protection). Some works done with the apparatus are reported in [23-24].

### 3. IMAGE HANDLING

Images are normally recorded on photographic films or using a video camera (a Panasonic WV-F15E) and a recorder (a professional Panasonic S VHS AG-7330). The camera or the video camera are mounted on the microscope (a Nikon SMZ-10). Photos can be scanned while recorded images can be directly discharged in the computers used for image elaboration (a Macintosh Centris 660 AV and a recently purchased Power Macintosh 7600/120). For the larger possibilities connected with the use of the video camera, this study is centered on this kind of images, even if the definition of the photographic prints is usually better. The methodology used by the following described programs is anyway independent from the image definition. Nominal resolution of the video camera is  $756 \times 581$  pixels and the corresponding images are digitized at 144 dpi (dots per inch). This allows to have one dot for each pixel.

The computer programs presented in this work have been developed in the MATLAB environment, particularly suitable for high-performance numerical computation and visualization. MATLAB's commands and functions have been used to form the so called "m-files". Over 40 m-files constitute this first version of the programs.

Many different kinds of problems have been encountered and solved in developing the programs. For space reasons only few of these are reported in this paper.

The images elaborated in the present work are obtained in static and in pure rolling tests made with the specimen of Figure 2 (one of some super-finished AISI

52100 steel bearing balls kindly furnished by SKF of Pinerolo, Italy). The sphere has a diameter of 24.606 mm and a roughness  $R_a=0.01 \mu\text{m}$ . The used disc is of crown glass with a semi-reflecting chromium layer of about 20 nm and a medium roughness  $R_a=0.015 \mu\text{m}$ .

All shown pictures are relative to lubricated contacts with a load  $F=7 \text{ N}$ . The used lubricant is SN600 with a viscosity  $\eta_0=0.25 \text{ N s/m}^2$  at the test temperature. The actual magnification of the images is evaluated using a calibration grid with a step of 0.5 mm.

#### 4. ELABORATION OF STATIC CONDITION IMAGES

The first computer program has been developed for elaboration of images obtained in static conditions. This kind of analysis allows to determine the phase change in reflection, an important data for absolute film thickness determination with monochromatic interferograms. In addition to this, static images are easier to elaborate than the ones obtained in dynamic conditions, and some procedures of this first developed program are easily adaptable to the dynamic case.

Captured monochromatic images, stored in tiff uncompressed format after discarding color information, are first imported in MATLAB and converted in intensity images. This grey-scale image is stored as a single matrix that contains values ranging from 0 (black) to 1 (white); each element of the matrix corresponds to an image pixel.

The center of the image is then determined. An investigation is made in horizontal (x) and vertical (y) directions to find the values of x and y for which the width of the central zone is maximum. This is determined choosing a value greater than all intensity values of the central zone; the choice is made using plots of some intensities in x and y directions. As an example, in

Fig. 3 an interferogram obtained in static conditions is shown with the six values of y used for the investigation (white lines). Values of y are normalized using the total number of pixels in y directions.

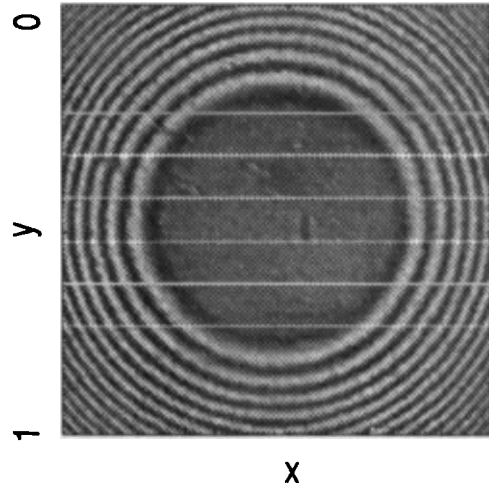


Figure 3. Static interferogram.

Related trends of the intensities are reported in Figure 4. On the x-axis there are numbers denoting pixel positions in the x direction (pixel coordinate). The stored image is in this case 5x5 cm large and the dimension of the corresponding matrix of intensity values is 284x284.

After having determined the center of the circular contact zone, points of maximum and minimum of intensity are determined along the horizontal and vertical lines. The lines and the calculated points are reported in Figure 5. Intermediate graphic results are shown during this calculation. Interactive corrections can also be made to overcome many particular conditions related to the several possible trends of intensity. A typical plot used for control is reported in Figure 6 (in the case shown here the determination of minimum points did not present particular difficulties). The circles correspond to the intensity values of points on the horizontal line on the right of the interference image center (in black the calculated minima).

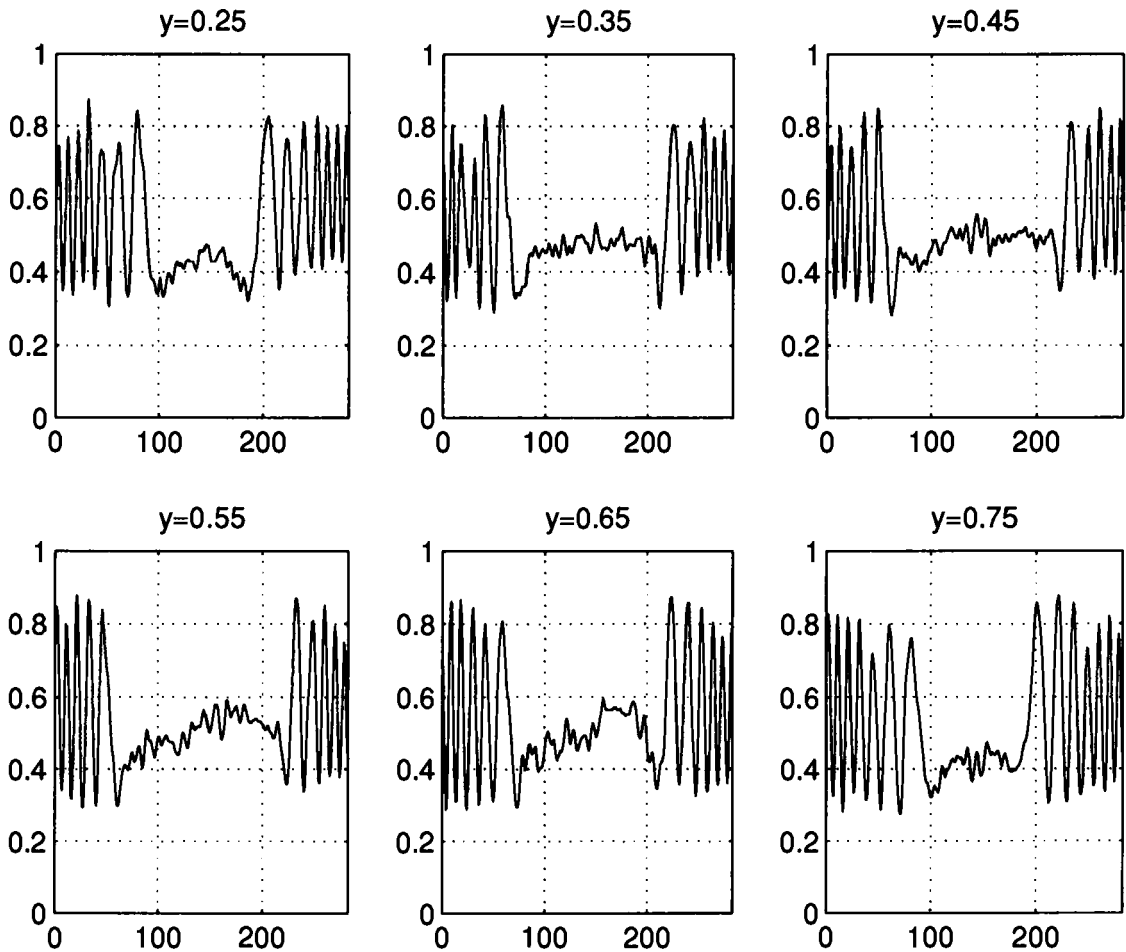


Figure 4. Variation of intensity versus  $x$  (pixel coordinate) for six normalized  $y$  values.

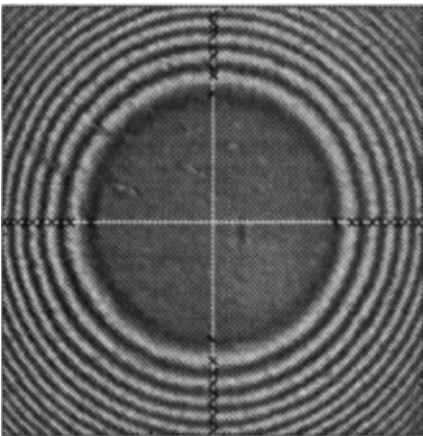


Figure 5. Directions for first investigation.

The points of maximum and minimum values found in the 4 main directions, left, right, top and bottom of the centre, are then used to determine the phase change  $\Phi$ . The correct evaluation of this quantity is necessary to calculate the absolute film thickness  $h$  using the following well known optical formulas:

$$h = \left( K + \frac{1}{2} + \frac{\Phi}{2 \cdot \pi} \right) \cdot \frac{\lambda}{2 \cdot n} \quad (K=0, 1, 2, \dots) \quad (1)$$

$$h = \left( K + \frac{\Phi}{2 \cdot \pi} \right) \cdot \frac{\lambda}{2 \cdot n} \quad (K=1, 2, 3, \dots) \quad (2)$$

( $K$  is the fringe order,  $\lambda$  the wavelength of the

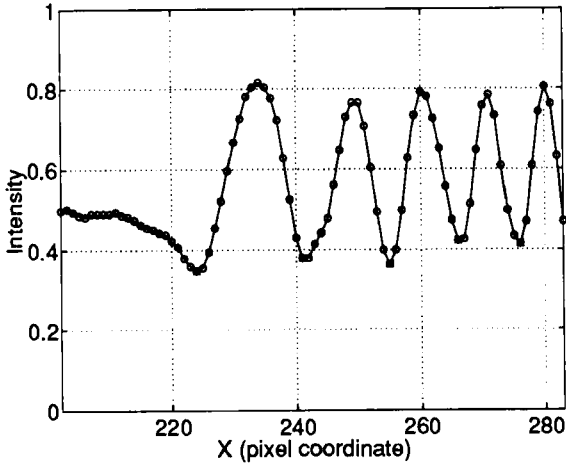


Figure 6. Example of intensity trend.

light,  $n$  the refractive index of the lubricant). Formula (1) is used for the dark fringes, (2) for the light ones.

On the other hand, the distance between two elastic bodies outside the static contact zone can be evaluated using a formula derived from the Hertzian theory:

$$h = \frac{a \cdot P_H}{E} \cdot \left[ \left( \frac{r^2}{a^2} - 2 \right) \cdot \cos^{-1} \left( \frac{a}{r} \right) + \sqrt{\frac{r^2}{a^2} - 1} \right] \quad (3)$$

where  $a = \sqrt[3]{1.5 \cdot F \cdot R/E}$  is the Hertzian radius,  $P_H = 1.5 \cdot F/(\pi \cdot a^2)$  is the maximum pressure,  $E = 2 \cdot [(1 - \nu_1^2)/E_1 + (1 - \nu_2^2)/E_2]^{-1}$  is the equivalent elastic modulus and  $r$  is the distance from the center of the contact ( $F$  is the load,  $R$  the radius of the sphere,  $E_1$ ,  $E_2$  and  $\nu_1$ ,  $\nu_2$  are elastic moduli and Poisson's ratio of the 2 bodies in contact).

Values used in this study are:

$E_1 = 2.0 \cdot 10^{11}$  N/m<sup>2</sup>,  $\nu_1 = 0.3$  for the steel ball,  
 $E_2 = 7.8 \cdot 10^{10}$  N/m<sup>2</sup>,  $\nu_2 = 0.2$  for the glass disk,  
 $R = 12.303 \cdot 10^{-3}$  m,  $n = 1.49$ ,  $\lambda = 546$  nm.

An iterative optimization technique is employed for the determination of  $\Phi$ . The differences of height values calculated with Hertzian and optical formulas are minimized using a least square method. The procedure can be repeated using only

some of the found points of maximum or minimum value. In Figure 7 an example of results obtained after optimization is shown. In this figure only values of heights calculated for the dark fringes on the left of the image center are reported, while optimization was made using all points represented with crosses in Figure 5. The difference between optical (hot) and Hertzian values (hHz) are small, but the trend shown in Figure 7 has been recorded in many other elaborations. Optimized values of  $\Phi$  are in good agreement with the normally used value for tests like these ( $\Phi = -2/5\pi \approx -1.26$  [25]) but only considering

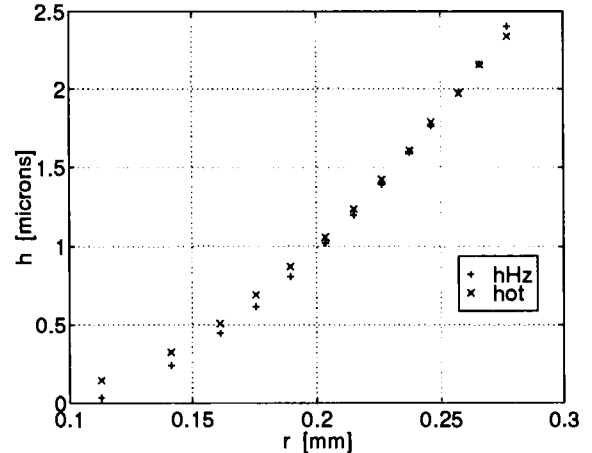


Figure 7. Thickness values calculated with Hertzian (hHz) and optical (hot) formulas.

very few points near the contact zone; considering a bigger number of points, calculated values of  $\Phi$  usually tend to diminish in absolute value. On the other hand, obtained results seem to be good because they don't vary much considering dark or light fringes, horizontal and vertical directions, different definition of the picture (the same image has been also memorized, only for test purpose, to 72, 200 and 300 dpi using the program "Photoshop"). As expected, different values are also found with the yellow and blue filters. The study of the problem of the correct determination of  $\Phi$  will be treated in a future work about the

possibility of determining the film thickness without prior knowledge of the fringe order in the interferogram and using only monochromatic patterns obtained with different wavelengths.

At this stage, the normally used value of  $\Phi$  for green images is adopted for determination of absolute heights of the first fringe in the last part of the program for analysis of static images. Using formulas (1) and (2) thickness in the previously determined points of minimum and maximum intensity is calculated. The principle of investigating intensities in directions at  $45^\circ$  was chosen to find additional image points where heights can be calculated. Starting points for this investigation are the previously determined ones on the horizontal and vertical lines and other points of minimum intensity on the first circular fringe. The central zone, corresponding to zero values of heights, is filled with points in suitable positions. In Figure 8 determined points are reported on the interference image. The related plot of calculated heights is reported in Figure 9.

The representation of Figure 9 is not very clear; much more indicative is a mesh

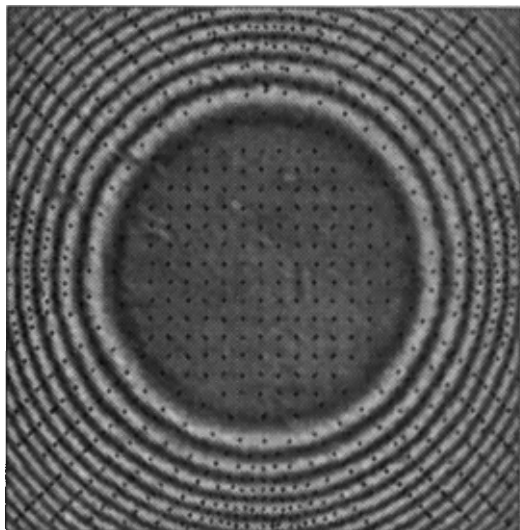


Figure 8. Interferogram with determined points for calculation of heights.

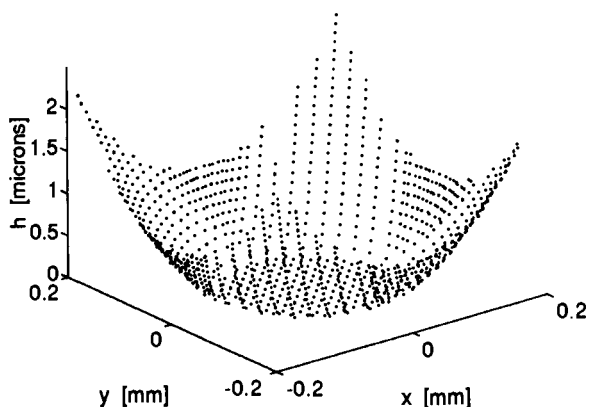


Figure 9. 3-D representation of the calculated heights.

surface plot. For this kind of plot an ordered grid of  $x$  and  $y$  values is usually needed. Unfortunately that is not the case of the points evaluated in the manner previously described. Anyway there are some methods allowing to interpolate evaluated data on a suitable grid. An m-file developed for this aim was realized. The output of this elaboration related to the case of Figure 9 is reported in Figure 10. To have a better feeling of the form of the deformed sphere in contact with the disc, values of heights have been set in reverse mode.

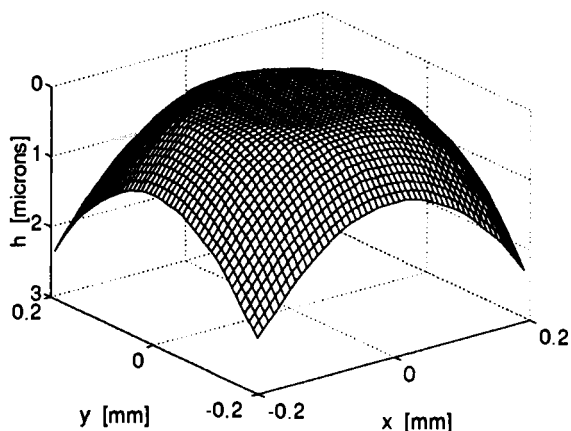


Figure 10. 3-D mesh surface plot of a ball-disc contact.



## 5. ELABORATION OF DYNAMIC CONDITION IMAGES

The elaboration of images obtained in dynamic conditions involves many different problems as in static conditions. Anyway some basic procedures used for the previous case can easily be extended to this one.

The developed program has been tested with images corresponding to the classical features of EHL contacts: constant film thickness in the central region and horse shoe shaped restriction in the outlet zone.

The basic concept used for film thickness evaluation is that the difference of heights between two successive fringes, one with maximum and one with minimum of intensity, can be found with the formula:

$$\Delta h = \frac{\lambda}{4 \cdot n} \quad (4)$$

The film thickness value in at least one point is needed. For this first version of the program, the minimum film thickness is evaluated using the formula for EHL elliptical contacts reported in [26].

One of the problems is to avoid crossing two times the same fringe and giving it two different values of heights while investigating a chosen line on the image. For this reason, after importation of the image and determination of an acceptable center of it using the mouse in a graph window, two points are determined for a convenient division of the image in four rectangular zones at the corners and a central strip (Figure 11). As for static images, points from which to start for a 45 degree investigation are then found. These points are marked with stars in the figure. Each investigation is made in one of the four separated lateral zones. Other points, represented with crosses in Figure 11, from which investigation is made along horizontal lines are then located in the central image strip.

The film thickness is finally evaluated

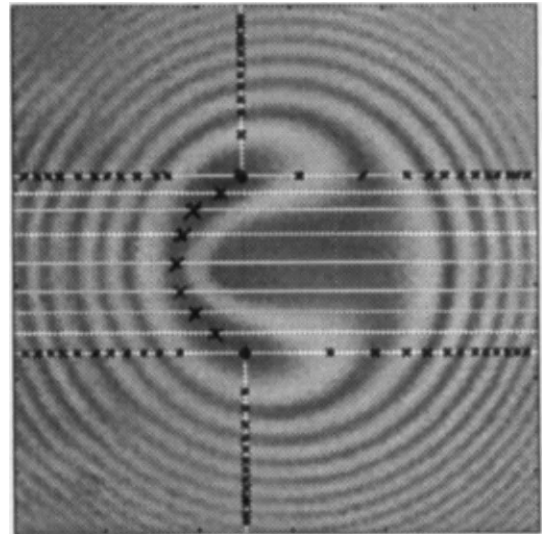


Fig. 11. Subdivision in investigation zones for a dynamic condition image ( $u=0.4$  m/s).

at each determined point of minimum or maximum intensity. Values of heights at the two points represented with black circles in Figure 11 and in the points represented with crosses are the initial data for the elaboration.

For a large zone of the same fringe, the program has also the possibility to calculate the position of points in which the difference of intensity is less than a given small value; in this point the height is also set equal to that of the nearest point of minimum or maximum.

Some results of elaboration of images obtained with two different velocities are shown in Figure 12.

## 6. CONCLUSIONS

Computer programs for the elaboration of monochromatic interference images are presented after a brief description of the apparatus used for experimental tests for lubricated contacts. The first elaborated program deals with images obtained in static conditions. A second one is developed for dynamic conditions.

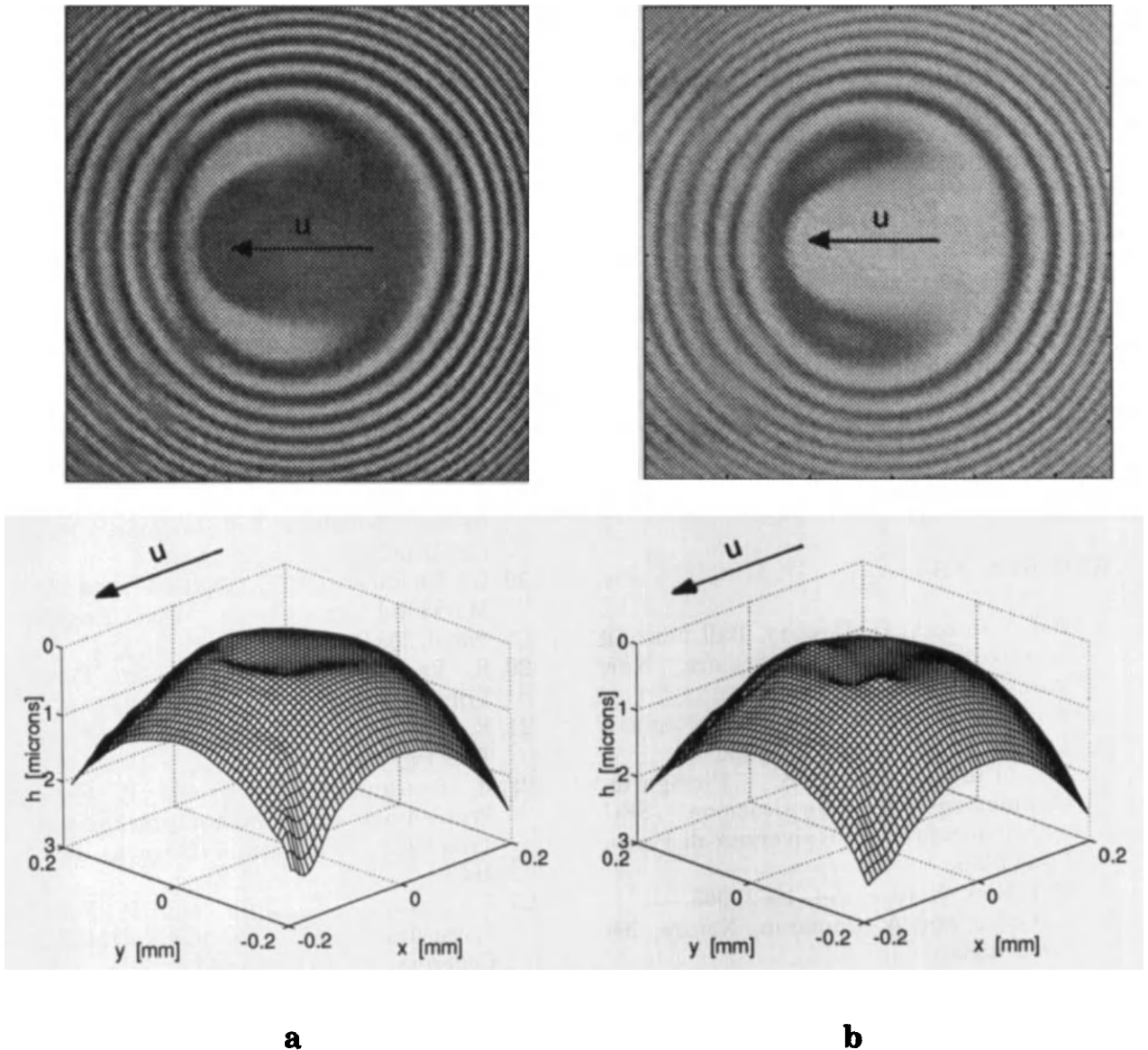


Fig. 12. Interference images and 3-D mesh surface plots of the film thickness for two different rolling speeds,  $u$ : a)  $u=0.09$  m/s, b)  $u=0.15$  m/s.

Some preliminary applications of both programs are shown.

The main advantages of the developed procedures are the possibility to have more detailed information about film thickness values and fluctuations, the overcoming of the uncertainty due to the human factor and the elaboration of large number of images in an almost automatic way avoiding long and

tedious manual work.

This work should be a starting point for other investigations.

A Study about the phase change  $\Phi$  with different wavelengths of the light, thicknesses of the coatings on the glass disc and loads are possible in a quick way. Starting from the determination of the correct  $\Phi$  for the different wavelengths, a

procedure for absolute film thickness determination using only monochromatic images without knowing the fringe order could be developed.

Information and results yielded by these programs can be combined with the ones given by methods for chromatic images as that reported in [19] to have very detailed and complete data.

A possible development involves the treatment of images obtained with bodies with greater roughness.

Numerical results will be obtained with a EHL finite element program considering thermal effect and different rheological behavior of lubricants already developed for linear contacts [27].

## REFERENCES

1. B.J. Hamrock, D. Dowson, Ball bearing lubrication, Wiley Interscience, New York, 1981.
2. R. Bassani and E. Ciulli, Tribologia e Lubrificazione, anno XXI (1986) 13.
3. E. Ciulli and B. Piccigallo, Complementi di lubrificazione, SEU (Servizio Editoriale Università di Pisa), Pisa, 1996.
4. M.T. Kirk, Nature, 194 (1962) 965.
5. R. Gohar and A. Cameron, Nature, 200 (1963) 458.
6. A. Cameron and R. Gohar, Proc. R. Soc. London, A 291 (1966) 520.
7. C.A. Foord, W.C. Hammann and A. Cameron, ASLE Trans., 11 (1968) 31.
8. G. Dalmaz and M. Godet, Tribology, June (1972) 111.
9. L.D. Wedeven, Nasa TN D-8087 (1975).
10. H. Czichos, Wear, 41 (1977) 1.
11. K.A. Koye and W.O. Winer, ASME Journal of Lubrication Technology, 103 (1981) 284.
12. M. Eis and J. Jakobsen, Tribologia, Finnish Journal of Tribology, 8, 1 (1989) 42.
13. O. Isaksson, Proceedings of Eurotrib '89, 2 (Helsinki 1989) 403.
14. M. Kaneta, Y. Kanzaki, K. Kameishi and H. Nishikawa, Proceedings of the Japan International Tribology Conference, (Nagoya 1990) 1695.
15. S.K. Sharma, N.H. Forster and L.J. Gschwender, Tribology Trans., 36, 4 (1993) 555.
16. D. Zhu, G. Biresaw, S.J. Clark and T.J. Kasun, Trans. of the ASME Journal of Tribology, 116, April (1994) 310.
17. H.A. Spikes and G. Guangteng, Proceedings of the 14th Leeds-Lyon Symposium on Tribology, *Interface dynamics*, (1988, Elsevier) 275.
18. G.J. Johnston, R. Wayteand H.A. Spikes, Tribology Transactions, 34, 2 (1991) 187.
19. L. Gustafsson, E. Höglund and O. Marklund, Proc. Instn. Mech. Engrs., Part J, 208 (1994) 199.
20. R. Bassani, E. Ciulli and P. Forte, Tribology international, 22, 3 (1989) 177.
21. R. Bassani, E. Ciulli and P. Forte, Tribology international, 22, 6 (1989) 363.
22. R. Bassani, E. Ciulli and P. Forte, Proceedings of the Japan International Tribology Conference, (Nagoya 1990) 1653.
23. R. Bassani, E. Ciulli and P. Forte, Proceedings of the 10th AIMETA Congress, 2 (Pisa 1990) 427.
24. R. Bassani and E. Ciulli, Proceedings of the 12th AIMETA Congress, III (Napoli 1995) 293.
25. C.A. Foord, L.D. Wedeven, F.J. Westlake and A. Cameron, Proc. Instn. Mech. Engrs. 184, Pt. 1, 28 (1969-1970) 487.
26. B.J. Hamrock, Fundamental of Fluid Film Lubrication, McGraw-Hill Inc., New York, 1994.
27. B. Piccigallo, Wear, 193 (1996) 56.

## Technique for measuring EHD film thickness in non-steady state contact conditions

J. Sugimura<sup>a</sup> and H. A. Spikes<sup>b</sup>

<sup>a</sup> Department of Energy and Mechanical Engineering, Kyushu University, Fukuoka 812-81, Japan

<sup>b</sup> Tribology Section, Imperial College, London SW7 2BX, United Kingdom

A technique has been developed for making film thickness measurements in rolling elastohydrodynamic contacts under non-steady state conditions. It is based upon ultrathin film interferometry and allows the central film thickness down to less than 5 nm, and also film profiles across the EHD contact, to be precisely measured every 0.02 seconds. The technique has been applied to experiments in which lubricated specimens alternately roll at a constant speed and stop. It is found that upon halting motion, both the central and the minimum film thicknesses fall rapidly within several hundredths of seconds to residual levels but that thereafter, film thickness falls further only slowly as lubricant is squeezed out from the contact. Upon sudden start of motion, there is a small overshoot in the film thickness followed by a small oscillation, after which film thickness stabilises to a constant level which corresponds to the thickness predicted by steady state theory. Results of constant acceleration/ deceleration tests are also presented.

### 1. INTRODUCTION

Elastohydrodynamic (EHD) lubrication has been extensively studied both experimentally and theoretically in tribology, and our understanding of EHD lubrication has reached the point where film thicknesses under given steady state conditions can be easily calculated [1]. However, many practical machine elements, such as rolling element bearings, gears, cams and traction drives, operate under non-steady state conditions where the load, speed or contact geometry are not constant over time. For example, involute gear teeth, even when they run at constant rotating speed, contact each other with varying load, varying slide-to-roll ratio, and varying contact radius. Recent applications in the precision, mechatronics industry involve components that undergo intermittent or reciprocating motions produced by stepper motors, for which bearings obviously have to support load under varying speed. It is often in such transient conditions that breakdown of lubrication films occurs which eventually gives rise to failure of the lubricated surfaces. It is therefore extremely important from the practical point of view to study non-steady state behaviour of EHD films and

establish proper models to predict film thicknesses under such conditions.

Several theoretical studies have been reported on non-steady state EHD problems. Vichard [2] developed equations for EHD line contact with time-varying load and contact radius based on Grubin's approximation. Others have conducted numerical studies to solve various types of non-steady state problem [3-6]. The main limitations of these investigations are (i) that almost all of them concentrate only on line contact problems, (ii) they do not give practically useful equations for calculating film thicknesses, and (iii) the validity of their results have yet to be properly tested experimentally. It seems that to conduct full numerical simulation of time-varying, two-dimensional EHD systems is still very difficult and time-consuming. Our knowledge of the rheological properties of lubricants within EHD contacts is also inadequate for carrying out such analysis with confidence.

Very few experimental attempts have been made to study non-steady state EHD. Vichard [2] employed capacitance measurement to determine film thickness in a cam on flat geometry, and Ren *et al.* used conventional optical interferometry [7].

However, neither was able to obtain accurate film thicknesses in well defined, controlled conditions. The reason for this lack of experimental work may be that to measure EHD film is very difficult even under steady state conditions, and there has been no fast and accurate measurement technique suitable for studying time-varying systems.

The most advanced and reliable technique to accurately measure steady state EHD film thickness is currently the ultrathin film interferometric method developed by Johnston *et al.* [8]. This uses a combination of a spacer layer and spectroscopic analysis to measure film thicknesses between 2 and 200 nm with a resolution of about 1 nm. The technique has been employed to study the behaviour of thin films of a wide variety of lubricant types in rolling and rolling/sliding EHD contacts. From the point of view of the current work, the advantage of ultrathin film interferometry is that it is based on the analysis of spectrometer images with a computer-based data acquisition system, which is potentially well-suited to be applied to measuring rapid changes in film thickness under non-steady state conditions.

The aim of the present study was to develop an extended system based on ultrathin film interferometry to directly measure EHD film thicknesses under non-steady state speed conditions. This paper describes the outline of the developed system and some preliminary results obtained.

## 2. ULTRATHIN FILM INTERFEROMETRY

The conventional ultrathin film interferometry technique [8] and the existing EHD test rig on which the present non-steady state measurement system is based is first briefly described.

The test set-up consists of a contact formed between a 19.05 mm diameter steel ball and a flat glass disc, both contained within a temperature-controlled chamber. The disc is driven by a DC servo motor, while the ball is either driven by the disc or by a shaft connected to a separate motor. The present study employs the former so that the ball and disc contact is in nominally pure rolling. The ball is loaded against the rotating glass disc, and half-immersed in lubricant so that fluid is carried into the contact by the rotation of the ball.

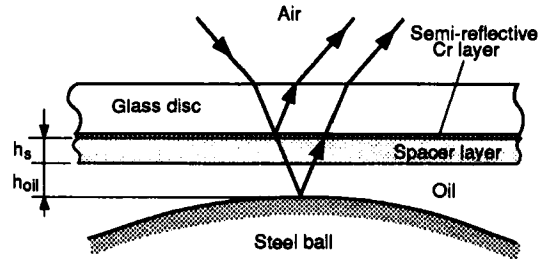


Figure 1. Spacer layer method

White light is shone onto the contact to produce interference images.

One significant change to conventional interferometry is the use of a spacer layer, *i.e.* a transparent layer of silica deposited on top of the semi-reflective layer of chromium with which the glass disc is coated. As shown schematically in Figure 1, some of the light shone through the disc is reflected from the underside of the glass disc, while some passes through the spacer layer and also any oil film before being reflected from the steel surface. The two beams of light travel different distances so that they interfere optically to produce bright and dark interfered light output depending on the optical path difference. Bright constructive interference occurs when:

$$h_{oil}n_{oil} + h_s n_s = (N - \phi)\lambda/2 \quad N=1,2,3,\dots \quad (1)$$

where  $h_{oil}$  and  $h_s$  are the film thicknesses of the oil film and the spacer layer, respectively,  $n_{oil}$  and  $n_s$  are their refractive indices at the wavelength concerned,  $\lambda$  is the wavelength,  $N$  is the optical order, and  $\phi$  the phase change. Hence the spacer layer acts as "solid oil" and enables optical interferometry to be used to measure oil film thicknesses of less than one quarter the wavelength of light.

Another important feature of ultrathin film interferometry is the use of a spectrometer and microcomputer image analysis to determine accurately the wavelength of maximum constructive interference instead of detecting the colour or intensity of the interfered light by human eye. The light reflected from a narrow strip across the contact is passed into a spectrometer through an entrance slit and diffracted into its component wavelengths before being detected by a

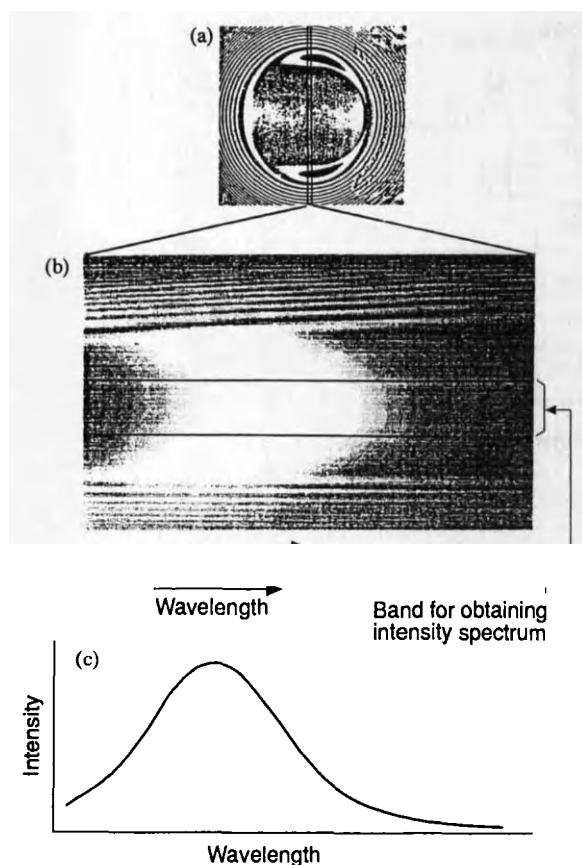


Figure 2. (a) An interference image of an EHD contact, (b) a spectrum image, and (c) a light intensity spectrum at the central band in (b)

monochrome CCD camera. A typical spectrometer image is shown in Figure 2. The horizontal axis of the image is wavelength, while the vertical co-ordinate refers to distance across on the contact. Lighter regions are regions of constructive interference of light of the corresponding wavelength. Thus the band in the middle of the image represents the relatively flat, central region of the EHD contact.

The spectrometer image is fed to a frame grabber on the microcomputer, and a computer program analyses the central band to determine the wavelength of maximum interference, from which the film thickness is calculated using Equation (1). Since the spacer layer thickness  $h_s$  is usually not constant over the whole disc surface, the measurement is made at only one or several pre-determined, circumferential positions on the disc, at which  $h_s$  has been previously determined

without oil in the chamber using Equation (1), *i.e.* with  $h_{oil}=0$ . In order to ensure that the frame grabber captures an image exactly when the glass disc is at the specified positions, the computer program monitors the rotational position of the disc from a rotary encoder on the driving shaft of the glass disc. The encoder outputs 512 rotational positions in the form of 9-bit parallel digital signal.

### 3. NON-STEADY STATE THICKNESS MEASUREMENT

#### 3.1 Design strategy

To carry out the measurement of oil film thickness in non-steady state conditions essentially requires that changes in thickness with time must be followed rapidly and accurately. This is theoretically possible using ultrathin film interferometry and a measurement system has been constructed based on the following principles.

- (i) Non-steady state conditions employed are those of varying speed with time. Several types of motions, which will be described later, are produced by using a function generator to control the DC servo motor which drives the disc.
- (ii) The conventional system uses a monochrome CCD camera, with a scan speed of 50 Hz, to obtain spectrometer images. Instead of analysing these images immediately after they are captured as in the existing system, they are recorded on video tape, to be analysed afterwards to determine film thickness. This allows film thickness determination at the maximum rate of 50 measurements per second, which is far faster than possible by immediate analysis.
- (iii) To follow rapidly-changing conditions, the film thickness must be measured at any location on the glass disc. Therefore, before the EHD oil film is measured, the spacer layer thickness around the whole track is determined.
- (iv) For post-capture analysis it is necessary to know, for each video image, the location on the disc and the speed at which the image was captured. To do this, a specially designed

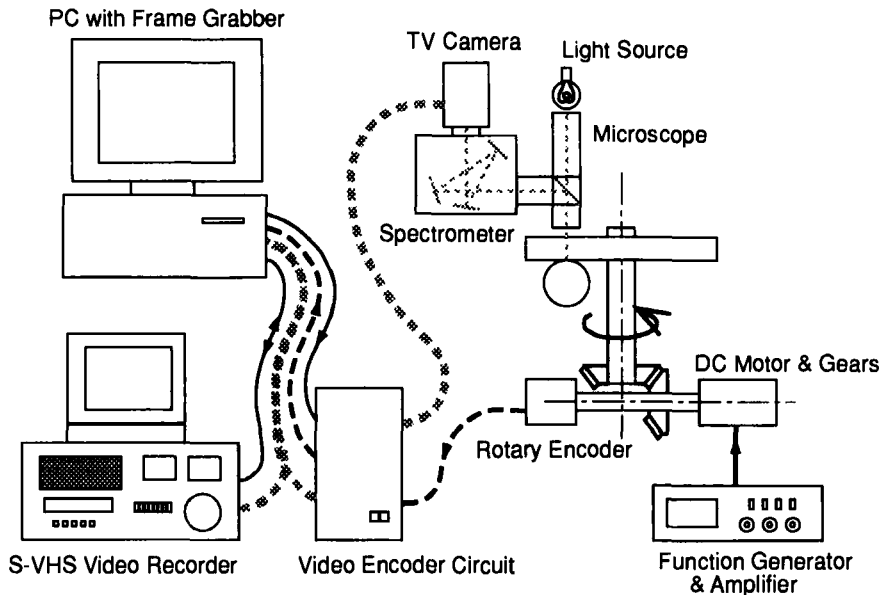


Figure 3. Schematic diagram of the new system

circuit was constructed to insert coded information regarding the position and the speed of the disc into each video image.

- (v) Computer programs were developed to analyse the many thousands of video frames obtained in order to determine film thickness rapidly and semi-automatically.

### 3.2 System hardware

Figure 3 shows a schematic diagram of the system configuration. In addition to the existing elastohydrodynamic optical rig, a function generator which gives several kinds of speed variation to the disc, an S-VHS video recorder for recording spectrometer images and a circuit to insert information on each image are indicated. The figure also shows how the various components are connected; thick dotted lines represent video lines, dotted lines are the encoder signals, and solid lines are command signals.

The function generator produces oscillating output voltage having square, triangle or sinusoidal form within the frequency range 0.1 Hz to 1 MHz. The output can also have a DC voltage offset so that it is possible to generate, for example, a clockpulse-like wave with one of the levels equal to zero volts by using the square wave with an offset. Since the motor is used in the range where

its speed is almost linearly proportional to given voltage, the disc can be driven with the above three types of speed variation. In practice, frequencies below 5 Hz were used in the current study in order to ensure proper response of the motor and to enable enough images to be obtained in one cycle to give a clear indication of the variation of film thickness with speed.

A conventional S-VHS video recorder, Mitsubishi BV-2000B, is used to record the monochrome spectrometer images. The advantage of this model is that it can be controlled by a microcomputer using very simple commands.

Before the images are recorded on tape, coded information in the form of a digital bar code is inserted near the top of each image field by a custom built circuit. This circuit is called a "video encoder". The bar code contains 48 bits of information, which includes 9 bits for the encoder position, 16 bits for the video field number that increases frame by frame, and 16 bits for the approximate speed of the disc. Here the term "field" denotes one of two interlaced image fields that constitute one image frame; the 50 Hz video signal has 50 fields in a second. The bar code thus allows the computer program to identify which video field and which encoder position it is analysing.

### 3.3 Reading data from video tapes

A very large number of images are recorded on tape during each experiment, far more than could be conveniently analysed manually. A series of Pascal computer programs were developed to read and process these semi-automatically.

The whole analysis is divided into several stages, in each of which the initial task is to obtain, from each image field, light intensity variations with wavelength in a central band on the images, to decode the barcode to obtain the field number and the disc position, and to store these on hard disc.

With the existing video recorder it was not possible to pause/still the video recorder whilst this was connected to the computer. Instead a program was written to automatically replay a selected section of the tape several times, using the RS-232C interface to control the video recorder, until all the fields in the section had been read. A procedure was devised which, while the tape is running, enables the frame grabber to grab a specified target field by using the decoded field number. This is effective even when there is instability in tape tracking.

In some cases considerable damage on the spectrometer image was found, probably due to the coating being worn off from the surface of the disc. Since it is very difficult to detect this kind of defect after the intensity spectrum curve has been obtained, the analysis program includes a routine that automatically checks the images and mark the condition in the stored file, in order for subsequent analyses to reject damaged fields.

### 3.4 Film thickness determination

Determination of film thickness variation from the images recorded on a tape is conducted by:

- (i) mapping the spacer layer thickness by recording images during one revolution of the disc in non-lubricated conditions at constant, slow speed, or in lubricated conditions at which the spacer film thickness at some locations is already known, and
- (ii) determining oil film thickness and corresponding speed or position in non-steady state speed conditions.

Instead of averaging the band in the central region of the EHD contact to obtain one averaged

Table 1  
Test fluids and their viscosities

| Oils  | Dynamic viscosities (cP) |      |       |
|-------|--------------------------|------|-------|
|       | 25°C                     | 40°C | 100°C |
| SN100 | 31.5                     | 16.6 | 3.24  |
| SN150 | 55.1                     | 27.1 | 3.81  |

central film thickness, the band can be divided into rows of thin bands of a few video lines to obtain a film profile across the EHD contact [9].

### 3.5 Validation of the system

In order to test the effectiveness of the recording and analysis system, experiments were conducted with a mineral oil SN150, listed in Table 1, under constant speed conditions at room temperature. A load of 20 N was used, which gave a Hertzian contact radius of 0.135 mm and a maximum Hertzian pressure of 0.526 GPa. The film thickness was measured at a series of speeds ranging between 4 mm/s and 0.124 m/s.

Figure 4 shows the spacer layer thickness obtained from a lubricated, rolling contact at a speed of 41.1 mm/s, about 10 rpm. The steady state EHD film thickness at this speed is known to be 25.9 nm, which is subtracted from the measured thickness to obtain the thickness profile of the spacer layer. It can be seen that there is a large undulation in the spacer layer thickness between about 505 to 525 nm around the circular track due to circumferential spacer layer thickness variation.

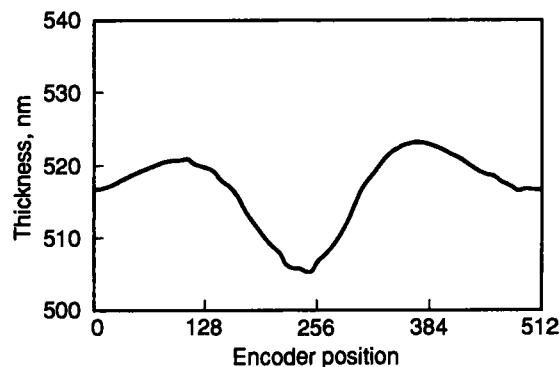


Figure 4. Spacer layer thickness variation



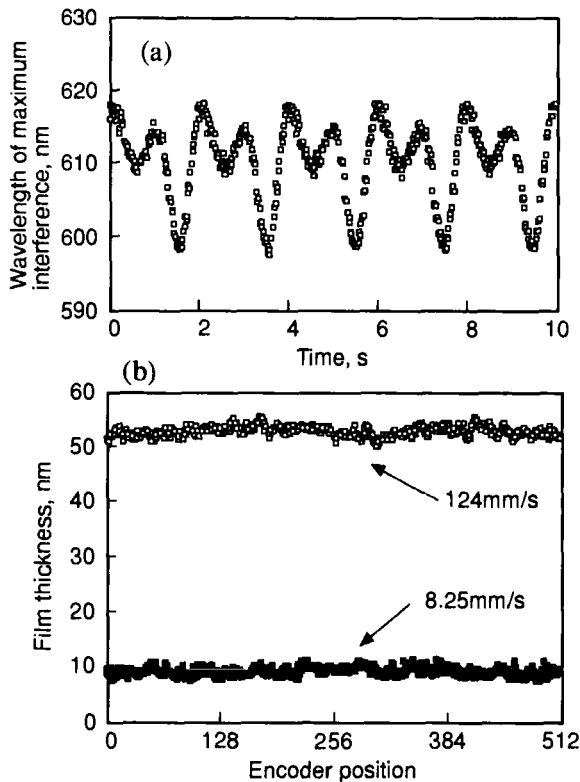


Figure 5. Steady state test result with SN150; (a) wavelength of maximum interference at 124 mm/s, and (b) film thickness variations with rotational position at 124 mm/s and 8.25 mm/s

Figure 5(a) is a plot of the wavelength of maximum interference against the rotational position of the disc from a lubricated rolling test at a rolling speed of 124 mm/s. It is clear that the wavelength fluctuates due to the variations in the spacer layer thickness; in this case the rotational speed is about 30 rpm, *i.e.* 0.5 revolutions per second. By using Equation (1) to subtract the spacer layer thickness from the total thickness, the oil film thickness is calculated. Figure 5(b) shows the result; the film thickness is quite constant round the disc, with a mean film thickness of 52.7 nm and a standard deviation of 0.88 nm. Also shown in Figure 5(b) is film thickness variation determined at a much lower speed of 8.25 mm/s. The mean and standard deviation are 9.0 nm and 0.74 nm, respectively, showing that good quality data can be determined in the 10 nm film thickness range.

The above example clearly demonstrates that the developed system is able to measure oil film thicknesses with accuracy within 2 nm, and can be used confidently in non-steady speed tests. In the next sections, some preliminary results of non-steady state tests conducted are shown.

## 4. NON-STEADY STATE EXPERIMENTS

### 4.1 Experimental conditions

Two mineral oils with different viscosities were used, as listed in Table 1. Several types of non-steady state speed motions were employed, including:

- (i) Rapid halting of motion
- (ii) Uni-directional on-off motion
- (iii) Reciprocation at nominally constant speed
- (iv) Acceleration/deceleration

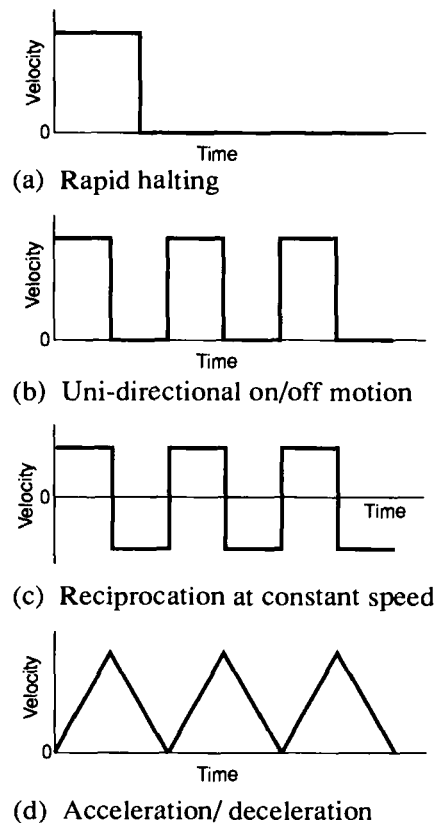


Figure 6. Non-steady state motions

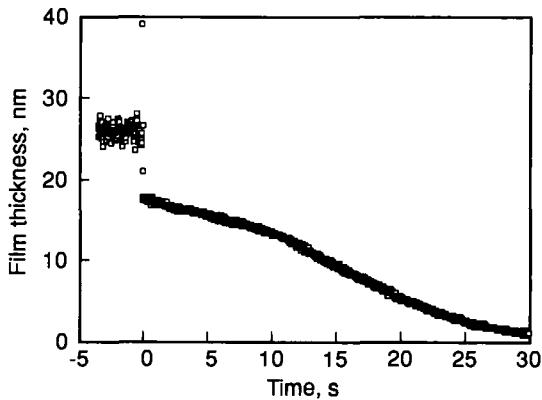


Figure 7. Changes in the EHD central film thickness in a rapid halting test; SN150, 25°C, from a velocity of 41.2 mm/s

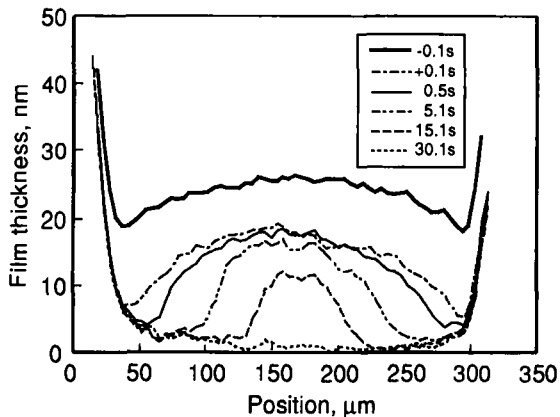


Figure 8. EHD film shapes across the contact in a rapid halting test shown in Figure 7

These motions are shown schematically in Figure 6. In motions (i), (ii) and (iii) the rolling speed was varied over the range from about 20 to 160 mm/s, whilst in (iv) the speed was varied between 0 and 165 mm/s. A load of 20 N was used in all the tests.

#### 4.2 Rapid halting of motion

Figure 7 shows the variation of the central film thickness during rapid halting of motion with the lubricant SN150. The data points in the figure represent film thicknesses taken at intervals of 0.02 seconds. When the motion is halted, which is

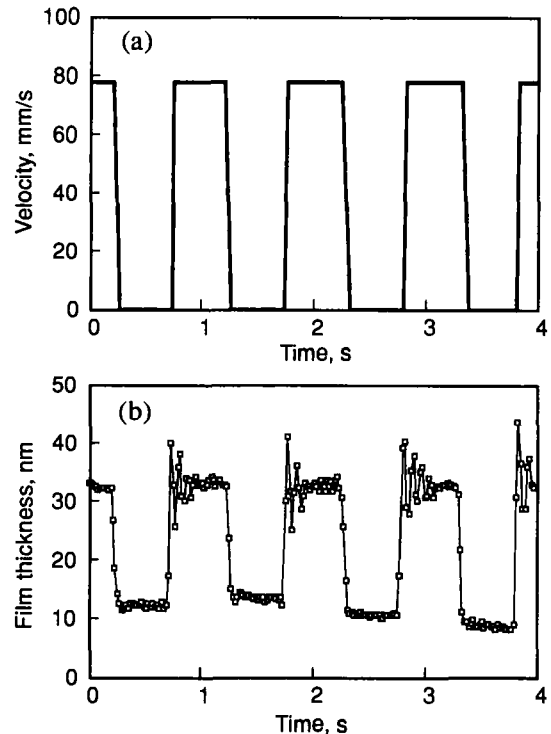


Figure 9. Changes in (a) velocity and (b) EHD central film thickness with time in a uni-directional on/off test; SN100, 25°C, 1 Hz, 78.8 mm/s

indicated on the abscissa to occur at 0 seconds, the EHD central film thickness collapses very rapidly, within a few hundredths of second. However, it does not drop immediately to zero but instead levels out at about half of the original thickness and there is then a very slow gradual decay of residual film.

This behaviour can be studied in detail by acquiring profiles of film thickness across the EHD contact, as described in Section 3.4. Figure 8 shows the changes in the film shape with time for the same test, from 0.1 seconds before the end of motion to 30.1 seconds after halting. The shape at  $-0.1$  seconds clearly represents the well-known EHD film shape, showing the side lobes at which the film thickness is a minimum. After halting of the disc, film thickness falls more rapidly at the sides than at the centre of the contact. Thereafter, gradual squeezing out of the lubricant is seen until the film becomes almost flat at 30.1 seconds, with a residual, thin film of a few nanometers thickness.

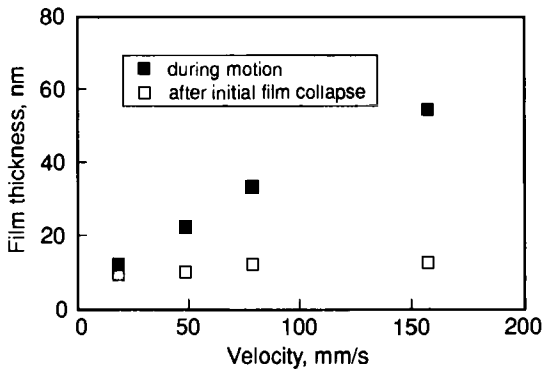


Figure 10. Central film thicknesses during motion and after initial film collapse in uni-directional on/off tests with SN100

#### 4.3 Uni-directional on-off motion

This is a motion which consists of cycles of constant speed followed by rest; equivalent to stepper motor action. The results at 1 Hz will be shown, where standstill of nominally 0.5 seconds follows 0.5 seconds of constant velocity motion.

Figure 9 shows typical film thickness variation with time with the oil SN100, together with the corresponding variation in velocity. As in the case with abrupt halting, film thickness drops very rapidly to an intermediate value with subsequent decay taking place much more slowly. When motion is resumed, film thickness increases abruptly and then oscillates for a few cycles before it stabilises to a level which corresponds to the steady state film thickness. The frequency of this oscillation is about  $12 \text{ s}^{-1}$ .

Quite similar behaviour is observed at different speeds. Figure 10 compares the film thicknesses during motion with the film thickness attained after the initial film collapse on halting for different rolling speeds, all at 1 Hz. The figure demonstrates that the latter film thicknesses are almost independent of the preceding speed and thus independent of initial film thickness. The above results show that under the present conditions, the EHD film never breaks down with the repetition of the on-off motion at 1 Hz.

#### 4.4 Uni-directional acceleration/deceleration

By using several triangular waves of different frequency while keeping the amplitude constant,

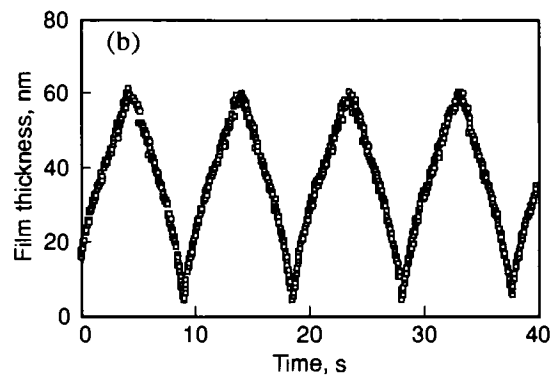
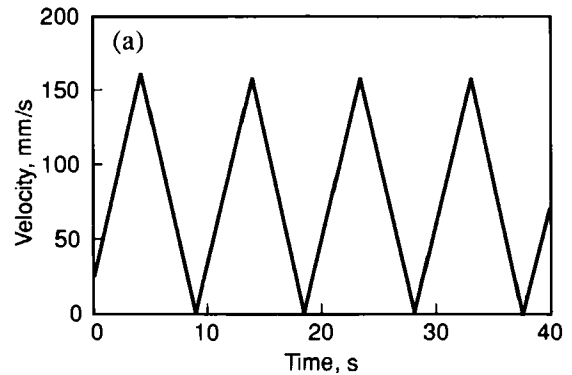


Figure 11. Changes in (a) velocity and (b) the EHD central film thickness in an acceleration/deceleration test; SN150, 25°C, 0.1 Hz, 0-165 mm/s

motions with different constant acceleration were generated. Figure 11 shows the velocity variation and the corresponding variation in the central film thickness when the speed changes between almost zero and 165 mm/s at a frequency of about 0.1 Hz with the oil SN150. The film thickness change matches the speed variation. The film thicknesses for several cycles of acceleration and deceleration are plotted against the speed in Figure 12(a). There is little difference in thickness between the increasing and decreasing results at the same speed. It can also be seen that the film thickness is not proportional to the speed but proportional to the speed to the power of about 0.7, as expected from EHD theory.

Figure 12(b) and (c) shows that, as the cycle rate is increased to 1 Hz and then 2 Hz, the thickness values diverge, with those formed during acceleration falling below those formed during deceleration. There is a delay in the film thickness

response to the change in speed. After the speed reaches the maximum, the film still continues to grow for a while. These results clearly show the non-steady state effect produced by acceleration.

## 5. DISCUSSION

It has been shown that the system is able to measure EHD oil film thicknesses in various non-steady state conditions. It should be noted that further improvement of the technique for faster data acquisition can be made relatively simply by employing a high speed video camera. Although only a few results are presented here, they provide some interesting insights.

When rolling is suddenly halted, the film thickness falls in two stages, a very rapid film collapse occurring over a time period of less than 0.1 seconds, followed by a much slower reduction. The former is accompanied by the rapid fall of the minimum film thickness in the side lobes. This loss of film thickness may have important implications when surface damage in low frequency stop/start motion is concerned. The latter proceeds as the lubricant flows out of the contact through the narrow gap at the sides of the contact, by the squeeze film action. This behaviour is qualitatively similar to that predicted by numerical analysis [3].

The present results also show the occurrence of oscillation in the film thickness when rolling is suddenly commenced. The overshoot of the film thickness and the subsequent damping may indicate the dynamic effect of the lubricant film and also the dynamics of the motor-to-disc driveline. It has been found that, upon sudden start-up, there is a small oscillation in the shaft driving the disc. Further investigation is needed in order to clarify how these effects operate.

One of the biggest limitations of the current system is that the speed of the ball was not monitored or controlled. Instead it was assumed that the ball was driven in nominally pure rolling by the disc. It is possible that, after sudden changes of the disc velocity, some skidding due to the inertia of the ball may have occurred. Skidding might also have affected the lag in film thickness found in the acceleration/ deceleration tests. At present, the authors believe that the non-steady

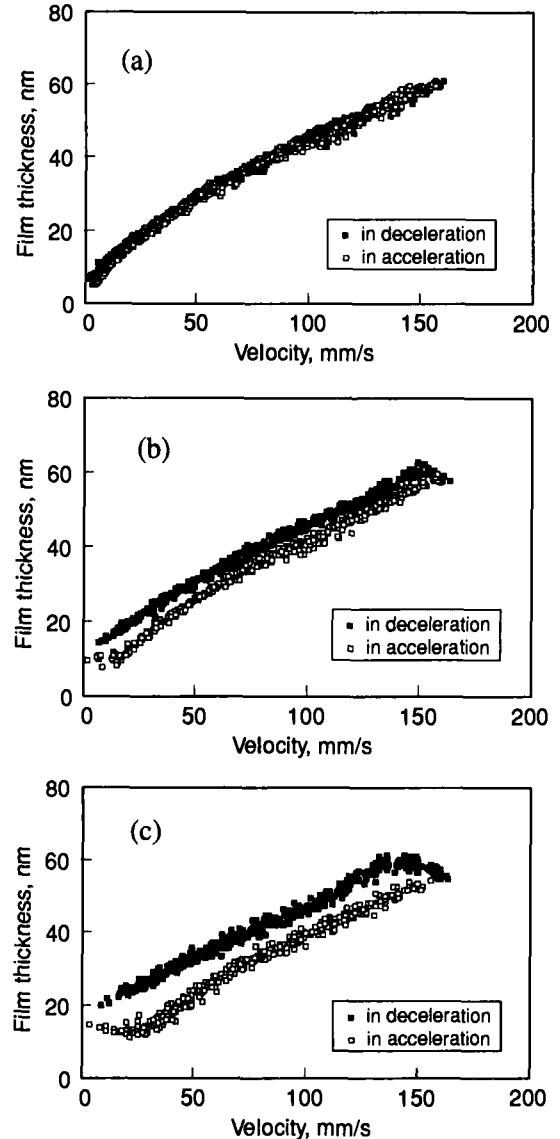


Figure 12. Variation of the EHD central film thickness with velocity (a) in the test shown in Figure 11, (b) at 1 Hz, and (c) at 2 Hz

effect caused by the inertia of the ball is insignificant under the present conditions. The reason is that the time constant of the exponential reduction of the ball speed upon the sudden halting of the disc should be less than one thousandth of a second. This is based on a very simple model in which the traction between the disc and the ball is proportional to the speed difference, with the

maximum traction coefficient being about 0.05 [10], and the inertia of the supporting bearings being neglected.

To overcome this limitation, future work will accurately monitor and control the ball motion as well as that of the disc, and will also measure traction forces between the disc and the ball.

## 6. CONCLUSIONS

A technique has been developed for making film thickness measurements in rolling elastohydrodynamic contacts under non-steady state conditions. This is based on ultrathin film interferometry in a ball on flat contact geometry, and employs a standard video recorder and a specially designed circuit which facilitates determination of the disc motion. The developed system can measure central film thickness and also film thickness profiles across the EHD contact down to less than 5 nm at very high accuracy every 0.02 seconds.

The technique has been applied to several non-steady state types of motion. It has been shown that, upon abrupt halting of rolling, both the central film thickness and the minimum film thickness fall rapidly within several hundredths of seconds but only to an intermediate level where a residual film remains. This residual film then flows out gradually due to squeezing out action. In uni-directional on/off motion, upon sudden start of motion, there is a small overshoot in the film thickness followed by a decreasing oscillation before film thickness stabilises to a constant level, which is the same as that formed under steady speed conditions.

It has also been shown that the film thickness in accelerating and decelerating motion lags behind that predicted from steady state theory, giving higher film thicknesses than steady state values when the speed is decreasing and lower film thicknesses when the speed is increasing.

The present approach shows great promise in being able to study non-steady state EHD behaviour. The main limitation of the study, which can be quite easily addressed in future work, is that the dynamics of motion of the ball was not precisely controllable.

## ACKNOWLEDGEMENTS

The authors would like to thank NASA for financially supporting this work, and Dr. R. Wayte, Dr. J. Hutchinson, Dr. C. Hamer, and Mr. M. Smeeth for their kind help.

## REFERENCES

1. Hamrock, B. T. and Dowson, D., *Ball Bearing Lubrication: the Elastohydrodynamics of Elliptical Contacts*, John Wiley and Sons, 1981.
2. Vichard, J. P., *Transient Effects of the Lubrication of Hertzian Contacts*, *J. Mech. Engr. Sci.*, 13, 3 (1971) 173-189.
3. Wu, Y. and Yan, S., *A Full Numerical Solution for the Non-steady State Elastohydrodynamic Problem in Nominal Line Contacts*, *Proc. 12th Leeds-Lyon Symp. on Trib.* (1986) 291-298.
4. Ai, X. and Yu, H., *A Full Numerical Solution for General Transient Elastohydrodynamic Line Contacts and its Application*, *Wear*, 121 (1988) 143-159.
5. Dowson, D., Taylor, C. M. and Zhu, G., *A Transient Elastohydrodynamic Lubrication Analysis of a Cam and Follower*, *J. Phys., D: Appl. Phys.*, 25 (1992) A313-A320.
6. Hooke, C. J., *The Minimum Film Thickness in Lubricated Line Contacts During a Reversal of Entrainment — General Solution and the Development of a Design Chart*, *Proc. Instn. Mech. Engrs.*, J208 (1994) 53-64.
7. Ren, N., Zhu, D. and Wen, S. Z., *Experimental Method for Quantitative Analysis of Transient EHL*, *Trib. Int.*, 24, 4 (1991) 225-230.
8. Johnston, G. J., Wayte, R. and Spikes, H. A., *The Measurement and Study of Very Thin Lubricant Films in Concentrated Contacts*, *Trib. Trans.*, 34 (1991) 187-194.
9. Smeeth, M. and Spikes, H. A., *Central and Minimum Elastohydrodynamic Film Thickness as High Contact Pressure*, accepted for publication in *ASME Trans.*
10. Smeeth, M., Gunsel, S. and Spikes, H. A., *Friction and Wear Reduction by Boundary Film-Forming Viscosity Index Improvers*, to be presented at SAE Meeting, San Antonio, October 1996.

## Amplitude Reduction of Waviness in Transient EHL Line Contacts

C.H. Venner<sup>a</sup>, F. Couhier<sup>b</sup>, A.A. Lubrecht<sup>b</sup>, J.A. Greenwood<sup>c</sup>

<sup>a</sup>University of Twente, Enschede, The Netherlands.

<sup>b</sup>Laboratoire de Mécanique des Contacts, UMR CNRS 5514, INSA de Lyon, France.

<sup>c</sup>Department of Engineering, University of Cambridge, UK.

The problem of surface waviness in ElastoHydrodynamic Lubrication is commonly considered as a first step towards understanding the lubrication of rough surfaces. Both problems are generally transient. The current paper investigates the deformation of sinusoidal waviness in the contact, more precisely it studies the amplitude reduction of one-sided waviness in a transient EHL line contact. The film thickness amplitude at  $X = 0$  is called  $A_d$  (deformed amplitude). It is shown that for waviness amplitudes smaller than the film thickness  $A_i < H_c$ , the ratio  $A_d/A_i$  is independent of the undeformed amplitude  $A_i$ . In other words: for small amplitudes the deformed amplitude depends linearly on the initial amplitude  $A_i$ . Rather surprisingly, the same behaviour is found for  $A_i > H_c$ . The results show that qualitatively waviness with short wavelengths  $\lambda/b < 1$  is hardly deformed, thus  $A_d \simeq A_i$ . Long wavelengths on the contrary, disappear nearly completely:  $A_d \ll A_i$  thus  $A_d/A_i \simeq 0$ . However, quantitatively the amplitude reduction was found to depend also on the contact operating conditions. With a generalized coordinate  $\nabla$ , instead of  $\lambda/b$ , the relative amplitude  $A_d/A_i$  can be described by a single function of  $\nabla$  for all operating conditions:  $A_d/A_i = F(\nabla), \forall (M, L)$ . A possible way of expressing  $\nabla$  is:  $\nabla = \lambda/b M^{3/4} / L^{1/2}$ .

### 1. Introduction

The interest in Elasto Hydrodynamic Lubrication (EHL) has gradually shifted from the steady state smooth surface problem to more complex geometries, i.e. the effect of surface features such as dents, bumps, waviness and roughness. In other words attention has moved from the macro contact to features that cover only a fraction of the contact area: the micro contact, and from the steady state to transient conditions. This change in interest can easily be explained when realizing that engineering surfaces are never perfectly smooth. The current trends in design are towards increased efficiency: higher loads, lower viscosity oils and higher operating temperatures and thus thinner lubricant films. As a result the surface topography becomes increasingly important when describing the performance of lubricated concentrated contacts. Experimental investigations into the influence of surface effects have been carried out using optical interferometry, Wedeven and Cusano (1979), Kaneta and Cameron (1980), and more recently Kaneta (1992) and Kaneta et

al. (1992,1993). Also more and more theoretical work is devoted to studying the influence of the surface topography. Most of these studies have been carried out using a steady state analysis, see for instance Goglia et al. (1984), Kweh et al (1989), and Lee and Hamrock (1990). However, in general both surfaces move and any feature present on the surface will move through the contact. Hence, in fact such theoretical studies require a transient analysis calculating the pressure and film thickness, see Ai and Cheng (1993, 1994a, 1994b, 1996), Chang (1989, 1992), Osborn and Sadeghi (1992) and Venner et al. (1991). A time step proportional to the spatial discretisation should be used to model the motion of the feature through the contact. In addition, the number of spatial nodes should be sufficiently large to study features on a sub-contact scale. Obviously, a prerequisite for such studies is an algorithm of very low complexity for the computation of the film thickness and pressure in the contact at each time step. Moreover, to simulate situations of practical interest, the algorithm should also be stable, especially since rough sur-

face problems tend to be more difficult to solve from a stability point of view than their smooth surface counterparts.

The introduction and further development of multilevel techniques to solve the EHL problem has yielded algorithms for the steady state line and point contact problem of  $O(n \ln n)$  complexity,  $n$  being the number of discretisation points. As a result these methods allow a fast computation of the pressure profile and film shape using large values of  $n$  and are well suited to accomplish the transient calculations.

This method has allowed detailed studies of transient features: Lubrecht et al. (1990, 1992) and Venner et al. (1991, 1994a, 1994b, 1994c, 1996).

A detailed analysis of the change of the wavelength of the waviness in an EHL contact was supplied by Greenwood and Johnson (1992), Greenwood and Morales-Espejel (1994) and Morales-Espejel (1993). The missing part of the puzzle remains the change of amplitude inside the contact; the amplitude reduction as a function of wavelength and operating conditions, which forms the topic of the current paper.

## 2. Nomenclature

|             |  |
|-------------|--|
| $A_d$       | dimensionless deformed amplitude<br>$A_d = [\max_T H(0, T) - \min_T H(0, T)]/2$                      |
| $\bar{A}_d$ | equivalent dimensionless deformed amplitude<br>$\bar{A}_d = [\max_\phi H(X=0) - \min_\phi H(X=0)]/2$ |
| $A_i$       | dimensionless initial amplitude<br>$A_i = a_i R/b^2$   |
| $b$         | half width of Hertzian contact<br>$b = \sqrt{(8wR)/(\pi E')}$  |
| $E'$        | reduced modulus of elasticity<br>$2/E' = (1 - \nu_1^2)/E_1 + (1 - \nu_2^2)/E_2$                      |
| $G$         | dimensionless materials parameter<br>$G = \alpha E'$   |
| $h$         | film thickness   |
| $H$         | dimensionless film thickness<br>$H = hR/b^2$   |
| $H_c$       | dimensionless central film thickness<br>$H_c = h_c R/b^2$  |

|                 |  |
|-----------------|--|
| $\bar{H}_c$     | mean central film thickness over time<br>$\bar{H}_c = (H_c^+ + H_c^-)/2$                     |
| $dH_c$          | central film thickness increase<br>$dH_c = \bar{H}_c - H_c$                                  |
| $H_0$           | integration constant   |
| $L$             | dimensionless material parameter (Moes) $L = G(2U)^{0.25}$                                   |
| $M$             | dimensionless load parameter (Moes)<br>$M = W(2U)^{-0.5}$                                    |
| $p$             | pressure   |
| $p_h$           | maximum Hertzian pressure<br>$p_h = (2w)/(\pi b)$  |
| $P$             | dimensionless pressure, $P = p/p_h$  |
| $R$             | reduced radius of curvature<br>$1/R = 1/R_1 + 1/R_2$   |
| $\mathcal{R}$   | dimensionless deviations from the smooth profile   |
| $t$             | time   |
| $T$             | dimensionless time $T = t\bar{u}/b$  |
| $u_1$           | velocity of lower (smooth) surface   |
| $u_2$           | velocity of upper surface  |
| $\bar{u}$       | mean velocity $\bar{u} = (u_1 + u_2)/2$  |
| $U$             | dimensionless speed parameter<br>$U = \eta_0 \bar{u}/(E' R)$                                 |
| $x$             | coordinate   |
| $X$             | dimensionless coordinate, $X = x/b$  |
| $X_a, X_b$      | dimensionless inlet, outlet boundary of the domain $X_a = x_a/b, X_b = x_b/b$                |
| $X_s$           | dimensionless position of waviness start   |
| $W$             | dimensionless load parameter<br>$W = w/(E' R)$   |
| $z$             | viscosity index (Roelands equation)  |
| $\alpha$        | pressure viscosity index   |
| $\bar{\alpha}$  | dimensionless parameter, $\bar{\alpha} = \alpha p_h$   |
| $\Delta_T$      | dimensionless time increment   |
| $\Delta_X$      | dimensionless space increment  |
| $\epsilon$      | coefficient in Reynolds equation<br>$\epsilon = (\bar{\rho} H^3)/(\bar{\eta} \bar{\lambda})$ |
| $\lambda$       | waviness wavelength  |
| $\bar{\lambda}$ | dimensionless speed parameter<br>$\bar{\lambda} = (12\eta_0 \bar{u} R^2)/(b^3 p_h)$          |
| $\eta$          | viscosity  |
| $\eta_0$        | viscosity at ambient pressure  |
| $\bar{\eta}$    | dimensionless viscosity, $\bar{\eta} = \eta/\eta_0$  |
| $\rho$          | density  |
| $\rho_0$        | density at ambient pressure  |
| $\bar{\rho}$    | dimensionless density, $\bar{\rho} = \rho/\rho_0$  |

### 3. Theory

For completeness this section presents the dimensionless equations to be solved.

$$\frac{\partial}{\partial X} \left( \epsilon \frac{\partial P}{\partial X} \right) - \frac{\partial(\bar{\rho}H)}{\partial X} - \frac{\partial(\bar{\rho}H)}{\partial T} = 0 \quad (1)$$

The boundary conditions are  $P(X_a, T) = P(X_b, T) = 0, \forall T$  where  $X_a$  and  $X_b$  denote the boundaries of the domain. Furthermore, the cavitation condition  $P(X, T) \geq 0, \forall X, T$  must be satisfied.  $\epsilon$  and  $\bar{\lambda}$  are defined according to:

$$\epsilon = \frac{\bar{\rho}H^3}{\eta\bar{\lambda}} \quad \bar{\lambda} = \frac{12\eta_0\bar{u}R^2}{b^3p_h}$$

The density  $\rho$  is assumed to depend on the pressure according to the Dowson and Higginson relation (Dowson and Higginson (1966)) and the Roelands viscosity pressure relation (Roelands (1966)) is used.

The film thickness equation is made dimensionless using the same parameters and accounting for a moving surface feature reads:

$$H(X, T) = H_0(T) + \frac{X^2}{2} - \mathcal{R}(X, T) - \frac{1}{\pi} \int_{X_a}^{X_b} P(X', T) \ln |X - X'| dX' \quad (2)$$

where  $\mathcal{R}(X, T)$  denotes the undeformed waviness geometry.

$$\mathcal{R}(X, T) = A(X, T) \cos \left[ 2\pi \frac{(X - X_s)}{(\lambda/b)} \right]$$

$$A(X, T) = A_s 10^{-10 (\max(0, \frac{|X - X_s|}{(\lambda/b)})^2)}$$

The exponential term in the amplitude smoothly suppresses the waviness for  $X - X_s > 0$ , i.e. without introducing any discontinuous derivatives. It allows the waviness to start effectively at  $X_s = X_{s,0} + Tu_2/\bar{u}$ , and thus allows the computations to start with the waviness well outside the contact and to move physically correct through the contact, from  $T = 0$  onwards.

At all times the force balance condition is imposed, i.e. the integral over the pressure must balance the externally applied contact load. This condition determines the value of the integration constant  $H_0(T)$  in equation (2). Expressed in the dimensionless variables it reads:

$$\int_{X_a}^{X_b} P(X, T) dX - \frac{\pi}{2} = 0, \quad \forall T \quad (3)$$

The equations were discretised with second order accuracy with respect to both space and time. Multilevel techniques were used to accelerate the convergence of the relaxation process, and to calculate the deformation integrals rapidly. These techniques are extensively described in Lubrecht (1987) and Venner (1991).

In our study we focus on the behaviour of the amplitude of the film thickness oscillations  $A_d$  in the center of the contact:

$$2A_d = \max_T H(0, T) - \min_T H(0, T) \quad (4)$$

where the maximum and minimum are taken over the period in which the film thickness variations have become periodic, thus excluding the period when the waviness enters the contact. We will refer to  $A_d$  as the (dimensionless) *deformed* amplitude.

#### 3.1. Numerical Accuracy

In this section the numerical accuracy of the results is analysed for a specific case ( $M = 100, L = 11$ ). The parameter values are:  $\alpha = 2.2 \times 10^{-8}$ ,  $z = 0.67$ ,  $\eta_0 = 4.0 \times 10^{-2}$  and  $P_0 = 1.96 \times 10^8$ . The domain was taken  $-2.5 \leq X \leq 1.5$ . The smooth problem value of the central film thickness is  $H_c = 1.417 \times 10^{-2}$  for level 8, 2048 points. The level 9 (4096 points) value is  $H_c = 1.422 \times 10^{-2}$ . The level 10 (8192 points) value is  $H_c = 1.423 \times 10^{-2}$ .

This indicates that the absolute error on level 9 is of the order of  $1 \times 10^{-5}$ . The problem of the determination of the amplitude reduction is, however, more difficult because of three reasons. First of all, one studies the behaviour of a difference between two amplitudes. Secondly, because these amplitudes are an order of magnitude smaller than  $H_c$ , and finally, because the problem



is transient the incremental error per timestep accumulates. This error accumulation can be easily monitored when comparing the waviness amplitude around  $X = -0.9$  and  $X = 0.9$ . These should remain identical as long as the pressure remains sufficiently high everywhere in the high pressure zone. For the above case with pure rolling,  $\lambda/b = 0.5$  and  $A_i/H_c = 0.1$ ,  $A_d/A_i = 0.395$  was obtained with level 8, level 9 resulted in  $A_d/A_i = 0.394$ , while the level 10 result was  $A_d/A_i = 0.393$ . Assuming second order accuracy, the level 9 results reported throughout the work are estimated to have an absolute error of approximately 1%. However, towards larger and smaller values of  $A_d/A_i$ , and for smaller values of  $\lambda/b$ , the situation is less favourable, and an overall relative error of 2-5% in  $A_d/A_i$  seems to be more realistic.

#### 4. Pure Rolling ( $u_2 = \bar{u}$ )

##### 4.1. Linear Behaviour $A_i \ll H_c$

The stationary Reynolds equation being already a complicated non-linear equation, the central idea was to study the behaviour of waviness with amplitudes  $A_i$  much smaller than the smooth film thickness  $H_c$ . It was hoped that for these small amplitudes the waviness deformation would be linear, i.e. independent of  $A_i$ . This linear behaviour is indeed obtained as can be concluded from Table 1. The differences between the columns are thought to be primarily caused by numerical errors.

| $\lambda/b$ | $A_i/H_c$ |       |       |
|-------------|-----------|-------|-------|
|             | 0.1       | 0.2   | 0.5   |
| 4.0         | 0.030     | 0.030 | 0.029 |
| 2.0         | 0.073     | 0.073 | 0.073 |
| 1.0         | 0.183     | 0.182 | 0.195 |
| 0.5         | 0.394     | 0.393 | 0.378 |
| 0.25        | 0.660     | 0.670 | 0.679 |
| 0.125       | 0.839     | 0.838 | 0.859 |

**Table 1**  $A_d/A_i$  for different initial amplitudes  $A_i/H_c$  and wavelengths  $\lambda/b$ ,  $M = 100$ ,  $L = 11$ .

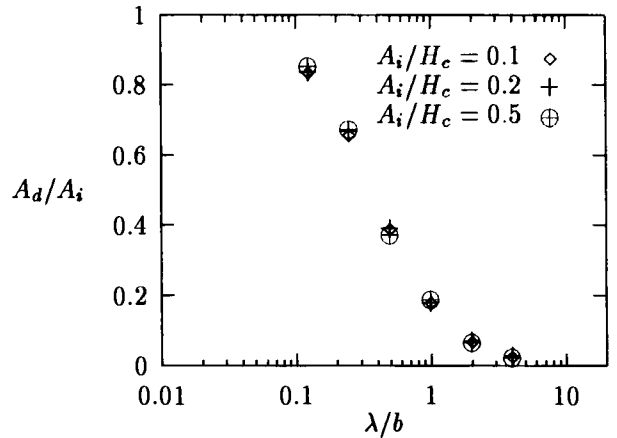


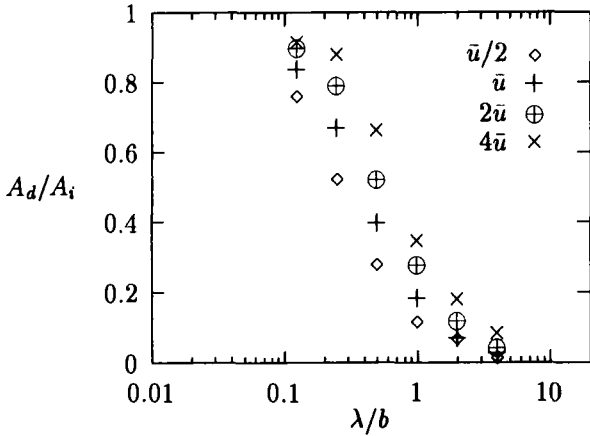
**Figure 1** Relative amplitude as a function of  $\lambda/b$ , for three different initial amplitudes and pure rolling,  $M = 100$ ,  $L = 11$ .

The same results are plotted in Figure 1, in order to observe the way  $A_d/A_i$  depends on  $\lambda/b$ . This figure shows that long wavelengths like  $\lambda/b = 4$  are almost completely deformed (flattened), while shorter wavelengths such as  $\lambda/b = 1/8$  deform only very little. However, as is demonstrated in the next section, the relative amplitude reduction depends on the specific operating conditions.

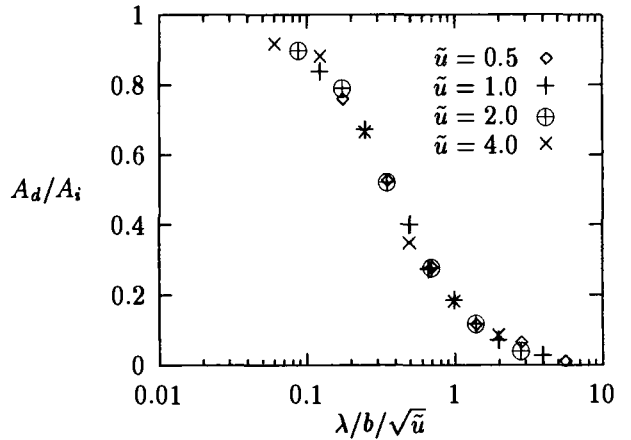
##### 4.2. Influence of Rolling Speed

Figure 2 shows how the amplitude reduction curve depends on the velocity  $\bar{u}$ . A series of constant horizontal shifts with respect to the coordinate  $\lambda/b$  was obtained. For increasing values of  $\bar{u}$  the curve tends to be shifted to the right. Since the relative amplitude  $A_d/A_i$  is independent of  $A_i$ , and since  $0 \leq A_d/A_i \leq 1$ , it seems logical to try and reduce the number of parameters by scaling the horizontal coordinate.

It was found that the horizontal shift can be counteracted by introducing a new parameter  $\lambda/b/\sqrt{\bar{u}}$ . In order to keep the scale of the horizontal axis similar to the ones used before, all velocities are scaled to the velocity  $\bar{u}$  in Figure 2. Figure 3 shows that the different curves all coincide when the new horizontal coordinate is used  $\lambda/b/\sqrt{\bar{u}}$ .



**Figure 2** Relative amplitude as a function of  $\lambda/b$ , for four different speeds and pure rolling.



**Figure 3** Relative amplitude as a function of  $\lambda/b/\sqrt{\bar{u}}$ , for four different speeds and pure rolling.

**4.3. Influence of Operating Conditions**

After this successful attempt, it was logical to try to reduce the curves with respect to load and material parameters as well. Remembering though, that the steady-state EHL problem can be described by two parameters only:  $\bar{\alpha}, \bar{\lambda}$  or  $M, L$ , the parameter  $\sqrt{\bar{u}}$  was abandoned, in favour of  $M$  and  $L$ .

Fixing the ratio of  $M$  and  $L$  to obtain  $1/\sqrt{U}$ , see above, and staying close to rational fractions for the exponents, the following dimensionless parameter  $\nabla$  was obtained:  $\nabla = \lambda/b M^{3/4}/L^{1/2}$ . This parameter allows a single description of  $A_d/A_i$  as a function of  $\nabla$  irrespective of the operating conditions, see Figure 4. This parameter can be rewritten, up to a constant as:  $\nabla = \lambda/b/\sqrt{\bar{\alpha}\bar{\lambda}}$ . Since the two expressions are identical up to a multiplicative constant, their approximation is equally good.

In a slightly different approach the parameter  $\nabla$  is made dimensionless with respect to the central film thickness, in dimensionless terms it reads:  $\nabla = \lambda/b/H_c^{3/4}$ . The reduction of all results onto a single curve is equally effective, as is shown by Figure 5.

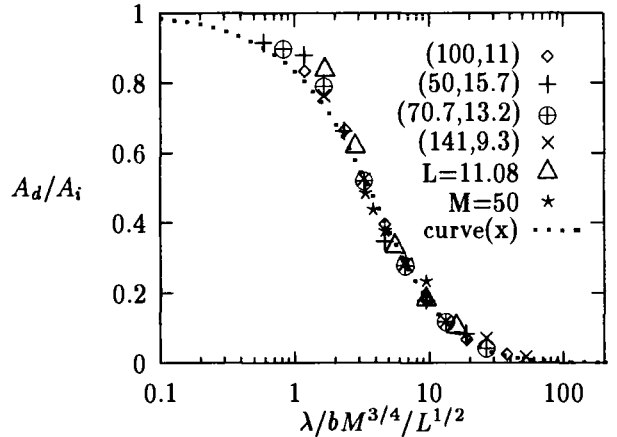


**Figure 4** Relative amplitude as a function of  $\nabla$ , for different conditions ( $M, L$ ) and pure rolling.

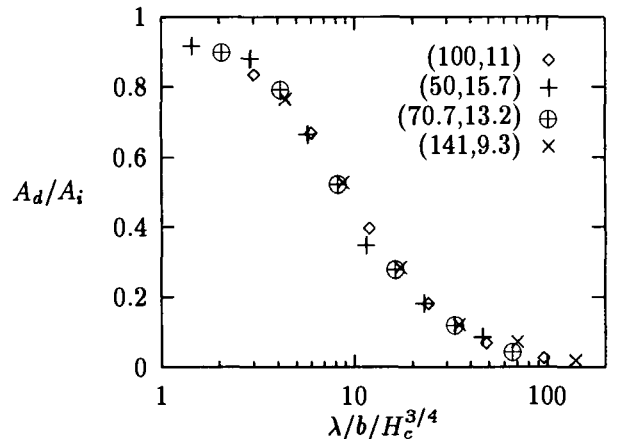


**Figure 5** Relative amplitude as a function of  $\nabla$ , for different conditions ( $M, L$ ) and pure rolling.

#### 4.4. Curve Fit

The single curve that describes the relative amplitude  $A_d/A_i$  as a function of  $\nabla$ , is approximated by the following equation:

$$\frac{A_d}{A_i} = \frac{1}{1 + 0.17\nabla + 0.03\nabla^2} \quad (5)$$

where  $\nabla = \lambda/bM^{3/4}/L^{1/2}$ . This equation naturally fulfills the two asymptotic values:  $\lim_{\nabla \rightarrow 0} A_d/A_i = 1$  and  $\lim_{\nabla \rightarrow \infty} A_d/A_i = 0$ . This curve, which is plotted in Figures 4 and 6, closely approximates the computed values for  $A_d/A_i \leq 0.5$ . For larger values,  $0.5 < A_d/A_i < 1$ , however, this curve seems to predict values which are too small. More complex approximations are possible to improve the fit for  $0.5 < A_d/A_i < 1$  but do not add to the insight.

Greenwood and Morales-Espejel (1994) predict a similar relation between amplitude and dimensionless wavelength, which can be rewritten using the notation of this paper as:

$$\frac{A_d}{A_i} = \frac{1}{1 + C^*\tilde{\nabla}} \quad (6)$$

where  $\tilde{\nabla} = \lambda/b/H_c$  and  $C^* \simeq 3.3$ . Since  $H_c \simeq 0.01$ , the point  $A_d/A_i = 0.5$  would be reached around  $\lambda/b = 0.003$ , whereas Figure 1 shows that this point occurs around  $\lambda/b = 0.3$ . Thus, qualitatively (6) gives a similar curve as (5), but as the predictions of (6) are two orders of magnitude lower, we are still left in the dark with respect to the ‘‘physical’’ mechanism determining the observed behaviour.

#### 4.5. Non-Linear Behaviour $A_i \simeq H_c$

When the waviness amplitude becomes comparable to the film thickness the above stated linear behaviour is expected to break down. However, an extension of Figure 1, including amplitudes  $A_i$  up to three times the film thickness value, show hardly any deviation from the linear behaviour, see Figure 6.

From this Figure it can be concluded that the amplitude reduction remains linear, even for amplitudes  $A_i$  much larger than the film thickness. However, for  $A_i/H_c \geq 2.0$  and  $A_d/A_i \geq 0.6$  this suggests that  $A_d > H_c$ , and that contact between

the two surfaces occurs. Indeed,  $A_d > H_c$ , but no contact occurs because the mean central film thickness value  $\bar{H}_c$  increases over the smooth surface value  $H_c$ , as is shown in Figure 7. In this Figure  $\bar{H}_c$  is defined as  $\bar{H}_c = (H_c^+ + H_c^-)/2$ , where  $H_c^+$  and  $H_c^-$  are the subsequent maximum and minimum value of  $H(X = 0, T)$  over time. For deformed amplitudes  $A_d$  that are larger than  $H_c$ ,  $\bar{H}_c$  tends asymptotically to  $A_d$ , which is logical, since no additional deformation seems to occur.

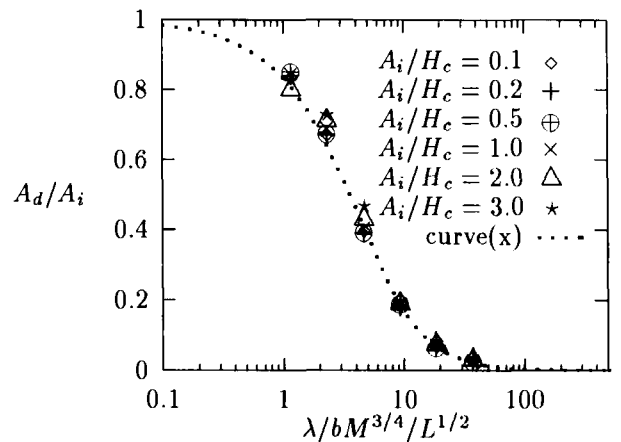


**Figure 6** Relative amplitude as a function of  $\nabla$ , for six different initial amplitudes and pure rolling,  $M = 100$ ,  $L = 11$ .

In Figure 8 the increase in the mean central film thickness  $dH_c$  is plotted against  $\lambda/b$ ,  $dH_c$  is defined as  $dH_c = (H_c^+ + H_c^-)/2 - H_c$ . The variation of  $dH_c$  with  $A_i$  is not linear, as is shown in Figure 8, it seems as if  $dH_c \propto A_i^{3/2}$ . A similar non linear behaviour was observed in Venner and Lubrecht 1994a, Figure 9.

#### 5. Simple Sliding ( $u_2 = 0$ )

The same analysis as in section 4 was performed for the stationary case of simple sliding, where the waviness is located on the stationary surface:

$$\mathcal{R}(X) = A_i \cos\left(\frac{2\pi X}{\lambda/b} - \phi\right)$$

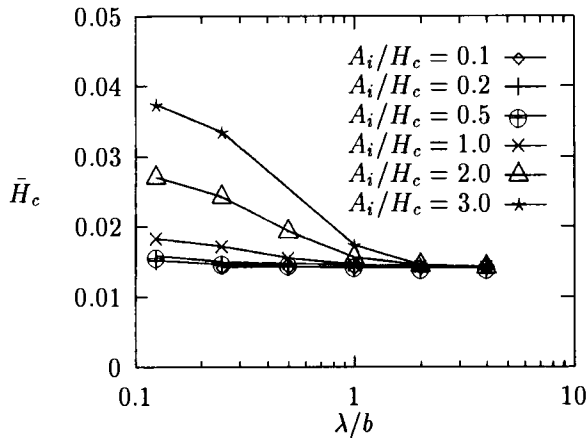


**Figure 7** Mean central film thickness as a function of  $\lambda/b$ , for six different initial amplitudes and pure rolling,  $M = 100$ ,  $L = 11$ .

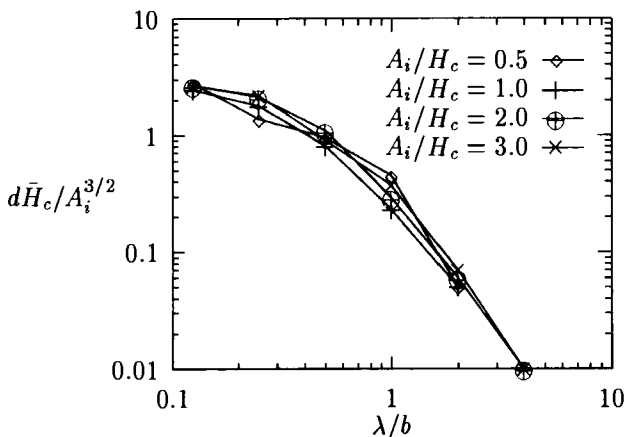


**Figure 8** Mean central film thickness difference as a function of  $\lambda/b$ , for six different initial amplitudes and pure rolling,  $M = 100$ ,  $L = 11$ .

In this form the problem has been studied extensively in the past, e.g. over a decade ago by Goglia et al. (1984b). They investigated in detail the effect of the waviness amplitude and phase-shift on the pressure profile and film shape. Here we revisit this problem, and investigate if a similar mastercurve exists as for the transient pure rolling problem.

As the problem is stationary  $A_d$  according to (4) is not defined. However, instead of  $T$  the phase-shift may be used to obtain an equivalent deformed amplitude (Couhier 1996):

$$2\bar{A}_d = \max_{0 \leq \phi \leq 2\pi} H(X=0) - \min_{0 \leq \phi \leq 2\pi} H(X=0) \quad (7)$$

Subsequently the behaviour of the equivalent relative amplitude  $\bar{A}_d/A_i$  was studied as a function of the operating conditions, see Figure 9. Firstly it appears that, as for the pure rolling cases, the results obtained for different loading conditions can be mapped on a single curve using the very same dimensionless parameter  $\nabla$ . However, the behaviour is essentially different. Indeed for  $\nabla > 1$  we see a similar behaviour as in Figure 4, however, for  $\nabla < 1$ , the quantity  $\bar{A}_d$  decreases. This behaviour reflects a fundamental difference between the transient solution and the steady state solution. The reduction of  $\bar{A}_d$  for  $\nabla < 1$  does not imply that the waviness itself is completely flattened. On the contrary, for small wavelengths the film thickness varies as a function of  $X$  with an amplitude that, even though it is small (and for larger wavelengths almost zero), increases with decreasing wavelength.

The reduction of  $\bar{A}_d$  for  $\nabla < 1$  is simply the consequence of its definition as a film thickness difference taken from a series of (uncoupled) solutions. Under pure sliding conditions the waviness in the inlet perturbs the pressure build-up in the transition zone (zone in which the Poiseuille flow term disappears). The extent of this zone is limited, but whenever the wavelength becomes smaller than its size, an averaging effect takes place, resulting in an insensitivity of  $H(X=0)$  to a phase-shift.

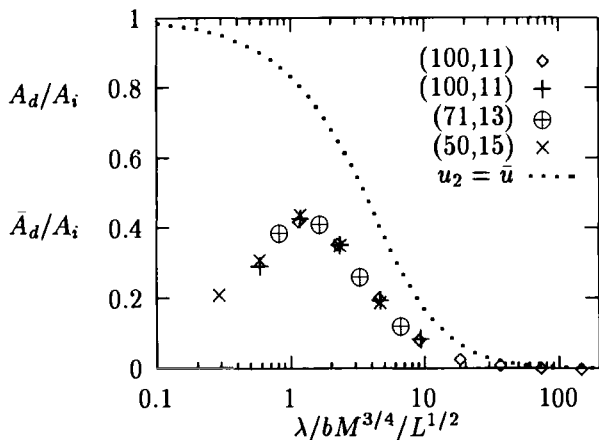


**Figure 9** Relative equivalent amplitude as a function of  $\nabla$  for different conditions ( $M, L$ ) and simple sliding. The dotted curve gives the relative amplitude as a function  $\nabla$  for pure rolling according to equation (5)

## 6. Discussion and Conclusion

The problem of waviness amplitude reduction in an EHL line contact has been studied in this paper by means of the amplitude  $A_d$  of the film thickness oscillations in the center of the contact. It was found that under pure rolling the relative amplitude  $A_d/A_i$  can be expressed as a single function of a dimensionless wavelength  $\nabla = \lambda/bM^{3/4}/L^{1/2}$ . This relation does not depend either on the contact operating conditions, nor on the initial amplitude or wavelength. For large amplitude waviness, the mean central film thickness  $d\bar{H}_c$  tends to increase with  $A_i$ .

The same study was carried out for the case of pure sliding. For this steady state problem an equivalent deformed amplitude can be defined using the phase of the wave relative to the contact. It was shown that the relative equivalent deformed amplitude  $\bar{A}_d/A_i$  is a function only of the very same dimensionless wavelength  $\nabla$ . For large  $\nabla$  the behaviour of  $\bar{A}_d/A_i$  is similar to the behaviour of  $A_d/A_i$  for pure rolling. However, for small  $\nabla$  the behaviour was quite different as  $\bar{A}_d/A_i$  tends to 0 whereas  $A_d/A_i$  tends to unity. This different behaviour is a consequence of the definition of  $\bar{A}_d$ .

Further work is required to analyse the amplitude behaviour under general rolling/sliding conditions.

In this paper we studied the deformed amplitude by means of the film thickness oscillations in the center of the contact. Strictly this is not exactly the deformed amplitude as the result includes changes of  $H_0$  as a function of time. The exact influence of these changes should be investigated. Subsequently attention should be directed to the case of two dimensional roughness in point contacts.

Finally, fast and stable numerical algorithms presently allow detailed studies of the transient effects of surface features on film and pressure in EHL contacts. Indeed, detailed simulations for individual features and load conditions can give much information, but the main question is to translate this knowledge into simple engineering tools for general use. The results presented here can be an important step in this direction. They facilitate computation of (an estimate of) the deformed film profile for pure rolling from the decomposition of the undeformed profile in its Fourier components and the application of equation (5) onto every single component amplitude.

## 7. Acknowledgement

The first author kindly acknowledges the support of the Royal Netherlands Academy of Arts and Sciences.

## 8. References

- Ai, X., Cheng, H.S., and Zheng, L., 1993, "A Transient Model for Micro-Elastohydrodynamic Lubrication with Three-Dimensional Irregularities," *ASME JOT*, **115**, pp. 102-110.
- Ai, X., and Cheng, H.S., 1994a, "The Influence of Moving Dent on Point EHL Contacts," *STLE Trib. Trans.*, **37**, pp. 323-335.
- Ai, X., and Cheng, H.S., 1994b, "A Transient EHL Analysis for Line Contacts with a Measured Surface Roughness using Multigrid Technique," *ASME JOT*, **116**, pp. 549-558.

- Ai, X., and Cheng, H.S.**, 1995 "The Effects of Surface Texture on EHL Point Contacts," submitted to *ASME JOT*.
- Chang, L., Cusano, C., and Conry, T.F.**, 1989, "Effects of Lubrication Rheology and Kinematic Conditions on Micro-Elastohydrodynamic Lubrication," *ASME JOT*, **111**, 344-351.
- Chang, L., and Webster, M.N.**, 1991, "A Study of Elastohydrodynamic Lubrication of Rough Surfaces," *ASME JOT*, **113**, 110-115.
- Chang, L.**, 1992, "Traction in Thermal Elastohydrodynamic Lubrication of Rough Surfaces," *ASME JOT*, **114**, 186-191.
- Couhier, F.**, 1996, "Influence des Rugosites de Surface sur les Mecanismes de Lubrification de Contact Elastohydrodynamique Cylindre-Plan", (in French) Ph.D. Thesis, INSA de Lyon, France.
- Dowson, D., and Higginson, G.R.**, 1966, "Elastohydrodynamic Lubrication, The Fundamentals of Roller and Gear Lubrication," Pergamon Press, Oxford, Great Britain.
- Goglia, P.R., Cusano, C., and Conry, T.F.**, 1984, "The Effects of Surface Irregularities on the Elastohydrodynamic Lubrication of Sliding Line Contacts. Part I - Single Irregularities," *ASME JOT*, **106**, 104-112.
- Goglia, P.R., Cusano, C., and Conry, T.F.**, 1984, "The Effects of Surface Irregularities on the Elastohydrodynamic Lubrication of Sliding Line Contacts. Part II - Wavy Surfaces," *ASME JOT*, **106**, 113-119.
- Greenwood, J.A., and Johnson, K.L.**, 1992, "The Behaviour of Transverse Roughness in Sliding Elastohydrodynamically Lubricated Contacts," *WEAR*, **153**, pp. 107-117.
- Greenwood, J.A., and Morales Espejel, G.E.**, 1994, "The Behaviour of Transverse Roughness in EHL Contacts," *Proc. IMechE*, **208**, pp. 121-132.
- Kaneta, M., and Cameron, A.**, 1980, "Effects of Asperities in Elastohydrodynamic Lubrication," *ASME JOLT*, **102**, 374-379.
- Kaneta, M.**, 1992, "Effects of Surface Roughness in Elastohydrodynamic Lubrication," *JSME*, **III**, **35**, 4, pp. 535-546.
- Kaneta, M., Sakai, T., and Nishikawa, H.**, 1992, "Optical Interferometric Observations of the Effects of a Bump on Point Contact EHL," *ASME JOT*, **114**, pp. 779-784.
- Kaneta, M., Sakai, T., and Nishikawa, H.**, 1993, "Effects of Surface Roughness on Point Contact EHL," *STLE Trib. Trans.*, **36**, **4**, pp. 605-612.
- Kweh, C.C., Evans, H.P., and Snidle, R.W.**, 1989, "Micro-Elastohydrodynamic Lubrication of an Elliptical Contact with Transverse and Three-Dimensional Roughness," *ASME JOT*, **111**, 577-583.
- Lee, R.T., and Hamrock, B.J.**, 1990, "A circular non-Newtonian Fluid Model: Part II - used in Micro-Elastohydrodynamic Lubrication," *ASME JOT*, **112**, 497-505.
- Lubrecht, A.A.**, 1987, "Numerical Solution of the EHL Line and Point Contact Problem Using Multigrid Techniques," Ph.D. Thesis, University of Twente, Enschede, The Netherlands, ISBN 90-9001583-3.
- Lubrecht, A.A., Venner, C.H., Lane, S., Jacobson, B., and Ioannides, E.**, 1990, "Surface Damage- Comparison of Theoretical and Experimental Endurance Lives of Rolling Bearings," *Proceedings of the 1990 Japan International Tribology Conference, Nagoya, Japan*, **1**, 185-190.
- Lubrecht, A.A., and Venner, C.H.**, 1992, "Aspects of two-Sided Surface Waviness in an EHL Line Contact," presented at the 1992 Leeds-Lyon Conference on Tribology, Leeds, U.K.
- Morales Espejel, G.E.**, 1993, "Elastohydrodynamic lubrication of smooth and rough surfaces," Ph.D. Thesis, University of Cambridge, Department of engineering.
- Osborn, K.F., and Sadeghi, F.**, 1992, "Time Dependent Line EHD Lubrication Using the Multigrid/Multilevel Technique", *ASME JOT*, **114**, 68-74.
- Roelands, C.J.A.**, 1966, "Correlational Aspects of the Viscosity-Temperature-Pressure Relationship of Lubricating Oils" Ph.D. Thesis, Technical University Delft, Delft, The Netherlands, (V.R.B., Groningen, The Netherlands).
- Venner, C.H.**, 1991, "Multilevel Solution of the EHL Line and Point Contact Problems," Ph.D. Thesis, University of Twente, Enschede, The Netherlands. ISBN 90-9003974-0.
- Venner, C.H., Lubrecht, A.A., and ten Napel, W.E.**, 1991, "Numerical Simulation of

the Overrolling of a Surface Feature in an EHL Line Contact," *ASME JOT*, **113**, 777-783.

**Venner, C.H., and Lubrecht, A.A.**, 1994a, "Transient Analysis of Surface Features in an EHL Line Contact in the case of Sliding," *ASME JOT*, **116**, pp. 186-193.

**Venner, C.H., and Lubrecht, A.A.**, 1994b, "Numerical Simulation of a Transverse Ridge in a Circular EHL Contact, under rolling/sliding", *ASME JOT*, **116**, pp. 751-761.

**Venner, C.H., and Lubrecht, A.A.**, 1994c, "Numerical Simulation of Waviness in a Circular EHL Contact, under rolling/sliding", *presented at the 1994 Leeds-Lyon Symposium on Tribology*.

**Venner, C.H., and Lubrecht, A.A.**, 1996, "Numerical Analysis of the influence of Waviness on the Film Thickness of a Circular EHL Contact", *ASME JOT*, **118**, pp. 153-161.

**Wedeven, L.D., and Cusano, C.**, 1979, "Elastohydrodynamic Film Thickness Measurements of Artificially Produced Surface Dents and Grooves," *ASLE Trans.*, **22**, 369-381.

## Effect of micro-cavitation on oil film thickness and pressure distributions in micro-EHL line contact

Shigeo KAMAMOTO<sup>a</sup>, Masaaki SAKURAGI<sup>a</sup>, Koji FUJIMOTO<sup>b</sup>  
and Takashi YAMAMOTO<sup>c</sup>

<sup>a</sup> Research & Development Center, Koyo Seiko Co., Ltd., 24-1 Kokubuhiganjyo-cho,  
Kashiwara-shi, Osaka 582, Japan

<sup>b</sup> Department of Aeronautics and Astronautics, University of Tokyo, 7-3-1 Hongo, Bunkyo-ku,  
Tokyo 113, Japan

<sup>c</sup> Department of Mechanical Systems Engineering, Tokyo University of Agriculture and Technology,  
2-24-16 Naka-cho, Koganei-shi, Tokyo 184, Japan

The micro-EHL problems taking into account the micro-cavitation caused by surface asperities were analysed numerically to determine the criterion of formation of micro-cavity and to study the effect of micro-cavitation on oil film thickness and pressure distributions. The numerical procedures consist of the Newton-Raphson method and the step by step method. The pressure in each micro-cavity is assumed to be the saturated vapor pressure of lubricant, and the negative gauge pressure is obtained at the region of each micro-cavity. It is found that the micro-cavities appear, when the surface roughness amplitude is large enough. With decrease of the dimensionless speed parameter  $U$  or the dimensionless materials parameter  $G$ , the micro-cavities appear even if the surface roughness amplitude is small.

### 1. INTRODUCTION

Micro-EHL problems have been studied in many lubricating conditions. It is already recognized that the effects of surface roughness on oil film thickness and pressure distributions cannot be excluded in real tribological problems. However, in the micro-EHL analyses, the effect of mutual interactions between micro asperities cannot be well simulated comparing the viscosity rising effect of lubricant due to contact pressure. Therefore, it is expected that the micro-cavitation caused by surface asperities may overcome this difficulty [1-3].

The damage by cavitation in journal bearings have been investigated, and reviewed by Dowson-Taylor [4]. The aspect of cavitation in lubricat are recognized gaseous and vaporous.

The boundary conditions of cavity in journal

bearings were investigated by Swift [5], Stieber [6], Coyne-Elrod [7] and Floberg [8], and the numerical procedures were presented [9-14]. However, these investigations treated only low contact pressure conditions in journal bearings. In the case of high contact pressure conditions as realized in rolling element bearings, the gaseous cavitation (gauge pressure) were studied [15-16].

In this paper, the micro-EHL problems taking into account the micro-cavitation caused by surface asperities were treated numerically to determine the criterion of formation of micro-cavity and to study the effect of micro-cavitation on EHL oil film thickness and pressure distributions. It is assumed that the pressure in each micro-cavity is equal to the saturated vapor pressure of lubricant. Loading conditions are simulated to the conditions of rolling element bearings.



2. LINE CONTACT MODEL

In conducting following numerical simulations, the line contact model between a rigid roller and an elastic half-space is used as shown in Figure 1.

A surface asperity profile is assumed to be a sinusoidal curve as shown in Figure 2. If the surface asperities are large enough, they produce micro-cavities as indicated in the figure. The pressure in each micro-cavity is assumed the saturated vapor pressure.

In order to simplify this numerical simulation, the micro-EHL problems of line contact between a rough-stationary rigid surface and a smooth-moving elastic surface are solved.

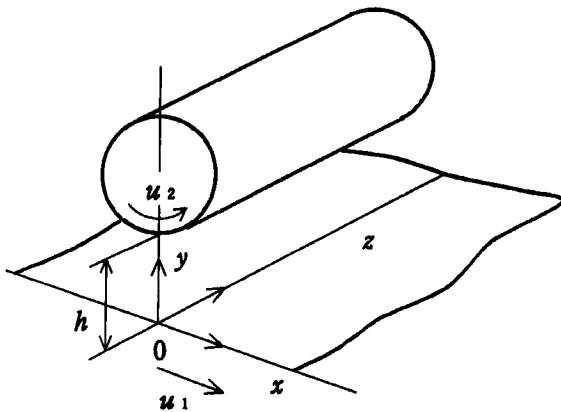


Figure 1. Line contact model

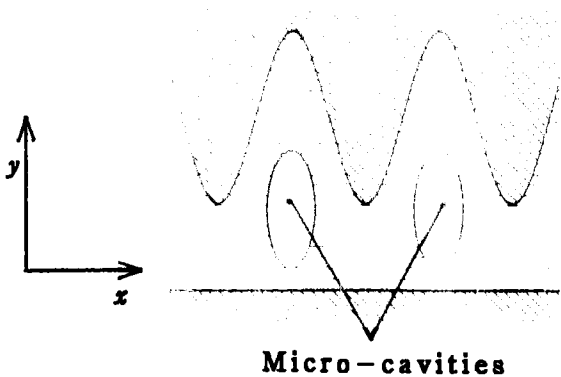


Figure 2. Rough surface micro-cavitation model

3. NUMERICAL CALCULATIONS

The numerical calculation procedures consist of two stages. At the first stage, the micro-EHL problem is solved to obtain the contact pressure distribution [17]. At the second stage, the locations where micro-cavities appear are determined.

3.1. Micro-EHL analysis

The isothermal, line-contact EHL problem can be represented with three dimensionless equation forms. The first one is the Reynolds equation. For each node  $i$  indicating virtual location in the Newtonian fluid, the Reynolds equation is expressed as follows :

$$f_i = H_i^3 \left( \frac{dP}{dX} \right)_i - \frac{3\pi^2 U \bar{\mu}_i}{4W^2} \left( H_i - \frac{(\bar{\rho}_m H_m)}{\bar{\rho}_i} \right) = 0 \quad (1)$$

where  $\bar{\mu}_i$  is given by the Roelands equation [18]:

$$\bar{\mu}_i = \exp \left[ \frac{G}{5.1 \times 10^{-9} z E'} \left( -1 + (1 + 5.1 \times 10^{-9} \rho_h P_i)^{0.7} \right) \right] \quad (2)$$

and  $\bar{\rho}_i$  is given by the Dowson-Higginson's equation [19] :

$$\bar{\rho}_i = 1 + \frac{0.6 \times 10^{-9} \rho_h P_i}{1 + 1.7 \times 10^{-9} \rho_h P_i} \quad (3)$$

where  $\rho_h$  is given by the maximum Hertzian contact pressure :

$$\rho_h = E' \sqrt{\frac{W}{2\pi}} \quad (4)$$

The term of  $(dP/dX)_i$  is important to solve the Reynolds equation. To keep the stability of numerical calculations, we use the Euler's difference formula [20-23]. The discrete version is introduced by the following technique :

$$\frac{d}{dX}(\bar{\mu}^{-1}) = \frac{d}{dP}(\bar{\mu}^{-1}) \frac{dP}{dX} \quad (5)$$

to obtain the accurate calculation results for Roelands equation. Therefore,  $(dP/dX)_i$  is given as :

$$\left(\frac{dP}{dX}\right)_i = \left[-G \sqrt{\frac{W}{2\pi}} (1+5.1 \times 10^{-9} p_h P_i)^{z-1}\right]^{-1} \times (\bar{\mu}_i) \frac{(\bar{\mu}_{i+1})^{-1} - (\bar{\mu}_i)^{-1}}{X_{i+1} - X_i} \quad (6)$$

The second one is the oil film thickness equation, that is,

$$H_i = H_0 + \frac{X_i^2}{2} - \frac{1}{2\pi} \sum_{j=1}^n D_{ij} P_j - \Omega_i \quad (7)$$

where  $\Omega$  is a term to take into account the surface asperity profile in these numerical simulation, that is,

$$\Omega_i = \frac{\Sigma \cos}{2} \cos \left\{ \frac{2\pi}{\Lambda \cos} (X_i - \Phi) \right\} \quad (8)$$

and  $D_{ij}$  is the influence coefficient obtained by Houpert–Hamrock [24]. By using the Lagrangian interpolation method to integrate the pressure, this term gives accurate calculation results of the elastic deformation.

The third one is the force equilibrium equation, that is,

$$S = \sum_{i=1}^n C_i P_i - \frac{\pi}{2} = 0 \quad (9)$$

Similarly, to obtain the accurate calculation results, the Lagrangian interpolation method is used to integrate the pressure in the equation (9). The term  $C_i$  is a weighting factor obtained by Houpert–Hamrock [24].

At the inlet and the outlet menisci, the Reynolds boundary conditions are used, that is,

$$\text{at the inlet meniscus : } X = X_{L1}, \quad P = 0$$

$$\text{at the outlet meniscus : } X = X_{L2}, \quad P = \frac{dP}{dX} = 0$$

These equations can be solved by the Newton–Raphson method. In the Newton–Raphson algorithm, the linear system of  $n+1$  equations is represented as follows :

$$\begin{bmatrix} \frac{\partial f_1}{\partial(\bar{\rho}_m H_m)} & \frac{\partial f_1}{\partial P_2} & \dots & \frac{\partial f_1}{\partial P_n} & \frac{\partial f_1}{\partial H_0} \\ \frac{\partial f_2}{\partial(\bar{\rho}_m H_m)} & \frac{\partial f_2}{\partial P_2} & \dots & \frac{\partial f_2}{\partial P_n} & \frac{\partial f_2}{\partial H_0} \\ \cdot & \cdot & \dots & \cdot & \cdot \\ \cdot & \cdot & \dots & \cdot & \cdot \\ \cdot & \cdot & \dots & \cdot & \cdot \\ \frac{\partial f_n}{\partial(\bar{\rho}_m H_m)} & \frac{\partial f_n}{\partial P_2} & \dots & \frac{\partial f_n}{\partial P_n} & \frac{\partial f_n}{\partial H_0} \\ 0 & C_2 & \dots & C_n & 0 \end{bmatrix}$$

$$\begin{bmatrix} \Delta(\bar{\rho}_m H_m) \\ \Delta P_2 \\ \cdot \\ \cdot \\ \cdot \\ \Delta P_n \\ \Delta H_0 \end{bmatrix} = \begin{bmatrix} f_1 \\ f_2 \\ \cdot \\ \cdot \\ \cdot \\ f_n \\ S \end{bmatrix} \quad (10)$$

The Doolittle method is used to solve this linear system to decrease the required computing time. Since the calculation results are summarized as correction values of unknowns, the new values of unknowns are given as follows :

$$(\bar{\rho}_m H_m)^{new} = (\bar{\rho}_m H_m)^{old} + \Delta(\bar{\rho}_m H_m)^{new} \quad (11)$$

$$P_i^{new} = P_i^{old} + \Delta P_i^{new} \quad (i=2 \dots n) \quad (12)$$

$$H_0^{new} = H_0^{old} + \Delta H_0^{new} \quad (13)$$

Since the value of term  $(\overline{\rho_m H_m})$  is obtained, the oil film thickness at the outlet meniscus is given by substituting  $P=dP/dX=0$  in equation (1).

$$H_m = (\overline{\rho_m H_m}) \quad (14)$$

Therefore, the outlet meniscus distance and number of node  $n$  are determined by comparison between oil film distribution and  $(\overline{\rho_m H_m})$  [24]. This method is effective to avoid the singular point in the equation of elastic deformation.

The iterative calculation is continued, until the convergence criterion is satisfied. The convergence criterion is defined as follows :

$$\sum_{i=2}^n |P_i| \leq 10^{-6} \quad (15)$$

The numerical method provides converged solutions in a wide region of dimensionless parameters  $G$ ,  $U$  and  $W$ . Based on this method, the complete resolutions can be obtained in a variety of operating conditions of rolling element bearings.

### 3. 2. Micro-cavitation

The micro-EHL problems are solved at the condition of large surface roughness amplitude, and the minus gauge pressure appears. If the minus gauge pressure is smaller than the value of saturated vapor pressure of lubricant, the cavity appears in the lubricant film.

When the Reynolds equation is applied to the region where lubricant does not exist, the physical inconsequence occurs. Therefore, the new outlet meniscus should be assumed at the starting point of the physical inconsequence in the Reynolds equation. The new inlet meniscus is assumed at the starting point where the Reynolds equation can be applied. The region between the new inlet meniscus and the new outlet meniscus is determined by micro-cavity.

If the micro-cavitation is considered to only remove the physically inconsequent Reynolds

equations, the second problem arises.

The flow continuous equation is taken into account, when the Reynolds equation is introduced from the Navier-Stokes equation. Even if the physical inconsequence in the Reynolds equations are removed, the flow continuous is not satisfied in each lubricated region separated by the micro-cavity. Since the condition of mass flow continuous must be satisfied, the disagreement of mass flow in each lubricated region is physical inconsequence. Therefore, by using the procedure of the starved EHL problem, the location of new meniscus is controlled to satisfy the mass flow continuous condition. At the lubricated region separated by the micro-cavity, the mass flow rate  $\overline{Q_{x,k}}$  must be satisfied as follows :

$$\overline{Q_{x,1}} = \overline{Q_{x,2}} = \dots = \overline{Q_{x,k}} = \dots = \overline{Q_{x,1}} \quad (16)$$

where the mass flow in each element is given as follows :

$$\overline{Q_{x,i}} = \overline{\rho_i} \left\{ -\frac{32 H_i^3 W^3}{3 \overline{\mu_i} \pi^3 U} \left( \frac{dP}{dX} \right)_i + \frac{8 H_i W}{\pi} \right\} \quad (17)$$

Since the cavities are formed at the regions located separately from the atmosphere, the pressure in each cavity is assumed to be the saturated vapor pressure of lubricant. In the real numerical analysis, the pressure at the element in a micro-cavity is assumed to be the known value  $P_v$ . The pressure in the micro-cavity is used to calculate the elastic deformation and force equilibrium equation, but the Reynolds equation is not applied in the micro-cavity.

In the conventional EHL analysis, the Reynolds boundary condition was used. The pressure in micro-cavities is the saturated vapor pressure of lubricant, the Reynolds boundary condition cannot be applied to the new meniscus formed by the micro-cavity.

In this paper, two boundary conditions for the micro-cavitation were discussed. At the new meniscus formed by the micro-cavity, the

boundary conditions are represented as follows :

(boundary condition I )

at the inlet meniscus :  $X=X_{c1,k}$  ,  $P=P_v$

at the outlet meniscus :  $X=X_{c2,k}$  ,  $P=P_v$   
 $\frac{dP}{dX}=0$

(boundary condition II )

at the inlet meniscus :  $X=X_{c1,k}$  ,  $P=P_v$

at the outlet meniscus :  $X=X_{c2,k}$  ,  $P=P_v$

If the boundary condition I is used, the oil film thickness at the new outlet meniscus is given by substituting  $P=P_v$  ,  $dP/dX=0$  in equation (1).

$$H_{c2} = \frac{(\overline{\rho_m H_m})}{\rho_{c2}} \tag{18}$$

where  $\overline{\rho_{c2}}$  is given by substituting  $P=P_v$  in the Dowson-Higginson's equation :

$$\overline{\rho_{c2}} = 1 + \frac{0.6 \times 10^{-9} \rho_h P_v}{1 + 1.7 \times 10^{-9} \rho_h P_v} \tag{19}$$

Therefore, the new outlet meniscus distance is determined by comparison between the oil film distribution and  $H_{c2}$ . The oil film thickness at the new inlet meniscus is given by the step by step approach to satisfy the continuity of mass flow.

If the boundary condition II is used, the new outlet meniscus distance is determined by the starting point of the saturated vapor pressure. Similarly, the oil film thickness at the new inlet meniscus is given by the step by step approach to satisfy the continuity of mass flow.

If the slope of the pressure is fixed to be 0 :

at the inlet meniscus :  $X=X_{c1,k}$  ,  $P=P_v$   
 $\frac{dP}{dX}=0$

, the mass flow continuity in each lubricated region separated by the micro-cavity cannot be satisfied. The flow chart of algorithm used in this paper is shown in Figure 3.

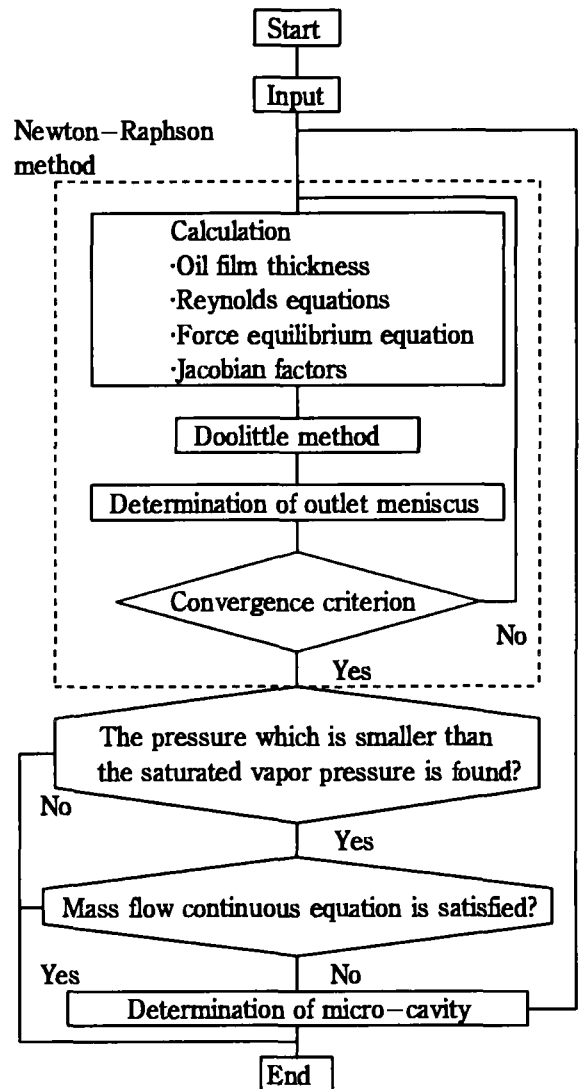


Figure 3. Flow chart of algorithm of micro-EHL analysis taking into account the micro-cavitation caused by surface asperities.

4. RESULTS AND DISCUSSION

4.1. Boundary condition

The calculation results of oil film thickness and pressure distribution are indicated in Figures 4 and 5 to compare the effects of boundary conditions I and II. Simulating conditions are as follows :

dimensionless parameters :  $G=6000, U=10^{-11},$

$$W=2.71 \times 10^{-4},$$

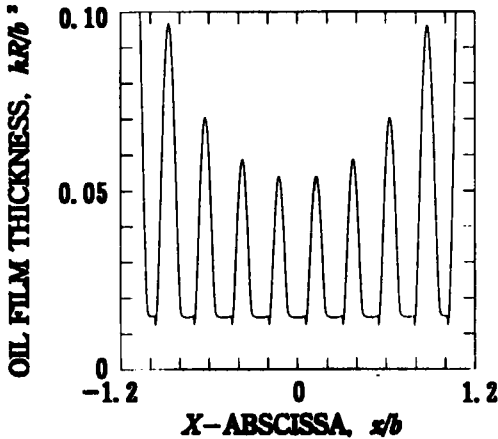
surface asperity profiles :  $\Sigma_{cos}=0.15,$

$$\Lambda_{cos}=0.25, \Phi=0$$

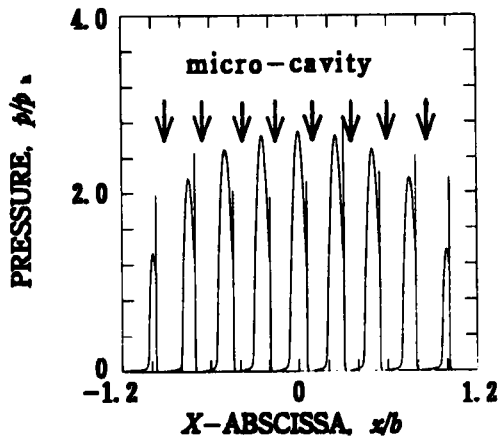
saturated vapor pressure :  $P_v=-6.66 \times 10^{-8}.$

If real properties of material for rolling

element bearings are applied, the maximum Hertzian contact pressure is calculated as 1.5GPa. Considering an increase of contact pressure by surface asperities, the maximum contact pressure is calculated as about 3.5GPa. The oil film shape of each bump is similar to that obtained in conventional macro-EHL analyses. The shape of the pressure distribution at each bump is similar to the shape of pressure spike obtained in conventional macro-EHL analyses. Micro-cavities are formed in these calculations. Since the disagreement of oil film thickness and pressure distribution are not remarkable as shown in Figures 4 and 5, the effect of difference in boundary condition is small.

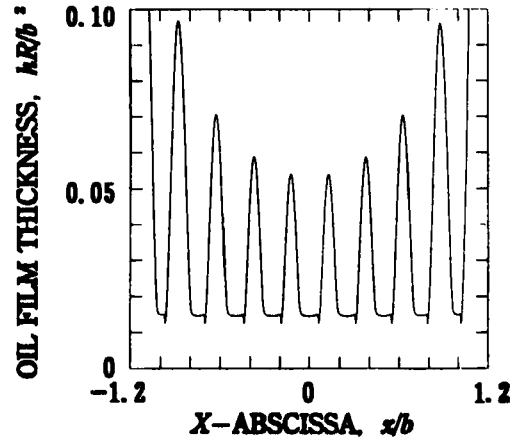


(a) Oil film thickness distribution

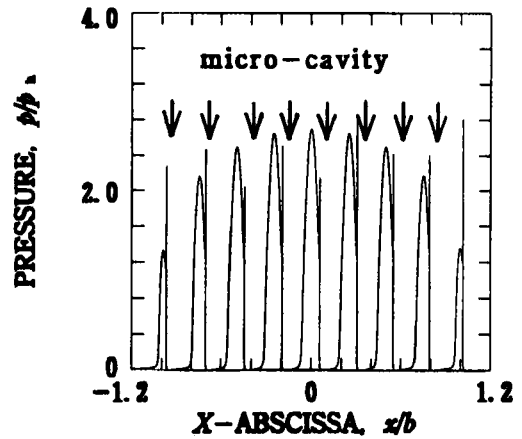


(b) Pressure distribution

Figure 4. Boundary condition I



(a) Oil film thickness distribution



(b) Pressure distribution

Figure 5. Boundary condition II

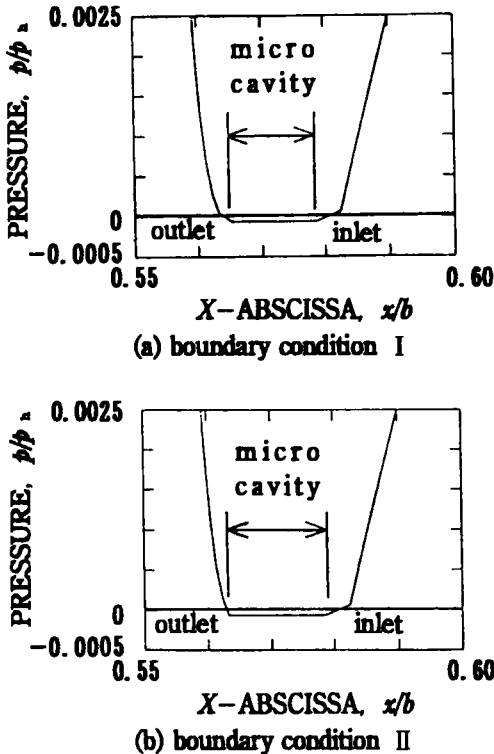


Figure 6. Pressure distribution at the micro-cavity

The pressure distributions of micro-cavity represented in Figures 4 and 5 are shown in Figure 6 in order to compare the effects of boundary conditions I and II. The disagreement of pressure distribution is remarkable at the micro-cavity starting point (outlet meniscus). The pressure in each micro-cavity indicates the minus gauge pressure (saturated vapor pressure). It is considered that the effect of boundary condition is slightly recognized due to the condition of mass flow continuity.

#### 4.2. Criterion of micro-cavity formation

The numerical calculations are compared to discuss the criterion of micro-cavity formation. In Figures 7 and 8, the pressure distribution, oil film thickness and micro-cavity are illustrated. The position of each micro-cavity is indicated by

the arrow mark. Simulating conditions are as follows: dimensionless parameters :  $G=3000$ ,  $U=10^{-11}$ ,

$$W=2.71 \times 10^{-4}$$

surface asperity profiles :  $\Sigma_{\cos}=0.15$ ,

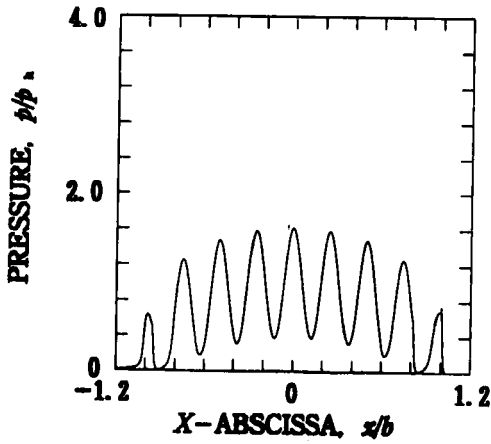
$$\Lambda_{\cos}=0.25, \Phi=0$$

saturated vapor pressure :  $P_v=-6.66 \times 10^{-6}$

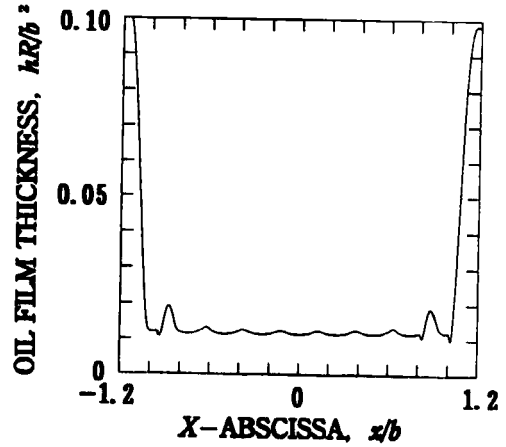
In these results, only the surface asperity amplitude is varied. The order of surface asperity amplitude of Figure 7(a) is the upper limit under which micro-cavities do not appear. Since the surface asperity amplitude is larger than that for (a), the micro-cavities are formed at the each side of contact region only as shown in Figure 7(b). In Figure 7(c), the micro-cavities are formed after each bump, because of the surface asperity amplitude is large enough.

In Figures 9 and 10, the dimensionless speed parameter  $U=10^{-11}$  is used to discuss the effect of  $U$  in the formation of micro-cavitation. Other simulating conditions are same as in the Figures 8 and 9. When the surface asperity amplitude of Figure 7(c) is used, the micro-cavity is not formed as shown in Figure 9 (a). In order to form the micro-cavities, the larger surface asperity amplitude is required. In Figures 9 (b) and (c), the micro-cavities are formed at the conditions of larger surface asperity amplitude. When the velocity parameter  $U$  increases, the larger surface asperity amplitude is required to form the micro cavity.

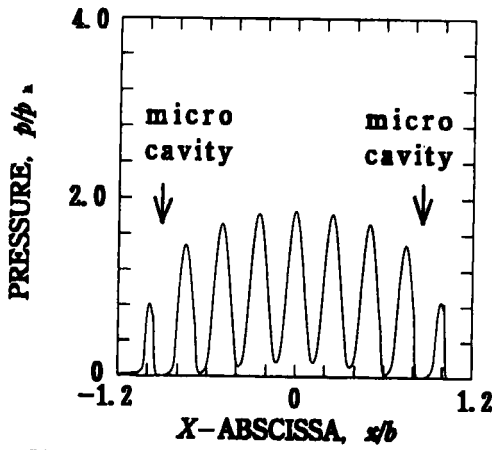
In Figures 11 and 12, the dimensionless materials parameter  $G=6000$  is used to discuss the effect of  $G$  in the micro-cavitation. Other simulating conditions are same as in the Figures 8 and 9. When the surface asperity amplitude is used larger than that for Figure 7(b), the micro-cavity is not formed as shown in Figure 11 (a). In order to form micro-cavities, the larger surface asperity amplitude is required. As shown in Figures 11 (b) and (c), the micro-cavities are formed at the conditions of larger surface asperity amplitude. When the materials parameter  $G$  increases, the larger surface asperity amplitude is required to form the micro-cavity.



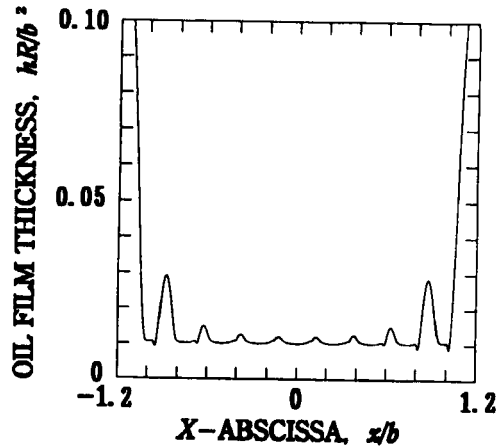
(a) Surface asperity amplitude,  $\Sigma=0.05$



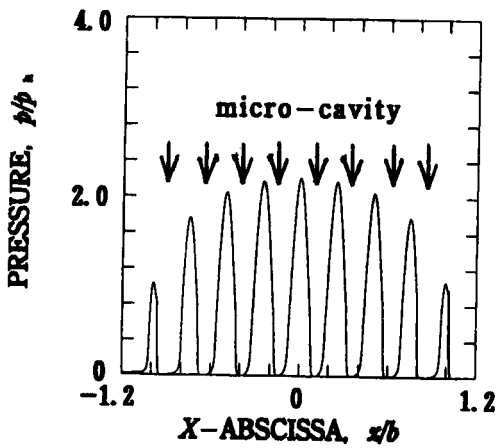
(a) Surface asperity amplitude,  $\Sigma=0.05$



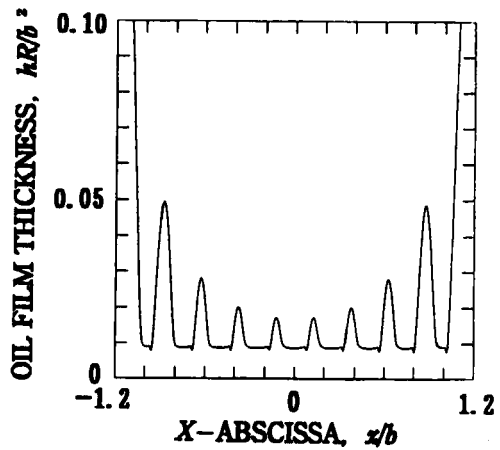
(b) Surface asperity amplitude,  $\Sigma=0.07$



(b) Surface asperity amplitude,  $\Sigma=0.07$



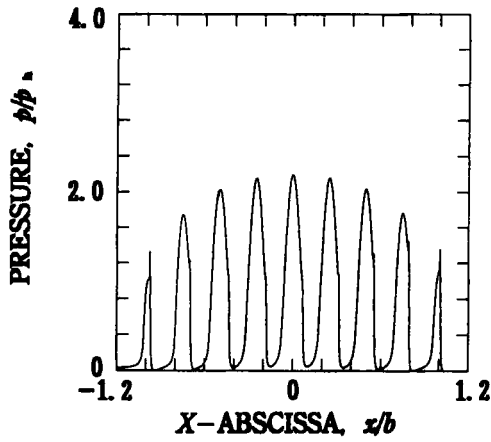
(c) Surface asperity amplitude,  $\Sigma=0.10$



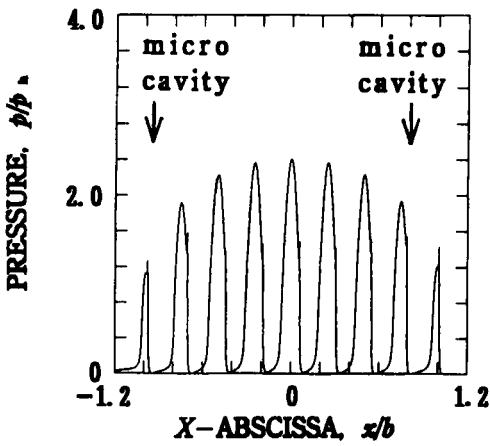
(c) Surface asperity amplitude,  $\Sigma=0.10$

**Figure 7. Pressure distribution**  
 ( $G=3000, U=10^{-11}, W=2.71 \times 10^{-4}, A=0.25$ )

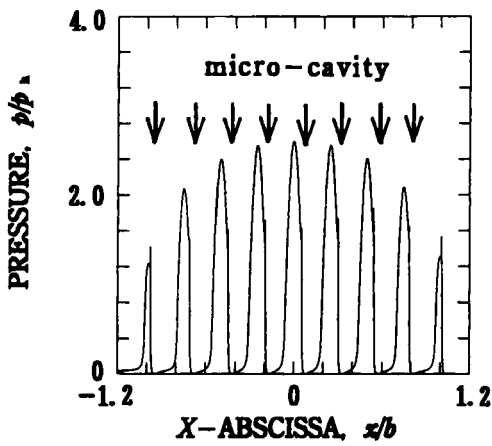
**Figure 8. Oil film thickness**  
 ( $G=3000, U=10^{-11}, W=2.71 \times 10^{-4}, A=0.25$ )



(a) Surface asperity amplitude,  $\Sigma=0.10$

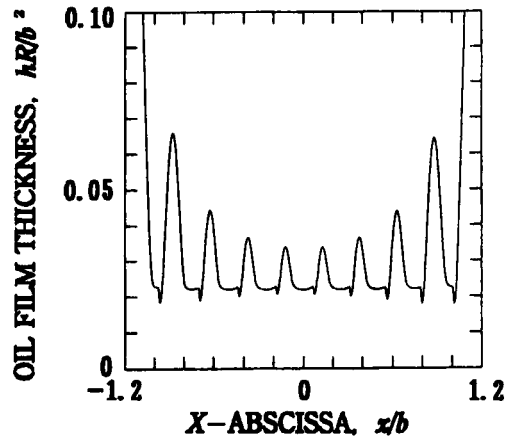


(b) Surface asperity amplitude,  $\Sigma=0.12$

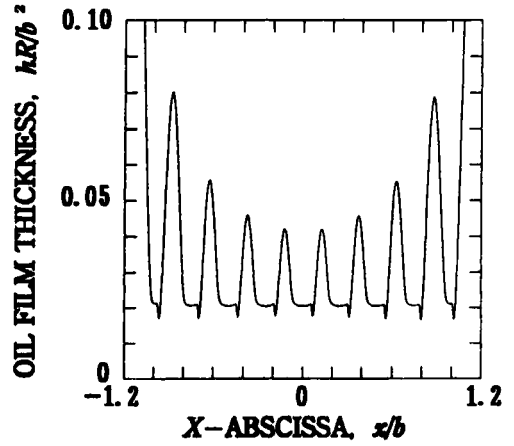


(c) Surface asperity amplitude,  $\Sigma=0.14$

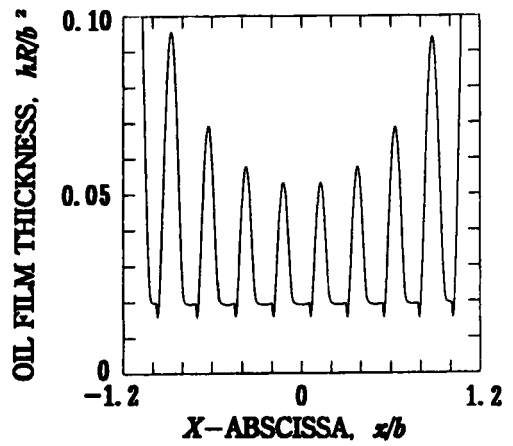
Figure 9. Pressure distribution  
( $G=3000, U=2.5 \times 10^{-11}, W=2.71 \times 10^{-4}, A=0.25$ )



(a) Surface asperity amplitude,  $\Sigma=0.10$



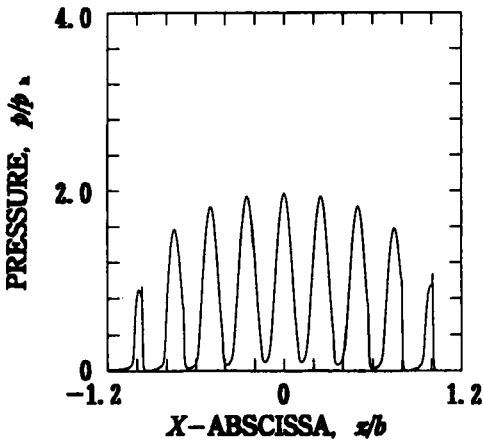
(b) Surface asperity amplitude,  $\Sigma=0.12$



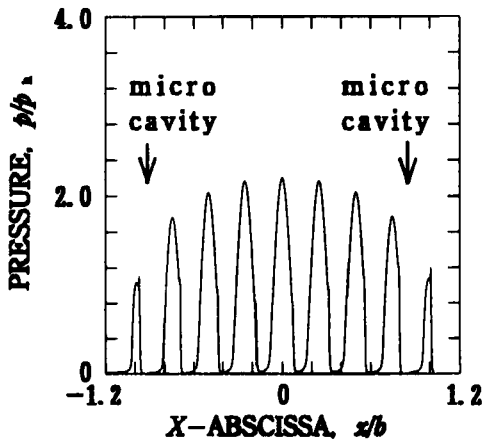
(c) Surface asperity amplitude,  $\Sigma=0.14$

Figure 10. Oil film thickness  
( $G=3000, U=2.5 \times 10^{-11}, W=2.71 \times 10^{-4}, A=0.25$ )

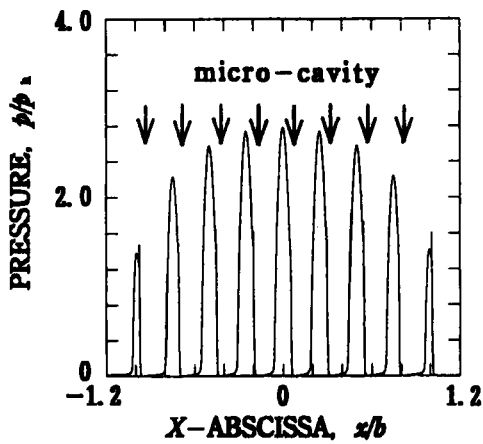




(a) Surface asperity amplitude,  $\Sigma=0.08$

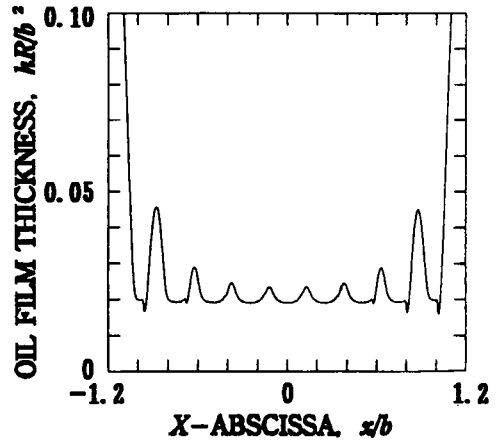


(b) Surface asperity amplitude,  $\Sigma=0.10$

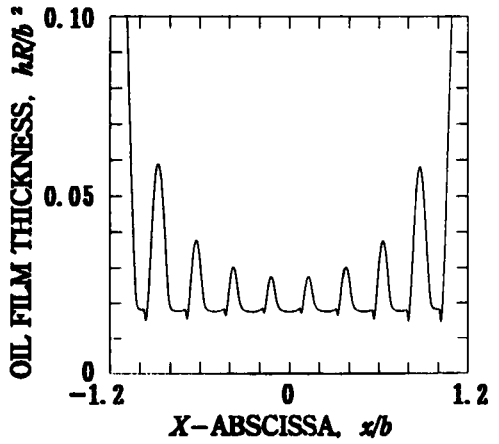


(c) Surface asperity amplitude,  $\Sigma=0.16$

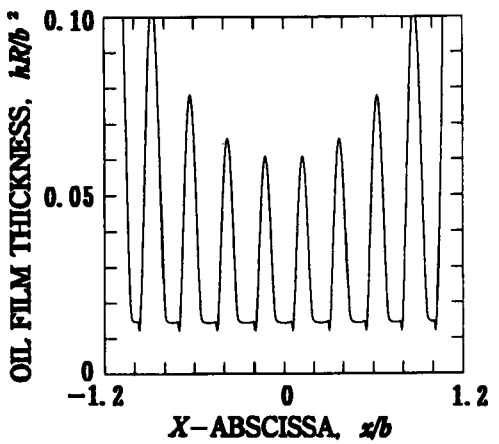
**Figure 11.** Pressure distribution ( $G=6000, U=10^{-11}, W=2.71 \times 10^{-4}, A=0.25$ )



(a) Surface asperity amplitude,  $\Sigma=0.08$



(b) Surface asperity amplitude,  $\Sigma=0.10$

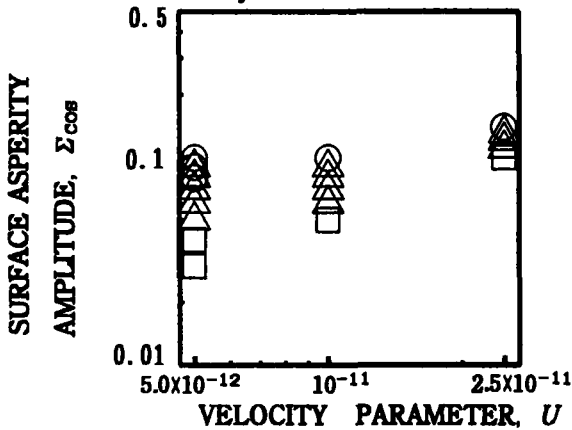


(c) Surface asperity amplitude,  $\Sigma=0.16$

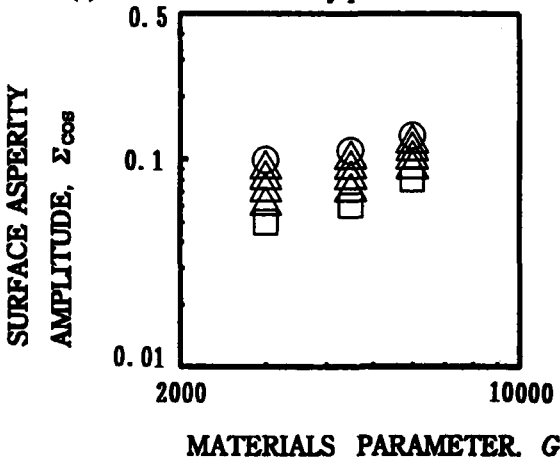
**Figure 12.** Oil film thickness ( $G=6000, U=10^{-11}, W=2.71 \times 10^{-4}, A=0.25$ )

The maximum contact pressure increases with an increase of the surface asperity amplitude as shown in Figures 7, 9 and 11. In Figure 11, the maximum contact pressure is calculated as about 4.2 GPa, in spite of the loading condition of  $W=2.71 \times 10^{-4}$ . This values of contact pressure is too large to obtain the converged solution. If the surface asperity does not exist, the maximum Hertzian contact pressure is calculated as 1.5 GPa at this loading condition. If the external load is smaller than  $W=2.71 \times 10^{-4}$ , the load is too small for the operating conditions realized in rolling element bearings. Therefore, the effect of

- : The micro-cavities are formed after all bumps in the Hertzian contact area.
- △ : Some micro-cavities are formed.
- : The micro-cavity is not formed.



(a) The effect of velocity parameter  $U$



(b) The effect of materials parameter  $G$

Figure 13. Criterion of micro-cavity formation

dimensionless load parameter  $W$  is not discussed.

The criterion of micro-cavity formation is shown in Figure 13. With the velocity parameter  $U$  increasing, the larger surface asperity amplitude is required. With the materials parameter  $G$  increasing, the larger surface asperity amplitude is required.

Since the surface profile must be smooth in order to satisfy one of the assumptions of the Reynolds equation which is introduced from the Navier-Stokes equation, the surface asperity profile is assumed to be sinusoidal curve in this study. The large surface asperity amplitude is required to form the micro-cavities. Therefore, the criterion of micro-cavity formation may be slightly overestimated.

## 5. CONCLUSIONS

The micro-EHL problems taking into account the micro-cavitation caused by surface asperities were investigated numerically.

- 1) It is found that the micro-cavities are formed, if the surface roughness amplitude is large enough.
- 2) Since the pressure in each micro-cavity is assumed to be the saturated vapor pressure of lubricant, a negative gauge pressure is obtained at the region of each micro-cavity.
- 3) In this paper, two boundary conditions at the micro-cavitation are compared, but the disagreement due to two boundary conditions is small. It is considered that the effect of two boundary conditions are slightly caused by the condition of mass flow continuity.
- 4) It is found that when the velocity parameter  $U$  increases, the larger surface asperity amplitude is required to form the micro-cavity.
- 5) When the materials parameter  $G$  increases, the larger surface asperity amplitude is required to form the micro-cavity.

## ACKNOWLEDGMENT

Authors gratefully acknowledge Prof. T. Nakahara and Dr. H. Okamura in discussing the micro-cavitation analysis.

## REFERENCES

1. T. Nakahara, Journal of Japanese Society of Lubrication, Vol. 26 (1981) 146.
2. T. Nakahara, Journal of Japan Soc. for Tech. of Plasticity, Vol. 36, 413 (1995-6) 566.
3. T. Nakahara, Journal of Japanese Society of Tribologists, Vol. 41, 1 (1996) 7.
4. D. Dowson and C. M. Taylor, Ann. Rev. Fluid Mech., (1979) 35.
5. H. W. Swift, Minutes of Proc. Inst. Civil Eng., 233, Paper No. 4809 (1931) 267.
6. W. Stieber, Das Schwimmlager, Krayn (1933).
7. J. C. Coyne and H. G. Elrod, Jr., Trans. ASME, Ser. F, 92, 3 (1970) 451.
8. L. Floberg, Acta Polytechnica Scandinavica, Mech. Eng. Ser. No. 19 (1965).
9. H. G. Elrod, Trans. ASME, Jour. of Lub. Tech., JULY, Vol. 103 (1981) 350.
10. G. A. LaBouff and J. F. Booker, Trans. ASME, Jour. of Trib., OCTOBER, Vol. 107 (1985) 505.
11. D. E. Brewe, Trans. ASME, Journal of Tribology, OCTOBER, Vol. 108 (1986) 628.
12. A. Kumar and J. F. Booker, Trans. ASME, Jour. of Tribology, APRIL, Vol. 113 (1991) 255.
13. A. Kumar and J. F. Booker, Trans. ASME, Jour. of Tribology, APRIL, Vol. 113 (1991) 276.
14. B. Vincent, P. Maspeyrot and J. Frene, Wear, 193 (1996) 155.
15. P. Huang and S. Z. Wen, Trans. ASME, Jour. of Tribology, JANUARY, Vol. 114 (1992) 42.
16. P. Huang and S. Z. Wen, Trans. ASME, Jour. of Tribology, JANUARY, Vol. 115 (1993) 148.
17. S. Kamamoto, M. Sakuragi and T. Yamamoto, Proceedings of the I. T. C., Yokohama 1995.
18. L. Houpert, Trans. ASME, Journal of Tribology, APRIL, Vol. 107 (1985) 241.
19. D. Dowson and G. R. Higginson, Elastohydrodynamic Lubrication (1977).
20. H. Okamura, Proceedings of the 9th Leeds-Lyon Symposium on Tribology (1982) 313.
21. E. J. Bissett and D. W. Glander, Trans. ASME, Journal of Tribology, APRIL, 110 (1988) 241.
22. H. Okamura and H. Fujiwara, Trans. Japan Soc. of Mech. Engrs. C, 58, 550 (1992-6) 211.
23. H. Okamura and H. Fujiwara, Trans. Japan Soc. of Mech. Engrs. C, 58, 550 (1992-6) 217.
24. L. G. Houpert and B. J. Hamrock, Trans. ASME, Journal of Tribology, JULY, 108 (1986) 411.

## APPENDIX

- $b$  = half Hertzian contact width (m)  
 $h$  = oil film thickness (m)  
 $i, j$  = node number  
 $k$  = micro-cavity number  
 $n$  = number of node  
 $p$  = pressure (Pa)  
 $p_h$  = Hertzian peak pressure (Pa)  
 $u$  = velocity (m/s),  $u = (u_1 + u_2)/2$   
 $u_{1,2}$  = velocity of surface 1, 2 (m/s)  
 $w$  = load per unit length (N/m)  
 $x$  = x-coordinate (m)  
 $\varepsilon$  = pressure-viscosity exponent (Roelands)  
 $\alpha$  = pressure-viscosity exponent (Barus)  
 $\lambda_{\text{COS}}$  = wave length of roughness (m)  
 $\mu$  = dynamic viscosity (Pa·s)  
 $\mu_0$  = dynamic viscosity at atmosphere (Pa·s)  
 $\sigma_{\text{COS}}$  = wave amplitude of roughness (m)  
 $\phi$  = wave phase of surface roughness (m)  
 $\overline{\rho_m H_m}$  = dimensionless constant  
 $C_1$  = wating factor used to integrate  $P$   
 $D_{1,1}$  = influence coefficient  
 $E'$  = equivalent Young's modulus (Pa)  
 $G$  = materials parameter,  $G = \alpha E'$   
 $H$  = dimensionless oil film thickness,  $H = h R/b^2$   
 $H_0$  = dimensionless constant  
 $P$  = dimensionless pressure,  $P = p/p_h$   
 $P_v$  = saturated vapor pressure,  $P_v = p_v/p_h$   
 $\overline{Q_x}$  = mass flow rate,  $\overline{Q_x} = Q_x/(\rho_0 uR)$   
 $R$  = equivalent radius (m)  
 $U$  = velocity parameter,  $U = \mu_0 u/(E'R)$   
 $W$  = load parameter,  $W = w/(E'R)$   
 $X$  = dimensionless X coordinate,  $X = x/b$   
 $X_{C1}$  = new inlet meniscus distance,  $X_{C1} = x_{C1}/b$   
 $X_{C2}$  = new outlet meniscus distance,  $X_{C2} = x_{C2}/b$   
 $X_{L1}$  = inlet meniscus distance,  $X_{L1} = x_{L1}/b$   
 $X_{L2}$  = outlet meniscus distance,  $X_{L2} = x_{L2}/b$   
 $\Lambda_{\text{COS}}$  = dimensionless wave length,  $\Lambda_{\text{COS}} = \lambda_{\text{COS}}/b$   
 $\Sigma_{\text{COS}}$  = dimensionless wave amplitude,  
 $\Sigma_{\text{COS}} = \sigma_{\text{COS}} R/b^2$   
 $\Phi$  = dimensionless phase of roughness,  $\Phi = \phi/b$

## A new relaxation scheme for solving EHL problems

(E. Nurgat and M. Berzins)<sup>a</sup>

<sup>a</sup>School of Computer Studies, University of Leeds,  
Leeds LS2 9JT, United Kingdom

A New Relaxation Scheme (NRS) is presented in this paper to solve Elasto Hydrodynamic Lubrication (EHL) point contact problems. The solutions obtained are compared with those obtained by Ehret [6] who employed the Distributive Relaxation Scheme (DRS) of Venner [2]. Results obtained using the two schemes are in close agreement which is very encouraging although it is too early to draw any conclusions. The new relaxation scheme thus provides an alternative approach to the distributive relaxation scheme.

### 1. INTRODUCTION

Over the last few decades various numerical algorithms have been presented for solving Elasto Hydrodynamic Lubrication (EHL) [1] point contact problems. One of the most effective technique to date for solving these problems is the use of multigrid methods. Extensive use of multigrid methods in solving EHL problems have been presented by Venner [2] and [3] and Venner and Lubrecht [4]. The development of multigrid multi-integration by Brandt and Lubrecht [5] and Venner [2] has also greatly enhanced the efficiency of multigrid methods for EHL problems. Venner [2] and more recently Ehret [6] employed Gauss-Seidel line and Jacobi distributive line relaxation schemes with multigrid multi-integration scheme to solve EHL problems. This scheme is known as the Distributive Relaxation Scheme (DRS).

The aim of this paper is to present a New Relaxation Scheme (NRS) to solve EHL point contact problems using the multigrid method. The new relaxation scheme employs Gauss-Seidel and Jacobi line relaxation schemes and is an alternative approach to the distributive relaxation scheme. In both the distributive relaxation scheme of Venner [2] and the new relaxation scheme, the choice of the relaxation scheme is dependent on the value of the coefficient  $\epsilon$  of the Reynolds equation. The main difference between these two approaches is in how they treat the contact region of the EHL problem. Various test problems are used in order to compare the

results obtained using the distributive relaxation scheme employed by Ehret [6] and the new relaxation scheme.

The layout of the rest of the paper is as follows. In section (2) we introduce the form of the equations to be solved. Multigrid method to be used is described in section (3) while section (4) describes different relaxation schemes which includes the distributive and the new relaxation schemes. Section (5) describes the test problems to be used in the comparison between the two relaxation schemes and the paper is concluded in section (6).

### 2. GOVERNING EQUATIONS

The mathematical model describing the isothermal EHL circular contact problem with oil entrainment in the positive X-direction consists of three non-dimensional equations. The Reynolds Equation relates pressure ( $P$ ) to the film thickness ( $H$ ) for a lubricant characterised by a pressure dependent viscosity  $\eta$  and density  $\rho$

$$L(P) = \frac{\partial}{\partial X} \left( \epsilon \frac{\partial P}{\partial X} \right) + \frac{\partial}{\partial Y} \left( \epsilon \frac{\partial P}{\partial Y} \right) - \frac{\partial (\rho H)}{\partial X} = 0, \quad X, Y \in [X_a, X_b] \times [Y_a, Y_b] \quad (1)$$

with the cavitation condition  $P \geq 0$  and the boundary condition  $P = 0$ . The non-dimensionalisation is expressed in terms of the so-called Moes parameters  $L$  and  $M$ , [7]. Pressure

is in units of the maximum Hertzian pressure

$$p_h = \frac{L}{\alpha\pi} \sqrt[3]{\frac{3M}{2}} \quad (2)$$

where  $\alpha$  is the pressure coefficient of viscosity of the lubricant.  $X$  and  $Y$  are in units of Hertzian radius ( $b$ ). Film thickness is in units of  $b^2/R$ , where  $R$  is the reduced radius of the contact.  $\epsilon$  is given by:

$$\epsilon = \frac{\rho H^3}{\eta\lambda} \quad (3)$$

where  $\rho = 1 + \frac{\mu p_h P}{1 + \nu p_h P}$  if  $P > 0$ , otherwise  $\rho = 1$  ( $\mu = 5.8 \times 10^{-10}$  and  $\nu = 1.68 \times 10^{-9}$ , [8]),  $\eta = \exp\left\{\frac{\alpha p_0}{z}[-1 + (1 + \frac{p_h P}{p_0})^z]\right\}$  ( $p_0 = 1.98 \times 10^8$  and  $z = 0.68$ , [9]) and  $\lambda = \frac{4\pi}{M} \sqrt[3]{\frac{2}{3M}}$ .

The Film Thickness Equation,  $H(X, Y)$ , computes the elastic distortion of the surfaces caused by the pressure in the film and is written as:

$$H(X, Y) = H_0 + \frac{X^2}{2} + \frac{Y^2}{2} + \frac{2}{\pi^2} \int_{Y_a}^{Y_b} \int_{X_a}^{X_b} \frac{P(X', Y') dX' dY'}{\sqrt{(X - X')^2 + (Y - Y')^2}} \quad (4)$$

where  $H_0$  is a constant.

The final equation is the Force Balance Equation which ensures that the integral over the pressure balances the external applied load:

$$\int_{Y_a}^{Y_b} \int_{X_a}^{X_b} P(X, Y) dX dY = \frac{2\pi}{3}. \quad (5)$$

### 2.1. Finite difference discretisation of governing equations

The governing equations are discretised with the direction of flow in the  $X$ -direction and mesh spacings  $h_x$  and  $h_y$  in the  $X$  and  $Y$  directions respectively. Due to symmetry, only half the domain is used in the  $Y$ -direction. Reynolds Equation (1) is discretised at each non boundary mesh point  $(i, j)$ ,  $((i-1)h_x + X_a, (j-1)h_y + Y_a)$  where  $X, Y \in [X_a, X_b] \times [Y_a, Y_b]$ , using central and backward differencing to get:

$$L_{i,j} = \epsilon_{i-\frac{1}{2},j}(P_{i-1,j} - P_{i,j}) + \epsilon_{i+\frac{1}{2},j}(P_{i+1,j} - P_{i,j}) + h_x^2 h_y^{-2} (\epsilon_{i,j-\frac{1}{2}}(P_{i,j-1} - P_{i,j}) + \epsilon_{i,j+\frac{1}{2}}(P_{i,j+1} - P_{i,j})) - h_x(\rho_{i,j} H_{i,j} - \rho_{i-1,j} H_{i-1,j}) \quad (6)$$

where,  $\epsilon_{i+\frac{1}{2},j}, \epsilon_{i-\frac{1}{2},j}, \epsilon_{i,j+\frac{1}{2}}$  and  $\epsilon_{i,j-\frac{1}{2}}$  ( $i = 2, \dots, m_x - 1$ ;  $j = 2, \dots, n_y - 1$ ) denote the values of  $\epsilon$  at the intermediate locations midway between mesh points.  $m_x$  and  $n_y$  are the maximum number of points in  $X$  and  $Y$  directions respectively.

The discretised film thickness equation (4) at a point  $(i, j)$  is given by:

$$H_{i,j} = H_0 + \frac{X_i^2}{2} + \frac{Y_j^2}{2} + d_{i,j} \quad (7)$$

where  $H_0$  is a constant and  $d_{i,j}$  is the elastic deformation of the material due to the applied load. The elastic deformation of the surface is derived by dividing the pressure distribution into rectangular blocks of uniform pressure. Thus the elastic deformation,  $d_{X,Y}$ , at a point  $(X, Y)$  due to the uniform pressure over the rectangular area  $2a2b$  is given by Venner [2]

$$d_{X,Y} = \frac{2P}{\pi^2} \int_{-b}^b \int_{-a}^a \frac{dX' dY'}{r} \quad (8)$$

where  $r = \sqrt{(X - X')^2 + (Y - Y')^2}$ .

If the entire domain is divided into equal rectangular areas, then from Dowson and Hamrock [10], the elastic deformation,  $d_{i,j}$ , at a point  $(i, j)$  due to contributions of all rectangular areas of uniform pressure is given by:

$$d_{i,j} = \frac{2}{\pi^2} \sum_{k=1}^{m_x} \sum_{l=1}^{n_y} K_{m,n} P_{k,l} \quad (9)$$

where,  $m = |i - k| + 1$ ,  $n = |j - l| + 1$ ,  $m_x$  and  $n_y$  are the maximum number of points in the  $X$  and  $Y$  directions respectively. The coefficients  $K_{m,n}$  are independent of pressure,  $P$ .

One advantage of a regular mesh is that the  $m_x n_y$  coefficients need only be calculated once and stored. In contrast, on an irregular mesh it is necessary to store  $m_x n_y$  coefficients for each mesh point.

The force balance equation (5) determines the value of the integration constant  $H_0$  and is discretised as follows:

$$h_x h_y \sum_{i=1}^{m_x} \sum_{j=1}^{n_y} P_{i,j} - \frac{2\pi}{3} = 0. \quad (10)$$

### 3. MULTIGRID METHOD

The use of multigrid methods in solving EHL problems was introduced by Lubrecht [11], who through his extensive work has made multigrid method an important technique in solving such problems. The use of multigrids for solving EHL line and point contact problems has been described by Venner [2].

The concept of multigrid iteration depends on the asymptotic nature of errors associated with iterative schemes and how the schemes reduce these errors. Smooth error components associated with low frequencies are hardly reduced with the classical iterative schemes, thus resulting in slow convergence. The opposite is true for error components with wavelength of the order of the mesh spacing. However, low frequency error components can be adequately represented on coarser grid. In a multilevel solver, which makes use of a series of coarser grids, each error component is reduced until it becomes smooth when the same procedure is applied on a coarser grid.

The FDMG Multigrid Software of Shaw [12] is used as a starting point for implementing the multigrid technique. FDMG employs Multigrid Full Approximation Scheme (FAS) to solve nonlinear systems of partial differential equations using either V or W coarse grid correction cycles. The Jacobi or Gauss Seidel iterative method can be used as a smoother. The option for the type of restriction is either injection or full weighting [7].

EHL problems are nonlinear. Thus, when using multigrids, the standard Correction Scheme can not be used and the Full Approximation Scheme must be used instead. In the cavitation region, in which negative pressures may be computed by the solver, the Reynolds equation is not valid and the computed negative pressures are set to zero in the standard manner as used by Venner [2]. The cavitation region is treated with the multigrid method by using injection near and in the cavitation region when transferring the residual to the coarse grid. Full weighting is used in the remaining part of the domain. The elastic deformation and force balance equations get updated on each grid using the updated pressure values. The only substantial modification to FDMG has

been to take symmetry boundary conditions and cavitation into consideration.

The solution for the isothermal point contact problem is obtained by making use of strong coupling in the direction of flow, the X-direction. Thus the discrete equations are solved simultaneously on a line of points, sweeping across the grid only in the positive Y-direction due to symmetry. On each line of points, the new relaxation scheme is employed, as described in section (4.3).

### 4. RELAXATION SCHEMES

The coefficient  $\epsilon$  of the Reynolds equation (1) varies several orders of magnitude over the calculational domain. In both the inlet and outlet regions  $\epsilon \gg 1$  whereas in the contact region  $\epsilon$  is very close to zero. Hence, in the dry contact region, i.e.  $(X^2 + Y^2) \leq 1$ , the integral aspect of the problem dominates whereas in the remaining part of the domain the problem behaves like a differential problem. When  $\epsilon$  is small Reynolds equation (1) reduces to  $\frac{\partial(\rho H)}{\partial X} = 0$  which is a relation in X-direction only. Consequently when discretised there is no direct coupling via pressure between adjacent grid points in Y-direction. When  $\epsilon$  is large the term  $\frac{\partial(\rho H)}{\partial X}$  in Reynolds equation (1) is small compared to the differential terms. Thus the Reynolds equation (1) has the form of the 2-D Poisson type equation. The value of  $\epsilon$  plays an important role in deciding which relaxation process to apply to the solution of discretised Reynolds equation (6) with  $H_{i,j}$  evaluated using equation (7). The relaxation process employed must be a stable error smoother over the entire domain and must be able to cope with the extreme values of  $\epsilon$  which are a nonlinear function of pressure. The general approach taken in the successful distributive relaxation scheme of Venner [2] (see also Ehret [6]) and also in the new relaxation scheme described here is to make the choice of relaxation scheme dependent on the value of  $\epsilon$ . The precise difference between the schemes will be described in section (4.4).

When  $\epsilon$  is large, (a Poisson type problem), a one point Gauss-Seidel relaxation provides good error smoothing and stability. This is where given

an approximation  $\tilde{P}_{i,j}$  and the associated approximation  $\tilde{H}_{i,j}$  to  $P_{i,j}$  and  $H_{i,j}$  respectively, a new approximation  $\bar{P}_{i,j}$  is computed using

$$\bar{P}_{i,j} = \tilde{P}_{i,j} + \left( \frac{\partial \tilde{L}_{i,j}}{\partial \tilde{P}_{i,j}} \right)^{-1} r_{i,j} \quad (11)$$

where  $r_{i,j}$  is the residual at the point  $(i,j)$  and  $\tilde{L}_{i,j} = L(\tilde{P}_{i,j})$  is given by equation (6). However, the performance of a one point Gauss-Seidel relaxation begins to deteriorate as  $\epsilon$  decreases. Firstly the relaxation becomes unstable - low frequency error components are amplified and the relaxation process diverges. Secondly, due to the loss of coupling in the Y-direction, the relaxation becomes ineffective in reducing high frequency error components in Y-direction.

The problem of stability can be overcome by using a relaxation scheme which has properties of both Gauss-Seidel and Jacobi relaxations. For a standard Gauss-Seidel relaxation the new updated solution get used immediately in relaxing subsequent equations whereas for a standard Jacobi relaxation the new updated solution replaces the old one at the end of a complete sweep. The relaxation scheme used in order to achieve stability depends very much on the value of  $\epsilon$  which is much smaller in the contact region than the non-contact region of the computational domain.

The problem of loss of coupling can be overcome by making use of line relaxation instead of point relaxation. This implies that instead of visiting the grid points one by one in some order, e.g. lexicographic order, and solving the discrete equation at each grid point, a system of discrete equations on a line of points are solved simultaneously. This must be done on a line which is in the direction of strong coupling. For EHL point contact problems their is strong coupling in the X-direction. Hence, we use points on a line in the X-direction, known as I-Line relaxation. That is on a line  $Y = j$  ( $j = 1, \dots, n_y$ ), where  $n_y$  is the maximum number of points in the Y-direction.

#### 4.1. I-Line relaxation

Suppose  $\tilde{P}$  is an approximation to the true solution  $P$  then at a point  $(i,j)$ ,  $\tilde{L}_{i,j} = L(\tilde{P})_{i,j} \neq 0$

and  $L_{i,j} = L(P)_{i,j} = 0$ . Taylors theorem gives:

$$L_{i,j} = \tilde{L}_{i,j} + \sum_{l=1}^{n_y} \sum_{k=1}^{m_x} \frac{\partial \tilde{L}_{i,j}}{\partial \tilde{P}_{k,l}} \Delta P_{k,l} + O(\Delta P)^2 \quad (12)$$

where  $\tilde{L}_{i,j} = L(\tilde{P}_{i,j})$  is the discretised Reynolds equation (6) at the point  $(X_i, Y_j)$ . If we only consider points at  $(i-1, j)$ ,  $(i, j)$  and  $(i+1, j)$  then equation (12) can be rewritten as:

$$\begin{aligned} \frac{\partial \tilde{L}_{i,j}}{\partial \tilde{P}_{i-1,j}} \Delta P_{i-1,j} + \frac{\partial \tilde{L}_{i,j}}{\partial \tilde{P}_{i,j}} \Delta P_{i,j} \\ + \frac{\partial \tilde{L}_{i,j}}{\partial \tilde{P}_{i+1,j}} \Delta P_{i+1,j} + \tilde{L}_{i,j} = 0. \end{aligned} \quad (13)$$

For a constant  $j$ , that is on a line  $Y = j$ , equation (13) results in a tridiagonal system of equations which are solved simultaneously for the correction term  $\Delta \underline{P}$ . Having obtained  $\Delta \underline{P}$ , a new approximation  $\bar{P}_{i,j}$  to  $\tilde{P}_{i,j}$  is computed using:

$$\bar{P}_{i,j} = \tilde{P}_{i,j} - W \Delta P_{i,j} \quad (14)$$

where  $W$  is a damping factor. A correct choice of  $W$  is critical to ensure convergence of the method.

#### 4.2. Distributive relaxation scheme

The distributive relaxation scheme works on the principle that the relaxation process remains local. That is relaxing at a point  $X_i$  has minimal effect at points  $X_j$  far away from  $X_i$ .

The distributive relaxation scheme employed by both Venner [2] and Ehret [6] makes use of Jacobi Distributive Line Relaxation (JDLR), Gauss-Seidel Line Relaxation (GSLR) and Point Gauss-Seidel (PGS) depending on the pressure values on the domain. JDLR is employed in regions of domain where pressure is large, which means  $\epsilon$  is small, whereas in the remaining part of the domain, excluding the cavitation region where PGS is employed, GSLR is employed. Gauss-Seidel line relaxation and point Gauss-Seidel schemes employed are as described in section (4).

When using JDLR a new approximation  $\bar{P}_{i,j}$  to  $\tilde{P}_{i,j}$  is computed using

$$\bar{P}_{i,j} = \tilde{P}_{i,j} + \delta P_{i,j} \quad (15)$$

where  $\delta P_{i,j} = \Delta P_{i,j} - \frac{1}{4}(\Delta P_{i-1,j} + \Delta P_{i+1,j} + \Delta P_{i,j-1} + \Delta P_{i,j+1})$ . A new approximation  $\bar{H}_{i,j}$  to  $\tilde{H}_{i,j}$  is also computed using

$$\bar{H}_{i,j} = \tilde{H}_{i,j} + \frac{2}{\pi^2} \sum_{k=i-1}^{i+1} \sum_{l=j-1}^{j+1} K_{i,k,j,l} \delta P_{k,l}. \quad (16)$$

It is not necessary to obtain the exact representation of  $\bar{H}_{i,j}$  as is shown by Wang [13]. The correction terms,  $\Delta \underline{P}$ , are obtained using line relaxation by solving a system of equations of the form given by

$$\begin{aligned} \frac{\partial \tilde{L}_{i,j}}{\partial \tilde{P}_{i-2,j}} \Delta P_{i-2,j} + \frac{\partial \tilde{L}_{i,j}}{\partial \tilde{P}_{i-1,j}} \Delta P_{i-1,j} + \\ \frac{\partial \tilde{L}_{i,j}}{\partial \tilde{P}_{i,j}} \Delta P_{i,j} + \frac{\partial \tilde{L}_{i,j}}{\partial \tilde{P}_{i+1,j}} \Delta P_{i+1,j} + \\ \frac{\partial \tilde{L}_{i,j}}{\partial \tilde{P}_{i+2,j}} \Delta P_{i+2,j} + \tilde{L}_{i,j} = 0. \end{aligned} \quad (17)$$

Since JDLR is a Jacobi relaxation scheme, the solution  $\underline{P}$  gets updated after a complete sweep. The numerical scheme employed makes use of the full multigrid solver and of the multi-integration techniques [2] and [5] to compute elastic deformation.

#### 4.3. New relaxation scheme

The new relaxation scheme makes use of Jacobi and Gauss-Seidel line relaxation schemes depending on the value of the coefficient  $\epsilon$  of the Reynolds equation (1). Jacobi and Gauss-Seidel line relaxation schemes are respectively employed in the contact and non-contact regions of the computational domain. This new relaxation scheme is employed in the following manner:

Having obtained  $\Delta \underline{P}$  using I-Line relaxation on the line  $Y = j$  and before applying I-Line relaxation on the line  $Y = j + 1$ , at every point on the line  $Y = j$  which lies in the non-contact region, as shown in Figure (1), a new approximation  $\bar{P}_{i,j}$  to  $\tilde{P}_{i,j}$  is computed using equation (14) with the damping factor  $W$  lying in the range 0.5 to 0.8. Besides this, all the correction terms  $\Delta \underline{P}$  in the contact region on the line  $Y = j$  are saved in order to update the solution in the contact region after a complete sweep.

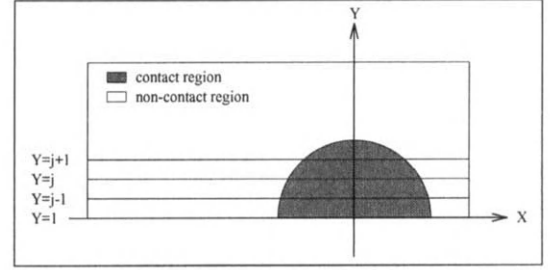


**Figure 1** Representation of contact and non-contact regions.

After all interior lines  $j$  have been visited, that is after a complete sweep, a new approximation  $\bar{P}_{i,j}$  to  $\tilde{P}_{i,j}$  is computed at every point on the entire grid which lies only in the contact region using equation (14) but this time the damping factor  $W$  lies in the range 0.1 to 0.2. Thus the saved values of the corrections  $\Delta \underline{P}$  for the portions of each of the lines in the contact region, shown as shaded region in Figure (1), are added en-masse at the end of the iteration. This corresponds to a block Jacobi method. Having updated all the pressure values on the entire grid, the elastic deformation at every point on the entire grid is recalculated using the new pressure values.

#### 4.4. Differences between DRS and NRS

The Distributive Relaxation Scheme (DRS) differs from the New Relaxation Scheme (NRS) in many ways and it is now possible to describe the differences between these two relaxation schemes.

The DRS makes use of Jacobi distributive and Gauss-Seidel line relaxation schemes in the contact and non contact regions of the computational domain respectively whereas the NRS makes use of Jacobi and Gauss-Seidel line relaxation schemes in the contact and non contact regions of the computational domain respectively. Besides this, the DRS also makes use of point Gauss-Seidel scheme in the cavitation region. In the DRS, regions of domain where JDLR is employed, the correction terms at the points  $(i, j)$ ,  $(i \pm 1, j)$  and  $(i, j \pm 1)$  are used to up-



date the solution at the point  $(i, j)$  as shown in equation (15) whereas in the remaining part of the domain, where Gauss-Seidel line relaxation and point Gauss-Seidel schemes are employed, the method used to update solution is similar to the one used in the NRS. The solution,  $P$ , at a point  $(i, j)$  in the NRS is updated using the correction term  $\Delta P_{i,j}$  as shown in equation (14). The correction terms in the NRS are obtained by solving a tridiagonal system of equations as can be seen from equation (13) whereas in the DRS, regions of domain where JDLR is employed, the system of equations are pentadiagonal as can be seen from equation (17). However, they will be tridiagonal in regions where Gauss-Seidel line relaxation scheme is employed. In DRS a new film thickness equation (16) is used when dealing with the couette term of the Reynolds equation (1). This is not the case in the NRS.

The main difference between the DRS and the NRS is in the contact region of the computational domain. This is where Jacobi distributive line relaxation scheme is employed by the DRS and Jacobi line relaxation scheme is employed by the NRS. The system of equations solved in order to obtain the correction terms and the way pressures are updated at a point  $(i, j)$  are also different in the two schemes. The results obtained, as shown in section (5), shows that the NRS appears to work as well as the DRS, though the NRS is a much simpler scheme than the DRS.

## 5. TEST PROBLEMS

Results obtained using Multigrid Multi-Integration method (MIM) [2], which employs distributive relaxation scheme, and Multigrid method (MM), which makes use of the new relaxation scheme are compared. Three test problems defined by Moes parameters  $M$  and  $L$  are considered where for each test problem Moes parameter  $L$  was fixed at 10, 14 and 28 while the Moes parameter  $M$  was varied from 10 to 200 for the three cases. A value of  $\alpha = 2.2 \times 10^{-8}$ , hence, the maximum Hertzian pressure varied from 0.44 GPa to 2.71 GPa, was considered in all the test problems.

Test problems solved using MIM employed

513  $\times$  513 mesh points on the finest grid and 17  $\times$  17 mesh points on the coarsest grid. When the Moes parameter  $L$  was fixed at 10 and 28, a finest grid of 129  $\times$  129 and a coarsest grid of 17  $\times$  17 was used when solved using MM. However, for the case  $L = 14$ , a finest grid with 257  $\times$  257 mesh points was employed. Both MIM and MM makes use of a full multigrid scheme and the discretisation schemes are the same for the two methods as described in section (2.1).

The minimum and central film thicknesses obtained using the two methods have been compared and the results are shown in Tables 1 and 2. The minimum and central film thicknesses obtained using the two methods are in general agreement especially for the case  $L = 14$  where the computational domains employed by the two schemes are the same and the mesh resolution of the solutions obtained using the MM scheme is higher than that of the other two cases,  $L=10$  and  $L=28$ . However, a discrepancy of about 5% is observed for the other two cases,  $L=10$  and  $L=28$ . This can be attributed to the different size of domains employed by the two schemes and primarily to the differences in the mesh resolution. For solutions obtained using the MIM scheme, the domain employed was dependent on the Moes parameter  $M$  and the following domains were employed:

$[M \leq 10 \Rightarrow -7 \leq X \leq 2 \text{ and } -4.5 \leq Y \leq 4.5]$ ,  
 $[10 < M \leq 50 \Rightarrow -5 \leq X \leq 2 \text{ and } -3.5 \leq Y \leq 3.5]$  and  $[50 < M \leq 500 \Rightarrow -4.5 \leq X \leq 1.5 \text{ and } -3 \leq Y \leq 3]$ . For solutions obtained using the MM scheme, the above domain was employed only for the case  $L = 14$ . However, when the Moes parameter  $L$  was fixed at 10 and 28 the domain employed was  $-4.5 \leq X \leq 1.5$  and  $-3 \leq Y \leq 3$ . Figure 2 shows the pressure profile for the case  $L = 14$  and  $M = 100$ .

The efficiency of the solution is based on the Root Mean Square Residual (RMSR) and the mean absolute residual (Norm0). The solutions obtained by Ehret using MIM, Norm0 was of the order  $1.0 \times 10^{-7}$  and hardly any change in Norm0 was observed after a number of iterations. For the solutions obtained using MM, the RMSR and Norm0 were of the order  $1.0 \times 10^{-4}$  and  $1.0 \times 10^{-5}$  respectively. Hardly any change was also observed in the RMSR and Norm0 after about 5

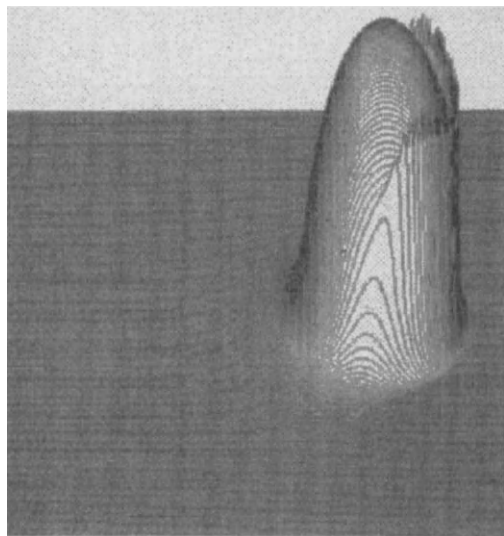


**Figure 2** 3D pressure profile for  $M=100$  &  $L=14$  on a  $257 \times 257$  mesh with domain  $[-4.5 \leq X \leq 1.5$  &  $-3 \leq Y \leq 3]$ .

to 6 multigrid iterations (V-cycles). An analysis of the residuals showed that the main reason in not achieving very small residuals was due to the free boundary in the cavitation region and the pressure spikes. Work is still being done in order to reduce residuals in these regions.

Results obtained by Ehret using MIM were carried out on a Sun Sparcstation 20 whereas an SGI R8000 was used for the solutions obtained using multigrid method which employed the new relaxation scheme. When using MIM, 5 V-cycles are performed in about 30 minutes whereas when MM is employed, time taken to do 5 V-cycles was about 60 minutes. The bulk of the difference in this computing time is due to the use of multi-integration method by Ehret. Adoption of this approach in the new relaxation scheme may well mean that the two procedures are more evenly matched computationally.

## 6. CONCLUSION

A new relaxation scheme for solving EHL problems have been presented in this paper and the

numerical results obtained are compared with those obtained by Ehret [6] who employed distributive relaxation scheme. The results obtained shows that the new relaxation scheme appears to work as well as the distributive relaxation scheme. This new relaxation scheme is very simple and the results obtained are very encouraging. However, it is too early to draw any conclusions at this stage as more work still needs to be done in order to analyse the accuracy of the solutions. An analysis of the residuals showed that in the free boundary cavitation and the pressure spike regions the residuals are relatively higher than those in the other regions of the computational domain. The results obtained also indicate that both the size of the computational domain and the mesh resolution does have an influence on the solutions.

## 7. ACKNOWLEDGEMENTS

The authors would like to thank EPSRC and Shell Research Ltd, Thornton Research Centre for funding this work through an EPSRC CASE Studentships for E.N. Our colleagues at Leeds in the Mechanical Engineering Department D. Dowson, C. Taylor and P. Ehret are thanked for providing much constructive advice and support. Gareth Shaw of NAG Ltd is thanked for supplying the FDMG code.

## REFERENCES

1. R. Gohar, *Elastohydrodynamics*, Ellis Horwood Limited, Chichester, England, 1988.
2. C.H. Venner, *Multilevel Solution of the EHL Line and Point Contact Problems*, PhD. Thesis, University of Twente, The Netherlands, ISBN 90-9003974-0, 1991.
3. C.H. Venner, *Higher-Order Multilevel Solvers for the EHL Line and Point Contact Problem*, *Journal of Tribology*, Vol. 116 (1994) 741-750.
4. C.H. Venner and A.A. Lubrecht, *Numerical Simulation of a Transverse Ridge in a Circular EHL Contact Under Rolling/Sliding*, *Journal of Tribology*, Vol. 116 (1994) 751-761.
5. A. Brandt and A.A. Lubrecht, *Multilevel Matrix Multiplication and Fast Solution of In-*

**Table 1** Minimum film thicknesses for  $L = 10$ ,  $L = 14$  and  $L = 28.3$ 

| $L = 10.0$ <span style="margin-left: 100px;"><math>U = 0.089 \times 10^{-10}</math></span> <span style="margin-left: 100px;"><math>G = 4869</math></span> |                        |         |                          |                         |
|---|------------------------|---------|--------------------------|-------------------------|
| M   | W ( $\times 10^{-6}$ ) | Ph(GPa) | MIM ( $\times 10^{-6}$ ) | MM ( $\times 10^{-6}$ ) |
| 20  | 0.173                  | 0.44    | 12.08                    | 12.31                   |
| 50  | 0.433                  | 0.60    | 10.26                    | 10.64                   |
| 100   | 0.867                  | 0.76    | 8.88                     | 8.99                    |
| 200   | 1.733                  | 0.96    | 7.43                     | 7.40                    |

| $L = 14.0$ <span style="margin-left: 100px;"><math>U = 0.343 \times 10^{-10}</math></span> <span style="margin-left: 100px;"><math>G = 4869</math></span> |                        |         |                          |                         |
|---|------------------------|---------|--------------------------|-------------------------|
| M   | W ( $\times 10^{-6}$ ) | Ph(GPa) | MIM ( $\times 10^{-6}$ ) | MM ( $\times 10^{-6}$ ) |
| 20  | 0.477                  | 0.62    | 28.98                    | 28.55                   |
| 50  | 1.191                  | 0.85    | 25.02                    | 25.28                   |
| 100   | 2.384                  | 1.07    | 21.87                    | 21.82                   |
| 200   | 4.767                  | 1.35    | 18.73                    | 18.71                   |

| $L = 28.3$ <span style="margin-left: 100px;"><math>U = 5.707 \times 10^{-10}</math></span> <span style="margin-left: 100px;"><math>G = 4869</math></span> |                        |         |                          |                         |
|---|------------------------|---------|--------------------------|-------------------------|
| M   | W ( $\times 10^{-6}$ ) | Ph(GPa) | MIM ( $\times 10^{-6}$ ) | MM ( $\times 10^{-6}$ ) |
| 20  | 3.927                  | 1.26    | 185.57                   | 190.83                  |
| 50  | 9.818                  | 1.72    | 166.12                   | 176.87                  |
| 100   | 19.64                  | 2.15    | 148.49                   | 148.19                  |
| 200   | 39.27                  | 2.71    | 129.87                   | 125.93                  |

- tegral Equations, Journal of Comp. Physics, No. 2 (1990) 348-370.
6. P. Ehret, D. Dowson, C.M. Taylor and D. Wang, Analysis of EHL Point Contacts with Multigrid Methods, To be Published in IMECHE, Part C.
  7. A.A. Lubrecht, W.E. ten Napel and R. Bosma, Multigrid - An Alternative Method of Solution for Two-dimensional Elastohydrodynamically Lubricated Point Contact Calculations, ASME Journal of Tribology, Vol. 109 (1987) 437-443.
  8. D. Dowson and G.P. Higginson, Elastohydrodynamic Lubrication, Pergamon Press, 1977.
  9. C.J.A. Roelands, Correlational Aspects of the Viscosity- Temperature-Pressure Relationship of Lubricating Oils, PhD. Thesis, Technische Hogeschool Delft, Netherlands, 1966.
  10. D. Dowson and B.J. Hamrock, Numerical Evaluation of the Surface Deformation of Elastic Solids Subjected to a Hertzian Contact Stress, ASLE Trans., Vol. 19 No. 4 (1976) 279-286.
  11. A.A. Lubrecht, W.E. ten Napel and R. Bosma, Multigrid - An Alternative Method of Calculating Film Thickness and Pressure Profiles in Elastohydrodynamically Lubricated Line Contacts, ASME Journal of Tribology, Vol. 108 No. 4 (1986) 551-556.
  12. G.J. Shaw, FDMG Multigrid Software Manual, version 3.0.

**Table 2** Central film thicknesses for  $L = 10$ ,  $L = 14$  and  $L = 28.3$ 

| <hr/>      |                        |                             |                          |                         |
|------------|------------------------|-----------------------------|--------------------------|-------------------------|
| $L = 10.0$ |                        | $U = 0.089 \times 10^{-10}$ | $G = 4869$               |                         |
| M          | W ( $\times 10^{-6}$ ) | Ph(GPa)                     | MIM ( $\times 10^{-6}$ ) | MM ( $\times 10^{-6}$ ) |
| 20         | 0.173                  | 0.44                        | 17.79                    | 18.27                   |
| 50         | 0.433                  | 0.60                        | 17.17                    | 18.02                   |
| 100        | 0.867                  | 0.76                        | 16.59                    | 17.24                   |
| 200        | 1.733                  | 0.96                        | 15.66                    | 16.59                   |
| <hr/>      |                        |                             |                          |                         |
| $L = 14.0$ |                        | $U = 0.343 \times 10^{-10}$ | $G = 4869$               |                         |
| M          | W ( $\times 10^{-6}$ ) | Ph(GPa)                     | MIM ( $\times 10^{-6}$ ) | MM ( $\times 10^{-6}$ ) |
| 20         | 0.477                  | 0.62                        | 41.54                    | 41.03                   |
| 50         | 1.191                  | 0.85                        | 40.30                    | 41.01                   |
| 100        | 2.384                  | 1.07                        | 39.13                    | 39.25                   |
| 200        | 4.767                  | 1.35                        | 37.71                    | 38.16                   |
| <hr/>      |                        |                             |                          |                         |
| $L = 28.3$ |                        | $U = 5.707 \times 10^{-10}$ | $G = 4869$               |                         |
| M          | W ( $\times 10^{-6}$ ) | Ph(GPa)                     | MIM ( $\times 10^{-6}$ ) | MM ( $\times 10^{-6}$ ) |
| 20         | 3.927                  | 1.26                        | 247.82                   | 252.94                  |
| 50         | 9.818                  | 1.72                        | 245.02                   | 255.99                  |
| 100        | 19.64                  | 2.15                        | 239.56                   | 245.61                  |
| 200        | 39.27                  | 2.71                        | 233.76                   | 241.44                  |

13. D. Wang, *Elastohydrodynamic Lubrication of Point Contacts for Layers of Soft Solids and for Monolithic Hard Materials in the Transient Bouncing Ball Problems*, PhD. Thesis, Department of Mechanical Engineering, University of Leeds, 1994.

Numerical simulation of the spatial elastohydrodynamic contact taking into account the complicated geometry of the inlet boundary of a lubricant film as well as the single surface irregularities

M.Ya. Panovko

Mechanical Engineering Research Institute of the Russian Academy of Sciences,  
4 Maliy Kharitonievsky Lane, Moscow 101830, Russia

Method of numerical analysis of heavily loaded spatial elastohydrodynamic (EHD) is presented. A numerical simulation of the point EHD contact, taking into account the complicated geometry of the inlet boundary of a lubricant film, single surface irregularities of the type of a bump or a dent, and also in the presence of the both factors are carried out. A significant influence of the above-mentioned factors on pressure and film thickness at the EHD contact, friction on the contact surface and subsurface octahedral shear stresses are shown.

## 1. INTRODUCTION

In the previously carried out numerical investigations of the point elastohydrodynamical (EHD) contact the surface of the contact was supposed to be smooth or rough under fully flooded conditions [1-5]. Those investigations have demonstrated the efficiency of the numerical method application for analysis of the basic effects in the EHD contact. However due to great dependence of reliability, fatigue life and wear resistance of the lubricated joints (e.g. bearings and gears) upon peculiarities of the lubricating, during recent years an increasing attention have been paid to influence of starved lubrication and single asperities on a contact surface. For example, a numerical simulation of the line EHD contact make it possible to form a more detailed conception of phenomena near asperities [6-8].

A numerical simulation for the heavily loaded point EHD contact, taking into account the complicated geometry of the inlet boundary of a lubricant film, single surface irregularity of the type of a bump or a dent to be situated on one of surfaces,

and also in the presence of the both factors are carried out in present paper. It allows to study the effects generated by factors mentioned above and their influence on parameters of the point EHD contact ( i.e. pressure distribution, film thickness, surface friction, tensor of the subsurface stresses).

## 2. GOVERNING EQUATIONS

The stationary problem of the heavily loaded point EHD contact (it is assumed that the lubricant behaves like a Newtonian incompressible fluid) under isothermal conditions is considered. Typical assumptions of the EHD lubrication theory are used in solving the problem [9,10]. The following dimensionless variables are introduced

$$(x', y') = \frac{(x, y)}{a_H}, \quad p' = \frac{p}{P_H}, \quad h' = \frac{h}{h_0}, \quad d' = \frac{d}{h_0}, \quad \mu' = \frac{\mu}{\mu_0}$$

$$V = \frac{24\mu_0 |v_1 + v_2| R_x^2}{P_H a_H^3}, \quad v = \frac{v_1 + v_2}{|v_1 + v_2|}, \quad H_0 = \frac{2R'_x h_0}{a_H^2}$$

$$\varepsilon = \frac{R'_x}{R'_y}, \quad \beta = \frac{a_H}{b_H}, \quad \varphi(\beta) = \frac{K(e) - D(e)}{\beta^4 D(e)}$$

$$D(e) = \frac{K(e) - E(e)}{e^2}, \quad e = \sqrt{1 - \beta^2}, \quad A' = \frac{2R'_x A}{a_H^2}$$

$$(x'_d, y'_d) = \frac{(x_d, y_d)}{a_H}, \quad (w'_x, w'_y) = \frac{(w_x, w_y)}{a_H}$$

where  $x, y$  - Cartesian coordinates in the contact plane,  $R'_x, R'_y$  - reduced radii of curvature of the contacting bodies,  $p$  - lubricant pressure,  $a_H$  and  $b_H$  - half-axes Hertzian contact region,  $e$  - eccentricity of the contact ellipse,  $p_H$  - maximum Hertzian pressure,  $h$  - film thickness,  $h_0$  - film thickness at the origin of coordinates,  $\mu$  - viscosity of lubricant,  $\mu_0$  - viscosity at ambient pressure ( $p=0$ ),  $v_1, v_2$  - vectors of the surface velocities,  $H_0$  - dimensionless film thickness at the origin of coordinates,  $V$  - load-velocity parameter,  $K(e)$  and  $E(e)$  - full elliptic integrals of the first and second kind,  $\beta$  - is determined from the equation  $\beta^2 \varphi(\beta) = R'_x/R'_y$ ,  $d$  - function describing surface irregularity,  $w_x$  and  $w_y$  - wavelength of the surface irregularity along the  $x$ - and  $y$ -directions respectively,  $x_d$  and  $y_d$  - coordinates of the irregularity centre,  $A$  - amplitude of the irregularity.

Configuration of the irregularity (of the type of a bump or a dent) is given (in dimensionless form, further without upper touches) by

$$d(x, y) = \frac{A}{H_0} 10^{-10} \left( \left( \frac{x - x_d}{w_x} \right)^2 + \left( \frac{y - y_d}{w_y} \right)^2 \right)_x$$

$$\cos \left( 2\pi \frac{x - x_d}{w_x} \right) \cos \left( 2\pi \frac{y - y_d}{w_y} \right)$$

This is generalization of the equation which was used in [7] for numerical simulation of the line EHD contact.

Equations of the point EHD contact in dimensionless form can be written as

$$L(p) = \nabla \cdot \left( H_0^2 \frac{h^3}{\mu} \nabla p - Vvh \right) = 0 \tag{1}$$

$$\nabla = \left( \frac{\partial}{\partial x}, \frac{\partial}{\partial y} \right), \quad v = (v_x, v_y)$$

$$h = 1 + \frac{x^2 + \varepsilon y^2}{H_0} + \frac{1}{\pi \beta^2 D(e) H_0} \times$$

$$\iint_{\Omega} \left( \frac{1}{\sqrt{(\xi - x)^2 + (\eta - y)^2}} - \frac{1}{\sqrt{\xi^2 + \eta^2}} \right) \times$$

$$p(\xi, \eta) d\xi d\eta + d(x, y) - d(0, 0) \tag{2}$$

$$\iint_{\Omega} p(\xi, \eta) d\xi d\eta = \frac{2\pi}{3\beta} \tag{3}$$

$$p \Big|_C = \frac{\partial p}{\partial n} \Big|_{C_e} = 0 \tag{4}$$

where  $C$  - boundary of the contact domain  $\Omega$ ,  $C_e$  - exit (free) boundary (part of the boundary where  $(v \cdot n) > 0$ ),  $n$  - single vector of the outward normal. The Barus viscosity-pressure relationship  $\mu = \mu_0 \exp(Qp)$ , where  $Q$  - piezoviscous parameter, was used in system (1)-(4)

System (1)-(4) is the nonlinear integro-differential system of the Reynolds equation (1), the gap between the two elastic bodies (2), force balance equation, i.e. the integral over the pressure equals to the externally applied contact load (3), and boundary conditions (4).

Complementarity conditions [1,11] are used to determine a free boundary, which separates the pressure-positive region from the cavitation region (pressure-null region). These conditions are written in following form

$$\begin{aligned} L(p) = 0, \quad p > 0 & \text{ in lubricant domain} \\ L(p) < 0, \quad p = 0 & \text{ in cavitation domain} \end{aligned} \tag{5}$$

Shape of the exit boundary, load-velocity parameter  $V$  (for heavily loaded

contact  $V \ll 1$ , vector of the velocity  $v(v_x, v_y)$ , parameters  $\varepsilon = R'_x/R'_y$ , and  $Q$  for system (1)-(5) are given.

Pressure  $p(x, y)$ , gap  $h(x, y)$ , exit (free) boundary  $x_c(y)$ , and film thickness  $H_0$  at the origin of coordinates are a solution of the system (1)-(5).

The known solution is used for determination of the friction stresses on contact surface with the aid of correlation

$$\tau = \frac{\mu s V}{12 h H_0} - \frac{h}{2} H_0 \nabla p$$

where first term - sliding shear stresses  $\tau_s = (\tau_{sx}, \tau_{sy})$ , second term - rolling shear stresses  $\tau_r = (\tau_{rx}, \tau_{ry})$ ,  $s = 2(v_2 - v_1)/|v_2 + v_1|$  - vector of the dimensionless sliding velocity.

Components of the stress tensor in subsurface layer  $\sigma_{ij}(x, y, z)$  is determined from known Boussinesq solution [12] and pressure on contact surface  $p(x, y)$  as

$$\sigma_{ij}(x, y, z) = \iint_{\Omega} B_{ij}(x, y, z, \xi, \eta) p(\xi, \eta) d\xi d\eta$$

where  $B_{ij}(x, y, z)$  - stress tensor in the Boussinesq solution. Subsurface octahedral shear stresses  $\tau_{oct}$  are calculated according to the known correlation (see e.g. [13]) with using the values of  $\sigma_{ij}(x, y, z)$ .

### 3. NUMERICAL METHOD

Computational domain in the plane  $(x, y)$  is given as rectangle and covered by nonuniform staggered grid with nodes  $(x_i, y_j)$  and  $(x_{i-1/2}, y_{j-1/2})$ . After integrating equation (1) over domain of the cell and transforming the double integral to the line integral over the contour of the cell (1) we obtain

$$L_1(p) = \int_{(1)} \left[ H_0^2 \frac{h^3}{\mu} (\nabla p \cdot n) - V(v \cdot n) h \right] dl = 0 \quad (6)$$

Operator  $L(p)$  in complementarity conditions (see (5)) is replaced by  $L_1(p)$ .

Solution of the EHD equations is carried out by Newton method. Linearizing equations (3), (4), (6) near solution  $(p(x, y), H_0)$  yields

$$\begin{aligned} & \int_{(1)} \left\{ \left[ 2H_{0,k} \frac{h_k^3}{\mu_k} \frac{\partial p_k}{\partial n} - V(v \cdot n) \frac{\partial h_k}{\partial H_{0,k}} + \right. \right. \\ & \left. \left. H_{0,k}^2 \frac{3h_k^2}{\mu_k} \frac{\partial p_k}{\partial n} \frac{\partial h_k}{\partial H_{0,k}} \right] \Delta H_{0,k+1} - \right. \\ & \left. H_{0,k}^2 \frac{h_k^3}{\mu_k^2} \frac{\partial \mu_k}{\partial p_k} \frac{\partial p_k}{\partial n} \Delta p_{k+1} + H_{0,k}^2 \frac{3h_k^2}{\mu_k} \frac{\partial h_k}{\partial p_k} \Delta p_{k+1} \frac{\partial p_k}{\partial n} + \right. \\ & \left. H_{0,k}^2 \frac{h_k^3}{\mu_k} \frac{\partial \Delta p_{k+1}}{\partial n} - V(v \cdot n) \frac{\partial h_k}{\partial p_k} \Delta p_{k+1} \right\} dl = \\ & = - \int_{(1)} \left[ H_{0,k}^2 \frac{h_k^3}{\mu_k} \frac{\partial p_k}{\partial n} - V(v \cdot n) h_k \right] dl \quad (7) \end{aligned}$$

$$\iint_{\Omega} \Delta p_{k+1}(\xi, \eta) d\xi d\eta = \frac{2\pi}{3\beta} - \iint_{\Omega} p_k(\xi, \eta) d\xi d\eta \quad (8)$$

$$\Delta p_{k+1} \Big|_c = 0 \quad (9)$$

In equations (7)-(9)  $k$  - number of the iteration,

$\Delta p_{k+1} = p_{k+1} - p_k$   
 $\Delta H_{0,k+1} = H_{0,k+1} - H_{0,k}$ ,  $\partial h_k / \partial p_k$  - line operator (Frechet derivative) which is applied to  $\Delta p_{k+1}$  and can be written as

$$\begin{aligned} & \frac{\partial h_k}{\partial p_k} \Delta p_{k+1} = \frac{1}{\pi \beta^2 D(e) H_0} \times \\ & \iint_{\Omega} \left( \frac{1}{\sqrt{(\xi - x)^2 + (\eta - y)^2}} - \frac{1}{\sqrt{\xi^2 + \eta^2}} \right) \times \\ & \Delta p_{k+1}(\xi, \eta) d\xi d\eta \end{aligned}$$

System (7)-(9) is used for developing the difference scheme. This numerical scheme satisfies the mass conservation law.

Matrix of the difference equations takes into account that the inlet boundary (there  $(\nu \cdot n) < 0$ ) of the lubricant film may be given by complicated shape (type of a hollow on inlet). Integral in the expression (2) is calculated according to the approach (see [14]) which is used for solution of the singular integral equations

$$\iint_{\Omega} \left( \frac{1}{\sqrt{(\xi - x_{m-1/2})^2 + (\eta - y_{n-1/2})^2}} - \frac{1}{\sqrt{\xi^2 + \eta^2}} \right) \times$$

$$p(\xi, \eta) d\xi d\eta \cong$$

$$\sum_{j=1}^{NY} \sum_{i=il(j)}^{i2(j)} \left( \frac{1}{\sqrt{(x_i - x_{m-1/2})^2 + (y_j - y_{n-1/2})^2}} - \right.$$

$$\left. \frac{1}{\sqrt{(x_i - x_{m0-1/2})^2 + (y_j - y_{n0-1/2})^2}} \right) \times$$

$$P_k(x_i, y_j)(x_{i+1/2} - x_{i-1/2})(y_{j+1/2} - y_{j-1/2})$$

where  $il(j)$ ,  $i2(j)$  - arrays describing the situation of the inlet and exit boundaries, respectively:  $m=1, \dots, NX+1$ ;  $n=1, \dots, NY+1$ . Array  $i2(j)$  is determined at every iteration according to the complementarity conditions (5). Node  $(m0-1/2, n0-1/2)$  is situated at the origin of coordinates.

The Hertzian solution for two elastic solids as initial approximation is used. One iteration step includes solution of the difference equations (7)-(9) for  $\Delta H_{0,k+1}$ ,  $\Delta P_{k+1}(x_i, y_j)$  by Gaussian method, calculation  $H_{0,k+1}$ ,  $P_{k+1}(x_i, y_j)$ ,  $h_{k+1}(x_{i-1/2}, y_{j-1/2})$  and determination of the exit boundary  $x_c(y)$ . Iteration procedure is finished when the given relative accuracy of a solution  $\delta$  satisfies the following condition

$$\max(|H_{0,k+1}/H_{0,k} - 1|, |P_{k+1}/P_k - 1|, |h_{k+1}/h_k - 1|, |x_{c,k+1}/x_{c,k} - 1|) < \delta.$$

#### 4. NUMERICAL RESULTS

Numerical simulation of the heavily loaded point EHD contact with a single surface irregularity or with a hollow (deepening) at the inlet boundary of lubricant film, and also in the presence of the both factors is carried out. For point EHD contact  $\varepsilon = 1$ ,  $\beta = 1$ ,  $D(0) = \pi / 4$ ,  $v_x = 1$ ,  $v_y = 0$  are given. Calculations are carried out on the grid  $30 \times 30$  under  $V=0.1$ ,  $Q=5$  and  $\delta = 0.00001$ . Sliding shear stresses for smooth surface are calculated under  $s=0.1$ . For description of the surface irregularity  $d(x,y)$  the following parameters are used  $w_x = w_y = 1$ ,  $A = \pm 0.1$  ( $A < 0$  - when bump,  $A > 0$  - when dent). Centre of the irregularity  $x_d, y_d$  is situated in the nodes of the grid with coordinates  $(-0.543, 0)$ ,  $(0, 0)$ ,  $(0.542, 0)$ . Calculations of the stress tensor  $\sigma_{ij}$  in subsurface layer are carried out under the Poisson's ratio  $\nu = 0.3$ .

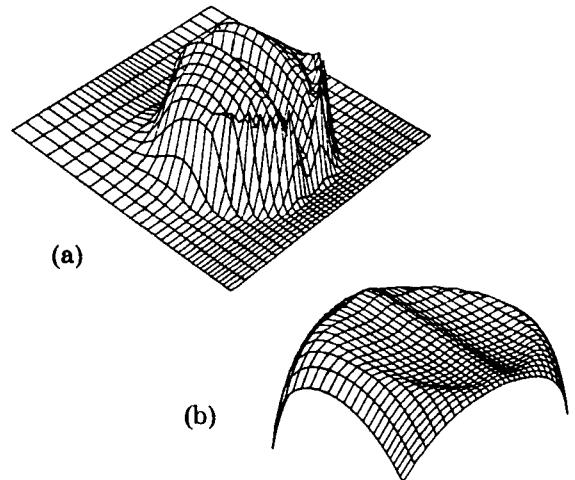


Figure 1. Pressure (a) and gap (b) distributions in the case with a hollow at the inlet boundary



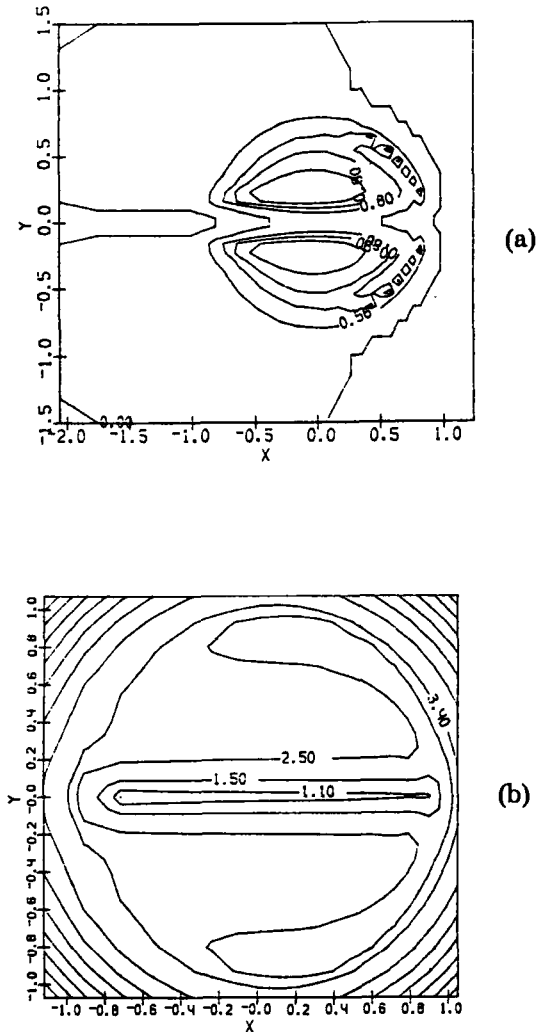


Figure 2. Pressure (a) and gap (b) isolines in the case with a hollow at the inlet boundary

Numerical simulation has shown that in the point EHD contact new phenomena take place under influence of the above-mentioned factors.

When the shape of the inlet boundary is complex, e.g. it has only one hollow, pressure distribution  $p(x,y)$  get a deep furrow in x-direction, and pressure spikes is locally vanished near outlet boundary (see Figure 1, (a)). In addition a

crest is formed for a gap in the x-direction, and contraction is locally absent near the exit boundary (see Figure 1, (b)). In this case a dimensionless thickness  $H_0$  decreases as follows : under fully flooded conditions  $H_0 = 0.1786$ , and when inlet boundary has a hollow  $H_0 = 0.05088$ . Calculations have shown that similar hollows cause a corresponding alterations in pressure and gap distributions.

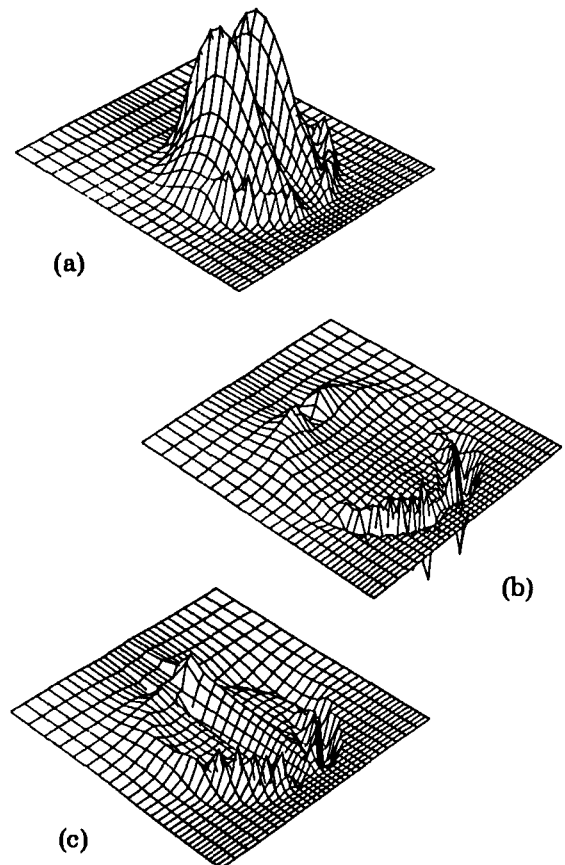
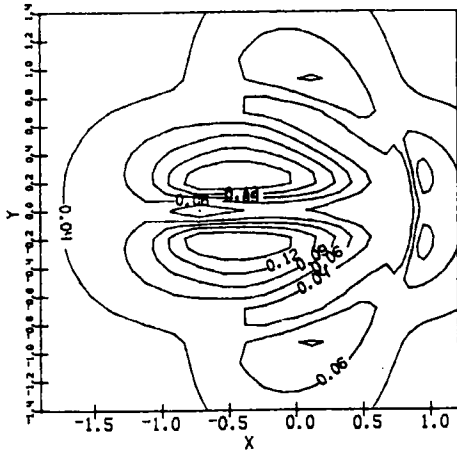
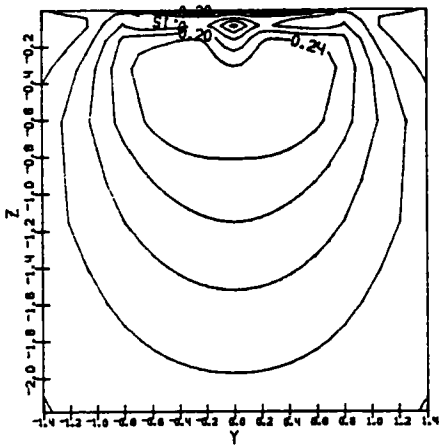


Figure 3. Distributions of the sliding in x-direction (a), rolling in x-direction (b) and y-direction (c) stresses

Details of the pressure and gap distributions are given by isolines in Figure 2. The hollow strongly influences distributions of the surface tangent stress



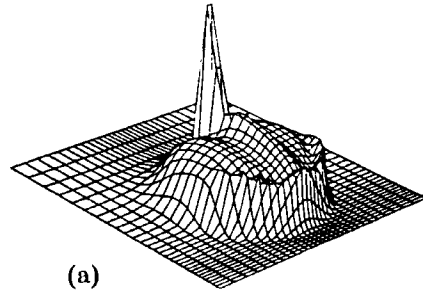
(a)



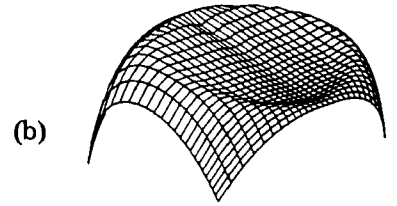
(b)

Figure 4. Octahedral shear stresses : (a) in plane  $z=-0.001$ ; (b) in plane  $x=0$

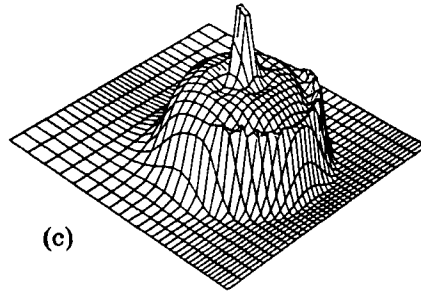
components and octahedral shear stresses. In Figure 3 sliding and rolling stresses are shown. Features of the sliding stresses are similar to pressure distributions. Features of the rolling stresses are determined by pressure gradient. In Figure 4 octahedral shear stresses by isolines in the plane sections ( $z=-0.001$ ,  $x=0$ ) when inlet boundary has a hollow are shown. One can



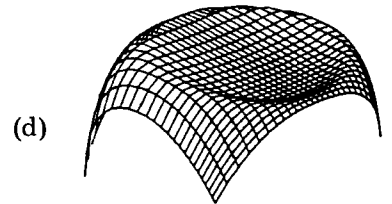
(a)



(b)



(c)



(d)

Figure 5. Pressure (a), (c) and gap (b), (d) distributions: (a), (b) - bump at  $x=-0.543$ ; (c), (d) - bump at  $x=0$ .

see that new local extremums of the octahedral shear stresses appear.

A single surface bump causes the spike in pressure distribution under fully flooded conditions (see Figure 5 (a), (c)). The bump situated near the inlet boundary affects pressure distribution downstream up to exit boundary. A crest is formed in the x-

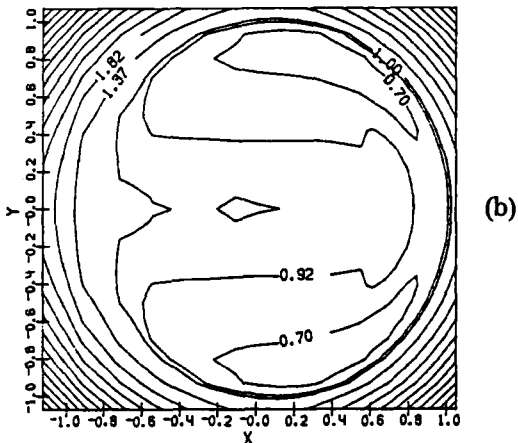
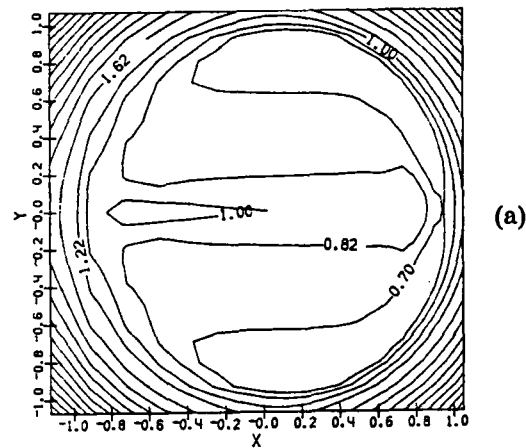


Figure 6. Gap isolines: (a) - bump is situated at  $x = -0.543$ , (b) - bump is situated at  $x = 0$

direction. When a bump is situated at the origin of the coordinates or near the exit boundary this crest is not formed. The gap distributions are shown on Figure 5 (b), (d) as a surface of solution and on Figure 6 as isolines. When a bump is situated near the inlet boundary, the gap has a furrow in  $x$ -direction. For other cases the gaps are similar to a gap with smooth surface. Details of the gap distributions are shown by Figure 6. Dimensionless thickness  $H_0$  in

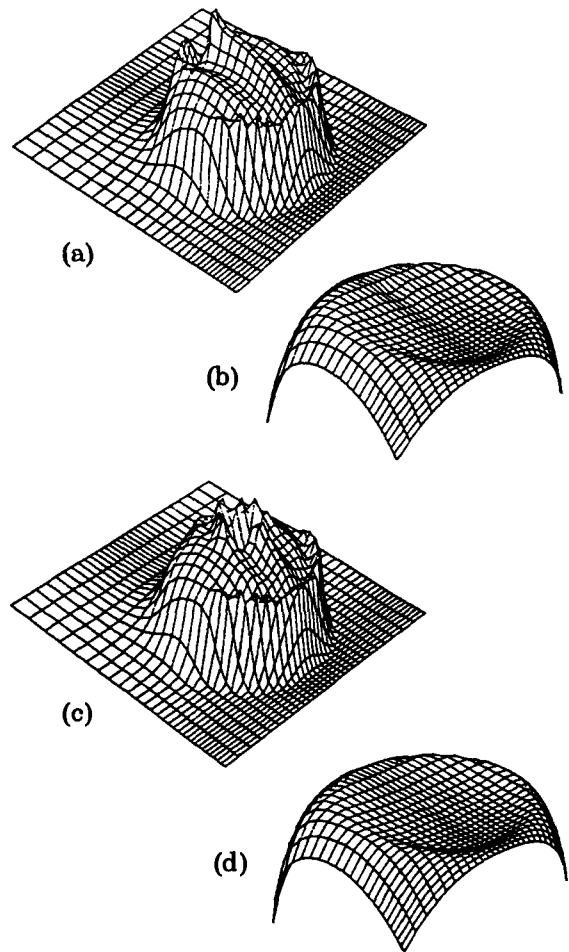
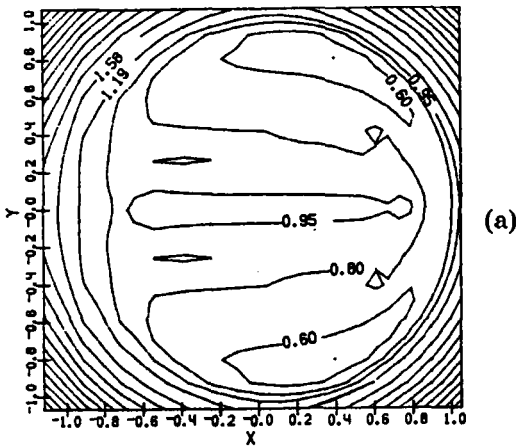


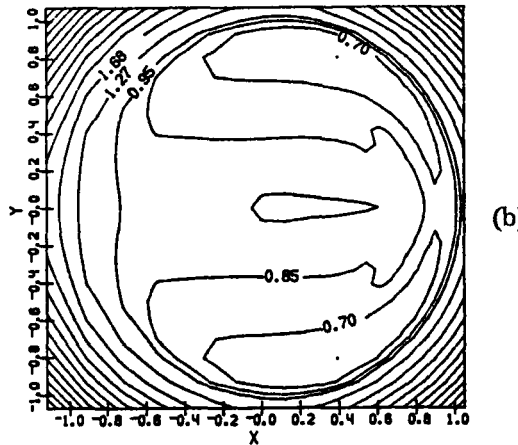
Figure 7. Pressure (a), (c) and gap (b), (d) distributions: (a), (b) - dent at  $x = -0.543$ ; (c), (d) - dent at  $x = 0$ .

these cases are:  $H_0 = 0.2009$  ( $x_d = -0.543$ ),  $H_0 = 0.18$  ( $x_d = 0$ ),  $H_0 = 0.1787$  ( $x_d = 0.542$ ).

When a single irregularity is a dent, the pressure distribution demonstrates a deep crater ( see Figure 7). Gap configurations in these cases to a certain extent more differ from that case when the contact operates under fully flooded conditions. Details of the gap distributions are shown in Figure 8. Dimensionless thickness  $H_0$  in these cases are:  $H_0 = 0.2065$  ( $x_d = -0.543$ ),  $H_0 = 0.1941$

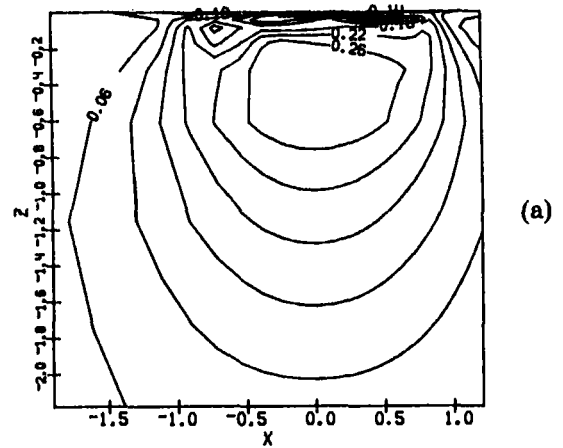


(a)

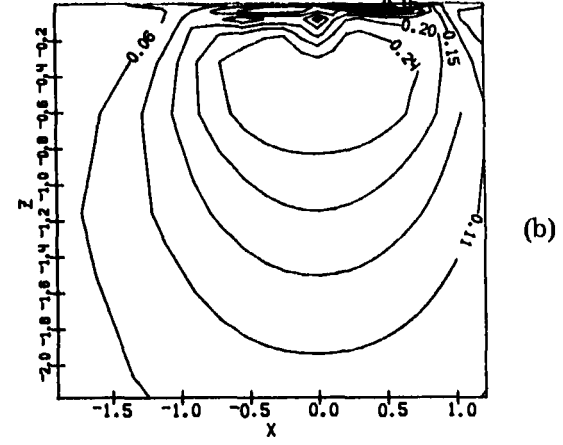


(b)

Figure 8. Gap isolines: (a) - dent is situated at  $x=-0.543$ , (b) - dent is situated at  $x=0$ .



(a)



(b)

Figure 9. Octahedral shear stresses in plane  $y=0$ : (a) - dent is situated at  $x=-0.543$ , (b) - dent is situated at  $x=0$ .

( $x_d=0$ ),  $H_0=0.1784$  ( $x_d=0.542$ ). Figure 9 demonstrates the isolines of the octahedral shear stresses in plane  $y=0$  when a dent is situated at above-mentioned coordinates. One can see that the local minimum is situated near the dent. Comparison Figure 9 (a) and Figure 9 (b) shows that a surface irregularity strongly alters distribution of the octahedral shear stresses.

Figure 10 demonstrates a combined influence of hollow and surface irregularity on parameters of the point EHD contact (case when a bump or dent are situated at

the origin of the coordinates:  $x_d=0, y_d=0$ ). Comparison of presented distributions with corresponding distributions when the hollow or surface irregularity takes place indicates that a combined case includes the main features of both cases. When combination "a cut + a bump" takes place the dimensional film thickness equals to  $H_0 = 0.05157$ . When combination "a cut + a dent" takes place the dimensional film thickness equals to  $H_0 = 0.06072$ .

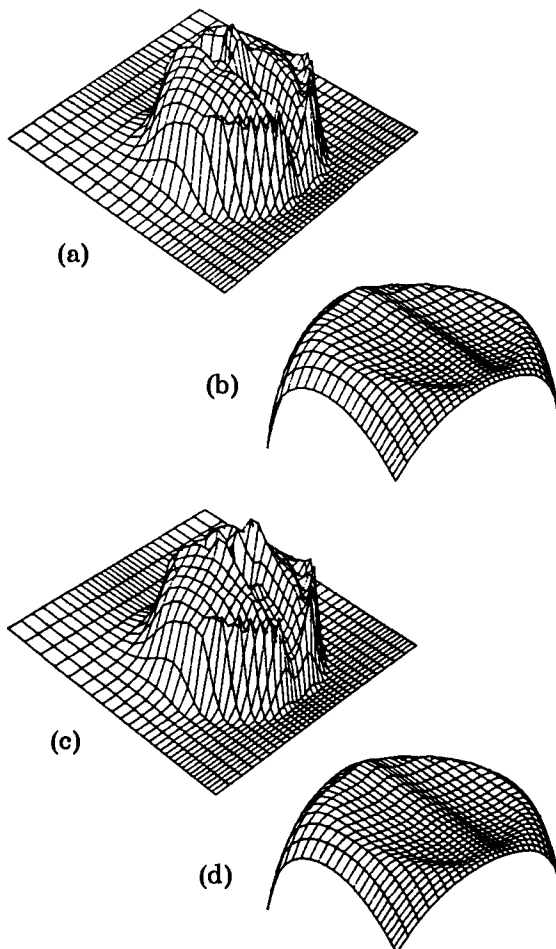


Figure 10. Pressure (a), (c) and gap (b), (d) distributions: (a), (b) - hollow+bump ; (c), (d) - hollow+dent.

## REFERENCES

1. K.P. Oh, ASME J. Tribol., 106(1984) 88.
2. H.P. Evans , R.W. Snidle, ASME J. Lubric. Technol., 103(1981) 547.
3. B.J. Hamrock , D. Dowson, ASME J. Lubric. Technol., 98(1976) 223.
4. A.A. Lubrecht , W.E. ten Napel , R. Bosma, ASME J. Tribol., 109(1987) 437.
5. D. Zhu , H.S. Cheng, ASME J. Tribol. 108(1988), 32.
6. P.R. Goglia, T.F. Conry, C. Cusano, ASME J. Tribol., 106(1984) 104.
7. C.H. Venner , A.A. Lubrecht , W.E. ten Napel, ASME J. Tribol. 113(1991) 777.
8. Rong-Tsong Lee, B.J. Hamrock, ASME J. Tribol., 112(1990) 497.
9. D. Dowson, G.R. Higginson, *Elasto-hydrodynamic lubrication*, New York, 1966.
10. M.A. Galakhov, P.B. Gusiaticnikov, A.P. Novikov, *Mathematical models of contact hydrodynamics*, "Nauka" publisher, Moscow, 1985.
11. M.M. Kostreva, *Intern. J. Numer. Methods in Fluids*, 4(1984) 377.
12. K.L. Johnson, *Contact mechanics*, Cambridge, 1987.
13. H.G. Hahn, *Theory of elasticity*, B.G. Teubner, Stuttgart, 1985.
14. S.M. Belotserkovsky, I.K. Lifanov, *Numerical methods in singular integral equations*, "Nauka" publisher, Moscow, 1985.

## Film thickness anomalies in very thin elastohydrodynamic oil films

F. M. Baskerville and A. J. Moore

BP Oil Technology Centre, Chertsey Road, Sunbury-on-Thames, Middlesex, TW16 7LN, UK

Experimental studies of very thin elastohydrodynamic (EHD) oil films have shown, or suggested, that several aspects of lubricant behaviour do not fully conform to the model presumed by classical EHD theory. This study examines three forms of behaviour which appear to be anomalous. The first concerns the pressure-viscosity response of the lubricant in the EHD inlet zone. Although this appears to be weaker than expected, the disparity appears more likely to arise from a modest systematic error in the method by which film thickness is determined than from the behaviour of the lubricant. The second phenomenon investigated is a mechanism by which additive systems improve the durability of rolling surfaces. A transition is detected at a film thickness of about 5 nm, below which the effective viscosity of an additive-treated lubricant approximately doubles. Finally, the effect of polymeric viscosity index improvers on film thickness is examined for both simple base oil solutions and a simplified range of fully formulated engine oils. Both film thickness enhancements and a severe film thinning phenomenon are observed at film thicknesses in the region of 10 nm.

### 1. INTRODUCTION

Studies of very thin elastohydrodynamic (EHD) oil films based on optical interferometry have indicated that EHD theory provides a largely accurate description of lubricant behaviour as film thickness ranges down to 10 nm [1, 2]. A number of departures from theory have also been identified, however, some with a high degree of certainty and some with less. Some forms of anomalous behaviour arise from the inherent structural (or solvation) properties of liquids in films of just a few molecular diameters thickness; these lie beyond the scope of this paper and are discussed elsewhere [3]. Attention is concentrated here on three aspects of behaviour considered to be of greater potential importance to commercial lubricants.

First to be considered is the pressure-viscosity response of lubricants in the EHD inlet region. Reported findings on this topic are somewhat at variance, with earlier studies pointing to quite good agreement between pressure-viscosity responses in EHD

and conventional viscometric experiments [2, 3] and more recent work suggesting that agreement may not be as good as first thought [4]. A common feature of these studies is the thin film optical interferometry technique used to determine film thickness. Whilst the basic principles of the technique have remained unchanged, the precise way in which they are applied has been subject to continual modification. The version of the technique used in the present study is similar to that employed by Guangteng and Spikes [4].

The second phenomenon investigated is the way in which additive systems are found to improve the protection afforded to rolling surfaces beyond that attributable to either a bulk viscosity increase or to boundary film formation. It has been noted in earlier work that the sometimes fragile silica spacer layer which lies at the heart of the thin film optical interferometry technique receives better protection from a lubricant containing an additive system than one that does not [2]. Experiments conducted at very low values of film thickness provide an insight as to why

this might be so.

Finally, a study is made of the behaviour of polymeric VI improvers when film thickness approaches the diameter of the polymer molecule. A variety of behaviours have been reported previously, ranging from film thickness enhancements for base oil solutions [5] to a film thinning phenomenon for fully formulated motor oils [2]. The present work shows that VI improvers are highly sensitive to the presence of other additives. The consequences can be seen both in the way film thickness develops and in the frictional behaviour of solutions in the boundary regime.

## 2. EXPERIMENTAL

### 2.1. EHD film thickness measurement

Film thickness was determined by the thin film optical interferometry technique developed by Johnson et al [1]. This technique overcomes the quarter wavelength resolution limit to conventional interferometry by exploiting the similarity in optical properties between oil and silica. A spacer-layer of silica sputtered onto a semi-reflective glass surface acts as an artificial oil film and allows constructive interference to occur at any real value of oil film thickness. Film thicknesses is deduced from shifts in the wavelength of constructive maxima, as detected by a diffraction grating spectrometer.

The apparatus and computer system used to measure film thickness were supplied by the Imperial College Tribology Section and PCS Instruments Ltd., respectively. Details of the experimental procedures are described elsewhere [4, 6].

Specimen properties and contact conditions between a steel ball and a coated glass plate were as summarised below.

Glass disc:

|                          |        |
|--------------------------|--------|
| Elastic Modulus          | 75 GPa |
| Poisson's Ratio          | 0.220  |
| R <sub>a</sub> roughness | 10 nm  |

Steel ball:

|                          |         |
|--------------------------|---------|
| Elastic Modulus          | 207 GPa |
| Poisson's Ratio          | 0.293   |
| Radius                   | 9.5 mm  |
| R <sub>a</sub> roughness | 10 nm   |

|                        |           |
|------------------------|-----------|
| Effective Modulus, $E$ | 116.9 GPa |
| Effective Radius, $R$  | 9.5 mm    |

|                     |          |
|---------------------|----------|
| Load, $W$           | 20 N     |
| Max. Hertz Pressure | 0.53 GPa |

|     |                  |   |
|-----|------------------|---|
| $k$ | see equation (3) | $0.0284 \text{ N}^{-0.14} \text{ m}^{0.58}$ |
|-----|------------------|---|

As will be seen later, the lower limit to which rolling speed could be taken depended on the robustness of the silica spacer layer on the glass disc. This varied from one batch of discs to another.

At each set value of rolling speed, film thickness was typically determined in batches of five consecutive measurements and then evaluated for statistical variation. Mean values were accepted if the standard deviation did not exceed 1 nm. At very low speeds, a higher standard deviation, typically 2.5 nm, was accepted but the sample size was then increased to 10 or 15 measurements. Whichever approach was taken, the standard error of the mean remained close to 0.5 nm. The long term repeatability of this type of measurement is generally found to be better than  $\pm 10\%$ .

### 2.2. Boundary friction measurements

Friction was measured using a Plint TE-77 test rig following the procedure described in detail elsewhere [7]. The specimen arrangement consisted of a cast iron pin reciprocating against a cast iron plate in a self-aligning, flat-on-flat configuration. The stroke length was 15 mm, the reciprocation rate 8 Hz, and the load 80N. The temperature of the plate surface was 100 °C.

Although the experiment is designed to introduce a small hydrodynamic influence in the central region of each stroke, mean friction coefficients reflect a predominantly boundary lubrication condition.

### 3. PRESSURE-VISCOSITY STUDIES

#### 3.1. Lubricants

Six fluids of known pressure-viscosity response were examined over a range of temperature. Viscous properties at temperatures relevant to each fluid are listed in Table 1. The first two lubricants, di(2-ethylhexyl)sebacate and di(2-ethylhexyl)phthalate, have been extensively characterised in the 1953 A.S.M.E. Pressure-Viscosity Report [8]. From the data reported therein, viscosities have been interpolated at 0 and 0.2 GPa pressure for each of the temperatures of interest. A pressure-viscosity coefficient,  $\alpha_0$ , has then been derived as

$$\alpha_0 = \frac{1}{\Delta p} \ln \frac{\eta}{\eta_0} \quad (1)$$

where  $\Delta p$  is the pressure range,  $\eta$  the dynamic viscosity at the higher pressure,  $p$ , and  $\eta_0$  the viscosity at atmospheric pressure.

The other fluids examined include a mixed isomeric form of dicyclohexylcyclohexane and three other naphthenic hydrocarbons. Pressure-viscosity data for these fluids were obtained using a rolling ball high pressure viscometer, again for the pressure range 0 to 0.2 GPa.

#### 3.2. Results

Film thickness measurements for di(2-ethylhexyl)sebacate and dicyclohexylcyclohexane are shown in Figures 1 and 2, respectively. The combinations of single and duplicate data sets in these figures illustrate both the satisfactory repeatability of the measurement and the low level of statistical

Table 1  
Viscometric properties of reference oils

| Reference oil             | $\theta / ^\circ\text{C}$ | $\eta_0 / \text{mPa s}$ | $\alpha_0 / \text{GPa}^{-1}$ | $\alpha_1 / \text{GPa}^{-1}$ |
|---------------------------|---------------------------|-------------------------|------------------------------|------------------------------|
| Di(2-ethylhexyl)sebacate  | 30                        | 14.78                   | 12.9                         | 9.6                          |
|                           | 60                        | 6.15                    | 10.8                         | 8.5                          |
|                           | 90                        | 3.30                    | 9.4                          | 7.0                          |
|                           | 120                       | 2.07                    | 8.3                          | 6.5                          |
| Di(2-ethylhexyl)phthalate | 30                        | 41.90                   | 18.3                         | 14.8                         |
|                           | 60                        | 11.87                   | 14.9                         | 12.1                         |
|                           | 90                        | 4.94                    | 12.3                         | 8.8                          |
|                           | 120                       | 2.59                    | 10.2                         | 7.3                          |
| Dicyclohexylcyclohexane   | 30                        | 59.70                   | 44.2                         | 32.2                         |
|                           | 45                        | 25.00                   | 34.7                         | 26.3                         |
|                           | 60                        | 12.70                   | 28.1                         | 19.8                         |
|                           | 90                        | 4.73                    | 19.9                         | 12.7                         |
| Naphthenic hydrocarbon A  | 30                        | 47.20                   | 31.2                         | 25.3                         |
|                           | 60                        | 12.58                   | 22.0                         | 16.1                         |
|                           | 90                        | 5.15                    | 16.8                         | 12.0                         |
|                           | 120                       | 2.71                    | 13.5                         | 11.2                         |
| Naphthenic hydrocarbon B  | 30                        | 10.99                   | 18.2                         | 14.0                         |
|                           | 60                        | 4.03                    | 13.7                         | 11.0                         |
| Naphthenic hydrocarbon C  | 30                        | 10.63                   | 22.7                         | 15.9                         |
|                           | 60                        | 4.30                    | 15.5                         | 11.8                         |



scatter in the mean values of film thickness.

At film thicknesses below 10 nm, the behaviour of some lubricant base stocks can be both complex and variable [3]. Although di(2ethylhexyl)sebacate, in Figure 1, obeys EHD theory down to film thicknesses of only 2 nm, behaviour below 10 nm was not highly consistent in repeated experiments. Departures reported for this fluid from the usual power law relationship between film thickness and speed [9] were usually found to occur below the speed range covered in Figure 1.

Dicyclohexylcyclohexane, in Figure 2, generates relatively thick oil films by virtue of its higher ranges of viscosity and pressure-viscosity coefficient. At the lowest temperature, film thicknesses range up to 400 nm. The range of film thickness covered for the whole set of fluids thus embraces both a molecular scale of thickness and a scale that is large in relation to the combined surface roughness.

**3.3. Interpretation**

Interpretation of film thickness data is based on the Hamrock and Dowson [10] equation for central film thickness,  $h_c$ :

$$h_c = k\alpha^{0.53}(u\eta_0)^{0.67} \tag{2}$$

where

$$k = 2.69KR^{0.46}W^{-0.067}E^{-0.073} \tag{3}$$

and  $u$  is the rolling speed,  $W$  the applied load,  $E$  the effective elastic modulus,  $R$  the effective radius and  $K$  a geometric parameter equal to 0.706 for circular point contacts. A least squares fit of  $h_c$  to  $u$  yields a relationship

$$\log(h_c) = \log(A) + b.\log(u) , \tag{4}$$

where

$$\log(A) = \log(k) + 0.53.\log(\alpha) + b.\log(\eta_0) \tag{5}$$

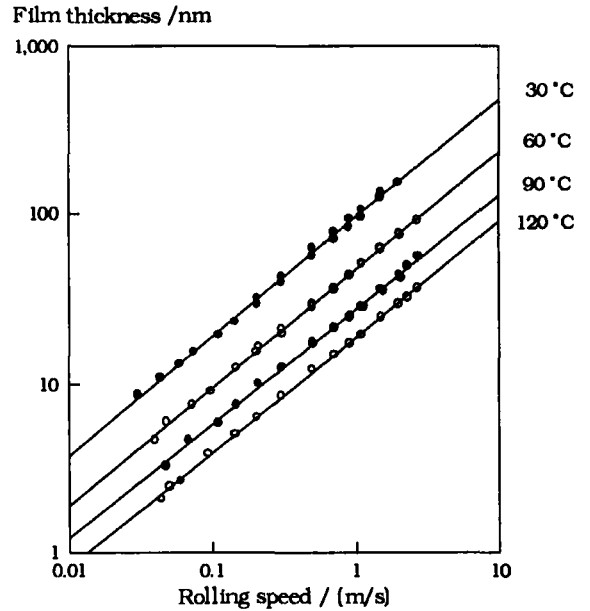


Figure 1. EHD film thickness for di(2-ethylhexyl)sebacate

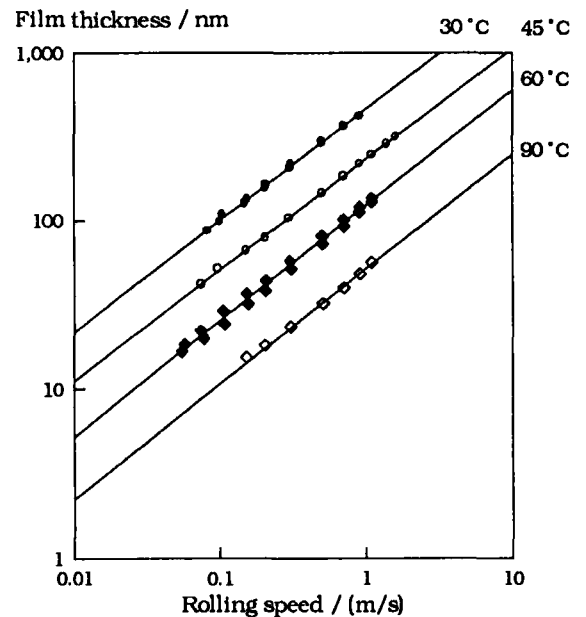


Figure 2. EHD film thickness for dicyclohexylcyclohexane

$b$ , of course, should prove equal to 0.67. A regression analysis of film thickness data thus yields an estimate first of  $A$  and then of the pressure-viscosity coefficient,  $\alpha$ .

For di(2-ethylhexyl)sebacate, in Figure 1, and dicyclohexylcyclohexane, in Figure 2, mean values of  $b$  are 0.685 and 0.673, respectively. In this respect, the Hamrock and Dowson expression, equation (2), is obeyed quite closely.

Estimates,  $\alpha_i$ , of the effective pressure-viscosity coefficient in the EHD inlet region are listed in Table 1. They prove lower than the values,  $\alpha_o$ , defined by conventional viscometry. Figure 3 shows that  $\alpha_i$  remains about 26% lower than  $\alpha_o$  irrespective of fluid type or temperature.

It has been suggested that low values of pressure-viscosity coefficient in the inlet region of very thin EHD oil films might stem from the response of lubricants to the severe conditions of shear [9]. Although this possibility can not be ruled out, the consistency of the relationship found in Figure 3 and the wide range of film thicknesses covered do not provide encouragement for it. An alternative

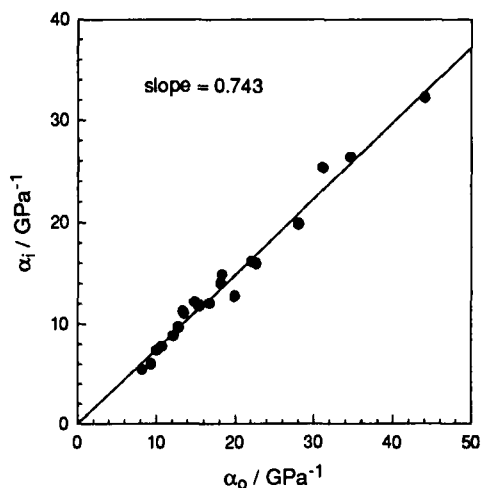


Figure 3. Comparison between pressure-viscosity coefficients determined by EHD and conventional forms of viscometry

inference is that the low values of  $\alpha_i$  derive from a systematic error in determinations of film thickness. An error of only 14.6% in the latter would account for the trend established in Figure 3.

## 4. ENGINE OIL STUDIES

### 4.1. Lubricants

Engine crankcase oils typically consist of a blend of two or more base oil components, a dispersant/inhibitor (DI) additive package and a polymeric viscosity index improver (VII). While the DI system confers the levels of anti-wear, anti-corrosion and engine cleanliness performance needed for particular applications, the VI improver reduces the rate at which viscosity varies with temperature. The enhancement in viscosity which results at high temperature helps to maintain hydrodynamically generated films in engine bearings at the thickness required.

For simplicity, the fluids examined here are based on a single hydrocracked base oil and a single DI system. The latter is used at a concentration of 14% w/w, a typical treat-rate for high performance products. The VI improvers studied are described in Table 2. Each is used in the form of a concentrate and is added at a level which yields a final polymer concentration of between 1 and 1.5% w/w. The resultant high temperature/high shear rate (HTHS) viscosity at 150 °C is then about 3 mPa.s.

HTHS viscosities, in Table 3, were determined using a Ravenfield concentric cylinder viscometer at temperatures of 100 and 150 °C and a shear rate of  $10^6 \text{ s}^{-1}$ . 100 °C viscosities, in Table 3, show that the base oil and DI solution remain Newtonian at high shear rate while the polymer solutions experience shear thinning.

### 4.2. Base oil and DI solution

Film thicknesses given by the base oil and DI solution are shown in Figure 4. A wider range of speed can be seen to be

Table 2  
Polymer concentrates

| Abbreviation | Polymer type                            | $M_n$   | $M_w$   | $M_w / M_n$ |
|--------------|---|---------|---------|-------------|
| PMA          | Polymethacrylate                        | 64,000  | 204,000 | 3.2         |
| SBCP         | Styrene-butadiene copolymer             | 113,100 | 143,400 | 1.3         |
| OCP          | Olefin copolymer                        | 46,000  | 145,000 | 3.2         |
| DOCP         | Dispersant olefin copolymer             | 50,300  | 127,500 | 2.5         |
| DAOCP        | Dispersant antioxidant olefin copolymer | 81,000  | 162,000 | 2.0         |

Table 3  
Base oil and solution properties

| Sample                      | Low shear viscosity / mPa·s |       |        | HTHS viscosity / mPa·s |        |
|-----------------------------|-----------------------------|-------|--------|------------------------|--------|
|                             | 30 °C                       | 65 °C | 100 °C | 100 °C                 | 150 °C |
| Base oil                    | 22.41                       | 6.95  | 3.21   | 3.20                   | 1.51   |
| Base oil + 5% w/w PMA       | 32.80                       | 10.73 | 5.09   | 4.40                   | 2.16   |
| Base oil + 10% w/w OCP      | 49.82                       | 14.15 | 6.22   | 4.95                   | 2.36   |
| Base oil + 10% w/w DOCP     | 53.27                       | 14.90 | 6.40   | 5.10                   | 2.47   |
| DI solution                 | 37.43                       | 10.71 | 4.68   | 4.69                   | 2.08   |
| DI solution + 5% w/w PMA    | 57.61                       | 16.94 | 7.51   | 6.00                   | 2.89   |
| DI solution + 12.5% w/w SB  | 56.30                       | 16.41 | 6.95   | 6.20                   | 2.92   |
| DI solution + 10% w/w OCP   | 74.64                       | 20.11 | 8.37   | 6.58                   | 3.09   |
| DI solution + 10% w/w DOCP  | 88.80                       | 23.00 | 9.24   | 6.90                   | 3.33   |
| DI solution + 10% w/w DAOCP | 91.15                       | 23.15 | 9.62   | 7.15                   | 3.29   |

covered for the DI solution than for the base oil. The necessity for this arose from the frailty of the silica spacer layer on the surface of the disc. While, for the base oil, damage to the disc surface began to occur when film thickness was taken below 10 nm, lower values were accessible for the DI solution. As in previous studies [2], it was inferred that the presence of the DI system enhanced the protection afforded to the silica spacer layer.

The increase in film thickness which results when the DI system is added to the base oil is due to a rise in viscosity. Comparison between observed and predicted effects of viscosity on film thickness may be

expressed in terms of the parameter  $\phi$ :

$$\phi = \frac{\text{determined film thickness ratio}}{\text{predicted film thickness ratio}} \quad (6)$$

Basing determined film thickness ratios on the regression parameter  $A$  (which is equivalent to the trend value of film thickness at the rolling speed of 1 m/s) and predicted ratios on the Hamrock and Dowson expression, equation (2), the values of  $\phi$  given in Table 4 are obtained for the three temperatures of Figure 4. In each case  $\phi$  lies close to 1, confirming that the change in viscosity accounts quite accurately for the observed variation in film thickness. The fact

Table 4  
Regression data for base oil and DI solution

| Sample      | $\theta / ^\circ\text{C}$ | $A / \text{nm}$ | $b$   | $\phi$ |
|-------------|---------------------------|-----------------|-------|--------|
| Base oil    | 30                        | 154.1           | 0.685 | -      |
|             | 65                        | 57.6            | 0.678 | -      |
|             | 100                       | 30.0            | 0.678 | -      |
| DI solution | 30                        | 210.9           | 0.684 | 0.97   |
|             | 65                        | 74.7            | 0.688 | 0.97   |
|             | 100                       | 37.8            | 0.678 | 0.98   |

that  $\phi$  is not exactly equal to one is due to the change in pressure-viscosity coefficient which results when a DI system is added to base oil [6]. The reduction implied by a  $\phi$  value of 0.97 is about 6%.

It will be noted, from Table 4, that the speed exponent,  $b$ , again lies close to the Hamrock and Dowson value of 0.67. With both base oil and DI solution showing such good agreement with EHD theory, there are no grounds for suspecting boundary film

formation of contributing to the improved durability of the silica coating.

Experiments carried out at a later date with a disc from a more robust batch of specimens allowed rolling speeds to be taken to substantially lower values. Over this wider range of speed, Figure 5 demonstrate that the base oil continued to obey EHD theory down to a film thickness of only 1.5 nm. The DI solution, however, underwent a change in behaviour at 5 nm film thickness to that of a more viscous medium. The implied increase in viscosity is by a factor of about two. A reversible physical phenomenon peculiar to very thin oil films is thus detected which is likely to be connected with the improved durability of the silica spacer layer.

#### 4.3. Friction studies

Studies of boundary friction were carried out to provide insights into the relative strengths of the surface activities of the various additive components. Base oil solutions of PMA, OCP and DOCP VI improves all yield lower friction coefficients

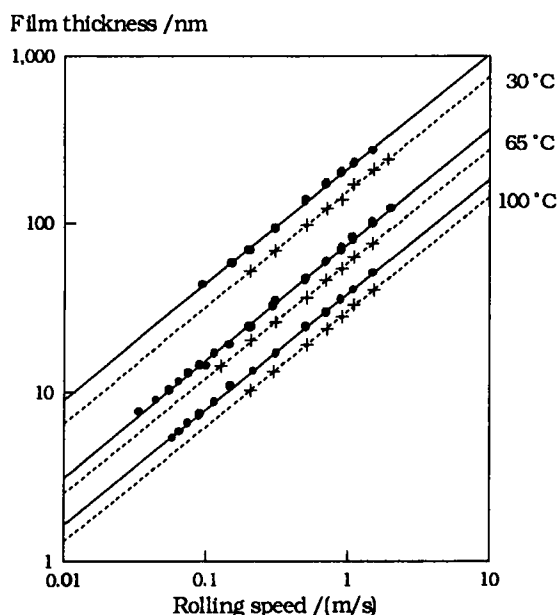


Figure 4. Film thickness behaviour of base oil (+) and DI solution (•).

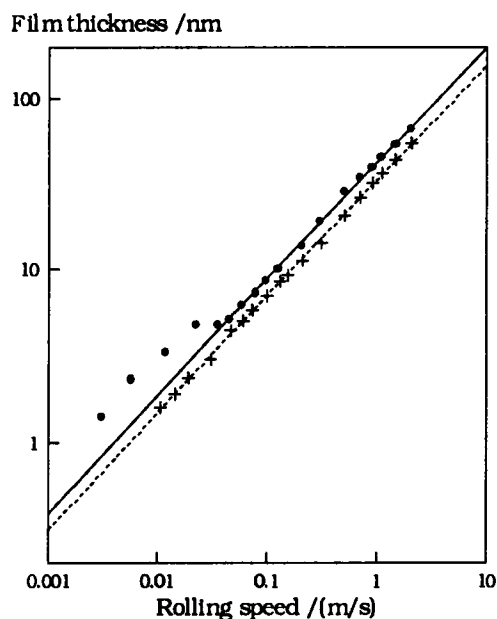


Figure 5. Film thickness behaviour of base oil (+) and DI solution (•) at 100 °C

than base oil alone, in Table 5, reflecting a measure of surface activity on the part of each polymer. Viscometric influences, it is emphasised, do not have significant influence on friction in these experiments.

Although the strongly adsorbing DI system does not obviously differ in frictional behaviour from the base oil, in Table 5, the similarity in friction coefficients is coincidental; observations of contact resistance during these measurements did reflect the greater activity of the DI system. A more tangible influence of the DI system is the inhibiting effect it has on the activity of VI improvers. Only the dispersant and antioxidant olefin copolymer, DAOCP, continues to exert a significant effect on friction in the presence of the DI system. This material is known to be a relatively powerful friction modifier capable of imparting significant fuel economy benefits in the ASTM Sequence VI fuel efficiency test [11].

Table 5  
Boundary friction coefficients,  $\mu$ , at 100°C

| Sample                      | $\mu$ |
|-----------------------------|-------|
| Base oil                    | 0.140 |
| Base oil + 5% w/w PMA       | 0.094 |
| Base oil + 10% w/w OCP      | 0.110 |
| Base oil + 10% w/w DOCP     | 0.092 |
| DI solution                 | 0.142 |
| DI solution + 5% w/w PMA    | 0.144 |
| DI solution + 10% w/w SB    | 0.141 |
| DI solution + 10% w/w OCP   | 0.145 |
| DI solution + 10% w/w DOCP  | 0.140 |
| DI solution + 10% w/w DAOCP | 0.116 |

#### 4.4. Film thickness for VI improved base oil

The surface activity of dispersant types of VI improver has been established through both EHD film thickness experiments [5] and force balance studies [12]. Of the materials examined here, the PMA VI improver, in Figure 6, can be seen to supplement the

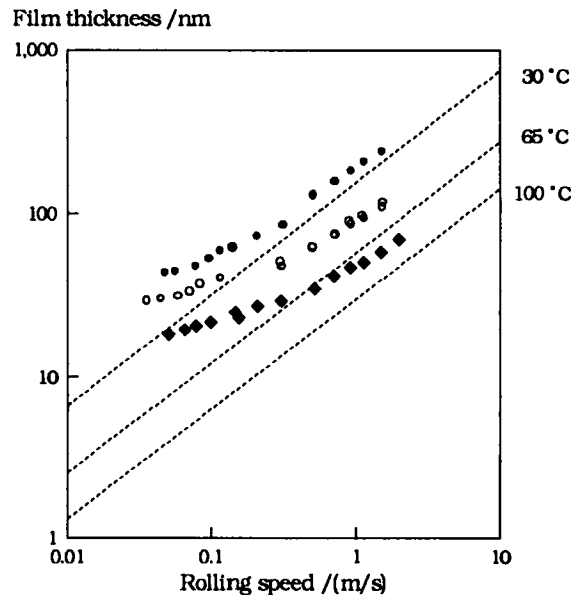


Figure 6. The influence of PMA VI improver on film thickness (symbols); dashed lines indicate the trends for untreated base oil.

hydrodynamically generated film with a boundary film ten to twenty nanometers thick. However, neither the non-dispersant nor the dispersant types of OCP polymer show a comparable effect. Indeed, both types of polymer result, in Figures 7 and 8, in a severe thinning of the oil film as film thickness falls below 10 nm.

#### 4.5. Film thickness for VI improved DI solutions

For the PMA polymer, inhibition of its surface activity by the DI system can again be inferred from the film-forming characteristics shown in Figure 9. At the two lower temperatures the thickness of the boundary film is clearly less than that suggested by Figure 7 while, at the highest, it completely disappears.

At the highest temperature, a film thinning phenomenon can again be identified in the regime below 10 nm. Film thickness then falls approximately to the level expected of base oil alone. This type of behaviour

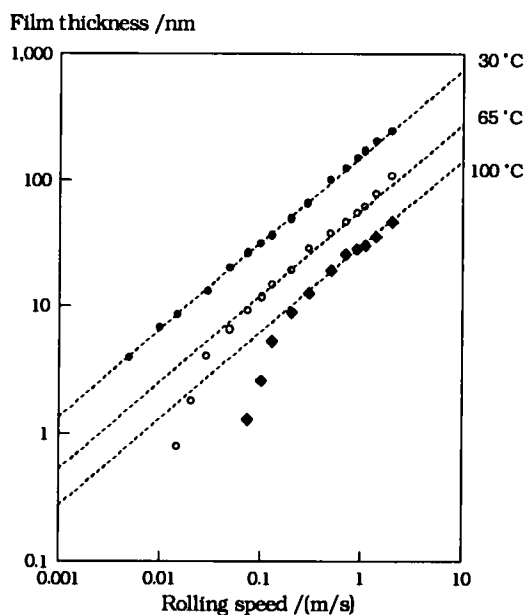


Figure 7. The influence of OCP VI improver on film thickness (symbols); dashed lines indicate the trends for untreated base oil.

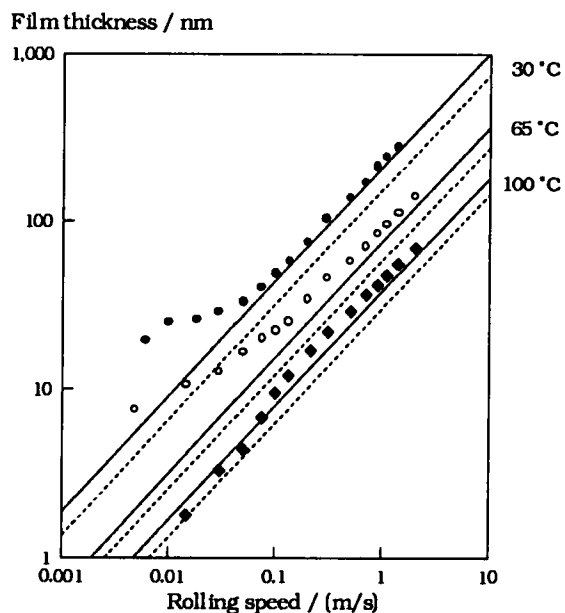


Figure 9. Film thickness behaviour for base oil (----), DI solution (—) and DI solution + PMA VI improver (symbols).

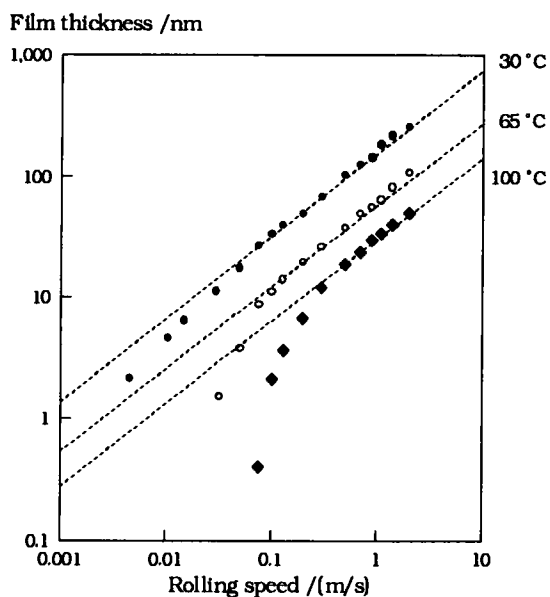


Figure 8. The influence of DOCP VI improver on film thickness (symbols); dashed lines indicate the trends for untreated base oil.

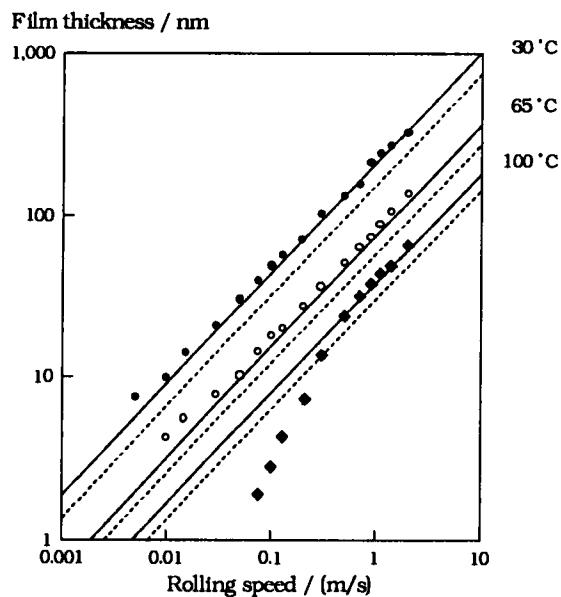


Figure 10. Film thickness behaviour for base oil (----), DI solution (—) and DI solution + OCP VI improver (symbols).

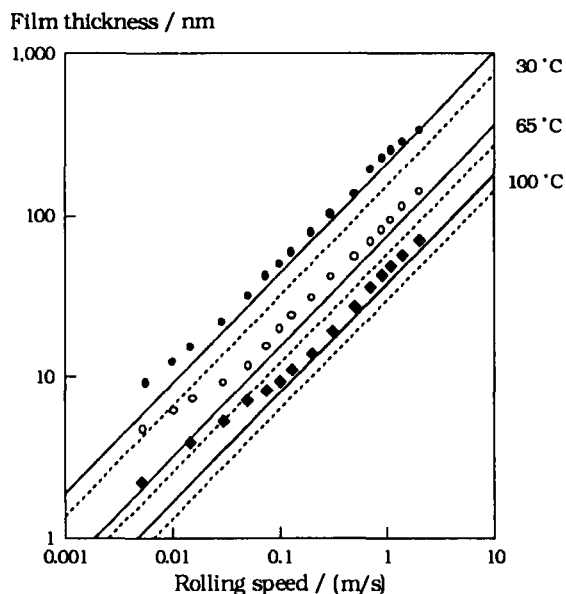


Figure 11 Film thickness behaviour for base oil (----), DI solution (—) and DI solution + DAOCP VI improver (symbols).

was not found to be highly repeatable, however, and eludes any generalised characterisation.

As for the base oil solution, the DI solution containing OCP polymer exhibits, in Figure 10, a more severe form of film thinning behaviour at the highest temperature. Below 10 nm, film thickness falls far below the level that can be sustained by the base oil alone. Again, it is noted that this type of behaviour was not highly repeatable.

DAOCP polymer, which, uniquely, retained a capacity for friction modification when the DI system was present, gives further evidence of boundary film formation in Figure 11. The effect persists at all temperatures, with no indications of film thinning.

## 5. DISCUSSION

Of the three potential anomalies in film

thickness behaviour explored in this paper, two have been confirmed. Lubricants containing a performance additive package undergo a step change in viscosity below about 5 nm film thickness, boosting film thickness and enhancing surface protection. Oils containing a polymeric VI improver may experience either an enhancement or a severe depletion in film thickness at low entraining velocities, depending on the chemical structure of the VI improver, the presence of other additive components and on temperature. An aspect of behaviour which does not appear to qualify as an anomaly is the pressure-viscosity response of lubricant base stocks. The low values of pressure-viscosity coefficient derived from EHD experiments are tentatively ascribed to a modest systematic error in the experimental method.

The increase in viscosity for the DI solution below 5 nm film thickness is a possible manifestation of the micropolarity phenomenon postulated for fluids containing polar molecular species [13]. It has been suggested that the viscosity of such fluids increases when film thickness approaches the dimensions of the polar entity as a result of restrictions on their freedom to rotate. The DI system investigated here contains three important species of polar molecule, a zinc dialkyldithiophosphate anti-wear additive, a phenate detergent and a succinimide dispersant. Approximate molecular diameters for the three are 1, 2 and 3 nm, respectively. Although it has not yet been established which species is responsible for the viscosity enhancement below 5 nm, the dispersant has the greatest influence on bulk viscosity and lies closest to the critical film thickness in molecular dimensions.

A possible explanation for the film thinning influence of VI improvers in Figures 7 to 10 is one that has been proposed in connection with a wear promoting effect in valve train wear tests [14]. It has been suggested that VI improver molecules accumulate in the EHD inlet zone and create a barrier to the base oil solvent. A form of

lubricant starvation then results. Hard sphere diameters for the polymer molecules considered here are typically in the range 5 to 8 nm, while the film thinning phenomenon first becomes apparent at a film thickness of between 10 nm and 20 nm. It is possible that a layer of polymer molecules, weakly bound to each of the two rolling surfaces, becomes detached under the high shear conditions of the inlet region to form a barrier approximately two molecular diameters in width. As film thicknesses diminishes, the barrier will move progressively away from the Hertzian pressure zone, accentuating the degree of starvation as it does so.

### ACKNOWLEDGEMENTS

Permission to publish this paper has been given by the British Petroleum Company plc.

### REFERENCES

1. Johnson, G. J., Wayte, R. and Spikes, H. A., "The measurement and study of very thin lubricant films in concentrated contacts", *Tribology Trans.*, 1991, 34, 187-194.
2. Cooper, D. and Moore, A.J., "Applications of the ultra-thin elastohydrodynamic oil film thickness technique to the study of automotive engine oils", *Wear*, 1994, 175, 93-105.
3. Moore, A. J., "Nanometer elastohydrodynamic lubrication", *Elastohydrodynamics - Fundamentals and Applications in Lubrication and Traction*, 23rd Leeds-Lyon Symposium on Tribology, Leeds, 1996.
4. Guangteng, G. and Spikes, H. A., "Behaviour of lubricants in the mixed elastohydrodynamic regime", *Lubricants and Lubrication*, Proceedings of the 21st Leeds-Lyon Symposium on Tribology, Elsevier, 1995.
5. Smeeth, M., Gunsel, S. and Spikes, H. A., "Boundary film formation by viscosity index improvers", to be published in *Tribology. Trans.*, preprint number 95-3B-TC-1.
6. Moore, A. J., Cooper, D. and Robinson, T. M., "Rheological properties of engine crankcase and gear oil components in elastohydrodynamic oil films", *SAE Trans.*, 1994, 103, Section 4, 1352-1364.
7. Moore, A. J., "Influences of lubricant properties on ASTM Sequence VI and Sequence VI-A fuel efficiency performance", *SAE 961138*, 1996.
8. A.S.M.E. Pressure-Viscosity Report, "Viscosity and density of over 40 lubricating fluids of known composition at pressures to 150,000 psi and temperatures to 425 °F", A.S.M.E., 1953, New York
9. Guangteng, G. and Spikes, H. A., "Boundary film formation by lubricant base fluids", to be published in *Trib. Trans.*, STLE Presentation No. 95-NP-7D-3.
10. Hamrock, B. J. and Dowson, D., "Isothermal elastohydrodynamic lubrication of point contacts", *Trans. A.S.M.E.*, A99, 264-276, 1977.
11. Stipanovic, A. J. & Schoonmaker, J. P., "The impact of organomolybdenum compounds on the frictional characteristics of crankcase engine oils", *SAE Trans.*, 102, Section 4, 1619-1630, 1993.
12. Georges, E., Georges, J.-M. and Diraison, C., "Steric repulsion of polymethacrylate layers", *SAE 961218*, 1996.
13. Prakash, J and Christensen, H., "A microcontinuum theory for the elastohydrodynamic inlet zone", *Trans. ASME, J. Lub. Tech.*, 99, 24-29, 1977.
14. Yoshida, K. and Sakurai, T., "Limitations of thin films in EHD contacts with dispersed phase systems as lubricants", *Wear*, 175, 71-79, 1994.



## An Experimental Study of Film Thickness in the Mixed Lubrication Regime

G. Guangteng and H. A. Spikes

Tribology Section, Imperial College, London SW7 2BX

This paper describes an experimental study of the influence of surface roughness on elastohydrodynamic film thickness in a steel ball on glass flat contact under nominally pure rolling conditions. Steel balls with a range of isotropic roughnesses have been employed and measurements have focused on the mixed lubrication regime where the film thickness is comparable to or below the composite surface roughness. It has been found that full film lubrication is only realised when the nominal lambda ratio ( $\lambda$ ) has a value of 2 or higher. Below this value, the film thickness decreases, first gradually and then rapidly, as the nominal smooth surface lambda ratio decreases. The mixed regime, where both roughness and entrainment velocity influence film separation, appears to span a large range in terms of the lambda ratio, from  $\lambda = 2$  to  $\lambda = 0.1$ .

The mean separation between rough surfaces in static contacts has been measured over a range of loads and the problem of the precise definition of lubricant film thickness in rough surface conditions is discussed.

### 1. BACKGROUND

Many machine components, such as gears, rolling element bearings, cams and tappets, etc. operate in the mixed lubrication regime where the lubricant film thickness is comparable to or below the composite roughness of the rubbing surfaces. In such situations, the ratio of film thickness to composite surface roughness, known as the "specific film thickness" or "lambda ratio", plays an important role in determining the actual lubrication state and the lifetime of those components.

A recent review of mixed lubrication was given in (1). A great deal of theoretical modelling has been carried out on mixed lubrication (2-7) and this has gradually increased in realism and relevance over the past two decades. Early work tended to examine only the influence of surface topography on fluid film behaviour but more recently the two coupled influences, of roughness on fluid flow and of fluid pressure on topography in contacts have been modelled together. Initial work also tended to consider only stationary roughness and Newtonian, isothermal fluid behaviour but models with moving roughness, and thermal, non-Newtonian fluid response have now been at least partially solved. However computing limitations still make it impossible to properly model systems

with realistic two-dimensionally rough moving surfaces and most work is still confined to cases in which the lambda ratio is relatively large, so as to avoid the problem of what happens at asperity contacts when any lubricant film thins to the point at which it can no longer be treated using continuum fluid models.

Limited experimental work has been carried out on mixed lubrication and the most widely used technique has been optical interferometry (8-14). The relatively poor film thickness resolution of this method means that studies have been mainly carried out to observe film behaviour resulting from artificially created features (bumps, dents, coated particles, etc.) rather than to make quantitative measurements of film thickness. The main findings fall into two main categories (i) how individual dents or bumps influence film thickness and how their shape is changed in contacts (ii) how roughness influences overall mean film thickness as compared to the smooth case. Some of the general conclusions reached from previous experimental work on the influence of roughness upon overall film thickness are summarised below.

- (a) For longitudinal roughness, i.e. 1-D roughness features parallel to the entrainment direction,

there is a reduction in mean film thickness compared to the smooth surface case.

- (b) For transverse roughness, where 1-D roughness features lie at right angles to the entrainment direction, some results have shown no measurable change (8) but some have shown a reduction in film thickness with roughness (13). There is also evidence of a roughness wavelength dependence effect, i.e. an increase in film thickness at long wavelengths and a reduction at short wavelengths (11).
- (c) Some researchers have reported that roughness generally reduces film thickness in sliding and rolling conditions (14).

It is clear that there is no general consensus about the effects of surface roughness upon film thickness. This is due partly to the fact that roughness itself is difficult to characterise and seemingly similar roughness values may have different characteristics, such as mean asperity slope, which influence the results. While previous experiments have certainly advanced our understanding of the influence of local surface features on local film separation, they have not provided reliable information about the effect of general randomly distributed roughness on overall film thickness. It should also be noted that although the lambda ratio is defined in terms of the out-of-contact roughness, the actual roughness within an EHD contact may change significantly at high pressures and when thin lubricant films are present due to elastic flattening..

The aim of the current study was to investigate directly the influence of isotropic surface roughness on EHD film thickness. The study was based upon the use of ultra thin film interferometry which is able to measure film separation with high precision in rolling, lubricated contacts (15).

## 2. TEST METHOD AND MATERIALS

The experimental technique employed to measure film thickness in this study was ultrathin film interferometry. This is able to measure films accurately down to 2 nm, which makes it possible to

explore the effects of realistic surface roughness upon EHD film thickness at low lambda ratios. The ball-on-plate test rig used for the EHD film thickness measurements is shown in Figure 1.

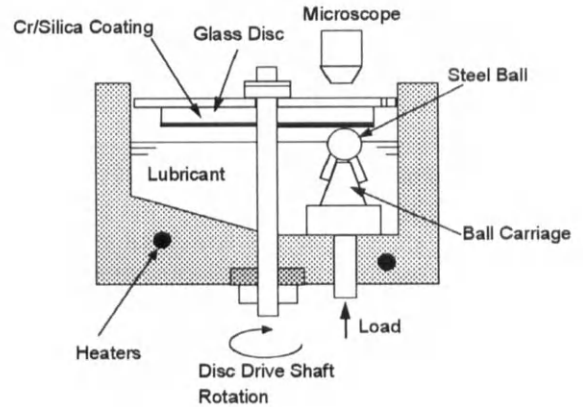


Figure 1. Schematic diagram of test rig

A steel ball (AISI 52100, 19.05 mm diameter) is loaded against the underside of a glass disc. The glass disc is driven by a motor via a series of speed-reduction gears to provide reliable speed holding down to 0.0002 m/s. The glass disc drives the steel ball in nominal pure rolling. The test lubricant is enclosed in a chamber and an insulated lid with a lubricant application hole sits on top of the glass disc. This helps to maintain constant test temperature and limits exposure of the lubricant to the outside environment. Temperature in the test chamber is maintained using a thermocouple in conjunction with feedback-controlled heater rods inserted in the chamber wall. Actual test temperature is measured near the contact inlet using a digital thermometer. All tests were carried out at a controlled temperature of  $25 \pm 0.5^\circ\text{C}$  and a constant load of 20 N, which produced a maximum Hertz pressure of 0.48 GPa in the contact. The test conditions are summarised in Table 1.

Table 1. Film thickness measurement test conditions

|                     |                                    |
|---------------------|------------------------------------|
| Max. Hertz pressure | 0.48 GPa                           |
| Bulk temperature    | $25^\circ\text{C}$                 |
| Rolling speed       | $0.001\text{-}2.0 \text{ ms}^{-1}$ |

Film thicknesses were measured at various rolling speeds, ranging from 0.001 m/s to about 2.0 m/s. For each test, the relevant rig parts were first thoroughly cleaned using analytical grade toluene and acetone. The rig was then assembled and the load applied. Test fluid was supplied through the application hole to the chamber and test temperature adjusted to 25°C. At the start of each test, before lubricant was supplied to the surfaces, the spacer layer thickness was measured in the static, loaded contact at a fixed position on the disc. Thereafter, film thickness measurements were triggered to be taken from this same position so that the lubricant film thickness could be determined from the difference between the measured separation and the spacer layer thickness. Film thickness measurements were the average over the central region of the contact.

Two base fluids were used in this study for the EHD film thickness measurements as listed in Table 2. Viscosities were measured using a cone-on-plate viscometer at varying temperatures and also using capillary viscometers at room temperature. Measured viscosities are listed in Table 2.

Table 2. EHD test fluids

| Fluid                      | Description           | Viscosity (PaS), 25°C |
|----------------------------|-----------------------|-----------------------|
| Di-(2-ethylhexyl Phthalate | Phthalate ester       | 0.0551                |
| SHF41                      | Synthetic hydrocarbon | 0.0238                |

Steel balls of three different roughness categories were chosen for the film thickness measurements, designated as 'Smooth', 'Rough1' and 'Rough2' respectively. The surface roughnesses of the balls and the glass plate were measured using a Talysurf 4 and the root-mean-

square (rms) roughness and mean asperity slope of the test balls are summarised in Table 3. The 'Smooth' balls had a roughness of 0.010  $\mu\text{m}$  (rms) and were commercial high precision ball bearings similar to those used in previous studies (16). The glass plate was optically smooth (0.004  $\mu\text{m}$ , rms). The composite roughnesses of the undeformed surfaces are also included in Table 3.

### 3. RESULTS

#### 3.1 Film thickness measurements

Figure 2 shows film thickness results for SHF41 in the conventional  $\log(\text{film thickness})$  versus  $\log(\text{speed})$  form. The film thickness of Rough1 is generally higher and persists to lower rolling speed than that of Rough2. It is noted that there are larger and larger variations in the film thicknesses as rolling speed reduces, perhaps showing the stochastic effect of the influence of asperities upon film thickness and vice versa

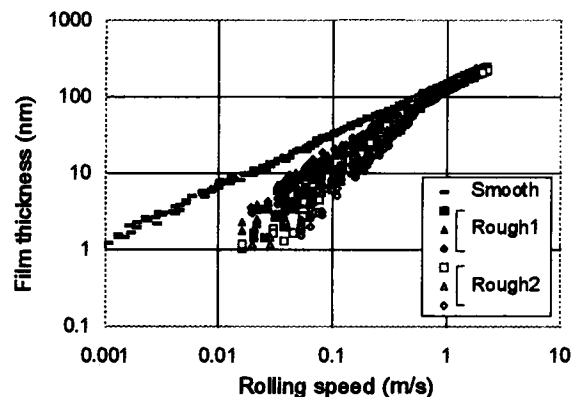


Figure 2. Influence of surface roughness on film thickness

Table 3. Test steel balls for film thickness measurements

| Ball Designation | Roughness (rms, $\mu\text{m}$ ) | Composite Roughness ( $\mu\text{m}$ ) | Mean Slope |
|------------------|---------------------------------|---------------------------------------|------------|
| Smooth           | 0.010                           | 0.011                                 | 0.8°       |
| Rough1           | 0.060                           | 0.060                                 | 2.2°       |
| Rough2           | 0.095                           | 0.095                                 | 3.4°       |

The film thickness results shown in figure 2 are also plotted in Figure 3 in terms of nominal lambda ratio. The abscissa is the ratio of film thickness measured with smooth surfaces to the composite surface roughness for Rough1 and Rough2 cases respectively. The ordinate is the ratio of film thickness measured with Rough1 and Rough2 balls to their corresponding composite roughnesses. The broken straight line represents a reference line for the case of smooth surfaces, necessarily diagonal with a slope of 1.

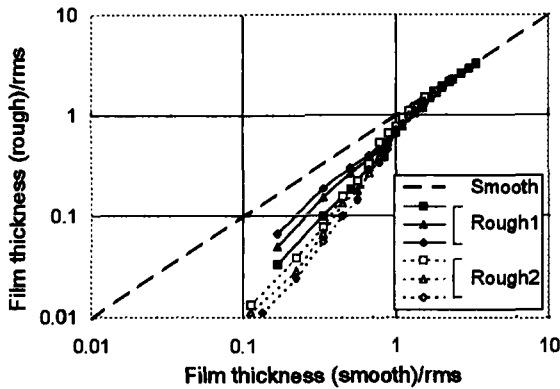


Figure 3. Measured versus smooth surface film thickness

The results show that full film lubrication is only realised when the nominal lambda ratio reaches 2 ( $\lambda = 2$ ). When the lambda ratio is below 2, the film thickness falls below the smooth case, operating in the mixed lubrication regime. As the lambda ratio further reduces ( $\lambda < 1$ ), the film thickness decreases more rapidly. At this stage, occasional asperity contacts are expected to occur but the film thickness results show that this may happen only with very thin films. The mixed regime seems to persist down to a very low lambda ratio, but there is no abrupt transition to indicate the lower end of the mixed regime or the borderline between the mixed and boundary lubrication regimes.

Figure 4 shows film thickness results for the phthalate ester in log(film thickness) versus log(speed) form. The general trend of film thickness reduction versus rolling speed is similar to that for SHF41, except that thicker films are generated and a measurable film persists to a lower speed than with

SHF41. This is to be expected since the phthalate ester has a higher viscosity than SHF41.

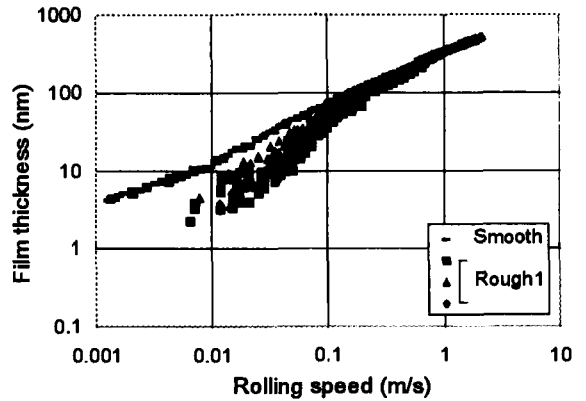


Figure 4. Influence of roughness on film thickness with phthalate ester

Figure 5 shows film thickness results in terms of nominal lambda ratio for the phthalate ester. The rate of decrease of film thickness for Rough1 balls with the phthalate ester is seen to be slightly smaller than that for Rough1 balls with SHF41. The reason is not yet clear but it may be due to the fact that the phthalate ester produces a boundary film, relatively more significant at low speeds, whilst SHF41 does not. This was found to be the case in a previous study using smooth surfaces (16) and can also be seen in Figure 4.

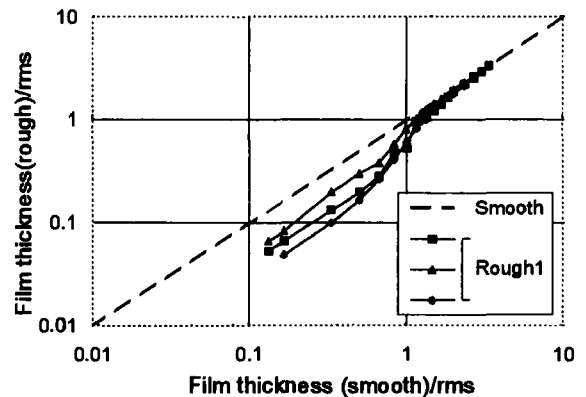


Figure 5. Measured versus smooth surface film thickness with phthalate ester

In the case of the phthalate ester, the roughness of Rough1 balls may be small enough or reduced in the EHD contact to such an extent that the boundary film effect is powerful enough to defer the film thickness reduction due to roughness.

### 3.2 True Mean Separation

It is important to understand what the above measured film thicknesses represent. To do this requires an appreciation of the separation in the static, loaded contact.

To begin with the smooth surface case, Figure 6(a) shows a schematic of two smooth surfaces in contact. Under static loading and without a lubricant, the coated spacer layer thickness is measured, which is subsequently subtracted from the total separation measured in rolling conditions and with a lubricant to give the difference as the lubricant film thickness.

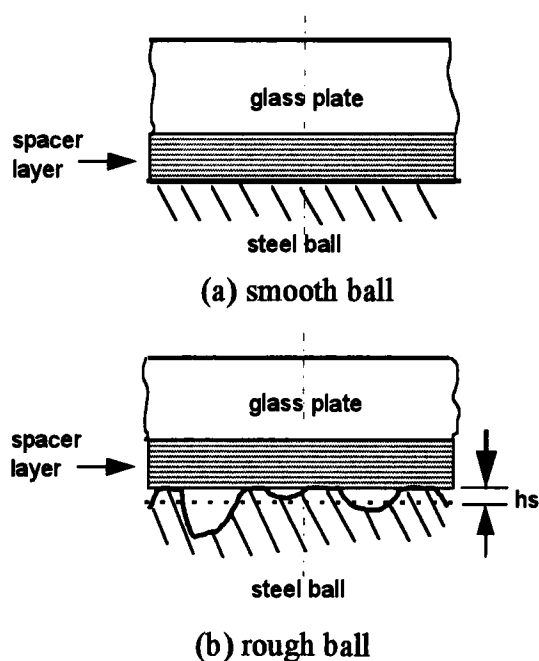


Figure 6. Mean separation in a static contact

For the contact of rough surfaces however, as shown in Figure 6(b), there are always pockets of air in the static contact due to the fact that asperities cannot flatten or conform sufficiently to fully close the gap between the two surfaces. This means that

even in the static contact there is a significant separation between the mean centrelines of the two solid surfaces. In the above film thickness measurements, this static separation was added to the spacer layer thickness and the total subtracted from subsequent rolling measurements. Thus for rough surface measurements the film thicknesses given in figures 2 to 5 represent the difference between the mean separation of the solid surfaces in the rolling case and the mean separation in the static case.

It is possible to measure the mean separation within the static contact, both by gradually increasing the load and observing the change in separation and also by introducing fluid of a different refractive index to air between the stationary surfaces and noting the consequent change in optical separation. Figure 7 shows how mean gap between a rough ball (Rough1) and the glass plate varies with static load. At the load used in film thickness measurements the gap is close to 10 nm. In the smooth surface case, a similar gap may exist but was measured and found to be less than 1 nm.

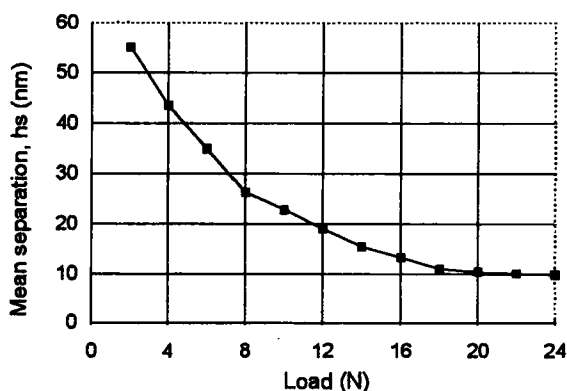


Figure 7. Dependence of mean separation on applied load in static contact

Using the mean separation in the static contact shown in Figure 7 it is possible to replot the measured film thickness results in terms of total mean surface separation versus rolling speed. Here the total mean surface separation is taken to be the measured film thickness plus the measured static gap. It represents the mean distance between the centrelines of the two solid surfaces at any given speed. Figure 8 shows the result for the smooth ball and the two different

roughness balls using SHF41. It can be seen that this measure of film thickness actually tracks the smooth surface case quite closely down to about 12 nm, although at very slow speeds it will, of course, asymptote to 10 nm.

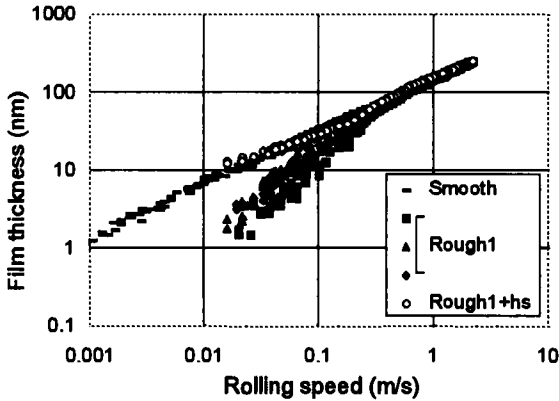


Figure 8. Influence of rolling speed on total mean separation for rough and smooth surfaces

4. DISCUSSION

It is generally believed that when the lambda ratio is large, the surface roughness has no influence on film thickness, friction or load support. As the lambda ratio becomes smaller ( $\lambda > 3$ ), occasional contacts may occur between the solid surfaces, but the asperities will still carry a negligible fraction of the load. When the lambda ratio becomes very small ( $\lambda < 0.5$ ), the load support is shared between the deforming asperities and the fluid film, and the surface roughness has significant influence upon the film generation, due to its influence on fluid flow pattern and load support. When the lambda ratio further reduces, the boundary regime is reached where the load is entirely supported by asperity contact and there is little fluid film pressure build up within the contact.

This is in general agreement with the experimental results from the current study which show that when  $\lambda > 2$  the film thicknesses generated with the rough surfaces approach those of the smooth surface case, indicating negligible influence of roughness on film formation. It is evident from

Figures 3 and 5 that, when the lambda ratio is in the range of  $\lambda = 2$  and  $\lambda = 0.1$  the film thickness is progressively but significantly reduced compared to the smooth case. In this region, surface roughness has a significant effect upon fluid flow behaviour and the surface roughness itself may be progressively flattened to some extent. The results shown in Figures 2 and 4 indicate that this happens when the lambda ratio is below 0.1 where there is no measurable fluid film.

Only one previous study, by Kaneta and Cameron has attempted to measure overall film thickness in a rough point contact (10). These authors used a steel ball artificially roughened by sputtering on the surface a grid of regularly spaced asperities, of height 254 nm. In their paper the authors give values for mean film thickness and also tip and valley film thicknesses. The latter are respectively between the asperity tips and the counterface and between the base of the asperities and the counterface. The results from this study are compared with those from the current work on a non-dimensional plot in Figure 9.

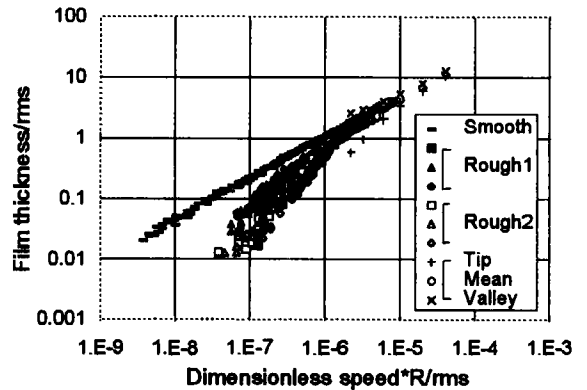


Figure 9. Comparison of current results with those of Kaneta and Cameron (10)

There is good agreement with the mean film thicknesses measured by Kaneta and those found in the present work, although it should be noted that Kaneta's measurements were made in the high lambda ratio region where roughness actually seems to have little effect on the film thickness. As expected, the tip and valley film thicknesses are smaller and larger than the mean respectively.

It is seen that the above discussed experimental results are well in line with general findings of various researchers but certain differences and new details emerge from this study. Although these experiments are by no means exhaustive they tend to indicate that (i) full film lubrication can be realised when  $\lambda > 2$ ; (ii) mixed regime spans a large lambda ratio range  $0.1 < \lambda < 2$ ; (iii) the border between mixed and boundary regimes is not clear but it seems at a rather low lambda ratio.

One problem which needs to be carefully addressed in describing film thickness in mixed lubrication is what to use as a baseline value. The static measurements of this study show that a considerable separation may exist between rough surfaces even when the latter are stationary and asperities are bearing all the load. In one sense, the film thickness generated must be regarded as the extent to which separation rises from this value when rolling and thus entrainment occurs and this has been the definition favoured in the current study. However it must be recognised that the actual mean gap between the two surfaces in rolling contact is probably always larger than this.

The static results provide some preliminary indications as to the likely value of the real surface roughness; or rather the extent to which separation varies, the "separation roughness" in an EHD contact. This is believed to be an important practical feature in determining, for example, fatigue life of rolling element bearings, but it is quite difficult to actually measure in thin film EHD contacts. It is acknowledged that the roughness in an EHD contact will be a good deal less than the out-of-contact composite roughness of the surfaces both because of overall elastic deformation and also the conformity of the two rubbing surfaces under high pressures.

It is known that the hydrodynamic pressure in an EHD contact is similar to that in static contact, with modifications such as extended pressure build up in the inlet region and possible pressure ripples. Because of this, the actual asperity deformation and hence the topography change will not be quite the same in a moving as a static contact but nonetheless Figure 7 does give an indication of the extent to which asperities can be flattened in an EHD contact.

The composite surface roughness in the static contact is found to be about five times less than that

in undeformed conditions. This is not unrealistic compared to the results from 2D contact analysis (17).

The experiments carried out in this study concentrated on measuring the mean film thickness in the central region of the contact and it should be pointed out that the central film thickness was used to calculate the nominal lambda ratios instead of the minimum film thickness. The ultrathin film method can also be used to give a film profile across the whole contact, which usually includes the minimum film thickness at the side restrictions (18). This can be used not just to show the minimum film thickness but also to investigate changes of surface structures across the contact. A recently developed technique (19) can also produce 2D maps of film thickness for very thin films in EHD contacts, which makes it possible to look directly at surface roughness itself in EHD/mixed contacts and enables film thickness profiles to be determined precisely. These features will be implemented in the future studies.

## 6. CONCLUSIONS

The following conclusions may be drawn from this study.

- (a). The ultra thin film interferometry technique can now be used to measure film thicknesses of rough surfaces in EHD contacts particularly at low nominal lambda ratios.
- (b). Full film lubrication is only realised when  $\lambda > 2$ ; the mixed lubrication regime spans a large lambda ratio range  $0.1 < \lambda < 2$  and there is no clear-cut for the border between mixed and boundary lubrication regimes.
- (c). It is now possible to explore the effective composite roughness in static contacts, serving as an indicator of the real roughness in EHD contacts.

## ACKNOWLEDGEMENT

The authors gratefully acknowledge the support of the EPSRC which enabled this study to be carried out.

## REFERENCES

1. H. A. Spikes, "Mixed lubrication- An overview.", presented at symposium "Tribology-Solving friction and wear problems", Esslingen, Jan. 1996, accepted for publication in *Lubrication Science*.
2. T. E. Tallian, "The theory of partial elastohydrodynamic contact." *Wear* 21, (1972), pp. 49-101.
3. N. Patir and H. S. Cheng, "Application of average flow models to lubrication between rough sliding surfaces." *ASME Trans, J. Lub. Tech.* 101, (1979), pp. 220-230.
4. C. C. Kweh, H. P. Evans and R. W. Snidle, "Micro-elastohydrodynamic lubrication of an elliptical contact with transverse and three-dimensional sinusoidal roughness." *ASME Trans, J. Tribology*, 111, (1989), pp. 577-584.
5. C. H. Venner and A. A. Lubrecht, "Transient analysis of surface features in an EHL line contact in the case of sliding and three-dimensional sinusoidal roughness." *ASME Trans, J. Tribology* 116, (1994), pp. 186-193.
6. L. Chang, A. Jackson and M. N. Webster, "Effects of 3-D surface topography on the EHL film thickness and film breakdown.", *Trib. Trans* 37, (1994), pp. 435-444.
7. L. Chang, "A deterministic model for line contact partial elastohydrodynamic lubrication" *Trib. Intern.* 28, (1995), pp. 75-84.
8. A. Jackson and A. Cameron, "An interferometric study of the EHL of rough surfaces", *ASLE Trans.* 19, (1976), pp. 50-60.
9. C. Cusano and L. D. Wedeven, "Elastohydrodynamic film thickness measurements of artificially produced non smooth surfaces", *ASLE Trans.* 24, (1980), p. 1014.
10. M. Kaneta and A. Cameron, "Effects of asperities in elastohydrodynamic lubrication." *ASME Trans. J. Lub. Techn.* 102, (1980), pp. 374-379.
11. G. M. S. de Silva, J. A. Leather and R. S. Sayles, "The influence of surface topography on lubricant film thickness in an elastohydrodynamic (EHD) point contact.", *Proc. 12th Leeds-Lyon Symp. Mechanisms and surface distress*, Sept. 1985, ed. D. Dowson et al., publ. Butterworths, London, 1986.
12. X. Liang and Z. Linqing, "A new method for the experimental investigation of contact in mixed lubrication." *Wear* 132 (1989), pp. 221-233.
13. K. Tondor and J. Jakobsen, "Interferometric studies of effects of striated roughness on lubricant film thickness under elastohydrodynamic conditions." *ASME Trans., J. of Tribology* 114, (1992), pp. 52-56.
14. M. Kaneta, T. Sakai and H. Nishikawa, "Effects of surface roughness on point contact EHL." *Trib. Trans*, 36, (1993), pp. 605-612.
15. G. J. Johnston, R. Wayte and H. A. Spikes, "The measurement and study of very thin lubricant films in concentrated contacts." *Trib. Trans* 34, (1991), pp. 187-194.
16. G. Guangteng and H. A. Spikes "Boundary film formation by lubricant base fluids.", *Trib. Trans.*, 39, (1996), pp. 448-454.
17. R. S. Sayles "Debris and roughness in machine element contacts: Some current and future engineering implications.", *Proc. Inst. Mech. Engrs.* J209, (1995), pp. 149-172.
18. Smeeth, M. and Spikes, H.A. "Central and minimum elastohydrodynamic film thickness as high contact pressure", to be presented ASME/STLE Conference, San Francisco, Oct. 1996, accepted for publication in *ASME Trans. J. of Tribology*
19. P. M. Cann, J. Hutchinson and H. A. Spikes "The development of a spacer layer imaging method (SLIM) for mapping elastohydrodynamic contact.", to be published in *Trib. Trans.*, Oct. 1996.



## Surface Elastic Deformation by Solvent Structural Force in Very Thin Film Lubrication

Takahisa Kato<sup>a</sup> and Hiroshige Matsuoka<sup>a</sup>

<sup>a</sup>Department of Mechanical Engineering, The University of Tokyo,  
7-3-1 Hongo, Bunkyo-ku, Tokyo 113, Japan  
e-mail: kato@mech.t.u-tokyo.ac.jp

Film thickness of the order of several nanometres is measured by using a precise experimental setup in which two molecularly smooth mica surfaces in crossed cylinder configuration are slid past each other with three kinds of liquid between the surfaces. It will be shown that the film thickness depends on liquid structure and the film is thickened when intervening liquid exhibits a strong solvent structural force. A new EHL theory which considers the deformation due to the structural force is introduced and results of the calculation are shown.

### 1. Introduction

With the advance of microfabrication technology machine elements have been remarkably downsized in recent years<sup>(1,2)</sup>. In accordance with this tribologists have been requested to control the friction and wear occurred in very small sliding systems because the tribological properties govern the overall machine efficiency in these systems more notably than in the ordinary size of sliding systems<sup>(3,4)</sup>. A request with great urgency is made by the computer magnetic slider/disk engineers who are considering to reduce flying height of the slider over the disk to ten nanometres or less in order to increase the recording density of the disk. This flying height is of the order of the surface roughness<sup>(5)</sup> thus thin liquid lubricant is an idea to avoid the contact between solid surfaces and to reduce wear<sup>(6)</sup>. When the solid surfaces reach the distance of several nanometres, surface forces cannot be neglected any more<sup>(7,8)</sup> and, in addition, very thin lubricant film shows different characteristics from those of isotropic lubricant as reported in the recent researches. Homola et al. <sup>(9)</sup> reported that the shear stress increased stepwise by the increase in load or by

the decrease in sliding velocity. Alsten and Granick <sup>(10)</sup> found the extremely enhanced dynamic viscosity of thin liquid film and suggested the phase transition to a solidlike structure. Georges et al. <sup>(11)</sup> proposed a model of "immobile" layer fluid on each solid surface. Guanteng and Spikes <sup>(12)</sup> found thicker films than predicted by EHL theory and suggested the existence of "boundary film" due to adsorption of liquid molecules on the solid surfaces. In order to design a small lubricating system we must know rheological and structural characteristics of thin film between solid surfaces and the applicable limit of conventional EHL theory <sup>(13)</sup>.

### 2. Experiments

The authors measured film thickness of the order of several nanometres by using a simple but precise experimental setup <sup>(14)</sup>. Figure 1 shows a schematic illustration of the setup in which two molecularly smooth mica surfaces in crossed cylinder configuration are slid past each other. One of the mica surfaces is supported by an elastic hinge and minute and controlled slide is realized ( $66.2 \mu \text{ m/mV}$ ). On

smooth cylindrical lenses with the curvature radius of 10.15 mm made of BK7 glass, cleaved mica sheets of thickness of 10 to 30 micrometres are glued carefully so that crystal axes of two mica sheets match each other during contacting and sliding. Roughness of mica surfaces measured by AFM is 0.048 nm ( $R_a$ ) and 0.62 nm ( $R_{max}$ ). Young's modulus of mica,  $E$ , is 34.5GPa and Poisson's ratio,  $\nu$ , is 0.205 which are measured by Scanning Acoustic Microscope. Hardness of mica is 1.43 GPa measured by micro Vickers tester.

Initially mica surfaces are made in contact by a small load, namely,

$$F_{contact} = F_{vdW} + F_m - F_0 \tag{1}$$

where  $F_{vdW}$  is van der Waals force,  $F_m$  is meniscus force and  $F_0$  is pull-off spring force (see Fig. 2(a)).

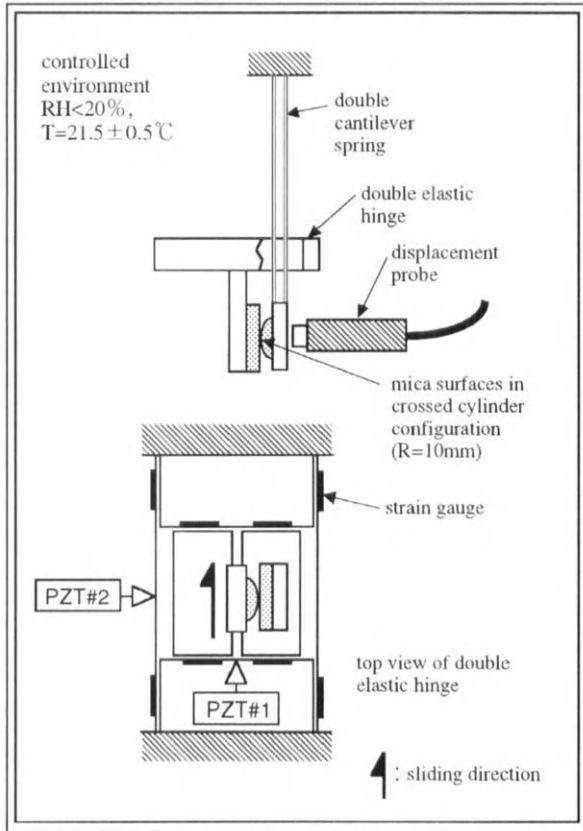


Fig. 1 Experimental setup

$F_{contact}$  is set positive but very small value so that surface contact is kept with negligible elastic surface deformation. If the pull-off force is not applied,  $F_{contact}$  would be as large as a few mN which would cause the surface elastic deformation of about ten nm. When the mica surface supported by an elastic hinge slides, the mating mica surface supported by a double cantilever spring recedes from the sliding surface because of formation of liquid film. Thus the film thickness between surfaces can be known by measuring the displacement of the mica surface supported by the double cantilever spring. Fluid force,  $F$ , is given by the similar equation to eq.(1), namely,

$$F = F_{vdW} + F_m - (F_0 - F_s) \tag{2}$$

$$F_s = k \cdot h \tag{3}$$

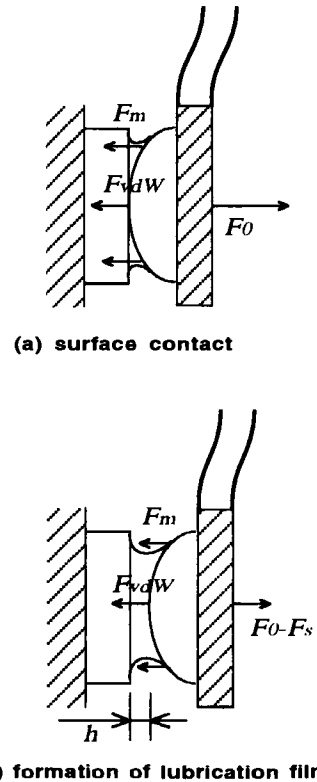


Fig. 2 Formation of lubrication film by sliding

where  $k$  is spring constant of the double cantilever spring (132.5 N/m) and  $h$  the film thickness (see Fig. 2(b)). Note that  $F_{vdW}$  and  $F_m$  are functions of film thickness<sup>(15)</sup>, thus their values in eq.(2) are different from those in eq.(1), respectively.

Using Hertz elastic contact theory<sup>(16)</sup>, the total elastic deformation of the surfaces,  $w$ , is given by

$$w = [(9F^2)/(4RE'^2)]^{1/3} \quad (4)$$

where  $E' = E/(1 - \nu^2)$ . Substituting material and geometric constants ( $E=34.5$  GPa,  $\nu = 0.205$  and  $R=10.15$  mm) into eq.(4), we obtain

$$w(m) = 0.56 \times 10^{-6} (F(N))^{2/3}. \quad (5)$$

As an example, eq.(5) gives  $w=5.6$ nm for  $F=1$  mN and  $w=1.2$ nm for  $F=0.1$  mN, thus minimizing  $F_{contact}$  is important in this experiment.

Fig. 3 shows an example of output of displacement probe (see Fig. 1) obtained at a slide with intervening liquid and illustrates the process for estimating the film thickness,  $h$ . Just after the start of a slide, the output shows a steep increase, which corresponds to the formation of liquid film, followed by a gradual increase. The gradual increase is at the rate of  $7 \times 10^{-5}$  and caused by the fact that the trace of sliding is not vertical to the displacement probe axis. In order to remove this effect from the output, the gradual increase in the figure is approximated by a straight line drawn by the least square method then y-

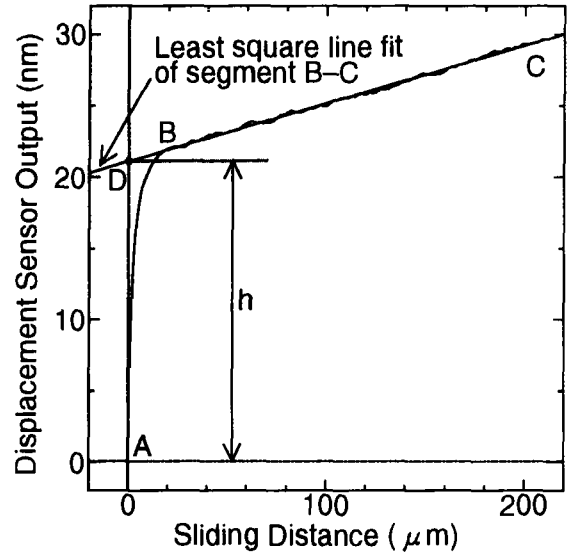


Fig. 3 Output of displacement sensor

intercept of the line is regarded as the film thickness,  $h$ . This process is on the assumption that the sliding condition is not changed during the slide. In fact the sliding distance of  $100 \mu\text{m}$  produces, in this example, a spring bend of  $7$  nm which causes the increase in  $F_{contact}$  of only  $0.93 \mu\text{N}$ . We also obtained the results in a preliminary experiment that the fitted line always passes the origin for the case of dry sliding. The displacement probe is of the type of non-contact capacitive having the resolution of  $0.7 \sim 0.8$  nm with the cutoff frequency of  $3 \sim 5$ Hz for 30 seconds.

Three kinds of nonpolar liquid<sup>(18)</sup> are used in the experiment. They are n-hexadecane, cyclohexane and OMCTS (octamethylcyclotetrasiloxane) and their properties are listed in Table 1.

| Liquid               | n-hexadecane <sup>(17)</sup>               | cyclohexane <sup>(18)</sup> | OMCTS <sup>(19)</sup>           |
|----------------------|--|-----------------------------|---------------------------------|
| chemical formula     | $\text{CH}_3(\text{CH}_2)_{14}\text{CH}_3$ | $(\text{CH}_2)_6$           | $[(\text{CH}_3)_2\text{SiO}]_4$ |
| diameter             | 0.4 nm                                     | 0.6 nm                      | 1.0 nm                          |
| refractive index     | 1.42                                       | 1.43                        | 1.40                            |
| absorption frequency | $1.82 \times 10^{16}$ rad/s                | $1.82 \times 10^{16}$ rad/s | $1.60 \times 10^{16}$ rad/s     |
| dielectric constant  | 2.05                                       | 2.02                        | 2.30                            |
| viscosity            | 3.35 mPas                                  | 0.980 mPas                  | 2.35 mPas                       |

Table 1 Properties of Liquids

Experiments are performed in a clean booth under the atmospheric pressure with controlled environment, namely, the temperature of  $21.5 \pm 0.5$  °C and the relative humidity less than 20%. It is ascertained by a preliminary experiment that the results are not affected by an aqueous vapor if the relative humidity is set within this range.

**3. Results and Discussion**

In the experiment a small amount of liquid (0.1 ~ 0.2cc) is dropped between surfaces then small load is applied. The load is varied by changing  $F_0$  in eq.(1) carefully so that  $F_{contact}$  is set positive but very small value as described in the previous section. Mica surfaces are then slid past each other. Sliding speed is controlled by using a microcomputer as 50, 100 or 200  $\mu$  m/s. The film thickness,  $h$ , is measured by the process described above and  $F_{vdW}$ ,  $F_m$  and  $F_s$  are calculated by using  $h$  value <sup>(14)</sup>, then fluid force,  $F$ , is calculated by eq. (2). The results are shown in Fig. 4 for n-hexadecane, in Fig. 5 for cyclohexane and in Fig. 6 for OMCTS. Prediction by EHL theory for concentrated contact is also shown in the figures. Lines

denoted by "R-I" are predicted minimum film thickness by rigid-isoviscous theory, those denoted by "E-I" are by elastic-isoviscous theory<sup>(20)</sup>. It is seen from these figures that the theoretical boundary between R-I and E-I regimes locates at  $h=1$  nm or less and the surface elastic deformation is considered negligible when the film thickness is larger than this value according to the conventional EHL theory. Fig.4 shows that the measured film thickness agrees well with the calculation by R-I theory down to two nm of film thickness when n-hexadecane is used as lubricant. For the film thickness smaller than this value, the thickened film suggests the increase in the viscosity near the solid<sup>(10)</sup>, or the formation of "immobile" layer<sup>(11)</sup> or "boundary film"<sup>(12)</sup>. It is seen that the thickness of this layer would be less than 0.5 nm, if exists, and it appears only when the surface separation is of the order of several nanometres..

When cyclohexane and OMCTS are used as lubricant (see Figs. 5 and 6), however, the film thickness deviates from the theoretical R-I curve at larger values of film thickness (5 -7 nm) then decrease stepwise with an increase in load. It is noted that the

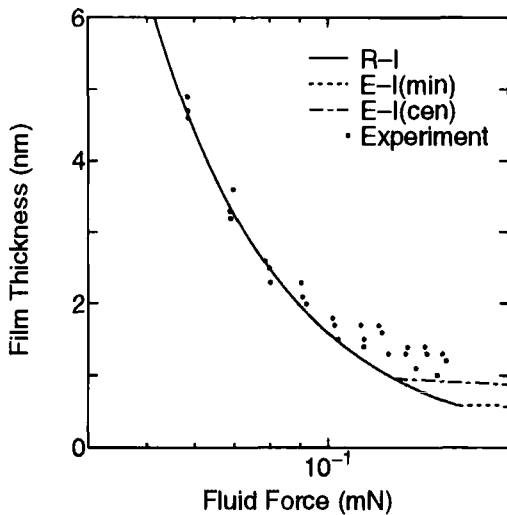


Fig. 4 Film thickness v.s. fluid force for n-hexadecane ( $u=200 \mu$  m/s)

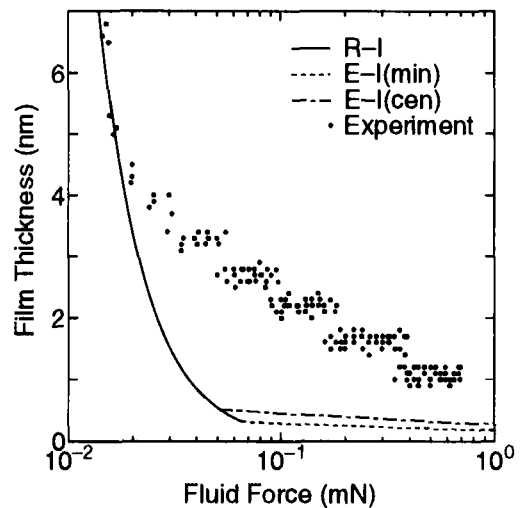


Fig. 5 Film thickness v.s. fluid force for cyclohexane ( $u=200 \mu$  m/s)

interval of the discrete film thickness is nearly equal to the liquid molecular diameter, namely, 0.6 nm for cyclohexane and 1.0 nm for OMCTS (see Table 1). If the difference between the measured and calculated fluid forces, namely,

$$F_s = F - F_{ehl} \tag{6}$$

is plotted against film thickness, it is found that the force,  $F_s$ , decays exponentially with the film thickness as shown in Fig. 7, in which, for the sake of simplicity, only the maximum value of  $F_s$  at each steplike film thickness is plotted. It is seen from the figure that  $F_s$  is not a dynamic force because the relation  $F_s - h$  does not depend on the sliding velocity. It is known that the van der Waals force decays with the separation between solid surfaces. Thus the possibility of the origin of this force being the van der Waals force must be checked. The van der Waals force, however, decays more quickly than this example as shown in Fig. 8 which shows the calculated van der Waals force for our experimental configuration. It is reported that cyclohexane and OMCTS have spherical molecular

shape and show strong structural force<sup>(19)</sup> compared to n-hexadecane. The structural force (or solvation force) depends on the structure of the liquid intervening between solid surfaces. This force is oscillatory with the film thickness and the period is almost equal to the molecular diameter of intervening liquid as shown in Fig. 9. It is considered that a repulsive or an attractive force acts according to dense or dilute condition of molecules between surfaces, respectively (see Fig. 10). The most dense condition is expected when the film thickness becomes some integral number times the

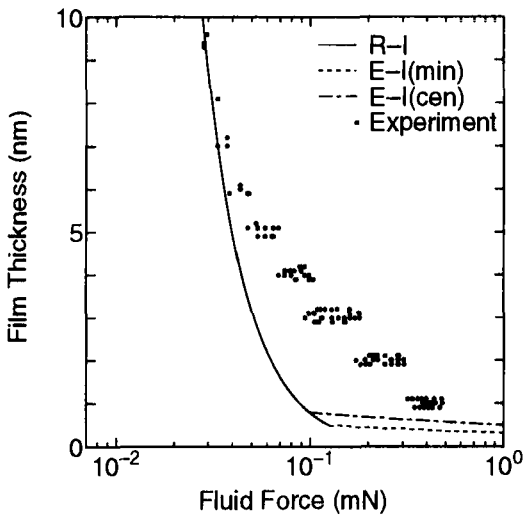


Fig. 6 Film thickness v.s. fluid force for OMCTS ( $u=200 \mu \text{ m/s}$ )

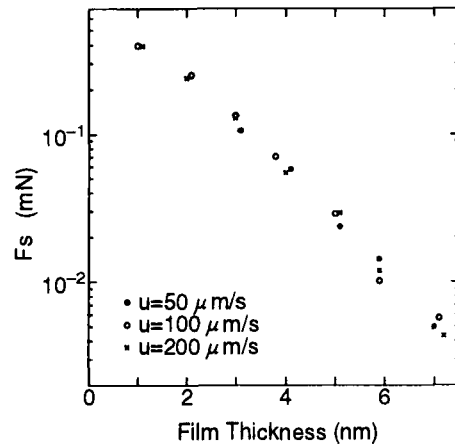


Fig. 7  $F_s$  for OMCTS

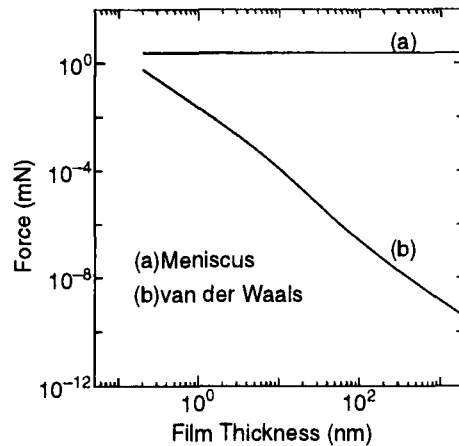


Fig. 8 Van der Waals force and meniscus force

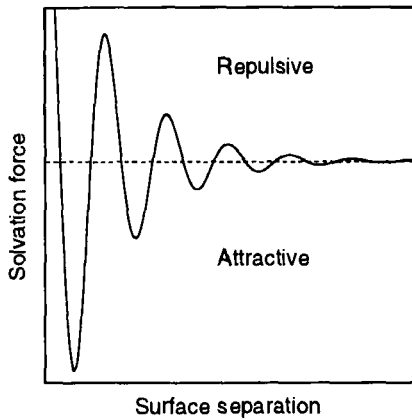


Fig. 9 Solvation force v.s. surface separation

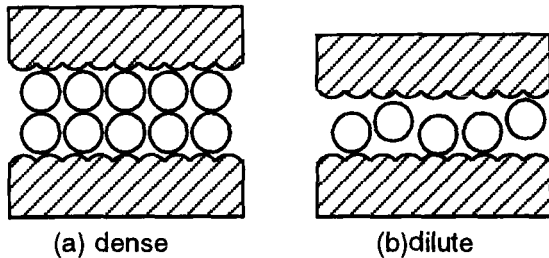


Fig. 10 Spherical molecules between surfaces

molecule diameter. The molecules would form "layered structure" in these cases. From these consideration it is concluded that the thickened film in Figs. 5 and 6 is attributed to the solvent structural force.

#### 4. Surface elastic deformation by structural force

When cyclohexane and OMCTS were used as lubricant with the film thickness of several nm, it was seen that an additional force of several mN was generated due to the solvent structural force. It is easily shown that this force produces surface elastic deformation of several nm by the Hertz elastic contact theory (see eq.(5)). Since this is of the same magnitude with film thickness, we cannot neglect the surface deformation any more in the analysis of this sort of lubrication problems. The authors developed a very thin film lubrication theory where solvation pressure

was dominant<sup>(15)</sup>. It is assumed the total pressure,  $p$ , is composed of three components, namely

$$p = p_s + p_{vdW} + p_h \quad (7)$$

where  $p_s$  is the pressure due to the liquid structural force,  $p_{vdW}$  is that due to the van der Waals force between the solid surfaces and  $p_h$  is hydrodynamic viscous force.  $p_h$  is obtained by solving the Reynolds equation and the calculation method of other components is written in detail elsewhere<sup>(15)</sup>. Similar to the conventional EHL calculation, the Reynolds equation is solved simultaneously with the equation of elastic deformation of solid<sup>(21)</sup>. As for the formation of equations and the boundary and initial conditions, the methods reported in the past are adopted in this study<sup>(21,22,23)</sup>. Examples of EHL calculation for OMCTS are shown in Figs. 11 (a) and (b). In figures the film thickness is normalized by the curvature radius of the mica surface,  $R = 10 \text{ mm}$ , and the pressure by the equivalent Young's modulus,  $E' = 35.9 \text{ GPa}$ . Fig. 11(a) shows the result for the total load of  $30 \mu \text{ N}$ . The surface deformation is not clear in this case (approximately  $0.5 \text{ nm}$  by Hertz theory) but the oscillatory pressure distribution which is due to the solvation structural force is observed. When the total load is  $100 \mu \text{ N}$ , the surface deformation and the pressure distribution similar to the Hertzian contact are observed as shown in Fig. 11(b). This is because the structural force, which is originally static like a point contact force, is dominant compared to the hydrodynamic force in this case.

It is clarified that the measured film thickness deviates from the R-I theoretical curve due to the surface deformation by the solvent structural force, although the R-I theory is thought applicable to the film thickness down to one nm in this sliding condition according to Hamrock-Dowson diagram<sup>(20)</sup>. The Hamrock-Dowson diagram for the point contact is shown in Fig.12 in which the range of the present

experiment is indicated by a solid long circle, namely  $F=10 \mu\text{ N} \sim 10\text{mN}$ ,  $u=1 \sim 500 \mu\text{ m/s}$ ,  $\alpha = 10 \sim 30\text{GPa}^{-1}$ ,  $R= 10\text{mm}$ . Symbols in the long circle indicate the sliding conditions under which the film thickness begins to deviate from the R-I theoretical curve for cyclohexane (+:  $200 \mu\text{ m/s}$ ) and for OMCTS ( $\circ$ :  $200$ ,  $\triangle$ :  $100$ ,  $\square$ :  $50 \mu\text{ m/s}$ ). The boundary line between R-I and E-I regimes on the diagram should pass this symbols because the elastic deformation begins to occur under these sliding conditions.

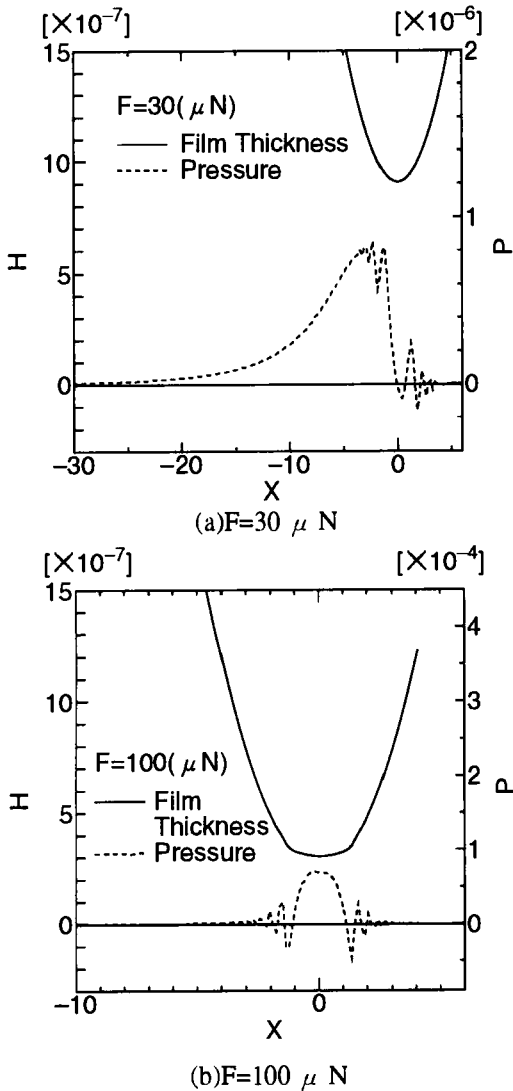


Fig. 11 Calculated film thickness and pressure distribution for OMCTS ( $H=h/R$ ,  $P=p/E'$ ,  $X=x/a$ ,  $a$ : radius of Hertzian contact)

5. Conclusions

Film thickness of the order of several nanometres is measured with liquid between mica surfaces in crossed cylinder configuration. The measured film thickness agrees well with the calculation by R-I (Rigid-Isoviscous) lubrication theory down to two nanometres of film thickness when n-hexadecane, which has a molecular structure of flexible chain, is used. When cyclohexane and OMCTS (octamethylcyclotetrasiloxane) which have spherical molecular shape are used, however, the film thickness deviates from theoretical R-I curve at larger values (5-7 nm) then decreases stepwise. It is considered that the deviation (thickened film) is attributed to solvent structural force. According to the newly developed EHL theory, it is seen that the surface elastic deformation due to the solvent structural force causes the thickened lubricant film. Thus the E-I (Elastic-Isoviscous) regime should be expanded in the Hamrock-Dowson diagram in the case of very thin film lubricating condition with very light load in which solvent structural force cannot be neglected any more compared to the ordinary fluid viscous force.

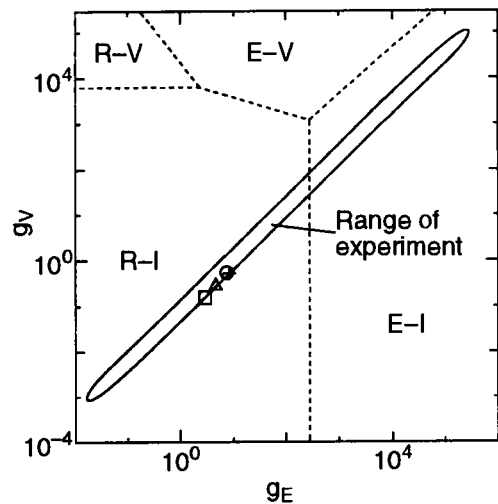


Fig. 12 Sliding condition on Hamrock-Dowson diagram ( $g_V$ : viscosity parameter,  $g_E$ : elasticity parameter <sup>(20)</sup>)

## References

- 1.F. Behi et al., "A Microfabricated Three-Degree-of-Freedom Parallel Mechanism," Proc. IEEE Micro Electro Mechanical Systems 1990, pp.159-165.
- 2.R. Legtenberg et al., "Electrostatic Microactuators with Integrated Gear Linkages for Mechanical Power Transmission," Proc. IEEE Micro Electro Mechanical Systems 1996, pp.204-209.
- 3.M.Mehregany et al., "Friction and Wear in Microfabricated Harmonic Side-Drive Motors," Proc. IEEE Micro Electro Mecha. Systems 1990, pp.17-22.
- 4.T. Yasuda, I. Shimoyama and H. Miura, "Microrobot Actuated by a Vibration Energy Field," Sensors and Actuators A, 43, 1994, pp.366-370.
- 5.C. Gao and B. Bhushan, "Tribological Performance of Magnetic Thin-Film Glass Disks: Its Relation to Surface Roughness and Lubricant Structure and Its Thickness," Wear 190, 1995, pp.60-75.
- 6.F. A. de Buyne and D. B. Bogy, "Numerical Simulation of the Lubrication of the Head-Disk Interface Using a Non-Newtonian Fluid," ASME Journal of Tribology, Vol.116, 1994, pp.541-548.
- 7.D. Tabor, "Surface Forces and Surface Interactions," J. of Colloid Interface Sci., Vol.58, 1977, pp.2-13.
- 8.P. M. McGuiggan and J. N. Israelachvili, "Adhesion and short range forces between surfaces. Part II: Effect of surface lattice mismatch," Journal of Material Research, Vol. 5, 1990, pp.2232-2243.
- 9.A. M. Homola et. al., "Measurement of and Relation between the Adhesion and Friction of Two Surfaces Separated by Molecularly Thin Liquid Film," ASME Journal of Tribology, Vol. 111, 1989, pp.675-682.
- 10.J. V. Alsten and S. Granick, "Molecular Tribometry of Ultrathin Liquid Films," Physical Review Letters, Vol.61, No. 22, 1988, pp.2570-2573.
- 11.J. M. Georges et al., "Drainage of Thin Liquid Film between Relatively Smooth Surfaces," Journal of Chemical Physics, Vol. 98, 1993, pp.7345-7360.
- 12.G. Guanteng and H. A. Spikes, "Behaviour of Lubricants in the Mixed Elastohydrodynamic Regime," Proc. Leeds/Lyon Symposium, 1994.
- 13.G. Guanteng and H. A. Spikes, "Boundary Film Formation by Lubricant Base Fluids," presented at the 50th STLE Annual Meeting in Chicago, No.95-NP-7D-3, 1995.
- 14.H. Matsuoka and T. Kato, "Discrete Nature of Ultrathin Lubrication Film between Mica Surfaces," ASME Journal of Tribology, in press.
- 15.H. Matsuoka and T. Kato, "An Ultrathin Liquid Film lubrication Theory- Calculation Method of Solvation Pressure and Its Application to the EHL Problem," ASME Journal of Tribology, in press (presented at the '96 ASME/STLE Tribology Conference in San Francisco, October, '96).
- 16.S. P. Timoshenko and J. N. Goodier, "Theory of Elasticity (Third Edition)," McGraw-Hill, Ltd.
- 17.J. N. Israelachvili, "Intermolecular and Surface Forces," 2nd edition, Academic Press, 1992.
- 18.H. K. Christenson, "Experimental Measurement of Solvation Forces in Nonpolar Liquids," Journal of Chemical Physics, Vol. 78, pp.6906-6913, 1983.
- 19.R. G. Horn and J. N. Israelachvili, "Direct Measurement of Structural Forces between Two Surfaces in a Nonpolar Liquid," Journal of Chemical Physics, Vol. 75, pp.1400-1411, 1981.
- 20.M. Esfahanian and B. J. Hamrock, "Fluid-Film Lubrication Regimes Revised," STLE Tribology Transactions, Vol. 34, 1991, pp.628-632.
- 21.B. J. Hamrock and D. Dowson, "Isothermal Elastohydrodynamic Lubrication of Point Contact, Part I- Theoretical formulation," ASME Journal of Lubrication Technology, Vol.98, 1976, pp.223-229.
- 22.J. F. Lin and H. Y. Chu, "A Numerical Solution for Calculating Elastic Deformation in Elliptical-Contact EHL of Rough Surface," ASME Journal of Tribology, Vol.113, 1991, pp.12-21.
- 23.H. P. Evans and R. W. Snidle "The Isothermal Elastohydrodynamic Lubrication of Spheres," ASME Journal of Lubrication Technology, Vol.103, 1981, pp.547-557.



## FAILURE OF VERY HIGH SPEED ELASTOHYDRODYNAMIC CONTACTS

D.J. HIRST and A.V. OLVER

*Imperial College, Tribology Section, Department of Mechanical Engineering, Exhibition Rd, South Kensington, London, UK.*

This paper describes a rig designed to simulate high speed ball bearing contacts under laboratory conditions. Measured amounts of spin and sliding can be imposed on the contact in addition to the very high rolling speed. Scuffing-type failures can be provoked by high slip conditions.

### 1. INTRODUCTION

The ball bearings found in aero-engine gas turbines operate at around 2.5 million DN or more and similar conditions are encountered in some machine tool bearings. Under these conditions, the gyroscopic forces become dominant, exceeding the spin moments present. Race control theory is not applicable as the rotational axis of the rolling element is almost parallel to the shaft axis, so that sliding and spinning motion occur at both ball-raceway contacts in addition to the rolling motion.

This paper describes a test rig designed to simulate this type of contact under controlled laboratory conditions, in order to study the limits of its performance.

### 2. BACKGROUND

A diagram of a typical bearing is shown in figure 1. The contact angles between the inner and outer raceways are  $\alpha$  and  $\beta$  respectively. Reaction forces at each contact are accompanied by tangential frictional forces and a spin moment as shown. High orbital and rotational speeds lead to a centrifugal force and a gyroscopic moment respectively.

The ball motion is determined by the equilibrium of the forces acting on it including

the contact reaction forces at both raceways and the cage together with the centrifugal and

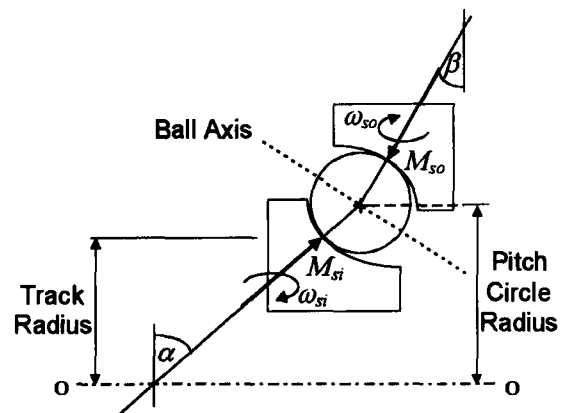


Figure 1 Ball bearing contact geometry

gyroscopic forces due to the motion. In addition, traction forces act on the ball leading to the occurrence of sliding and spinning motion at the contacts.

The net effect of these forces on the ball is uncertain, and although it is known that in principle, relative spin and slip of the contact could be detrimental to the performance of the bearing, observations of failure phenomena have not been widely reported.

## 2.2 Ball Motion

Ball motion can be predicted from theory in several ways. Race control theory, in which dry friction is assumed (1, 2) is valid for low speeds. The controlling contact (usually the outer at high speed) is assumed to undergo pure rolling whilst the other encounters both rolling and spin. Alternatively, if the speeds are sufficiently high the gyroscopic forces may become very large compared to the spin moments, a situation which we term "Gyroscopic Control". The rotational axis of the ball is therefore parallel to the bearing axis and spinning and sliding occur at *both* raceway contacts. It might be assumed that this would occur at very high speed because of the expected low friction coefficient and high gyroscopic moment.

For a more general case, several commercial computer packages are available which contain explicit fluid friction models. One example is 'ADORE' - the original theory and listing appears in (3)

This approach takes into account the fluid friction arising from the oil. The high pressure contact between the ball and raceway is separated by a film of oil the thickness of which can be determined from the well-known regression equations of Dowson and Hamrock (4), subjected to a suitable correction factor combining both inlet shear heating and loading effects (5). Starvation may also occur in real bearings although this can be combated using, for example, through-race lubricant supply.

Experimental measurements of ball motion present difficulties due to the high rotational speeds - cage speed measurements are more common and easier. In a recent paper Chapman (6) describes a rotating prism that optically freezes the ball and cage motion in a full bearing rig, thereby allowing closed circuit TV to record the tests.

The contact studied in this project is subjected to simulated gyroscopic and centrifugal forces at high loads, speeds and temperatures and, as a result, encounters slip and spin at the contacting interfaces. The main objective was

to identify contact conditions which could lead to failure of the ball raceway contact.

## 3. RIG DESIGN

In order to determine performance limiting conditions, an experimental rig was designed to simulate high speed ball bearing contacts such that the bearing element motion could be measured. It was designed to operate at around an equivalent DN of 3 million, with the option of higher speeds if required.

### 3.1 Basic Design

A simplified diagram showing the principle of the test rig is presented in figure 2: a driven disc rotates a non-orbiting lubricated follower (test ball) which is loaded against it. This system gives an equivalent cage speed of zero so that the required ball speed can be obtained from approximately half the usual driveshaft speed.

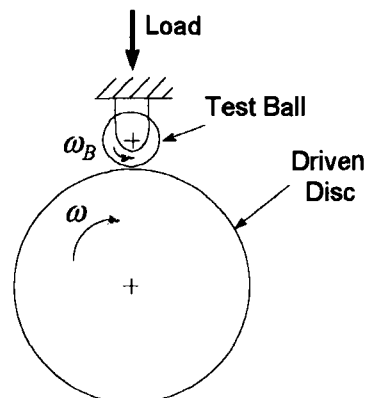


Figure 2 Schematic diagram of the test rig

The ball is loaded into a conforming groove formed from a split inner raceway pair in a gothic arch shape. This forces the ball axis of rotation to be parallel to the bearing axis thereby achieving the required simulated gyroscopic control.

This method of testing was chosen over the conventional disc machine method, which can test elliptical contacts with crowned rollers

without the imposed spin motion, or full bearing testing which was rejected on grounds of size, cost, power consumption and the difficulties of monitoring ball motion.

### 3.2 Test Ball

The test ball was located and loaded into the rotating groove using a combined hydraulic ram and hydrostatic bearing - a 'biro'. The biro admits high pressure oil, which flows through an orifice to maintain the pressure across the back of the ball. This both loads and lubricates the contacts as well as providing a lubricating film between the ball and biro. The system is shown in figure 3.

Measurable amounts of sliding and spinning were imposed upon the contacting interfaces at high rolling speed by variations in the raceway profile geometry.

Ball motion was measured by use of a magnetic search coil system located on the biro housing. The active coil detects the movement of the magnetised ball. The output has sinusoidal form, the frequency being proportional to the rotational speed of the ball; changes in wave amplitude are proportional to the relative positions of the ball magnetic pole, the spin axis and the coil.

Both the ball and the raceways were of M50 VIM-VAR steel. Bulk oil and biro temperatures were measured using thermocouples. The lubricant supplied throughout was Castrol Aerojet 5, an ester-based turbine oil, which was run through 3  $\mu\text{m}$  filters. The test rig was driven by a 25 kW d.c. motor, which is

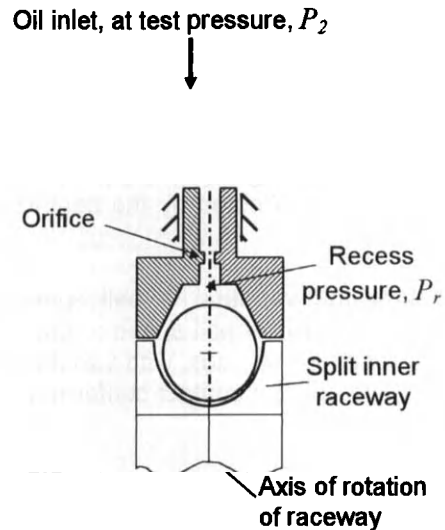


Figure 3 The test ball and biro system loaded in a grooved rotor

stepped up to the driveshaft via a POLY-V belt and pulley system. A control system triggered by abnormal instrumentation readings was installed to cut electrical power to the rig in the event of a failure.

## 4. RESULTS

Table 1 presents the contact conditions for the two types of tests run - for contact angles of 35° and 40° - where  $P$  is the load in N,  $p_0$  is the maximum contact pressure (Pa),  $a$  and  $b$  are the contact semi-major and semi-minor widths respectively (mm), and  $h_0$  ( $\mu\text{m}$ ) is the minimum film thickness assuming fully flooded conditions.

| $P$ (N) | Contact Angle, $\alpha = 40^\circ$ |                         | Contact Angle, $\alpha = 35^\circ$ |                         |
|---------|------------------------------------|-------------------------|------------------------------------|-------------------------|
|         | $p_0$ (Pa)                         | $h_0$ ( $\mu\text{m}$ ) | $p_0$ (Pa)                         | $h_0$ ( $\mu\text{m}$ ) |
| 5000    | $1.25 \times 10^9$                 | 2.92                    | $9.73 \times 10^8$                 | 2.92                    |

Table 1 Table of full load and speed contact conditions at 100°C, for contact angles of 40° and 35°

The effect of decreasing the contact angle is to decrease the maximum contact pressure. The theoretical film thickness, ignoring any possible starvation effects, is unaffected by the contact angle.

The results show the variation in ball speed (indicated as  $\Omega$  - the ratio of ball speed to shaft speed) and PV for different loads, with variation in the contact angle and the contact conformity.

**4.1 Ball Speed**

Figure 4 shows the variation of ball to shaft speed ratio with load. Although the test was repeated for various shaft speeds, the shaft rotated at constant speed throughout the duration of each test.

The first few points are at a very low speed ratio, indicative of skidding behaviour. The speed ratio then rises to a plateau close to the theoretical rolling ratio depending on the shaft speed: the magnitude of slip rises with the shaft rotational velocity

It was noted that low  $\Omega$  values could be avoided by controlling the shaft speed such that it increased concurrently with the load so that skidding conditions (low load, high speed) were not reached. Figure 5 shows an example of this type of test with the ball speed only plotted as ordinate, due to the variable shaft velocity. Shaft speed was increased in equal steps until the desired final speed was reached - shown by the flat parts of some of the curves. The speed ratio in this case very quickly reached high values close to the theoretical rolling limit.

Ball speed was taken from direct measurement of frequency of the magnetic signal. An oscillatory variation of the signal with a period of approximately 30 seconds was observed. This may indicate skewing of the ball axis due to unequal contact geometry, but no firm conclusions were drawn.

First tests were run at up to three-quarter driveshaft speed. Later tests were run up to full

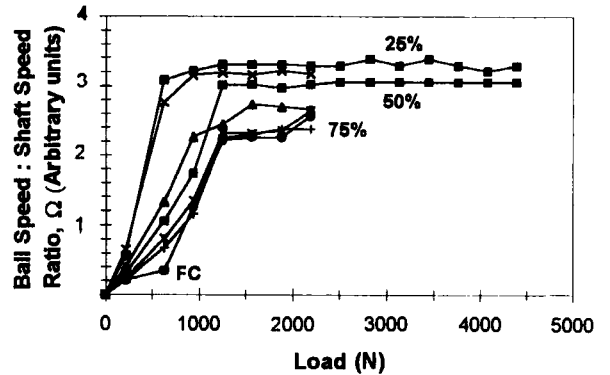


Figure 4 Ball to shaft speed ratio vs load under constant driveshaft conditions (indicated as a percentage of full speed) and for  $\alpha = 40^\circ$ . Points taken at 5 minute intervals. FC = Region of approximate failure conditions.

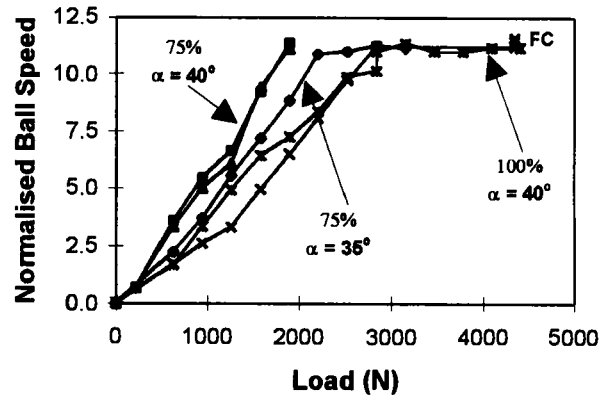


Figure 5 Normalised ball speed vs load for variable driveshaft conditions (the ball speed is normalised by dividing it by the final shaft speed which is indicated as a percentage of full speed). Measured points taken at 5 minute intervals, after each increment to the shaft speed until final speed is achieved. FC = Region of failure conditions

speed - with simultaneously increasing load - whereupon they were tested until the maximum load was reached. Tests were repeated with variations in the contact angle.

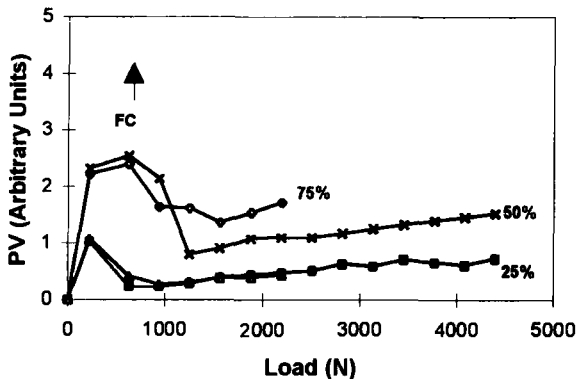


Figure 6 PV vs Load for constant driveshaft test conditions (indicated as percentages of full speed) and for  $\alpha = 40^\circ$ . Points taken at 5 minute intervals. FC = Region of approximate failure conditions.

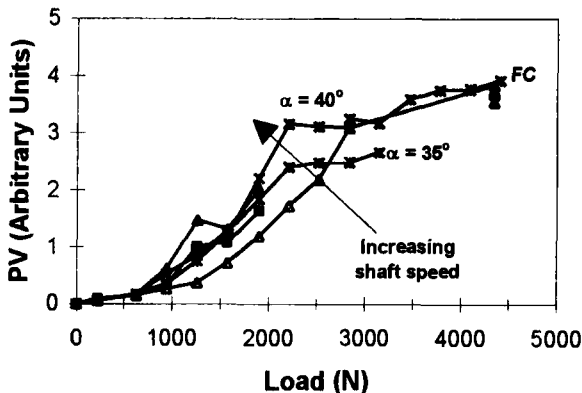


Figure 7 Effect of load on PV for variable driveshaft test conditions with different contact angles. Measured points taken at 5 minute intervals, after each increment to the shaft speed until final speed is achieved. FC = Region of failure conditions.

#### 4.2 PV

PV is an indicator, widely used in bearing design, of the maximum permissible load and speed conditions achievable in a bearing. It is given by the maximum value of the product of

the local contact pressure ( $P$ ) and the local, relative surface velocities ( $V$ ).

The PV curves for the same conditions shown in figures 4 and 5 are presented in figures 6 and 7.

The PV peak corresponding to the skidding conditions at low load can be seen in Figure 6. The curve drops off and thereafter follows a consistent gradient, once the applied load is sufficiently high.

Figure 7 shows the avoidance of the PV peak associated with the skidding condition by virtue of the lower shaft speeds at low load. PV levels fall both as the contact angle is decreased, and as the shaft speed falls with the contact angle remaining constant.

#### 4.3 Failure

Contact failures have been noted at the speed and load conditions indicated in figures 4-7. It was noted that failures are associated with PV peaks, although higher levels are possible for the high spin condition. Contact temperatures just before failure have been recorded at around  $120^\circ\text{C}$ , which rises significantly with the onset of failure.

The mechanism of failure has not been determined. The three factors that have been observed are: seizure in the biro; destruction of the lubricating film and damage to the ball and raceway contact. It appears that initial wear at the ball-raceway contact may eventually lead to debris being lodged in the biro so that the friction is increased at the ball-race interface, whilst at the same time restricting lubricant flow to the test ball.

Failure cases were examined with both visual and scanning electron microscopy methods. Large areas of plastic flow were noted on the surface of the ball and evidence of severe surface and sub-surface heating was also found around the wear scars. Two images taken with the scanning electron microscope are presented in figures 8 and 9. First the catastrophic wear capable of this type of contact is shown. Scuffing has taken place: the

smooth ball surface is just visible in the foreground with a large area of local welding behind it. The second image shows the surface away from the site of the scuffing failure. The surface is severely worn in the rolling direction and surface cracks across the direction of rolling can be clearly seen.

## 5. DISCUSSION

The test rig has several advantages over full scale bearing tests in terms of reduced power, space and cost requirements. In addition the method of determining the ball motion has been found to be successful, as the single, non-orbiting ball allows more ease of measurement than a rotating cage. It is, however, uncertain how the presence of other balls in the system would affect the contact conditions created in the rig. It is believed that a high speed rotating element is starved of oil by the motion of the preceding element, which effectively pushes the lubricant away from the track. This is not simulated in the rig, though the flow of the lubricant through the biro onto the test ball is also uncertain and unproven.

Two types of condition appear to lead to failure. At low loads there is skidding which, in the rig, is predominantly a consequence of frictional drag from the biro. In a real bearing, a similar condition can arise from cage interaction at high speed and low load. In contrast, high load conditions can also precipitate failure; here, high spin velocities constitute the larger part of the slip. Post failure examination suggests that both failure mechanisms are similar, although the relative amount of damage increases with the ball speed.

PV values increase with shaft speed; a PV peak is accompanied by an associated drop in the speed ratio,  $\Omega$ , indicating an increase in the slip levels. The PV values under which the two types of failure occurred are rather similar, suggesting that this is a useful parameter for gauging useful bearing performance limits.

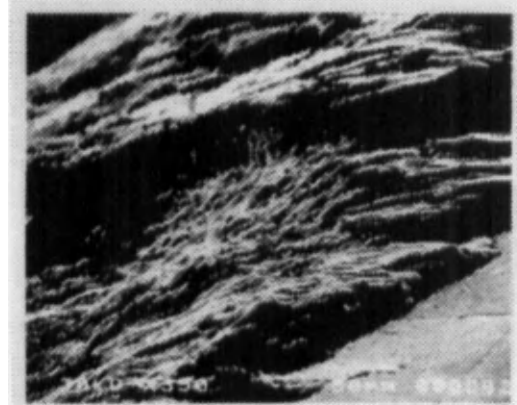


Figure 8 Failed ball element surface showing catastrophic damage area due to local welding (Scanning electron micrograph x350).

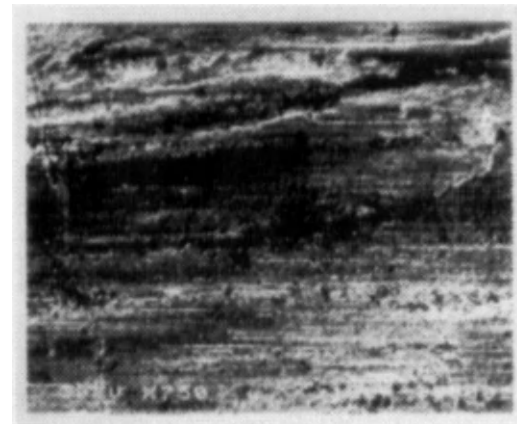


Figure 9 Worn track of ball element, showing surface cracks normal to the rolling direction (Scanning electron micrograph x 750).

## 6. CONCLUSIONS

A test rig which reproduces the contact conditions of very high speed ball bearings has been developed. The rig consists of a single ball pressed into a gothic-arch inner raceway using a hydrostatic bearing.

Failures of the ball-raceway contact can be provoked either by skidding (low load, high

speed) or by spin (high load, high speed) motions. The failures appear to be due to scuffing at a test temperature of around 120°C.

The failures obtained to date are at an approximately constant level of PV.

#### ACKNOWLEDGEMENTS

The authors gratefully acknowledge the financial and technical support of The Torrington Company Ltd in the funding of this project and in the design and manufacture of the test rig and test components. The support of PALL Filters Ltd is also gratefully acknowledged.

#### REFERENCES

- [1] Jones, A.B., (1959), *Ball Motion And Sliding Friction In Ball Bearings*, Trans. ASME, J. Basic Eng., D81(1), pp1-12.
- [2] Harris, T.A., (1966), *Rolling Bearing Analysis*, John Wiley & Sons.
- [3] Gupta, P.K., (1984), *Advanced Dynamics Of Rolling Elements*, Springer-Verlag.
- [4] Hamrock, B.J, and Dowson, D., (1981), *Ball Bearing Lubrication*, John Wiley & Sons.
- [5] Gupta, P.K., Cheng, H.S., Zhu, D., Forster, N.H., Schrand, J.B., (1992), *Viscoelastic Effects In MIL-L-7808-Type Lubricant, Part I: Analytical Formulation*, Trib. Trans., Vol 35, 2, pp269-274.
- [6] Chapman, J.J., (1994), *Angular Contact Ball Bearing Dynamics, An Experimental And Theoretical Investigation*, Proc. XXI Leeds-Lyon Symp., Elsevier.

## ELASTOHYDRODYNAMIC LUBRICATION OF SOFT SOLIDS

C. J. HOOKE

School of Manufacturing and Mechanical Engineering, The University of Birmingham, Edgbaston,  
Birmingham, B15 2TT.

### SYNOPSIS

Lubricated soft contacts are characterised by the large magnitude of the surface deformations compared to the thickness of the fluid film separating them. Thus over most of the conjunction the pressures remain close to the dry contact values. It is only in narrow inlet and exit regions and, occasionally near other pressure singularities, that there is substantial divergence. The dry contact pressure distribution, therefore, largely dictates the nature of the lubrication process and the magnitude of the film thickness.

This paper reviews the behaviour of soft contacts concentrating, particularly, on the relationship between the lubrication behaviour and dry contact pressures.

### 1. INTRODUCTION

The lubrication of soft contacts is distinguished from that of the more familiar metallic, or hard, surfaces by two characteristics. The first is the relatively low contact pressures in the conjunction with values around 1 to 10 MPa being typical. This ensures that the effects of pressure on viscosity, on which hard EHL relies, are almost entirely absent.

The second characteristic of soft contacts is the very large magnitude of the surface deformation. Displacements of some hundreds of microns are common and, since film thicknesses are typically around 1  $\mu\text{m}$ , the contact pressures and surface deformations are largely unaffected by the lubrication process. The other consequence of these large deformations is that the Hertz approximation is generally no longer valid and a more complex analysis of the deformation process becomes necessary.

These two differences have major consequences in the lubrication process. The absence of piezo-viscous effects simplifies the lubrication analysis. It means that there can be no pressure spikes at the contact exit, that the contact friction can be calculated without reference to complex, high pressure rheological characteristics and that the effects of surface roughness are somewhat easier to

understand. However, this simplification is balanced by far more complex elastic behaviour and, because of the large deformations, it is these that control the lubrication process.

The use of modern multi-level calculation methods means that it is now straightforward to calculate the film thickness in any soft contact under either steady or dynamic conditions. This paper will, therefore, concentrate on the general characteristics of this type of problem and will, in particular, emphasise the relationship between the solution of the dry contact pressure distribution and the EHL film thickness.

#### 1.1 Notation

- a semi-contact width
- a amplitude of residual sinusoidal roughness
- A initial amplitude of sinusoidal roughness
- e entrainment length - twice the distance from dry contact end to maximum pressure gradient
- $e_{\text{exit}}$  exit length - distance from  $h_{\text{min}}$  to cavitation

$$E^* = \frac{2}{E'} = \frac{1-\nu_1^2}{E_1} + \frac{1-\nu_2^2}{E_2} \text{ - equivalent elastic}$$

modulus

- $g_3$  elasticity parameter

$$= \left[ \frac{W^2}{\eta \mu E' R} \right]^{0.5} \text{ for cylindrical contacts}$$



$$= \left[ \frac{W^2 \tan \alpha}{\eta u a E'} \right]^{0.5} \text{ for wedge contacts}$$

$h$  clearance

$h'$  non-dimension clearance

$$= \frac{Wh_{\min}}{\eta u R} \text{ for cylindrical contacts}$$

$$= \frac{Wh_{\min} \tan \alpha}{\eta u a} \text{ for wedge contacts}$$

$h_m$  clearance at maximum pressure

$h_{\min}$  minimum clearance

$k$  inlet coefficient

$L$  wavelength of sinusoidal roughness

$n$  distance from end of contact measured into the conjunction

$p$  pressure

$P_H$  maximum pressure in Hertz line contact

$R$   $\frac{1}{R} = \frac{1}{R_1} + \frac{1}{R_2}$  - equivalent radius

$W$  load per unit length of contact

$t$  layer thickness

$t$  time

$u = (u_1 + u_2)/2$  - entrainment velocity

$x, y$  coordinates

$\alpha$  wedge angle

$\delta$  elastic deformation

$\eta$  dynamic viscosity

$\phi$  phase of residual roughness

$\lambda = 2\pi/L$  - roughness frequency

$\psi$  attenuation factor

## 2. LINE CONTACTS

Any discussion of soft contacts must start with an examination of the pressure distribution between the surfaces under frictionless, unlubricated conditions. Modern finite element methods provide easy means of calculating this distribution [1,2,3] although care is required because of the presence of infinite pressure gradients. Although these programs allow for large strains through the use of large strain elasticity models, strains are generally moderate and neo-Hookean, incompressible elastic models are generally sufficiently accurate.

The very large surface displacements mean that the dry contact pressure will be present, largely unchanged, when the surfaces are lubricated. Because Reynolds' equation defines the relationship

between fluid pressure and clearance it follows that the dry contact pressure distribution controls the clearances in the contact and, hence, the lubrication behaviour.

For line contacts in steady motion, this relationship was first explored by Blok [4] who developed an inverse analysis using the integrated form of Reynolds' equation:

$$\frac{dp}{dx} = 12\eta u \frac{h - h_m}{h^3} \quad [1]$$

Essentially, the maximum value of the pressure gradient determines  $h_m$ :

$$h_m = \frac{4}{3} \sqrt{\frac{\eta u}{[dp/dx]_{\max}}} \quad [2]$$

and from this the clearance,  $h$ , at every point in the conjunction may be found. Where two solutions for  $h$  exist, the larger value is chosen to the left of the point of maximum gradient (assuming entrainment on the left of the contact); the lower to the right.

### 2.1 Inlet control

The simplest and most widely analysed contact, is that between two cylindrical surfaces - the Hertz line contact. Under dry conditions, the pressure distribution is given by:

$$p = P_H \sqrt{1 - (x/a)^2} \quad [3]$$

where  $P_H$  is the maximum pressure under the contact and  $a$  is the semi-contact width. The critical feature here is that the pressure gradient becomes infinite at the ends of the contact. Thus direct application of Blok's inverse analysis predicts that the clearance will be zero. What in fact occurs as was demonstrated by Dowson and Higginson [5] and later, in more detail, by Herrebrugh [6] is that a pressure sweep forms at the inlet to the conjunction over-riding the initial section of the dry contact profile.

Fig. 1 shows typical pressures and clearances for this contact for a range of values of  $g_3$ , a parameter proposed by Johnson [7] to represent the extent of the elastic deformation of the contact. It may be

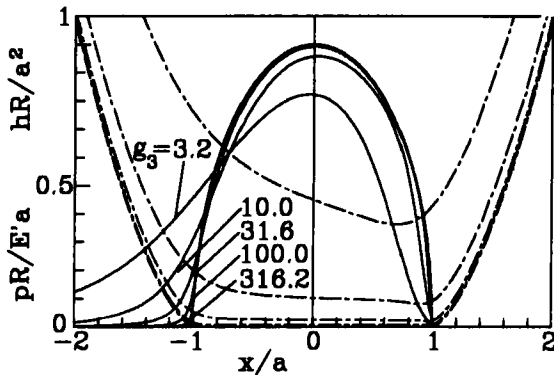


Fig. 1 Pressures and clearances in a lubricated Hertzian contact

seen that, as  $g_3$  increases, the pressure becomes increasing close to the dry contact distribution and that the extent of the inlet sweep reduces. For high values of  $g_3$  the maximum positive pressure gradient occurs in the inlet and the maximum negative gradient in the exit. Thus it is the inlet region that controls the mean clearance,  $h_m$ , and the exit region that determines the minimum clearance.

Under these highly deformed conditions, the inlet and exit can be treated in isolation [8,9] and it may be shown that:

$$kh_m \left[ \frac{E'}{\eta\mu k} \right]^{0.6} = 1.98$$

and that  $h_{min} = 0.795h_m$  [4]

where  $k$  is determined by the dry contact pressure adjacent to end of the conjunction where it has the form:

$$p = E'(kn)^{0.5} \tag{5}$$

where  $n$  is the distance from the end of the contact measured into the conjunction.

The effect of this may be seen in Fig. 2 where the minimum clearance is plotted against  $g_3$ . The two chained lines represent the clearances predicted for a rigid contact and those obtained from the inlet analysis of equation 4. It can be seen that, for Hertz contacts, there is a smooth transition from rigid behaviour to inlet controlled behaviour and that use of the appropriate limit expression will yield a good

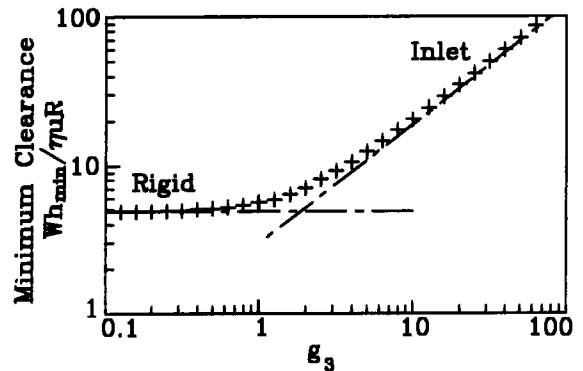


Fig. 2 Variation of minimum film thickness with  $g_3$  for Hertz contact

estimate of the minimum film thickness. It may also be noted that at the values of  $g_3$  typically found in elastomeric contacts, it is the inlet region that controls the contact's lubrication.

Elasticity theory dictates [8] that the pressure gradient at the ends of all contacts will be infinite unless there is a change in slope in the undeformed surfaces at that point. Thus inlet controlled behaviour will, potentially, be found in all contacts. Where the dry contact pressure gradient decreases uniformly from inlet to exit, behaviour of the general type shown above will be found. A typical example is the behaviour of O-ring seals, discussed later, where the clearance is determined solely by the pressure coefficient,  $k$ , at the inlet.

However, in some situations, the dry contact pressure distribution is more complex and this may alter the overall lubrication process.

### 2.2 Maximum pressure gradient control

The simplest modification of the inlet control is where the pressure gradient does not decrease uniformly from inlet to exit but shows a maximum part way through the contact. This situation is found in the lubrication of some elastomer lined surfaces. This contact problem has been widely examined, both theoretically and experimentally, [8,10-13] since it provides, perhaps, the most easily manufactured type of elastomeric conjunction. The dry contact pressure distribution is easily calculated, although the early, semi-analytical methods of Meijers [14] and Ablas and Kuipers [15] have been replaced by more accurate Fourier transform

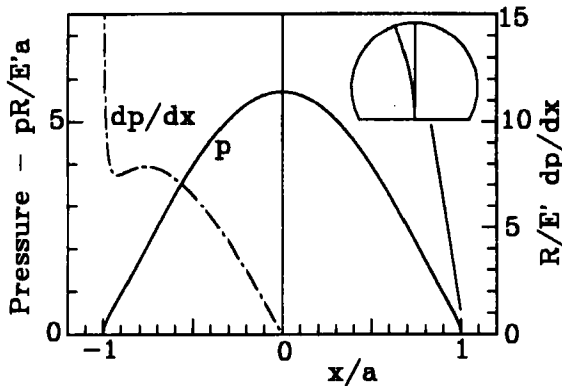


Fig. 3 Pressure between a cylinder and an elastomer layer on a rigid substrate,  $a/t = 5$ .

procedures [16]. Fig. 3 shows the pressure and pressure gradient for an elastomer layer with a semi-contact width of five times the layer thickness. Here, a maximum in the pressure gradient occurs about one quarter of the way from the inlet to the contact centre with a value of gradient close to  $8E'/R$ . It may also be noted that, at the ends of the contact, the pressure adopts the form given by equation 5 and that the pressure gradient becomes infinite.

The inlet analysis described in the previous section can be used to determine the clearance,  $h_m$ . From this the maximum pressure gradient in the inlet can be found using equation 1. For values of  $g_3$  above 250 this gradient is higher than the maximum in the dry contact profile. However, for lower values, the calculated gradient in the inlet becomes smaller than that in the dry contact profile. Under these conditions the inlet sweep will override the inlet. When this occurs the maximum dry contact pressure gradient controls the clearance and the inverse theory of equation (4) may be used to determine  $h_m$ . From this the other clearances may be obtained (except of course in the inlet and exit zones where the pressures are modified).

The type pressures and clearances that result are shown, for  $g_3 = 31.6$ , in Fig. 4a. At higher values of  $g_3$  the extent of the inlet sweep is reduced and eventually the position of the maximum pressure gradient moves from the flank of the dry contact profile back to the inlet, as shown for  $g_3 = 398$  in Fig. 4b. It may be noted that, because the extent of the exit restriction is small, the position of the most

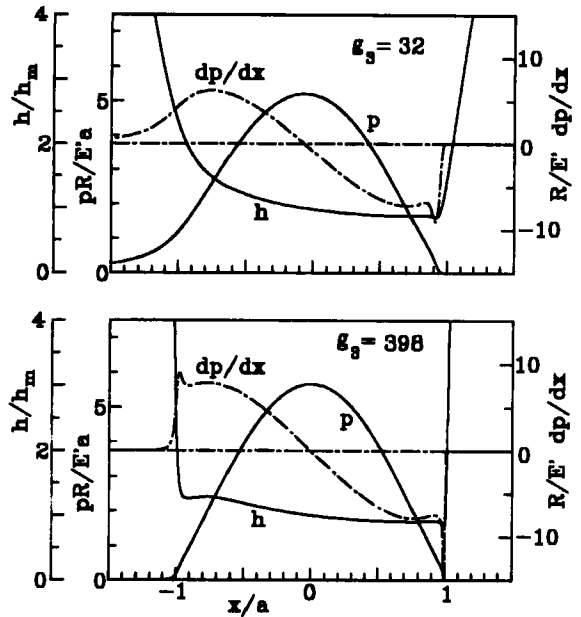


Fig. 4 Clearances in lubricated layer contact  
a)  $g_3 = 31.6$ , b)  $g_3 = 398$

negative pressure gradient occurs in the end section of the pressure curve for both values of  $g_3$ . Thus, for both values of  $g_3$ , the ratio of  $h_{min}$  to  $h_m$  is determined by the exit zone and not by the dry contact pressure gradient.

The overall behaviour of this conjunction is summarised in Fig. 5 where the minimum clearance is plotted against  $g_3$ . The three chained lines correspond to the clearances calculated assuming a) a rigid contact, b) the clearance to be determined by the maximum pressure gradient and c) the clearance to be determined by the inlet. The crosses represent

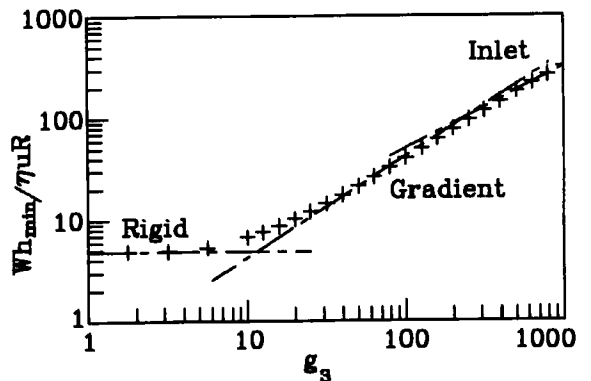


Fig. 5 Variation of minimum clearance with  $g_3$  for layered contact

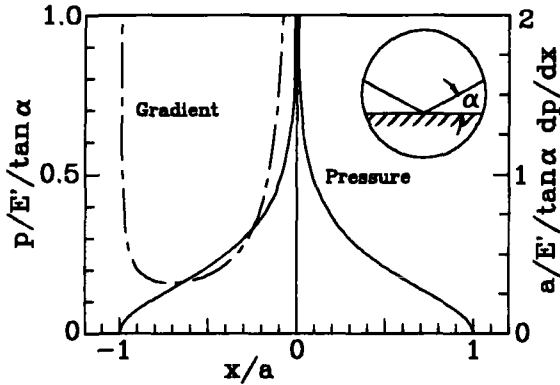


Fig. 6 Pressure between a rigid flat surface and an elastomer wedge

the results of individual multi-level solutions of the problem such as those shown in Fig. 4. It may be seen that the actual behaviour blends these limit curves and that good estimates of clearance can be obtained simply by taking the three limit lines and using these to construct a piecewise relationship between clearance and operating conditions.

### 2.3 Pressure singularities

As well as an infinite pressure gradient occurring at the inlet and exit, singularities can exist inside the contact. Where the elastomer surface has a sharp change in slope, as in the wedge shaped contact shown in Fig. 6, the pressure becomes infinite [17] at the centre of the wedge:

$$p = \frac{E' \tan \alpha}{2\pi} \cosh^{-1}(a/x) \quad (6)$$

If the pressure gradient is examined it may be seen that near the centre of the contact the gradient varies as  $x^{-1}$  while adjacent to the ends of the contact it varies as  $x^{-0.5}$ . As a result, as the elasticity parameter increases and the extent of any pressure sweep decreases, the pressure gradient at the centre becomes dominant and controls the clearances. Inverse theory then dictates the remaining clearances. High film thicknesses will form in front of the point of maximum pressure gradient and clearances close to  $h_{\min}$  will form behind it.

Fig. 7 shows a typical clearance profile for  $g_3 = 31.6$ . The elasticity parameter,  $g_3$ , is similar to that used in Hertz contacts and is defined by:

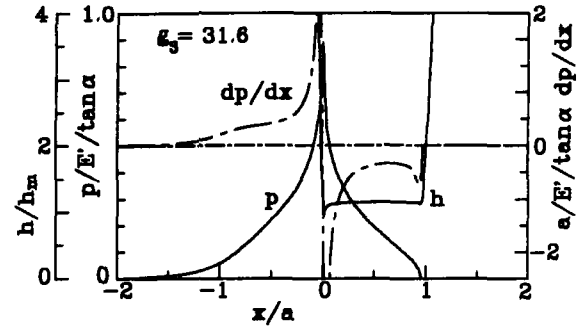


Fig. 7 Pressures and clearance under a lubricated wedge

$$g_3 = \left[ \frac{W^2 \tan \alpha}{\eta u a E'} \right]^{1/2} \quad (7)$$

In calculating the results the start of film formation has been taken a distance  $2a$  in front of the contact centre.

The minimum clearance occurs just after the centre of the contact at the point of maximum negative pressure gradient and there is another, smaller, restriction at the exit. At this value of  $g_3$  the inlet region has been completely smoothed with the pressure gradient increasing uniformly from the inlet to contact centre.

Fig. 8, curve a, summarises the relationship between minimum film thickness,  $h'$ , and  $g_3$  for this problem and it may be noted that, at high values of  $g_3$ , the clearance tends to a value close to 8.0. Noting that  $h'$  is given by:

$$h' = \frac{W h_{\min} \tan \alpha}{\eta u a} \quad (8)$$

and that the load per unit length on the contact is:

$$W = 0.5 E' a \tan \alpha \quad (9)$$

suggests that where there is a change in gradient of  $2\alpha$  in the slope of the contact, the discontinuity will generate a minimum clearance of:

$$h_{\min} = \frac{4 \eta u}{E' \tan^2 \alpha} \quad (10)$$

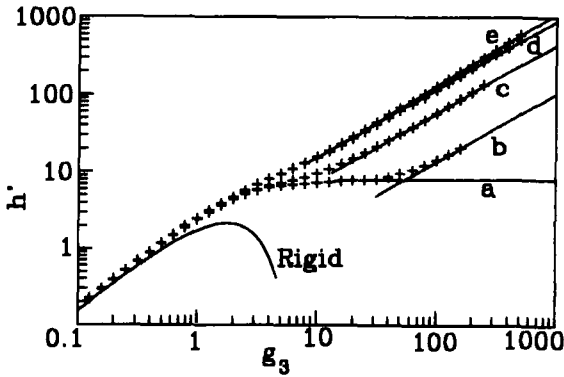


Fig. 8 Variation of clearance with  $g_3$  for wedge  
 a) sharp wedge  
 b) 0.05a tip radius  
 c) 0.1a tip radius  
 d) 0.25a tip radius  
 e) 0.25 tip radius smoothly blended to wedge

**2.4 Pressure gradient singularities**

The second location where a singularity in pressure gradient may occur is at a change in curvature of the conjunction. This is illustrated by curve a in Fig. 9 where the apex of the wedge has been replaced by an arc of a circle. (The pressure distributions are readily calculated using the analysis of Muskhelishvili [18] - or from equation 2.41 of ref. 17). The junction between the wedge and circle has been taken at  $x=0.25a$ . It may be seen that the pressure profile is rounded but that the gradient becomes infinite at the point where the curvature changes. In this case the gradient varies as  $\ln(x)$  from the discontinuity.

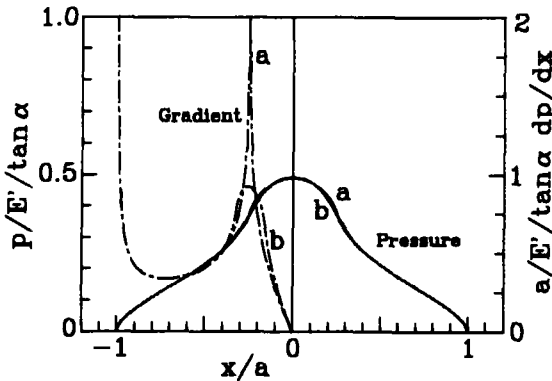


Fig. 9 Pressure distribution under a wedge with 0.25a tip radius  
 a) unsmoothed junction  
 b) smoothed junction

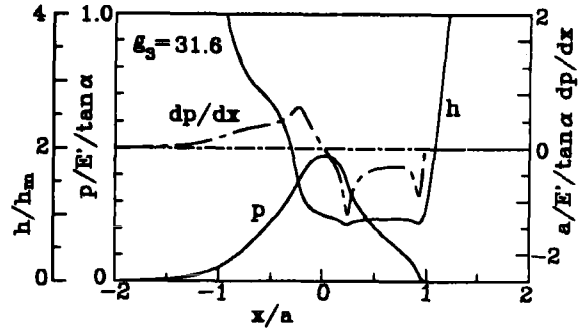


Fig. 10 Pressure and clearance distribution under a wedge with 0.25a tip radius

Fig. 10 shows the clearance distribution for the same operating conditions as the sharp wedge. The value of  $h_m$  is now determined by the curvature discontinuity with relatively large clearances in front of it and low clearances after. The minimum clearance occurs at the downstream change in curvature but a second minimum can be seen at the contact exit.

The effect of radiusing the wedge on the minimum film thickness can be seen in Fig. 8 where  $h'$  is plotted against  $g_3$  for three tip radii. The clearances follow the wedge results until the pressure sweep at the centre becomes smaller than the length of the tip and then diverge to curves b, c and d.

For comparison, in curve b in Fig. 9, the discontinuity in curvature has been removed by inserting a linear change in radius over a short length of the contact. This has little effect on the dry contact pressure distribution but has the effect of removing the gradient singularity and replacing it with a simple maximum in the pressure gradient curve. The value of the maximum is only weakly dependent on the length used for blending and gives rise to very similar clearances to those of the sharp change. Curve e in Fig. 8 shows minimum clearance for the blended profile, curve d for the unblended. It can be seen that the minimum clearance has changed by less than 10%.

In estimating the effect of curvature changes, therefore, it would seem sensible to replace the singularity by an averaged pressure gradient and to treat it as a point of maximum pressure gradient.

Finally, it may be noted that, at very high values of  $g_3$ , clearance control switches back to the inlet with the minimum film thickness given by:

$$h' = 4.5g_3^{0.8} \quad (11)$$

The transition occurs above the highest values of  $g_3$  plotted in Fig. 8 and, in order to avoid confusion, the limit curve for the inlet has been omitted.

### 2.5 Clearance calculation

In highly deformed, soft line contacts the clearance can be controlled by any one of the four types of point in the dry contact pressure gradient: the inlet to the conjunction, any step change in surface slope, any step change in surface curvature and any maximum in the pressure gradient. The latter is likely to occur where the surface curvature changes rapidly. The minimum film thickness may be calculated for each of these and where more than one exists the lowest calculated clearance will be the one that controls the conjunction.

## 3. DYNAMIC BEHAVIOUR

Although the above discussion has considered a wide range of different types of dry contact pressure distribution, in the great majority of contacts the clearance will be controlled by the inlet region.

If the Hertzian contact of Fig. 1 is considered, for a value of  $g_3$  of 100 - a value typical of many soft contacts, it may be seen that the pressure deviates from the dry contact distribution only in the very narrow inlet and exit zones. Under steady conditions the clearances are generated in the inlet zone, pass through the contact, being slightly reduced in transit, and emerge through the exit zone where a very localised restriction forms.

Although analysis of this type of contact is now most easily carried out using multi-level techniques, it is, perhaps, worth examining the earlier approach developed initially by Hirano [19,20].

### 3.1 Inverse analysis

Under the centre of the contact the pressures are closely defined and Reynolds' equation

$$\frac{\partial}{\partial x} \left[ \frac{h^3}{12\eta} \frac{\partial p}{\partial x} \right] + \frac{\partial}{\partial y} \left[ \frac{h^3}{12\eta} \frac{\partial p}{\partial y} \right] = u \frac{\partial h}{\partial x} + \frac{\partial h}{\partial t} \quad (12)$$

can be regarded as an equation with the clearance  $h$  as the unknown rather than its more conventional interpretation as an equation in  $p$ .

With this interpretation, equation 12 can be replaced by three ordinary differential equations

$$\frac{dx}{dt} = u - \frac{h^2}{4\eta} \frac{dp}{dx}$$

$$\frac{dy}{dt} = - \frac{h^2}{4\eta} \frac{dp}{dy}$$

and

$$\frac{dh}{dt} = \frac{h^3}{12\eta} \left[ \frac{d^2 p}{dx^2} + \frac{d^2 p}{dy^2} \right] \quad (13)$$

The first two equations define paths through the conjunction, the third defines the variation of clearance along those paths. These equations may be readily integrated to obtain the clearance distribution. It is, of course, necessary to know the clearance where any path enters the conjunction.

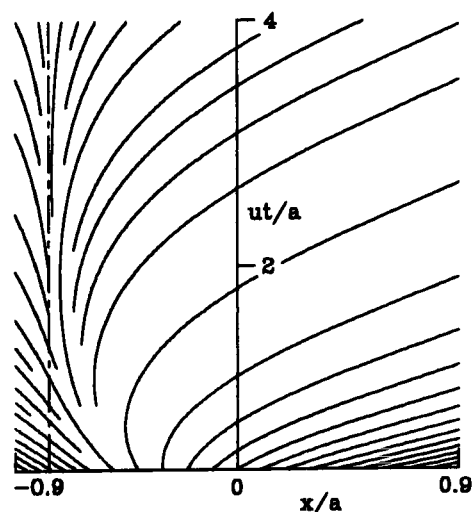


Fig. 11 Paths from inverse analysis for layer contact with  $b/t = 5$ . Large initial clearance.

In one dimensional contacts, for cases where the clearance is controlled by a maximum pressure gradient under the conjunction, solution is fairly straightforward. Figure 11 shows the paths, as a function of position and time in the lubrication of the layered contact shown in Fig. 3. The analysis starts with a high, uniform clearance in the contact and follows the formation of the steady state solution. Initially, the paths diverge from near the centre of the contact as fluid is squeezed out. Then, as steady state conditions are approached, the paths fan out from the position of maximum pressure gradient.

### 3.2 Inlet control

For inlet controlled contacts the behaviour is slightly more complex. Here, paths will generally originate in the inlet to the conjunction where the pressures deviate from the dry contact values. Similarly, the lowest clearances are likely to occur in the exit region. If Hirano's approach is to be followed it is necessary to separate the end regions from the bulk of the contact and to carry out full, dynamic EHL calculations there [21,22]. Clearances generated in the inlet region form the starting clearance for paths entering the centre of the conjunction. Similarly, the clearance of paths leaving the centre form the inner clearance of the exit region.

Because the EHL calculations are restricted to the very limited end regions, analysis tends to be rapid compared with multi-level solutions (factors of 1:100 are typical). However, the major reason for considering this approach is that it simplifies any interpretation of the results.

Figures 12 shows two examples of the paths calculated using this method, while Fig. 13 shows the variations of clearance. The first example is for an elastomer layer with a semi-contact width twice the layer depth. The contact is reciprocating sinusoidally with a maximum velocity  $u_0$ . The second is for an O-ring seal with 10% nip and a sealed pressure of  $0.1E'$  reciprocating with a constant entrainment velocity in each direction. In the first case the entrainment length swept during the oscillation ( $\int u dt$ ) is twice the full contact width, in the second case 0.85 of the full contact width. To aid interpretation the paths in Fig. 12 have been extended from the central region into the inlet and

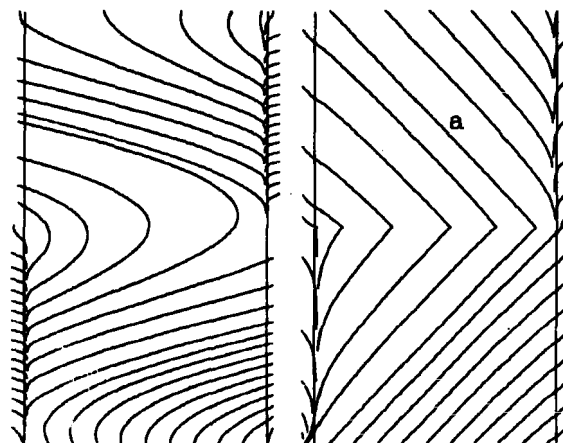


Fig. 12 Paths from inverse analysis  
 a) layer contact,  $a/t = 2$ ,  $u = u_0 \sin(u_0 t / 4a)$   
 b) O-ring,  $P_{\text{seal}} = 0.1E'$ , entrainment distance =  $1.7a$

exit zones. The vertical lines in the figure represent the boundaries of the dry contact. The end zones, which vary in size through the calculation, occupy an equal length each side of these lines.

It may be seen that the paths originate close to the end of the conjunction and once inside the contact move at a speed close to the entraining velocity. What deviations there are are limited to the end zones.

The clearances in Fig. 13 are in the form of isometric plots and show the clearance distribution at a number of equi-spaced intervals throughout a cycle.

Figure 13a shows the sinusoidal oscillation. At the start entrainment is changing from the right of the contact to the left. Under the majority of the contact clearances are high, having been generated at a point in the cycle where the entrainment velocity was large. On the right, lower clearances occur due to the fall in entrainment velocity towards the end of the cycle while on the left a deep exit restriction is visible.

As entrainment occurs on the left, low clearances are initially generated because of the low velocity. However, the clearances inside the conjunction are large and are squeezed out by the adverse pressure gradient. The results is a very sharp step in film thickness as the two meet. This step is convected through the conjunction at close to the entraining velocity and is followed by higher

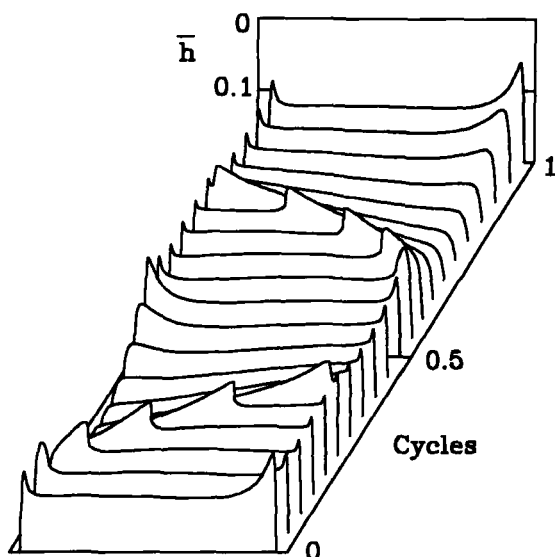


Fig. 13a Clearances from inverse analysis,

$$\text{layer contact, } \bar{h} = h \left[ \frac{E'}{\eta\mu_0 R} \right]^{0.5}$$

clearances. Then, at the end of the half cycle an inlet restriction begins to form because of the falling entrainment velocity and eventually the process repeats.

Figure 13b shows the clearances under the O-ring. On the left of the conjunction clearances are generated at constant entrainment velocity and tend to vary little with time. These penetrate most of the way through the conjunction before the velocity reverses and they then return to the left of the conjunction forming a nearly uniform exit restriction. Similar behaviour occurs on the right of the contact. It may be noted that, with the sealed pressure on the left, larger clearances are generated there than on the right because of the lower value of the inlet coefficient,  $k$ .

However, a small section of the paths never leave the conjunction, sweeping back and forth inside it. Path a in Fig 12 is typical. Here, the clearances fall uniformly with time and the values shown are the result of 20 oscillations after steady state entrainment from the right. The resulting band of low clearance is clearly visible in the figure and, if the oscillation pattern persists, will result in the collapse of the fluid film - behaviour demonstrated experimentally by Hirano [23].

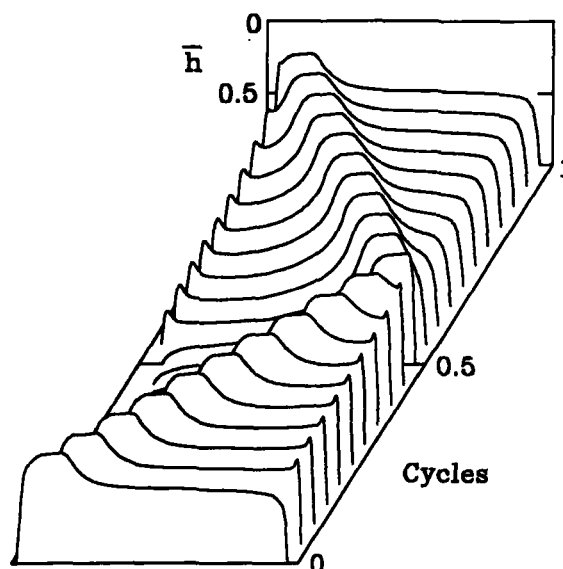


Fig. 13b Clearances from inverse analysis

$$\text{O-ring, } \bar{h} = h \left[ \frac{E'}{12\eta\mu r} \right]^{0.5}$$

#### 4. ROUGHNESS EFFECTS

The effect of surface roughness in soft contacts is somewhat more straightforward than in hard conjunctions where the effect of piezo-viscosity complicates the behaviour.

It is not possible to include a full discussion here but it is, perhaps, worth mentioning the most straightforward situation. A large number of soft contacts consist of a relatively smooth, hard surface sliding over a rough elastomer surface. Typical, here, are shaft seals.

##### 4.1 Small amplitude roughness

Consider an elastomer surface with a sinusoidal surface roughness of low amplitude as shown in Fig. 14. It is assumed that the wavelength is small compared with the contact width and that, over the region being considered, the mean clearance is uniform and equal to  $hm$ . This roughness will generate a nearly sinusoidal pressure ripple that will, in turn, distort the surfaces and change the phase and amplitude of the surface profile. Following Greenwood and Johnsons' analysis [24], it will be assumed that an initial surface roughness,



$A\cos(\lambda x)$  is changed to  $a\cos(\lambda x - \varphi)$  under the centre of the conjunction. Then, since the mean clearance at this point in the contact is assumed to be close to  $h_m$ , equation 1 can be integrated to obtain the pressure ripple:

$$\Delta P = \frac{12\eta u}{h_m^3 \lambda} a \sin(\lambda x - \varphi) \quad (14)$$

This pressure ripple will distort the surface by an amount,  $\delta$ , where  $\delta$  is given [17] by:

$$\delta = \frac{12\eta u}{h_m^3 \lambda} \frac{4}{\lambda E'} a \sin(\lambda x - \varphi) \quad (15)$$

Then, since the final surface roughness must be the sum of the initial roughness and the distortion:

$$A \cos(\lambda x) + \frac{48\eta u}{h_m^3 E' \lambda^2} a \sin(\lambda x - \varphi) = a \cos(\lambda x - \varphi)$$

or  $a = A \cos \psi$

$$\text{where } \tan \psi = \frac{48\eta u}{h_m^3 E' \lambda^2} \quad (16)$$

Thus, for long wavelength roughnesses where  $\lambda$  is small and the angle  $\psi$  is close to  $\pi/2$ , the roughness will be almost completely smoothed. For short wavelengths where  $\lambda$  is large the roughness will remain unchanged.

Where the clearance under the contact is controlled by the inlet, equation 16 can be simplified. Noting [9] that:

$$h_m = 1.982 \left[ \frac{\eta u}{E'} \right]^{0.6} k^{-0.4} \quad (17)$$

and that the entrainment length,  $e$ , defined here as twice the distance from the end of the dry contact to the point of inflection in the EHL pressure distribution, is given by [9]:

$$e = 1.98 \left[ \frac{\eta u}{E'} \right]^{0.4} k^{-0.6} \quad (15)$$

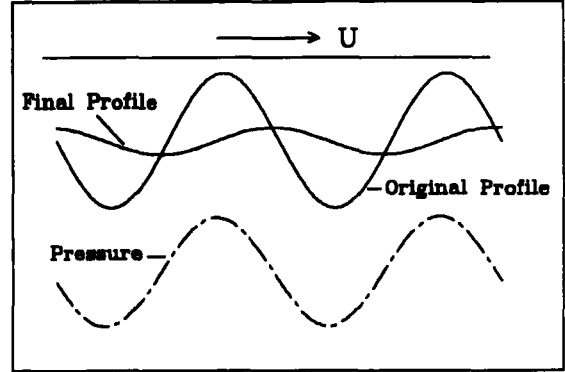


Fig. 14 Attenuation of sinusoidal surface roughness under the centre of the conjunction in a sliding contact.

$$\text{gives } \tan \psi = 0.612 \left[ \frac{L}{e} \right]^2 \quad (16)$$

where  $L$  is the wavelength of the surface roughness.

The ratio of the length of the inlet to the roughness wavelength, therefore, appears to control the extent to which the roughness is attenuated. Roughnesses of longer wavelength will be smoothed while roughnesses of shorter wavelength will be virtually unchanged in height.

#### 4.2 Large amplitude behaviour

While the above analysis gives some information about the behaviour of rough contacts it is limited to very low amplitudes of residual roughness. Actual behaviour is more complex. Figure 15 shows the variation of the clearance at the centre of the conjunction,  $h_c$ , and in the exit,  $h_{\min}$ , with roughness wavelength. A Hertzian contact has been chosen with a value of  $g_3$  of 31.6. The initial amplitude of the roughness is equal to  $0.5h_m$ .

The left hand vertical dashed line shows the position where  $\tan \psi$  is equal to 1. The right hand dashed line shows the equivalent location for the exit. This has been calculated using an exit length equal to the distance from the minimum clearance to the point of cavitation. The horizontal chained lines show  $h_c/h_m$  and  $h_{\min}/h_m$  for smooth contacts (1 and 0.795 respectively) while the curved dotted line presents the estimate of  $h_c$  obtained using the small amplitude analysis. Finally, the horizontal dashed lines represent the results of an EHL analysis with

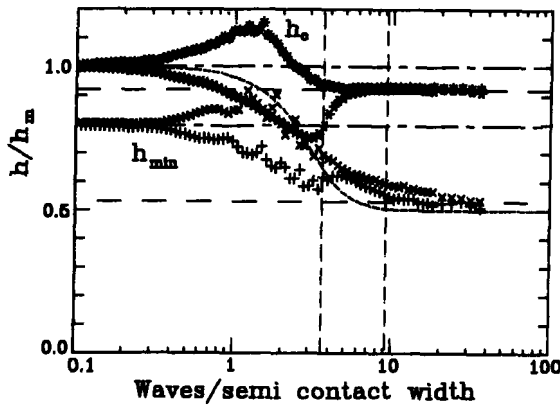


Fig. 15 Variation of central and minimum clearance with roughness wavelength and phase.

$g_3 = 31.6$ ,  $A/h_m = 0.5$ .

vertical dashed lines -

left -  $L/e = 1.3$ , right -  $L/e_{\text{exit}} = 1.3$

chained lines - smooth contact solution

dashed lines - averaged flow solution

dotted curve - small amplitude prediction,  $h_m$

symbols - multi-level analysis

averaged flow parameters obtained from a stochastic analysis [25-27].

Eight phases of the initial surface roughness relative to the dry contact were investigated for each wavelength and the symbols represent the highest and lowest values found. Again, these detailed results were obtained from a multi-level solution.

Considering, first, the central clearance (i.e. the lowest clearance near the centre of the conjunction); for wavelengths longer than the contact width the clearance may be either increased or reduced depending on the phase of the roughness. This appears to be simply a result of the curvature change of the conjunction and the consequent alteration in the dry contact profile. Then, as the wavelength becomes shorter than the contact, the minimum clearance reduces. The phase of the roughness still has a large effect. Finally, as the wavelength becomes shorter than the inlet length the central clearance converges rapidly on the averaged flow solution and phase becomes unimportant.

The minimum clearance follows a roughly similar pattern, with slightly more variation in the clearances since the phasing of the roughness at both inlet and exit are significant. Final

convergence on the averaged flow solution is also delayed until the wavelength is short compared with the exit length.

Although the behaviour of the actual contact is more complex than that predicted by the small amplitude analysis it is clear that the general predictions are valid. Roughnesses with wavelengths longer than the inlet are smoothed (but may still affect the clearance by altering the dry contact pressure distribution). Roughnesses with shorter wavelengths enter the contact unsmoothed. Their effect on the contact may then be readily calculated using the average flow coefficient model.

Broadly similar behaviour is found for longitudinal and two dimensional roughness distributions and it would appear possible to use the inlet length as a measure of the attenuation, incorporating longer wavelength roughnesses into the dry contact analysis and treating shorter wavelengths by an averaged flow model.

## 6. CONCLUSIONS

Soft contacts are typically characterised by the large magnitude of the elastic deformation relative to any film thickness. This means that, over much of the contact, the pressures will remain close to those obtaining under dry, frictionless conditions.

The large magnitude of the deformation means that most conjunctions are non-Hertzian. Clearances are, however, controlled by the dry contact pressure distribution and this makes it possible to estimate the likely behaviour of any contact from an elasticity analysis. For line contacts, the clearance may be controlled by the inlet to the conjunction, any maximum in the dry contact pressure gradient or by singularities in the pressure or pressure gradient distribution.

However, in most contacts the clearance will be determined by the inlet to (and exit from) the conjunction. Thus it is the narrow region at the ends of line contacts (and around the boundaries of two dimensional contacts) that determine the contacts' behaviour. The remainder of the conjunction simply transports the clearances generated at the inlet. The transport velocity is close to that of entrainment and there are only slight changes in clearance during the passage.

Additionally, the narrow inlet region appears to act as a filter smoothing out roughnesses with

and that the entrainment length,  $e$ , defined here as twice the distance from the end of the dry contact to the point of inflection in the EHL pressure distribution, is given by [9]:

$$e = 1.98 \left[ \frac{\eta \mu}{E'} \right]^{0.4} k^{-0.6} \quad (15)$$

$$\text{gives } \tan \psi = 0.612 \left[ \frac{L}{e} \right]^2 \quad (16)$$

where  $L$  is the wavelength of the surface roughness.

The ratio of the length of the inlet to the roughness wavelength, therefore, appears to control the extent to which the roughness is attenuated. Roughnesses of longer wavelength will be smoothed while roughnesses of shorter wavelength will be virtually unchanged in height.

#### 4.2 Large amplitude behaviour

While the above analysis gives some information about the behaviour of rough contacts it is limited to very low amplitudes of residual roughness. Actual behaviour is more complex. Figure 15 shows the variation of the clearance at the centre of the conjunction,  $h_c$ , and in the exit,  $h_{\min}$ , with roughness wavelength. A Hertzian contact has been chosen with a value of  $g_3$  of 31.6. The initial amplitude of the roughness is equal to  $0.5h_m$ .

The left hand vertical dashed line shows the position where  $\tan \psi$  is equal to 1. The right hand dashed line shows the equivalent location for the exit. This has been calculated using an exit length equal to the distance from the minimum clearance to the point of cavitation. The horizontal chained lines show  $h_c/h_m$  and  $h_{\min}/h_m$  for smooth contacts (1 and 0.795 respectively) while the curved dotted line presents the estimate of  $h_c$  obtained using the small amplitude analysis. Finally, the horizontal dashed lines represent the results of an EHL analysis with averaged flow parameters obtained from a stochastic analysis [25-27].

Eight phases of the initial surface roughness relative to the dry contact were investigated for each wavelength and the symbols represent the highest and lowest values found. Again, these detailed results were obtained from a multi-level solution.

Considering, first, the central clearance (i.e. the lowest clearance near the centre of the conjunction):

for wavelengths longer than the contact width the clearance may be either increased or reduced depending on the phase of the roughness. This appears to be simply a result of the curvature change of the conjunction and the consequent alteration in the dry contact profile. Then, as the wavelength becomes shorter than the contact, the minimum clearance reduces. The phase of the roughness still has a large effect. Finally, as the wavelength becomes shorter than the inlet length the central clearance converges rapidly on the averaged flow solution and phase becomes unimportant.

The minimum clearance follows a roughly similar pattern, with slightly more variation in the clearances since the phasing of the roughness at both inlet and exit are significant. Final convergence on the averaged flow solution is also delayed until the wavelength is short compared with the exit length.

Although the behaviour of the actual contact is more complex than that predicted by the small amplitude analysis it is clear that the general predictions are valid. Roughnesses with wavelengths longer than the inlet are smoothed (but may still affect the clearance by altering the dry contact pressure distribution). Roughnesses with shorter wavelengths enter the contact unsmoothed. Their effect on the contact may then be readily calculated using the average flow coefficient model.

Broadly similar behaviour is found for longitudinal and two dimensional roughness distributions and it would appear possible to use the inlet length as a measure of the attenuation, incorporating longer wavelength roughnesses into the dry contact analysis and treating shorter wavelengths by an averaged flow model.

## 6. CONCLUSIONS

Soft contacts are typically characterised by the large magnitude of the elastic deformation relative to any film thickness. This means that, over much of the contact, the pressures will remain close to those obtaining under dry, frictionless conditions.

The large magnitude of the deformation means that most conjunctions are non-Hertzian. Clearances are, however, controlled by the dry contact pressure distribution and this makes it possible to estimate the likely behaviour of any

longer wavelengths and leaving roughnesses with shorter wavelengths unchanged.

## REFERENCES

- 1 Strozzi, A. Static stresses in an unpressurised, rounded, rectangular seal. *ASLE Trans.*, 29 (1986) 558.
- 2 Lindgren, H. Pressure distribution in scraper ring contacts. *Wear*, 115 (1987) 31.
- 3 Kanters, A.F.C. On the calculation of leakage and friction of reciprocating elastomeric seals. Proefschrift, Technische Universiteit Eindhoven, 1990.
- 4 Blok, H. Inverse problems in hydrodynamic lubrication and design directives for lubricated, flexible surfaces. *Proc Int Symp. Lubr and Wear*. Eds Muster, D. & Sternlicht, B., Houston (1963) 9.
- 5 Dowson, D. & Higginson, G.R. A numerical solution to the elasto-hydrodynamic problem. *J. Mech. Engng Sci.*, 1 (1959) 6.
- 6 Herrebrugh, K. Solving the incompressible and isothermal problem in elastohydrodynamic lubrication models. *J. Lubr. Tech.*, 106 (1968) 262.
- 7 Johnson, K.L. Regimes of Elastohydrodynamic lubrication. *J. Mech. Engng Sci.*, 12 (1970) 9.
- 8 Hooke, C.J. & O'Donoghue, J.P. Elastohydrodynamic lubrication of soft, highly deformed contacts. *J. Mech. Engng Sci.*, 14 (1972) 34.
- 9 Hooke, C.J. The Elastohydrodynamic lubrication of heavily loaded contacts. *J. Mech. Engng Sci.*, 19 (1977) 149.
- 10 Gupta, P.K. On the heavily loaded elastohydrodynamic contacts of layered solids. *J. Lubr. Tech.*, 114 (1976) 367.
- 11 Cudworth, C.J. & Mennie, G.J. Elastomer-lined bearings: an analysis of a heavily loaded cylinder sliding on a compliant layer. *Wear* 67 (1981) .
- 12 Jaffar, M.J. Two-dimensional elastohydrodynamic lubrication of elastic strips. *Wear* 139 (1990) .
- 13 Varnam, C.J. & Hooke, C.J. Non-Hertzian elastohydrodynamic contacts: An experimental investigation. *J. Mech. Engng Sci.*, 19 (1977) .
- 14 Meijers, P. The contact problem of a rigid cylinder on an elastic layer. *Appl. Sci. Res.* 18 (1968) 353.
- 15 Alblas, J.B. & Kuipers, M. On the two-dimensional problem of a cylindrical stamp pressed into a thin elastic layer. *Acta Mechanica*, 9 (1970) 292.
- 16 Gladwell, G.M.L. On some unbounded contact problems in plane elasticity theory. *J. Appl. Mech.* 43 (1976) 263.
- 17 Johnson, K.L. *Contact Mechanics*. Cambridge University Press, 1985.
- 18 Muskhelishvili, N.I. Some basic problems of the mathematical theory of elasticity. (English translation Radok, J.R.M.)P. Noordhoff, 1963.
- 19 Hirano, F. Dynamic inverse problems in hydrodynamic lubrication. *Proc. Third Int. Conf. on Fluid Sealing*, 1967. B.H.R.A. Paper F1.
- 20 Hirano, F. & Kaneta, M. Dynamic behavior of flexible seals in reciprocating motion. *Proc. Fourth Int. Conf. on Fluid Sealing*, 1969. B.H.R.A. 11.
- 21 Hooke, C.J. The elastohydrodynamic lubrication of soft, highly deformed contacts under conditions of non-uniform motion. *J. of Tribology*, 108 (1986).
- 22 Hooke, C.J. The calculation of film thickness in soft, highly deformed contacts under dynamic conditions. *Proc. Instn Mech. Engrs.* 201 (1987) 171.
- 23 Hirano, F. & Kaneta, M. Elastohydrodynamic condition in elliptic contact in reciprocating motion. *Proc. Sixth Int. Conf. on Fluid Sealing*, (1973) B.H.R.A. 11.
- 24 Greenwood, J.A. & Johnson, K.L.. The behaviour of transverse roughness in sliding elastohydrodynamic contacts. *Wear*, 153 (1992) 107.
- 25 Tzeng, S.T & Saibel, E. Surface roughness effect on slider bearing lubrication. *ASLE Trans.* 10 (1967) 334.
- 26 Christensen, H. & Tonder, K. Hydrodynamic lubrication of rough bearing surfaces of finite width. *J of Lubr. Tech.*, 93 (1971) 324.
- 27 Patir, N. & Cheng, H.S. An average flow model for determining effects of three-dimensional roughness on partial hydrodynamic lubrication. *J of Lubr. Tech.*, 100 (1978) 12.

## Film thickness measurements in elastohydrodynamically-lubricated elastomeric contacts

S.A. Johnson<sup>a</sup>, M.J. Adams<sup>a</sup>, A. Arvanitaki<sup>b†</sup> and B.J. Briscoe<sup>b</sup>

<sup>a</sup>Unilever Research Port Sunlight Laboratory,  
Quarry Road East, Bebington, Wirral, Merseyside, L63 3JW, United Kingdom.

<sup>b</sup>Dept. of Chemical Engineering and Chemical Technology, Imperial College of Science, Technology and Medicine,  
Prince Consort Road, London, SW7 2BY, United Kingdom.

This paper reports measurements of the thick (1 - 100  $\mu\text{m}$ ) fluid films generated by isoviscous elastohydrodynamic lubrication (IEHL) in elastomer/glass contacts operating at relatively high sliding velocities and with relatively high viscosity fluids. These measurements were made using an optical displacement transducer focused through the glass onto the centre of the elastomer/glass contact. Close agreement is demonstrated between the experimental results and predictions generated from established IEHL theories, which have been verified previously only for data from experiments where the film thicknesses were much thinner.

### 1. INTRODUCTION

Camera-based white-light interferometry has become a popular method for measuring the thickness of EH films in the regime 0.2 - 1.5  $\mu\text{m}$  when at least one of the contacting bodies is flat and transparent [1]. The most important reason for this is that the central film thicknesses generated in non-conformal contacts are often within this range. As a consequence, white light produces vividly-coloured Newton's rings that can be readily interpreted as film thickness contours. A second reason for the popularity of the technique is that it is inherently insensitive to any movement of the whole contact pair normal to the contact plane (resulting from mechanical and thermal disturbances).

Monochromatic light from a filtered mercury or tungsten discharge lamp also produces Newton's rings, and has advantages for profiling EH films greater than about 1  $\mu\text{m}$  thick. This is because the fringes have greater contrast than those produced with white light [2,3]. Laser interferometry can also be used to quantify the thickness of fluid films but, as with using filtered light from discharge lamps, absolute thickness measurements by fringe counting can be difficult if a suitable datum (most commonly the first fringe) is not conveniently available [4].

Using laser interferometry, Schlesinger *et al.* [5] have demonstrated that measuring the thinning of draining films that are initially greater than 500  $\mu\text{m}$  thick is possible. Besides the problems with establishing the zero-thickness datum when using monochromatic light interferometry, the film thickness information in the 0.2 - 1.5  $\mu\text{m}$  region is less detailed than that obtainable with white light [6,7].

For films much thinner than about 0.2  $\mu\text{m}$ , conventional white light interferometry becomes inappropriate. Spikes and his co-workers [8] have developed a modified technique to overcome this limitation. In this technique, a spacer layer is deposited on the surface of the flat transparent body. This produces a composite structure that does give coloured interference patterns for fluid films substantially less thick than visible optical wavelengths. In fact, it has been demonstrated that the method can be used to measure films as thin as 1 nm [9]. It is also possible to determine central film thicknesses down to about 10 nm using monochromatic laser light. This is done by measuring the light intensity relative to the first dark and light fringe [10]. However, this method is not as precise or convenient as that developed by Spikes and his colleagues.

---

<sup>†</sup> Current address is P.D. Papoutsanis S.A.I.C, Athens, Greece.

Once the central film thicknesses become greater than about  $1.5\ \mu\text{m}$ , interferometry is a less convenient technique because of the zero datum problem and the complexities of fringe counting. However, displacement measurements relative to a remote fixed point become more practical. In this paper, the development of such a method is described that enables the quantification of central film thicknesses in the range  $1 - 100\ \mu\text{m}$ . This uses a commercial optical displacement transducer and the method developed has been applied to an investigation of the films generated in sliding glass/elastomer contacts at relatively high sliding velocities in the presence of relatively high viscosity fluids.

The displacement transducer is of a type commonly employed for non-contact surface topography measurements. A similar device and technique has previously been used to measure the real area of contact between a rough elastomer and a smooth glass plate under both dry [11] and squeeze film conditions [12]. The present study has extended the use of the method to the measurement of the fluid film thickness generated in sliding contacts.

The experimental data are compared with those calculated using established IEHL solutions [10,13], and implications for the tractions in such contacts are discussed.

## 2. EXPERIMENTAL

### 2.1. Apparatus

Figure 1 shows a schematic diagram of the experimental apparatus. A twin-lapped low thermal expansion borosilicate glass disc (100 mm diameter and 6 mm thick) was drilled centrally and mounted vertically on a commercial air-bearing spindle (M107-42, Westwind Air Bearings, Poole, U.K.). This was rotated by an induction motor powered through an inverter drive (CDS 150, Imo Precision Controls, London, U.K.) which enabled effective rotational speed control in the range  $1 - 50\ \text{Hz}$ .

The laser displacement transducer (Laser Stylus RM 600 LS10, Rodenstock, Munich, Germany) was mounted so as to focus through the glass disc and onto the elastomeric specimen. This device operates in the near-infrared at  $780\ \text{nm}$ , gives a spot size of about  $1.5\ \mu\text{m}$  in diameter on the measured surface, has a distance resolution of  $1\ \text{nm}$  and an operational range of  $\pm 400\ \mu\text{m}$ . The 'stand-off' distance between the

end of the transducer and the measured surface is about  $10\ \text{mm}$ , in air, and the full included cone angle of the focused beam is approximately  $47^\circ$ . This transducer is an example of an 'optical follower' that utilises auto-focusing optics, derived from compact disc technology, to 'lock-onto' an interface and to measure its displacement relative to an internal reference position; such devices are described in some detail by Whitehouse [14] and Visscher [15]. In addition to the measurement of film thickness, this device was used to evaluate the 'runout' of the rotating disc ( $\pm 2\ \mu\text{m}$ ), the inherent stability of the optical path ( $0.5\ \mu\text{m}$  over several minutes), and the disc rotational speed (from the frequency of runout-induced displacement oscillations).

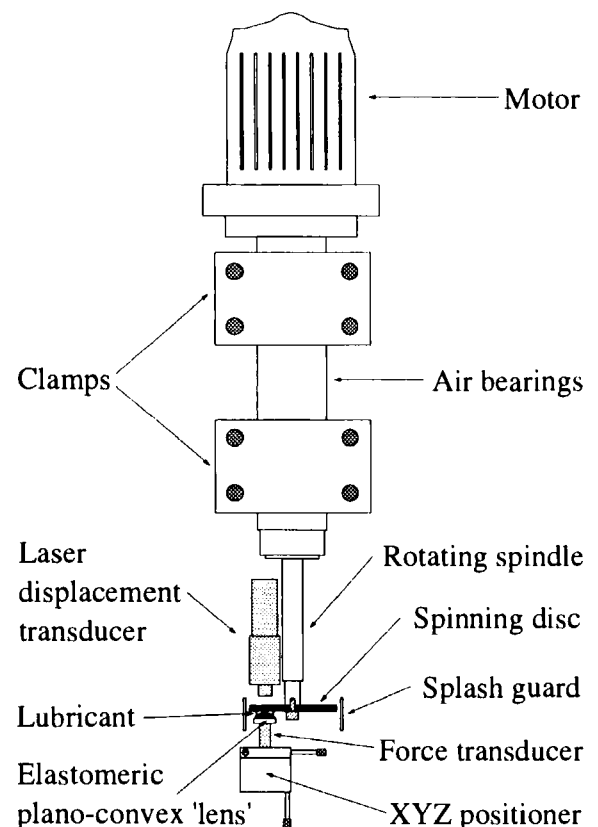


**Figure 1.** A plan view of the spinning disc apparatus. The air bearing spindle, the displacement transducer and the XYZ positioner were all firmly clamped to an optical table.

## 2.2. Materials

The elastomeric specimens were prepared using a two part, fast-setting silicone liquid (Silflo, J&S Davis, Potters Bar, U.K.) used at a mixing ratio of 1:50. This material is commercially used as a dental impression material. Specimens were usually cast between a concave glass lens (with a radius of curvature,  $R$ , of 9.4 mm) and a small glass window in order to produce optically-smooth plano-convex elastomeric specimens. Some of the silicone was cast similarly into a concave cylindrical glass lens to produce hemicylindrical elastomeric specimens. After the elastomer had cured, the window on which the specimen was attached was glued to a bolt to act as a stub. This was then used to mount the elastomer in close proximity to the glass disc, and within the optical capture distance of the laser probe. The elastic modulus of the elastomer was measured to be 1.5 MPa, which represents an average value obtained from a simple Hertzian analysis of a wide range of low strain-rate, sphere against flat, force/displacement curves.

Silicone oils (Dow Corning 200 fluids, Hopkin & Williams, Chadwell Heath, U.K., and Fluka Chemicals, Gillingham, U.K.) of viscosities between 12 and 12200 mPas were used as lubricants.

## 2.3. Measurement procedures

The elastomeric specimens were positioned using manual micrometer-driven translation stages. The most important of these moved the elastomer perpendicular to the plane of the disc. Once in contact, further motion of this stage caused deformation of the specimen and a finite normal load at the contact. This load was monitored by a piezoelectric force transducer (9311A, Kistler Instruments Ltd., Hartley Wintney, U.K.). The radial distance,  $r$ , between the centre of the elastomer/glass contact and the centre of the disc was between 29 - 40 mm, a range governed by both the size of the disc and the diameter of the displacement transducer. This, in combination with the spindle rotational velocity range, allowed the imposition of linear sliding velocities at the contact of between about 0.02 and 12 m/s.

Lubricants were continually 'drip-fed' to the contact using either a peristaltic pump or by gravity from a reservoir. Lubricant was directed to the front of the contact region by using the outside of a hypodermic needle angled at about 45° to the horizontal. A cylindrical splash guard was placed

around the disc to both collect excess lubricant and to prevent fluid from contaminating the unlubricated side of the disc.

Initially, the elastomeric specimen was aligned such that the displacement transducer was focused onto the centre of the contact region. This was most easily accomplished for the glass/elastomer contact in air, where there was a large reduction in the light intensity reflected from within the contact circle. Typically, 12, 5, 5 and 4 % of the incident intensity was reflected back through the transducer's optics from the air/elastomer, glass/elastomer, silicone oil/elastomer and air/glass interfaces respectively. Reflection from the glass/oil or glass/water interfaces was too low for the transducer to lock-onto, and, indeed, the current method relies on the effectiveness of this refractive index matching in order for fluid film thickness measurements to be made.

A calibration curve between the measured 'optical',  $h_o$ , and actual lubricant film thicknesses,  $h$ , was obtained using one of the translation stages to vary the gap between the elastomer and the stationary glass disc over a range of 0 - 100  $\mu\text{m}$  in a controlled manner ( $\pm 1 \mu\text{m}$ ). For silicone fluids, the calibration was found to be linear and such that  $h = 1.66h_o$ .

## 3. IEHL FILM THICKNESS SOLUTIONS

Hamrock and Dowson [13,16] were the first workers to generate numerical solutions for the IEH film thickness profiles generated in smooth point contacts and Newtonian fluids. Expressions for both the central and minimum film thicknesses,  $h_c$  and  $h_{min}$  respectively, were derived for the case of elliptical contact geometries where the direction of motion coincided with the minor axis of the ellipse. The expression these workers give for the minimum film thickness, which is located either on the centre-line or in the side lobes of the contact [13,17], is

$$H_{min} = 7.43 M^{0.65} N^{-0.21} (1 - 0.85 e^{-0.31k}) \quad (1)$$

where  $H_{min}$ ,  $M$  and  $N$  are dimensionless groups and  $k$  is the contact ellipticity.  $H_{min}$  is the dimensionless minimum contact film thickness given by

$$H_{min} = \frac{h_{min}}{R_x} \quad (2)$$

where  $h_{min}$  is the actual minimum film thickness towards the rear of the contact, and  $R_x$  is the effective radius of curvature in the direction of motion,  $x$ , which is given by

$$\frac{1}{R_x} = \frac{1}{r_{ax}} + \frac{1}{r_{bx}} \quad (3)$$

where  $r_{ax}$  and  $r_{bx}$  are the radii of curvature of the two contacting bodies,  $a$  and  $b$ , in the direction of motion.  $M$  is a dimensionless velocity parameter given by

$$M = \frac{\eta U}{E' R_x} \quad (4)$$

where  $\eta$  is the shear viscosity of the lubricant in the inlet zone of the contact (as distinct to that within the contact which may be different due to non-Newtonian behaviour at the higher shear rates),  $U$  is the mean surface velocity (i.e. the entrainment velocity) in the direction of motion and is given by

$$U = \frac{u_a + u_b}{2} \quad (5)$$

where  $u_a$  and  $u_b$  are the absolute surface velocities of the two contacting bodies in the direction of motion, and  $E'$  is the effective elastic modulus given by

$$\frac{1}{E'} = \frac{1 - \nu_a^2}{2E_a} + \frac{1 - \nu_b^2}{2E_b} \quad (6)$$

where  $E_a$  and  $E_b$  are the elastic moduli, and  $\nu_a$  and  $\nu_b$  are the Poisson's ratios of the two contacting bodies.  $N$  is a dimensionless load parameter given by

$$N = \frac{W}{E' R_x^2} \quad (7)$$

where  $W$  is the applied load.  $k$  represents the ratio between the semi-major and semi-minor axes of the contact ellipse. The following expression is valid for  $0 < k < 20$ :

$$k = \left( \frac{R_y}{R_x} \right)^{2/\pi} \quad (8)$$

where  $R_y$  is the effective radius of curvature in a direction,  $y$ , transverse to the direction of motion and is given by

$$\frac{1}{R_y} = \frac{1}{r_{ay}} + \frac{1}{r_{by}} \quad (9)$$

Hamrock and Dowson [13,16] also give the following expression for the dimensionless and actual central film thicknesses,  $H_c$  and  $h_c$  respectively:

$$H_c = \frac{h_c}{R_x} = 7.32 M^{0.64} N^{-0.22} (1 - 0.72 e^{-0.28k}) \quad (10)$$

These equations enable film thickness calculations to be made for any rolling or sliding non-conformal circular or elliptical contact (where the direction of motion coincides with the minor axis of the ellipse) involving smooth polymers or elastomers in the presence of excess Newtonian lubricants.

In previously reported studies [18,19] we used an earlier equation for the minimum film thickness given by Roberts and Tabor [10], which has the following form:

$$h_{min} = 0.79 (\eta V)^{0.6} R^{0.6} E^{-0.4} \left( \frac{W}{2a} \right)^{-0.2} \quad (11)$$

where  $2a$  is the contact diameter. This equation, although derived from a numerical solution for the line-contact problem by Herrebrugh [20], was found to give predictions in close agreement with experimental measurements of the IEH films generated in sliding elastomeric sphere/glass flat contacts. These films were in the thickness range 50 - 200 nm.

## 4. RESULTS

In the current study, the contact configuration involved a stationary elastomeric 'lens' of, unloaded, radius of curvature  $R$ , elastic modulus  $E$ , and Poisson's ratio  $\nu$ , sliding against a flat glass disc rotating at a frequency  $\omega$ . In this case,  $r_{ax} = r_{ay} = R$ ,  $r_{bx} = r_{by} = \infty$ , and eqns. 3 and 9 give  $R_x = R_y = R$ . Eqn. 8 then gives  $k = 1$  which is the value for a circular contact. In addition, because the elastic modulus of glass is much greater than that of rubber, eqn. 6 reduces to



$$E' \approx \frac{2E}{1-\nu^2} \quad (12)$$

The linear sliding velocity at the contact,  $V$ , is given by  $V = 2\pi r\omega$ . Now  $u_a = 0$  and  $u_b = V$  and therefore  $U = V/2$  (eqn. 5).

If the elastomer is assumed to have a Poisson's ratio equal to 0.49, substitution and rearrangement of eqns. 1-9 and 12 gives the following expression for the minimum film thickness:

$$h_{min} = 1.17(\eta V)^{0.65} R^{0.77} E^{-0.44} W^{-0.21} \quad (13)$$

Eqn. 10 can be developed in the same way to give

$$h_c = 1.43(\eta V)^{0.64} R^{0.80} E^{-0.42} W^{-0.22} \quad (14)$$

This expression, developed here from the numerical solutions of Hamrock and Dowson [13,16], can be used to generate predictions for comparison with data from the current experiments. Figure 2 shows the measured central film thickness,  $h_c$  (expt.), as a function of the sliding velocity and load for four silicone fluids of viscosity 12, 110, 970 and 12200 mPas. This is plotted as a function of the values predicted by eqn. 14; agreement is seen to be close. The broken straight line in Fig. 2 represents the bisector of the rectangle, and, because of the chosen scales, indicates the line of perfect agreement.

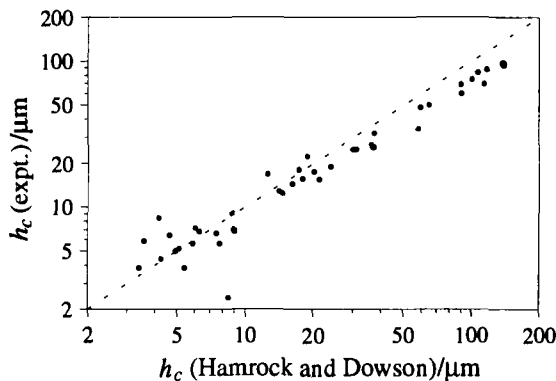


**Figure 2.** A comparison between the measured central film thicknesses and predictions generated from eqn. 14.

For the case of a compliant sphere of radius  $R$ , elastic modulus  $E$ , and Poisson's ratio  $\nu$ , in contact with a rigid flat, the appropriate Hertz equation for the

contact radius is [21]

$$a^3 = \frac{3WR(1-\nu^2)}{4E} \quad (15)$$

Substitution of this expression for the contact radius into eqn. 11, collecting up terms, and assuming  $\nu = 0.49$ , enables the Roberts and Tabor [10] equation to be couched in a form more readily comparable with eqn. 13:

$$h_{min} = 0.87(\eta V)^{0.6} R^{2/3} E^{-7/15} W^{-2/15} \quad (16)$$

For the predictions of experimental film thickness data shown in Fig. 2, eqns. 13 and 14 on average give  $h_c = 1.47 h_{min}$ . Using the value of the proportionality constant in this expression to scale eqn. 16, Fig. 3 shows how well this equation predicts the experimental data. Again, the broken straight line in Fig. 3 indicates the line of perfect agreement. Comparison of Fig. 3 with Fig. 2 suggests that eqn. 16 is a slightly better predictor than eqn. 14, although the differences are relatively small.

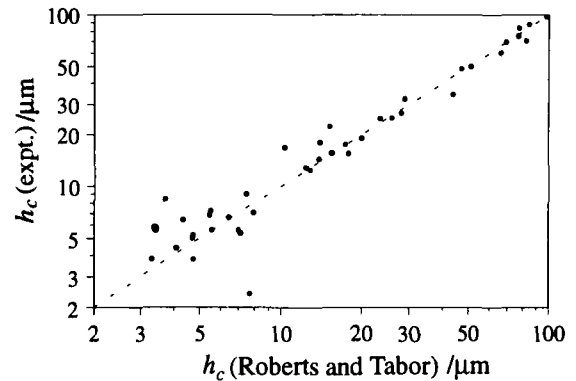


**Figure 3.** A comparison between the measured central film thicknesses and predictions generated from eqn. 16 and using  $h_c = 1.47 h_{min}$ .

## 5. DISCUSSION

### 5.1. Laser displacement probe

The earlier work of Visscher and his co-workers [12,15] demonstrated the potential usefulness of optical followers for investigating elastomeric surfaces in the presence of fluids. Such devices contain an infrared laser whose output is focused onto the interface to be measured using an internal lens,

and the reflected light examined in the back focal plane using photodiodes and appropriate optics. If the interface subsequently moves, then the focal point becomes temporarily out of focus and the photodiodes produce an error signal. This signal is used to dynamically-regulate the position of the lens (using a moving coil actuator) in a feedback loop, to re-establish the focused condition. The position of the lens is simultaneously measured with a separate displacement transducer, and this gives the required position of the interface relative to an internal reference point in device.

The current work has successfully extended the method to measure fluid film thicknesses between an elastomer and a glass disc. The success of this approach required two main conditions to be met. First, that the fluid's refractive index (RI) at the wavelength of the laser (780 nm) was sufficiently close to that of the glass (RI = 1.47 for low thermal expansion borosilicate glass) for the glass/fluid interface to become 'transparent' to the laser. In practice, both the silicone oils (RI = 1.40) and water (RI = 1.33) have refractive indices close enough to that of the glass to satisfy this condition. However, this was certainly not true for air (RI = 1), where both the glass/air and the air/elastomer interfaces were sufficiently reflective that the laser could lock-onto either interface, or even in between the two depending on their relative separation. This led to a rather complex relationship between the thickness of the air gap and that derived from the changing position of the lens in the optical follower's auto-focusing mechanism. This was in contrast to the case for either silicone fluids or water where the calibration was almost linear over the 0 -100  $\mu\text{m}$  range.

The second condition that had to be satisfied was that the fluid/elastomer interface was sufficiently reflective for the laser's auto-focusing mechanism to operate effectively. The white elastomer used was chosen for this purpose. An alternative would have been to metal-coat a transparent elastomer but this would have been more susceptible to wear.

Using a simple paraxial approximation, it might be expected that the ratio between the optical and actual film thicknesses would be given by the air/oil refractive index ratio. The value obtained for silicone fluids of 1.66 is much higher than would be expected on this basis (1.40). However, the values did match if either the elastomer was replaced with a mirror, or if the thickness of the glass disc was measured, in air, by

monitoring how far it was necessary to move the whole probe to lock onto first one, and then the other glass surface. In this case, the actual and optical glass thicknesses were measured to be 5.961 and 4.006 mm, and the ratio of 1.49 is very close to that expected from the refractive index (1.47). The calibration factor would therefore appear to be sensitive to the optical properties of the solid interface opposite to the glass, as well as to that of the fluid. In the case of the white elastomer, it could be that diffuse scattering from within the bulk of the sample was influencing the position of the focal point.

## 5.2. Film thickness

In Section 4 it was shown that the experimental data are in close agreement with predictions from existing theories, particularly those associated with Hamrock and Dowson (eqn. 14 and Fig. 2) and Roberts and Tabor (eqn. 16 and Fig. 3). The differences between the predictions from these two theories are relatively small and illustrated in Fig. 4, which shows a comparison between the two for the experimental conditions. A power law fit gives

$$h_{min} [\text{eqn.13}] = 0.96 (h_{min} [\text{eqn.16}])^{1.09} \quad (17)$$

and the associated curve is drawn on Fig. 4, together with a broken straight line that represents the line of perfect agreement. Practically, for the range of values of the variables spanned by the experimental points, eqn. 13 predicts values for the film thickness that are between 0.1 % (low  $V$ ) and 42 % (high  $V$ ) greater than that predicted by eqn. 16 using the 1.47 scaling factor discussed earlier.

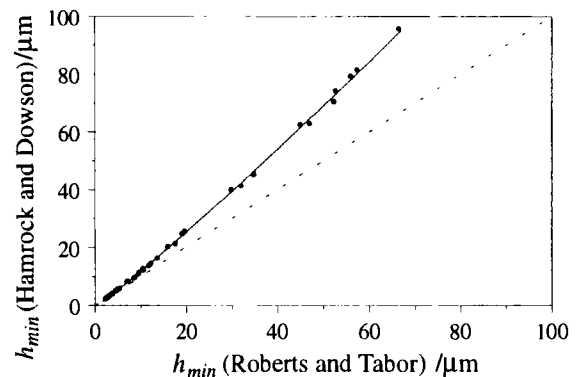


**Figure 4.** A comparison between predictions generated using eqns. 14 and 16.

At present, the repeatability of the film thickness measurements is *ca.*  $\pm 2 \mu\text{m}$ , a value determined partly by the runout of the spinning disc, and partly by other mechanical instabilities in the apparatus. It was in an effort to minimise these effects that an air-bearing spindle was chosen, and that the optical path was made horizontal so that all the components could be rigidly mounted to an optical table. On this basis, it would appear that the deviations of the experimental data from that predicted from the expressions given by Hamrock and Dowson are real. Such deviations might be expected, given that these expressions were only verified using data from experiments where the maximum film central thickness generated was only about a micron [22] - the film thicknesses generated in the current experiments were much larger than this. Of perhaps more importance, in the current study the contact area cannot be treated as small in comparison to the elastomer radius, and also the larger film thicknesses are not small in comparison to either the elastomer deformation or the contact diameter. Both these factors might be expected to modify the 'standard' IEH behaviour.

Nevertheless, the agreement between the present data and the predictions calculated from the minimum film thickness formula (eqn. 16) given by Roberts and Tabor [10] is excellent, although an assumption has to be made about the ratio between minimum and central film thicknesses. This is because only the latter was measured in the current work. It should be noted, for future work, that the high spatial resolution of the laser displacement probe ( $\sim 1 \mu\text{m}$ ) would enable the measurement of film thickness line profiles across the whole contact region. This could be done by translating the elastomeric lens in the vertical or horizontal direction at the same time as rotating the disc. Roberts and Tabor also found close agreement between their measured minimum film thickness data and predictions from eqn. 11 [10]. These data were obtained for IEH films generated during the sliding of a glass plate across an elastomeric hemisphere, but the maximum film thickness measured was only about 200 nm. The expression used by Roberts and Tabor was derived from the appropriate equations given by Herrebrugh [20] for elastomeric line contacts. They simply assumed that, because of side-leakage, the values of the minimum film thickness would be 40 % less for a circular contact than for a line contact. Previously, Roberts and Swales [2] confirmed the validity of Herrebrugh's line contact solutions in

analogous sliding experiments involving elastomeric cylinders. Agreement was found to be particularly close for films less than  $2 \mu\text{m}$  in thickness, although films up to  $10 \mu\text{m}$  were measured. Later, McClune [3] also found close agreement with theory for relatively heavily-loaded elastomeric cylinders sliding against a rotating glass disc, and explained deviations at small loads due to side-leakage and late pressure build-up. McClune and Briscoe [23] also found satisfactory agreement in similar experiments involving the squeeze IEH films generated between an elastomeric cylinder and a glass flat where the maximum central deformations measured were up to about  $30 \mu\text{m}$ .

In Hamrock and Dowson's iterative numerical solutions of the governing equations appropriate for point contacts [13], the elasticity and hydrodynamic equations are solved separately [24]. From a starting pressure distribution, the elasticity equation is used to calculate a film shape using particular values of  $k$ ,  $M$  and  $N$ . The Reynold's equation is then solved with this film shape to give an improved pressure distribution and then this cycle repeated until convergence occurs. In contrast, Herrebrugh's approach [20] was to couple the elasticity and hydrodynamic equations appropriate for line contacts into one integral equation containing the film thickness as the only variable. This equation was then solved by a combination of successive approximation or analytic continuation methods. In comparing the results appropriate for the current experiments from the two methods, the only major difference to be expected is in the treatment of side-leakage effects that are ignored in Herrebrugh's line contact solutions.

In the current configuration ensuring a fully-flooded conjunction was quite difficult. In an attempt to avoid starvation and the reduced central film thicknesses this leads to [25], lubricant had to be fed continuously to the front of the contact, which was subjected to normal load only after the disc was rotating at a constant velocity. In spite of these precautions, it is possible that there was some contact starvation, which would be more easily avoidable if the configuration was made vertical rather than horizontal, as with many interferometric EHL instruments [1,8].

### 5.3. Traction

In the case of full-film IEHL it is possible to estimate the traction, and the associated friction coefficient,  $\mu_{IEHL}$ , assuming that the work done

involves shearing a disc of Newtonian fluid of a particular thickness and radius. The central film thickness,  $h_c$ , can be treated as characteristic for the purposes of this calculation. The contact diameter produced under static loading can be treated as the characteristic lateral dimension of the fluid disc and, as a result, the latter is given by the Hertzian elastic contact equation above (eqn. 15). Therefore

$$\mu_{IEHL} = \frac{F}{W} = \frac{\tau \pi a^2}{W} \quad (18)$$

where  $\tau$  is a shear stress. This shear stress can be calculated using the central film thickness, and the viscosity of the fluid in the gap which is subjected to a characteristic shear rate of  $V/h_c$ . Provided the film thickness is greater than about 10 - 20 nm [8,10], it can be assumed that the fluid exhibits its bulk viscosity within the contact region and thus:

$$\tau = \eta \frac{V}{h_c} \quad (19)$$

Substitution of eqns. 15 and 19 into eqn. 18, together with the two film thickness expressions (with  $h_c = 1.47 h_{min}$  in the case of eqn. 16), gives

$$\mu_{IEHL} = 1.69 \left( \frac{\eta V}{\sqrt{EW}} \right)^{0.4} \quad (20)$$

using the Roberts and Tabor [10] expression for the film thickness (eqn. 16), and

$$\mu_{IEHL} = 1.51 \left( \frac{\eta V}{W^{0.314} E^{0.686} R^{0.372}} \right)^{0.36} \quad (21)$$

for the film thickness expression calculated from the solutions of Hamrock and Dowson (eqn. 14) [13]. In order to aid a more ready comparison between eqns. 20 and 21, the latter can be approximated by an expression of the form

$$\mu_{IEHL} = c \left( \frac{\eta V}{\sqrt{WRE^2}} \right)^{0.36} \quad (22)$$

where  $c$  is only a very weak function of the variables. The main difference is in the denominator where eqn. 22 predicts that the friction coefficient should

decrease slightly as the specimen radius increases, whereas eqn. 20 shows no dependence. For the bracketed group to be dimensionless in eqns. 21 and 22, the powers of  $E$  and  $W$  necessarily differ from those in eqn. 20 to compensate for the presence of a finite power of  $R$ .

Eqns. 20 and 21 can be used as the basis for interpreting experimental traction data for sphere-on-flat sliding contacts between smooth elastomers and rigid bodies. For instance, a plot of  $\log(\mu)$  against  $\log(\eta V/\sqrt{EW})$  should give a slope of 0.4 in the IEHL regime and this is indeed found to be approximately the case [19,26]. It should be noted that the effect of the magnitude of the elastic modulus and load on the friction coefficient is predicted to be relatively weak, with a factor of 100 increase in either of these quantities only leading to about a 250 % decrease in the friction coefficient (eqn. 20) - provided that the contact remains within the IEHL regime.

## 6. CONCLUSIONS

A laser displacement transducer, based on compact disc player technology, has been used successfully to measure the thickness of IEH films generated in sliding elastomer/glass contacts. The method offers some advantages over other optical techniques for investigating relatively thick lubricant films. The film thicknesses measured are in close agreement with theoretical predictions.

## ACKNOWLEDGEMENT

A. Arvanitaki is grateful to Unilever Research for the provision of a student bursary.

## REFERENCES

- [1]. B.O. Jacobson, 'Rheology and Elastohydrodynamic Lubrication', Elsevier, Amsterdam (1991).
- [2]. A.D. Roberts and P.D. Swales, Brit. J. Appl. Phys. Ser. 2 2, 1317 (1969).
- [3]. C.R. McClune, 'The Properties of Liquid Films between Highly Elastic Surfaces', Ph.D Thesis, University of Cambridge (1974).

- [4]. B.J. Briscoe and C.R. McClune, *J. Colloid Interface Sci.* **61**, 485 (1977).
- [5]. M. Schlesinger, D. De Kee and M.N. Godo, *Rev. Sci. Instrum.* **57**, 2535 (1986).
- [6]. M.T. Kirk, *Nature* **194**, 965 (1962).
- [7]. R. Gohar and A. Cameron, '**The Mapping of Elastohydrodynamic Contacts**', ASLE Lubrication Conference, LC-21, Minneapolis, Oct. 1966.
- [8]. H.A. Spikes, *Proc. Instn. Mech. Engrs.* **208**, 3 (1994).
- [9]. D. Cooper and A.J. Moore, *Wear* **175**, 93 (1994).
- [10]. A.D. Roberts and D. Tabor, *Proc. Roy. Soc. Lond. A* **325**, 323 (1971).
- [11]. C.P. Hendriks and M. Visscher, *J. Tribology* **117**, 607 (1995).
- [12]. M. Visscher, C.P. Hendriks and K.G. Struik, '**The Real Area of Contact Measured on Elastomers**', in '**Thin Films in Tribology**', Proc. 19th Leeds-Lyon Symposium on Tribology, eds. D. Dowson *et al.*, p. 705, Elsevier, Amsterdam (1993).
- [13]. B.J. Hamrock and D. Dowson, *ASME J. Lubric. Technol.* **100**, 236 (1978).
- [14]. D.J. Whitehouse, '**Handbook of Surface Metrology**', IOP, Bristol (1994).
- [15]. M. Visscher, '**The Measurement of the Film Thickness and the Roughness Deformation of Lubricated Elastomers**', Ph.D. Thesis, Eindhoven University of Technology (1992).
- [16]. B.J. Hamrock, '**Elastohydrodynamic Lubrication - Status of Understanding**', in '**Tribology in the 80's**', NASA Conf. Pub. **2300** Vol. 2, 507 (1984).
- [17]. C.J. Hooke, *Proc. Instn. Mech. Engrs.* **209**, 225 (1995).
- [18]. S.A. Johnson, D.M. Gorman, M.J. Adams and B.J. Briscoe, '**The Friction and Lubrication of Human *Stratum Corneum***', in '**Thin Films in Tribology**', Proc. 19th Leeds-Lyon Symposium on Tribology, eds. D. Dowson *et al.*, p. 663, Elsevier, Amsterdam (1993).
- [19]. A. Arvanitaki, B.J. Briscoe, M.J. Adams and S.A. Johnson, '**The Friction and Lubrication of Elastomers**', in '**Lubricants and Lubrication**', Proc. 21st Leeds-Lyon Symposium on Tribology, eds. D. Dowson *et al.*, p 503, Elsevier, Amsterdam (1995).
- [20]. K. Herrebrugh, *ASME J. Lubric. Technol.* **90**, 262 (1968).
- [21]. S.P. Timoshenko and J.N. Goodier, '**Theory of Elasticity**', McGraw-Hill, New York (1970).
- [22]. W.E. Jamison, C.C. Lee and J.J. Kauzlarich, *ASLE Trans.* **21**, 299 (1978).
- [23]. C.R. McClune and B.J. Briscoe, *J. Phys. D.* **10**, 587 (1977).
- [24]. R.J. Chittenden, D. Dowson, J.F. Dunn and C.M. Taylor, *Proc. Roy. Soc. Lond. A* **397**, 245 (1985).
- [25]. B.J. Hamrock and D. Dowson, *ASME J. Lubric. Technol.* **101**, 92 (1979).
- [26]. A. Arvanitaki, B.J. Briscoe, M.J. Adams and S.A. Johnson, '**The Elastohydrodynamic Lubrication of Elastomers**', Proc. of the International Tribology Conference, Yokohama (1995).

## Some Aspects of the Contact Mechanics and Lubrication of Low Modulus Materials in Rough Interfaces

Sayles, R.S., Lee-Prudhoe, I. & Bouvet, C.

Tribology Section  
Mech. Eng. Dept.  
Imperial College  
South Kensington  
London SW7 2BX

### Synopsis

Low modulus materials will by definition elastically deform under relatively light loads and can thus offer the contact conditions where relatively low viscosity fluids, such as water, can form effective isoviscous EHD films in relation to the interface roughness. Some aspects of this form of EHD will be demonstrated in relation to material modulus and geometry, and in relation to the magnitude and form of roughness where effective films can be generated.

An important example of film generation with low modulus materials can occur with human skin on wet interfaces. Research will be described on the contact mechanics and frictional aspects of skin where the topography is found to be a very good example of a self-affine fractal, and when under the appropriate conditions may well form effective EHD films against other interfaces in the presence of water as a lubricant.

The implications of the results to slipping and sliding are discussed.

### Introduction

There are many important areas of tribology where the lubrication of low modulus materials are involved. Some of these aspects have received attention in the academic press, for example elastomeric sealing [1] and similar areas, the prediction of film thickness in smooth low modulus Hertzian-like contacts [2,3], but in particular, in relation to human joints [4-9], where considerable research has been performed.

Introducing roughness aspects to such problems was initially confined to defining lambda values (the ratio of theoretical film thickness for smooth surfaces to the measured rms roughness of the contact), which is fraught with difficulty due to the very conforming nature of the surfaces when subject to loading. However in more recent work in relation

to human joints [6-9] considerable efforts have been made to produce film thickness predictions by combining the hydrodynamic and elastic aspects of rough asperity contacts.

The main lubrication mechanism involved with most of these situations is thought to be *elastic isoviscous elastohydrodynamics* which is usually referred to as *soft-ehd*. A useful and interesting demonstration of this mechanism is described in [10], where a shelled hard-boiled egg is shown to glide freely on a smooth surface in the presence of water as a lubricant. In the same paper some aspects of roughness are introduced to this demonstration to examine the level of elastic deformation in relation to predicted lambda values, and the subsequent ability to form soft-ehd films as a function of the structure of the roughness.

What was evident from [10] was that the nature of the roughness in relation to the contact mechanics played a vital role in the ability to form fluid films, and that although lambda values based on the elastically deformed interface roughness were a better indicator of potential film formation, other aspects of contact were also important. This paper describes some aspects of the overall topic, some of which are based on work carried out in 2 undergraduate research projects. One project involved aspects of slipping at wet interfaces of rubber soled shoes on various walkway surfaces in relation to lambda values [11], and the other was concerned with the roughness and contact aspects of human skin [12].

### **Roughness and Contact of human Skin**

Relatively crude experiments were performed using a Form-Talysurf to measure the profile of the finger print area of human skin. The finger was held as steady as possible beneath the stylus whilst a profile was recorded. This rather crude measurement method proved to be relatively reliable, probably due to the quite high levels of roughness involved in relation to smooth engineering surfaces. Sensitivity tests involving several measurements over the same finger area were performed with the finger kept as still as possible, and with the introduction of various types of movement, to quantify the possible errors (described later).

Further preliminary tests revealed that profiles of 2mm in length, taking less than 1 minute to collect were adequate for further analysis. A total of 25 undergraduate students were subjected to such measurements involving various fingers, but in all cases the left hand index finger was included, giving a total profile data base of over 100 entries.

Profiles were then subjected to various forms of analysis, which confirmed some earlier preliminary measurements from, and by, one individual (Mr Lee-Prudhoe), that surprisingly revealed that the topography of each finger measured usually represented a very good example of a self-affine fractal (this is not generally the case for engineering surfaces). This form of fractal reveals itself as a straight line when the structure function of the

profile is plotted on logarithmic scales [13]. Figure 1 shows a typical structure function plot from a finger print profile.

Self affine fractals can be defined in terms of 2 parameters from such plots; the fractal dimension  $D$ , and the Topothesy  $\Delta$  on the basis of the following equation given by Thomas and Thomas [13] describing the structure function.

$$S(\tau) = \Delta^{2D-2} \tau^{2(2-D)} \quad (1)$$

The definition of fractal dimension  $D$  and topothesy  $\Delta$  is that  $D$  represents the basic shape of a profile feature at any scale of size, and is dimensionless, and the topothesy  $\Delta$  is a scaling parameter with units of length that modifies the height to width characteristics of this feature depending on the scale of size in question. The physical interpretation of  $D$  and  $\Delta$  for self affine fractal profiles in relation to what we have come to accept as roughness is thus, in general, not straightforward because of the interrelationship of the 2 parameters. This interrelationship can be seen from Equation (1) where both  $D$  and  $\Delta$  are needed to define the intercept of the structure function's line.

However for self-similar fractals, where only the fractal dimension is needed, as the shape of the feature doesn't change with scale,  $D$  is called a space filling parameter, analogous to a relative roughness, where  $D=1$  represents a straight line, and  $D=2$  is an infinite roughness. Thus for self-affine fractal profiles of constant topothesy,  $D$  will represent the relative roughness of the profile, and conversely if the fractal dimension is constant the topothesy reflects the roughness. This latter case seems to occur with fractured sedimentary rocks [14].

The sensitivity tests on the measurement method briefly described earlier, revealed that if the finger was kept still a maximum error in  $D$  of less than 3% can be expected, but the topothesy could vary by as much as 20%. With intentional finger movements  $D$  and  $\Delta$  always increased, but with very small intentional movements, the increase in  $D$  was

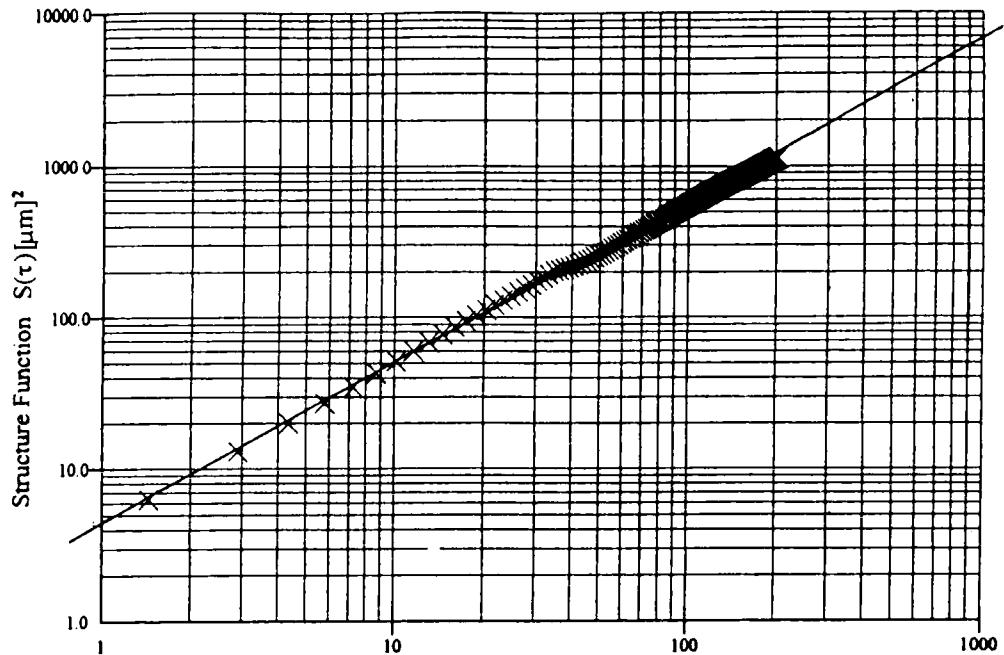


**Figure 1** A structure function plot of a finger profile. The continuous line is a best fit line used in conjunction with equation (1) to determine the fractal parameters. The abscissa is the delay length in units of microns.

| last name | country    | sex    | age | height | finger      | Fra. Dim | Topothesy |
|-----------|------------|--------|-----|--------|-------------|----------|-----------|
| Bouvet    | France     | male   | 22  | 1m88   | left index  | 1.045    | 0         |
| Cardinne  | France     | male   | 22  | 1m72   | left index  | 1.099    | 0         |
| Lie       | Hong Kong  | male   | 21  | 1m71   | left 5      | 1.131    | 0.00001   |
| Whatling  | England    | male   | 19  | 1m67   | left index  | 1.143    | 0.00006   |
| Morgan    | England    | male   | 19  | 1m84   | left 5      | 1.146    | 0.00108   |
| Schneider | Germany    | male   | 23  | 1m80   | left 5      | 1.154    | 0.00004   |
| Lin       | Singapore  | male   | 23  | 1m64   | right index | 1.164    | 0.00001   |
| Leach     | England    | male   | 21  | 1m98   | left index  | 1.171    | 0.00001   |
| Ho        | Hong Kong  | male   | 22  | 1m72   | left 5      | 1.172    | 0.00115   |
| Bhaskar   | Malaysia   | male   | 22  | 1m86   | right index | 1.173    | 0.00008   |
| Polydakis | Greece     | male   | 21  | 1m70   | right index | 1.189    | 0.104     |
| Matin     | Bangladesh | male   | 22  | 1m72   | right index | 1.194    | 0.00155   |
| Rust      | England    | male   | 19  | 1m81   | left index  | 1.201    | 0.00097   |
| Coxon     | England    | female | 22  | 1m70   | right index | 1.204    | 0.00028   |
| Lenouvel  | France     | male   | 23  | 1m75   | left 5      | 1.217    | 0.00005   |
| Tin       | Malaysia   | male   | 20  | 1m79   | right index | 1.219    | 0.00673   |
| Holland   | England    | male   | 23  | 1m88   | right index | 1.223    | 0.0258    |
| Baker     | England    | female | 19  | 1m69   | left 5      | 1.229    | 0.224     |
| Grajales  | France     | female | 22  | 1m69   | left index  | 1.25     | 0.0206    |
| Noon      | England    | male   | 21  | 1m80   | left index  | 1.269    | 13.94     |
| Samad     | Malaysia   | male   | 21  | 1m67   | left index  | 1.273    | 0.0402    |
| Soulinnac | France     | male   | 22  | 1m70   | left index  | 1.302    | 0.0620    |
| Chan      | Hong Kong  | male   | 21  | 1m70   | left index  | 1.355    | 0.384     |

**Table 1** Fractal parameters and other details of finger print skin measurements.



limited to a few percent, however  $\Delta$  varied significantly. Thus in all measurements the lowest values were taken as the most accurate.

Table 1 gives the data collected on the basis of the best measurements (lowest parameter values) and in ascending order of fractal dimension. The full data set of all measurements indicated a trend of Asian students possessing a higher fractal dimension than Europeans. This was thought to possibly represent a feature related to climatic/thermal influences, but on analysis of only the most reliable data shown in Table 1 such a trend is not evident, and any such possibility is far from conclusive, and very likely simply represents the ability of Europeans to keep their finger's still.

The definition of skin topography in terms of self-affine fractals is thus promising, but the large variation in topography seen in the data, which is related to its sensitivity to values of  $D$ , casts some doubt on this method of defining a self-affine fractal and more research is needed on this aspect.

### Contact Mechanics of Skin

The interface frictional and slipping potential of gripping objects is related to the contact geometry, stresses and lubricant aspects at the contact interface. Using a numerical rough surface contact algorithm [15] it was possible to examine many of these aspects for the finger print profiles measured.

To perform the numerical contact analysis the mechanical properties of skin are needed. The skin is closely attached to the underlying tissue and any load applied to the skin surface will produce deformation of the dermas and subcutaneous (hypodermal) layers. However Vasblom [16] showed that for small deformations in the plane of the skin the contribution of the subcutaneous tissue was relatively unimportant.

Variations in mechanical properties are almost certainly involved in this form of analysis, and use of multilayer contact methods [17] were considered, but it was decided to use a simple homogeneous model approach to this initial study in order to

determine the relevant aspects. The method used was to place a small piece of glass on to an inked finger and by measuring the approximately circular contact patch, calculate the effective modulus via Hertzian theory. For a load range of .041N to 0.145N this method revealed moduli between 210 and 160 KPa, assuming a Poisson's ratio of 0.4, and a value of 200KPa was adopted for the analysis.

Contact analysis was performed for various finger profiles against hypothetical cylinders of 20mm diameter with differing modulus over a load range. A stiff and a relatively low modulus contact are shown in Figures 2 and 3 respectively. For the stiff cylinder the mean nominal contact pressure is about 12.5 KPa, producing a real contact area of around 27% where the real mean contact pressures are around 40KPa. The low modulus contact is under a nominal contact pressure of about 2.5KPa with peak real pressures of about 20KPa and a mean real pressure of around 8KPa. The nominal finger loads associated with these pressures are around 1N and less.

Table 2 shows the effect of real contact area with load for various moduli contacts.

| E cyl. MPa | 100  | 1    | 0.5  | 0.2  | 0.1  | 0.05 |
|------------|------|------|------|------|------|------|
| Nom.Pres.  |      |      |      |      |      |      |
| 2.5 KPa    | 11.2 | 11.9 | 15.6 | 18.7 | 26.8 | 51.2 |
| 5 KPa      | 16.9 | 16.9 |      | 27.5 |      |      |
| 7.5 KPa    | 19.4 | 24.4 |      |      |      |      |
| 10 KPa     | 24.4 | 30   |      |      |      |      |
| 12.5KPa    | 27.5 |      |      |      |      |      |

**Table 2** Ratios of real to nominal contact area (%) for finger contact with various modulus cylinders of 20mm diameter.

The results suggest that the real contact area is reluctant to increase with load when gripping relatively high modulus materials.

This effect is shown more clearly in Figure 4 which shows the effect of changing modulus on contact area, at a constant contact pressure, in this case a relatively low nominal pressure of 2.5KPa.

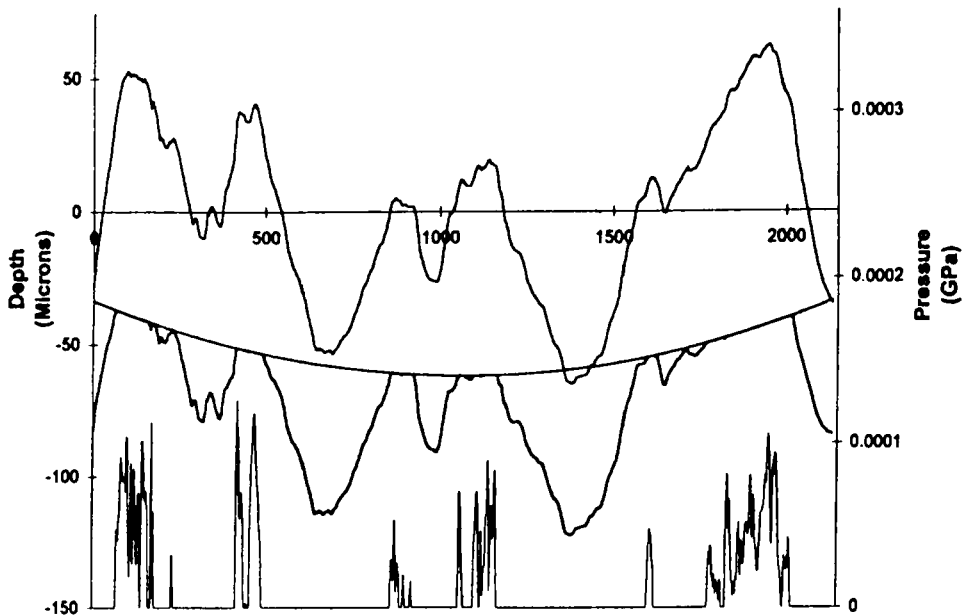


**Figure 2** Elastic contact geometry over 2mm of a finger profile in contact with a relatively stiff ( $E=100\text{MPa}$ ) 20mm radius cylinder under a nominal pressure of 12.5KPa. The upper trace is the undeformed finger profile and the lower plot represents the contact pressure distribution.

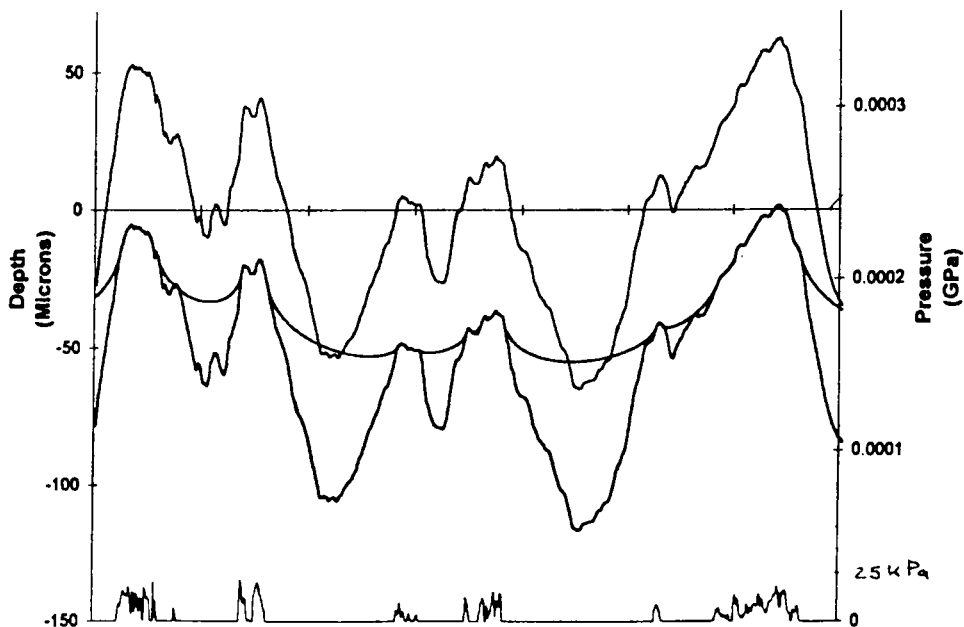


**Figure 3** Elastic contact geometry over 2mm of the finger profile shown in Fig. 2 in contact with a relatively soft ( $E=0.05\text{MPa}$ ) 20mm radius cylinder under a nominal pressure of 2.5KPa. The upper trace is the undeformed finger profile and the lower plot represents the contact pressure distribution. Note how the elastic conformity creates a contact area similar to Fig. 1, but this is achieved at a much lower pressure

The real area of contact is seen to change very little for high moduli, but then increases rapidly due to conformity when the modulus of the surface being gripped approaches the finger's modulus.

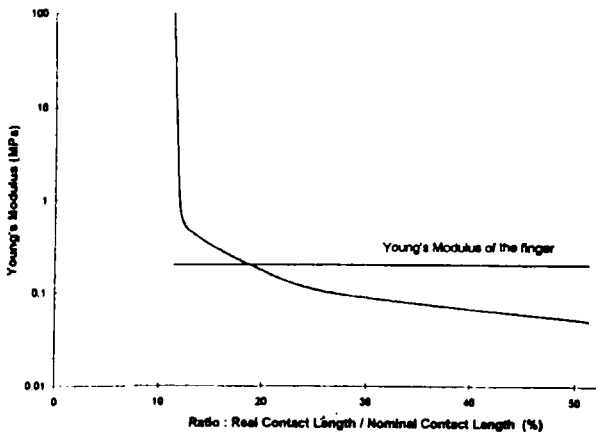


**Figure 4** The effect of cylinder modulus on finger contact area at a nominal pressure of 2.5KPa

No correlation could be defined between the fractal parameters and the contact conditions for the various finger profiles analysed.

**Frictional Effects of Skin on Glass**

Some preliminary tests of the frictional behaviour of fingers against an oscillating glass flat were performed in a rig designed to examine cv joint lubrication effects [18]. No specific lubricant was used other than natural finger boundary films.

A typical friction cycle for a relatively highly loaded finger (around 30KPa nominal pressure and a real contact area of 80-90%) is depicted in figure 5. Stick and slip regions are evident on the trace as might be expected.

Coefficients of friction were estimated to be around 0.9 (static) and 1.3 (dynamic) from provisional results at this higher load. Lower loads were examined and somewhat surprisingly revealed much higher coefficients. but this latter effect could not be confirmed with any quantitative certainty.

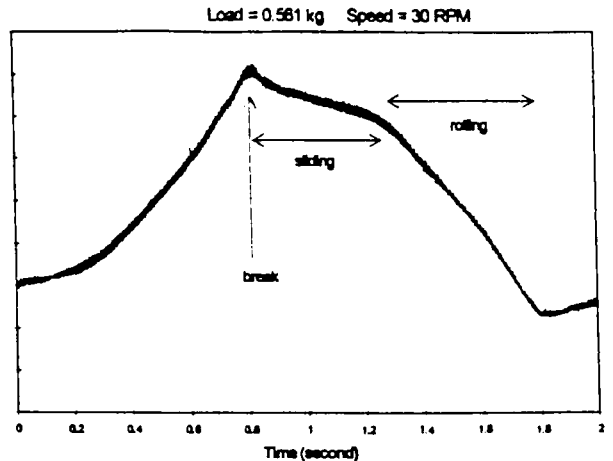


**Figure 5** A cycle of shear resistance measured from a finger pressed against an oscillating glass flat.

**Lubrication/Slipping of Conformal Surfaces**

The results of finger contact geometry effects in contact and other conformal contacts can be assessed in terms of their ability to form soft ehd films in the manner described in [10] where the dry contact geometry is used to calculate an equivalent roughness based on the contact gap and comparing this with the theoretical soft-ehd film thickness. In effect by examining the lambda value based on a modified contact roughness. Film thicknesses with water vary from around 40µm for a 50 KPa modulus egg at 1.5 m/s to about 4µm for a 10000KPa rubber soled shoe for similar radii materials and speeds against stiff surfaces. Thus finger films should be around 20 - 30 µm under similar conditions.

We have performed several analyses on this basis and shown that the potential for conformity of low modulus materials suggests that roughness can exist to form a wavy but uniform film much less in extent than the measured roughness.

Some analyses of rubber soled shoes on various surfaces are shown in Figures 6,7 and 8 representing the contact with varnished wood, a conventional concrete paving surface and the surface of South Kensington subway. The first and latter surfaces are qualitatively considered as slippery under wet conditions.

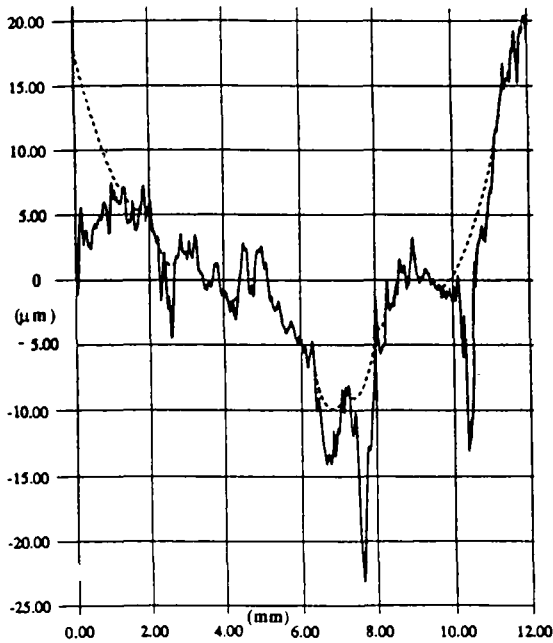


**Figure 6** Contact of a smooth rubber soled shoe ( $E=10\text{MPa}, R=100\text{mm}$ ) with a varnished wood surface ( $\sigma=7.3\mu\text{m}$ ) for an 80Kg load.

The lambda value of a rubber soled shoe sliding at 1m/s in the presence of water on varnished wood is calculated as about 0.38 using the film thickness equations of Hook et al[2,3] and talysurf roughness values from wood samples. When the elastic conformity shown in Fig.6 is used as a filter to allow calculation of the roughness of the gap, rather than the undeformed surface, then lambda increases to 2.5, and contact occurs over about 64% of the nominal area.

Similarly for the concrete pavement of Fig.7 lambda increases from 0.03 to 0.06 with only 9.3% real contact, and for South kensington subway from 0.05 to 0.1 with a real area of 18%.

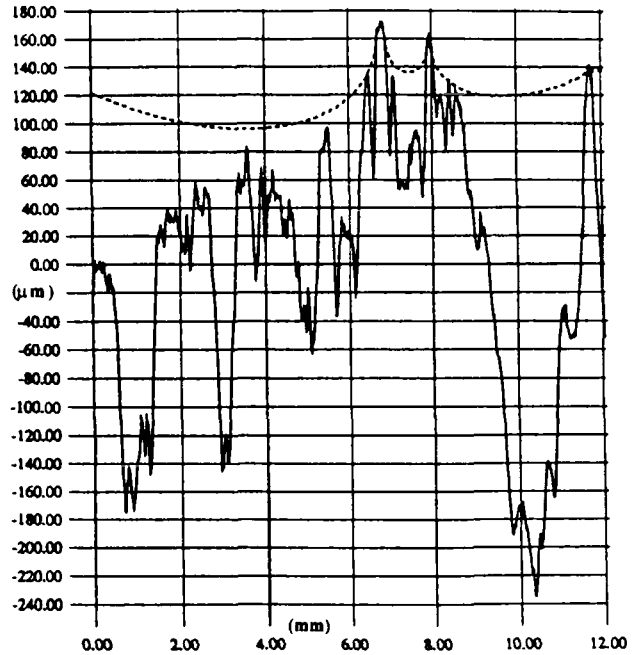


**Figure 7** Contact of a smooth rubber soled shoe ( $E=10\text{MPa}, R=100\text{mm}$ ) with a concrete paving surface ( $\sigma=94\mu\text{m}$ ) for an 80Kg load.

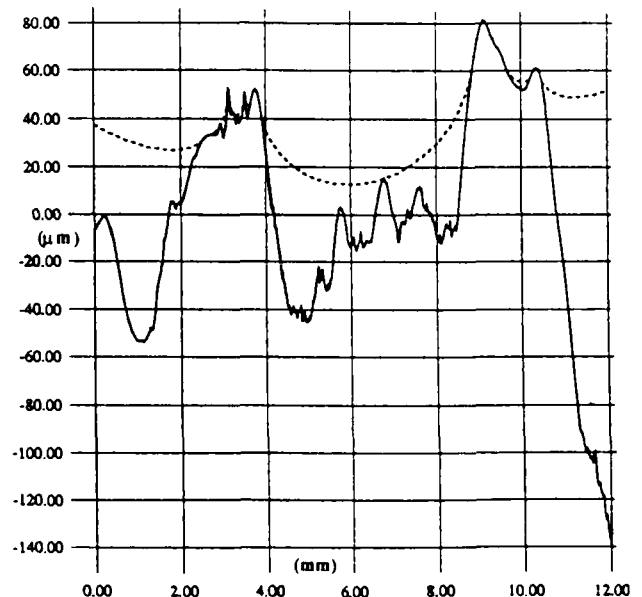


**Figure 8** Contact of a smooth rubber soled shoe ( $E=10\text{MPa}, R=100\text{mm}$ ) with South Kensington subway surface ( $\sigma=58\mu\text{m}$ ) for an 80Kg load.

In terms of comparing the lambda values of these three surfaces on the basis of the modified roughness method described, the rubber soled shoe on varnished wood can be explained, as can be the concrete pavement. But the South Kensington surface seems rough enough to prevent film formation, and yet it can be slippery.

Considering the contact of fingers in gripping objects in a similar way it would seem that the process of trying to grip a very low modulus material under wet conditions can create the conformity necessary to allow high relative lambda values to occur and soft ehd films to occur. However in the case of rigid materials slipperiness can often be experienced, but it seems unlikely to be the total result of steady state soft-ehd films. (Try picking up a wet glass quickly and then slowly to experience the influence of transient effects.)

Thus a further aspect worth considering as a transient film forming effect is the result of squeeze films and trapped lubricant in allowing the velocity to increase to a high enough level to allow the development of soft ehd films that become thick enough to nullify the roughness.

In terms of wet pavement surfaces, and in particular the South Kensington subway surface, the wet surface, as with road surfaces, seems much slipperier when a small amount of water is present and when the surface is dusty and contaminated with debris. In this situation the effective viscosity of the two-phase mixture is increased and perhaps creates a more conducive effect to create such transient effects. It is also noticeable from Fig. 8, and in relation to Fig. 4, that a relatively small reduction in modulus might create a significant improvement in conformity and thus potential for slipping.

## Conclusions

The roughness of human skin in relation to fingers is shown to be a good example of self-affine fractals. However the use of the structure function and defining the fractal in terms of topography as well as fractal dimension needs further work to create reliable results.

The contact mechanics of skin and other conforming materials is analysed in relation to the conformity and ability to create soft ehd films with low modulus materials such as water. Some sense can be made of such analyses, but it does not explain all aspects of slipping seen in realistic situations.

A further transient mechanism such as squeeze-film lubrication seems necessary to initiate velocities high enough to allow soft ehd films to form. However the form of the roughness is also important as micro-ehd films of sufficient extent in terms of the proportion of real area can allow a similar effect to occur as with squeeze films. The sliding of an egg on rough glass reported in [10] is an example of this latter effect.

## References

- [1] Gabelli, A. Micro-Elastohydrodynamic Lubrication Film Formation in Rotary Lip-Seal Contacts, Proc. 15th Leeds-Lyon Symp., Elsevier 1989
- [2] Hooke, C.J. and O'Donoghue, J.P. The Elastohydrodynamic Lubrication of Soft Highly Deformed Contacts, J. Mech. Eng'g. Sci., V14, 1972
- [3] Hooke, C.J., A note on the elastohydrodynamic lubrication of Soft Contacts, Proc. Instn. Mech. Engs., V200 No C3, 1986
- [4] Dowson, D. Modes of lubrication in synovial joints., Proc. Instn. Mech. Engs., V181, 1967
- [5] Higginson, G.R., Elastohydrodynamic Lubrication of Human Joints, Proc. Instn. Mech. Engs., V191, 1977

- [6] Dowson,D. and Jin,Z.M., Micro-elastohydrodynamic lubrication in synovial joints., Engng.Medicine, V15, 1986
- [7] Dowson,D. and Jin,Z.M., Micro-elastohydrodynamic lubrication of low elastic solids on rigid substrates, J.Phys.,D(25). 1992
- [8] Unsworth,A. The lubrication of human joints. In The Biomechanics of Human Joints. Ed. Wright,V. & Radin,E.L., Marcel-Dekker; New York, 1993
- [9] Yao,J.O. & Unsworth,A. Asperity lubrication in human joints, Proc.Instrn.Mech.Engrs., V207, 1993
- [10] Sayles,R.S., "Debris and Roughness in Machine Element Contacts: Some Current and Future Engineering Implications", Proc.Instrn.Mech.Engrs., V.209, 1995
- [11] Kurbany,R. Friction and Lubrication of Conforming Surfaces, Imperial College, Mech.Eng.Dept. Final Year Undergraduate Project, 1994
- [12] Bouvet,C.A. Fractal Topography of Skin, Imperial College, Mech.Eng.Dept. Final Year Undergraduate Project, 1996
- [13] Thomas, A. & Thomas, T.R., Fractals and Engineering Surface Roughness, Surf.Top., V1, 1988
- [14] Poon, C.Y., Sayles, R.S. & Jones, T.A., Surface Measurement and Fractal Characterisation of Naturally Fractured Rocks. J.Phys.D., Appl.Phys.V25, 1992
- [15] Webster,M.N. & Sayles,R.S., A Numerical Model for the Elastic Frictionless Contact of Real Rough Surfaces. ASME, J.of Tribology, V108, 1986
- [16] Vasblom 1967
- [17] Cole, S.J. and Sayles, R.S., A Numerical Model for the Contact of Layered Elastic Bodies with Real Rough Surfaces. ASME V114, 1991  
Sayles I.Mech.E
- [18] Rutlin,H.C., Sayles,R.S. & Starkey,M. An Optical EHD Study Using a Reciprocating Hertzian Contact Rig Designed to Simulate the Kinematics of Constant Velocity Joints, 23rd Leeds-Lyon Syp.1996

## The sealing and lubrication principles of plain radial lip seals: an experimental study of local tangential deformations and film thickness

Harry van Leeuwen and Marcel Wolfert  
Eindhoven University of Technology, Dept. of Mechanical Engineering,  
P.O. Box 513, 5600 MB Eindhoven, Netherlands

Tangential deformations of the seal surface at the contact zone between a shaft and a radial lip seal are determined by image analysis of video camera pictures. These displacements are thought to be essential for the sealing mechanism. The results show that all seals tested have an asymmetric pattern of tangential deformation, which is of the order of  $10\ \mu\text{m}$ . Local fluid film thickness has been studied on a separate test rig. This rig employs a new method for distance measurements in the shaft/seal contact, based on an opto-electronic system as used in CD players. The preliminary results indicate that the investigated seal has a film thickness of the order of  $1\ \mu\text{m}$  under normal operational conditions, which is much higher than expected. Possible causes and improvements are discussed.

### 1. INTRODUCTION

Radial lip seals, also called rotating shaft seals, are very widely used machine elements, providing good performance at relatively low costs. They are employed to seal rotating and reciprocating shafts. They prevent (1) leakage of a fluid under low static pressure or that is splashed at the shaft, and (2) entrance of dust, dirt, etc., into the sealed fluid. The plain rotating shaft seal is the most interesting of the two, since the operational principles are still unclear. Figure 1 shows the configuration of a rotating shaft seal. The contact width is very narrow and of the order of  $0.1\ \text{mm}$ . The design of this modern lip seal is more than 60 years old.

In the ideal case, the geometry of a shaft seal is rotationally symmetric. Reynolds' equation explains that there is no reason why a continuous fluid film should develop, because it would be parallel. There is no entrainment action. Nevertheless, since 40 years researchers generally agree on the existence of a coherent fluid film, after Jagger (1957) concluded that the measured film thickness is of the order of  $1\ \mu\text{m}$ . More support for full film lubrication conditions stems from the exceptional low seal wear, after a run in period. During this run in period, which may take a few 100 hours, a wear track is formed. The surface roughness of this track is vital to the sealing properties (Horve 1991, 1992). The

lubrication mechanism is not obvious and has not found general agreement yet.

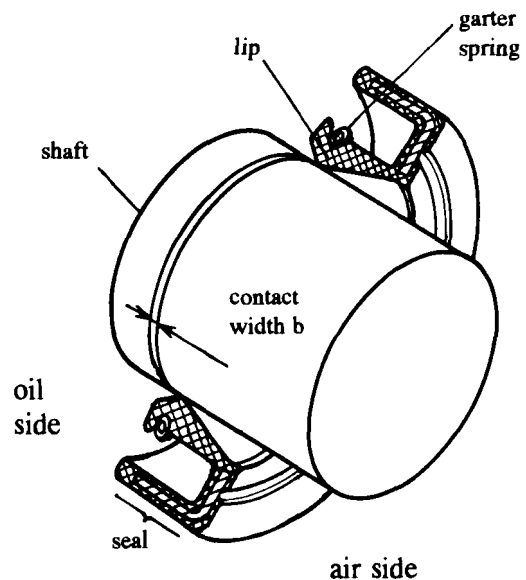


Figure 1: Plain radial lip seal for rotating shafts

If the existence of a full film is accepted, leakage would be expected. Fortunately, a properly operating plain lip seal does not leak after running in. Experienced seal designers know that a lip seal can pump fluid from the air side to the oil side, even

against a pressure head. This upstream pumping ability allows leakage free operation of the seal. The sealing mechanism is not obvious and still being disputed.

It is clear that experiments play an important role in the quest for the physical explanation of the lubrication and sealing mechanism. Most of the experimental studies on radial lip seals that have been published concern global quantities like friction torque, radial load, or leakage. As part of the solution lies in the surface roughness, these global measurements cannot solve the problem. Local measurements are needed to generate ideas for the understanding of the operating principles. This paper reports on local measurements of tangential deformations and of film thickness in the contact between shaft and seal, to provide more support for some recent theoretical models. A brief review of theories and experiments will be given first.

### 1.1. Notation

|           |  |                      |
|-----------|--|----------------------|
| $b$       | seal contact width                       | [m]                  |
| $h$       | fluid film thickness                     | [m]                  |
| $h_{av}$  | average value of film thickness          | [m]                  |
| $n$       | index of refraction                      | [-]                  |
| $p_{av}$  | average contact pressure                 | [Nm <sup>-2</sup> ]  |
| $R$       | shaft radius                             | [m]                  |
| $T_f$     | friction torque                          | [Nm]                 |
| $y$       | axial position in contact zone           | [m]                  |
| $y=0$     | indicates contact edge at oil side       |                      |
| $y_{max}$ | indicates maximum tangential deformation |                      |
| $\eta$    | dynamic fluid viscosity                  | [Nsm <sup>-2</sup> ] |
| $\omega$  | shaft angular speed                      | [s <sup>-1</sup> ]   |

## 2. SEALING AND LUBRICATION

### 2.1. Theory

Many models have been suggested to explain the lubrication and sealing mechanism of rotating shaft seals in the past 40 years. Recent contributions to the theory with state of the art surveys of existing models can be found in Müller (1987), Stakenborg (1988), Salant and Flaherty (1995) and Van Bavel et al. (1996). From these references it can be concluded that fluid film formation can be explained by entrainment action, caused by deviations from a nominal smooth and parallel film. It is much more difficult to explain the sealing mechanism, however.

Kuzma (1969) was the first to present a radical departure from then existing sealing theories, by developing a concept based on tangential deformations of the seal surface due to viscous shear forces. He claims that his theory is applicable to lip seals too. The latest theories can explain both fluid film formation as well as upstream pumping by adopting this concept of tangential deformation (Salant and Flaherty (1995), Van Bavel et al. (1996)). These theories rely on the observations by Kammüller (1986), who found that the seal surface has a roughness texture, which is deformed in sliding (tangential) direction due to viscous shear stress. To yield upstream pumping, there is no need for an axial asymmetry in the static pressure distribution, but the tangential deformation should necessarily be axially asymmetric. The asperities in the contact now act like microvanes, which pump fluid, like in an asymmetric spiral groove bearing. Kammüller's work is discussed in more detail in section 2.2.1.

In the recent models it is assumed that the tangential deformation is inside the bulk material. Hence the asperities do not deform themselves, and the only interaction between them is caused by the hydrodynamic pressures. This implies that both new and run in seals should show the same tangential deformation pattern.

### 2.2. Experiments

Recent reviews on local measurement methods for seals can be found in Stakenborg (1988), Visscher and Kanters (1990), Visscher (1992), Poll and Gabelli (1992), and Poll et al. (1992). These measurements include tangential deformation, meniscus position, surface distance, fluid film thickness, film and surface temperature, lip motion, and static pressure. No pressures measurements under running conditions have been reported. In this section local measurements of tangential deformation and film thickness are briefly discussed.

#### 2.2.1. Tangential deformations

Kawahara et al. (1980) state that shear stresses will deform the lip surface in tangential direction. This deformation has an asymmetric distribution over the contact zone. Kawahara et al. (1980) only provided a schematic graph, and gave no experimental support, nor did they relate the deformations to pump flow. It was Kammüller (1986) who showed results of tangential deformation measure-



ments, and related them to flow rates. Kammüller determined tangential deformations of a 68 mm diameter seal surface at a shaft speed of about  $20 \text{ min}^{-1}$ , under supposedly full film regime conditions. Using light microscopy, he measured the distance of travel of a threshold between a highly reflecting layer of gold, evaporated on the lip, and the lip's elastomer. He documented 4 measurements. Two of them are reproduced in Figure 2.

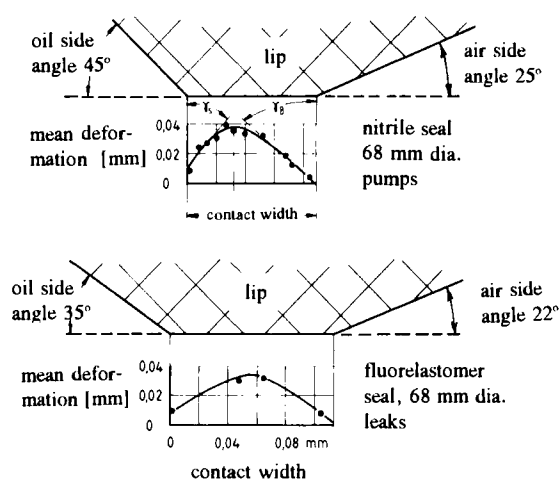


Figure 2: Tangential displacements of the seal surface in the contact zone, from Kammüller (1986).

This figure shows the averaged values of the deformation at two different circumferential positions. Only the relative deformations in the contact zone are of interest, not the bulk deformation of the lip, since the latter does not contribute to the pump flow. Kammüller plotted a few readings within the contact zone only. At the oil side a small offset appears. The maximum tangential displacement amounts to about  $40 \mu\text{m}$ , and the offset is roughly  $10 \mu\text{m}$ . These values are consistent with calculations by Salant and Flaherty (1995) and Van Bavel et al. (1996). In practice, the mechanical behaviour of a seal is not rotationally symmetric. So it can be anticipated that the tangential deformation will not be the same at different circumferential positions.

### 2.2.2. The importance of seal surface roughness

Practice tells that some shaft surface roughness, somewhere in between  $0.2$  and  $0.8 \mu\text{m}$  (CLA), is

needed to create a properly run in seal surface. Kawahara and Hirabayashi (1979) found that, after running in, the sealing flow rate is determined by the seal surface roughness only. Nakamura and Kawahara (1984), Nakamura et al. (1985), and Nakamura (1987) concluded that the seal microgeometry is decisive for sealing. Horve (1991) showed that the seal surface roughness is of crucial importance for the pumping ability. Horve concluded that rough wear tracks, with an abundance of microasperities, give good sealing properties. On the other hand, smooth wear tracks with a few microasperities give poor sealing performance. It is clear that, to assess the effect of surface roughness on fluid film formation and on pump flow rate, local film thickness measurements are needed.

### 2.2.3. Torque

Many authors interpret a Stribeck-like graph of friction torque vs. the so-called Gümbel number  $G$  ( $=\eta\omega/p_{av}$ ) for elastomer seals as if they were dealing with bearings. In the latter case, the friction minimum is associated with a transition from mixed to full film lubrication conditions, which can be proved by simple measurements (e.g., Ohmic resistance). The validity of this interpretation in lubricated elastomeric contact has never been demonstrated. Film pressures are usually low in elastomer contacts. If it is true that film thicknesses are very low (yielding very high shear stresses), high values of the coefficient of friction will result, which may be even higher than under unlubricated conditions. For example, the Gümbel number does not take into account any elastomer property, which may be of importance here. Van Leeuwen and Stakenborg (1990) performed a theoretical study and found a friction minimum under full film lubrication conditions. Experimental evidence can be found in Hoffmann et al. (1996). As a consequence, the lubrication condition cannot be determined by the friction behaviour alone. The film thickness is conclusive.

### 2.2.4. Film thickness in lip seals

Film thickness can be deduced from global friction torque measurements or leakage flow, see Jagger (1957), but this can only serve as a check of the results. In the past, film thickness has been measured directly by means of electrical, magnetic,

and optical methods. These methods are briefly reviewed here.

Jagger (1957), Iny and Cameron (1961), and Schouten (1978) used the capacity of the oil film between the shaft and a specially treated lip seal. Film thickness was found to be of the order of 1  $\mu\text{m}$ . Kawahara et al. (1981) and Ogata et al. (1987) employ the Ohmic resistance between shaft and lip. The resistance measurement is used for determining the lubrication mode, hence for qualitative purposes only. The necessary seal treatment will change the mechanical properties and the roughness texture after running in.

A different approach is the measurement of the magnetic inductance between a shaft mounted sensor (a tape recorder head) and the seal with a magnetised fluid in between, by Poll and Gabelli (1992). The measured film thickness was of the same order as the capacitance measurements, 2 till 10  $\mu\text{m}$ , for a seal with very low small interference. The seal material remains unchanged.

Optical methods can also refrain from changes in the elastomer. McClune and Tabor (1978) found film thicknesses between a smooth rubber annulus and a glass disc lubricated with a special fluid by means of interferometry. Fluid film formation was attributed to intentional radial misalignment and of the order of 2  $\mu\text{m}$ . Poll et al. (1992) used fluorescent radiation in the contact between a hollow glass shaft and seal lubricated with a special fluid. The average film thickness does not markedly change with speed, and is about 0.35  $\mu\text{m}$ .

A new method, not applied before in film thickness measurements, is open loop focus error signal (fes) detection. This method was originally developed by Philips Research Laboratories for application in CD players. The potentials of fes detection in film thickness measurement are investigated by Visscher (1992), who also explains the principles (pp. 23-37)). He performed preliminary film thickness measurements on a cylindrical elastomer specimen and a flat glass plate, and concluded that the results were qualitatively in agreement with theory. See also Visscher and Struik (1994) and Visscher et al. (1994). The measured values of the film thickness were of the order of 10  $\mu\text{m}$ . The focus error signal is a ratio of photodiode

signals, and should therefore be more or less independent of the surface reflectance. Visscher claims that, in theory, surface roughness features are quantifiable by fes detection. The so-called radial error signal (res) is used for tracking purposes in CD players. Visscher shows that the res signal may be used to correct the fes signal for asperity slopes (Visscher (1992), pp. 35-36, 152-158). The spatial resolution of the fes measurement can be made very small: of the order of 1  $\mu\text{m}$  in a direction parallel to the fluid film, and of the order of 0.01  $\mu\text{m}$  in film thickness direction. It is therefore chosen to measure film thickness in radial lip seals.

It can be concluded that at present the film thickness in radial lip seals is not known to an accuracy which is desirable to assess the effects of surface roughness on their operation, and that the lubrication condition in a real shaft/seal system is not known either.

### 3. TEST EQUIPMENT

#### 3.1. Test specimens

Two brands of seals were used throughout the experiments, designated brand R and brand S. Brand R had a rough wear track, and brand S showed a smooth surface after running in. Data are given in the Appendix. Friction coefficients were also determined on a pin disc apparatus, where Shell Ondina 68 oil has been used under lubricated conditions. Each seal, of a total of 15, obtained 6 evaporated strips of about 1 mm width in groups of 3, the two groups 120° apart along the circumference, see also under 3.2.2. This allows comparisons for the rotational symmetry of the seal. In total 10 seals were run in, the remainder was in new (virgin) state. The seals investigated in this paper were run in on rig RLS1 (see below) at 1000  $\text{min}^{-1}$  during 25 up to 52 hours in Shell Tellus 46 oil. The steel shaft had a CLA surface roughness of about  $R_a \approx 0.5 \mu\text{m}$  in axial direction. The seals were cleaned three times in hexane before the were evaporated.

#### 3.2. Test rig RLS1

RLS1 is a universal seal test apparatus, used earlier by Schouten (1978) and Stakenborg (1988).

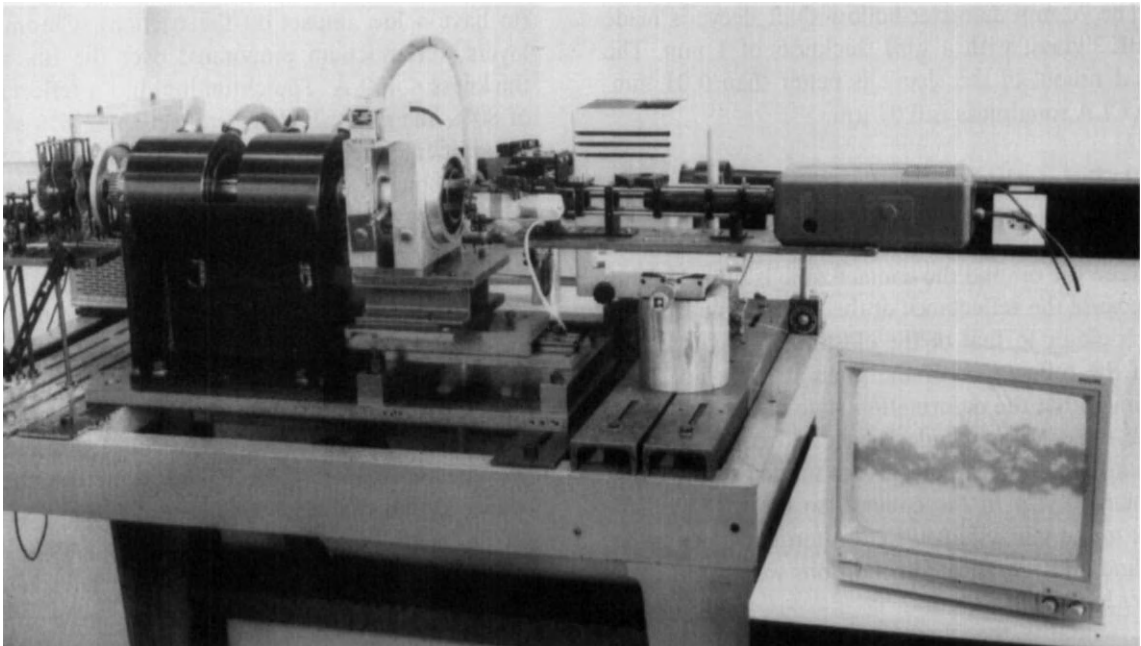


Figure 3: Photograph of the RLSI test rig for optical measurements in the contact zone.

A picture of the arrangement is shown in Figure 3. Note the image on the monitor screen, which shows the contact zone of a seal of type R.

### 3.2.1. Description

The steel shaft is supported by two air bearings. At one end a hollow glass sleeve is fitted. The other side is connected to a motor by means of a low ratio transmission, allowing shaft speeds of the order of  $100 \mu\text{m/s}$ . At assembly the seal is slid over the glass shaft and mounted in a cylindrical housing, which is

supported on an air film, allowing torque measurements. To measure small displacements a long distance microscope was built, using a Spindler and Hoyer Microbench kit. The layout is given in Figure 4. The light is produced by a high pressure mercury source, and is filtered to obtain monochromatic light. For a sharp image with sufficient irradiance, an angle of incidence of  $90^\circ$  of the light rays on the seal surface was chosen. The images were taken in by a black and white videocamera and recorded on videocassette. A monitor and videoprinter were connected.

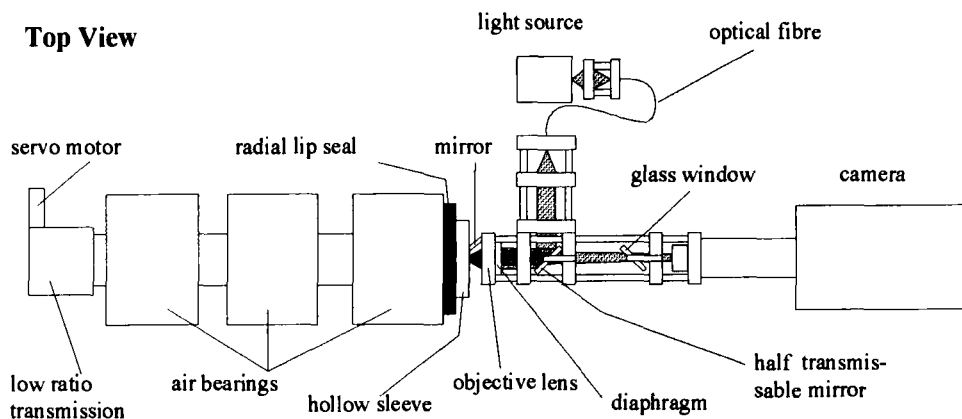


Figure 4: Layout of the modified test rig RLSI

The 70 mm diameter hollow shaft sleeve is made of BK7 glass, with a wall thickness of 4 mm. The radial runout of the sleeve is better than 0.01 mm. The CLA roughness is 0.04  $\mu\text{m}$ .

### 3.2.2. Test method

The seals were operated dry and at very low speeds. If the contact is lubricated, the difference between the oil and the contact zone is blurred. This is because the reflectance of the oil/glass interface is much closer to that of the elastomer/glass interface than the reflectance of the glass/air interface. It is assumed that the deformation state of the seal is the same under dry as under lubricated conditions. To simulate a lubricated state, it is needed to introduce permanent slip in the contact, so the seal will not stick to the glass shaft. Friction torque values under dry and under lubricated conditions were fairly close under low sliding speeds.

Essentially the method is based on distance measurement of moving markers. Several marker methods were tested: the border of an ink layer, of a vacuum evaporated layer, and speckles available in the contact zone. The ink layer was found to peel off easily. The number of useful speckles was only about 6 per image, which was considered too low. The edge between a highly reflecting layer and the low reflecting rubber marks a line, of which the deformation can be followed. This layer should be thin (not to affect the surface roughness) and narrow

(to have a low impact on the friction). Chromium layers were vacuum evaporated over the lip, with thickness  $< 400 \text{ \AA}$ . The chromium has a reflectance of 80%, the glass shaft will reflect about 4% at the glass/air interface, and the glass/rubber contact will reflect about 1%. Reflected light will therefore be white, grey, and black, respectively, and a sharp contrast between the contact and the glass/air interface results.

At first the coordinates of the undeformed and the deformed state were determined by hand from videoprints. The inaccuracy was  $\pm 5 \mu\text{m}$ , and could only be improved by repeating this tedious process many times for each print separately. In addition, this method depended on personal skills, which can lead to systematic errors and reproducibility errors. As the deformations are of the order of 10  $\mu\text{m}$ , a method with lower inaccuracy and independent of the executor has to be used.

Digital image analysis has less drawbacks. The videosignal (from the videocamera or VCR) is digitised by means of a PC equipped with a framegrabber and image processing software (TIM-win). Figure 5 shows two seal images. The smooth seal S has only a few microasperities, and therefore a smooth edge and a lip surface that is fitted tight to the shaft. On the contrary, the rough seal R has many asperities and many distinct contact spots, a very irregular contact edge, and a lip surface that does not fit close to the shaft.

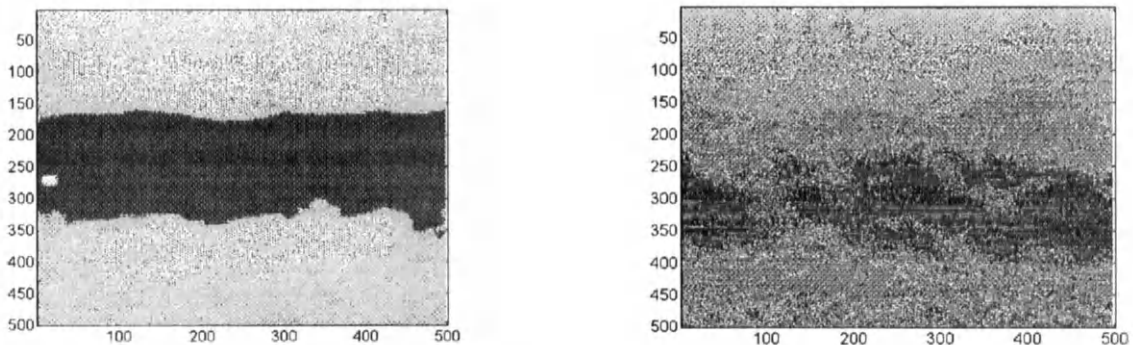


Figure 5: Images of the contact zone of a smooth seal S (left) and a rough seal R (right)

The data are arranged in a matrix and loaded into MATLAB. The Thresholding and Contour functions proved to be very convenient. A distinct speckle on the image of the seal served as a (moving) reference. In a MATLAB program the coordinates of initial contour lines are subtracted from coordinate values obtained under slip.

### 3.2.3. Calibration, reproducibility and inaccuracy

The magnification is determined by measuring a calibrated grid on the glass shaft. The transverse magnification factor was found to be about 300x. The video output signal showed that the image had a uniform irradiance distribution. The distribution is of utmost importance, while an intensity different from initial conditions necessitates a different value of the threshold, which would render a lower reliability. The inaccuracy of the method was determined by following the edge of the chromium layer on several seals, when the glass shaft sticks to the seal. In this case the relative deformation should

be zero. It was found that for the largest deformations the inaccuracy was better than  $\pm 2\mu\text{m}$ . If the same threshold value is chosen, and the initial adjustments are unchanged, the reproducibility is very good and independent of the person.

### 3.3. Test rig RLS2

Test rig RLS2 is a new apparatus, especially designed for film thickness determination in radial lip seals through fcs detection.

#### 3.3.1. Description

The RLS2 apparatus consists of a hollow steel shaft, which holds a lens system and electronics, and is supported in two precision angle contact bearings. At one end a hollow glass sleeve is glued on this shaft. At the other side a pulley is mounted, which is driven by a toothed belt. The maximum shaft speed is  $600\text{ min}^{-1}$  and is closed loop controlled. Two seals are mounted in tandem geometry in a small housing, that can move axially with respect to the shaft.

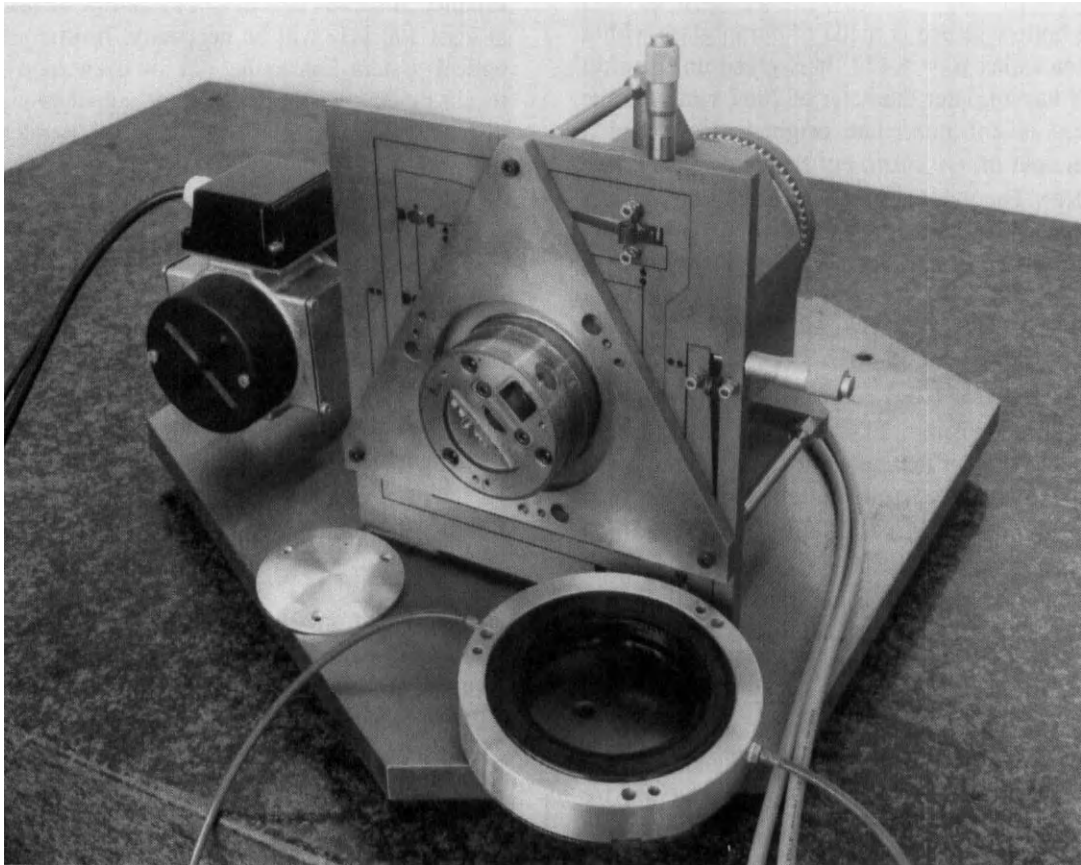


Figure 6: Photograph of RLS 2 test rig for film thickness measurements (the test seal is removed). See text.

| Measurement # | type of surface           | distance to sleeve [mm] | reflectance [-] | sensitivity [mV/ $\mu$ m] |
|---------------|---------------------------|-------------------------|-----------------|---------------------------|
| 1             | flat metal plate          | 2                       | 20 %            | 570                       |
| 2             | polished metal plate      | 2                       | 60 %            | 690                       |
| 3             | polished metal plate      | 0,1                     | 60-80 %         | 630                       |
| 4             | flat NBR specimen         | 2                       | 2 %             | 170                       |
| 5             | ring of NBR               | <0,1                    | 2 %             | ? unclear ?               |
| 6             | ring of NBR with oil film | <0,1                    | <<1 %           | 20                        |

Table 1: Sensitivity of the fes detection system with different specimens and variable object distance

Figure 6 shows the RLS2 test rig with the housing disassembled. The seal housing is mounted on a base plate with elastic pivots, allowing very small motions in two perpendicular directions. These motions are realised by means of two micrometers. At present, it is not possible to measure friction on this apparatus.

The hollow sleeve is made of duran glass with a refraction index  $n_s = 1.477$ . It is glued on the steel shaft. It has an outer diameter of 70h7 mm, and the thickness is 2.0 mm. The original sleeve had a radial runout of  $\pm 2 \mu\text{m}$ , but this one cracked (see under 5.2). The measurements reported in this paper were performed with a substitute that had a total runout of  $\pm 10 \mu\text{m}$  at the lens position. S type seals were used.

The lens system consists of a Philips GaAlAs laser, type CP065 (output 0.25 mW, laser wave length  $\lambda = 780 \text{ nm}$ ), an achromatic collimator lens with focal distance  $f = 20.0 \text{ mm}$ , and an aspherical objective lens with focal distance  $f = 9.0 \text{ mm}$ . The spot size is about  $3.5 \mu\text{m}$  in sliding direction, and the linearity range is  $\pm 13 \mu\text{m}$ . The laser light beam is reflected by the specimen, and diverted to 4 photodiodes by means of a beam splitter. The 4 diode signals are fed into an amplifier, built into the rotating shaft, which processes the diode signals to a low ohmic current. Brush contacts subsequently transmit the diode signals to a custom built instrumentation amplifier, that changes the diode signals into a focus error signal and a radial error signal. The sensitivity of the fes signal is about  $700 \text{ mV}/\mu\text{m}$  on a polished metal specimen in air.

With optical profilometry the unit is usually used in closed loop (autofocus) mode. This mode cannot be operated beyond 600 Hz due to mass inertia. If fluid film formation in radial lip seals is assumed to occur at sliding speeds of at least 0.1 m/s, and a distance measurement at every  $10 \mu\text{m}$  is to be sampled at speeds of 1 m/s, a sampling frequency of at least 100 kHz will be necessary. In this case the optical system has to be run in open loop (fixed focus) mode, and the focus error signal is used for distance measurement. The maximum frequency of the amplifiers is 300 kHz.

### 3.3.2. Test method

The test rig was operated in a speed range between 0 and  $600 \text{ min}^{-1}$ . The oil used is a mix of Shell Ondina oils, and optically almost identical to the duran glass sleeve (see Visscher (1992), p. 150). The fes output signal is used for measuring the distance from the light spot, and the seal elastomer. If the outside of the glass sleeve is in focus, the fes signal equals zero. It is assumed that the fes output signal has the same sensitivity under dynamic conditions as under static conditions.

### 3.3.3. Calibration

The fes signal was calibrated on the rig by focusing the lens on a flat specimen, and lifting this specimen relative to the nonrotating shaft. This could easily be accomplished by adjusting one of the two micrometers. Different specimens were used for calibration, see Table 1.

It follows from measurement 1, 2, and 4 that the sensitivity of the fes signal decreases as the

reflectance of the specimen decreases. If the specimen is closer to the shaft, reflection at the glass/air interface at the shaft outside will become more important, and now acts as a noise signal. Again, the sensitivity decreases (measurements 2 and 3). To calibrate the fcs output on NBR seals, the lip of a seal was trimmed away, leaving a cylindrical ring of 70.2 mm inner diameter around the shaft. This NBR ring has a low reflectance, which results in a very low sensitivity at a very small distance of less than 0.1 mm. Presumably the reflected light from the rubber interferes with the reflected light from the glass/air interface. If the space between shaft and a NBR ring is filled with the Ondina oil, the sensitivity decreases to  $0.020 \text{ V}/\mu\text{m}$ . This is consistent with Visscher (1992, p. 61).

## 4. MEASUREMENT RESULTS

### 4.1. Tangential deformations (RLS1)

Not all chromium layers adhered equally well on the elastomer surface. The accessibility to the seal's tip is difficult. In addition, adhesion depends on the substrate roughness and the cleanliness. Oil rests will remain on the seal, even after thorough cleaning. The chromium layer sticks better to seal S than to seal R. A few seals were not useful, because the chromium came off too easily, or the tip of the

lip had no chromium deposit at all, or the chromium would peel off under continuous shear. Another problem arising with rough seals is the variation of the real contact area during shaft rotation. If a contact spot comes loose, light will be reflected at the glass/air instead of the glass/elastomer interface. This results in a local increase of the reflectance, obscuring the elastomer valley under it, and making the measurement unreliable. For these reasons most results were obtained on smooth seals

Figure 7 shows some results. The oil side is at the left, the air side at the right. Figure 7b presents the tangential deformation under the no slip (stick) condition, see also under 3.2.3. Figure 7c and 7d show the tangential deformation on a new seal S8, at two distinct circumferential positions. In Figure 7e and 7f two graphs are shown of a run in rough seal R4, again at two separate positions along the circumference.

From observations of the monitor screen it follows that the axial position of the contact zone varies along the circumference, but the contact width is almost constant. This is also corroborated by the graphs from Figure 7c - 7f. Running in (at least until 50 hours at  $1000 \text{ min}^{-1}$ ), does not significantly change the contact width nor the tangential deflections. The contact width is found to be in between 0.037 mm and 0.065 mm.

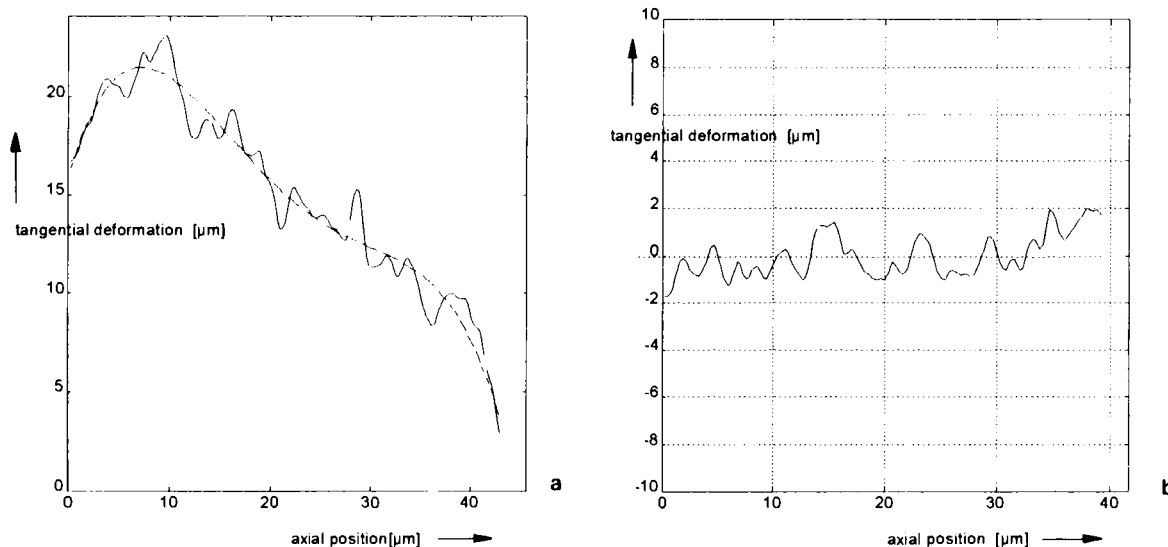


Figure 7: Tangential deformation of seals. The oil side is at the left. S = smooth, R = rough. (a) run in smooth seal S3, (b) run in smooth seal S3 under stick conditions

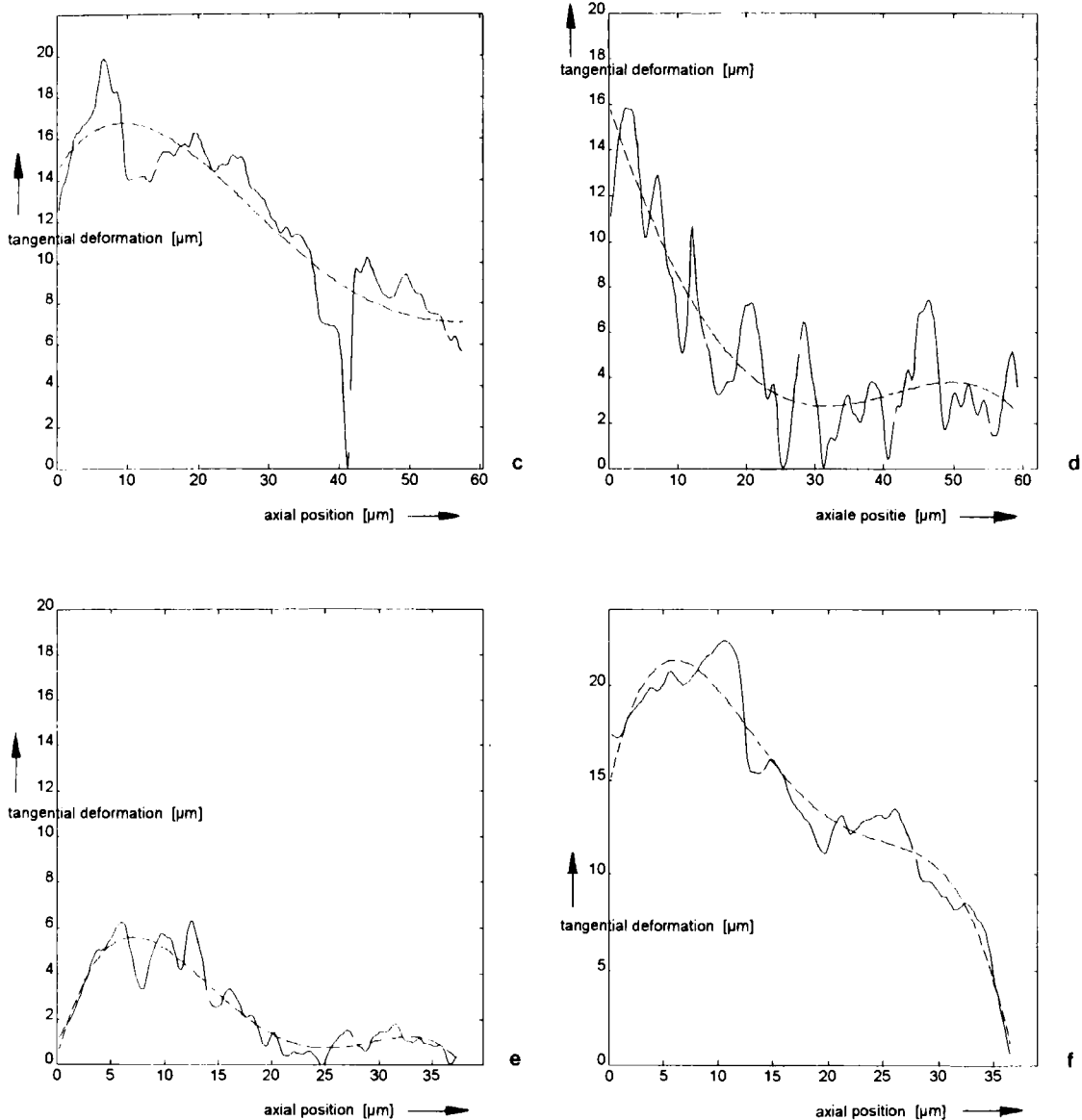


Figure 7 (cont.): (c) new smooth seal S8.1, (d) new smooth seal S8.2, at  $120^\circ$  from (c) (e) run in rough seal R4.1, (f) run in rough seal R4.2, at  $120^\circ$  from (e)

The maximum tangential deformation is in between 6 and 20  $\mu\text{m}$ . This maximum occurs at a position in between 0 and 30% of contact width  $b$  from the oil side edge, with a mean of about  $y_{\text{max}} \approx 0.2b$ . The tangential deformation has an offset in sliding direction at the oil side, which is between 1 and 15  $\mu\text{m}$ . At different circumferential positions the deformation pattern can differ considerably.

#### 4.2. Film thickness (RLS2)

The first results obtained on RLS2 give an impression of the potentials of open loop fes detection for film thickness measurement in elastomer seals. The low reflectance of the elastomer complicates the focusing on the outside of the shaft so much that the fes signal could not be set zero. Figure 8 shows the fes signal expressed in  $\mu\text{m}$  for 6  $\text{min}^{-1}$  and for 600  $\text{min}^{-1}$ .



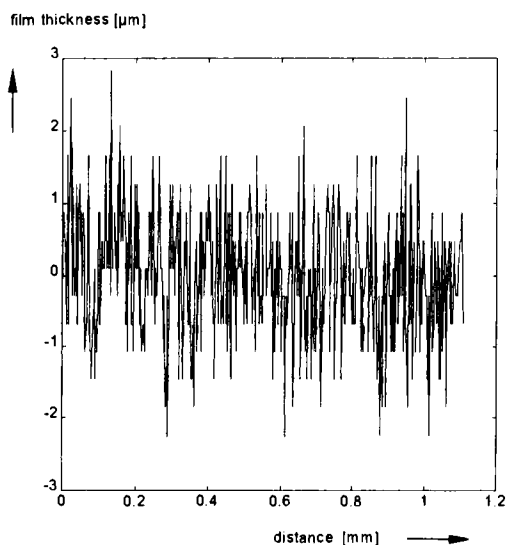


Figure 8a: Film thickness measurement for 6 min<sup>-1</sup>

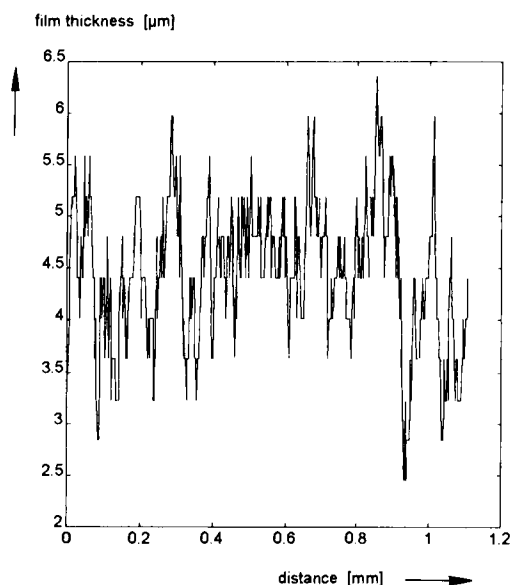


Figure 8b: Film thickness measurement for 600 min<sup>-1</sup>

It appears that the  $f_{es}$  signal contains very steep gradients, originating from noise. The noise level is about 40 mV, which corresponds to 2  $\mu\text{m}$  film thickness. The autopower spectrum of the noise signal (with nonrotating shaft) contains frequencies in a wide band ranging far over 100 kHz. The highest amplitudes occur below 60 kHz. Earlier (in section 3.3.1) it was concluded that frequencies of the order of at least 100 kHz could be of interest for roughness effects. Hence it is not functional to filter the noise.

## 5. DISCUSSION

### 5.1 Tangential deformations in the contact zone (RLS1)

#### 5.1.1. Tangential deformations

Some results show very sharp gradients in the deformation, which cannot originate from shear stresses. See, e.g., Figure 7c. Sharp peaks may be ascribed to imperfect adhesion of the chromium layer. Due to shear stresses the deposited layer may come loose, in which case it is transported along a longer distance than when it would adhere perfectly to the seal surface. Sharp craters could originate from valleys in the surface texture. Valleys are not in contact with the glass shaft. They are only moved because the surrounding asperity peaks, which are in contact, force them to do so. The valleys may lag behind, and have less deformation. Thus the measured distribution cannot be smooth.

The offset at the oil side is evident, and amounts 16 till 100 % of the maximum tangential deformation. Van Bavel et al. (1996) have assumed an offset of 25 % of a presumed maximum deformation of 10  $\mu\text{m}$ , and found an increase of at least 2 orders of magnitude in pump rate compared to zero offset (Ruijl (1994)). Salant and Flaherty (1995) calculated an offset of 25 till 30 % of a maximum displacement of 70 till 80  $\mu\text{m}$  for a surface covered with microasperities. Therefore this offset seems essential for sealing.

The tangential deformation is not uniform along the circumference of the same seal. This can be attributed to seal imperfections (in material and geometry), causing deviations from rotatory symmetry. This implies that areas having large deformation are followed by zones with low deformation. In other words: areas with a high reverse pump rate are succeeded by zones with a low (or even negative) pump rate. For a well operating seal, fluid that is accidentally leaked to the air side in a certain zone, will be pumped back into the oil side at another zone.

It is not possible to distinguish the tangential deformation of run in seals from that of new ones. This suggests that, on the whole, the tangential deformation is independent of the surface roughness texture. Hence, tangential deformations are

determined by the bulk of the lip rather than by the surface roughness.

The influence of time on the deflection could not be measured. Due to wear of the chromium layer the threshold value had to be adjusted continuously. This is unacceptable, see section 3.2.3. Initial experiments, using videoprints, indicate that an almost uniform displacement is added to the existing deformation in time. Hence the deformation distribution does not change substantially.

### 5.1.2. Contact width

The contact width of a new seal appears to be about 0.060 mm. This is in line with FEM analysis results of Stakenborg (1988), who calculated  $b = 0.073$  mm for this shaft/seal combination. It is also supported by calculations by Sponagel et al. (1987) for the same seal and shaft size ( $b = 0.080$  mm), and by experiments of Nakamura and Kawahara (1984) and Nakamura (1987), who find contact widths of run in seals with 85 mm diameter in between 0.050 and 0.100 mm.

Even after running in, this narrow contact band will not become markedly wider. Thus the static contact pressure distribution will not change considerably, and maintain the same average value. This is remarkable, since Gabelli et al. (1992) came to opposite conclusions. They calculated a contact width of about  $b \approx 0.150$  mm for a new 110 mm diameter seal, and  $b \approx 0.400$  mm for a run in seal. Consequently, their average static contact pressure drops correspondingly.

It follows that the contact width and the wear track width can differ notably. During running in the width of the wear track increases with time. In a different series of experiments on RLS1, the wear track width was found to be in between 0.050 and 0.30 mm for smooth seals S, for running times between 5 minutes and 50 hours. Shaft motions (bending, radial runout) result in an axial translation and in rotation of the seal lip with respect to the shaft, yielding a wear track that is wider than the contact width. Gawlinski and Konderla (1984) did a FEM analysis of the seal dynamics and found that the contact width varied a factor of almost 2 during a shaft revolution. Seal geometry and assembly imperfections will only increase this difference and render an even wider running track on the shaft.

## 5.2 Film thickness (RLS2)

### 5.2.1. Film thickness values

If fluid film formation can be neglected at a speed as low as  $6 \text{ min}^{-1}$ , this speed could serve as a reference for zero film thickness. The fes signal was determined at several shaft speeds, at the same part of the seal circumference (constant sampling length of 1.1 mm), and centre line averaged. Subsequently, 5 measurements were done at each speed and the average of these 5 was determined ( $h_{av}$ ). The value of  $h_{av,6}$  at  $6 \text{ min}^{-1}$  was set equal to zero, and the other readings were corrected correspondingly. This results in Figure 9.

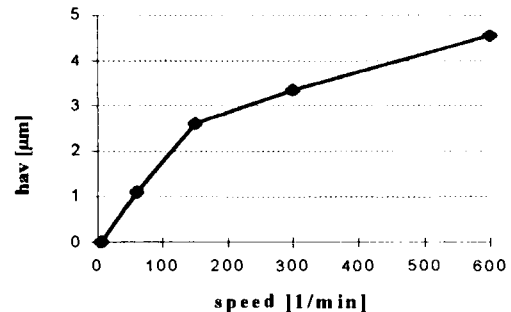


Figure 9: Averaged film thickness values vs. speed

Figure 9 suggests that film thickness increases with speed, as in a hydrodynamic bearing, and amounts up to  $4.5 \mu\text{m}$  at  $600 \text{ min}^{-1}$ . A simple Petroff model for the friction torque of the parallel smooth seal, see Jagger (1957)), yields

$$h_{av} \approx \{(2\pi \eta \omega b R^3)/T_f\}$$

for the average film thickness  $h_{av}$ , where  $T_f$  represents the friction torque. If it is assumed that at  $\eta = 0.01 \text{ Pa}\cdot\text{s}$  (at 333 K),  $\omega = 600 \text{ min}^{-1} = 62.8 \text{ s}^{-1}$ ,  $b = 2 \cdot 10^{-4} \text{ m}$ ,  $R = 35 \cdot 10^{-3} \text{ m}$ ,  $T_f = 0.8 \text{ Nm}$ , it is found that  $h_{av} \approx 0.04 \mu\text{m}$ . Therefore, it may be concluded that the measured averaged film thickness is about 2 orders of magnitude higher than expected. In addition, the signal to noise ratio is too low.

The first glass sleeve cracked during operation, see also section 3.3.1. An analysis of the temperature rise in a simple geometrical model was undertaken with MARC FE software. If it is assumed that one seal dissipates  $60 \text{ W}$  at  $600 \text{ min}^{-1}$ , and that, far away from the contact, the oil has attained a temperature of 303 K, and the air of 293 K, a

maximum contact temperature of 630 K can be attained. These high temperatures can be reached in a few seconds. Therefore, high thermal stresses are created in the glass sleeve. At lower speeds the temperature rise is less dramatic: 470 K at 300 min<sup>-1</sup>, 385 K at 150 min<sup>-1</sup>, 335 K at 60 min<sup>-1</sup>, and 306 K at 6 min<sup>-1</sup>. If, e.g., a sapphire sleeve had been used, the maximum contact temperature at 600 min<sup>-1</sup> would have been 318 K.

A substantial temperature rise has a large impact on the film thickness measurement, see Visscher (1992) pp. 217-229. Depending on the actual temperatures, an over as well as an underestimation of the film thickness is possible. If the temperature of the lubricant is 413 K, of the shaft 393 K, and of the lens system 303 K, respectively, the film thickness will be overestimated by about 4 μm. The influence of pressure on the film thickness measurement is less than 0.15 μm. It follows that the measured behaviour of film thickness with speed may be mainly attributed to temperature effects. Several corrective measures to compensate for these effects are conceivable.

It is clear that in test rig RLS2 the accuracy of fes detection is affected considerably by temperature, and therefore the temperature should be kept under control.

#### 5.2.2. Noise

Reflectances can be estimated by measuring the laser diode signals under various conditions. It is concluded that the reflectance of the oil/elastomer interface is about 0.4 %, and that the internal reflectance in the sensor unit amounts approximately 0.8 %. In this respect the reflectance on the shaft inside (air/glass interface) can be neglected. See also under 3.3.3.

Visscher (1992, pp. 189-190), in discussing the noise problem, concludes that the signal level should be increased. He suggests a laser source with higher light intensity and a thin metallic coating on the seal. Other feasible improvements are a decrease in the internal sensor reflectance and the use of a high refraction index glass shaft. If glass with an index of refraction of  $n = 1.7$  is used, the reflection on the oil/elastomer surface rises from 0.4 % to 1.8 %.

What is considered as noise could partly originate from asperity slopes. The effect of slopes on the fes signal can be accounted for by using the res signal, see under 2.2.4. As the surface slopes are

statistically distributed over the seal contact, their influence on the fes signal may be disguised as noise. The RMS roughness of the tested seals amounts 1 - 2.5 μm. Considering the wave length scale of about 10 μm, this results in steep slopes of far over 0.1 (for a dismounted seal). This should be further explored.

## 6. CONCLUSIONS

- (1) On the whole, Kammüller's hypothesis of an asymmetric tangential deformation distribution is corroborated by the experiments on RLS1.
- (2) The tangential deformations are not constant along the circumference.
- (3) The tangential deformation is determined by the bulk of the lip and not by the roughness texture.
- (4) New and run in seals both show the same tangential deformation pattern.
- (5) The contact width does hardly change under operation and is obviously smaller than the wear track width.
- (6) The reflectance on the oil/elastomer interface on test rig RLS2 is about 0.4 %. The sensitivity of the fes signal in an oil lubricated seal amounts about 20 mV/μm. This is considered sufficient for fes measurements.
- (7) The S/N ratio of the fes signal on the current RLS2 rig is too low. Corrective measures are suggested.
- (8) The poor conductance of the glass sleeve introduces high contact temperatures, which result in a considerable overestimation of the film thickness. Different materials, like sapphire, should be considered.

## 7. ACKNOWLEDGEMENTS

The authors gratefully acknowledge the support of, and stimulating discussions with, Prof. E.A. Muijderman and Mr. P.G.M. van Bavel, the technical skills of Mr. J.A. Peels, the help of student Mr. W.A. Monden, the advice of Mr. K.G. Struik and Mr. R. Petterson, and the Central Technical Services of the University, for designing and building RLS2.

## REFERENCES

- van Bavel, P.G.M. et al., 1996, *Trans. ASME, J.o.Tribology*, Vol. 118, pp. 266-275
- Gabelli, A., et al., 1992, in: *Fluid Sealing*, by B.S. Nau (ed.), Kluwer, Dordrecht, pp. 21-39
- Gawlinski, M.J., and Konderla, P., 1984, in: *Proceedings 10th Int. Conf. on Fluid Sealing*, BHRA, Cranfield, pp. 139-155
- Hoffmann, C., et al., 1996, *Konstruktion*, Vol. 48, pp. 94-98
- Horve, L., 1991, *SAE Paper*, No. 910530, 8 pp.
- Horve, L.A., 1992, in: *Fluid Sealing*, by B.S. Nau (ed.), Kluwer, Dordrecht, pp. 5-19
- Iny, E.H., and Cameron, A., 1961, *Proc. 1st Int. Conf. on Fluid Sealing*, BHRA, Barlow, Paper A2, 15 pp.
- Jagger, E.T., 1957, *Proc. Conf. on Lubrication and Wear*, I.Mech.E., London, Paper 93, pp. 409-415
- Kammüller, M., 1986, "On the sealing action of rotating shaft seals" (in German), *Ph.D. Thesis*, Stuttgart University, pp. 49-59
- Kawahara, Y., and Hirabayashi, H., 1979, *ASLE Trans.*, Vol. 22, pp. 46-55
- Kawahara, Y., et al. 1980, *ASLE Trans.*, Vol. 23, pp. 93-102
- Kawahara, Y., et al. 1981, in: *Proceedings 9th Int. Conf. on Fluid Sealing*, pp. 73-85
- Kuzma, D.C., 1969, in: *Proceedings 4th Int. Conf. on Fluid Sealing*, BHRA, Cranfield, Paper 18, pp. 165 -173
- van Leeuwen, H.J., and Stakenborg, M.J.L., 1990, *Trans. ASME, J.o.Tribology*, Vol. 112, pp. 584-592
- McClune, C.R., and Tabor, D., 1978, *Tribology International*, Vol. 11, pp. 219-227
- Müller, H.K., 1987, in: *Proc. 11th. Conf. on Fluid Sealing*, Elsevier, London, pp. 698-709
- Nakamura, K., and Kawahara, Y., 1984, in: *Proceedings 10th Int. Conf. on Fluid Sealing*, BHRA, Cranfield, pp. 87-105
- Nakamura, K., et al., 1985, in: *Proc. JSLE Int. Trib. Conf.*, Elsevier, Amsterdam, pp. 805-810
- Nakamura, K., 1987, *Tribology International*, Vol. 20, No. 2, pp. 90-101
- Ogata, M., et al., 1987, in: *Fluid Film Lubrication - Osborne Reynolds Centenary*, by D. Dowson, et al. (eds.), Elsevier, Amsterdam, pp. 553 - 560
- Poll, G., and Gabelli, A., 1992, *Trans. ASME, J.o.Tribology*, Vol. 114, pp. 290 - 297
- Poll, G., et al., 1992, in: *Fluid Sealing*, by B.S. Nau (ed.), Kluwer, Dordrecht, pp. 55-77
- Ruijl, T.A.M., "Theoretical concept of the pumping effect of radial lip seals" (in Dutch), *M.Sc. Thesis*, Eindhoven University of Technology, 68 pp.
- Salant, R.F., and Flaherty, A.L., 1995, *Trans. ASME, J.o.Tribology*, Vol. 117, pp. 53-59
- Schouten, M.J.W., 1978, *FKM-Heft*, No.72, Maschinenbau Verlag Frankfurt, pp. 45-56
- Sponagel, S., et al., 1987, in: *Proc. 11th. Conf. on Fluid Sealing*, by B.S. Nau (ed.), Elsevier, London, pp. 748-772
- Stakenborg, M.J.L., 1988, "On the sealing and lubrication mechanism of radial lip seals", *Ph.D. Thesis*, Eindhoven University of Technology, 92 pp.
- Visscher, M., and Kanters, A.F.C., 1990, *Lub. Engng.*, Vol. 44, pp. 785-191
- Visscher, M., 1992, "The measurement of the film thickness and the roughness deformation of lubricated elastomers", *Ph.D. Thesis*, Eindhoven University of Technology, 249 pp.
- Visscher, M., and Struik, K.G., 1994, *Precision Engineering*, Vol. 16, pp. 192 - 198.
- Visscher, M., et al., 1994, *Precision Engineering*, Vol. 16, pp. 199 - 204.

## A. Data of seals R and S

*Seal R (rough wear track)*

material: NBR (nitrile)  
 size: 70x100x10 mm  
 inner diameter  $68.5 \times 10^{-3}$  m  
 garter spring stiffness 0.062 N/m  
 initial spring force 1.920 N  
 coefficient of friction (on pin and disc):  
   dry 0.7-0.75, speeds up to 0.03 m/s  
   lubricated 0.6-0.2, speeds up to 0.16 m/s  
 index of refraction  $n = 1.30$

*Seal S (smooth wear track)*

material: NBR (nitrile)  
 size: 70x100x10 mm  
 inner diameter  $68.6 \times 10^{-3}$  m  
 garter spring stiffness 0.095 N/m  
 initial spring force 1.911 N  
 coefficient of friction (on pin and disc):  
   dry 0.3-0.65, speeds up to 0.03 m/s  
   lubricated 0.6-0.2, speeds up to 0.16 m/s  
 index of refraction  $n = 1.30$

## A Simple Formula for EHD Film Thickness of Non-Newtonian Liquids

Scott Bair, Principal Research Engineer and Ward O. Winer, Chair

The George W. Woodruff School of Engineering  
Georgia Institute of Technology  
Atlanta, Georgia 30332-0405

The classical EHD numerical solutions have provided the machine designer with simplified formulae for prediction of concentrated contact film thickness when the lubricant is Newtonian. Many liquids which function as lubricants display non-linear shear response in the range of shear stress critical to the pressure boosting zone of a concentrated contact. A recently developed numerical scheme for incompressible, isothermal line contact is used with a simplified rheological model to obtain a film thickness correction formula for non-Newtonian liquids using a minimum of parameters. The resulting prediction is compared with experiment.

### 1. INTRODUCTION

The designer of nonconformal contacting machine components can avail himself of formulae which predict the thickness of films formed by any piezoviscous Newtonian liquid which he may choose as a lubricant. These formulae have been verified by experiment for many lubricant types. Often, however, experimental measurement yields films considerably thinner than predicted by the isothermal Newtonian solutions. These discrepancies are usually attributed to thermal reduction of viscosity by viscous dissipation or shear thinning for the non-Newtonian liquid. Corrections are available for viscous heating (e.g., ref. [1]). No such correction is known for shear thinning. We should keep in mind, when making comparisons with experiment, that the classical EHD film thickness formulae are not exact solutions. The pressure relationships that have been used for compressibility and viscosity for example are not universal.

Numerical methods have been worked out to generate complete film profiles for certain rheological models (e.g., ref. [2]). Recently, Ostensen [3] introduced an iterative method for computing a mean effective viscosity by

assuming that the mean effective inlet shear rate is equal to one-half of the ratio of rolling velocity,  $u$ , to central film thickness. Bair and Khonsari [4] used a very simple numerical method to simulate inlet flow which departed from convention by not using the Reynolds equation. Realistic constitutive laws could be utilized. In this paper, the latter numerical method is used to generate many central film thickness solutions for a useful rheological model. These numerical "experiments" are then used to regress the parameters for a shear thinning correction formula.

### 2. METHOD

The numerical method of ref. [4] which was refined in ref. [5] is applied to study the effects of the rheological parameters as well as operating conditions on central film thickness,  $h_0$ , in incompressible, isothermal line contact. The same method is used to find the central film thicknesses,  $h_N$  and  $h_{NN}$ , for the corresponding Newtonian and non-Newtonian cases. This method assumes that the shape,  $h(x)$ , of the contacting solids is unaffected by the presence of the liquid as originally suggested by Grubin. Local pressures are

**Table 1**

Numerical Results

 $\alpha = 25\text{GPa}^{-1}$ ;  $\phi$  from equation (6)

| $\bar{p}$<br>GPa | $R$<br>m | $\mu_0$<br>Pa·s | $\tau_c$<br>Pa | $h_N/nm$<br>( $m=1$ ) |      |      | $h_N/h_{NN}$<br>( $\phi$ ) |        |        |         |        |        |           |        |        |
|------------------|----------|-----------------|----------------|-----------------------|------|------|----------------------------|--------|--------|---------|--------|--------|-----------|--------|--------|
|                  |          |                 |                |                       |      |      | $m = .4$                   |        |        | $m = 0$ |        |        | $m = -.7$ |        |        |
|                  |          |                 |                | $u/ms^{-1} =$         | 10   | .1   | 0.1                        | 10     | 1      | 0.1     | 10     | 1      | 0.1       | 10     | 1      |
| 1                | .01      | 1               | $10^1$         | 15900                 | 3080 | 540  | 15.3                       | 13.6   | 11.2   | 77      | 60     | 46     | 864       | 616    | ---    |
|                  |          |                 |                |                       |      |      | (15.1)                     | (11.8) | (9.6)  | (93)    | (62)   | (44)   | (930)     | (502)  | ---    |
| 1                | .01      | 1               | $10^0$         | 15900                 | 3080 | 540  | 6.5                        | 5.4    | 4.3    | 18.7    | 14.3   | 10.5   | 96        | 65     | 41     |
|                  |          |                 |                |                       |      |      | (6.4)                      | (5.0)  | (4.1)  | (22)    | (14.9) | (10.5) | (108)     | (59)   | (35)   |
| 1                | .01      | 1               | $10^2$         | 15900                 | 3080 | 540  | 2.8                        | 2.2    | 1.66   | 5.0     | 3.5    | 2.4    | 11.6      | 6.4    | 4.0    |
|                  |          |                 |                |                       |      |      | (2.8)                      | (2.2)  | (1.77) | (5.4)   | (3.6)  | (2.6)  | (12.7)    | (7.0)  | (4.2)  |
| 1                | .01      | .01             | $10^0$         | 564                   | 96.3 | 16.1 | 4.5                        | 3.5    | 2.9    | 10.7    | 7.6    | 5.7    | 43        | 26     | ---    |
|                  |          |                 |                |                       |      |      | (4.0)                      | (3.3)  | (2.7)  | (10.2)  | (7.4)  | (5.4)  | (33)      | (20)   | ---    |
| 1                | .01      | .01             | $10^2$         | 564                   | 96.3 | 16.1 | 1.74                       | 1.45   | 1.27   | 2.6     | 1.86   | 1.49   | 4.2       | 2.8    | 1.96   |
|                  |          |                 |                |                       |      |      | (1.75)                     | (1.47) | (1.27) | (2.54)  | (1.90) | (1.49) | (4.1)     | (2.6)  | (1.83) |
| 1                | .01      | .01             | $10^0$         | 564                   | 96.3 | 16.1 | 1.06                       | 1.02   | 1.00   | 1.09    | 1.03   | 1.00   | 1.15      | 1.05   | 1.00   |
|                  |          |                 |                |                       |      |      | (1.05)                     | (1.02) | (1.01) | (1.08)  | (1.03) | (1.01) | (1.13)    | (1.05) | (1.02) |
| .5               | .01      | .01             | $10^0$         | 657                   | 118  | 20.6 |                            |        |        | 2.2     | 1.72   | 1.35   |           |        |        |
|                  |          |                 |                |                       |      |      |                            |        |        | (2.3)   | (1.72) | (1.36) |           |        |        |
| 1                | .04      | .01             | $10^2$         | 782                   | 134  | 21.6 |                            |        |        | 2.1     | 1.64   | 1.27   |           |        |        |
|                  |          |                 |                |                       |      |      |                            |        |        | (2.1)   | (1.62) | (1.34) |           |        |        |
| 2                | .002     | .01             | $10^2$         | 314                   | 54.1 | 8.97 |                            |        |        | 3.6     | 2.5    | 1.92   |           |        |        |
|                  |          |                 |                |                       |      |      |                            |        |        | (3.6)   | (2.6)  | (1.97) |           |        |        |

found from integration of the momentum equation starting from a position eight contact half-widths from the Hertzian contact edge. The volume flow rate at the contact center,  $uh_0$ , is conserved throughout to find the local shear stress profile across the film. The rheological equations for effective viscosity are

$$\eta = \mu \quad (1)$$

$$\eta = \mu \left[ 1 + \left( \frac{\tau}{\tau_c} \right)^2 \right]^{\frac{m-1}{2}} \quad (2)$$

for the Newtonian and non-Newtonian cases respectively. The limiting low shear viscosity is  $\mu$ ,  $\tau_c$  is a critical shear stress and  $m$  is a dimensionless parameter which controls the sensitivity of effective viscosity to shear stress,  $\tau$ . A significant departure from Newtonian occurs for shear stress greater than the critical value. The boundary condition applied at the Hertzian contact edge is that the isoviscous pressure is very close to the asymptotic value. For details, see ref. [4 and 5].

### 3. NUMERICAL RESULTS

The operating conditions for our numerical simulations are shown in Table 1. Average Hertzian pressure,  $\bar{p}$ , varied from 0.5 to 2 GPa. Reduced radius,  $R$ , varied from 2 to 10 mm, and rolling velocities,  $u$ , of 0.1, 1.0 and 10 m/s were used. The ambient low shear viscosity,  $\mu_0$ , was 1 and 0.01 Pa·s. The Newtonian solutions are tabulated as  $h_N$  in Table 1. Non-Newtonian results are tabulated as  $h_N / h_{NN}$  for various values of  $\tau_c$  and  $m$ . Low shear viscosity followed the Barus Law with  $\alpha = 25\text{GPa}^{-1}$ .

### 4. DEVELOPMENT OF A CORRECTION FACTOR

Experience with solutions for  $h_{NN}$  [4 and 5] suggested that a correction could be applied to  $h_N$  and that the form of the correction should be as follows. The Newtonian and non-Newtonian thicknesses approach one another at low film thickness (or low speed). At higher

thickness  $h_{NN}$  diverges from  $h_N$  which shows a power-law dependence on rolling speed. The non-Newtonian thickness,  $h_{NN}$ , also displays a power-law relationship at high speed. The above characteristics suggest a correction of the form  $h_{NN} = h_N / \bar{\phi}$  where  $\bar{\phi}$  is approximated by  $\phi$  which has a form similar to equation (2).

$$\phi = \left[ 1 + A \left( \frac{u\mu_o}{h_N\tau_c} \right)^B \right]^{\frac{C}{B}[F(m)]^D} \quad (3)$$

The term  $u\mu_o / h_N\tau_c$  is a dimensionless shear stress which controls the transition of film thickness from Newtonian-like values. The parameters A, B, C and D are dimensionless and can be fitted using a least-squares type of program. F(m) should be zero for Newtonian ( $m=1$  in equation (2)) liquids. We investigated two forms for F(m):

$$F(m) = 1 - m \quad (4)$$

and

$$F(m) = 1 - \frac{1}{2 - m} \quad (5)$$

Both have the necessary property that  $F(m = 1) = 0$  and both yield about equally good fit to the  $h_N / h_{NN}$  values in Table 1. The regressed parameters are given in Table 2.

**Table 2**

Correction parameters regressed from the results of Table 1

| F(m)                | A     | B     | C      | D      | $\sum \left( \frac{\phi - h_N / h_{NN}}{h_N / h_{NN}} \right)^2$ |
|---------------------|-------|-------|--------|--------|--|
| 1-m                 | 4.740 | 1.726 | 0.5971 | 0.8524 | 0.34   |
| $1 - \frac{1}{2-m}$ | 4.436 | 1.687 | 2.127  | 1.781  | 0.40   |

Liquids which approach rate independent behavior (limiting shear stress behavior) at

some high value of shear stress must have very large negative values of m. This presents a problem for equation (4). When used as a correction to the classical film thickness solutions for  $h_N$ , one gets with (4) a film thickness which decreases with speed which seems unreasonable in an isothermal situation. For this reason, we recommend the use of equation (5) and the correction factor becomes

$$\phi = \left[ 1 + 4.44 \left( \frac{u\mu_o}{h_N\tau_c} \right)^{1.69} \right]^{1.26(1 - \frac{1}{2-m})^{1.78}} \quad (6)$$

Equation (6) in combination with a solution for  $h_N$  gives a prediction for EHD film thickness for shear thinning liquids. Note that for  $m \rightarrow -\infty$  and large dimensionless shear stress,  $\phi \propto (u / h_N)^{2.13}$ . Then,  $h_{NN} \propto h_N^{3.13} / u^{2.13}$ . Now ordinarily  $h_N$  varies approximately with  $u^{0.7}$  so that  $h_{NN}$  should become essentially independent of speed for liquids which are rate independent in the inlet zone. Equation (6) was used to calculate values of  $\phi$  shown in Table 1 in parentheses.

It is instructive to apply equation (6) to a real elastohydrodynamic contact. We assume that the correction worked out here is appropriate for point contact as well as line contact. Such an approach neglects the effect that shear thinning may have on side leakage. The curve marked  $h_N$  in Figure 1 is the point contact solution of Hamrock and Dowson [6]. Central film thickness is plotted against the product  $u\mu_o$  for a steel ball of radius 0.076 m rolling against a sapphire flat with a load of 11.8 N. These are the operating conditions for the experiments presented in the next section. The pressure-viscosity coefficient was taken as  $25 \text{ GPa}^{-1}$  for an example. The correction formula (6) is applied to the Hamrock and Dowson solution in the curves marked with the  $(\tau_c, m)$ . The character of the non-Newtonian solution depends on the value of  $\tau_c$ .

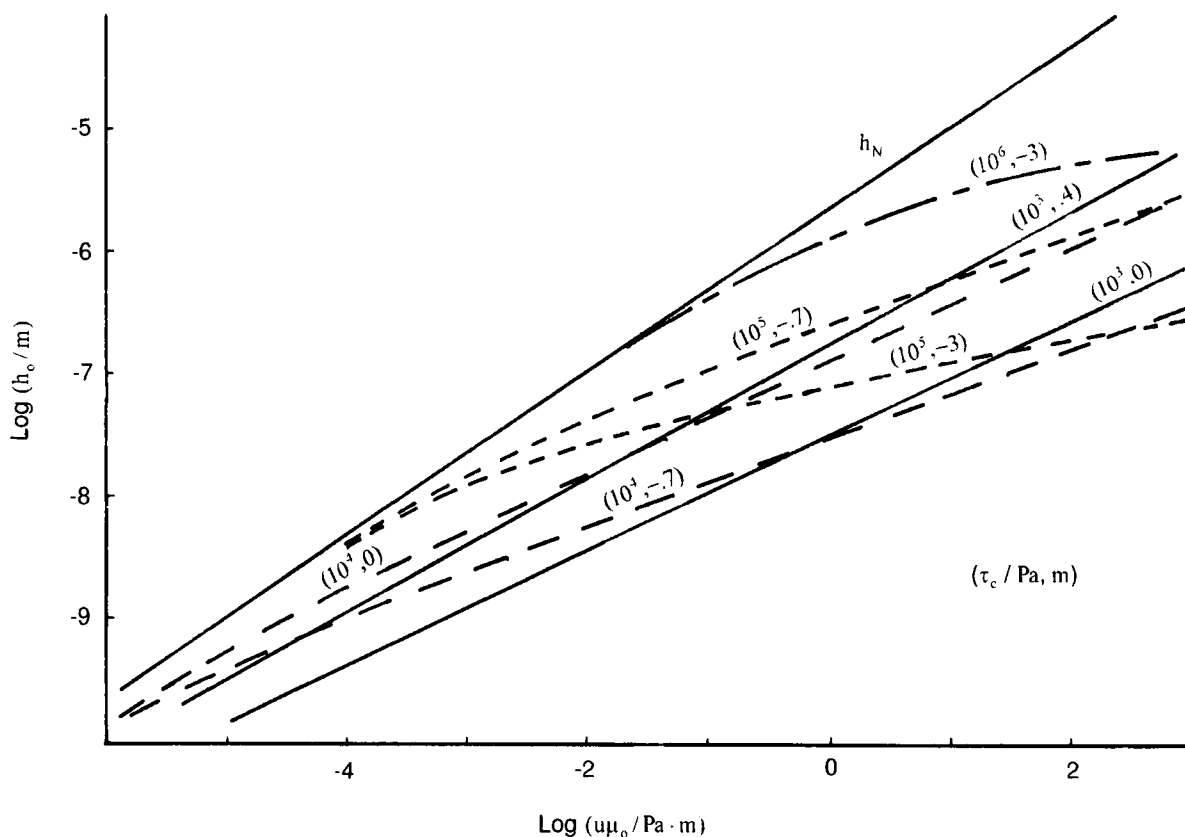


Figure 1. Application of the correction formula (6) to the Hamrock and Dowson equation [6].

## 5. COMPARISON WITH EXPERIMENT

Flow curves for a blend of mineral oil and polybutene are shown in Figure 2 for pressures of 200 and 241 MPa. The high shear stress data were obtained in torsional flow [7] with a High-Pressure Rheogoniometer and low shear results were taken with a falling body. The curves fitted to the points in Figure 2 are equation (2) with  $m = 0.462$  and  $\tau_c = 5400\text{Pa}$ .

Central film thickness was measured using interferometry for the liquid of Figure 2 in point contact with average Hertz pressure of 0.6 GPa and plotted as the points in Figure 3. The classical Newtonian solution [6] is shown as the dashed curve and the corrected solution (with equation (6)) is shown as the solid curve. The improvement in predictive power is excellent.

Flow curves for a high viscosity polyalphaolefin were obtained with a High-Shear Stress Viscometer [8] in circular Couette flow and are shown in Figure 4. The curves are equation (2) for  $\tau_c = 4500\text{Pa}$  and  $m=0.5$ . Film thickness results are shown in Figure 5 using the same format as in Figure 3. Our correction slightly overestimates the loss in thickness due to shear thinning. Similarly, flow curves and film thickness results for a medium viscosity polyalphaolefin are given in Figures 6 and 7 respectively. Here,  $\tau_c = 1.5\text{MPa}$  and  $m=0.4$ .

The calculations above require values of ambient viscosity,  $\mu_0$ , and pressure viscosity coefficient. These properties were obtained from ref. [4 and 9]. The reciprocal asymptotic isoviscous pressure was used for the pressure viscosity coefficient in the Newtonian solution.



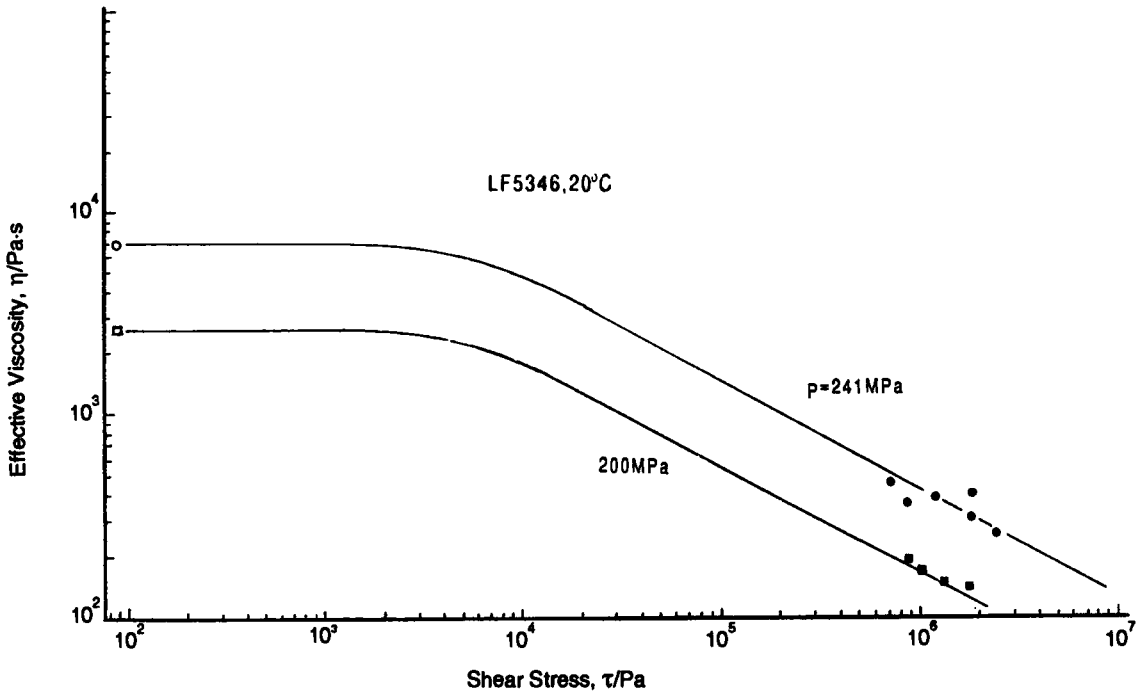


Figure 2. Flow chart for a blend of mineral oil + 20% polybutene.

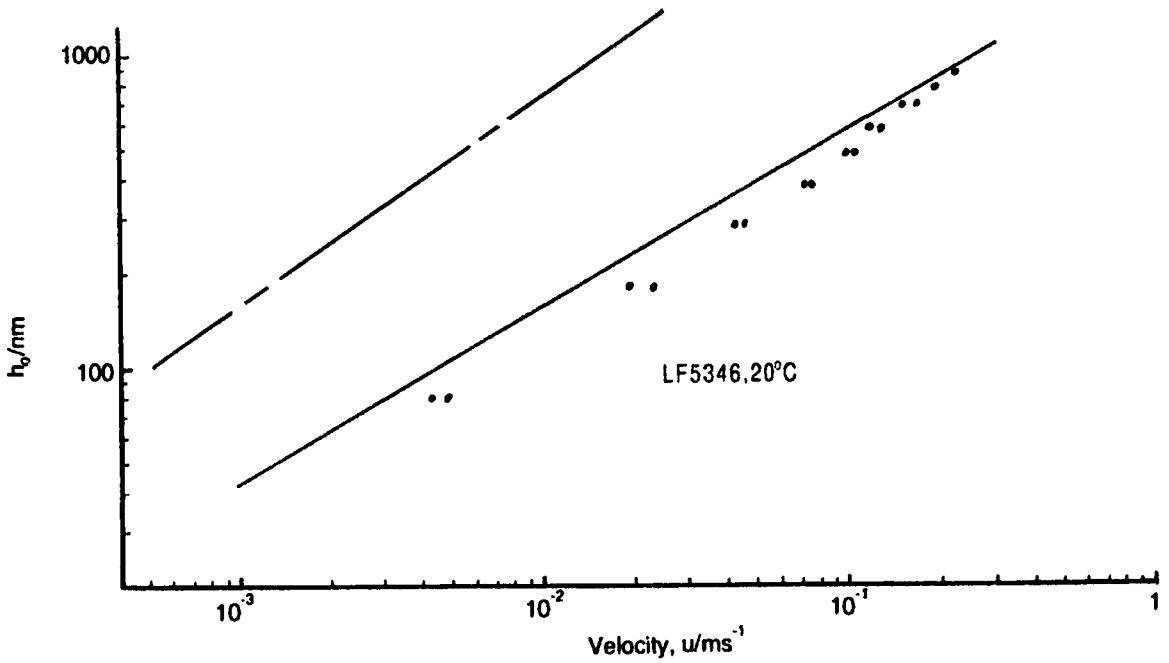


Figure 3. Central film thickness for mineral oil plus polybutene.

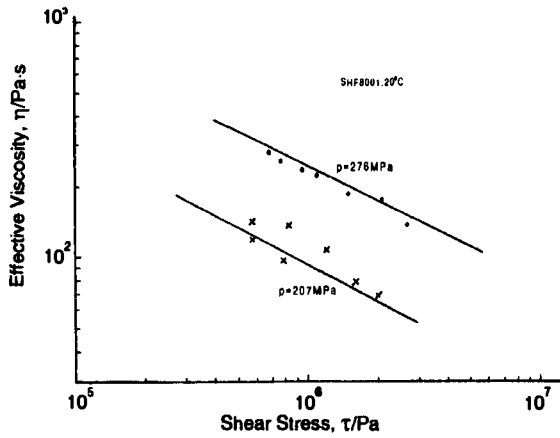


Figure 4. Flow chart for high viscosity polyalphaolefin.

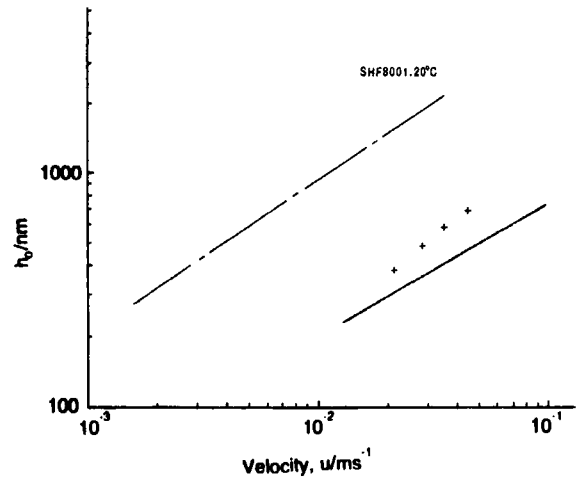


Figure 5. Film thickness for high viscosity polyalphaolefin.

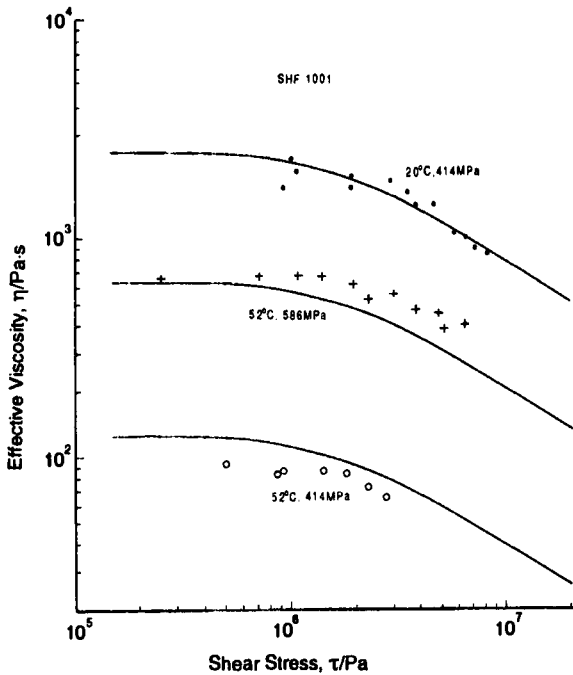


Figure 6. Flow chart for medium viscosity polyalphaolefin.

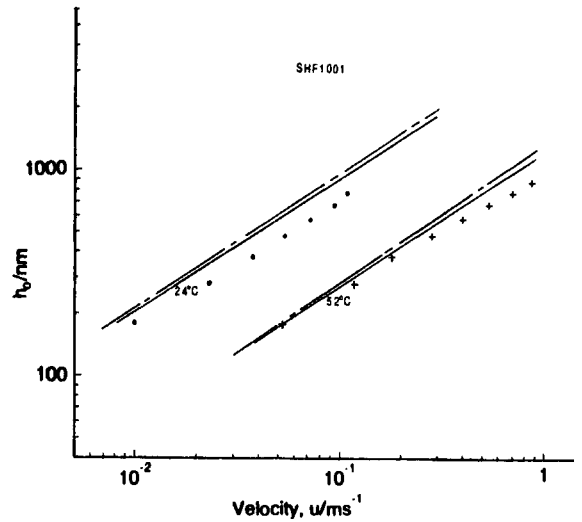


Figure 7. Film thickness for medium viscosity polyalphaolefin.

6. DISCUSSION

Clearly, the shear-thinning correction,  $h_{NN} \cong h_N / \phi$ , where  $\phi$  is given by equation (6), improves the prediction of film thickness.

The mineral oil/polymer blend is expected to display a second Newtonian with a viscosity equal to or slightly greater than the low shear viscosity of the base oil. The base oil viscosity is, however, about one thousand times less

than the blend viscosity. Extrapolation from Figure 2 shows that the second Newtonian would not be observed for shear stress less than about 1 GPa. This magnitude of shear stress is not expected in the inlet region and, consequently, the film thickness prediction is not effected by the absence of the second Newtonian in the assumed rheological model (2). It was necessary to perform the rheological measurements of the medium viscosity polyalphaolefin at pressures greater than those characteristic of the inlet region. Consequently, the value of  $\tau_c$  obtained is greater than would be appropriate for a film thickness analysis. A smaller  $\tau_c$  would improve the correction of film thickness for the medium viscosity polyalphaolefin.

We offer a non-Newtonian correction formula for concentrated contact film thickness requiring only two rheological parameters beyond those currently used for the Newtonian solution. These new parameters,  $\tau_c$  and  $m$ , may be obtained using existing rheometers.

## ACKNOWLEDGEMENT

The authors acknowledge the financial support of the Office of Naval Research, Peter Schmidt, Science Officer.

## REFERENCES

1. Cheng, H.S. (1967), "Calculation of Elastohydrodynamic Film Thickness in High-Speed Rolling and Sliding Contacts," Mechanical Technology Technical Report MTI-67TR24.
2. Vergne, F., Chaomleffel, J.P. and Dalmaz, G. (1990) "Elastohydrodynamic Lubrication of Point Contact with a Rhee-Eyring Fluid: Film Thickness and Traction," J. Rheol. **34**, 8, pp. 1357-1371.
3. Ostensen, J.O. (1995) "Prediction of Film Thickness in an Elastohydrodynamic Point Contact Lubricated with a Viscosity Index Improved Base Oil," Proc. Instn. Mech. Engrs. **209**, pp. 235-242.
4. Bair, S. and Khonsari, M. (1995) "An EHD Inlet Zone Analysis Incorporating the Second Newtonian," ASME J. Tribology **118**, 2, pp. 341-343.
5. Bair, S. (1996) "Elastohydrodynamic Film Forming with Shear Thinning Liquids," submitted to ASME J. Tribology.
6. Hamrock, B.J. (1991) Fundamentals of Fluid Film Lubrication, NASA Ref. Pub. 1255, p. 507.
7. Bair, S., (1996) "Normal Stress Difference in Liquid Lubricants Sheared under High Pressure," Rheol. Acta **35**, pp. 13-23.
8. Bair, S. and Winer, W.O. (1993) "A New High-Pressure High-Shear Stress Viscometer and Results for Lubricants," STLE Tribology Trans. **36**, 4, pp. 721.
9. Bair, S. and Winer, W.O. (1995) "Application of the Yasutomi Free Volume Model to Various Liquids," Proc. Inter. Symp. Tribology Yokoham.

## Behavior of some vegetable oils in EHL contacts

N. Ohno<sup>a</sup>, A. Shiratake<sup>a</sup>, N. Kuwano<sup>a</sup> and F. Hiranob<sup>b</sup>

<sup>a</sup>Department of Mechanical Engineering, Saga University,  
1, Honjyo, Saga, 840, JAPAN

<sup>b</sup>Professor Emeritus of Kyushu University,  
4-10-12, Takamiya, Minamiku, Fukuoka, 815, JAPAN

EHL oil film thickness measurements for rape seed oil, camellia oil, olive oil, castor oil and glycerol have been carried out by optical interferometry. The experimental results showed that the central film thickness of castor oil and glycerol under rolling conditions was 0.5-0.9 times thinner compared with the Hamrock - Dowson central film thickness formula. This fact was considered to be attributed to their poor wettability at the liquid/solid interface, which was estimated by observing the contact angle with the aid of a goniometer. Furthermore, the largest contact angle of glycerol was lowered by adding surfactant and brought about an increase in film thickness. It is suggested that the interfacial phenomena near the inlet side of the EHL contact region affects the EHL central film thickness, in particular, in case of vegetable oils and glycerol. Further, comparing oils with equal viscosity grades, vegetable oils with lower pressure-viscosity coefficients show lower traction coefficients than the paraffinic mineral oils. The effect of wettability on the traction coefficient was unrecognized.

### 1. INTRODUCTION

The main component of vegetable oils comprises glyceride of fatty acids, biodegradable oils have a superior to the performance for boundary lubrication. However, the limitation of vegetable oils has been their high cost, and their thermal and oxidation instability. Therefore, it was mainly used for metal working lubricants. Recently the demand for biodegradable lubricating oil is increasing, vegetable oils as environmentally acceptable fluids are noticed [1].

So far in experimental research of elastohydrodynamic oil films mineral oils and synthetic oils were widely used, the use of vegetable oils was failed to notice. Thus, the traction and EHL film thickness measurements for vegetable oils were carried

out by optical interferometry. As compared with mineral oils, behavior of vegetable oils show considerable deviation concerning the EHL film thickness, in particular, in maps of liquid/solid transition lubrication [2][3] and traction coefficient [4]. It is confirmed that the difference in wettability plays a significant role of this fact. Further, comparing oils with equal viscosity grades, vegetable oils with lower pressure-viscosity coefficients show lower traction coefficients than mineral oil series. The effect of wettability on the traction coefficient was unrecognized.

The present investigations were carried out to clarify merits or demerits of vegetable oils concerning EHL oil film thickness and traction. Furthermore, using the entrapment of oil between normally approaching elastic bodies, it is ascertained

the interfacial phenomena's effects on the EHL central film thickness.

## 2. EXPERIMENTAL METHOD

The apparatuses used in the present investigation for measuring basic properties of lubricants are the viscometer of a falling ball type, and the high pressure cylinder for the density measurement at pressure up to 1.2 GPa and at temperatures from 0 to 100°C as described in the authors' previous report in detail [5]. Hence, the general views of these apparatuses are omitted.

For measurement of traction forces and observation of EHL patterns by means of the usual interferometric method, a rolling/sliding contact apparatus was used. It was composed of a pyrex glass or a sapphire optical flat of 40 mm diameter and 5 mm thick and a 23.8 mm diameter bearing steel ball for ellipticity parameter  $k = 1$ . For ellipticity parameter  $k = 3.6$  a barrel shaped roller of 23.6 mm in maximum outer diameter and 84 mm in radius of curvature in the meridian plane was used. Fig. 1 shows a schematic diagram of the experimental apparatus used in this study.

The experimental conditions in the traction measurements are as follows:

Maximum rolling speed  $u$  : 1100 mm/s

Contact load  $w$  : 86 N

Mean Hertzian contact pressure  $p$   
in circular contact,  $k=1$

with pyrex glass : 0.45 GPa,

with sapphire : 0.90 GPa,

in elliptic contact,  $k=3.6$

with pyrex glass : 0.26 GPa,

with sapphire : 0.52 GPa

Temperature : room temperature

The film thickness measurements were carried out at mean Hertzian pressure 0.26 GPa for  $k = 3.6$  and 0.45 GPa for  $k =$

1.

The names and properties of tested lubricants are listed in Table 1. The main series are classified into the following types:

1. Vegetable oils : rape seed oil, camellia oil, olive oil and castor oil

2. Glycerol  $C_3H_5(OH)_3$

3. Surfactant containing oil:

Polyoxyethylene 5% by weight used in solution in glycerol.

4. Paraffinic mineral oils P60N, P150N, P500N, PBSN

Values of pressure-viscosity coefficient  $\alpha$  listed in Table 1 were all determined as follows. Provided the validity of relation,  $\ln \eta_i = \ln \eta_0 + \alpha p_i$ ,  $\alpha$  was derived from the slope of plot using method of least squares. For this, experimental data points in range  $\eta_i < 10^3$  Pa·s and  $p_i < 0.33$  GPa were used [5].

## 3. RESULTS AND DISCUSSIONS

### 3.1 Film Thickness Measurements

Fig. 2 shows the interference pattern for paraffinic mineral oil PBSN. We can see the well-known film shape having the flat

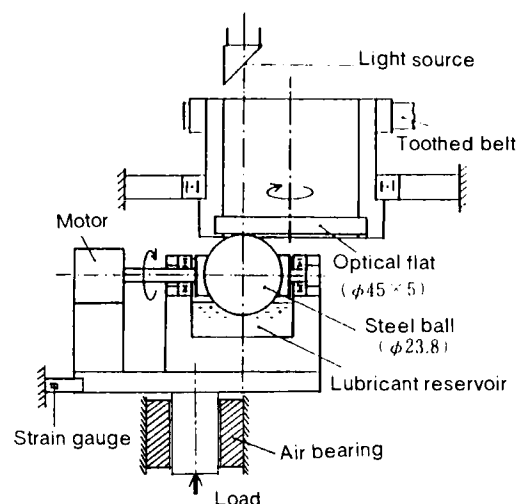


Fig. 1 Schematic diagram of rolling - sliding apparatus

Table 1 Properties of Oils

|                             | $\rho$ , g/mL |       | $\nu$ , mm/s <sup>2</sup> |      | $\alpha$ , GPa <sup>-1</sup> | $\phi^\circ$ | $\sigma_L$ , mN/m |
|-----------------------------|---------------|-------|---------------------------|------|------------------------------|--------------|-------------------|
|                             | 15°C          | 40°C  | 100°C                     | 40°C | 23°C                         | 23°C         |                   |
| rape seed oil               | 0.9189        | 35.7  | 8.06                      | 9.0  | 12.0                         | 34.1         |                   |
| camellia oil                | 0.9168        | 39.3  | 8.28                      | 7.0  | 12.9                         | 33.2         |                   |
| olive oil                   | 0.9137        | 39.6  | 8.24                      | 8.1  | 11.8                         | 33.1         |                   |
| castor oil                  | 0.9666        | 241.0 | 17.50                     | 11.3 | 18.7                         | 33.1         |                   |
| glycerol                    | 1.2631        | 209.3 | 12.00                     | 3.7  | 48.1                         | 40.1         |                   |
| glycerol<br>+ surfactant 5% | 1.2549        | 181.0 | 11.45                     | 3.4  | 23.4                         | 31.4         |                   |
| P60N                        | 0.8552        | 8.0   | 2.38                      | 11.7 | 12.2                         | 27.0         |                   |
| P150N                       | 0.8620        | 29.9  | 5.28                      | 12.7 | 11.0                         | 28.3         |                   |
| P500N                       | 0.8716        | 89.8  | 10.99                     | 14.1 | 14.2                         | 32.2         |                   |
| PBSN                        | 0.8772        | 379.3 | 29.10                     | 16.4 | 12.9                         | 31.2         |                   |

$\rho$  : density,  $\nu$  : kinematic viscosity,  $\alpha$  : pressure-viscosity coefficient

$\phi$  : contact angle,  $\sigma_L$  : surface tension, surfactant : polyoxyethylene

plateau region bounded by the horseshoe shaped constriction and the wake at the outlet region. When we compare the theoretical film thickness and the experimental film thickness, it is based on the lubrication regime. It is common practice for identification of the lubrication regime of point contacts to use Hamrock-Dowson diagram [6] in which the regimes are divided as follows: isoviscous-rigid IR, piezo-viscous-rigid PR, isoviscous-elastic IE, and piezoviscous-elastic PE. The authors [3] previously pointed out that the most suited representation for estimated of the solidified film thickness at high pressure EHL contacts is concluded to use the liquid/solid transition lubrication diagram, where the product of pressure-viscosity coefficient  $\alpha$  and mean Hertzian pressure  $p$  as the abscissa and dimensionless parameter  $GU^{1/4}$  as the ordinate are used. It is composed by combining Greenwood diagram [2], Hamrock-Dowson diagram and liquid/solid transition condition given by  $\alpha p$ , i.e., for liquid  $\alpha p < 13$ , for viscoelastic solid  $13 < \alpha p < 25$ , and for elastic-plastic

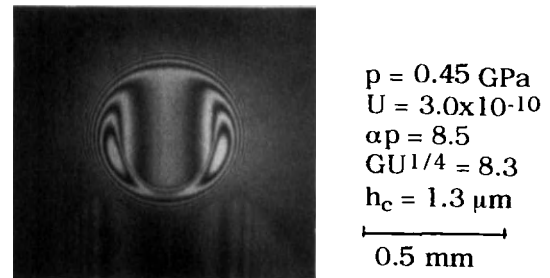


Fig. 2 EHL pattern in rolling contact (Paraffinic mineral oil PBSN)

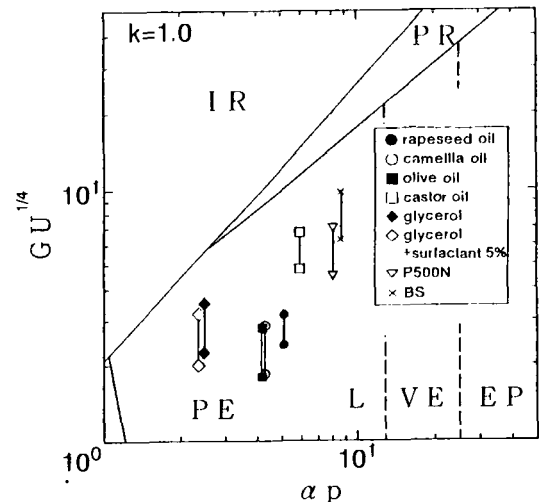


Fig. 3 Experimental points in liquid/solid transition lubrication diagram

solid  $25 < \alpha p$  [7]. The author's experimental ranges for circular contact  $k=1$  are plotted in Fig. 3. In our experimental range, the state of the lubricants is liquid and the lubrication regime is PE, therefore, the central film thickness calculated by the formula of Hamrock-Dowson for elastohydrodynamic lubrication.

Fig. 4 shows central film thicknesses obtained under conditions of pure rolling with a load of 86 N for the case of  $k=3.6$ , where pure rolling was obtained by removing the drive shaft from the barrel shaped roller and allowing the barrel shaped roller to be driven by the disk. For paraffinic mineral oil PBSN the measured film thickness is 1.1 times of the predicted value. The measured film thickness for castor is 0.9 times of the predicted value. In particular, for glycerol that is main component of vegetable oil it is one half of the predicted value.

So far with regard to the measured film thickness lower than predicted value Wedeven, Evans and Cameron [8] and Chiu [9] observed the effects of oil starvation on film thickness. Hirata and Cameron [10] reported the viscosity loss of the polymer thickened oils. In this study experiments are done under fully flooded condition, we couldn't observe the oil starvation, and also the tested lubricants contain no polymer. Therefore, we investigated the effects of interfacial phenomena on the film thickness.

The contact angle was measured on the glass disk with an aid of goniometer. Table 1 show the values of the contact angles. The contact angle of glycerol is so much higher. Therefore, it has poor wettability.

Fig. 5 shows the relation between the contact angle  $\phi$  and the nondimensional measured film thickness  $h_{exp}/h$ , i.e., the ratio

of the predicted central film thickness  $h$  to the measured central film thickness  $h_{exp}$ . The nondimensional measured film thickness  $h_{exp}/h$  decreases with an increase the contact angle  $\phi$ . This fact was considered to be attributed to their poor wettability at the liquid/solid interface. Furthermore, the largest contact angle of glycerol was lowered by adding surfactant and brought about an increase in film thickness. It is suggested that the interfacial phenomena near the inlet side of the EHL contact region effects the EHL central film thickness, in particular, in the case of castor oil and glycerol.

Moreover, it was supported that the recovering time  $t$  of the wake after the sudden stop decreases with a decrease in the contact angle  $\phi$ . Fig. 6 shows the relation between nondimensional measured cen-

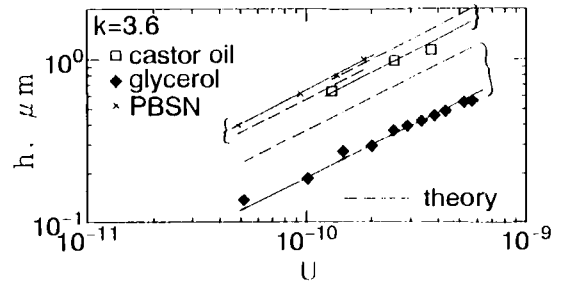


Fig. 4 Central film thickness in rolling contact ( $p = 0.26$  GPa)

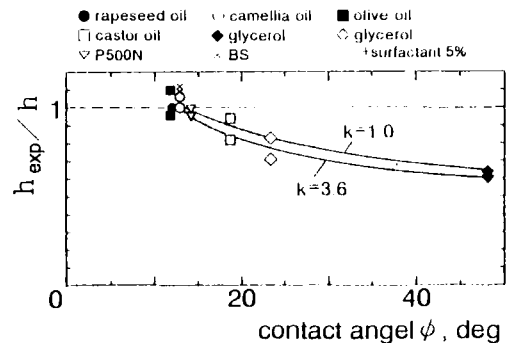


Fig. 5 Effect of contact angle on central film thickness (rolling contact)

tral film thickness  $h_{exp}/h$  and non-dimensional number for interfacial phenomena  $\eta a/\sigma_L t$ , where  $\sigma_L$  is surface tension listed in Table 1,  $a$  is the semi-width of the contact ellipse in perpendicular to the direction of motion and  $t$  is recovering time of wake. It is suggested that the behavior of the inlet region under the EHL condition is similar to the behavior of the outlet region.

Next, we attempted to measure the entrapment of oil between normally approaching elastic bodies to verify the effects of the interfacial phenomena on the EHL film thickness. A schematic diagram of the experimental apparatus [11] is shown in Fig.7. An optical flat of pyrex glass is clamped to the upper part. On the other hand, a bearing steel ball is attached to the upper end of a spindle supported by an air bearing. The impact load is applied by releasing an electromagnet at the end of a lever. The steel ball with a static load 86 N was separated from the glass disk with a clearance of 0.06 mm.

Fig. 8 shows the changes of interference fringe patterns with the elapse of time for castor oil. The authors previously pointed out that under the condition showing  $\alpha p_0$  greater than 25, no leakage occurs corresponding to the elastic-plastic solidification, where  $p_0$  is the maximum Hertzian pressure. When  $\alpha p_0$  is lower than 13, leakage occurs within a short period. Under the intermediate condition  $13 < \alpha p_0 < 25$ , sealing effect is incomplete, but according to the value of  $\alpha p_0$  it maintains for a considerably long period [12].

In this study,  $\alpha p_0$  of tested oils is in the range of 3.7 to 12.5, leakage occurred within a short period. So we recorded the sequence of fringe patterns in a VTR and decided the maximum entrapped film thick-

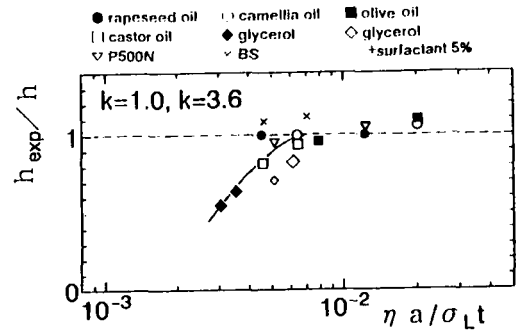


Fig. 6 Relation between central film thickness and non-dimensional number for interfacial phenomena

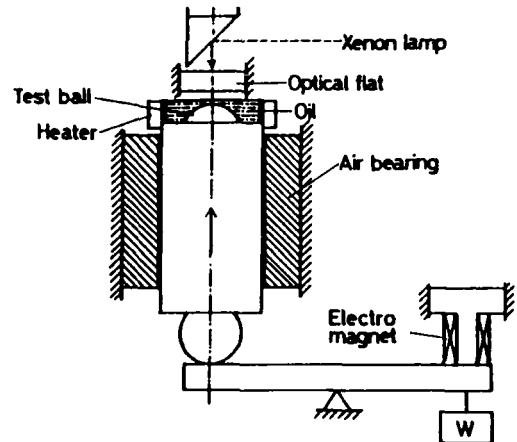


Fig. 7 Schematic diagram of impact test apparatus

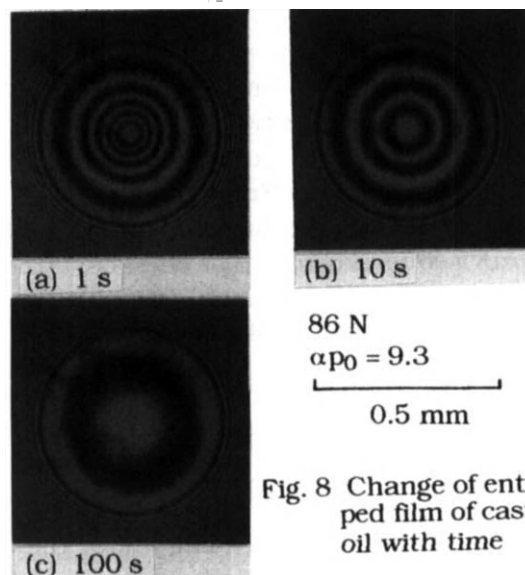


Fig. 8 Change of entrapped film of castor oil with time



ness  $h_{e,max}$  of each oil. Fig. 9 plots  $h_{e,max}$  determined as such for all the 9 tested oils as a function of the lubricant parameter [13]  $\alpha\eta_0$ . The cross points in this figure rearranges for the lubricant parameter  $\alpha\eta_0$  at the previous results [11]. It shows that the maximum entrapped film thickness  $h_{e,max}$  of the mineral oil series, rape seed oil, camellia oil and olive oil tends to increase with increasing the lubricant parameter  $\alpha\eta_0$ , a single relation is obtained irrespective of oils. However, the experimental points of castor oil and glycerol with poor wettability show some deviation from the well-established relation in the case of the mineral oil series. Furthermore, the surfactant containing glycerol brought about an increase in the film thickness. Therefore, using the entrapment of oil between normally approaching elastic bodies, it was ascertained the interfacial phenomena's effects on the EHL central film thickness.

**3.2 Traction Measurements**

The authors previously pointed out that the most suited representation to estimate the traction characteristics is concluded to use the liquid/solid transition lubrication diagram [4]. The author's experimental ranges of elliptical contact  $k = 3.6$  at mean Hertzian pressure  $p = 0.26$  GPa are plotted in Fig. 10. From this figure, it is recognized that the lubrication regime is piezoviscous elastic (PE). The absolute values of the traction coefficient were measured varying slip ratios in positive and negative directions. Fig. 11 plots traction coefficients of castor oil as a function of  $GU^{1/4}$  under mean Hertzian pressure 0.26 GPa ( $k = 3.6$ ), 0.45 GPa ( $k = 1$ ), 0.52 GPa ( $k = 3.6$ ) and 0.90 GPa ( $k = 1$ ). It shows that traction coefficient under the constant pressure tends to decrease with

increasing  $GU^{1/4}$ , while in the range of lower  $GU^{1/4}$  value the traction coefficient reach constant high level  $\mu_{op,max}$  and to increase with increasing mean Hertzian pressure [4]. A number of  $\mu_{op,max}$  for each test oil at mean Hertzian pressure 0.26 GPa, 0.45 GPa, 0.52 GPa and 0.90 GPa are shown in Fig. 12. The results show the traction coefficients of vege-

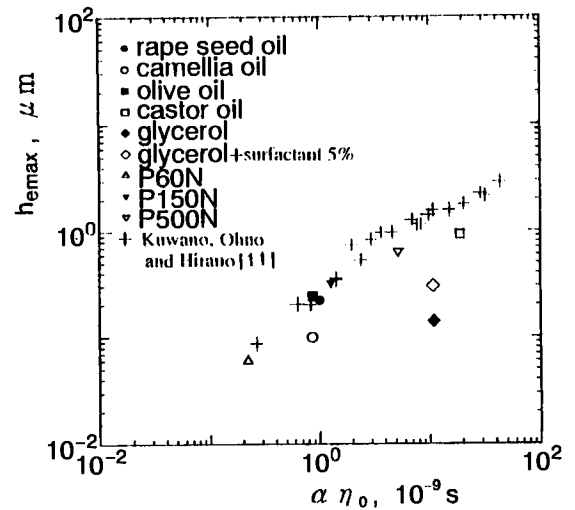


Fig. 9 Relation between entrapped film thickness and lubricant parameter

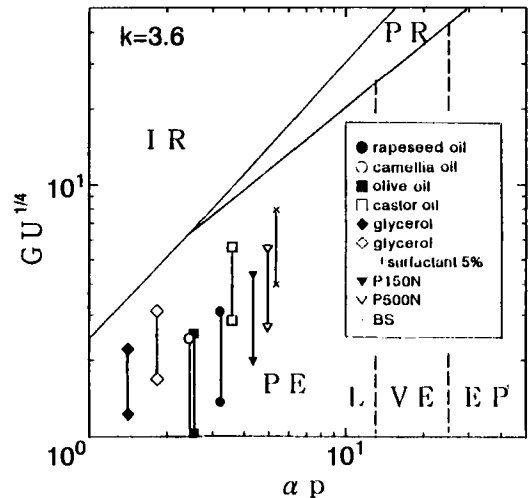


Fig. 10 Experimental points in liquid/solid transition lubrication diagram

table oils with lower pressure-viscosity coefficients  $\alpha$  shown in Table 1 is lower than the mineral oil series of equal viscosity grades at each mean Hertzian pressure. Furthermore, there is a linearly increasing relation between the  $\mu_{\alpha p \max}$  at each mean Hertzian pressure and the pressure-viscosity coefficient  $\alpha$  of oils.

Then, the traction coefficients of glycerol and surfactant containing glycerol is shown about the same values at each mean Hertzian pressure. The effect of wettability on the traction coefficient was unrecognized.

Fig. 13 shows the maximum traction coefficients  $\mu_{\alpha p \max}$  of each oils and the product of the pressure-viscosity coefficient  $\alpha$  and mean Hertzian pressure  $p$ . It shows the  $\mu_{\alpha p \max}$  tends to rise with increasing  $\alpha p$ , where  $\alpha p$  is a measure of free volume of lubricant [4,5,7].

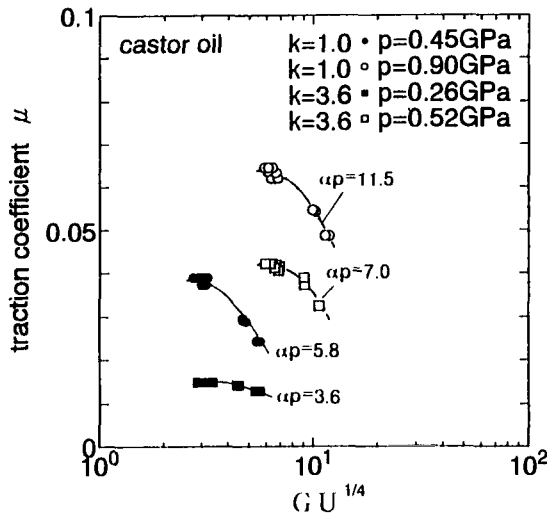


Fig. 11 Effects of  $\alpha p$  and  $GU^{1/4}$  on traction coefficient  $\mu$

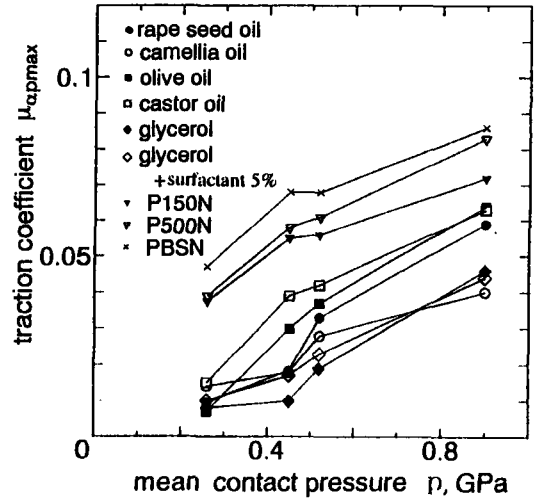


Fig. 12 Effect of mean contact pressure on traction coefficient  $\mu_{\alpha p \max}$

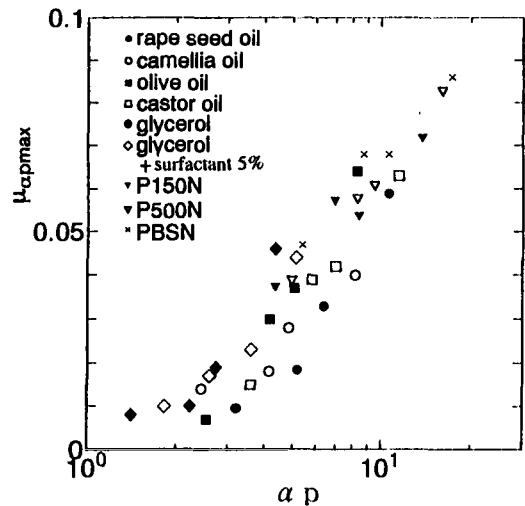


Fig. 13 Effect of  $\alpha p$  on traction coefficient  $\mu_{\alpha p \max}$

#### 4. CONCLUSIONS

Summarizing the experimental results, the following conclusion are drawn concerning the behavior of some vegetable oils in EHL contacts.

(1) The central film thickness of castor oil and glycerol with poor wettability under rolling condition is 0.5-0.9 times thin-

ner compared with the predicted values.

(2) The largest contact angle of glycerol is lowered by adding surfactant and brings about an increase in central film thickness.

(3) Furthermore, using the entrapment of oil between normally approaching elastic bodies, it is ascertained.

(4) These facts show the interfacial phenomena near the inlet side of the EHL contact region affects the EHL central film thickness.

(5) In the full EHL regime, the traction coefficients of vegetable oils are lower than the paraffinic mineral oils with equal viscosity grades. It is caused by lower pressure-viscosity coefficients of vegetable oils. Then, the effect of wettability on the traction coefficient is unrecognized.

(6) The maximum traction coefficient under the constant  $\alpha p$  tends to rise with increasing  $\alpha p$  both the vegetable oils and the paraffinic mineral oils.

## 5. ACKNOWLEDGMENTS

The authors wish to express their thanks Mr. Y. Nakahara, Saga University, for his efforts in preparing the experimental apparatuses; and also to Messrs. T. Isobe and M. Funaguti for their cooperation. The paraffinic minerals and the surfactant were supplied by Idemitsu Kosan Co., Ltd.

## REFERENCES

1. Product review, Biodegradable fluids and lubricants, *Industrial Lubrication and Tribology*, **48**, 2 (1996) 17-26.
2. J.A. Greenwood, Film thickness in circular elastohydrodynamic contacts, *Proc. Instn. Mech. Engrs.*, **202**, C1 (1988) 11-17.
3. N. Ohno, N. Kuwano and F. Hirano, Diagrams for Estimation of the Solidified Film Thickness at High Pressure EHD Contacts, *Proceedings of the 20th Leeds-Lyon Symposium on Tribology, Lyon, September 1993; Dissipative Processes in Tribology*, Elsevier Science B. V., (1994) 507-518.
4. N. Ohno, N. Kuwano and F. Hirano, Traction Control by Considering Free Volume of Lubricating oil, *Proceedings of the International Tribology Conference, Yokohama*, (1995).
5. N. Ohno, N. Kuwano and F. Hirano, Effect of Bulk Modulus of Solidified Oils Under High Pressure on Trictional Behavior, *Japanese Journal of Tribology*, **38**, 10 (1993) 1361-1372.
6. B.J. Hamrock and D. Dowson, *Ball Bearing Lubrication*, John Wiley & Sons (1986).
7. N. Ohno, N. Hattori, N. Kuwano and F. Hirano, Some observations on the Relationship between Rheological Properties of Lubricants at High Pressure and Regimes of Traction (Part 1) The Rheological Properties of Lubricants at High Pressure, *J.JSLE*, **33**, 12 (1988) 922-928.
8. L.D. Wedeven, D. Evans and A. Cameron, Optical analysis of ball bearing starvation, *Trans. ASME, JOLT*, **93** (1971) 349-363.
9. Y.P. Chiu, An analysis and prediction of lubricant film starvation in rolling contact systems, *ASLE Trans.*, **17** (1974) 22-35.
10. M. Hirata and A. Cameron, The Use of Optical Elastohydrodynamics to Investigate Viscosity Loss in Polymer-thickened Oils, *ASLE Trans*, **27**, 2 (1984) 114-121.
11. N. Kuwano, N. Ohno and F. Hirano, Investigation on Entrapment of Mineral Oils under Impact, *J. JSLE*, **31**, 7 (1986) 477-484.

12. F. Hirano, N. Kuwano and N. Ohno. Fundamental Study of Static Sealing Characteristics of Solidified Oils at High Pressure. in *Fluid Sealing*, Nau, B. S., ed., Kluwer Academic Publishers, Dordrecht, The Netherlands (1992) 109-120.
13. Mobil EHL Guidebook, Mobil Oil Corporation, New York (1979)

### Notation

- a semi-width of contact ellipse in y direction
- b semi-width of contact ellipse in x direction
- E' effective elastic modulus  
 $[2/E' = (1 - \nu_1^2)/E_1 + (1 - \nu_2^2)/E_2]$
- G material parameter,  $a E'$
- h film thickness
- $h_e$  entrapped film thickness
- k ellipticity parameter,  $a/b$
- p mean Hertzian pressure
- $p_0$  maximum Hertzian pressure
- $R_x$  radius of curvature in x direction
- t recovering time of wake
- U speed parameter,  $\eta_0 u / E' R_x$
- u mean entrainment velocity
- $\alpha$  pressure-viscosity coefficient
- $\phi$  contact angle
- $\eta_0$  absolute viscosity at atmospheric pressure
- $\mu$  traction coefficient
- $\nu$  kinematic viscosity
- $\rho$  lubricant density
- $\sigma_L$  surface tension
- IE isoviscous-elastic
- IR isoviscous-rigid
- PE piezoviscous-elastic, EHL
- PR piezoviscous-rigid
- L liquid
- VE viscoelastic solid
- EP elastic-plastic solid

## Estimation of pressure viscosity coefficient by high speed and high pressure traction drive test

T. Nakamura, F. Itoigawa and T. Matsubara<sup>a</sup>

<sup>a</sup>Department of Mechanical Engineering,  
Nagoya Institute of Technology,  
Gokiso-cho, Showa-ku, Nagoya 466 Japan

Traction tests under high speed condition are carried out for a traction fluid and the pressure viscosity coefficient of the traction fluid pressurized in an extreme short duration is estimated by comparing calculated results with the experimental results. Traction tests are performed on two roller traction drive apparatus in the surface velocity range from 18.9 to 44.0 m/s. The experimental results suggest a practical use of traction drive device with the traction fluid used in this experiment. A relationship between the maximum traction coefficient which is important value for the practical design of the traction drive and the rheological properties including the pressure viscosity coefficient is numerically introduced. The effect of the surface velocity on the rheological properties is discussed with comparisons between the calculated results and the experimental results. Consequently, no effect of the short duration on the pressure viscosity coefficient of the traction fluid is found in this experimental condition.

### 1. INTRODUCTION

For a practical use of EHD traction drive, it is necessary to estimate rheological properties of traction fluids at the pressure and temperatures existing within the conjunction of the contact. In the viscoelastic model which indicates non-linear stress-strain behavior proposed by Johnson and Tevaarwerk [1], elastic shear modulus of the film, Eyring stress and viscosity under the high pressure are those of properties to find out the magnitude of traction force. Many investigations have been carried out to measure the elastic shear modulus and Eyring stress in practical traction test at the temperatures existing or not [2–5]. On the other hands, the viscosity under high speeds and high pressures has not been measured in practical situations but done in static tests, for instance DAC, or in isothermal traction test [2]. From the standpoint of the practical design and construction for the lubricated parts, for example, rolling bearing, gear tooth, CVT, and so on, it is important to clarify the relationship between pressure and viscosity under a high speed condition. Although several traction tests under high speed condition were reported [6,7], the relationship between pressure and viscosity was not discussed in these reports. The duration in which the fluid is subjected to extremely high pressure through the contact becomes shorter with the increase in the surface velocity. The short duration

may have an influence on the rheological properties of traction fluid for the practical application of the high speed traction.

In this report, traction tests are carried out for a traction fluid. The pressure viscosity coefficient is estimated under high speed and high pressure condition on the traction drive test by taking note of the maximum traction coefficient which determines the design of traction device. Experiments are carried out in the surface velocity range from 18.9 to 44.0m/s at two pressure condition, 0.78 and 0.93 GPa, for the traction fluid “Santotrac 32” which correspond to “Santotrac 50” manufactured by Monsanto Corporation.

### 2. TRACTION TEST APPARATUS

A traction test apparatus used in this research consists of two rollers which are independently driven by speed controlled motors as shown in Fig. 1. Both rollers are spherical and in the same dimension, so it can be assume that the elastic contact between two rollers forms circular and flat contact plane. In this configuration, influence of a misalignment between two axes on the fluctuation of the pressure in the contact can be reduced rather than the case on two flat disk machine in line contact, especially under high speed.

The rollers are supported by high precision angular contact bearings at the both ends. The traction forces

acting on the driver roller and the follower roller are detected by strain gauges attached on the torque tubes and are recorded through slip rings connected at the shaft ends. Rotational speeds of both rollers and a speed difference between them are also recorded. The traction fluid is poured into the conjunction at a rate of 0.34 ℓ/min, and traction fluid temperature is kept constant at 30°C in this report. Roller specification and properties of traction fluid “Santotrac 32 ” are listed in table 1.

In this system, traction forces of the driver roller, which are measured with the gauges, positively include a friction force of one side of support bearing, on the contrary, negatively in the case of follower roller. Figure 2, where elastic tangential compliances of the rollers have been added, shows experimental results of traction coefficient on the follower side in the region of low slip speed. The traction coefficients at zero slide/roll ratio almost take value -0.002, regardless of the applied normal load and roller surface velocity. This negative traction at zero slide/roll ratio can be considered as a result of friction force of the support bearing. Accordingly, measured traction coefficients are corrected by adding the value 0.002 in all conditions.

Table 1  
Roller specification and properties of traction fluid

|                |                   |                  |                                     |
|----------------|-------------------|------------------|-------------------------------------|
| Roller         | Material          | SUJ2 (AISI52100) |                                     |
|                | Surface roughness | 0.18             | μm Ra                               |
|                | Diameter          | 120              | mm                                  |
| Traction fluid |                   |                  |                                     |
|                | Santotrac 32*     |                  |                                     |
|                | Viscosity (40°C)  | 0.027            | Pa·s                                |
|                | Density (20°C)    | 0.901            | × 10 <sup>3</sup> kg/m <sup>3</sup> |

\* corresponding to Santotrac 50 manufactured by Monsanto Corporation

### 3. TRACTION CURVE UNDER HIGH SPEED CONDITION

Traction curves which represent a variation of traction coefficient,  $\mu (= \bar{\tau}/\bar{p})$ , with slide/roll ratio,  $\lambda (= \Delta U/\bar{U})$ , are plotted in Figs. 3 and 4. The former is

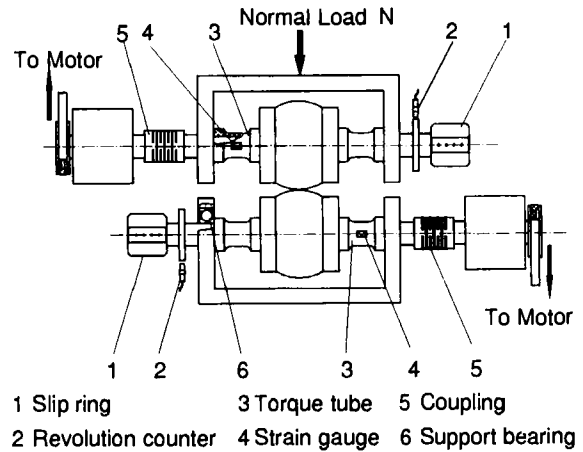


Figure 1. Illustration of traction test apparatus

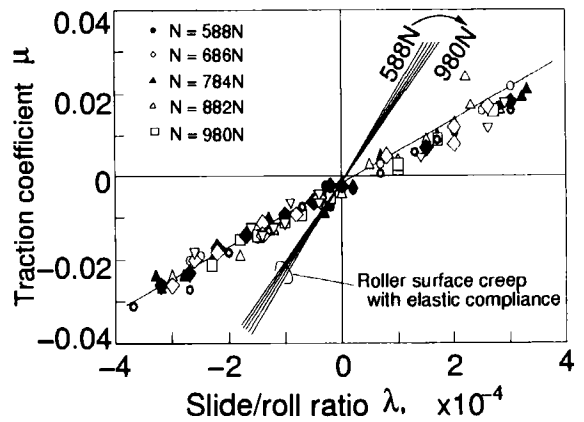


Figure 2. Estimation of support bearing friction and creep motion of roller surface due to elastic compliance

obtained under high pressure,  $\bar{p} = 0.93\text{GPa}$ , the latter is low pressure,  $\bar{p} = 0.78\text{GPa}$ , and roller surface velocity range is from 18.9 to 44.0 m/s in both cases. The elastic compliance of the roller is not negligible in these conditions as shown in Fig. 2. So, the measured slide/roll ratio,  $\lambda$ , is corrected by subtracting the creep motion/roll ratio,  $\lambda_e$ , of the roller, which is obtained by following equation [8],

$$\lambda_e = 1.46 \frac{\bar{p}}{(1 - \nu)E'} \mu, \tag{1}$$

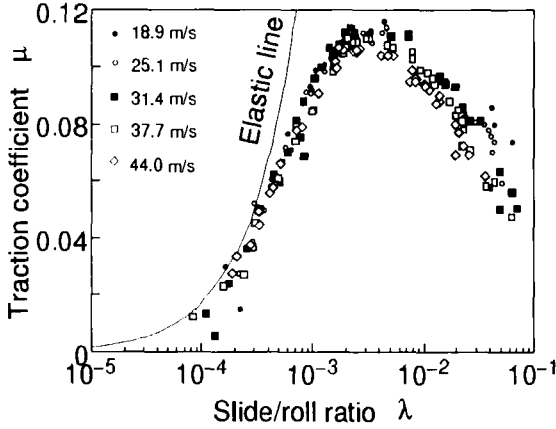


Figure 3. Traction curves obtained in several velocity condition, mean contact pressure  $\bar{p}=0.93\text{GPa}$

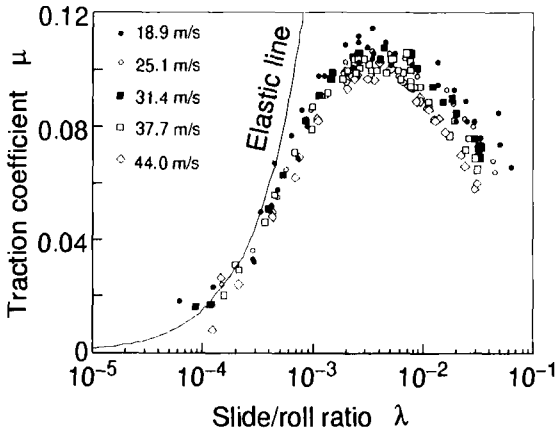


Figure 4. Traction curves obtained in several velocity condition, lower mean contact pressure than in Fig.3,  $\bar{p}=0.78\text{GPa}$

where  $\nu$  is Poisson ratio of roller material and  $E'$  is reduced elastic modulus.

In Figs. 3 and 4, it can be seen that the roller surface velocity has little effect on the initial slope of traction curve at low slide/roll ratio in both pressure conditions. This slope is proportional to the elastic shear modulus,  $G$ , of the traction fluid in the nip and inversely proportional to the aspect ratio of film shape,  $h/a$ . The little change of slope is the consequence of

increase in the elastic shear modulus and increase in the film thickness as the roller surface velocity is increased.

On the other hand, the variations of the traction curves with both the roller surface velocity and the contact pressure can be observed from non-linear region to thermal region. The traction curves begin to leave from the initial slope line if the slide/roll ratio exceeds about 0.0003. The difference in the magnitude of traction coefficient between different velocity conditions increases as the slide/roll ratio becomes larger.

Each curve has a maximum traction coefficient,  $\mu_{max}$ , at a slide/roll ratio,  $\lambda_m$ . The values of  $\mu_{max}$  and  $\lambda_m$  are decreased with increasing the roller surface velocity. Nevertheless, the maximum traction coefficient exceeds 0.1 for almost every testing condition in this experiment. The slide/roll ratio at  $\mu = 0.1$  is smaller than 0.003. The same results were reported for "Santotrac 32" when the inlet temperature was  $40^\circ\text{C}$  [5]. These results suggest a practical use of traction drive device with the traction fluid used in this experiment.

#### 4. PRESSURE VISCOSITY COEFFICIENT AND EYRING STRESS

In this experiment, the traction tests are carried out in non-linear viscoelastic regime because  $\alpha\bar{p}$  is in the range from 18 to 24 [9]. Thus, the stress-strain behavior of EHD film can be represented with the following constitutive equation proposed by Johnson and Tevaarwerk [1],

$$\dot{\gamma} = \frac{1}{G} \dot{\tau} + \frac{\tau_0}{\eta} \sinh\left(\frac{\tau}{\tau_0}\right). \quad (2)$$

If elastic shear modulus,  $G$ , Eyring stress,  $\tau_0$ , and viscosity,  $\eta$ , under high pressure in the EHD contact are known, the behavior of mean shear stress and shear strain can be obtained by integrating this equation over the EHD contact area. The elastic shear modulus,  $G$ , can be obtained from the initial slope of traction curve, because Deborah number,  $D$ , exceeds tenth in the experiment. So,

$$G = \frac{3Nh_0}{8a^3} \frac{\mu_0}{\lambda_0}, \quad (3)$$

where  $N$  is normal load,  $a$  is Hertzian contact radius and suffix "0" denotes the value at low slide/roll ratio.

Assuming that the film thickness,  $h$ , is uniform [10] and the contacting footprint corresponds to Hertzian contact circle, equation (2) may be written non-dimensionally as,

$$\frac{\eta U}{\tau_0 h} \lambda = \frac{U \eta}{a G} \frac{ds}{dX} + \sinh(s) \quad (4)$$

where  $s = \frac{\tau}{\tau_0}$ ,  $X (= \frac{x}{a})$  is non-dimensional distance in the peripheral direction of the roller. Temperature rise,  $\Delta\theta$ , from the inlet fluid temperature,  $\theta_0$ , is:

$$\Delta\theta = \frac{0.154 \mu N \Delta U}{a(k' \rho' c' U)^{0.5}} + \frac{\mu N h \Delta U}{8 \pi a^2 k}, \quad (5)$$

where  $k'$ ,  $\rho'$  and  $c'$  are thermal conductivity, density and specific heat of the roller material respectively and  $k$  is the thermal conductivity of the traction fluid. With this temperature rise,  $\Delta\theta$ , the viscosity in the contact,  $\eta$ , is determined from Barus expression as,

$$\eta = \eta_i \exp(\alpha \bar{p} - \beta \Delta\theta), \quad (6)$$

where  $\eta_i$  is viscosity under atmospheric pressure at the inlet fluid temperature. Consequently, the constitutive equation can be rewritten as,

$$D_i \frac{ds}{dX} = \Sigma_i \lambda - \exp(\zeta \lambda \bar{s} - \alpha \bar{p}) \sinh(s), \quad (7)$$

where

$$D_i = \frac{\eta_i U}{a G}, \quad \Sigma_i = \frac{\eta_i U}{\tau_0 h}, \quad \bar{s} = \frac{\mu \bar{p}}{\tau_0} \text{ and}$$

$$\zeta = \beta \tau_0 \left\{ 0.484 \left( \frac{a U}{k' \rho' c'} \right)^{0.5} + \frac{h U}{8 k} \right\}.$$

To obtain the shear stress distribution,  $s(X)$ , above equation is integrated by using boundary condition at  $X = 0, s = 0$ . Furthermore, integrating this shear stress distribution over whole contact area, mean non-dimensional shear stress,  $\bar{s}$  is obtained as,

$$\bar{s} = \frac{1}{\pi} \int_{-1}^1 \int_0^{2\sqrt{1-Y^2}} s(X) dX dY. \quad (8)$$

The right-hand of above equation depends on  $\bar{s}$ ,  $\lambda$ ,  $\zeta$  and  $h$ . Though  $h$  is represented as

$$h = h_i \exp(0.67 \zeta \lambda \bar{s}), \quad (9)$$

where  $h_i$  is obtained by center film thickness formula under isothermal condition, both  $h$  and  $\zeta$  are regarded as function of  $\bar{s}$  and  $\lambda$ . Consequently, right-hand of equation (8) depends on  $\bar{s}$  and  $\lambda$ .

From the point of view of the application, for example, designing for a practical traction drive machine, it is useful to introduce a relationship between the rheological properties and the maximum traction coefficient and the slide/roll ratio. Then, the mean shear stress  $\bar{s}$  derived above is differentiated with respect to  $\lambda$ :

$$\frac{\partial \bar{s}}{\partial \lambda} = \frac{1}{\pi} \frac{\partial}{\partial \lambda} \left\{ \int_{-1}^1 \int_0^{2\sqrt{1-Y^2}} s(X) dX dY \right\} \quad (10)$$

$$= \frac{1}{\pi} \int_{-1}^1 \int_0^{2\sqrt{1-Y^2}} \frac{\partial s(X)}{\partial \lambda} dX dY.$$

Though  $\partial \bar{s} / \partial \lambda$  is included in the right-hand of above equation, its value is equal to zero at maximum traction. So, above equation may be represented as the form of  $g(\bar{s}, \lambda) = 0$ . Here, equation (8) can be rewritten as:

$$f(\bar{s}, \lambda) = \pi \bar{s} - \int_{-1}^1 \int_0^{2\sqrt{1-Y^2}} s(X) dX dY = 0. \quad (11)$$

From these equations, if the rheological properties, that is, the pressure viscosity coefficient,  $\alpha$ , and Eyring stress,  $\tau_0$ , are known,  $\bar{s}$  and  $\lambda$  at the maximum in the traction curve are derived by solving both  $f(\bar{s}, \lambda) = 0$  and  $g(\bar{s}, \lambda) = 0$  simultaneously. Because integrations included in both equations can not be performed analytically and both equations are implicit expression with respect to  $\bar{s}$  or  $\lambda$ , these parameters can be derived only numerically.

Integrating with Simpson's rule and solving simultaneous equation with respect to  $\bar{s}$  and  $\lambda$  with Newton-Raphson method are performed when  $\alpha$  and  $\tau_0$  change in the ranges from 14 to 34 GPa<sup>-1</sup> and from 4 to 15 MPa, respectively. In Fig. 5, the trajectories of the maximum in the traction curve are illustrated for the various value of parameter  $\tau_0$ . If the magnitude of  $\tau_0$  is increased, the trajectory line considerably moves upward but slightly changes in the position with respect to  $\lambda$ . The value of slide/roll ratio,  $\lambda$ , at which the traction coefficient reaches a maximum decreases as the roller surface velocity is increased. This trend agrees with the experimental results.



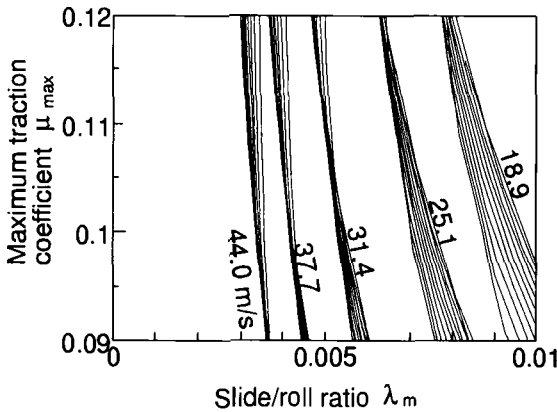


Figure 5. Variations of maximum point in traction curves with  $\alpha$  for various value of parameter  $\tau_0$ , Santotrac 32,  $\bar{p} = 0.93\text{GPa}$

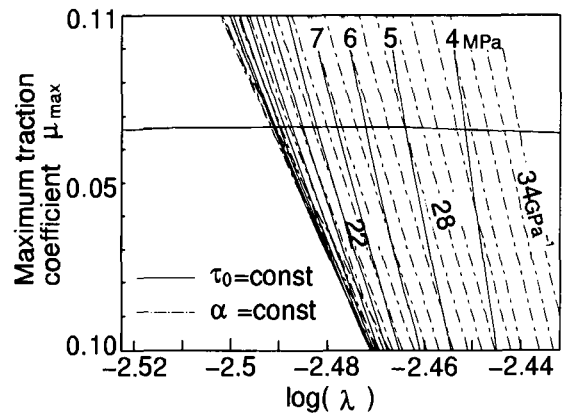


Figure 7. Detailed illustration corresponding to rectangular region of ABCD in Fig.6

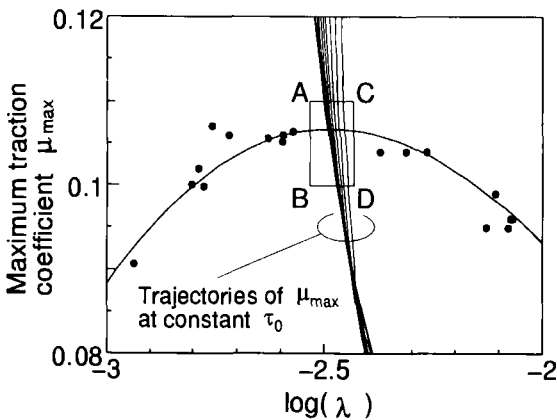


Figure 6. Traction curve by fitting polynomial expression(12) to experimental results and variation of maximum point calculated for Santotrac 32,  $\bar{p} = 0.93\text{GPa}$

5. DISCUSSION

It is considered that the the value of pressure viscosity coefficient,  $\alpha$ , under high speed condition will be found from the position of maximum in the traction curve.

The following polynomial expression with respect to  $\log(\lambda)$  is fitted to the traction test results with the least square method:

$$\mu = \sum_{k=0}^m a_k \{ \log(\lambda) \}^k \tag{12}$$

This fitting result gives both the magnitude of the maximum traction coefficient,  $\mu_{max}$ , and slide/roll ratio,  $\lambda_m$ , corresponding to the maximum point. The values of  $\alpha$  and  $\tau_0$  may be obtained by comparing the fitting result with the calculated results illustrated in Fig. 5 on the  $\lambda$ - $\mu_{max}$  diagram. The diagram shown in Fig. 6 is the case under the high speed and high pressure condition(the roller surface velocity  $U = 44.0\text{m/s}$ , the mean contact pressure  $\bar{p} = 0.93\text{GPa}$ ). A rectangular region ABCD on the diagram is expanded into Fig. 7. By taking it consideration that the ranges of the value  $\alpha$  and  $\tau_0$  are from 14 to 34GPa<sup>-1</sup>, from 5 to 15MPa respectively in these figures, it is revealed that the variations of the magnitude of  $\alpha$  and  $\tau_0$  scarcely change the value of  $\lambda_m$  which indicates the maximum point. It is hard to find the values of  $\alpha$  and  $\tau_0$  simultaneously from this diagram. Accordingly, the pressure viscosity coefficient,  $\alpha$  is estimated by taking a moderate value of  $\tau_0$  into account.

The film temperature rise with the increase in the roller surface velocity is very slight because a rate of increase in film thickness are considerably counterbalanced by a rate of decrease in  $\tau\dot{\gamma}$  at the maximum point, and the roller surface temperature rise is inversely proportional to  $U^{1/2}$ . Evans and Johnson reported a weak effect of pressure on Eyring stress,  $\tau_0$ ,

of the traction lubricant “Santotrac 50” which corresponds to “Santotrac 32” used in this experiment [2]. So, it is assumed that  $\tau_0$  has a constant value in this experiment. Thus,  $\alpha$  can be measured with the diagrams in Fig. 6.

Figs. 8 and 9 show calculated results of the maximum traction coefficient,  $\mu_{max}$ , with roller surface velocity,  $U$ , for the various value of pressure viscosity coefficient,  $\alpha$ . In these calculations, the value of Eyring stress,  $\tau_0$ , was fixed in 10 MPa. This value was decided from experimental results of  $\tau_0$  obtained for Santotrac 32, surface velocity,  $U = 20$  m/s by Saito et al. [5]. The filled circles in these figures denote experimental results of maximum traction coefficient which are measured by fitting polynomial expression mentioned above. The experimental results show reductions of  $\mu_{max}$  with the increase in  $U$  in the same manner as the calculated results where  $\alpha$  is fixed at a constant value. These results suggest that the pressure viscosity coefficient,  $\alpha$ , is maintained nearly at constant regardless of the roller surface velocity.

Fig. 10 shows film temperature rises calculated in the same condition as Figs. 8 and 9, and the elastic shear moduli estimated from experimental results. Calculated results show small changes of temperature rise with the mean contact pressure and roller surface velocity. The elastic shear modulus,  $G$ , increases as the roller surface velocity is increased. This tendency agrees with results reported by Johnson et al. [1] and Loewenthal [3].

## 6. CONCLUSIONS

Traction drive tests under high speed condition are carried out for a traction fluid “Santotrac 32” and the pressure viscosity coefficient of the fluid is estimated by comparing calculated results based on the non-linear Maxwell model proposed by the Johnson and Tevaarwerk with the experimental results.

Obtained conclusions are as follows;

1. The maximum traction coefficient of the traction fluid decreases as the roller surface velocity is increased. Nevertheless, the value of the maximum traction coefficient exceeds the value 0.1 in for almost every testing condition.
2. Calculated results show that the value of slide/roll ratio at which the traction coefficient

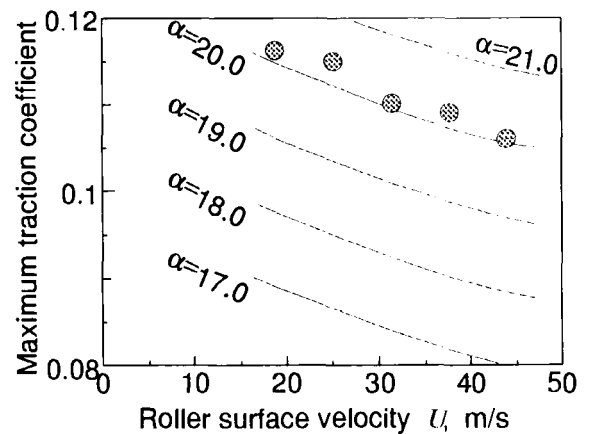


Figure 8. Estimation of pressure viscosity coefficient,  $\bar{p} = 0.93\text{GPa}$ ,  $\tau_0 = 10\text{MPa}$

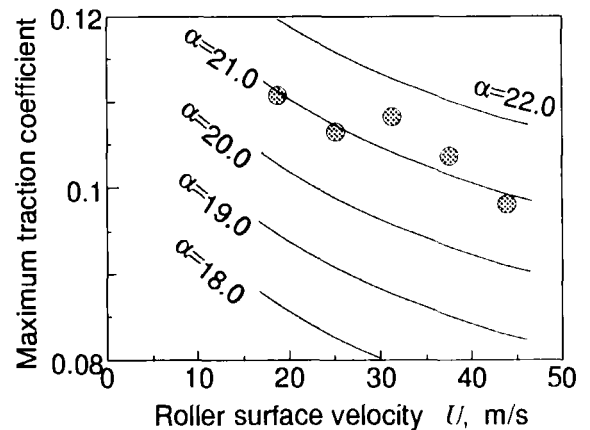


Figure 9. Estimation of pressure viscosity coefficient,  $\bar{p} = 0.78\text{GPa}$ ,  $\tau_0 = 10\text{MPa}$

reaches a maximum decreases as the roller surface velocity is increased. This trend agrees with the experimental results.

3. It is hard to find both the pressure viscosity coefficient and Eyring stress simultaneously by comparing experimental result of the maximum traction point with calculated results.
4. Variations of the pressure viscosity coefficient with the roller surface velocity can be estimated

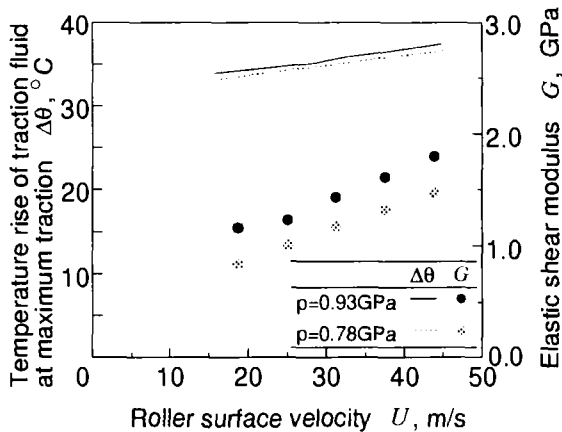


Figure 10. Film temperature calculated at the same condition as Figs. 8 and 9, and elastic shear modulus estimated with experimental results

by fixing the Eyring stress.

- The duration in which the traction fluid through the pressurized contact has little effect on the pressure viscosity coefficient in the surface velocity range from 18.9 to 44.0 m/s.

## REFERENCES

- Johnson, K. L., and Tevaarwerk, J. L., "Shear behavior of elastohydrodynamic oil films," *Proc. Roy. Soc. Lond., Series A.*, vol. 356, 1977, pp. 215-236.
- Evans, C. R., and Johnson, K. L., "The rheological properties of elastohydrodynamic lubricants," *Proc. instn. Mech. Engrs.*, vol. 200, No. C5, 1986, pp.303-312.
- Loewenthal, S. H., and Rohn, D. A., "Elastic Model of the Traction Behavior of Two Traction Lubricants," *ASLE trans.*, Vol. 27, No. 2, 1983, pp.129-137.
- Muraki, M., and Kimura, Y., "Traction Characteristics of Lubricating Oils (4th Report)," *J. Jpn. Soc. Lub. Engrs.*, vol. 30, No. 1, 1985, pp.45-52. (in Japanese)
- Saito, T., and Kawase, T., *Proc. of JAST annual meetings in Tokyo*, 1996, pp. 88-90 (in Japanese)
- Hewko, L. O., "Contact Traction and Creep of Lubricated Cylindrical Rolling Elements at very High Surface Speeds," *ASLE trans.*, vol. 12, 1969, pp. 151-161.
- Maruyama, H., and Ohyama, T., "Rolling Contact at Higher Speeds," *J. Jpn. Soc. Lub. Engrs.*, vol. 23, No. 11, 1978, pp. 808-813. (in Japanese)
- Johnson, K. L., *Contact mechanics*, Cambridge University Press, 1985, pp. 257.
- Evans, C. R., and Johnson, K. L., "Regimes of traction in elastohydrodynamic lubrication," *Proc. Instn. Mech. Engrs.* vol. 200, No. C5, 1986, pp. 313-324
- Johnson, K. L., and Roberts, A. D., "Observations of viscoelastic behaviour of an elastohydrodynamic lubricant film," *Proc. Roy. Soc. Lond., Series A*, vol. 337, 1974, pp. 217-242.

## ACKNOWLEDGMENT

Authors wish to express great thanks for the support of this research from Nippon Oil Company Limited and NTN Company limited.

## Simulated lubricant non-Newtonian behaviour under elastohydrodynamic conditions

S. Chynoweth, R.C. Coy, A.J. Holmes and L.E. Scales

Shell Research and Technology Centre, Thornton, P.O. Box 1, Chester CH1 3SH, U.K.

Non-Equilibrium Molecular Dynamics Simulation (NEMDS) has been used to model the behaviour of simple lubricant-like liquids under extremes of pressure and shear rate, typical of those encountered in elastohydrodynamic (EHD) lubricated contacts. From these simulations, a 'molecular' constitutive equation has been developed and used to compute friction in an EHD line contact. NEMDS is carried out under constant volume conditions and the resultant pressure is obtained, whereas in real EHD conditions pressure is applied to the fluid and the volume changes. Previously reported results [1] using the molecular constitutive equation gave similar oil film thicknesses and friction coefficients to simple Newtonian lubricants at low load and speed conditions. At higher contact pressures, the Newtonian fluids gave unrealistically high friction coefficients, whereas the molecular constitutive equation gave sensible values reasonably close to experiment. However, at the most severe conditions tested, the molecular constitutive equation also gave unrealistically high friction values. In this paper, we correct the molecular constitutive equation to constant pressure and consider the effects of changing the parameters in the constitutive equation for two simple fluids: normal hexadecane and 2,2,4,4,6,8,8-heptamethyl-nonane.

### 1. INTRODUCTION

Classical Newtonian theory has been successfully employed by many researchers for the prediction of lubricant film thickness under elastohydrodynamic (EHD) lubrication conditions [2-4]. This is because the hydrodynamic film thickness is primarily determined by the low pressure inlet region. However, friction is dependent upon the rheology of the lubricant within the high pressure contact zone and the assumption of Newtonian behaviour for lubricants in elasto-hydrodynamic (EHD) lubrication has been shown in many cases to lead to large errors in the prediction of friction.

There have been many models developed to overcome this deficiency. Those based around shear thinning have been successful in predicting friction [5,6], especially those models that invoke a 'limiting shear stress' for the lubricant which is linearly dependent on pressure [7]. The basis for this assumption lies in the experimental measurement of fluid properties at very high pressures and shear rates. The theoretical basis for this is less certain and many constitutive models have been put forward broadly based on a view that the lubricant flows as a plastic solid at some shear stress which varies with temperature and pressure.

In this paper a constitutive equation derived from molecular dynamics simulations of normal and branched alkanes over a wide range of pressures and shear rates is used. This is a shear-thinning model based around the ideas of Rouse for polymer melts [8] and a four parameter flow curve originally proposed by Cross [9]. Using this constitutive model with a new robust numerical EHD solver, we demonstrate that it is possible to get realistic friction values for simple fluids. In a previous paper [1], we have shown that the assumption of constant volume in NEMDS did not correspond to experiment, where constant pressure is the norm. In this paper we correct the molecular constitutive equation to constant pressure and consider the effect of changing the parameters in the constitutive equation for two simple fluids, *n*-hexadecane (*n*-C<sub>16</sub>) and heptamethyl-nonane (*i*-C<sub>16</sub>).

### 2. EHD SOLVER

The software used for the macroscopic EHD simulations in this paper is a black box solver that has been developed for the accurate solution of line contact problems with a compressible or incompressible, isothermal or thermal, Newtonian or non-Newtonian fluid under steady or transient conditions [10,11].

Non-Newtonian behaviour is characterized in the present work by a shear dependent viscosity law derived from molecular dynamics simulations (see Section 3). The software accurately solves problems over an extremely wide parametric range from the highest loads for which solutions have been reported in the literature [12] down through the transition to the hydrodynamic regime. It uses a robust solution strategy based upon state of the art nonlinear equation techniques, linear algebra acceleration and adaptive meshing. The isothermal model employed here takes as input load, reduced elastic modulus, reduced radius, surface velocities, standard viscosity and pressure coefficient of viscosity, along with viscosity and density model parameters. The outputs include pressure distribution, oil film shape, elastic deflections, viscosity distribution, minimum and central film thicknesses, friction force and coefficient of friction.

### 3. NON-EQUILIBRIUM MOLECULAR DYNAMICS SIMULATIONS

Non-equilibrium molecular dynamics simulations [13-15] have indicated that liquids exhibit non-Newtonian behaviour at shear rates which, albeit high, are likely to be found in the lubricated contacts of automotive engines and other highly rated machinery operating under realistic EHD conditions. A concise statement of this behaviour at any state point for one specific alkane, *n*-C<sub>16</sub>, has been presented elsewhere [16]. This can be extended to any linear alkane, hence providing, in effect, a constitutive equation for linear alkanes. This equation is sufficient to provide the flow curve of any linear alkane given its zero-shear-rate viscosity at the appropriate state point and assuming the liquid phase. It is derived by drawing upon the strong analogy between the rheology of molecular liquids and that of polymer solutions which has been established in earlier studies. This approach for *n*-alkanes has been applied to the calculation of oil film thickness and friction under EHD conditions [1].

Whereas NEMDS is carried out at constant volume, shear dilation effects mean that most experimental measurements are better characterised by constant pressure. As small volume changes have been observed under limiting shear stress conditions, pressure corrections must be applied to the NEMDS

results in order to simulate the experimental conditions more closely. At every shear rate  $\gamma$ , the density  $\rho$  was 'manually' adjusted so that corresponding constant volume NEMDS simulations could yield the same pressure  $p(\gamma)$  as at equilibrium ( $\gamma = 0$ ). The size of the pressure correction is only significant at the highest shear rates. The results are presented in Figure 1. The consequence of this correction is to increase the steepness of the flow curve, which we represent by increasing the value of the Cross exponent  $n$ .

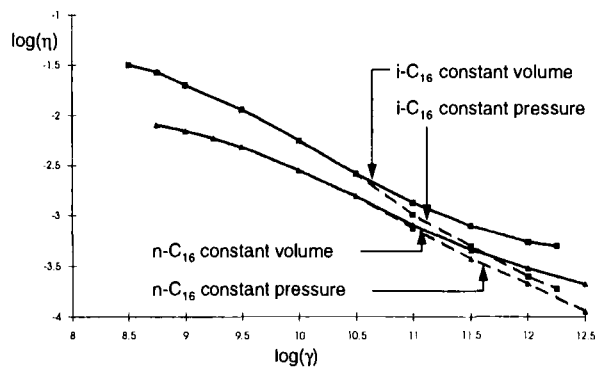


Figure 1: Effect of constant density / pressure on viscosity.

The Cross Equation [9] has the correct features to describe the flow curve ( $\eta(\gamma)$ , where  $\eta$  is the viscosity and  $\gamma$  is the shear rate) of linear alkanes. The equation can be written:

$$\eta(\gamma) = \eta_{\infty} + \frac{\eta_0(p) - \eta_{\infty}}{1 + (\lambda\gamma)^n} \quad (1)$$

which has four parameters: the asymptotic low and high shear-rate values of viscosity (denoted  $\eta_0(p)$  and  $\eta_{\infty}$ ) and  $n$  and  $\lambda$ , which govern the slope and position (in terms of shear-rate) of the shear-thinning region in which the bulk of the transition between the two asymptotes takes place. If  $\gamma_{crit}$  is the shear rate at which the viscosity is mid-way between  $\eta_0$  and  $\eta_{\infty}$ , then

$$\lambda = \frac{1}{\gamma_{crit}} \quad (2)$$

We also have

$$\left(\frac{\partial \eta}{\partial \gamma}\right)_{\gamma=\gamma_{crit}} = -\frac{(\eta_0 - \eta_\infty)n\lambda}{4} = -\frac{(\eta_0 - \eta_\infty)n}{4\gamma_{crit}} \quad (3)$$

and so  $\lambda$  and  $n$  together govern the steepness of the transition, given  $\eta_0$  and  $\eta_\infty$ .

The parameters  $n$  and  $\eta_\infty$  are material constants for the given class of molecular structures, independent of the state-point and the molecular weight. This can be physically justified because at high shear-rates the molecules are aligned along the direction of flow so that the shear stresses are virtually independent of the length of the molecule.  $\eta_\infty$  is fitted from the simulation data.

$\eta_0$  encompasses the pressure dependence of viscosity according to a modified Roelands law:

$$\eta_0(p) = \eta_{atm} \exp\left\{\frac{\alpha p_0}{z} \left[\left(1 + \frac{p}{p_0}\right)^z - 1\right]\right\} \quad (4)$$

The value of  $\eta_{atm}$ , the viscosity at atmospheric pressure, is available experimentally.  $\alpha$  is the pressure coefficient of viscosity and  $z$  is a parameter that modifies the increase in viscosity at high pressures. These parameters are both obtained by fitting experimental data and, if treated independently of each other (necessary for the liquids in the present study), can give excellent fits for a wide range of fluids.  $p_0$  is a universal constant.

The shear-rate at which shear-thinning takes place is governed by the characteristic relaxation time of the molecule, marking the point at which aligning effects of the hydrodynamic flow are sufficient to overcome the thermodynamic relaxation of the molecule. Accordingly, we have estimated the parameter  $\lambda$  by the Rouse relaxation time [8]:

$$\lambda = \frac{1}{\gamma_{crit}} = \frac{K\eta_0(p)}{T\rho(p)} \quad (5)$$

where  $\gamma_{crit}$  is the shear rate at which the viscosity is mid-way between  $\eta_0$  and  $\eta_\infty$ ,  $K$  is a structure

dependent constant,  $T$  is the temperature and  $\rho(p)$  is the density given, according to Dowson and Higginson [3], by

$$\rho(p) = \rho_{atm} \left(1 + \frac{\mu p}{1 + \nu p}\right) \quad (6)$$

$\mu$  and  $\nu$  are parameters obtained by fitting experimental data and  $\rho_{atm}$  is the density at atmospheric pressure. For  $n$ -alkanes [1]

$$K = 6M / \pi^2 R \quad (7)$$

where  $M$  is the molecular weight and  $R$  is the gas constant. For branched alkanes,  $K$  is fitted from the simulation data. Combining Equations (1-7), we obtain viscosity as the function

$$\eta = \eta(\gamma, \eta_{atm}, \eta_\infty, n, K, \rho_{atm}, T, p, \alpha, z, \mu, \nu) \quad (8)$$

This paper studies the normal and branched hydrocarbons  $n$ -C<sub>16</sub> and  $i$ -C<sub>16</sub>, for which the data in Table 1 pertaining to equations (1-7) have been obtained by fitting to experimental data or from NEMDS simulations, as appropriate. The values for  $n$  are those derived from constant volume simulations and are too low. Therefore the effect on friction of varying  $n$  will be explored in Section 4.

|                              | $n$ -C <sub>16</sub>   | $i$ -C <sub>16</sub>   |
|------------------------------|------------------------|------------------------|
| $\eta_{atm}$ (Pa s)          | $3.078 \times 10^{-3}$ | $3.474 \times 10^{-3}$ |
| $\eta_\infty$ (Pa s)         | $1.34 \times 10^{-4}$  | $3.63 \times 10^{-4}$  |
| $K$                          | 0.0165                 | 0.0125                 |
| $n$                          | 0.65                   | 0.76                   |
| $\alpha$ (Pa <sup>-1</sup> ) | $1.15 \times 10^{-8}$  | $1.30 \times 10^{-8}$  |
| $z$                          | 0.13                   | 0.80                   |
| $p_0$ (Pa <sup>-1</sup> )    | $1.96 \times 10^8$     | $1.96 \times 10^8$     |
| $\rho_{atm}$                 | 770                    | 808                    |
| $\mu$ (Pa <sup>-1</sup> )    | $1.2 \times 10^{-9}$   | $1.0 \times 10^{-9}$   |
| $\nu$ (Pa <sup>-1</sup> )    | $3.2 \times 10^{-9}$   | $2.3 \times 10^{-9}$   |

Table 1: Viscosity parameters for  $n$ -C<sub>16</sub> and  $i$ -C<sub>16</sub>.

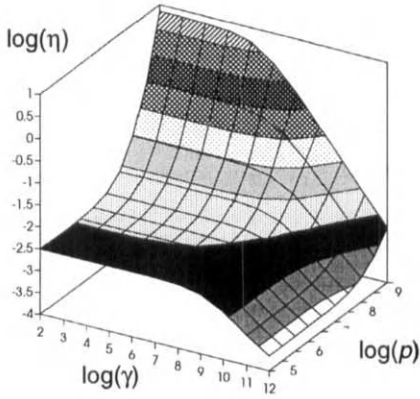


Figure 2a:  $n\text{-C}_{16}$  viscosity function,  $n = 0.65$ .

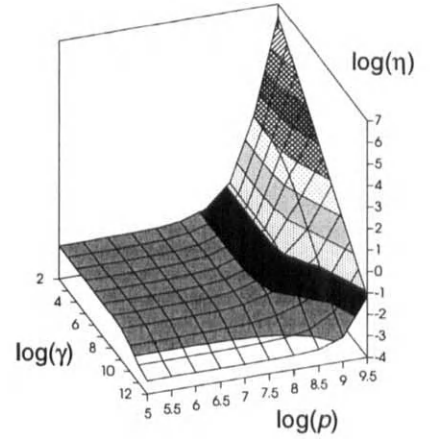


Figure 3a:  $i\text{-C}_{16}$  viscosity function,  $n = 0.65$ .

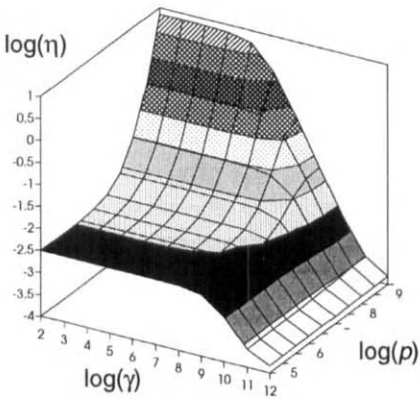


Figure 2b:  $n\text{-C}_{16}$  viscosity function,  $n = 1.00$ .

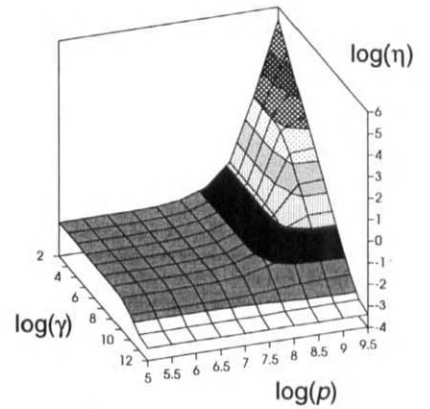


Figure 3b:  $i\text{-C}_{16}$  viscosity function,  $n = 1.00$ .

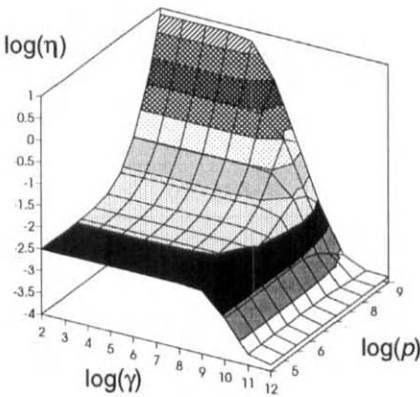


Figure 2c:  $n\text{-C}_{16}$  viscosity function,  $n = 1.35$ .

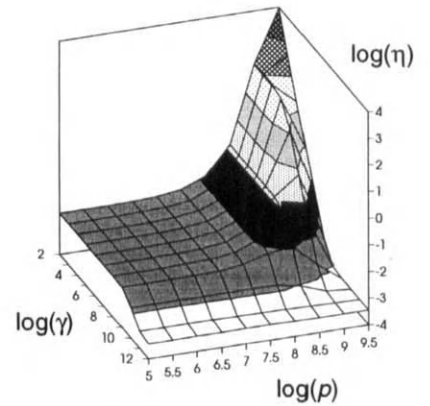


Figure 3c:  $i\text{-C}_{16}$  viscosity function,  $n = 1.35$ .

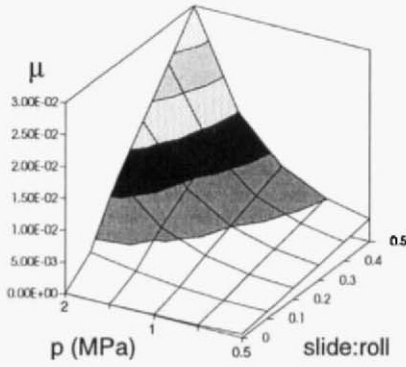


Figure 4a:  $n$ -C<sub>16</sub> friction coefficients, Newtonian.

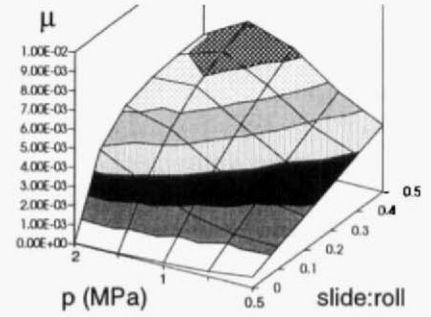


Figure 4d:  $n$ -C<sub>16</sub> friction coefficients,  $n = 1.35$ .

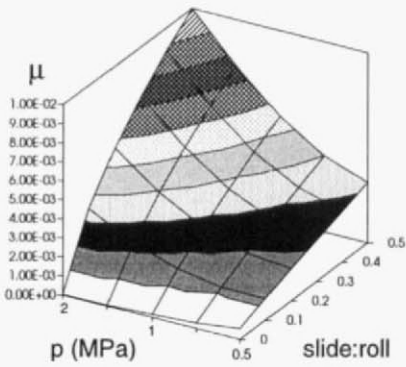


Figure 4b:  $n$ -C<sub>16</sub> friction coefficients,  $n = 0.65$ .

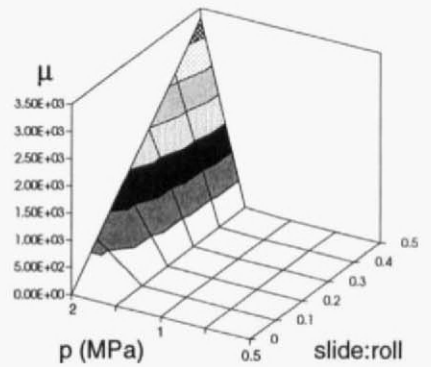


Figure 5a:  $i$ -C<sub>16</sub> friction coefficients, Newtonian.

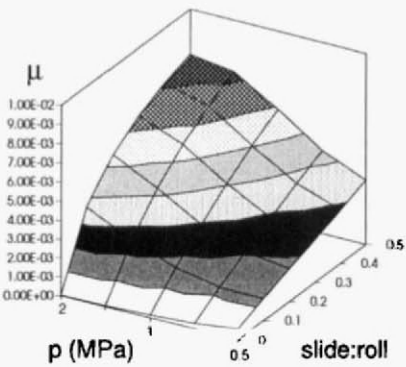


Figure 4c:  $n$ -C<sub>16</sub> friction coefficients,  $n = 1.00$ .

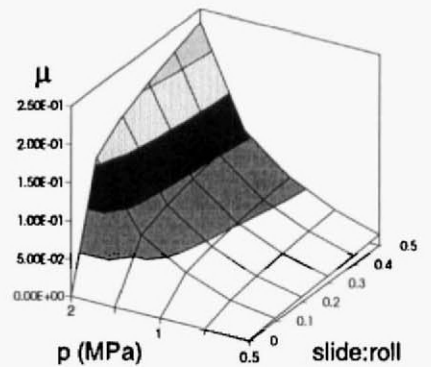


Figure 5b:  $i$ -C<sub>16</sub> friction coefficients,  $n = 0.76$ .



#### 4. APPLICATION OF THE NEMDS CONSTITUTIVE EQUATION TO EHD LUBRICATION

The EHD solver has been used to compare the Newtonian ( $\partial\eta/\partial\gamma = 0$ ) and non-Newtonian cases using the constitutive equation (1) for  $n$ -C<sub>16</sub> and  $i$ -C<sub>16</sub>. The calculations are for isothermal conditions. Figures 2 and 3 plot the viscosity  $\eta$  as a function of shear rate  $\gamma$  and pressure  $p$  as given by equation (1) for  $n = 0.65, 1.0$  and  $1.35$ . Figures 4 and 5 show the variation of friction coefficient  $\mu$  with pressure (logarithmic scale) and slide/roll ratio for  $n$ -C<sub>16</sub> and  $i$ -C<sub>16</sub> in both the Newtonian case and with a variety of  $n$  values.

In practical EHD situations, such as in gears, valve trains and traction drives, contact pressures over 1GPa are common. Film thicknesses can be very small (of the order of a few tens of nanometers) and, for example, in valve trains shear rates over  $10^8$  s<sup>-1</sup> can be inferred [17]. In traction drives, the slide/roll ratio is one of the most important parameters in determining the friction, hence Figures 2-5 cover most practical applications.

#### 5. DISCUSSION

A molecular geometric analysis provides valuable microscopic understanding to the observed macroscopic EHD non-Newtonian behaviour. The intermolecular rearrangement caused by the applied shear manifests itself in changes to the molecular orientation functions [13]. These go from being essentially spherical when the molecules are randomly oriented (at equilibrium and in the first Newtonian region) to becoming more ellipsoidal as  $\gamma$  is increased, indicating an increasing intermolecular alignment. This is the underlying mechanism for shear thinning and is also a possible explanation for limiting shear stress.

Figure 2 depicts the viscosity (equation (1)) for  $n$ -C<sub>16</sub> as a function of pressure and shear rate for three different values of the Cross exponent  $n$ . The increase in the steepness of the transition in the shear thinning regime with increasing  $n$  is clearly seen, both at low and high pressures. For a given value of  $n$ , there is also an increase in steepness with

pressure, since, via equation (5), pressure thickening is incorporated in  $\lambda$  in equation (3). More importantly, increasing  $\lambda$  in this way has exactly the same effect in equation (1) as increasing shear rate. Therefore the whole transitional region is moved towards lower shear rates as the pressure increases. This effect is greater the higher the value of  $n$ , and in Figure 2c is seen to lead to an actual drop in viscosity with increasing pressure at the highest pressures for  $n = 1.35$ .

Figure 3 depicts the corresponding viscosity functions for  $i$ -C<sub>16</sub>. This liquid has much stronger pressure thickening characteristics than  $n$ -C<sub>16</sub> ( $\alpha$  and  $z$  in Table 1) and behaves rather more in the manner of a traction fluid. It shows the same characteristics as  $n$ -C<sub>16</sub> but in a more exaggerated form. In particular, the fall-off in viscosity at high pressure is very marked. This effect is likely to be important in the performance of traction drives (real traction fluids have much stronger pressure thickening properties even than this).

Figure 4 depicts coefficient of friction  $\mu$  as a function of maximum Hertzian pressure and slide/roll ratio for  $n$ -C<sub>16</sub> as computed for a complete contact by the EHD model. Figure 4a shows that, for the Newtonian case, friction increases with both slide/roll ratio and pressure to a value of 0.03. In Figures 4b-4d, the shear thinning non-Newtonian constitutive equation is used for three values of the Cross exponent  $n$ . The effect of increasing  $n$  is to progressively reduce the coefficient of friction at the highest pressure and slide/roll ratio from 0.01 at  $n = 0.65$  to 0.006 at  $n = 1.35$ . This is a consequence of the reduction in viscosity at high pressures discussed above. The levelling out and eventual turn-down of the coefficient of friction at higher slide/roll ratios with increasing pressure is a result of the increasing importance of shear thinning behaviour within the contact under the given operating conditions. This mimics experimental results run under approximately isothermal conditions [18].

The effect of changing structure from linear to branched is partially illustrated in Figure 5. The Newtonian model (Figure 5a) gives unrealistically high coefficients of friction of over 3000. The shear thinning model (Figure 5b) shows the levelling out of coefficient of friction to about 0.25 with slide/roll

ratio, even for a value of  $n = 0.76$ . This is a consequence of the different response of the two fluids to pressure, as discussed above. There is much less pressure thickening with the former at high pressures and hence a lower coefficient of friction, other things being equal. This is illustrated in Figure 6, which shows that  $z$  has a much stronger influence on the coefficient of friction than  $\alpha$ . This reflects the effect that different molecular structures have on the response of the fluid at high pressure.

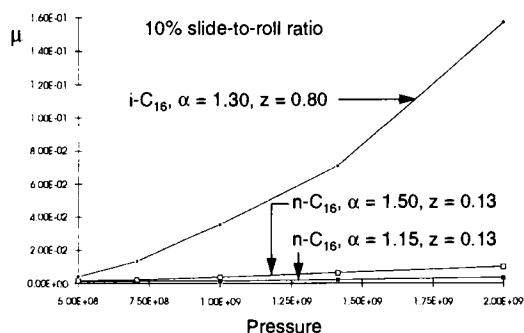


Figure 6: Effect of viscosity pressure coefficient on  $\mu$ .

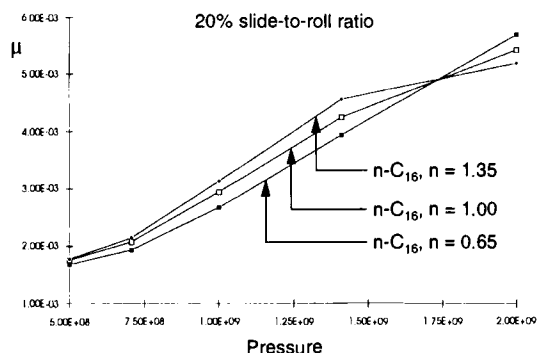


Figure 7: Effect of Cross equation exponent on  $\mu$ .

The effect that changing  $n$  has on the coefficient of friction for  $i\text{-C}_{16}$  for a given slide/roll ratio is clarified in the example given in Figure 7. Here, the coefficient of friction is plotted against pressure at 20% slide/roll ratio. Initially the coefficient of friction is highest with  $n = 1.35$ , but, as the pressure increases, the order reverses so that  $n = 0.65$  gives the highest coefficient of friction. This is in response

to the steeper drop in viscosity and the earlier onset of shear thinning at higher pressures.

The analysis of our molecular model combined with the macroscopic EHD solver provides insight into the role of molecular structure in determining friction under realistic conditions. The importance of non-Newtonian effects on calculating coefficient of friction and how they vary with structure has been demonstrated. Current work is being directed to modelling friction with a wider range of molecular structures.

## 6. CONCLUSIONS

1. We have demonstrated that a shear thinning constitutive equation for simple fluids can be derived from non-equilibrium molecular dynamics simulations.
2. The effect of constant pressure simulations rather than constant volume is to effectively increase the Cross exponent  $n$ .
3. This constitutive equation can be applied to the continuum equations for EHD lubrication under realistic conditions.
4. The effect of increasing  $n$  can be to increase or decrease friction depending upon the pressure.
5. Increasing the pressure coefficient of viscosity increases friction.
6. The NEMDS constitutive model shows that realistic friction coefficients can be derived in comparison with the simple Newtonian case.

## 7. ACKNOWLEDGEMENTS

The authors would like to thank their colleagues at Thornton Research Centre for their assistance and Shell Research for permission to publish.

## REFERENCES

1. S. Chynoweth, R.C. Coy, Y. Michopoulos and L.E. Scales, Simulated lubricant behaviour under elastohydrodynamic conditions, Proceedings of the International Tribology Conference, Yokohama, **2** (1995) 663-668.
2. D. Dowson. and G.R. Higginson. A numerical solution to the elastohydrodynamic problem, *J. Mech. Eng. Sci.*, **1** (1959) 7-15.
3. B.J. Hamrock and D. Dowson, *Ball Bearing Lubrication - The elastohydrodynamic lubrication of elliptical contacts*, John Wiley and Sons, New York (1981).
4. C.C. Kweh., H.P. Evans and R.W. Snidle, Elastohydrodynamic lubrication of heavily loaded circular contacts, *Proc. Inst. Mech. Engrs.*, **203** (1989) 133-148.
5. C.R. Evans and K.L. Johnson, The rheological properties of EHD lubricants, *Proc. Inst. Mech. Engrs.*, **200** (1986).
6. S. Bair and W.O. Winer, The high pressure, high shear stress rheology of liquid lubricants, *ASME J. Tribology* **114** (1992) 1.
7. S. Bair and W.O. Winer, The high shear stress rheology of liquid lubricants at pressures of 2 to 200 mPa, *ASME J. Tribology*, **112** (1990) 246.
8. P.E. Rouse Jr., A theory of the linear viscoelastic properties of dilute solutions of coiling polymers, *J. Chem. Phys.*, **21** (1953) 1272-1280.
9. M.M. Cross, Rheology of non-Newtonian fluids: A new flow equation for pseudoplastic systems. *J. Colloid Sci.*, **20** (1965) 417.
10. A.G. Schlijper, L.E. Scales and J.E. Rycroft, Current tools and techniques for EHL modelling, *Tribology International*, **29** (1996) 669-673.
11. L.E. Scales, J.E. Rycroft, N.R. Horswill and B.P. Williamson, Simulation and observation of transient effects in elastohydrodynamic lubrication, SP-1182, SAE International Spring Fuels and Lubricants Meeting, Dearborn, Michigan, (1996) 23-34.
12. C.H. Venner, W.E. ten Napel and R. Bosma, Advanced multilevel solution of the EHL line contact problem, *J. Tribology*, **112** (1990) 426-432.
13. A. Berker, S. Chynoweth, U.C. Klomp and Y. Michopoulos, Non-equilibrium molecular dynamics (NEMD) simulations and the rheological properties of liquid n-hexadecane, *J. Chem. Soc. Faraday Trans.*, **88** (1992) 1719.
14. D.J. Evans and G.P. Morriss, *Statistical mechanics of nonequilibrium liquids*, Academic Press, London, (1990).
15. P.J. Davis, D.J. Evans and G.P. Morriss, Computer simulation study of the comparative rheology of branched and linear alkanes, *J. Chem. Phys.*, **97** (1992) 616.
16. S. Chynoweth, R.C. Coy and Y. Michopoulos, Simulated non-Newtonian lubricant behaviour under extreme conditions, *Proc. Inst. Mech. Engrs.*, **209(J4)** (1995) 243-254.
17. B.P. Williamson, and H.N. Perkins, The effects of engine oil rheology on the oil film thickness between a cam and rocker follower, SAE 92, 2346.
18. B.O. Jacobson, Rheology and elastohydrodynamic lubrication, Elsevier Tribology Series, **19** (1991) 202.

## Elastohydrodynamics of gears

R W Snidle and H P Evans

School of Engineering  
University of Wales Cardiff, Cardiff CF2 1YF

The paper describes recent experimental and theoretical work on the elastohydrodynamic lubrication of gears. Gear tooth contacts tend to operate under conditions where the film is thin compared to surface roughness. This feature is shown to have a significant effect on scuffing capacity and friction and is also thought to be a factor in micropitting. Recent developments in thin film micro EHL theory are described and these should lead to a better understanding of the behaviour and modes of surface distress in gears. The application of EHL analysis to the special types of contacts occurring in conformal and worm gears and thrust cones is also described.

### 1. INTRODUCTION

The mechanism responsible for the protection of the surfaces of heavily loaded rolling/sliding contacts such as those between gear teeth is elastohydrodynamic lubrication (EHL). However, an important feature of gear tooth contacts is that the surfaces produced by present day manufacturing methods have roughness features that are of the same order or even significantly greater than the thickness of the oil film predicted by classical EHL theory [1]. Consequently they operate under conditions described as "partial", "mixed" or "micro" EHL. In theoretical solutions of both the dry contact and micro-EHL problems the presence of significant roughness leads to a severe rippling in the contact pressure distribution with maximum values far in excess of the Hertzian values expected when the surfaces are perfectly smooth. A practical problem which is directly associated with these effects in hardened steel gears is that of "micropitting". A second form of surface failure in which roughness effects appear to play a part is that of scuffing. In this case the presence of gaps between the loaded surfaces in the nominal contact region allows leakage and escape of oil from the contact which can lead to complete collapse of the EHL film.

Unlike rolling element bearings, which tend to have relatively good surface finish, most gears rarely have a finish better than about  $0.4\mu\text{m}$  roughness

average ( $R_a$ ) and nominal oil films are typically  $1\mu\text{m}$  (far less than this value under high temperature or low speed conditions).

The particular problems of gear tooth contact lubrication have been highlighted by the British Gearing Association (BGA) [2] in its document: "Framework for transmission engineering research for the UK". The case prepared by BGA for basic research was founded upon an extensive survey of the gearing industry, and detailed requirements have been assessed by the Gear Research Foundation. The practical need for research on gearing in general is thus well made by BGA. In relation to tooth lubrication theory BGA concluded that "Conventional EHL theory does not satisfactorily explain lubrication of the gear mesh"

The aim of this paper is to draw attention to the need for research on gear tooth contact lubrication that will lead to a better understanding of the problems of micropitting and scuffing and gear lubrication in general.

### 2. SCUFFING

Scuffing is a form of surface distress that can affect gears running at high speeds or at high temperatures. Although there is no accepted explanation for the mechanism of scuffing it appears to be linked (in some situations) to the physical failure of the EHL mechanism. In attempting to

avoid scuffing problems the gear designer often specifies the use of chemically active extreme pressure (EP) additives in the lubricating oil or some form of surface treatment for the gears such as hardening or nitriding or a combination of these. Recently Patching et al [3] have shown experimentally that an improvement in the surface finish of hardened and ground steel discs can produce a significant improvement in scuffing performance. Scuffing tests to compare the performance of conventionally ground with superfinished (polished) discs showed an increase in the load at scuffing by a factor of about two. An additional benefit of the polishing process was that significantly lower friction and bulk metal temperatures were produced (see §4). It should be emphasised that the ground and superfinished discs were of the same steel which was case-carburised and hardened to the same specification for both types of finish. The quality of the polishing process used is illustrated in Figure 1. Collected results from the series of scuffing tests to compare ground and superfinished discs are shown in Figure 2.

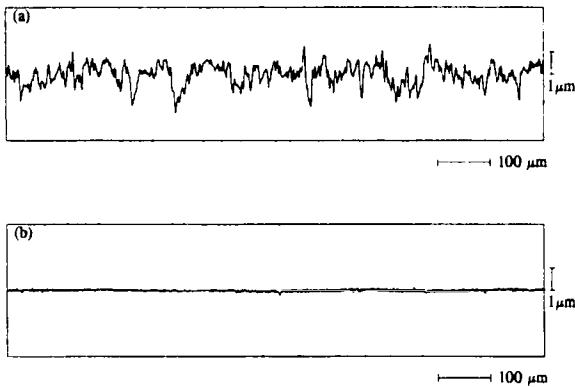


Figure 1. Comparison of (a) ground and (b) superfinished surfaces used in disc machine experiments.

Analysis of EHL between typical gear tooth surfaces in contact strongly suggests that scuffing can be explained by the physical failure of the lubrication mechanism due to sideways leakage of lubricant near the edges of nominal point contacts, and within nominal line contacts due to waviness in the direction transverse to that of rolling/sliding.

Figure 3 shows a scuffing scar at the edge of an elliptical contact: it is easy to envisage the leakage of oil from the loaded area in a transverse direction along the relatively deep valleys between asperities produced by the grinding process.

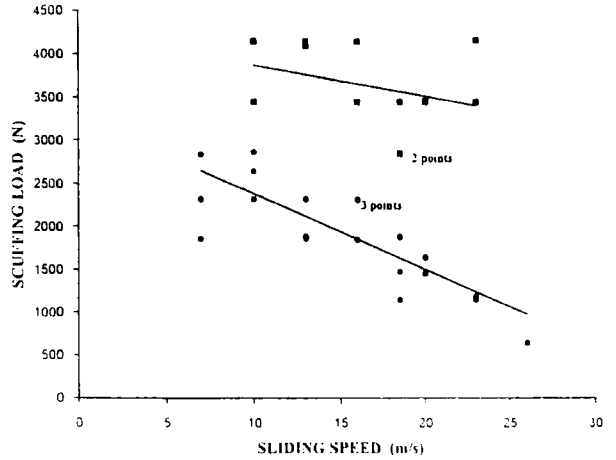


Figure 2. Results of scuffing experiments using steel discs. Lubricant: Mobiljet 2; oil feed temperature 100 degC.

● ground surfaces; ■ superfinished surfaces.

Roughness valleys are therefore seen as vulnerable features of the surface when considering lubrication effects. This idea has been pursued theoretically [4] in a simple model of EHL film failure in which a dry contact analysis has been used to provide the geometry of gaps (due to valley features of roughness) between lubricated surfaces under thin film conditions. The magnitude of the transverse pressure gradients needed to cause significant sideways leakage in these gaps, and hence collapse of the film, is consistent with that present at the edges of real EHL contacts under similar operating conditions.

In a more sophisticated development of this model now being pursued the transverse pressure gradient is no longer regarded as a disposable quantity but is calculated on the basis of a detailed analysis of oil flow in the gaps when subjected to boundary conditions at the edges of real contacts. This approach to modelling of film thinning and loss in real contacts shows promise as a means of explaining the physical limits of EHL films.

### 3. MICROPITTING

Micropitting is pitting (rolling contact fatigue) on the scale of the roughness, as opposed to classical pitting which is on the scale of the nominal Hertzian contact dimension. With increased use of hardened gears micropitting has become of widespread concern. Although micropitting affects gears of all types it has become particularly troublesome in heavily loaded gears with hardened teeth. The problem has been studied by researchers [5] [6] [7] [8] and is well known to gear designers [9]. Micropitting is also described as "frosting" or "grey staining" in the industry. It is characterised by the presence of fine surface pits and the occurrence of local plastic deformation and shallow surface cracks. The condition can lead to significant wear of the surfaces causing loss of profile of the teeth. More serious cases precipitate scuffing and even complete fracture of the tooth. The problem is widespread and its solution has a high industrial priority.

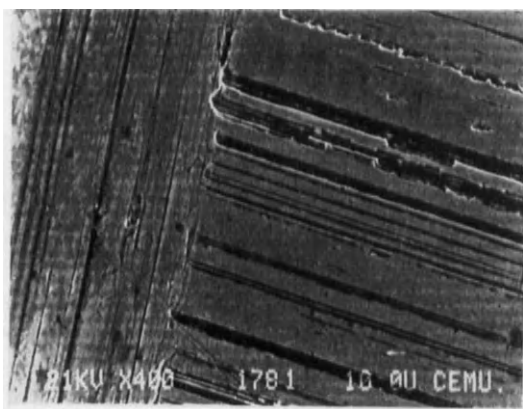


Figure 3. Scuffing scar (vertical mark) on surface of a ground steel disc at edge of contact region.

The causes of micropitting are not fully understood, but it is generally agreed that surface roughness and the high contact stresses at asperity contacts within the overall Hertzian contact are the key factors. A thorough understanding of the stresses at asperity contacts is clearly needed. Useful information can be obtained using elastic contact simulation [10] [11] or elastic/plastic contact simulation [12] which ignore the presence of the oil film. However, it is necessary to consider micro-EHL effects since these influence the contact

pressures and, through non-Newtonian and time-dependent behaviour, determine the traction forces at the micro contacts. The important sub-surface stress field is therefore affected by the presence of a micro EHL film.

The mechanism of plastic ratchetting brought about by asperity pummelling or cyclic stressing at the edges of micro contacts described by Kapoor and Johnson [13] may be a factor in micropitting. Work which has so far been directed towards an understanding of failure of railway wheel contacts undergoing plastic deformation may also have relevance to the problem [14].

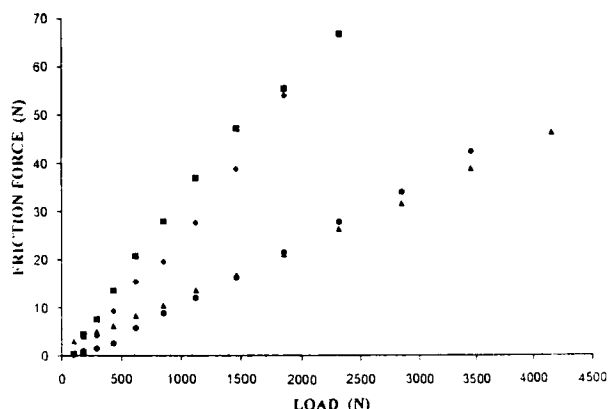


Figure 4. Friction force at disc contact.

- ◆ ground surfaces;
- ▲ superfinished surfaces.

### 4. FRICTION AND HEAT TRANSFER

The efficiency of work transfer in a gear mesh is generally in excess of ninety percent, so in many industrial applications overall efficiency of a geared transmission system is not a major issue. However, in high technology applications such as aerospace the losses arising from friction can become of critical importance. For example, the need for ever greater efficiency of propulsion systems for large transport aircraft has led to serious consideration of geared propeller engines or "geared fans" where a reduction gear drive is used to match the speed of an optimum-efficiency gas turbine to that of an efficient propeller or fan. The powers involved are high, typically 30 MW or even higher. In these applications reduced gear tooth friction can

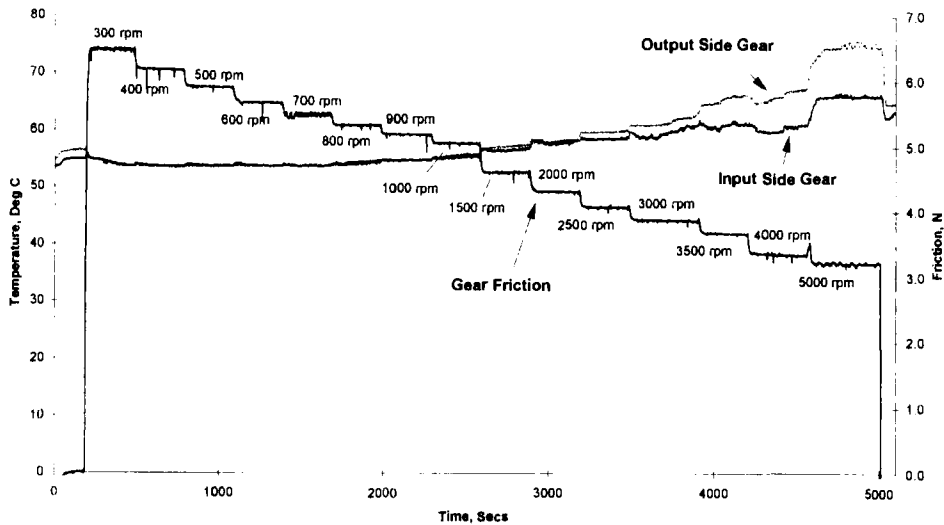


Figure 5. Results of gear friction test. Graphs show gearbox friction force and gear tooth bulk temperatures.

potentially lead to significantly lower amounts of heat being generated at the tooth contacts and hence less bulky cooling arrangements.

Measurements of bulk temperatures in a high speed two-disc machine used to simulate aerospace tooth contact conditions shows the potential benefits of superfinishing of the surfaces [15]. Figure 4 shows a typical comparison of disc friction values in this rig under the same operating conditions of rolling and sliding speed.

In current research at Cardiff measurements of losses in gearing are being made using a special gearbox mounted on trunion bearings. At high speeds the nature of the convective heat transfer between the oil jet and the gears becomes a significant factor in determining their temperature. Figure 5 shows some preliminary results of overall losses and gear tooth bulk temperatures as a function of speed obtained from the rig. In future work losses and temperatures will be compared with conventionally ground and superfinished gears and experimental values of friction with predictions from micro EHL theory. For this work it will be necessary to use the thin film EHL solver described by Elcoate, Evans and Hughes [16] (see §5). The solver will be developed for thermal, non-Newtonian, time-dependent conditions for this purpose.

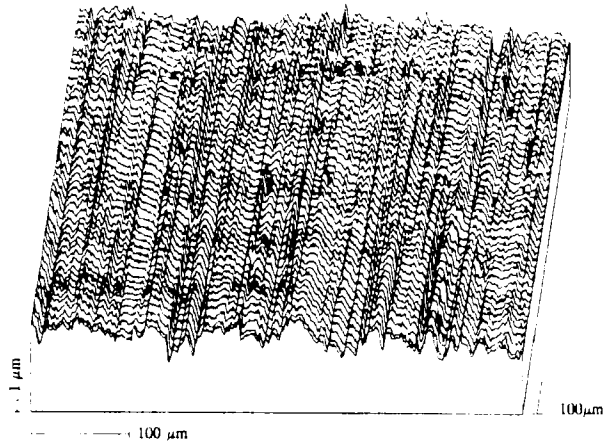


Figure 6. Three-dimensional visualisation of surface of a ground steel gear tooth.

## 5. MICRO EHL THEORY

Considerable progress has been made with modelling of roughness in EHL contacts starting with idealised single features or sinusoidal waves and progressing to measured (real) roughness on both line and point contacts. Most analyses are based on the two-dimensional or nominal line contact assumption. This is a reasonable assumption in the case of conventional involute,

parallel axis gears where rolling/sliding takes place across the finishing marks which are close to being two-dimensional, as may be judged from Figure 6.

The early attempts to model micro EHL were based upon a sinusoidal representation of roughness under steady state conditions (Goglia et al [17]; Lubrecht et al [18]; Kweh et al [19]; Elsharkawy and Hamrock [20]) More recently real surfaces as represented by profilometer traces of actual surfaces have been used in steady-state solutions (Sadeghi [21]; Kweh et al [22]; Venner, et al [23]). The problem of non-steady (i.e. moving roughness) conditions has been addressed by Chang and Webster [24], Chang [25], and Chang et al [26] using sinusoidal roughness, and by Ai and Cheng [27] with random roughness. The influence of non-Newtonian effects in micro EHL solutions in general has been reviewed and studied by Chang and Zhao [28].

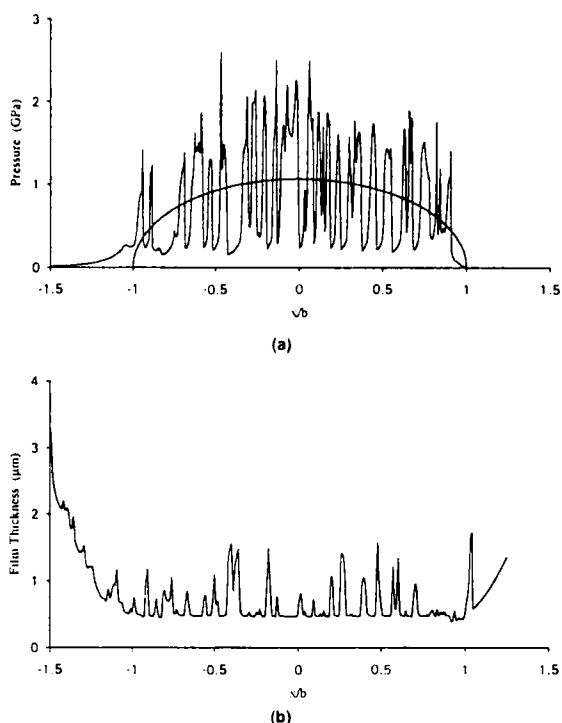


Figure 7. Results of micro-EHL analysis of ground steel surfaces. (a) pressure distribution shown relative to Hertzian; (b) film thickness profile.

A comparison of micro EHL of ground and superfinished surfaces [29] is shown in Figures 7

and 8. The surface profiles shown in these simulations were taken from discs used in the experimental work described in §2.

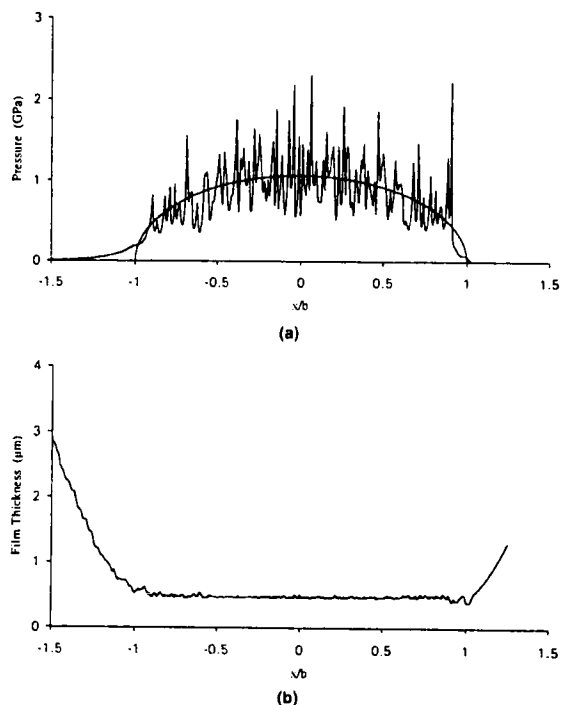


Figure 8. Results of micro-EHL analysis of superfinished steel surfaces. (a) pressure distribution shown relative to Hertzian; (b) film thickness profile.

The main problem with such solutions is in simulating conditions in which the oil film is of the same order or much smaller than the roughness amplitude, as it apparently is in many gears. These simulations of rough EHL contacts show sharply rippled pressure distributions with maximum pressures typically exceeding twice the corresponding Hertzian maximum pressure. The latest solutions of this type show that the inclusion of non-Newtonian lubricant behaviour and consideration of the roughness moving relative to the contact tend to reduce the pressure ripples but also tend to give thinner oil films. Rippling of the pressure distribution clearly has implications for surface fatigue effects such as pitting and micro-pitting and the reduction of pressure in valley features, if extreme, can produce a sharp decrease of



viscosity and hence greatly enhance the tendency of the oil to leak from the contact in the sideways direction.

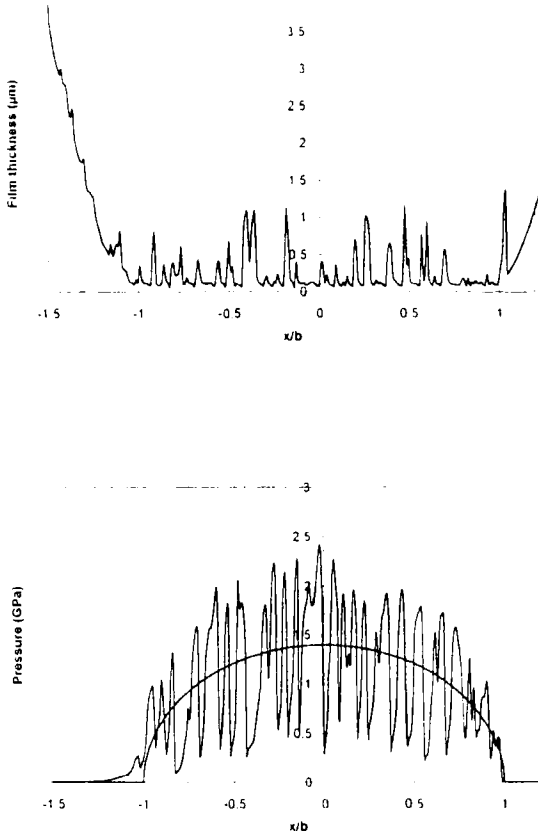


Figure 9. Results of micro-EHL analysis under very thin film conditions. Minimum film thickness 0.05 µm; rolling speed 22m/s; sliding speed 27.3m/s; lubricant Mobiljet 2 at 192 degC.

The effects of non-Newtonian lubricant behaviour and the transient (moving roughness) problem have been included in the most recent numerical models. However, the practically important case of high (roughness/film thickness) seems to present a very difficult numerical problem. In order to study real gear tooth contact problems it will be necessary to model cases where the depth of roughness features is at least ten times greater than the minimum film. For this purpose a special line contact micro EHL solver has been developed by Elcoate et al [16]. With this solver it is possible to investigate conditions in which the minimum film is extremely

thin compared to the deepest valley features of roughness as shown in Figure 9.

6. THRUST CONES

Thrust cones are conical rims placed on the end faces of single helical gears in order to react the axial force that occurs when the gears are transmitting torque. If the apex angle of the mating thrust cones is large (i.e. close to 180 degrees) and equal, then the geometrical conformity of the line contact between the cones is high, and conditions favour the generation of a thick EHL film. There appears to have been little basic work on the modelling of thrust cones and the approach taken by designers has been to use cones having apex angles giving very high conformity.

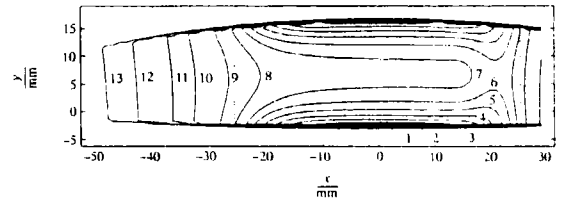


Figure 10. Severe thinning at the edge of a thrust cones contact. Load 106kN; central film thickness 12.6µm; minimum film thickness 0.31µm.

Contour key

|    |      |    |      |    |      |
|----|------|----|------|----|------|
| 1  | 1µm  | 2  | 2µm  | 3  | 4µm  |
| 4  | 6µm  | 5  | 8µm  | 6  | 10µm |
| 7  | 12µm | 8  | 15µm | 9  | 20µm |
| 10 | 30µm | 11 | 40µm | 12 | 60µm |
| 13 | 80µm |    |      |    |      |

Full elastohydrodynamic lubrication analysis of a typical thrust cones design [30] shows that in theory these devices can generate substantial oil films which should provide complete separation of the lubricated surfaces. A typical film at the centre of the contact region is about 12µm. The Ra of surfaces used in thrust cones applications is likely to

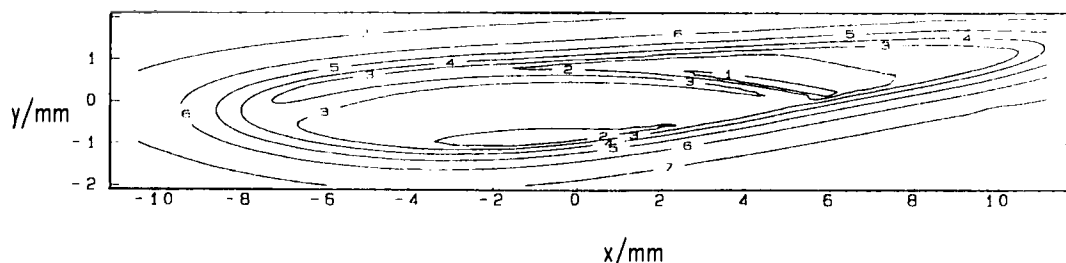


Figure 11. Film thickness contours for a worm gear tooth contact. Load 11.6 kN.

Contour key

1, 0.25 $\mu\text{m}$ .; 2, 0.50 $\mu\text{m}$ .; 3, 1.00 $\mu\text{m}$ .; 4, 2.00 $\mu\text{m}$ .; 5, 4.00 $\mu\text{m}$ .; 6, 8.00 $\mu\text{m}$ .; 7, 20.00 $\mu\text{m}$ .

be 1 $\mu\text{m}$  or less. This "central" value of the film thickness correlates well with the value predicted from classical EHL theory [1]. However, the analysis also predicts severe thinning of the film at the edges of the contact region as shown in Figure 10. Whereas the central film thickness is almost independent of the load (as we would expect from classical theory), the minimum film thickness falls sharply with the load to levels at which some asperity interaction is expected. The side-thinning effect places a practical limitation on the loading of thrust rims of purely conical form. Misalignment further increases the possibility of edge contact. Edge effects in thrust rims of purely conical geometry are therefore likely to reduce their effectiveness and durability.

A better solution is achieved by crowning one of the surfaces to give a self-aligning or point contact between the thrust rims. Analysis of naturally relieved contacts of this type shows significantly less thinning with load [30], [31].

## 7. WORM GEARS

The lubricated contacts in worm gears are similar to those occurring in high conformity Wildhaber-Novikov gears [32] giving rise to particularly severe conditions because of the elongated shape of the dry contact region. The contact geometry is non-

symmetrical/non-Hertzian and although entrainment of the oil is predominantly along the major axis of the contact its direction varies throughout the area of the conjunction (i.e. a significant spin component of velocity is present). High sliding and heat generation in the contact necessitate a thermal/non-Newtonian EHL treatment. A typical solution obtained for a worm gear contact is shown in Figure 11.

In the design of worm gears it is usual to aim for close conformity of the worm and wheel surfaces in the entraining direction, but too high a degree of conformity can result in the contact reaching the inlet edge of the wheel tooth. Conditions for effective film generation are therefore severely worsened. Some degree of mismatch of the tooth curvatures is required to provide the necessary converging inlet to the contact. For unidirectional drives it is possible to arrange for the position of the contact on the wheel tooth to be biased towards the outlet of the contact to provide an optimum inlet region whilst making best use of the potential area of contact in order to minimise contact pressures. Hydrodynamic lubrication considerations clearly have their part to play in worm gear design and detailed EHL analysis allows these effects to be properly quantified.

## 8. CONCLUSION

The distinguishing features of EHL contacts in gears are:

- (i) surface roughness effects including micro EHL under non-steady conditions;
- (ii) the presence of significant sliding and frictional heating;
- (iii) non-Hertzian and non-symmetrical contact geometries;
- (iv) edge effects and the importance of edge relief and self-aligning configurations.

Progress is being made in the analysis of roughness/micro EHL but the main requirement is the ability to model the severe conditions under which scuffing and micropitting failure occur. This requires EHL solvers capable of dealing with cases in which roughness amplitude is typically an order of magnitude greater than the minimum film. Such solvers must include thermal, non-Newtonian and time-dependent effects, and in order to model the sideways leakage of oil from valley features of roughness in gears, it will be necessary to include two-dimensional effects.

The worm gear contact embodies all the above features and represents a major challenge for EHL modellers.

## REFERENCES

- [1] Dowson, D and Higginson, G R, 1966, *Elastohydrodynamic Lubrication*, Pergamon Press, Oxford.
- [2] British Gear Association, 1990, "Transmission engineering research for the United Kingdom"
- [3] Patching, M J, Kweh, C C, Evans, H P and Snidle, R W, 1994, "Conditions for scuffing failure of ground and superfinished steel discs at high sliding speeds using a gas turbine engine oil", *Trans ASME Journal of Tribology* Vol 117, pp 482-489.
- [4] Evans, H P and Snidle, R W, 1995, "A model for elastohydrodynamic film failure in contacts between rough surfaces having transverse finish", *Trans ASME Journal of Tribology* (in press).
- [5] Berthe, D, Flamand, L, Foucher, D and Godet, M, 1980, "Micro-pitting in Hertzian contacts", *Trans ASME, J. Lubr. Tech.*, Vol 102, pp 478-489.
- [6] Olver, A V, 1983, "Micro-pitting and asperity deformation", *Proc 10th Leeds-Lyon Symposium on Tribology*.
- [7] Zhou, R S, Cheng, H S and Mura, T, 1989, "Micropitting in rolling and sliding contact under mixed lubrication", *Trans ASME, J. of Tribology*, Vol 111, pp 605-613.
- [8] Webster, M N and Norbart, C C J, 1995, "An experimental investigation of micropitting using a roller disk machine", *Tribol. Trans*, Vol 38, pp 883-895.
- [9] Shotter, B A, 1981, "Micropitting, its characteristics and implications, in performance and testing of gear oils and transmission fluids", *Institute of Petroleum*.
- [10] Webster, M N and Sayles, R S, 1986, "A numerical model for the elastic frictionless contact of real rough surfaces", *Trans ASME, J. Tribology*, Vol 108, pp 314-320.
- [11] Snidle, R W and Evans, H P, 1994, "A simple method of elastic contact simulation", *Proc. Instn Mech. Engrs Part J Jn of Engng Tribology* Vol 208, pp 291-293.
- [12] Mayeur, C, Sainsot, P and Flamand, L, 1995, "A numerical elastoplastic model for rough contact", *Trans ASME, J. of Tribology*, Vol 117, pp 422-429.
- [13] Kapoor, A and Johnson, K L, 1995, "Plastic ratchetting as a mechanism of erosive wear", *Wear* Vol 190, pp 86-91.

- [14] Tyfour, W R and Beynon, J H, 1994, "The effect of rolling direction reversal on fatigue crack morphology and propagation", *Tribology International*, Vol 27, pp 273-282.
- [15] Patching, M J, 1994, *The effect of surface roughness on the micro-elastohydrodynamic lubrication and scuffing performance of aerospace gear tooth contacts*, PhD Thesis, University of Wales.
- [16] Elcoate, C D, Evans, H P and Hughes, T G, "Fully coupled elastohydrodynamic solution techniques for the analysis of real rough line contacts using finite element and finite difference models", paper for presentation at 23rd Leeds-Lyon Symposium on Tribology, 1996.
- [17] Goglia, P R, Cusano, C and Conry, T F, 1984, "The effects of surface irregularities on the elastohydrodynamic lubrication of sliding line contacts. Part I - single irregularities; Part II - wavy surfaces", *Trans ASME, Jn. of Tribology*, Vol. 106, pp 104-112, 113-119.
- [18] Lubrecht, A A, Ten Napel, W E and Bosma, R, 1988, "The influence of longitudinal and transverse roughness on the elastohydrodynamic lubrication of circular contacts", *Trans ASME Jn of Tribology*, Vol 110, pp 421-426.
- [19] Kweh, C C, Evans, H P, and Snidle, R W, 1989, "Microelastohydrodynamic lubrication of an elliptical contact with transverse and three-dimensional roughness", *J. of Tribology, Trans ASME*, Vol 111, pp 577-584.
- [20] Elsharkawy, A A and Hamrock, B J, 1991, "Subsurface stresses in micro-EHL line contacts", *ASME Journal of Tribology*, Vol 113, pp 645-655.
- [21] Sadeghi, F, 1991, "A comparison of the fluid model's effect on the internal stresses of rough surfaces", *ASME Journal of Tribology* Vol 113, pp 142-149.
- [22] Kweh, C C, Patching, M J, Evans, H P, and Snidle, R W, 1991, "Simulation of elastohydrodynamic contacts between rough surfaces", *J. of Tribology, Trans ASME, Paper 91-Trib-36*.
- [23] Venner, C H and ten Napel, W E, 1992, "Surface roughness effects in an EHL line contact", *ASME Journal of Tribology*, Vol 114, pp 616-622.
- [24] Chang, L and Webster, M N, 1991, "A study of elastohydrodynamic lubrication of rough surfaces", *ASME Journal of Tribology*, Vol 113, pp 110-115.
- [25] Chang, L, 1992, "Traction in thermal elastohydrodynamic lubrication of rough surfaces", *ASME journal of Tribology*, Vol 114, pp 186-191.
- [26] Chang, L, Webster, M N and Jackson, A, 1993, "On the pressure rippling and roughness deformation in elastohydrodynamic lubrication of rough surfaces", *ASME Journal of Tribology*, Vol 115, pp 439-444.
- [27] Ai, X and Cheng, H S, 1993, "A transient EHL analysis for line contacts with measured surface roughness using multigrid technique", *ASME Journal of Tribology, Paper No 93-Trib-56*.
- [28] Chang, L and Zhao, W, 1995, "Fundamental differences between Newtonian and non-Newtonian micro-EHL results", *ASME Journal of Tribology*, Vol 117, pp 29-35.
- [29] Patching, M J, Evans, H P and Snidle, R W, 1996, "Micro-EHL analysis of ground and superfinished steel discs used to simulate gear tooth contacts", *STLE preprint No. 96-AM-7C-1*.
- [30] Barragan de Ling, FdM, Evans, H P and Snidle, R W, "Thrust cone lubrication part I: elastohydrodynamic analysis of conical rims", *Proc. Instn Mech. Engrs Part J Jn of Engng Tribology*, Vol 210, pp 85-96, 1996.

- [31] Barragan de Ling, FdM, Evans, H P and Snidle, R W, "Thrust cone lubrication part 1: elastohydrodynamic analysis of crowned rims", Proc. Instn Mech. Engrs Part J Jn of Engng Tribology, Vol 210, pp 97-105, 1996.
- [32] Evans, H P and Snidle, R W, 'Wildhaber-Novikov circular arc gears: Elastohydrodynamics', Trans ASME Jn of Tribology, Vol 115, pp 487-492, 1993.

## LUBRICATION TESTS IN WORM GEARMOTORS

by

**TORELLI** Corrado, **ZANOTTI** Vittoriano  
**ROSSI MOTORIDUTTORI** S.p.A. - Modena - ITALY  
**SAVELLI** Paolo, **FLABBI** Luciano  
**AUSIMONT** S.p.A. - Bollate - ITALY

### 1. SUMMARY

This work reports practical data that underline the lubricating performances of perfluoropolyethers using a worm gearmotor bench test, in comparison with the conventional fluids currently used.

Mineral oils, synthetic oils and fluorinated oils were tested at very severe operating conditions (high torque, low service factor, high thermal stress) in order to evaluate the effect of chemical structure and viscosity on the performance.

The computer controlled bench test, consisting mainly of a D.C. motor connected to a worm reducer generator via an overgear, was equipped with thermocouples and inductive torque meter.

All the data were continuously monitored and the temperature and torque were recorded as a function of time.

At the end of the tests all the lubricants were analyzed to detect the amount of solid particles. These results were used as a reference to evaluate the wear of the gears during the operation.

Among the fluid tested, linear perfluoroether with viscosity of 280 cSt at 20°C ( M30 ) showed the best performance in terms of low wear, high power transmission ability and low operating temperature.

### 2. PURPOSE OF THE WORK

The objective of this work was to evaluate the behaviour of fluorinated oils as lubricants in worm reducers.

The two key operating parameters of worm reducers are the very high sliding speed in this particular coupling (about 1,75 m/s), and the very low pressure between the teeth of worm and the worm wheel. This value is about 200 N/mm<sup>2</sup>, compared with 1,600 N/mm<sup>2</sup> of the gear reducers having spur-bevel gears.

The effect of the following parameters

- base fluid
- fluid structure
- fluid viscosity

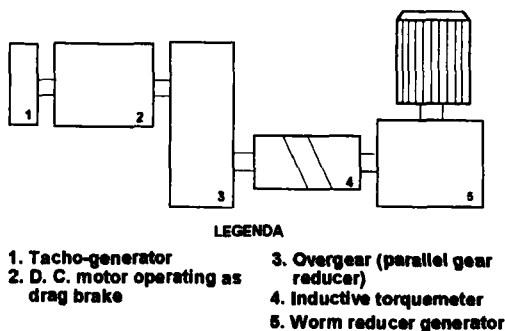
on the final performances of the products was evaluated.

### 3. EXPERIMENTAL

#### 3.1. Equipment

The scheme of the bench test is shown in Fig. 1

Fig. 1  
LUBRICATION TESTS IN WORM GEARMOTORS



The gearmotor was type MRV 63 UO2A - 90Lb 4 220.380 B5/70 produced by ROSSI MOTORIDUTTORI.

The technical characteristics of the worm reducers were:

- trasmission ratio            20
- output speed                 70 min<sup>-1</sup>
- input speed                  1400 min<sup>-1</sup>
- oil quantity                 0,8 l
- materials :
- worm     : steel (16 Ni Cr 4),  
                                casehardened and hardened
- worm wheel: phosphorous bronze  
(PB2.BS 1400-73, P=0,15-0,21%)

The electric motor was type 90 Lb 4 220.380 B5, P1=1,85 KW

The overgear, connected to the slow axle, was a parallel gear reducer type R2I 63 UP2A with trasmission ratio  $i = 10,7$ .

One termocouple was placed into the worm reducer (to measure the oil temperature), one on worm reducer casing and one in the room as reference (ambient temperature).

Two worm reducers were used alternatively, after a running-in period to reach the same mechanical characteristics.

The bench test was managed and checked via a computer.

All the data were collected and elaborated by a continuous monitoring system.

### 3.2. Procedure

The worm reducer was washed with solvent, then dried and filled with the oil sample.

The test started at room temperature.

The torque was increased gradually without exceeding the power limit of the electrical motor.

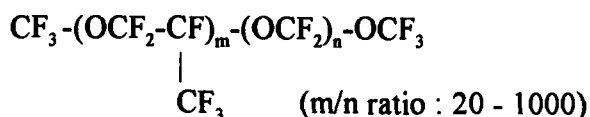
The test was stopped when the variation of the oil temperature of the sample was below 2 °C/hr (steady state temperature) at the maximum power absorption of the electric motor, corresponding to the maximum torque.

At the end of the test the oil sample was analysed to determine the quantity and the type of wear particles and its physico-chemical properties were re-checked.

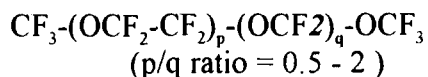
### 3.3. Fluids tested

#### 3.3.1. Fluorinated lubricants

Perfluoropolyethers (PFPE) are synthetic fluids obtained by a liquid phase photooxidation process from hexafluoropropene (HFP) or tetrafluoroethene (TFE) and, at the end of production process, they have the following structures: Branched PFPE ( Y fluid ), from HFP



Linear PFPE ( M fluid ), from TFE



The presence of strong chemical bonds of covalent nature, such as C-O, C-F, C-C, and the absence of hydrogen in the structure, together with neutral character, provides to these fluids an excellent thermal and oxidation stability associated with other specific properties.

Tab. 1 - Main properties of PFPE lubricants

- Good lubricating properties
- Good viscostaticity
- High thermooxidative resistance
- Low pour point
- Low surface tension
- Chemical inertness
- Low volatility
- High specific gravity
- Resistance to radiation
- Good dielectric properties
- Non flammability
- Compatibility with plastics,elastomers and metals
- Solubility in perfluorinated organic solvent only
- Biological inertness

Three grades of PFPE of each structure ( Y and M ) were tested . Their physical properties are reported in the following table.

Perfluoropolyethers - typical properties

|                           | M 15 | M 30 | M 60 | Y 25 | Y 45 | YR   |
|---------------------------|------|------|------|------|------|------|
| Kinematic viscosity       |      |      |      |      |      |      |
| at 20°C, cSt              | 180  | 280  | 550  | 250  | 470  | 1200 |
| at 40°C, cSt              | 85   | 159  | 310  | 81   | 147  | 345  |
| at 100°C, cSt             | 22   | 45   | 86   | 10   | 16   | 33   |
| Viscosity index           | 286  | 338  | 343  | 108  | 117  | 135  |
| Pour point °C             | -75  | -65  | -60  | -35  | -30  | -25  |
| Weight loss               |      |      |      |      |      |      |
| at 204°C, 22 hs,%         | 3    | 0.7  | 0.4  | 15   | 1.7  | 1.2  |
| Density g/cm <sup>3</sup> | 1.83 | 1.85 | 1.86 | 1.90 | 1.91 | 1.91 |

PFPE 3.3.2. Conventional lubricants

The following three current lubricants used in worm reducers, were used as reference, for comparison purpose :

- Lubricant A : Mineral oil with E.P. additive
  - Lubricant B : Polyglycol with anti wear additive .
  - Lubricant C : Polyglycol with E.P. additive
- Their properties were the following :

| lubricant | Kin. Viscosity<br>at 40 °C | viscosity<br>Index |
|-----------|----------------------------|--------------------|
| A         | 210                        | 97                 |
| B         | 224                        | 216                |
| C         | 225                        | 220                |

#### 4. RESULTS AND DISCUSSION

The time necessary to reach the thermal steady state resulted about 4 hours.

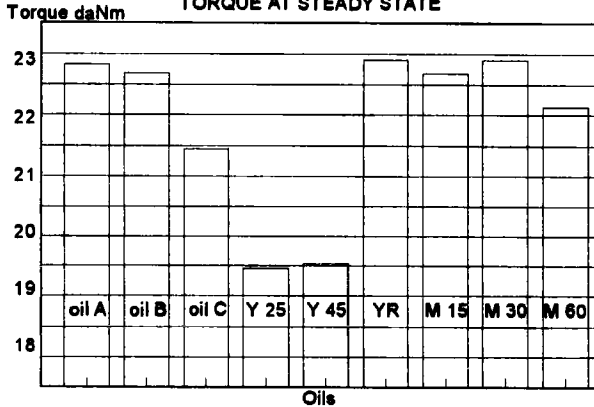
The theoretical value of the torque of worm reducers used during the tests was 16 daNm.

During the test the value of the torque was increased up to 23 daNm (according to the lubricating oils) in order to obtain a very severe operating test condition .

Tab. 2 shows the value of the torque of the sample oils at steady state.

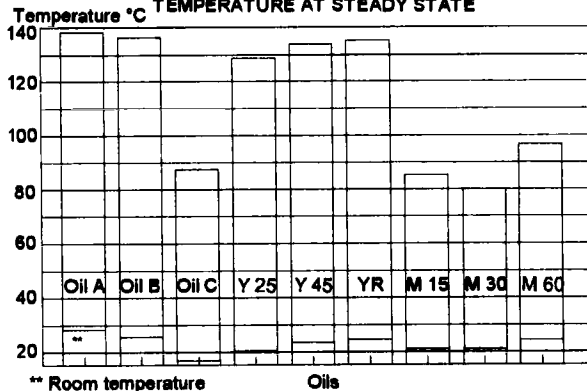


tab. 2 - LUBRICATION TESTS IN WORM GEARMOTORS  
TORQUE AT STEADY STATE



Tab. 3 shows the value of the temperature of the sample oils at steady state.

tab.3 - LUBRICATION TESTS IN WORM GEARMOTORS  
TEMPERATURE AT STEADY STATE



\*\* Room temperature

#### 4.1. Fluorinated lubricants

##### Branched PFPE ( Y fluids )

The data ( Fig. 2a / 2b ) show that the temperature of these oils increases quickly reaching a very high value up to 140 °C. The oils of this serie showed a poor performance.

fig. 2 A - Y Fluids - Torque vs time

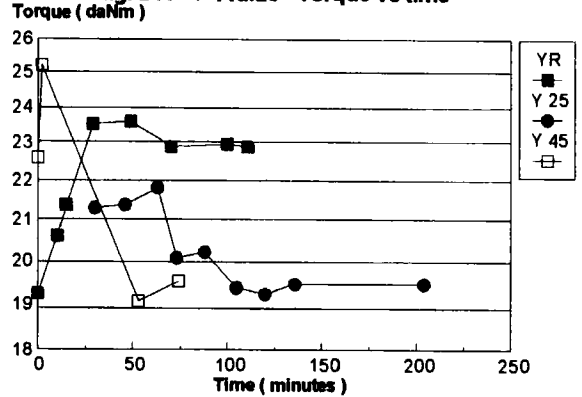
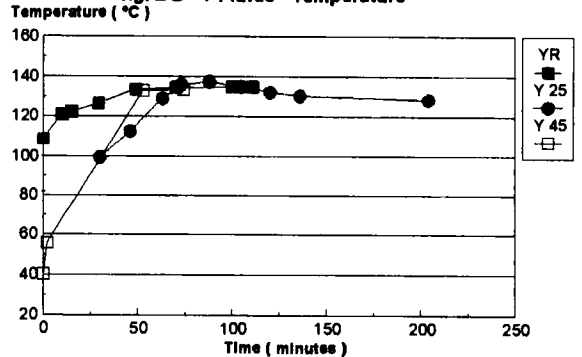


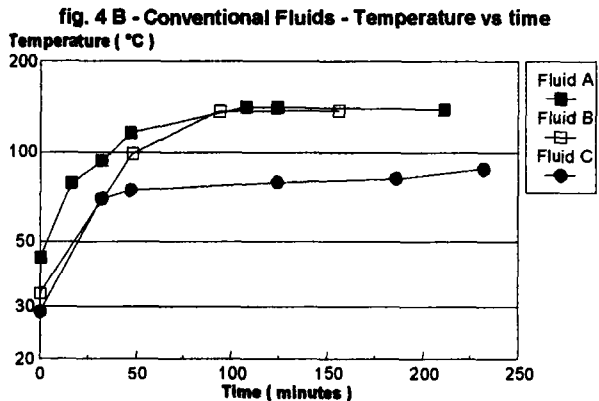
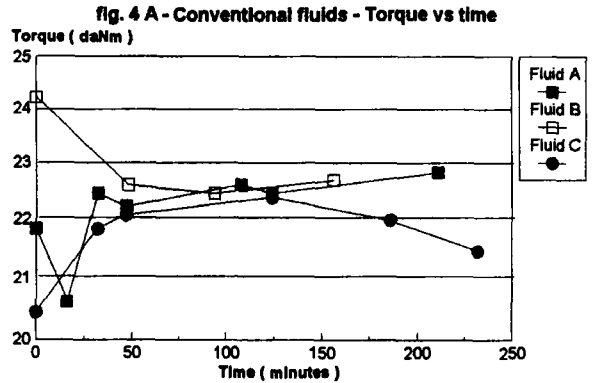
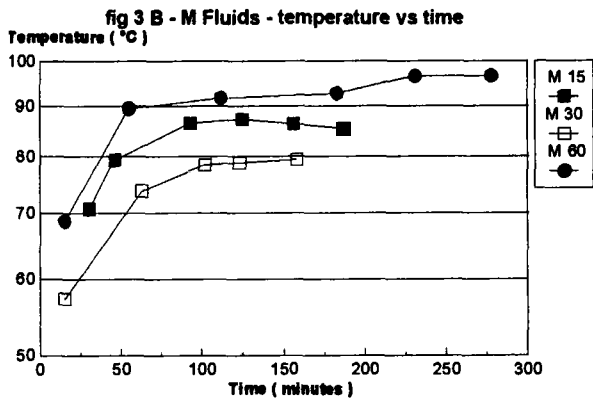
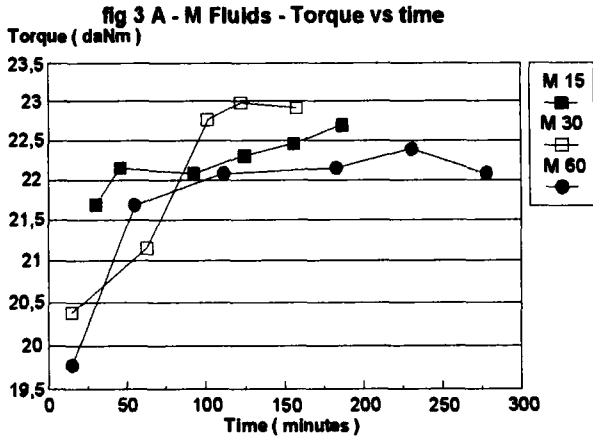
fig. 2 B - Y Fluids - Temperature



With Fomblin YR was reached a very high torque value at steady state, but the temperature was definitely too high for long term operations.

##### Linear PFPE ( M fluids )

All these lubricants showed a good performance (Fig.3a/3b). The temperatures were quite low (80-100 °C) and the values of the torque were over 22 daNm. The best results were obtained with fluid M30.



4.2. Non fluorinated lubricants

Lubricant A and Lubricant B showed high torque, but high temperature.

The better performance was obtained with Lubricant C that showed the highest torque and the lowest temperature. ( Fig. 4a/4b )

4.3. Lubricant analysis.

At the end of each test a properly homogenized sample of 600 g of each lubricating oil was analysed to evaluate the composition and the quantity of solid content. The results are reported in table 4 .

tab. 4- LUBRICATION TESTS IN WORM GEARMOTORS  
ANALYSIS OF THE OIL RESIDUE AFTER TEST

| Type of Lubricant | Dry content g | Metallic elements % |    |    |    |
|-------------------|---------------|---------------------|----|----|----|
|                   |               | Cu                  | Sn | Fe | Zn |
| Oil C             | 1.1345        | 46                  | 8  | 1  | 7  |
| PFPE Y 25         | 0.3580        | 24                  | 3  | 7  | 1  |
| PFPE Y 45         | 0.2192        | 14                  | 1  | 1  | 1  |
| PFPE YR           | 0.3219        | 12                  | 1  | 1  | 1  |
| PFPE M 15         | 0.6303        | 20                  | 2  | 1  | 1  |
| PFPE M 30         | 0.2032        | 26                  | 1  | 2  | 1  |
| PFPE M 60         | 0.4281        | 20                  | 1  | 3  | 1  |

Among the fluids with the best performance in operation, linear PFPE M 30 showed a lower amount of solid content compared to Lubricant C.

More particularly the low content of Copper and Tin can be taken as a clear indication of the less wear occurred with the use of the linear PFPE fluid M30

## 5 . CONCLUSION

Among all the lubricants tested, linear PFPE M 30 showed the best performance, in terms of high torque and low temperature in operation .This result was obtained without the need of any additive.

- Among the conventional lubricants, presently used, the better performance was achieved with the synthetic lubricant C, containing E.P. additive.

- The structure of the fluorinated fluids influenced the performance .Linear perfluoropolyethers ( M fluids ) showed better behaviour than perfluoropolyethers with branched structure ( Y fluid ), with the same viscosity.

- High viscosity lubricants negatively affected the results , due to the high temperature generated by the viscous friction.

- Fluorinated oils showed the less wear as demonstrated by the lower amount of solid particles found in the oils after the test.

## Lubrication of thrust cone bearings

L M Rudd<sup>a</sup>, H P Evans<sup>b</sup>, R W Snidle<sup>b</sup> and D W Parkins<sup>c</sup>

<sup>a</sup> DERA, Pyestock, Hants, GU14 0LS, UK

<sup>b</sup> University of Wales, Cardiff, CF2 1XF, UK

<sup>c</sup> Cranfield University, Bedford, MK43 0AL, UK

### SYNOPSIS

This paper describes investigations into various aspects of the lubrication dynamics of thrust cone bearings. When single helical gears are used to transmit power between parallel shafts there is an axial component of force between the two gears. The common way of reacting this force is by the use of separate thrust bearings mounted on the shafts of the gears. An alternative arrangement involves the use of thrust cones which are conical rims mounted on the edges of the gears close to the teeth. The results of full EHL analyses, validated by film thickness experiments using the interference method, have revealed a very load-sensitive film thinning effect at the edges of such contacts. With a rational comparison to rolling element bearing design and based on the work reported here, it is suggested that edge relief in the form of a circular arc is applied to one of the cone tracks (a 'crowned' cone) to avoid this effect and provide a self aligning elongated elliptical point contact. As a result of the work, validated lubrication design guides for both straight and crowned thrust cones have been produced and descriptions of these will follow in papers to be published elsewhere.

### NOTATION

|                |  |
|----------------|--|
| $E_1, E_2$     | Elastic moduli of the bearing surfaces     |
| $E'$           | $2/E' = (1-\nu_1^2)/E_1 + (1-\nu_2^2)/E_2$ |
| $h$            | Film thickness                             |
| $h_{cen}$      | Central film thickness                     |
| $h_{min}$      | Minimum film thickness                     |
| $p$            | pressure                                   |
| $R'$           | Relative radius of curvature               |
| $u$            | Entraining velocity                        |
| $w'$           | Load per unit length (line contacts)       |
| $\alpha$       | Pressure - viscosity coefficient           |
| $\beta$        | Thrust cone angle                          |
| $\eta_0$       | Dynamic viscosity at ambient pressure      |
| $\nu_1, \nu_2$ | Poisson's ratios of the bearing surfaces   |

### 1. INTRODUCTION

The work described has been part of a wider ranging study involving collaboration between the Defence Evaluation and Research Agency (DERA), the University of Wales College of Cardiff (UWC), Cranfield University (CU), Leicester University (LU) and Imperial College, London (ICL). In essence the main objective of the work reported here

was to provide validated lubrication design guidance to effect the full economic potential of thrust cone bearings. In particular information relating to localised film thinning and how best to avoid it was obtained.

### 2. DESCRIPTION OF THRUST CONES

In essence, thrust cone bearings consist of annular rings concentric with the gear axes that form a flange outside the pinion gear addendum circle, with a similar feature on the wheel gear, but inside the wheel dedendum circle, as shown schematically in Figure 1. Apart from the economic and noise benefits afforded by the use of single helical gears, thrust cones have the advantage of compactness and the axial space needed for high power intensity drives can be significantly reduced. Also, as the contact can occur close to the pitch line of the gears further design advantages are possible with reduced bending of the gears and frictional losses. These bearing surfaces may be referred to as rims, rings, cones or tracks and form a nominally rigid 'overlap' thus reacting the out of mesh forces and preventing relative axial movement of the gears. If the track on

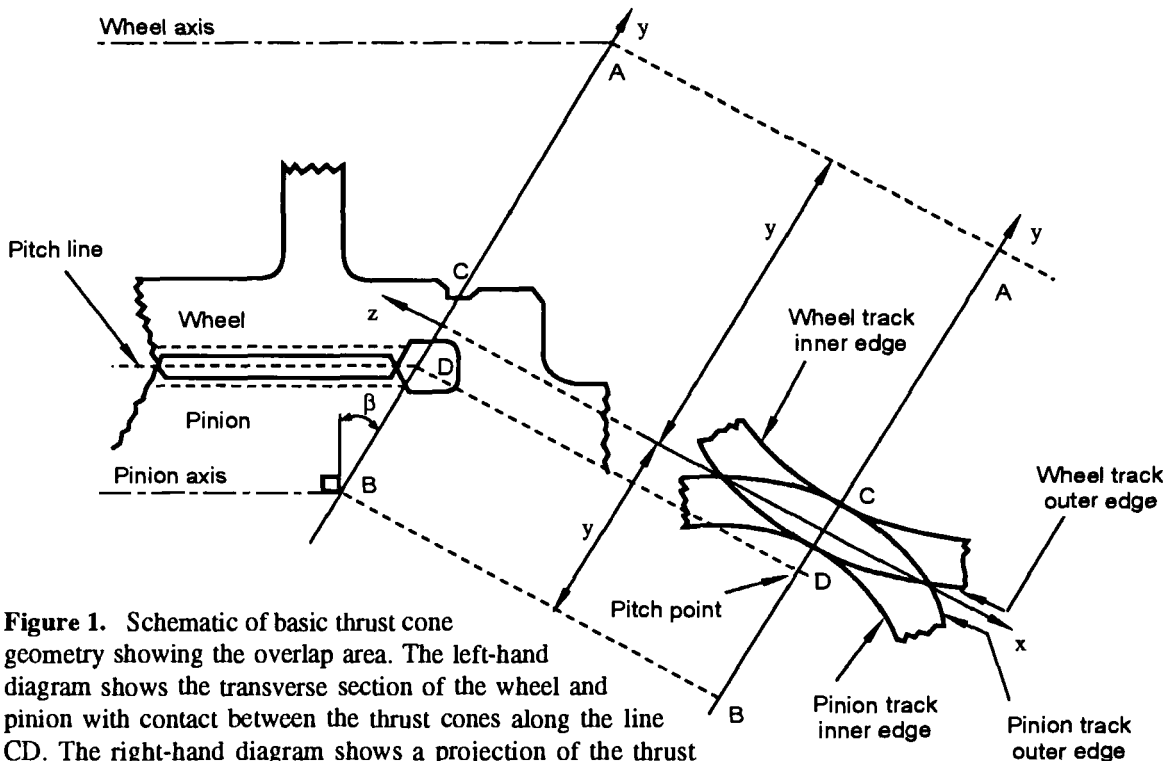


**Figure 1.** Schematic of basic thrust cone geometry showing the overlap area. The left-hand diagram shows the transverse section of the wheel and pinion with contact between the thrust cones along the line CD. The right-hand diagram shows a projection of the thrust cones edge into the common tangent plane at the line of contact.

the wheel and the flange on the pinion were made perpendicular to the gear axes, then contact would occur over the whole of the overlap area. Although, resulting in a low theoretical contact stress, the generation of an oil film at the contact would be ineffective as the converging clearance necessary for hydrodynamic oil film formation would not exist. Consequently the surfaces are inclined at a small angle to the end face of the gears, called the thrust cone angle, such that a nominal conical geometry results. This allows the formation of a hydrodynamic oil film in the presence of an oil and appropriate angular velocity. Typically, the tracks are no more than 30mm wide with a cone angle of between one half and two degrees.

Thrust cones are by no means a recent invention and although their origin is not clear, it is apparent they have been used with success for some considerable time. In fact some aspects of their lubrication dynamics have already been reported by Langer [1] and Simon [2]. In general their work was appropriate to lightly loaded thrust cones operating

at high speeds where the effects investigated in the work reported here are insignificant. Although Simon forewarned of misalignment producing a point contact at the edges of a thrust cone overlap, no general quantitative design guidance was offered.

### 3. PRELIMINARY LUBRICATION APPRAISAL

Considering the geometry of these bearings, at first sight, and on the basis of a simple analysis, low contact pressures, thick oil films and good tribological performance are implied. To explain this, in concept a thrust cone with a straight radial profile (or 'straight' cone) may be taken as a line contact. The small change in relative radius of curvature ( $R'$ ) across the track width is neglected, which is a reasonable omission for small cone angles.

Referring to Figure 2, the radii of curvature of rollers of identical radii to the cone tracks at mid-point,  $R_1$  and  $R_2$ , are:-

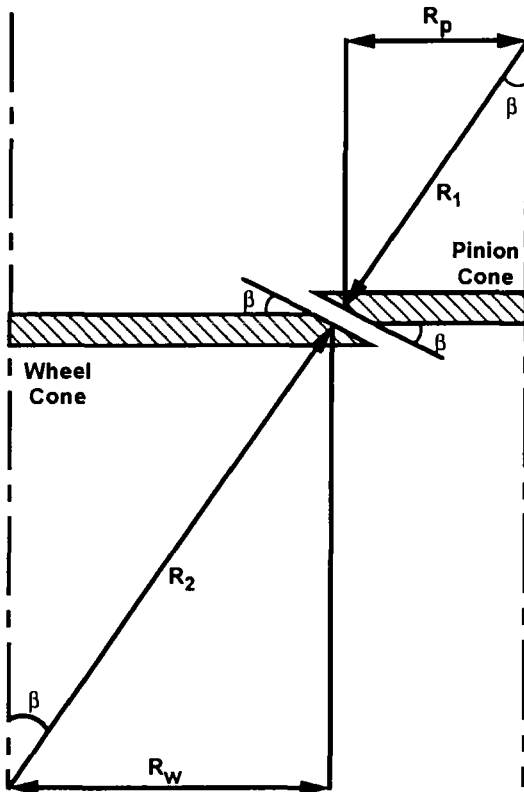


**Figure 2.** Schematic showing the development of radii of curvature of rollers of identical radii to the cone tracks at mid-point.

$$R_1 = \frac{R_p}{\sin \beta} \quad (1)$$

$$R_2 = \frac{R_w}{\sin \beta} \quad (2)$$

Then for a thrust cone configuration it can be shown that  $R'$  is given by:-

$$R' = \frac{R_w R_p}{(R_w + R_p) \sin \beta} \quad (3)$$

Thus for thrust cone contacts, where the angle  $\beta$  is close to zero,  $R'$  is surprisingly large when compared

to the cone track radii. In the limit as  $\beta$  tends to zero the surfaces become plane and  $R'$  tends to infinity as expected. As the contact stress in a line contact is inversely proportional to  $(R')^{1/2}$ , low contact pressures can be achieved with smaller angle cone tracks. Allied to this, the formula for calculating the minimum oil film thickness in a line contact is given by Dowson and Higginson [3] as:-

$$h_{\min} = \frac{1.63(\alpha)^{0.6} (\eta_0 u)^{0.7} (E')^{0.03} (R')^{0.43}}{(w')^{0.13}} \quad (4)$$

Here  $h_{\min}$  is proportional to  $(R')^{0.43}$  and therefore for small cone angles substantial oil films are expected.

Relevant data for the design conditions initially investigated are given in Table 1. The minimum oil film thickness at the mean centre line of the cone track was calculated with equation 4 and estimated at  $16\mu\text{m}$ . Given the short width of the contact some thinning of this centre line value was also anticipated due to side leakage. (In the work that follows and described in section 5, a reduction of more than 20% was computed). In comparison to the nominal surface roughness of the ground steel cone tracks of  $0.4\mu\text{m Ra}$ , complete surface separation could be expected. However, it was realised that the actual minimum film thickness could occur at the edges of the contact due to a combination of side leakage and elastic deflection across the cone tracks, implying a possible load dependency not usually anticipated from a cursory analysis using the chosen design formula. Therefore some form of edge relief is appropriate for what may be considered a special case of a short roller.

**Table 1.** Conditions and parameters considered.

|                                   |                    |
|-----------------------------------|--------------------|
| Maximum normal load on contact    | 106kN              |
| Mid-track entraining velocity     | 24.2m/s            |
| Cone angle                        | $1^\circ$          |
| Nominal cone track width          | 20mm               |
| Young's Moduli of both cones      | 200GPa             |
| Relative Radius of Curvature      | 11.6m              |
| Operating temperature             | $70^\circ\text{C}$ |
| Lubricant - ISO VG 68 mineral oil |                    |

#### 4. QUALITATIVE COMPARISON WITH ROLLING ELEMENT BEARING DESIGN

Before proceeding with a description of the EHL analyses and validation experiments, it is worth making a simple comparison to standard rolling element profile design to rationalise *a priori* the suggestion of crowning highly loaded thrust cone bearing tracks. For roller bearings, a so called 'dub-off' radius is used to provide relief at the roller ends

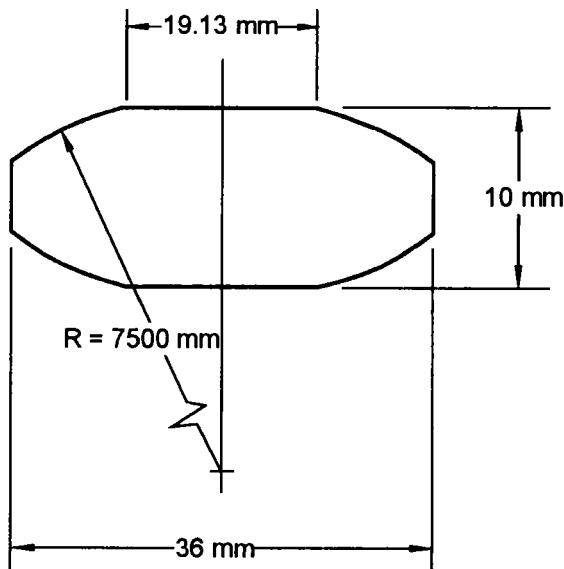


Figure 3. A typical roller profile design. (after Hartnett [4])

which improves film forming ability, tolerance to misalignment and reduction in contact stress, all resulting in improved fatigue life. Typically these radii are applied on the end quarters of rollers and may be over a thousand times the roller radius to achieve the correct effect. Figure 3 is extracted from work by Hartnett [4] who developed the design methodology for economic application of this type of end relief in the production process. However, a useful comparison can be made with the contact aspect ratio (roller width/contact length) of Hartnett's roller contact and the thrust cone contact defined here. For Hartnett's roller, made of steel and loaded to 20 kN against a steel shaft of 50mm diameter this ratio is approximately 70. In comparison, for the thrust cone set it is 0.4. Therefore it may be implied that for nominal line

contacts of small aspect ratio (straight thrust cones), a radical end or edge relief is required. As effective tribo-design practice of rollers having large contact aspect ratio dictates the form of end relief shown in Figure 3, then for thrust cones a centrally located circular arc across one of the cone tracks seems appropriate. With this in mind, on completion of isothermal EHL analyses relevant to the thrust cone design outlined here, further modelling work was centred on developing a methodology for selection of a crowning radius.

#### 5. RESULTS OF THE STRAIGHT CONES EHL ANALYSES

A description of the model used in the analysis of the straight cone case considered is given elsewhere by Barragan de Ling *et al* [5]. Therefore only a brief review of the results is presented. Several analyses were completed at part-load conditions up to the full load also accounting for the fact that the gearing considered was connected to a final drive where the thrust load was proportional to the square of the speed. Although a full thermal EHL analysis was not completed an estimation of temperature rise in the inlet region was made and accounted for in the analysis.

Figures 4 and 5 show pressure and film thickness plots along the nominal cone track overlap centre line (or longitudinal direction) for 25% and full load conditions. As expected for such a contact the value of minimum film thickness was not particularly sensitive to this change in load. However, shown in Figures 6,7 and 8 are similar plots in the radial direction across the cone track (or transverse direction). As originally anticipated these demonstrate the marked effect of load on film thinning at the edges of the contact with a reduction in minimum film thickness there from 6  $\mu\text{m}$  at 25 % load to 0.3  $\mu\text{m}$  at full load conditions. Compared to the surface roughness this implies the strong possibility of running in mixed lubrication conditions with the prospect of attendant wear and failure mechanisms associated with this lubrication regime.

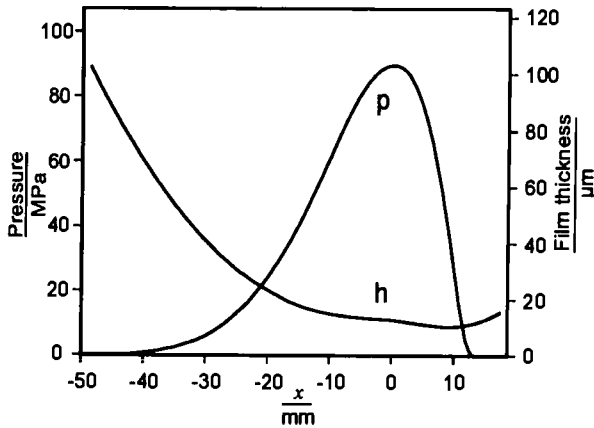


Figure 4. The longitudinal film thickness (h) and pressure distribution (p) at 25% load.

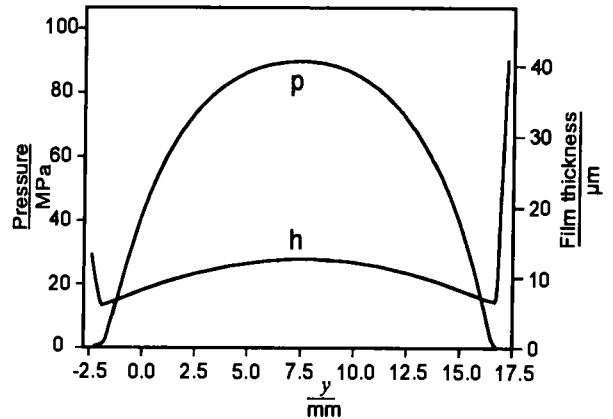


Figure 6. The transverse film thickness (h) and pressure distribution (p) at 25% load.

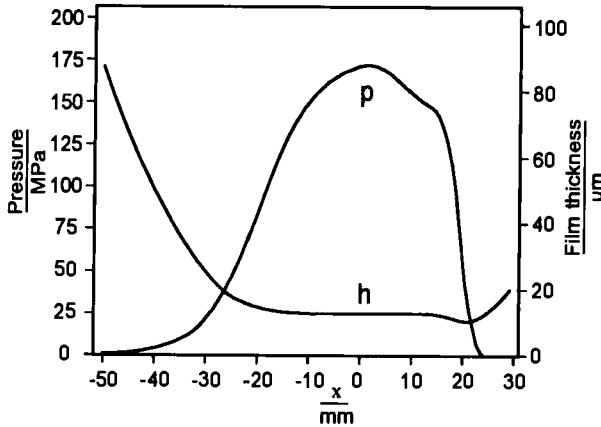


Figure 5. The longitudinal film thickness (h) and pressure distribution (p) at full load.

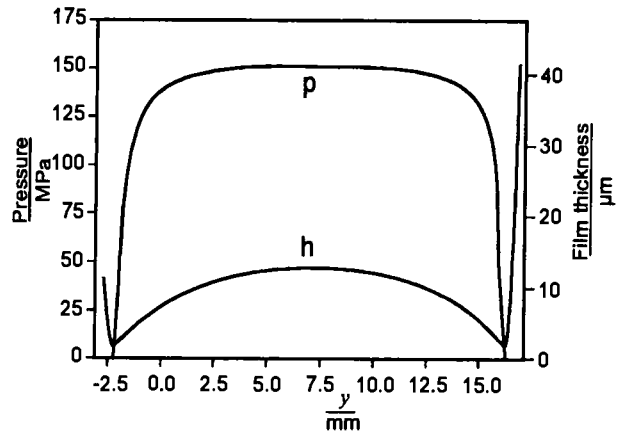


Figure 7. The transverse film thickness (h) and pressure distribution (p) at 80% load.

## 6. INTRODUCTION OF EDGE RELIEF BY CROWNING

Given confirmation of the load driven film thinning effect with the straight cone profile, further analytical work concentrated on developing the existing model to analyse a crowned cone track profile. This results in a slightly asymmetric elongated elliptical point contact for which some lubrication design formulae may be considered appropriate, for instance those offered by Chittenden *et al* [6]. However, the model development that followed and reported by Barragan de Ling *et al* [7], also accounted for starvation effects in both the longitudinal and transverse directions resulting from

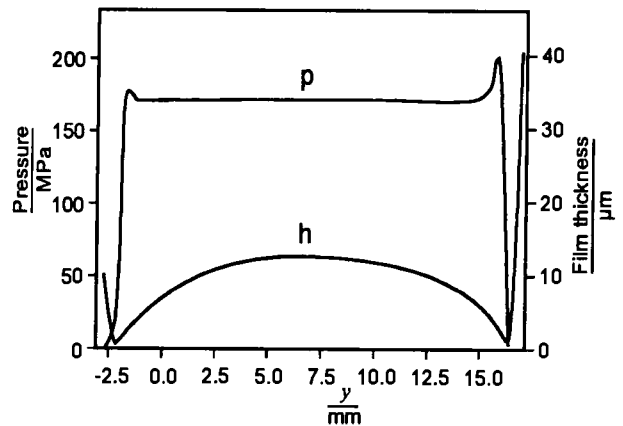
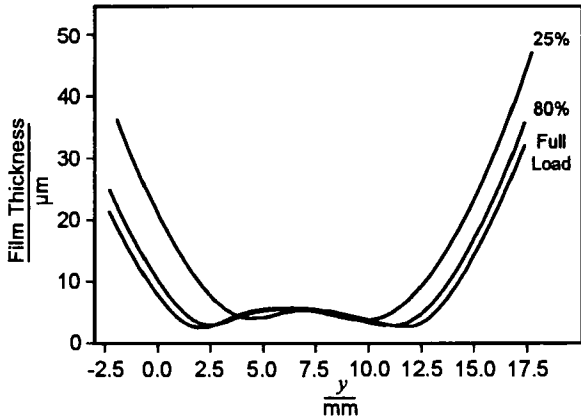


Figure 8. The transverse film thickness (h) and pressure distribution (p) at full load.





**Figure 9.** The transverse film thickness at 25%, 80% and full load with a 1 m crown radius.

the influence of reduced pressure generation area associated with the proximity of the cone track overlap edges. In associated work concentrating on more general cases and reported by Barragan de Ling [8], at certain conditions this effect was found to be very influential on the film forming ability of

crowned thrust cones. This has led to a design rationale for selection of crown radius accounting for the starvation effect caused by transverse misalignment of cone tracks and this will be described in papers that are in preparation.

With the original model modified to account for the lubrication dynamics of crowned cones, analyses were made for the same conditions used in the straight cone work with various crown radii. Figure 9 shows a film thickness plot in the transverse direction for a crown radius of 1m. Although the centre line film thickness value (or central film) reduced to approximately 5µm because of this geometry modification, the minimum films were located inside the cone track edges and had increased to between 3µm and 2µm for the 25% and full load condition respectively.

**7. EXPERIMENTAL WORK**

In support of the modeling work a special test facility was developed and used to provide

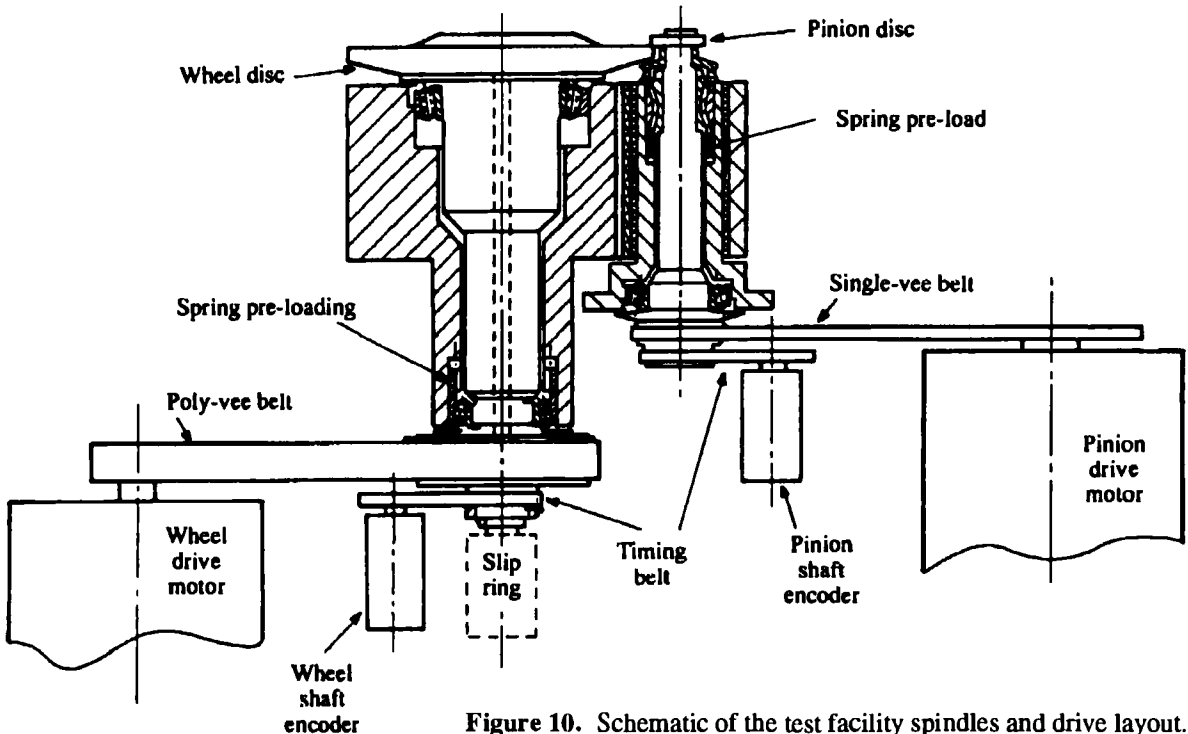


**Figure 10.** Schematic of the test facility spindles and drive layout.

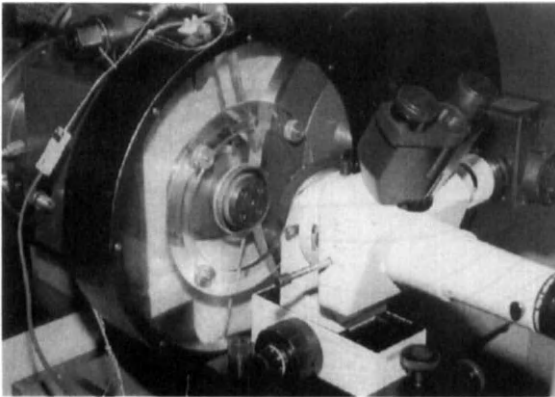


**Figure 11.** Close up of the wheel and pinion overlap.

experimental oil film thickness data to validate the numerical work. This facility is more completely described by Parkins and Rudd [9]. Although the facility is unique by virtue of configuration and scale, the essence of the method used to measure film thickness is not. The light interference technique was first used to measure oil film thickness by Kirk [10] and has been developed since that time by a number of workers. A schematic of the test facility layout is shown in Figure 10 while Figure 11 shows a close up of the contact overlap made between the steel wheel specimen and glass pinion specimen. When viewing the contact with either a standard metallurgical microscope for crowned cones or a wide field macro system, for the straight cone experiments, light interference patterns were observed. A wide field macro system was used for the straight cone simply because the contact area was much larger. In both cases a white light source was used with a Kodak Wratten No. 12 filter resulting in a duo-chromatic system of vivid red and green light fringes.

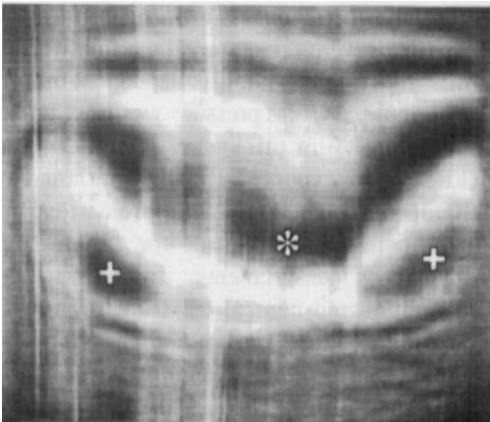
The inference of film thickness information from such fringe patterns required careful calibration of the interference fringes. This was completed in a similar manner to that described by Foord *et al* [11]. The calibrations established the separation of two surfaces (in air) corresponding to each fringe colour up to a maximum of approximately  $1.4 \mu\text{m}$ . The calibration was carried out both in-situ using the contact between the thrust cone elements and separately with a specially designed calibration rig so that good agreement was confirmed. To obtain

the oil film thickness, the corresponding fringe colours in air were divided by the refractive index of the oil. This latter value was dependent on pressure and the nominal Hertz pressure was used in the case of the central film thickness. The minimum film thickness was expected from numerical work to occur at substantially lower pressures, and no pressure correction was made for the minimum oil film thickness measurements. In this way relations of minimum and central oil film thickness with speed were obtained for both straight and crowned cone track profiles.

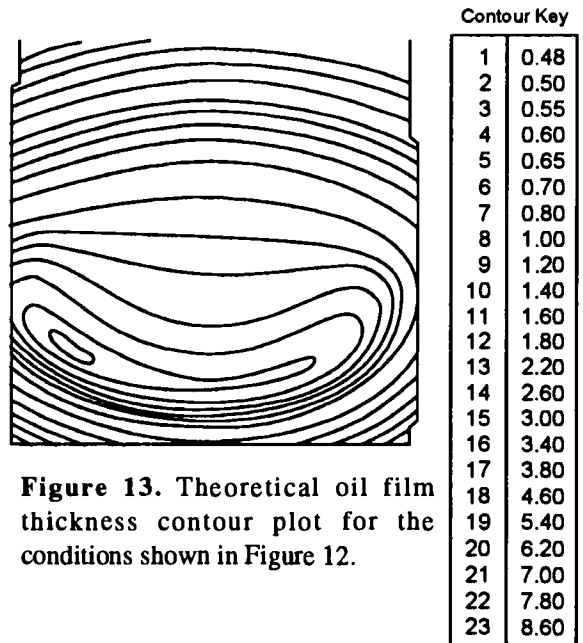
Experiments were performed at a constant load and oil supply temperature, with the pinion and wheel gearing set for pure rolling at the track overlap centre line to avoid damage to the reflective coatings on the glass pinion. An experiment consisted of varying the speed gradually and recording the light interference fringe detail on video for subsequent evaluation of the oil film thickness data.

Figure 12 shows a typical frame from the video recording of a nominally straight cone experiment which has been reconstructed as a black and white image for the purpose of producing this paper. The 'fringes' illustrate the main features of contact between nominally straight cone tracks. The film thickness within the contact region was greatest in the region of the centre of the track and is essentially flat in the direction of lubricant entrainment. There was a 'nip' to the rear of the contact which is characteristic of the oil films found in elastohydrodynamic line contacts. The contacts differed significantly from standard line contact behaviour with a significant degree of thinning of the oil film towards the edges of the contact as determined by the associated modelling, as Figure 13 shows.

In the 'fringe' pattern shown in Figure 12, the minimum film thickness can be seen formed inboard of the edge of the track. The apparent degree of thinning was of the same order as that expected from the theoretical treatment. However, the difference in location was due to a slight rounding of the nominally straight steel track. This slight error of form was apparent at the end of the polishing process necessary to obtain the appropriate degree of reflectivity and fineness of surface finish.



**Figure 12.** A reconstructed black and white image of a video frame for a straight cone experiment. Entraining velocity 0.375 m/s, load 400N. \*  $h_{cen}$  - 3rd green fringe at a thickness of  $0.63 \mu\text{m}$ ,  $0.63 \mu\text{m}$  by model. +  $h_{min}$  - 2nd green fringe at a thickness of  $0.47 \mu\text{m}$ ,  $0.46 \mu\text{m}$  by model. Refractive index approximately 1.48.



**Figure 13.** Theoretical oil film thickness contour plot for the conditions shown in Figure 12.

When measured this slight rounding at the wheel edges equated to a nominal crowning radius of approximately 3 metres. This was taken into account in the modelling and it did not affect the results sufficiently to warrant a further expensive, and probably impossible, finishing operation.

Figure 14 shows a typical frame from the video recording of a crowned cone experiment which again has been reconstructed as a black and white image. The 'fringes' illustrate the main features of an EHL contact with crowned cone tracks. Again, the film thickness within the contact region was greatest at the centre of the track. It was essentially flat in the direction of lubricant entrainment and the characteristic 'nip' was seen to the rear of the contact. The nip developed into minimum film thickness lobes towards the edges of the nominal Hertz contact area. The film shape and thickness was found to agree well with the full EHL analysis and sufficient data was acquired to directly validate the relevant numerical models.

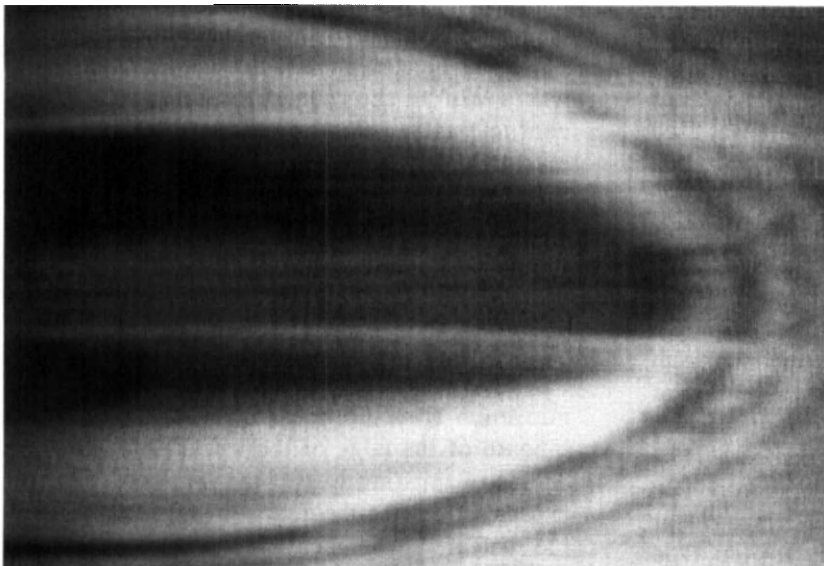


**Figure 14.** A reconstructed black and white image of a video frame from a crowned cone experiment. Entraining velocity 0.5 m/s, load 660N, crown radius 300mm.

Figures 15 and 16 show logarithmic plots of oil film thickness with speed for a

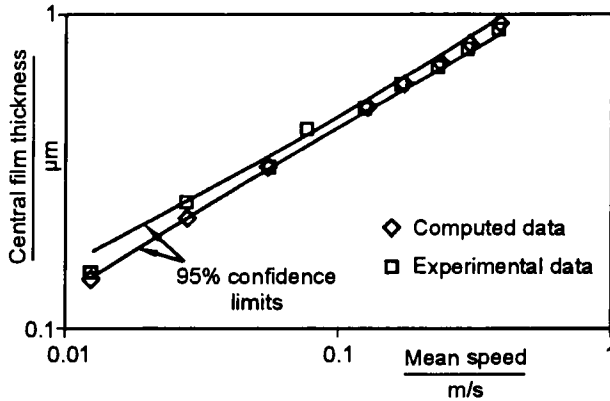


Figure 15. Measured and computed central film thickness for a crown cone experiment

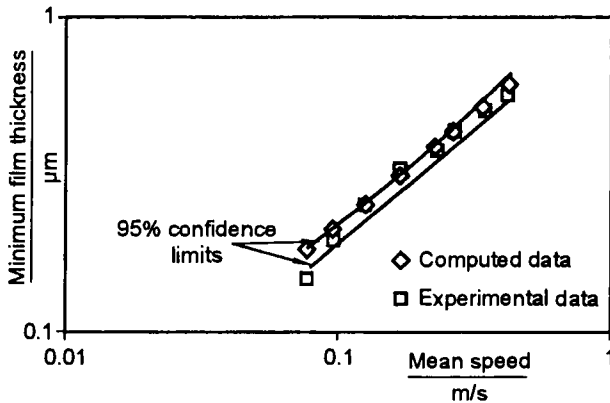


Figure 16. Measured and computed minimum film thickness for a crown cone experiment

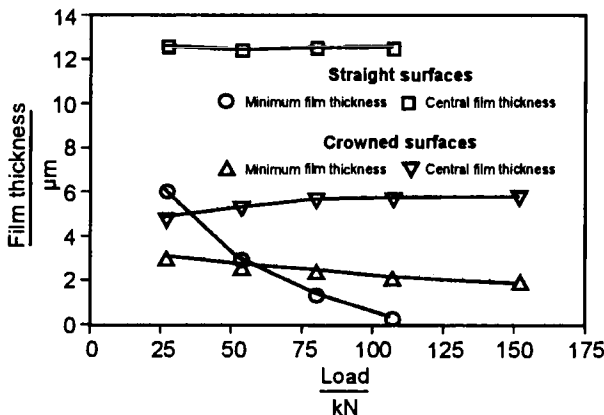


Figure 17. Comparison of the variation of film thickness with load for straight and crowned thrust cone tracks.

crowned cone experiment. The linearity is reassuringly good and it can be seen that theory and experiment agree within the 95% confidence limits derived from the experimental data.

### 8. DISCUSSION

It has been shown that thrust cone bearings with straight cone tracks have a nominal line contact and may be compared to a rolling element bearing. To this end when compared with best tribo-design practice for such bearings, as the transverse width of the thrust contacts may not be significantly larger than the nominal Hertzian contact dimension a radical degree of edge relief is implied. In the case of highly loaded slow speed thrust cones it has been shown that the lubrication of such configurations can suffer significantly from the effects of side leakage, and load-driven edge film thinning. To avoid such problems, it is suggested that edge relief in the form of a circular arc is applied to one of the cone tracks to effectively crown one of the surfaces to promote better minimum oil film thinning resistance with respect to load, as justified by the data shown in Figure 17. Although such a modification is an 'on cost', even for more lightly loaded higher speed thrust cones where such effects may be less evident, it has a further advantage in that it leads to an intrinsically self aligning contact which can be made more tolerant to misalignment. It will be realised from the comparisons made that crowning also has the effect of increasing contact pressure. However, given the film forming advantage and the fact that for such high conformity bearings contact pressures are generally much lower than those in the associated gear contacts, concern about fatigue resistance is unlikely to dictate any restriction on the use of crowning.

### 9. CONCLUSIONS

1. Under certain loading conditions straight thrust cones can suffer from severe oil film thinning at the contact edges.
2. To counter the edge film thinning effect, profiling one of the cone tracks with a circular arc and effectively edge relieving a nominal line contact by 'crowning', leads to more load-stable minimum oil films.

## 10. ACKNOWLEDGEMENTS

The authors gratefully acknowledge the support made available by MoD. We also thank Paul Maillardet and Forbes Morgan of MoD; Norman Hopkinson and Chris Bartlett of DRA; Eric Frisk of Ealing Optics for supply of the excellent quality glass discs and Harry Shearman of Micro Instruments for the supply of the two special optical systems.

## REFERENCES

- [1] Langer, H., Hydrodynamische axiale Kraftübertragung bei wellen schjnellaufender getriebe, Konstruktion, 1982, 34, 473-478.
- [2] Simon, V., Thermal elastohydrodynamic lubrication of rider rings, Trans ASME, J. Trib., 1984, 106, 492-498.
- [3] Dowson, D. and Higginson, G. R. Elastohydrodynamic Lubrication, 1977 (Pergamon, Oxford)
- [4] Hartnett, M. J., The analysis of contact stress in rolling element bearings, JLT, Vol 101, 105 - 109, 1979.
- [5] Barragan de Ling, FdM., Evans, H.P. and Snidle, R.W., Thrust Cone Lubrication: elastohydrodynamic analysis of conical rims, Proc. I.Mech.E, JET, Vol 210, 85-96, 1995.
- [6] Chittenden R.J., Dowson, D., Dunn, J.F., and Taylor, C.M. A theoretical analysis of the isothermal lubrication of concentrated contacts, Pt 1 & 2, Proc. Roy. Soc., Ser.A, 397,245, (Pt1), 271, (Pt2), 1985.
- [7] Barragan de Ling, FdM., Lubrication of thrust cones. PhD thesis, University of Wales, 1993.
- [8] Barragan de Ling, FdM., Evans, H.P. and Snidle, R.W., Thrust Cone Lubrication: elastohydrodynamic analysis of crowned rims, Proc. I.Mech.E, JET, Vol 210, 97-105, 1995.
- [9] Parkins, D. W. and Rudd, L. M., Thrust Cone Lubrication: a test facility and preliminary measured data, Proc. I.Mech.E, JET, Vol 210, 107-112, 1995.
- [10] Kirk, M. T., Hydrodynamic Lubrication of Perspex, Nature, 1944, 1962, 965.
- [11] Foord, C. A., Wedeven, L. D. Westlake, F. J. and Cameron, A., Optical Elastohydrodynamics, Proc. I. Mech. E, Vol 184, Pt1 and Pt2, 1969-70.

(c) British Crown Copyright 1996/DERA

Published with the permission of the controller of Her Britannic Majesty's Stationery Office

## **An Optical EHD Study Using a Reciprocating Hertzian Contact Rig Designed to Simulate the Kinematics of Constant Velocity Joints**

**H.C. Rutlin<sup>a</sup>, R.S. Sayles<sup>a</sup> and M.S. Starkey<sup>b</sup>**

a Tribology Section, Imperial College of Science, Technology and Medicine,  
Exhibition Road, London, SW7 2BX.

b GKN Technology Ltd, Birmingham New Road, Wolverhampton, WV4 6BW.

A test rig employing a reciprocating Hertzian contact and designed to simulate constant velocity joint (CVJ) motion, has been used to study the essential aspects of CVJ tribology. This paper describes the use of chromatic optical interferometry to study EHD film behaviour under reciprocating conditions.

Film measurements are reported as a function of stroke length, position and speed for different lubricants and the transient nature of film formation is described in terms of different modes of film behaviour and how these relate to operating conditions.

Results are compared with the predictions of steady state theory where it is shown that significant deviations are often evident. The implications of the results to CVJ operation are discussed.

### **1. INTRODUCTION**

Constant velocity joints (CVJs) are a special type of universal joint designed to transmit torque between two non-aligned shafts at constant angular velocity. Their main application is in the drive lines of cars and light vans. Research has been going on for some years at Imperial College aimed at improving our tribological understanding of CVJs, in particular that of ball joints. These joints consist of an outer race connected to one shaft, an inner race connected to the second shaft and balls which transmit the torque. A cage constrains the balls to the homokinetic plane, that is the plane that bisects the angle between the two non-aligned shafts, and so ensures constant angular velocity. This causes the balls to reciprocate along the tracks of the inner and outer races as the shafts and joint rotate.

A test rig was developed to simulate the essential aspects of CVJ operation. This test rig has been used to study some aspects of CVJ tribological behaviour through the measurement of film thickness and friction in reciprocating contacts (1).

The overall aim of this and associated research projects is a better understanding of the tribological conditions within a CVJ and the identification of important parameters for future modelling of such systems.

This paper reviews the background to this research and describes some of the initial film thickness results obtained.

### **2. BACKGROUND**

To improve the operation and design of CVJs it is necessary to understand, and be able to predict, lubricating conditions and frictional effects within a joint. There are two principal reasons why this is difficult: firstly CVJs have a complex reciprocating motion affecting several integral components, and as a result much of the lubrication associated with these components is of a transient nature; and secondly CVJs are lubricated with complex greases.

Well established models exist to describe fluid film behaviour under steady state conditions and are being developed further for the transient case (2,3). However the behaviour of complex CVJ greases, which are formulated to exploit several lubrication regimes, is even more difficult to predict, and film behaviour cannot usually be accurately defined for the steady state or transient cases.

Speed, temperature, contact surface roughness, local conditions of lubricant supply as well as lubricant type, will all influence the lubrication of the contacts within a CVJ. Reciprocating motion and low entrainment speeds suggest that the elastohydrodynamic (EHD) component is likely to be small. As yet no real model exists that accurately reflects the lubrication of CVJs, although a great deal more is now known as a result of research such as that reported here.

### 3. CVJ OPERATION

Although the individual components within a CVJ are rotating at the speeds of the shafts, the balls reciprocate only a few millimetres on their tracks, consequently entrainment velocities are low. Ball speeds vary sinusoidally with respect to the tracks, and a mid-stroke (i.e. maximum) speed of 0.08m/s is typical of service conditions. The geometry of CVJs forces the balls to move by a combination of rolling and sliding.

High loads and small contact areas lead to high pressures; 1 - 3 GPa being normal, with higher stresses possible. The normal working temperature of joints lies in the range 50 to 80 °C.

### 4. TEST RIG AND EXPERIMENTS

The test rig used for the experimental work has been designed to simulate the essential features of the motion of a ball within a CVJ (1). Figure 1 depicts the contact configuration of the rig with it's associated friction force transducers and optics. Reciprocation of the plate holder, (in and out of Fig. 1), combined with synchronised rotation of the ball, form the basic kinematics of the rig.

The rig, in the configuration\* depicted in Figure 1, consists of a horizontal sapphire plate loaded against a steel ball supported upon two rolling element bearings. The plate and ball are synchronised and driven in simple harmonic motion.

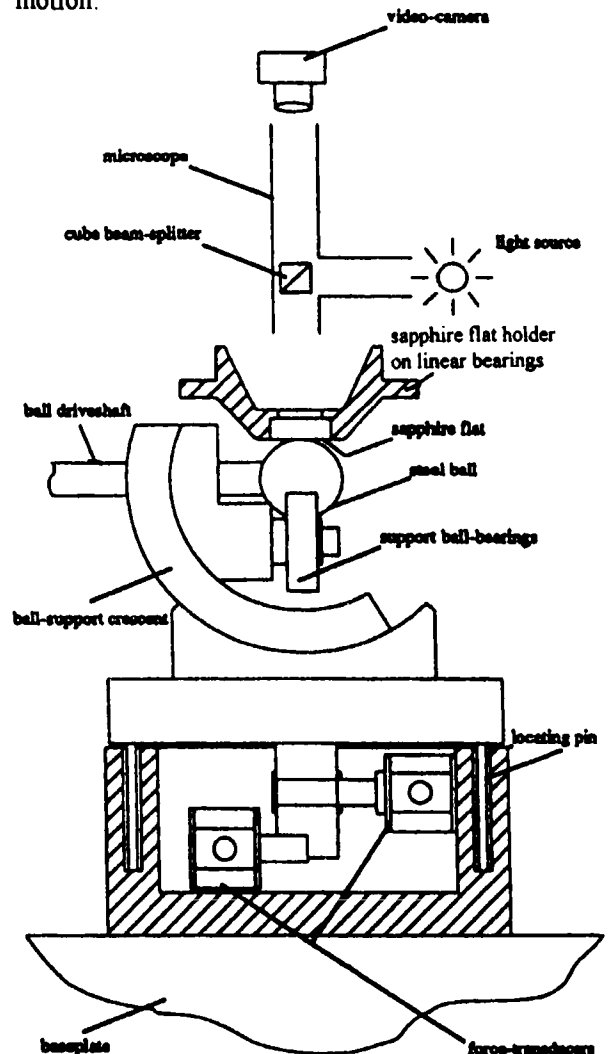


**Figure 1** Specimen configuration and associated measurement arrangements of the rig for a ball-on-flat geometry. The plane of reciprocation of the flat holder is in and out of the figure. The support crescent allows a spin component to be imposed on the contact.

\* Sapphire or glass plates have been used for optical studies as depicted in Figure 1, however steel plates of different roughness etc. have also been used to study friction and wear effects. Elliptical contact effects have also been examined by replacing the ball with a spherical roller.

The stroke length and frequency can be anything up to 25 mm and 11Hz respectively, and the slide/roll ratio can be varied from pure rolling to full sliding.

Frictional forces are measured with force transducers in two orthogonal directions in the plane of reciprocation (see Fig. 1). The contact force is known from the dead-weight loading system which gives an upper limit on maximum nominal contact pressure, for the ball-on-flat configuration shown in Figure 1, of around 4 GPa.

The contacting specimens and their environment can also be heated up to a maximum temperature of about 140°C for tests at elevated temperature.

Film thickness is measured by chromatic optical interferometry between a glass or sapphire flat with a semi-reflective chromium coating and a steel ball. This gives a working range from approximately 120 to 1000 nanometers with a resolution of about 25 nanometers. The contact is observed via a video camera and the images recorded on videocassette. Film thickness can thus be determined for each increment of time which can then be related back to stroke position. This method also allows observation of the inlet meniscus, wake and any particles that may be present. The resolution of the image is such that markings or small defects on the ball can be detected and this helps determine position in the cycle.

## 5. RESULTS

Film thickness results are reported for three test lubricants at room temperature; a high viscosity reference oil HVI650; a base oil for a CVJ grease; and a CVJ grease. For this test work the rig was configured for pure rolling. In general, all the lubricants generated films that were greatest in the centre of the stroke where the speed is highest and reduced at the ends as the speed fell to zero, but behaviour was more complex than that predicted by steady state theory.

### 5.1 HVI650 REFERENCE OIL

For this lubricant, which has a viscosity of 1.2Pas at 23°C, and is about 3 times higher than that of the

CVJ base oil, the film thickness generated throughout the stroke by the reciprocating motion was found to be less than that predicted by steady state EHD theory. Some differences however were observed with increasing frequency.

Figures 2-4 show film thicknesses measured during a half cycle. At low frequencies (Figure 2), no measurable oil film is generated at the ends (turn-around-points) of the motion. Moving away from the ends, film thickness increases with increasing speed and reaches a maximum at the midpoint of the reciprocating motion.

At slightly higher reciprocating speeds (Figure 3) squeeze films are detected at each end of the motion, where steady state theory predicts a film rapidly falling to zero.

When test frequency is increased further, a third type of behaviour is observed which results in a very distorted film profile (Figure 4). The film thickness generated is much less than that predicted by steady state theory and film thickness appears to be controlled by some parameter other than entrainment velocity.

Observation of the inlet meniscus showed that as test frequency increased, it moved closer to the contact, and it would seem that oil starvation is influencing the results.

### 5.2 CVJ GREASE BASE OIL

Figures 5 & 6 show measurements recorded for the much less viscous CVJ grease base oil. The results are different from those of HVI650, and instead of the measured film thickness always lagging the steady state theoretical prediction, the recorded values exceed steady-state predictions for a substantial part of the stroke. Both Figures 5 and 6, which were obtained at different frequencies, show that squeeze films have been recorded at the ends of the motion or turn-around-points where there is reversal of entrainment. Restrictions on the experimental method meant that it was not possible to run the test at frequencies substantially greater than 3.2 Hz to see if this oil also then shows the effects of starvation.



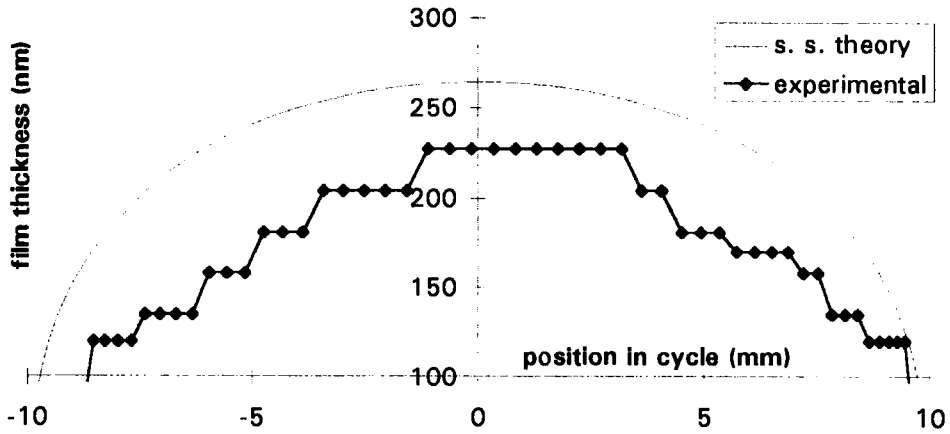


Figure 2. Graph of central film thickness versus position in cycle for experimental reciprocating motion and steady state theory; HVI650; 0.191 Hz.

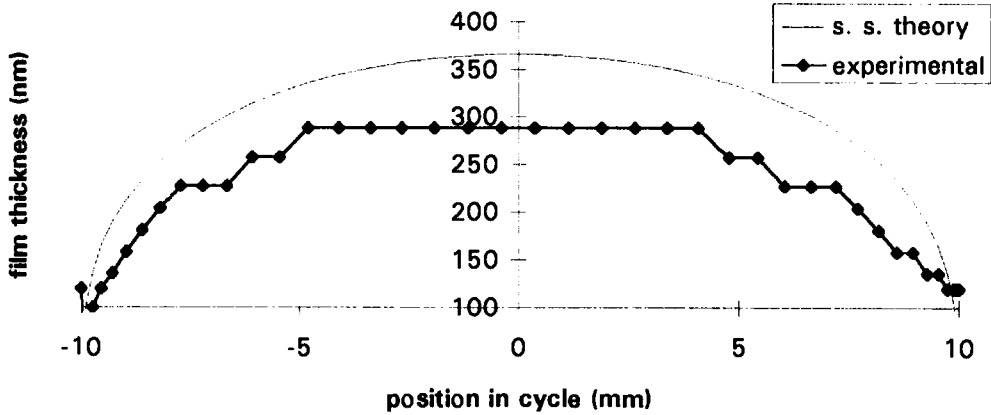


Figure 3. Graph of central film thickness versus position in cycle for experimental reciprocating motion and steady state theory; HVI650; 0.310 Hz.

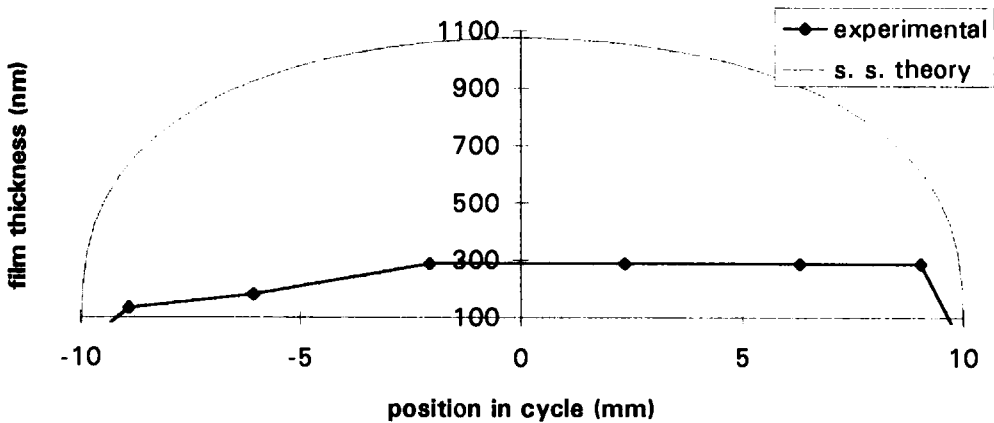


Figure 4. Graph of central film thickness versus position in cycle for experimental reciprocating motion and steady state theory; HVI650; 1.55 Hz.

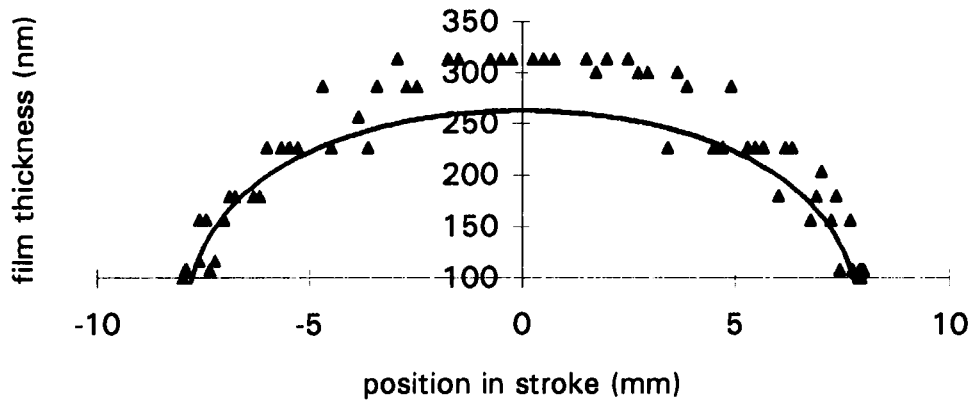


Figure 5. Graph of central film thickness versus position in cycle for experimental reciprocating motion (points) and steady state theory (solid line); CVJ grease base oil; 1.63 Hz.

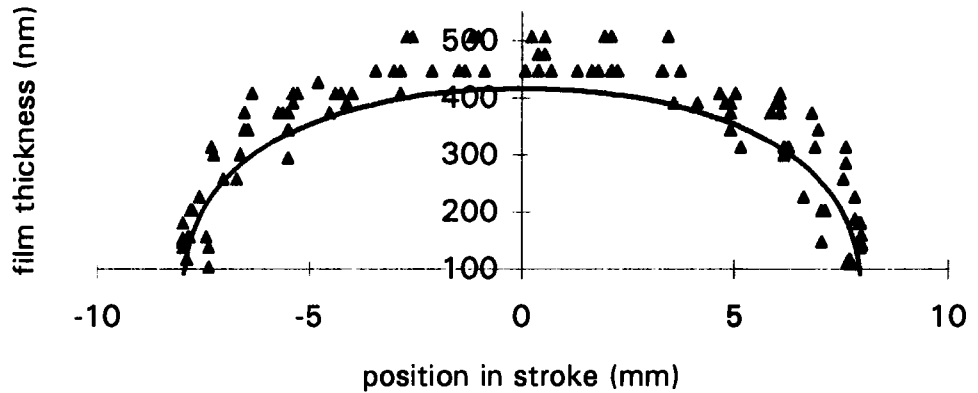


Figure 6. Graph of central film thickness versus position in cycle for experimental reciprocating motion (points) and steady state theory (solid line); CVJ grease base oil; 3.22 Hz.

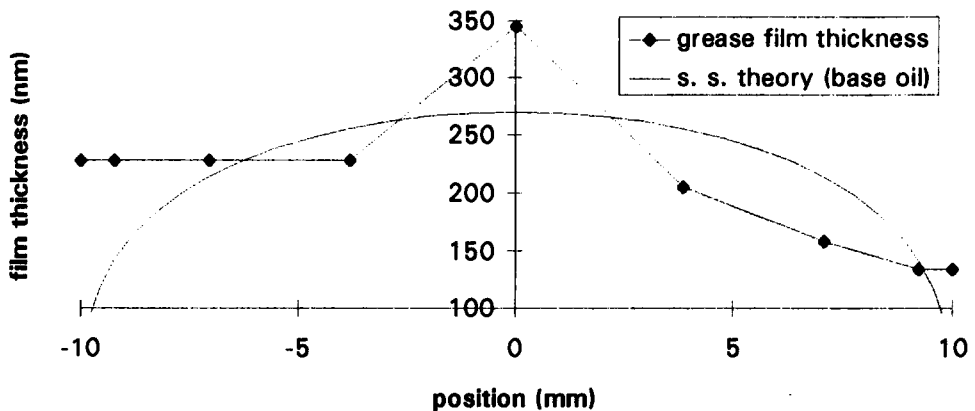
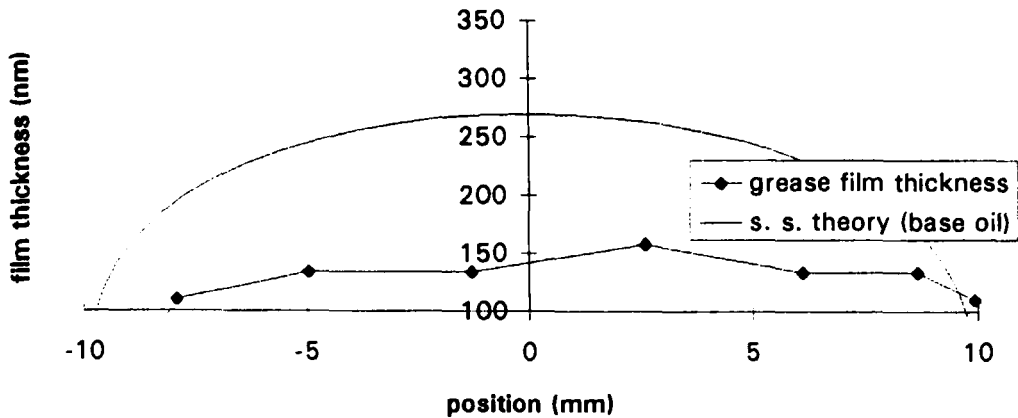


Figure 7. Graph of central film thickness versus position in cycle for grease under reciprocating motion and steady state theory for base oil; 1.56 Hz; at start.



**Figure 8.** Comparison of central film thickness versus position in cycle for grease under reciprocating motion and steady state theory for base oil; 1.56 Hz; after 8 secs.

**5.3 CVJ GREASE**

Film thicknesses have also been measured for a typical CVJ grease. The behaviour of the grease is more complicated than that of the base oil in that the measured film thickness also varies with running time. The grease initially forms a thicker film than steady state EHD theory predicts, as shown in Figure 7 which illustrates the film generated in the first recorded half cycle of the test.

Maximum film thickness was found to decay with each half cycle until after 8 seconds running a condition is reached where the film generated is much less than that predicted by steady state theory and almost speed independent, Figure 8.

**6. DISCUSSION.**

The results of the test rig show that the supply condition is particularly important for reciprocating motion. The fluid CVJ grease base oil, and the more viscous HVI650 oil when run at low frequencies, most closely follow the behaviour predicted from steady state theory; the small differences in thickness may be partially attributed to small differences in temperature. Squeeze film effects prevent the film decaying to zero at entrainment reversal.

With both the CVJ grease and HVI650 at higher test frequencies, starvation influences the film thickness generated until eventually, at longer running times/higher frequencies, film thickness is independent of entrainment speed.

Figure 9 shows this effect for the CVJ base oil when test results from a conventional steady-state optical EHD rig are compared with results from the reciprocating rig at the same speeds.

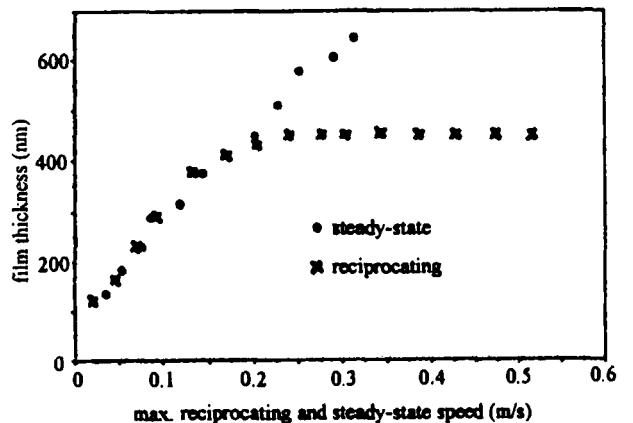


**Figure 9** Comparison of steady state (ball-on-disc) and reciprocating film-thickness measurements, over a range of speeds, for the grease base oil at room temperature.

Film thickness in reciprocating tests plateau's out due to starvation effects at a speed related to the viscosity. Further tests similar to those represented in Fig.9 have shown that the higher the viscosity, the lower will be the speed when the reciprocating films deviate from the steady state values. This effect has also been reported when some greases are used as the lubricant, even under steady state conditions (4).

Under conditions of marginal starvation it was found that the film thickness was not symmetric about mid stroke, that is it was sensitive to the direction of travel. This asymmetry can be seen in many of the results, but is very prominently illustrated in the results of Figures 4 and 8. As the ball starts moving at -10 mm, it turns back into a region freshly cleared of grease: (in the case of an oil it would be a freshly cavitated region). This hinders film formation as it limits the amount of lubricant available for film generation and the film builds more slowly than predicted by steady state theory.

As the ball slows down at the ends of each cycle, the film often decays more slowly than predicted, probably due to squeeze effects. This can accentuate the asymmetry due to the larger quantity of lubricant available in this region relative to the start of each stroke, when the ball is turning back into a region freshly cleared of lubricant. Also as frequency increases, the time available for re-supply decreases, and a greater area of the track is affected by lubricant starvation until the film thickness along the majority of the track is controlled by the availability of the lubricant, e.g. Figs. 4 and 8.

On the test rig the ball motion is restricted so that a track is formed on both the ball and the plate. In a joint, the ball is free to rotate and spin about any axis and is also observed to precess. Wear is not restricted to a single track but is distributed around the whole surface of the ball. Each time that the ball moves onto a fresh surface it will draw fresh grease into the contact. Thus whilst grease starvation must play a role in CVJ lubrication, it is unlikely to be as extreme as that found in the reported tests.

## 7. CONCLUSIONS

- 1) With an adequate supply of lubricant, EHD film formation in reciprocating motion is similar to that predicted from steady state theory and under some conditions may exceed it.
- 2) Significant squeeze films can form at the point of entrainment reversal.
- 3) Films formed under reciprocating motion are particularly sensitive to starvation: at the end of motion, the ball turns back into a freshly cavitated region or a region freshly cleared of lubricant.
- 4) Under conditions dominated by starvation, film thickness is constant over much of the cycle.

## 8. REFERENCES

- (1) Rutlin H.C., (1991), "An Investigation of the Lubrication of Constant Velocity Joints", *M.Sc thesis*, Dept. of Mech. Eng., Imperial College, London SW7 2BX.
- (2) Hooke C.J., (1994), "The minimum film thickness in lubricated line contacts during a reversal of entrainment - general solution and the development of a design chart", *Proc Instn Mech Engrs*, Vol 208, pp. 53-64.
- (3) Scale L.E., Rycroft J.E., Horswill N.R., Williamson B.P., (1996), "Simulation and Observation of Transient Effects in Elastohydrodynamic Lubrication", *SAE Technical Paper Series 961143*, Reprinted from: *New Studies in Engine Oil Rheology and tribology (SP-1182)*.
- (4) Cann P. M., Spikes H. A., "Film Thickness Measurements of Lubricating Greases Under Normally Starved Conditions", *NLGI Spokesman*, May 1992, pp21-27

## The amplitude of the complementary function for wavy EHL contacts.

J A Greenwood<sup>a</sup> and G.E. Morales-Espejel<sup>b</sup>

<sup>a</sup>Department of Engineering, University of Cambridge, UK.

<sup>b</sup>Instituto Tecnológico de Monterrey, ITESM, Monterrey, Mexico

In an EHL line contact between wavy rollers, it is known that the behaviour in the Hertz zone consists of two terms: a direct response, which has the original wavelength and moves with the speed of the roller carrying the original wave, and an induced response, which has a different wavelength and moves at the mean roller speed. Attempts (largely unsuccessful) to predict the magnitude of this induced response are described

### 1. INTRODUCTION.

Considerable progress has been made in recent years towards understanding of the behaviour of transverse roughness in an EHD contact. In the 'Hertzian' region of the contact, the pressure is so high and the viscosity reaches such enormous values that viscous shearing ceases, and instead of the Reynolds equation, the governing equation for one-dimensional flow becomes simply

$$\bar{u} \frac{\partial(\rho h)}{\partial x} + \frac{\partial(\rho h)}{\partial t} = 0. \quad (1)$$

This is a *transport equation*, and its solutions are of two types, which in the case of a roller with a wavy surface may be described as a 'forced vibration' and a 'free vibration'. The 'forced vibration' consists of a pressure fluctuation which induces sinusoidal elastic deformation in the rollers, largely cancelling out the original waviness: the amplitudes of the pressure fluctuation and of the resulting film-thickness variations are determined by the competition between the compressibility of the lubricant and the deformability of the rollers, but, especially for long wavelengths, this results in film-thickness variations which are very much smaller than the original waviness, and pressure variations almost as large as those needed to flatten the waviness completely, as in a dry contact.

The 'free vibration' can be anything! – any wave travelling with speed  $\bar{u}$  is a solution of the transport equation. But it must, of course, be stimulated in some way, and the excitation consists of the waviness arriving at the end of the inlet with a *frequency*  $(u_1 / \lambda)$ , where  $u_1$  is the speed of the wavy surface and  $\lambda$  is the wavelength. (If both rollers are wavy,

there will be two excitations). This excitation will induce a free vibration of the same frequency, and therefore, since its speed  $\bar{u}$  is set, of wavelength  $\lambda' = \bar{u} / (u_1 / \lambda)$  *differing from that of the original waviness*. Also, the free vibration consists of a film thickness variation and a pressure variation, but the pressure variation is normally smaller than that of the pressure variation in the forced vibration, while the film thickness variation is normally much larger than the film thickness variation of the forced vibration, so that what we see is the pressure variation of the first (wavelength  $\lambda$ , speed  $u_1$ ) and the film thickness variation of the second (wavelength  $\lambda'$ , speed  $\bar{u}$ ). This is confusing enough when the roughness is a single, sinusoidal wave; but it becomes worse when the roughness is of some other form, which must be reduced by Fourier analysis to a set of sinusoidal components.

The picture just described is based on work and insights from many papers from different authors, especially [1,2,3,4,5,6,7,8]. But what none of these papers contain is any rule for determining the amplitude of the free vibration. Venner et al [9,10] have attempted to fill this gap by determining the amplitude numerically, and, for the case of pure rolling, have produced a master curve from which the amplitude may be predicted. This paper reports (largely unsuccessful) attempts to explain this master curve.

The compressibility of the fluid plays a major part in determining the amplitude of the film thickness variations, and indeed, is almost entirely responsible for any film thickness variation in the 'forced vibration': but in this first attempt at a theory it will be

neglected and only *incompressible* fluids considered.

### 1.1 Equations.

Throughout the paper, we consider a lubricated roller contact with an initial waviness  $z = z_1 \sin(2\pi x / \lambda)$ , and that the pressure fluctuates correspondingly about its smooth surface values. It is assumed that the elastic deformation may be calculated using the equations for a half-space covered by sinusoidal waves. Then from [7], but with a slight change of notation:

$$\text{let } A = \frac{2\lambda \bar{p}}{\pi \bar{h} E'}, \quad B = \frac{\pi \bar{h}^2 \bar{p}}{6\bar{u}\lambda\eta_0 \exp(\alpha p)} \quad (2)$$

where  $\bar{p}$  is a representative pressure (conveniently taken as the Hertz pressure) and  $\bar{h}$  the mean film thickness in the Hertz region. Then in the high pressure region we have:

#### Forced vibration:

The amplitudes  $p_1$  of the pressure fluctuations and  $h_1$  of the film thickness fluctuations are given by:

$$\frac{p_1 / \bar{p}}{z_1 / \bar{h}} = \frac{-1}{\sqrt{(B^2 + A^2)}}; \quad \frac{h_1}{z_1} = \frac{B}{\sqrt{(B^2 + A^2)}} \quad (3)$$

#### Free vibration:

The amplitudes  $p_1$  of the pressure fluctuations and  $v_1$  of the film thickness fluctuations are related by:

$$\frac{p_1 / \bar{p}}{v_1 / \bar{h}} = \frac{1}{A'} \quad \text{or} \quad \frac{p_1}{v_1} = \frac{\pi E'}{2\lambda'} \quad (4)$$

where  $A'$  is  $A$  except that  $\lambda'$  replaces  $\lambda$ . For pure rolling where  $u_1 = \bar{u}$  the two are the same.

## 2. PURE ROLLING WITH A WAVY ROLLER.

What will be the amplitude of the excitation of the 'free vibration'? If the amplitude of the roughness  $z_1$  is unchanged at the inlet, then according to simple gear pump theory,  $z_1$  is precisely the amplitude of the varying additional flow into the contact, which has to be accommodated in and carried through the

high pressure zone. If, as is usually true, the 'forced vibration' consists of pressure ripples which completely flatten the roughness, then the amplitude of the additional flow must be the amplitude of the induced wave:

$$z_T = z_1. \quad (5)$$

#### Roughness deformation in the inlet.

Assuming that no deformation occurs in the inlet seems rather extreme, and certainly the amplitude given by (5) is too large. Suppose that the amplitude reduction given by equation (3) is assumed to take place in the inlet, even though it has been calculated by assuming an infinite number of equal pressure ripples: and that the point at which the gearpump mechanism operates is near the end of the inlet, where the pressure is just beginning its steep rise, ie where  $\alpha p = 1$ . (called by Couhier [9] the **magic point**). Then (5) becomes

$$z_T = z_1 / \sqrt{1 + A^2 + B^2}. \quad (6)$$

$$\text{Now, } \frac{A}{B} = \frac{12\lambda^2 \eta_0 \bar{u} \exp(\alpha p)}{\pi^2 E' \bar{h}^3} = \frac{12e \lambda^2 \eta_0 \bar{u}}{\pi^2 E' \bar{h}^3} \quad (7)$$

on setting  $\alpha p = 1$ . How does this compare with the variable  $\nabla = \frac{\lambda}{b} \frac{M^{3/4}}{L^{1/2}}$  found by

Venner et al to determine the amplitude? Rewriting in terms of the non-dimensional variables gives

$$\frac{A}{B} = \frac{3e}{32} \left( \frac{\lambda}{b} \right)^2 \frac{1}{M^2 H^3} \quad (8)$$

Approximating the film thickness by the simple Kapitza equation

$$\bar{h} \sim 1.5(\alpha \eta_0 \bar{u})^{2/3} R^{1/3}$$

(see [11]) then simple manipulation gives

$$A/B \approx 0.16 \left( \frac{\lambda}{b} \right)^2 \frac{M^{3/2}}{L} \frac{1}{P} = 0.16 \nabla^2 \cdot \frac{1}{P}$$

where  $P = \alpha p_0 = L \sqrt{M/2\pi}$ : so that for constant  $P$  the two are directly related and the simple model appears to give the correct dependence. Fig 1 shows a comparison of the excitation function predicted by equations (6) and (7) with some early results by Venner et al [9] in which  $L$  and  $M$  were held constant ( $L=11.3$ ,  $M=98.3$ ) and only the wavelength  $\lambda$  varied, and there is general agreement. But

sadly, later results established conclusively that the additional  $P$  term gives a spurious dependence not found in the numerical results. Even worse, it seems doubtful whether there is any justification for applying equation (3) in the inlet *in a case of pure rolling, which is governed by the unsteady Reynolds equation.*

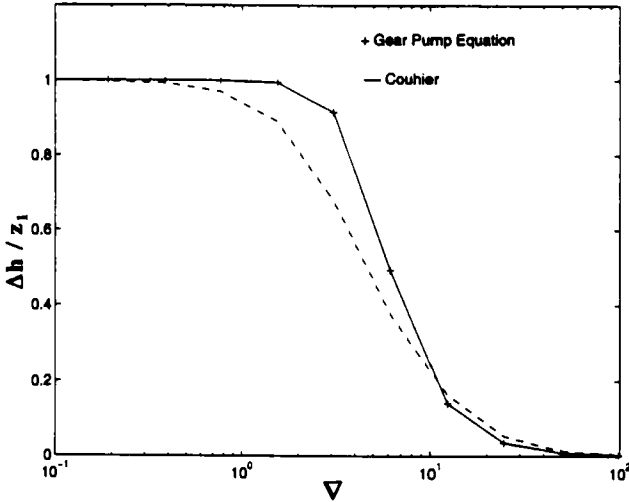


Fig 1. Amplitude reduction in rolling according to the gearpump equation and equation (6) for  $L=11.3$ ,  $M=98.3$ .

### 3. The wavy-Grubin model.

Venner et al [10] give a second set of numerical solutions, for the case of simple sliding of a smooth plane over a wavy roller (see also [3, pt 2]. Here the film-thickness variation along the channel is small and may be ignored: but the mean film thickness depends on how the roughness is positioned with respect to the contact. Venner et al show that the ratio of the amplitude of this, almost-sinusoidal, variation of the mean film thickness to that of the original waviness is governed by the same non-dimensional group  $\nabla$ . To what extent can we reproduce these results?

The governing equation is now the *steady Reynolds equation*

$$\frac{dp}{dx} = 12\eta\bar{u} \frac{h - \bar{h}}{h^3}. \quad (9)$$

We use the Ertel-Grubin model, in which the inlet is assumed to have the Hertz shape

$$h = h_0 + \left(\frac{b^2}{2R}\right) \left(\xi \sqrt{\xi^2 - 1} - \cosh^{-1} \xi\right) \quad (10)$$

where  $\xi = x / b$ , except that here we add a fixed waviness  $z = z_1 \cos(2\pi(x + b) / \lambda + \phi)$ .

This immediately raises a difficulty: within the Hertz region, if the waviness is undeformed, the film thickness will be

$$h = h_0 + z_1 \cos\left(\frac{2\pi(x + b)}{\lambda} + \phi\right), \quad (11)$$

and will periodically attain the critical value  $h = \bar{h}$  at which the pressure is a maximum or minimum. These maxima must all take the same value (certainly the maxima of the reduced pressure  $q \equiv (1/\alpha)(1 - \exp(-\alpha p))$  must be very nearly the same), so that we cannot, as in the ordinary Grubin theory, take  $\bar{h}$  to be  $h_0$ . Instead, the two must be related

$$\text{by} \quad \bar{h} \int_0^\lambda \frac{dx}{h^3} = \int_0^\lambda \frac{dx}{h^2} \quad (12)$$

The phase angle  $\phi$  is irrelevant, so we can write  $h = h_0(1 + k \cos \theta)$  with  $k = z_1 / h_0$  and obtain the well-known integrals of Sommerfeld journal bearing theory: hence

$$\bar{h} = h_0 \frac{2 - k^2}{2 + k^2}. \quad (13)$$

Having found  $\bar{h}$ , we then determine the point  $x_k$  in the Hertz region at which  $h = \bar{h}$  (here  $\phi$  is relevant), and apply the modified Grubin condition

$$\int_{x_k}^{\infty} \frac{h - \bar{h}}{h^3} dx = \frac{1}{12\alpha\eta_0\bar{u}} \quad (14)$$

to determine  $h_0$  (by iteration).

Changing the variables to  $H = Rh / b^2$  and  $\xi = x / b$ , equation (14) becomes

$$\int_{\xi_k}^{\infty} \frac{H - \bar{H}}{H^3} d\xi = \frac{b^3}{12\alpha\eta_0\bar{u}R^2}. \quad (15)$$

The integral depends only on  $H_0$  and  $\lambda / b$ :

the RHS may be rewritten  $\frac{4}{3} \left(\frac{2}{\pi}\right)^{3/2} \frac{M^{3/2}}{L}$ , so

the result of the calculation must be of the form

$$H_0 = F(\lambda / b, M^{3/2} / L). \quad (16)$$

Fig. 2 shows the results of varying the two parameters separately: over almost the entire range, combining the two parameters into

$$\nabla = (\lambda / b)(M^{3/2} / L)^{1/2} \quad (17)$$

brings all the points on to a single curve. Only when  $\nabla$  is small (and the film thicknesses very nearly all the same, barely dependent on the phase angle) are the points also dependent on  $\lambda / b$ .

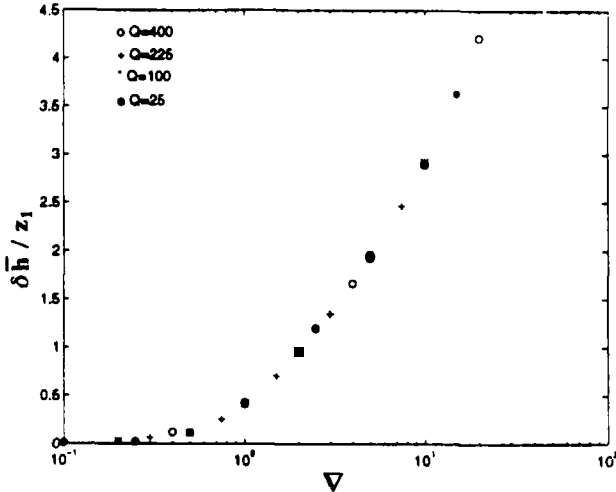


Fig 2. Amplitude reduction in simple sliding.

$$Q = M^{3/4} / L^{1/2} ; \nabla = (\lambda / b) \cdot Q$$

Unfortunately, although the amplitude depends on the correct parameter, the variation is completely wrong: the amplitude can be much larger than that of the waviness causing it, and steadily increases with  $\nabla$  instead of rising to a low maximum ( $\sim 0.3z_1$ ) and then falling to zero.

Clearly the assumption that the roughness is undeformed is unacceptable: and indeed we know what the film thickness variation along the Hertzian zone will be. From equation (3), which now is valid (see [2],[7],[8]), the amplitude is

$$\frac{z_1}{\sqrt{1 + A^2 / B^2}} \sim 6 z_1 \frac{P}{\nabla^2} \cdot \frac{1}{(\exp(P - 1))^2}$$

where here we use the pressure in the Hertz zone rather than the value  $\alpha p = 1$  at the magic point. For all likely values of  $P$  (and certainly  $P \geq 10$ ) this will be undetectable.

The simplest model would be to assume the waviness undeformed outside the

Hertzian region and completely flattened within it; and certainly this is not far from the truth! But as the phase of the waviness varies, this would result in a wave being arbitrarily truncated at  $x = -b$ , so generating a discontinuity: Instead, the waviness is postulated to continue unchanged as far as the pressure maximum at which the reduced pressure first reaches  $1 / \alpha$ , and then to disappear: this seems to imply that now  $\bar{h} = h_0$ . Again there is a complication: normally the relevant maximum lies in the Hertz zone, but sometimes a higher maximum occurs in the inlet: the Grubin model, of course, requires the higher value to be chosen. The result is rather unfortunate for higher amplitudes of waviness, as the film thickness values corresponding to the two locations vary with phase angle very differently, and the composite curve resulting is distinctly non-sinusoidal. But for small amplitudes the problem is minor. Fig 3 shows the results.

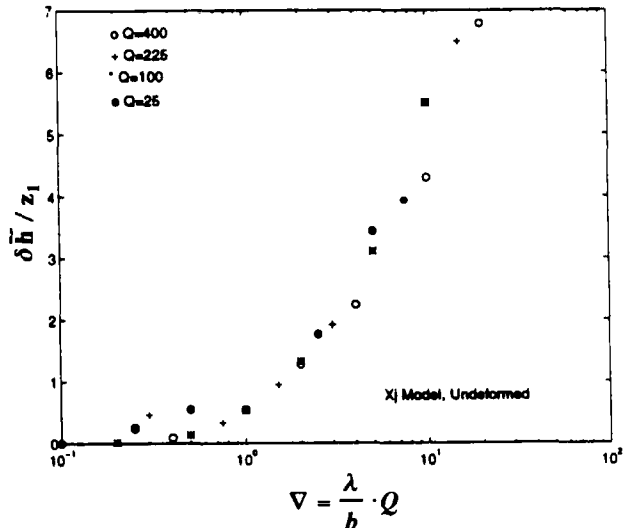


Fig 3. Amplitude reduction in simple sliding, assuming complete flattening in the Hertz zone.

It is not clear from these two models exactly where the waviness generates the film thickness changes. In order to throw some light on this, two artificial models were tried: in the first, the waviness was arbitrarily reduced by a factor  $(\bar{h} / h)$  so that the waviness is only appreciable near the end of the inlet: in the second the complementary



factor  $(1 - \bar{h} / h)$  was used. Using the first factor had a negligible effect: using the second largely eliminated the dependence of the film thickness on the waviness. This gives general support to Couhier's concept of a **magic point**, though not, of course, establishing that it is a *point* rather than a narrow *region* which matters.

Accordingly, the experiment was tried off again attenuating the roughness by using the factor from equation (6),

$$z_T = z_1 / \sqrt{1 + A^2 / B^2}$$

using the viscosity at the magic point,  $\alpha p = 1$  so that  $\bar{h}$  is again given by equation (7). The smooth surface film thickness  $\bar{h}$  was used to calculate  $A / B$ ; it was found by a preliminary iterative solution of the Grubin equations using the Crook approximation  $\bar{H} = 0.515(L / M^{3/2})^{3/4}$  as an initial guess.

There are now *three* independent variables,  $\lambda / b$ ,  $(L / M^{3/2})$ , and  $P$ . Even holding  $P$  constant results in a considerable scatter when the film thickness variation is plotted against  $\nabla$ , though the results are now of the right form, with the largest amplitude for intermediate values of  $\nabla$  (Fig. 4): when  $P$  is varied the scatter becomes excessive.

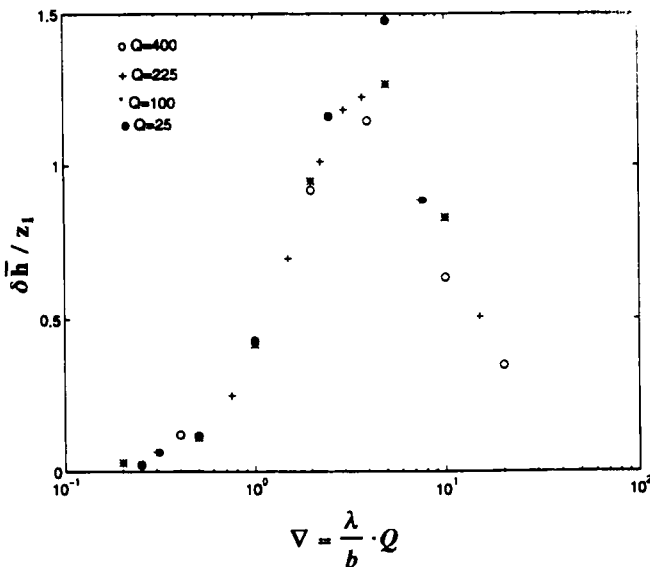


Fig 4. Amplitude reduction in simple sliding when the initial amplitude is reduced according to equation (6).

It would seem that it is correct to regard the response as due to two factors: the direct response of the film thickness to the phase of the waviness, which is responsible for the ineffectiveness of short wavelength waviness, and the attenuation of the waviness at the end of the inlet, which is complete for long wavelengths and so makes long wavelengths ineffective. If so, then the size of the largest response will depend on how the two factors combine, and will be changed by a shift in one factor. Thus, redefining the magic point as the point where  $\alpha p = 2$  will increase  $A / B$  by a factor  $e$  and shift the falling part of the curve to the left while leaving the rising part alone: the effect is to reduce the maximum considerably, but of course, has no effect on the scatter.

**CONCLUSION**

The amplitude of the film-thickness fluctuations between two wavy rollers in pure rolling can be predicted to a first approximation by using the gear-pump equation with the waviness modified by a factor based on conditions at the **magic point** defined as the point where the pressure reaches the value  $\alpha^{-1}$ , but this introduces an additional, spurious, factor involving  $P \equiv \alpha p_0$  compared with the parameter  $\nabla = (\lambda / b)(M^{3/4} / L^{1/2})$  on which the numerical solutions depend.

The mean film-thickness when a smooth surface slides past a stationary, wavy roller is usually higher than for two smooth rollers, but depends on the exact location of the waviness with respect to the Hertzian zone. The variation of the mean film thickness with the phase of the waviness is almost sinusoidal, and the amplitude is governed by the interaction of two factors: the direct response of the film thickness to the waviness, which is responsible for the ineffectiveness of waviness of short wavelength, and the attenuation of the waviness at the end of the inlet, which is complete for long wavelengths and so makes long wavelengths ineffective.

Computations based on a simple Grubin analysis show that the first factor

depends on  $\nabla$ ; the remaining factor is not too different from the factor used here to obtain the pure rolling results above. But this factor,  $z_T = z_1 / \sqrt{1 + A^2 / B^2}$ , offered here is inadequate: possibly because the attenuation is not determined by the behaviour at a single point in the inlet; possibly because the approximation of calculating the elastic deflection as if there were an infinite number of waves of the same amplitude is too poor. It is not clear that either of these changes would actually produce the right sort of change in the results: our factor depends on  $\nabla$  and  $P$ , and the dependence on  $P$  needs to be reduced. Perhaps the location of the magic point depends on the Hertz width rather than occurring at a particular inlet pressure?

#### ACKNOWLEDGEMENT.

This project has been partly supported by CONACyT, Mexico.

#### REFERENCES.

- [1] Kweh, C.C., Evans, H.P. and Snidle, R.W. Micro-elastohydrodynamic lubrication of an elliptical contact with transverse and three-dimensional roughness. *Trans. ASME, J. Trib.*, 1984, **111**, p577.
- [2] Greenwood, J.A. and Johnson, K.L. The behaviour of transverse roughness in sliding EHL contacts. *Wear*, 1992, **153**, p107.
- [3] Goglia, P.R., Cusano, C. and Conry, T.F. Effects of irregularities on the EHL of sliding line contacts. *Trans. ASME, J. Trib.*, 1984, **106**, p104.
- [4] Venner, C.H. Multilevel solution of the EHL line and point contact problems. PhD thesis, University of Twente, Enschede., The Netherlands, 1991.
- [5] Venner, C.H. and Lubrecht, A.A. Transient analysis of surface features in an EHL line contact in the case of sliding. *Trans. ASME, J. Trib.*, 1994, **116**, p186.
- [6] Chang, L., Webster, M.M. and Jackson, A. On the pressure rippling and roughness deformation in elastohydrodynamic lubrication of rough surfaces. *Trans. ASME, J. Trib.*, 1993, **115**, p439.
- [7] Greenwood, J. A. and Morales-Espejel, G.E. The behaviour of transverse roughness in EHL contacts. *Proc. Instn. Mech. Engrs. J. Eng. Trib.* 1994, **208J**, p121
- [8] Morales-Espejel, G.E. EHL of smooth and rough surfaces. Ph.d Thesis, University of Cambridge, 1993.
- [9] Couhier, F., Influence des rugosités de surface sur les mécanismes de lubrification de contact elastohydrodynamique. Ph.d Thesis, INSA de Lyon, 1996
- [10] Venner, C.H. , Couhier, F., Lubrecht, A.A., and Greenwood, J. A. Amplitude reduction of waviness in transient EHL line contacts. 23rd Leeds-Lyon Symposium, Leeds 1996
- [11] Archard, J.F. and Cowking, E.W. Elastohydrodynamic lubrication at point contacts. *Proc Instn. Mech. Engrs.* 1965-66, **180** pt 3B, p47

## Time-Dependent Solutions with Waviness and Asperities in EHL Point Contacts

P. Ehret, D. Dowson, and C.M Taylor <sup>a</sup>

<sup>a</sup> Institute of Tribology, Department of Mechanical Engineering. The University of Leeds

The effects of various surface textures, described either by an orientated waviness or an uniform distribution of asperities, are compared under pure rolling conditions for elastohydrodynamic lubricated point contacts. Time-dependent solutions, obtained with a Multigrid Multi-Integration method, reveal that the orientation of the waviness, in these conditions, has only a moderate effect on the values of minimum film thickness and maximum pressure. These results are in contrast to those obtained under pure sliding conditions, where the orientation of the surface texture leads to important differences in terms of minimum film thickness. In pure sliding, it is shown that the best lubrication condition is produced for the transverse waviness.

### 1. INTRODUCTION

Reliability and durability of all heavily loaded concentrated contacts rely upon the existence of a thin film of lubricant in order to separate the bounding surfaces in relative motion. Over the years, technological and economic issues have necessitated the transfer of higher loads over the contact area, leading modern mechanisms to sustain stringent elastohydrodynamic lubrication conditions, where film thickness is approximately of the same magnitude as the surface roughness. Under such severe conditions, the characteristics of the surface texture, and more importantly, the properties of the deformed surface texture to allow lubricant to flow between peaks and valleys and to protect every part of the contact, have a considerable impact on the success of the lubrication conditions.

In a previous study [1], the effects of a surface texture described by a waviness were analysed under different orientations of the surface compared to the entrainment velocity. The findings revealed that the orientation of the waviness affected considerably the lubrication conditions and therefore the minimum film thickness. Under isothermal and pure sliding conditions (motionless waviness), the results obtained showed that transverse waviness provides a substantial enhancement in lubrication capabilities, and pro-

duced even larger minimum film thickness than the smooth surface case. The reason is explained by the fact that valleys created by leakage flows at the entrance of the contact supply a regular flow of lubricant in remote parts of the contact. On the other hand, for other orientations, lubrication conditions become non-homogeneous. The orientation thus leads to an accumulation of the lubricant in the valleys of the waviness at the entrance of the contact, which propagates in a straight line all over the contact in the direction of the entrainment velocity. The minimum film thickness then decreases reaching the smallest values for an orientation approximately equal to 60°. Similar simulations were performed by Ai [2] with transverse, oblique and longitudinal orientations of a surface texture described either by a waviness, or by a random roughness.

This paper presents an extension to these studies in which the effects of the surface texture are investigated in pure rolling conditions. The influence of waviness orientation is again considered, but surface patterns which contain uniformly distributed asperities on the surface are also examined. The aim of this study is to identify the effects of the surface texture on the flow of lubricant through the contact. The ultimate purpose is to propose surface textures which improve the lubrication conditions, alleviating stress on the

bounding surfaces, and increasing the fatigue life of the machine elements.

The effects of the surface texture on elastohydrodynamic lubrication has attracted great attention over the years. In the 1970s, the surface roughness orientation in EHL contacts was studied by Patir and Cheng [3] using a stochastic approach to define the surface characteristics. Nevertheless such approaches present fundamental flaws in elastohydrodynamic conditions since the micro-geometries are deformed under high pressure, and cannot be presumed known in the contact area. The representation of the surface texture in a deterministic manner requires, however, handling a very demanding numerical problem involving fine levels of discretization to define accurately the micro-geometries, but also the solution of the strongly non-linear Reynolds equation.

For point and elliptical contacts, studies with a deterministic representation of the micro-geometry were initiated by Seabra, [4], Barrangan de Ling [5], Kweh [6], and Lubrecht [7]. The development of the multigrid multi-integration technique [8], [9] [10] has impressively overcome the limits of the more traditional numerical schemes, by allowing high level of discretization and, fast and stable convergence. Using this technique, Venner [10] studied extensively the effect of micro-geometries in point contacts. Recently Venner and Lubrecht [11] [12] [13] have proposed time-dependent simulations of EHL point contacts with transverse waviness under various rolling/sliding conditions. Their study confirmed Greenwood and Morales Espejel's [14] theory which considers the film thickness as the result of wave combination propagating through the contact at different speeds.

### 1.1. Notation

$a$  radius of the Hertzian contact [m],  
 $a = \left(\frac{3FR}{2E^*}\right)^{\frac{1}{3}}$   
 $\mathcal{A}$  Dimensionless amplitude,  
 $\mathcal{A} = amp/h_h$

$amp$  Micro-geometry amplitude [m]  
 $E'$  Reduced Elasticity Modulus [Pa],  
 $\frac{2}{E'} = \frac{(1-\nu_1^2)}{E_1} + \frac{(1-\nu_2^2)}{E_2}$   
 $E_1$  Elasticity Modulus of Body 1 [Pa]  
 $E_2$  Elasticity Modulus of Body 2 [Pa]  
 $G$  Dimensionless Material Parameter,  
 $G = \alpha E'$   
 $h_h$  Maximum Hertzian Deformation [m],  
 $h_h = \frac{a^2}{R}$   
 $h_{cen}$  Central Film Thickness [m]  
 $h_{min}$  Minimum Film Thickness [m]  
 $h_{00}$  Motional Separation of Rigid Surfaces [m]  
 $H_{00}$  Constant of integration  
 $H_{00} = h_{00}/h_h$   
 $H$  Dimensionless film thickness,  
 $H = h/h_h$   
 $L$  Dimensionless Material Parameter (Moes),  
 $L = G(2U)^{1/4}$   
 $M$  Dimensionless Load Parameter (Moes),  
 $M = W(2U)^{-3/4}$   
 $p$  Pressure [Pa]  
 $p_h$  Maximum Hertzian Pressure [Pa],  
 $p_h = \frac{3F}{2\pi a^2}$   
 $p_R$  Reference Pressure [Pa],  
 $p_R = 0.198 \cdot 10^9 Pa$   
 $P$  Dimensionless pressure  $P = p/p_h$   
 $R$  Radius of the Ball [m]  
 $r$  Half length of the Asperities [m]  
 $t$  Time  
 $\bar{t}$  Dimensionless time  $\bar{t} = tu_e/a$   
 $u_e$  Entrainment Velocity [m/s]  
 $U$  Dimensionless Velocity Parameter,  
 $U = \frac{\eta_0 u_e}{E^* R}$   
 $x, y$  Coordinates [m]  
 $X, Y$  Dimensionless Coordinates  
 $X_0, Y_0$  Initial Location of Asperity Centre  
 $X = x/a, Y = y/a$   
 $z$  Pressure Viscosity Parameter  
 $w$  Load [N]  
 $\tilde{w}$  Wavelength [m]  
 $W$  Dimensionless Load Parameter,  
 $W = \frac{w}{E^* R}$   
 $\mathcal{W}$  Dimensionless wavelength,  
 $\mathcal{W} = \tilde{w}/a$   
 $\alpha$  Pressure Viscosity Index [Pa<sup>-1</sup>]  
 $\frac{\alpha_2 R}{z} = \ln \frac{\eta_0}{\eta_R}$   
 $\eta$  Viscosity [Pa s]

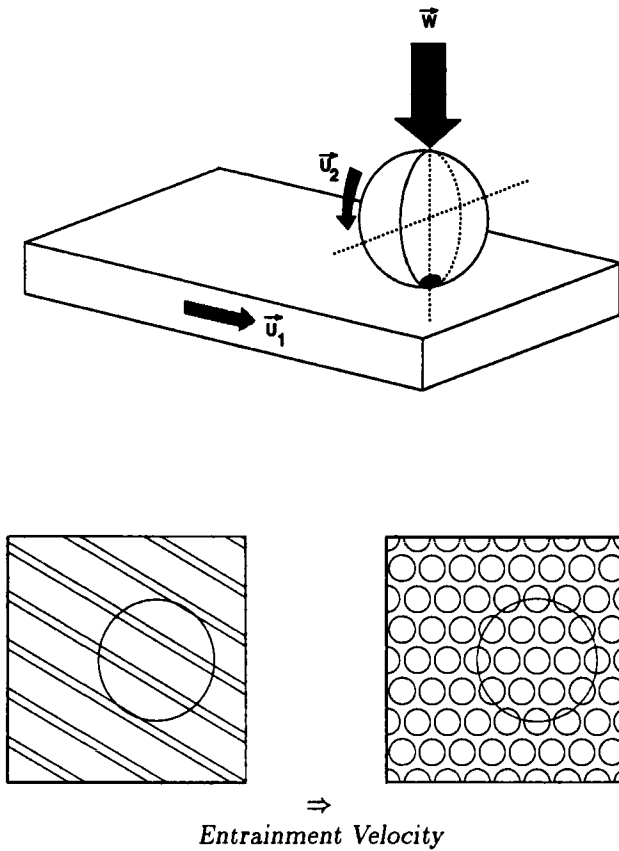


Figure 1: Kinematic condition and Geometry. On the plane, the surface texture is defined either as an orientated waviness or as a uniform distribution of asperities

|            |   |
|------------|---|
| $\eta_0$   | Viscosity at Ambient Pressure [Pa s]  |
| $\eta_R$   | Reference Viscosity [Pa s],<br>$\eta_R = 6.32 \cdot 10^{-5} \text{ Pa s}$     |
| $\epsilon$ | Reynolds Equation Coefficients,<br>$\epsilon = \frac{\rho H^3}{\eta \lambda}$ |
| $\lambda$  | Dimensionless parameter<br>$\lambda = \frac{12\eta_0 u_e R^2}{a^3 \rho_h}$    |
| $\nu_1$    | Poisson's ratio of Body 1   |
| $\nu_2$    | Poisson's ratio of Body 2   |

## 2. THEORY

The lubrication conditions of the contact between a smooth ball and a plane containing micro-geometries are examined under pure rolling conditions (Figure 1). The ball and the plane have same kinematic conditions, and move with an entrainment velocity  $u_e$ . Kinematic and loading conditions are not dependent on time. Isothermal conditions are assumed. Furthermore the lubricant is considered as a Newtonian compressible and piezoviscous fluid. The change of density with pressure is given by the Dowson and Higginson relation [15]:

$$\rho(p) = \rho_0 \left( 1 + \frac{0.6p}{1 + 1.7p} \right) \quad (1)$$

The viscosity variation obeys the Roelands equation [16]:

$$\eta(p) = \eta_0 \left( \frac{\eta_0}{\eta_R} \right)^{\left[ \left( 1 + \frac{p}{p_R} \right)^s - 1 \right]} \quad (2)$$

The domain of study is rectangular, and the coordinates are defined such that the axis  $0x$  has the same direction as the surface velocity. The origin of the frame is located at the centre of the contact. The set of equations which have to be satisfied at each instant  $\bar{t}$  are represented in a dimensionless form as follows:

- the Reynolds equation,

$$\nabla(\nabla\epsilon P) = \frac{D}{Dt}(\bar{\rho}H) \quad (3)$$

- the Elasticity equation

$$H = H_{00} + \frac{X^2}{2} + \frac{Y^2}{2} - \mathcal{R}(X, Y, \bar{t}) + \frac{2}{\pi^2} \int_{-\infty}^{+\infty} \int_{-\infty}^{+\infty} \frac{P(X', Y', \bar{t}) dX' dY'}{\sqrt{(X-X')^2 + (Y-Y')^2}} \quad (4)$$

- the Balance equation

$$\int \int_{\Omega} P(X, Y, \bar{t}) dX dY - \frac{2\pi}{3} = 0 \quad (5)$$

The operator  $\frac{D}{Dt}(\cdot)$  of the Reynolds equation represents the time derivative following the average motion of the fluid through the contact ;

$$\frac{D}{Dt}(\cdot) = \frac{\partial}{\partial \bar{t}}(\cdot) + \frac{\partial}{\partial X}(\cdot)$$

This defines respectively the squeeze and Couette terms.

The boundary conditions for the Reynolds equation are :

$$P = 0 \quad \text{on each side of the computation domain}$$

$$P = \frac{\partial P}{\partial X} = 0 \quad \text{at the boundary cavitation}$$

### 2.1. Surface Texture

The function  $\mathcal{R}(X, Y, \bar{t})$  defines the micro-geometry located on the plane. Two types of surface texture are considered :

- a waviness orientated at a given angle  $\phi$  compared to the entrainment velocity  $u_e$ . Specifically, the orientation angle  $\phi = 0^\circ$  corresponds to a transverse waviness, and  $\phi = 90^\circ$  defines a longitudinal waviness.

$$\begin{cases} X_a = X \cos(\phi) - Y \sin(\phi) \\ X_d = (X_s + \bar{t}) \cos(\phi) \\ \mathcal{R}(X, Y, \bar{t}) = \mathcal{A} (1 + \cos(2\pi \frac{X_a - X_d}{\mathcal{W}})) \end{cases} \quad (6)$$

- a uniform distribution of asperities.

$$\begin{cases} X_{c_i} = X_{0_i} + \bar{t} \\ z_i = 1 - \left( \frac{X - X_{c_i}}{r} \right)^2 + \left( \frac{Y - Y_{c_i}}{r} \right)^2 \\ \mathcal{R}(X, Y, \bar{t}) = \mathcal{A} \sum_i \sqrt{z_i} \end{cases} \quad (7)$$

Only the positive values of  $z_i$  are considered. The distribution of the asperity centres  $X_{0_i}, Y_{0_i}$  is such that each asperity is surrounded by five other asperities. The distance between each asperity centre equals  $\mathcal{W} = 2r$ .

Compared to a traditional definition, the waviness has been translated to the value  $\mathcal{A}$  in order to compare results obtained from the two micro-geometries. After translation, it follows that, for both surface textures, the function  $\mathcal{R}(X, Y, \bar{t})$  remains positive or nil everywhere in the domain of study.

### 2.2. Conditions of Study

The conditions of study are related to one of Kaneta's experiments [17], and are the same as used by Venner and Lubrecht [11] in simulations of a moving ridge. The parameters of study are presented in Table 1. The height of the micro-geometry remains constant in the whole study. Its value is chosen equal to  $0.120 \mu\text{m}$  which corresponds respectively to  $\mathcal{A} = 0.0225$  for the waviness, and  $\mathcal{A} = 0.045$  for the asperity distribution.

|                       |                       |                     |
|-----------------------|-----------------------|---------------------|
| $E'$                  | $1.17 \cdot 10^{11}$  | [Pa]                |
| $\alpha$              | $2.2 \cdot 10^{-8}$   | [Pa <sup>-1</sup> ] |
| $\eta_0$              | 1.22                  | [Pa s]              |
| $u_e$                 | 0.01075               | [ms <sup>-1</sup> ] |
| $R$                   | $1.27 \cdot 10^{-2}$  | [m]                 |
| $a$                   | 0.184                 | [mm]                |
| $p_h$                 | 0.54                  | [GPa]               |
| $h_h$                 | 2.67                  | [ $\mu\text{m}$ ]   |
| $F$                   | 38.3                  | [N]                 |
| $h_{min, smooth}$     | 0.062                 | [ $\mu\text{m}$ ]   |
| $h_{cen, smooth}$     | 0.142                 | [ $\mu\text{m}$ ]   |
| Dimensionless Numbers |                       |                     |
| $M$                   | 235.8                 |                     |
| $L$                   | 5.27                  |                     |
| $W$                   | $2.0 \cdot 10^{-6}$   |                     |
| $U$                   | $8.82 \cdot 10^{-12}$ |                     |
| $G$                   | 2574                  |                     |

**Table 1** Smooth surface parameters, and loading conditions

### 2.3. Numerical Method

The multigrid multi-integration method [10], [18] [19] is used to solve the set of equations at each time step. The finest mesh is defined by a

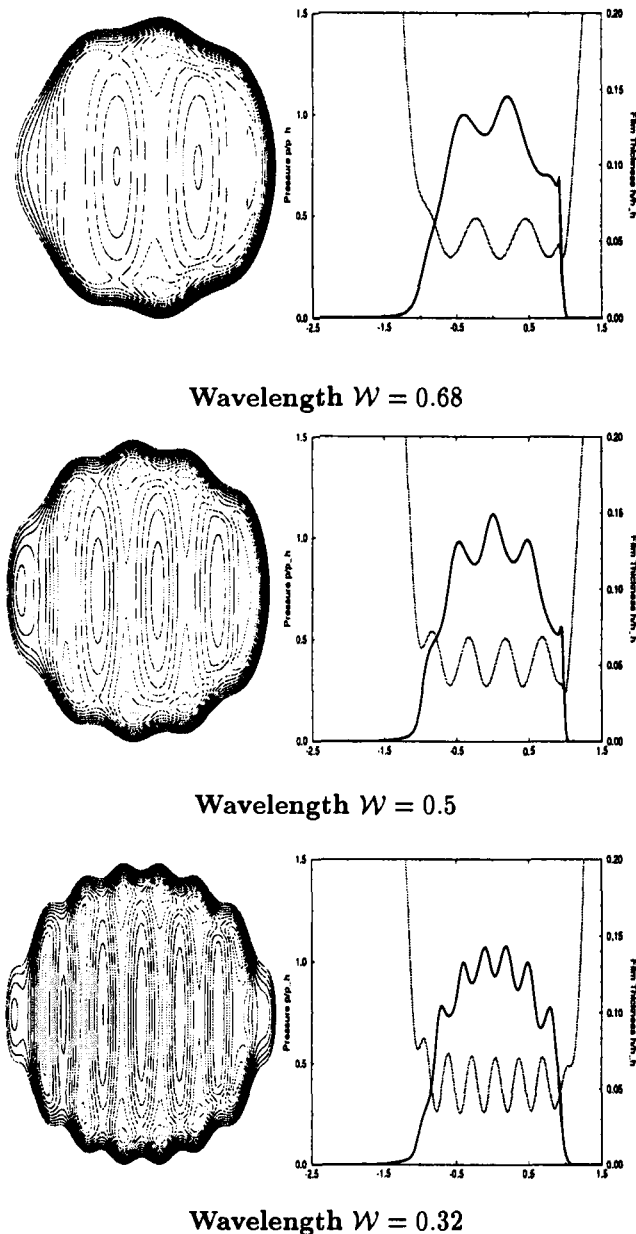


Figure 2: Contours of film thickness, pressure and film thickness profiles at  $Y=0$ , for transverse waviness, under pure rolling conditions, at  $\bar{t} = 3.6$

grid of  $257 \times 257$  points, and the coarsest grid contains  $17 \times 17$  points. In order to increase the efficiency of the numerical scheme, the F-cycle is employed. The solution, obtained at the previous time step, is not used directly as a first guess to solve the set of equations at the current time, but it is decomposed according to its smooth (low frequency) and detailed (high frequency) components by transferring it on different grids. The solution at the current time is then constructed from low to high frequencies by correcting the components obtained at the previous time with the Full Approximation Scheme [8].

As pointed out by Venner, it is essential to employ a second order scheme to discretize the Couette and squeeze terms of the Reynolds equation. For transient solutions, under pure rolling conditions, the use of the first order scheme leads to a decrease in the amplitude of the surface feature as it moves towards the contact. The solution exhibits an overprediction of the pressure and surface deformation. This numerical artifact is explained by the fact that first order schemes have difficulties in representing the local changes in the solution. Parts of the solution history are thus misrepresented or forgotten, leading to a solution similar to that obtained in steady-state. For second order schemes, this problem can also appear when the time step is not small enough considering the changes in the solution between two instants. This is the case when a large number of surface features are present in the contact, involving a multitude of simultaneous changes at each time step. For these reasons, time-dependent simulations of real rough surfaces remains questionable since a very large spatial discretization, and a very fine time step are required to represent and conserve the high frequency features of the surface topography.

There is a simple test which allows us to control if the time step is sufficiently small to account for all the changes which take place in the contact. It consists of checking the pressure and film thickness profiles at  $Y = 0$  during the passage of transverse waviness under pure rolling conditions. For this case, the solution is well known.

The waviness must travel without any change in the contact, since there is no pressure induced flow in the high pressure area of the contact. In this part of the contact, the viscosity is so high that the elliptical part of the Reynolds equation vanishes. As a result, the deformation of the waviness and the pressure ripples are only produced by the squeeze action which takes place when the surface feature enters the contact. Subsequently these ripples cannot increase when the waviness moves towards the contact. It follows that the increase in the pressure ripples as observed in some of Lubrecht and Venner's simulations [12] [13] can only be explained by the numerical damping of the waviness, and should disappear by decreasing the time step. Using the same spatial discretization as Venner and Lubrecht, the previous condition on the transport of the surface features in pure rolling conditions leads us to employ a time step twice as small as theirs. The transport of the waviness is clearly seen in Figure 2 for 3 different wavelengths, as an instant far from the start-up. For all the cases presented,  $\Delta X = \Delta Y = 0.015625$ , and  $\Delta t = 0.0078125$ . The computational domain is defined as  $-2.5 \leq X \leq 1.5$  and  $-2 \leq Y \leq 2$ .

The initial condition chosen corresponds to the deformed smooth geometry on which is superimposed the underformed micro-geometry. As a result, the pressure field at time  $t = 0$  remains close to the pressure field obtained with the smooth geometry. The initial condition can be considered as a representation of the geometry according to the  $\Lambda$  ratio (smooth minimum film thickness to the composite roughness). In this present study, the  $\Lambda$  ratio is about 1, although a value at least larger than 3 is commonly recommended to assure satisfactory elastohydrodynamic lubrication. The start-up of the numerical simulation presents the transition between the micro-geometry defined by the  $\Lambda$  ratio and the real conditions of lubrication. Since the minimum film thickness is smaller than the height of the micro-geometry, there are local interferences between the two bounding surfaces during a short period of time at the start-up. No special numerical treatment of the Reynolds equation has been made to handle this aspect,

although an accurate and rigorous solution of the start-up conditions should require solving the problem of contact between solid/solid in the areas where local interferences exist.

### 3. RESULTS

#### 3.1. Transition Period

Figures 3, 4 and 5 display the evolution of the film thickness, and pressure profiles for a transverse waviness, an orientated waviness ( $\phi = 45^\circ$ ), and an asperity distribution during the period when the surface features, set at  $t = 0$  in the conjunction, pass through the contact. Thereafter periodic results are obtained and are independent of the initial solution. In order to improve the visualization of the film thickness contours, a maximum and a minimum threshold are selected, which correspond respectively to  $H = 0.0525$ , and  $H = 0.02$ . As a result, the zones without any contour represent the new locations of the initial surface textures (minimum threshold), and the positions of the valleys filled with lubricant (maximum threshold), which are created when new surface features arrive in the contact.

These simulations show that the initial surface features, as they move through the contact, hardly sustain any deformation. This is explained by the fact that the lubricant, in the high pressure region, and the initial micro-geometry possess same velocities.

The transition between the initial condition and the arrival of new surface features is clearly seen on the film thickness profiles. They show that the entrance of new surface feature are always accompanied by a substantial entrainment of lubricant in the contact, leading to an increase in the separation between the bounding surfaces. It is also interesting to note that most of the deformation to which the surface feature is subjected is produced when the micro-geometry enters the contact due to the squeeze action. This effect is especially evident for the asperity feature (Figure 4) which changes shape as it squeezes the lubricant.



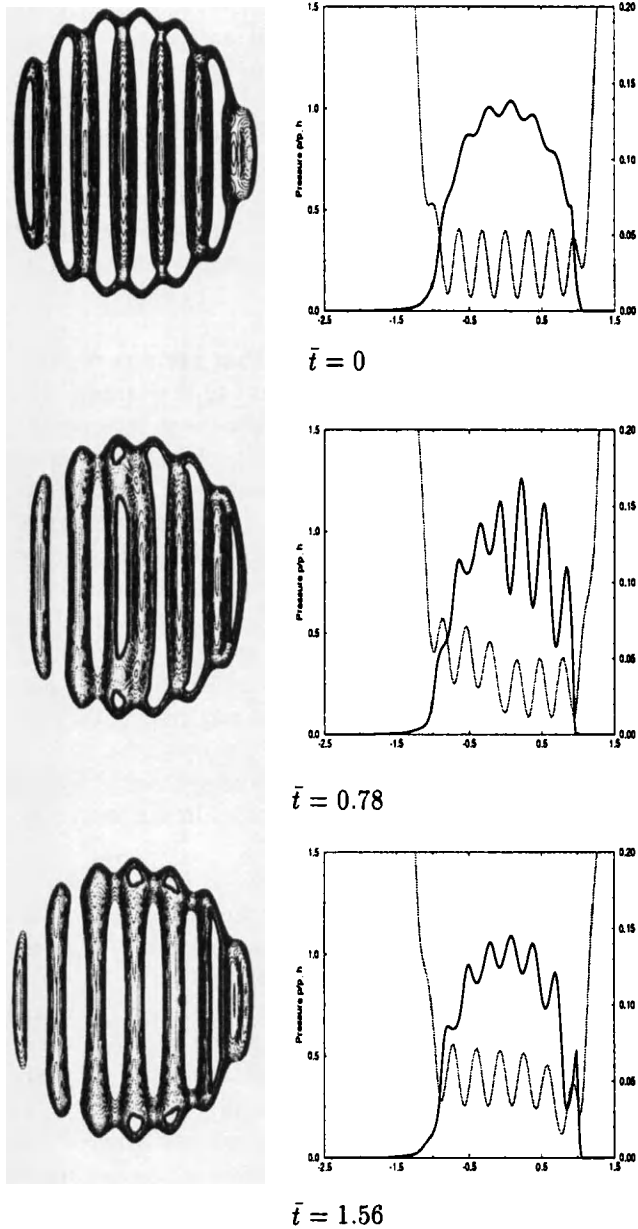


Figure 3: Contours of film thickness, pressure and film thickness profiles at  $Y=0$ , for a transverse waviness,  $W = 0.32$ , under pure rolling conditions

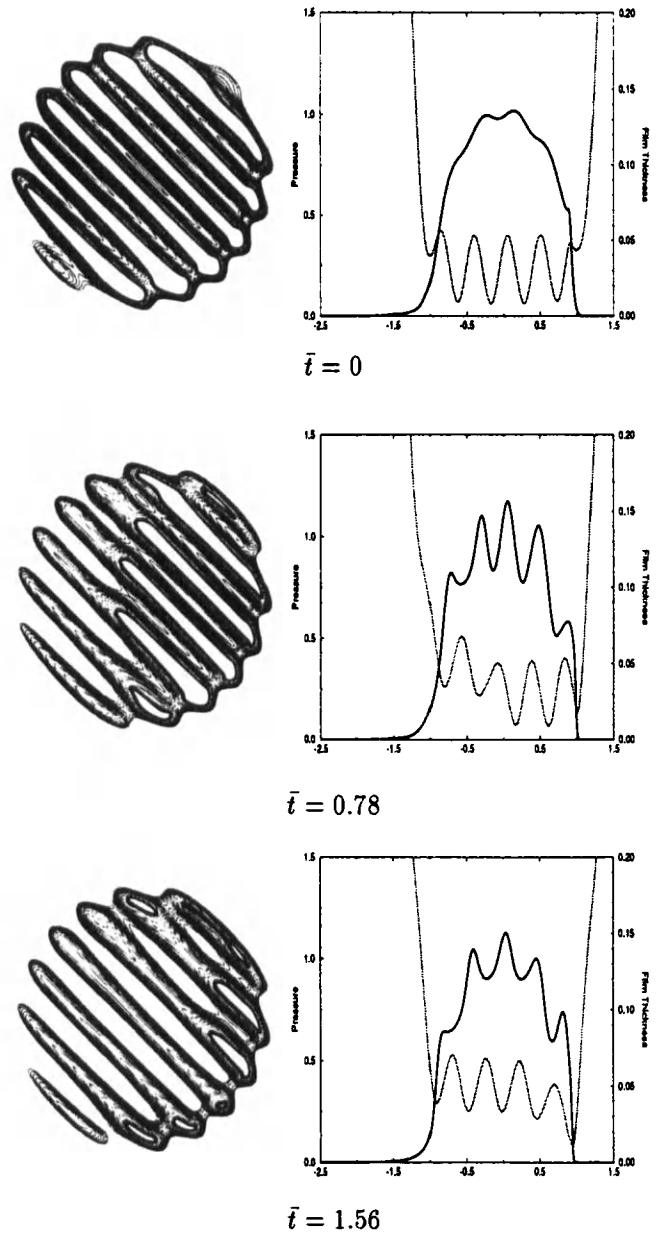


Figure 4: Contours of film thickness, pressure and film thickness profiles at  $Y=0$ , for an orientated waviness,  $\phi = 45^\circ$ ,  $W = 0.32$ , under pure rolling conditions

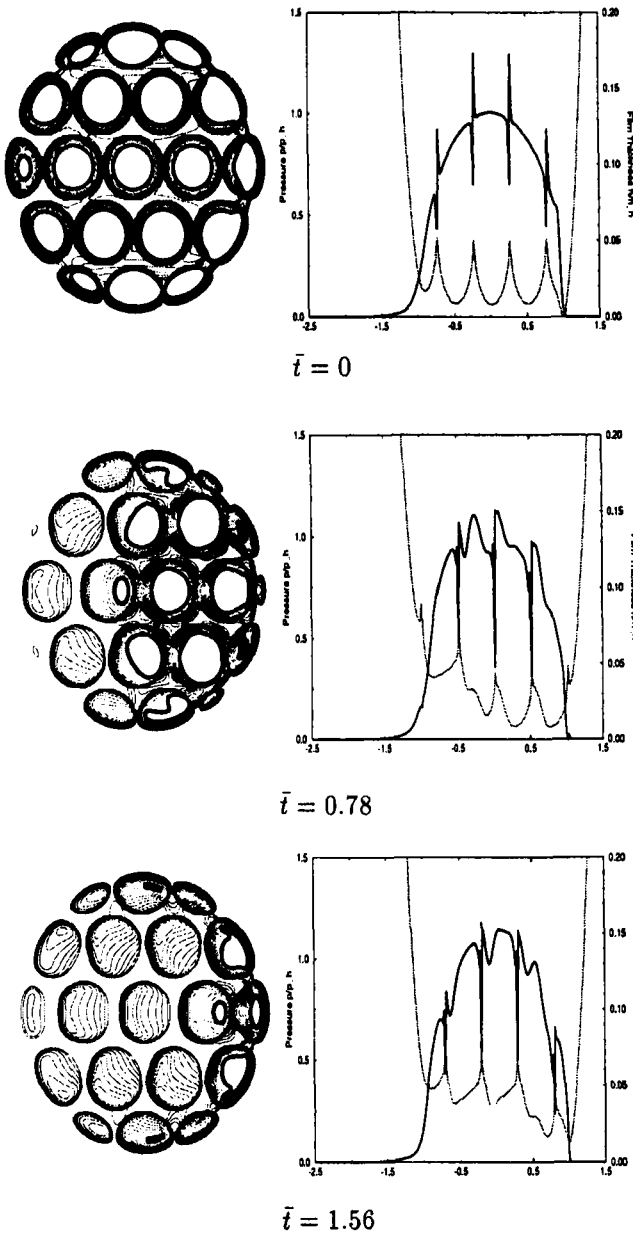


Figure 5: Contours of film thickness, pressure and film thickness profiles at  $Y=0$ , for an asperity distribution,  $W = 0.5$ , under pure rolling conditions

### 3.2. Lubricant Flow

The entrance of identical surface features in the contact, at regular time intervals, splits up the continuous inlet flow, and subsequently forms patchy lubrication conditions. For the transverse and orientated wavinesses (Figure 3 and 4), this aspect is illustrated by areas of the contact where lubricant, is entrapped between the ridges of the waviness, and propagates at the same speed as the surface micro-geometry.

In Figure 5, it is shown that the asperity distribution allows the lubricant to flow around the surface features. Note also the space between the asperities in the transverse direction which forms longitudinal valleys. In this case, conditions at the entrance of the contact do not lead to formations of valleys filled with lubricant as obtained in the previous cases. The situation remains, however, similar to that observed for the transverse and orientated wavinesses; pressure induced flow is non-existent at the centre of the contact and the asperities travel without any change through the contact. Contrary to the waviness, the results obtained with this micro-geometry depend on the position of the asperities in the transverse direction.

### 3.3. Minimum Film Thickness

The evolution of the minimum film thickness as a function of time is presented in Figure 6 for a waviness which is characterized by a wavelength  $W = 0.32$ . Four different orientations of the surface texture have been examined which are ;  $\phi = 0^\circ$ ,  $\phi = 22.5^\circ$ ,  $\phi = 45^\circ$ ,  $\phi = 67.5^\circ$ . As previously mentioned, interferences between the bounding surfaces are produced at the beginning of the simulations since the micro-geometry is larger than the smooth minimum film thickness. This is described on the figure by a minimum film thickness equal to zero. As new surface features arrive in the contact, they draw a larger quantity of lubricant and the minimum film thickness gradually increases. At time  $\bar{t} > 2$ , it can be estimated that the solution no longer depends on the initial condition since the evolution of the minimum film thickness becomes periodic. After this stage, results can thus be compared in order to analyse

the influence of the surface texture. These periodic results do not show important differences in terms of the magnitude of their oscillating components, although the frequency of their variation is dependent upon the waviness orientation, since the orientation affects the number of ridges which crosses the centreline  $Y = 0$  of the conjunction.

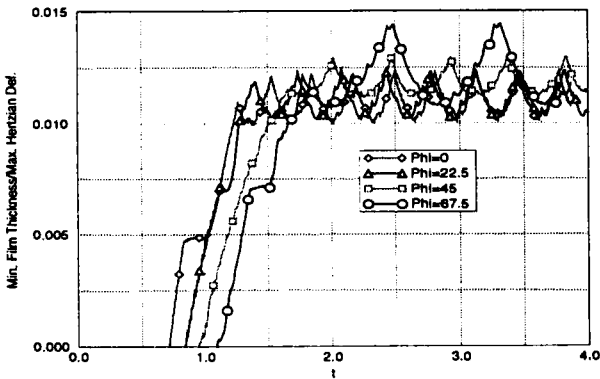


Figure 6: Variation of the minimum film thickness, as function of the time, in pure rolling conditions, for wavnnesses,  $\mathcal{W} = 0.32$ ,  $\phi = 0^\circ$ ,  $\phi = 22.5^\circ$ ,  $\phi = 45^\circ$ ,  $\phi = 67.5^\circ$

These results are completed with two other orientation angles  $\phi = 11.25^\circ$  and  $\phi = 78.75^\circ$ , and are condensed in Figure 7. Symbols represent the average values of the minimum film thickness when periodic results are reached, while the error bar defines the lowest and highest values of the time-variations. With this graph, it is then apparent that the minimum film thickness slightly increases with the orientation of the waviness in the conjunction. It is interesting to compared these results with those obtained in pure sliding conditions with a motionless waviness and a configuration where a ridge of the waviness is located at the centre of the contact. For this case, the minimum film thickness exhibits a completely opposite trend. The maximum value of film thickness is obtained in these sliding conditions for a transverse waviness and declines as the orientation angle increases.

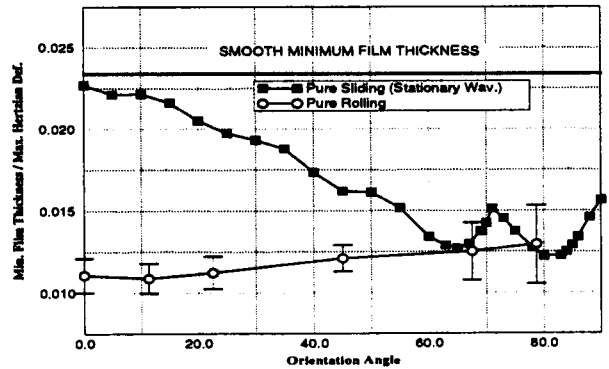


Figure 7: Comparison of the minimum film thickness, in pure sliding and in pure rolling conditions, as function of the orientation angle, for a wavnness,  $\mathcal{W} = 0.32$

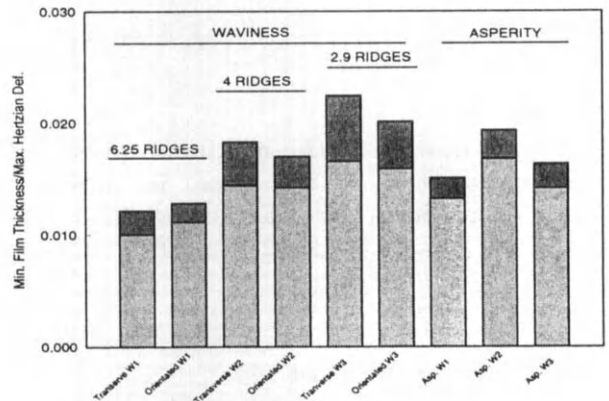


Figure 8: Minimum film thickness, in pure rolling conditions, for transverse waviness, orientated waviness  $\phi = 45^\circ$ , and asperity distribution, under different wave-lengths  $\mathcal{W}1 = 0.32$ ,  $\mathcal{W}2 = 0.5$ , and  $\mathcal{W}1 = 0.68$

Figure 8 summarizes the values of minimum film thickness obtained under different wave-lengths of the surface texture ;  $\mathcal{W} = 0.32$ ,  $\mathcal{W} = 0.5$  and  $\mathcal{W} = 0.68$ . A transverse waviness, an

orientated waviness ( $\phi = 45^\circ$ ), and an asperity distribution are analysed. For all the wavinesses, whatever the orientations considered, the increase in the wavelength leads to a rise in the minimum film thickness. On the other hand, for the asperity distribution, a decrease in minimum film thickness occurs when the wavelength passes from  $W = 0.5$  to  $W = 0.68$ . For this case, the latter wavelength is too large, and the transverse space between the asperities which forms longitudinal valleys cannot be created in the extreme part of the contact, where the minimum film thickness takes place.

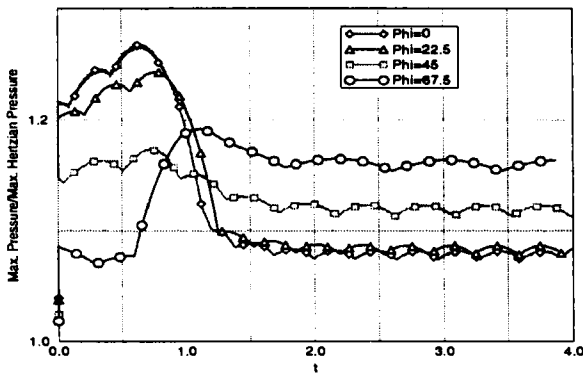


Figure 9: Variation of the maximum pressure, as function of the time, in pure rolling conditions, for wavinesses,  $W = 0.32$ ,  $\phi = 0^\circ$ ,  $\phi = 22.5^\circ$ ,  $\phi = 25^\circ$ ,  $\phi = 67.5^\circ$

### 3.4. Maximum Pressure

The evolution of the maximum pressure as a function of the time is shown in Figure 9 for the same micro-geometries as proposed in the previous section. The variations of pressures which occur during the transition period are due to the progression of the initial surface geometry. Since the initial micro-geometry has been set artificially in the contact, these pressures are not relevant to real cases. The periodic results are again condensed in order to show the variations of maximum pressure as a function of the orientation angle. With Figure 10, it is shown that pressures,

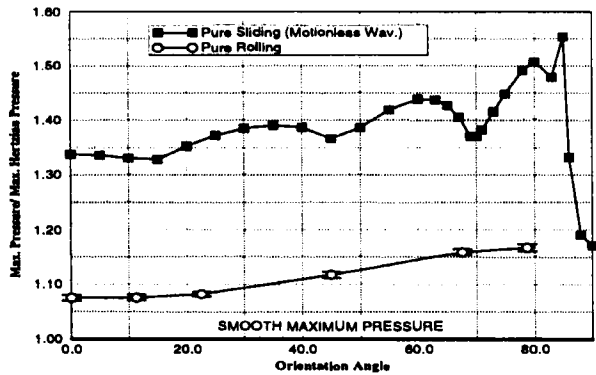


Figure 10: Comparison of the maximum pressure, in pure sliding and in pure rolling conditions, as function of the orientation angle, for a waviness,  $W = 0.32$

under pure rolling conditions, remains much lower than those obtained in pure sliding cases, for any of the orientation angles. Note that the maximum pressure slightly increases with the orientation angle, and its value tends towards that obtained, in pure sliding conditions, for the longitudinal waviness.

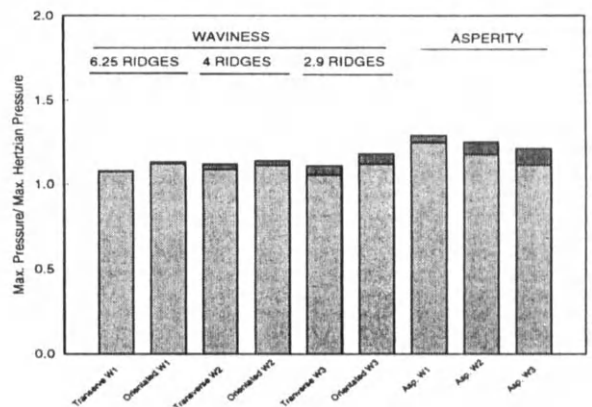


Figure 11: Maximum pressure, in pure rolling conditions, for transverse waviness, orientated waviness  $\phi = 45^\circ$ , and asperity distribution, under different wavelengths  $W1 = 0.32$ ,  $W2 = 0.5$ , and  $W1 = 0.68$

Figure 11 regroups the results obtained with the surface textures and orientation described in the previous section. The values of maximum pressure, for the transverse and orientated wavinesses, in pure rolling conditions, remain close to that of the smooth surface problem. This again points out the small deformation that the micro-geometry has to sustain in these running conditions. Maximum pressure, for the asperity distribution, remains slightly higher than for transverse waviness, due to higher pressure spikes which are formed at the end of each asperity.

#### 4. CONCLUSIONS

In pure rolling conditions, minimum film thickness and maximum pressure are not very sensitive to the orientation of the waviness, or the pattern of the surface texture. The minimum film thickness of transverse and orientated wavinesses is governed by the flow of lubricant drawn, at the entrance of the contact, under the ridges of the waviness. It also depends on the deformation of the ridges as they enter the contact. The magnitude of the deformation is mainly related to the wavelength of the ridge compared to the size of the contact. Results show that short wavelength surface features are less deformed compared to those of long wavelength.

For the asperity distribution, lubrication conditions are similar to the transverse waviness since again, minimum film thickness depends upon both entrainment of the lubricant and deformation of surface features at the entrance of the contact. The asperity distribution however improves the situation when the transverse space between the asperities, which form longitudinal valleys, are located at the extremity of the contact.

#### 5. ACKNOWLEDGEMENT

This research was funded by a research grant from EPSRC under a project to study Non-Newtonian Lubrication of Elastohydrodynamic

Elliptical Contact with 3D Surface Roughness.

#### REFERENCES

1. **Ehret, P., Dowson, D., and Taylor, C.M.** Waviness Orientation in EHL Point Contact. *22nd Leeds-Lyon Symp. (Leeds)* (ed Dowson D., Taylor C.M, Godet M., and Berthe D.), 1995.
2. **Ai, X., and Cheng, H.S.** The Effects of Surface Texture on EHL Point Contacts. *J. Trib. (Trans. ASME F)*, 118:59-66, 1995.
3. **Patir, N., and Cheng, H.S.** Effect of Surface Orientation on the Central Film Thickness in EHD Contacts. *5th Leeds-Lyon Symp. (Leeds)* (ed Dowson D., Taylor C.M, Godet M., and Berthe D.), pages 15-21, 1978.
4. **Seabra, J., and Berthe, D.** Elastohydrodynamic Point Contacts part 2 : Influence of Surface Speeds, Surface Waviness and Load on the Contact Behaviour. *Wear*, 130:319-335, 1989.
5. **Barragan de Ling, Fdm., Evans, H.P, and Snidle R.W.** Micro-Elastohydrodynamic Lubrication of Circumferentially Finished Rollers : The Influence of Temperature and Roughness . *J. Trib. (Trans. ASME F)*, 111:730-736, 1989.
6. **Kweh, C.C., Evans, H.P., and Snidle R.W.** Micro-Elastohydrodynamic Lubrication of Elliptical Contact with Transverse and Three-Dimensional Roughness . *J. Trib. (Trans. ASME F)*, 111:577-584, 1989.
7. **Lubrecht, A.A., ten Napel, W.E., and Bosma, R.** The Influence of Longitudinal and Transverse Roughness on the Elastohydrodynamic Lubrication of Circular Contacts. *J. Trib. (Trans. ASME F)*, 110(3):421-426, 1988.
8. **Brandt, A.** Multi-Level Adaptive Solutions to Boundary-Value Problems. *Mathematics of Computation*, 31(138):333-389, 1977.
9. **Lubrecht, A.A., ten Napel, W.E., and Bosma, R.** Multigrid, an Alternative Method of Solution for Two-Dimension Elastohydrodynamically Lubricated Point Contact Calculations. *J. Trib. (Trans. ASME F)*,

- 108(3):551-556, 1986.
10. **Venner, C.H.** *Multilevel Solution of the EHL Line and Point Contact Problems*. PhD thesis, Twente University, The Netherlands, 1991.
  11. **Venner, C.H. and Lubrecht, A.A.** Numerical Simulation of a Transverse Ridge in a Circular EHL Contact Under Rolling/Sliding. *J. Trib. (Trans. ASME F)*, 116:751-761, 1994.
  12. **Venner, C.H., and Lubrecht, A.A.** Numerical Simulation of Waviness in a Circular EHL Contact, under Rolling/Sliding. *21th Leeds-Lyon Symp. (Leeds) (ed Dowson D., Taylor C.M, Godet M., and Berthe D.)*, 1994.
  13. **Venner, C.H., and Lubrecht, A.A.** Numerical Analysis of the Influence of Waviness on the Film Thickness of a Circular EHL Contact. *presented at the 1995 ASME/STLE Tribology Conference*, 95-TRIB-8, 1995.
  14. **Greenwood, J.A., and Morales Espejel, G.E.** The Behaviour of Transverse Roughness in EHL Contacts. *Proc IMechE*, 208:121-132, 1994.
  15. **Dowson, D., and Higginson, G.R.** *Elasto-Hydrodynamic Lubrication, The Fundamentals of Roller and Gear Lubrication*. Pergamon Press, Oxford, Great Britain, 1966.
  16. **Roelands, C.** *Correlational Aspects of the Viscosity-Temperature-Pressure Relationship of Lubricating Oils*. PhD thesis, Delft University, (V.R.B Groningen) The Netherlands, 1966.
  17. **Kaneta, M., Sakai, T., and Nishikawa, H.** Effects of Surface Roughness on Point Contact EHL. *STLE Tribology Transactions*, 36(4):605-612, 1993.
  18. **Brandt, A., and Lubrecht, A.A.** Multilevel Matrix Multiplication and Fast Solution of Integral Equations. *J.of Comp. Phys.*, 2:348-370, 1990.
  19. **Ehret, P., Dowson, D., and Taylor, C.M.** Analysis of EHL Point Contacts with Multigrid Methods. *Submitted for publication, Proc Instn Mech Engrs (IMechE part C)*, 1995.

## Finite Element Modelling of Surface Fatigue Crack in EHD Contact

S. Bogdański

Institute of Aeronautics and Applied Mechanics, Warsaw University of Technology, Nowowiejska 22/24, 00-665 Warsaw, Poland

The interaction of EHD contact with a shallow angle surface breaking crack is analysed. The crack, which in reality is assumed to be embedded in one member of the EHD contact couple, and the member itself are modelled as a 2D prism containing plane, zero thickness discontinuity of material of a given length and an angle of inclination to the horizontal  $\alpha$ . The cycle of loading is simulated by assuming that the stresses having a EHD distribution travel along the prism such that one passage is equivalent to one cycle of rolling. Friction between the crack faces as well as the stick/slip phenomena are accounted for in the analysis. An influence of crack slope and friction between the crack faces on the values and ranges of mode I and mode II SIF is investigated. Comparison with the others results of analyses, which assume Hertzian pressure distribution, is presented.

### 1. INTRODUCTION

Very often happens in engineering practice that a surface breaking rolling-contact fatigue crack is exposed, after its initiation, to the pure EHL conditions for a period of time which is sufficient for creating pits. As S. Way already pointed out in 1935 [1], such situation is possible even for fully developed EHD lubrication, which prevents the interacting surfaces from metallic contacts.

Since that time, the phenomena involved with rolling contact fatigue have been a subject of research for many investigators [2 - 18]. Despite many approaches and technics have been applied, the mechanism of creating pits is not fully explained, and is still a topic of interest to many researchers.

L. M. Keer and M. D. Bryant [2] simulated by computer the propagation phases of the experiments of Way [1] and Yamamoto [3]. They applied 2D model of a crack embedded in an elastic half plane. Loading cycle was simulated by assuming that stresses having a Hertzian distribution travel across the half space. They predicted cycles of stress intensities large enough to cause crack growth, but they have not indicated the mechanism, which could be responsible for propagating contact fatigue cracks.

Bower [4] utilised similar 2D model for explaining the characteristic features of rolling contact fatigue cracks, which have been observed experimentally.

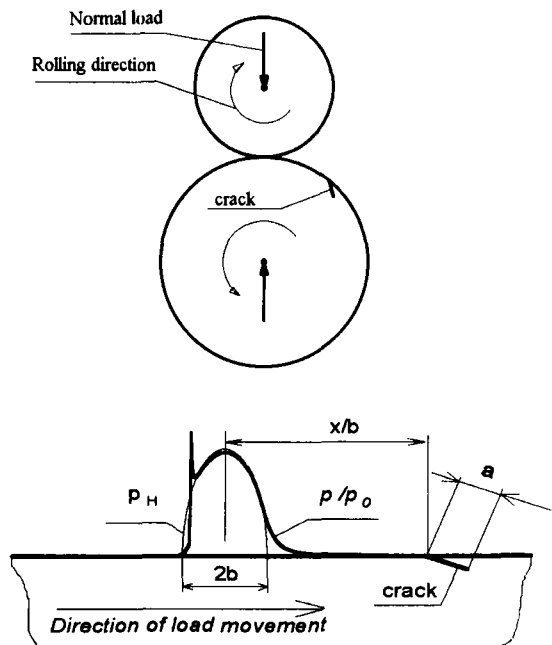


Fig. 1. a). The members of an EHD contact couple, b). Geometry of a crack and load configuration.

He stated that a satisfactory explanation for pitting must account for the influence of fluid lubricant, and explain the direction of crack growth, which is always in agreement with the direction of the load motion. He pointed out additionally, that the model used for analysis should explain also the effect of tractive force direction. His model incorporated three possible mechanisms of crack growth.

The first accounted for friction reduction effect caused by lubrication of the crack faces, the second one based on "the hydraulic action of liquid" inside the crack interior and the third one assumed an occurrence of fluid entrapment phenomenon. The results obtained from the analyses for the first and the third mechanisms seem to give an explanation for "the preferred" direction of cracks growth, and the effect of tractive force direction. The fluid influence could be also explained there in two ways, firstly as the necessary medium for lubricating the crack faces, and secondly as a medium necessary for entrapment phenomenon. However, in the light of unsuccessful experimental attempts of growing mode II cracks, and due to the lack of experimental data for non proportional mode I and mode II cycles, which are the result of the fluid entrapment mechanism, it is difficult to predict the direction or rate of the crack growth on the basis of these results.

The similar method based on the distribution of dislocations has been applied to multiple cracks by Duborg, Godet and Villechaise [5]. The cracks have been located also in an elastic half plane, and contact load was approximated by the theoretical Hertz' pressure distribution.

Bogdański, Olzak and Stupnicki [6], [7] utilised 2D FEM model in the form of a cylinder and prism for the analysis of lubricating and hydraulic effects of liquid on the behaviour of surface breaking rolling contact fatigue cracks.

### Nomenclature

|   |  |  |
|---|--|--|
| a - length of the crack, [m].   | intensity factor, $K'_{II} = K_{II}/(p_0\sqrt{b})$                 | W - load parameter, $W = F/E'R'L$ .                        |
| b - Hertzian line contact footprint half width, [m].  | N - normal load, [N]   | $\alpha$ - angle of crack inclination, [°].                |
| E' = equivalent Young modulus, $E' = 2/(1-\nu_1)^2/E_1 + (1-\nu_2)^2/E_2$                   | L - contact length, [m].   | $\alpha'$ - piezocoefficient of oil viscosity              |
| F - normal load intensity, $F = N/L$  | p - oil pressure in EHD film, [MPa].                               | $\lambda$ = traction to normal load ratio,                 |
| G - material parameter, $G = \alpha' E'$  | $p_0$ - maximum Hertzian contact pressure, [MPa].                  | $\lambda = q_0/p_0$ .                                      |
| H - oil film thickness, [m].  | R - roller radius, [m].  | $\mu$ - coefficient of friction between crack faces.       |
| $K_I$ - mode I stress intensity factor, [MPa $\sqrt{m}$ ].                                  | R' = equivalent radius of rollers, $R' = R_1R_2/(R_1+R_2)$ .       | x, x' - co-ordinates, [m].                                 |
| $K'_I$ - dimensionless mode I stress intensity factor, $K'_I = K_I/(p_0\sqrt{b})$           | S - slip parameter, $S = 2(u_1-u_2)(u_1+u_2)$ .                    | $\eta_0$ = viscosity of oil in ambient conditions, [Pa s]. |
| $K_{II}$ - mode II stress intensity factor, [MPa $\sqrt{m}$ ].                              | u - velocity, [m/s].   | <i>Indices:</i>  |
| $K'_{II}$ - dimensionless mode II stress intensity factor, $K'_{II} = K_{II}/(p_0\sqrt{b})$ | u' - average entrapment rolling speed, $u' = (u_1+u_2)/2$ , [m/s]. | 1, 2 - for lower and upper roller, respectively.           |
|   | U - dimensionless speed parameter, $U = \eta_0 u' / E' R'$ .       | a - for the point of the first pressure maximum.           |

They determined normal and tangential contact interactions between cylinder and prism through the complete solutions of the contact problems for the consecutive positions of cylinder rolling over the prism. Using similar model, they investigated the fluid entrapment effect combined with tractive force and residual stresses acting in the vicinity of crack [8], [9], [10]. Murakami and Nasser [11] have developed a "body force method" which was applied to the analyses of three dimensional rolling contact fatigue cracks by Kaneta and Murakami [12], [13] and Kaneta, Murakami and Yatsuzuka [14]. The method is very interesting and the results cover wide scope of cases, but again cracks are embedded in the elastic half - space and contact load is approximated by the Hertzian pressure.

The 3D real geometry model of "squat" type of crack, which occurs in the rail head, has been attempted for the first time by Bogdański, Olzak and Stupnicki [9], [15]. They applied FEM model for a wheel and a section of rail containing a typical "squat" shape crack. Using the flexibility matrices and utilising the iterative procedure, they solved a series of consecutive contact problems which occur between rail and wheel during rolling of the wheel over the crack. They indicated on the significant differences between the contact pressure distributions obtained through the solution of the real geometry contact problem and those predicted by Hertz' theory.



Using similar model, they investigated an influence of face friction on the crack behaviour as a result of lubrication of the crack faces [16].

Most of the results of the above discussed analyses can be at least partially used for explanation of the phenomena occurring during the development of rolling contact fatigue cracks in gears, bearings and railway tracks. However, the particular contact couples have their specific features, which should be taken into account when creating the more adequate and precise models. The EHD contact is an example of such a couple. Fully developed EHD oil film prevents the co-operating surfaces from the direct metallic contacts of surface asperities. Hence, solving the contact problem in this case is not necessary nor even assuming the Hertzian pressure distribution. The only proper approach seems to be an application of a real EHD pressure and traction distributions as a contact load. The permanent presence of oil in the contact zone, and consequently in the vicinity of a crack mouth, when it is passing along this zone creates conditions for occurrence of all discussed here mechanisms of liquid interactions.

These mechanisms should be modelled on the basis of fluid mechanics, and the models should account for the dynamic effects associated with fluid sucking in, and flowing out from the crack interior. Referring to the above, the first step of such an approach in modelling of the RCF cracks exposed to EHD contact has been undertaken, and is described in this paper.

## 2. MODELLING

The two-dimensional finite element model of a oblique, surface breaking crack has been applied to investigate the state of stress in the vicinity of a crack tip, during cyclic EHD contact loading. The EHD contact couple (Fig. 1a.) is modelled here as a plane prism with the length of  $32b$  and height of  $7b$ , which is subjected to the travelling EHD pressure and traction distributions (Fig. 1b.). One passage of such load is equivalent to one cycle of rolling. The cycle of loading starts for the position of the load centre at  $x = -5b$ , and ends at  $x = 7b$ .

The crack, which is modelled here as a plane discontinuity of material, is embedded in the centre of the prism, and is characterised by the length "a"

and an angle of inclination to the horizontal " $\alpha$ ". The crack mouth is located at  $x = 0.0$ .

Fully developed EHD conditions have been assumed, which assure an existence of the continuous oil film, thick enough to prevent the surface asperities from touching each other. As an approximation of a real pressure and traction distributions acting in the EHD oil film, those of a numerical solution of thermo-elastohydrodynamic problem for  $U = 3 \cdot 10^{-11}$  has been taken for the analysis (Fig. 2.), [17], [18].

The tangential and normal interactions between the crack faces are taken into account through the contact problem being subsequently solved during simulation of the cycle of loading. Three states of the crack faces interactions are distinguished; crack open, crack being in sticking contact and crack in sliding contact. Penetration of a crack interior by oil and the consequent reduction of friction is also taken into account. The deformed geometry of body being in contact is incorporated into the model, and several angles of crack inclination are analysed. On the basis of the linear fracture mechanics, values, ranges and histories of fluctuations of the stress intensity factors SIF;  $K_I$ ,  $K_{II}$  at the crack tip are determined for the cycle of contact loading.

The analysis has been performed for several values of friction coefficient at the crack faces. The results are compared with those obtained by others, who either used the theoretical Hertz' contact pressure distribution as an approximation of the real contact pressure [4], or solved a number of consecutive contact problems for the co-operating surfaces [5].

## 3. RESULTS

For each cycle of loading the state of stress in the vicinity of a crack has been determined and consequently the history diagrams of mode I and mode II Stress Intensity factors (SIF). The diagrams are shown as the curves plotted for the values of the particular SIFs against the position of the load centre. The history diagram for the mode II SIF shown in Fig. 3 has been chosen here as an example for explaining how to read such diagrams in this paper. The above mentioned diagram concerns the case of EHD pressure distribution presented in Fig. 2 (the curve for  $U = 3 \cdot 10^{-11}$ ).

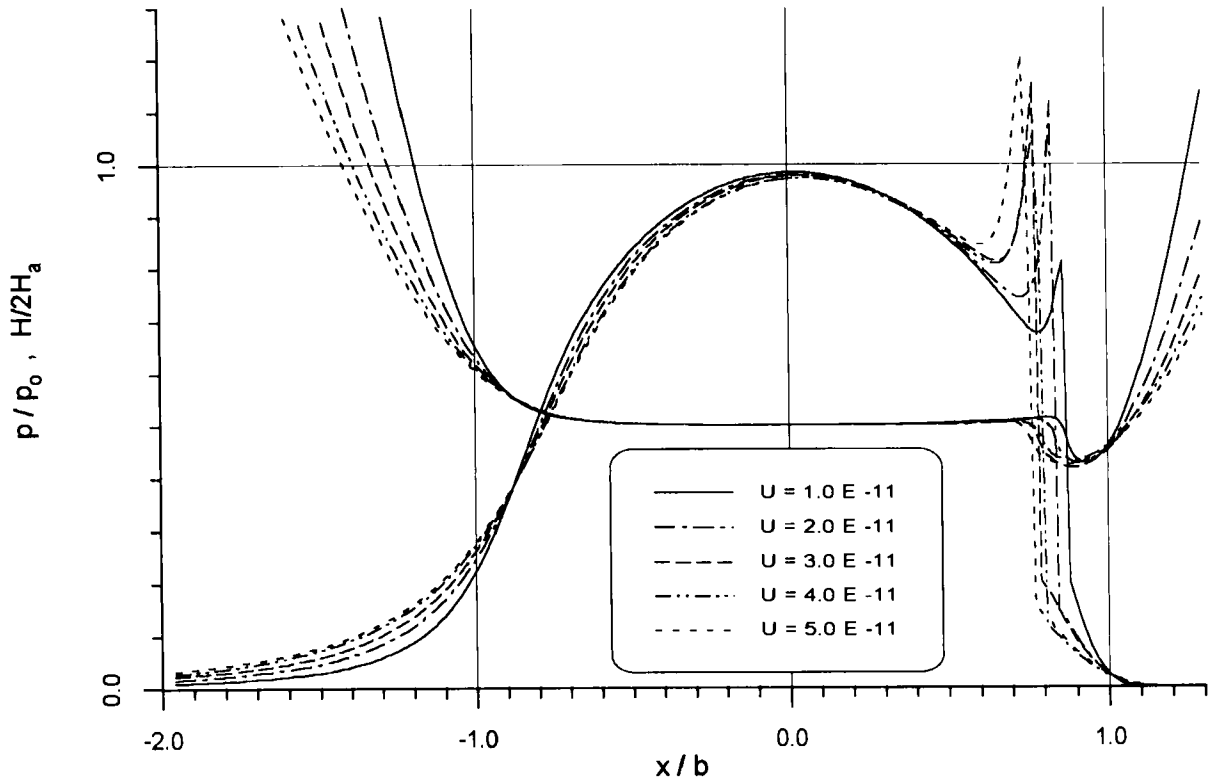


Fig. 2. Dimensionless pressure profiles and film shapes for varying dimensionless speed parameter. The load, material and slip parameters are constant:  $W = 5.0 \cdot 10^{-5}$ ,  $G = 3000$ ,  $S = 0.2$ .

This pressure distribution travels along the prism containing the crack of the length  $a = b/2$ , inclined to the horizontal at an angle  $\alpha = 25^\circ$ .

As shown in Fig. 3, the axis  $x'/b$  along which the EHD pressure profile is defined travels from the left to right across the co-ordinate system  $x/b$  having their origin ( $x'/b = 0.0$ ) at the crack mouth. Values of the mode II and mode I SIFs are plotted for various locations of the load centre (load centre is located at  $x'/b = 0.0$ ) as the curves of the SIF cycle, which corresponds to one rolling cycle of the system shown in Fig. 1a. Friction coefficients " $\mu$ ", which are written in the diagram legends, describe friction between the crack faces. The traction ratio  $\lambda = q_0/p_0$  describes friction at the surfaces of members being in contact.

The above mentioned EHD pressure profile is shown in detail in Fig. 2 (curve for  $U = 3 \cdot 10^{-11}$ ), and the EHD contact parameters for the chosen case are as follows;

Maximum theoretical Hertz' pressure,  
 $p_0 = 638.0 \text{ MPa}$ ;

Hertzian line contact footprint half-length,  
 $b = 0.226 \text{ mm}$   
 Load parameter,  $W = 5 \cdot 10^{-5}$ ;  
 Material parameter,  $G = 3000$ ;  
 Speed parameter,  $U = 3 \cdot 10^{-11}$ ;  
 Slip parameter,  $S=0.2$ ;  
 Minimum film thickness parameter,  
 $(h_{\min} R')/b^2 = 0.2302$   
 Global traction coefficient,  $\lambda = 0.5612 \cdot 10^{-1}$ ;

It should be pointed out, that the global traction coefficient reflects here the tangential interactions between the fluid film and the solid surface, which vary along the contact length. Similarly as traction coefficient  $\lambda = q_0/p_0$  used in the Hertz contact, it is defined as a ratio of the resultant tractive load to the normal load, but here this quantity is specific for the given EHD conditions. In the cases of Hertz' pressure distribution used in RCF crack analyses this ratio does not influence the pressure profile, and can be assumed arbitrarily.

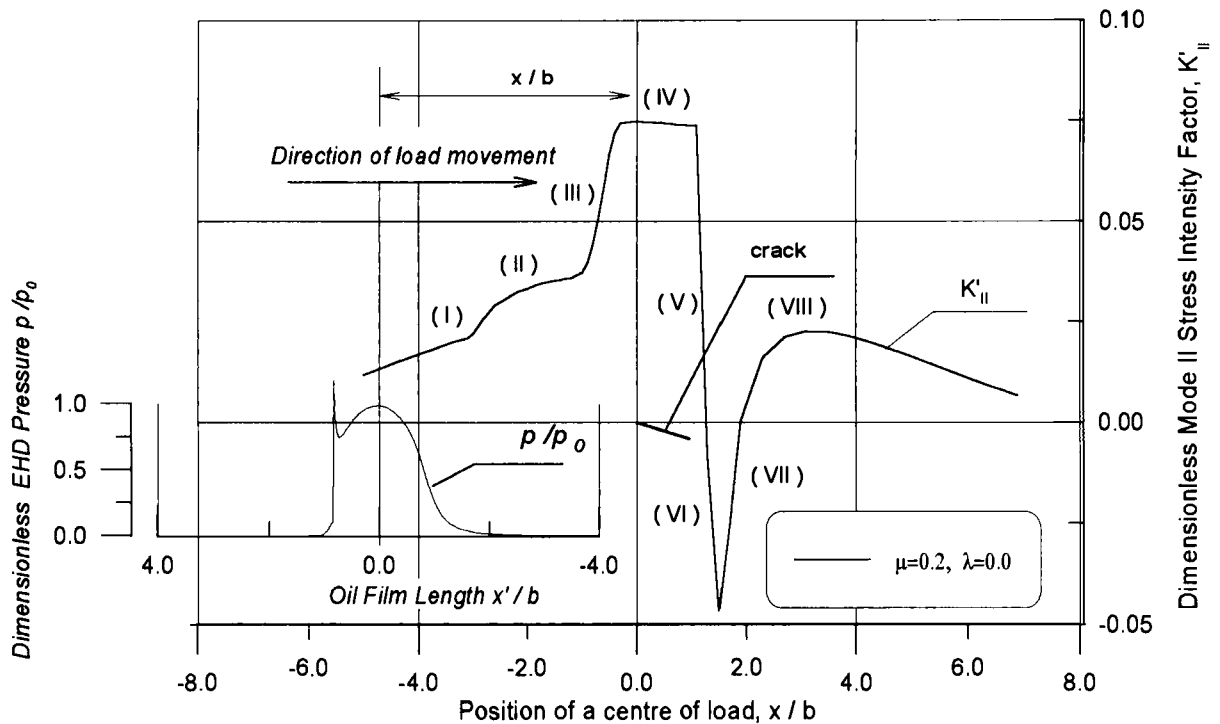


Fig. 3. The typical history diagram for mode II SIF for the case of EHD pressure distribution.  $P_0 = 638.0$  MPa,  $\alpha = 25^\circ$ ,  $b = 0.226$  mm,  $a = b/2$ ,  $\mu = 0.2$ ,  $\lambda = 0.0$ . Crack located at  $x/b = 0.0$ .

Here, this coefficient depends mainly on the slip and material parameter, and is constant for the fixed EHD contact parameters. Hence, it is not possible to assume various tractive forces in the present analysis for the fixed pressure distribution. To obtain various traction coefficients it is necessary to change some of the above mentioned parameters. The best way is to alter the slip - the parameter having the greatest influence on traction, but such a change will always alter the pressure distribution. For all analyses reported in this paper, the above mentioned case of EHD contact has been assumed, with only one common value of global traction coefficient;  $\lambda = -0.06$ . However, it was possible to use this pressure and traction distributions for loading cracks of various geometry and with various friction coefficients controlling their face slippage.

### 3.1. Hertz' pressure profiles.

As already mentioned, the results of the RCF crack analyses for the EHD conditions are not available in the literature as the investigators have always applied a simplified Hertzian pressure

distribution for the similar analyses. To make the results comparable, some calculations for the cases with Hertzian pressure distribution have been carried out, before attempting the analysis for the cases with the EHD pressure distributions. Having both, the results for EHD and Hertzian pressure distributions, obtained from the same method of analysis, gives an additional opportunity to compare them and determine the possible consequences resulting from the simplifications applied to the EHD contact pressure distribution.

The comparison of the mode II SIF cycle obtained by the author and by Bower [4] is presented in Fig. 4. Both calculations have been carried out for the Hertzian contact pressure distribution, for the same friction coefficient  $\mu = 0.1$  at the crack faces and the same ratio  $q_0/p_0 = -0.1$ . The length of the crack in both cases was  $a = b/2$ , and it was inclined at an angle of  $\alpha = 25^\circ$  to the horizontal. The curves presenting the mode II SIF cycles have similar shapes but the curve presenting the Bower's results seems to be shifted down a certain distance. The range of this SIF fluctuation in Bower's case is about  $\Delta K'_{II} = 0.31$ ,

which is approximately 19% larger as compared to  $\Delta K'_{II} = 0.26$  obtained by the author. The mode I SIF cycles can not be compared, because they are not available in Bower's paper.

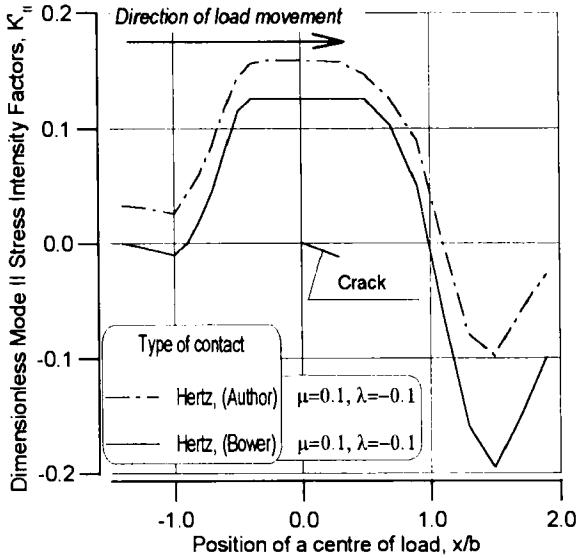


Fig. 4. Comparison of the Mode II SIF cycles for Hertzian pressure distribution obtained by Bower [5] and author. The results obtained for;  $a = b / 2$ ,  $\alpha = 25^\circ$ ,  $\mu = 0.1$ ,  $\lambda = -0.1$ .

**3.2 EHD pressure profiles.**

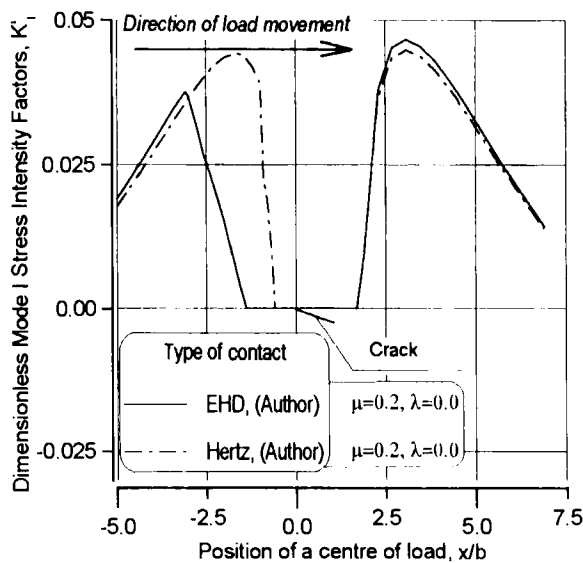
The typical history diagram of the mode II SIF for the case of EHD pressure profile is shown in Fig. 3. Friction coefficient for crack faces was assumed as  $\mu = 0.2$ , and no traction forces have been included ( $\lambda = 0.0$ ). The crack of the length  $a = b/2$  was inclined at an angle of  $\alpha = 25^\circ$  to the horizontal.

**The phases of the mode II SIF cycle.**

The whole cycle of the SIF  $K_{II}$  variation can be divided into eight phases, which correspond to the current state of the crack faces, i. e. their position and relative motion against each other.

The phase I can be defined by the range of  $x$  coordinate  $5.0 < x / b < 3.0$ . This part of the cycle shows the initial stage of crack opening (Fig. 5.) during which the SIF  $K_I$  and  $K_{II}$  increase as the load approaches the crack mouth. The upper side of the crack is not loaded yet, as the pressure profile begins at  $x' / b = -3.0$ . Starting from the load position of  $x / b = -3.0$ , the phase II begins, which is manifested by the growth of the mode II SIF with higher gradient. As shown in Fig. 5, the mode I SIF decreases in this phase, due to the action of the part of the low gradient pressure profile, which pressurises the upper wedge of the crack. When the travelling load starts to cover the crack mouth by the higher gradient part of pressure profile,

a).



b).

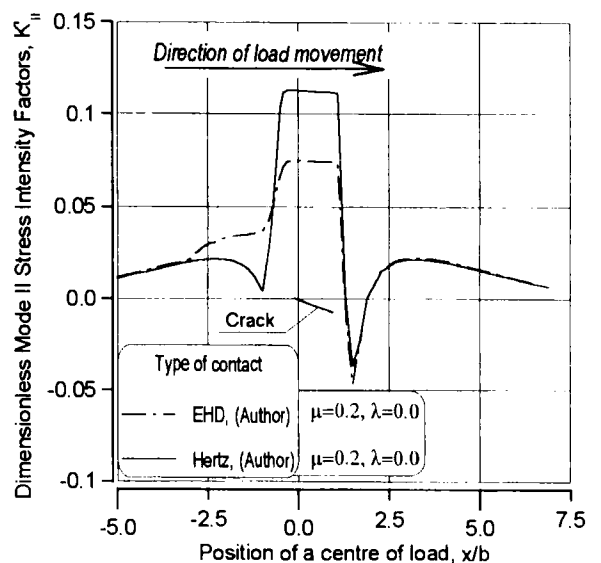


Fig. 5. Comparison of the SIF cycles for the EHD and the Hertzian pressure distributions applied as the crack load, a). mode I cycle, b). mode II cycle. No tractive force.

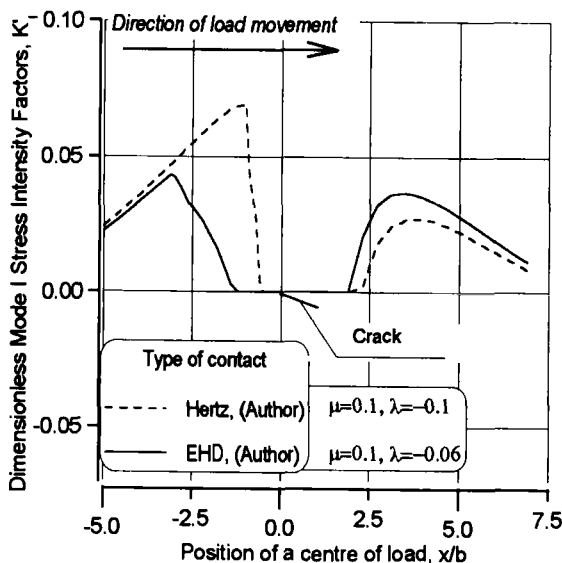
the phase III commences with very steep rise of the discussed SIF. This rapid growth of the SIF is caused by the intensive loading of the upper wedge of the crack by the part of the pressure profile, which is close to the high pressure region. Depending on the value of friction coefficient, the phase IV begins sooner or later, which represents the phenomenon of the blockade of crack faces. During the part of phase III and the whole phase IV, the value of mode I SIF remains zero. For the load position approximately at  $x/b = 1.0$  the blockade finishes, and the released crack faces slip against each other, unloading the crack tip. This is the phase V, during which the value of the SIF  $K_{II}$  drops to zero. During this phase the value of the mode I SIF is still zero. After the load relaxation, starting from the load position for which the SIF  $K_{II}$  attains zero value, the crack tip shearing changes direction to negative, and the upper face of the crack starts to slip upwards to the left in relation to the lower face. This is the phase VI, during which the crack is locked in the vicinity of its tip, with the mode I SIF value is still equal to zero. This phase is very short, as the SIF  $K_{II}$  drops very rapidly to the maximum negative value. The phase VII is associated with relaxation of load imposed on the crack faces during

previous phase. At the end of this phase the SIF  $K_{II}$  attains zero value for the second time in the cycle. The last phase, numbered as VIII, covers the ending part of the cycle for  $2.0 < x < 7.0$ , during which the SIF initially increases, and after reaching its local maximum positive value, begins to decrease. This fluctuations are accompanied by the similar variation of the SIF  $K_I$ .

#### Comparison between EHD and Hertz' cases.

As already mentioned, some cases with Hertzian pressure distribution have been analysed to make it possible to evaluate an impact of simplifications on the results. Two pairs of cases have been analysed. For the first one the friction coefficient  $\mu = 0.2$  has been assumed, and traction has been neglected,  $\lambda = 0.0$ . The second one has been analysed with the face friction coefficient  $\mu = 0.1$ , and in the presence of driving tractive force,  $\lambda = -0.06$  and  $\lambda = -0.1$  for Hertz' and EHD pressure profile, respectively. The comparison of the results for both cases is presented in Fig. 5. and Fig. 6. As shown, both cycles of loading obtained by the two various methods of load modelling are different in shapes and ranges of fluctuations. For the first pair of cases (Fig. 5.), the ranges of the SIF fluctuations for the EHD pressure profile case are less as compared to the Hertzian profile case, by 17% and

a).



b).

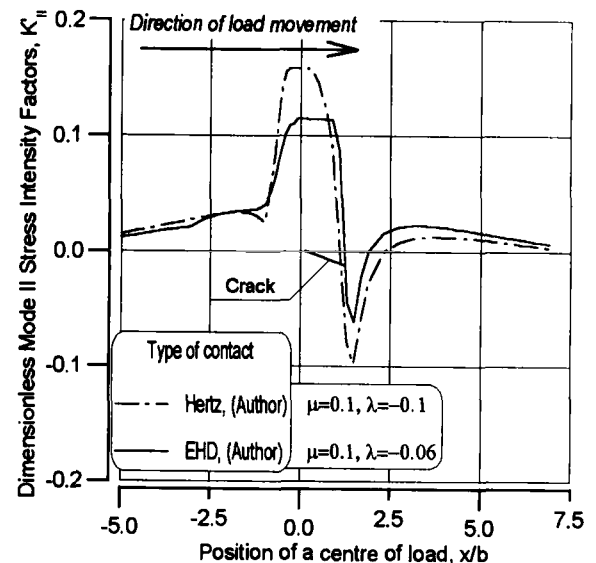


Fig. 6. The SIF cycles for the EHD and the Hertzian pressure profiles applied as a crack load, in the presence of tractive force,  $p_0 = 638$  MPa,  $b = 0.226$  mm,  $a = b/2$ ,  $\alpha = 25$ ; a). mode I cycle, b). mode II cycle.

22.6%, for mode I and mode II loading, respectively. For the second pair of analysed cases (Fig. 6.), the reduction of the SIF ranges is even higher, but it is partly caused by the inconsistency of the ratio  $\lambda$ , which is  $\lambda = -0.06$  for the EHD pressure profile, and  $\lambda = -0.1$  for the Hertz' pressure profile.

**Influence of friction.**

The phenomenon of friction between the crack faces is recently a subject of the great interest, because some results of the experimental investigations and numerical analyses indicate on the significant role of liquid in the crack growth [8], [9].

Liquid if present in the crack interior, can reduce friction between its faces considerably, enabling them to slip against each other. Referring to the above, the calculations for several friction coefficients have been carried out and the results are presented in Fig. 7 and Fig. 8. As shown, the ranges of the mode II SIF fluctuation strongly depend on the value of the friction coefficient between the crack faces. This SIF varies within the greatest ranges for the case, which neglects friction between the crack faces ( $\mu = 0.0$ ). The cycle for these cases has the characteristic sharp shape without the horizontal section, which

represents the blockade of the crack faces. The ranges of the SIFs fluctuations depend also on the crack slope, taking the higher values for steeper cracks. The length of the cycle sections, during which the crack faces are blocked, depends on the value of the friction coefficient, and on the crack slope. The smaller the crack inclination angle the longer the blocking period of the cycle, and the earlier the beginning of this phase of cycle. For crack inclined at an angle of  $\alpha = 60^\circ$  to the horizontal, this blocking phenomenon vanishes, even for such high value of friction coefficients as  $\mu = 0.4$  (Fig 8.b). The comparison of the mode I SIF cycles for various friction coefficients is not presented here, because this cycles are influenced by friction very insignificantly, and the curves remain identical within the whole range of load positions.

**Influence of crack slope.**

The effect of crack slope on the values and shapes of the mode I and mode II SIF cycles can be investigated trough the comparison of the particular cycles determined for various angles of crack inclination. Such cycles are presented in Fig. 9 and Fig. 10 for the two face friction coefficients  $\mu = 0.2$  and  $\mu = 0.6$ , respectively. Both, the mode I and mode II SIF cycles are dependent on the crack slope, but the latter are influenced more intensively.

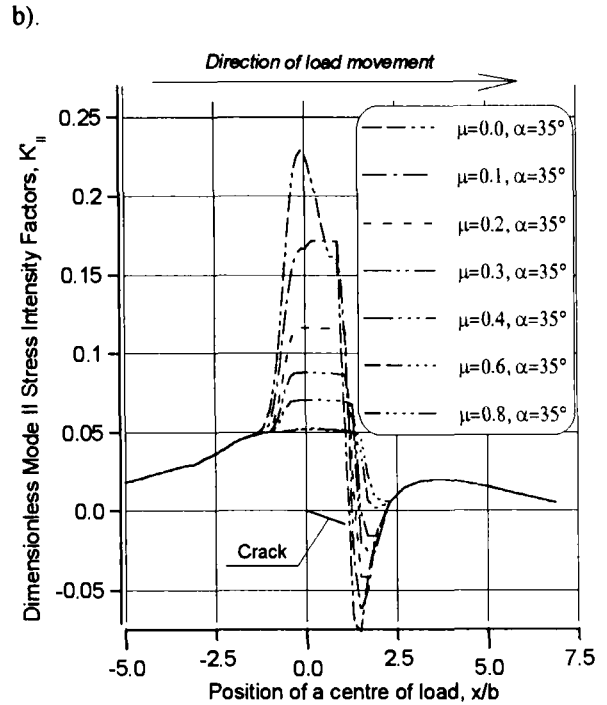
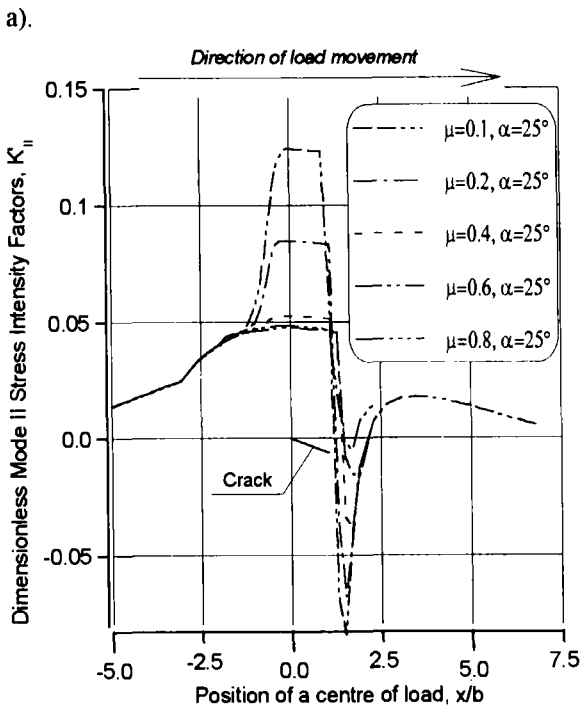


Fig. 7. The cycles of the mode II SIF for various friction coefficients between the crack faces. The EHD pressure profile;  $p_0 = 638$  MPa,  $b = 0.226$  mm,  $a = b / 2$ ,  $\lambda = -0.06$ ; a).  $\alpha = 25^\circ$ , b).  $\alpha = 35^\circ$

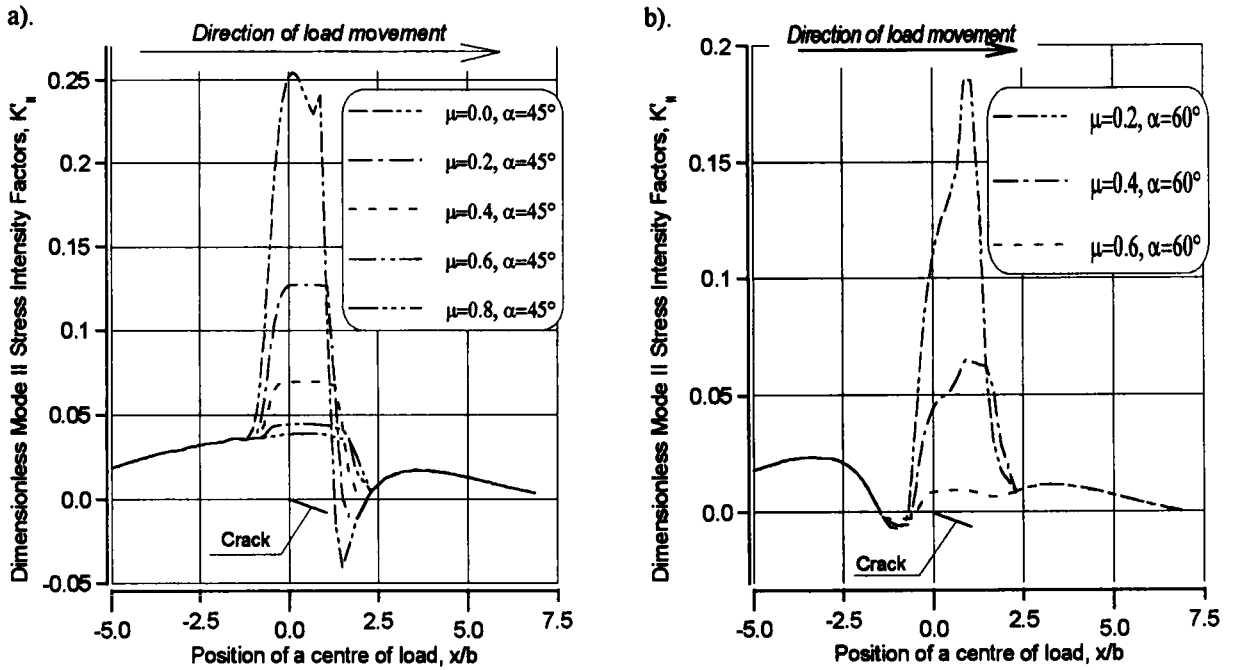


Fig. 8. The cycles of the mode II SIF for various friction coefficients between the crack faces. The EHD pressure profile;  $p_0 = 638$  MPa,  $b = 0.226$  mm,  $a = b/2$ ,  $\lambda = -0.06$ . a).  $\alpha = 45^\circ$ , b).  $\alpha = 60^\circ$ .

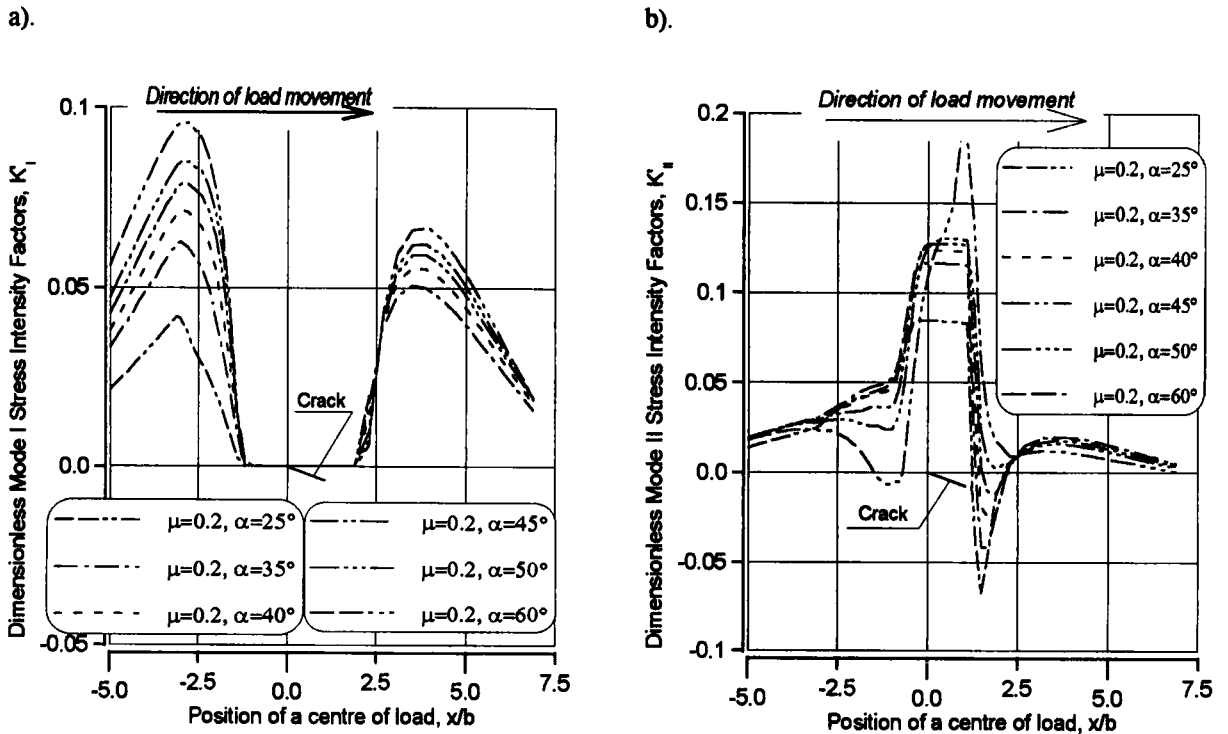


Fig. 9. The cycles of the SIFs for various crack slopes. The EHD pressure profile;  $p_0 = 638$  MPa,  $b = 0.226$  mm,  $a = b/2$ ,  $\lambda = -0.06$ ,  $\mu = 0.2$ ; a) mode I cycles b). mode II cycles

The steeper the crack slopes the higher the ranges of the SIFs fluctuations. For the coefficient of friction  $\mu = 0.2$  (Fig. 9b), the shapes of the mode II SIFs cycles are similar for all crack slopes less than  $\alpha = 60^\circ$ , for which the face blocking does not occur. This similarity does not appear for higher face friction coefficients. The mode II cycles shown in Fig. 10b ( $\mu = 0.6$ ) have completely different shapes, especially for angles higher than  $40^\circ$ .

**Influence of tractive force.**

As already mentioned, traction in the EHD contact depends on the EHD parameters. For given complete set of these parameters, the only one value of traction load can be obtained. As a consequence of the above, in this paper, an influence of tractive force can be investigated through the comparison of the cases with traction load to the cases, which neglect traction. Such exemplary comparisons for the driving tractive force are shown in Fig. 11. As shown, the presence of this force increases the ranges of both the mode I and mode II SIF cycles even for very small value of the traction ratio, which was in these case equal to  $\lambda = -0.06$ .

**4. CONCLUSIONS**

- FE modelling of rolling contact fatigue cracks is a convenient tool which enables the characteristic features of the contact problem to be accounted for.
- Simplification of the EHD contact pressure distribution to the Hertzian pressure profile in the EHD contact fatigue cracks analysis leads to the higher values and ranges of the mode I and mode II SIF fluctuations during the rolling cycles. The differences depends on the crack geometry and loading conditions. It was shown in this paper, that these differences can be close to 20%. As the rate of crack growth depends on the discussed ranges, it seems to be safe to rely in the engineering practice on the analyses giving higher estimates of these decisive quantities. However, apart from the quantitative differences, the discussed simplification implies also some qualitative misinterpretations of the crack behaviour during the cyclic loading.
- Friction between the crack faces plays an important role during the whole loading process of the EHD contact fatigue crack. This role is especially important for the cracks growing in the EHD environment, which assures the permanent presence of a lubricant in the form of fluid

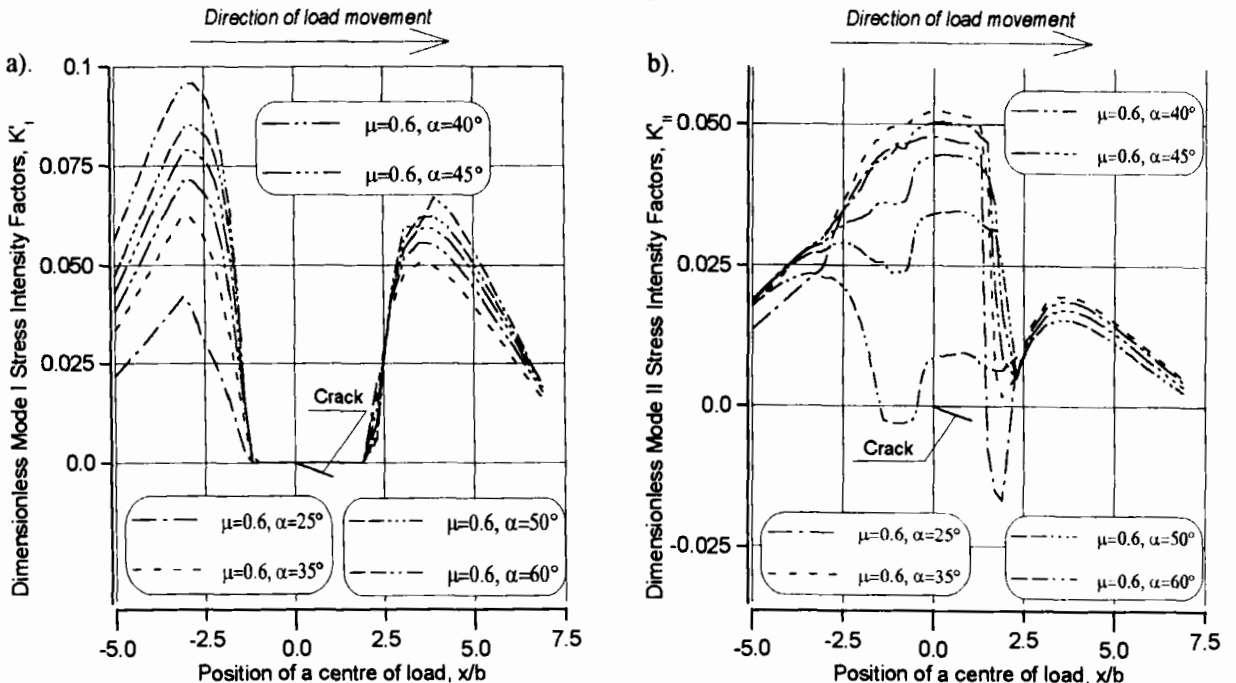


Fig. 10. The cycles of the SIFs for various crack slopes. The EHD pressure profile;  $p_0 = 638$  MPa,  $b = 0.226$  mm,  $a = b / 2$ ,  $\mu = 0.6$ ,  $\lambda = -0.06$  (driving), a). mode I cycles, b). mode II cycles.



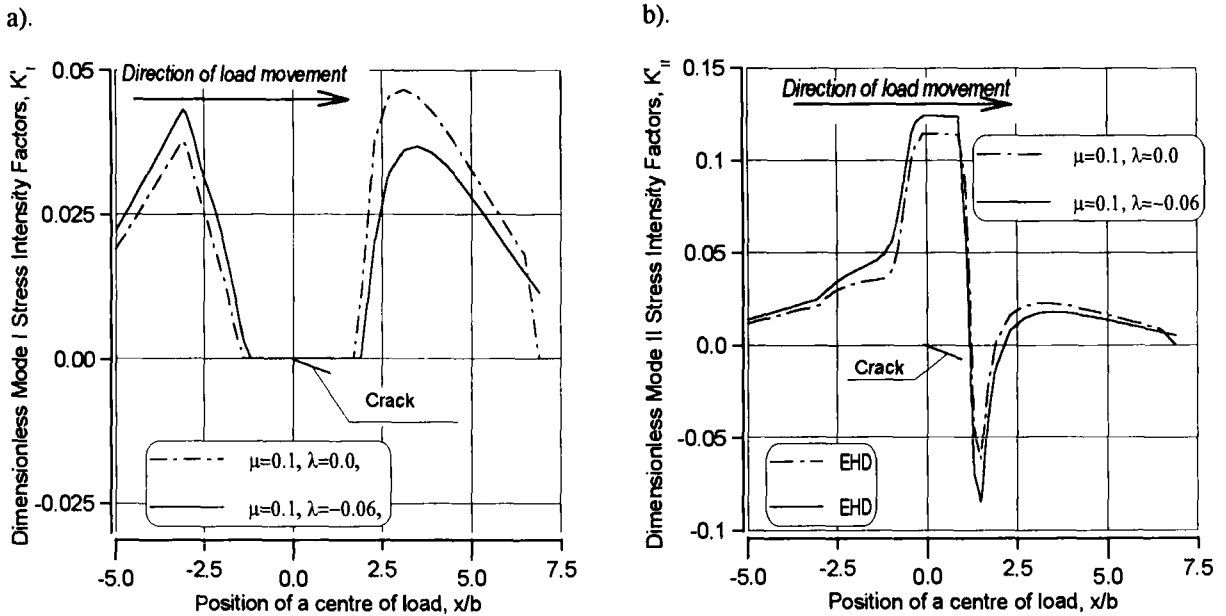


Fig. 11. Comparison of the SIF cycles for cases with and without tractive force. The EHD contact,  $p_0 = 638$  MPa,  $\alpha = 25^\circ$ ,  $a = b/2$ ,  $\mu = 0.6$ ,  $\lambda = -0.06$  (driving); a). mode I cycles, b). mode II cycles.

continuous film, and hence in the vicinity of the crack mouth during its passage through the contact zone. This continuous supply of oil makes it easier to fill the crack interior in some circumstances. Oil present between the crack faces can lubricate them and reduce friction, as well as separate them, or keep them apart in certain conditions, which also leads to the similar final effect of enabling crack faces to move against each other. Such conditions can cause the significant increases of the mode II SIF ranges of variation. From the another point of view, the increase of face friction coefficient alters sometimes severely the shape of the mode II crack tip loading cycle, and changes the physical character and sequence of the phenomena occurring during the rolling process ( see Fig. 10b for the large angles  $\alpha$ ).

- In the contrary to the most of methods applied to the RCF crack analyses, the method used in the presented paper accounts for the tangential contact interactions, which can vary along the contact zone. This allows for more precise modelling of the tractive force distribution in the vicinity of the crack mouth, when it is crossing the contact patch. Such modelling is especially desired when analysing the EHD contacts with high

values of slip. The results obtained in this analysis proof that even such a small tractive driving force, which results from the EHD liquid interaction for rather small slip parameter  $S = 0.2$ , can significantly increase the range of the mode II SIF, by increasing the positive maximum before the crack mouth and the negative minimum after it ( Fig. 11b ). This effect is the most intensive for the shallow crack angles. The mode I SIF history diagram is also influenced significantly by the action of tractive force ( Fig. 11a ). The maximum  $K_I$  values attained during the initial opening phase of the cycle is increased, as well as the local maximum reached after the crack mouth.

## REFERENCES

1. S. Way, Pitting due to rolling contact, *Trans. ASME, J. of Appl. Mech.*, 2, (1935), pp. 49-58.
2. L M. Keer and M. D. Bryant, A pitting model for rolling contact fatigue, *J. Lubr. Technol., Trans. ASME*, 105 (1983) 198 - 205.
3. T. Yamamoto, Crack Growth in Lubricating Rollers, *Solid Contact and Lubrication*, Ed. H. S. Cheng and L. M. Keer, ASME AMD, Vol. 39, 1980, pp. 223 - 236.

4. A. F. Bower, The influence of crack face friction and trapped fluid on surface initiated rolling contact fatigue cracks, *ASME, Journal of Tribology*, 110, (1988), pp. 704-711
5. M. C. Dubourg, M. Godet and B. Villechaise, Analysis of multiple fatigue cracks; Part I and Part II, *Transactions of ASME, Journal of Tribology*, 114, (1991), pp. 455-468.
6. S. Bogdański, M. Olzak and J. Stupnicki, An effect of internal stress and liquid pressure on crack propagation in contact area, *Proceedings of the 6 th. International Congress on Tribology - EUROTRIB '93, Budapest 30 th Aug. - 2 nd Sept. 1993. Vol. 5 pp. 310-315.*
7. Stress Analysis of Rail Rolling Contact Fatigue Cracks - The European Rail Research Institute, Utrecht, The Netherlands, *Report No. 11* (1988 - 1992).
8. Stress Analysis of Rail Rolling Contact Fatigue Cracks - The European Rail Research Institute, Utrecht, The Netherlands, *Annual Report - 1994*.
9. S. Bogdański, M. Olzak., J. Stupnicki, Numerical stress analysis of rail rolling contact fatigue cracks, *Wear*, 191 (1996), pp. 14-24.
10. S. Bogdański, M. Olzak., J. Stupnicki, Influence of Liquid Interaction on Propagation of Rail Rolling Contact Fatigue Cracks, *Proceedings of 2nd Mini Conference on Contact Mechanics and Wear of Rail/Wheel Systems, 29-31 July, 1996, Budapest.*
11. Y. Murakami and S. Nemat - Nasser, Growth and stability of interacting surface flaws of arbitrary shape, *Engineering Fracture Mechanics*, Vol. 17, No. 3, 1983, pp. 193 - 210.
12. M. Kaneta and Y. Murakami, Effects of oil pressure on surface crack growth in rolling/sliding contact, *Tribology International*, 20, (1987), pp. 210-217.
13. M. Kaneta, Y. Murakami, Propagation of semi-elliptical surface cracks in lubricated rolling/sliding elliptical contacts, *ASME, Journ. of Tribology*, Vol. 113 (1991) pp. 270-275.
14. M. Kaneta, Y. Murakami, and H. Yatsuzuka, Analysis of surface crack propagation in rolling line contact, *ASLE Trans.*, 28, (1985), pp. 60-68.
15. Stress Analysis of Rail Rolling Contact Fatigue Cracks - The European Rail Research Institute, Utrecht, The Netherlands, *Annual Report - 1993*.
16. S. Bogdański, M. Olzak., J. Stupnicki, The Effects of Face Friction and Tractive Force on Propagation of 3D 'Squat' Type of Rolling Contact Fatigue Crack, *Proceedings of 2nd Mini Conference on Contact Mechanics and Wear of Rail/Wheel Systems, 29-31 July, 1996, Budapest.*
17. S. Bogdański, Z. Paturski, R. Wolff, PC Version of Newton - Raphson Method for Solving EHD Line contact Problem.", *Archive of Machine Design* ", vol. 39, No. 3, 1992 pp 223 - 238.
18. S. Bogdański, Z. Paturski , R. Wolff , 1992, " Numerical Solution To The Thermal EHD Line Contact Problem ", *Archive of Machine Design* ", vol. 40, No. 2, 1993.

## Thermal and non-Newtonian effects on traction in an elliptical EHD contact under high loads and sliding speeds

Ming-Tang Ma<sup>a</sup> and Shilong Wang<sup>b</sup>

<sup>a</sup>Department of Engineering and Product Design,  
University of Central Lancashire, Preston, PR1 2HE, UK

<sup>b</sup>Department of Mechanical Engineering,  
Jilin Institute of Technology, Changchun, 130015, P. R. China

Predictions of the traction with good accuracy in elastohydrodynamic (EHD) contacts are of primary importance. An expedient non-Newtonian thermal EHL model for heavily loaded point contacts has been developed by the authors. The computer model, incorporating several different rheological laws of lubricants, is capable of effectively and accurately predicting the traction in elliptical EHD contacts when the applied load is high ( $p_0 > 1$  GPa). The influence of temperature rises and the non-Newtonian behaviour of a lubricant on the traction has been examined using this model. The main purpose of this paper is to report and discuss some data obtained. Results show that, in thermal conditions, for lower sliding speeds ( $U_s < 1$  m/s) the non-Newtonian effect on the traction is significant and should be taken into account, whereas, when sliding speeds are higher the use of the Newtonian law is sufficient for evaluating the traction.

### 1. INTRODUCTION

One of the primary purposes of EHL studies is to determine the traction in machine elements such as gears, cams and rolling-element bearings. Over the decades, a large volume of predictive EHL models has been developed by various researchers in order to obtain the film thickness and traction in lubricated EHD contacts. Most of them were based on isothermal conditions in the lubricant. It is well known, however, that when sliding is introduced in the EHD contact, the isothermal assumption is not sufficient, particularly for predicting the traction. Hence, thermal effects have been considered by numerous workers in modelling the EHL problems. On the other hand, a vast majority of the previous EHL analyses assume that lubricants follow the Newtonian law. Experiments show (and it is widely accepted), however, that a liquid lubricant in the EHD contact usually exhibits a nonlinear (non-Newtonian) characteristic. There is little doubt that this will influence the traction in the contact. In order to take the non-Newtonian effect into account in EHL theories, various alternative rheological laws

have been proposed by a number of researchers, e.g. [1–3]. A summary of these rheological models can be found in reference [4].

Thermal and non-Newtonian effects in the EHL have already been considered by some researchers. Early theoretical studies of the combined rheological and thermal effects on traction [5–7] are based on the assumption that the pressure distribution is Hertzian and the film thickness is uniform. This provides a first approximation, but it is not adequate, particularly in light loading conditions. Recently, the complete solutions to the non-Newtonian thermal EHL of line contacts have been obtained by some researchers. Wang and Zhang [8] obtained a numerical solution based on mean values of the lubricant properties across the film. They incorporated a modified version of Bair and Winer's rheological model in the analysis, and found that both thermal and non-Newtonian effects on the traction were significant. Yang and Wen [9] derived and solved a generalized Reynolds equation which can accommodate different rheological laws. Their results show that the effect of the non-Newtonian property on the traction is not significant even when

slide-roll ratios are small. This result appears to be unusual and contrary to the findings of the other studies (e.g. [8]). Sui and Sadeghi [10] incorporated the Eyring rheological model in their thermal EHL (TEHL) analysis. Their results indicate that the thermal effect on the traction is significant. The Eyring model was also used by Wang *et al.* [11, 12] in their line contact analyses. Hsiao and Hamrock [13] used a circular rheological model in their EHL analysis. They have also confirmed the significance of temperature rises on the traction.

This brief review reveals that almost all of the previous non-Newtonian TEHL models deal with line-contact problems, and in many cases the loads considered were low. Most of these models employed the Eyring law and were involved in a complete numerical solution of the generalised Reynolds equation. The procedure from such complete approaches is very expensive in terms of CPU time. This may be not suitable and unnecessary for practical purposes.

In this study, an empirical and economical numerical approach to the non-Newtonian TEHL of elliptical contacts has been developed by the authors. The computer model, incorporating several different rheological laws, is applicable to engineering practices where the applied loads are high ( $p_0 > 1$  GPa). From an empirically corrected Hertzian pressure distribution, the generalised momentum and energy equations were solved simultaneously. The three-dimensional distributions of the velocity, temperature, shear stress and film thickness in the contact were obtained. Then the priori assumed pressure distribution was verified, and modified if necessary, with the aid of the flow continuity condition (equation). Because the solution of the Reynolds equation for the pressure was avoided, the computer algorithms developed from this approach were highly economical in terms of computing cost. The CPU time required for a complete run on a DELL 450/L (50 MHz) was about 80 seconds for a general case.

The computer model has been used to investigate the thermal and non-Newtonian effects on the traction in an elliptical contact. The main objective of this paper is to present and discuss the results obtained. It is shown that the non-Newtonian behaviour of lubricants has a dominant effect on the traction when slide-roll ratios are low, whereas, the thermal effect is controlling in high sliding speed conditions.

## 2. SUMMARY OF THE ANALYTICAL MODEL

Details of the model and numerical techniques are presented in a separate paper [14]. For completeness, the governing equations are listed in the present paper.

### 2.1. Equations of motion

The three-dimensional generalised equations of motion (momentum equations) for non-Newtonian fluids were derived by the authors [14] and they can be written as

$$\frac{\partial p}{\partial x} = \frac{\partial}{\partial z} \left[ \frac{\eta}{F(\tau_e)} \left( \frac{\partial u}{\partial z} - A_G \frac{d\tau_{xz}}{dt} \right) \right] \quad (1a)$$

$$\frac{\partial p}{\partial y} = \frac{\partial}{\partial z} \left[ \frac{\eta}{F(\tau_e)} \left( \frac{\partial v}{\partial z} - A_G \frac{d\tau_{yz}}{dt} \right) \right] \quad (1b)$$

where  $A_G = 1/G_L$  and  $F(\tau_e)$  is a so-called 'rheology function' which takes different forms for different rheological models. (See Appendix for notation.) For example, for Bair and Winer's model [3], it is defined by

$$F(\tau_e) = - \frac{\ln(1 - \tau_e/\tau_L)}{(\tau_e/\tau_L)}.$$

When  $A_G = 0$  and  $F(\tau_e) = 1$ , equations (1a) and (1b) become the common forms of the simplified Navier-Stokes equations.

For the problem under investigation, the boundary conditions for equations (1a) and (1b) are:

$$\begin{aligned} u = U_1, \quad v = 0 \quad \text{for } z = 0 \quad (\text{at surface 1}); \\ u = U_2, \quad v = 0 \quad \text{for } z = h \quad (\text{at surface 2}). \end{aligned}$$

### 2.2. Continuity equation

The continuity equation in the integral form can be expressed as

$$\int_0^h \frac{\partial (\rho_L u)}{\partial x} dz + \int_0^h \frac{\partial (\rho_L v)}{\partial y} dz = 0 \quad (2)$$

### 2.3. Energy equation

The temperature distribution in the film can be obtained through solving the energy equation. For

the problem under investigation, the generalised energy equation is expressed as [14]

$$\rho_L C_L \left( u \frac{\partial T}{\partial x} + v \frac{\partial T}{\partial y} \right) - K_L \frac{\partial^2 T}{\partial z^2} = - \frac{T}{\rho_L} \frac{\partial \rho_L}{\partial T} \left( u \frac{\partial p}{\partial x} + v \frac{\partial p}{\partial y} \right) + \frac{F(\tau_e)}{\eta} \tau_e^2 \quad (3)$$

#### 2.4. Temperatures on the contact surfaces

In solving the energy equation, the temperatures on the contact surfaces need to be known beforehand. These surface temperatures can be specified approximately by

$$T_1(x, y) = T_0 + \frac{1}{\sqrt{\pi K_1 C_1 \rho_1 U_1}} \int_{x_{in}}^x K_L \frac{\partial T}{\partial z} \Big|_{z=0} \frac{d\xi}{\sqrt{x-\xi}} \quad (4a)$$

$$T_2(x, y) = T_0 + \frac{1}{\sqrt{\pi K_2 C_2 \rho_2 U_2}} \int_{x_{in}}^x -K_L \frac{\partial T}{\partial z} \Big|_{z=h} \frac{d\xi}{\sqrt{x-\xi}} \quad (4b)$$

#### 2.5. Elastic deformation

The equivalent local deformation of the two solid surfaces at contact is given by

$$D(x, y) = \frac{2}{\pi E'} \iint_A \frac{p(\xi, \zeta) d\xi d\zeta}{\sqrt{(x-\xi)^2 + (y-\zeta)^2}} \quad (5)$$

#### 2.6. Film thickness

The film thickness in the conjunction is calculated by

$$h(x, y) = h_c + \frac{x^2}{2R_x} + \frac{y^2}{2R_y} + D(x, y) - D(0,0) \quad (6)$$

#### 2.7. Load equilibrium

The applied load must be balanced by the resultant of the fluid film pressures. Thus,

$$W = \iint_A p(x, y) dx dy \quad (7)$$

#### 2.8. Lubricant viscosity–pressure–temperature relation

The viscosity of lubricants is a strong function of temperature and pressure. A viscosity–pressure–temperature relation proposed by Roelands [15] was used in this study and it can be expressed as

$$\eta = \exp \left[ \left( \ln(\eta_0) + 9.67 \right) \left( 1 + \frac{p \times 10^{-6}}{196.2} \right)^{S_p} \left( \frac{T_0 + 135}{T + 135} \right)^{S_T} - 9.67 \right] \quad (8)$$

where  $S_p = S_1 - S_2 \ln(1 + T/135)$ , and  $S_1$ ,  $S_2$  and  $S_T$  are the lubricant dependent coefficients.

#### 2.9. Lubricant density–pressure–temperature relation

As a function of pressure and temperature, the lubricant density is determined by a relation proposed by Dowson and Higginson [16]:

$$\rho = \rho_0 \left[ 1 + \frac{C_A p}{1 + C_B p} - D_T (T - T_0) \right] \quad (9)$$

where  $C_A$ ,  $C_B$  and  $D_T$  are the lubricant dependent constants.

### 3. BRIEF DESCRIPTION OF THE COMPUTATION PROCEDURE

It is known that in heavily loaded conditions ( $p_0 > 1$  GPa) the pressure distribution in the contact conjunction is close to Hertzian. Thus, as an 'input parameter', a Hertzian pressure distribution was initially corrected in the inlet, outlet and side leakage regions of the solution domain according to an empirical procedure. The computation domain was chosen to be slightly larger than the Hertzian contact area with an extended inlet zone. Details of the establishment of the initial pressures and numerical scheme are presented elsewhere [14]. But, the global solution procedure is described as follows:

- (i) From the corrected Hertzian pressure distribution, the elastic deformations and film thicknesses were calculated.
- (ii) The surface temperatures at a given column or 'base point' on the Oxy plane were computed;

the nodal temperatures across the film thickness at the given base point were initialised empirically.

- (iii) The computation was conducted iteratively to obtain the shear stresses. The Newton-Raphson method and an under-relaxation scheme were used in the iteration process.
- (iv) The equations of motion and the energy equation were solved simultaneously and iteratively in conjunction with the updating of the lubricant properties until the convergent temperatures were obtained.
- (v) After the shear stresses and film temperatures at the given column converged separately, their consistency between two consecutive global cycles was checked. If necessary, the solution process was repeated from step (iii).
- (vi) The same procedure was applied to the next column (base point) until the computation was completed over the entire solution domain. Then, the central film thickness was updated. If necessary, the procedure was repeated from step (ii) until the film thickness converged.
- (vii) The flow continuity condition (equation) was checked at each column. In case this was not fulfilled, the priori assumed pressure distribution was modified and the entire computation process

was repeated. Only a few number (normally 2 – 4) of the pressure modifications was required to meet the continuity condition over the solution domain.

The computer program developed from the procedures described above is highly economical and efficient in terms of CPU time. This is principally because a very limited number of updates of the elastic deformations is required as only a few number of pressure modifications is normally involved. For the mesh ( $N_x = 55$ ,  $N_y = 15$  and  $N_z = 10$ ) used for most of the cases presented in this paper, the CPU time taken for a run on a DELL 450/L PC was generally about 80 seconds.

#### 4. RESULTS AND DISCUSSION

The contact between a steel ball and a steel roller, having the diameters of 40 mm and 96 mm, was simulated to examine the significance of thermal and non-Newtonian effects on traction. The equivalent sizes of the ball and roller and their properties are presented in Table 1. The properties of a paraffinic base oil, Tellus 145, used by Brüggemann and Kollmann [17] were adopted to conduct the simulation. These properties are listed in Table 2.

Table 1. Properties of the steel ball and roller used

|                                     |   |
|-------------------------------------|---|
| Equivalent radius in $x$ -direction | $R_x = 0.014$ m                                       |
| Equivalent radius in $y$ -direction | $R_y = 0.02$ m  |
| Modulus of elasticity               | $E_1 = E_2 = 200 \times 10^9$ Pa                      |
| Poisson's ratio                     | $\nu_1 = \nu_2 = 0.3$                                 |
| Specific heat capacity              | $C_1 = C_2 = 460$ J kg <sup>-1</sup> °C <sup>-1</sup> |
| Density                             | $\rho_1 = \rho_2 = 7865$ kg m <sup>-3</sup>           |

Table 2. Lubricant properties

|  |  |
|--|--|
| Inlet (bulk) temperature                 | $T_0 = 50$ °C                                    |
| Inlet viscosity                          | $\eta_0 = 0.058$ Pa s                            |
| Inlet density                            | $\rho_0 = 875$ kg m <sup>-3</sup>                |
| Coefficient for pressure-viscosity index | $S_1 = 0.72$                                     |
| Coefficient for pressure-viscosity index | $S_2 = 0.26$                                     |
| Temperature-viscosity index              | $S_T = 1.14$                                     |
| Coefficient of compressibility           | $C_A = 0.326 \times 10^{-9}$ Pa <sup>-1</sup>    |
| Coefficient of compressibility           | $C_B = 0.283 \times 10^{-9}$ Pa <sup>-1</sup>    |
| Thermal expansivity                      | $D_T = 0.35 \times 10^{-3}$ °C <sup>-1</sup>     |
| Thermal conductivity                     | $K_L = 0.13$ W m <sup>-1</sup> °C <sup>-1</sup>  |
| Specific heat capacity                   | $C_L = 2010$ J kg <sup>-1</sup> °C <sup>-1</sup> |
| Elastic shear modulus                    | $G_L = 1000 \times 10^6$ Pa                      |

The current analysis can accommodate various rheological models. In order to demonstrate the capability of the computer model and to investigate the effect of non-Newtonian behaviour of the lubricant, the Eyring law and Bair and Winer's rheological model were considered:

1) The Eyring (nonlinear viscous) model [1],

$$\dot{\gamma}_{ij} = \frac{\tau_{ij}}{\eta} F(\tau_e) \quad (10)$$

$$\text{where } F(\tau_e) = \frac{\sinh(\tau_e/\tau_0)}{(\tau_e/\tau_0)};$$

2) Bair and Winer's (visco-elastic-plastic) model [3],

$$\dot{\gamma}_{ij} = A_G \frac{d\tau_{ij}}{dt} + \frac{\tau_{ij}}{\eta} F(\tau_e) \quad (11)$$

$$\text{where } F(\tau_e) = -\frac{\ln(1-\tau_e/\tau_L)}{(\tau_e/\tau_L)}.$$

Experiments [18] show that the shear strength of liquid lubricants is nearly directly proportional to the pressure. Hence, the limiting shear stress for Bair and Winer's model (referred to as the B-W model hereafter) was evaluated by

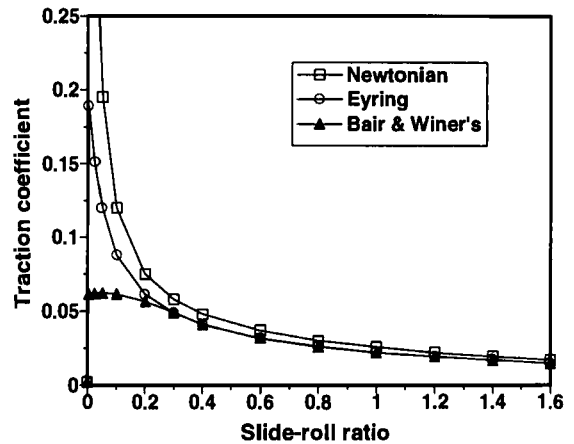
$$\tau_L = \gamma p_0 \quad (12)$$

The constant of proportionality,  $\gamma$ , was taken to be 0.045. The reason for this will be discussed in section 4.2. For the Eyring model, the representative (Eyring) stress was assumed to be one third of the limiting shear stress, i.e.,  $\tau_0 = \tau_L/3$ . This assumption was also employed by Wolff and Kubo [19].

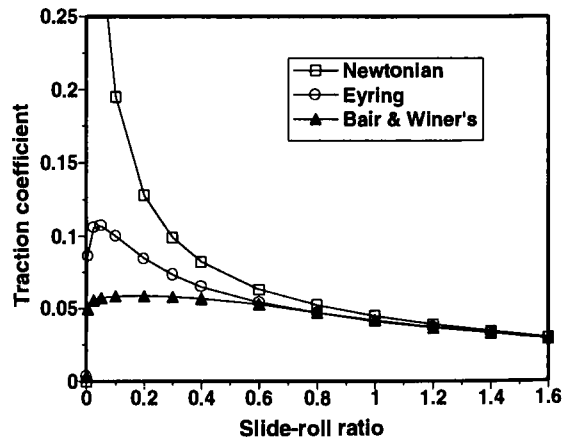
#### 4.1. Non-Newtonian effect

In order to demonstrate the non-Newtonian effect on the traction, Figures 1 (a) and (b) show comparison of the traction coefficients predicted by the Eyring and B-W models with that obtained using the Newtonian law for a range of slide to roll ratios in thermal conditions. Figure 1 (a) shows the results for  $p_0 = 2$  GPa and  $U_m = 4$  m/s, while Figure 1 (b) presents the data in a less severe condition with  $p_0 = 1.2$  GPa and  $U_m = 2$  m/s. It can be seen that for the lower slide-roll ratios, the prediction of the Newtonian law is dramatically higher than those of

the non-Newtonian models. (In the figures, the values over 0.25 are truncated for the Newtonian model.) In fact, the maximum traction coefficient predicted by the Newtonian law was over 1.0 for  $p_0 = 2$  GPa. This is far from being realistic. Further, for the lower slide-roll ratios the use of the Eyring model does predict the lower traction coefficient than the Newtonian law, but this is not adequate, and the prediction is significantly higher than that of the B-W model, particularly under the heavier load. The B-W rheological model appears to be more realistic in the present conditions. (This is evident from Figure 2 which will be discussed in the next subsection.) Therefore, the results presented in rest of this paper have been obtained by employing the B-W model.



(a)  $p_0 = 2$  GPa,  $U_m = 4$  m/s



(b)  $p_0 = 1.2$  GPa,  $U_m = 2$  m/s

Figure 1. Comparison of the traction coefficients calculated using three different rheological models in thermal conditions.

When slide-roll ratios are higher, however, the traction coefficients obtained using the three rheological models become similar. This is due to a dominating thermal thinning effect, which will be discussed later.

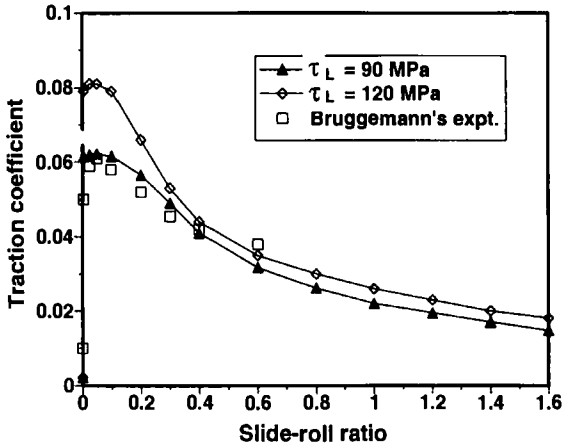


Figure 2. The effect of the magnitude of limiting shear stress on the traction coefficient:  $p_0 = 2 \text{ GPa}$ ,  $U_m = 4 \text{ m/s}$ .

**4.2. Effect of the magnitude of the limiting shear stress**

Figure 2 shows variation of the traction coefficients with the slide-roll ratio for two values of the limiting shear stress in thermal conditions at  $p_0 = 2 \text{ GPa}$  and  $U_m = 4 \text{ m/s}$ , and comparison with the experimental results obtained by Brüggenmann and Kollmann [17]. The two limiting shear stresses of 120 MPa and 90 MPa correspond to  $\gamma = 0.06$  and  $\gamma = 0.045$  respectively. It is noted that, in general, the higher limiting shear stress results in the higher traction coefficient. But the difference is notable only when the slide-roll ratio is smaller (i.e.,  $s < 0.3$ ). This occurs since the limiting shear stress dominates the shear stress distribution in the contact when sliding speeds are lower. Consequently, the traction (coefficient) predicted for  $\tau_L = 120 \text{ MPa}$  is markedly higher than that obtained for  $\tau_L = 90 \text{ MPa}$ . For higher slide-roll ratios, the effect of the limiting shear stress on the traction is less significant because of the thermal effect.

It is particularly noteworthy that the predictions for  $\tau_L = 90 \text{ MPa}$  ( $\gamma = 0.045$ ) are in better correlation with Brüggenmann and Kollmann's measurements.

Therefore, the slope of the limiting shear stress–pressure relation,  $\gamma$ , was taken to be 0.045 in this work.

**4.3. Thermal effect, and temperature and shear stress profiles**

Figure 3 illustrates the coefficients of traction as a function of slide-roll ratio, predicted in thermal and isothermal conditions for two rolling (average) speeds of 2 m/s and 4 m/s at  $p_0 = 2 \text{ GPa}$ . The isothermal condition considers a uniform temperature throughout the contact conjunction with its value being equal to the inlet (bulk) temperature of 50 °C. In the isothermal condition, the traction coefficient hardly changes with the slide-roll ratio after attaining its limiting value at a very small slide-roll ratio. Also, the traction coefficient is almost independent of the average speed ( $U_m$ ). These are to be expected because of the dominating effect of limiting shear response. In the thermal condition, however, the calculated traction coefficient reduces significantly with the slide-roll ratio after reaching its maximum value, particularly for the higher average velocity. This is due to the dominating thermal effect.

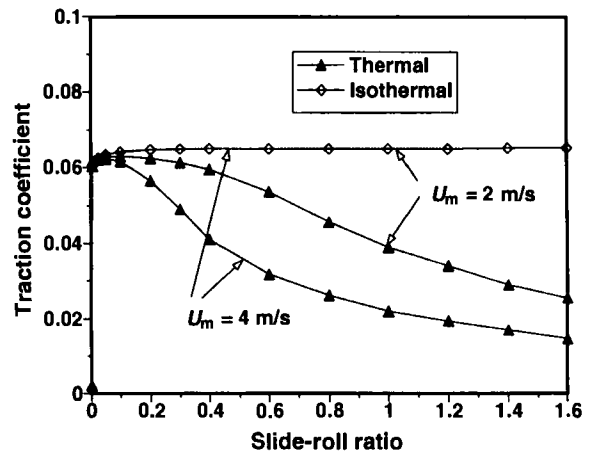


Figure 3. The thermal effect on traction for  $p_0 = 2 \text{ GPa}$ .

Figure 4 shows the temperature distribution on the horizontal plane of symmetry for a slide-roll ratio of 1 at  $p_0 = 2 \text{ GPa}$  and  $U_m = 4 \text{ m/s}$ . As can be seen, there is a large temperature rise in the film. (The shape of the temperature profile is similar to that of the pressure distribution which is depicted in Figure 5. It is noted that the pressure distribution is close to



Hertzian except there is a 'ridge' in the exit region of the contact.) Because of the significant temperature rise over most of the contact area, the lubricant viscosity is greatly reduced. Consequently, the lower shear stresses result. This is evident from Figure 6 where the corresponding shear stress distribution is presented. Clearly, the shear stresses are well below the limiting value of 90 MPa, particularly in the outlet region of the contact conjunction. As a result, for increasing the slide-roll ratio a decrease in the traction (coefficient) is observed.

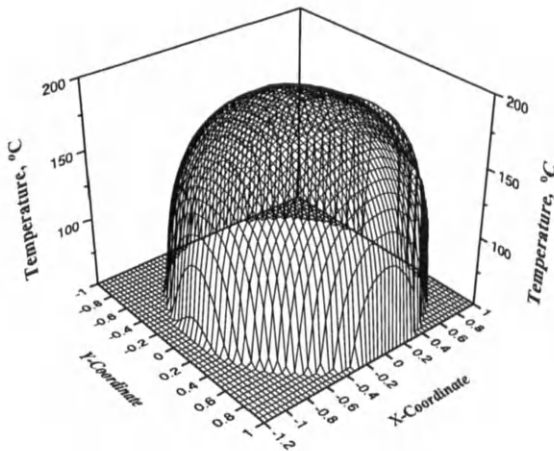


Figure 4. Temperature distribution on the horizontal plane of symmetry ( $Z = 0.5$ ):  $p_0 = 2$  GPa,  $U_m = 4$  m/s,  $s = 1$ .

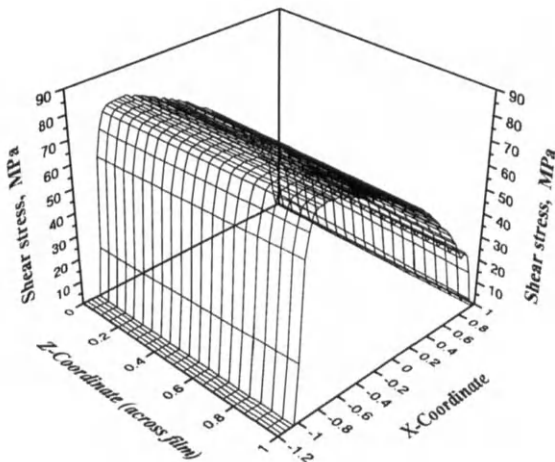


Figure 5. Film pressure distribution:  
 $p_0 = 2$  GPa,  $U_m = 4$  m/s,  $s = 1$ .

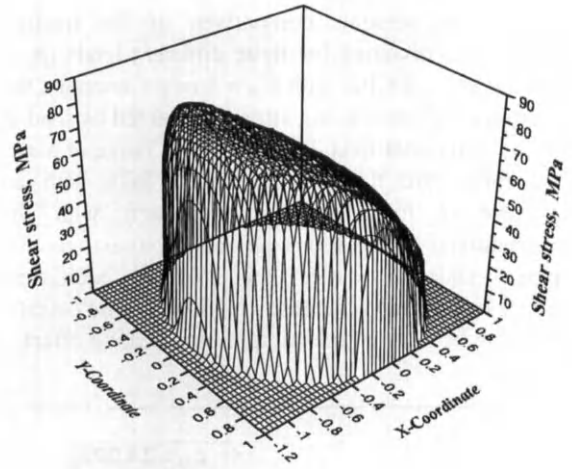


Figure 6. Equivalent shear stress distribution ( $\tau_e$ ) at surface 1:  $p_0 = 2$  GPa,  $U_m = 4$  m/s,  $s = 1$ .

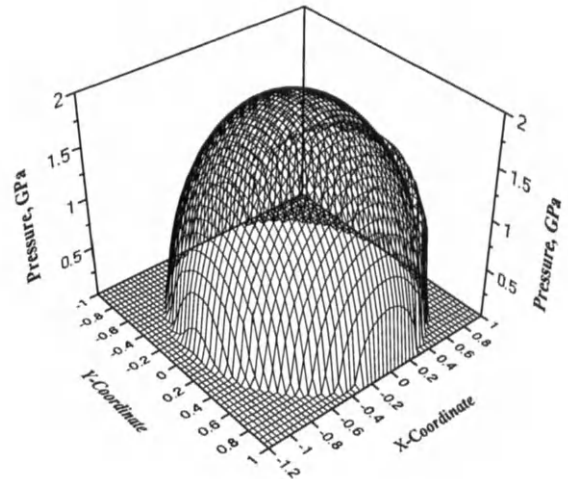


Figure 7. Equivalent shear stress distribution ( $\tau_e$ ) on the vertical plane of symmetry ( $Y = 0$ ):  
 $p_0 = 2$  GPa,  $U_m = 4$  m/s,  $s = 1$ .

Figure 7 depicts the shear stress profile on the vertical plane of symmetry through the Hertzian contact centre in the same conditions as discussed above. It can be seen that the equivalent shear stress profiles at different layers of the film are very similar. This result is to be expected. Thus, this may suggest that the traction is effectively and efficiently transmitted from one surface to the other of the contact bodies through the film.

#### 4.4. Influence of load

Figure 8 presents comparison of the traction coefficients obtained for three different loads ( $p_0 = 1.2, 2.0$  and  $2.8$  GPa) with  $U_m = 4$  m/s. Generally, the traction coefficient is not strongly affected by load in the present conditions. But, in a lower range of slide-roll ratios the traction coefficient falls with an increase in load. This is consistent with the conventional observations [20]. In contrast, for the higher slide-roll ratios the traction coefficient reduces with an increase in load. This occurs probably because of the compression heating effect.

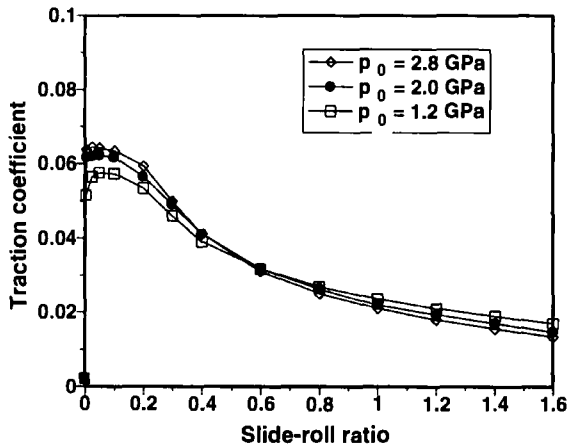
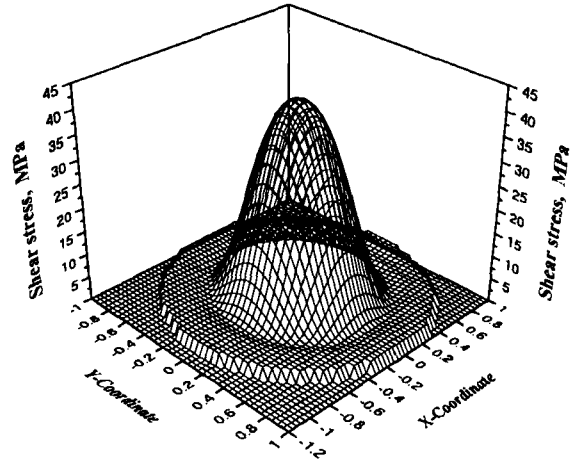
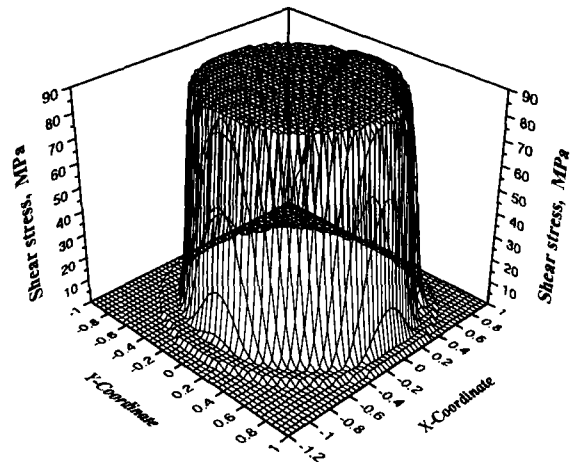


Figure 8. The influence of load on the traction coefficient for  $U_m = 4$  m/s

Figures 9 (a) and (b) show the equivalent shear stress distributions for two loads ( $p_0 = 1.2$  GPa and  $2.0$  GPa) at a very small slide-roll ratio of  $0.00001$  and a rolling speed of  $4$  m/s. It can be seen that the shapes of the shear stress distributions for the two loads are significantly different. For the lighter load, the shear stresses fail to reach the limiting value of  $54$  MPa at the given slide-roll ratio. Whereas, for the higher load they obtain the limiting shear stress of  $90$  MPa over the central area of the contact. This explains why the traction (coefficient) increases with load for the lower slide-roll ratios and why it attains its maximum value at a very small slide-roll ratio in the heavy loading conditions. It is interesting to note there is a 'skirt' round the central distribution (area), particularly for the lighter load. This occurs because the effect of pressure-induced flow (shearing) is relatively significant in the vicinity of edge of the contact as the Couette flow is less dominant at such a small slide-roll ratio.



(a)  $p_0 = 1.2$  GPa



(b)  $p_0 = 2.0$  GPa

Figure 9. The effect of maximum Hertzian pressure on the equivalent shear stress distribution at surface 1:  $U_m = 4$  m/s,  $s = 0.00001$ .

## 5. CONCLUSIONS

A practical and effective model of the non-Newtonian TEHL for elliptical contacts has been developed by the authors. Using this computer model, the calculations have been conducted to examine the applicability of the Eyring law and Bair and Winer's rheological model and the influences of the non-Newtonian character of a lubricant and temperature rises on the traction. From the results

presented in this paper, the following points can be obtained:

- Bair and Winer's rheological model is more realistic than the Eyring law in evaluating the traction in the EHD contact of heavy loads.
- In thermal conditions, for lower sliding speeds ( $U_s < 1$  m/s) the non-Newtonian effect is significant and should be taken into account when evaluating the traction; whereas, for higher sliding speeds the use of the Newtonian law is sufficient.
- For the non-Newtonian lubricant, the thermal effect on the traction is significant when sliding speeds are relatively high and this influence increases with an increase in slide-roll ratio.
- When sliding speeds are lower, the magnitude of the limiting shear stress has a considerable influence on the traction.
- When the non-Newtonian effect is considered, the traction appears to be less sensitive to the load in the heavy loading conditions.

## REFERENCES

1. H. Eyring, Viscosity, plasticity, and diffusion as examples of absolute reaction rates, *J. Chem. Physics*, 4 (1936) 283–291.
2. K.L. Johnson and J.L. Tevaarwerk, Shear behaviour of elastohydrodynamic oil film, *Proc. R. Soc. London, Series A*, 356 (1977) 215–236.
3. S. Bair and W.O. Winer, A rheological model for elastohydrodynamic contacts based on primary laboratory data, *ASME J. Lubric. Technol.*, 101 (1979) 258–265.
4. A.J. Moore, The behaviour of lubricants in elastohydrodynamic contacts, Presented at the *Annual House Meeting of the IMechE Tribology Group*, I.Mech.E., London, 1995.
5. E.G. Trachman and H.S. Cheng, Thermal and non-Newtonian effects on traction in EHL contacts, *Proc. Instn. Mech. Engrs.*, (1972), 142.
6. T.F. Conry, Thermal effects on traction in EHD lubrication, *ASME J. Lubric. Technol.*, 103 (1981) 533–538.
7. L. Houpert, L. Flamand and D. Bethe, Rheological and thermal effects in lubricated E.H.D. contacts, *ASME J. Lubric. Technol.*, 103 (1981) 526–532.
8. S.H. Wang and H.H. Zhang, Combined effects of thermal and non-Newtonian character of lubricant on pressure, film profile, temperature rise, and shear stress in E.H.L., *ASME J. Tribol.*, 109 (1987) 666–670.
9. P. Yang and S. When, A generalized Reynolds equation for non-Newtonian thermal elastohydrodynamic lubrication, *ASME J. Tribol.*, 112 (1990) 631–636.
10. P.C. Sui and F. Sadeghi, Non-Newtonian thermal elastohydrodynamic lubrication, *ASME J. Tribol.*, 113 (1991) 390–397.
11. S. Wang, T.F. Conry and C. Cusano, Thermal analysis of elastohydrodynamic lubrication of line contacts using the Ree-Eyring fluid model, *ASME J. Tribol.*, 113 (1991) 232–244.
12. S. Wang, C. Cusano and T.F. Conry, Thermal non-Newtonian elastohydrodynamic lubrication of line contacts under simple sliding conditions, *ASME J. Tribol.*, 114 (1992) 317–327.
13. H.-S. S. Hsiao and B.J. Hamrock, A complete solution for thermal-elastohydrodynamic lubrication of line contacts using circular non-Newtonian fluid model, *ASME J. Tribol.*, 114 (1992) 540–552.
14. M.-T. Ma, An expedient approach to the non-Newtonian thermal EHL in heavily loaded point contacts. Submitted to *Wear* for publication, 1996.
15. C.J.A. Roelands, J.C. Vlutger and H.I. Watermann, The viscosity temperature pressure relationship of lubricating oils and its correlation with chemical constitution, *ASME J. Basic Engng.*, 1963, p. 601.
16. D. Dowson and G.R. Higginson, *Elastohydrodynamic lubrication*, Pergamon Press, 1966.
17. H. Brüggemann and F.G. Kollmann, A numerical solution of the thermal elastohydrodynamic lubrication in an elliptical contact, *ASME J. Lubric. Technol.*, 104 (1982) 392–400.
18. S. Bair and W.O. Winer, Shear strength measurements of lubricants at high pressure, *ASME J. Lubric. Technol.*, 101 (1979) 258–265.
19. R. Wolff and A. Kubo, A generalised non-Newtonian fluid model incorporated into elastohydrodynamic lubrication, *ASME J. Tribol.*, 118 (1996) 74–82.
20. K.L. Johnson, Introductory review of lubricant rheology and traction, *Proceedings of 5th Leeds-Lyon Symposium on Tribology*, Mechanical Engineering Publications Limited, London, 1978, 155–161.

**APPENDIX: Nomenclature**

|            |  |                     |  |
|------------|--|---------------------|--|
| $a$        | semi-minor axis of Hertzian contact ellipse, m                                 | $T$                 | film temperature, °C   |
| $A$        | area of solution domain, m <sup>2</sup>  | $T_0$               | inlet (bulk) temperature, °C   |
| $A_G$      | $1/G_L$ , Pa <sup>-1</sup>   | $T_1$               | temperature at the contact surface of lower speed (surface 1), °C          |
| $b$        | semi-major axis of Hertzian contact ellipse, m                                 | $T_2$               | temperature at the contact surface of higher speed (surface 2), °C         |
| $C_1, C_2$ | specific heat capacity of two bodies, J kg <sup>-1</sup> °C <sup>-1</sup>      | $u$                 | velocity in $x$ -direction, m s <sup>-1</sup>                              |
| $C_A, C_B$ | coefficients of compressibility of lubricant, Pa <sup>-1</sup>                 | $U_1$               | velocity at surface 1, m s <sup>-1</sup>                                   |
| $C_L$      | specific heat of lubricant,  | $U_2$               | velocity at surface 2, m s <sup>-1</sup>                                   |
| $D$        | elastic deformation, m   | $U_m$               | average (rolling) speed, $(U_1 + U_2)/2$                                   |
| $D_T$      | thermal expansivity, °C <sup>-1</sup>  | $U_s$               | sliding speed, $U_2 - U_1$ , m s <sup>-1</sup>                             |
| $E_1, E_2$ | elastic moduli of two contact bodies, Pa                                       | $v$                 | velocity in $y$ -direction, m s <sup>-1</sup>                              |
| $E'$       | equivalent modulus of elasticity, $2/[(1-\nu_1^2)/E_1 + (1-\nu_2^2)/E_2]$ , Pa | $w$                 | velocity in $z$ -direction, m s <sup>-1</sup>                              |
| $G_L$      | elastic shear modulus of lubricant, Pa   | $W$                 | applied load, N  |
| $h$        | film thickness, m  | $x$                 | coordinate along rolling direction, m                                      |
| $h_c$      | central film thickness, m  | $x_{in}$            | location of inlet boundary of solution domain, m                           |
| $K_1, K_2$ | thermal conductivity of two bodies, W m <sup>-1</sup> °C <sup>-1</sup>         | $X$                 | dimensionless coordinate, $X = x/a$  |
| $K_L$      | thermal conductivity of lubricant, W m <sup>-1</sup> °C <sup>-1</sup>          | $y$                 | coordinate perpendicular to $x$ -axis on the plane of contact, m           |
| $N_x$      | number of mesh intervals along $x$ -direction                                  | $Y$                 | dimensionless coordinate, $Y = y/b$  |
| $N_y$      | number of mesh intervals along $y$ -direction                                  | $z$                 | coordinate in film thickness direction, m                                  |
| $N_z$      | number of mesh intervals along $z$ -direction                                  | $Z$                 | dimensionless coordinate, $Z = z/h$  |
| $p$        | pressure, Pa   | $\gamma$            | slope of limiting shear stress–pressure relation                           |
| $p_0$      | maximum Hertzian pressure, Pa  | $\dot{\gamma}_{ij}$ | shear strain rate tensor, s <sup>-1</sup>                                  |
| $R_x$      | equivalent radius of curvature of the contact bodies in $x$ -direction, m      | $\eta$              | lubricant viscosity, Pa s  |
| $R_y$      | equivalent radius of curvature of the contact bodies in $y$ -direction, m      | $\eta_0$            | inlet viscosity of lubricant, Pa s   |
| $s$        | slide to roll ratio, $U_s/U_m$   | $\nu_1, \nu_2$      | Poisson's ratios of two bodies   |
| $S_0$      | temperature–viscosity index  | $\rho_0$            | inlet lubricant density, kg m <sup>-3</sup>                                |
| $S_1, S_2$ | coefficients for determining pressure–viscosity index                          | $\rho_1, \rho_2$    | densities of two bodies, kg m <sup>-3</sup>                                |
| $S_p$      | pressure–viscosity index   | $\rho_L$            | lubricant density, kg m <sup>-3</sup>                                      |
| $S_T$      | temperature–viscosity index  | $\tau_0$            | Eyring shear stress, Pa  |
| $t$        | time, s  | $\tau_L$            | limiting shear stress, Pa  |
|            |  | $\tau_e$            | equivalent shear stress, $\tau_e = (\tau_{xz}^2 + \tau_{yz}^2)^{1/2}$ , Pa |
|            |  | $\tau_{ij}$         | shear stress tensor, Pa  |
|            |  | $\tau_{xz}$         | shear stress in $x$ -direction, Pa   |
|            |  | $\tau_{yz}$         | shear stress in $y$ -direction, Pa   |
|            |  | $\xi, \zeta$        | dummy variables  |

## Influence of Geometry of Conjunction on Elastohydrodynamic Film Formation in Knee Prostheses with Compliant Layer

N. Ohtsuki<sup>a</sup>, T. Murakami<sup>b</sup>, S. Moriyama<sup>b</sup> and H. Higaki<sup>b</sup>

<sup>a</sup>Graphic Science, Faculty of Engineering, Kyushu University, Ropponmatsu, Chuo-ku, Fukuoka, 810 Japan

<sup>b</sup>Department of Intelligent Machinery and Systems, Faculty of Engineering, Kyushu University, Hakozaki, Higashi-ku, Fukuoka 812-81 Japan

In most of existing knee prostheses with low geometrical congruity, the sufficient fluid film is unlikely to be formed to prevent a direct contact between femoral and tibial component. The difference in geometry of conjunction of knee prostheses may exert an influence on lubricating film formation. Fluid film formation and frictional behavior in several kinds of knee prostheses with compliant layer different in geometry of conjunction were examined in knee joint simulator tests under walking conditions. The femoral component is the sphere of 30mm radius made of stainless steel. The tibial components were made of conductive silicone rubber layer of 3mm thickness supported by acrylic resin. Four kinds of tibial components were prepared for a different conjunction geometry. Silicone oils were used as lubricants. The geometrical shapes of conjunction are classified into three kinds of shape, i.e., a longitudinally long ellipse, a transversely long ellipse to the sliding direction and a circle. Four kinds of data ( tibial axis load, flexion angle, frictional torque and degree of separation ) were measured. The data of 25th cycle were evaluated. As a result, the ability of the fluid film formation of the transverse geometry of conjunction was higher than the longitudinal geometry of conjunction.

### 1. INTRODUCTION

In most of existing knee prostheses composed of corrosion-resistant metal or ceramics and ultrahigh molecular weight polyethylene with low geometrical congruity, the sufficient fluid film is unlikely to be formed to prevent a direct contact between femoral and tibial component.

The application of compliant materials for rubbing surface in knee prostheses appears to enhance the elastohydrodynamic film formation [1-6]. Furthermore, optimum geometrical design to improve the geometrical congruity seems to enhance the fluid film formation [4,7]. The difference in geometry of conjunction may exert an influence on lubricating film formation. The geometry of conjunction of the knee prostheses is determined by a combination of femoral and tibial component of the prostheses.

In this paper, the fluid film formation and frictional behaviour in several kinds of knee prostheses with compliant layer different in geometry of conjunction were examined in knee joint simulator tests under walking conditions and then the difference in geometrical design was evaluated.

### 2. EXPERIMENTAL METHODS

#### 2.1 Knee joint simulator

Figure 1 shows the 3D solid model of the knee joint

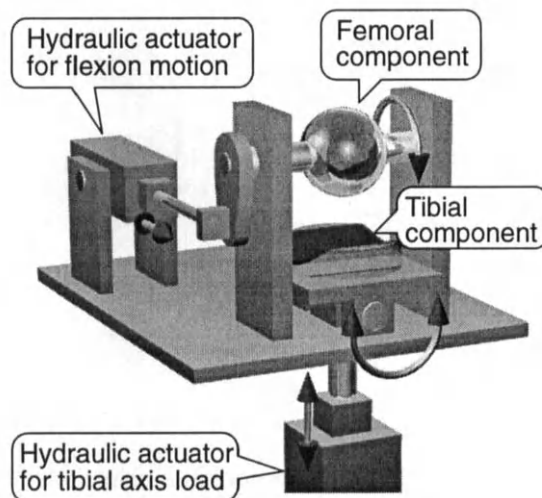


Figure 1. The knee joint simulator modeled by 3-D software.

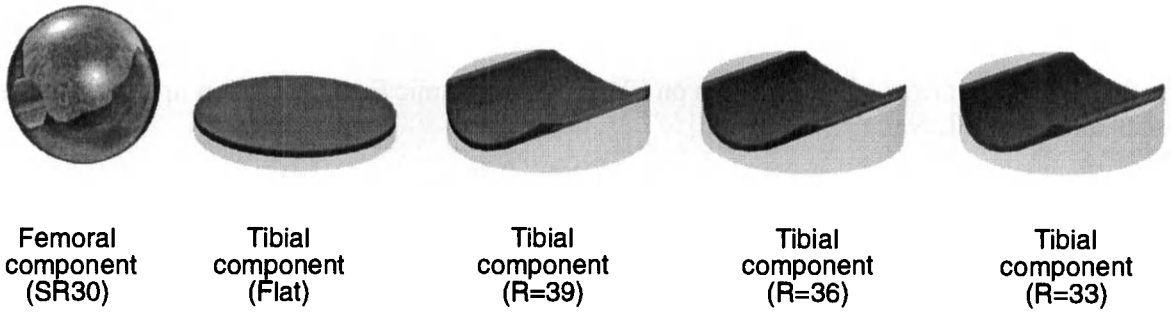


Figure 2. A spherical femoral and 4 types of tibial components for knee joint simulator tests.

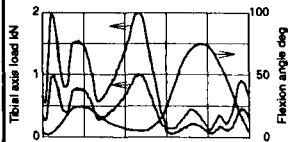
simulator used for the experiment. A walking motion was simulated by using this knee joint simulator. Flexion-extension motion of the femoral component and time-dependent tibial axis load were achieved by personal computer controlled hydraulic system. A strain gauges were attached on the femoral flexion-extension shaft for the measurement of the frictional torque. A degree of separation to correspond to fluid film formation can be measured by the electric resistance method [1-4].

**2.2 Specimens**

The specimens used for the knee joint simulator tests are shown in the Fig. 2. The femoral component is the sphere of 30mm radius made of stainless steel (SUS316). The tibial components were made of conductive silicone rubber layer of 3mm thickness supported by acrylic resin. Root mean square values for surface roughness are 0.065µm for stainless steel and 3.3µm for silicone rubber, respectively.

Four kinds of tibial components were prepared for a different conjunction geometry. Figure 3 shows the

Table1. Experiment condition

|                                   |  |
|-----------------------------------|--|
| Temperature                       | 30 - 32 °C   |
| Lubricant                         | Silicone oil S-30<br>(kinetic viscosity is 30 mm <sup>2</sup> /s at 25°C)          |
| Walking period                    | 2 s  |
| 2 types of load and flexion angle |  |
| Femoral material                  | SUS316 ( JIS )   |
| r.m.s roughness                   | 0.065 µm   |
| Tibial material                   | Conductive silicone rubber layer of 3mm thickness supported by plastic resin       |
| r.m.s roughness                   | 3.3 µm   |

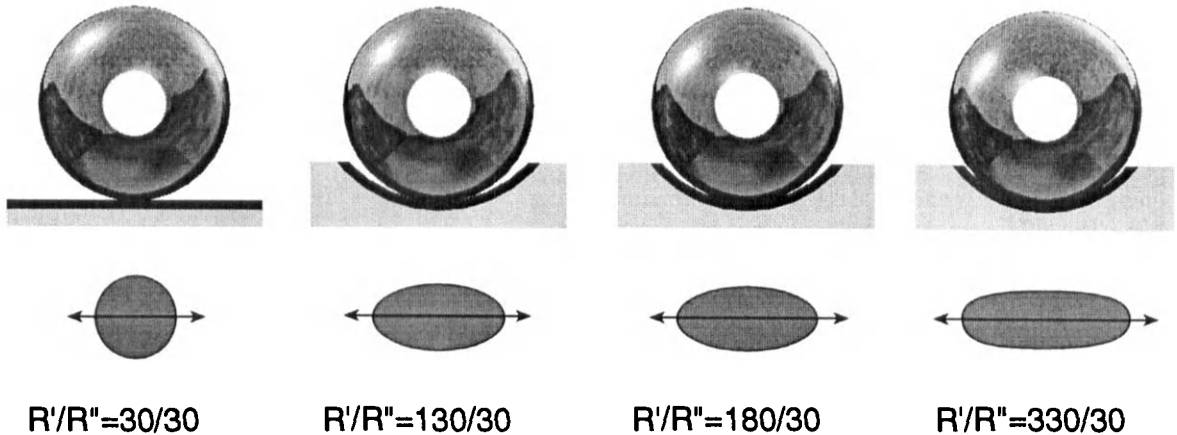


Figure 3. The 4 fundamental combinations of the tibial and femoral components, and the corresponding geometries of conjunction which was examined under the static load.

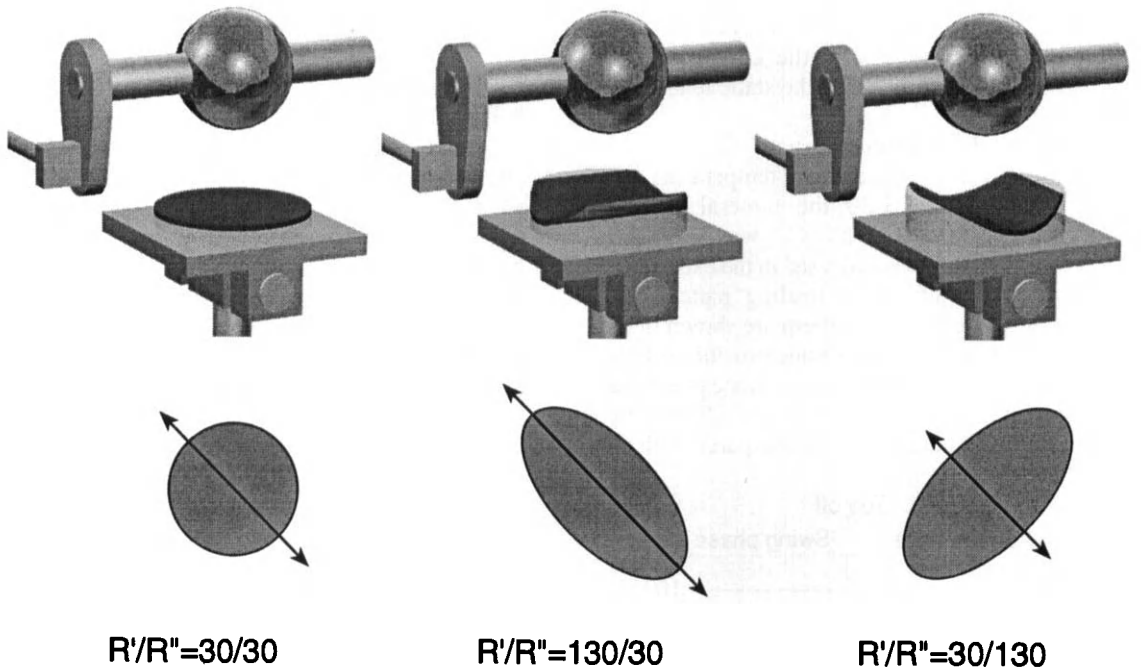


Figure 4. The 3 fundamental arrangements for 3 geometrical shapes of conjunction.

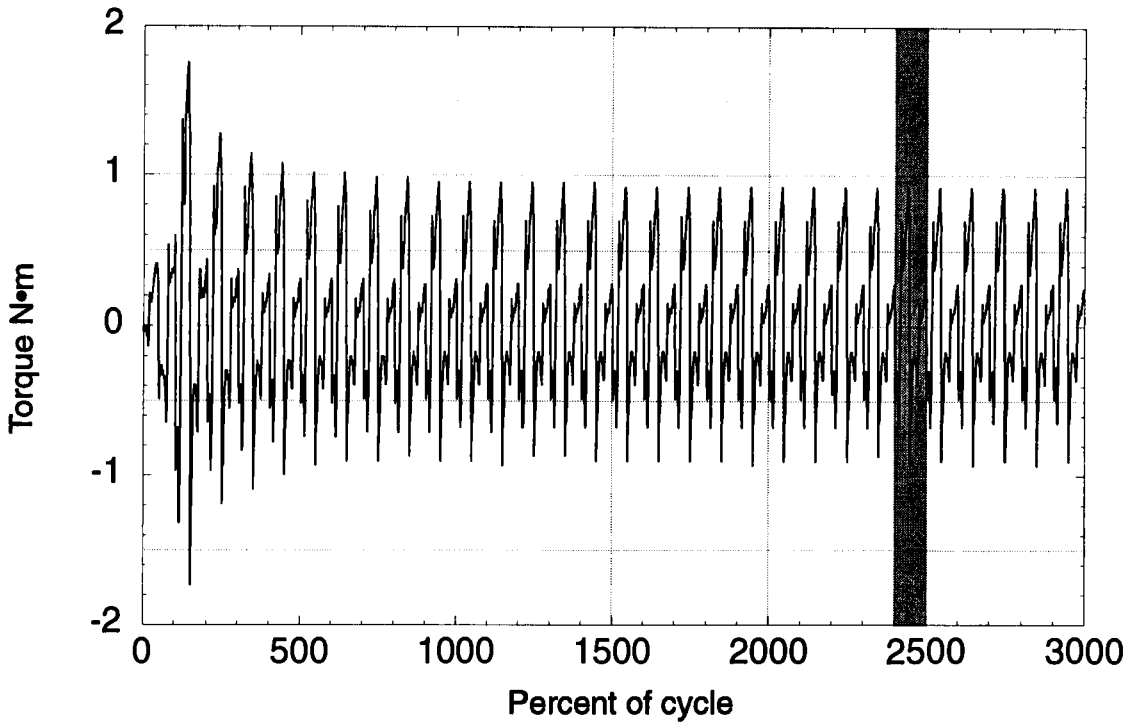


Figure 5. Changes in torque for 30 walking periods, in which the torque at the 25th cycle was evaluated.

four kinds of fundamental combinations of the tibial and femoral components and the corresponding geometries of conjunction under the static load.

**2.3 Experimental condition**

All tests were carried out at room temperature ( 30 - 32 °C ). Silicone oil ( S-30, the numeral means a kinetic viscosity mm<sup>2</sup>/s at 25 °C ) was used as a lubricant. The period of walking used in the experiment is 2 seconds, and two kinds of loading patterns and a common flexion-extension pattern are shown in the Table 1. Usual total condylar knee prostheses have both medial and lateral contact zones. Knee prostheses used in this test have single contact zone. Therefore, both half and full loading patterns compared with the

previous tests [1-4] were applied.

**2.4 Experimental procedure**

The geometrical shapes of conjunction are classified into three kinds of shape, i.e., a longitudinally long ellipse, a transversely long ellipse to the sliding direction and a circle. The experiments were carried out using the arrangements of specimens shown in the Fig. 4 for three kinds of geometrical shapes of conjunction. Each experiment was carried out for 30 cycles.

**2.5 Data processing**

Using the knee joint simulator, four kinds of data (tibial axis load, flexion angle, frictional torque and degree of separation) were measured in the experiment.

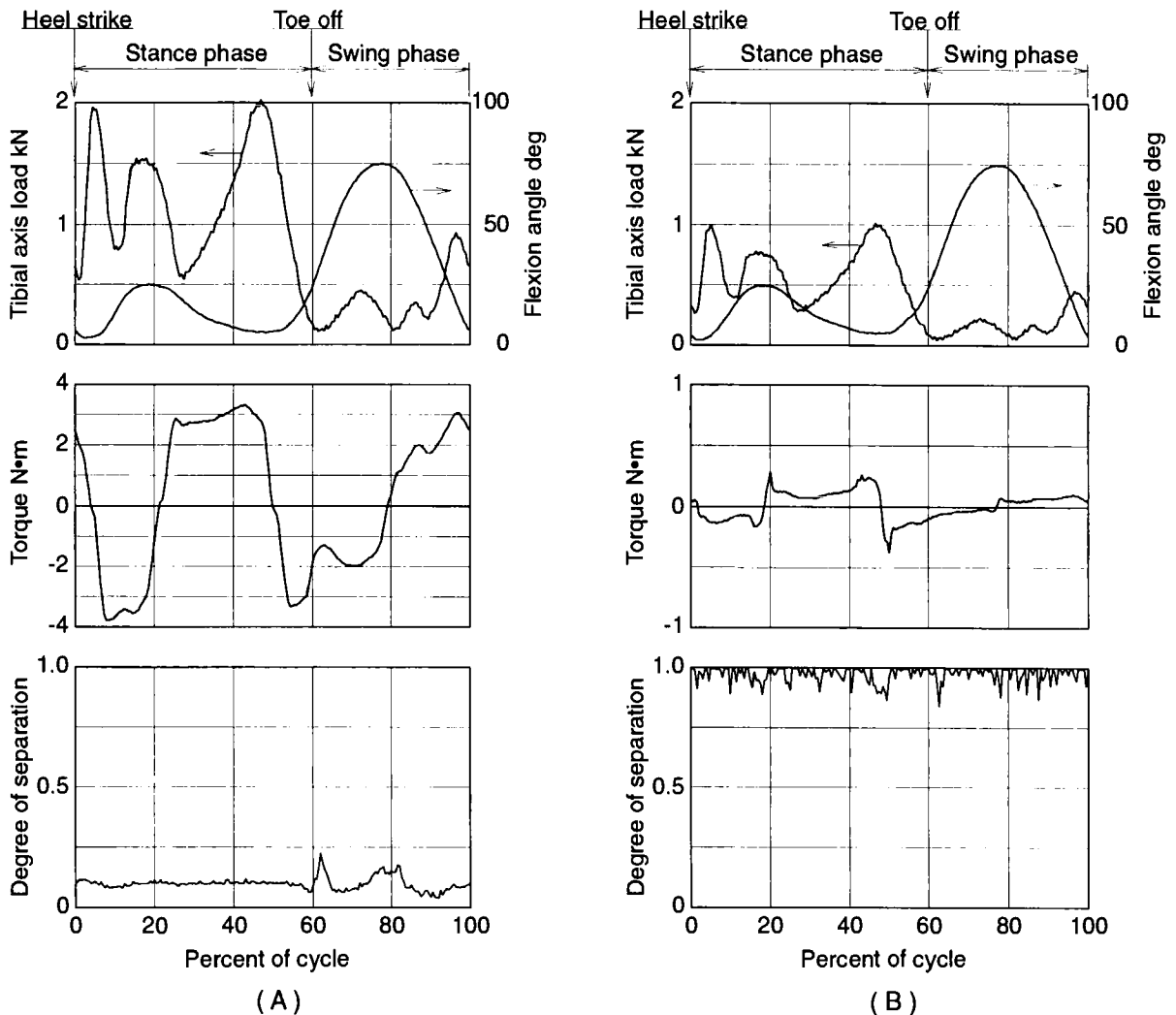


Figure 6. Examples of the graph of the data on the 25th period used for the evaluation when it has a circular geometry of conjunction. ( A: peak load of 2kN. B: peak load of 1kN. )



A degree of separation is defined as the ratio of measured voltage to applied voltage of 100mV. (degree of separation is 1 : full separation, degree of separation is 0 : contact)

As shown in Fig. 5 which means the change in the frictional torque for 30 cycles, the data of 25th cycle which are considered to be stable are evaluated in this paper. Figure 6 shows examples of the graph of the data on the 25th period used for the evaluation when it has a circular geometry of conjunction.

### 3. RESULTS

Experimental results were classified as two groups in relation to geometrical shapes of conjunction, i.e., longitudinal or transverse conjunction. Each group has two graphs classified by the peak load ( 2kN and 1kN ). All graphs have two columns. Left columns show a series of graphs of the frictional torque, and right columns show a series of graphs of the degree of separation. The top graphs are frictional torque and degree of separation in the case of the circular contact. Each series of graphs are arranged in longitudinal or transverse as increasing order of geometrical congruity from the top to the bottom.

#### 3.1 The case of which the geometrical shapes of conjunction is a longitudinally long ellipse to the sliding direction.

##### 3.1.1 Full load condition;peak load of 2kN. (Fig. 7)

The longitudinally longer the elliptical shape of conjunction is, the lower the frictional torque is. A degree of separation is almost 0.1 when the geometrical shape of conjunction is circular. As the geometrical shape of conjunction becomes gradually long, the degree of separation increases gradually to almost 0.8.

##### 3.1.2 Half load condition;peak load of 1kN. (Fig. 8)

The longitudinally longer the elliptical shape of conjunction is, the higher the frictional torque is. But, the frictional torque is lower than 0.7 N•m. As the geometrical shapes of conjunction becomes long gradually, the degree of separation decreases gradually. However, the degree of separation is higher than 0.5 at least.

#### 3.2 The case of which the geometrical shapes of conjunction is a transversely long ellipse to the sliding direction.

##### 3.2.1 Full load condition;peak load of 2kN. (Fig. 9)

When the geometrical shape of conjunction is circle,

a frictional torque is high, and a degree of separation is almost 0.1.

On the other hand, at all the cases that the geometrical shapes of conjunction are transversely long elliptical to the sliding direction, a frictional torque is low, and a degree of separation is almost 1 except for the especially severe phase.

##### 3.2.2 Half load condition;peak load of 1kN (Fig.10)

The frictional torque is lower than 0.3 N•m. The degree of separation is almost 1. An influence by differences of the geometrical shapes of conjunction is little observed.

### 4. DISCUSSIONS

As pointed out based on the authors' previous studies [1-4] and tribological viewpoint of cushion form bearing [5, 6, 8], the application of compliant layer for rubbing surface of knee prostheses appears to enhance fluid film formation. In this paper, the authors examined the effect of conjunction geometry on lubricating film formation for the same material combination different in tibial geometry. The factor which influences an elastohydrodynamic film formation is discussed in the following by classifying it in the longitudinal and the transverse geometry of conjunction.

Except for the graph in the case of the circular conjunction in the top in Figs.7, 8, 9 and 10, experimental results for frictional torque and degree of separation are compared. Obviously the frictional torque for transverse conjunction in Figs. 9 and 10 is smaller than for longitudinal conjunction in Figs.7 and 8. This is supported by fluid film formation. The degree of separation in Figs. 9 and 10 is higher than in Figs. 7 and 8.

If it is said in other words, friction in the case of the transverse geometry is smaller than the longitudinal one, and a degree of separation is higher under the condition of the transverse conjunction. For transverse conjunction, a friction coefficient is about 0.01 in the phase of the maximum load before the moment of the toe off, and a degree of separation is almost 1 in the whole cycle except just before toe off at full load condition. As mentioned above, considerable elastohydrodynamic fluid film is likely to prevent direct contact between rubbing surfaces in knee prosthesis with silicone rubber layer, which has transverse elliptic conjunction.

On the other hand, in the case of longitudinal conjunction in Figs. 7 and 8, degree of separation is low under the severe condition. This means that fluid film is partly broken down and local direct contact occurs. Coefficient of friction was almost 0.05 at the

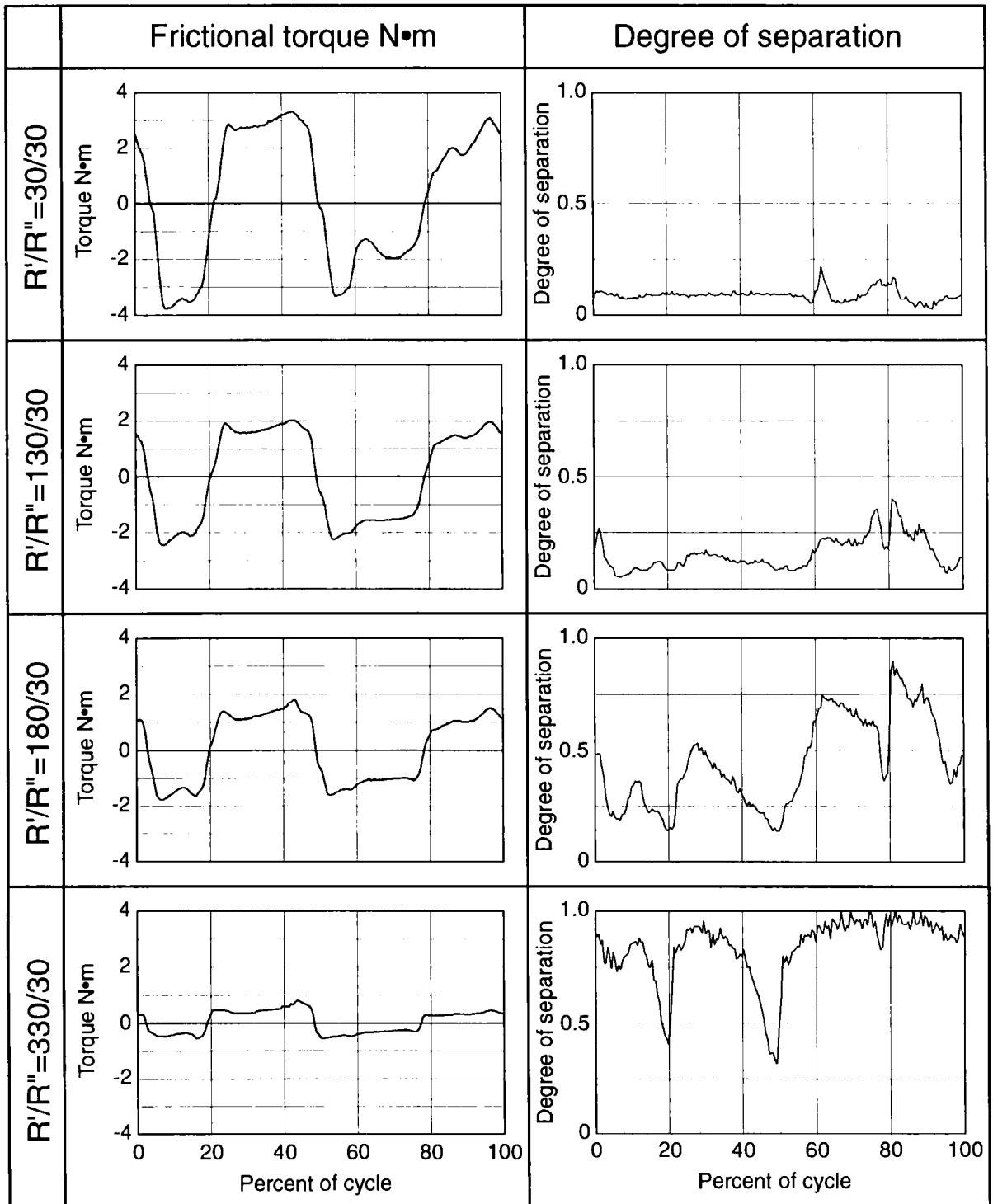


Figure 7. A series of graphs of data which has circular and three longitudinal geometries of conjunction when a peak load is 2kN, as arranged in longitudinal order from the top to the bottom. The left column is the graphs of the data of the frictional torque. The right column is the graphs of the data of the degree of separation.

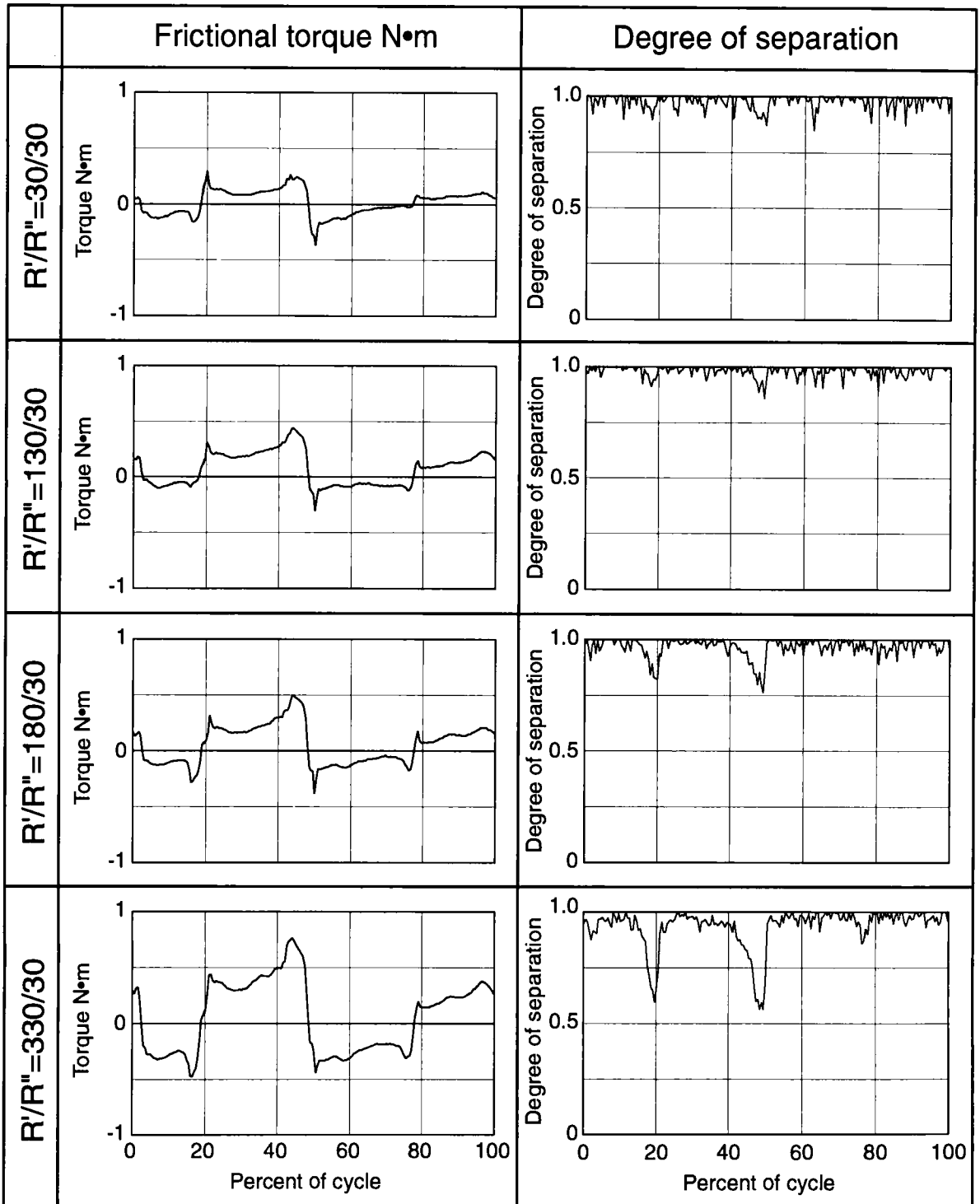


Figure 8. A series of graphs of data which has circular and three longitudinal geometries of conjunction when a peak load is 1kN, as arranged in longitudinal order from the top to the bottom. The left column is the graphs of the data of the frictional torque. The right column is the graphs of the data of the degree of separation.

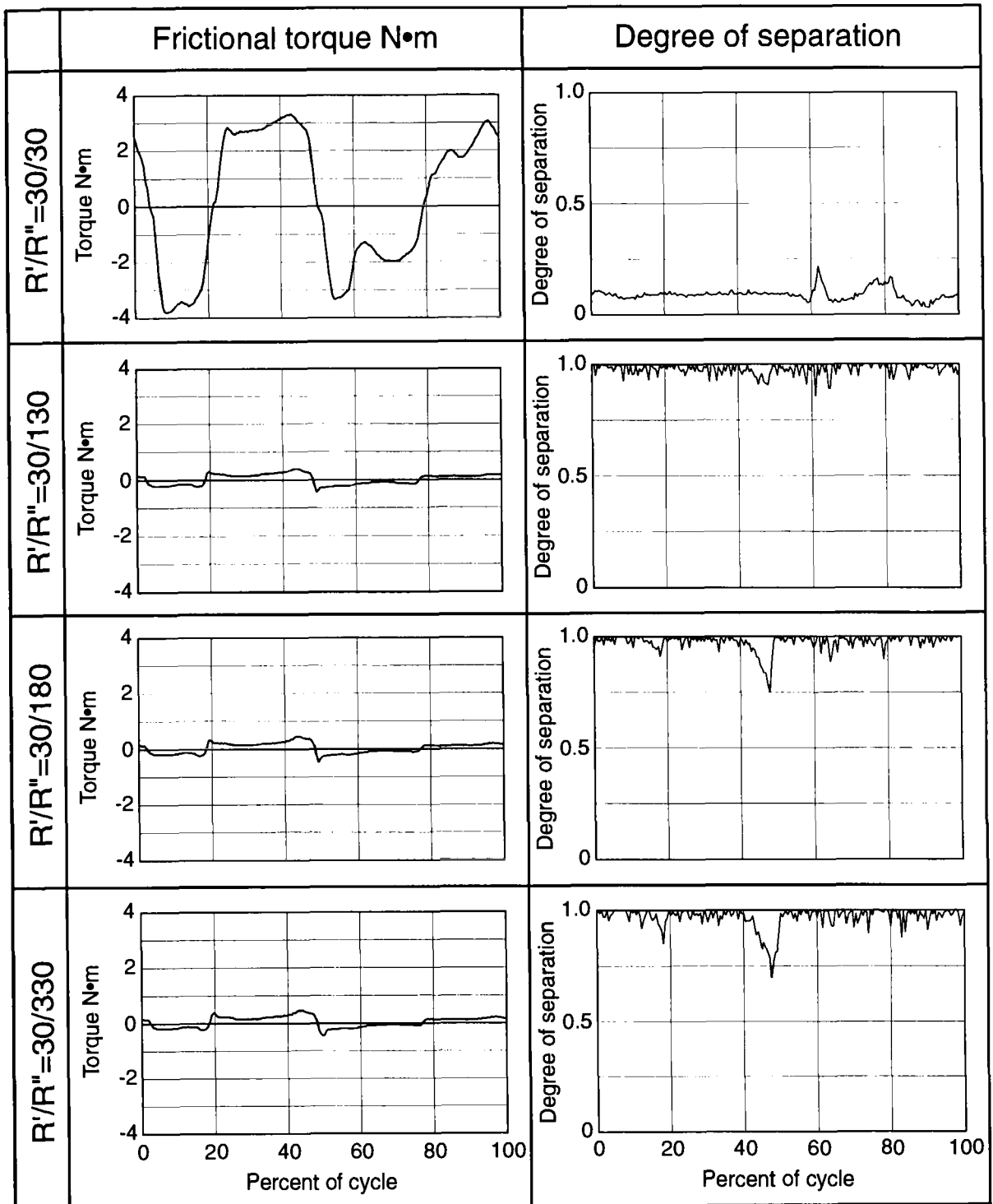


Figure 9. A series of graphs of data which has circular and three transverse geometries of conjunction when a peak load is 2kN, as arranged in transverse order from the top to the bottom. The left column is the graphs of the data of the frictional torque. The right column is the graphs of the data of the degree of separation.

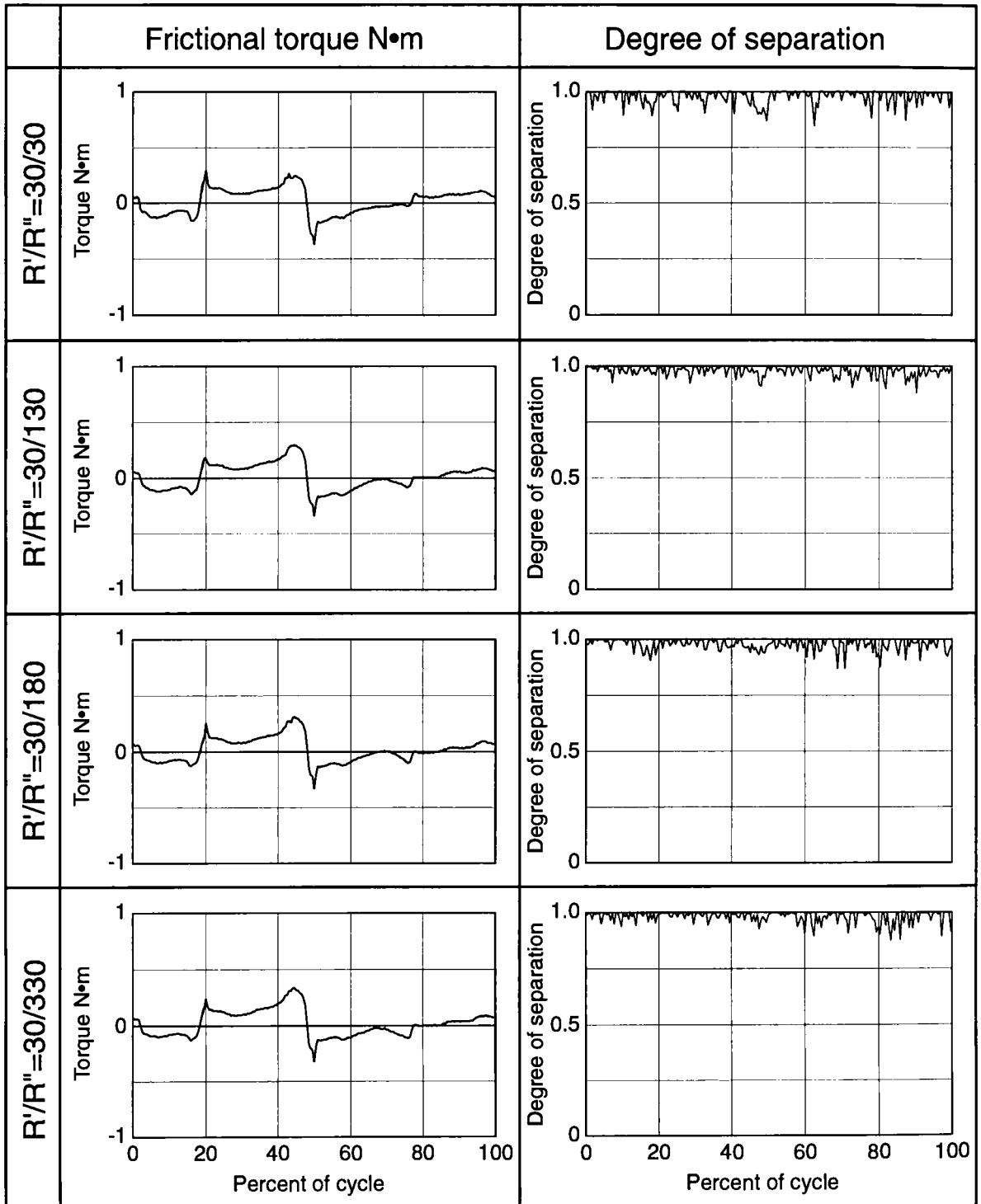


Figure 10. A series of graphs of data which has circular and three transverse geometries of conjunction when a peak load is 1kN, as arranged in transverse order from the top to the bottom. The left column is the graphs of the data of the frictional torque. The right column is the graphs of the data of the degree of separation.

phase of maximum load before toe off for severe case. Therefore, transverse geometry is more desirable than the longitudinal one from the viewpoint of fluid film formation.

Next, the influence of difference of equivalent radius or contact area on fluid film formation is discussed in the case of longitudinal conjunction as shown in Figs. 7 and 8. Under high load condition in Fig.7,  $R'=330$  mm corresponding to longer and larger contact area shows lower friction and higher separation than smaller conjunctions. On the other hand, under half load condition in Fig.8,  $R'=330$  mm exhibits higher friction and lower separation than other conjunction with smaller  $R'$ , while frictional value is not so high.

These results indicate the influence of longitudinal geometry of conjunction varies depending on the severity of operating condition. One of parameter controlling severity is load or contact pressure. Figure 11 shows the changes in contact area. This indicates the mean contact pressure increases as  $R'$  is smaller under the same load condition (2 kN,  $R'=330$  mm: 3.6 MPa  $\rightarrow$   $R'=30$  mm: 5.4 MPa) and increases with increasing load for the same  $R'/R''$  ( $R'/R''=130/30$ , 1 kN:3.4 MPa  $\rightarrow$  2 kN:4.9 MPa).

Under mild condition in Fig.8 where fluid film is maintained during walking in circular conjunction, the fluid film becomes thinner probably due to an increase in side leakage flow, as geometry of conjunction becomes longer in frictional direction. That is, under mild condition, fluid film has a tendency to break down as the longitudinal width becomes longer, in spite of decreasing contact pressure. In contrast, under severe condition in Fig.7 where considerable direct contact occurs between rubbing surfaces, friction becomes higher as the longitudinal width becomes shorter, which is probably due to increasing tendency of contact stresses. In circular conjunction under high load condition, fluid film formation is little expected and significantly high frictional torque is observed.

From the viewpoint of optimum geometrical design, it is noticed that the longest conjunction with larger contact area is little varied by increase in load, although local contact easily occurs under mild condition.

Next, the influence which a geometry of transverse conjunction exerts on fluid film formation is discussed. As shown in Figs. 9 and 10, the circular conjunction shows high friction and low separation under high load condition, but exhibits low friction and almost full separation except local drop under half load condition. It is noted under severe high load condition that transverse conjunction can maintain low friction condition and good fluid film formation except some local contact before toe off. This remarkable difference in fluid film formation between circular and transverse

elliptic conjunctions may be due to higher film thickness with increasing ellipticity ratio [9] and lower contact pressure in transverse conjunction under the same load condition. However, the drop in degree of separation is a little larger in larger  $R''$ . This suggests the existence of optimum geometry for fluid film formation.

As described above, there was no difference between transverse conjunctions ( $R''=130, 180$  and  $330$ ) in Fig.10 under mild condition. And, there was small difference under high load condition. So, additional tests were carried out under severer operating condition lubricated with silicone oil S-10 of lower viscosity. The experimental results are shown in Fig.12. Only the results of  $R''=180$  and  $R''=330$  are shown in Fig.12. All other graphs showed high friction and low separation in the same way as the case of  $R''=180$ . The area of the conjunction in  $R''=330$  is the highest as shown in the Fig.11. This fact suggests the beneficial effect of larger transverse contact area. However, it is required to examine the fluid film formation in further tests using models of transverse conjunction with the same contact area but with different geometry, to evaluate the influence of conjunction geometry.

5. CONCLUSIONS

The frictional torque and the degree of separation were measured by using the knee joint simulator to

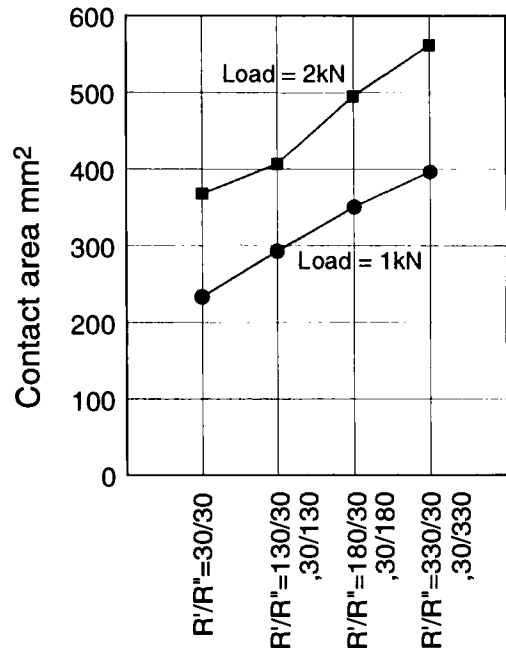


Figure 11. The areas of the conjunctions in the load 1kN and 2kN.

examine the ability of the fluid film formation by changing the geometry of conjunction for both longitudinal and transverse elliptical contacts. As a result, it was obviously proved that the ability of the fluid film formation of the transverse geometry of conjunction is higher than the longitudinal geometry of conjunction.

If the longitudinal length for longitudinal conjunction became long, it was found out that friction increased due to fluid film thinning by side leakage under milder loading condition. In contrast, under excessively high loading condition, the friction increased as the longitudinal length became shorter, probably due to excessively increased contact pressure.

An experimental and theoretical study to investigate the geometrical shapes of conjunction which is the most suitable for the fluid film formation is necessary.

#### ACKNOWLEDGMENTS

Financial support was given by the Grant-in-Aid for Scientific Research of The Ministry of Education, Science, Sports and Culture, Japan.

#### REFERENCES

1. T.Murakami and N.Ohtsuki, Fluid Film Lubrication - Osborne Reynolds Centenary, ed. by D. Dowson, et al., Elsevier, (1987) 387.
2. N.Ohtsuki and T.Murakami, Proc. Jpn. Int. Trib. Conf. Nagoya, 2 (1990) 713.
3. T.Murakami, JSME International Journal, Series III, 33, 4 (1990) 465.
4. T.Murakami, N.Ohtsuki and H.Higaki, Thin Films in Tribology, ed. by D. Dowson et al. Elsevier (1993) 673.
5. D.D.Auger, D.Dowson and J.Fisher, Proc. Instn. Mech. Engrs., 209, Part H (1995) 73.
6. D.D.Auger, D.Dowson and J.Fisher, Proc. Instn. Mech. Engrs., 209, Part H (1995) 83.
7. T.Sasada, Y.Tsukamoto and K.Mabuchi, Biotribology, (in Japanese), Sangyo-Tosyo(1988) 60.
8. D.Dowson, J.Fisher, Z.M.Jin, D.D.Auger and B.Jobbins, Proc. Instn. Mech. Engrs., 205, Part H (1991) 59.
9. D.Dowson and J.Q.Yao, Proc. Instn. Mech. Engrs., 208, Part J (1994) 43.

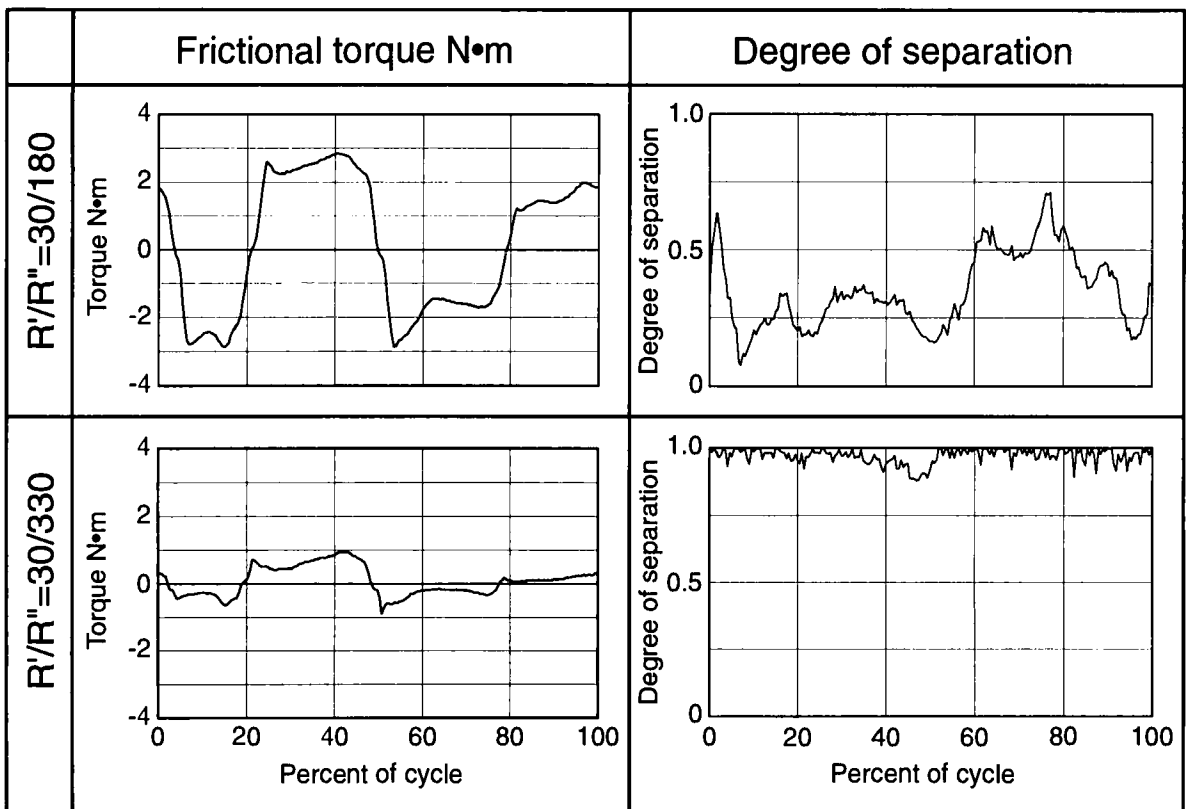


Figure 12. Friction and fluid film formation for two transverse geometries of conjunctions when a peak load is 2kN and lubricant is low viscosity silicone oil.

## Micro-Elastohydrodynamic Squeeze-Film Lubrication of Compliant Layered Surfaces Firmly Bonded to a Rigid Substrate

Z M Jin<sup>a</sup> and D Dowson<sup>b</sup>

<sup>a</sup>Department of Mechanical and Manufacturing Engineering, Bradford University, UK.

<sup>b</sup>Department of Mechanical Engineering, Leeds University, UK.

The micro-elastohydrodynamic lubrication mechanism associated with asperities superimposed upon a compliant layered bearing surface firmly bonded to a rigid substrate under squeeze-film motion has been considered in this study. A simple cosine has been assumed for the roughness profile. Both Reynolds' equation and the elasticity equation have been solved simultaneously and results for the pressure distribution and film profile have been obtained for a wide range of roughness amplitudes and wavelengths. It has been found that the roughness on the compliant layered bearing surface is hardly deformed under squeeze-film motion, particularly in the centre of the contact, where the lubricant flow is minimum, while a slight increase in micro-elastohydrodynamic action occurs near the edge of the contact region. The consequence is that both the minimum film thickness and the squeeze-film velocity are reduced and the pressure distribution is only slightly modified compared with the smooth surface solution. Therefore, it is concluded from this study that micro-elastohydrodynamic action is less pronounced under pure squeeze-film motion than with sliding motion.

### 1. INTRODUCTION

Normal approach, or squeeze-film motion, occurs when two solids separated by a viscous fluid move towards each other. This subject has been extensively reported in the literature because of its practical importance. In many machine components, squeeze-film lubrication is very important in protecting the bearing surfaces during start-up or stopping. In other situations when both the load and the velocity change with time, squeeze-film action is also very important when the velocity becomes zero or the load is extremely high and the sliding velocity is very low. This latter situation can be found in natural synovial joints during walking and squeeze-film lubrication has been shown to play a dominant role in preventing the two articulating surfaces from touching each other (Higginson, 1977).

The analyses of various rigid bearing surfaces under squeeze-film motion have been summarised by Moore (1972). The first analysis considering elastic deformation of the bearing surface was carried out by Christensen (1962) for two cylinders.

An interesting observation was the formation of a pocket in the centre of the contact. Later, Christensen extended his analysis to the squeeze-film lubrication problem between two spheres (Christensen, 1970). The elastohydrodynamic squeeze-film lubrication between two cylinders with relatively low elastic modulus was solved by Herreburgh (1970). An approximate solution to the elastohydrodynamic squeeze-film lubrication problem of both cylindrical and spherical surfaces was obtained by Higginson (1978) using a Grubin-type assumption. Following the same line, Cudworth and Mykura (1980) extended the analysis to a compliant layered bearing surface and good agreement between the simplified theory and experiment was found by these authors.

Another exciting recent development in the field of tribology is micro-elastohydrodynamic lubrication (micro-EHL for short) (Dowson, 1995). It has been shown that significant pressure perturbations can be generated by surface asperities, which in turn largely smooth out the original roughness. Most of the micro-EHL studies reported in the literature



have been concerned with materials of high elastic modulus and sliding motion. Therefore the purpose of the present study is to investigate the micro-elastohydrodynamic lubrication mechanism of a compliant layered bearing surface with low elastic modulus under squeeze-film motion.

**1.1 Notation**

- a Amplitude of roughness;
- A Non-dimensional amplitude of roughness,  $a/h_0$ ;
- b Half dry contact width;
- B Non-dimensional half dry contact width,  $b/d$ ;
- C<sub>s</sub> Dimensionless compliance defined in equation (8),  $\frac{2D(1-2\nu)}{(1-\nu)^2}$ ;
- d Layer thickness;
- D Non-dimensional layer thickness,  $d/R$ ;
- E Elastic modulus ;
- E' Equivalent elastic modulus,  $\frac{2E}{(1-\nu^2)}$ ;
- h Film thickness ;
- $h_{min}$  Minimum film thickness;
- $h_0$  Central film thickness ;
- H Non-dimensional film thickness,  $h/R$ ;
- R Bearing radius ;
- p Pressure ;
- $p_0$  Maximum pressure;
- $\Delta p$  Pressure perturbation due to roughness;
- P Non-dimensional pressure,  $p/E'$  ;
- s Central squeeze-film velocity,  $\frac{dh_0}{dt}$  ;
- S Non-dimensional central squeeze-film velocity,  $\frac{\eta s}{E' R}$  ;
- x Horizontal co-ordinate ;
- $x_e$  exit distance;
- X Non-dimensional horizontal co-ordinate,  $x/d$ ;
- w Load ;
- W Non-dimensional load,  $\frac{w}{E' R}$  ;
- $\eta$  Lubricant viscosity ;
- $\delta$  Elastic deformation ;

- $\delta_0$  Elastic deformation at the centre of the conjunction,  $x=0$ ;
- $\nu$  Poisson's ratio;
- $\lambda$  Wavelength of roughness;
- $\Lambda$  Non-dimensional roughness wavelength,  $\lambda/b$ ;

**2. PHYSICAL MODEL AND THEORETICAL AND NUMERICAL FORMULATION**

The problem considered in the present study is a smooth rigid cylinder moving towards a rough compliant layered bearing surface firmly attached to a rigid substrate as shown in Figure 1.

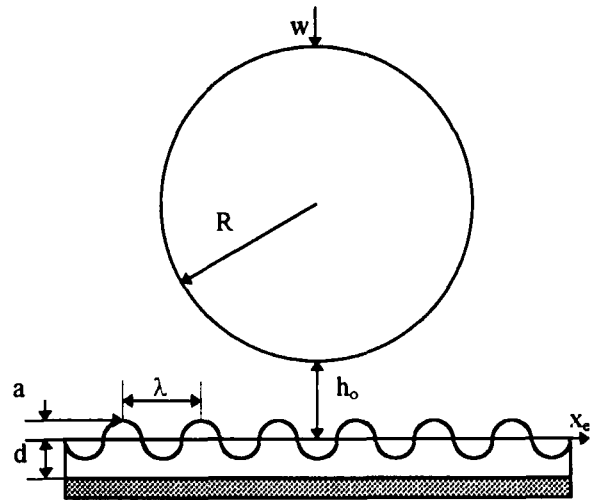


Figure 1 A micro-elastohydrodynamic squeeze-film lubrication model of a smooth rigid cylinder moving towards a rough compliant layered bearing surface.

The governing equations for this model are Reynolds' equation ,

$$\frac{\partial}{\partial x} \left( h^3 \frac{\partial p}{\partial x} \right) = 12\eta \frac{\partial h}{\partial t} \tag{1}$$

and the film thickness equation considering the roughness in the form of a simple cosine function,

$$h = h_0 + \frac{x^2}{2R} + a \cos\left(\frac{2\pi x}{\lambda}\right) + \delta - \delta_0 \quad (2)$$

where  $(\delta)$  is the elastic deformation of the compliant layered surface, calculated relative to the centre of the contact. Therefore,  $(h_0)$  is the central film

thickness. The squeeze-film velocity  $\left(\frac{\partial h}{\partial t}\right)$  is, in

general, not constant within the contact region because of the change of the elastic deformation with time (often referred to as local squeeze-film velocity). In the present study, the local squeeze-film velocity is neglected and the squeeze-film velocity is taken to be that at the centre of the contact ( $x=0$ ,  $h=h_0$ ). Therefore,

$$\frac{\partial h}{\partial t} = \frac{dh_0}{dt} = s \quad (3)$$

Under this assumption, Reynolds' equation can be further simplified to,

$$\frac{dp}{dx} = 12\eta s \frac{x}{h^3} \quad (4)$$

The boundary conditions are

$$\frac{dp}{dx} = 0 \quad \text{at } x=0 \quad (5a)$$

and

$$p = 0 \quad \text{at } x=x_e \quad (5b)$$

where  $(x_e)$  is the exit distance shown in Figure 1. Furthermore, the integration of the pressure distribution must satisfy the specified load

$$w = 2 \int_0^{x_e} p dx \quad (6)$$

The following non-dimensional parameters are adopted in the present study :

$$X = \frac{x}{d}; H = \frac{h}{R}; P = \frac{p}{E}; S = \frac{\eta s}{E R}; W = \frac{w}{E R};$$

$$D = \frac{d}{R}; B = \frac{b}{d}; A = \frac{a}{h_0}; \Lambda = \frac{\lambda}{b}; \quad (7)$$

where  $(b)$  is the contact half width and is estimated from the following equations depending upon Poisson's ratio of the compliant layer (Johnson, 1985);

for Poisson's ratio not equal or close to 0.5

$$B = \left(1.5 \frac{WC_s}{D^2}\right)^{1/3} \quad (8)$$

where

$$C_s = 2D \frac{1-2\nu}{(1-\nu)^2}$$

and for Poisson's ratio equal to 0.5

$$B = \left(60W / D^2\right)^{1/5} \quad (9)$$

Equations (2), (4) and (6) can be written in non-dimensional form as follows :

$$\frac{dP}{dX} = 12SD^2 \frac{X}{H^3}, \quad (10)$$

$$H = H_0 + D^2 \frac{X^2}{2} + AH_0 \cos\left(\frac{2\pi X}{\Lambda B}\right) + \frac{\delta - \delta_0}{R} \quad (11)$$

and

$$W = 2D \int_0^{X_e} P dX \quad (12)$$

A straight forward iteration method was used to solve equations (10) and (11) subject to the boundary conditions represented by equations (5a) and (5b). The solution was started by specifying a central film thickness ( $h_o$ ) and assuming a pressure distribution, which enabled the elastic deformation to be calculated from the displacement coefficients based upon the theoretical work of Meijers (1968). The pressure distribution between two adjacent nodes was assumed to be uniform and the details of the numerical calculation have been published elsewhere (Dowson and Jin, 1990). An initial squeeze-film velocity was also assumed, which, together with the calculated elastic deformation, enabled the solution to the Reynolds' equation to be obtained using a simple central difference scheme. The pressure distribution thus obtained was then integrated using a simple trapezoidal formula and the result was compared with the load specified. If different, the squeeze-film velocity was modified using a bisection routine. After the load had converged, the pressure distribution was then compared with the initial assumed form and if different, a new pressure distribution was assumed based upon both the initially assumed and the correctly calculated pressure distribution with some weighting factors. The number of nodal points taken in the present study was generally between 500 and 1000 and the exit distance was chosen to be 2.5 times the dry contact half width. The computing time required to obtain a convergent solution generally depends on the cases considered. It was found that when the film thickness became comparable with the elastic deformation, a large damping factor had to be introduced in order to stabilise the pressure iteration process. Furthermore, in order to facilitate the iteration, the initial pressure distribution was specified from a convergent solution obtained under less severe conditions. This was found to significantly reduce computing time and to stabilise the pressure iteration process.

### 3. RESULTS AND DISCUSSION

The following parameters were chosen for analysis in the present study :

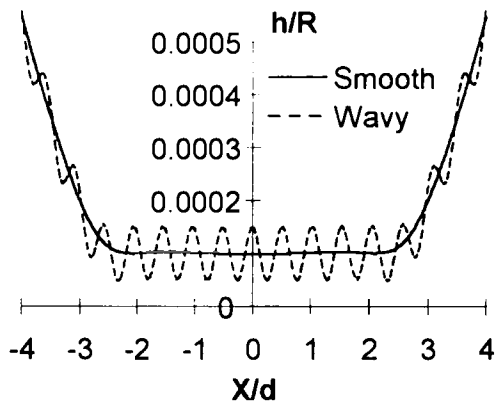
$$W=10^{-3} ; H_o=10^{-4} ; D=10^{-2} ; \nu=0.4$$

with the roughness parameter range

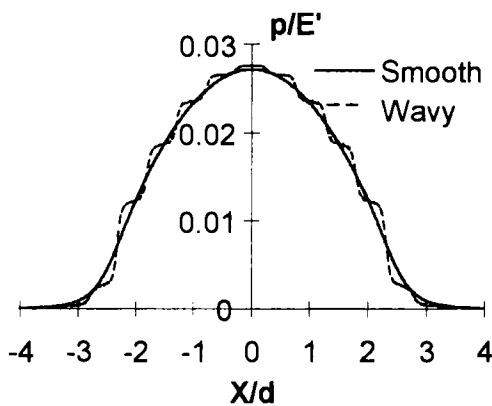
$$\frac{a}{h_o} = 0 \text{ to } 0.8 \text{ and } \frac{\lambda}{b} = 0.0667 \text{ to } 1$$

The results for the squeeze-film velocity, film profile and pressure distribution have been obtained for various combinations of the roughness parameters. Figure 2(a) shows the comparisons of the film profiles between the smooth bearing surface and the rough one, with a ratio of the roughness amplitude to the central film thickness of 0.5 and a ratio of the roughness wavelength to the dry contact half width of 0.2. The corresponding comparison of the pressure distribution is shown in Figure 2(b) and the corresponding pressure perturbation due to the roughness in Figure 2(c). The film profiles, the pressure distributions and the pressure perturbations for various roughness amplitudes are shown in Figures 3(a), 3(b) and 3(c) respectively for a fixed ratio of the roughness wavelength to the dry contact half width of 0.2. The effect of the roughness wavelength is shown in Figures 4(a), 4(b) and 4(c) for a fixed ratio of the roughness amplitude to the central film thickness of 0.5. The effects of the roughness amplitude on the predicted non-dimensional squeeze-film velocities, the minimum film thicknesses and the maximum contact pressures are shown in Figures 5(a), 5(b) and 5(c) and the effect of the roughness wavelength can be seen in Figures 6(a), 6(b) and 6(c).

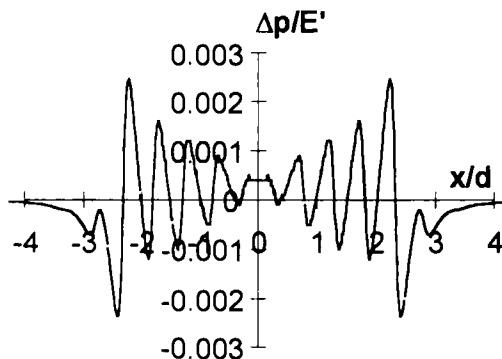
It is clear from Figure 2(a) that the film profile for the smooth surface is almost constant within the contact region, with a slight reduction towards the edge of the conjunction. The formation of the pocket within the centre of the contact, which has well been described for semi-infinite solids, is less pronounced for the layered bearing surface considered in the present study. When roughness is introduced, little deformation of the asperities has been found, particularly in the centre region of the contact. At larger distances from the centre of the conjunction, where the mean lubricant velocity relative to the roughness perturbations is larger, the micro-elastohydrodynamic effect is more pronounced.



(a)



(b)



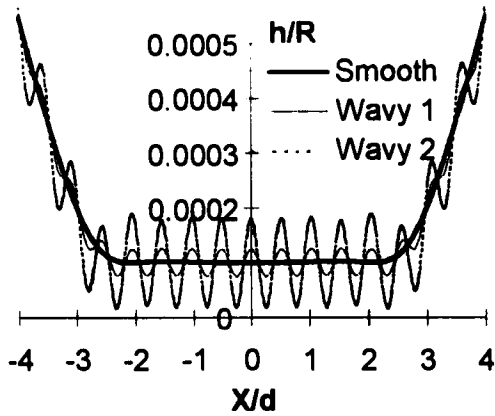
(c)

Figure 2 Comparison of the predicted (a) film profile and (b) pressure distribution between a smooth surface and a wavy surface ( $a/h_0 = 0.5$  and  $\lambda/b = 0.2$ ) and (c) the corresponding pressure perturbations.

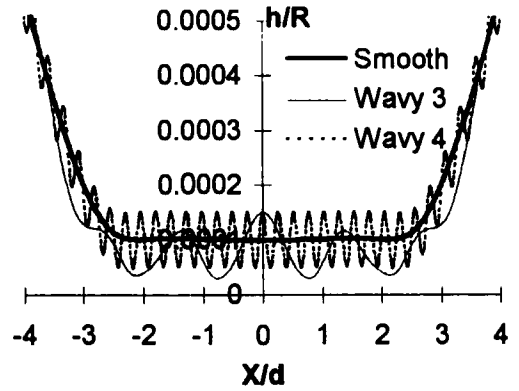
This is significantly different from the features of micro-EHL associated with sliding motion under which the original roughness has been found to be largely smoothed out (Dowson and Jin, 1992). Furthermore, the pressure distribution is only slightly modified due to roughness. It is interesting to note from Figure 2(c) that the pressure perturbation is very small in the centre of the contact, and is slightly increased towards the edge of the contact. This is consistent with the observation that micro-elastohydrodynamic action is mainly associated with the relative flow of the lubricant with respect to the bearing surface (Dowson and Jin 1992). In the centre of the contact, there is an insignificant lateral lubricant flow, while towards the exit from the conjunction, the lubricant flow is increased. However, it is noted that the pressure perturbation generated within the contact region is not sufficient to deform the original roughness to any significant extent.

The effects of the roughness amplitudes on the predicted film profiles, pressure distributions and the pressure perturbations can be seen in Figures 3(a), 3(b) and 3(c). Again it is observed that the original roughness is largely preserved and the pressure distributions are only slightly modified. Although an increase of the roughness amplitude results in an increase in the pressure perturbation, the magnitude of the pressure perturbation is not large enough to cause an appreciable deformation of the original asperities. Figures 4(a), 4(b) and 4(c) show the effects of the roughness wavelength. It is noted that the largest changes in the film profile are predicted for a relatively large roughness wavelength. This can also be seen from the pressure distribution and the pressure perturbation as shown in Figures 3(b) and 3(c). It is clear that micro-elastohydrodynamic action is more pronounced when the roughness wavelength is relatively large.

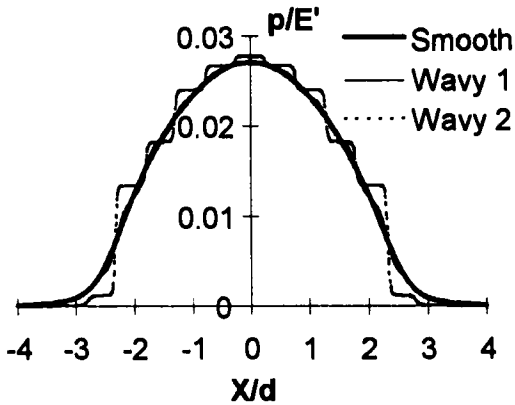
The effect of the roughness amplitude and the roughness wavelength on the predicted squeeze-film velocity, minimum film thickness and maximum pressure can be explained by the fact that the original roughness is largely preserved under squeeze-film motion. An increase in the roughness amplitude results in a partial closing of the gap between the rough and the smooth surface and



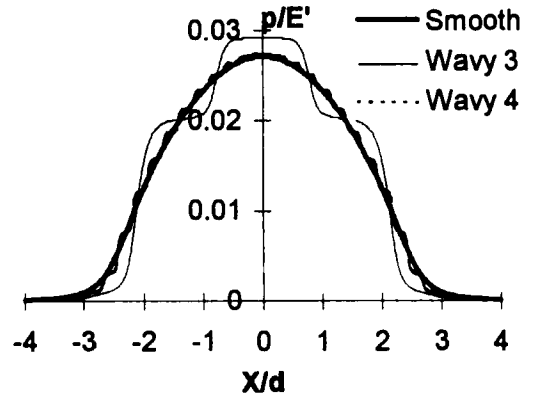
(a)



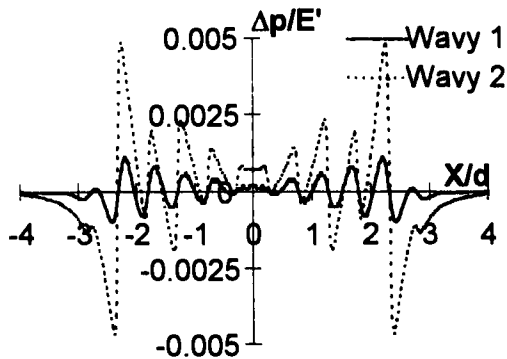
(a)



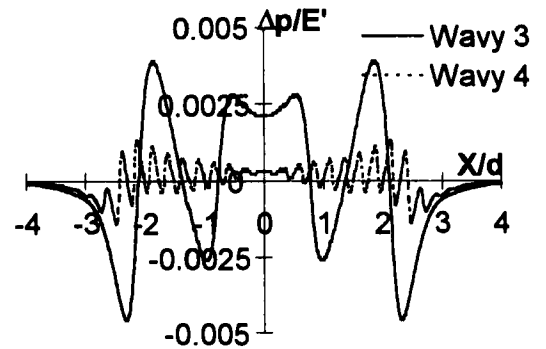
(b)



(b)



(c)



(c)

Figure 3 Effects of the roughness amplitude on the predicted (a) film profile, (b) pressure distribution and (c) pressure perturbation for two wavy surfaces (Wavy 1 :  $a/h_0 = 0.2$ ,  $\lambda/b=0.2$ ; Wavy 2 :  $a/h_0 = 0.8$ ,  $\lambda/b=0.2$ )

Figure 4 Effects of the roughness wavelength on the predicted (a) film profile, (b) pressure distribution and (c) pressure perturbation for two wavy surfaces (Wavy 3 :  $a/h_0 = 0.5$ ,  $\lambda/b=0.5$ ; Wavy 4 :  $a/h_0 = 0.5$ ,  $\lambda/b=0.1$ )

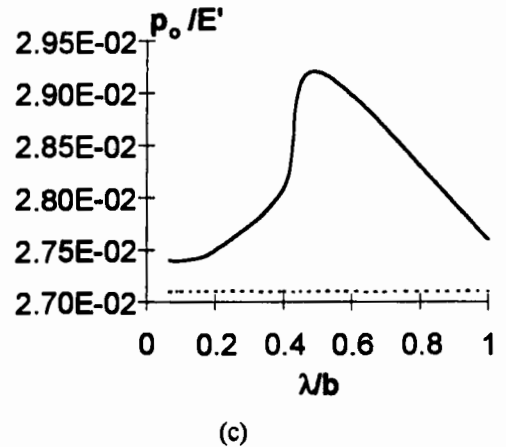
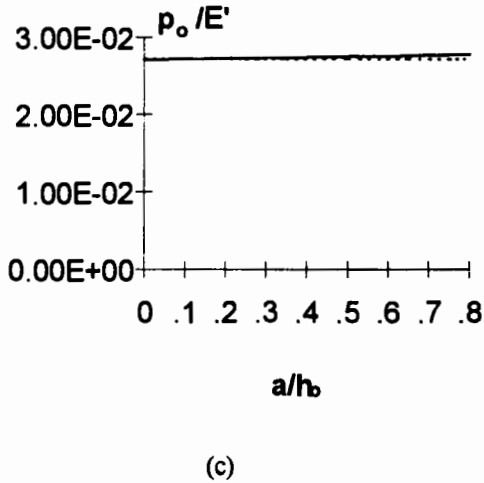
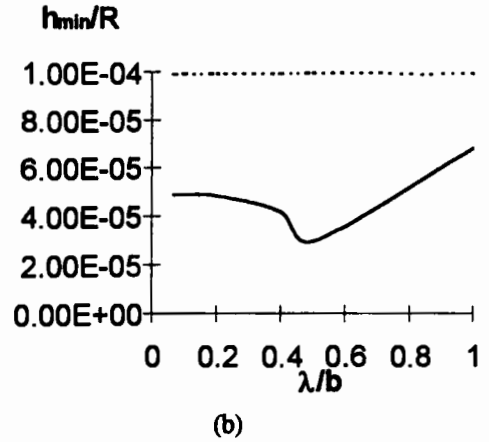
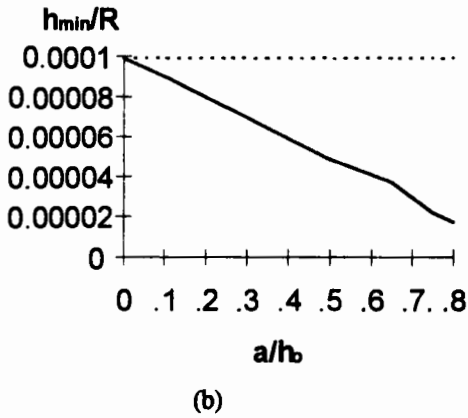
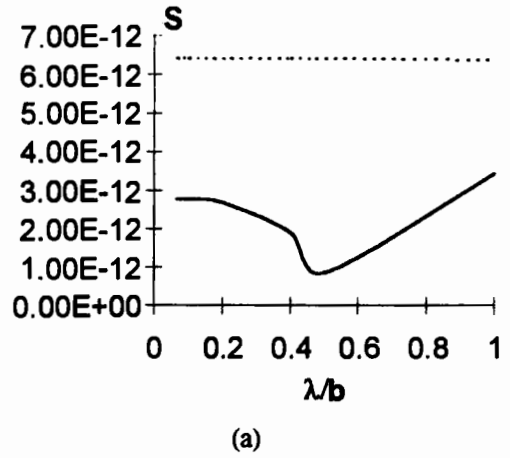
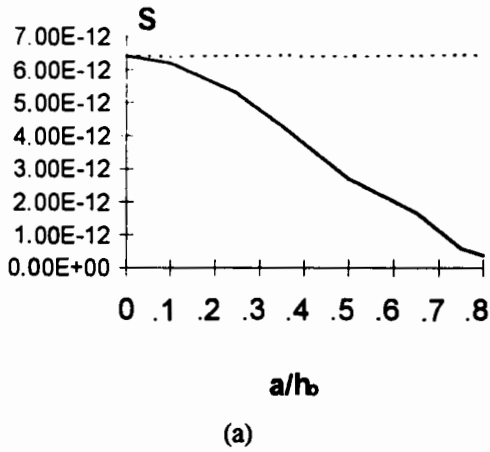


Figure 5 Comparison of the predicted non-dimensional (a) squeeze-film velocity, (b) minimum film thickness and (c) maximum pressure between a smooth surface (dashed line) and a wavy surface (solid line) with various amplitudes ( $\lambda/b = 0.2$ )

Figure 6 Comparison of the predicted non-dimensional (a) squeeze-film velocity, (b) minimum film thickness and (c) maximum pressure between a smooth surface (dashed line) and a wavy surface (solid line) with various wavelengths ( $a/h_0 = 0.2$ )

hence in a decrease in the squeeze-film velocity as seen in Figure 5(a) and an increase in the squeeze-film time. The minimum film thickness is significantly reduced compared with the smooth surface solution. It is possible to estimate the minimum film thickness by simply subtracting the roughness amplitude from the minimum smooth film thickness for the conditions considered in the present study. Furthermore, a slight increase in the predicted maximum pressure is found as the roughness amplitude increases. The predicted squeeze-film velocity is also significantly affected by the wavelength of the roughness profile in relation to the contact half width, reaching a minimum value close to ( $\lambda/b = 0.5$ ) as shown in Figure 6(a). It is also interesting to note that when the roughness wavelength is reduced, the predicted squeeze-film velocity approaches an asymptotic value. Similar observations can be made for both the minimum film thickness and the maximum pressure as shown in Figures 6(b) and 6(c).

The roughness amplitude considered in the present study is of a similar order of magnitude to the central film thickness. When either the roughness amplitude increases or the central film thickness decreases during the squeeze-film process, it can be expected that micro-EHL action associated with asperities will increase. However, it is unlikely that a significant deformation of the asperities can occur and this may result in the direct contact of the asperities. The practical implication of this finding can be related to the lubrication of synovial joints. It has been shown that squeeze-film motion between articular cartilage and a glass surface results in the formation of large pools of entrapped synovial fluid with a high concentration of hyaluronic acid in the so called "boosted lubrication" theory (Walker et al 1968). The present study provides further theoretical support for this theory.

#### 4. CONCLUSIONS

The micro-elastohydrodynamic lubrication squeeze-film problem of a compliant layered bearing surface firmly bonded to a rigid substrate has been solved in this study. The following conclusions can be drawn :

- The original roughness under squeeze-film motion has been found to persist, particularly in the centre of the contact region, with a slight increase in the micro-elastohydrodynamic action being found towards the edge of the conjunction.
- The effect of the roughness under squeeze-film motion has been found to reduce both the minimum film thickness and the squeeze-film velocity.
- The present study has provided further theoretical support for the "boosted lubrication" theory proposed for synovial joints.

#### REFERENCES

- Christensen, H. (1962). Oil Film in a Closing Gap, Proc. of the Royal Society, A266, 312-328.
- Christensen, H. (1970). Elastohydrodynamic Theory of Spherical Bodies in Normal Approach, Trans ASME., J. Lubric. Technol., 92(1), 145-154.
- Cudworth, C.J. and Mykura, J.F. (1980). Normal Approach of a Cylinder Towards an Elastic Layer, J. of Mech. Eng. Sci., 22(2), 65-70.
- Dowson, D. (1995). Elastohydrodynamic and Micro-elastohydrodynamic Lubrication, Wear, 190, 125-138.
- Dowson, D. and Jin, Z. M. (1990). The Influence of Elastic Deformation upon Film Thickness in Lubricated Bearings with Low Elastic Modulus Coatings. in Mechanics of Coating, Proc. of 16th Leeds-Lyon Symp. on Tribology (Eds D. Dowson, C. M. Taylor and M. Godet), 263-270 (Elsevier, Amsterdam).
- Dowson, D. and Jin, Z. M. (1992). Microelastohydrodynamic Lubrication of Low-elastic-modulus Solids on Rigid Substrates, J. Phys. D: Appl. Phys., 25, A116-A123.
- Herreburgh, K. (1970). Elastohydrodynamic Squeeze Films Between Two Cylinders in Normal Approach, Trans ASME., J. Lubric. Technol., F92, 292-302.

Higginson, G.R. (1977). Elastohydrodynamic Lubrication of Synovial Joints, Proc. Instn. Mech. Engrs., 191, 33-77.

Higginson, G.R. (1978). Squeeze Films Between Compliant Solids, Wear, 46, 387-395.

Johnson, K.L. (1985). Contact Mechanics, Cambridge University Press, 1985.

Meijers, P. (1968). The Contact Problem of a Rigid Cylinder on an Elastic Layer, Appl. Sci. Res., 18(5), 353-383.

Moore, D.F. (1972). Friction and Lubrication of Elastomers, Pergamon Press.

Walker, P. S., Dowson, D., Longfield, M. D. and Wright, V. (1968). Boosted Lubrication in Synovial Joints by Fluid Entrapment and Enrichment. Ann. Rheum. Dis., 27(6), 512-520.



## The Adaptive Multimode Lubrication in Knee Prostheses with Artificial Cartilage during Walking

T. Murakami<sup>a</sup>, Y. Sawae<sup>a</sup>, H. Higaki<sup>a</sup>, N. Ohtsuki<sup>b</sup> and S. Moriyama<sup>a</sup>

<sup>a</sup> Department of Intelligent Machinery and Systems, Faculty of Engineering, Kyushu University, Hakozaki, Higashi-ku, Fukuoka, 812-81 Japan

<sup>b</sup> Graphic Science, Faculty of Engineering, Kyushu University, Ropponmatsu, Chuo-ku, Fukuoka, 810 Japan

The lubricating performance of total knee prosthesis models with compliant layer as artificial cartilage was evaluated and discussed from the viewpoint of adaptive multimode lubrication. The minimum film thickness and inclination of rubbing surface during walking were estimated by numerical analysis based on the plane inclined surface model for polyvinylalcohol (PVA) hydrogel and polyurethane. The numerical results show the effectiveness of softer material on fluid film formation during walking, although surface inclination during swing phase is larger for polyurethane than PVA hydrogel. The actual fluid film formation in knee prostheses during walking was examined by measurement of degree of separation by electric resistance method and frictional force in simulator tests. Under walking condition lubricated with lubricants of appropriate viscosity, considerable elastohydrodynamic film was formed corresponding to numerical analysis. Under thin film conditions lubricated with low viscosity lubricants where significant local direct contact occurred between rubbing surfaces due to breakdown of fluid film, the addition of proteins remarkably decreased friction and suppressed stick-slip for PVA, but increased friction for polyurethane. The addition of phospholipid liposomes had an effect in reducing of friction after repetition of rubbing process in walking motion. The adsorbed film formation of synovia constituents on stainless steel plate was observed by atomic force microscopy.

### 1. INTRODUCTION

For most of the clinical application of total joint replacements particularly for diseased hip and knee joints, material combinations of ultrahigh molecular weight polyethylene (UHMWPE) and corrosion-resistant metals or bioceramics have been used as bearing surfaces. Recent considerable progress in development of new implant materials, new design including fixation methods, manufacturing, and operation under sterile condition has improved clinical results. However, in certain cases, serious tribological problems such as wear and loosening have occurred. This is attributable to the poorness of the fluid film formation in existing joint prostheses, which results in high wear and high friction. Wear debris attacks the living tissue inducing the loosening of joint prostheses [1, 2].

Most of existing joint prostheses appear to operate in mixed lubrication mode. Particularly, in many

kinds of knee prostheses with low geometrical congruity, the sufficient fluid film is unlikely to be formed to prevent the direct contact between femoral and tibial components, as suggested by the authors (3-7).

To attain long endurance of joint prostheses, it is required to improve the lubricating film formation in various daily activities. Both the geometrical optimum design for combinations of polyethylene and metal [8-10] and application of compliant materials such as silicone rubber, polyurethane and hydrogel [3-7, 11-21] are likely to improve the fluid film formation. For the latter with compliant layer, the design considerations for cushion form bearing are discussed on lubrication mechanisms and contact mechanics [14-18]. Furthermore, it is pointed out that porous hydrogels gave lower friction than non-porous polyurethane or silicone rubber at start up or after breakdown of fluid film [16, 20, 21].

The authors proposed the design concept of the

adaptive multimode lubrication for joint prostheses (5-7). This design concept aims to realize the application of lubrication mechanisms in natural synovial joints to the total replacement joints. In natural joints, the macro- and micro-soft-EHL mechanisms appear to play main lubricating roles in daily activities such as walking. Under severer thin film conditions, various supplemental lubrication modes such as weeping, boundary and gel-film lubrication mechanisms seem to synergistically operate to protect articular cartilages. This lubrication mechanism is called as the adaptive multimode lubrication [5-7, 22].

In this paper, firstly the recent researches on the lubrication modes in natural synovial joints were shortly reviewed from both the experimental and theoretical viewpoints. Next, the lubricating performance of total knee prosthesis models with compliant layer as artificial cartilage was evaluated by numerical analysis and simulator tests.

The minimum film thickness and inclination of rubbing surface during walking were estimated by the plane inclined surface (PI) model proposed by Medley et al. (23, 24) as simplified elastohydrodynamic analysis for soft layer of polyvinylalcohol (PVA) hydrogel or polyurethane. The effectiveness of soft material on fluid film formation was discussed. The changes in rubbing surface inclination during walking were examined. Then, the measurement of fluid film formation and frictional force were carried out in simulator tests. As lubricants, sodium hyaluronate solutions were used with or without serum proteins and/or phospholipid. The difference in frictional behaviours was discussed from the viewpoint of adaptive multimode lubrication on the basis of the observation of adsorption of synovia constituents in tapping mode in liquid by atomic force microscopy (AFM).

## 2. ADAPTIVE MULTIMODE LUBRICATION IN NATURAL SYNOVIAL JOINTS

Concerning the excellent lubrication mechanism of the natural synovial joints with very low friction and long durability, various proposals (5) such as hydrodynamic (rigid, isoviscous), elastohydrodynamic, microelastohydrodynamic, weeping, biphasic or triphasic, boosted, mixed, elastomixed, gel film and boundary lubrication have been proposed. As pointed out by Dowson [25], Unsworth et al. [26], Sasada [27], Murakami [5] and Ikeuchi [28], not

single mode but multimode lubrication probably operates in various daily activities. Stachowiak et al. [29] paid special attention to the relative importance of synovial fluid and cartilage, and indicated the existence of a secondary lubrication mechanism at the cartilage surface layer when synovial fluid is unable to prevent contact between cartilage surfaces.

As discussed in detail by Murakami (5), the elastohydrodynamic film formation, which is enhanced by the elastic deformation of articular surfaces and viscous effect of synovial fluid, appears to play the main role in preserving both low friction and low wear during walking. Under thin film conditions, the various supplemental lubrication mechanisms are likely to be capable of protecting the rubbing surfaces depending on the severity of operating conditions. As described above, this lubrication mechanism is denoted as the adaptive multimode lubrication.

As discussed later, fluid film formation changes according to operating condition during walking in natural synovial joints with compliant articular surfaces and lubricated with synovial fluid. The flattening of initial asperities of articular cartilage in conjunction zone indicated by micro-EHL analyses [30, 31] appears to achieve the fluid film lubrication during walking. In diseased joint with low viscosity synovia, however, the local direct contact may occur even during walking. At starting motion after long standing, some local direct contact may occur even in normal natural joints. Therefore, the protecting performance of adsorbed film or gel-film on articular cartilage becomes important.

The authors [22, 32-34] evaluated the protecting role of proteins and phospholipids by pendulum tests of pig shoulder joints. Coefficient of friction was estimated from the damping of amplitude. Typical experimental results on effect of protein and phospholipid on friction in natural synovial joints are shown in Fig.1. Although the detail is described in elsewhere [34], test condition under mixed lubrication regime was selected, i.e., immediately after loading of 100N lubricated with saline solution of 0.2 wt% sodium hyaluronate (HA, molecular weight =  $9.6 \times 10^5$ ) as low viscosity lubricant.

First, the pendulum tests were carried out by using fresh joints lubricated with HA solutions, in which low friction coefficient of 0.0075 as average was obtained. After the first tests, the joints were rinsed with the saline solution of 10 wt% polyoxyethylene p-t-octylphenyl ether (Triton X-100),

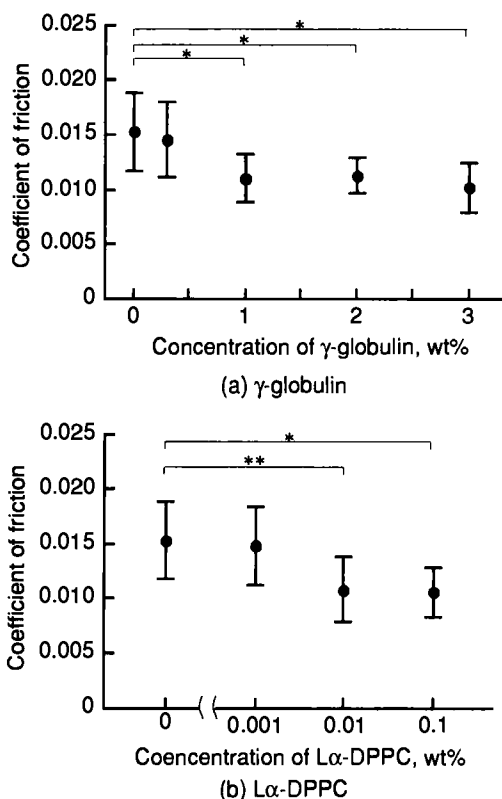


Figure 1. Lubricating effects of addition of  $\gamma$ -globulin and  $L\alpha$ -DPPC in pendulum tests of pig shoulder joints ( $N=6$ , Error bars indicates S.D., \* $p<0.005$ , \*\* $p<0.01$ )

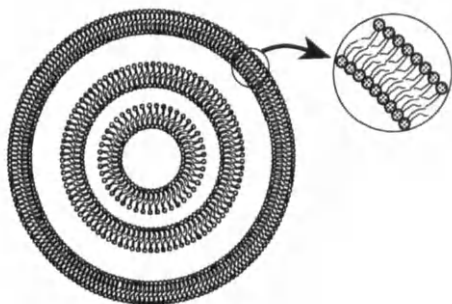


Figure 2. Multilamellar liposome of  $L\alpha$ -DPPC

which is highly surface active non-ionic surfactant to remove the adsorbed film on the articular cartilage surfaces, in 30 min in ultrasonic bath and then rinsed again with saline in 30 min. The removal of adsorbed film mostly composed of phospholipids was confirmed by significant reduction in contact angle occurring when a droplet of

water was placed upon dried cartilage surfaces [35]. The change from hydrophobic to hydrophilic surface was observed. Then, the second pendulum tests were carried out lubricated with HA solutions. The second tests showed significant increase in friction as average coefficient of friction of about 0.015, which indicates the loss of protection by adsorbed film under mixed lubrication regime.

After the second tests for 0.2 wt% HA solution, the joints were rinsed with saline and then the third pendulum tests were conducted under lubricated condition with new lubricants such as HA solutions with and without serum proteins and liposome of phospholipid  $L\alpha$ -DPPC (dipalmitoyl phosphatidylcholine). The liposome diameter as multilamellar vesicles of  $L\alpha$ -DPPC in Fig.2 has the range of 0.1 to 0.5  $\mu\text{m}$ . As shown in Fig.1, 1.0 wt%  $\gamma$ -globulin and 0.01 wt%  $L\alpha$ -DPPC exhibit the effectiveness in protecting role in natural synovial joints. It is noticed that  $L\alpha$ -DPPC of similar concentration to that in human joint is sufficiently effective, while higher concentration of  $\gamma$ -globulin is needed. And, even 3.0 wt% serum albumin was little valid.

These results support the boundary lubricating ability of phospholipids, particularly oligolamellar one proposed by Hills et al. [35, 36]. However, not only phospholipids but proteins or lubricating glycoprotein [37, 38] appear to function as effective boundary lubricants.

In the authors' studies [39, 40] on reciprocating friction tests for articular cartilage and Langmuir-Blodgett films on glass plate, mixed LB films composed of  $L\alpha$ -DPPC and  $\gamma$ -globulin exhibited superior frictional behaviour to LB films of  $L\alpha$ -DPPC alone.

The boundary lubricating ability of proteins and phospholipid to artificial cartilage in knee prostheses is examined later from the viewpoint of adaptive multimode lubrication.

### 3. NUMERICAL ANALYSIS OF FLUID FILM FORMATION

#### 3.1 Minimum film thickness based on PI model

To estimate the minimum fluid film thickness in cylindrical knee prostheses, PI (plane inclined surface) model proposed by Medley et al. [23, 24] was applied. Equation (2) was derived from Reynolds equation (1) for the cylindrical model of equivalent radius of  $R$  with soft layer thickness  $t_s$  as shown in Fig.3.

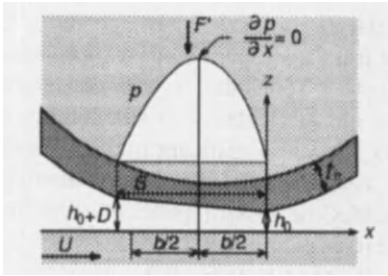


Figure 3. Plane inclined surface model

$$\frac{\partial}{\partial x} \left( h^3 \frac{\partial p}{\partial x} \right) = 12\eta \left( \frac{\partial h}{\partial t} + \frac{U}{2} \cdot \frac{\partial h}{\partial x} \right) \quad (1)$$

$$\frac{dh_0}{dt} = \frac{D^3 F' (2h_0 + D)}{12\eta B^3 \left\{ 2D - (2h_0 + D) \ln \left( 1 + \frac{D}{h_0} \right) \right\}} + \frac{D}{B} \cdot \frac{U}{2} \quad (2)$$

Changes in minimum film  $h_0$  during walking was obtained based on the method by Gladstone and Medley [24].  $B$  and  $D$  were determined based on steady state conditions. When  $U$  is nearly zero, Eq. (2) is reduced to

$$\frac{dh_0}{dt} = -\frac{F' h_0^3}{\eta B^3} \quad (3)$$

Here,

- $b$  : dry contact length
- $B$  : bearing length
- $D$  : bearing inclination
- $F'$  : load per unit width
- $h$  : film thickness
- $h_0$  : minimum film thickness
- $p$  : fluid pressure
- $t$  : time
- $U$  : sliding velocity
- $\eta$  : viscosity
- $x, z$  : coordinate

### 3.2 Changes in minimum film thickness and inclination of plane surface during walking

The changes in minimum film thickness and inclination  $B/D$  in cylindrical knee prostheses with flat compliant layer are shown in Fig.4. Equivalent radius of cylindrical surface is 30 mm, and soft layer thickness is 2 mm and lubricant viscosity is 0.01 Pa·s. Two values of elastic modulus of 1.0 and 40 MPa approximately correspond to PVA hydrogel and polyurethane, respectively. As described in

Figure 4. Changes in fluid film formation and surface inclination in knee prostheses with artificial cartilage during walking

previous studies [3, 5-7, 21], the fluid film gradually decreases during stance phase and then recovers to higher level during swing phase. The effect of the inclination of plane surface is observed at high speed and low load conditions during swing phase. Therefore, mainly squeeze film action can contribute to preserve fluid film during stance phase in knee joint. Similar variations of the transient film thickness with time are predicted by EHL analysis for ankle and hip joints [40]. Furthermore, It is noted that the film thickness is thicker for PVA than polyurethane, although the inclination of polyurethane is larger than PVA. PVA shows about three times higher film thickness than polyurethane due to soft-EHL effect.

It is required to analyze the fluid film formation by micro-EHL theory for compliant articular surfaces with considerable asperities. Dowson and Jin [30] pointed out that the significant flattening of compliant surface asperities enables to avoid direct contact between rubbing surfaces during walking. In present study, it is very difficult to measure actual surface profiles of PVA hydrogel layer containing high content of water, although its image by scanning electron microscopy at low vacuum

environment suggests the existence of asperities of several  $\mu\text{m}$ . So, the occurrence of direct contact under walking condition is discussed based on experimental results.

4. SIMULATOR TESTS

4.1 Specimens and lubricants

Two kinds of geometric designs for knee prostheses were prepared as shown in Fig.5. As femoral component, the cylindrical stainless steel (SUS316, JIS) specimen of 30 mm radius was used. Surface roughness  $R_{ms} = 0.02 \mu\text{m}$ . As tibial components, flat type and concave type were used.

As soft layer supported by PMMA, PVA hydrogel and polyurethane sheet were used.

PVA hydrogel specimen was prepared by the

repeated freezing-thawing method [42]. Average degree of polymerization is 2000 and average degree of saponification is 98.5~99.4 mol%. The elastic modulus  $E$  depends on equivalent water content (EWC). In this study, two kinds of PVA hydrogel of high water content different in thickness ( $EWC=79\%$ ,  $E=0.8 \text{ MPa}$  for  $t=3 \text{ mm}$ ,  $E=1.1 \text{ MPa}$  for  $t=2 \text{ mm}$ ) were used.

For comparison, medical grade poly(ether)-polyurethane (Pellethane,  $E = 37 \text{ MPa}$ ) was used. The sheet has surface roughness of  $R_{ms} = 0.4 - 0.5 \mu\text{m}$ .

As lubricants, saline solutions of two kinds of sodium hyaluronate (HA-1: $M$  (molecular weight) =  $9.6 \times 10^5$ , HA-2: $M=1.95 \times 10^6$ ) were used. The viscous property measured by cone/plate viscometer is shown in Fig.6. In some tests, silicone oils were used.

To examine the effect of proteins and phospholipids on friction and lubrication, human serum albumin and  $\gamma$ -globulin, and liposome of  $L\alpha$ -DPPC were added to HA solutions. DPPC was selected as predominant phospholipid in synovial fluids and on cartilage surfaces. Liposomes of  $L\alpha$ -DPPC were prepared by the method by Bangham et al. [43]. Sizes of the diameter of liposomes observed by negative staining method in transmission electron microscopy were distributed from 0.1 to 0.5  $\mu\text{m}$ .

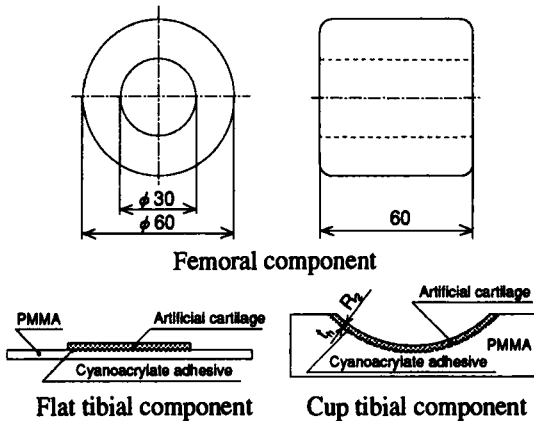


Figure 5. Cylindrical knee prostheses

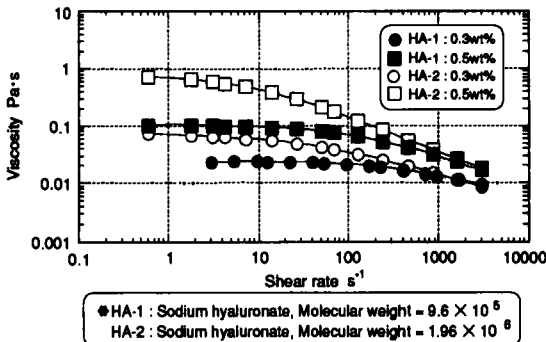


Figure 6. Viscous property of HA solutions

4.2 Experimental methods in simulator

A walking motion was simulated by using two types of knee joint simulators. Detailed structure of old type was described in the previous papers [3-7]. New type is shown in Fig.7. Both types have similar hydraulic control system except some

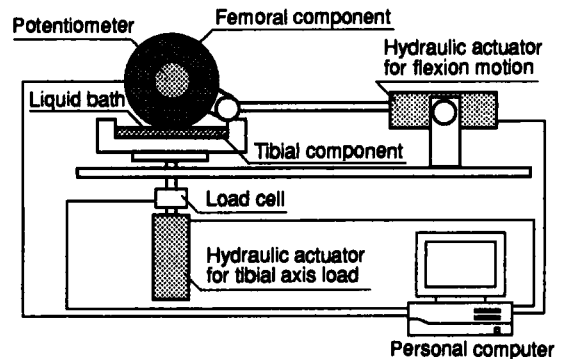


Figure 7. Knee joint simulator

mechanical components. Flexion-extension motion of a femoral component and time-dependent tibial axis load were applied by the personal computer controlled hydraulic system. In these tests at room temperature, the walking period is 1 or 2 s, and the flat tibial component was fixed to holder but anterior-posterior movement was restricted by friction for the concave tibial components.

To examine in detail the frictional behaviour, the torque of upper driving axis was measured by using strain gauges attached to the shaft. This torque value in new simulator approximately corresponds to frictional torque, since the torque due to the offset loading is negligible and inertia effect is scare for concentric cylindrical femoral component. The lubricating film formation during walking motion was examined by the electric resistance method. The extent of fluid film formation with conductive PVA hydrogel was evaluated by the degree of separation, which is defined as the ratio of measured voltage to the applied voltage of 100 mV (degree of separation is 1 : full separation, degree of separation is 0 : contact). For PVA hydrogel layer with low electric resistance, the degree of separation = 0 was corrected as the corresponding voltage for unlubricated condition.

**4.3 Observation of adsorbed film by AFM**

To investigate the influence of adsorbed film on stainless steel on frictional behaviour, the adsorbed film formation on stainless steel flat surfaces was observed in saline by AFM as fluid tapping mode after immersion in test fluid for 5 min.

**5. RESULTS AND DISCUSSIONS ON SIMULATOR TESTS**

**5.1 Fluid film formation in knee prosthesis with PVA hydrogel layer**

As described above, considerable fluid film is likely to be formed due to soft-EHL in knee prostheses with compliant layer during walking.

The example of fluid film measurement by electric resistance method for sliding pair of conductive PVA hydrogel and stainless steel in old type of knee joint simulator is shown in Fig.8 for lubricated condition with silicone oil of 0.13 Pa·s. In both numerical analysis based on PI model and measured value for degree of separation, fluid film gradually decreases during stance phase and then recovers to thicker level during swing phase. Some

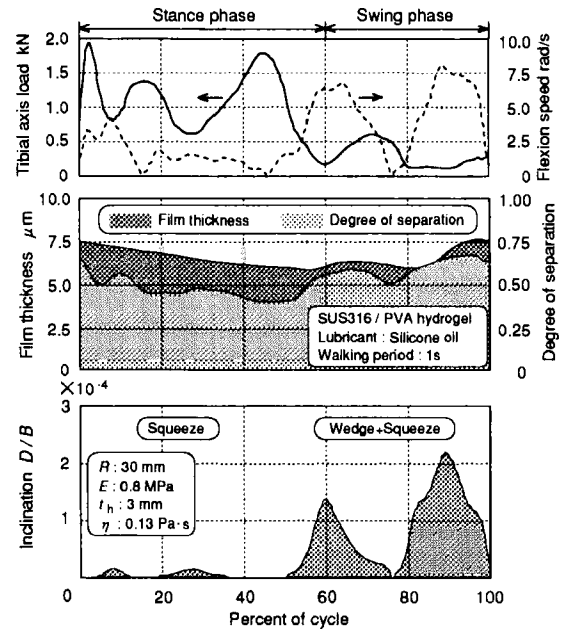


Figure 8. Fluid film formation in knee prosthesis with PVA hydrogel layer during walking

variations in degree of separation during stance phase are considered to be caused by the actual surface profile changes and the occurrence of local contacts. As suggested from changes in inclination of plane surface, the squeeze film action plays main role during stance phase, and the wedge or entraining action becomes important during swing phase for fluid film formation. In the knee prostheses with compliant layer, considerable fluid film appears to be formed with lubricants of medium viscosity. However, under lubricated conditions with lower viscosity lubricants, the significant direct contact between rubbing surfaces may occur. It is difficult to evaluate the quantitative severity by the degree of separation, since the degree of separation is sensitive for slight local contact and electric conductivity of PVA hydrogel changes depending on loading conditions. So, the frictional behaviour was investigated by measurement of torque of femoral axis in new type of knee joint simulator.

**5.2 Frictional behaviour in knee prostheses with polyurethane and PVA hydrogel layer**

Changes in frictional torque in cylindrical knee prostheses with flat tibial components with soft layer

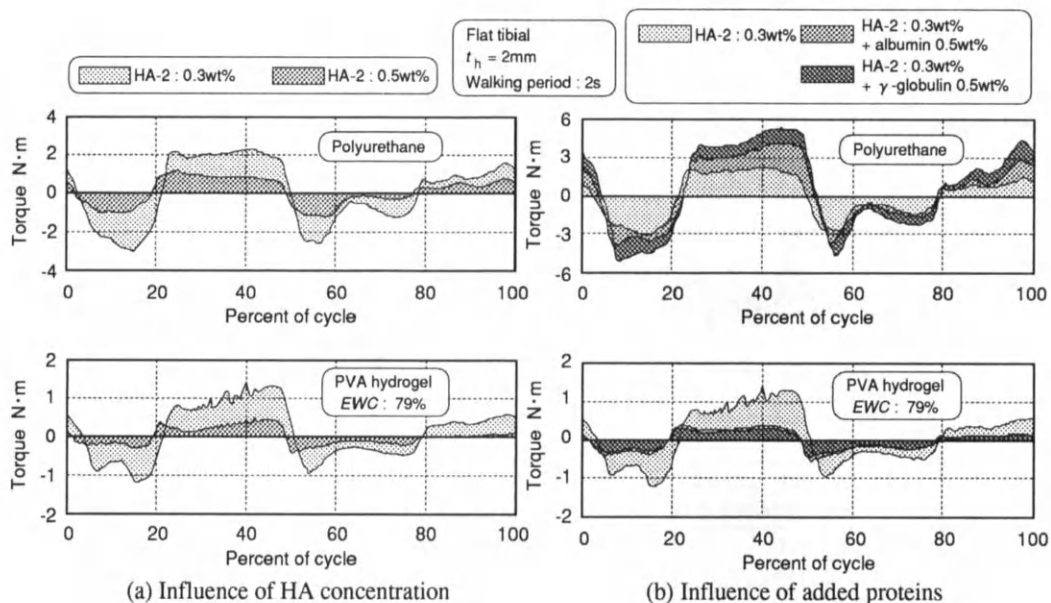


Figure 9. Influence of HA concentration and addition of proteins on frictional behaviours of cylindrical knee prostheses with polyurethane or PVA layer during walking

of polyurethane or PVA hydrogel are shown in Fig.9. Figure 9(a) indicates the influence of HA concentration on frictional behaviour. Higher HA concentration corresponds to higher viscosity. The lubrication regimes under these operating conditions seem to be belonged to mixed lubrication. So, with increasing concentration of HA, or with increasing viscosity, friction is reduced for both polyurethane and PVA hydrogel. Furthermore, PVA hydrogel layer exhibits significantly lower friction than polyurethane, as suggested by calculated thicker film thickness in Fig.4, although the estimation for the flattening of surface asperities based on micro-EHL analysis and effective viscosity at high shear rate is required for exact evaluation. For PVA lubricated with 0.3 wt% HA, considerable stick-slip was observed during stance phase. This stick-slip was attenuated by increasing HA concentration.

Figure 9(b) shows the influence of addition of serum proteins in HA solutions on frictional behaviour. It is noticed that there are remarkable difference in influence of proteins between polyurethane and PVA hydrogel. The addition of albumin or  $\gamma$ -globulin significantly decreases frictional value and diminishes stick-slip phenomena

in PVA hydrogel. In contrast, the addition of proteins considerably increased friction for polyurethane. Particularly,  $\gamma$ -globulin affects strongly. These results exhibit the superiority of lubricating property for PVA hydrogel layer in human body environment.

The difference in frictional behaviour is considered to be caused by difference in lubrication mode. So, frictional behaviour was expressed as the form of coefficient of friction in Fig.10. It is confirmed that better lubrication is achieved in knee prosthesis with PVA layer lubricated with HA solution containing protein. Low coefficient of friction of about 0.01 is maintained during high loading stance phase. This means that the adsorbed film of proteins can effectively protect the rubbing surfaces. Similar low frictional behaviour was observed in PVA hydrogel lubricated with pig synovial fluid [20]. On the other hand, for polyurethane layer, the severity increases with addition of proteins. This may be brought about by obstruction to entrainment of fluid flow or interaction due to entanglement of protein molecules under extremely thin film condition.

AFM images in Fig.11 show the changes in

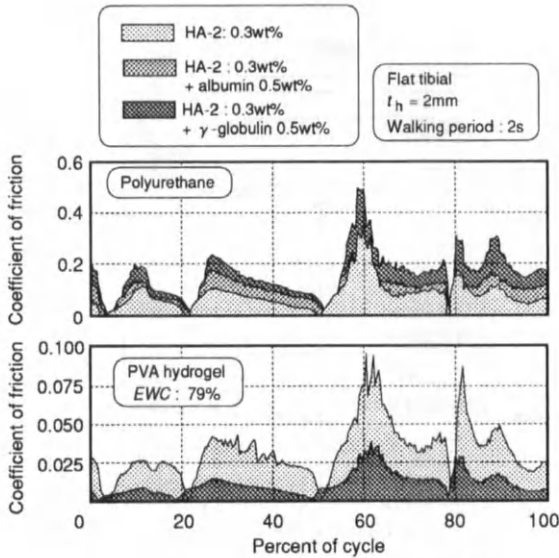


Figure 10. Influence of proteins on frictional behaviour in knee prostheses with compliant layer

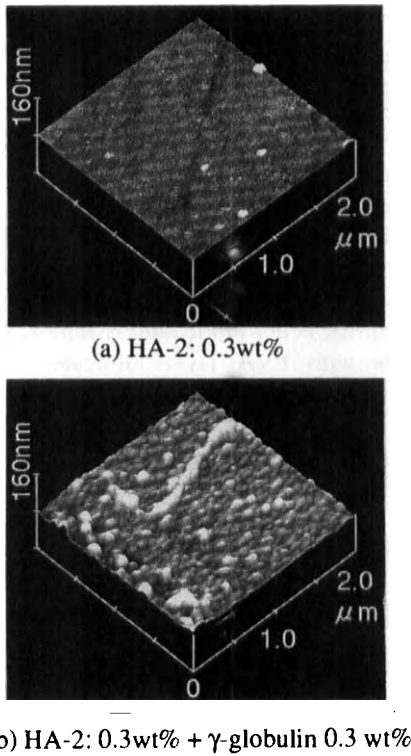


Figure 11. AFM images of adsorbed film on stainless steel

adsorbed film on stainless steel plate with addition of  $\gamma$ -globulin to HA solution. Globular molecules of  $\gamma$ -globulin appears to adsorb on stainless steel surface, although some hyaluronate molecules may adsorb on surface. These images correspond to adsorbed film on non-contact zone. The rubbing process probably changes the adsorbed state. In this test, the actual femoral surface could not be observed due to excessive size of specimen in this AFM system. However, adsorbed film similar to images in Fig.11 is considered to induce the difference in frictional behaviour between polyurethane and PVA hydrogel, depending upon difference in lubrication mode.

**5.3 Influence of geometric congruity on frictional behaviour in knee prostheses with PVA hydrogel**

Although PVA hydrogel shows the possibility of excellent candidate biomaterial as artificial cartilage, geometrical modification is required to reduce contact stresses for longer durability. So, the influence of geometrical congruity on friction characteristics was investigated by using cup tibial components.

As shown in Fig.12, the better geometrical congruity reduce friction for HA solutions with and without protein. For HA solution without protein, the improvement in frictional behaviour brought about by enhanced fluid film formation is remarkable and stick-slip is attenuated. For HA solution

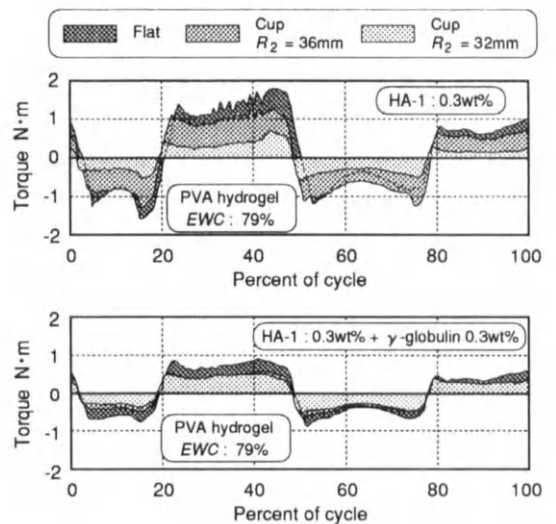


Figure 12. Influence of geometrical congruity on frictional behaviour



with  $\gamma$ -globulin, friction is a little decreased with increase in congruity, since the addition of protein shows low friction even for flat tibial component. In better geometrical congruity, fluid film lubrication plays main role and the influence of adsorbed film is attenuated.

#### 5.4 Effect of protein and phospholipid on frictional behaviour for PVA hydrogel

As mentioned above, proteins were effective particularly for PVA hydrogel and liposomes of phospholipid were effective for natural articular cartilage. Therefore, the effect of protein and phospholipid was examined in simulator tests.

Figure 13 shows the frictional behaviours in cylindrical knee prostheses of flat tibial component with PVA hydrogel layer. In this case, 7 runs of 30 cycles were carried out for each condition. The results for 16th cycle in the first and 3rd runs are shown. As shown above,  $\gamma$ -globulin exhibits remark-

able and steady improvement in frictional behaviour.

The addition of 0.1 wt%  $\alpha$ -DPPC alone to HA solution has little effect in the first run, but in the 3rd run gradual decreasing in friction and attenuation of stick-slip are observed. This means the adsorbed film of phospholipid might be formed after repeated rubbing.

Next, the frictional property lubricated with HA solution containing both  $\gamma$ -globulin and liposomes of  $\alpha$ -DPPC was examined. In the first run, friction is little decreased but stick-slip is attenuated, which means the occurrence of interaction between  $\gamma$ -globulin,  $\alpha$ -DPPC and HA.

In order to elucidate these phenomena, the adsorbed film formation on stainless steel plate was examined by tapping mode of AFM.

As observed in Fig.14(c), HA solution containing both  $\gamma$ -globulin and liposome of  $\alpha$ -DPPC exhibits clear spherical molecules. In contrast, HA solution with  $\gamma$ -globulin alone (Fig.14 (a)) lacks clearness.

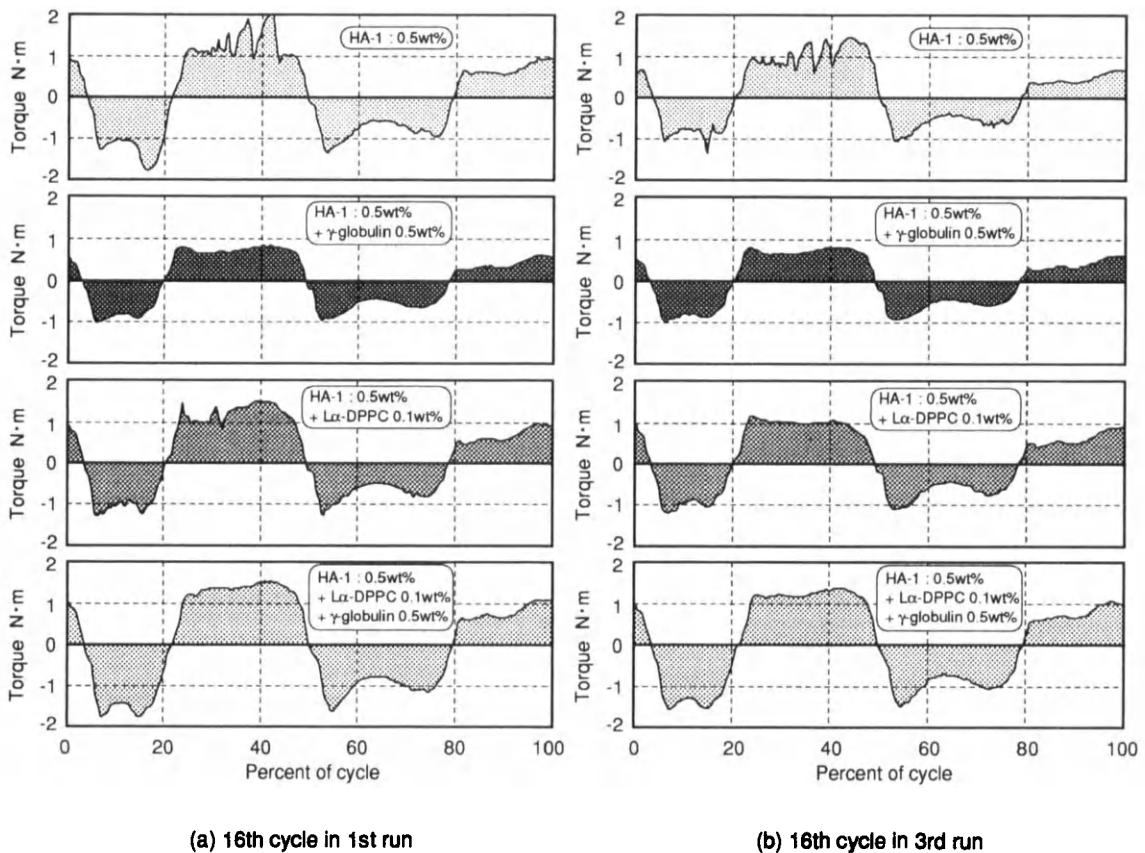
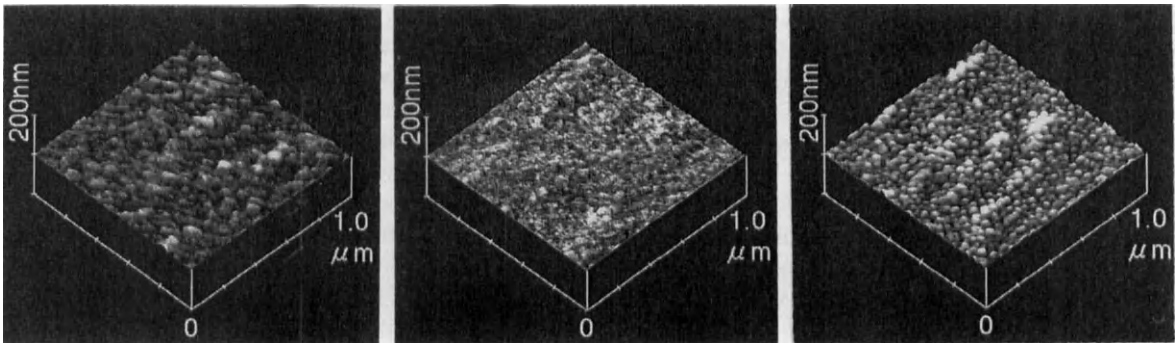


Figure 13. Influence of protein and phospholipid on frictional behaviour in knee prosthesis with PVA hydrogel layer



(a) HA-1:0.5wt% +  $\gamma$ -globulin 0.5wt%    (b) HA-1:0.5wt%+L $\alpha$ -DPPC 0.1wt%    (c) HA-1:0.5wt%+ $\gamma$ -globulin 0.5wt% + L $\alpha$ -DPPC0.1wt%

Figure 14. AFM images of adsorbed film on stainless steel plate

For HA solution with L $\alpha$ -DPPC alone, distinct adsorbed molecules were not found in Fig.14 (b), which means that large liposomes scarcely adsorb or adsorbed phospholipid molecules are too small by this AFM observation.

Clear adsorbed molecules for coexistence of  $\gamma$ -globulin, L $\alpha$ -DPPC and HA may have either less intensive adsorbed ability or high shearing resistance. In the former case, the adsorbed film is desorbed by rubbing process. In the latter case, the adsorbed molecules show high resistance to shearing action.

## 6. DISCUSSIONS

As described in the first half of this paper, the application of compliant material as an artificial cartilage in knee prosthesis is likely to significantly promote fluid film formation accompanied with enlargement of apparent contact areas. In knee prostheses with compliant layer lubricated with lubricant of appropriate viscosity under walking condition, considerable elastohydrodynamic film formation was observed in simulator tests. The fluid film varies in similar to numerical analysis based on PI model except some slight variation during stance phase. When viscosity of lubricants is extremely low, however, some direct contact occurred between articular surfaces, depending on the severity of operating conditions. Therefore, the authors proposed the design concept of the adaptive multimode lubrication mechanism to protect

articulating surfaces and reduce friction even under severe conditions.

In this paper, frictional behaviour for polyurethane and PVA hydrogel were compared. PVA hydrogel had better fluid film formation and the improvement of friction in condition lubricated with HA solution containing proteins. On the other hand, the addition of protein to HA solution increased friction for polyurethane. The difference in these materials may be caused by difference in compliance and porosity containing water.

For PVA hydrogel layer, the addition of liposomes of L $\alpha$ -DPPC into HA solution had an effect in reducing of friction and suppressing of stick-slip, after repetition of rubbing process. As pointed out by Hills [35], low friction may be achieved for sliding pair of PVA and stainless steel by some form of molecular ordering with successive rubbing process after immersion in lubricant containing liposomes. In contrast, coexistence of  $\gamma$ -globulin, liposome of L $\alpha$ -DPPC and HA affected frictional behaviour of PVA hydrogel. However, PVA lubricated with pig synovial fluid showed low friction similar to HA solution with protein as described above [20]. As AFM images in Fig.14, the difference in forms of adsorbed molecules seems to have harmful influence. Clear spherical adsorbed molecules in Fig. 14 (c) may be reflected by the formation of lipoproteins. In human body, hyaluronic acid may be stabilizing the adsorption of surface active phospholipid to articular surfaces. Besides, both proteins and mucopolysaccharides

could act as carriers for phospholipid by entering into reversible chemical associations with phospholipids as lipoproteins and lipopolysaccharides, respectively [35]. Further researches are required to elucidate lubrication mechanism in joint prostheses with hydrogel layer in human body.

Furthermore, frictional characteristics at start-up or breakdown of fluid film should be clarified for various daily activities. On the lubrication mechanism in joint prosthesis with PVA hydrogel, weeping or exudation of fluid from PVA seems to make lubrication better, particularly at start-up or at breakdown of fluid film.

One of the unsolved problems on the clinical application of compliant hydrogel as a artificial cartilage is their short durability. Mean values of static contact pressure for polyurethane and PVA hydrogel flat layer at 2 kN were about 6 MPa and 2 MPa, respectively. For PVA hydrogel with inferior mechanical strength to polyurethane, this value seems to be too large. So, it is better to reduce the contact pressure in knee prosthesis by improving the geometrical congruity. But, excessive geometrical congruity induces lubricant starvation or excessive deformation. Excessive larger thickness of soft layer has a harmful effect upon frictional behaviour [22]. So, the optimum geometrical design is required to preserve the lubricating film formation supplemented by various lubrication mechanism particularly under low viscosity conditions.

## 7. CONCLUSIONS

The lubricating film formation in cylindrical knee prostheses with compliant layer as artificial cartilage during walking was evaluated based on numerical analysis and simulator tests.

In the cylindrical knee prosthesis with compliant tibial layer, the elasto-hydrodynamic film appears to be considerably established depending on its compliance during walking, as indicated by numerical analysis. However, particularly under lubricated condition with low viscosity lubricant, significant local direct contact occurred. Therefore, the design concept of the adaptive multimode lubrication was discussed to improve lubricating performance of joint prostheses even under low viscosity conditions.

Cylindrical knee prostheses with PVA hydrogel layer exhibited the improvement in frictional behaviour lubricated with hyaluronate solution

containing proteins. The addition of protein had adverse effect on frictional behaviour in polyurethane. Liposomes of phospholipid had an effect on friction after repeated rubbing process for PVA hydrogel layer. The difference in influence of synovia constituents was discussed based on the observation of adsorbed film by atomic force microscopy.

Further studies on optimum design and improvement of durability are required to realize a knee prosthesis with a compliant artificial cartilage for clinical use.

## ACKNOWLEDGMENTS

The authors wish to express their appreciation to Mr. Y. Nakanishi, graduate student at Kyushu University for his cooperation and Dr. J. B. Medley, University of Waterloo, for his advice on PI model. The measurement of AFM was conducted using AFM at the Center of Advanced Instrumental Analysis, Kyushu University. Sodium hyaluronate was prepared by Seikagaku Corporation and polyurethane was supplied by Dow Chemical Japan Ltd. Financial support was given by the Grant-in-Aid for Scientific Research of The Ministry of Education, Science, Sports and Culture, Japan ((A) No.07558256, (B) No.07458237, International Scientific Research (Joint Research) No.07044159).

## REFERENCES

1. H.G. Willert and M. Semlitsch, *J. Biomed. Mater. Res.*, 11 (1977) 157.
2. I. C. Clarke and P. Cambell, *Progress in Bioengineering*, ed. by J.P. Paul, et al., Adam Hilger (1989) 104.
3. T. Murakami and N. Ohtsuki, *Fluid Film Lubrication - Osborne Reynolds Centenary*, ed. by D. Dowson, C.M. Taylor, M. Godet, and D. Berthe, Elsevier, (1987) 387.
4. N. Ohtsuki and T. Murakami, *Proc. Jpn. Int. Trib. Conf. Nagoya*, 2 (1990) 713.
5. T. Murakami, *JSME International Journal, Series III*, 33, 4 (1990) 465.
6. T. Murakami, N. Ohtsuki and H. Higaki, *Thin Films in Tribology*, ed. by D. Dowson et al. Elsevier (1993) 673.
7. T. Murakami, *Design of Amenity*, ed. by Y. Ando and T. Sakamoto, Kyushu Univ. Press (1995)319.
8. T. Sasada and K. Mabuchi, *Proc. JSLE Int. Trib.*

- Conf., (1985), 949.
9. K. Mabuchi and T. Sasada, *Wear*, 140 (1990) 1.
  10. T. Sasada, Y. Tsukamoto and K. Mabuchi, *Biotribology*, ( in Japanese ), Sangyo-Tosyo, (1988) 60.
  11. T. Sasada, M. Takahashi, M. Watakabe, K.Mabuchi, Y. Tsukamoto and M. Nanbu, *J. Jpn. Soc. Biomaterials* (in Japanese), 3, 3, (1985) 151.
  12. A. Unsworth, M.J. Percy, E.F.T. White and G. White, *Proc. Inst. Mech. Eng.*, C219/87 (1987) 715.
  13. M. Oka, T. Noguchi, P. Kumar, K. Ikeuchi, T. Yamamuro, S.H. Hyon and Y. Ikada, *Clin. Mater.*, 6 (1990) 361.
  14. D.D. Auger, J.B. Medley, J. Fisher and D. Dowson, *Mechanics of Coatings*, ed. by D. Dowson, et al. , Elsevier (1990) 264.
  15. D. Dowson, J. Fisher, Z.M. Jin, D.D. Auger and B. Jobbins, *Proc. Instn. Mech. Engrs.*, 205, Part H, (1991) 59.
  16. L. Caravia, D. Dowson, J. Fisher, P.H. Corkhill and B.J. Tighe, *J. Mater. Sci., Mater. in Medicine*, 4 (1993) 515.
  17. D.D. Auger, D. Dowson and J. Fisher, *Proc. Instn. Mech. Engrs.*, 209, Part H (1995) 73.
  18. D.D. Auger, D. Dowson and J. Fisher, *Proc. Instn. Mech. Engrs.*, 209, Part H (1995) 83.
  19. Y. Sawae, T. Murakami, H. Higaki and S. Moriyama, *JSME International Journal, Ser. C*, 39, 2 (1996) 356.
  20. Y. Sawae, T. Murakami, H. Higaki, *Proc. Int. Tribol. Conf. Yokohama 1995*, to be published in 1996.
  21. T. Murakami, Y. Sawae and H. Higaki, *J. Jpn. Soc. Clin. Biomech. & Rel. Res.*, 16 (1996) to be published.
  22. T. Murakami, N. Ohtsuki and H. Higaki, *Proc. Int. Tribol. Conf. Yokohama 1995*, to be published in 1996.
  23. J.B. Medley and D. Dowson, *ASLE Trans.*, 27, 3 (1984) 243.
  24. J.R. Gladstone and J.B. Medley, *Mechanics of Coateing*, ed. by D. Dowson et al. Elsevier (1990) 241.
  25. D. Dowson, *Proc. Instn. Mech. Engrs.*, 181, Pt 3J, (1966-67) 45.
  26. A. Unsworth, D. Dowson and V. Wright, *Ann. Rheum. Dis.*, 34 (1975) 277.
  27. T. Sasada, *J. Jpn. Soc. Lubr. Eng.*, (in Japanese), 23, 2 (1978) 79.
  28. K. Ikeuchi, *Lubricants and Lubrication*, ed. by D. Dowson et al., Elsevier (1995) 65.
  29. G.W. Stachowiak, A.W. Batchelor and L.J. Griffiths, *Wear*, 171 (1994) 135.
  30. D. Dowson and Z-M. Jin, *Engng. Med.*, 15 (1986) 63.
  31. D. Dowson and Z-M. Jin, *Fluid Film Lubrication - Osborne Reynolds Centenary*, ed. by Dowson, D. et al, Elsevier Sci. Pub., (1987) 375.
  32. H. Higaki, T. Murakami and Y. Nakanishi, *Proc. 4th China-Japan-USA-Singapore Conf. Biomechanics*, Int. Academic Pub. (1995) 154.
  33. H. Higaki, T. Murakami and Y. Nakanishi, *Trans. Jpn. Soc. Mech. Eng. (in Japanese)*, C 61, 588 (1995) 3396.
  34. H. Higaki, T. Murakami, N. Nakanishi, T. Katagiri, H. Miura and T. Mawatari, Submitted to *Trans. Jpn. Soc. Mech. Eng. (in Japanese)*.
  35. B. A. Hills, *J. Rheumatol.*, 16 (1989) 82.
  36. B.A. Hills and B.D. Butler, *Ann. Rheum. Dis.*, 43 (1984) 641.
  37. D.A. Swann, *The joints and synovial fluids*, Academic Press (1978) 374.
  38. W.H. Davis, Jr., S.L. Lee and L. Sokoloff, *Trans ASME, J. Biomech. Engng.*, 101 (1979) 185.
  39. H. Higaki and T. Murakami, *Proc. Int. Tribol. Conf. Yokohama 1995*, to be published in 1996.
  40. H. Higaki, T. Murakami and Y. Nakanishi, *Trans. Jpn. Soc. Mech. Eng. (in Japanese)*, C , to be published.
  41. Z.M. Jin, D. Dowson and J. Fisher, *Thin Films in Tribology*, ed. by D. Dowson et al, Elsevier (1993) 545.
  42. M. Nanbu, Published unexamined patent application (in Japanese), Shou-57-130543, 58 36630.
  43. A.D. Bangham, M. M. Standish and J.C. Watkins, *J. Mol. Biol.*, 13 (1965) 238.

## Effects of Electric Field on Lubricating Ability of Synovia Constituents

Y.Nakanishi, T.Murakami and H.Higaki

Department of Intelligent Machinery and Systems, Faculty of Engineering, Kyushu University,  
Hakozaki, Higashi-ku, Fukuoka, 812-81, JAPAN

The lubricating ability of synovia constituents and the effects of an electric field applied between rubbing surfaces have been investigated in the wide range of lubrication regime using a reciprocating tester and a roller-on-flat tester. Sliding materials were a conductive silicone rubber and a stainless steel. In friction tests for a conductive silicone rubber against a stainless steel, the existence of protein in lubricant caused a rise of friction coefficient that was derived from the adsorption of protein onto sliding surfaces accompanied with considerable local contacts. When a stainless steel slid against a stainless steel, on the other hand, the adsorption of protein onto rubbing surfaces seemed to promote both stability of frictional characteristics and low wear rate. For a conductive silicone rubber sliding on a stainless steel within mixed lubrication regime using water solution of sodium hyaluronate with  $\gamma$ -globulin present, remarked decrease in friction was observed by means of applying a low frequency alternating current. Furthermore, on the observation by atomic force microscopy (AFM) for specimens after this friction test, the decline of adsorbates that had dotted whole rubbing area was confirmed. Mechanism based on the electrical potential of sliding surface was proposed to explain frictional behaviour.

### 1. INTRODUCTION

Natural synovial joint is constructed as an excellent tribology system which sustains both low friction and minimum wear throughout lifetime of most people, in which elastohydrodynamic lubrication plays the main role in protecting the compliant surface. On the other hand, at sever condition where a joint keeps stationary state under heavy load or sliding velocity is too low to generate sufficient fluid film, the various supplemental lubrication mechanisms, such as boundary lubrication, start functioning. This mechanism is called as the adaptive multimode lubrication (Murakami, et al. [1-2], Dowson [3]).

The adaptive multimode lubrication is derived from the interaction with physical and chemical properties of the articular cartilage and synovial fluid. Therefore, if one of these elements is substituted for artificial substance, it is debatable whether the lubricating ability being match for natural

synovial joint is reproduced or not.

Synovial fluid is a dialysate of blood plasma with addition of hyaluronic acid (polysaccharide) and phospholipids. Hyaluronic acid is responsible for high viscosity, which plays an important part in the viscous effect of lubrication. Each ingredient may adsorb onto the surfaces of not only articular cartilage but artificial materials, so that tribological characteristics must be changed in the boundary or the mixed lubrication regime. Higaki, et al. [4] used lubricants containing various synovia constituents. According to their pendulum friction tests in pig shoulder joints, the adsorption of  $\gamma$ -globulin and phospholipids onto cartilage improved the frictional characteristics.

The driving force in adsorption of synovia constituents onto rubbing surface varies depending on the property of materials and its environment, i.e. hydrophobic (or hydrophilic), potential (including zeta

potential), pH and concentration of solution, temperature, and so on (Lyklema, et al. [5-6]). To put it the other way round, there is possibility that the adsorption/desorption of synovia constituents onto sliding surfaces is controlled by means of the modifying the only one of factors which were mentioned above.

It is well known that certain industrial bearings may have to operate in the presence of electrical potentials which are applied across the sliding interfaces either externally or from the sliding process itself (Bowden.[7]). These potentials may influence tribological characteristics in both dry and wet sliding condition. Although the potentials of sliding interfaces have been an object of study for a long time (Yamamoto,Y. et al.[8]), only few attempts have so far been made at prosthetic materials using lubricants which contains synovia constituents.

Zaki et al.[9] undertook to explore the influences of externally electrical potentials on the frictional behaviour of cartilage and prosthetic materials using a pin-on-disc friction tester. They showed marked variations in the coefficient of friction for sliding surfaces when electrical potentials were applied.

This paper is intended as an investigation of the influence of synovia constituents on tribological behaviour in artificial rubbing surfaces and a consideration of the aggressive control of the lubricating ability by means of an electric field.

2. MATERIALS

2.1 Sliding pair

Mechanical properties for rubbing materials are shown in Table 1. Stainless steel was treated mechanically to ensure the use of smooth, clean rubbing surface. Before tests, all specimens were wiped with ethyl alcohol spilled onto cloth to keep the surfaces free from contaminants.

Conductive silicone rubber (conductive SR)

which contains carbon particles inside has not only similar elastic modulus to articular cartilage but conductivity. With applying the compressive load, the increased joining sections of carbon particles bring about the change of conductivity. Within the loading conditions which were adopted in this paper, however, the transition of conductivity during a test was scarcely seen (Fig.1).

Table 1. Mechanical properties for sliding materials

|                            | Roughness, $R_{rms}$ $\mu\text{m}$ | Young's Modulus, MPa |
|----------------------------|------------------------------------|----------------------|
| Stainless steel            | 0.02 (flat)<br>0.1 (sphere)        | $2.1 \times 10^5$    |
| Conductive silicone rubber | 3.3 (replica of resin)             | 9.1                  |

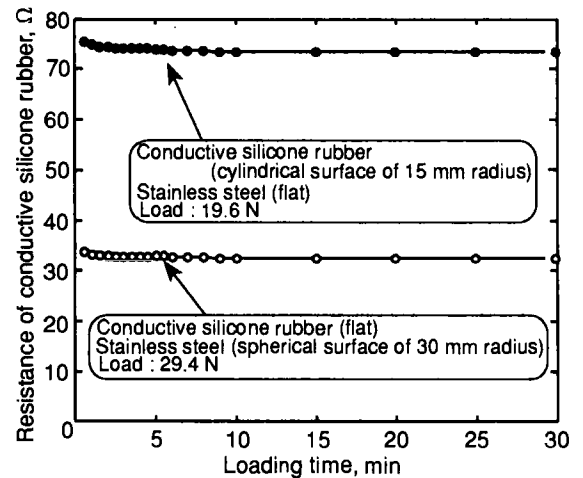


Figure 1. Relation between viscoelastic deformation and conductivity of conductive silicone rubber

2.2 Lubricants

The composition of lubricants and each viscosity which was measured by a cone / plate viscometer are shown in Table 2 and Fig.2, respectively.

Table 2 Constituents of lubricants used for tribological tests

| Constituents (wt%)<br>Lubricant | Solvent         | Sodium hyaluronate | Human serum $\gamma$ -globulin | Human serum Albumin |
|---------------------------------|-----------------|--------------------|--------------------------------|---------------------|
| A, B                            | Distilled Water | 0.1                | (0.3)                          | —                   |
| C, D                            | Distilled Water | 0.5                | (0.3)                          | —                   |
| E, F                            | Distilled Water | 1.0                | (0.3)                          | —                   |
| G, H                            | Saline          | —                  | (0.3)                          | (2.0)               |

Lubricants were water or saline solution with or without sodium hyaluronate (HA, Molecular weight =  $8.8 - 9.6 \times 10^5$ ), human serum  $\gamma$ -globulin and albumin, respectively.

At low shear rates, the viscosity of HA solution shows a high viscosity in proportion to the concentration of HA, whereas at higher shear rates the viscous effect is fading, clearly portraying non-Newtonian behaviour (Yanaki, et. al. [10]).

### 3. EXPERIMENTAL EQUIPMENT

#### 3.1 Roller-on-flat friction tester

The roller-on-flat friction tester shown in Fig.3 was used to elucidate the tribological characteristics in the wide range of lubrication modes. The upper roller had spherical surface of 30 mm radius. This roller was clamped to the rotating shaft. The lower flat specimen was fastened in a holder with a liquid bath. The wide range of constant load (1.96 - 29.4 N) and sliding speed (0.01 - 0.18 m/s) were applied by the lever system and the motor unit, respectively. The frictional characteristics were continuously observed by the strain gauges.

#### 3.2 Reciprocating friction tester

The reciprocating friction tester shown in Fig.4 was used to observe the changes in frictional behaviour by means of an electricfield and to examine the states of

( ) : with (B,D,F,H) or without (A,C,E,G)

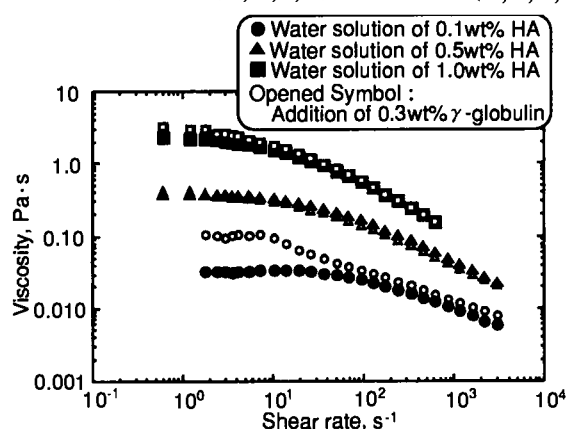


Figure 2. Viscosity and non-Newtonian behaviour of water solution of HA with or without  $\gamma$ -globulin

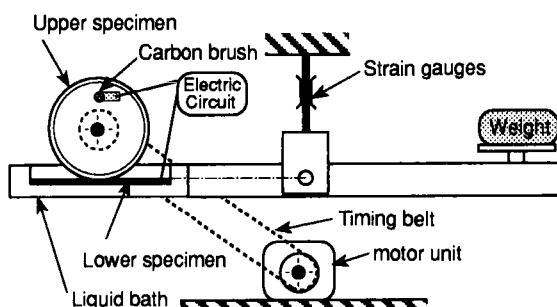


Figure 3. Schematic representation of roller-on-flat friction tester

lower specimens after those tests by AFM. The upper specimen was fastened by the cylindrical holder jig of 15mm radius. The

lower flat specimen was fastened in a holder with a liquid bath. Only one rubbing condition (Normal load : 19.4 N, Stroke : 20 mm, Period 4 s ) was adopted to operate in the mixed lubrication mode, in which water solution of HA with or without  $\gamma$ -globulin were used as lubricants. The friction coefficient in this study was defined as the ratio of the highest tangential force measured in one stroke to the normal load.

### 3.3 Electric circuit for externally applied electric field

Three types of electric circuit were utilized for an externally applied electric field between rubbing surfaces; a variable direct current circuit with a constant voltage, an electric circuit for degree of separation and an alternative current circuit.

To begin with, the variable direct current circuit is shown in Fig.5. The optional current value with a constant voltage could be operated by means of the parallel circuit including a variable resistor and a switch to elucidate the influence of the current value on frictional characteristics.

Then, the lubricating film formation during tests was examined by the electric resistance method, in which the electric circuit for degree of separation shown in Fig.6 was used. The voltage and current value between sliding surfaces may be changed during a test because of the resistance associated with lubricating film formation (see Fig.5). Although the degree of separation is generally defined as the ratio of measured voltage to the applied voltage (degree of separation is 1 : full separation, degree of separation is 0 : contact), the value had to be revised in such a case as the conductive SR - rubbing surface which had a low conductivity shown in Fig.1. The notable example of this revising is shown in Fig.7.

Finally, in externally applying alternative current (A.C.) tests, the function generator was used as an alternating current circuit to investigate the relation between frequency (Hz) and frictional behaviour.

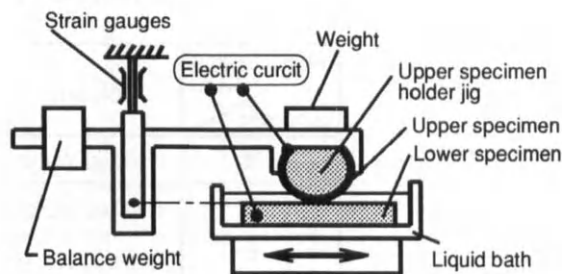


Figure 4. Schematic representation of reciprocating friction tester.

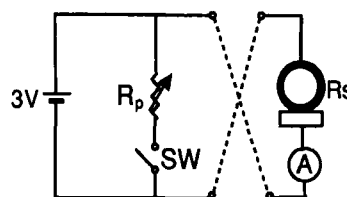


Figure 5. The electric circuit for externally applied electric field ( a variable current - constant voltage )

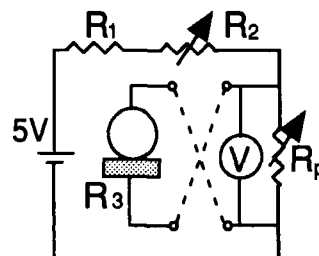


Figure 6. The electric circuit for degree of separation

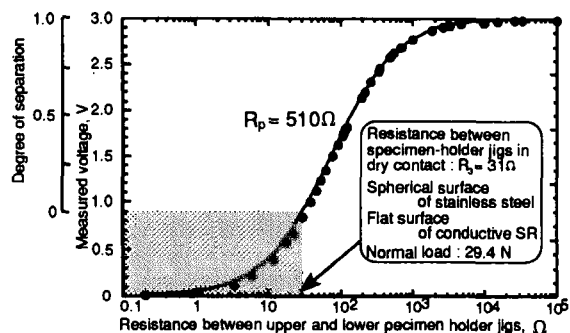


Figure 7. Example of expression in the degree of separation



## 4. EXPERIMENTAL PROCEDURE

### 4.1 Influence of synovia constituents on tribological characteristics

Tribological characteristics under constant speed and load conditions were investigated on a Roller-on-flat tester shown in Fig.3, using all lubricants and counterfaces shown in Table 1 and Table 2, respectively. Friction tests were undertaken over wide range of load and speed condition to observe the tribological behaviour in different lubrication modes. Running time or sliding distance was decided by the criterion in which frictional equilibrium had achieved or where sufficient wear to be evaluated had been obtained.

The theoretical values for central and minimum film thickness were also estimated in those tests. The main formulae for soft-layered solids at elliptical contacts proposed by Dowson, et al.[11] are shown below.

$$H_{cen} = 3.66U^{0.54}L^{0.37}W^{-0.18}(1 - 0.61e^{-0.12k})$$

$$H_{min} = 3.54U^{0.56}L^{0.36}W^{-0.20}(1 - 0.64e^{-0.15k})$$

where

$U, L$  and  $W$  are dimensionless parameter groups; speed, layer and load, respectively.  
 $k$  : ellipticity ratio

Since the rubbing conditions in this study were different from the physiological conditions in natural synovial joints, the viscosity of lubricants didn't seem to be estimated as twice that of water (see Dowson, et al. [11-12]). The approximate exponential functions (correlation coefficient > 0.88) were defined applying the data presented in Fig.2 and the assumed value of 0.002 Pa · s at high shear rates, being  $10^6 - 10^7$  s<sup>-1</sup>. The convergence method was undertaken by means of these functions.

### 4.2 Influence of electric field on adsorption of synovia constituents and frictional behaviour

The state of adsorption of synovia constituents and frictional behaviour were

examined in a reciprocating friction test for sliding pair of a conductive SR cylindrical surface and a stainless steel plate, using water solution of HA with  $\gamma$ -globulin.

To start with, an electric field of 3V was applied by means of either a constant voltage circuit shown in Fig.5 or an alternative current circuit to rubbing surfaces for 30 minutes after 30 minutes' running-in to allow frictional equilibrium to be achieved. Next, the lubricant clung excessively on the lower specimen (stainless steel) was removed by the flowing distilled water. Lastly, the treated lower flat specimen was observed by AFM (Tapping Mode in distilled water).

### 4.3 The lubrication mode where an electric field can affect the frictional characteristics

The lubrication mode in which an electric field could affect the frictional behaviour was investigated on a roller-on-flat friction tester shown in Fig.3. Sliding pair was a spherical stainless steel / conductive SR plate. Lubricants were water solution of HA with or without  $\gamma$ -globulin. Fluid film formation was also evaluated by means of the circuit presented in Fig.6. The way of applying electric field was as the same as in paragraph 4.2.

## 5. RESULTS

### 5.1 Influence of synovia constituents on tribological characteristics

Results of roller-on-flat friction tests and theoretical results are shown in Figs.8,9 and 10, respectively.

The value of friction coefficient (Fig.8) is adopted at 30 minutes testing time achieved frictional equilibrium. The value of viscosity included in abscissa value is adopted from the result of the convergence calculation presented in paragraph 4.1.

The friction coefficient gradually declines along the abscissa value, falls right down to the lowest point at about  $5.2 \times 10^{-5}$  m<sup>-1</sup> and then slightly increases. Those frictional

characteristics suggest that the lubricating conditions in these tests range from the mixed lubrication to the elastohydrodynamic lubrication regime. Theoretical results (Fig.9) represent the increase of film thickness up to about  $3\ \mu\text{m}$  in proportion to abscissa value, and the viscous effect can be expected owing to decrease of shear rate at milder condition ( $>10^{-4}\ \text{m}^{-1}$ ).

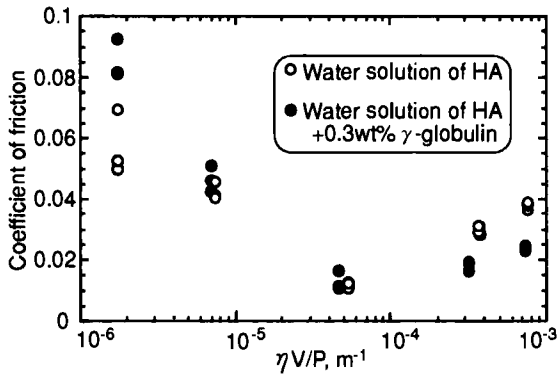


Figure 8. Influence of synovia constituents on frictional behaviour (spherical surface : stainless steel, flat surface : conductive SR, in a roller-on-flat tester.)

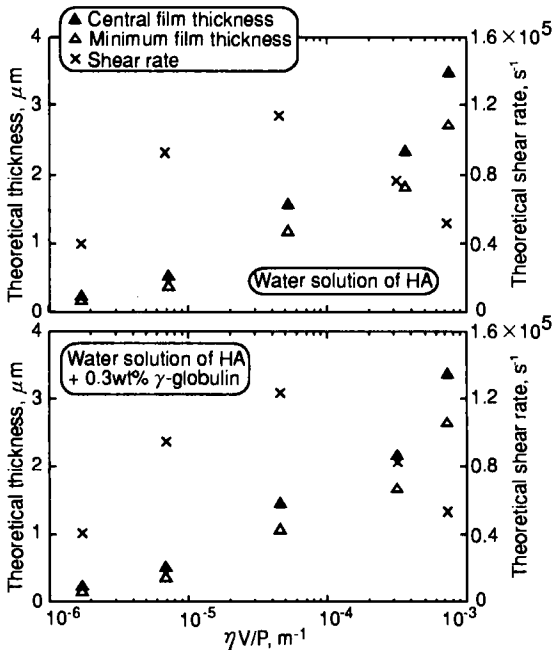


Figure 9. Theoretical results of film thickness and shear rate (in a roller-on-flat-tester)

Marked increase of friction coefficient in the presence of  $\gamma$ -globulin was measured in the severer mixed lubrication mode where local contact could be considerable.

For a spherical stainless steel sliding on a flat stainless steel (Fig.10), on the other hand, the stability of frictional behaviour was observed in the presence of protein. Furthermore, the wear rate using saline solution of protein was about half as much as that using saline only.

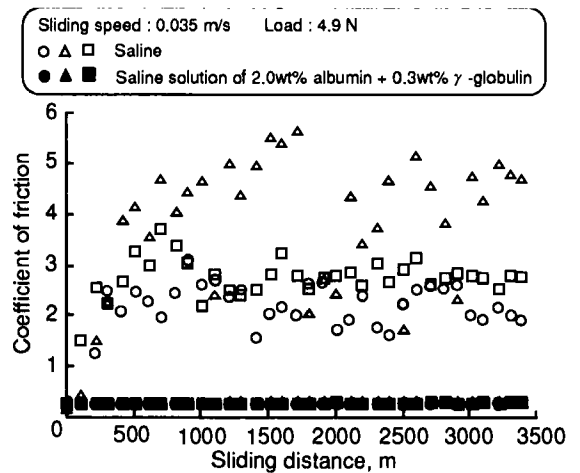


Figure 10. Effect of protein on tribological characteristics (stainless steel against stainless steel in a roller-on-flat tester)

### 5.2 Influence of electric field on adsorption of synovia constituents and frictional behaviour

Changes in maximum values for coefficient of friction during reciprocation are plotted against running time in reciprocating tests in Fig.11. Figure 12 shows AFM images of lower stainless steel surfaces after tests.

In applying a direct current (D.C.) tests, the frictional characteristics were improved in an electric field where the stainless steel plate was the anode, but with application of an electric field in which the stainless steel plate was the cathode, the frictional characteristics were deteriorated except for the high current value ( $R_p = \infty\ \Omega$  ; 5-7 mA).

In applying an alternative current (A.C.) tests, improvement of frictional behaviour

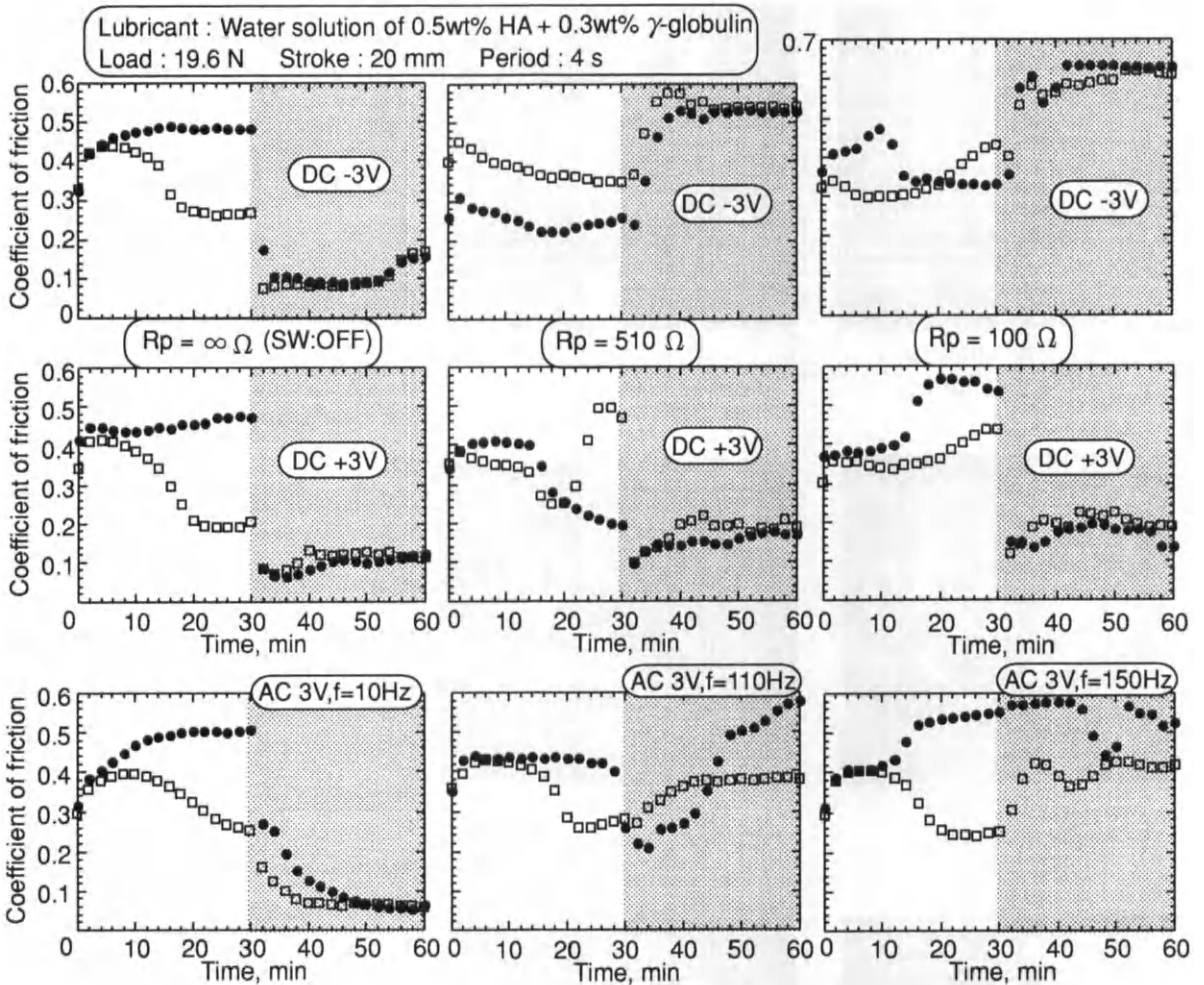


Figure 11. Influence of externally applied voltage on frictional behaviour (upper cylindrical surface : conductive SR, lower flat surface : stainless steel, in a reciprocating test)

was observed by means of the low frequency ( $f=10\text{Hz}$ ) A.C. in comparison with the high frequency ( $f=150\text{Hz}$ ) A.C.

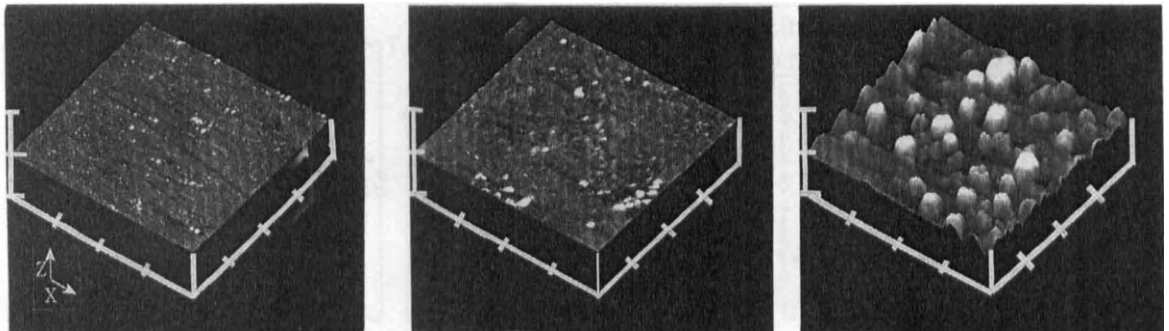
The states of stainless steel surface after these tests (Fig.12) suggest that the adsorbing behaviour on sliding materials is related to the line of electric force and a current value. It is noted that the decline of adsorbates on the rubbing area is caused with application of A.C. electric field or the electric field in which the stainless steel plate is the cathode and a high current value. The gentle adsorbed film is formed

with application of the electric field where stainless steel is the anode.

### 5.3 The lubrication mode where an electric field can affect the frictional characteristics

Figure 13 shows results of a roller-on-flat friction tests in the presence of water solution of HA.

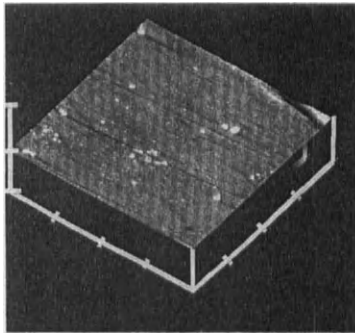
The adsorbed film appears to be promoted with applying the D.C. electric field according to the increase of the degree of separation in the severer mixed lubrication regime



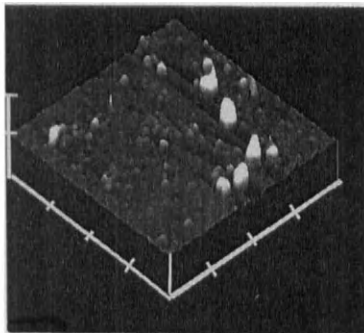
(A) Lapped surface  
(Before testing)

(B) Contact area  
(Applied voltage : -3V DC)  
 $R_p = \infty \Omega$  (SW:OFF)

(b) Non-contact area  
(Applied voltage : -3V DC)  
 $R_p = \infty \Omega$  (SW:OFF)

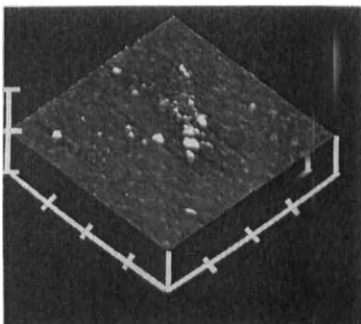


(C) Contact area  
(Applied voltage :  
3V AC, f=10Hz)

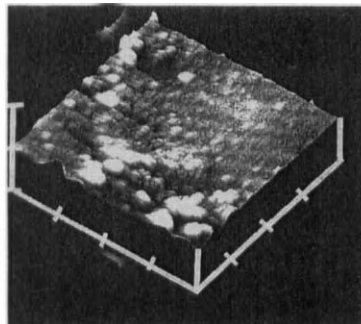


(D) Contact area  
(Applied voltage : -3V DC)  
 $R_p = 510 \Omega$

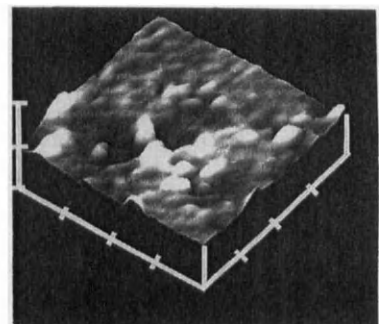
Reciprocating tests  
 Upper specimen : Conductive SR  
 Lower specimen : Stainless steel  
 Lubricant : 0.5wt%HA  
                   + 0.3wt% $\gamma$ -globulin  
 Load : 19.6 N  
 Stroke : 20 mm  
 Period : 4 s  
 GND : Upper specimen  
 X : 500nm/div    Z : 100 nm/div



(E) Contact area  
(Applied voltage :  
3V AC, f=150Hz)



(F) Contact area  
(Applied voltage : +3V DC)  
 $R_p = \infty \Omega$  (SW:OFF)



(f) Non-contact area  
(Applied voltage : +3V DC)  
 $R_p = \infty \Omega$  (SW:OFF)

Figure 12. The observation by atomic force microscopy (AFM) for lower specimens (stainless steel) after reciprocating friction tests

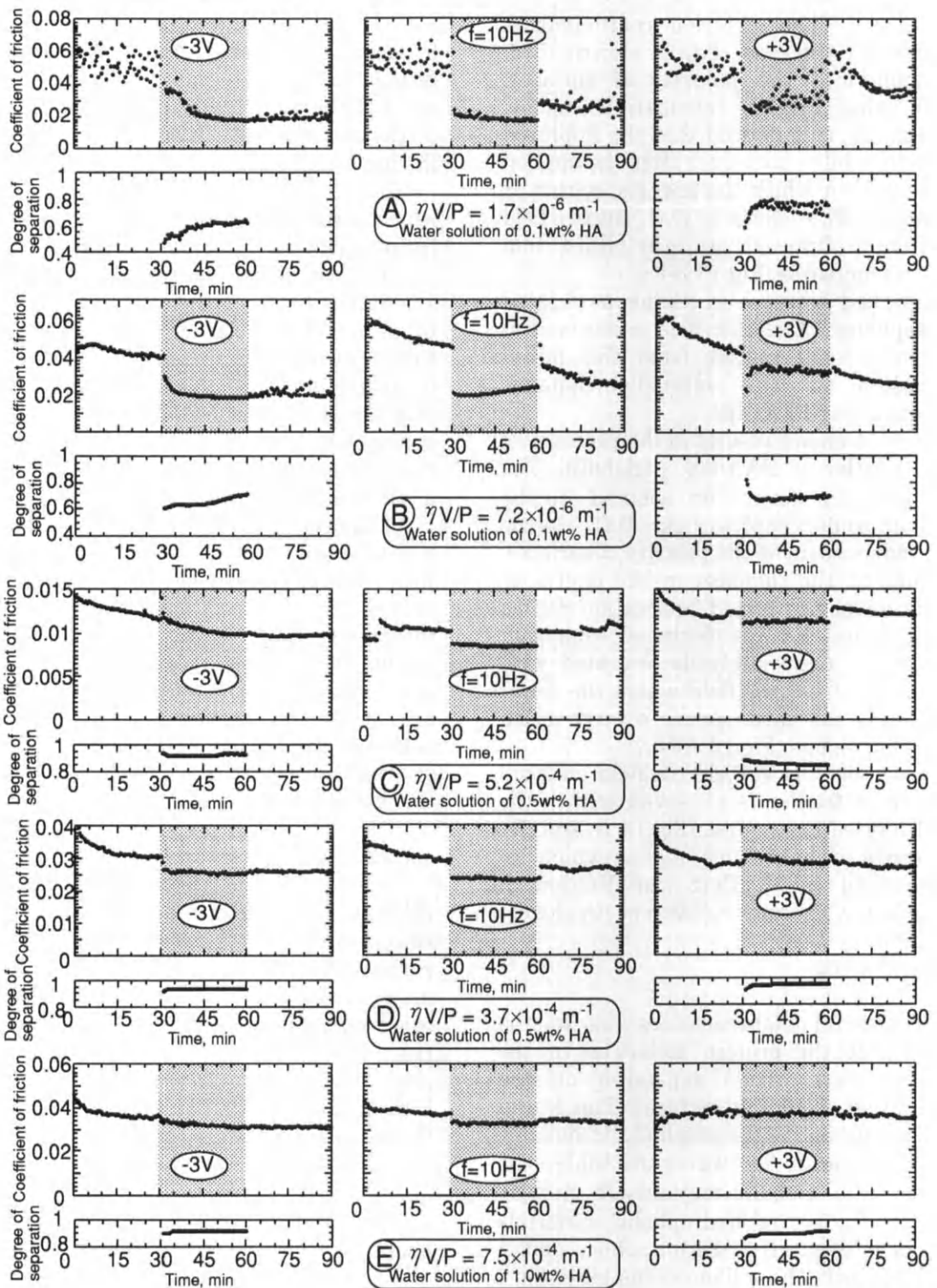


**Figure 13.** Influence of externally applied voltage on frictional behaviour (upper spherical surface : stainless steel, lower flat surface : conductive SR, in a roller-on-flat tester)

(Fig.13 A). The friction coefficient is decreased in the case of D.C. electric field, independent of the polarity of surfaces, within the mixed lubrication regime. Furthermore, it is noticed that the improved lubricating ability continues after the applied electric field in which the lower specimen is the cathode. The effects of D.C. electric field on friction diminish as the fluid film thickness increases (Fig.13 B-E).

Remarkable decrease in friction associated with applying A.C. electric field is observed in the transitional regime from the mixed lubrication to the elastohydrodynamic lubrication (Fig.13 A - E).

Figure 14 shows results in the presence of water solution of HA with  $\gamma$ -globulin. The adsorbed film formation seemed to be promoted under applying the D.C. electric field, independent of the polarity of surfaces, according to the increase in the degree of separation in the mixed lubrication regime (Fig.14 A and B). The frictional behaviour, however, is remarkably deteriorated with application of electric field where the lower specimen is the anode in the severe mixed lubrication regime (Fig.14 A).

Under applying A.C. electric field, marked decrease in friction is observed within the mixed lubrication regime (Fig.14 A and B). The range of lubrication regime which an electric field could affect was limited in comparison with water solution of HA alone.

## 6. DISCUSSION

Frictional characteristics due to the existence of the protein molecules in the lubricant were varied depending on the combination of sliding surfaces (Figs.8 and 10). Since protein is the amphiphilic molecule and  $\gamma$ -globulin is water-insoluble, the molecule of  $\gamma$ -globulin may adsorb strongly onto the surface of hydrophobic materials such as a conductive silicon rubber and a stainless steel. These phenomena may offer, in the boundary or the mixed lubrication mode, a high adhesion leading to an increase in friction for softer materials (Fig.8), but act

as the sacrificial film to keep the stability of frictional characteristics and the low wear rate for harder materials (Fig.10). Walker, et al. [13] also reported that the adsorption of  $\gamma$ -globulin onto Vitallium counterface played the important role in friction and wear.

Since HA forms the random-coil structure which acquires high negative charges due to its dissociation, HA may adsorb onto the surface which is charged positively. The adsorbed film formation which is promoted by applying D.C. electric field may improve the frictional characteristics within the boundary and the mixed lubrication modes (Fig.13) and if the rubbing severity for the surface which is charged positively is milder than the other one, there is the possibility of a continuous low friction.

As shown in Fig.13, the effects of applying a low frequency A.C. on frictional behaviour was observed in the wide range of lubrication modes. These results lead to one idea that the applying A.C. electric field plays roles in not only the promoting the adsorption of HA onto rubbing surfaces due to the electric force but also the producing the weak-bond between the adsorbed HA film and the sliding material due to a continuous changing the polarity of surfaces.

The observation by AFM for the sliding surfaces after tests (Fig.12) gives the precise information of the adsorption behaviour of HA and  $\gamma$ -globulin. As mentioned above, since HA must be easy to adsorb onto the surface charged as positive potential, the major ingredient of the adsorbed film observed in Fig.12 (F) and (f) seems to be HA. Since spherical adsorbates were observed on the surface which led to a high friction (Fig.12 (D)), the major ingredient of those adsorbates is thought to be  $\gamma$ -globulin. Those results suggest that  $\gamma$ -globulin behaves as a positively charged particle and the same may be said, no doubt, of the observation shown in Fig.12(b).

Judging from the above, the frictional characteristics shown in Fig.11 can be explained; Under applying D.C. electric field where the lower specimen whose rubbing

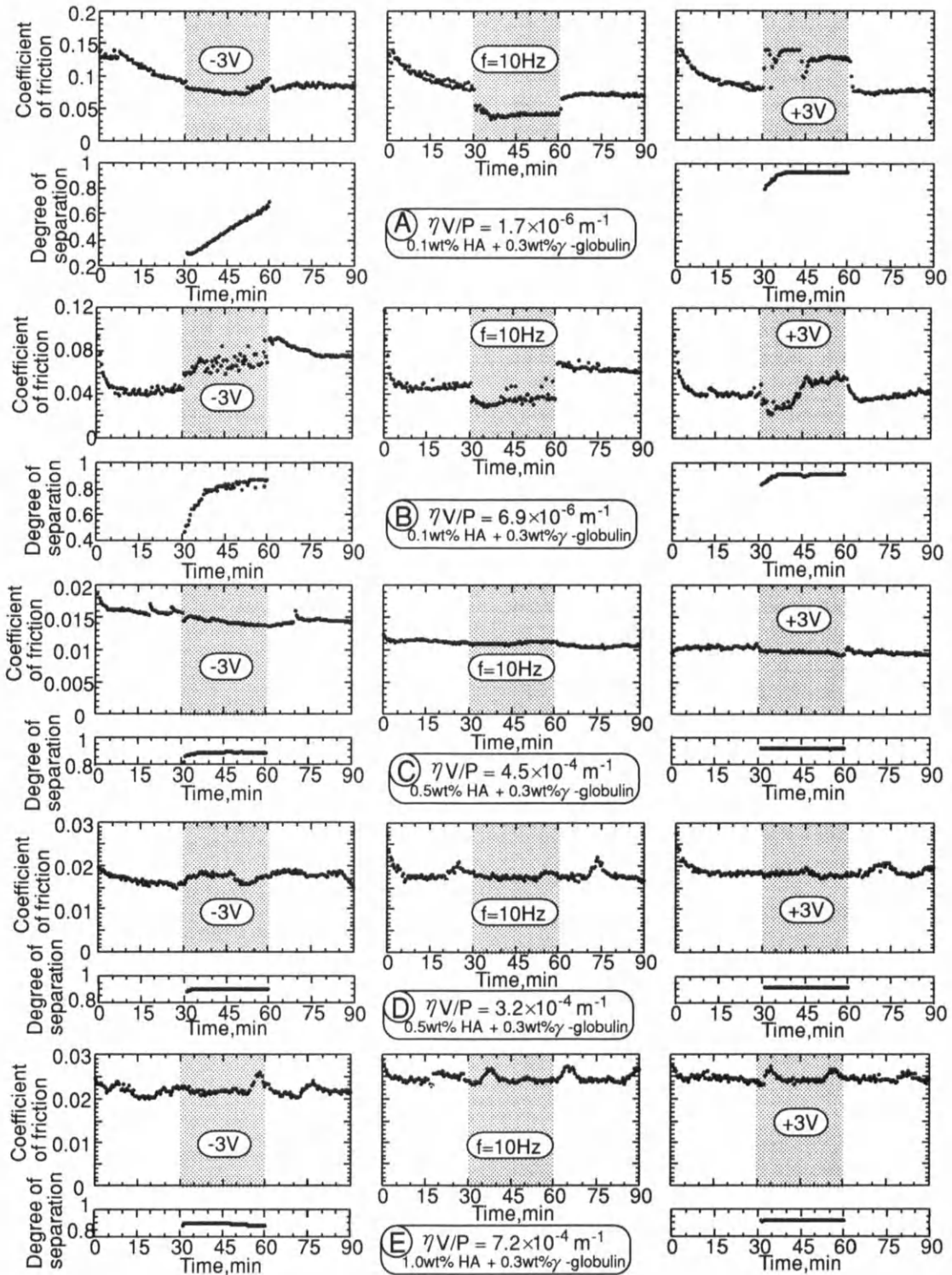


**Figure 14.** Influence of externally applied voltage on frictional behaviour (upper spherical surface : stainless Steel, lower flat surface : conductive SR, in a roller-on-flat tester)



condition is milder than upper specimen in reciprocating tests is the anode, the desorption of  $\gamma$ -globulin and the adsorption of HA onto lower specimen's surface seemed to be promoted, so that frictional characteristics might be improved. On the other hand, under applying D.C. electric field where the lower specimen is the cathode, the adsorption of  $\gamma$ -globulin and the desorption of HA onto lower specimen's surface seemed to be promoted, so that frictional behaviour might be deteriorated. There is an exception to the rule; The current value also cannot be ignored. The hydrogen gas, more or less, must be generated from the surface which is charged as negative potential. The sufficient hydrogen gas might bring about producing the weak-bond between the adsorbed protein film and the sliding material, which caused the abrupt decrease in friction.

The mechanism of the improved frictional characteristics with applying low frequency A.C. electric field using HA solution with  $\gamma$ -globulin seems to be as the same as that of HA solution lubrication. The reason why frictional characteristics were deteriorated under a high frequency A.C. electric field might be that the rapid changing in the polarity of surfaces prevented HA and  $\gamma$ -globulin from adsorbing onto sliding materials.

## 7. CONCLUSIONS

An experimental investigation has demonstrated the effects of an electric field on the lubricating ability of synovia constituents. Important features are summarized below:

1.  $\gamma$ -Globulin in lubricants adsorbed onto the hydrophobic sliding surfaces and changed tribological characteristics in the boundary and the mixed lubrication.
2. The application of an electric field between rubbing surfaces resulted in the changes of adsorption / desorption of synovia constituents and frictional characteristics.

3. The lubrication modes which an electric field could be effective were mainly in the mixed lubrication regime.

## 8. ACKNOWLEDGMENT

Sodium hyaluronate was supplied by Seikagaku Corporation, Japan. This research was supported by Grants-in-Aid for Scientific Research of the Ministry of Education, Science, Sports and Culture, Japan and Research Fellowships of the Japan Society for the Promotion of Science for Young Scientists.

## REFERENCES

1. T. Murakami, JSME Intern. J., Ser. III, 33, 4, (1990), 465.
2. T. Murakami, N. Ohtuki and H. Higaki, Thin Films in Tribology, (1993), 673, Elsevier.
3. D. Dowson, Proc. I.M.E., 181, Pt 3J, (1966-76), 45.
4. H. Higaki, T. Murakami and Y. Nakanishi, Proc. 4th CJUS Conf. Biomechanics, (1995), 154, International Academic Publishers.
5. J. Lyklema and W. Norde, Croat. Chem. Acta., 45, (1973), 67.
6. W. Norde and J. Lyklema, J. Colloid Interface Sci., 66, (1978), 266.
7. F. P. Bowden and T. Tabor, The Friction and Lubrication of Solids, (1950), Oxford.
8. Y. Yamamoto, J. Yagi and H. Higaki, JSME Intern. J., Ser. III, 35, 4, (1990), 641.
9. M. Zaki and D. Dowson, Mixed Lubrication and Lubricated Wear., (1985), 230, Butter worth.
10. T. Yanaki and M. Yamaguchi, Chem. Pharm. Bull., 42, (1994), 1651.
11. D. Dowson and J. Q. Yao, Proc. I.M.E., 208 (1994), 43.
12. D. Dowson and Z. M. Jin, Fluid Film Lubrication - Osborne Reynolds Centenary., (1986), 375, Elsevier.
13. P. S. Walker and M. J. Erkman, Wear, 21, (1972), 377.



## A MODEL TO EXPLAIN EHL IN A NON-FLOODED OR STARVED ROLLING ELEMENT BEARING

J.W. Kannel

Battelle, 505 King Avenue, Columbus, Ohio 43201-2693

### ABSTRACT

Are elastohydrodynamic lubrication (EHL) theories as applied to real machine elements too complicated? Is it possible that the EHL film is simply equal to the residual layer of lubricant in the ball (or roller) tracks in a bearing that occurs after a few rotations of a prelubricated bearing? The paper introduces this hypothesis. If the initial lubricant layer in a bearing exceeds the EHL film thickness, the steady-state theoretical film thickness is about 0.728 times the flooded EHL film. However, if the initial layer of lubricant in a bearing is much less than the flooded EHL film, the film thickness simply equals the initial layer thickness. The EHL film will prevail as long as there is lubricant in the bearing.

In traction tests we have found that under high-speed conditions, it is not easy to flood the interface. As a result the film thickness (as implied from traction measurements) is about 0.728 times the expected film thickness.

If the hypothesis put forth in the paper is valid, the EHL film thickness can be calculated by very indirect methods. Efforts have been made to compute the film thickness based on surface pressure measurements made in an 85 mm bore bearing with some (limited) success.

### 1. INTRODUCTION

Elastohydrodynamic lubrication (EHL) is the lubrication associated with heavily loaded rolling contact elements such as ball or roller bearing, gears, and many others (c.f. Dowson, 1959). The primary questions asked in EHL are: how does the lubricant impact life, and how does it impact traction. One key parameter with regards to both questions is the EHL film thickness. Life is affected by the degree of separation of the surface asperities. Traction is affected by the shear rate associated with slip divided by film thickness. Numerous traction measurements have been made including work at Battelle using twin disk machines. Disks are loaded together under lubricated rolling contact. Slippage is introduced between the disks and the resultant tractive force measured.

In recent tests, Gleeson (1995) made a very interesting observation. Under high-speed conditions, the traction seemed to be higher at high speeds than at low speeds, which was counter to experience. This suggests the EHL film thickness is decreasing with increasing speed. The traction curves were normally very "clean" and reproducible. Occasionally, however,

the traction curves seemed to be erratic and jump from one level to another and back. After much consternation, carefully controlled tests were conducted to determine the role on the lubricant supply system. When the lubricant jet was properly directed and driven by adequate pressure, the traction was low, implying a thick film. When the jet was improperly directed, the traction was high, implying a thin film. Both films were steady. The work presented here was conducted to help analyze and understand the traction data.

The effect of lubricant starvation has been analyzed by several researchers over the past three decades. Wolveridge et al. (1971) did early theoretical work on the subject and varied the position of the inlet boundary. Chiu (1974) developed a starvation parameter based on oil-air surface tension. Hamrock and Dowson (1977) analyzed lubrication of point contacts using full EHL solutions and varied starvation by moving the inlet boundary. Goksem and Hargreaves (1978) extended the starvation analyses to include traction. In a recent paper by Olaru and Gafitanu (1993), a starvation criterion for a ball bearing was developed based on consideration of lubricant retention due the lateral oil meniscus.

In addition to the excellent work done analytically, several researchers have evaluated the role of starvation experimentally. Wedeven et al. (1971) measured film thickness under various conditions of starvation by an optical technique. Again the inlet film layer was a critical parameter. Hargreaves and Higginson (1976) determined the effect of the quantity of oil on the starvation and on roller bearing torque. Pemberton and Cameron (1979) studied roller bearing lubrication using an optical window in a bearing. They observed that the inlet boundary length was itself controlled by the film thickness in the unloaded zone. Very recent work has been conducted by Kingsbury et al. (1990) and also by Schritz et al. (1994) on the subject of parched EHL.

Bearings can be marginally or well lubricated, with or without a flood lubrication system. Many bearings operate for years with a single charge of lubricant without replenishment. Even under conditions of marginal lubrication, bearings operate without new lubricant added. The questions that initiate the analysis given herein were as follows. Why in our recent traction studies could we get two distinct plateaus of film thickness? How can a bearing provide long life when each roller must be lubricated by the lubricant left behind the previous roller, over and over again for thousands or perhaps millions of cycles? Several lubrication theories have of course addressed this, but is there something we have overlooked?

The purpose of this paper is to present a reforming inlet EHL theory. In this theory, the thickness of the layer of lubricant in the bearing increases near the inlet of the conjunction region between ball and race. This thick layer allows for the formation of a good EHL film that can endure for millions of cycles. Solutions to equations using the Grubin (1949) approach with the Bell (1962) inlet approximation can be used to estimate the magnitude of this EHL film.

## 2. FLUID FLOW IN THE INLET REGION

It is helpful to divide the conjunction region between two elastic contacts into three regions (See Figure 1).

- The contact (slug flow) region
- The inlet region where the EHL film is formed
- The pre-inlet region where a lubricant layer builds up.

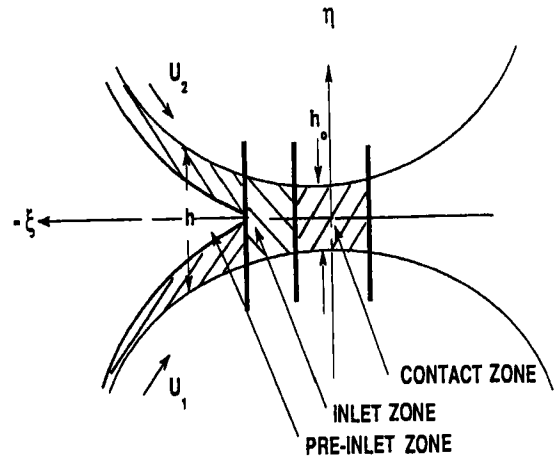


Figure 1. The inlet and pre-inlet region.

### 2.1. The Contact Region

In this region the flow of lubricant is given by the equation

$$Q = u_0 h_0 \quad (1)$$

### 2.2. The Inlet Region

In this region, the standard Reynolds equation is assumed to apply. Reynolds equation can be written

$$\frac{dp}{dx} = 6\mu(u_1 + u_2) \frac{h - h_0}{h^3} \quad (2)$$

When both surfaces are moving with identical velocities, the equilibrium equation appears.

$$\frac{1}{\mu} \frac{dp}{dx} \left( \frac{y^2 - yh}{2} \right) = u - u_0 \quad (3)$$

Combining Eqs. (2) and (3) yields

$$6(u_1 + u_2) \frac{h - h_0}{h^3} \left( \frac{y^2 - yh}{2} \right) = u - u_0 \quad (4)$$

or

$$6 \left( 1 - \frac{h_0}{h} \right) (\eta^2 - \eta) = \frac{u}{u_0} - 1 \quad (5)$$

At the center of the film ( $\eta = 1/2$ )

$$-\frac{3}{2} \left( 1 - \frac{h_0}{h} \right) = \frac{u}{u_0} - 1 \quad (6)$$

Note: all of the flow will be positive if  $u(\text{center}) = 0$  so

that

$$\frac{h_0}{h} = \frac{1}{3} \tag{7}$$

and

$$4(\eta^2 - \eta) = \frac{u}{u_0} - 1 \tag{8}$$

If lubricant layer were to grow in the pre-inlet region such that

$$h = 3h_0 \tag{9}$$

then all of the lubricant would flow through the contact region and continuously reform the film.

**2.3. Pre-inlet Region**

Assume that the equilibrium equation for the pre-inlet region is given by

$$\frac{dp}{dx} = \frac{\partial}{\partial y} \left( \mu \frac{\partial u}{\partial y} \right) \tag{10}$$

This equation, although convenient, is definitely an approximation because the shape of the pre-inlet boundary is variable and not necessarily parallel to the moving surface.

As the pre-inlet approaches the inlet region, a dynamic pressure builds as the lubricant on the surface of the layer slows down. Using the standard equation for dynamic pressure

$$p = \frac{1}{2} \rho u^2 \tag{11}$$

Combining Eqs. (10) and (11) and assuming flow is isoviscous and incompressible there results in the expression

$$\frac{1}{2} \rho \frac{\partial u^2}{\partial x} = \mu \frac{\partial^2 u}{\partial y^2} \tag{12}$$

In dimensionless form this equation becomes

$$\frac{\partial \bar{u}^2}{\partial(x/h_0)} = \frac{2}{\lambda \bar{h}^2} \frac{\partial^2 \bar{u}}{\partial \eta^2} \tag{13}$$

Equation (12) can be solved backward from the inlet region by using a “marching technique” starting from the edge of the inlet region and going outward. The equations to be solved are:

$$\frac{\partial \bar{u}^2}{\partial \xi_1} = - \frac{2}{\lambda \bar{h}^2} \frac{\partial^2 \bar{u}}{\partial \eta^2} \tag{14}$$

and at the inlet-pre-inlet boundary,

$$\bar{u} = 1 - 4(\eta^2 - \eta) \tag{15}$$

Also,

$$\bar{h} = \frac{1}{2} \left[ \int_0^{1/2} \bar{u} d\eta \right]^{-1} \tag{16}$$

A solution to the equations for ( $\lambda = 1$ ) are presented graphically in Figure 2.

**3. SOLUTION FOR FILM THICKNESS**

The film thickness equation attributed to Grubin could be written:

$$\frac{h_G}{R} = 0.998 \left( \frac{P_H}{E'} \right)^{-\frac{2}{11}} \left( \frac{\mu_0 \gamma u}{R} \right)^{\frac{8}{11}} \tag{17}$$

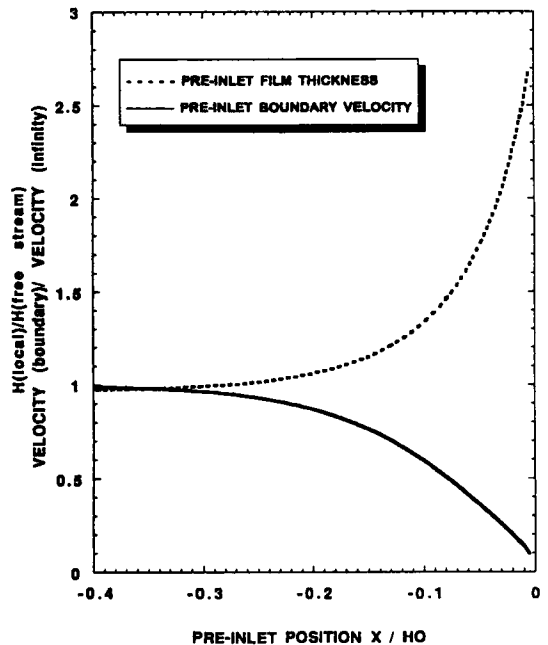


Figure 2. Pre-inlet film shape.

This equation is based on the assumption that there is

an infinite quantity of lubricant available in the inlet region. It is helpful to rederive this theory based on a limited inlet layer. The solution involves solving Reynolds equation (Eq. 2) with the inlet shape equation.

The inlet shape equation used in the Grubin analysis is the dry contact shape for concentrated contacts. This shape equation can be written:

$$h = h_o(1 + r) \tag{18}$$

$$r = \frac{4w'}{\pi E'h_o} \left[ \xi\sqrt{\xi^2 - 1} - \ln(\xi + \sqrt{\xi^2 - 1}) \right] \tag{19}$$

The Reynolds equation could be written:

$$\frac{dp}{d\xi} = \frac{dp}{dr} \frac{dr}{d\xi} = -6\mu u_o a \frac{h - h_o}{h^3} \tag{20}$$

Bell (1962) found an approximation for the expression  $\sqrt{\xi^2 - 1}$  such that

$$\frac{dr}{d\xi} = 3.04 \left[ \frac{w'}{E'h_o} \right]^{\frac{5}{8}} r^{\frac{3}{8}} \tag{21}$$

Combining E's. (17), (18), (20), and (21) yields:

$$\left( \frac{h_o}{h_G} \right)^{\frac{11}{8}} = 2.52 \int_0^{\frac{h_i}{h_o} - 1} \frac{r^{\frac{5}{8}}}{(1+r)^3} dr \tag{22}$$

If a bearing were initially filled with a complete charge of lubricant, then the Grubin equation would give the initial film thickness. However, if no lubricant were added, the Grubin film thickness would become the available layer of lubricant. In the pre-inlet region, this layer could increase by a factor of three before entering the inlet region. The predicted film thickness would be somewhat less than the initial film thickness, but eventually the film thickness would not degrade any further and it would reach a steady-state film thickness.

The inlet layer could be expressed as

$$h_i = 3h_o + \text{fill} \tag{23}$$

where the fill is any makeup lubricant that is added to the bearing. Then

$$\frac{h_i}{h_G} = 3 \frac{h_o}{h_G} + \frac{\text{fill}}{h_G} \tag{24}$$

and

$$\frac{\text{fill}}{h_G} = \left( \frac{h_o}{h_G} \right) \left( \frac{h_i}{h_o} \right) - 3 \frac{h_o}{h_G} \tag{25}$$

In the computations, it is straightforward to assume a value of  $h_i/h_o$  and compute  $h_o/h_G$ . Using these two parameters, the value of  $\text{fill}/h_G$  can be determined.

Figure 3 presents the ratio of "starved film thickness" versus the lubricant fill added after the initial charge. It is easy to conclude that an adequately lubricated bearing will operate in one of two modes. The steady-state film thickness is 0.728 times that which would occur if the inlet zone were flooded. For non-flooded conditions, the film thickness is just the layer of lubricant in the bearing.

Traction curves from Gleeson's tests are given in Figures 4 and 5. Note the traction tends to vary between two very sharp limits. This is most likely due to variation in lubricant supply. Either the inlet is starved or flooded. There is no in between region.

If the bearing only has a small lubricant layer initially, then this layer will become the film thickness. If this initial layer is increased, it will eventually start to flood the inlet and the film thickness will be as given by standard theory. This is illustrated by the graph of Figure 6.

### 3.1. Film Thickness from Pressure Measurements

If a bearing is initially flooded with lubricant but allowed to operate with no further make-up lubricant, the inlet region should begin at a point where the gap is three times the film thickness. Using the so-called Grubin (Hertzian) inlet equation, it should be possible to determine the film thickness by knowing the length of the inlet zone.

Using Eq. (18) and setting  $h/h_o = 3$  results in

$$r = 2$$

Using the Hertzian equations, this equation can be written as

$$h_o \left( \frac{R}{b^2} \right) = \frac{1}{4} \left[ \xi\sqrt{\xi^2 - 1} - \ln(\xi + \sqrt{\xi^2 - 1}) \right] \tag{26}$$

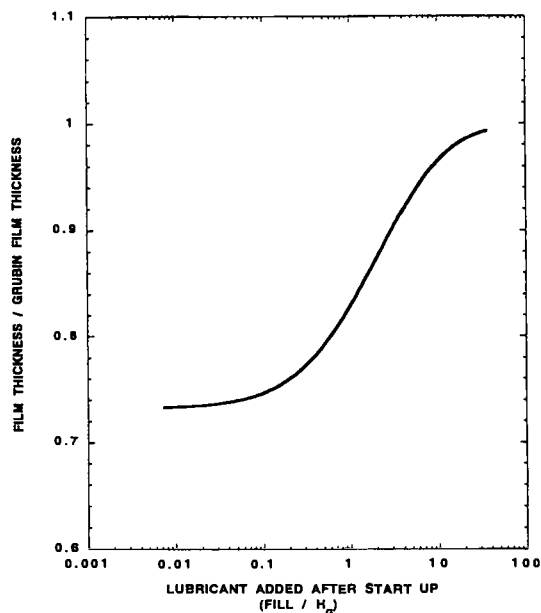


Figure 3. Effect of adding lubricant on EHL film.

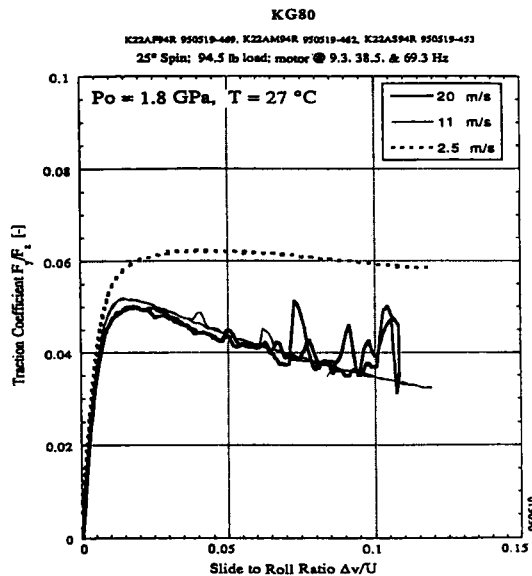


Figure 5. Traction tests with adequate lubricant supply rate.

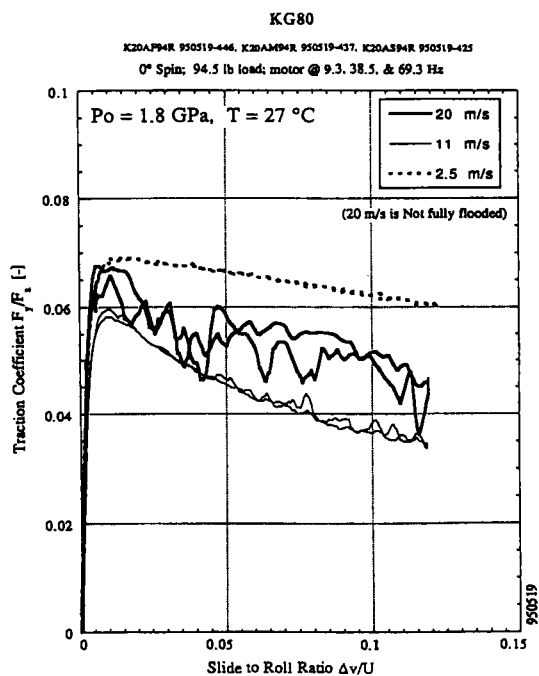


Figure 4. Effect of inadequate lubricant supply rate on traction (Gleeson data).

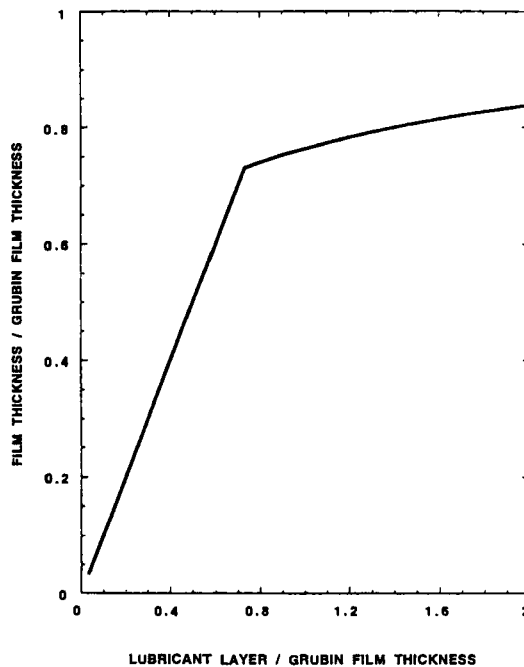


Figure 6. Effect of residual lubricant layer on EHL film (lubricant layer is the layer on one surface plus the layer on the other surface).

Figure 7 shows film thickness as a function of the inlet zone shape.

Pressure measurements were made at Battelle (Kannel et al., 1968) by using a thin film manganin transducer. This technique has been described in the literature. Figure 8 shows a sketch of the transducer on an 85 mm bore bearing. The general specifications for the bearing are

- ID 85 mm
- OD 150 mm
- Bearing width 28 mm
- Ball diameter 13/16 inch
- Contact angle 25 degrees
- Roll curvature 52 percent
- Number of balls 15

Typical pressure traces are given in Figures 9 and 10 for tests with two lubricants: a mineral oil and a polyphenyl ether. The viscosities for the lubricants are as follows.

|                  | 38°C    | 100°C   | Density |
|------------------|---------|---------|---------|
| Mineral Oil      | 50.8 cs | 6.8 cs  | 0.859   |
| Polyphenyl Ether | 306 cs  | 11.5 cs | 1.185   |

The film thickness as computed using the Grubin theory (at 30 C) is as follows.

$$\begin{aligned}
 h_G &= 2.0 \text{ microns (HRMO)} \\
 h_G &= 13.5 \text{ microns (5P4E)}
 \end{aligned}
 \tag{27}$$

Using the length of the inlet zone approximation, the film thicknesses would be

$$\begin{aligned}
 h_{in} &= 0.95 \text{ microns (HRMO)} \\
 h_{in} &= 4.4 \text{ microns (5P4E)}
 \end{aligned}
 \tag{28}$$

It appears that the operating film thickness in a bearing is somewhat less than would be expected for flooded lubrication. However, bearing temperature could be considerably higher than assumed, which of course would impact the film thickness computation by Grubin's theory.

#### 4. CONCLUSIONS

A bearing can run indefinitely on a single charge of lubricant provided there is nothing drawing the

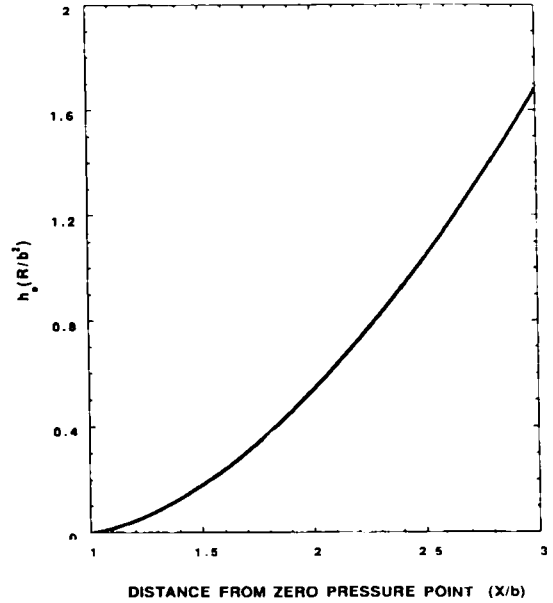


Figure 7. Film thickness theory based on inlet shape.

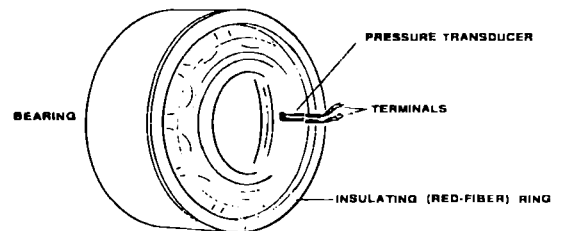


Figure 8. Schematic drawing showing surface-pressure transducer in an 85-millimeter split inner ring bearing.

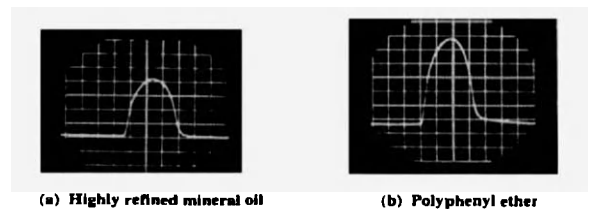


Figure 9. Film pressure measurement in 85-mm bearing scope speed 25 microseconds/division. Max. Pressure (1.4 GPa). Note: Scale factor on traces were different.

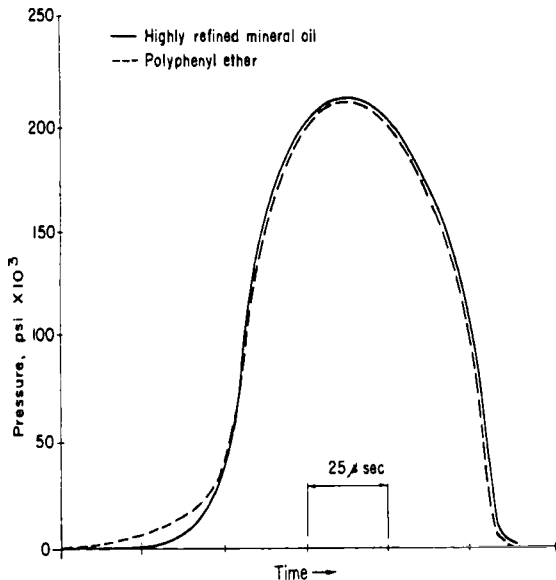


Figure 10. Comparison of ball-race pressure pattern in 85-mm bearing with lubricant type. Shaft speed - 2,500 rpm; contact load - 205,000 psi maximum Hertz pressure.

lubricant out, such as evaporation. If the bearing is initially flooded, the steady-state film thickness will be about 0.728 times the film computed using standard theory. If the bearing is not flooded with lubricant, the film thickness is basically equivalent to the layer of lubricant pre-deposited on the balls plus the races.

## 5. REFERENCES

1. S. Bair and M. Khonsari, "An EHD Inlet Zone Analysis Incorporating the Second Newtonian," Presented at the 1995 Jt. ASME/STLE Tribology Conference, Paper 95-TRIB-24, Orlando, Florida, October 8-11, 1995.
2. J.C. Bell, "Lubrication of Rolling Surfaces by a Ree-Eyring Fluid," *Trans. ASLE*, Vol 5, 1962, pp 160-171.
3. P. Castle and D. Dowson, "A Theoretical Analysis of the Starved Elastohydrodynamic Lubrication Problem for Cylinders in Line Contact," *Institution of Mechanical Engineers, Elastohydrodynamic Lubrication*, 1972, pp 131-137.
4. Y.P. Chiu, "An Analysis and Prediction of Lubricant Film Starvation in Rolling Contact Systems," *Trans. ASLE*, Vol. 17, 1974, pp 22-35.
5. D. Dowson and G.R. Higginson, "A Numerical Solution to the Elasto-hydrodynamic Problem," *J. Mech. Eng. Sci.*, Vol. 1, 1959, 1, pp 6-15.
6. J.B. Gleeson, "Lubricant Traction Measurements," Report to Aerospace Corporation, June 1995.
7. P.G. Goksem and R.A. Hargreaves, "The Effect of Viscous Shear Heating on Both Film Thickness and Rolling Traction in an EHL Line Contact, Part I: Fully Flooded Conditions, Part II: Starved Condition," *Trans. ASME, J. Lubric. Technol.*, Vol. 100, 1978, pp 346-358.
8. A.N. Rubin and I.E. Vinogradova, "Investigation of the Contact of Machine Components," Moscow, TsNIIT-MASh, Book No. 30, 1949, (D.S.I.R., London, Translation No. 337).
9. B.J. Hamrock and D. Dowson, "Isothermal Elastohydrodynamic Lubrication of Point Contacts, Part IV--Starvation Results," *J. Lubric. Technol.*, January 1977, p 15.
10. R.A. Hargreaves and G.R. Higginson, "Some Effects of Lubricant Starvation in Cylindrical Roller Bearings," *Trans. ASME, J. Lubric. Technol.*, Vol. 98, 1976, pp 66-72.
11. J.W. Kannel, J.C. Bell, J.A. Walowit and C.M. Allen, "A Study of the Influence of Lubricants on High-Speed Rolling-Contact Bearing Performance, Part VIII. Research on Elastohydrodynamic Lubrication on High-Speed Rolling Contacts," Report to Air Force Aero Propulsion Laboratory, Technical Documentary Report ASD-TDR-61-643, Part VIII, June 1968.
12. E. Kingsbury, B. Schrittz and J. Prah, "Parched Elasto Hydrodynamic Lubrication Film Thickness Measurement in an Instrument Ball Bearing," *Tribology Transactions*, Vol. 33, 1990, 1, pp 11-14.
13. D.N. Olaru and M.D. Gafitanu, "Starvation in Ball Bearings," *Wear*, Vol. 170, 1993, pp 219-234.
14. J.C. Pemberton and A. Cameron, "An Optical Study of the Lubrication of a 65 mm Cylindrical Roller Bearing," *J. Lubric. Technol.*, Vol. 101, July 1979, p 327.
15. J.C. Pemberton and A. Cameron, "A Mechanism of Fluid Replenishment in Elasto-Hydrodynamic Contacts," *Wear*, Vol. 37, 1976, pp 185-190.

15. B. Schrittz, W.R. Jones, Jr., J. Prah and R.. Jansen, "Parched Elastohydrodynamic Lubrication: Instrumentation and Procedure<sup>o</sup>," *Tribology Transactions*, Vol. 37, 1994, 1, pp 13-22.
16. L.D. Wedeven, D. Evan and A. Cameron, "Optical Analysis of Ball Bearing Starvation," *J. Lubric. Technol., Trans. ASME*, Series F, Vol. 93, No. 3, July 1971, pp 349-363.
17. P.E. Wolveridge, K.P. Baglin and J.G. Archard, "The Starved Lubrication of Cylinders in Line Contact," *Proc. Inst. Mech. Eng.*, Vol. 185, 1971, p 1159-1169.

## 6. NOMENCLATURE

|       |  |
|-------|--|
| b     | nip half width   |
| E     | Young's modules  |
| $E^l$ | $\frac{1}{E^l} = \frac{1}{2} \left[ \frac{1-v_1^2}{E_1} + \frac{1-v_2^2}{E_2} \right]$ |
| $h_i$ | lubricant layer in bearing (surface 1 plus surface 2)                                  |
| h     | gap between rollers  |
| $h_o$ | minimum gap  |

|             |  |
|-------------|--|
| $h_G$       | film thickness computed by Grubin's equation (17)                            |
| $\tilde{h}$ | $h/h_o$  |
| p           | pressure   |
| $P_H$       | maximum Hertz pressure   |
| Q           | flow of lubricant  |
| $R_1, R_2$  | radii of rollers   |
| R           | relative radius $\left( \frac{1}{R} = \frac{1}{R_1} + \frac{1}{R_2} \right)$ |
| u           | velocity   |
| $u_1, u_2$  | surface velocity of rollers  |
| $u_o$       | velocity in center of contact  |
| $\tilde{u}$ | $u/u_1$  |
| x           | coordinate variable  |
| y           | coordinate variable  |
| $w'$        | load per unit width  |
| v           | Poisson's ratio  |
| $\gamma$    | pressure velocity coefficient  |
| $\eta$      | $y/h$  |
| $\xi$       | $x/b$  |
| $\xi_1$     | $-x/h_o$   |
| $\lambda$   | $\frac{\rho u_1 h_o}{\mu_o}$   |
| $\mu$       | viscosity  |
| $\mu_o$     | base viscosity   |
| $\rho$      | mass density   |



## Track Depletion and Replenishment in a Grease Lubricated Point Contact: A Quantitative Analysis

P.M.E. Cann<sup>a</sup>, F. Chevalier<sup>b</sup>, A.A. Lubrecht<sup>b</sup>

<sup>a</sup>Tribology Section, Imperial College of Science, Technology & Medicine, London, SW7 2BX, UK.

<sup>b</sup>Laboratoire de Mécanique des Contacts, UMR CNRS 5514, INSA de Lyon, France.

At present there are no quantitative models available for the prediction of grease film thickness in rolling element bearings. The problem is a difficult one as it involves both rolling bearing parameters (geometry and kinematics) and grease properties. It is the role of the grease that is considered in this paper.

Grease behaviour in rolling contacts is very complex. At low shear stress grease behaves as a plastic solid and once pushed aside by the passage of a rolling element it will not spontaneously flow back to replenish the track. Thus, unless there is an external mechanism supplying bulk lubricant to the inlet, such contacts operate under severely starved conditions. Grease film thickness is determined by the flow balance existing between the loss from the track and local resupply mechanisms. It is difficult, however, to quantify these effects as we know little of the mechanisms involved. One approach to this problem is through a starved fluid film model, as this might be regarded as the simplest form of starved grease lubrication.

Fluid film starvation has been studied both experimentally, and theoretically where the loss mechanisms have been identified. In the modelling work, oil loss from a circular EHD contact was quantified, and a very simple relation between oil film reduction and number of overrollings obtained. In the current paper this analysis is extended to grease lubricated point contacts. The aim is to quantify lubricant reflow and to identify the important replenishment mechanisms involved.

A series of experiments was conducted where film thickness change with repeated overrolling was measured for different grease and operating parameters. After many overrollings the film thickness approaches the steady-state condition where film depletion and replenishment are balanced. By varying the test conditions it is thus possible to quantify loss and supply and to identify the important model parameters.

This analysis is performed using a simple loss and replenishment model, an extension from earlier starvation work. Using this model the film thickness decay as a function of the number of overrollings  $n$  is obtained. From this analysis the required oil replenishment rate to obtain a steady state film thickness is also derived.

### 1. Introduction

Lubricating performance is rarely considered when choosing a grease for rolling element bearings and, yet, this is the most important parameter in determining the life of the bearing. The main reason for this is that, compared to fluid film lubrication, we have little detailed knowledge of the mechanisms of grease lubrication and the way in which they control the film thickness. Thus, it is neither possible to predict lubrication performance from bulk grease properties nor to design pertinent screening tests to measure the relevant parameters

Several different lubrication mechanisms have

been suggested and these can be classified according to the efficiency of the contact supply mechanism as full flow (inlet maintained) [1-3] or restricted (starved) [4, 5]. The full flow models can be used to predict film thickness from empirical rheological properties and reasonable agreement is found. However the main assumption of the continued flow of bulk grease into the inlet is not realistic and it is difficult to apply such a model to film prediction in real bearings. Thus the full flow model will provide an 'upper limit' for the lubricating film thickness. This will occur when bulk grease replenishment has been initiated by the operation of the bearing, for instance due to cage movement, ball spin or vibration. It is un-

likely that this will provide a continual flow of grease and that starvation, and thus film decay, will inevitably occur during most of the bearing operating cycle. Observation of grease behaviour [6-8] in a simple rolling contact has shown that, under most conditions, the film decays rapidly as the grease is pushed aside and the track is progressively depleted. Thus it is the supply mechanisms which occur under bulk starved conditions that will determine the lubrication performance of a grease.

The conventional view of grease lubrication in rolling element bearings is that the grease provides a controlled flow of base oil into the track thus maintaining a separating film [4]. This idea was first suggested over 40 years ago, however it has remained a vague concept, almost hearsay, as there is little supporting experimental evidence barely any advance in the development of this model was made in the intervening years. The second restricted flow model was suggested by Scarlett [5] in his review of grease lubrication in bearings. He maintained that there was no bulk movement of either grease, or base oil, to replenish the track and that the rolling surfaces were separated by a film of grease deposited in the first few minutes of operation before the bulk grease has cleared. This film is composed of heavily worked grease, although it retains a high viscosity, and is thus held in the track. Neither model can be used to predict film thickness for a specific grease or bearing operation parameters. This paper is one of the first attempts to provide a scientific basis for these physical models and to develop a framework for future analysis.

The problem of fluid film starvation has been studied both experimentally and theoretically in recent years and significant advances have been made. It is of interest here as starved fluid film lubrication is, perhaps, the simplest form of starved grease lubrication. Experimental studies [9-12] have shown that the degree of starvation depends on the amount of oil available, rolling speed and oil viscosity. In the starved regime film decay occurs progressively as oil is lost from the contact due to the passage of the ball. Numerical models [11, 12] have been developed to predict the film decay with the number of overrollings and good

agreement has been found.

In the current study the fluid film starvation analysis [12] is extended to grease lubricated contacts. The predictions of the model are compared to experimental measurements of grease film decay and stabilisation. Such a comparison can provide an insight into the important model parameters and the mechanisms of film decay. The aim is to develop a physical and numerical model capable of describing, and predicting, grease behaviour under heavily starved conditions.

## 2. Nomenclature

|                   |  |
|-------------------|--|
| $h_{cff}$         | fully flooded central film thickness   |
| $h_c$             | central film thickness under starved conditions  |
| $h_{oil}$         | inlet oil film thickness   |
| $n$               | number of overrollings or disk revolutions   |
| $r$               | relative inlet oil film thickness,<br>$r = h_{oil}/h_{cff}/\bar{\rho}(p_h)$              |
| $dr$              | mean replenishment rate for a given $\mathcal{R}$ value                                  |
| $\mathcal{R}$     | central film thickness reduction or relative film thickness, $\mathcal{R} = h_c/h_{cff}$ |
| $\bar{\rho}(p_h)$ | compressibility factor at the maximum Hertzian pressure                                  |
| $\Phi$            | mean flux per revolution replenishing the contact track                                  |
| $\gamma$          | reduction parameter for the central film thickness, $\mathcal{R} = r/\sqrt{1+r^\gamma}$  |

## 3. Experimental Procedure

Central film thickness was measured for a series of simple greases in a rolling point contact device. The contact is formed by a steel ball loaded and rolling against a glass disc. The ball is mounted on a shaft that is connected to an electric motor by a flexible mounting. The disc is driven by the ball in nominal pure rolling. Thin film optical interferometry was used to measure film thickness in the centre of the contact. This technique is described in detail in earlier publications [13].

The aim of this study was to quantify grease film loss, and replenishment, in a contact where there is no bulk supply to the inlet. It was necessary therefore to develop a test method where

the amount of grease available was carefully controlled. The experimental procedure was as follows: a small amount of grease (0.5ml) is applied as a single charge over one revolution of the disc. The ball shaft is rotated by hand and a syringe is used to inject the grease directly into the inlet region. In this way an even amount of grease is applied around the track. The ball motor was then started at a preset speed and film thickness measured, at constant speed, as a function of disc revolution. Typically the tests ran for 1000 - 2000 revolutions with rolling speeds in the range 0.01 - 0.1 m/s. In a parallel series of experiments the decay function for the base oils, under starved conditions, was also measured. Oil was progressively removed from the ball and disc, until the contact starved and film thickness decay was then measured in a similar manner.

For the purposes of the starvation analysis it was necessary to measure grease film thickness under fully flooded conditions. A separate series of tests was thus run where a small reservoir was pushed up against the underside of the disk. This collected the displaced grease and channeled it back into the track, thus ensuring fully flooded conditions. Film thickness was measured as a function of increasing rolling speed for the range 0.01 to 0.5 m/s. A maximum Hertz pressure of 0.48 GPa and bulk temperature of 25°C were used in all the tests.

#### 4. Model Greases

A matrix of four test greases was used in this work. The greases were specially made by a single manufacturer and they consisted of a paraffinic base oil with lithium hydroxystearate thickener. The greases contained no additives. Two base oil viscosities and two thickener concentrations were used. These are listed in Table 1.

A set of simple greases was chosen in order to limit the number of variables. The single origin of the greases guarantees that the thickener composition and manufacturing processes are similar. The absence of additives ensures that it is the effect of the physical properties of the grease on replenishment that is studied. The matrix of two viscosities and two thickener concentrations per-

mits a systematic study of these properties.

| Grease | Base oil viscosity [Pa s] | Soap concentration % w/w |
|--------|---------------------------|--------------------------|
| A      | 0.1                       | 8                        |
| B      | 0.1                       | 11                       |
| C      | 0.4                       | 8                        |
| D      | 0.4                       | 11                       |

Table 1

*Model grease properties.*

## 5. Results

### 5.1. Fully Flooded

A representative fully flooded curve is plotted in Figure 1 for grease A. Generally, film thickness increased with rolling speed in a similar manner to classical fluid film results. Film thickness enhancement, relative to the base oil, was measured and this could be related to thickener concentration. Figure 1 also shows a starved speed result for grease A. In this test 0.5 ml of grease was applied to the track and the speed increased in the normal way. The channeling device was not used. Initially the starved curve follows the fully flooded curve. At 0.05 m/s the starved curve starts to deviate from the fully flooded one, and drops rapidly to an initial level of 30-40 nm. However, this level is time dependent and a further drop to a much lower level of 6 nm occurs within a few minutes at constant speed. It is this progressive starvation and subsequent stabilisation of the film that is studied in this paper.

### 5.2. Base Oil Decay

The model used in this work is based upon a starved fluid film analysis. It was therefore necessary to measure the base oil decay curves. The analysis quantifies starvation relative to the fully flooded film. Therefore, in all the figures that follow, the relative film thickness  $\mathcal{R}$  is plotted, this is the starved film thickness divided by the fully flooded value.

In Figures 2 and 3 the relative film thickness is plotted for the two base oils. In both cases the

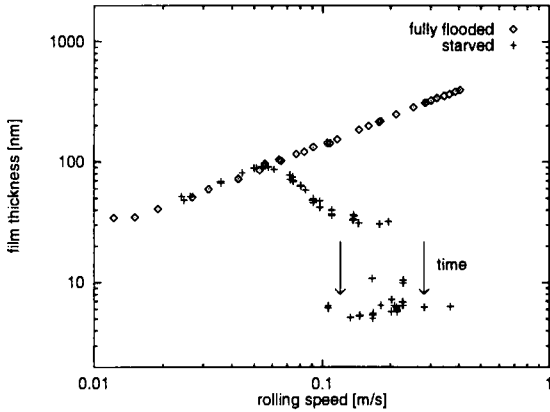


**Figure 1** Film thickness as a function of speed, fully flooded and starved: Grease A.

relative film thickness decays over the first 100 disk revolutions, before stabilising at a level determined by the local replenishment action. For a given oil, and a given set of operating conditions (in this case speed) the replenishment action depends solely on the initial amount of oil available on the track. In these tests it was not possible to control carefully the amount of oil, however, it is the gradient in the decay region that is of primary interest in this analysis and the final steady state value does not influence this gradient.

In the same Figures the theoretical decay curve is represented by a dotted line. The 0.1 Pa s base oil gives a  $\gamma = 3.5$ , whereas the 0.4 Pa s base oil gives  $\gamma = 3.1$ . These values are computed according to the method described in [12] (see also the appendix). As was found in that paper, the agreement between experimental results and theoretical predictions is very good.

**5.3. Grease Decay**

The grease decay curves, represented in the Figures 4-7, all have the same overall behaviour. The shape of the decay curves is far more complex than for the base oils. The base oils decay immediately before leveling off whereas three distinct regions can be observed for the greases.

Region I: a relatively constant film thickness exists during the first few overrollings.

Region II: a rapid decay, similar to the one observed with the base oils.

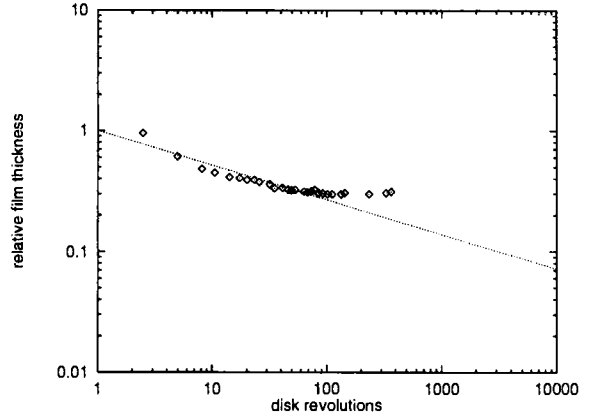


**Figure 2** Relative film thickness as a function of the number of overrollings for 0.1 m/s base oil of 0.1 Pa s, compared with the  $\gamma = 3.5$  curve.

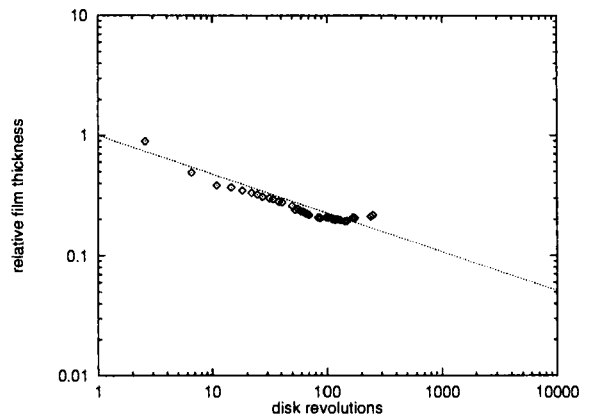


**Figure 3** Relative film thickness as a function of the number of overrollings for 0.1 m/s base oil of 0.4 Pa s, compared with the  $\gamma = 3.1$  curve.

Region III: an evolution towards a constant value.

For certain cases, zone III was not stable and a second rapid decrease was observed leading to very thin films.

In Figure 4 grease A at 0.05 m/s shows no reduction of the film thickness at all, region I merges with region III without any starvation effects at all. From Figure 1, one can conclude that for this speed, the starved results and the fully flooded ones are very close. At higher speeds region I extends to approximately 50 disk revolutions. From there on a steep decay seems to occur, followed by stabilisation and subsequent increase in the film thickness. This increase is particularly marked for the 0.075 m/s curve.

Grease B in Figure 5 gives a very similar set of curves, except that even at 0.01 m/s a reduction of the film thickness to 30% occurs. At higher speeds (0.05, 0.1 m/s) the film thickness stabilises at much lower values.

Grease C in Figure 6 behaves in a similar fashion to the two previous greases, whereas the grease D response, in Figure 7, is unstable in zone III at 0.1 m/s.

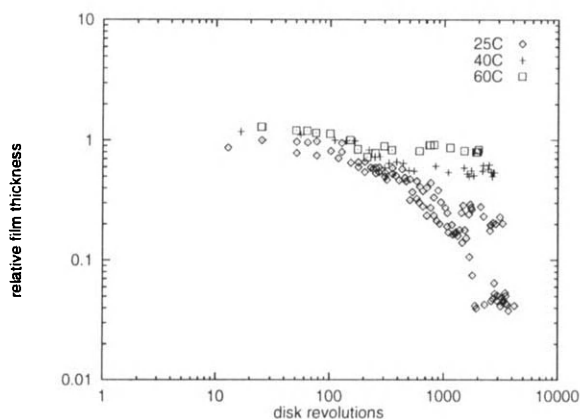


**Figure 4** Relative film thickness as a function of number of overrollings for 3 speeds; Grease A.

## 6. Analysis and Discussion

In this section, the three different zones described briefly in the previous section are analysed in de-

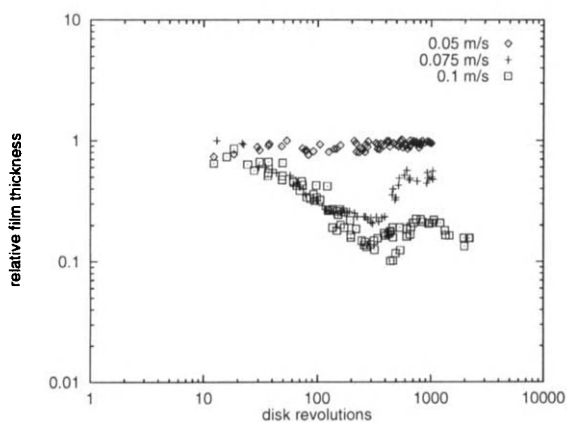


**Figure 5** Relative film thickness as a function of number of overrollings for 3 speeds; Grease B.

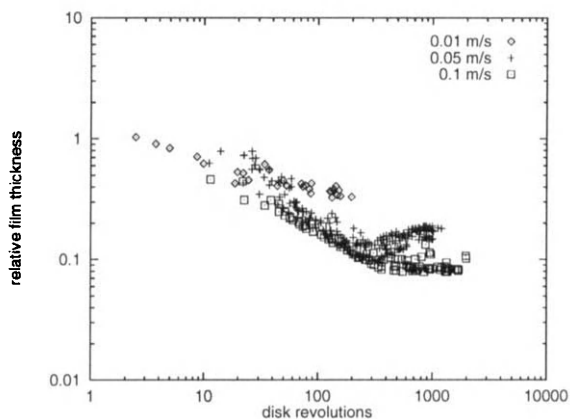


**Figure 6** Relative film thickness as a function of number of overrollings for 3 speeds; Grease C.

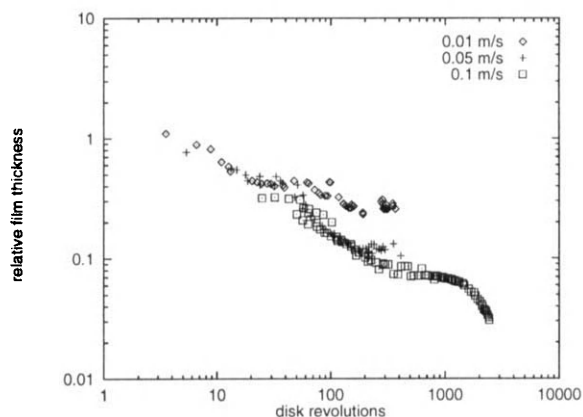


**Figure 7** Relative film thickness as a function of number of overrollings for 3 speeds; Grease D.

tail.

### 6.1. Zone I

During the initial overrolling of fresh grease at the start of the test a thick 'high viscosity' layer is deposited in the track. The bulk grease is then pushed away from the track and the inlet is starved. This can be seen in Figure 8, which is an image of grease A taken at the start of the test. The film in the contact has a classical EHD shape although there is no bulk oil present in the inlet. The EHD film thickness distribution is therefore generated from the deposited layer of grease. At the beginning of the test this deposited grease has not been significantly shear degraded and thus retains most of its original properties. In the low pressure region, the shear strength of the grease prevents lateral flow from the track. In the high pressure region, the increased base oil viscosity prevents lateral flow. Only in a limited intermediate region, can the lubricant escape from the contact track, thus explaining why the film thickness hardly decreases. The breakdown of the grease in this layer during subsequent overrollings leads to zone II, whenever fresh grease is no longer fed into the contact. The degree of breakdown depends on the grease shear stability and the shear stress level in the contact (speed).

The duration of this zone will be very dependent on the amount of fresh grease being fed into the contact. This can be caused by continuously resupplying the grease, but also by minor geometrical misalignments and vibrations. The soap thickener properties will also influence this zone.

### 6.2. Zone II

The breakdown of the thickener structure in region I releases base oil which is then expelled from the contact. Therefore it is considered that it is this loss which dominates the film decay. Consequently the decay curve should be similar to that obtained for the base oil alone. Thus, the decay in Figures 4 and 5, and in Figures 6 and 7, should be similar; which is approximately true. From the Figures 4 - 7 it seems as if this slope is much higher for the grease lubricated contacts. However it should be remembered that the logarithmic graph is misleading in this respect. In Figure

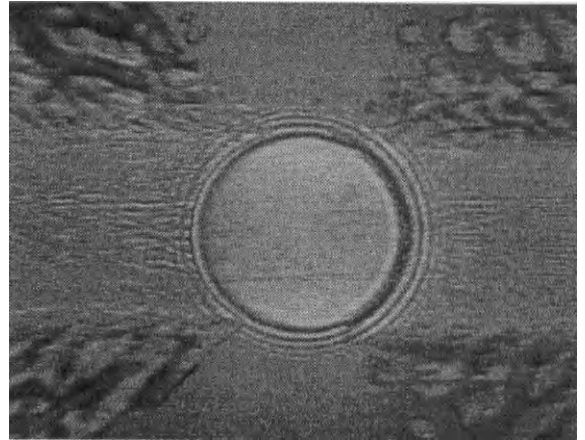


**Figure 8** Interference picture of grease A after only few revolutions.

9 the results for grease B at 0.1 m/s have been replotted with region I removed. In this Figure, the theoretical base oil decay (Figure 2) is plotted as well. The slopes are similar, but the film thickness value is too low. This can be partially explained by the fact that the film thickness is divided by the fully flooded grease film thickness, whereas the base oil fully flooded film thickness is 20 % lower.

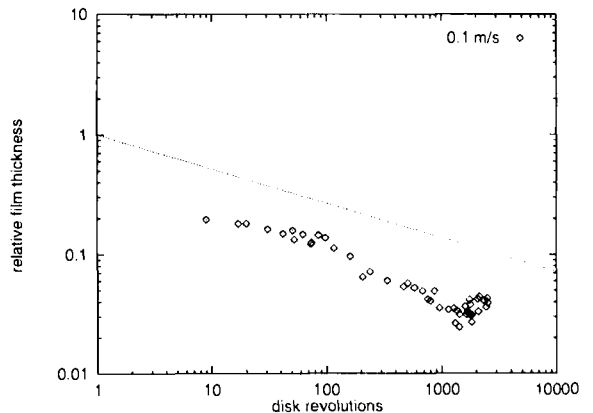


**Figure 9** Relative film thickness as a function of the number of overrollings for 0.1 m/s; Grease B, zone I removed.

### 6.3. Zone III

In zone III the film thickness stabilises and, in some cases, an increase is observed. This is thought to be due to two effects; an increasing availability of free base oil from the worked grease reservoir close to the track and a decrease in the amount of oil being expelled from the contact due to the reduction in absolute film thickness. Thus a flow balance is achieved and, hence, film thickness stabilisation. For real applications this steady-state film thickness value will determine successful operation or failure.

It is possible to translate the stabilised  $\mathcal{R}$  values in terms of the mean replenishment rate  $dr$  (see the appendix for full explanation).  $dr$  is defined as the mean oil film thickness increase over the Hertzian track, during one overrolling. These results are given in Table 2.

| Grease | $u$   | $\mathcal{R}$ | $dr$               | $\Phi$          |
|--------|-------|---------------|--------------------|-----------------|
| A      | 0.05  | 1.0           | -                  | -               |
|        | 0.075 | 0.5           | $1. \cdot 10^{-2}$ | $3. \cdot 10^4$ |
|        | 0.1   | 0.2           | $2. \cdot 10^{-4}$ | $9. \cdot 10^2$ |
| B      | 0.01  | 0.35          | $2. \cdot 10^{-3}$ | $2. \cdot 10^2$ |
|        | 0.05  | 0.1           | $1. \cdot 10^{-5}$ | $1. \cdot 10^1$ |
|        | 0.1   | 0.03          | $2. \cdot 10^{-7}$ | $1. \cdot 10^0$ |
| C      | 0.01  | 0.4           | $8. \cdot 10^{-3}$ | $2. \cdot 10^3$ |
|        | 0.05  | 0.2           | $5. \cdot 10^{-4}$ | $2. \cdot 10^3$ |
|        | 0.1   | 0.09          | $2. \cdot 10^{-5}$ | $2. \cdot 10^2$ |
| D      | 0.01  | 0.3           | $2. \cdot 10^{-3}$ | $4. \cdot 10^2$ |
|        | 0.05  | 0.1           | $3. \cdot 10^{-5}$ | $1. \cdot 10^2$ |
|        | 0.1   | -             | -                  | -               |

Table 2

Approximate mean replenishment values  $dr$  corresponding to the stabilised  $\mathcal{R}$  values from Figures 4 - 7, speed  $u$  in [m/s],  $\Phi$  in [ $\mu\text{m}^3/\text{s}$ ].

Note that the  $dr$  values from Table 2 can not be directly compared since they include  $h_{cff}$  values which are different due to the different viscosities and speeds (time). Therefore, the mean flux into the track  $\Phi$  was defined as the flow into the track per revolution.  $\Phi$  is given by:

$$\Phi = dr h_{cff} 2b 2\pi R / T_{overrolling}$$

$$= dr h_{cff} 2b 2\pi R / (2\pi R / u)$$

$$= 2b u dr h_{cff}$$

with the track radius  $R = 40$  mm, and the Hertzian half width  $b = 0.167$  mm. One needs to keep in mind that  $\Phi$  is a mean quantity, and that both the exact oil profile (as a function of  $Y$ ) and the flux as a function of time might be very different, which may result in a different film behaviour. The figures given in this Table indicate that only a minute quantity of base oil needs to reflow into the track to build up a stationary film.

The reflow rates given by this analysis appear astonishingly small, however, it must be remembered that the tests were carried out at room temperature. In more recent work grease starvation has been measured at higher temperatures and the results show that the reflow rate  $\Phi$  for grease B increases over 100 fold from 25 to 60 °C.

## 7. Conclusion

This paper has sought to establish the ground rules for the quantitative analysis of base oil reflow from grease in the starved regime. Film thickness decay has been measured in a rolling point contact for a range of greases and the results compared to predictions from a numerical model. The analysis is derived from a simple fluid film starvation model; although the experimental results have shown the grease behaviour to be far more complex.

The grease film decay behaviour displays three distinct regions which encompass both the high viscosity layer and base oil bleeding mechanisms suggested by earlier workers [1, 2]. The predominance of the either mechanism depends upon operating conditions and grease properties.

The durability of the high viscosity layer in region I, is very dependent on the initial addition and will be investigated properly in the future. It is not, therefore, discussed here.

Behaviour in region II can be described in terms of the base oil decay, which has been extensively described elsewhere.

Using a simple equilibrium equation, the replenishment flow in zone III has been approximated.

The agreement between experimental and numerical results, taking into account the simplifications assumed in the model and experimental errors, is good. One problem with the analysis is that the composite film thickness for the grease is used. Earlier studies have shown that such films contain a solid component and, superimposed on this, a hydrodynamically derived oil film. In future studies it will be necessary to measure both components at the end of the test to give a more accurate estimation of the the residual oil film and, hence, reflow. However, the current results can be regarded as an upper limit.

This study has been confined to low temperatures and is, thus, not representative of bearing operation where bulk temperatures of 40 - 80°C are usual. Initial results suggest that base oil reflow increases rapidly at the higher temperatures. Future work will thus seek to extend the test conditions (higher temperatures and rolling speeds) and refine the model.

It is hoped that such an approach will, eventually, allow the prediction of real reflow, and film stabilisation levels in grease lubricated bearings and the development of more pertinent screening tests.

## 8. References

- [1] Kauzlarich, J.J., and Greenwood, J.A., "Elastohydrodynamic Lubrication with Herschel-Bulkley Model Greases", ASLE Trans., 15, pp 269-277, (1972).
- [2] Zhu, W.S., and Neng, Y.T., "A Theoretical and Experimental Study of EHL Lubricated With Grease.", J. Tribol. ASME Trans., 110, pp 38-43, (1988).
- [3] Cheng, J., "Elastohydrodynamic Grease Lubrication Theory and Numerical Solution in Line Contact.", STLE Trib. Trans., 37, pp 711-718, (1994).
- [4] Baker, A.E., "Grease Bleeding - A Factor in Ball Bearing Performance.", NLGI Spokesman, 22, pp 271-279, (1958).
- [5] Scarlett, N.A., "Use of Grease in Rolling Bearings.", Proc. IMechE. 3A, 182, pp 585-593, (1967).
- [6] Åstrom, H, Östenson, J.O., and Höglund, E., "Lubricating Grease Replenishment in an Elastohydrodynamic Point Contact", ASME JoT, Vol. 115, pp. 501-506, (1993).
- [7] Cann, P.M.E., and Spikes, H.A., "Film Thickness Measurement of Greases under Normally Starved Conditions", NLGI Spokesman, Vol. 56, pp. 21-26, (1992).
- [8] Cann, P.M.E. "Understanding Grease Lubrication", presented at the 22nd Leeds-Lyon Symposium on Tribology (1995).
- [9] G. Guantang, P.M. Cann and H. Spikes "A Study of Parched Lubrication", Wear 153, pp. 91-105, (1991).
- [10] Chiu, Y.P., "An Analysis and Prediction of Lubricant Film Starvation in Rolling Contact Systems", ASLE Trans, 17, 1, pp. 22-35, (1974).
- [11] Chevalier, F., Lubrecht, A.A., Cann, P.M.E., Colin, F., and Dalmaz, G., "Starvation Phenomena in EHL Point Contacts, Influence of Inlet Flow Distribution", Proc. 22nd Leeds-Lyon Symposium on Tribology, Lyon (1995).
- [12] Chevalier, F., Lubrecht, A.A., Cann, P.M.E., Colin, F., and Dalmaz, G., "Film Thickness in Starved EHL Point Contacts", paper accepted for publication in the ASME JoT.
- [13] Johnston, G.J., Wayte, R., and Spikes, H.A., "The Measurement and Study of very Thin Lubricant Films in Concentrated Contacts", Tribology Transactions, 2, 34, pp. 187-194, (1991).

## 9. Appendix

It was shown in reference [11] that a starved oil lubricated contact could be described by:

$$\mathcal{R} = \frac{r}{\sqrt[3]{1+r^\gamma}}$$

with  $\mathcal{R} = h_c/h_{c_{ff}}$  and  $r = h_{oil}/h_{c_{ff}}/\bar{\rho}(p_h)$ .

For the cases treated, the values of  $\gamma$  are respectively 3.5 and 3.1 for the base oil viscosities of 0.1 and 0.4 Pa.s at the speed of 0.1 m/s.

If the mean outlet film thickness across the Hertzian width is approximated by the  $h_c \bar{\rho}(p_h)$  value, the film decay can be evaluated, in case of zero replenishment, by:

$$\mathcal{R}(n) = \frac{1}{\sqrt[3]{1/r_0^\gamma + n}} \approx n^{-1/\gamma}$$



The theoretical base oil decay is represented in Figures 2 and 3.

To extend this analysis, we can now consider the mean replenishment rate over the Hertzian width, depending on the initial quantities available on the track and on the rheological properties of the lubricant. The equilibrium between in-flow and out-flow is reached when the sum of the mean outlet film thickness and the mean replenishment is equal to the mean inlet value. Thus, if  $dr$  is the mean replenishment rate, this equilibrium reads (see Figure 10):

$$r = \mathcal{R} + dr$$

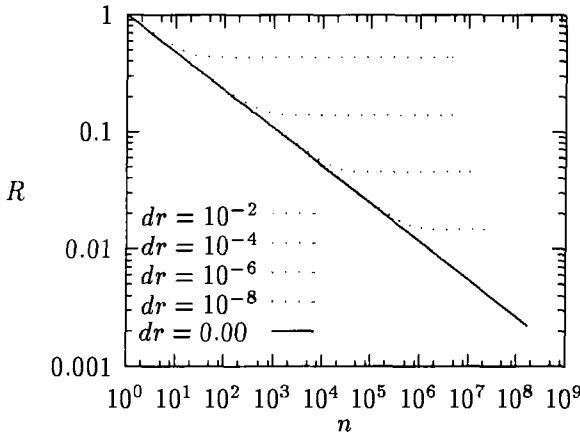


**Figure 10** Relative film thickness decay for different values of replenishment rate  $dr$  into the track.

If the film thickness is stabilized at a given value  $\mathcal{R}$ , the mean replenishment can be evaluated by:

$$dr = \frac{\mathcal{R}}{\sqrt{1 - \mathcal{R}^\gamma}} - \mathcal{R}$$

Figure 11 represents the evolution of  $dr$  as a function of the stabilised  $\mathcal{R}$  values for  $\gamma = 3.1$  and  $\gamma = 3.5$ .

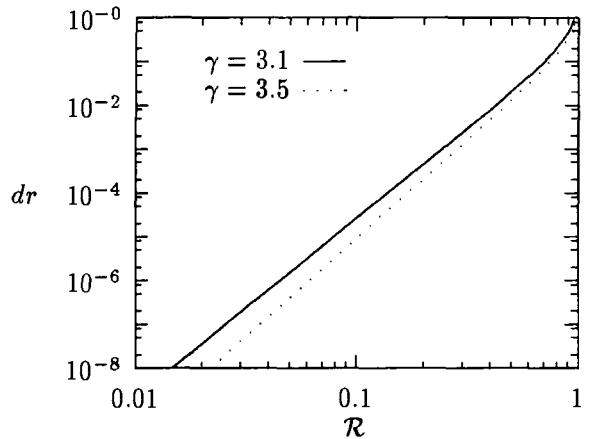


**Figure 11** Mean replenishment rate  $dr$  as a function of the stabilised central film thickness reduction  $\mathcal{R}$  for  $\gamma = 3.1$  and  $\gamma = 3.5$

So if one supposes that the film thickness is only composed of base oil, which is not completely true, the mean replenishment quantities can be evaluated from the stabilised film thickness in Figures 4-7.

## Oil film thickness and shape in Lundberg's profile roller contacts

X. -Y. Chen<sup>a</sup>      S. -Q. Zhou<sup>a</sup>      J. -J. Ma<sup>b</sup>

<sup>a</sup> Research Institute of Bearings, Shanghai University,  
 P.O. Box 224, 149 Yangchang Road, Shanghai, 200072, P. R. China

<sup>b</sup> Department of Mechanical Engineering, Zhejiang University,  
 20 Yugu Road, Hangzhou, 310027, P. R. China

In order to study the effects of amount of crowning on the elastohydrodynamic of lubrication (EHL) of rollers with Lundberg's profile, optical interferometry is applied to measure the oil film thickness between a profiled taper roller and a glass plate under pure rolling conditions. It was found from the experiments that there exists an optimum value of crowning of Lundberg's profile in the given working condition by which the maximum evenness in axial direction of the oil film thickness and the pressure distribution can be obtained. The optimum crowning value obtained in EHL state is larger than the design value obtained in dry contact state for the same working conditions.

### 1. INTRODUCTION

Roller bearings are used to support heavy loads, frequently at high rotational speeds. When a roller of finite length contacts with a raceway of greater width and if the generatrix of the contact pair is absolutely straight (which is the basic idea behind roller bearings), compressive stress peaks, known as edge effects, will arise at the ends of the contact surfaces, since the material in the raceway is under tension at the roller ends because of depression of the raceway outside of the roller ends. The edge stresses will considerably shorten the bearing fatigue life. And this effect will be even more pronounced in a misalignment state. To avoid this, rollers are usually slightly modified toward the ends.

According to elastostatic analysis, Lundberg[1] had found the logarithmic generatrix to be the best profile for finite line contacts, which yields a substantially optimized stress distribution under most conditions of loading, and gave out the logarithmic profile function:

$$\begin{cases} C_r(y) = \frac{2Q}{\pi E' L_{we}} \ln \frac{1}{1 - (2y/L_{we})^2} & y \neq \pm \frac{L_{we}}{2} \\ C_r(y) = \frac{2Q}{\pi E' L_{we}} (1.1932 + \ln \frac{L_{we}}{2a}) & y = \pm \frac{L_{we}}{2} \end{cases}$$

Where

$$E' = \frac{2}{(1 - \nu_1^2) / E_1 + (1 - \nu_2^2) / E_2}$$

$$a = \sqrt{\frac{4QD_w}{\pi E' L_{we}}}$$

in which  $Q$  is total load on roller,  $L_{we}$  is the effective contact length of roller,  $D_w$  is the nominal diameter of roller,  $E_1$  and  $E_2$  are the Young's modulus of materials, and the  $\nu_1$  and  $\nu_2$  are Poisson's ratios of materials.

But this profile was not used in roller bearings at that time, probably due to lack of efficient manufacturing methods for producing this profile. After many years of investigation and with the assistance of mathematical tools such as finite difference and finite element methods supported by modern computers[2], rigorous numerical methods have been developed for calculating the distribution and magnitude of surface stresses in any "line" contact situation, and consequently proved that Lundberg's profile is the optimum line contact geometry for all kinds of modified line contacts. So it is being widely used in commercial roller bearings now[3] along with the development of manufacturing technology. While the crowning value roller is ideally designed for only one condition of loading.

However, it is well known that the rollers and races are separated by a viscous oil film during rolling, which results in the EHL state and the pressure distribution of oil film is different from that in elastostatic contact state. It is because the optimum crowning value of Lundberg's profile given by elastostatic analysis does not consider the effects of lubricant and rolling speed on the

contact stress. Obviously, the oil film thickness is also not estimate by this method.

There are many researchers studying EHL problems during the past five decades. But most of the researches are restricted to the case of infinite line contacts or elliptical contacts, only a few works have been done for finite line contacts. The first investigation of EHL performance for both blended and unblended roller was made by Gohar and Cameron[4] who measured oil film thickness using optical interferometry in sliding contact, which gave several important pictures of the effect of roller blending. A great improvement in fringe quality was obtained by Wymer and Cameron[5] who adopted some new good techniques described by Foord *et al.* [6] and developed a very flexible loading system which enabled the optical interferometry usable to study EHL of finite line contacts under pure rolling and high contact pressure conditions. They showed clearly that the oil film shapes and thicknesses of blended and unblended rollers were quite different, especially near the edge region of the roller. The other publications on this topic were mostly under high speed and lightly loaded conditions[7-10].

A numerical analysis of the EHL problem of axially profiled cylindrical roller under flooded, moderate load and material parameter conditions was done by Mostofi and Gohar[11], Park and Kim[12]. They showed that the minimum film thickness was effected by different radii of dub off and crown profiles, as well as pointed out that the maximum pressure and the minimum film thickness are highly dependent on the local

geometry there. A preliminary work of the EHL numerical solution of finite roller contacts with Lundberg's profile was carried out by J.-J. Ma, X.-Y. Chen and S.-B. Liu [13]. They showed the effects of speed and crowning amount on the variations of pressure distribution, film shape and thickness.

In this paper, the effects of crowning amount of Lundberg's profile roller on EHL is studied by optical interferometry. For rollers of two different crowning values, the oil film thicknesses and shapes near the edge region are compared.

## 2. APPARATUS

The main object of the design of the apparatus was to simulate a taper roller bearing in which the oil film shape and thickness between a taper roller and the transparent glass disk could be measured by optical interferometry method.

A sectional view of the apparatus is shown in Fig. 1, and Fig. 2 is a photograph from above. The rolling element is a tapered steel roller of 7.96 mm mean diameter, 11 mm long, and  $8^{\circ} 40'$  total cone angle, and is held by a fixed brass cage with a 52.67 mm mean radius of gyration. The single tapered roller runs between an upper flat glass disk and a lower steel race which is tilted at the total conical roller angle. The steel

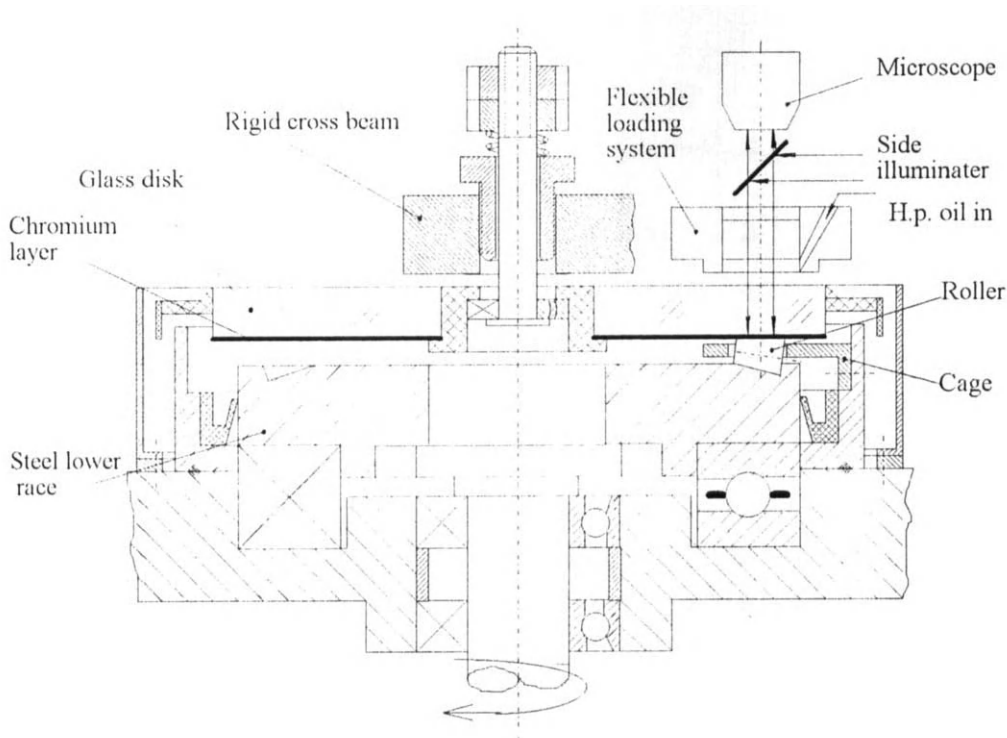


Figure 1. Sectional view of the finite line contact apparatus

race is supported by a heavy series ball thrust bearing and is driven via a toothed belt from a motor and a stepless speed regulation. With the roller stationary, the glass disk rotates in the opposite direction to the race. The whole system, in fact, is a thrust bearing with a single tapered roller .

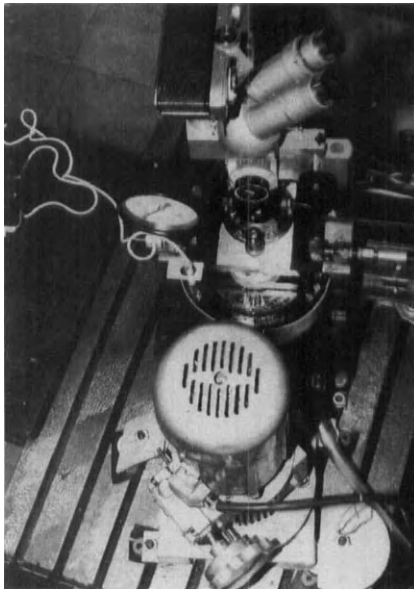


Figure 2. View of the apparatus from above

The glass disk is supported by a self aligning bearing which is suspended from a central shaft. The center shaft can be freely moved vertically in a guide by a fine adjusting screw. This allows the glass disk to align itself with the roller. It is necessary for the glass disk to have a good self alignment properties in order to ensure a uniform load distribution along the length of the contact. The weight of the glass, self aligning bearing, central shaft and other attachments is balanced by an adjustable compression spring.

Immediately above the roller, on the upper surface of the flat glass disk, is a flexible hydrostatic thrust bearing loading system acting through an adaptive pneumatic spring, two elastic pipes and a rolling seal diaphragm, as shown in Fig. 3. The glass disk is loaded locally against the roller by the very flexible loading system to minimize the variation of the film thickness of hydrostatic bearing due to small oscillations of the glass disk caused by driving system and give more stationary fringe patterns.

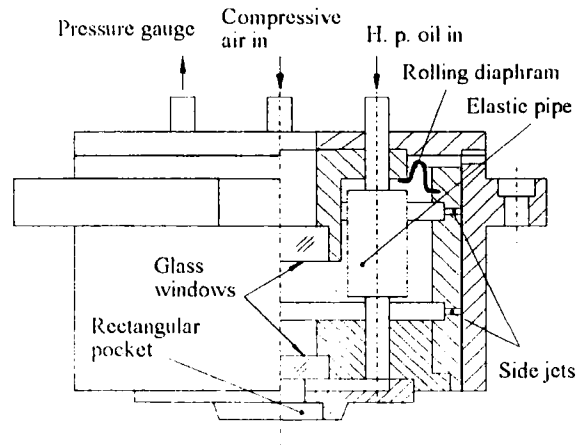


Figure 3. Flexible loading system

The hydrostatic bearing has two built-in glass windows which allow light ray to pass. All glass/air interfaces are coated with anti-reflection layers specially designed for the helium-neon laser to cut down possible spurious patterns as far as. Because the glass and oil have the same refractive index[6], a microscope and interferometry system is capable of viewing the interference patterns at the contact.

A standard microscope with an 100 mm working distance with an  $1.6 \times$  objective and  $25 \times$  eyepiece is mounted above the loading system. Between them is a semi-reflecting mirror. A helium-neon laser source is used as side illuminator. The rotational speed of the glass disk is measured by digital tachometer. The oil pressure of hydrostatic bearing and the air pressure of pneumatic spring are measured by three pressure gauges. And the temperature is obtained by a thermometer.

### 3. TEST CONDITIONS

The upper flat glass disk is made of crown glass and optically polished to  $1.2 \times 10^{-5}$  mm integral mean deviation of profile (Ra). Its surfaces are parallel to within  $2.0 \times 10^{-3}$  mm. And a  $200 \text{ \AA}$  semi-reflecting layer of chromium is vacuum deposited onto the lower surface, to allow the formation of interference fringes. This is in accordance with the usual practice when employing optical interference techniques to measure the oil film of EHL.

The tapered rollers used are made of chromium steel 15 from bearing roller manufacturers' factory which are made with refined lapping manufacturing method, and their surface roughness are about  $8.0 \times 10^{-5}$  mm Ra. It is not easy to obtain a roller of a higher surface finish because of the difficulty in forming the required profile.

Only two rollers of different crowning amounts are tested in this work. Their profiles are measured by Form Talysurf 120. The results are shown in Fig. 4. And Fig. 5 shows their

pressure distribution in elastostatic contact state, which is calculated using the method of reference [14]. It is clear from Fig. 5, the pressure distribution of the roller with the smaller crowning is a more even than that with the larger crowning.

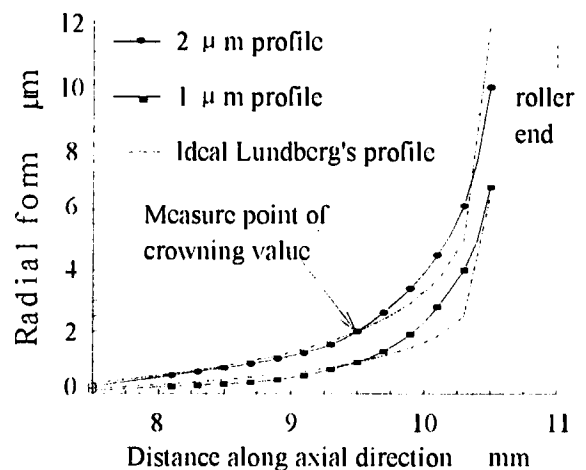


Figure 4. Measured profiles of tested rollers

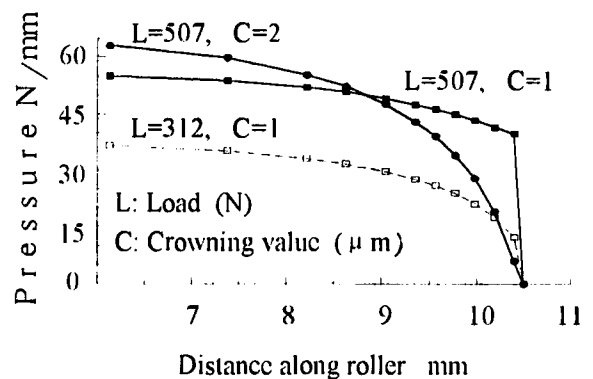


Figure 5. pressure distribution of elastostatic contact state

There are  $0.4 \pm 0.2$  mm round chamfers at both ends of the roller, so the effective contact

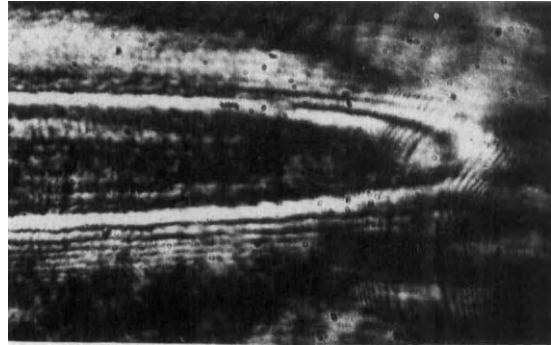
length of the tapered roller on glass disk must be shorter than 10 mm and the load on the roller needed to produce 0.5 GPa contact pressure is about 507 N. This load is produced by the flexible hydrostatic thrust bearing loading system under conditions that the required oil pressure is about 1.3 MPa and the compressed air pressure is about 0.27 MPa.

Although the two taper rollers are selected carefully from a multitude of rollers which the authors have obtained, it is still found that the position of contact zone is oscillating in axial direction during rotation and very severely so at high speeds, which is caused because of the axes of the round chamfer and large end spherical face of the tapered roller are minutely misaligned with that of the roller. Therefore the experiments could not be carried on to higher speeds. This difficulty should be overcome in a further work. Lubricating oil is supplied onto the lower steel race and is retained by the outer rib. And the temperatures is accurate to  $\pm 1^\circ\text{C}$ . As the contact is in pure rolling, the test conditions are considered isothermal.

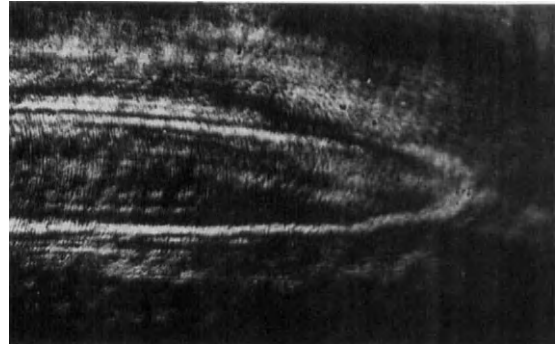
#### 4. RESULTS AND DISCUSSION

Fig. 6 shows the photographs of interference pictures at the end of line contact for different crowning values with the other parameters kept constant. The direction of rolling speed is from bottom to top. The inlet, as far as can be seen, is fully flooded with oil. The significant feature is that the side closures are a little different.

The way the film shape varies with load and rolling speed, for a constant entry film thickness



(a) Crowning value is  $1\ \mu\text{m}$



(b) Crowning value is  $2\ \mu\text{m}$

Figure 6. Interference photographs of different crowning values at end of roller. For each the load is 507 N and the speed is 112 mm/s.



Figure 7. Interference photograph of small crowning value roller at the end. The load is 312 N and the speed is 95 mm/s. Crowning value is  $1\ \mu\text{m}$ .

and the large crowning value of the two, is shown in Fig. 7. The significant feature is that both the contact zone and the side closure become different to Fig. 6a, with the latter difference more pronounced than that between the fringe patterns of Fig. 6a and Fig. 6b.

The film profiles across side closure along axial direction are plotted in Fig. 8. Because of the difficulty of estimating the pressure distribution and therefore the refractive index change in the thicker film cases, all the profiles of Fig. 8 are plotted using the refractive index at

atmospheric pressure. It is clear from Fig. 8, the side closure of the roller with the smaller crowning is a little severer than that with the larger crowning, and the position of minimum film thickness in axial direction from the end of the roller is a little longer in the latter case as compared to the former case. That means, it is more advantageous for the oil film to form with the large crowning value of the two. And for the same crowning amount, the oil film profile in the lighter loaded condition is more even than that in the more heavily one.

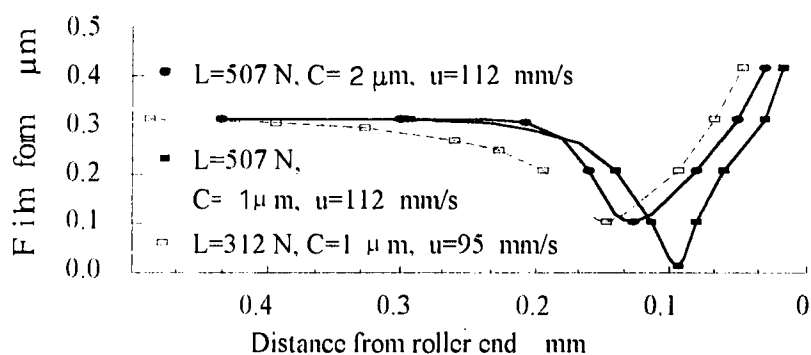


Figure 8. Film profiles across side closure along axial direction

These two comparisons indicate there must be an optimum crowning value which will induce the thickest and most even oil film in EHL state for a given working condition, and this value is larger than the design value in dry contact state for the same working conditions.

## 5. CONCLUSIONS

A finite line contact optical EHL apparatus is used to measure the oil film thickness and shape under pure rolling, generous oil supply, not too

high rolling speed, moderate load and material parameters conditions. The experiments reported have shown how the oil film thickness and shape is affected by crowning value of rollers with Lundberg's profile. Which indicate there must be an optimum crowning value which will induce the thickest and most even oil film in EHL state for a given working condition, and this value is larger than the design value in dry contact state for the same working conditions.



## 6. ACKNOWLEDGMENTS

This work is sponsored by Science and Technological Commission of Shanghai Municipal Government and National Natural Science Foundation of China. The authors wish to thank Prof. Z. Zhang and Prof. Z.-X. Yi of Research Institute of Bearings of Shanghai University for their valuable advices, and Engineer Z.-Q. Zhang of Shanghai Grinder Research Institute of Shanghai Machine Tool Works for his assistance in making the apparatus. Thanks are also due to all those who have helped in carrying out this work.

## REFERENCES

1. G. Lundberg. *Forschung auf dem Gebiete des Ingenieurwesens*, Bd.10, Nr.5 (1939) 201.
2. H. Reusner. *Ball Bearing Journal*, No.230 (1987) 2.
3. F. -J. Markert. *Ball Bearing Journal Special'89* (1989) 28.
4. R. Gohar and A. Cameron, *ASLE Trans.*, 10 (1967) 215.
5. D. G. Wymer and A. Cameron, *Proc. I. Mech. E.* 188 (1974) 221.
6. A. Foord and L. D. Wedeven, F. J. Westlake, A. Cameron, *Proc. I. Mech. E.* 184 (1969-70) 487.
7. H. Bahadoran and R. Gohar, *J. Mech. Eng. Sci.*, 16 (1974) 386.
8. J. C. Pemberton and A. Cameron, *ASME, J. Lub. Tech.*, 101 (1979) 327.
9. R. A. J. Ford and C. A. Foord, *Mech. E. Trans., Australia*, (1981) 140.
10. N. Dmytrychenko and A. Aksyonov, R. Gohar, G. T. Y. Wan, *Wear*, 151 (1991) 303.
11. A. Mostofi and R. Gohar, *ASME, J. Lub. Tech.*, 105 (1983) 598.
12. T.-J. Park and K.-W. Kim, *Paper of Proc. Int. Trib. Conference, Yokohama*, 1995.
13. J.-J. Ma and X.-Y. Chen, S.-B. Liu, *Proc. Int. Sym. Trib.*, Beijing, 1(1993)132.
14. X.-Y. Chen and J.-J. Ma, *Tribology (Mocaxue Xuebao)*, 13(1993)25. (in Chinese)

## **A Theoretical Analysis of Shear Stresses and Roller Slip in Rolling Bearings During Low-Temperature Starting**

V. Wikström\*, R. Larsson and E. Höglund, Div. of Machine Elements, Luleå University of Technology, S-971 87 Luleå, SWEDEN

\* Address for correspondence: SKF Engineering&Research Centre, Postbus 2350, 3430 DT Nieuwegein, The Netherlands

### **ABSTRACT**

A simple quasi-static model of roller motion in cylindrical roller bearings has been used to investigate the amount of roller slip during one bearing revolution. Also, surface shear stresses and total bearing friction has been studied for different settings of the input parameters to see whether there exist conditions under which lubricant non-Newtonian characteristics become important. The investigation utilises the concept of factorial design, commonly used in experimental design, to find important parameters and cancel out those which have less influence on the factors under study. The method allows the investigator to calculate the relative effect of each the different parameters, taking into consideration the settings of the other parameters. The result indicates that the limiting shear stress as well as the limiting shear stress-pressure coefficient is of little importance also at low temperatures. However, roller slip is present to a large extent at low temperature starting, especially if the contact area between roller ends and outer ring flanges is large. The outer ring friction torque will be higher if lubricant viscosity and shaft speed are increased simultaneously, whereas the effects of other parameters under study are negligible.

### **1. INTRODUCTION**

Presently, when choosing grease for bearings designated to operate in low-temperature conditions, the main thing considered is NLGI number and, sometimes, low-temperature torque as measured in i. e. ASTM D1478<sup>1</sup> (ball bearings) or ASTM D4693<sup>2</sup> (tapered roller bearings). However important for a rolling bearing, not only friction is of interest but also the rolling/sliding motion of the rolling elements as well as the prevailing lubricant

film thickness between rollers/balls and races. At low temperature, which in this case may be below +20°C, base oil bleeding ceases. In combination with decreasing base oil replenishment due to increased viscosity, there will be lubricant starvation and, occasionally, metal-to-metal contact. Wikström and Jacobson<sup>3</sup> have shown that this is significant at higher shaft speeds when the time for replenishment between passing rollers is short.

The importance of maintaining a lubricating film between race and rollers also at low temperature has been acknowledged by some users who have their own standards<sup>4</sup> where criteria other than friction are taken into consideration, aiming to ensure that the grease manages to separate the surfaces also at low temperatures. The temperature where metal contact frequently occurs is called the Low Temperature Performance Limit (LTPL) for the specific grease. However, this limit is merely valid for a specific combination of grease and bearing, and its use is still limited.

Rolling element slip, or skidding, is an un-wanted state in a bearing, which may be described as gross sliding of a contact surface relative to the opposing surface. It differs from micro-slip, which is defined as slip within the roller/race contact ellipse and contrary to roller slip, micro-slip cannot be seen from the outside. Roller slip has been treated experimentally by a number of authors<sup>5,6,7,8</sup> using magnetic transducers. The referred investigations all concentrate on the temperature range +23°C and above, and predominantly on high speeds of rotation ( $\Omega > 500$  rpm). In Wikström et al.<sup>9</sup>, roller slip is measured in an oil lubricated cylindrical roller bearing using image analysis. Here, the end surface of three evenly spaced rollers were painted black and white, enabling registration of rolling/sliding motion with a video camera. In the investigation<sup>9</sup>, roller slip at  $\Omega = 100$  rpm and bearing OR temperature -20°C was measured, and a significant difference in roller slip between rollers

differing in diameter (but still within the manufacturing tolerances) was noted.

Roller slip, especially as the roller enters the loaded zone, may lead to so called smearing failures, predominantly in large bearings. The origins of smearing is still not fully understood, but roller slip does result in surface shear stresses of significant magnitude if occurring in the loaded region of the bearing. If a roller enters the loaded zone with no or low speed of rotation, the contact pressure and the shear stresses caused by the applied load and relative speed of the surfaces might be sufficiently high to create surface spalling and smearing damage. The subject has been treated extensively by Hamer et al.<sup>10</sup>, who argue that one potential smearing mechanism could be shear heating with heat dissipation to the contact inlet, causing a drop in inlet oil viscosity and hence a decrease in the film thickness. They included shear heating in their analysis, but even though there was a decrease in  $h_{min}$ , they found that to trigger the heat induced smearing, the roller had to be near to stationary relative to the cage prior to entering the loaded zone. Using a specially designed disc machine, they also made an experimental study, showing that no smearing occurred if  $\omega_r$  was greater than 20% of  $\omega_r$  at pure rolling (corresponding to, in their case,  $\Delta = 1.7$ ). However, even though no visible smearing damages are present, roller slip may result in small pitting damages or residual stresses in the material which will shorten the bearing life.

Under certain circumstances, such as high contact pressure, high lubricant viscosity and high rotational speeds, it may be assumed that a non-Newtonian behaviour such as the limiting shear stress<sup>11</sup> might be of importance. This is also suggested by Hamer et al.<sup>10</sup>, but it is not evident from their paper whether the limiting shear stress is ever used within the calculations. If the limiting shear stress is reached, the sliding friction will be limited and less than the "Newtonian" friction at that shear rate. In the literature, non-Newtonian effects are sometimes considered as insignificant<sup>12</sup>, but no evidence has hitherto been presented to prove if this is a reasonable assumption for all operational conditions, for example conditions of low-temperature lubrication with different types of lubricants, different bearing clearances, radial loads and so on.

Theoretical investigations of roller and cage slip, for specific lubricants at high temperatures, have been made by i. e. Harris<sup>13</sup> and Chang et al.<sup>14,15</sup>. Östensen et al.<sup>16</sup> compared their experimental results with theory, using a similar model as in the present investigation, and the agreement between theory and experiments was seen to be excellent, but due to problems measuring the roller slip at low temperatures with accuracy, their comparison was made only at +20°C. Östensen et al.<sup>16</sup> only considered viscous effects and did not include different roller slip due to different running conditions or altered lubricant parameters, nor did they study the magnitude of the shear stresses. Considering temperatures of +20°C and above is

indeed important as the bearing reaches steady-state running conditions, but increasing knowledge about the mechanisms of low-temperature starting and the influence of cold starting on bearing life is of equal importance. Since both  $\eta$  and  $\alpha$  increase<sup>17</sup>, whereas  $\gamma$  decreases for polyalphaolefines<sup>18</sup>, with decreasing temperature, the influence of lubricant parameters at low-temperature operation has to be looked into. Recently, simulating the rib-roller end contact and varying viscosity (still in the high temperature region), contact geometry and axial load, Prisacaru et al.<sup>19</sup> have found that piezoviscous-rigid lubrication conditions may develop in an axially loaded cylindrical roller bearing. The magnitude of the shear stresses are not looked into in their paper, and it is therefore difficult to assess the risk of surface damage.

Boness<sup>5</sup>, who made a theoretical and experimental investigation of roller motion using three different paraffinic mineral oils in a SKF CRM16 cylindrical roller bearing at +37°C, has shown that for low load, both roller and cage slip increases with increasing lubricant supply up to about 0.9 l/min. It may be noted that 0.9 l/min. is a relatively large supply when compared to what is necessary to obtain sufficient film thickness in a rolling bearing. Wikström and Jacobson<sup>3</sup> showed that 0.5 ml applied between the races may be enough to run a spherical roller bearing for up to 75 h, which indicates that oil supplies much lower than Boness' levels are of interest, at least when run-in grease lubricated bearings are considered. Boness<sup>5</sup> did include lubricant viscosity in the analysis, however

not in combination with other parameters which makes it difficult to draw conclusions valid e. g. for the low-temperature torque test rig<sup>1</sup>.

In order to bring clarity to how lubricant parameters in combination with different loads, speed and small alterations of bearing design affect roller slip and bearing torque, the present investigation has been made as a parameter simulation of roller motion and bearing friction. The results are evaluated and presented using a method this far utilised by experimenters, enabling the study of relative effects of altogether 8 different parameters, single or in combination with each other. The model bearing is a cylindrical roller bearing (SKF NU 1024) with inner diameter 120 mm, outer diameter 180 mm and width  $w = 28$  mm, Figure 1. There are 23 rollers in the bearing, the roller mean diameter is 14.98 mm and the effective roller length (minus crowning radii) is 13.5 mm, see Figure 1. The outer ring of the bearing is stationary, which means that  $\Omega_o=0$ .

## 2. THEORY

To investigate roller slip, surface shear stresses and outer ring friction torque, a computer program was written, based on a quasi-static model used by, e. g., Östensen et al.<sup>16</sup> and Prisacaru et al.<sup>20</sup>. Quasi-static in this case implies that roller motion is treated in a "snapshot" way: for roller  $j$  in position  $\varphi_j$ , angular velocity of the roller is changed until force equilibrium is reached. This is repeated in 138 points for  $0 < \varphi < 2\pi$ , included the positions

$\varphi_j = j \frac{2\pi}{Z}$  where rollers are situated, creating a "snapshot" view of  $\omega_r$  and  $(\tau)_{i,o}$  in the bearing. Also, friction torque will be of snapshot character, but this is irrelevant as steady-state conditions are assumed. Actually, due to the method applied in friction torque summation, there will be a slight change in friction torque when the rollers are between the chosen  $\varphi_j$ 's (because of the different normal load at different angular positions), but the effect is insignificant when compared with the much larger contribution from viscous friction between roller ends and flanges and between cage and outer ring.

The quasi-static model used in this paper has both positive and negative features, extensively reviewed by Gupta<sup>21</sup>. Among its advantages may be mentioned its simplicity and capability to obtain accurate estimates of roller motion in a bearing. The disadvantages consist mainly of the assumption that cage speed is constant and equal to the theoretical epicyclic value for stationary outer ring<sup>22</sup>, Equation (1),

$$\omega_c = \frac{\Omega}{2(1+s)} \quad (1)$$

an assumption that will imply misleading results at shaft speeds above 1000 rpm<sup>5,6</sup> when cage slip becomes significant. Of course, for very lightly loaded bearings, cage slip may occur even though shaft speed is low. That the assumption of no cage slip is valid under conditions similar to those

investigated here has been verified experimentally by Östensen et al.<sup>16</sup> who could see that cage speed was epicyclic within  $\pm 5\%$ . Another disadvantage with the quasi-static model is that it does not allow treatment of time-varying loads or race speeds.

In the present analysis, thermal effects are assumed to be negligible since the surface velocities involved are relatively low. As shown by Conry<sup>23</sup>, shear rates have to be of the order  $10^6 \text{ s}^{-1}$  before heating starts to significantly affect traction. Also, it must be remembered that the application considered is bearing start-up which means that the time considered is short.

The model is based on force equilibrium of the roller, Figure 2a, taking into account tangential forces due to roller - race friction,  $F_{i,o}$ , viscous forces from the contact roller - cage pocket (both on roller ends and roller mantle),  $(F_p)_{1,2}$ . Also, viscous forces arising from the contact between roller ends and outer race flanges,  $F_F$ , are included. Roller inertia, which may be important in the transition between unloaded and loaded zone, is also included as are centrifugal forces  $F_C$  and gravity  $mg$ . However, none of these body forces showed to be significant in bearing geometries of the size considered here, see also Östensen et al.<sup>16</sup>.

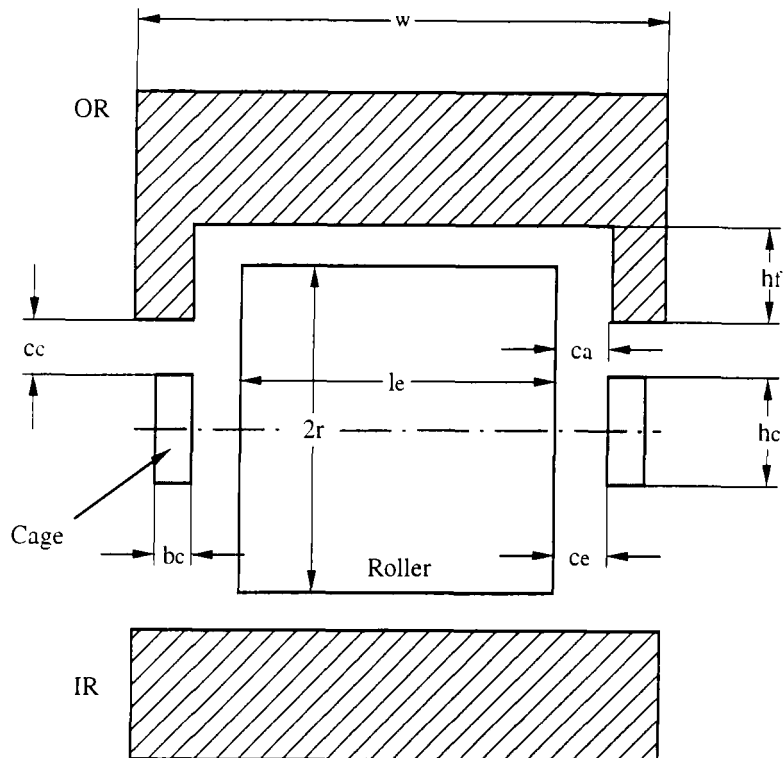


**Figure 1:** View of the roller and cage in bearing tangential direction.

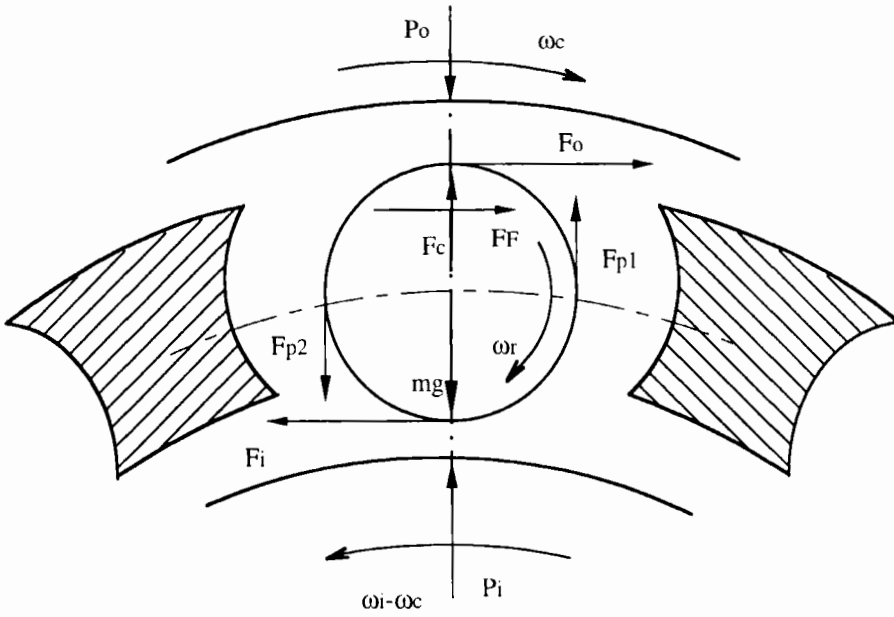


**Figure 2a:** View of the roller and cage in bearing axial direction, forces and rotational speeds.

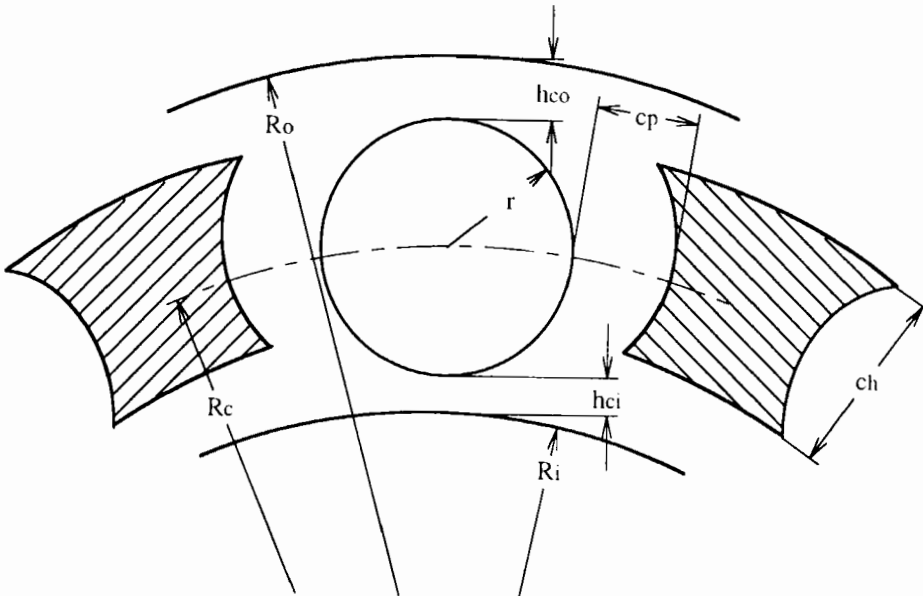


**Figure 2b:** View of the roller and cage in bearing axial direction, measures.

Full-film lubrication is assumed everywhere in the bearing.

In the equations, which are applied in all 138 points of calculation,  $\omega_r$  is changed until roller equilibrium  $\sum T_r = T_D - T_B = 0$  is achieved for the load/viscosity conditions in that point. The driving forces on the roller are  $F_F$  (when  $\omega_r < \omega_c$ ) and the tangential friction forces  $(F)_{i,o}$ . The braking forces are  $F_p$ , produced from the rotation of the roller in the cage pocket, and the forces arising from grease churning at roller ends. An approximation of the latter is given by Gupta<sup>21</sup>, and has been used here, but according to Gupta, no truly accurate approximations exist. The moment of inertia is also included, and depending on whether the roller is accelerating (from unloaded zone to loaded zone) or decelerating (loaded to unloaded), it will act either braking or driving.

The tangential friction forces  $F_{i,o}$  at the roller-race contact are calculated differently in the loaded and unloaded zone. In the loaded zone, elastohydrodynamic conditions are assumed whereas in the unloaded zone, the Dowson and Higginson<sup>22</sup> theory for isoviscous, rigid contacts has been used in the same way as was made by Boness<sup>5</sup>, Hamer et al.<sup>10</sup> and Östensen et al.<sup>16</sup>.

The forces counteracting roller rotation arising from the contact between roller and cage,  $F_p$ , are calculated according to Newtonian theory using  $\eta_0$ , Equation (2),

$$F_p = \eta_0 \frac{\omega_r r}{c_p} A_p \quad (2)$$

$c_p$  has been measured in the mounted bearing, and the initial calculations were made with the roller centred in the cage pocket ( $c_p = 220 \mu\text{m}$ ).

## 2.1 Unloaded zone

In the unloaded zone,  $F_{i,o}$  and also the film thickness  $(h_c)_{i,o}$  are calculated using the Dowson and Higginson<sup>22</sup> hydrodynamic theory. Since the external load on the rollers in the "unloaded" zone consists of a combination of gravity and centrifugal force only, the rollers may be considered rigid and the theory for lightly loaded rigid cylinders has therefore been used, Equations (3) - (4).

$$F_{i,o} = -4.5 \eta_0 (u_s)_{i,o} \sqrt{\frac{(R_x)_{i,o}}{(h_c)_{i,o}}} + 3.48 \eta_0 (u_d)_{i,o} \sqrt{\frac{(R_x)_{i,o}}{(h_c)_{i,o}}} \quad (3)$$

$$(P_j)_{i,o} = 2 \times 2.45 (u_s)_{i,o} \eta_0 \left( \frac{R_x}{h_c} \right)_{i,o} \quad (4)$$

$(h_c)_j$  and  $(h_c)_o$  are related to each other via the total radial clearance  $c_T$  in the bearing. This was measured in the mounted loaded bearing. At each position  $\phi_j$ , the normal load at the roller-inner race contact was calculated using  $\sum P_y = P_i + F_c - mg = 0$ . In the case  $F_C > mg$ ,  $P_o$  was calculated instead.  $(P_j)_{i,o}$  is the left-hand-side in Equation (4) and with the initial



assumption of pure rolling,  $(h_c)_i$  may be calculated and then  $(h_c)_o$  using  $cT$  (or, in the case  $FC > mg$ ,  $(h_c)_o$  is calculated from Equation (4)). These initial approximations of  $(h_c)_i$  and  $(h_c)_o$  are used to get the first approximation of  $F_{i,o}$  which is then used in the check for roller equilibrium.

**2.2 Loaded zone**

The extension of the loaded zone is given by geometry and may be found in e. g. Hamrock<sup>17</sup>

$$\frac{\pi}{2} - a \cos\left(\frac{c_d}{2\delta_m}\right) \leq \varphi \leq \frac{\pi}{2} + a \cos\left(\frac{c_d}{2\delta_m}\right) \quad (5)$$

Inside this zone,  $(h_c)_i$  and  $(h_c)_o$  were calculated through the Hamrock and Dowson<sup>17</sup> minimum film thickness formula for line contact, Equation (6).

$$H_{mi,o} = 1.714 W^{-0.128} U^{0.694} G^{0.568} \quad (6)$$

The reason for approximating the EHD film thickness with minimum instead of central film thickness was to simulate a run-in grease lubricated concentrated contact which is more likely to run with less lubricant available than the corresponding oil lubricated contact<sup>24</sup>. Also, since one main purpose of the investigation was to check whether the limiting shear stress might be significant, a conservative analysis had to be conducted. If  $h_c$  had been used instead of  $h_{min}$  it would have implied somewhat smaller shear stresses.

The tangential friction force at the roller race contacts driving the roller are, Equation (7)

$$(F_{EHD})_{i,o} = (A_c \tau)_{i,o} = 2b_{i,o} l_e \tau_{i,o} \quad (7)$$

As long as the shear stresses at the inner and outer roller/race contacts are below the limiting shear stress at a specific angular location, they are calculated according to the Newtonian relationship, Equation (8),

$$\tau_{i,o} = \left( \eta_R \frac{\partial u}{\partial z} \right)_{i,o} \quad (8)$$

where

$$\left( \frac{\partial u}{\partial z} \right)_i = \frac{u_i - u_r}{(h_{min})_i} = \frac{(\Omega - \omega_c) R_i - \omega r}{(h_{min})_i} \quad (9)$$

and  $\eta_R$  is calculated using the average pressure in the contact (normal load divided by contact area). The error introduced using average pressure will not affect the average shear stress, which is what is calculated from Equations (8)-(9), in the EHD contact significantly. In the roller-outer race contact we have, for stationary outer ring, Equation (10),

$$\left( \frac{\partial u}{\partial z} \right)_o = \frac{u_o - u_r}{(h_{min})_o} = \frac{\omega_c R_y - \omega r}{(h_{min})_o} \quad (10)$$

If the shear stress at a specific angular location would exceed  $\tau_L$ , then  $(\tau)_{i,o} = (\tau_L)_{i,o}$ .

The limiting shear stress, which varies with  $\varphi$ , is calculated throughout the loaded zone using the Johnson and Tevaarwerk<sup>25</sup> relationship

$$(\tau_L)_{i,o} = \tau_o + \gamma(p_{av})_{i,o} \quad (11)$$

In Equation (11),  $\tau_0$  is assumed to be negligible<sup>26</sup> compared to the term  $\gamma p_{av}$ . The use of a limiting shear stress means that a small error may be introduced regarding the film thickness, where no shear stress limit is included. Jacobson and Hamrock<sup>27</sup> have shown, that for high sliding speeds and moderate normal loads, EHD film thickness will depend on the shear stresses at the contact inlet. However, the decrease in film thickness due to sliding is small (less than 10% of the Newtonian film thickness) irrespective of the value of  $\gamma$ , which implies that the error also will be small. Thinner film would result in higher tangential shear stresses and might therefore reduce roller slip further in the loaded zone.

In the present investigation, the magnitude of the actual shear stress as a roller passes through different positions in the loaded zone is compared to the limiting shear stress at that position. This makes it easier to find the critical zones in the bearing where the limiting shear stress will be reached if roller slip increases further, i. e. through the introduction of cage slip.

The amount of roller slip is defined using the slide-to-roll ratio according to Hamrock<sup>17</sup>, Equation (12),

$$\Delta = \frac{u_d}{u_s} = 2 \frac{u_i - u_r}{u_i + u_r} \quad (12)$$

a definition implying  $\Delta = 2$  at pure sliding ( $\omega_r = 0$ ) and  $\Delta = 0$  at pure rolling when  $\omega_r r = \Omega R_i$ .

### 2.3 Bearing Friction

The total bearing outer ring friction torque under steady-state conditions is calculated as

$$T_T = T_C + \sum_{j=1}^Z (T_{HD})_j + (T_{EHD})_j + (T_F)_j \quad (13)$$

i. e. the friction forces at each angular location  $\Phi_j$ , where a roller is present at time  $t$ , are multiplied with their lever, or, explicitly, Equation (14) - (15),

$$(T_{HD})_j = (F_o)_j R_y \quad (14)$$

$$(T_{EHD})_j = (F_o)_j R_y \quad (15)$$

The friction torque arising from the contact roller end-outer race flange is assumed to be Newtonian, Equation (16) - (17),

$$(T_F)_j = (\tau_F)_j A_F (R_y - r + r_F) \quad (16)$$

where

$$\tau_F = \eta_0 \frac{\partial u}{\partial z} = \eta_0 \frac{\omega_c (R_y - r + r_F) - \omega_r r_F}{c_A} \quad (17)$$

and  $\omega_r = \omega_r(\varphi)$ . In using Equation (17), it has been assumed that the roller is axially centered in the cage pocket.

The sum, together with the torque acting on the outer ring from the cage-outer ring contact at that time, equals the total bearing torque, Equation 13. The torque arising from the contact cage - outer ring is

$$T_c = \tau_c A_c (R_i + r + r_f) \quad (18)$$

where

$$\tau_c = \eta_0 \frac{\partial u}{\partial z} = \eta_0 \frac{\omega_c (R_i + r + r_f)}{c_c} \quad (19)$$

### 3. INPUT DATA AND THE FUNDAMENTALS OF FACTORIAL DESIGN

The investigated output parameters, also denoted the *responses*, are maximum roller slip  $\Delta_{max}$  ( $0 < \varphi < 2\pi$ ) and the outer ring friction torque  $T_T$ . Also, the actual shear stress in each computational point is compared to the limiting shear stress at that location. The ratio may be seen as the amount of "non-Newtonian-ness",  $N_p$ , and it will vary with angular location  $\varphi$ . Since one of the scopes of the present investigation is to detect whether non-Newtonian effects may be of importance to the function of a bearing,  $N_p$  was also examined as a response. It is of course possible to study also the absolute stress level at both inner and outer race contacts, but this has not been done here.

In the first stage of the present investigation, 7 parameters were assumed to have an influence on  $\Delta_{max}$ ,  $N_p$  and  $T_T$ , see Table 1, parameters A-G. To enable a condensed interpretation of the results, the concept of factorial design was used, described in detail below. The seven parameters were input to the roller motion simulation program described, and after running the program for all combinations of the different levels, the relative effect on roller slip, surface shear stress

and bearing torque were evaluated using Yates algorithm<sup>28</sup> and the statistics package Statgraphics<sup>29</sup>.

The levels of the parameters were chosen to correspond to low-temperature ( $\eta_0$ ,  $\gamma$  and  $\alpha$ ) and/or fast or slow starting ( $\Omega$ ) for two somewhat different bearing designs ( $c_d$  and  $h_f$ ). The bearing geometry, except  $c_d$  and  $h_f$  which are subjected to variation according to Table 1, corresponds to a SKF NU 1024 cylindrical roller bearing. This is the same bearing as was used by Östensen et al.<sup>16</sup> and Wikström et al.<sup>30,31</sup>.

Since it was reported by Östensen et al.<sup>16</sup> that there was an increase in roller slip when the roller was moved closer to one side of the pocket, a second analysis was carried out where the rollers were placed closer to the pocket wall, see Table 1 (H). For simplification,  $c_d$  (G),  $\alpha$  (D) and  $\gamma$  (C) were held constant at (+), (-) and (+) level respectively in the second run since they were seen to have small

effect on all three responses.  $\Omega$ ,  $\eta_0$ , C/P and  $h_f$  were varied according to Table 1 also in the second run.

Nowadays, the concept of factorial design is frequently used in screening experiments since it is a powerful method to compare the effect of different parameters, thereby sorting out parameters of little or no interest. Also, factorial design may be used to find combinations of parameters, *interactions*, under which the parameter under study, the response, will behave differently. Interactions are difficult to reveal if the parameters are varied one at the time, at least when the number of parameters is large.

In theoretical investigations however, the method is scarcely used, but it has been suggested by Bergman<sup>32</sup> that factorial design could be used in combination with i. e. extensive FEM problems to save CPU time in the initial stage when little is known about the results. Besides less CPU, the method has another and even more important advantage: if, as has been done in the present investigation, as many as 7 parameters are varied at the same time, it is almost impossible to assess the relative effects of the parameters, leave out interactions of second or third order, using common methods.

#### 4. EVALUATION OF RESULTS

The total sum of input data combinations is 144 ( $2^7+2^5/2$ ), which makes presentation of results difficult if one would like to show the effect of different parameters on  $\Delta_{max}$ ,  $N_p$  and  $T_T$  for all

combinations. Therefore, the results are presented as so-called Pareto plots, showing the relative size of the effect on the studied response (may be slip or torque) of changing a factor or a combination of factors from the chosen low to the chosen high level, Figure 3a-c and Figure 7.

The effect of a factor on a response is defined as the change in the response variable as the factor is changed from (-) to (+) level, and the effect may be either "main" or "interactive" (due to one or more factors). As three-factor-interactions are scarce<sup>28</sup>, only main effects and two-factor-interactions have been considered here. The relationship between responses and interacting parameters may be displayed graphically in the form found in Figures 4-6. If an interactive effect is examined using such a diagram, four points are marked and lines are drawn between them. To understand the meaning of such a diagram, an example may be helpful: In Figure 5a, the point representing the average  $N_p$  at (+) level of both  $\Omega$  and  $\eta_0$  may be found in the upper right corner. Here, factor A ( $\Omega$ ) is on the x-axis and factor B ( $\eta_0$ ) is the curve parameter. On the y-axis, average  $N_p$  may be found. Since the (+)- (+) combination of A and B occurs at  $2^7/2^2 = 32$  different combinations of the other 5 parameters C - G, this single point represents a mean of  $N_p$  of all the 32 combinations. The implication is, that with high accuracy, it may be predicted that  $N_p$  will be close to 4.5% when the combination of high  $\Omega$  and high  $\eta_0$  is present, irrespective of the settings of the other parameters. These interaction diagrams may then be used to see which combinations of

then be used to see which combinations of parameters that will be likely to increase i. e. roller slip.

The evaluation method suffers from one drawback when used together with theoretical results: since the variance seen within the effects is “exact” (the same result will appear on the screen even though the calculation is repeated!), there is no proper method to decide which effects may be cancelled out. When conducting experiments, the standard deviation and hence the noise level, may be assessed in different ways, but in this case, the line between significant and insignificant effects has to be drawn subjectively, see Bergman<sup>26</sup>. Nevertheless, the method may be used without problems when large differences between different effects are present, as in Figure 3a and c.

## 5. RESULTS AND DISCUSSION

The results from the first series, including all parameters A-G, are shown in Figure 3a-c. Figure 3a clearly shows that parameter G, the outer race flange height  $h_f$ , has the largest influence on  $\Delta_{max}$ . If the effect of changing the flange height is analysed separately, see Figure 4, it is found that an increase in flange height from 2.25 to 3.25 mm decreases maximum roller slip from, on average, 1.09 to 0.83, irrespective of the settings of the other parameters. No other parameters were considered significant to  $\Delta_{max}$  when compared to flange height. Also, lubricant viscosity (parameter B) seems to be of relatively little significance, which

suggests that low-temperature starting might not cause large roller slip in this type of bearing, at least not within the investigated range of parameters.

Regarding  $N_p$  at inner ring/race contact, Figure 3b indicates that the parameters having the largest influence when changed are lubricant viscosity at atmospheric pressure (B), possibly in combination with shaft speed (A). The interaction AB was therefore investigated separately, see Figure 5, and here, the large difference in  $N_p$  response when changing viscosity from 0.1 to 5 Pas at  $\Omega=10$  rpm is clearly demonstrated. Also, the BC, BD, AD, AC and CD interactions are probably important, however not shown here. Interesting to note regarding  $N_p$  is that bearing load E is of little influence, Figure 3b.

The conclusion is that high shaft speed and high viscosity together will cause shear stresses closer to the limiting shear stress in a cylindrical roller bearing. To reduce the risk of unnecessary high surface shear stresses at low temperature starting, a low  $\gamma$  value is recommended.

When analysing the effects on surface shear stress, Figure 3b, all effects are relatively small ( $N_p$  varies between 0 and 0.08), which makes it hard to conclude where one should draw the line between significant and less significant parameters. Since it is the quotient between actual and limiting shear stress that is studied, it is not surprising that

**Table 1: Parameters and levels**

|   | Parameter                    | Low (-) level            | High (+) level     |
|---|------------------------------|--------------------------|--------------------|
| A | $\Omega$ (rpm)               | 1                        | 10                 |
| B | $\eta_0$ (Pas)               | 0.1                      | 5                  |
| C | $\gamma$                     | 0.03                     | 0.08               |
| D | $\alpha$ (Pa <sup>-1</sup> ) | $2 \times 10^{-8}$       | $3 \times 10^{-8}$ |
| E | C/P                          | 67                       | 11                 |
| F | $c_d$ ( $\mu\text{m}$ )      | 10                       | 40                 |
| G | $h_f$ (mm)                   | 2.25                     | 3.25               |
| H | $c_p$ ( $\mu\text{m}$ )      | 110 (closer to one side) | 220 (centred)      |

parameter C, the  $\gamma$ -value, has such large effect even though the limiting shear stress is never reached within the calculations. This is due to the relatively low shear rates at the entrance/exit of the loaded zone and the almost pure rolling conditions found within the loaded zone.

Studying  $T_T$ , Figure 3c, it is obvious that the main thing to consider is viscosity, B, in combination with shaft speed A (AB interaction, Figure 3c). Flange height G together with viscosity, B, may also be important to look at, but the effect is relatively small compared to AB. The reason for AB's large influence is the large contribution of viscous friction

between roller ends and flange,  $T_F$ , together with cage-outer ring friction  $T_C$ .  $T_{HD}$  and  $T_{EHD}$  arising from HD and EHD friction in the unloaded and loaded zone respectively are small in comparison (1: 20). Note that  $\gamma$ , parameter C, and  $\alpha$ , parameter D, have no effect on friction torque since the main contribution comes from contacts where the pressures are low. The AB interaction is shown in detail in Figure 6, and here, the large increase in friction torque when increasing viscosity  $\eta_0$  from 0.1 to 5 Pas at high shaft speed is demonstrated. If the same operation is performed at low speed ( $\Omega = 1$  rpm), the effect on bearing friction is negligible.

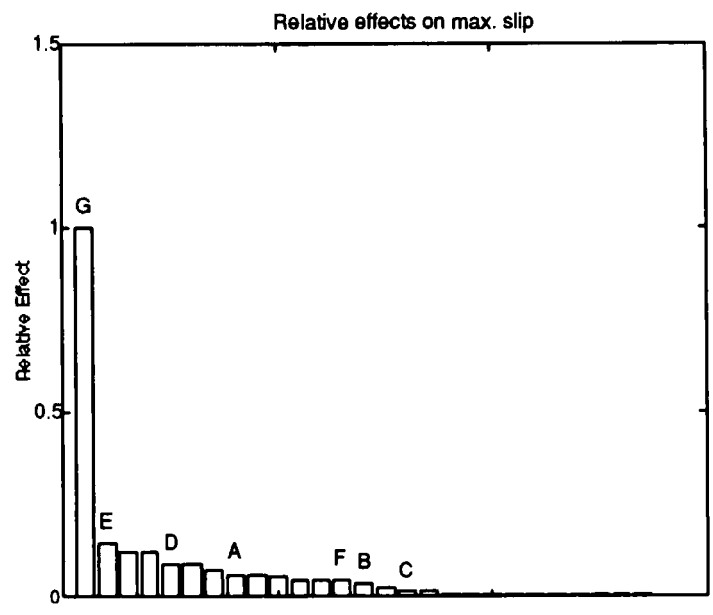


Figure 3a: Normalised Pareto plot for  $\Delta_{max}$

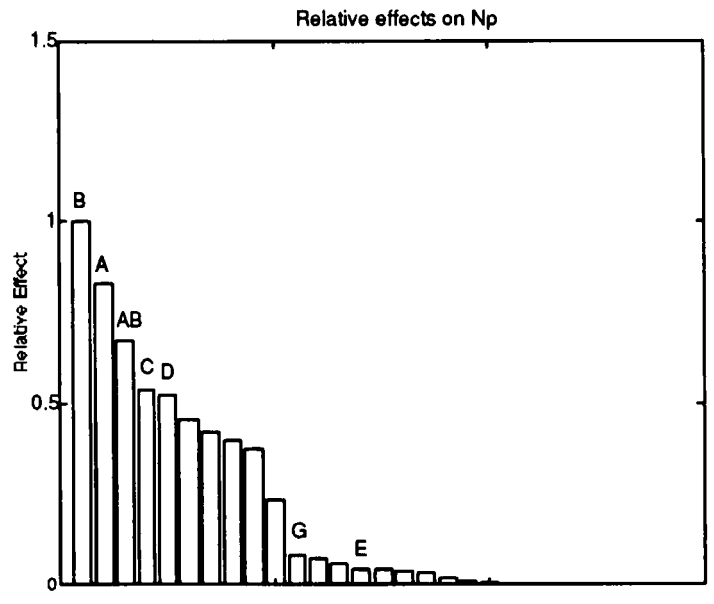


Figure 3b: Normalised Pareto plot for  $N_p$

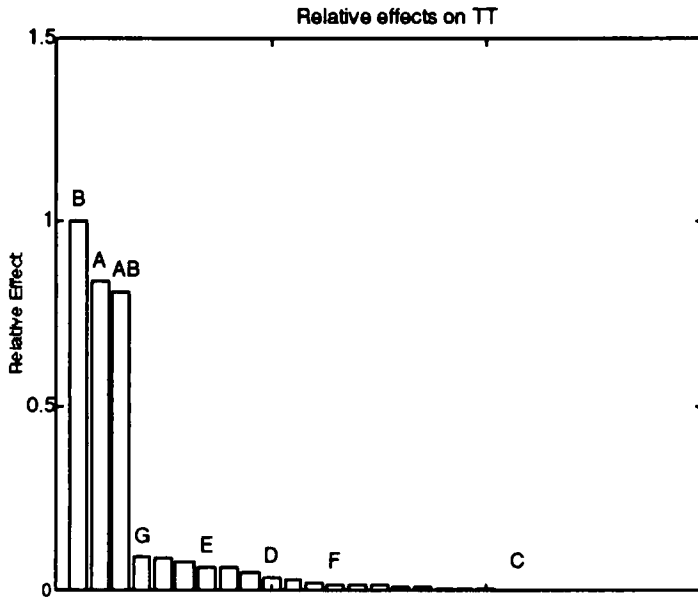


Figure 3c: Normalised Pareto plot for  $T_T$ .

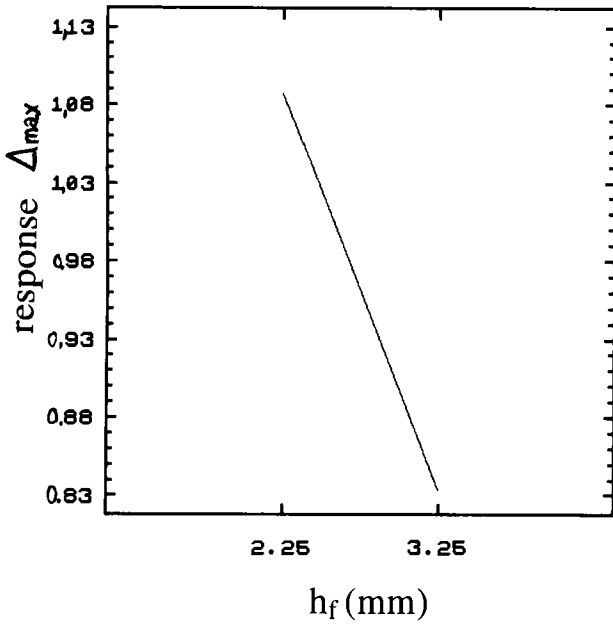


Figure 4: The effect of flange height on  $\Delta_{max}$ .

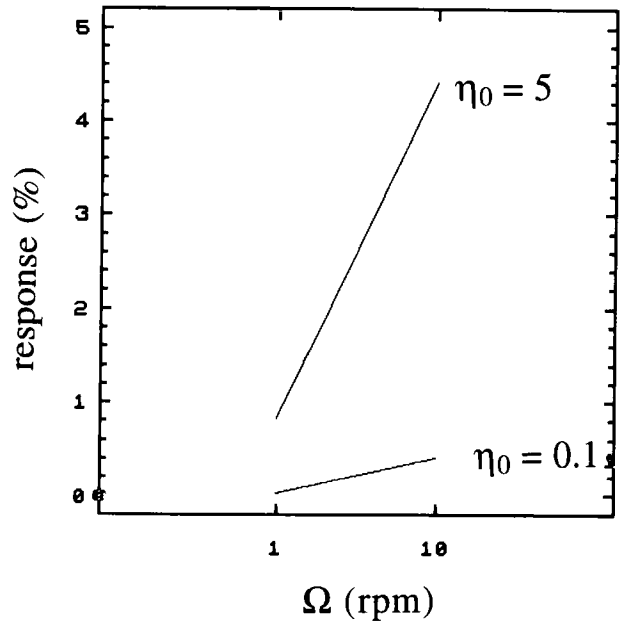
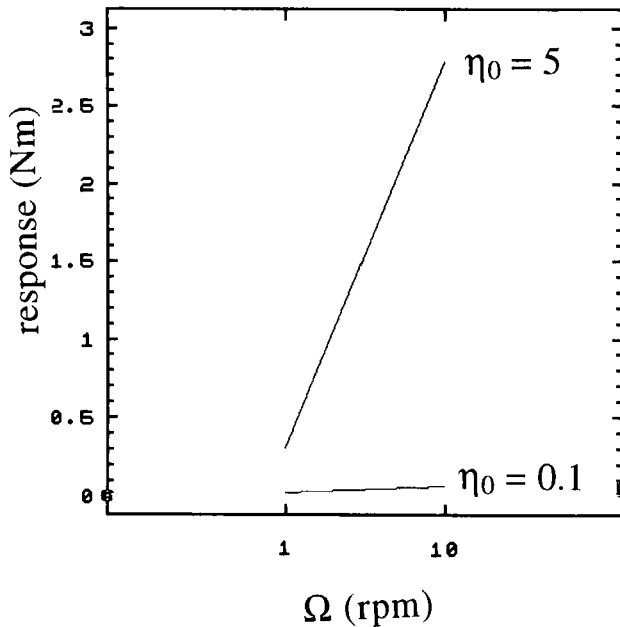


Figure 5: The interaction effect between  $\Omega$  and  $\eta_0$  on  $N_p$ . (the AB effect).





**Figure 6:** The interaction effect between  $\Omega$  and  $\eta_0$  on  $T_T$  (the AB effect).

The result of the second run, where parameters C, D and F were held constant and the parameter H, placement of the roller in the cage pocket, was introduced, is presented in Figure 7. Interesting to note here, is that even though flange height is still the most important parameter to affect roller slip, roller location has a considerable influence. Östensen et al.<sup>16</sup> made a slight alteration in roller location and compared it with a change in viscosity, however not comparing the relative effect of the two. Looking at Figure 7a however, the difference in effect between the two parameters is clearly seen, and it is also clear that no time has to be wasted varying radial load, E, or shaft speed A, at least not within this range, to study roller slip. In Figure 7b, the effect of moving the roller in the cage pocket is studied separately, together with the influence of flange height. The effect on  $\Delta_{max}$  when changing roller location is smaller than that of altering flange

height, but it must be remembered that the roller, in the case of cage slip, will be in close contact with the cage, separated in the extreme case only by an additive layer. Decreasing  $c_p$  further increases the shear stress, and hence the breaking torque on the roller, dramatically. The implication is that even a small amount of cage slip causes the rollers to slow down even more in the unloaded zone, and, eventually, the conditions are present where heat induced smearing is triggered, see Hamer et al.<sup>10</sup> and *Introduction*. Also, a decrease in  $c_p$  due to smaller tolerances between roller and cage may easily increase roller slip.

When the absolute levels of the friction torque results are studied, Figure 6, they predict bearing friction well below the level that has been measured by Wikström et al.<sup>30,31</sup> and Östensen et al.<sup>16</sup>, especially at low temperatures. The maximum friction torque calculated in the present investigation was 3.4 Nm, occurring when all input parameters were at + level, which may be compared with the 20-30 Nm obtained experimentally in a lightly run-in bearing under the same conditions. The difference between the two is probably due to the relatively large amount of lubricant present in the test bearing, even in a bearing that has been run-in for 60 s before starting which was the case in the experiments. The calculations assume that the contacts are fully flooded, but there are no bulk grease reservoirs with high apparent viscosity in front or behind the rollers as will be the case in the experiments. However, if one turns to manufacturers' equations<sup>33,34</sup> for prediction of

friction torque, intended for run-in bearings, the agreement with the present investigation is excellent.

Östensen et al.<sup>16</sup>, who compared calculated and measured roller slip at +20°C found the agreement between theory and experiments to be good, but experiments should still be made to verify the theoretical results of the present investigation also

at lower temperatures. Due to the time-demanding procedure applied when roller slip is to be measured, together with the difficulties involved in identifying the centre-line of the rollers when lubricant is affluent and highly viscous, this has not been included in the present work.

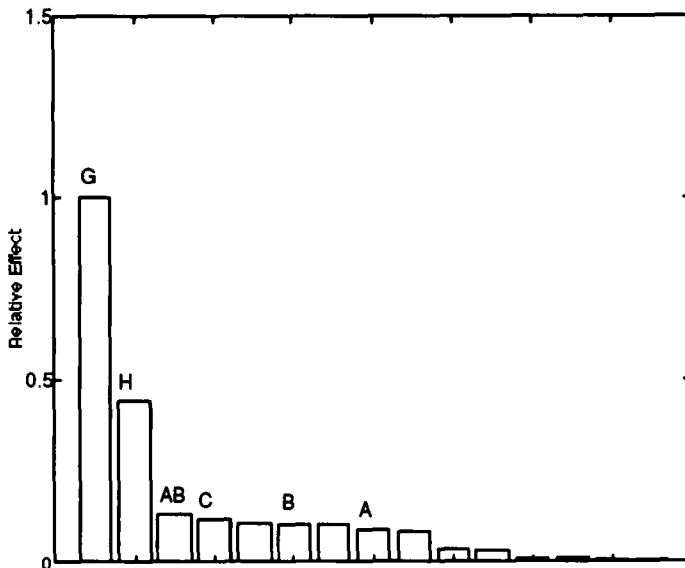


Figure 7a: Normalised Pareto plot for  $\Delta_{max}$ , second run including roller placement in cage pocket.

Examples of  $\Delta(\phi)$  for some extreme cases are shown in Figure 8. In Figure 8a-b, the effect on  $\Delta_{max}$  of changing  $h_f$  from 2.25 to 3.25 mm is shown to illustrate how the large main effect G seen in Figure 3a may look when studied in detail. It will not affect  $\Delta_{max}$  significantly if all parameters were changed, as long as  $h_f$  is kept constant, which is the essence of Figure 3a.

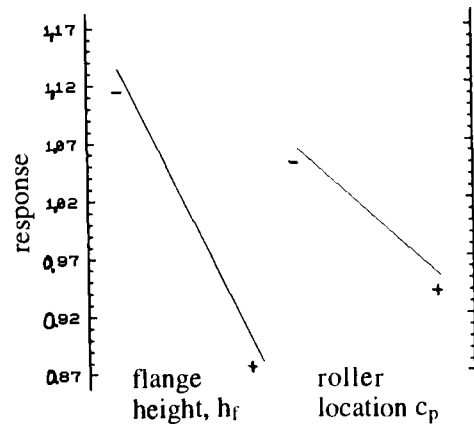
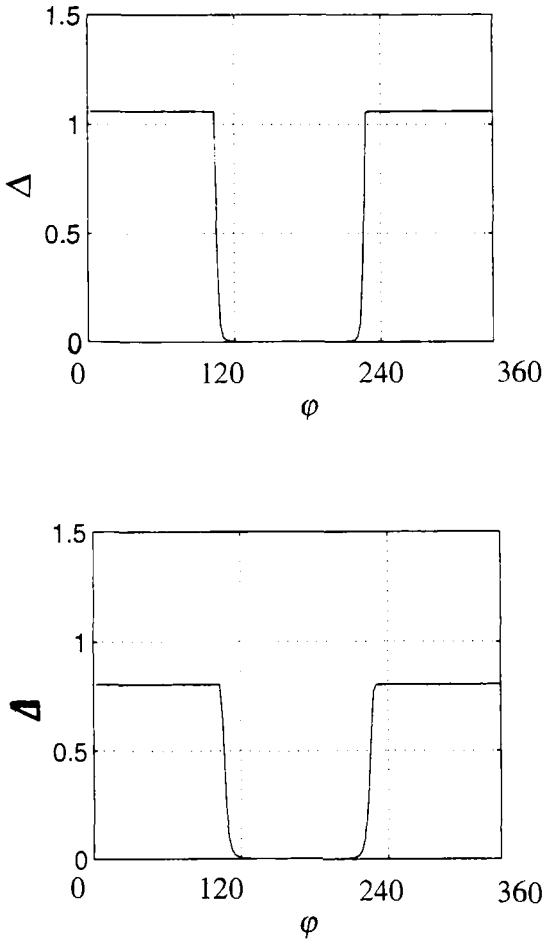


Figure 7b: The effect of flange height and roller placement in cage pocket on  $\Delta_{max}$ .



**Figure 8:**  $\Delta(\varphi)$  for a)  $\Omega = 1$  rpm,  $\eta_0 = 5$  Pas,  $\gamma = 0.03$ ,  $\alpha = 3 \times 10^{-8}$  Pa $^{-1}$ ,  $P = 12\,000$  N,  $c_d = 10$   $\mu$ m and  $h_f = 2.25$  mm. b)  $\Omega = 10$  rpm,  $\eta_0 = 5$  Pas,  $\gamma = 0.03$ ,  $\alpha = 3 \times 10^{-8}$  Pa $^{-1}$ ,  $P = 12\,000$  N,  $c_d = 10$   $\mu$ m and  $h_f = 3.25$  mm.

### Conclusions

The influence of eight different parameters combined in 144 different ways on roller slip, friction torque and the level of shear stress in a cylindrical roller bearing has been investigated

using a quasi-static simulation model. The aim of the investigation was to see whether non-Newtonian effects, under any conditions, may be present in this type of bearing, especially at low temperature starting.

As the maximum amount of shear stress, when compared to the limiting shear stress, never exceeded 10% under any settings of the input parameters, it must be concluded that non-Newtonian effects are unlikely to appear in cylindrical roller bearings. This is due to the low sliding speed in the loaded zone, and to the relatively fast acceleration phase, still at low normal force, entering the zone.

It has also been verified that the maximum roller slip, appearing in the main part of the loaded zone, can be decreased significantly if the outer race flange height is decreased slightly. The effect of changing flange height is several orders of magnitude larger than changing any other parameter. Only when roller placement in the cage pocket was altered, an effect of the same order as flange height was seen. To keep roller slip to a minimum is important, at least in large size rolling bearings where a combination of normal and sliding motion may endanger the separating film, Lundberg et al.<sup>35</sup>. The tangential shear stress will be largest when speed and viscosity are high, which points out the direction in which to continue further work on smearing and pitting damages in bearings.

The practical implications of the study is that bearings should have as low flange as possible to reduce roller slip. Also, a low value of the limiting shear stress-pressure coefficient of the lubricant may become important to keep bearing friction down at low temperature if cage slip occurs. However, for bearings that have not been run in for a longer period of time, the amount of lubricant within the bearing is probably the far most important parameter.

## References

- 1 "Low Temperature Torque of Ball Bearing Greases", Standard no. ASTM D-1478. In: *1987 Annual Book of ASTM Standards*, vol. 05.01., American Society for Testing and Materials, Philadelphia, PA, (1987).
- 2 "Low-Temperature Torque of Grease-Lubricated Wheel Bearings", Standard no. ASTM D-4693. In: *1988 Annual Book of ASTM Standards*, vol. 05.03., American Society for Testing and Materials, Philadelphia, PA, (1988).
- 3 Wikström, V., Jacobson, B., "Loss of Lubricant from Oil Lubricated Near-Starved Spherical Roller Bearings", SKF Internal Report, to be published, (1996).
- 4 Lubrecht, A. A., *Grease Performance at Temperatures Below +70\_C*, SKF Internal Report - unpublished, (1989).
- 5 Boness, R. J., "The Effect of Oil Supply on Cage and Roller Motion in a Lubricated Roller Bearing", *ASME Journal of Lubrication Technology*, January, pp. 39-53, (1970).
- 6 Kaido, H., Doi, Y., "Cage Slip and Its Effect on Damages in High Speed Roller Bearings, in: *Proceedings of the JSLE International Tribology Conference*, July 8-10, Tokyo, Japan, pp. 591-596, (1985).
- 7 Kawakita, K., Halling, J., "A New Method for the Study of Ball Motion in Ball Bearings", *Wear*, vol. 69, pp. 241-248, (1981).
- 8 Ariyoshi, S., Kawakita, K., Hirano, F., Kondo, T., "Motion of a Ball in a Deep-Groove Ball Bearing Under Static Moment Loading", *Journal of JSLE Int. Ed.*, No. 4, pp. 109-115, (1983).
- 9 Wikström, V., Östensen, J. O., Höglund, E., "Friction Torque and Slip of Rollers in Roller Bearings Under Arctic Conditions", In: *Proceedings of the 4th NORDTRIB Symposium*, Hirtshals, Denmark, June 10-13, pp. 95-103, MacKeenzie, Copenhagen, (1990).
- 10 Hamer, J. C., Sayles, R. S., Ioannides, E., "An Experimental Investigation Into the Boundaries of Smearing Failure in Roller Bearings", *ASME Journal of Tribology*, vol. 113, pp. 102-110, (1991).
- 11 Jacobson, B.O., *Rheology and Elastohydrodynamic Lubrication*, Elsevier Tribology Series 19, Elsevier, Amsterdam, ISBN 0-444-88146-8, (1991).
- 12 Harris, T. A., *Rolling Bearing Analysis*, 3rd ed., John Wiley&Sons, (1991).
- 13 Harris, T. A., "An Analytical Method to Predict Skidding in Thrust-Loaded, Angular-Contact Ball Bearings", *ASME Journal of Lubrication Technology*, vol. 93, pp 17-24, (1971).
- 14 Chang, L., Cusano, C., Conry, T. F., "Analysis of High-Speed Cylindrical Roller Bearings Using a Full EHD Lubrication Model. Part 1: Formulation", *STLE Tribology Transactions*, vol. 33, no. 2, pp. 274-284, (1990).
- 15 Chang, L., Conry, T. F., Cusano, C., "Analysis of High-Speed Cylindrical Roller Bearings Using a Full EHD Lubrication Model. Part 2: Results", *STLE Tribology Transactions*, vol. 33, no. 2, pp. 285-291, (1990).
- 16 Östensen, J. O., Åström, H., Höglund, E., "Analysis of a Grease-Lubricated Roller Bearing Under Arctic Conditions", *Proc Instn*

- Mech Engrs, Part J: J. of Engineering Tribology*, vol. 209, pp. 213-220, (1995).
- <sup>17</sup> **Hamrock, B. J.**, *Fundamentals of Fluid Film Lubrication*, Mc Graw-Hill, Inc., ISBN 0-07-025956-9, (1994).
- <sup>18</sup> **Wikström, V., Höglund, E.**, "Investigation of Parameters Affecting the Limiting Shear Stress-Pressure Coefficient: A New Model Incorporating Temperature", *ASME Journal of Tribology*, vol. 116, July, pp. 612-620, (1994).
- <sup>19</sup> **Prisacaru, G., Bercea, I., Cretu, S., Mitu, N.**, "Non-Newtonian Behaviour of Mineral Oils in Cylindrical Roller Bearing", in: *Proceedings of the 10th International Colloquium on Tribology, Part II*, Jan. 9-11, Esslingen, Germany, pp. 1617-1623, (1996).
- <sup>20</sup> **Prisacaru, G., Bercea, I., Mitu, N., Cretu, S., Silion, D., Croitoru, L.**, "Analysis of Quasi-Dynamic Equilibrium in Cylindrical Roller Bearings", in: *Proceedings of NORDTRIB '94*, 6th Nordic Symposium on Tribology, June 12-15, Uppsala, Sweden, pp. 721-731, (1994).
- <sup>21</sup> **Gupta, P. K.**, *Advanced Dynamics of Rolling Elements*, Springer Verlag, New York, ISBN 0-387-96031-7, (1984).
- <sup>22</sup> **Dowson, D., Higginson, G. R.**, *Elasto-Hydrodynamic Lubrication. The Fundamentals of Roller and Gear Lubrication*, Pergamon Press Ltd., Oxford, (1966).
- <sup>23</sup> **Conry, T. F.**, "Thermal Effects on Traction in EHD Lubrication", *ASME Journal of Lubrication Technology*, vol. 103, October, pp. 533-538, (1981).
- <sup>24</sup> **Muennich, H. C., Gloeckner, H. J. R.**, "EHD Lubrication of Grease-Lubricated Rolling Bearings", *ASLE Transactions*, Vol. 23, No. 1, pp. 45-52, (1980).
- <sup>25</sup> **Johnson, K. L., Tevaarwerk, J. L.**, "Shear Behaviour of Elastohydrodynamic Oil Films", *Proc. Royal Society*, London, A 356, pp 215-236, (1976).
- <sup>26</sup> **Jacobson, B. O.**, "On the Lubrication of Heavily Loaded Spherical Surfaces Considering Surface Deformations and Solidification of the Lubricant", *Acta Polytechnica Scandinavica, Mech. Eng. Series No. 54*, (1970).
- <sup>27</sup> **Hamrock, B. J., Jacobson, B. O.**, "Non-Newtonian Fluid Model Incorporated Into EHD Lubrication of Rectangular Contacts", NASA Report No TM 83318, (1983).
- <sup>28</sup> **Box, G. E. P., Hunter, W. G., Hunter, J. S.**, *Statistics for Experimenters*, Wiley Interscience, John Wiley&Sons Inc. NY, ISBN 0-471-09315-7, (1978).
- <sup>29</sup> **Statgraphics®**, Version 7.1. Statistical Graphics Corporation (STSC) Ind, 2115 East Jefferson St., Rockville, Maryland, USA.
- <sup>30</sup> **Wikström, V., Höglund, E.**, "Starting and Steady-State Friction Torque of Grease-Lubricated Rolling Element Bearings at Low Temperatures, Part I: A Parameter Study", presented at the STLE/ASME Tribology Conference, Kissimmee, Florida, Oct. 8-11. *STLE Preprint No. 95-TC-2D-1*, (1995).
- <sup>31</sup> **Wikström, V., Höglund, E.**, "Starting and Steady-State Friction Torque of Grease-Lubricated Rolling Element Bearings at Low Temperatures, Part II: Correlation with Less-Complex Test Methods", presented at the STLE/ASME Tribology Conference, Kissimmee, Florida, Oct. 8-11. *STLE Preprint No. 95-TC-2D-2*, (1995).
- <sup>32</sup> **Bergman, B.**, *Industriell Försöksplanering och Robust Konstruktion*, (Industrial Experimental Design), in Swedish, Linköping University, Inst. of Technology, Linköping , Sweden, (1992).
- <sup>33</sup> **SKF General Catalogue**, SKF Industries Inc., (1989).
- <sup>34</sup> **INA Huvudkatalog**, INA Wälzlager Schaeffler KG, Germany, (1987).
- <sup>35</sup> **Lundberg, J., Östensen, J. O., Åström, H.**, "High Speed Video Photographs of Lubrication Breakdown in Squeeze-Sliding Contact", *Wear*, Vol. 157, pp. 427-433, (1992).

## NOMENCLATURE

|               |   |               |  |
|---------------|---|---------------|--|
| $A_c$         | Contact area between roller and race,<br>$A_c = 2bl_{eff}$ , m <sup>2</sup> .   | $(H_m)_{i,o}$ | Minimum film thickness in the loaded zone, dimensionless.                                |
| $A_F$         | Flange shear area, contact between roller end and outer ring flange, 16.6 mm <sup>2</sup> , see also Figure 1.  | $h_{min}$     | Minimum film thickness, $\mu\text{m}$ .  |
| $A_p$         | Contact area between roller circumference and cage pocket,<br>$A_p \approx \arcsin\left(\frac{h_c}{2r}\right)lr$ , see also Figure 2b, m <sup>2</sup> . | $(h_c)_{i,o}$ | Central film thickness in the unloaded zone, $\mu\text{m}$ .                             |
| $b_c$         | Cage width, measured to 3 mm, see Figure 1.   | $h_f$         | Flange height, mm.   |
| $(b)_{i,o}$   | Hertzian contact width, m.  | IR            | Abbreviation for inner ring.   |
| $C$           | Bearing basic dynamic capacity, N.  | $l$           | Total roller length, 14.98 mm.   |
| $C/P$         | Load ratio.   | $le$          | Effective roller length, $l-2r_c$ , m.   |
| $c_A$         | Axial clearance between roller end and flange, see Figure 1, 35 $\mu\text{m}$ .   | $m$           | Roller mass, kg.   |
| $c_c$         | Clearance between cage and OR flange, see Figure 1, $\mu\text{m}$ .   | $N_p$         | Amount of "non-Newtonian-ness",<br>$\frac{\tau_{i,o}}{(\tau_L)_{i,o}} \times 100$        |
| $c_d$         | Bearing diametral clearance, unloaded bearing: 40 $\mu\text{m}$ .   | OR            | Abbreviation for outer ring.   |
| $c_e$         | Clearance between roller end and cage, see Figure 1, 460 $\mu\text{m}$ .  | $P$           | Bearing radial load, N.  |
| $c_h$         | Cage height, 8.8 mm.  | $(P_j)_{i,o}$ | Normal load on roller $j$ at inner/outer race contact.                                   |
| $c_p$         | Radial clearance between roller and pocket, see Figure 2b, $\mu\text{m}$ .  | $p_{av}$      | Average contact pressure,<br>$(p_{av})_{i,o} = \frac{(p_j)_{i,o}}{2(b)_{i,o} l_e}$ , Pa. |
| $c_T$         | Bearing diametral clearance, loaded bearing 12 kN: 70 $\mu\text{m}$ .   | $R_c$         | Cage mean radius, see Figure 2b, mm.   |
| $E'$          | Effective Young's modulus,<br>$2\left(\frac{1-\nu_a^2}{E_a} + \frac{1-\nu_b^2}{E_b}\right)^{-1}$ .  | $R_i$         | Inner race radius, see Figure 2b, mm.  |
| $E_{a,b}$     | Young's modulus for surfaces a and b in contact, Pa.  | $(R_x)_{i,o}$ | Equivalent radii in x direction, m.  |
| $F_{i,o}$     | Tangential traction at inner- and outer roller/race contact, N.   | $R_y$         | Outer ring radius, m.  |
| $F_C$         | Centrifugal force on roller, N.   | $r$           | Roller radius, 7.50 mm.  |
| $F_F$         | Viscous forces between roller ends and OR flange, N.  | $r_c$         | Roller crowning radius, 0.8 mm.  |
| $(F_p)_{1,2}$ | Viscous forces between roller mantle and cage pocket, see Figure 2a, N.   | $r_F$         | Flange shear radius, 6.2 mm, see Figure 1.   |
| $G$           | Dimensionless material parameter, $G = \alpha E'$ .   | $s$           | $s = \frac{r}{R_i}$  |
|               |   | $T_B$         | Braking torque on roller, Nm.  |
|               |   | $T_C$         | Friction torque contribution from cage acting on the outer ring, Nm.                     |
|               |   | $T_D$         | Driving torque on roller, Nm.  |
|               |   | $(T_{EHD})_j$ | Friction torque contribution from roller $j$ in the loaded zone, Nm.                     |
|               |   | $T_F$         | Friction torque arising from roller end-outer race flange contact, Nm.                   |
|               |   | $(T_{HD})_j$  | Friction torque contribution from roller $j$ in the unloaded zone, Nm.                   |

|                |   |                                 |   |
|----------------|---|---------------------------------|---|
| $T_r$          | Total torque on roller, Nm.   | $\tau_F$                        | Shear stress between roller – OR flange, Equation (17).                           |
| $T_T$          | Total bearing friction torque on outer ring, Nm.                                  | $\tau_o$                        | Limiting shear stress at atmospheric conditions, Pa.                              |
| $U$            | Dimensionless speed parameter,<br>$U = \eta_0 \frac{u_r + u_{i,o}}{2E' R_{i,o}}$  | $(\tau_L)_{i,o}$                | Limiting shear stress at inner/outer contacts, Pa.                                |
| $u_i$          | Peripheral speed of the shaft, $u_i = (\Omega \omega_c)R_i$ , m/s.                | $\Omega$                        | Shaft angular velocity, rad/s.  |
| $u_r$          | Peripheral speed of the roller, $u_r = \omega_r r$ , m/s.                         | $\omega_c$                      | Cage angular velocity around shaft axis, rad/s.                                   |
| $u_s$          | Mean velocity,<br>$(u_s)_{i,o} = \left( \frac{u_1 + u_2}{2} \right)_{i,o}$ , m/s. | $\omega_r$                      | Roller angular velocity relative to the cage, rad/s.                              |
| $u_d$          | Velocity difference, $(u_d)_{i,o} = (u_1 - u_2)_{i,o}$ , m/s.                     | $\frac{\partial u}{\partial z}$ | Shear rate, relative speed divided by film thickness/clearance, s <sup>-1</sup> . |
| $W$            | Dimensionless load parameter,<br>$\frac{P_j}{E' R_{i,o} l_{eff}}$                 |                                 |   |
| $w$            | Bearing width, see Figure 1, mm.  |                                 |   |
| $Z$            | Number of rollers.  |                                 |   |
| $\alpha$       | Pressure-viscosity coefficient, Pa <sup>-1</sup> .                                |                                 |   |
| $\delta_m$     | Maximum deflection, $\mu\text{m}$ .   |                                 |   |
| $\Delta$       | Roller slip, $\Delta = 2 \frac{u_i - u_r}{u_i + u_r}$                             |                                 |   |
| $\Delta_{max}$ | Maximum roller slip for a roller, $0 < \varphi < 360$ .                           |                                 |   |
| $\varphi$      | Angular location, °. $\varphi = 0$ on the load line but opposite the load.        |                                 |   |
| $\varphi_j$    | Angular location where a roller is placed, $(1 < j < Z)$ , °.                     |                                 |   |
| $\gamma$       | Limiting shear stress-pressure coefficient, dimensionless.                        |                                 |   |
| $\eta_o$       | Viscosity at atmospheric pressure, Pas.   |                                 |   |
| $\eta_R$       | Viscosity according to Roelands. Pressure dependence included, Pas.               |                                 |   |
| $\nu$          | Poisson's ratio, 0.3.   |                                 |   |
| $(\tau)_{i,o}$ | Tangential shear stress at inner and outer contacts, Pa.                          |                                 |   |

## Analysis of an EHL circular contact incorporating rolling element vibration

Y.H. Wijnant and C.H. Venner

University of Twente, Enschede, The Netherlands

The dynamics of rolling bearings is governed by both the dynamics of its structural components, and the elastohydrodynamic lubricated (EHL) contacts connecting these structural elements. In this paper, as an initial stage in quantifying the influence of the lubricant on the vibrations in rolling bearings, the influence of the lubricant on the vibration of *one* rolling element is investigated. For that purpose, inertia forces of the rolling element are incorporated into the analysis of an EHL circular contact. The model thus obtained includes both squeeze and entraining motion and hence it is time-dependent. It is shown that, to incorporate inertia forces, only one additional dimensionless parameter, the natural frequency, is needed. First, a Hertzian dry contact is investigated, as its solution will serve as an asymptote for the lubricated case. Subsequently, for a given load condition and different values of the natural frequency parameter, numerical solutions are presented showing both the influence of the lubricant on the vibration of the rolling element, as well as the influence of the vibration on film thickness and pressure.

### 1. Introduction

A realistic investigation of the dynamics of rolling element bearings should combine the dynamics of the housing, rolling elements, cage and shaft as well as their interactions. It is evident that a full numerical study of such a complex system goes beyond today's computer capabilities and limitations of existing models. Hence, simplifications are essential. One of these simplifications is the introduction of a "contact model" to represent the contact between roller and raceway, like "spring and damper" models. Nevertheless, such a model should provide an accurate representation of the influence of the lubricant film on the vibrating signal of the rolling element. In the present work, as an initial stage in developing such a simplified model, the influence of the lubricant on the vibrating signal of *one* rolling element is studied.

When studying EHL contacts, it is common to assume a constant load. Entraining motion causes the build up of pressure, resulting in a contact force, i.e. the integral over pressure, which is normally demanded to equal the applied load. The analysis done in this way is often time-independent. Transient calculations, i.e. the incorporation of squeeze motion, need only be per-

formed if surface features like waviness, dents and bumps are simulated, see [13,19–21].

However, when inertia forces are accounted for, the contact force will, in general, not be equal to the applied load and an oscillation around an equilibrium position will occur. This oscillation results in a squeeze motion and subsequently both squeeze and entraining motion need to be accounted for. Therefore, even for smooth surfaces, the model thus obtained is time-dependent.

Until now, squeeze and entraining motion have only been addressed in cases where inertia forces were neglected, whereas, on the other hand, inertia forces were taken into account only when pure squeeze motion was considered.

Studies on combined squeeze and entraining motion for rigid surfaces were carried out by Ghosh et al. [7]. EHL line contacts were studied by Yang and Weng [24], Bedewi et al. [2] and Lee and Hamrock [15]. All authors neglected inertia forces of the rolling element, i.e. their analyses is dynamically quasi-static, and a constant or sinusoidal load was assumed.

Pure squeeze motion, neglecting inertia forces, was discussed by Christensen [3,4], Herrebrugh [9], Vichard [21] and Lee and Cheng [16]. Inertia forces were taken into account in the analysis of



pure squeeze motion by Yang and Wen [23], Larsson and Höglund [11,12] and Dowson and Wang [6].

The model presented in this paper accounts for both squeeze and entraining motion as well as inertia effects. First, to determine the asymptotic behaviour, the so-called Hertzian dry contact is investigated. Subsequently, we move to the results obtained from a transient numerical simulation of the lubricated model.

## 2. Nomenclature

|           |   |                  |  |
|-----------|---|------------------|--|
| $a$       | radius Hertzian contact circle<br>$a = ((3fR)/(2E'))^{1/3}$   | $n1, n2$         | number of points   |
| $A$       | amplitude   | $p$              | pressure   |
| $C$       | integration constant  | $p_h$            | maximum Hertzian pressure<br>$p_h = (3f)/(2\pi a^2)$                           |
| $C_2$     | integration constant  | $p_0$            | constant<br>$p_0 = 1.96 \cdot 10^8$  |
| $dX$      | meshsize in $X$ -direction  | $P$              | dimensionless pressure<br>$P = p/p_h$  |
| $dY$      | meshsize in $Y$ -direction  | $R$              | reduced radius of curvature<br>$R^{-1} = R_1^{-1} + R_2^{-1}$                  |
| $dT$      | meshsize in $T$ -direction  | $S$              | domain   |
| $E_{1,2}$ | elasticity modulus body 1,2   | $t$              | time   |
| $E$       | variable  | $T$              | dimensionless time<br>$T = (tu_s)/(2a)$  |
| $E'$      | reduced modulus of elasticity<br>$2/E' = (1 - \nu_1^2)/E_1 + (1 - \nu_2^2)/E_2$   | $T_n$            | period of oscillation  |
| $f$       | contact force   | $u_s$            | sum velocity<br>$u_s = u_1 + u_2$  |
| $f_n$     | natural frequency   | $U$              | dimensionless speed parameter<br>(Hamrock/Dowson)<br>$U = (\eta_0 u_s)/(2E'R)$ |
| $F$       | variable  | $W$              | dimensionless load parameter<br>(Hamrock/Dowson)<br>$W = f/(E'R^2)$            |
| $g_{2,3}$ | constants   | $x$              | coordinate in direction of flow  |
| $G$       | dimensionless material parameter<br>(Hamrock/Dowson)<br>$G = \alpha E'$   | $X$              | dimensionless coordinate<br>$X = x/a$  |
| $h$       | film thickness, meshsize  | $y$              | coordinate perpendicular to $x$  |
| $H$       | dimensionless film thickness<br>$H = hR/a^2$  | $Y$              | dimensionless coordinate<br>$Y = y/a$  |
| $H_c$     | central film thickness  | $z$              | pressure viscosity parameter<br>(Roelands), variable                           |
| $H_{min}$ | minimum film thickness  | $Z$              | variable<br>$Z = \sqrt{\Delta}$  |
| $i$       | imaginary unit<br>$i = \sqrt{-1}$   | $\alpha$         | pressure viscosity index   |
| $I$       | intensity   | $\bar{\alpha}$   | dimensionless parameter<br>$\bar{\alpha} = \alpha p_h$                         |
| $L$       | dimensionless material parameter (Moes)<br>$L = G(2U)^{1/4} = \alpha E' \left( \frac{\eta_0 u_s}{E'R} \right)^{1/4}$    | $\gamma$         | variable   |
| $m$       | mass of rolling element   | $\delta$         | mutual approach  |
| $M$       | dimensionless load parameter (Moes)<br>$M = W(2U)^{-3/4} = \frac{f}{E'R^2} \left( \frac{E'R}{\eta_0 u_s} \right)^{3/4}$ | $\delta_\infty$  | $\delta$ at equilibrium  |
|           |   | $\delta_0$       | $\delta$ at $t = 0$  |
|           |   | $\dot{\delta}_0$ | velocity at $t=0$  |
|           |   | $\Delta$         | dimensionless mutual approach  |
|           |   | $\Delta_\infty$  | $\Delta$ at equilibrium  |
|           |   | $\Delta_0$       | $\Delta$ at $T = 0$ or $T = 0$   |
|           |   | $\dot{\Delta}_0$ | dimensionless velocity at $T = 0$<br>or $T = 0$                                |

|               |  |
|---------------|--|
| $\epsilon$    | coefficient<br>$\epsilon = (\bar{\rho}H^3)/(\bar{\eta}\lambda)$          |
| $\eta$        | viscosity  |
| $\eta_0$      | viscosity at ambient pressure  |
| $\bar{\eta}$  | dimensionless viscosity<br>$\bar{\eta} = \eta/\eta_0$                    |
| $\lambda$     | dimensionless speed parameter<br>$\lambda = (6\eta_0 u_s R^2)/(a^3 p_h)$ |
| $\Lambda$     | dimensionless wavelength<br>$\Lambda = 0.05$                             |
| $\phi$        | phase angle  |
| $\nu_{1,2}$   | Poisson's ratio body 1,2   |
| $\rho$        | density  |
| $\rho_0$      | density at ambient pressure  |
| $\bar{\rho}$  | dimensionless density<br>$\bar{\rho} = \rho/\rho_0$                      |
| $\Omega$      | dimensionless frequency<br>$\Omega = \sqrt{4fR/(mu_s^2)}$                |
| $\tau$        | dimensionless time<br>$\tau = \gamma T$                                  |
| $\wp$         | Weierstrass function   |
| $\mathcal{R}$ | geometry of undeformed gap   |
| $\mathcal{T}$ | dimensionless time<br>$\mathcal{T} = t((4fRE'^2)/(9m^3))^{1/6}$          |
| $T_n$         | period   |

### 3. Dry Contact

Consider a rolling element subjected to a load  $f$ , running on a raceway of a rolling bearing. If the mass of the raceway is large compared to the mass of the rolling element, we can assume it to be a solid of infinite mass. Let the mass of the rolling element be  $m$ . The rolling element and the solid will deform elastically and, using the elastic half-space assumption, the pressure field  $p$  can be solved from the complementarity problem on the domain  $S$ ; see Johnson [10]:

$$\begin{aligned}
 hp &= 0, \\
 h &= -\delta(t) + \mathcal{R}(x, y, t) \\
 &\quad + \frac{2}{\pi E'} \int_S \frac{p(x', y', t) dx' dy'}{\sqrt{(x-x')^2 + (y-y')^2}}, \\
 p &\geq 0, \quad h \geq 0,
 \end{aligned} \tag{1}$$

where  $h$  is the film thickness,  $\delta(t)$  the mutual approach of the two bodies and  $\mathcal{R}(x, y, t)$  the geometry of the undeformed gap.

The equation of motion for the rolling element follows from Newton's second law:

$$m \frac{d^2 \delta}{dt^2} + \int_S p(x, y, t) dx dy = f, \tag{2}$$

with the initial conditions

$$\delta_{(t=0)} = \delta_0 \quad \text{and} \quad \frac{d\delta}{dt}_{(t=0)} = \dot{\delta}_0. \tag{3}$$

For perfectly smooth surfaces the undeformed gap between the two bodies can be accurately approximated by parabolas. The solution of this dry contact problem has been given by Hertz [8,10] and has been referred to as the Hertzian contact since then. For arbitrary functions  $\mathcal{R}(x, y, t)$ , Eq.(1) must be solved numerically, e.g. using the multilevel algorithm presented by Lubrecht and Ioannides [14].

#### 3.1. Hertzian contact

According to the Hertzian theory the shape of the contact region is an ellipse and the pressure field is semi-ellipsoid. Although the present analysis can be performed for elliptical contacts too, for simplicity we will restrict ourselves to a circular contact. Then, the contact force is related to the mutual approach  $\delta$  by:

$$\int_S p(x, y, t) dx dy = \frac{2}{3} \sqrt{RE'} \delta^{3/2}. \tag{4}$$

Substituting Eq.(4) in Eq.(2) yields:

$$m \frac{d^2 \delta}{dt^2} + \frac{2}{3} \sqrt{RE'} \delta^{3/2} = f, \tag{5}$$

which describes the oscillation of the rolling element around its equilibrium position  $\delta_\infty = (3f/2\sqrt{RE'})^{2/3} = a^2/R$ . Provided the second term in Eq.(5) is set to zero when  $\delta$  becomes negative, the equation is valid for all values of  $\delta$ .

To reduce the number of parameters Eq.(5) can be written in dimensionless form. Defining

$$\Delta = \delta R/a^2 \tag{6}$$

and

$$T = t \left( \frac{4fRE'^2}{9m^3} \right)^{1/6} \tag{7}$$

the equation of motion is transformed into

$$\frac{d^2\Delta}{dT^2} + \Delta^{3/2} = 1, \tag{8}$$

with initial conditions

$$\Delta(T=0) = \Delta_0 \text{ and } \frac{d\Delta}{dT}(T=0) = \dot{\Delta}_0. \tag{9}$$

Hence, the problem is fully described by the variables  $\Delta$  and  $T$  and thus its solution is uniquely determined by the initial conditions  $\Delta_0$  and  $\dot{\Delta}_0$ .

Eq.(8) can be integrated once, yielding:

$$\frac{1}{2} \left( \frac{d\Delta}{dT} \right)^2 + \frac{2}{5} \Delta^{5/2} = \Delta + C, \tag{10}$$

where  $C$  is a constant of integration. The individual terms in this equation can be interpreted as the kinetic energy, the potential energy and the work done by the unit force (as given in the r.h.s. of Eq.(8)), respectively. The value of  $C$  ranges from  $-3/5$  for the steady-state situation to 0 for the oscillation where  $\Delta$  just becomes zero, but remains positive.

Eq.(8) can be solved efficiently by numerical integration, however, analytical solutions do exist. For small oscillations, i.e. when  $C$  approaches  $-3/5$ , Eq.(8) can be linearized around the equilibrium position  $\Delta = 1$ . The solution to this linearized problem is:

$$\Delta = 1 + A \cos(\sqrt{3/2} T + \phi), \tag{11}$$

where the amplitude  $A$  and phase angle  $\phi$  are determined by the initial conditions, see appendix A. The natural frequency is  $f_n = \sqrt{3/2}/2\pi \approx 0.195$ . Thus, the period of one oscillation equals  $T_n = 1/f_n \approx 5.130$ .

Secondly, for  $C = 0$  the solution is given in terms of the Weierstrass elliptic function  $\wp(z; g_2, g_3)$ , see appendix A, with  $g_2 = 0$  and  $g_3 = -1/800$ , i.e.

$$\Delta = 400 \wp(T - i\sqrt{20}C_2; 0, -1/800)^2. \tag{12}$$

$C_2$  is a constant of integration, representing a phase shift. Between the zeros of this function,

there are alternating regions where the solution is bounded and regions where it goes to infinity. The period of the bounded solution can be shown to be

$$T_n = 2 \int_{\frac{1}{10}\sqrt[3]{\frac{2}{3}}}^{\infty} (4t^3 + 1/800)^{1/2} dt \approx 5.383. \tag{13}$$

Thus, for this case,  $f_n \approx 0.186$ . The maximum mutual approach is  $(5/2)^{2/3}$ . This shows, as one would expect from such a non-linear system, that the oscillation is asymmetric around the equilibrium position  $\Delta = 1$ .

For general values of  $C$  the equation of motion can easily be solved numerically, e.g. by the so called Newmark scheme, see appendix B and [17,1]. This scheme is a second order scheme and shows no numerical amplitude decay. This latter property will be especially important when the lubricated case is considered. As will be shown, the lubricant will damp the oscillation and one must make sure that artificial viscosity is sufficiently small.

In Fig. 1 the mutual approach  $\Delta$  is given for three different values of the integration constant  $C$ . In this figure the asymmetry of the solution with increasing amplitude clearly shows.

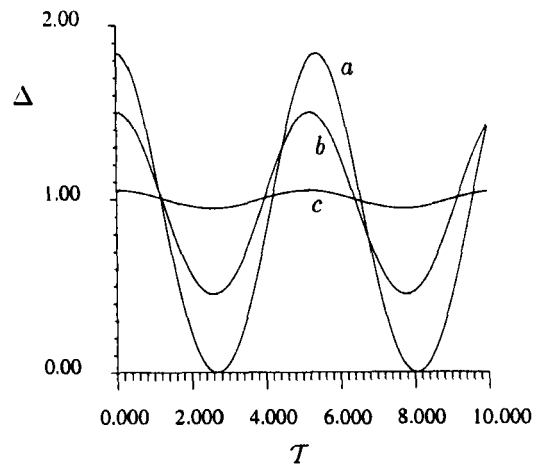


Figure 1.  $\Delta$  as a function of  $T$  for  $C = 0.00$  (a),  $C = -0.398$  (b) and  $C = -0.598$  (c).

Comparing the three solutions, one observes that the difference in natural frequency is small. In fact, the difference in natural frequency between the linearized and the Weierstrass solution is only about 4.7%. Thus,  $f_n$  is almost independent of the amplitude of the oscillation.

#### 4. Lubricated circular contact

Next, we extend the model by introducing a lubricant between rolling element and solid. In that case there is no direct relation between the contact force and the approach  $\delta$ . Hence, Eq.(2) should be solved together with the equation for the film thickness and the equations describing the lubricant flow and behaviour, i.e. in the present work, Reynolds' equation, Roelands' pressure viscosity law [18] and the compressibility equation of Dowson and Higginson [5].

##### 4.1. Equations

The equations describing the lubricant flow and the position of the rolling element have been made dimensionless using:

$$\begin{aligned}\bar{\rho} &= \rho/\rho_0, & \bar{\eta} &= \eta/\eta_0, \\ X &= x/a, & Y &= y/a, \\ P &= p/p_h, & H &= hR/a^2, \\ \Delta &= \delta R/a^2, & T &= tu_s/(2a),\end{aligned}$$

where  $p_h$  is the maximum Hertzian pressure and  $a$  the radius of the Hertzian contact circle in case of equilibrium:

$$p_h = 3f/(2\pi a^2), \quad a^3 = 3fR/(2E'). \quad (14)$$

Note that the time  $t$  is made dimensionless by the time in which a fluid particle passes the Hertzian contact, which differs from the time scale  $T$  introduced in the Hertzian model, see Sec. 3.1. The other variables are explained in the nomenclature.

In terms of these dimensionless variables the Reynolds equation reads:

$$\begin{aligned}\frac{\partial}{\partial X} \left( \frac{\bar{\rho} H^3}{\bar{\eta} \lambda} \frac{\partial P}{\partial X} \right) + \frac{\partial}{\partial Y} \left( \frac{\bar{\rho} H^3}{\bar{\eta} \lambda} \frac{\partial P}{\partial Y} \right) \\ - \frac{\partial(\bar{\rho} H)}{\partial X} - \frac{\partial(\bar{\rho} H)}{\partial T} = 0.\end{aligned} \quad (15)$$

At all  $T$  the solution is subjected to the cavitation condition  $P \geq 0$ ,  $\forall(X, Y) \in S$  and  $P = 0$  on the

boundary  $\partial S$ .  $\lambda$  denotes the dimensionless speed parameter:

$$\lambda = \frac{6 u_s \eta_0 R^2}{a^3 p_h}. \quad (16)$$

Roelands' viscosity-pressure equation and Dowson and Higginson's relation are,

$$\bar{\eta}(P) = \exp \left\{ \left( \frac{\alpha p_0}{z} \right) \left( -1 + \left( 1 + \frac{P p_h}{p_0} \right)^z \right) \right\} \quad (17)$$

and

$$\bar{\rho}(P) = \frac{0.59 \cdot 10^9 + 1.34 P p_h}{0.59 \cdot 10^9 + P p_h}. \quad (18)$$

In Roelands' equation  $p_0$  is a constant;  $p_0 = 1.96 \cdot 10^8$ . All results presented in this paper have been obtained using  $z = 0.67$  and  $\alpha = 2.2 \cdot 10^{-8}$ . The dimensionless film thickness equation reads:

$$\begin{aligned}H(X, Y, T) = -\Delta + \frac{X^2}{2} + \frac{Y^2}{2} \\ + \frac{2}{\pi^2} \int_S \frac{P(X', Y', T) dX' dY'}{\sqrt{(X - X')^2 + (Y - Y')^2}}.\end{aligned} \quad (19)$$

The dimensionless equation of motion is given by:

$$\frac{1}{\Omega^2} \frac{d^2 \Delta}{dT^2} + \frac{3}{2\pi} \int_S P(X', Y', T) dX' dY' = 1, \quad (20)$$

where  $\Omega$ , as will be shown, is the dimensionless natural frequency with respect to the timescale  $T$ :

$$\Omega = \sqrt{\frac{4fR}{mu_s^2}}. \quad (21)$$

Finally the following initial conditions should be satisfied:

$$\Delta_{(T=0)} = \Delta_0 \quad \text{and} \quad \frac{d\Delta}{dT}_{(T=0)} = \dot{\Delta}_0. \quad (22)$$

We further introduce  $\Delta_\infty$  to denote the mutual approach at equilibrium.

Alternatively, the set of equations can be made dimensionless using the time scale  $T$  introduced in Sec. 3.1. In that case, Reynolds' equation and the equation of motion are

$$\begin{aligned}\frac{\partial}{\partial X} \left( \frac{\bar{\rho} H^3}{\bar{\eta} \lambda} \frac{\partial P}{\partial X} \right) + \frac{\partial}{\partial Y} \left( \frac{\bar{\rho} H^3}{\bar{\eta} \lambda} \frac{\partial P}{\partial Y} \right) \\ - \frac{\partial(\bar{\rho} H)}{\partial X} - \Omega \frac{\partial(\bar{\rho} H)}{\partial T} = 0,\end{aligned} \quad (23)$$

and

$$\frac{d^2 \Delta}{dT^2} + \frac{3}{2\pi} \int_S P(X', Y', T) dX' dY' = 1. \quad (24)$$

**4.2. Numerical Simulation**

In the present paper, numerical solutions of Eq. (15) to (22) are presented for  $\lambda = 1.756 \cdot 10^{-2}$  and  $\bar{\alpha} = 9.109$  or, in terms of the Moes dimensionless parameters,  $M = 125$  and  $L = 5$ . Two values of  $\Omega$  are considered i.e.,  $\Omega = 10.0$  and  $\Omega = 5.2$ . The equations have been discretised, see appendix B, and the discrete equations have been solved by multilevel methods, see [13,19,21]. However, instead of using the double discretisation as in [21], the second order system of equations was solved directly. Furthermore, Gaussian elimination using partial pivoting was used for solving the (truncated) system of equations resulting from the line-relaxation. The calculations were performed on the domain  $-2.5 \leq X \leq 1.5$  and  $-2.0 \leq Y \leq 2.0$ .

**4.2.1. Stationary results**

First, the solution to the steady state problem was calculated. A meshsize  $dX = dY = 0.0156$  was used. For this case, the mutual approach  $\Delta_\infty = 0.917$ .

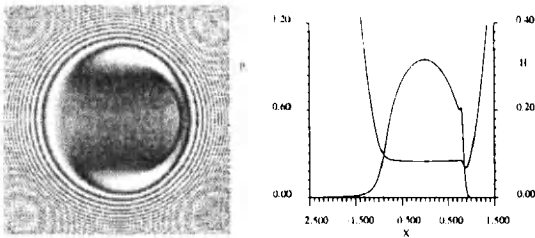


Figure 2. Pseudo interference plot and centreline pressure and film thickness ( $M = 125$  and  $L = 5$ ).

Fig. 2 shows the film thickness by means of a so-called pseudo interference plot together with the pressure and film thickness profile for  $Y = 0$ . In the pseudo interference plot, the film thickness is plotted by means of the intensity  $I$ , defined by:

$$I(X, Y, T) = 0.5 + 0.5 \cos \left( \frac{2\pi H(X, Y, T)}{\Lambda} \right), \quad (25)$$

where  $\Lambda = 0.05$  is the dimensionless wavelength. A white square of size  $dX \times dY$  is plotted when  $I = 1$  whereas a black square is plotted for  $I = 0$ . For  $0 < I < 1$  grey tones are plotted according to the value of  $I$ .

For the medium loaded case considered, the film displays the well known horse shoe shape and the pressure distribution is almost semi-ellipsoid.

**4.2.2. Transient results**

Transient calculations were performed using a meshsize  $dX = dY = 0.03125$ . In order to minimize artificial viscosity the time increment  $dT$  was taken equal to the meshsize, i.e.  $dT = 0.03125$ . On the grid used for the transient calculations the equilibrium position is  $\Delta_\infty = 0.916$  which approximately equals the one used on the grid for the steady state calculations ( $\Delta_\infty = 0.917$ ).

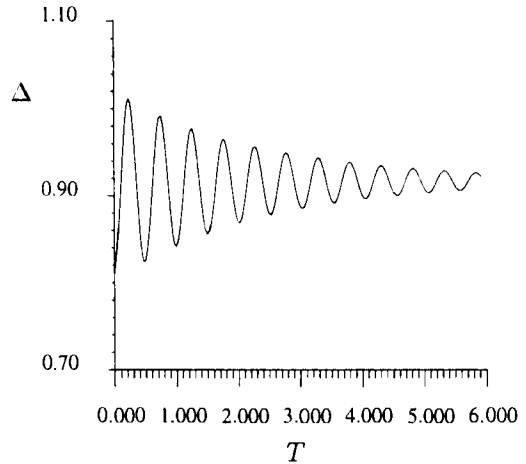


Figure 3.  $\Delta$  as a function of  $T$ . ( $\Delta_0 = 0.8$ ,  $\dot{\Delta}_0 = 0.0$ ,  $M = 125$ ,  $L = 5$  and  $\Omega = 10.0$ )

To take the rolling element out of its equilibrium position we can either take  $\Delta_0$  different from  $\Delta_\infty$  or take  $\dot{\Delta}_0$  different from zero. As a result of these initial conditions the rolling element will start an oscillatory motion that resembles the motion of the Hertzian contact shown before. However, as a result of viscous losses in the lubricant, the amplitude of the oscillation will decrease and

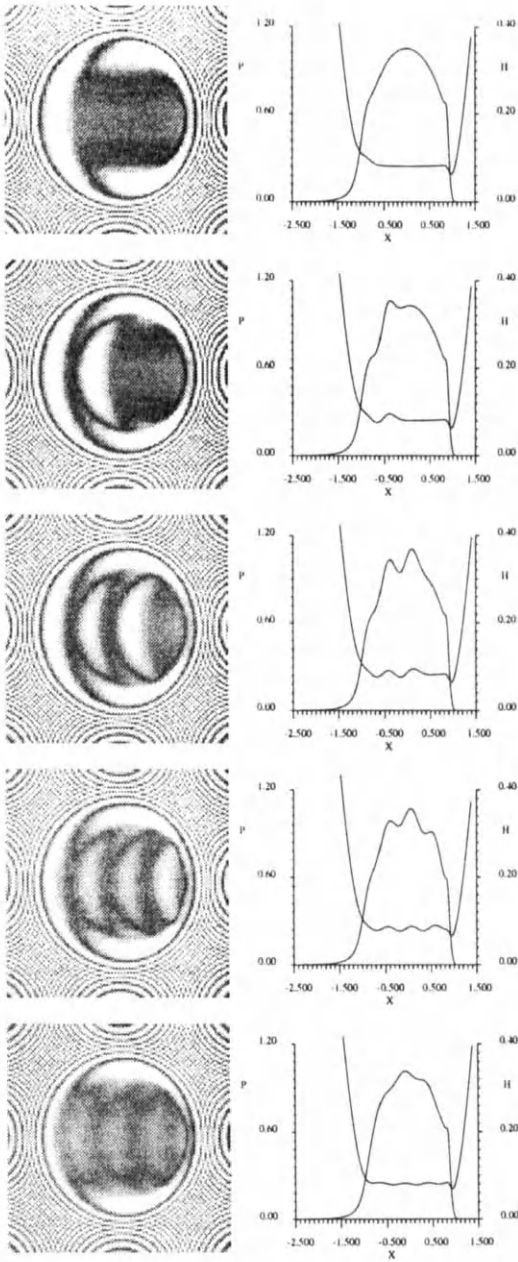


Figure 4. Pseudo film thickness interference plots and pressure and film thickness pressure at centerline on time  $T = 0.47, 1.09, 1.72, 2.97$  and  $5.94$  respectively.  $\Omega = 10.0$ .

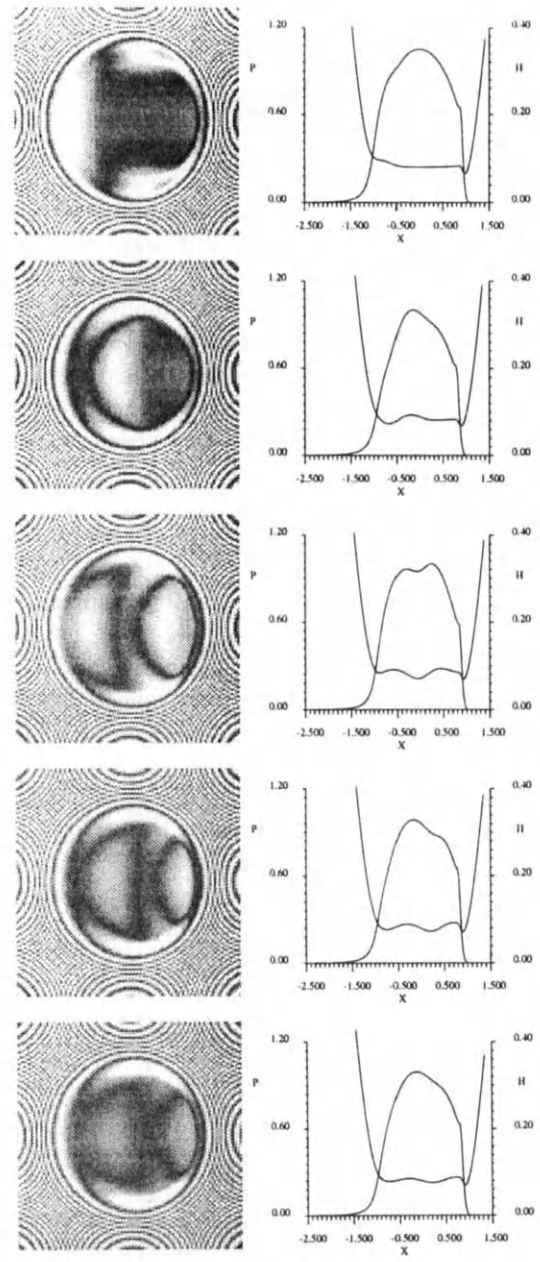


Figure 5. Pseudo film thickness interference plots and pressure and film thickness pressure at centerline on time  $T = 0.47, 1.09, 1.72, 2.97$  and  $5.94$  respectively.  $\Omega = 5.2$ .

eventually become zero, i.e. the solution returns to the steady state solution. Fig. 3 shows this oscillatory motion of the rolling element as a function of time for  $\Omega = 10.0$  and initial conditions  $\Delta_0 = 0.8$  and  $\dot{\Delta}_0 = 0.0$ .

To illustrate the changes in film thickness and pressure during the oscillatory motion, Fig. 4 shows snapshots of the film and pressure profile at different times.

Even though the surfaces are smooth, one observes film thickness modulations in the high pressure region. These modulations have a particular wavelength and propagate through the high pressure zone at the dimensionless speed of unity. This can be explained as follows.

Because  $\Delta_0 < \Delta_\infty$ , the rolling element is lifted from the solid and, when released, starts to accelerate towards the solid. Because of the lubricant's large viscosity in the high pressure zone, the central film thickness hardly reduces. Instead, the high pressure zone expands and only near the edge of the Hertzian circle does squeeze motion occur.

Subsequently, the film thickness reduction induced at the inlet of the contact, is propagated through the high pressure zone. This immediately follows from the Reynolds equation. In the high pressure zone Poiseuille flow is virtually absent and Reynolds' equation reduces to

$$-\frac{\partial(\bar{\rho}H)}{\partial X} - \frac{\partial(\bar{\rho}H)}{\partial T} \approx 0, \quad (26)$$

with the solution  $\bar{\rho}H = \bar{\rho}H(X - T)$ . Because the lubricant's compressibility is limited, eventually  $H$  is a function of  $(X - T)$  only. This shows that film thickness modulations are propagated at a dimensionless speed of unity.

This explanation is valid for any mechanism causing film thickness modulations at the entrance of the contact. Indeed, it has been observed for surface features in e.g. [19,20].

Finally, when the rolling element moves away from the solid, the contact region becomes smaller, resulting in a larger inlet film thickness, which again propagates through the contact. This process is then repeated periodically, until the steady state solution is obtained.

Fig. 5 shows the solution for  $\Omega = 5.2$ . Note

that the film thickness modulations have a larger wavelength than for  $\Omega = 10.0$ . This phenomenon can be explained as follows. At the end of Sec. 3.1 it was concluded that the dimensionless period of oscillation for the dry contact is almost independent of the amplitude. Given in terms of  $T$  the period equals  $T_n = 5.130$  for the smallest oscillation. For the largest oscillation  $T_n = 5.383$ . Thus it is justified to assume that the period is a constant and  $T_n \approx 5.2$ . Assume that one can neglect the influence of the lubricant on the period of oscillation. Hence, for the lubricated contact it is assumed that  $T_n \approx 5.2$ .

Furthermore, the timescales  $T$  and  $T$  are related by:

$$T = \Omega T. \quad (27)$$

Thus, in terms of  $T$ , the dimensionless period of oscillation is  $T_n = T_n/\Omega \approx (5.2/\Omega)$  and equals the dimensionless wavelength of the film thickness modulations induced. This explains the larger wavelength observed for  $\Omega = 5.2$ . The dimensionless frequency in terms of  $T$  equals  $f_n = \Omega/5.2$  and hence  $\Omega$  is a dimensionless frequency.

Alternatively, within the high pressure zone Eq. (23) reduces to

$$-\frac{\partial(\bar{\rho}H)}{\partial X} - \Omega \frac{\partial(\bar{\rho}H)}{\partial T} \approx 0. \quad (28)$$

Thus, in terms of  $T$ ,  $H = H(X - (T/\Omega))$ , and  $1/\Omega$  is the dimensionless speed at which film thickness modulations travel through the high pressure zone.

## 5. Numerical Accuracy

Since a second order scheme was used for time and the spatial coordinates and the meshsize is small compared to the scale on which changes in the solution occur, the numerical solution converges quickly towards the solution of the continuum problem. Let  $h = 0.03125$ , i.e.  $dX = h$  is the meshsize used for the transient calculations presented in Sec. 4.2.2. Then, we will denote grids by their meshsizes  $2h$ ,  $h$  and  $h/2$ , where  $dY = dT = dX$ .

The second order convergence with decreasing meshsize in the spatial coordinates, is shown by

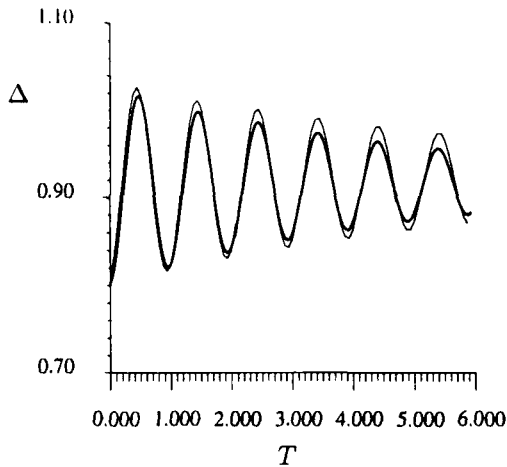


Figure 6.  $\Delta$  as a function of  $T$  on mesh  $dX = dT = 0.0625$  (thin line) and  $dX = dT = 0.0313$  (thick line). ( $\Delta_0 = 0.8$ ,  $\dot{\Delta}_0 = 0.0$ ,  $M = 125$ ,  $L = 5$  and  $\Omega = 5.2$ )

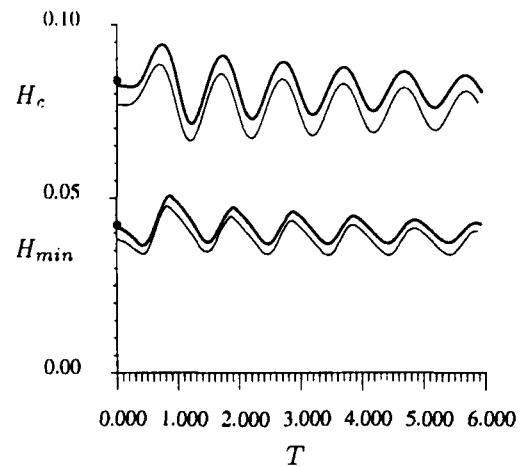


Figure 7.  $H_c$  and  $H_{min}$  as a function of  $T$  on mesh  $dX = dT = 0.0625$  (thin line) and  $dX = dT = 0.0313$  (thick line). ( $\Delta_0 = 0.8$ ,  $\dot{\Delta}_0 = 0.0$ ,  $M = 125$ ,  $L = 5$  and  $\Omega = 5.2$ )

means of  $\Delta_\infty$ . Its value equals 0.922, 0.917 and 0.916 on grid  $2h$ ,  $h$  and  $h/2$ , respectively. Thus, on grid  $h$ ,  $\Delta_\infty$  is accurate within approximately 1%.

Next, we consider the discretisation error in time. Fig. 6 shows  $\Delta$  as a function of  $T$ , solved on grid  $h$  and  $2h$ . Comparing these results shows that the discretisation error in the transient result manifests itself in two ways. Firstly, the initial deviation from the equilibrium position is slightly larger for the coarse mesh and secondly the solution converges to an equilibrium position which is also slightly larger for the coarse mesh. Note that both effects are related to the spatial accuracy. Also the rate of decline of the amplitude of oscillation with  $T$  is approximately the same for both solutions. Hence, the incremental discretisation error must be small compared to the discretisation error in space (negligible artificial damping) and the Sec. 4.2.2 result is estimated to be accurate up to 2%.

Alternatively, we can check the accuracy of the solution by means of the central,  $H_c$ , and minimum film thickness,  $H_{min}$ , see Fig. 7. The initial central film thickness equals 0.0769 and 0.0812 on grid  $2h$  and  $h$ , respectively. On grid  $h/2$ , used in

the steady state calculations,  $H_c(T = 0) = 0.0839$  and is indicated by a dot in Fig. 7. On grid  $h$ ,  $H_c$  is thus solved within approximately 4%. The initial minimum film thickness is equal to 0.0386, 0.0416 and 0.0424 on grid  $2h$ ,  $h$  and  $h/2$ , indicating an error of approximately 2% in the grid  $h$  results. Throughout time, it is observed that the difference between the film thickness on both grids remains approximately constant. This indicates that the time incremental error in  $H$  is less than the spatial discretisation error and is at most  $O(dT^3)$ . Hence the accuracy of  $H$  at a given time is indeed  $O(dT^2) = O(dX^2)$ .

## 6. Discussion and Conclusion

A Hertzian contact model incorporating inertia effects for the rolling element has been presented. Choosing appropriate scales, the model reduces to a non-parameter problem where the dimensionless mutual approach of the rolling element and solid,  $\Delta$ , is a function of the dimensionless time  $T$  only. The Hertzian model is conservative, i.e. the total energy remains constant and its value determines the amplitude of the oscillation. Two analytical solutions have been obtained, showing that the period of oscillation is



approximately constant, i.e. independent of the amplitude.

The model has been extended to a lubricated contact. Apart from the known parameters describing the EHL equations, e.g. the Moes parameters  $M$  and  $L$ , the dimensionless natural frequency  $\Omega$ , is sufficient to account for inertia forces of the rolling element.

If  $\Omega \gg 1$ , surface speeds are much less than the speed at which the two bodies approach each other and squeeze motion dominates. E.g. impact elastohydrodynamics is the study of problems where  $\Omega \gg 1$  and the initial condition  $\Delta_0 \leq 0$ . On the other hand, for  $\Omega \ll 1$ , surface speeds are much larger than the squeeze speed. Then, the solution reduces to the steady state solution where  $\Delta$  is constant and is equal to  $\Delta_0$ .

Numerical solutions have been obtained which show that the oscillation is damped by the lubricant. For the values of the parameters considered, the period of oscillation is hardly affected by the lubricant. Although the surfaces are smooth, the oscillation of the rolling element induces film thickness modulations which propagate at a dimensionless speed of unity. The wavelength of the induced modulations roughly equals  $5.2/\Omega$ .

### 7. Appendix A

Linearizing the equation of motion, Eq.(8), around  $\Delta = 1$  yields:

$$\frac{d^2 \Delta}{dT^2} + \frac{3}{2} \Delta = \frac{3}{2}, \tag{29}$$

with initial conditions  $\Delta_0$  and  $\dot{\Delta}_0$ . The solution is:

$$\Delta = 1 + A \cos(\sqrt{3/2} T + \phi), \tag{30}$$

where  $A \ll 1$  for the linearization to be valid.

The solution for  $C = 0$  can be derived by defining  $\Delta = Z^2$  and rewriting Eq.(10):

$$\frac{dZ^2}{dT} + \frac{1}{5} Z^3 - \frac{1}{2} - \frac{C}{2Z^2} = 0. \tag{31}$$

Let  $T = \gamma\tau$ . This gives:

$$\frac{dZ^2}{d\tau} + \frac{\gamma^2 Z^3}{5} - \frac{\gamma^2}{2} - \frac{C\gamma^2}{2Z^2} = 0. \tag{32}$$

For  $C = 0$  and taking  $\gamma^2 = -20$ , the differential equation reduces to:

$$\frac{dZ^2}{d\tau} - 4Z^3 + 10 = 0. \tag{33}$$

This equation is solved by the Weierstrass elliptic function  $\wp(z; g_2, g_3)$  with invariants  $g_2 = 0$  and  $g_3 = 10$ , see Whittaker and Watson [25], i.e.

$$Z = \wp(\tau + C_2; 0, 10). \tag{34}$$

Note that, with  $T$  real,  $\tau$  and  $C_2$  must be imaginary.  $C_2$  is the second constant of integration and it represents a phase shift. Finally, using one of the properties of homogeneity:  $\wp(\lambda z; \lambda^{-4} g_2, \lambda^{-6} g_3) = \lambda^{-2} \wp(z; g_2, g_3)$  and back-substitution of  $\Delta = Z^2$ , yields:

$$\Delta = 400 \wp(T - i\sqrt{20} C_2; 0, -1/800)^2, \tag{35}$$

where the argument becomes real again.

### 8. Appendix B

The Reynolds' equation has been discretised according to the following second order scheme:

$$\begin{aligned} & (dX)^{-2} (\epsilon_{i+1/2,j,k} (P_{i+1,j,k} - P_{i,j,k}) \\ & \quad - \epsilon_{i-1/2,j,k} (P_{i,j,k} - P_{i-1,j,k})) \\ & + (dY)^{-2} (\epsilon_{i,j+1/2,k} (P_{i,j+1,k} - P_{i,j,k}) \\ & \quad - \epsilon_{i,j-1/2,k} (P_{i,j,k} - P_{i,j-1,k})) \\ & - (dX)^{-1} (1.5\bar{\rho}_{i,j,k} H_{i,j,k} - 2.0\bar{\rho}_{i-1,j,k} H_{i-1,j,k} \\ & \quad + 0.5\bar{\rho}_{i-2,j,k} H_{i-2,j,k}) \\ & - (dT)^{-1} (1.5\bar{\rho}_{i,j,k} H_{i,j,k} - 2.0\bar{\rho}_{i,j,k-1} H_{i,j,k-1} \\ & \quad + 0.5\bar{\rho}_{i,j,k-2} H_{i,j,k-2}) = 0. \end{aligned} \tag{36}$$

$dX$  and  $dY$  are the meshsizes in  $X$ - and  $Y$  direction, respectively.  $i$  and  $j$  are the spatial grid indices whereas  $k$  denotes the time index.  $\epsilon$  is defined according to:

$$\epsilon_{i,j,k} = (\bar{\rho}_{i,j,k} H_{i,j,k}^3) / (\bar{\eta}_{i,j,k} \lambda) \tag{37}$$

The elastic deformation integral is discretised according to:

$$\begin{aligned} H_{i,j,k} = & \Delta_k + X_i/2 + Y_j/2 \\ & + \frac{2}{\pi^2} \sum_{r=1}^{n1} \sum_{s=1}^{n2} K_{irjs} P_{r,s,k}, \end{aligned} \tag{38}$$

where  $K_{irj_s}$  are influence coefficients, see Lubrecht [13].

The equation of motion is discretised according to the Newmark integration scheme. This implicit second order scheme is widely used in transient finite element calculations and its derivation can be found in e.g. [1]. The Newmark scheme is given by:

$$\Delta_{k+1} = \Delta_k + dT \dot{\Delta}_k + \frac{1}{2} dT^2 \left( \frac{1}{2} \ddot{\Delta}_k + \frac{1}{2} \ddot{\Delta}_{k+1} \right) \quad (39)$$

and

$$\dot{\Delta}_{k+1} = \dot{\Delta}_k + dT \left( \frac{1}{2} \ddot{\Delta}_k + \frac{1}{2} \ddot{\Delta}_{k+1} \right). \quad (40)$$

For Eq.(20) the Newmark scheme yields:

$$\Delta_{k+1} + E \frac{3}{2\pi} dXdY \sum_{i=1}^{n1} \sum_{j=1}^{n2} P_{i,j,k+1} = F, \quad (41)$$

where

$$E = \frac{1}{4} \Omega^2 dT^2 \quad \text{and} \quad (42)$$

$$F = \frac{1}{4} \Omega^2 dT^2 + \Delta_k + dT \dot{\Delta}_k + \frac{1}{4} dT^2 \ddot{\Delta}_k, \quad (43)$$

which can be solved by Newton Raphson iteration. Once  $\Delta_{k+1}$  is known,  $\dot{\Delta}_{k+1}$  and  $\ddot{\Delta}_{k+1}$  can be calculated from Eq.(39) and (40).

For the Hertzian contact, Eq.(41) reduces to

$$\Delta_{k+1} + E \Delta_{k+1}^{3/2} = F \quad (44)$$

where

$$E = \frac{1}{4} dT^2 \quad \text{and} \quad (45)$$

$$F = \frac{1}{4} dT^2 + \Delta_k + dT \dot{\Delta}_k + \frac{1}{4} dT^2 \ddot{\Delta}_k, \quad (46)$$

This equation can easily be solved by the Newton Raphson iteration process:

$$\Delta_{k+1,l+1} = \Delta_{k+1,l} - \frac{\Delta_{k+1,l} + E \Delta_{k+1,l}^{3/2} - F}{1 + 3/2 E \Delta_{k+1,l}^{1/2}}, \quad (47)$$

where  $\Delta_{k+1,0} = \Delta_k$ . Numerical tests have shown that, for sufficiently small timesteps, Eq.(47) is solved well below discretisation error within only two or three iterations.

## 9. Acknowledgement

The authors wish to thank Dr. D. Dijkstra and Ir. H. Moes for their valuable contributions in finding the analytical solutions to the Hertzian problem. The authors gratefully acknowledge the support of the SKF Engineering & Research Centre B.V., Nieuwegein, the Netherlands.

## REFERENCES

1. Bathe, K.J., (1982), "Finite element procedures in engineering analysis," Prentice-Hall Inc..
2. Bedewi, M.A., Dowson, D., Taylor, C.M., (1984), "Elastohydrodynamic lubrication of line contacts subjected to time dependent loading with particular reference to roller bearings and cams and followers." *Proc. 12th Leeds Lyon Symposium on Tribology*, 289-303.
3. Christensen, H., (1962), "The oil film in a closing gap," *Proc. R. Soc. London, Series A*, **226**, 312-328.
4. Christensen, H., (1970), "Elastohydrodynamic Theory of Spherical Bodies in Normal Approach," *J. Lubr. Technol. Trans. ASME*, **92(1)**, 145-154.
5. Dowson, D. and Higginson, G.R., (1966), "Elasto-hydrodynamic lubrication, The fundamentals of roller and gear lubrication," Pergamon Press, Oxford, United Kingdom.
6. Dowson, D. and Wang, D., (1995), "Impact elastohydrodynamics," *Proc. 21th Leeds Lyon Symposium on Tribology*, 565-582.
7. Ghosh, M.K., Hamrock, J. and Brewster, D., (1985), "Hydrodynamic Lubrication of Rigid Nonconformal Contacts in Combined Rolling and Normal Motion," *ASME JOT*, **107**, 97-103.
8. Hertz, H., (1881) "On the contact of elastic solids," *J. Reine Angew. Math*, **92**, 156-171.
9. Herrebrugh, K., (1970), "Elastohydrodynamic squeeze films between two cylinders in normal approach," *ASME J. Lub. Techn.*, **92**, 292-302.
10. Johnson, K.L., (1985), "Contact mechanics," Cambridge University Press, ISBN 0-521-25576-7.

11. Larsson, R., and Höglund, E., (1994), "Elastohydrodynamic lubrication at pure squeeze motion," *WEAR*, **179**, 39-43.
12. Larsson, R., (1996), "Elastohydrodynamic Lubrication under Non-Steady Conditions," Doctoral Thesis, Luleå University of Technology, Sweden. ISSN 0348-8373.
13. Lubrecht, A.A., (1987), "The numerical solution of the elastohydrodynamically lubricated line- and point contact problem using multi-grid techniques," PhD. Thesis, University of Twente, Enschede, ISBN 90-9001583-3.
14. Lubrecht, A.A., Ioannides, E., (1989), "A fast solution of the dry contact problem and the associated sub-surface stress field, using multilevel techniques," *ASME JOT*, **113**, 128-133.
15. Lee, R-T., Hamrock, B.J., (1989), "Squeeze and entraining motion in nonconformal line contacts. Part II-Elastohydrodynamic lubrication," *ASME JOT*, **111**, 8-16.
16. Lee, R-T., Cheng, H.S., (1973), "The Pressure and Deformation Profiles Between Two Normally Approaching Lubricated Cylinders," *ASME J. Lub. Techn.*, **95**, 308-317.
17. Newmark, N.M., (1959), "A method of computation for structural dynamics," *A.S.C.E. Journal of Engineering Mechanics Division*, **85**, 76-94.
18. Roelands, C.J.A., (1966). "Correlational aspects of the viscosity- temperature-pressure relationship of lubricating oils." PhD. Thesis, Technische Hogeschool Delft, The Netherlands, (V.R.B., Groningen, The Netherlands.)
19. Venner, C.H., (1991), "Multilevel solution of the EHL line and point contact problems," PhD. Thesis, University of Twente, Enschede, The Netherlands. ISBN 90-9003974-0.
20. Venner, C.H., and Lubrecht, A.A., 1994, "Numerical Simulation of a Transverse Ridge in a Circular EHL Contact, under rolling/sliding", *ASME JOT*, **116**, 751-761.
21. Venner, C.H., and Lubrecht, A.A., 1995, "Numerical Analysis of Influence Waviness on the Film Thickness of a Circular EHL Contact", *ASME JOT*, **118**, 153-161.
22. Vichard, J.P., 1971. "Transient effects in the lubrication of Hertzian contacts", *J. Mech. Eng. Sci.*, **13-3**, 173-189.
23. Yang, P.R., and Wen, S.Z., (1991), "Pure squeeze action in an isothermal elastohydrodynamically lubricated spherical conjunction. Part 1 and 2," *WEAR*, **142**, 1-16, 17-30.
24. Yang, P., Wen, S., 1992, "The behavior of non-Newtonian thermal EHL film in line contacts at dynamic loads", *ASME JOT*, **114**, 81-85.
25. Whittaker, E.T., and Watson, G.N., (1962), "A course of modern analysis," Cambridge University Press, (4<sup>th</sup> edition)

## Direct measurement of boundary lubricating films

V Anghel, P M Cann and H A Spikes

Tribology Section, Imperial College, London SW7 2BX, United Kingdom

Using an advanced form of optical interferometry it is now possible to measure lubricant film thickness in rolling, concentrated contacts down to 1 nm. This enables a direct study of the presence and properties of boundary films in such contacts.

It is shown that a simple hydrocarbon fluid exhibits no boundary effects down to 1 nm and obeys elastohydrodynamic theory down to this thickness. However solutions of long chain surfactants, such as stearic and oleic acid in base fluid form boundary films, typically 2 to 6 nm thick in lubricated contacts. These films appears to be partially viscous and partially solid-like in that a proportion of the film, usually 1 to 2 nm is retained for long periods in the stationary contact. In some cases, these boundary lubricating films are quite thick, up to 20 nm, indicating some degree of multilayer formation. This thick film-forming behaviour is, however, difficult to obtain repeatably and may be highly sensitive to the cleanliness of the rubbing surfaces.

### 1. BACKGROUND

The first deliberate use of additives to improve the boundary lubricating properties of liquid lubricants was reported by Wells and Southcombe in 1920 (1). They showed that the addition of small proportions of long chain carboxylic acids to mineral oils reduced friction and ameliorated seizure tendencies to such an extent that a refined mineral oil attained comparable boundary lubricating properties to a natural animal or vegetable oil.

Wells and Southcombe ascribed this behaviour to a modification of the surface tension of the oil. However this hypothesis was very rapidly superseded by the concept that long chain polar surfactants adsorb on metal surfaces to form close-packed monolayers able to prevent direct contact and adhesion of rubbing solids. In the early 1920s, Hardy demonstrated that the extent of friction reduction produced by surfactant solutions increased with chain length up to a critical number of carbon atoms, above which it remained constant (2). He suggested that the longer the vertically oriented chains, the more effectively the solid surfaces were separated.

It was then shown by Desvaux (3), Langmuir (4) and later by Bowden (5) that single monolayers

of surfactant deposited on surfaces were able to reduce friction coefficient down to values characteristic of those found using surfactant solutions in hydrocarbons. The protection afforded by a single deposited monolayer broke down after a short period of sliding whilst deposited multilayers lasted somewhat longer. From this, the concept was developed of a protective monolayer on each surface which was subject to continuous damage by rubbing but which could be repaired by adsorption from solution. This model was subsequently extended to suggest that adsorbed monolayers are always disrupted to some extent at asperity contacts and that their main role is to limit the extent of junction growth in contacts, thereby reducing the extent of solid-solid adhesion (6). The development of the monolayer model has been illustrated by Adamson (figure 1) and by the 1970s was widely accepted.

Despite the supremacy of the monolayer model outlined above, there were, between 1920 and 1970, a number of advocates of the view that boundary lubrication involves surface films which are much thicker than monolayers. Thus Trillat, in the 1920s, used X-ray diffraction to show that a lubricant could form an organised layer many molecules thick on metal surfaces (8). Work in the 1940s and 1950s, on the normal approach of lubricated flats found that

there remained a residual, separating film, resistant to high load, typically hundreds of nanometers in thickness with surfactant-containing oils but not with pure, non-polar hydrocarbons (9)(10). Other work used a method of displacing lubricant from a steel ball using mercury to show, from capacitance measurements, that a thick, residual surface film on the steel was far more slowly displaced than the bulk fluid (11).

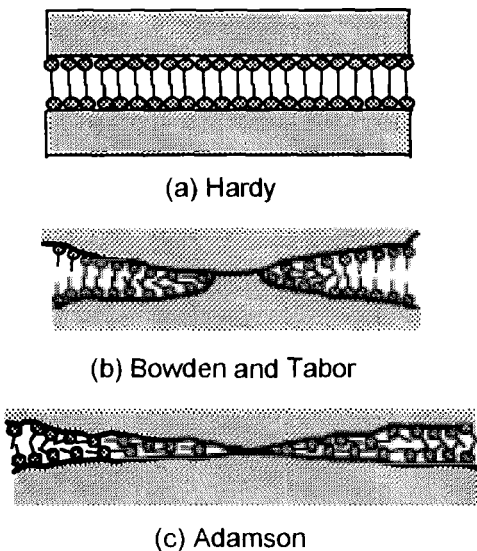


Figure 1. Monolayer adsorption models of boundary lubrication (7)

Thus the exact nature of boundary lubricating films in real, high pressure contacts remains unclear; whether they are monolayer or multilayer films; whether they have essentially solid-like properties or are mobile and viscous like. The controversy has been fully reviewed by Allen and Drauglis (12).

The problem in resolving this issue lies in the indirect and inferential nature of most boundary lubrication studies. Boundary lubricant films are very thin and, when operating, are contained and concealed within two relatively very large, opaque bodies where they cannot be observed directly. This has led to there being two alternative, both somewhat unsatisfactory approaches to studying boundary lubricating films. One is simply to measure friction

properties in real contacts and attempt to deduce the nature and properties of the films from the observed behaviour and its dependence, for example, on surfactant chain length, concentration or temperature. The second is to move away from a real lubricated contacts and to examine the adsorption properties or rheology of near surface films, using techniques such as X-ray diffraction, force balance or infrared adsorption. The problem here is that the films being studied are subject to very different and usually far gentler conditions than those prevailing in real contacts.

The first of these approaches has shown that monolayers can reduce friction to boundary lubrication levels but has not been able to definitely establish whether films present in real contacts are indeed only monolayers. The second has shown that additive solutions can interact with polar solid surfaces to form layers of modified rheology many nanometres thick, but has not been able to establish whether such thick film effects survive or have any relevance in real contact conditions.

The aim of the work, whose first stages are described in this paper, is to apply the technique of ultrathin film interferometry to measure the true thickness and nature of boundary films in lubricated contacts. As the paper will show, the answer is not yet clear-cut and boundary film thickness may depend critically on the history, cleanliness and pre-treatment of the metal surfaces.

## 2. EXPERIMENTAL TECHNIQUE AND MATERIALS

### 2.1 Ultrathin film interferometry

The principle of the ultrathin film interferometric technique is shown in figure 2.

A contact is formed between the flat surface of a glass disc and a reflective steel ball. The glass disc is coated with a thin, semi-reflecting layer of chromium on top of which is a layer of silica about 500 nm thick. White light is shone into the contact and some is reflected from the chromium layer whilst some passes through the spacer layer and any lubricant film present to be reflected from the steel ball. The two beams recombine and interfere and

the spacer layer ensures that interference will occur even if no oil film is present.

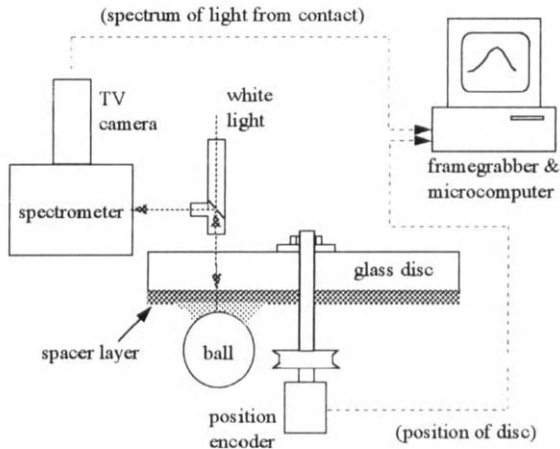


Figure 2. Schematic diagram of ultrathin film method.

The interfered light from a strip across the contact is then passed into a spectrometer where it is dispersed and detected by a solid state black and white TV camera. A frame grabber is used to capture this image at a preselected moment and a microcomputer program determines the wavelength of maximum constructive interference in the central region of the contact. The lubricant film thickness is then calculated from the difference between the measured film thickness and the thickness of the silica spacer layer at that position (13). Accurate determination of film thickness, particularly in the thin film region, requires a number of careful corrections to be made including allowance for the non-linearity of response of the system to wavelength and the variation of refractive index of lubricant and spacer layer with wavelength.

In each test, the silica spacer layer thickness is initially recorded using an angular encoder, at a series of set positions around the disc using a dry contact. Lubricant is then applied and a series of film thickness measurements are made at different rolling speeds. In doing this, the position encoder is used to ensure that interference images are detected and grabbed from these same positions where the spacer layer thickness has already been determined.

The test rig used is shown in figure 3. Both ball and disc can be independently driven but in the work described here the disc was rotated and itself drove the ball in nominally pure rolling. The studies described here all employed commercial, 19 mm diameter, AISI 52100 steel balls of root mean square surface roughness 11 nm and were made at a load of 20 N which corresponds to a maximum contact pressure of 0.52 GPa. Under these conditions the central part of the contact experiences about  $2 \mu\text{m}$  of elastic flattening and forms a circular contact of between 250 and 270  $\mu\text{m}$  diameter.

The whole contact is contained in a temperature-controlled chamber and in this work the temperature was maintained at  $25^\circ\text{C} \pm 0.5^\circ\text{C}$ . The quantity of lubricant used was typically  $3 \text{ cm}^3$  per test. This was applied to the ball at the beginning of the test. After lubricant application, some tests were started immediately but more commonly, ball and disc were held stationary at the set temperature for a fixed "presoak" period before motion was begun. This was to investigate the existence of any time-dependent adsorption effects.

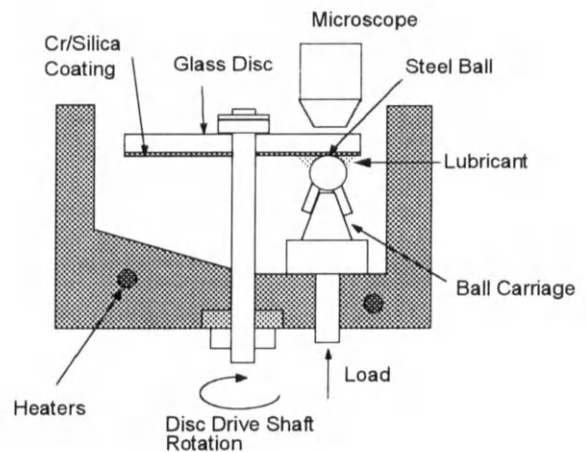


Figure 3: Test rig for film thickness measurements.

## 2.2 Steel ball cleaning technique

As will be indicated in the results, the thickness of film formed appears to be very dependent upon the cleaning technique used. In this study, the ball support and glass disc were heated in

boiling analar toluene for about 30 minutes. They were then cooled to about 80°C, removed from the toluene and rinsed with analar acetone.

Two different techniques were used for cleaning the ball. In one the steel ball was boiled in toluene and then rinsed in acetone in a similar fashion to the glass disc. In the second, the ball was Soxhletted in analar chloroform for one hour and then rinsed in analar propan-2-ol (isopropanol) before being dried in an oven at 60°C for ten minutes.

### 2.3 Materials Used

In all work the lubricant base fluid used was hexadecane. This was purified by mixing with activated alumina and silica gel and was filtered prior to use.

The boundary lubricant additives employed were hexadecanoic (palmitic) acid, octadecanoic (stearic) acid and oleic acid. The stearic acid and oleic acid were 99+ grade and was used as received. The palmitic acid was recrystallised from ethanol.

## 3. FILM THICKNESS OF HEXADECANE

Figure 4 shows a plot of log(film thickness) versus log(rolling speed) for purified hexadecane. Four sets of results are included to indicate the level of repeatability.

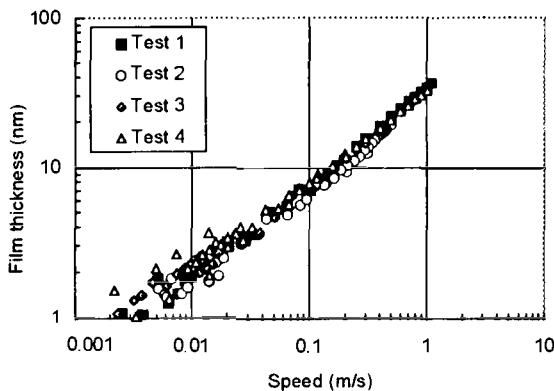


Figure 4. Film thickness/speed plot for hexadecane at 25°C

According to elastohydrodynamic theory, central film thickness,  $h_c$  is given by (14):

$$h_c \approx k(U\eta)^{0.67} \alpha^{0.53} \quad (1)$$

where  $U$  is the mean rolling speed  $(U_1+U_2)/2$ ,  $\eta$  is the dynamic viscosity of the lubricant in the inlet at atmospheric pressure and  $\alpha$  is the pressure viscosity coefficient of the lubricant  $(d\ln\eta/dp)$ . Thus a log/log plot should be a straight line of gradient about 0.67. Since figure 4 forms a straight line plot close to this gradient and is linear down to 1 nm, this suggests that hexadecane obeys EHD theory down to this thickness. It is important to note that EHD film thickness is determined not by the viscosity of the lubricant within the contact itself but by the viscosity of the fluid in the immediate contact inlet, where the film gap reduces from about  $2h_c$  to  $h_c$  at the inlet edge (15). Thus the fact that equation 1 is obeyed down to 1 nm thickness for hexadecane indicates that its viscosity remains at the bulk value within 2 nm of the surfaces. Previous work has shown similar behaviour for other saturated hydrocarbon fluids (15).

## 4. FILM THICKNESS OF SURFACTANT SOLUTIONS

Figure 5 shows results of two tests using 0.1% wt. palmitic acid in hexadecane with the toluene/acetone cleaning method described above. The behaviour of hexadecane is shown by a solid line. Two sets of data points are included for each test. One shows how film thickness varies as speed is steadily increased (fwd) in the first half of a test whilst the second shows the response of film thickness to the speed being subsequently decreased (back). It can be seen that both tests give quite similar, thick boundary films of about 15 nm thickness at slow speed. In the second stage of each test, this boundary film thickness is somewhat reduced to between 4 and 8 nm. At high speeds, the film thickness follows the classical Dowson and Hamrock relationship with a  $\log(\text{film thickness})/\log(\text{speed})$  gradient of about 0.7. Interestingly, the film thickness at high speeds

appears to be rather lower than that formed by hexadecane.

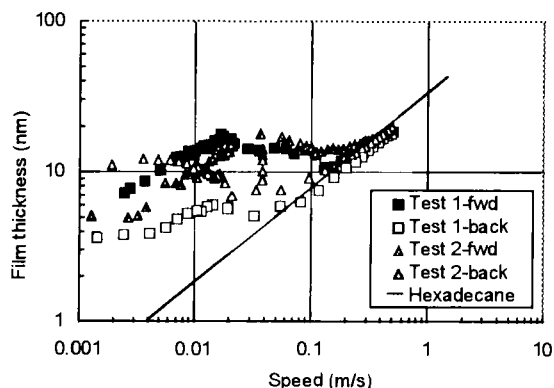


Figure 5. Film thickness/speed plot for 0.1% wt. palmitic acid at 25°C

Figure 6 shows similar results for stearic acid in hexadecane at two concentrations. The behaviour is broadly similar to that for 0.1% wt. palmitic acid although the boundary film thickness is considerably less, at 7 to 10 nm. There appears to be no significant concentration effect.

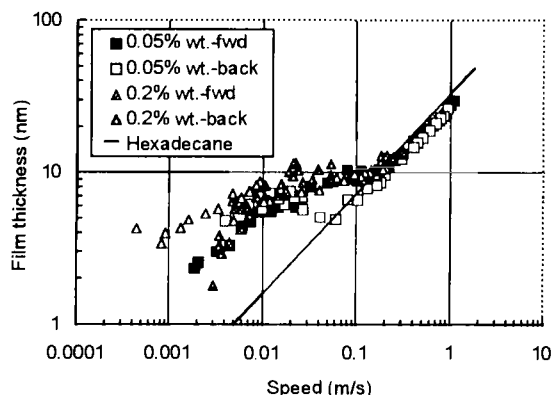


Figure 6. Film thickness/speed plots for stearic acid solutions at 25°C.

A large number of tests have been carried out. Whilst many show the thick boundary film behaviour exemplified in figure 5 and 6, in others a

thinner boundary film, only about 2 nm thick, formed initially although sometimes a thicker film was evident in the second stage of the test. Pre-soaking the ball in the additive solution did not appear to influence film formation.

In an attempt to reduce scatter, the second, the more rigorous cleaning procedure involving chloroform and isopropanol outlined above was adopted. This had the effect of increasing the proportion of tests in which a thick film formed but did not entirely remove the variation. Figure 7 shows a test in which the normal film measurement procedure was deliberately extended. The normal test procedure was first carried out, measuring film thickness as the speed was raised and then lowered. Then the whole measurement procedure was repeated. It can be seen that there is a time effect; the boundary film is initially about 2 nm but increases during running to about 8 to 10 nm.

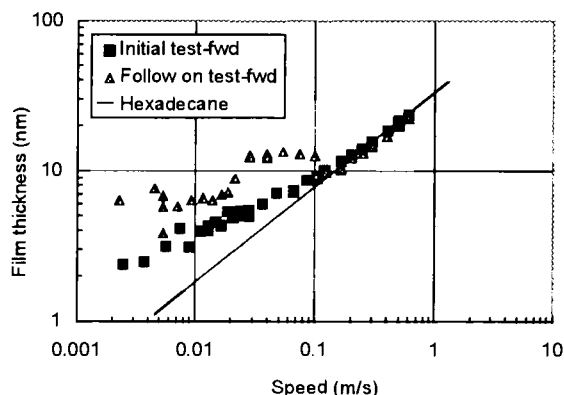


Figure 7. Two stage film thickness/speed results for palmitic acid solution at 25°C (chloroform/isopropanol cleaning)

This time effect was explored further. Figure 8 shows results from an extended test using a 0.1% wt. solution of oleic acid and employing the toluene/acetone cleaning procedure. Three successive sets of film thickness measurements were made, each separated by a one hour period during which the ball was rolled against the disc at 0.1 m/s. The first two stages show no measurable film formation and, indeed, a thinner film than for



hexadecane. This is probably due to some removal of spacer layer. By the third stage, however, a boundary film about 6-8 nm in thickness has clearly formed.

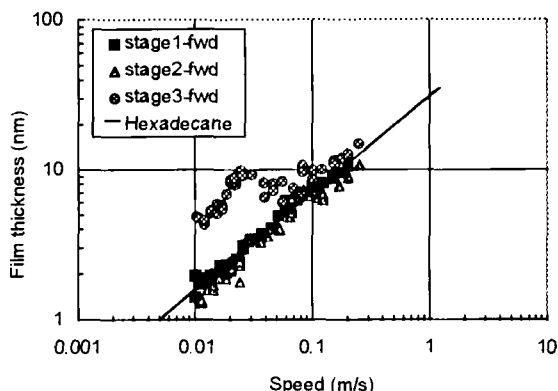


Figure 8. Three stage film thickness/speed results for oleic acid solution at 25°C (chloroform/isopropanol cleaning)

## 5. DISCUSSION

It is important to note at the outset that the base fluid, purified hexadecane, exhibits classical EHD behaviour down to about 1-2 nm, indicating that it gives no anomalous rheological behaviour or boundary film down to this thickness. This makes it possible to interpret effects seen with additive solutions as resulting from the surface behaviour of the additive molecules themselves; i.e. as boundary film effects.

The results using surfactant solutions so far carried out show considerable scatter, with behaviour varying between alternative two modes of behaviour, thick film formation and thin film formation.

### 5.1 Thick Boundary Films

There is clear evidence that in some conditions, long chain carboxylic acids form quite thick films, up to and even in excess of 10 nm thickness. Such a value implies many equivalent

monolayers since the surfactants used in this study have chain lengths of between 2 and 2.5 nm when fully aligned. These boundary films appear to become thinner at very slow speeds and are also partially lost on halting the rolling motion. This type of behaviour has previously been seen with polar polymer solutions and is believed to indicate the presence of a surface film of enhanced viscosity (16). It is not yet known whether these thick films represent ordered multilayers or a more disordered, paste-like material.

As the speed is raised, these films often exhibit some instability, reflected in very variable and often decreasing film thickness in the intermediate speed range of about 0.1 m/s. At high speeds the influence of thick boundary films on overall film thickness appears minimal and, indeed, the film thickness observed is often less than that of pure hexadecane. This may result from some EHD starvation at high speeds. It was observed that the rubbed track of the ball out of contact often appeared dry even though the contact was surrounded by a meniscus of oil at all times. This is likely to result from the formation of oleophobic layers on the surfaces. It has previously been noted that highly organised surfactant layers on solid surfaces can render the surfaces non-wetting by solvents (17).

The boundary films formed by palmitic acid were consistently higher than those formed with stearic acid. This may possibly be related to a "chain matching" effect since palmitic acid and hexadecane have the same number of carbon atoms (18).

### 5.2 Thin Boundary Films

When no thick boundary film was initially formed, a much thinner boundary film of about 2 nm was often seen. This is approximately equivalent to one vertically oriented monolayer and may indicate the presence of approximately monomolecular films in accord with the conventional boundary lubrication model. This film was generally found to remain in the contact after halting, suggesting that it was a more immobile or "solid like" film than the thick film.

### 5.3 Variability of Film Formation

Thus far the study has not been able to obtain fully repeatable results. This precludes, so far, the possibility of quantitative interpretation but it does clearly show that two alternative modes of behaviour can take place. It also sheds some light on the long-standing controversy in the literature over the thickness of boundary films. Nominally very similar test conditions may result in either monomolecular or considerably thicker films.

From the results carried out so far it appears that the extent of thick film formation is determined by a coupling of cleaning method and running time. As the rigour of the cleaning technique used is increased, it becomes more likely that a thick boundary film will form rapidly. However, even with a less rigorous cleaning, extended rolling will eventually form a thick film.

Boundary lubrication studies are notoriously sensitive to the influence of surface cleaning and contamination and many different cleaning procedures have been described in the literature. These all tend to be based on one or two solvent cleaning stages, often followed by a mechanical cleaning process such as fine polishing or ionic bombardment. The former is designed to remove adsorbed or reacted oily molecular species, including any preservative oil present on the metallic surfaces. The latter presumably has the effect of abrading any solvent-irremovable film and possibly also any residues left from the evaporating solvent itself. With an already highly polished ball it is quite difficult to carry out a final mechanical cleaning procedure. It is thus quite likely that the ball surface remains partially contaminated even after solvent cleaning. Such contamination would need to be only a fraction of a monolayer thick to disrupt the formation of a complete adsorbed surfactant layer.

Two possible hypothesis are advanced to explain the observed variation of thick film formation with cleaning and time. One is that the formation of multilayers and thus thick boundary films is critically contingent on the initial formation of a coherent monolayer to provide the template for further layer formation. Only when a regular and even monolayer is formed can further layers develop. Thus thick boundary film formation will be

especially sensitive to surface cleanliness and it is possible that extended rolling helps to form the crucial single monolayer by conditioning the surfaces. Alternatively it is possible that, whilst monolayers can be formed by direct adsorption of surfactant monolayers, multilayers can only be formed by carboxylic acid salts or soaps. In this case, cleanliness might determine the accessibility of metallic oxides for reaction with surfactant and extended running might promote the formation of insoluble soaps on the surfaces.

Clearly further work must be carried out to investigate the influence of cleaning and other experimental factors on thin versus thick boundary film formation and this is currently being undertaken.

## 6. CONCLUSIONS

Using ultrathin film interferometry it is now possible to measure lubricant film thickness in concentrated, rolling contact down to about 1 nm. This shows that purified hexadecane continues to show conventional EHD behaviour down to below 2 nm, with no evidence of anomalous rheological behaviour.

Long chain surfactant solutions in hexadecane show very variable boundary film behaviour and this is believed to represent subtle variations of the ball and disc cleaning procedure and also subsequent running time. Some tests show clear evidence of the formation of quite thick boundary films, up to 15 nm thickness. These films are equivalent to several monolayers of surfactant. The films appear to behave in a partially viscous fashion in that film thickness falls at very slow speed. In an alternative mode of behaviour, other tests show the presence of boundary films of the order of 2 nm thickness, which is equivalent to about one vertically oriented surfactant molecular layer. The presence of these two alternative types of behaviour in tests carried out under nominally identical conditions may help explain the thin versus thick boundary film controversy present in the literature.

## 7. ACKNOWLEDGEMENTS

The authors wish to thank both EPSRC and Exxon Chemicals for kindly supporting this work.

## REFERENCES

1. Wells, H.M. and Southcombe, J.E., "The Theory and Practice of Lubrication: The 'Germ' Process." *J. Soc. of Chem. Ind.* **39**, pp. 51T-60T, (1920).
2. Hardy, H.B. and Doubleday, I., "Boundary Lubrication, - The Paraffin Series" *Proc. Roy. Soc. Lond.* **A100**, pp. 550-757, (1922).
3. Desvaux, H., "Le Frottement des Solides: Epaisseur Minimum d'un Enduit Lubrifiant", *J. de Phys. et la Radium*, **5**, p. 845 (1924).
4. Langmuir, I., "The Mechanism of the Surface Phenomena of Flotation", *Trans. Farad. Soc.* **15**, pp. 62-74, (1920).
5. Bowden, F.P. and Leben, L., "The Friction of Lubricated Metals", *Phil. Trans. Roy. Soc.* **A239**, pp. 1-27, (1940).
6. *The Friction and Lubrication of Solids, Part II, Chapter IV*, F.P. Bowden and D. Tabor, publ. Clarendon Press, Oxford, 1964.
7. *Physical Chemistry of Surfaces. IX-7B*. A. W. Adamson. 2nd Edition, publ. J. Wiley & Sons, 1967.
8. Trillat, J.J., "The Adsorption of Oils in Relation to Lubrication", *I. Mech. E. Proceedings of the General Discussion on Lubrication and Lubricants* **2**, pp. 55-59, (1937).
9. Needs, S.J., "Boundary Film Investigations", *Trans. ASME* **62**, pp. 331-339, (1940).
10. Fuks, G.I., "The Properties of Solutions of Organic Acids in Liquid Hydrocarbons at Solid Surfaces", in "Research in Surface Forces", Vol 1, 1960, ed. B.V. Deryaguin, Transl. by Consultants Bureau, NY, 1964.
11. Smith, A.J. and Cameron, A., "Rigid Surface Films." *Proc. Roy. Soc. Lond.* **A328**, pp. 541-560, (1972).
12. Allen, C. M. and Drauglis, E., "Boundary Layer Lubrication: Monolayer or Multilayer", *Wear* **14**, pp. 363-384 (1969).
13. Johnston, G.J., Wayte, R. and Spikes, H.A., "The Measurement and Study of Very Thin Lubricant Films in Concentrated Contacts", *Trib. Trans.* **34**, pp. 187-194, (1991).
14. *Ball Bearing Lubrication: the Elastohydrodynamics of Elliptical Contacts*, B T Hamrock and D Dowson, publ. J Wiley, New York, 1981.
15. Guangteng, G. and Spikes, H.A., "Boundary Film Formation by Lubricant Base Fluids", *Trib. Trans.* **39**, pp. 448-454, (1996).
16. Smeeth, M., Gonsel, S. and Spikes, H.A. "The Formation of Viscous Surface Films by Polymer Solutions: Boundary or Elastohydrodynamic Lubrication". *Trib. Trans.* **39**, pp. 720-725, (1996).
17. Bigelow, W.C., Glass, E. and Zisman, W.A. "Oleophobic Monolayers. II Temperature Effects and Energy of Adsorption", *J. Coll. Sci.* **2**, pp. 563-591, (1947).
18. Hirano, F., Sakai, T., Kuwano, N. and Ohno, N. "Chain Matching Between Hydrocarbon and Fatty Acid as Interfacial Phenomena", *Tribology Int.* **20**, pp. 186-204, (1987).

## Performance of Environmentally Adapted Hydraulic Fluids at Boundary Lubrication

JENS RIEGLERT and ELISABET KASSFELDT  
Luleå University of Technology  
Division of Machine Elements  
Luleå, S-971 87, Sweden

### Abstract

The lubricating performance of environmentally adapted hydraulic fluids in boundary lubrication situations has been examined and compared to that of a conventional mineral oil based hydraulic fluid.

The oils tested were all fully formulated hydraulic oils with the same ISO viscosity grade. Oil A was a conventional mineral oil whilst oil's B and C were mixtures of rape seed and synthetic ester oils; oil C containing a significantly higher amount of synthetic ester than oil B. Oil D was a pure synthetic ester based hydraulic fluid.

The ability of the test oils to reduce friction and wear was investigated in a Plint and Partner High Frequency Friction Machine (TE 77B). In all the tests the contact geometry was of the cylinder-plate type and the contact surfaces were of roller bearing steel. The sliding friction force was measured at different oscillating sliding speeds, contact pressures and temperatures. The wear tests were performed at constant load, speed and temperature.

Multifactor analysis showed that the main factors affecting the coefficient of friction at the contact were oil type, temperature, sliding speed and load. The coefficient of friction decreased with increasing sliding speed and load and increased with increasing temperature. The environmentally adapted hydraulic fluids were seen to give lower friction compared to the conventional mineral oil based hydraulic fluid.

Further analysis of variance showed that combined interaction effects exists, but at much lower order of magnitude than the main effects.

A comparison between friction measurements in elasto-hydrodynamic lubrication and boundary lubrication showed that the environmentally adapted hydraulic fluids gave lower friction under both lubricating conditions. This implies low shear stress and minimal temperature rise in concentrated contacts, which increase life of both hydraulic equipment and fluid.

The wear tests indicated that the environmentally adapted hydraulic fluids resulted in higher wear rate than the mineral oil based hydraulic fluid. This is thought to be a result of the competition between the polar molecules of the environmentally adapted base oils and the anti-wear (AW) and extreme pressure (EP) additives, in covering metal surfaces. The superior lubricity of the environmentally adapted hydraulic fluids seems not to be sufficient to replace the use of AW and/or EP additives in a fully formulated product. When choosing EP or AW additives for a non mineral oil based product, the interference between base oil molecules and additive molecules must be considered.

### 1. Introduction

Environmental awareness has increased in recent years and the fact that the environment can't cope with the pollution rate that exists today has forced the petroleum industries to produce so called environmentally adapted lubricants. Mobile hydrau-

lic systems in the forest industry contains a large quantity (app. 400 litres) of hydraulic fluid. These machines are used in environmentally sensitive forests where leakage caused by a broken hydraulic hose could cause severe damage. For this reason it is necessary to substitute mineral oils with environmentally adapted oils.

The main task of a hydraulic fluid is to transfer energy from the pump to a "consumer" such as an actuator or motor. The most critical component in a hydraulic system is the pump. In mobile hydraulic systems much effort has been aimed at reducing the weight of components and flow rates of hydraulic oil. To reduce an actuators weight and the flow rate, the piston area has to be minimised whilst, in order to maintain the actuators load capacity, the system pressure has to be increased. The result of these changes are higher system temperatures and pump requirements. The hydraulic fluid must be able to reduce wear and friction at high temperatures in pumps that are at the limits of their capabilities.

The aim of this paper is to compare the performance of three environmentally adapted hydraulic fluid with a conventional mineral oil based hydraulic fluid in boundary lubrication conditions. Boundary lubrication was selected for investigation because it is the dominant lubrication regime in highly loaded hydraulic pumps. Boundary lubrication performance is mainly characterised by the fluids ability to reduce friction and wear in contacts where sliding surfaces are not fully separated by a fluid film. In these contacts the asperities come into contact with each other and micro welding, seizure and wear can occur.

## 2. Experimental Method

The tests described in this paper were performed using a Plint and Partner High Frequency Friction Machine (TE 77B). In all tests the contact geometry was of cylinder-plate type and the contact surfaces of roller bearing steel. The main parts of the equipment are shown in Figure 1.

### 2.1 Friction measurements

Measurements were made with the contact area flooded with oil and the oil bath held at constant temperature, with a maximum error of  $\pm 0.5^\circ\text{C}$ . In order to increase repeatability, all friction measurements were performed with new cylinder surfaces and a plate that had been run in. The friction machine moves the steel cylinder in a sinusoidal motion relative to the plate, with a amplitude of 2.5 mm. The cylinder-plate geometry was created by using the flat end of the larger roller as the plate and the smaller roller as cylinder. (See Figure 1.) The steel cylinder and plate were standard bearing rollers of hardness Vickers 850.

In the friction tests the load was varied between 40-80 N, in five steps. This corresponds to a maximum pressure according to Hertz of ca. 350 to 500 MPa. The maximum relative sliding speed was varied in five steps from 0.08 to 0.3 m/s. The temperature in the oil bath was varied in three steps between 40 and  $80^\circ\text{C}$ .

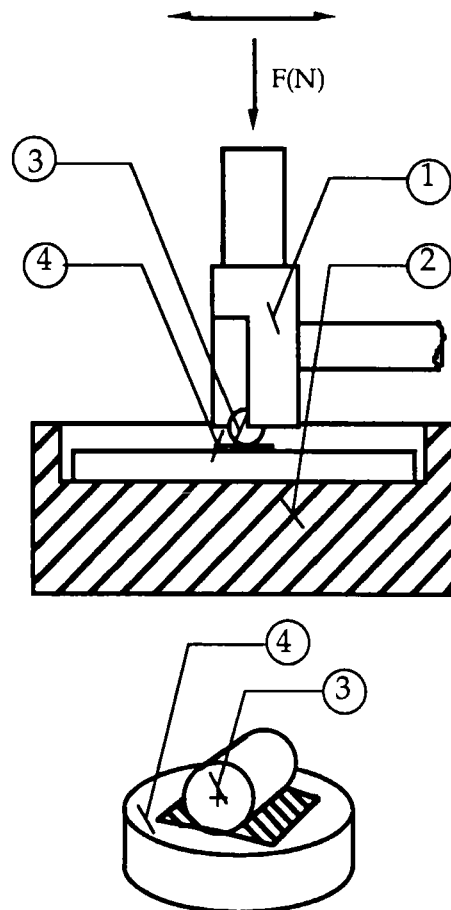


Figure 1. Moving plint (1) with upper specimen (3) and oil bath (2) with fixed specimen (4).

### 2.2 Wear measurements

Because of the short duration of the friction measurements, there are very little wear. In order to create a significant wear scar, the tested tribo contact was run at a higher load than used in the friction measurements for 22 hours. The wear scar on the cylinder from each oil test was measured and the removed material volume calculated.

In the wear tests the temperature was held at  $80^\circ\text{C}$ , the maximum relative sliding speed was 0.08 m/s and the normal load 200 N. The normal load in the

wear tests corresponds to a 780 MPa maximum pressure according to Hertz. This pressure is only present in the beginning of the wear test due to the growing wear scar.

### 2.3 Tested oils

The tested oils were all hydraulic oils within the same ISO viscosity grade. These oils are fully formulated and three of them are put out on the market as environmentally adapted hydraulic fluids and one is a conventional mineral oil based hydraulic fluid. Oil data from the manufacturer and data from earlier research are presented in table 1 and 2.

### 2.4 Lubricating film thickness

The minimum lubricating film thickness ( $h_{min}$ ) was calculated for the line contact between cylinder and

plate using the theory of elasto-hydrodynamic lubrication in rectangular contacts. Houpert and Hamrock (1986).

The minimum lubricating film thickness is given by:

$$h_{min} = 1.714(E')^{0.002} (w'_z)^{-0.128} (\eta_0 \bar{u})^{0.694} \xi^{0.568} R_x^{0.434}$$

Due to the sinusoidal motion of the plint, the relative velocity between cylinder and plate will reach it's maximum at the midpoint of travel. Any possible full film lubrication is thus only likely to be present during a limited part of the total stroke.

Table 1  
Physical Data for tested hydraulic oils.

|  | A       | B                          | C                          | D               |
|--|---------|----------------------------|----------------------------|-----------------|
| Base oil. <sup>1</sup>   | Mineral | Rape seed and synth. ester | Rape seed and synth. ester | Synthetic ester |
| Viscosity 40°C [mm <sup>2</sup> /s]. <sup>1</sup> .                                | 44.8    | 37.7                       | 47.9                       | 46.7            |
| Viscosity 100°C [mm <sup>2</sup> /s]. <sup>1</sup> .                               | 11.68   | 8.90                       | 10.70                      | 9.30            |
| Viscosity index  | 268     | 228                        | 222                        | 187             |
| Limiting shear strength proportionality constant ( $\gamma$ ) 40°C. <sup>2</sup> . | 0.054   | 0.038                      | 0.038                      | 0.039           |
| Limiting shear strength proportionality constant ( $\gamma$ ) 80°C. <sup>2</sup> . | 0.053   | 0.036                      | 0.037                      | 0.038           |
| EP, AW additives. <sup>1</sup> .   | ZDDP    | S, P <sup>3</sup> .        | TPPT                       | P <sup>3</sup>  |

Table 2  
Chemical analysis for tested hydraulic oils. <sup>1</sup>.

|          | A    | B    | C   | D   |
|----------|------|------|-----|-----|
| S [ppm]  | 1525 | 1500 | 338 | 0   |
| P [ppm]  | 414  | 714  | 385 | 233 |
| Ca [ppm] | 100  | 26   | 18  | 11  |
| Zn [ppm] | 545  | 28   | 26  | 19  |

<sup>1</sup> Data from manufacturer.

<sup>2</sup> Data from Kassfeldt et al. (1996).

<sup>3</sup> The EP, AW additives exact formula and proportions are not known.

The relative velocity as a function of time is derived as:

$$\dot{X} = \frac{2\pi f L}{\bar{u}} \cos(2\pi f t)$$

$\bar{u} = V_{max}$  = maximum relative sliding speed

In order to determine the state of lubrication, the dimensionless film parameter was calculated.

$$\Lambda = \frac{h_{min}}{\sqrt{R_{q,a}^2 + R_{q,b}^2}}$$

$R_{q,a}$  = rms surface finish of surface a

$R_{q,b}$  = rms surface finish of surface b

The four regimes of lubrication corresponds to the following film parameter intervals.

- Hydrodynamic lubrication,  $5 \leq \Lambda < 100$
- Elastohydrodynamic lubrication,  $3 \leq \Lambda < 10$
- Partial lubrication,  $1 \leq \Lambda < 5$
- Boundary lubrication,  $\Lambda < 1$

The film parameter was calculated for all oils at every combination of speed, temperature and load. The calculations show that the film parameter never reaches more than about 0.9 for the lowest temperature and load at the highest speed and thus boundary lubrication is the dominant lubrication regime in all friction measurements made in this paper. At the highest load and temperature and lowest speed, the film parameter was about 0.1.

### 3. Friction measurement results

A multifactor analysis of variances shows that the main factors affecting the coefficient of friction are oil type, temperature, sliding speed and load. The coefficient of friction decreases with increasing sliding speed and load, and increases with increasing temperature.

The oil type effect shows that the environmentally adapted hydraulic fluids give less friction compared to the conventional mineral oil based hydraulic fluid. This behaviour is consequent for all temperatures speeds and loads.

Figure 2. shows the 99% confidence intervals of mean coefficients of friction for each oil. Oil A clearly gave the highest friction coefficient whilst oil C gave slightly higher friction than oil B.

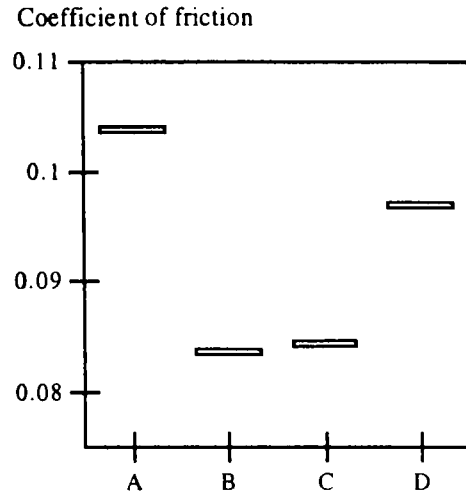


Figure 2. 99% confidence intervals of friction coefficients for respective oil.

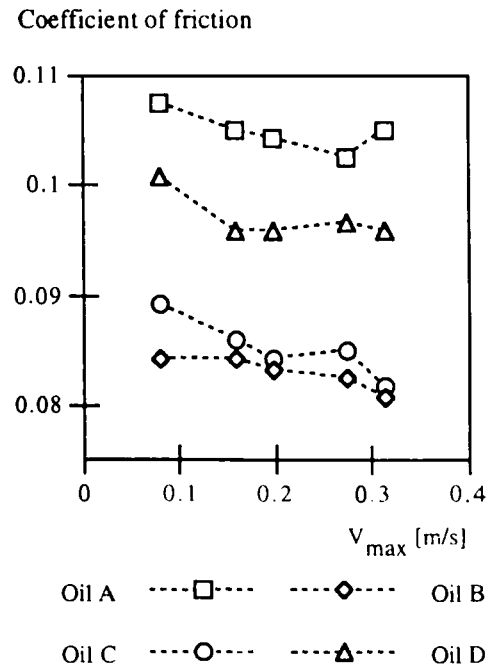


Figure 3. Coefficient of friction vs. maximum sliding speed.

Figure 3 shows the environmentally adapted hydraulic fluids superior ability to reduce friction at 60°C and 430 MPa maximum Hertzian pressure.

The friction behaviour when changing load and sliding speed is shown in Figure 4; the coefficient

of friction increasing with increasing temperature. The coefficient of friction decreases with increasing load and speed. It can also be seen from Figure 4 that oil D shows the lowest speed and load dependency.

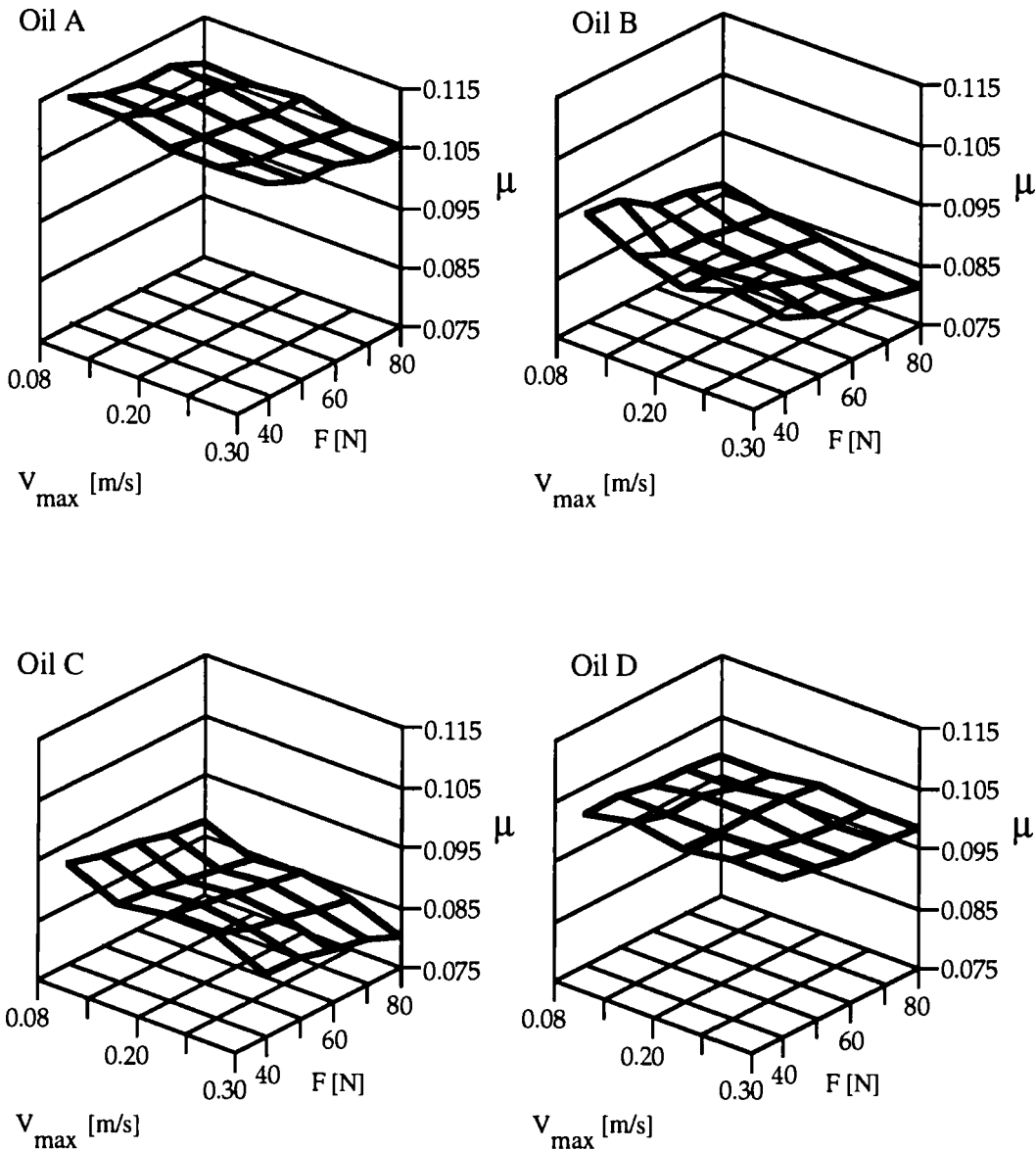


Figure 4. Friction behaviour at 80°C.



#### 4. Wear measurement results

The results from the wear tests show that the environmentally adapted oils give approximately 3-6 times greater wear volume than the conventional mineral oil.

The coefficient of friction was measured during the wear tests. These measurements showed that the mineral oil resulted in higher coefficient of friction but lower wear rate compared to the environmentally adapted oils.

#### 5. Discussion

Synthetic esters have good built in boundary lubrication properties under mild wear conditions. The long polar molecules of the synthetic ester base oil adhere to surfaces by adsorption. These anti-wear molecules are not very powerful because they tend to be sheared off under more severe wear conditions and are disadsorbed when the surface temperature rises much over 100°C. Mortier et al. p 273 (1994).

In a fully formulated hydraulic oil, the polar ester groups will compete with anti-wear additives in covering the metal surfaces. If the ester groups are too polar, they, and not the anti-wear additives, will preferentially cover the metal surfaces. This can lead to an increase in wear rate because of the polar ester groups low anti-wear efficiency under severe wear conditions. Van der Waal (1985).

Rape seed base oils contain long polar molecules and therefore have good built in boundary lubrication properties. The polar molecules in the rape seed oil function in the same way as the polar ester groups and can thus interfere with anti-wear additives.

Data from additive manufacturers show that TPPT, which is the anti-wear additive in oil C, shows better anti-wear performance than ZDDP when used in a mineral oil. This implies that the base oil characteristics can interfere with the additive performance, as suggested by Van der Waal.

The interference of the polar molecules with the anti-wear additive can be an explanation for the poor anti-wear results that oil B, C and D gave in the tests presented in this paper.

The wear tests carried out showed that the AW properties of the environmentally adapted hydraulic fluids are not comparable to a standard mineral oil with AW and EP additives such as ZDDP.

Pure base oils of rape seed and/or synthetic esters gives better AW results compared to pure mineral oil, as shown by Kabuya et al. (1995). These results are, however, not applicable to fully formulated products with AW and EP additives due to the interference of the polar ester and rape seed oil molecules with these additives.

A comparison with friction measurements at elasto-hydrodynamic lubrication, Kassfeldt et al. (1996), shows that the environmentally adapted hydraulic fluids result in lower friction under both elasto-hydrodynamic and boundary lubrication conditions. This implies low shear stress and low temperature rise in concentrated contacts, which extends life of both hydraulic equipment and fluid.

Experience from field tests shows that hydraulic machinery with environmentally adapted hydraulic fluids has lower system temperatures than equivalent systems filled with conventional hydraulic fluids. This can not be explained solely by the lower friction losses. According to Wits (1989), synthetic esters have a 5-10% higher specific heat capacity compared to mineral oils. This will directly reduce the temperature rise of the oil by a corresponding 5-10%. The thermal conductivity is also higher for the synthetic esters compared to mineral oil, Wits (1989). High thermal conductivity will reduce surface temperatures in concentrated contacts.

## 6. Conclusions

The environmentally adapted hydraulic fluids give lower friction under both elasto-hydrodynamic lubrication and boundary lubrication conditions.

The environmentally adapted oils result in higher wear rates than the mineral oil.

The environmentally adapted hydraulic fluids superior lubricity is not sufficient to replace AW and/or EP additives in a fully formulated product.

When choosing EP or AW additives for a non mineral oil based product, the interference between base oil molecules and additive molecules must be considered.

The environmentally adapted oils ability to reduce friction at mild wear conditions indicates low flash temperatures in concentrated contacts.

## References

- Hamrock B. J. 1994. **Fundamentals of Fluid Film Lubrication**. McGraw -Hill series in mechanical engineering.
- Mortier R.M. and Orzulik S.T. **Chemistry and Technology of Lubricants**. 1994 Blackie Academic and Professional. p 273.
- Van der Waal, G. 1985. **The Relationship Between the Chemical Structure of Ester Base Fluids and their Influence on Elastomer Seals and Wear Characteristics**. J. Syn. Lub. 1(4), 281.
- Kabuya, A. and Bozet, J. L. 1995. **Comparative analysis of the lubricating power between a pure mineral oil and biodegradable oils of the same mean iso grade**. Proc. Leeds-Lyon conf. 1994.
- Kassfeldt, E. and Dave, G. 1996. **Environmentally adapted hydraulic oils**. Presented at Nordtrib 1996, Bergen.
- Witz, JJ. 1989. **Diester Compressor Lubricants in Petroleum and Chemical Plant Service**. J. Syn. Lub. 5, 319.

## Influence of Lubricant Additives on Friction in a Disc Machine

H. Yu and J.B. Medley

Department of Mechanical Engineering  
University of Waterloo, Waterloo, ON N2L 3G1, Canada

The friction behaviour of base stock and formulated lubricating oils under conditions of continuous elastohydrodynamic lubrication (ehl) and micro-ehl were investigated in a side-slip disc machine by varying the surface roughness of the discs. Under micro-ehl conditions, the friction was 2 - 3 times larger than under ehl conditions and the additives produced significant differences in the friction. For ehl, small but distinct and repeatable differences in friction were produced by the additives. These differences permitted the derivation of a limiting shear stress expression as a function of pressure, using an empirical approach suggested in the literature, for each of the lubricants. The friction measured under micro-ehl conditions along with an estimation of the real area of contact allowed an alternative evaluation of the limiting shear stress which agreed quite well with the predictions based on the friction measured under ehl conditions. Thus, it was suggested that friction measurements under ehl conditions could be used to evaluate and explore the influence of additives on the limiting shear stress. Furthermore, a simple model for friction in micro-ehl was developed which was consistent with the results of the present investigation.

### NOMENCLATURE

|                      |   |
|----------------------|---|
| $a$                  | radius of Hertzian contact circle             |
| $A_a, A_r$           | apparent, real area of contact                |
| $d_{avg}, d_{avg}^*$ | average surface, asperity height              |
| $E'$                 | reduced elastic modulus                       |
| $F$                  | load  |
| $F_f$                | friction force                                |
| $h_c$                | central film thickness                        |
| $m$                  | limiting shear stress index number            |
| $n$                  | asperity density                              |
| $p$                  | pressure                                      |
| $R$                  | reduced radius                                |
| $T$                  | lubricant supply temperature                  |
| $u$                  | entrainment velocity                          |
| $z_m, z_m^*$         | dimensionless surface, asperity separation    |
| $\alpha$             | pressure-viscosity coefficient                |
| $\beta$              | average asperity tip radius at separation $z$ |
| $\eta_0$             | viscosity at atmospheric pressure             |
| $\lambda$            | lambda ratio                                  |
| $\mu$                | coefficient of friction                       |
| $\nu$                | kinematic viscosity                           |
| $\rho$               | lubricant density                             |
| $\sigma, \sigma^*$   | std deviation of surface, asperity heights    |
| $\sigma_C$           | composite RMS surface roughness               |
| $\sigma_T, \sigma_B$ | RMS roughness of top, bottom discs            |
| $\tau_L$             | limiting shear stress                         |
| $\phi$               | skew angle                                    |

### 1. INTRODUCTION

Crankcase oils are "graded" according to their viscosity variation with temperature but their "service category" depends on performance in full engine tests which is influenced significantly by the efficacy of their additive packages. One aspect of additive performance is how they accommodate shear. This rheological behaviour influences friction and, in engines, friction is an important part of the overall energy efficiency and is related ultimately to engine wear.

New additives are proposed frequently by lubricant chemists but it is much too expensive to evaluate them in full engine tests. The simplified standard lubricant tests, such as those involving 4-ball (ASTM D2266) and Timken (ASTM D2509) devices, may be helpful indicators of the combined rheological-chemical additive behaviour but cannot be related, with precision, to performance in full engine tests. Therefore, it is useful to develop new simple and inexpensive tests for evaluating rheological behaviour of lubricant additives which, on their own or in conjunction with existing standard tests, can give a better indication of lubricant performance in full engine tests.

In many engine bearings, elastohydrodynamic lubrication (ehl) films are thin enough to allow individual asperities to play a role in the tribology. These asperity interactions may be "cooperative" in that

they interact with each other to maintain a relatively continuous lubricant film. However, as the surfaces approach more closely, there may be a transition to "isolated" micro-ehl in which each asperity contact acts as an individual bearing. Eventually, surface films of molecular dimensions may begin to interact and the friction is governed by the chemical behaviour of these surface films rather than lubricant rheology. This is known as boundary lubrication. Additive packages are often considered to be developed for boundary lubrication but micro-ehl may be a much more common state and thus performance of additives under these conditions may be important.

The purpose of the present study is to explore the influence of additives on friction in ehl and micro-ehl using a side-slip disc machine of a particular nominal point contact geometry. In the long term, a simple, low cost test procedure for quantifying additive rheological behaviour is sought.

Disc machines have been used to study ehl for many years. The lubricant film can be subjected to various combinations of rolling and sliding velocity and friction forces can be measured accurately.

Jefferis and Johnson (1968) used a disc machine to study the influence of surface roughness on friction in lubricated contacts. They found that when lubricant film thickness decreased, friction increased only slightly with asperity interaction and suggested that, even with very rough surfaces, the lubricant rheology dominated the traction between the discs. More recently, disc machine experiments by Evans and Johnson (1987), Johnson and Higginson (1988) and Sutcliffe (1991) supported this view with more data, directly linking friction at asperity contacts to bulk lubricant rheology. Unfortunately, the role of lubricant additives on the friction at asperity contacts was not examined.

Lubricant additives were examined by Snyder et al (1984) using the disc machine of the present study but their investigation emphasized the influence of additives on ehl film thickness rather than rheology. Much of their work was performed under conditions of continuous fluid film lubrication and they reported that no significant changes in their peak traction coefficients were seen with any of the additives.

Recently, sophisticated instrumentation has been developed for measuring two dimensional maps of shear stress within ehl contacts (Cann and Spikes, 1989; Spikes, 1994) and profiles of shear through ehl film thicknesses (Bair et al, 1993). Such devices provide a much more direct measurement of lubricant rheology

than an overall friction force measurement from a disc machine and can be used to investigate additive behaviour, but they may not be so suitable as simple, low cost test procedures.

## 2. MATERIALS AND METHODS

### 2.1. Lubricants

Three formulations of a low viscosity mineral oil (from Imperial Oil Ltd) were used in the present study (Table 1). The first oil was base stock alone (MCT 5) while the second was base stock with 0.5 % by weight of a friction modifier (MCT 5 + FM). The friction modifier was a long chain polar molecule that attached ionically to the metal surfaces. In automobile engine tests, the fuel consumption would decrease because of this additive. The third oil was the base stock with 2 % by weight of an extreme pressure additive (MCT 5 + EP). The extreme pressure additive was *anglamol 33*, a sulphur-phosphorus compound, and the efficacy of this additive could be demonstrated in a 4-ball test (ASTM D2566).

The supplier (Imperial Oil Ltd) provided the kinematic viscosity ( $\nu$ ) and the density ( $\rho$ ) at the appropriate standard temperatures for each lubricant (Table 1). Following the established ASTM procedures, an absolute viscosity ( $\eta_0$ ) was predicted at the lubricant supply temperature in the present experiments for each of the lubricants. These values of  $\eta_0$  were checked by measurements with a Brookfield viscometer and showed acceptable agreement.

Table 1  
Lubricant Specifications

|               | T<br>(°C) | MCT 5 | MCT 5<br>+ FM | MCT 5<br>+ EP |
|---------------|-----------|-------|---------------|---------------|
| $\nu$ (cSt)   | 40        | 18.47 | 19.12         | 18.46         |
| $\nu$ (cSt)   | 100       | 3.796 | 3.803         | 3.800         |
| $\rho$ (g/ml) | 15        | 0.851 | 0.854         | 0.858         |

### 2.2. Disc machine

A side-slip disc machine (Fig 1 and 2) was used to provide a simple method of subjecting a lubricating oil to high pressures and a range of low shear rates, while maintaining an almost constant ehl film thickness. The load was applied by hanging weights on the top disc.

An oil damper was placed below the weights and a pivot was provided in the hanger rod so that the weights did not move when the top disc was skewed (rotated in the plane of the contact zone). Both of these features acted to reduce the mechanical vibrations at the higher rolling speeds and loads. A DC motor drove the bottom disc which in turn drove the top disc, at about the same surface velocity, by virtue of friction acting through the contact. By skewing the top disc manually, a side-slip velocity was imposed and continuously increased, thus causing a friction (traction) force which acted sideways (perpendicular to the rolling direction). The friction force was measured by a load cell which used strain gauges and the skew angle ( $\phi$ ) was measured with a displacement transducer. A digital data acquisition board (PC-LPT-16 from National Instruments, Austin, Texas) was used with a purpose-built signal conditioning unit (Wheatstone bridge, amplifier and an analog anti-aliasing filter). To help record and process the data, a software package (LabView for Windows from National Instruments) was employed.

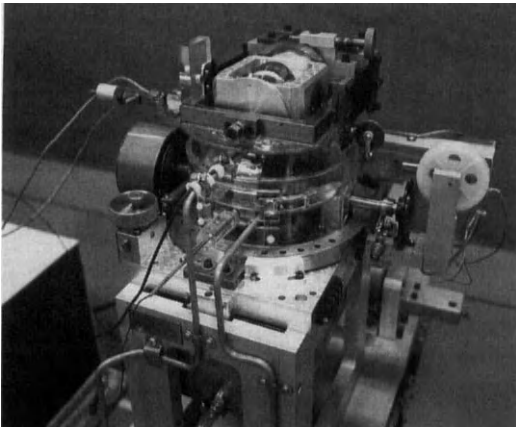


Figure 1. Side-slip disc machine which is mounted on a high stand with the weights hanging below.

Thermocouples were placed in light contact with the disc surfaces and in the inlet oil stream in order to determine an appropriate inlet oil temperature. In addition, a simple circuit was fabricated to determine the electrical resistance of the oil film. The resistance measurements provided some insight into the beginning and extent of asperity interaction.

It is important to realize that if the application of this disc machine is established for evaluating additive performance, much of the instrumentation described above can be simplified or eliminated.

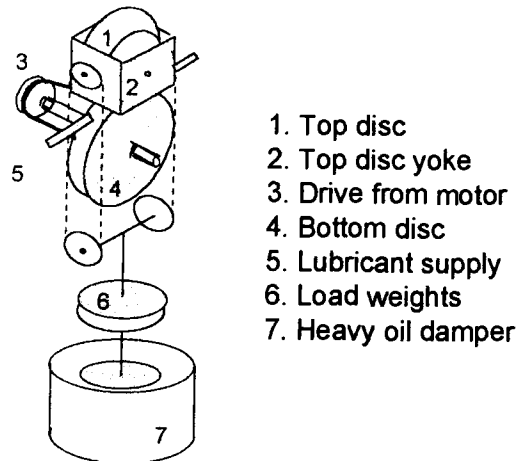


Figure 2. Schematic representation of the side-slip disc machine.

### 2.3. Disc fabrication

The discs were machined from wrought tool steel (SAE O1 for the bottom disc and Atlas Steel's Keewatin for the top disc). Then, they were hardened by heat treatment to a Rockwell C value of 63, precision cut on a lathe with a diamond tip cutting tool and lapped with fine diamond paste until an RMS roughnesses ( $\sigma_T$  and  $\sigma_B$ ) in the range of 0.08 - 0.11  $\mu\text{m}$  were measured with a profilometer device (Talysurf 5, made by Rank Taylor Hobson, Leicester, UK). Two rough top discs were fabricated by adding the additional step of sand blasting with a graded silica sand (No. 60 AFA with a mean diameter of about 1.5 mm) to achieve a  $\sigma_T$  in the range of 1.0 - 1.5  $\mu\text{m}$ .

### 2.4. Operating conditions

A number of procedural guidelines were developed to select the operating conditions. The thermocouples in the inlet zone were monitored and rolling speeds kept low enough that inlet shear heating was not detected.

When using the smooth discs at a particular load, the electrical resistance measurements allowed a range of rolling speeds to be set that proceeded gradually through the initial breakdown of the ehl film. Likewise, with the rough top discs, the rolling speeds were set to approach the point at which the resistance dropped close to zero, thus suggesting a breakdown of micro-ehl films had occurred. It was recognized that the electrical resistance could give an inaccurate indication of the extent of film breakdown because of oil deposit and oxide layers on

the surface. However, by choosing a range of rolling speeds and various load, it was ensured that measurements were made in regions of experimental interest.

Loads up to about 829.5 N were applied to the smooth disc contacts but the testing with the rough upper discs used only loads of 147.0 N and 244.5 N because of the risk of progressive plastic deformation changing the surface roughness continually. In all testing, run-in was allowed to occur until the surface roughness had stabilized in the contact zone.

The tests always proceeded from using pure base stock oil to using base stock oil with FM and then EP additives. Before introducing a new lubricant, the top disc was cleaned with solvents (varsol and acetone) and lightly polished with abrasives while the bottom disc was just cleaned with the solvents.

A total of 84 individual tests were included in the present study, with the lubricant supply temperature (T) always at 30 °C. Each test consisted of manually skewing the top disc from one side to the other, repeating this act for the opposite direction of rolling (Fig 3) and, finally, repeating the entire procedure a second time. The reversal in rolling direction, allowed the origin of the friction force versus skew angle to be determined exactly and the symmetry of the friction in the four quadrants provided a check on the precision of the disc machine. In most cases, a single quadrant was selected to represent the friction in each individual test and the other seven values only provided an indication of reliability. While an “averaging” procedure might be appropriate, it was not implemented at this stage.

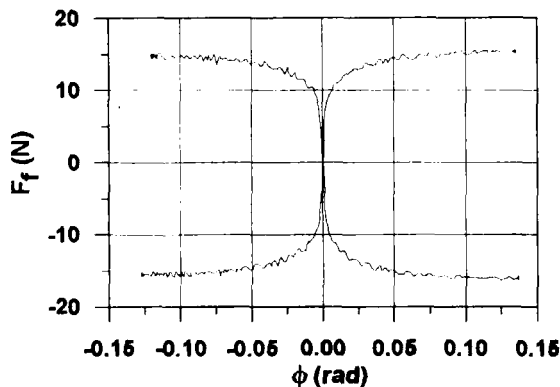


Figure 3. Typical traction curve from the side-slip disc machine for smooth disc surfaces.

An outline of the experimental input parameters is provided in Table 2. Detailed data lists will be available

in the first author’s PhD thesis. In Table 2, a composite root mean square (RMS) roughness is calculated as follows:

$$\sigma_C = \sqrt{\sigma_T^2 + \sigma_B^2} \quad (1)$$

Also, the rough top discs R1 and R2 have the same combinations of loads and velocities as the smooth top discs S1 and S2, respectively.

Table 2  
Input parameters for the experiments

| Top Disc | $\sigma_C$ ( $\mu\text{m}$ ) | F (N)        | u (m/s)   |
|----------|------------------------------|--------------|-----------|
| S0       | 0.094                        | 244.5 -829.5 | 1.6 - 3.8 |
| S1       | 0.095                        | 147.0        | 0.6 - 3.1 |
| S2       | 0.095                        | 244.5        | 0.7 - 3.3 |
| R1       | 1.146                        | 147.0        | 0.6 - 3.1 |
| R2       | 1.061                        | 244.5        | 0.7 - 3.3 |

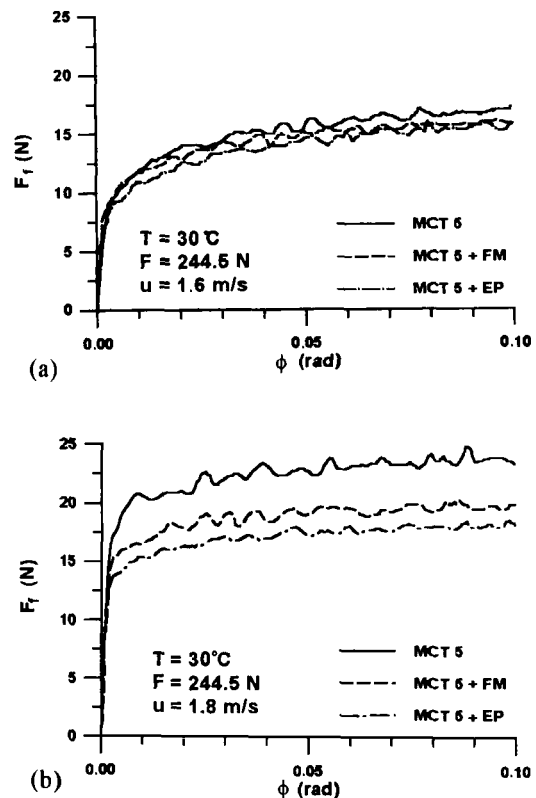


Figure 4. Typical effect of additives on friction for (a) smooth top disc (S2) and (b) rough top disc (R2).

### 3. RESULTS

As expected with a side-slip disc machine (Johnson and Tevaarwerk, 1977), the friction force ( $F_f$ ) increased rapidly to a maximum value as the skew angle ( $\phi$ ) increased from zero (Fig 3 and 4). Although,  $F_f$  was not much influenced by the additives for the smooth top disc, a distinct and repeatable decrease in friction did occur. This effect was much more pronounced when the rough top disc was used. In general, the EP additive reduced  $F_f$  more than the FM additive. At  $\phi > 0.05$  rad (corresponding to a slide-roll ratio of about 5%), the friction force remained relatively constant and thus this value was considered to correspond to  $F_{f\max}$  in the subsequent analysis of the present study.

### 4. ANALYSIS

#### 4.1. Friction and lambda ratio

One rather obvious analysis to perform in tribology is to examine the influence of the lambda ratio ( $\lambda$ ) on the maximum friction coefficient ( $\mu_{\max}$ ) where

$$\lambda = \frac{h_c}{\sigma_c} \quad (2)$$

The central film thickness ( $h_c$ ) is calculated, assuming isothermal ehl, for  $\eta_0$  at 30 °C of 24.5 mPa s,  $E'$  of 219.8 GPa,  $R$  of 22.58 mm and  $\alpha$  of 22.1 GPa<sup>-1</sup> along with various values of  $u$  and  $F$  using

$$\frac{h_c}{R} = 1.90 \left( \alpha E' \right)^{0.53} \left( \frac{\eta_0 u}{E' R} \right)^{0.67} \left( \frac{F}{E' R^2} \right)^{-0.067} \quad (3)$$

from Hamrock and Dowson (1981).

The  $\sigma_c$  values are taken from Table 2. Electrical resistance measurements through the contact indicated that a continuous fluid film occurred for about  $\lambda > 3$ . As mentioned previously, the  $F_{f\max}$  was specified as occurring at  $\phi = 0.05$  rad ( corresponding to a slide-roll ratio of 5%) and dividing by the load gives the maximum friction coefficient ( $\mu_{\max}$ ). By eliminating  $\phi$  from further consideration, a concise overview of the present experiments can be shown in Figure 5 (except the testing with top disc S0).

Broadly similar behaviour of  $\mu_{\max}$  versus  $\lambda$  was found using top discs S1 and R1 with  $F = 147.0$  N (Fig 5a) and top discs S2 and R2 with  $F = 244.5$  N (Fig 5b). However, the friction for the rough disc tests,

corresponding to the low  $\lambda$  regions, differed enough to suggest that the variations in their surface texture such as asperity tip radius ( $\beta$ ) and maximum contact density ( $n_{\max}$ ) influenced friction.

In general,  $\mu_{\max}$  remained constant for  $\lambda > 1$  but increased significantly as  $\lambda$  dropped further. For  $\lambda$  just below 0.2,  $\mu_{\max}$  was two or three times its value for  $\lambda > 1$ . The additives had a small but repeatable effect of reducing  $\mu_{\max}$  in the region of  $\lambda > 3$  which persisted until  $\lambda < 1$ , whereupon both types of additives reduced the  $\mu_{\max}$  significantly compared with base stock alone.

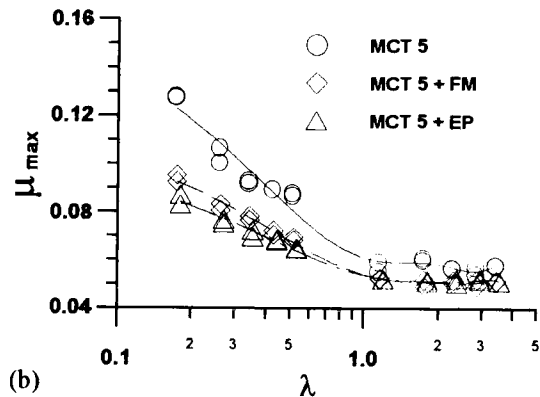
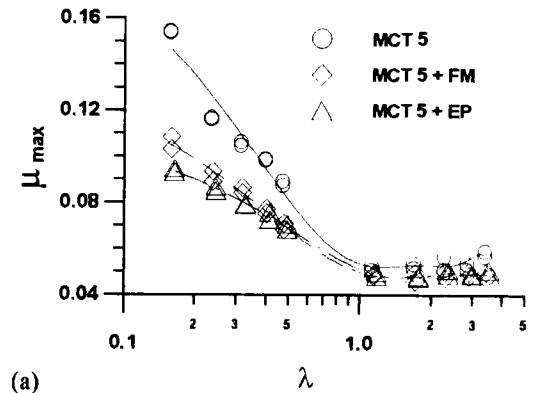


Figure 5. Plots of  $\mu_{\max}$  versus  $\lambda$  for (a)  $F = 147.0$  N (top discs S1 and R1) and (b)  $F = 244.5$  N (top discs S2 and R2).

#### 4.2. Limiting shear stress from ehl friction

The effect of the additives when  $\lambda > 3$  was puzzling because a continuous fluid film sufficient to separate the asperities occurred and was verified by electrical resistance measurements. To quantify this behaviour, it was decided to estimate the limiting shear stress from

the  $F_{r,max}$  obtained for the tests with top disc S0. These tests involved four loads (244.5 N, 439.5 N, 634.5 N and 829.5 N). Following the procedure of Wu and Cheng (1994), the values of the limiting shear stress index number ( $m$ ) were determined for the lubricants as described in detail in Appendix A.

Once  $m$  was determined, eqn (A4) was used to generate an expression of the form (with  $\tau_L$  and  $p$  in Pa)

$$\tau_L = C p^{2m} \tag{4}$$

where  $C$  = average of the four load levels,

which was evaluated (Table 3) for the lubricants of the present study .

Table 3  
Constants for eqn (4)

|     | MCT 5    | MCT 5<br>+ FM | MCT 5<br>+ EP |
|-----|----------|---------------|---------------|
| $m$ | 0.615    | 0.565         | 0.523         |
| $C$ | 0.000569 | 0.00436       | 0.0243        |

**4.3. Real area of contact for the rough discs**

To analyze the friction behaviour for the rough discs (discs R1 and R2) which had  $\lambda < 1$ , it was decided to ignore the lubricant, for the moment, and estimate the real area of contact. The “alpha” roughness parameter of Greenwood et al (1984) was 0.135 for disc R1 and 0.111 for disc R2. According to Greenwood et al, the apparent area of contact ( $A_a$ ) was influenced by the rough surface such that if Hertzian theory (which assumed smooth surfaces) was used to calculate  $A_a$ , it would be about 20% smaller than the actual value. However, it was considered relevant to note that for elastic contact of a surface with Gaussian distributions of surface and asperity heights, the real area of contact ( $A_r$ ) might depend mostly on the load and be relatively independent of the  $A_a$ .

In any case, it was assumed that the  $A_r$  was represented accurately by a flat rough surface, with an  $A_a$  equal to the smooth surfaced Hertzian value, loaded against a smooth flat surface. A portion of a typical Talysurf profilometer trace of one of the rough top discs is shown in Figure 6. The data from the profilometer

processing unit was analyzed to give the characteristic features of the surface and asperity height distributions (Appendix B and C). The Hertzian value for  $A_a$  was calculated with the following standard expression.

$$A_a = \pi \left( \frac{1.5 FR}{E'} \right)^{\frac{2}{3}} \tag{5}$$

Then, the procedure outlined in Appendix D was used to estimate  $A_r$  (Table 4). The standard deviation of the surface heights ( $\sigma$ ) was not equal to the RMS roughness of the disc ( $\sigma_r$ ) because the actual surface height distribution was only Gaussian in the region of the asperity tips (Appendix C, Fig C1) because of the deep valleys and rounded peaks found in the run-in surface profile (Fig 6).

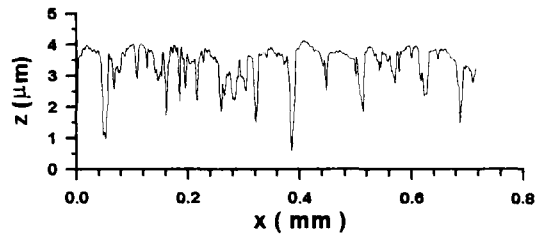


Figure 6. Typical surface of one of the rough top discs after run-in.

Table 4  
Calculation of the real area of contact

| Parameter               | Disc    |         |
|-------------------------|---------|---------|
|                         | R1      | R2      |
| $F$ (N)                 | 147.0   | 244.5   |
| $d_{avg}$ ( $\mu m$ )   | 0.      | 0.      |
| $\sigma$ ( $\mu m$ )    | 0.48    | 0.55    |
| $d_{avg}^*$ ( $\mu m$ ) | 0.11    | 0.03    |
| $\sigma^*$ ( $\mu m$ )  | 0.47    | 0.45    |
| $n_{max}$ ( $mm^{-2}$ ) | 2442.   | 3116.   |
| $z_m$                   | 0.2373  | 0.1574  |
| $z_m^*$                 | 0.00735 | 0.1257  |
| $\beta$ (mm)            | 0.1423  | 0.1132  |
| $A_r$ ( $mm^2$ )        | 0.05108 | 0.07723 |



**4.4. Limiting shear stress from micro-ehl friction**

Assuming that isolated micro-ehl occurred for the rough disc tests somewhere in the range  $0.25 < \lambda < 0.5$ , the measured  $F_{fmax}$  divided by the calculated  $A_r$  gave an estimate for  $\tau_{L,avg}$ . These values of  $\tau_{L,avg}$  were calculated for  $\lambda = 0.25$  and  $0.5$  and the corresponding pressure was taken to be the average value obtained by dividing  $F$  by  $A_r$ . In this manner, a small range of  $\tau_{L,avg}$  values were estimated with a corresponding  $p_{avg}$  for the lubricants in each of the tests with top discs R1 and R2.

**4.5. Comparison of the limiting shear stress from ehl and micro-ehl friction measurements**

In the experiments involving top disc S0,  $\tau_{L,avg}$  was determined by dividing the measured  $F_{fmax}$  by the Hertzian contact area which was calculated using eqn (5). Substituting  $p_{avg}$  into eqn (4) gave a prediction of  $\tau_{L,avg}$  and when the measured values were compared to the predicted ones for the example of the base stock oil (MCT 5) close agreement was obtained (Table 5). Assuming an absolutely precise value of  $m$  had been obtained from Appendix A, eqn (A4) was manipulated to show that the percent error ( $\% err$ ) in estimating a value of  $\tau_{L,avg}$  using  $p_{avg}$  in an expression such as eqn (4) would be

$$\% err = \left| \frac{m + 1}{1.5^{2m}} - 1 \right| \times 100 \quad (6)$$

and evaluating this equation for the  $m$  values obtained in the present study gave a maximum percent error of less than 2%. Thus, for the present ehl experiments, eqn (4) with  $p = p_{avg}$  could give an accurate estimate of  $\tau_{L,avg}$ .

Table 5  
The use of eqn (4) in predicting  $\tau_{L,avg}$  for the base stock lubricant (MCT 5)

| F (N) | $p_{avg}$ (GPa) | $\tau_{L,avg}$ (MPa) |           |
|-------|-----------------|----------------------|-----------|
|       |                 | measured             | predicted |
| 244.5 | 0.692           | 43.0                 | 42.5      |
| 439.5 | 0.842           | 54.7                 | 54.1      |
| 634.5 | 0.952           | 63.4                 | 62.9      |
| 829.5 | 1.041           | 71.1                 | 70.2      |

Remembering that the film pressure in isolated micro-ehl of a surface with spherical tipped asperities could be approximated as number of localized Hertzian

distributions, it seemed reasonable to use eqn (4) to predict the average limiting shear stress in micro-ehl with the understanding that the pressure in eqn (4) would be the average pressure of all the micro-contacts.

Finally, a direct comparison could be made between the  $\tau_{L,avg}$  predicted from ehl friction and that predicted from micro-ehl (Fig 8). Surprisingly, considering the assumptions and simplifications made in the analysis, the agreement was quite good, particularly for the testing at  $F = 244.5$  N with top disc R2. This agreement suggested that the  $\tau_L$  expression given by eqn (4) which was determined from ehl friction measurements was reasonably accurate and thus a useful technique for finding  $\tau_L$  had been found which was sensitive enough to give different values for the different additives.

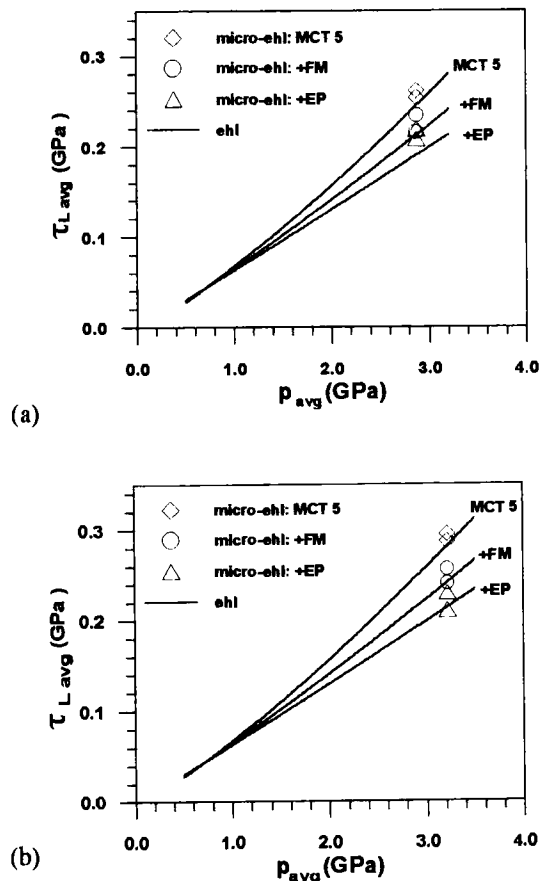


Figure 8. Comparison of the average limiting shear stress predictions based on ehl and micro-ehl friction measurements for (a)  $F = 147.0$  N and (b)  $F = 244.5$  N.

## 5. DISCUSSION

A disc machine of relatively simple construction has been used to investigate the influence of additives on lubricant rheology. For the present experiments, a plausible analysis has been made which explains the friction as *arising from the lubricant reaching a limiting shear stress*. This analysis remains consistent for lambda ratio greater than 0.25, thus suggesting that micro-ehl can persist down to these low values. The limiting shear stress was influenced by the additives used in the present experiments.

The limiting shear stress could be evaluated at a lambda ratio greater than 3, where full fluid film lubrication occurs and where neither extensive characterization of the disc surfaces nor frequent monitoring of progressive damage to the disc surfaces is required. *It is here that we believe the main contribution of the present study lies*. Side-slip disc machine friction measurements can be used under conditions of continuous ehl to evaluate limiting shear stress that is a useful parameter for predicting friction in the mixed film regime under conditions of micro-ehl. The limiting shear stress is influenced by the additives, thus suggesting that lubricant chemistry could be designed to give an optimal limiting shear stress using the disc machine measurements for guidance.

However, our enthusiasm for this approach must be tempered with some uncertainty regarding the generality of the procedure. Although additional data has been generated for the first author's PhD thesis and it seems to support the findings of the present paper, more testing is required with other additives and higher lubricant temperatures. The developed procedures for finding the limiting shear stress index value and the real area of contact are both very sensitive to small changes in the input parameters. Continued work is required to improve the precision of all of the procedures described in the present study. Maintaining the experimental studies under micro-ehl conditions is advocated to check the estimated values of limiting shear stress obtained under continuous ehl conditions and another type of viscometer (as opposed to a disc machine) is recommended to provide additional, perhaps more precise, confirmation of these estimated values. Devices such as those used by Cann and Spikes (1989) and Bair et al (1993) may be good choices for this future work.

## 5. CONCLUSIONS

- The limiting shear stress was estimated from friction measurements under continuous ehl conditions and agrees quite closely with that obtained under isolated micro-ehl conditions.
- The limiting shear stress was influenced by lubricant additives.
- The limiting shear stress combined with an evaluation of the real area of contact provided a simple friction model for isolated micro-ehl.
- A simple, low cost test procedure using a side-slip disc machine under conditions of continuous ehl was suggested for screening lubricant additives.

## ACKNOWLEDGEMENTS

Financial support was provided by Imperial Oil Ltd and NSERC and skillful technical assistance was provided by E. Huber, P. Renkma and D. Raude.

## REFERENCES

- Bair, S., Qureshi, F. and Winer, W.O.** (1993) Observations of shear localization in liquid lubricants under pressure. *ASME J. of Trib.*, **115**, 507-514.
- Bair, S. and Winer, W.O.** (1992) The high pressure high shear stress rheology of liquid lubricants. *ASME J. of Trib.*, **114**, 1-13.
- Bair, S. and Winer, W.O.** (1979) A rheological model for elastohydrodynamic contacts based on primary laboratory data. *ASME J. of Lubr. Technol.*, **101**, 258-265.
- Cann, P.M. and Spikes, H.A.** (1989) Determination of the shear stresses of lubricants in elastohydrodynamic contacts. *STLE Tribology Trans.*, **32**, 414-422.
- Cooper, M.G., Mikic, B.B. and Yovanovich M.M.** (1969) Thermal contact conductance. *Int. J. Heat Mass Transfer*, **12**, 279-300.
- Evans, C.R. and Johnson, K.L.** (1987) The influence of surface roughness on EHD traction. *Proc. Inst. Mech. Engrs.* Pt C, **201**, 145-150.
- Greenwood, J.A., Johnson, K.L. and Matsubara, E.** (1984) A surface roughness parameter in hertz contact. *Wear*, **100**, 47-57.
- Greenwood, J.A. and Tripp, J.H.** (1967) The elastic contact of rough spheres. *ASME J. of Appl. Mech.*, **89**, 153-159.
- Greenwood, J.A. and Williamson, J.B.P.** (1966) Contact of nominally flat surfaces. *Proc. Royal Soc. A*, **295**, 300-319.

**Hamrock, B.J. and Dowson, D.** (1981) *Ball Bearing Lubrication - The Elastohydrodynamics of Elliptical Contacts*. McGraw-Hill.

**Jefferis, J.A. and Johnson, K.L.** (1968) Sliding friction between lubricated rollers. *Proc Instn Mech Engrs*, **182** (1), 281-92.

**Johnson, K.L. and Higginson, J.G.** (1988) A non-Newtonian effect of sliding in micro-el. *Wear*, **128**, 249-264.

**Johnson, K.L. and Tevaarwerk, J.L.** (1977) Shear behavior of elastohydrodynamic oil film. *Proc. Roy. Soc. Lond., Ser. A*, **356**, 215-236.

**McCool, J.I.** (1986) Comparison of models for the contact of rough surface. *Wear*, **107**, 37-60.

**Snyder, F.L., Tevaarwerk, J.L. and Schey, J.A.** (1984) Effects of oil additives on lubricant film thickness and traction. *SAE Tech. Paper Series*, **840263**, SAE, Warrendale, Pennsylvania.

**Spikes, H.A.** (1994) The behaviour of lubricants in contacts: current understanding and future possibilities. *Proc Instn Mech Engrs, Part J: J of Eng Tribology*, **208**, 3-15.

**Sutcliffe, M.P.** (1991) Traction measurements in mixed elastohydrodynamic lubrication with a controlled circumferential roughness. *Proc Instn Mech Engrs, Part C: J Mech Engineering Science*, **205**, 265-273.

**Wu, S. and Cheng, H.S.** (1994) Empirical determination of effective lubricant rheological parameters. *STLE Tribology Trans.*, **37**(1), 138-46.

## APPENDIX A

### Determining the limiting shear stress index number from friction measurements with a disc machine

In elastohydrodynamic contacts, the lubricant may be subjected to high pressures and shear rates. The resisting shear stress in the lubricant often reaches a limiting value ( $\tau_L$ ) which depends on pressure and temperature but is independent of the shear rate (Johnson and Tevaarwerk, 1977; Bair and Winer, 1979). This model for lubricant behaviour is very simple and there is some debate regarding the extent to which it applies in elastohydrodynamic contacts (Bair and Winer, 1992; Bair et al, 1993).

In the present study, an empirical approach following Wu and Cheng (1994) was adopted to determine a limiting shear stress index number ( $m$ ). This approach used friction measurements from a disc machine and was based on the assumption that the lubricant had reached limiting shear stress throughout

the contact zone, the values of which depended on local film pressure. It was further assumed that the limiting shear stress was reached before shear heating was significant and thus the inlet temperature of the lubricant prevailed throughout the contact.

Wu and Cheng (1994) applied their technique to a nominal point contact with circular contact area and approximated the local film pressure as Hertzian using the standard formula

$$p = p_{\max} \sqrt{1 - \left(\frac{r}{a}\right)^2} \quad (A1)$$

$$\text{where } p_{\max} = \frac{1.5 F}{\pi a^2}, \quad a = \left(\frac{1.5 FR}{E'}\right)^{\frac{1}{3}}$$

and then assumed that the limiting shear stress has the following distribution

$$\tau_L = \tau_{L \max} \left(1 - \left(\frac{r}{a}\right)^2\right)^m \quad (A2)$$

where  $m$  = limiting shear stress index number.

It followed that the maximum friction force as measured with a disc machine was

$$F_{f \max} = \int_0^{2\pi} \int_0^a \tau_L r dr d\theta$$

and substituting in from eqn (A2) along with elementary integrations gave

$$F_{f \max} = \tau_{L \max} \frac{\pi a^2}{m + 1} \quad (A3)$$

Eqns (A1), (A2) and (A3) were combined to give

$$\tau_L = (m + 1) \frac{F_{f \max}}{\pi a^2} \left(\frac{p}{p_{\max}}\right)^{2m} \quad (A4)$$

To determine the value of  $m$  for a particular lubricant, the maximum friction force was measured at each of four applied loads (244.5 N, 439.5 N, 634.5 N, 829.5 N). At the same pressure ( $p$ ), eqn (A4) indicated that some value of  $m$  must exist such that the same limiting shear stress could be calculated for each applied load.

Wu and Cheng (1994) did not indicate clearly how this  $m$  value was determined. In the present study, a value of  $p$  was chosen equal to the maximum Hertzian pressure for the lowest of four levels of applied load. An  $m$  value was specified and eqn (A4) used to calculate four values for  $\tau_L$ . An average of the four  $\tau_L$  values was

calculated and then the sum of the squared residuals were determined as follows:

$$\epsilon = \sum_{i=1}^4 [\tau_{L i} - \tau_{L, avg}]^2 \tag{A5}$$

This calculation was repeated for ranges of *m* values, starting from 0 - 1 and refining within that range until the *m* value to three significant digits was determined which gave a minimum  $\epsilon$ . In the present study, a single minimum occurred at around *m* = 0.6 in all cases. Slight changes in *m* occurred when a different value of *p* was chosen. More substantial changes in *m* occurred when 2 or 3 rather than 4 load levels were used but the changes between 3 and 4 load levels were much less than those between 2 and 3 load levels. Thus, it was apparent that *m* was influenced by the inevitable scatter in the friction measurements and the best course of action was to use at least 4 load levels and perhaps repeat the measurements at each load level more than once. In this respect, the present study was deemed adequate but in future work more load levels and friction measurements would be used and continuing efforts would be made to improve the precision of the measurements.

**APPENDIX B**

**Contact spot density between flat rough and smooth surfaces**

If the topography of a nominally flat surface region can be measured giving an accurate three dimensional map, it is relatively simple to ascertain the number of asperity contacts when a smooth flat plane is located at a particular separation. With a specified apparent area of contact (*A<sub>a</sub>*), a direct measurement of contact spot density (*n*) could be made at that separation.

However, if a profilometer trace is used to measure surface topography giving a two dimensional graph, it is somewhat more difficult to establish an expression for contact spot density which is related to the features of the profilometer trace. To address this problem, a rigid smooth plane (represented in two dimensions as a horizontal line) located at some separation (*z*), is considered to be in contact with an isotropically rough surface which is measured by a profilometer (Fig B1). A line representing the average of the rough surface heights is also horizontal and the rough surface undergoes perfectly plastic deformation. The *n* at *z* is the same if the two surfaces deform elastically but it is

convenient for visualization in the present development to consider the above rigid-plastic pair.

An expression relating *n* to the high spot count (HSC) and bearing area (BA) at *z* can be developed. Following standard definitions, the HSC is one half the number of times the rough surface profile crosses the horizontal line representing the smooth surface divided by the profile length while the BA is the sum of the length of the horizontal line segments contained within the rough surface profile divided by the profile length (Fig B1). The HSC and BA are provided as functions of height (or separation) *z* by the 5M processor of the Talysurf profilometer which was used in the present study. However, this processor selects the heights internally and often does not supply the required parameters at enough heights. When this occurred, additional values were obtained by interpolation with a third order polynomial.

Following Greenwood and Tripp (1967), the asperities are assumed to have spherical tips of about the same radius of curvature but various heights. When a smooth flat plane is pressed into such a spherical tip the contact circle increases rapidly after initial contact, then more slowly as the separation *z* decreases. As a result, the contact spots all have about the same radius of curvature ( $\bar{a}$ ) when the smooth flat surface is at some height *z* despite the variation in asperity heights.

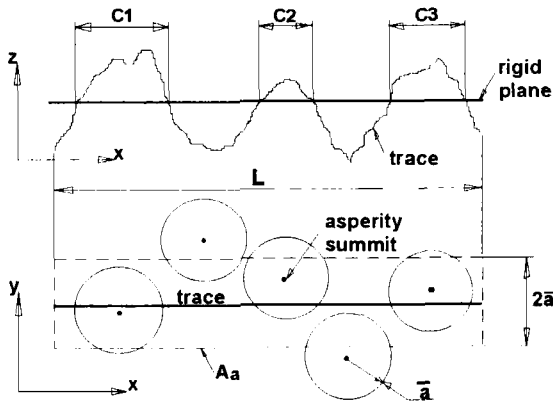
It is convenient to consider the *A<sub>a</sub>* shown in Fig B1 and to note that if asperity contact areas are larger and smaller than those shown, some extra contact spots would be include and some would be missed but on a long trace *n* should stay about the same. It follows that

$$n = \frac{HSC}{2\bar{a}} \tag{B1}$$

To determine an expression for  $\bar{a}$ , consider a long trace that, for the given *z*, intersects many contact spots. The average length of trace within the contact spots (Fig B2) is

$$\frac{BA}{HSC} = 2\bar{x} \tag{B2}$$

where from calculus  $\bar{x} = \frac{\frac{1}{2} \pi \bar{a}^2}{2\bar{a}} = \frac{\pi \bar{a}}{4}$



in this case

$$BA = \frac{c_1 + c_2 + c_3}{L} \quad HSC = \frac{3}{L} \quad n = \frac{3}{A_a}$$

Figure B1. Representation of a rigid plane in contact with a perfectly plastic rough surface, obtained from a two dimensional profilometer trace.

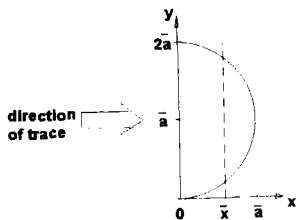


Figure B2. Half of a contact spot.

Eqs (B1) and (B2) imply that

$$n = \frac{\pi}{4} \frac{HSC^2}{BA} \tag{B3}$$

The above expression is valid for elastic surfaces because only size and not the number or the location of the contact spots changes. This same expression was derived in a somewhat different way by Cooper et al (1969).

**APPENDIX C**

**Determining the surface and asperity height distributions**

The HSC and BA were measured for decreasing z using a profilometer with interpolation as mentioned in Appendix B. It was then possible to determine n for

each z value using eqn (B3). As expected, n increased with decreasing z until a maximum value ( $n_{max}$ ) was reached at a particular separation ( $z_L$ ) as a result of the merging of asperities.

Since the BA represented a cumulative frequency plot of the surface heights, the type and features of the surface height distribution was obtained by plotting BA on probability paper (Fig C1). For both disc 1 and 2, the BA data fit a straight line on the probability paper for the asperity tip region of the surfaces. In other words, the surface height distribution was Gaussian in the part of the surface which would make intimate contact with the smooth disc surface. The features of the distribution included the average surface height ( $d_{avg}$ ) and the standard deviation ( $\sigma$ ) both of which could be determined from the plot on probability paper. The location of the z-axis was adjusted so that  $z = 0$  corresponded to the average surface height for convenience in later calculations.

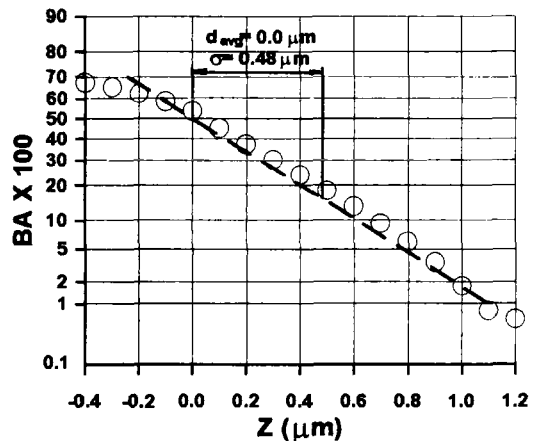


Figure C1. Plot of BA on probability paper (disc R1).

If an asperity was considered to be any summit on the surface which has a height greater than  $z_L$ , then the cumulative frequency of the asperity (as opposed to surface) height distribution was given by  $n/n_{max}$  which could then be plotted on probability paper (Fig C2). Once again, the data fit a straight line for the outermost region of the surfaces for both disc 1 and 2, thus indicating a Gaussian distribution. The features of the distribution included the average asperity height ( $d_{avg}^*$ ) and the standard deviation ( $\sigma^*$ ) which could be determined from the plot on probability paper.

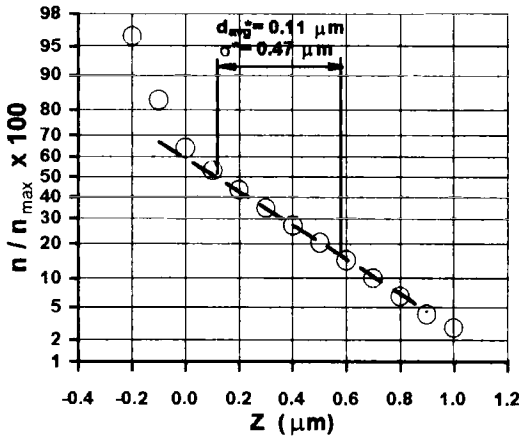


Figure B2. Plot of  $n/n_{max}$  on probability paper (disc R1).

In both the BA and the  $n/n_{max}$  plots on probability paper, the fitted lines were estimated “by eye”. Clearly, software must be developed to perform the curve fits and a criterion must be developed for excluding the points in the low  $z$  regions which are not distributed in a Gaussian fashion. However, this shortcoming in the present analysis was not expected to influence the overall findings significantly.

**APPENDIX D**

**Determining the real area of contact for a specified load**

If the separation  $z$  were known for a specified load and the deformation was perfectly plastic, the ratio of real to apparent area of contact would equal the BA at that  $z$  (considering an apparent area that was the length of the trace and of infinitesimally width). Unfortunately,  $z$  was not known and the deformation was elastic in the present study. However, assuming that all contacting asperities at a particular  $z$  have spherical tips with about the same radii of curvature, which could be represented adequately by an average value, and that they deform independently, a procedure was developed to find  $z$ . Following Greenwood and Williamson (1966), Hertzian equations were applied to individual asperity contacts and Gaussian distributions of surface and asperity height distributions were employed to yield the following equations:

(i) for the surface heights

$$A_r = \frac{1}{2} A_a F_0(z_m) \tag{D1}$$

(because Hertzian contact areas were half those of purely plastic deformation)

(ii) for the asperity heights

$$A_r = \pi \beta A_a n_{max} \sigma^* F_1(z_m^*) \tag{D2}$$

$$F = \frac{2}{3} \beta^{0.5} E' A_a n_{max} (\sigma^*)^{1.5} F_{1.5}(z_m^*) \tag{D3}$$

where 
$$z_m = \frac{z - d_{avg}}{\sigma} \quad , \quad z_m^* = \frac{z - d_{avg}^*}{\sigma^*}$$

$$F_j(\zeta) = \frac{1}{\sqrt{2\pi}} \int_{\zeta}^{\infty} (s - \zeta)^j e^{-\frac{s^2}{2}} ds$$

for  $j = 0, 1, 1.5$

$E'$  = effective elastic modulus

$\beta$  = average tip radius for all contacting asperities at separation  $z$

Eqs (D1) and (D2) gave an expression for the asperity tip radius at a particular  $z$

$$\beta = \frac{F_0(z_m)}{2 \pi n_{max} \sigma^* F_1(z_m^*)} \tag{D4}$$

and substituting into eqn (D3) yielded

$$F_0(z_m) - \frac{9\pi}{4} \left( \frac{1}{n_{max}} \right) \left( \frac{F}{\sigma^* E' A_a} \right)^2 \frac{F_1(z_m^*)}{[F_{1.5}(z_m^*)]^2} = 0 \tag{D5}$$

which was solved for the separation  $z$  which corresponded to the specified load  $F$ . A computer program was written in Fortran to perform the solution of eqn (D5) which contained a secant root finding algorithm that used the discrete values of the  $F_j$ 's given by McCool (1986) and a natural cubic spline routine to provide interpolated values when required.

Once the  $z$  value had been determined, the corresponding  $z_m$  value was calculated and eqn (D1) gave the real area of contact. Also, it was possible to calculate the average tip radius for all contacting asperities using eqn (D4).

## Boundary Film Formation by Low Molecular Weight Polymers

H Mitsui<sup>a</sup>, H A Spikes<sup>b</sup> and Y Suita<sup>a</sup>

<sup>a</sup> Showa Shell Sekiyu K.K., 123-1 Shimokawairi, Atsugi-shi, Kanagawa 243-02, Japan

<sup>b</sup> Tribology Section, Imperial College, London SW7 2BX, United Kingdom

Recent work using ultrathin film interferometry has shown that some polymers can form viscous boundary lubricating films in rolling and sliding contacts (1)-(3). This behaviour results from the adsorption of polymer molecules on metal or other polar surfaces which produces a layer on each surface of thickness approximately equivalent to one polymer coil diameter with enhanced polymer concentration and thus enhanced viscosity.

This paper describes film thickness measurements using a range of well-defined, narrow molecular weight distribution polymers in a variety of base fluids. The influence of polymer type, molecular weight and concentration on film thickness is investigated. It is found that the nature and thickness of the boundary film formed depend upon polymer type and molecular weight. One polymer, polystyrene forms lower film thicknesses in the thin film region than predicted from thick film behaviour, which may result from polymer depletion at the solid surfaces.

### 1. BACKGROUND

Polymers are widely used in solution in liquid lubricants for a number of reasons; to modify the viscometric properties of the fluid, as dispersants, as pour point depressants and to inhibit foaming. Oil-based viscosity modifiers are typically polymethacrylates, ethylenepropylene polymers or styrene-butadiene polymers having mean molecular weights in the range 50000 to 500000. Below this range, polymers make only a small contribution to viscosity at economically viable concentrations. Above it, most polymers, with the exception of some star structures, are mechanically degraded under the high shear stresses found in lubricated contacts, resulting in a steady loss of blend viscosity over time. Polymers are also used to thicken aqueous lubricants and polyethylene oxide is commonly employed for this purpose.

Dispersants are commonly polyisobutene succinimides which characteristically have mean molecular weights in the range 1000 to 5000 but in recent years there has been a trend towards the use of higher molecular weights up to 30000 in order to obtain some degree of viscosity modification from

the dispersant additive. Pour point depressants generally lie in the molecular weight range 20000 to 50000 and are typically polyalkylmethacrylates, polyalkylstyrenes or polyalkylnaphthalenes.

The influence of dissolved polymers on the lubricating ability of their blends is complex and still not fully understood. Broadly speaking, polymers have three types of effect on lubricant film formation and thence on friction and wear.

Firstly, polymers raise the viscosities of their solutions to an extent which depends strongly on molecular weight and concentration (4). This enhancement of viscosity results in an increase of hydrodynamic and elastohydrodynamic (EHD) film formation. However this increase in film thickness is generally considerably less than predicted theoretically from the bulk viscosity of the polymer solution because of temporary and also permanent shear thinning of polymer solutions in high shear stress hydrodynamic and EHD contact conditions (5)-(8).

Secondly, it has been suggested that under transient shear conditions, as are found in dynamically loaded contacts, polymers solutions may exhibit viscoelastic behaviour which may result

in an increase in load support and thus film thickness (9)(10).

The third way that polymers in solution can influence lubrication is by boundary film formation. It has recently been shown using both force balance and ultrathin film interferometry that polymers in solution can selectively adsorb at solid interfaces to form surface layer, tens of nanometres thick, of very different rheological properties from the bulk solution. These layers were initially considered to be "solid-like" or "immobile", (11)(12) but it is now recognised that they are simply much more viscous than the bulk solution by virtue of having an enhanced polymer concentration due to adsorption (1)(13).

In the force balance approach, two very smooth surfaces coated with test lubricant are brought into close approach using piezo translators and the forces between the surfaces are measured. A very small oscillatory motion is also applied to one surface to produce squeeze or shear and this can be used to estimate the viscosity of the separating fluid film. With this technique it has been shown that both melts and solutions of polyisoprene form surface layers of much higher effective viscosity than the bulk solution (11). These layers also possess viscoelastic properties. The layers have a thickness on each surface of about twice the bulk solution radius of gyration and are thus believed to result from the adsorption of polymer molecules in a semi-random coil arrangement on the surfaces, with polymer tails extending outward beyond the diameter of gyration. A similar effect has been found with dispersant type commercial viscosity modifiers (14).

The conditions present in force balance apparatus are far less severe than those present in practical contact conditions. However similar polymer boundary film-forming effects have also been observed in realistic, lubricated contacts using ultrathin film interferometry. Figure 1, taken from (1) shows a plot of  $\log(\text{film thickness})$  versus  $\log(\text{rolling speed})$  in a rolling point contact for a series of commercial viscosity modifiers, all at between 1 and 3% wt. in the same mineral base oil.

The solid line shows film formation by the polymer-free base oil. The base oil and many of the polymers show conventional EHD behaviour down to 2 nm thickness with a straight line  $\log/\log$  plot of

gradient between 0.65 and 0.75 in accord with EHD theory (15). However it can be seen that three of the polymers show anomalous behaviour at low speeds, forming much thicker films than the base oil. This is believed to result from the preferential adsorption of the polymer molecules on the two surfaces since the effect is seen by the three polymers with significant polarity and not by other, fully-saturated hydrocarbon polymers. The boundary film thickness is approximately 20 nm, which is close to the hydrodynamic diameter of the polymers employed and comparable to the findings of force balance studies. Similar behaviour has also been observed using polyisoprene where it has been found that boundary film thickness increases with  $(\text{molecular weight})^{0.6}$ , again suggesting that the boundary film thickness results from the adsorption of polymer coils on the surfaces (13).

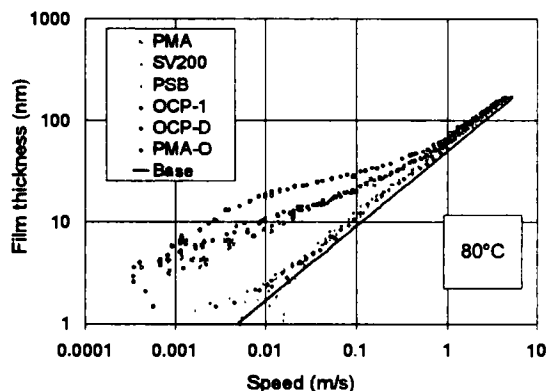


Figure 1 Film thickness behaviour of commercial viscosity index improvers solutions (1).

Very recently these boundary films formed by viscosity modifiers have been shown to persist in mixed sliding/rolling contacts as well as in pure rolling, indicating that they are able to withstand sliding conditions and it has also been demonstrated that they are able to reduce friction and wear in the mixed regime, by contributing to surface separation at intermediate to slow speeds (3).

The above work using both force balance and ultrathin film interferometry has largely been carried out on commercial viscosity modifiers. These are mixtures with a considerable range of



molecular weights, which makes it difficult to assess the precise influence of molecular weight on boundary film formation. Only one well-defined, narrow molecular weight distribution polymer, polyisoprene, has been investigated.

The aim of the work described in the current paper was to extend the study of boundary film formation by polymers in solution by examining a series of well-defined, model polymers and thereby to investigate, systematically, the influence of polymer type, molecular weight and concentration on boundary film formation.

## 2. TEST METHOD

In this study, ultrathin film interferometry was employed to map the variation of lubricant film thickness in a rolling ball on flat contact down to very thin films, thereby investigating the presence and characteristics of any boundary film (16).

The technique is shown schematically in figure 2.

into the contact and some is reflected from the chromium layer whilst some passes through the spacer layer and any lubricant film present to be reflected from the steel ball. The two beams recombine and interfere and the spacer layer ensures that interference will occur even if no oil film is present.

The interfered light from a strip across the contact is then passed into a spectrometer where it is dispersed and detected by a solid state, black and white TV camera. A frame grabber is used to capture this image and a microcomputer program determines the wavelength of maximum constructive interference in the central region of the contact. The lubricant film thickness is calculated from the difference between the measured film thickness and the thickness of the silica spacer layer at that position. The technique can detect and measure film separations down to less than 2 nm.

The test rig used is shown in figure 3. The ball is loaded upwards against the underside of the glass disc and both ball and disc are held within a temperature-controlled, stainless steel chamber.

In the work described in this study, the disc was rotated and itself drove the ball in nominally pure rolling. A new 19 mm diameter, steel ball of rms surface roughness 11 nm was used for each test. The load applied was 20 N which corresponds to a maximum contact pressure of 0.52 GPa.

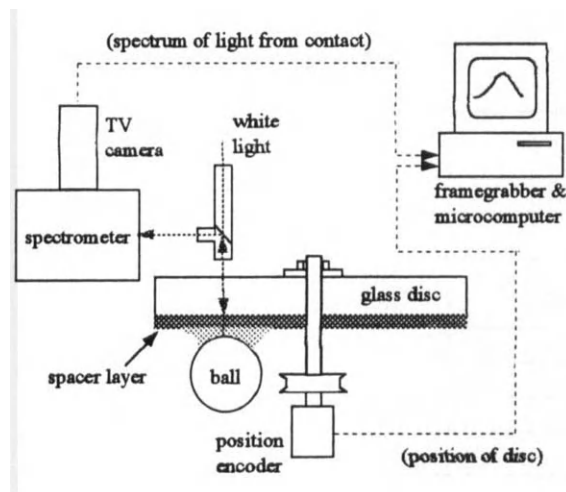


Figure 2. Schematic diagram of ultrathin film method.

A high pressure contact is formed between the flat surface of a glass disc and a reflective steel ball. The glass disc is coated with a thin, semi-reflective layer of chromium on top of which is a layer of silica, about 500 nm thick. White light is shone

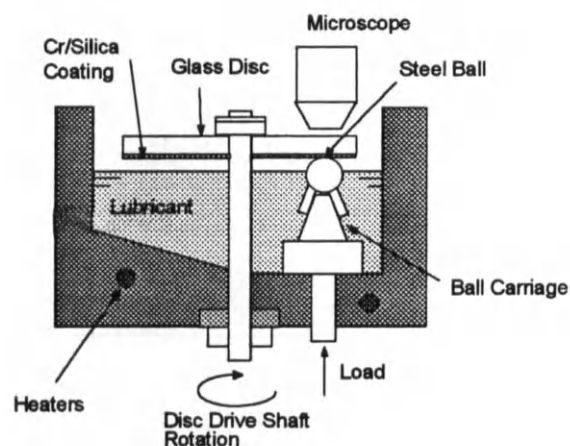


Figure 3: Test rig for film thickness measurements.

### 3. MATERIALS

This study required commercially available samples of polymer at several different average molecular weight values each having a very narrow molecular weight range distribution (i.e. low polydispersity index). In practice there are very few polymer structures which are thus available and these tend to have very simple monomer structures, far less complex than those present in commercial viscosity modifiers. They tend to be used primarily for calibration purposes in chromatography and also for fundamental rheological studies.

The polymers employed in the current study were polyisoprene, polymethylmethacrylate and polystyrene, as listed in table 1. They were obtained from Polymer Laboratories.

A practical problem with two of these polymers, polymethylmethacrylate (PMMA) and polystyrene (PS) is that they are too polar to be significantly soluble in conventional lubricants such as mineral oils, synthetic hydrocarbons and most esters. Suitable solvent base fluids were selected on three bases;

- (i) polarity; polarity matching was made using solubility parameter determination in order to identify solvents able to dissolve PMMA and PS
- (ii) viscosity; relatively low viscosity base fluids were chosen to minimise hydrodynamic film formation so that the boundary lubrication regime could be reached at attainably low speeds
- (iii) base fluids chosen had different chemical bond structure from the polymer solute. This was done in order to permit the infrared adsorption spectrum of the solute to be easily differentiated from the solvent for a separate study not reported here.

Using these criteria, the solvent base fluids chosen for each polymer, together with their viscometric properties, are listed in table 2. Also shown in table 2 is the test temperature at which each base fluid and its polymer solutions was tested.

Table 3 lists the measured low shear rate viscosities of each polymer solution, and the test temperatures used.

Table 1  
Polymers used in this study

| Polymer  | Mp     | Mw     | Mw/Mn |
|--|--------|--------|-------|
| Polymethyl methacrylate (PMMA)<br>$-(\text{CH}_2\text{C}(\text{CH}_3)(\text{COOCH}_3))_n-$ | 4,700  | 4,609  | 1.10  |
|  | 9,400  | 8,902  | 1.10  |
|  | 17,000 | 17,065 | 1.06  |
|  | 48,600 | 49,099 | 1.05  |
|  | 68,000 | 66,680 | 1.07  |
|  | 95,000 | 95,102 | 1.04  |
| Polystyrene (PS)<br>$-(\text{CH}_2\text{CH}(\text{C}_6\text{H}_5))_n-$                     | 5,050  | 5,011  | 1.04  |
|  | 22,000 | 21,870 | 1.03  |
|  | 30,300 | 30,162 | 1.02  |
|  | 52,000 | -      | 1.03  |
| Polyisoprene (PIP)<br>$-(\text{CH}_2-\text{C}(\text{CH}_3)=\text{CH}-\text{CH}_2)_n-$      | 7,450  | 7,396  | 1.03  |
|  | 32,400 | -      | 1.02  |
|  | 86,000 | 86,812 | 1.02  |

(Mp = peak average, Mw = weight average, Mn = number average molecular weight)

Table 2  
Base fluids used in this study

| Base fluid   | Abbrev. | Polymer solute | Test temp. °C | Viscosity, cP, at test temperature | Refractive index at test temperature |
|--|---------|----------------|---------------|------------------------------------|--------------------------------------|
| Polyalphaolefin synthetic hydrocarbon                            | SHF61   | PIP            | 40            | 23.82                              | 1.451                                |
| Linear dialkylbenzene<br>$C_6H_4R_2$ (R=C10-C13)                 | LADB    | PIP            | 40            | 17.97                              | 1.473                                |
| Di-2-ethylhexylphthalate<br>$C_6H_4-1,2-COOR$ , R=2-ethylhexyl   | DOP     | PS             | 60            | 11.68                              | 1.470                                |
| Tripropyleneglycol monoalkylether<br>$H-(OCH(CH_3)CH_2)_3-OCH_3$ | TPGME   | PMMA           | 30            | 4.767                              | 1.427                                |

Table 3  
Polymer solutions tested and their viscosities

| Polymer | Molecular weight (Mp) | concentration of polymer wt. % | Base oil | Test temp., °C | Viscosity, cP at test temperature |
|---------|-----------------------|--------------------------------|----------|----------------|-----------------------------------|
| PIP     | 7450                  | 5.98                           | LDAB     | 40             | 27.93                             |
| PIP     | 7450                  | 6.31                           | SHF 61   | 40             | 34.02                             |
| PIP     | 86000                 | 5.82                           | LDAB     | 40             | 104.44                            |
| PIP     | 86000                 | 5.78                           | SHF 61   | 40             | 106.17                            |
| PIP     | 86000                 | 1.27                           | LDAB     | 40             | 28.68                             |
| PIP     | 86000                 | 2.64                           | LDAB     | 40             | 44.68                             |
| PIP     | 86000                 | 4.10                           | LDAB     | 40             | 66.16                             |
| PS      | 5050                  | 6.0                            | DOP      | 60             | 17.99                             |
| PS      | 22000                 | 6.0                            | DOP      | 60             | 25.86                             |
| PS      | 30300                 | 6.0                            | DOP      | 60             | 28.74                             |
| PS      | 52000                 | 6.0                            | DOP      | 60             | 36.62                             |
| PS      | 22000                 | 2.0                            | DOP      | 60             | 14.93                             |
| PS      | 22000                 | 4.0                            | DOP      | 60             | 19.47                             |
| PS      | 22000                 | 8.0                            | DOP      | 60             | 34.25                             |
| PS      | 22000                 | 10.0                           | DOP      | 60             | 47.55                             |
| PMMA    | 4700                  | 6.0                            | TPGME    | 30             | 7.29                              |
| PMMA    | 9400                  | 6.0                            | TPGME    | 30             | 7.96                              |
| PMMA    | 17000                 | 6.0                            | TPGME    | 30             | 9.33                              |
| PMMA    | 48000                 | 6.0                            | TPGME    | 30             | 15.32                             |
| PMMA    | 68000                 | 6.0                            | TPGME    | 30             | 17.61                             |
| PMMA    | 95000                 | 6.0                            | TPGME    | 30             | 25.11                             |

4. RESULTS

Figure 4 contains plots of log(film thickness) versus log(rolling speed) for the four base fluids used in this study. All these show linear behaviour, with

a gradient of around 0.67, in accord with EHD theory. This linearity persists down to less than 10 nm, indicating that the base fluids show no significant boundary effects of such thickness.

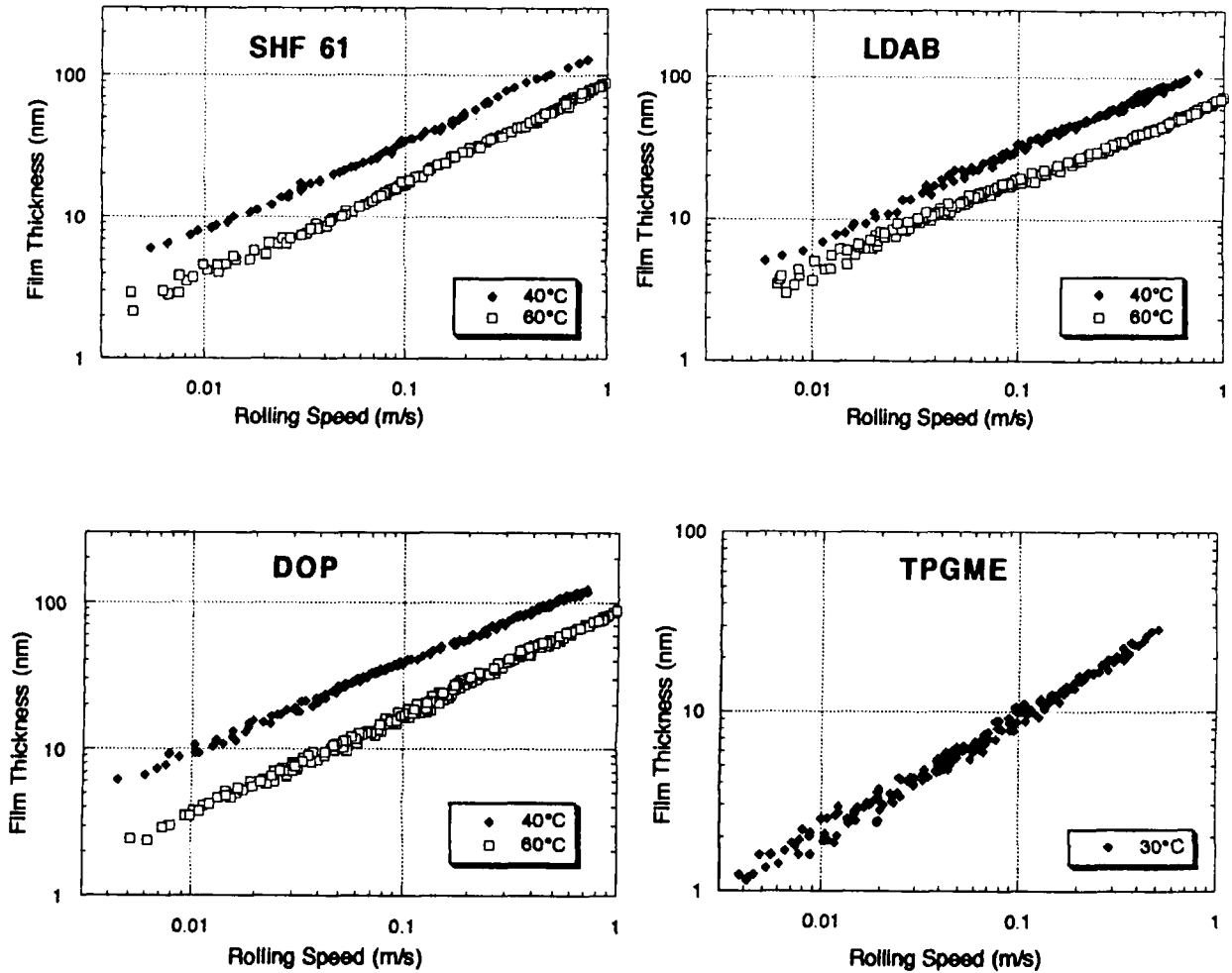


Figure 4. Film thickness results for the base oils.

Figure 5 compares plots of film thickness versus rolling speed for ~ 6% wt. solutions of low and high molecular weight polyisoprenes in two base fluids, LADB and SHF61. Also shown on each plot are the base fluid film thickness (a solid line) and the theoretical EHD film thickness based upon the low shear rate viscosity of the polymer solution and on the pressure viscosity coefficient of the base fluid.

The higher molecular weight PIP ( $M_p = 86000$ ) shows quite similar behaviour in both solvents, with clear evidence of a boundary film. In this study, the boundary film is approximately estimated as the difference between the measured film thickness at the lowest speed reached and the expected EHD film thickness component at this

speed, determined by extrapolating the linear, high speed part of the film thickness curve down to low speed. This gives a boundary film thickness of 15 nm in LADB and 22 nm in SHF61. The latter is very close to that predicted from previous work based on lower molecular weight polyisoprenes in synthetic hydrocarbon (13).

In the high speed, thick film region, the solutions exhibit a shear thinning effect, with the film thickness lying below that predicted from the low shear rate viscosity. The shear thinning appears greater in LADB than in SHF61. This shear thinning behaviour will be analysed in some detail in a later paper (17).

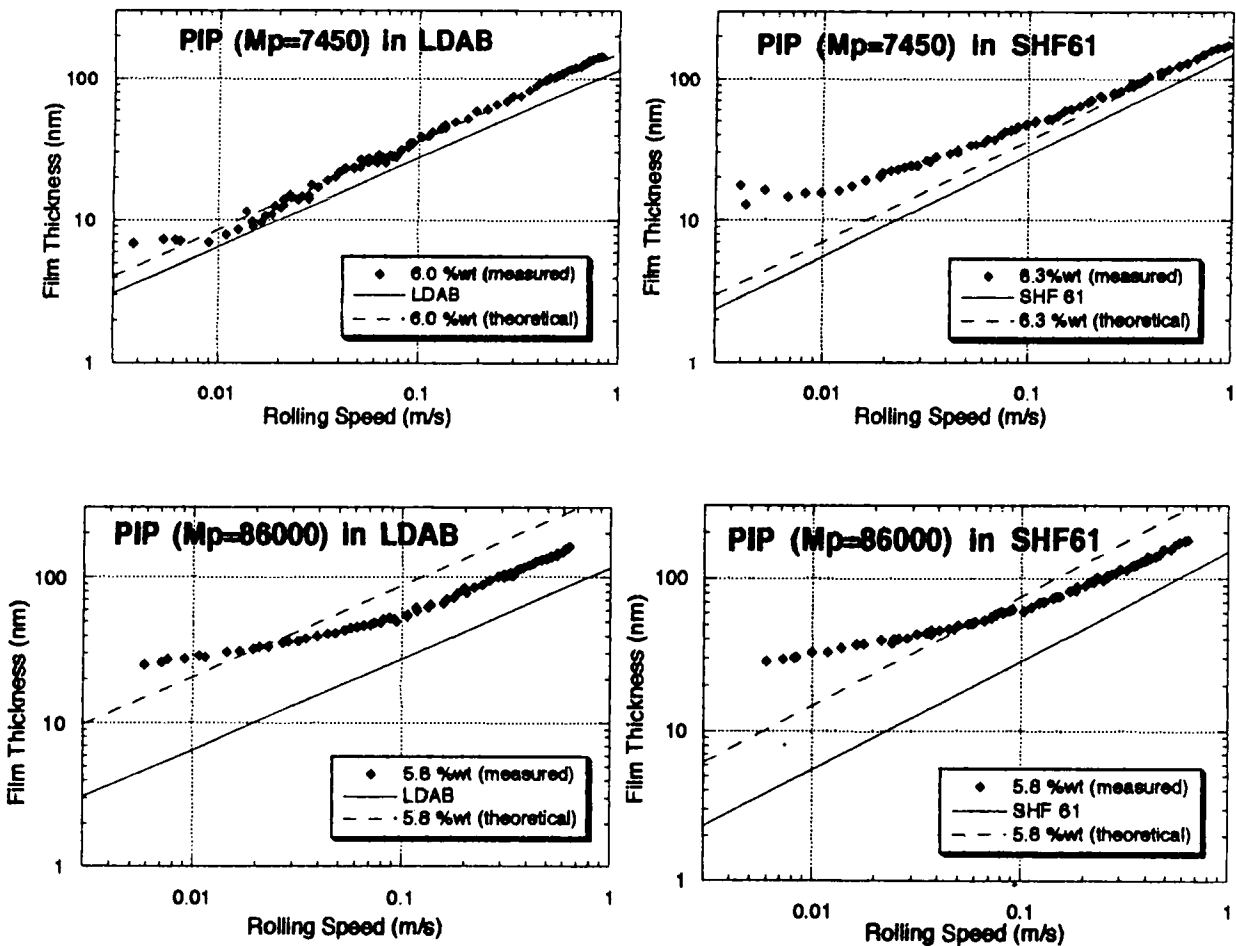


Figure 5: Comparison of film thickness results for polyisoprene (PIP) solutions in SHF61 and LADB.

The low molecular weight PIP solution appears to form a boundary film about 4-6 nm thick in LADB and about 10 nm thick in SHF61. In this case, the former value is closer to that predicted from previous work on polyisoprenes of 6-7 nm (13).

Figure 6 shows the influence of polymer concentration of boundary film formation for the solutions of PIP ( $M_p = 86000$ ) in LADB. Boundary film thickness appears to increase only marginally with concentration, from about 12 nm at 1.3% wt. to 15 nm at 5.8% wt.; the variation of the EHD component to film thickness with polymer concentration is higher than that of the boundary film component, even in the thin film region. Figure 7 shows the film-forming behaviour of solutions of

6% wt. polystyrenes in DOP. The lower molecular weight polymer shows negligible shear thinning or boundary film formation. However the highest molecular weight shows a striking reduction in film thickness in the thin film, slow speed region. At high speeds the film formed is slightly less than that predicted from the low shear rate viscosity (dashed line), presumably due to shear thinning.

At slow speeds, however, the film thickness falls down to a value close to that of the polymer-free base fluid and considerably below that expected from the high speed behaviour. This phenomenon will be discussed in the next section of this paper.

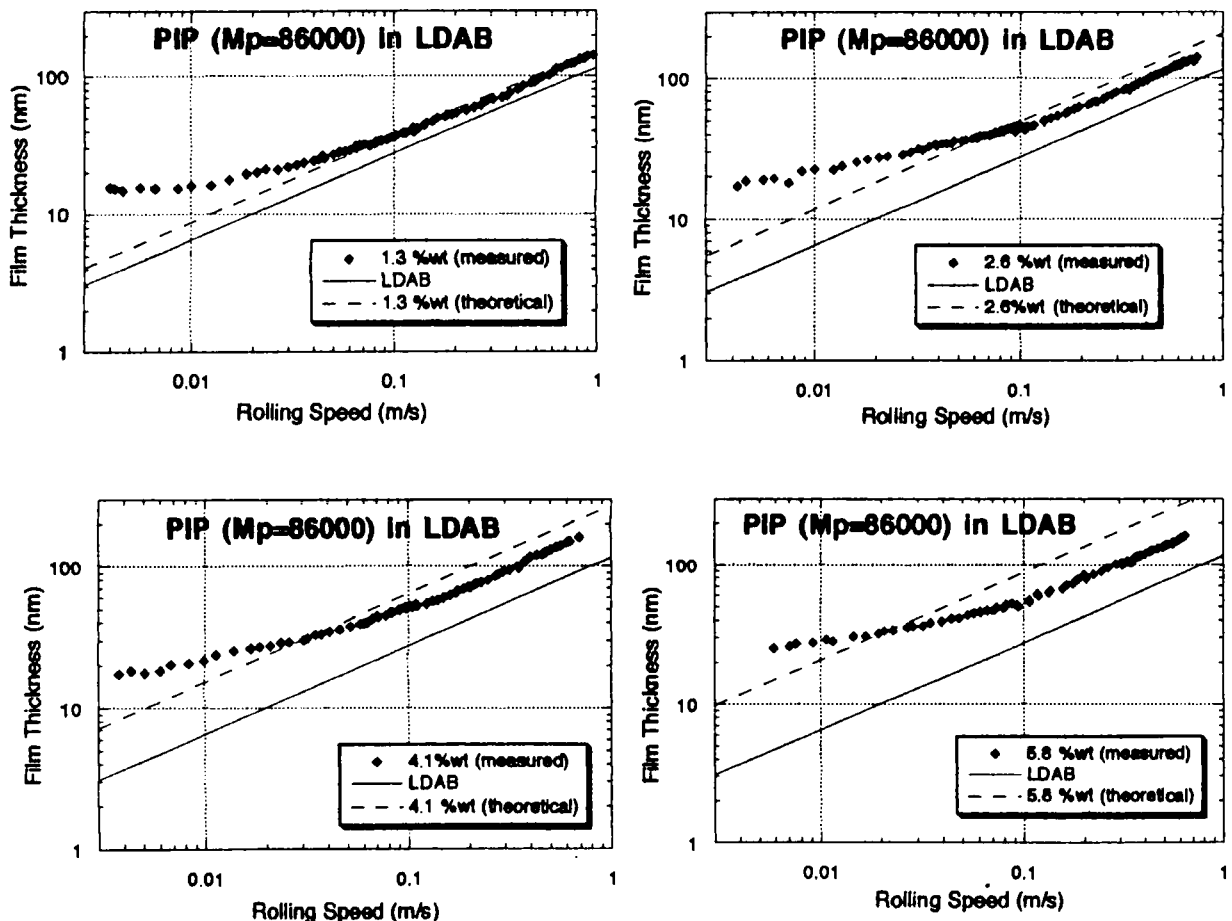


Figure 6. The influence of polymer concentration on film thickness for PIP ( $M_p = 86000$ ) in LADB.

Figure 8 examines the influence of polymer concentration on film-forming behaviour for an intermediate molecular weight polystyrene. This also shows a decrease in film thickness in the thin film, slow speed region but only at 8-10% wt. polymer. A similar trend was also seen with concentration for other molecular weights; the reduction in film thickness at slow speeds was most evident for high molecular weight polymers and at high polymer concentrations.

Results for the third polymer type, PMMA are shown in figure 9 at six different molecular weights.

Again, the solid line indicates the base fluid behaviour and the dashed line shows the theoretical EHD behaviour of the polymer solution. It is clear from these plots that PMMA does form a boundary film in this solvent, of thickness up to about 7 nm. However the results are noteworthy for the very large scatter found in the boundary film region. This is believed to be real and may reflect spatial variations in film thickness on the solid surfaces, perhaps due to uneven adsorption. This will be further discussed in the next section.

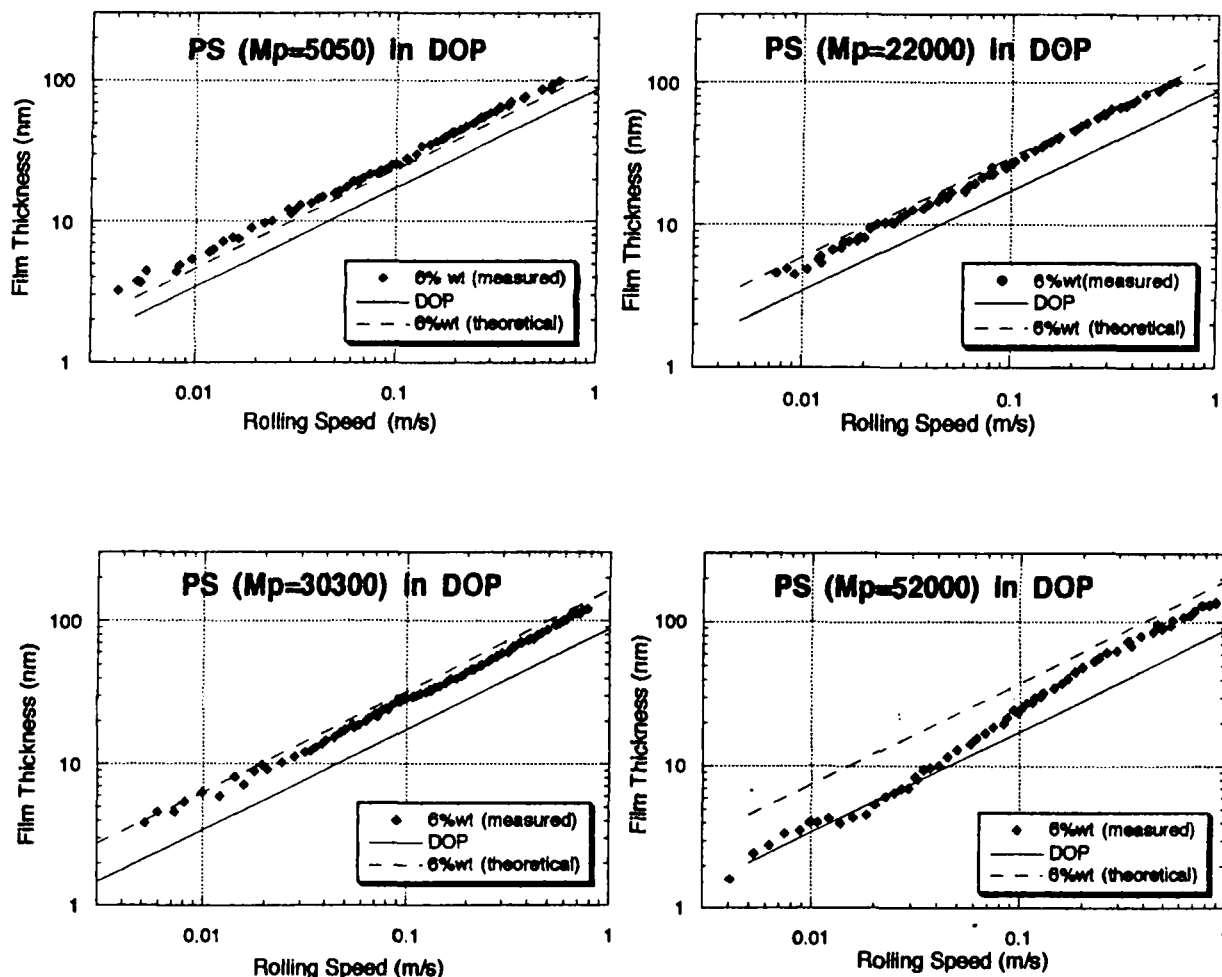


Figure 7. Film thickness results for solutions of 6% wt. polyisoprene (PIP) in DOP.

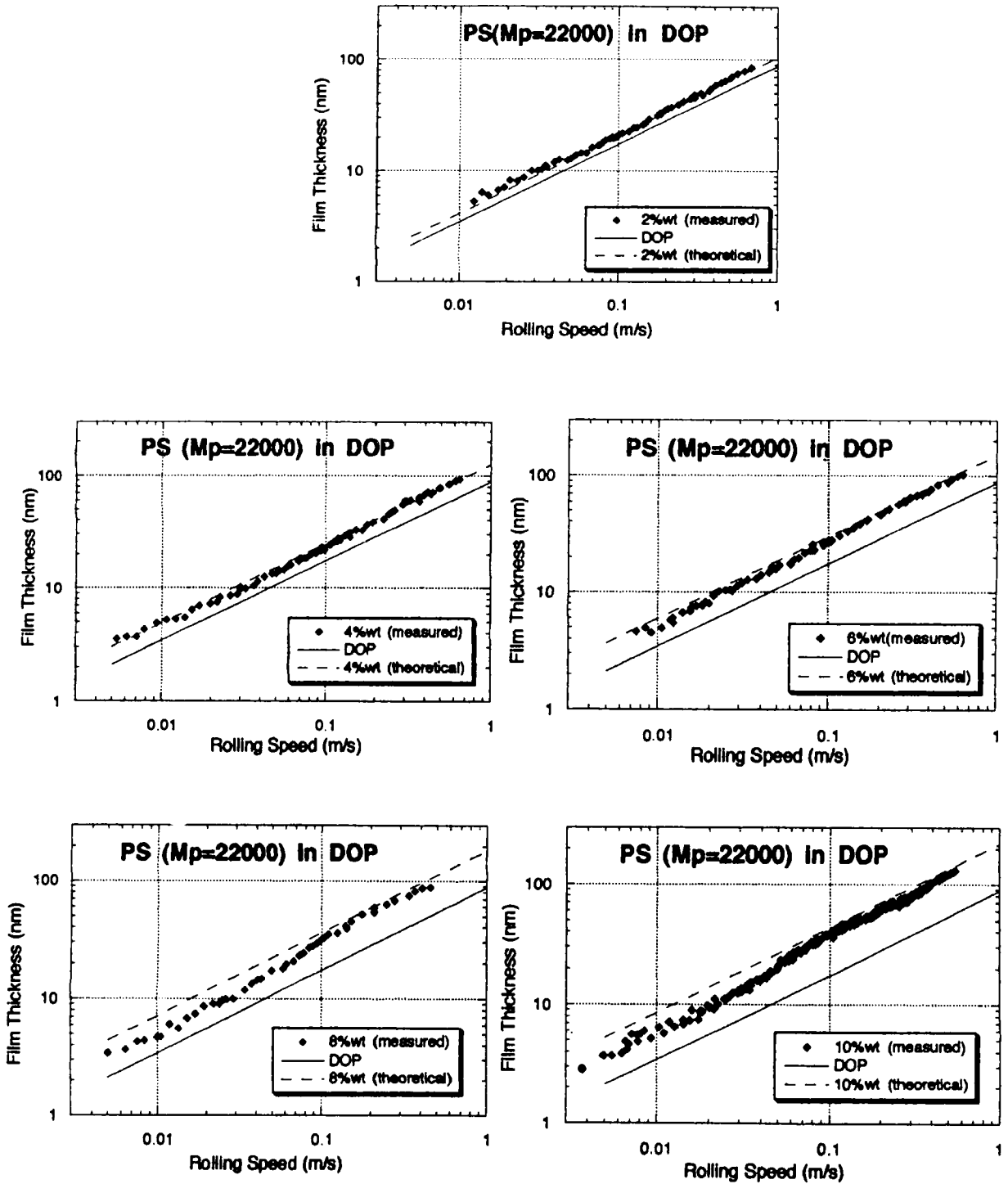


Figure 8. The influence of polymer concentration on film thickness for polystyrene (PS), ( $M_p = 22000$ ) in DOP.



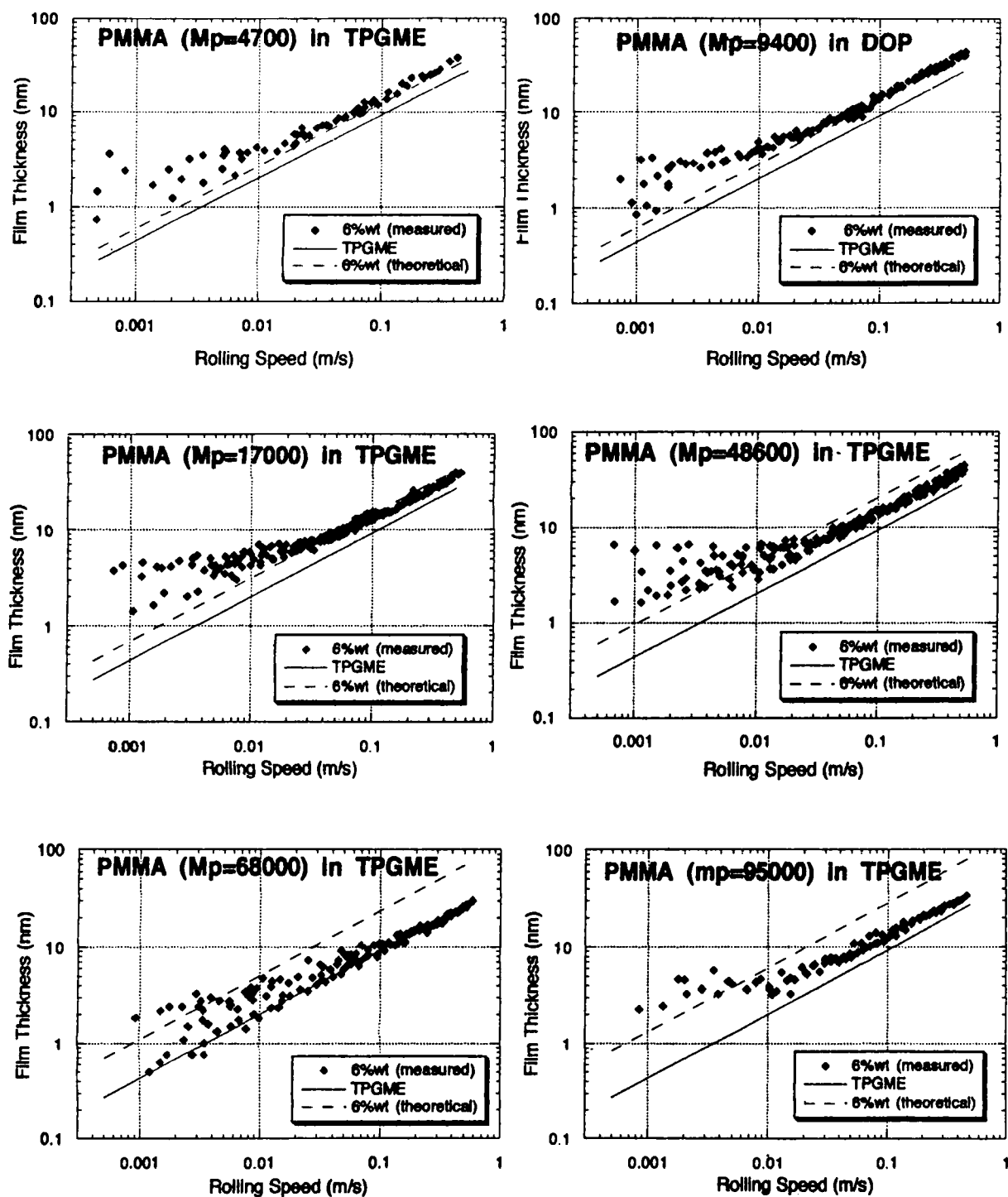


Figure 9. Film thickness results for solutions of 6% wt. polymethylmethacrylate (PMMA) in TPGME.

## 5. DISCUSSION

The three polymers can be seen from this study to each exhibit very different boundary film behaviour.

Polyisoprenes show very clear and very stable film formation, indicating a clearly-defined and evenly-distributed film. These thicknesses found are consistent with those found in previous work. There may be a solvent effect, with PIP in LADB forming slightly thinner films than in SHF61, perhaps reflecting a smaller gyration radius in the former base fluid. Previous work has shown that at very slow speeds, the boundary film thickness falls, indicating that it is not a solid-like but a highly viscous film of concentrated polymer solution. In this study no attempt was made to go to very slow speeds where this phenomenon occurs. Even so, examination of the boundary film thickness (total film minus EHD component), indicates that this falls with speed, suggesting that the surface film is viscous and probably has viscosity varying with distance from the solid surfaces.

Polystyrene in DOP shows no boundary film formation but instead exhibits a reduced film thickness in the thin film regime for high concentrations of the higher molecular weight polymers. Two possible explanations for this type of behaviour are as follows. One is polymer depletion. Polymers having negligible adsorption on solid surfaces should, for spatial reasons, show a reduced concentration of polymer segments within one hydrodynamic radius of the surface (18). Experimental work using fluorescence has shown that this can occur for styrene copolymers in ethyl acetate on deactivated glass surfaces (19). Such an effect might be expected to yield a layer of reduced viscosity, approaching that of the base fluid close to solid surfaces. Alternatively it has been suggested in the past that some polymers may behave similarly to suspended solid particles and be carried by fluid flow around the edges of the contact inlet, so that the inlet zone effectively filters out the polymer particles when the gap is very small (20). To explain the observed results, however, larger polymer molecules would have to be more easily diverted from the inlet than smaller ones.

The PMMA results are very different from both PIP and PS. A boundary film appears to be

formed but this is very thin (less than 5 nm for all polymers except  $M_p = 48600$ ) and the measurements have large scatter. This was found for all solutions tested and is believed to represent a true variation in boundary film thickness, either temporal or spatial. It is noteworthy that measurements tend to lie between two quite repeatable extremes, that corresponding to zero boundary film and that representing about 5 nm of film. Unlike with PIP, there appears to be no systematic increase in boundary film thickness with molecular weight. One possible explanation for this is that boundary film formation may not be due to polymer molecules adsorbed in a standard coiled arrangement as found in solution but instead result from molecules being adsorbed in a much flatter conformation. Alternatively polymers may be adsorbed as coils of thickness of the same scale as found in solution but at such low and irregular density on the solid surfaces that they have only a partial and irregular influence on inlet viscosity and this film thickness.

This behaviour is very different from that observed with commercial polyalkylmethacrylates, where thin and even boundary film formation has been observed (1). The difference may arise from solvent/polymer competition for the solid surfaces. TPGME is a highly polar solvent, which is why it is able to dissolve PMMA. It is possible that in consequence it absorbs in preference to PMMA molecules on the steel and silica surfaces, thereby inhibiting boundary film formation.

## 6. CONCLUSIONS

The boundary film-forming properties of solutions of three, well-defined model polymer systems, polyisoprene, polystyrene and polymethylmethacrylate have been studied using ultrathin film interferometry.

The three show very different behaviour. Polyisoprene forms regular boundary films whose thickness depends upon molecular weight in a manner suggesting the formation of single layers of adsorbed polymer in a largely random coil arrangement on the solid surfaces. The film thickness is strongly dependent on molecular weight, somewhat dependent upon base fluid type but only

very marginally dependent upon polymer concentration.

Polystyrene forms thinner films at slow speeds than predicted from their high speed, thick film behaviour. This is most easily explained in terms of polymer depletion; that the polystyrene concentration is reduced below that of the bulk solution within a hydrodynamic diameter of the surfaces. This phenomenon is quite well known in colloid chemistry and occurs when the solvent is much more strongly adsorbed on the solid surfaces than is the polymer.

Polymethylmethacrylate shows very thin and very irregular boundary film formation, which may reflect only partial adsorption of the polymer on the surface. The film thickness is not significantly dependent on molecular weight. This behaviour is quite different from that seen for commercial polyalkylmethacrylates and may reflect competition for surface adsorption between solvent and polymer.

#### ACKNOWLEDGEMENTS

The authors wish to thank Showa Shell Sekiyu K.K., Japan for supporting the work described in this paper.

#### REFERENCES

1. Smeeth, M., Gunsel, S. and Spikes, H.A. "Boundary Film Formation by Viscosity Index Improvers". Accepted for publication in Tribology Transactions, preprint no. 95-3B-TC-1.
2. Guangteng, G., Smeeth, M., Cann, P.M. and Spikes, H.A. "The Measurement and Modelling of the Boundary Film Properties of Polymeric Lubricant Additives", Proc. I. Mech. E. Ser. J210, (1996), p. 1-15.
3. Smeeth, M., Gunsel, S. and Spikes, H.A. "Friction and Wear Reduction by Boundary Film-Forming Viscosity Index Improvers", to be presented at SAE Meeting, San Antonio, October 1996.
4. *Rheological Properties of Lubricants*, Briant, J., Denis, J. and Parc, G., Chapter 8. Publ. Inst. Franc. du Petrole, Editions Techip, Paris, 1989.
5. "The Relationship Between High-Temperature Oil Rheology and Engine Operation - A Status report", ASTM Data Series DS 62, Publ. ASTM, Philadelphia, (1984).
6. McMillan, M.L. and Murphy, C.K. "Temporary Viscosity Loss and its Relationship to Journal Bearing Performance", SAE 780374, (1978).
7. Hirata, M. and Cameron, A. "The Use of Optical Elastohydrodynamics to Investigate Viscosity Loss in Polymer-thickened Oils", ASLE Trans. 27, (1984), pp. 114-121.
8. Spikes, H.A., Cann, P.M., Coy, R.C. and Wardle, R.W.M. "An 'In Lubro' Study of VI Improvers in EHD Contacts." Lub. Science 3, (1990), pp. 45-62.
9. Hutton, J.F., Jackson, K.P. and Williamson, B.P. "The Effect of Lubricant Rheology on the Performance of Journal Bearings", ASLE Trans. 29, (1986), pp. 52-60.
10. Bates, J.W., Williamson, B.P., Spearot, J.F. and Murphy, C.K. "The Importance of Oil Elasticity", Ind. Lub. and Trib. 40, (1988), pp. 4-19.
11. Georges, J.M., Millot, S., Loubet, J.L. and Tonck, A. "Drainage of Thin Liquid Films Between Relatively Smooth Surfaces", J. Chem. Phys. 98, (1993), pp. 7345-7360.
12. Cann, P.M. and Spikes, H.A. "The Behavior of Polymer Solutions in Concentrated Contacts: Immobile Surface Layer Formation." Trib. Trans. 37, (1994), pp. 580-586.
13. Smeeth, M., Gunsel, S. and Spikes, H.A. "The Formation of Viscous Surface Films by Polymer Solutions: Boundary or Elastohydrodynamic Lubrication", Trib. Trans. 39, (1996), pp. 237-241.
14. Georges, E., Georges, J-M., Diraison, C. "Rheology of Copolymer Layers Adsorbed on Solid Surfaces", STLE Preprint, TC-3C-2, presented at ASME/STLE Meeting, Orlando, Oct. 1995.
15. *Ball Bearing Lubrication: the Elastohydrodynamics of Elliptical Contacts*, 1981, Hamrock, B.T. and Dowson, D. Publ. J. Wiley, New York.

- 16 Johnston, G.J., Wayte, R. and Spikes, H.A. "The Measurement and Study of Very Thin Lubricant Films in Concentrated Contacts." *Trib. Trans.* 34, (1991), pp. 187-94.
- 17 Mitsui, H. and Spikes, H.A. "Predicting EHD Film Thickness of Lubricant Polymer Solutions", paper to be presented at World Tribology Congress, September 1997 and submitted to STLE.
18. *Solid/Liquid Dispersions*, 1987, ed. Th. F. Tadros, Chapter 6, "Adsorption of Polymers at the Solid/Liquid Interface", T Cosgrove, Publ. Academic Press, London.
19. Allain, C., Ausserre, D. and Rondelez, F. "Direct Observation of Interfacial Depletion Layers in Polymer Solutions", *Phys. Rev. Lett.* 49, (1982), pp. 1694-1697.
20. Yoshida, K., Hosonuma, K. and Sakurai, T. "Behaviour of Polymer-Thickened Oils in Lubricated Concentrated Contacts", *Wear* 98, (1984), pp. 63-78.

## The Role of Boundary Lubrication in Scuffing Reactions

R.J. Smalley<sup>1</sup> and A. Cameron<sup>2</sup>

<sup>1</sup>SKF Engineering and Research Centre B.V., Postbus 2350, 3430 DT Nieuwegein, The Netherlands.

<sup>2</sup>Visiting Professor, Anglia Polytechnic University, Victoria Road S., Chelmsford, Essex CM1 1LL, UK.

*In this paper the role of the development of the boundary lubricant as a function of surface roughness is covered and its effect on the scuffing reaction between hardened steel and a relatively soft, scuffing susceptible brass material investigated. The surface roughness of the hardened material plays a dominant role due to its effect on oil film collapse.*

### INTRODUCTION

The dominant role of boundary lubrication in the protection of practical sliding surfaces has been exhaustively demonstrated. A good review has been made by Ludema [1].

It is generally accepted that the dominant feature of this type of lubrication is that polar molecules are attached to the surface. At lower temperatures these are, to a great extent, absorbed reversibly. This can be regarded as physical attachment which is easily broken by sliding contact though the contacts are readily reformed. At higher temperatures some compounds are found to be irreversibly attached and can only be removed by, for example mechanical action. In this case components of the surface take part in the reaction giving rise to oxide components or with the oil components to "organo-metallic compounds". A definition of boundary lubrication, taking into account thermodynamically reversible as well as irreversible attachment was proposed at the NSF/NIST 1st. American Limits of Lubrication conference at Williamsburg, (April 1996. Submitted to Tribology Letters)

Various techniques are available for the detection of the physically and chemically adhered layers. Those used at our laboratories include both a high frequency capacitance technique and a resistance method developed by Furey [2] and Lunn [3]. Both methods are elegant means of demonstrating the build up of the physically and chemically reacted

film. Full quantitative analysis of the film by the resistance approach is not possible though it has been found to be very sensitive to temperature changes and is mainly used to detect the temperature zones at which various boundary film reactions occur. A qualitative approach has been utilised in this work based on a resistance technique to determine the extent to which an electrically resistant surface separating film occurs under quasi-static temperature conditions. This present paper reviews work carried out to determine the effect of the build-up of the boundary oil film and its subsequent breakdown under increasing load and temperature development.

### EXPERIMENTAL

Two apparatuses have been utilised in this investigation. The first, the Mills-Cameron reciprocating rig [4] is a block on plate configuration and the second a partially conforming block on ring. In the first rig, the normally used ball on plate has been modified to accommodate the block specimen. This rig had been developed for the study of the build-up and subsequent breakdown of additive films as a function of temperature. The second apparatus was specifically directed at the solution of pure sliding problems. Diagrams of the two apparatuses are shown in Figs. 1 and 2.

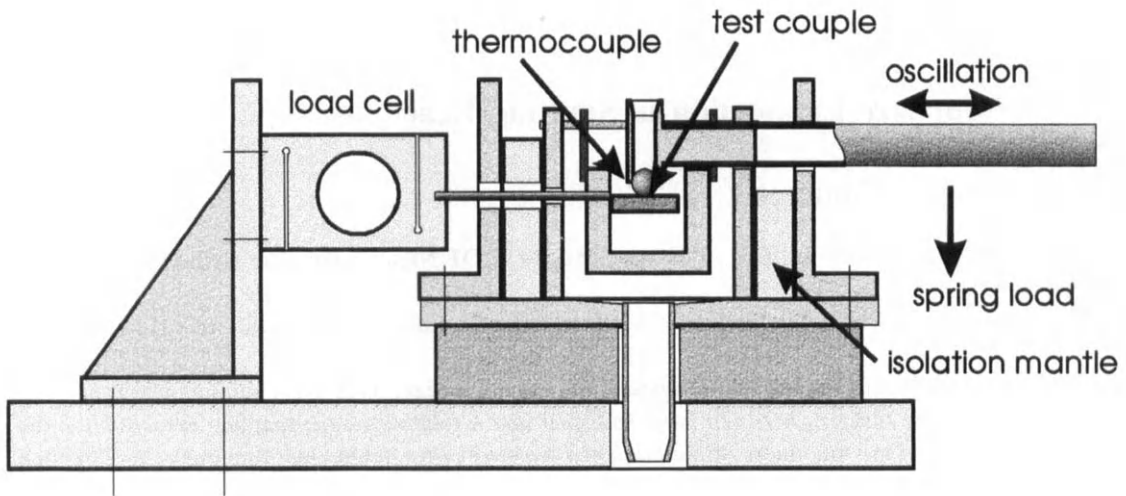


Fig. 1 Mills-Cameron oscillating rig

**Reciprocating rig**

In its standard form, a loaded 6 mm steel ball is reciprocated linearly against a stationary flat metal specimen. In the modified form used here, the ball is replaced by a brass sample as shown in Fig. 3. The progression of the formation and breakdown of the surface films is monitored by low voltage resistance measurements. The contact between the components acts as one side of a voltage dividing circuit. Zero resistance shows metal-metal contact while high resistance values  $> 1 \text{ M}\Omega$  indicate open circuit by the formation of a non-conducting film. The applied voltage is 15 mV which is stated in the literature as not influencing the formation of films or oxides by the presence of electrical fields or by discharge through the oil film. Some doubt has been expressed that this is indeed the case though the quoted work by Furey [2] demonstrated that no effect on the measured resistance values was found up to an applied voltage of 1500 mV. Oil was supplied to the contact zone by a syringe keeping the area flooded. Controlled heating was applied to the sample chamber by a variable temperature air stream. The standard testing temperature range of 20-200 °C is sufficient to cover the various boundary film reaction zones.

For the second apparatus, a partially conforming

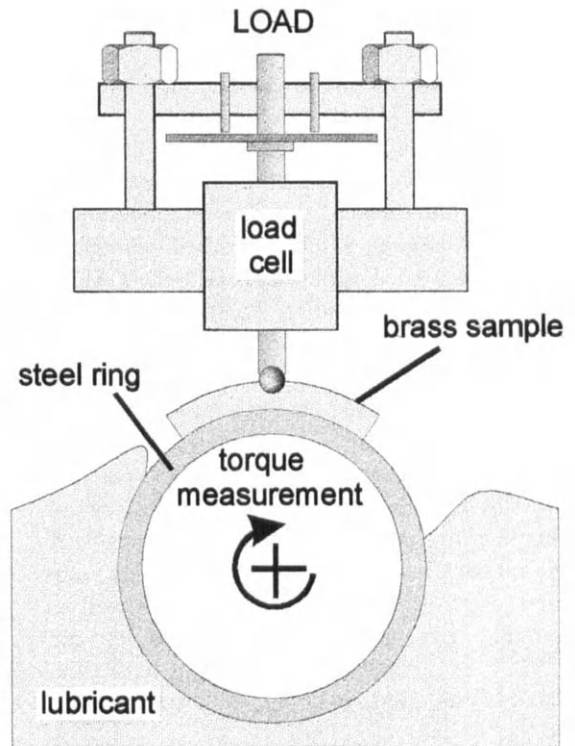


Fig. 2 Block on ring apparatus

line contact was used. This reduces the contact

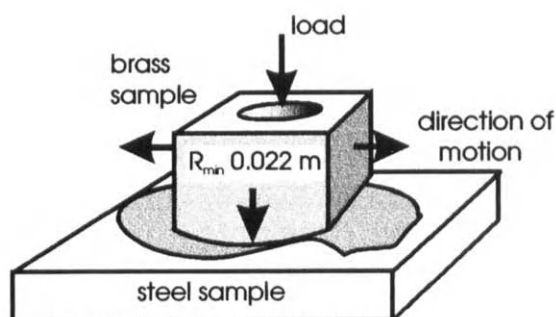


Fig. 3 Brass block on plate configuration

pressure from the GPa range down to 5-30 MPa.

#### Formation of boundary films

The lubricant used in these studies was a standard turbine oil (Mobil DTE light). This class of oil is formulated from high stability base stocks with only the addition of oxidation inhibitors to provide resistance to high temperature degradation. They are general purpose industrial lubrication oils, used for example in the papermaking industry. These will initially act as normal boundary lubricants at medium temperatures, and as the temperature rises react to give higher strength boundary films.

In this part of the work the effect of changing the surface roughness and the orientation of the grinding pattern on the build-up of the protective film was investigated.

The sample couple used was a hardened 52100 steel plate as the stationary member and a CuZn38Pb2 brass reciprocating curved block.

Three sample configurations were tested. In the first, both the brass block and the steel plate were polished to Ra value of  $0.05 \mu\text{m}$ . In the second and third tests the polished brass block was retained, but was loaded against a ground version of the steel plate. The grinding direction was a./ parallel and b./ transverse to the oscillating direction. The roughness values of the steel plate transverse to the grinding direction were as follows: while a topographical plot is given in Fig. 4.

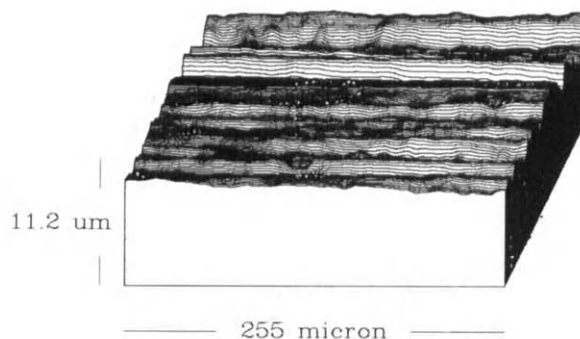


Fig. 4 Topographical plot of ground steel surface

|           |                      |
|-----------|----------------------|
| Ra        | 0.29 $\mu\text{m}$ . |
| Skew      | -0.55                |
| RMS slope | 7.7°                 |

A resistance plot for the first testing configuration is shown in Fig. 5 where the temperature range was from 20-200 °C. Three distinct zones can be detected as shown schematically in the lower diagram. It is suggested that the following mechanisms can be demonstrated. The first zone indicates the development of the hydrodynamic oil film and its subsequent breakdown at 70 °C. This can be attributed to loss of the hydrodynamic film due to viscosity reduction. The second zone develops from 90 to 170 °C. and is a combined competing process of physical absorption up to 120 °C and desorption above this temperature where the mechanical action of the oscillating contact plays a dominant role. It is suggested that two separate reaction constants are applicable to the total physical absorption process. This concept has been demonstrated by Cheng [5]. Chemical reaction of the surface to form organometallics becomes the dominant reaction above 140 °C on both surfaces. It is significant that the physically absorbed film is weaker than either the hydrodynamic or the chemically reacted film as demonstrated by the nature of the trace in the original resistance graph, Fig. 5.

The influence of ground surfaces can have a drastic effect on the formation of boundary films as shown in Fig. 6. Identically ground samples of hardened

Reaction characteristics of brass in  
contact with hardened 52100 steel.  
Lubricant: DTE light.

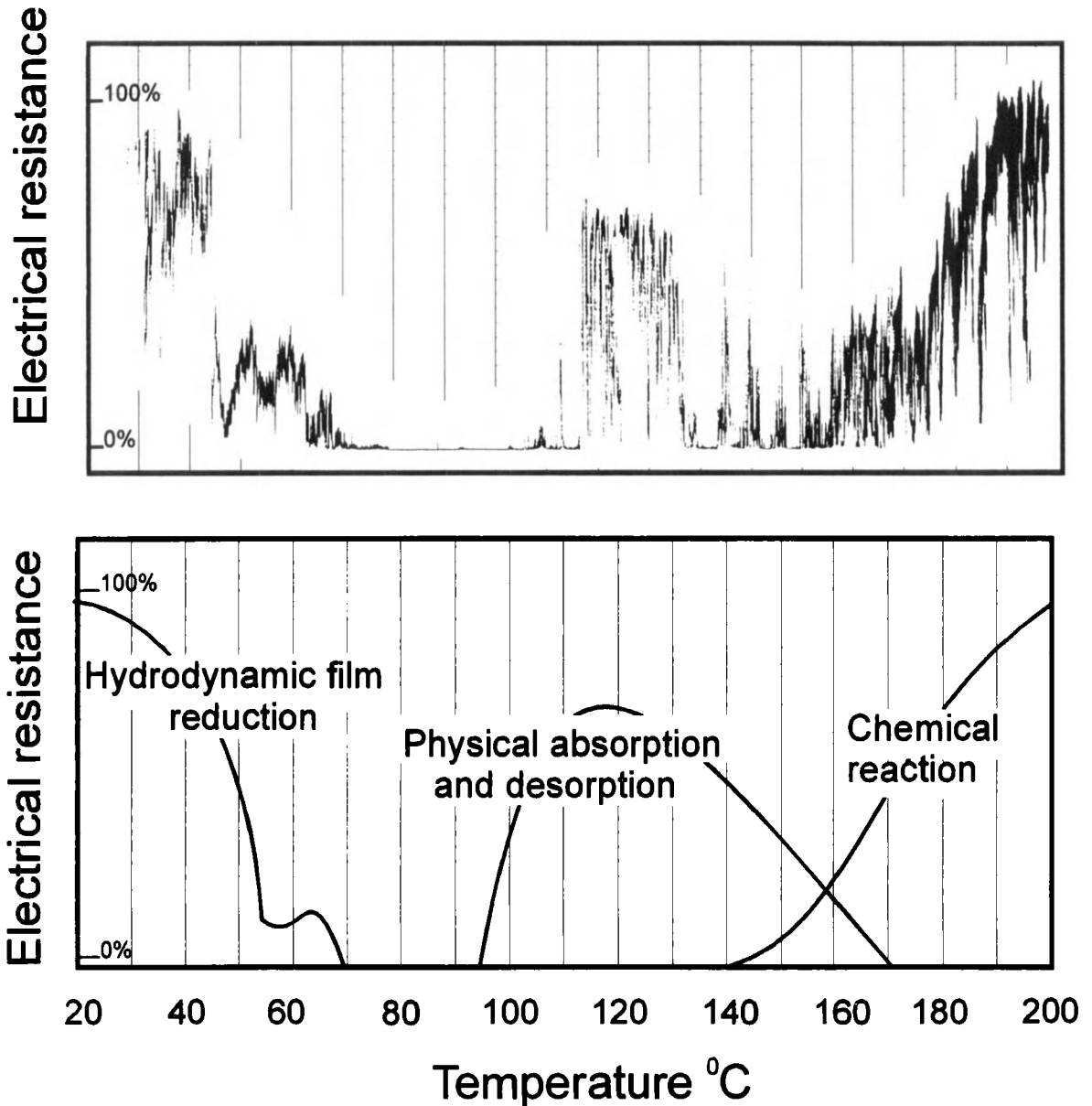


Fig. 5 Proposed model for formation of surface films detected by electrical resistance technique.



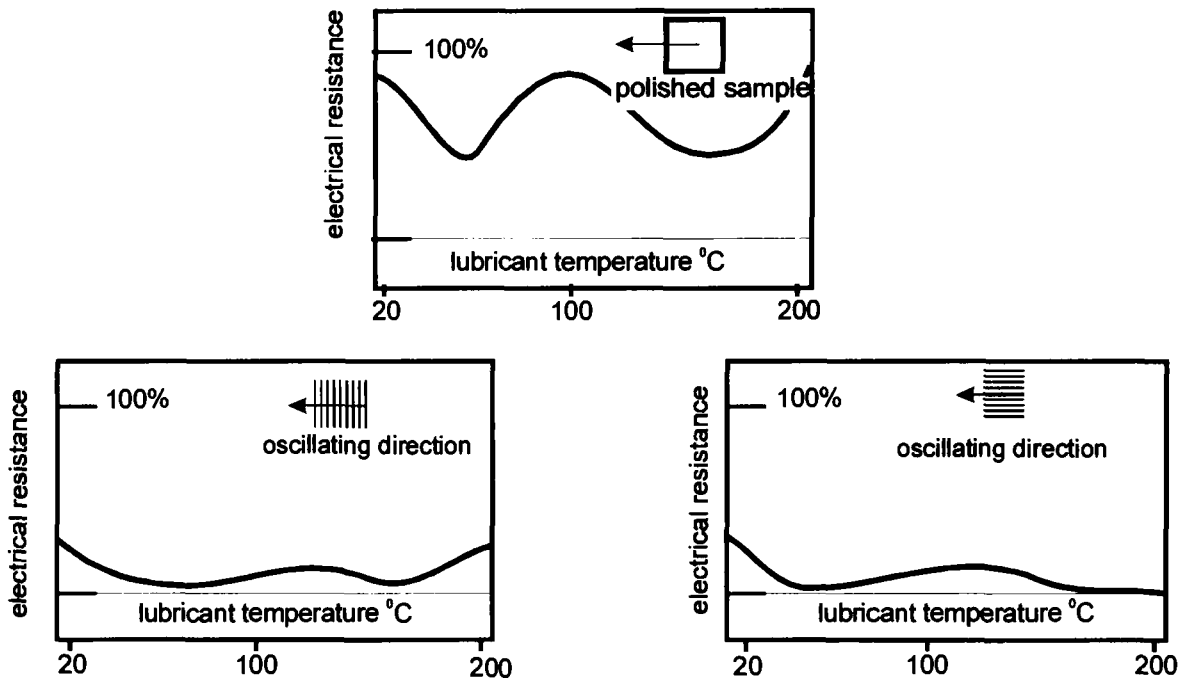


Fig. 6 Effect of grinding direction on build up of surface films.

52100 steel were used in both the parallel and perpendicular direction against the oscillating polished brass sample ( $R_a$  0.08  $\mu\text{m}$ ). A drastic reduction in the boundary film formation occurred. The effect was most pronounced when the grinding direction was parallel to the oscillating direction. In this case the pressure on the asperities was sufficient to cause complete suppression of the organometallic film formation, due to the competing effect of mechanical abrasion. Although when oscillation occurred perpendicular to the grinding direction the organo-metallic reaction in the third stage was reduced, it was not completely absent. In this configuration oil resident in the roughness channels may have been sufficient to provide a reservoir, though straightforward thermodynamic effects are not excluded.

#### Material evaluation under sliding conditions

To evaluate the scuffing susceptibility under full sliding conditions, use was made of the block on

ring rig shown in Fig. 2. The sample configuration was a brass ring segment loaded against the outer diameter of a hardened 52100 steel ring (diameter 83.5 mm). To facilitate optimum hydrodynamic film formation, the non-conforming diameter of the brass contacting surface had a diameter difference of 100  $\mu\text{m}$ . This clearance was arrived at as a result of numerous tests. To reduce the incidence of line contact a four pad contacting pattern was used, each pad having the dimensions 4 x 8 mm. Loading of the sample was made through a centrally located ball so allowing full alignment of the block on the ring. The loading cycle was applied through a servo controlled air pressure cylinder directly controlled by a PC. Measurement of the load was made using a load cell directly connected in the loading shaft. The resulting transverse load on the sample couple was taken from a torque cell located in the ring driving shaft. Fully flooded lubrication was ensured by running the ring in an oil bath, the temperature being

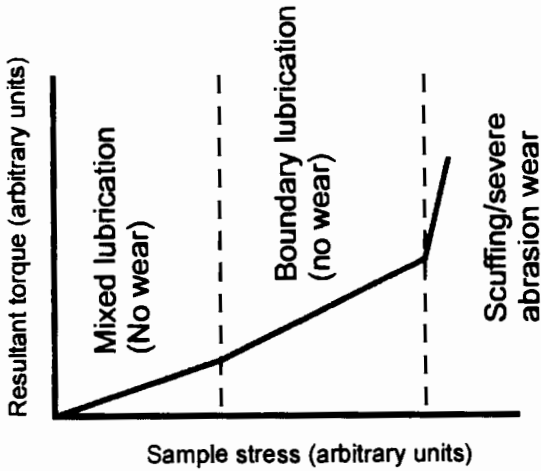


Fig. 7 Typical load/torque graph.

measured directly in the inlet zone.

A typical load/torque graph is shown in Fig. 7 where three distinct zones are detected: firstly the initial mixed lubrication, secondly the physical absorption zone and thirdly "chemical" boundary lubrication leading to catastrophic wear. This depended on the surface roughness and resulted either in strong laminated abrasion wear or in severe scuffing. The progression of the reaction curves as a function of temperature is shown in Fig. 8. The sharp transition between the boundary lubrication zone and catastrophic failure was found to be strongly temperature dependent and to be strongly pronounced above 45 °C bulk oil temperature. This suggests that the gap between zero hydrodynamic lubrication and severe wear/scuffing is filled by physical absorption type boundary lubrication.

**Conclusions**

This work confirms the known fact that asperity contact formed from grinding can negatively

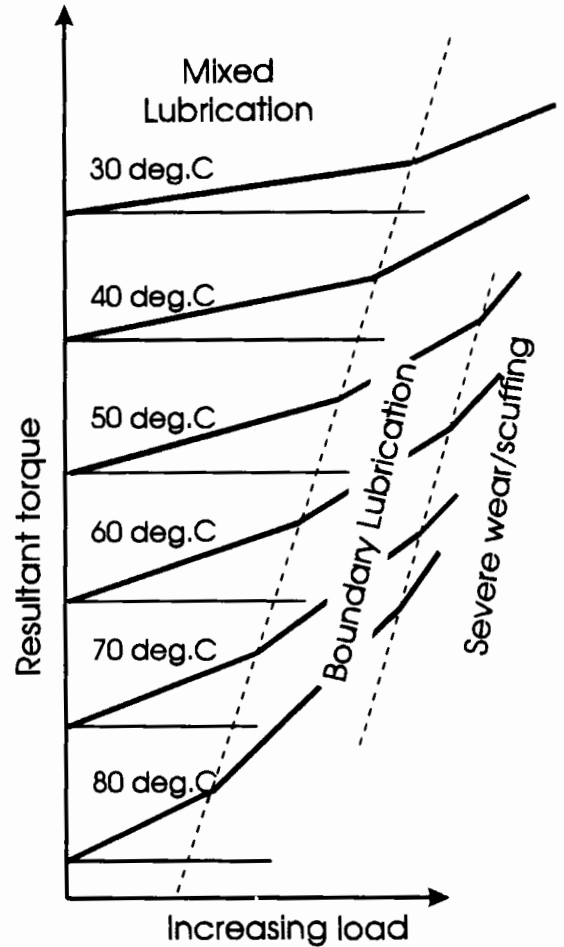


Fig. 8 Effect of temperature on load/torque curves.

influence and even suppress organometallic film formation.

The application of the reciprocating rig is paralleled by testing on the block on ring apparatus.

In contrast to the known steel-steel contacts the physical strength of boundary films formed on brass are at a lower level and easily damaged.

Development of the reciprocating technique will be necessary to cover those areas where partial hydrodynamic lubrication plays a major role. This effect has been highlighted by the present work using brass-steel contacts.

### **Acknowledgement**

The authors would like to thank Dr. E. Ioannides, Director of Product Research of SKF Engineering & Research Centre for permission to publish this work.

### **References**

1. Ludema K.C. "Lubricated Sliding-A Review of Chemical and Physical Effects". Lubricants and Lubrication. D. Dowson et al. (Editors). 1995 Elsevier Science B.V.
2. Furey M.J. "Metallic Contact and Friction between Sliding Surfaces". ASLE Trans 4, 1-11 (1961).
3. Lunn B. "Epilamen-und Mischreibung aus der Sicht de Metallkundlers". VDI-Berichte Bd. 20, 1957.
4. Mills T.N. and Cameron A. "Basic Studies on Boundary, EP, and Piston-Ring Lubrication Using a Special Apparatus". ASLE Trans. 25, 1, 117-124.
5. Cheng H.S. "Modelling of Scuffing Failure in Mixed Lubrication". 1st. Int. Symposium on Tribology, Beijing. Oct. 18-23 1993.

## MODELLING NON-STEADY EHL WITH FOCUS ON LUBRICANT DENSITY

Erik Höglund and Roland Larsson

Division of Machine Elements, Luleå University of Technology, S-971 87 Luleå, Sweden

A pressure increase has an effect on several physical and rheological properties such as, e.g., viscosity and density in an ehl contact. Results from dynamic dilatometry measurements, using a split-Hopkinson bar test rig, and the Roeland viscosity-pressure relation have been introduced into the governing equations for EHL pressure and oil film thickness. 5P4E shows a relatively stiffer behaviour than given by the conventionally used Dowson-Higginson equation whereas PAO shows a weaker behaviour. This difference results in different pressure and film thickness profiles. The stiffer 5P4E gives a slightly higher first pressure maximum and a considerably higher pressure spike approaching that of an incompressible fluid. The corresponding central film thickness is higher for 5P4E whereas the minimum film thickness is more or less the same in the two cases. The difference in pressure profiles leads to different von Mises sub-surface stress mainly just below the surface at the location of the pressure spike.

### 1. INTRODUCTION

This is a paper on the modelling of elastohydrodynamic lubrication during non-steady conditions. It comprises a literature review on the subject and also an experimental and theoretical investigation of how lubricant compressibility varies with pressure and how this influences on the conditions in the ehl contact.

### 2. BACKGROUND

The vast majority of ehl investigations utilise the assumption of a steady state, i.e. constant load, velocity, geometry, temperature etc. The lubricant is, however, in conditions that are far from those of steady state. The normal contact time in a rolling element bearing or in a gear is of the order of one thousandth of a second and the pressure will be elevated from ambient to 1-2 GPa in that time. The lubricant will also be subjected to very high shear rates during the short contact period.

Many components operate with varying load, velocity and geometry. To predict the operation of these components it is necessary to consider these transient effects.

Components such as gears, cams and followers, reciprocating seals and engine bearings are typical examples of elastohydrodynamically lubricated contacts that are subjected to transient conditions.

The meshing teeth in a gear are subjected to varying load, rolling/sliding velocities and radii of curvature. The load varies since the total load is sometimes

carried by one pair of gear teeth and sometimes by two pairs. The load may also vary due to dynamic effects such as overall gear vibrations or pitch errors. The gear teeth in action are rolling and sliding toward each other and the velocities and the degree of slip vary along the line of action. Even the shape of the gear teeth varies along the line of action.

The cam and follower of an automobile valve train experience the same problems as the gear. Load, velocities and geometry change during the operating cycle. The load varies due to dynamic forces coming from the reciprocating movement of the follower. The radius of the cam varies in order to obtain the correct valve lift characteristics and the sliding velocity between the cam and the follower may cease and change direction. When the sliding velocity approaches zero, i.e. when lubricant entrainment ceases, the separation of the surfaces has to be accomplished by pure squeeze action.

A reciprocating seal is also subjected to a change in direction of the relative motion of the surfaces. During the reversal of entrainment there is no other lubricating effect apart from the squeeze action.

Connecting rod bearings in an internal combustion engine are conformal, hydrodynamically lubricated bearings, but analysis of these usually has to be transient and elastohydrodynamic. The variation of load is rapid and the load is high enough to give significant deformation of the bearing surfaces.

A steady loaded rolling element bearing at constant rotational speed is also an example of transient loading. The roller or the ball moves into a converging gap

between the outer and inner races as it enters the loaded zone and the load starts to increase. A few moments later it comes out from the loaded zone again and the contacts between the rolling element and the races never met a constant load.

There are also other applications where time dependency is important. In the study of ehl there is growing interest in the effects of surface roughness and particle entrainment. The assumption of smooth surfaces is, of course, a simplification as the surface roughness height is of the same order of magnitude as the lubricant film thickness. When two rough surfaces come into contact there is squeeze action between the asperities. The surface texture changes all the time so there is a non-steady state at the asperity level. Particles, in the form of wear debris or dirt, give the same effect. The flow of particles into and around the lubricated conjunction makes the lubricant entrainment fluctuate.

Lubricant properties that are not normally considered in the ehl analysis may be important at very rapid lubrication processes. If the load is suddenly increased it takes some time for the molecules to orient to their new positions. That means that it takes some time for the lubricant to relax to its new viscosity and density. This relaxation time can be important if load or some other operating condition varies significantly during that period.

The fluid inertia is the final example of effects that are dependent on time. The fluid inertia forces are normally very small in comparison with the viscous forces but when dynamics are considered they become more important. If effects such as surface roughness and particles also are introduced into the analysis it becomes even more interesting. A small lubricant element that flows between two rough surfaces has to change its flow direction all the time and it might be questionable to neglect inertia forces in the determination of the flow pattern.

### 2.1. The squeeze effect

The main difference between steady and non-steady conditions is the effect of squeezing the lubricant through narrow passages (constrictions). The lubricated surfaces will approach or recede from each other if there is a rapid change of load, rolling/sliding velocity or geometry. If the surfaces approach each other, the excess lubricant has to be squeezed out from the contact region. The lubricant cannot leave the contact infinitely

fast due to the viscosity induced flow resistance of the lubricant. The pressure will then increase to overcome this resistance which will increase the viscosity even more. As the pressure increases the load carrying capacity also increases and prevents the surfaces from coming into direct contact. This effect is called the squeeze effect. When the surfaces recede from each other the opposite happens. More lubricant must flow into the contact region but it cannot be supplied fast enough and the pressure falls. If the negative squeeze is large, the pressure may fall to zero and the lubricant film cavitates.

The squeeze effect gives rise to a force that opposes all motion and which can thus be seen as a viscous damping effect.

## 3. TRANSIENT EHL - A LITERATURE REVIEW

Christensen [1] was 1962 one of the first to consider squeeze action in a theoretical ehl analysis. He studied the motion of two infinitely long cylinders in normal approach. He solved the Reynolds equation and obtained pressure distributions and load carrying capacities for squeeze films. He showed that very high pressures developed in the lubricant film. The pressure at the contact centre could exceed the corresponding maximum Hertzian pressure. He also discovered that the minimum film thickness does not occur at the contact centre but at the edges of the contact. Instead, a lubricant entrapment, the characteristic dimple, developed at the contact centre.

In the experimental part of [1] Christensen presented the results of a ball drop experiment. Balls impacted lubricated and dry surfaces. The contact pressure increased as the drop height increased and gave a permanent deformation at a certain drop height. The deformation was found to be deeper if the surface had been lubricated than if it had been dry. The theoretical finding of higher pressure in the lubricated case was thus confirmed. Similar results had been found by Rabinowicz [2] in the 1940's.

Experimental evidence of the existence of a lubricant entrapment was given by Dowson and Jones [3] 1967. They utilised optical interferometry to measure the deformed shapes of a ball's and a glass disc's surfaces when the ball impacted the lubricated glass disc.

Christensen continued to study squeeze problems and in 1970 he presented an analysis of two spherical bodies in normal approach [4]. The results once again

showed that the pressure could reach levels higher than in a corresponding non-lubricated case. In the same year, Herrebrugh [5] presented an analysis of two cylinders in normal approach.

Further steps towards understanding of pure squeeze action were taken by Lee and Cheng [6] 1973 and by Conway and Lee [7] 1975. They did not use the assumption of constant approach velocity which Christensen and Herrebrugh had used, but they solved the equation of motion to obtain the true normal approach velocity. They did not, however, consider elastic deformation in their analyses.

A very interesting experiment was carried out by Safa and Gohar 1986 [8]. They used thin film transducers to measure the pressure distribution in the contact between an impacting ball and a lubricated flat surface. They found clear evidence for a secondary pressure peak at the very end of the total impact time.

A full transient ehl analysis of the ball impacting problem was not given until 1991 when Yang and Wen [9] solved the first 1/3 of the impact. Larsson and Höglund [10,11] later gave the full transient solution of Reynolds equation while ball inertia was considered by a simultaneous solution of the ball's equation of motion. The experimental results of Safa and Gohar [8] were confirmed and there was a good correspondence between experiments and theory. At the same time, Dowson and Wang [12,13] presented results from a similar theoretical investigation. In 1995, Larsson and Lundberg [14], presented an experimental film thickness measurement in a contact between an impacting steel ball and a lubricated glass disk. The effects of impact velocity and lubricant viscosity were studied.

There is a combination of squeeze and entraining motions in most of the practical applications of transient ehl. Investigations, both theoretical and experimental, are rather few. In 1971 Vichard [15] made one of the first transient ehl analyses which could be applied to gears. He utilised a Grubin type of approximation and was able to calculate the minimum film thickness for the case of a sinusoidal load. There was also an experimental part of his paper where a capacitive transducer was used to measure film thickness between a rotating eccentric disc and a flat surface. Ten years later, in 1981, Wang and Cheng [16,17] applied Vichard's analysis on gears and their papers give a comprehensive investigation of film thickness, temperature and load in spur gear transmissions. Another full transient ehl analysis of a spur gear contact was pre-

sented by Hua et. al. 1991 [18]. This analysis was later, in 1995, extended by Hua and Khonsari [19] who studied the effects of different gear parameters on film thickness and contact pressure. A full transient ehl analysis of a spur gear was presented by Larsson [20]. One additional effect, a non-Newtonian lubricant, had been incorporated in the model. Larsson showed that transient variations in load may influence the minimum film thickness much more than static load variations do. In fact, the film thickness actually increased as the load was increased transiently. Scales et. al. [21] obtained the same results in their analysis of a spur gear.

Cams and followers have been studied by e.g. Dowson et. al. [22] who in 1992 presented a transient analysis of such a system. A quasi-static assumption had been used in earlier investigations. This assumption leads to the erroneous prediction of zero film thickness at the reversal of lubrication entrainment. This reversal of entrainment has been investigated by Hooke [23,24] and he presented design charts to determine minimum film thickness when the entraining velocity ceases and changes direction. A sudden change in rolling velocity, both in magnitude and direction, was also investigated by Scales et. al. [21]. It was found, both theoretically and experimentally, that the minimum film thickness never falls to zero even if the entraining direction changes.

Other more general theoretical transient ehl analyses have been presented by Hamrock et. al. [25,26,27], by Bedewi et. al. [28] and by Yang and Wen [29].

Film thickness measurements in dynamically loaded contacts are rare but, in 1991, Ren et. al. [30] used a high-speed film camera to study the contact between a rolling ball and a lubricated glass disc, while the ball was subjected to a harmonically varying load. They showed that the minimum film thickness occurred at the outlet of the contact and that a central dimple occurs even if rolling is superimposed.

Some very interesting applications of experimental transient ehl can be found in the study of lubricants and their properties. In 1972, Paul and Cameron [31] presented the impact viscometer. A ball impacts a lubricated transparent surface and the film thickness between the ball and the flat surface is measured by means of optical interferometry. The pressure field was derived from the elastic distortion. The density in the contact was found from refractive index measurements. Since film thickness, pressure and density were known, Reynolds equation could be used to obtain the viscos-

ity distribution in the contact. The impact viscometer has recently been further developed in Hong-Kong by Wong et. al. [32,33].

The jumping-ball apparatus is another example where transient ehl has been used to investigate lubricants. A ball was guided as it fell without rotation until it impacted a flat lubricated surface. The angle of impact was adjusted until the ball achieved pure rolling as it rebounded from the surface. A study of the motion after impact enabled the limiting shear strength of the lubricant to be determined. This technique was presented in 1985 by Jacobson [34]. It was later improved with an optical measuring system, see Höglund [35].

A comprehensive study of lubrication at combined squeeze and sliding motions has been carried out by Lundberg et. al. [36-40]. In their apparatus a rotating roller impacted a lubricated ball. The presence of metal-to-metal contact between the roller and the ball was detected electrically. They found that lubricant film breakdown was always initialised at the end of the impact time, and not when the impact force reached its maximum. They also found that the risk for lubricant film failure increased if the sliding velocity increased. This phenomena contradicts elastohydrodynamic theory and is still not fully understood.

Ramesh and his co-workers [41,42] also revealed lubricant properties by using impacts. They used the Kolsky bar technique. The lubricant sample was compressed between two bars by giving one of them an impact. The strain waves in the bars were measured and this enabled the derivation of density and limiting shear strength.

The effect of surface roughness on film formation has been studied intensively during recent years. Greenwood and Morales Espejel [43] and Venner and Lubrecht [44,45] have all utilised transient ehl in the study of rough surfaces. Venner and Lubrecht have also improved the numerical technique to solve such problems.

Among the many parameters influencing film thickness and friction in transient ehl this paper will from now-on focus on density.

#### 4. LUBRICANT PROPERTIES

To calculate film thickness, pressure distribution and friction in ehl it is necessary to know the viscosity, compressibility and density of the lubricant and how

they are affected by pressure, temperature and loading rate. Several investigations have been performed concerning the compressibility of lubricants, however, most of these investigations have been made under static conditions, i.e. no influence of temperature gradients and loading-unloading time is included. In a real lubricated contact, the loading-unloading cycle is usually transient. In for example a bearing or a gear, pressures often reach several GPa and the loading-unloading time is a few hundred microseconds.

##### 4.1 Dilatation and density

Dilatation or relative change in volume, is defined as

$$\frac{\Delta V}{V_0} \quad (1)$$

For lubricating oils it has been measured statically up to 400 MPa, Dowson and Higginson [46], and to 2.2 GPa, Hamrock et.al. [47]. Several other authors have also presented static dilatometry measurements, e.g., Jacobson-Vinet [48] and Alsaad et.al. [52]. In a real ehl contact however the loading cycle is usually very short which affects the dilatation's and density's dependence on pressure. At short loading times the temperature rise due to adiabatic compression may make the dilatation-pressure relation weaker and the density increase lower than in an isothermal case. Ramesh [42] and Feng and Ramesh [41] performed transient measurements under conditions with shorter loading times, 1-10  $\mu$ s, compared to a real conjunction. At static measurements there is a significant change in behaviour, a phase transition, at a certain pressure, Hamrock et.al [47]. This phase transition may occur also in dynamic measurements but it is not obvious at what pressure it will occur.

Based on transient measurements up to 5 GPa Ramesh [42] and Feng and Ramesh [41] suggested the following relationship between dilatation and pressure:

$$p = \frac{K\{1 - V / V_0\}}{[1 + a\{V / V_0 - 1\}^2]} \quad (2)$$

Their measurements gave one point per "shot" for the compressibility, so a lot of experiments had to be made before a tendency could be seen.

Density can be derived directly from the dilatation by assuming constant mass. The most well known den-

sity-pressure relationship is the one of Dowson and Higginson [46], Eq. (2).

$$\frac{\rho}{\rho_0} = 1 + \frac{0.6p}{1 + 1.7p} \quad (3)$$

#### 4.2 Split-Hopkinson bar test rig

Below a new way of measuring the dilatation, and the density's dependence on pressure at transient loading is presented.

A modified split-Hopkinson pressure bar set-up is used to determine the dilatation (relative volume change)-pressure relation of lubricants. The set-up makes it possible to test oils and greases under conditions similar to those found in a real ehl contact; loading-unloading times of 100 and 300  $\mu$ s respectively and pressures up to 1.9 GPa.

A schematic picture of the experimental set-up can be seen in Fig. 1. Details can be found in Lindqvist et al. [49].

The tested lubricant is confined in a cylindrical hole ( $\varnothing$ 8 mm) in a pre-stressed container made of cemented carbide and steel. It is pressurized by two axially movable pistons that are in contact with the two rods. The radial clearance between piston and hole is between 1 and 2  $\mu$ m thus minimizing leakage but still giving a low friction force. One of the rods is axially impacted by a projectile generating a compressive elastic wave.

Strain gauges are used to measure the strains in the rods as a function of time at two positions on each rod. One dimensional wave propagation theory is used to calculate the pressure, the dilatation and the dilatation rate at the contact between the confined oil and the piston on both sides of the oil column.

#### 4.3 Results of dilatation measurements

Data for seven tested oils are found in Table 1 and in Fig. 2 a comparison of the different dilatation-pressure curves is seen. The dependence between the different molecular structure of the oils and the dilatation-pressure relation is interesting. Long straight molecules like PAO, esters and polyglycols have a relatively weak behaviour. The molecules in a well refined mineral oil like the naphthenic or the paraffinic oils have less possibilities to adopt different kind of configurations, and the oil is therefore expected to have a stiffer behaviour. The 5P4E has the stiffest behaviour of the tested oils.

Table 1  
Properties of the tested oils.

| Type of oil or grease | Name                                       | Viscosity (20°C) [mPas] | Viscosity (40°C) [mPas] | Viscosity (70°C) [mPas] | Density (15°C) [kg/m <sup>3</sup> ] |
|-----------------------|--|-------------------------|-------------------------|-------------------------|-------------------------------------|
| Mineral oil           | Naphthenic base oil                        | 66                      | 24                      | 7.5                     | 894                                 |
| Mineral oil           | Paraffinic base oil                        | 71                      | 29                      |                         | 870                                 |
| Synthetic oil         | Polyphenyl Ether 5P4E                      | 4400                    | 385                     |                         | 900                                 |
| Synthetic oil         | Polyalphaolefin PAO base oil               | 85                      | 36                      | 14                      | 829                                 |
| Synthetic oil         | Santotrac traction fluid                   | 86                      | 30                      |                         | 907                                 |
| Synthetic oil         | Rape seed oil (68%) +synthetic ester (32%) | 100                     | 46                      |                         | 926                                 |
| Synthetic oil         | Polyglycol hydraulic fluid                 | 128                     | 41                      |                         | 981                                 |

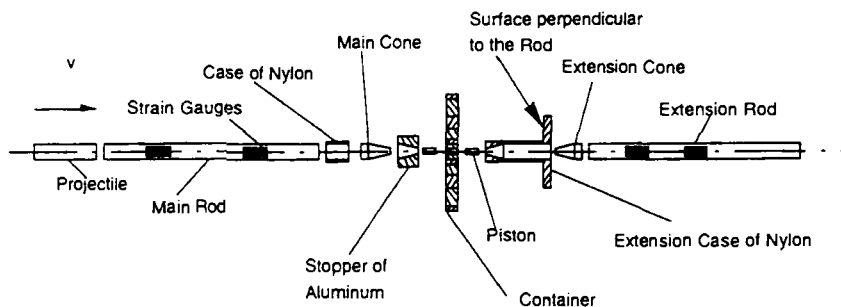


Figure 1. Blow-up picture of the mechanical parts for the experimental set-up, from Lindqvist et al. [49].



Table 2

A comparison of the Dowson and Higginson, Feng & Ramesh and present investigation expressions for both the dilatation-pressure relation and the density-pressure relation.

|                       | Pressure-dilatation relation   | Pressure-density relation   | Type of oil and Constants:   |
|-----------------------|--|---|--|
| Dowson & Higginson    | $p = \frac{\frac{\Delta V}{V_0}}{0.6 - 2.3 \frac{\Delta V}{V_0}}$                | $\frac{\rho}{\rho_0} = 1 + \frac{0.6p}{1 + 1.7p}$   | Mineral oil:<br>(Shell HVI650)   |
| Feng & Ramesh         | $p = \frac{K\{1 - V/V_0\}}{[1 + a\{V/V_0 - 1\}]^2}$                              | $\frac{\rho}{\rho_0} = \frac{1}{1 - \frac{1}{2a^2 \frac{p}{K}} \left[ 1 + 2a \frac{p}{K} - \sqrt{1 + 4 \frac{p}{K}} \right]}$ | Mineral:<br>K=1.4 [GPa]<br>a=3.5<br>Synthetic:<br>K=4.3 [GPa]<br>a=1.0 |
| Present investigation | $p = c_1 \frac{\Delta V}{V_0} + c_2 \left( \frac{\Delta V}{V_0} \right)^2 + c_3$ | $\frac{\rho}{\rho_0} = \frac{1}{1 + \frac{c_1}{2c_2} \left[ 1 + s \sqrt{1 + \frac{4c_2(p - c_3)}{c_1^2}} \right]}$            | See table 3.   |

[41] equations. Eq. (4) is more adopted to different kinds of lubricants under more ehl-like conditions. The equation has been rewritten as a new density-pressure model for the ehl calculations presented below. In Table 2 and Fig. 3 a comparison between the three models can be seen.

$$\frac{\rho}{\rho_0} = \frac{1}{1 + \frac{c_1}{2c_2} \left[ 1 + s \sqrt{1 + \frac{4c_2(p - c_3)}{c_1^2}} \right]} \quad (4)$$

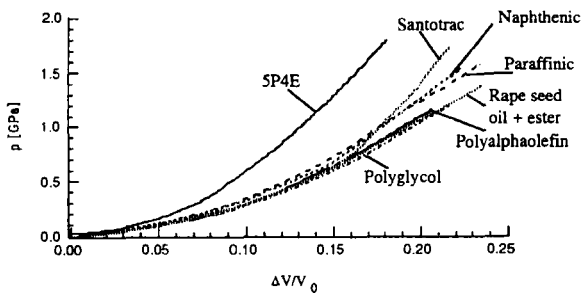


Figure 2. A comparison of measured dilatation-pressure relations for seven tested oils, from [49].

Based on the experiments an empirical equation (4) describes the density-pressure relation in a more detailed way than previously presented models like the Dowson and Higginson [46] or the Feng and Ramesh

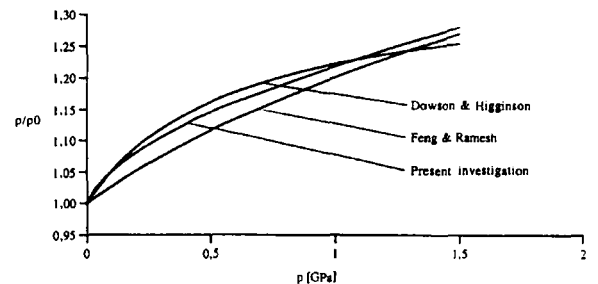


Figure 3. Relative density as a function of pressure for mineral oil.

In Table 3 the constants  $c_1$ - $c_3$  in Eq. (4) are given for the tested oils. In many cases  $c_3$  can be omitted and the density-pressure relation is sufficiently described by a second order polynomial. This is indicated by -- for  $c_3$  in Table 3.

**Table 3**  
Results of the polynomial curve fit for the constitutive constants for the seven oils.

| Type of oil or grease | Name                                  | T [°C] | Press. $p_1$ [GPa] | Press. $p_2$ [GPa] | Constants [GPa] up to pressure $p_1$ |       |       |     | Constants [GPa] between pressure $p_1$ and $p_2$ |       |       |     |
|-----------------------|---------------------------------------|--------|--------------------|--------------------|--------------------------------------|-------|-------|-----|--|-------|-------|-----|
|                       |                                       |        |                    |                    | $c_1$                                | $c_2$ | $c_3$ | $s$ | $c_1$  | $c_2$ | $c_3$ | $s$ |
| Mineral oil           | Naphthenic base oil                   | 20     | 0.5                | 1.5                | 1.0                                  | 22.4  | --    | -1  | -0.2   | 32.3  | --    | +1  |
| Mineral oil           | Paraffinic base oil                   | 20     | 1.0                |                    | 1.7                                  | 19.7  | --    | -1  |  |       |       |     |
| Synthetic oil         | Polyphenyl Ether 5P4E                 | 20     | 1.8                |                    | 1.1                                  | 49.1  | --    | -1  |  |       |       |     |
| Synthetic oil         | Polyalpha-olefin PAO base oil         | 20     | 1.2                |                    | 0.7                                  | 19.5  | --    | -1  |  |       |       |     |
| Synthetic oil         | Santotrac traction fluid              | 20     | 0.45               | 1.9                | 0.9                                  | 20.6  | --    | -1  | -16.6  | 90.7  | 1.1   | +1  |
| Mineral grease NLGI 2 | Naphthenic base oil+ Li-12-OH (13.2%) | 20     | 2.1                |                    | 0.5                                  | 33.0  | --    | -1  |  |       |       |     |
| Synthetic oil         | Polyglycol hydraulic fluid            | 20     | 1.2                |                    | 0.3                                  | 27.1  | --    | -1  |  |       |       |     |

## 5. EFFECT OF COMPRESSIBILITY IN EHL LINE CONTACTS

The effect of compressibility on ehl parameters such as film thickness and pressure spikes has been studied by several authors. Hamrock et. al. [50] studied the influence of compressibility on the pressure spike and found that an incompressible lubricant gives rise to much higher (or infinite) pressure at the pressure spike than lubricants that are compressible according to the Dowson-Higginson density-pressure relation, Eq. (2). They also showed that the minimum film thickness is not influenced by compressibility while the film thickness at the contact centre becomes somewhat smaller in case of compressible lubricants. Venner and Bos [51] did also study the effects of compressibility. They compared the incompressible lubricant with two different compressibility models, the Dowson-Higginson relation and the Jacobson-Vinet density-pressure relation [48]. The latter one implies a more compressible lubricant than described by the Dowson-Higginson relation.

The central film thickness was thus smaller in case of the Jacobson-Vinet model. They also pointed out the total dominance of Couette flow at the central region of an ehl contact. The Reynolds equation is thus reduced to:

$$\frac{\partial}{\partial x}(\rho h) \approx 0 \quad (5)$$

Since the net lubricant mass flow is approximately independent of the compressibility model, they showed that the ratio between the central film thickness using different compressibility models is the same as the inverse ratio of the densities at the centre of the contact, i.e.:

$$\frac{h_{J-V}}{h_{D-H}} = \frac{\rho_{D-H}}{\rho_{J-V}} \quad (6)$$

In this paper the ehl line contact problem is solved for two different density models. The first one, corresponding to a more compressible lubricant, such as a poly-alpha-olefin (PAO), and one corresponding to a less compressible lubricant, such as the 5P4E synthetic lubricant. Both static and transient loading are considered.

### 5.1. Modelling

The density-pressure relation for the two lubricants, is given by Eq. (4) where  $c_1=0.7$ ,  $c_2=19.5$  in case of PAO and  $c_1=1.1$ ,  $c_2=49.1$  in case of 5P4E, see Table 3. The density-pressure relations are shown in Fig. 4 together with the Dowson-Higginson relation.

The other assumptions are: pure rolling conditions, isothermal conditions, viscosity-pressure relation according to Roelands and Newtonian lubricant behaviour. The lubricants are assumed to be identical except for their different compressibility.

### 5.2. Results and discussion

Figure 5 shows a set of pressure distributions and film thickness profiles obtained from a static load ehl analysis with the two different density models. The dimensionless load is  $W=1.14 \times 10^{-4}$  and the dimensionless material parameter is  $G=4760$ . The dimensionless speed parameter,  $U$ , is varied from  $2.5 \times 10^{-11}$  to  $12.5 \times 10^{-11}$ . Steel surfaces are assumed, i.e. the maximum Hertzian pressure,  $p_H$ , is 1.2 GPa. It is seen that the compressibility has a very small effect on the minimum film thickness. The film thickness at the centre

of the contact is, however, influenced by the different compressibility models. The ratio between the central film thicknesses is constant 1.09 for all three cases and corresponds well to the proposed [45] ratio of the densities at the contact centre, Eq. (6).

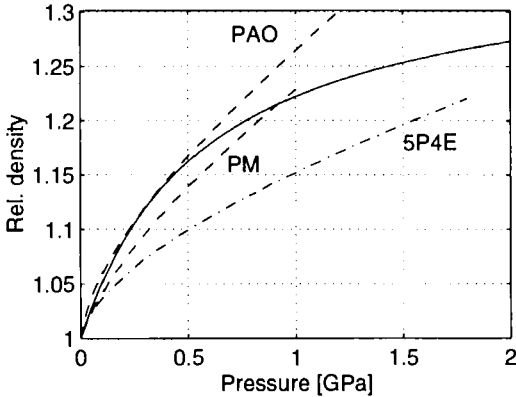


Figure 4. The Dowson-Higginson (D-H) density-pressure relation compared to density models for different lubricants, 5P4E, PAO and a paraffinic mineral oil (PM) at 20°C.

The difference in pressure is, as expected, most pronounced in the higher speed case, Fig. 5c, since the effect of a lubricant, i.e. hydrodynamic action, becomes greater as the speed (or the viscosity) increases. In all three cases it is seen that the pressure spike becomes higher for the 5P4E lubricant and the difference increases as  $U$  increases. At  $U=12.5 \times 10^{-11}$  the pressure spike amplitude is about 40 per cent higher in the 5P4E case. It is also seen that the difference in central pressure increases as the speed parameter increases. At the highest speed this difference is about 2 per cent.

The difference in pressure between the two density models influences the sub-surface stresses. Figure 6 shows the von Mises equivalent stress at the highest speed,  $U=12.5 \times 10^{-11}$ . The maximum von Mises stress is 67 per cent of the maximum Hertzian pressure ( $0.67 p_H$ ) for 5P4E and it occurs only 3 per cent of the contact semi-width ( $0.03b$ ) from the surface. For the PAO the maximum von Mises stress is  $0.50p_H$  at the same depth and it is not greater than  $0.52p_H$  within  $0 \leq z/b \leq 0.2$ . The risk of surface fatigue is thus much greater for a lubricant with low compressibility, such as the 5P4E, than for more compressible lubricants, such as the poly-alpha-olefins. Stress differences as large as in this case may change the operational life by several times.

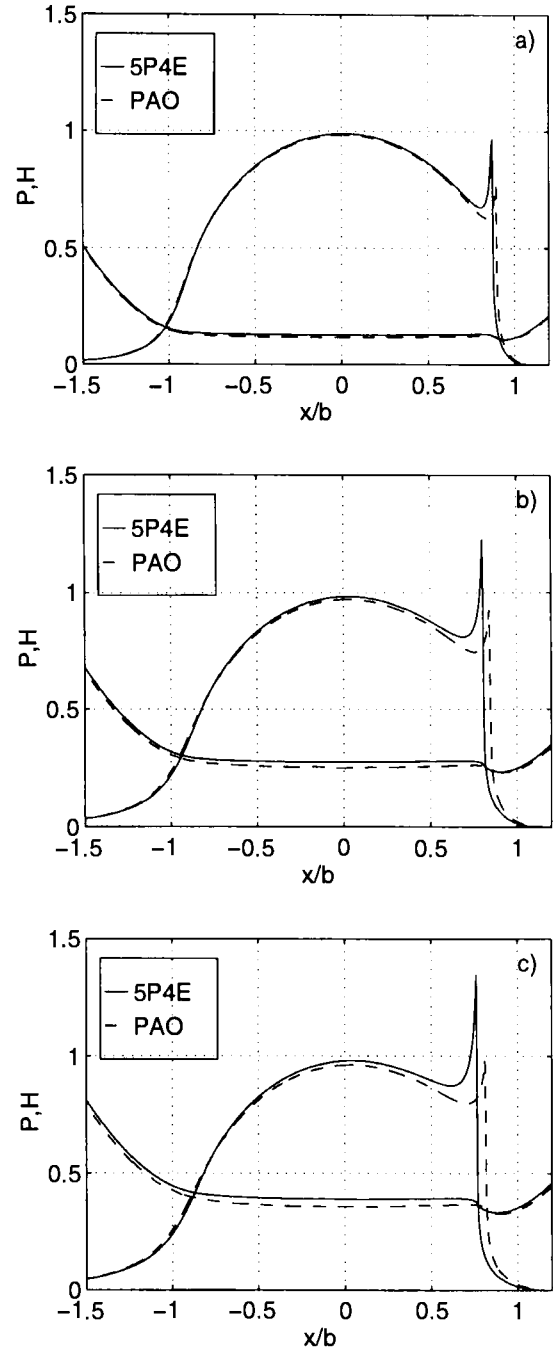


Figure 5. Pressure distributions and film thickness profiles at a)  $U=2.5 \times 10^{-11}$  b)  $U=7.5 \times 10^{-11}$  c)  $U=12.5 \times 10^{-11}$ .

One should remember that the two lubricants are the two extremes in the experiments, the most and the

least compressible, and the difference should be smaller if the PAO is compared with a paraffinic mineral oil. But the difference in operational life time, due to different compressibility only, can still be significant at certain running conditions. The effect of lubricant compressibility on sub-surface stress is largest at moderate or high load and conditions that makes the pressure distribution to deviate much from the Hertzian pressure, e.g. at high speed or high viscosity.

Since most ehl contacts are subjected to transient loads, a transient analysis is also carried out. The load is assumed to vary transiently from  $W=4.1 \times 10^{-5}$  to  $W=12.3 \times 10^{-5}$  and back again within 0.16 ms, Fig. 7a. The dimensionless speed and material parameters are held constant at  $U=2.5 \times 10^{-11}$  and  $G=4760$ . Fig. 7b shows minimum and central film thicknesses for the two different lubricants. It is again seen that the more compressible lubricant (PAO) gives smaller central film thickness while the difference in minimum film thickness is negligible. The transient character of the problem can be seen as the minimum film thickness occurs at the end of the loading cycle where the load is low and as an increasing central film thickness as the load increases and in the opposite way when the load decreases again.

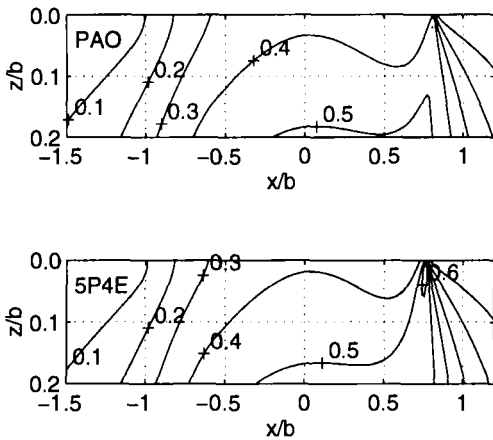


Figure 6. Sub-surface stresses,  $\sigma/p_H$ , von Mises equivalent stress, at  $U=12.5 \times 10^{-11}$ . Contour level lines at every  $0.1 p_H$ .

The maximum pressure and the pressure at the contact centre are shown in Fig. 7c. The 5P4E lubricant causes higher maximum pressure, especially at the pressure spike, than the PAO. The pressure at the contact centre is, however, approximately the same for both

lubricants. The pressure spike is not fully resolved which can be seen as irregularities in the maximum pressure curve of Fig. 7c. The trend is, however, clear: the 5P4E causes much higher pressure and thus increased risk of surface fatigue.

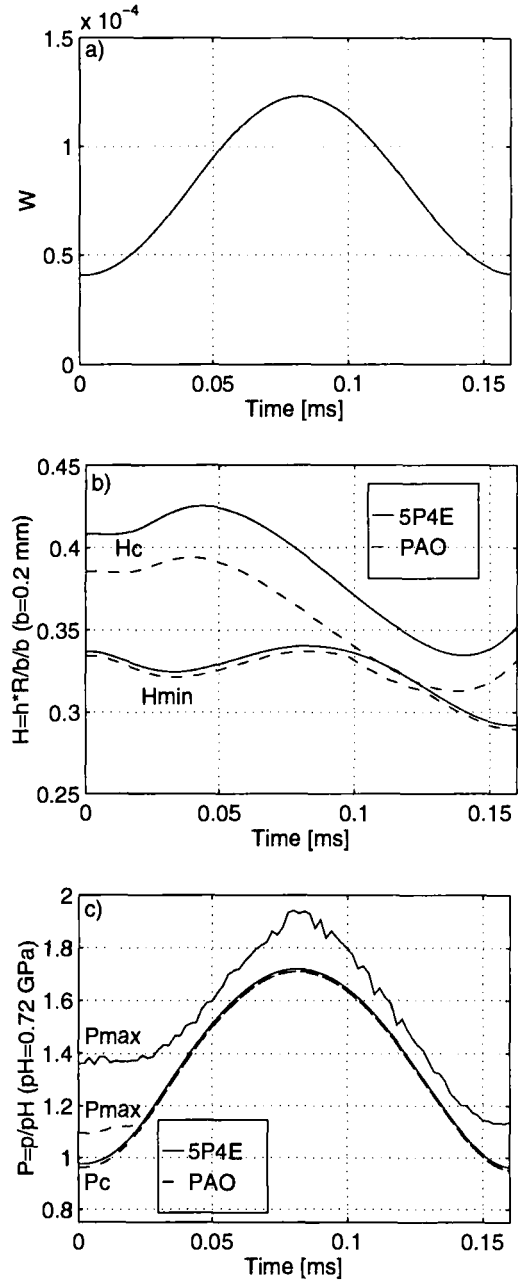


Figure 7. Transient analysis results a) transient load, b) central and minimum film thickness, c) central and maximum contact pressure.

## 5. CONCLUSIONS

The findings of this paper can be concluded as such:

- Different lubricant types exhibit different dilatation-pressure and density-pressure relations.
  - Long straight molecules found in esters, polyglycols and PAO give a weaker dilatation-pressure connection.
  - Naphthenic and paraffinic oils, with ring-shaped molecules, give a stiffer connection.
  - 5P4E has the most compact molecule and consequently the stiffest dilatation-pressure connection.
  - High temperature gives a weaker behaviour.

Applying two of the different models, those of 5P4E and PAO, in a numerical ehl analysis results in the following:

- The central film thickness becomes smaller as the lubricant compressibility increases, whereas the minimum film thickness remains almost unaffected.
- The pressure at the contact centre becomes a few percent lower when using more compressible lubricants, while the pressure spike magnitude may differ by 40 percent.
- The differences in pressure cause large differences in sub-surface stresses. A second stress maxima, located below the pressure spike, develops. This second maxima is more severe in the case of a less compressible fluid.
- Surface fatigue may shorten the operational life of a component by several times when using a less compressible lubricant.

## REFERENCES

1. H. Christensen, "The oil film in a closing gap", *Proc. R. Soc. London, Ser. A*, 226, (1962) 312-328.
2. F.P. Bowden and D. Tabor, *The friction and lubrication of solids*, Clarendon Press, Oxford, 1950 (1986) ISBN 0-19-852026-3.
3. D. Dowson and D.A. Jones, "Lubricant entrapment between approaching elastic solids", *Nature*, 214, (1967), 5091, pp. 947-948.
4. H. Christensen, "Elastohydrodynamic theory of spherical bodies in normal approach", *ASME Journal of Lubrication Tech.*, 92, (1) (1970), p.145-154.
5. K. Herrebrugh, "Elastohydrodynamic squeeze films between two cylinders in normal approach", *ASME J. of Lubrication Tech.*, 92 (1970) pp. 292-302.
6. K.M. Lee and H.S. Cheng, "The pressure and deformation profiles between two normally approaching lubricated cylinders", *ASME J. of Lubrication Tech.*, 95 No. 3 (1973) pp. 308-317.
7. H.D. Conway and H.C. Lee, "Impact of a lubricated surface by a sphere", *J. of Lubrication Tech.*, 97 (1975) pp. 613-615.
8. M.M.A. Safa and R. Gohar, "Pressure distribution under a ball impacting a thin lubricant layer", *ASME J. of Tribology*, 108 (1986) pp. 372-376.
9. P. Yang and S. Wen, "Pure squeeze action in an isothermal elastohydrodynamically lubricated spherical conjunction. Part 1. Theory and dynamic load results.", *WEAR*, 142 (1) (1991) pp 1-16.
10. R. Larsson and E. Höglund, "Numerical simulation of a ball impacting and rebounding a lubricated surface". Presented at the 1994 ASME/STLE Tribology conference, Maui, USA and published in *ASME Journal of Tribology*, 117 (Jan. 1995) pp. 94-102.
11. R. Larsson and E. Höglund, "Elastohydrodynamic lubrication at impact loading", *ASME Journal of Tribology*, 116 (Oct. 1994) pp. 770-776.
12. D. Dowson and D. Wang, "Impact elastohydrodynamics", *Lubricants and Lubrication, Proc. of 21st Leeds-Lyon Symp. on Tribology*, Leeds, England (1994).
13. D. Dowson and D. Wang, "An analysis of the normal bouncing of a solid elastic ball on an oily plate", *WEAR*, 179 (1994) pp. 29-38.
14. R. Larsson and J. Lundberg, "Study of lubricated impact using optical interferometry". Presented at *Austrib'94*, Perth, Australia Dec. 5-8 1994 and published in *WEAR*, 190 (1995) pp. 184-189.
15. J.P. Vichard, "Transient effects in the lubrication of Hertzian contacts", *J. of Mech. Eng. Sci.*, 13 No. 3 (1971) pp. 173-189.
16. K.L. Wang and H.S. Cheng, "A numerical solution to the dynamic load, film thickness, and surface temperatures in spur gears, Part I - Analysis", *ASME J. of Mech. Design*, 103 (1981) pp. 177-187.
17. K.L. Wang and H.S. Cheng, "A numerical solution to the dynamic load, film thickness, and surface temperatures in spur gears, Part II - Results", *ASME J. of Mech. Design*, 103 (1981) pp. 188-194.

18. D.Y. Hua, H.H. Zhang and S.L. Zhan, "Transient elastohydrodynamic lubrication of involute spur gears", Proc. Japan int'l. Trib. Conf., Nagoya Japan, 1990.
19. D.Y. Hua and M.M. Khonsari, "Application of transient elastohydrodynamic lubrication analysis for gear transmissions", STLE Tribology Trans., 38 (1995) 4 905-913.
20. R. Larsson, "Transient non-Newtonian elastohydrodynamic lubrication analysis of an involute spur gear", presented at the Seventh International Conference in Tribology - NORDTRIB'96, Bergen, Norway, June 16-19 1996.
21. L.E. Scales, J.E. Rycroft, N.R. Horswill, and B.P. Williamson, "Simulation and observation of transient effects in elastohydrodynamic lubrication", New studies in engine oil rheology and tribology (SP-1182), pp. 23-34 (1996), SAE Technical Paper Series no. 961143.
22. D. Dowson, C.M. Taylor and G. Zhu, "A transient elastohydrodynamic lubrication analysis of a cam and follower", J. Phys. D: Appl. Phys. 25 (1992) pp. A313-A320.
23. C.J. Hooke, "The minimum film thickness in line contacts during reversal of entrainment", ASME J. of Tribology, 115 (1993) pp. 191-199.
24. C.J. Hooke, "The minimum film thickness in lubricated line contacts during a reversal of entrainment - general solution and the development of a design chart", Proc. IMechE., J. of Eng. Tribology, 208 No. J1 (1994) pp. 53-64.
25. S. Kuroda and B.J. Hamrock, "Normal squeeze motion incorporated into conventional elastohydrodynamic lubrication.", Mech. Eng. Trans., Inst. of Eng., Australia, (1989), pp. 35-39.
26. R-T. Lee and B.J. Hamrock, "Squeeze and entraining motion in nonconformal line contacts. Part II- Elastohydrodynamic lubrication", ASME J. of Tribology, 111 (1989) pp. 8-16.
27. H. Iivonen and B.J. Hamrock, "Numerical simulation of the combined squeeze and sliding motion in elastohydrodynamically lubricated contacts", Proc. of the 5th Nordic Symposium on Tribology, in Tribologia-Finnish J. of Trib., 11 No.3 (1992) pp. 140-148.
28. M.A. Bedewi, D. Dowson and C.M. Taylor, "Elastohydrodynamic lubrication of line contacts subjected to time dependent loading with particular reference to roller bearings and cams and followers", Mechanisms and surface distress, Proc. of the 12th Leeds-Lyon Symposium on Tribology, Butterworths, London, England (1986) 289-304.
29. P. Yang and S. Wen, "The behaviour of non-Newtonian thermal ehl films in line contacts at dynamic loads", ASME J. of Tribology, 114 (1992) pp. 81-85.
30. N. Ren, D. Zhu and S.Z. Wen, "Experimental method for quantitative analysis of transient EHL", Tribology International, 24 (1991), Aug.91, no. 4, pp 225-230.
31. G.R. Paul and A. Cameron, "An high-pressure microviscometer based on refractive index", Proc. Roy. Soc., Ser. A, 331 (1972) pp. 171-184.
32. P.L. Wong, S. Lingard, and A. Cameron, "The high pressure impact microviscometer, STLE Tribology Transactions, 35 No. 3 (1992), pp 500-508.
33. P.L. Wong, S. Lingard, and A. Cameron, "High pressure viscosity and shear response of oil using the rotating optical micro-viscometer", Lubricants and Lubrication, Proc. of 21st Leeds-Lyon Symp. on Tribology, Leeds, England (1994).
34. B. Jacobson, "A high pressure-short time shear strength analyzer for lubricants", ASME J. of Tribology, 107 (1985) pp. 220-223.
35. E. Höglund, "The relationship between lubricant shear strength and chemical composition of the base oil", WEAR, 130 (1989) pp. 213-224.
36. J. Lundberg, E. Höglund and S.I. Bergström, "Apparatus for squeeze/sliding lubrication studies", Proc. Nordtrib'90, Hirtshals, Denmark, June 1990, No. 2.4, pp.83-94.
37. J. Lundberg, E. Höglund, "Velocity measurements in a squeeze/sliding lubricated contact". Tribologia-Finnish J. of Trib., 10 No. 4 (1991) pp. 32-47
38. J. Lundberg, "Viscosity dependence of squeeze/sliding lubrication", WEAR, 155 (1992) pp. 31-36.
39. J. Lundberg, J.O. Östensen and H. Åström, "High-speed video photographs of lubricated breakdown in a squeeze/sliding contact", WEAR, 157 (1992) pp. 427-433.
40. J. Lundberg, "Influence of surface roughness on normal-sliding lubrication", Tribology Int., 28 No. 5 (1995) pp. 317-322.
41. R. Feng and K.T. Ramesh, "The rheology of lubricants at high shear rates", J. of Tribology, 115 (1993) pp. 640-649.

## Efficient numerical method for various geometries of gas lubricated bearings

R.H.M. van der Stegen and H. Moes<sup>a</sup>

<sup>a</sup>Tribology Group, Dept. of Mechanical Engineering, University of Twente, P.O. Box 217, 7500 AE Enschede, The Netherlands

This paper discusses the development of a numerical solver for the Reynolds equation in aerodynamic lubricated bearings, utilizing a finite difference method with multigrid. The advantages of the numerical method are that the number of operations and the memory capacity needed are almost proportional to the number of gridpoints involved. It is second order accurate and can cope with various bearing geometries. A survey is also given of the implemented modifications of the Reynolds equation. The efficiency of the method is demonstrated by two examples, namely: the dynamic tracking of the centre of a herringbone grooved journal bearing and the equilibrium position of a hard disk slider.

### 1. Introduction

An analytical solution of the Reynolds equation for gas lubricated bearings is only available in some special situations. Therefore, in general, a numerical approach is required.

During the last decades several methods have been proposed for discretising the Reynolds equation. They may be divided in two groups, namely "finite element methods (FEMs)" and "finite difference methods (FDMs)". An early survey of numerical methods was published by Castelli and Pirvics (1968). Recently, substantially improved methods have been introduced. Useful FEMs have been developed, among others, by Bonneau, Huitric and Tournerie (1993) and by Nguyen (1991). The advantage of the FEMs is that they can be applied to a large variety of geometries. Nevertheless, the FDM is still used; see for example Lipschitz, Basu and Johnson (1991).

The numerical solution of the set of equations, constructed with the methods mentioned above, is quite expensive for a large number of points, i.e. the number of operations and the memory capacity needed are at least  $O(n^2)$ , with  $n$  the number of grid points involved. The numerical simulation is further complicated by the nonlinear character of the Reynolds equation and the wide velocity range of gas bearings. However, a multigrid solver in combination with a FDM decreases

the number of operations and the memory capacity needed and makes them directly proportional to the number of grid points involved. Therefore, this method is applied for solving the Reynolds equation.

A numerical method is presented that solves the Reynolds equation second order accurate, in arbitrarily shaped bearings. The grid points are equally spaced on the domain, but the location of these points is independent of the shape of the bearing surfaces.

To begin with, the bearing model will be presented and some possible modifications of the Reynolds equation are specified that extend its applicability. Next the numerical solver will be composed of a FDM and a multigrid solver. Finally two applications will be shown, namely a hard disk slider and a herringbone journal bearing.

### 2. Bearing model

Let us consider a model of a gas lubricated bearing of which the behaviour is to be analysed.

If the bearing is not defined in a rectangular domain, it has to be transformed onto it by a co-ordinate transformation. For instance, a journal bearing is unwrapped to a plain bearing and a thrust bearing is described in polar coordinates.

Figure 1 shows a schematic representation of a

bearing on the domain  $((0, l_x), (0, l_y))$ . The surfaces may have waviness, pockets or alternative groove geometries, like straight, herringbone or spiral grooves. The surfaces move in the tangential direction with a constant velocity  $\underline{u}$ .

The bearing clearance ( $h$ ) is a function of the given surface geometry and a global function with some degrees of freedom. Three combinations are of special interest, namely:

- the static solution; with no degrees of freedom for the clearance,
- the equilibrium solution; a steady state global function needs to be solved for every degree of freedom of the clearance,
- the time dependent solution; a transient global function needs to be solved for every degree of freedom of the clearance.

The boundary conditions complete the model. The values of the pressure ( $p$ ) are known along the external boundary parallel to the  $x$ -axis (Dirichlet boundary). The boundary parallel to the  $y$ -axis can, respectively, be of the Neumann or the Dirichlet type:

- a cyclic bearing condition, i.e.  $p(x=0, y) = p(x=l_x, y)$ ,
- a slider bearing condition, i.e. the pressures  $p(x=0, y)$  and  $p(x=l_x, y)$  are known.

Algorithms have been derived for the six possible combinations.

### 3. Lubrication model

The Reynolds equation is generally used to describe the behaviour of the lubricant film. It is derived from the Navier Stokes equations and the continuity equation by assuming very thin gaps. However, modifications can be made in order to extend the applicability of the Reynolds equation.

The Reynolds equation is written in the divergence form, neglecting the external forces, and reads:

$$\nabla \cdot \left( \frac{\rho h^3}{12\eta} \nabla p - \frac{\rho h \underline{u}}{2} \right) - \frac{\partial \rho h}{\partial t} = 0, \quad (1)$$

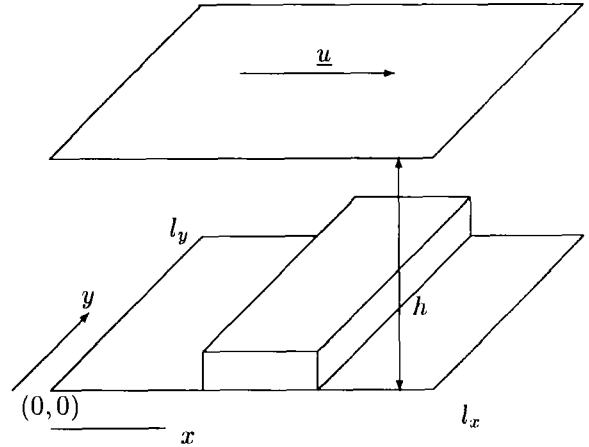


Figure 1. Schematic presentation of a bearing.

with  $\underline{u}$  and  $h$  for the sum velocity of the bearing surfaces and the clearance, respectively. The time is  $t$ . The pressure, the density and the viscosity are denoted by respectively,  $p$ ,  $\rho$  and  $\eta$ .

Further it is assumed that the flow is isoviscous and isothermal. Therefore the density  $\rho$  may be replaced by the pressure  $p$  according to  $p = \rho R_g \vartheta$ , with  $\vartheta$  and  $R_g$  for the temperature and the gas constant.

Because a number of assumptions have been made during the derivation, restrictions are necessary in order to obtain an accurate approximation for the flow in a clearance.

Special attention is paid to the flow of gas in an ultra thin gap, like between a hard disk and a slider. The original Reynolds equation is restricted to flows where the molecular mean free path is negligible as compared to the thickness of the gap. Whenever both lengths are comparable, slip between the gas and the wall produces an effect that is similar to a reduction of the viscosity.

The Reynolds equation can be adopted to ultra thin gaps by applying well known theories. The characteristic parameter is the Knudsen number ( $Kn$ ). It represents the ratio between the mean free path ( $\lambda$ ) and the gap ( $h$ ):

$$Kn = \frac{\lambda}{h}. \quad (2)$$



A first order approximation of the molecular slip velocity may be derived from the kinetic gas theory. It was implemented in the Reynolds equation by Burgdorfer (1959):

$$\nabla \cdot \left( \left( \frac{\rho h^3}{12\eta} + \frac{\lambda_0 p_0 h^2}{2\eta} \right) \nabla p - \frac{\rho h \underline{u}}{2} \right) - \frac{\partial \rho h}{\partial t} = 0, (3)$$

with  $\lambda_0$  for the mean free molecular path at the pressure  $p_0$ .

Higher order approximations for the slip in the Reynolds equation were investigated by Hsia and Domoto (1983) and Mitsuya (1993). Fukui and Kaneko (1988) derived a molecular gas equation which looks familiar to the Reynolds equation. This equation is specifically suited for very large Knudsen numbers.

Other well known adaptations are the incorporation of centrifugal effects (Pinkus and Lund, 1981) and turbulence (Taylor and Dowson, 1974). These models were originally derived for incompressible flow, but may quite as well be used for compressible flow.

All these modifications of the Reynolds equation will be neglected in the construction of the numerical method.

#### 4. Numerical procedure

A numerical procedure will now be presented that solves the Reynolds equation with second order accuracy. It is a combination of a FDM-discretisation and a multigrid method.

Point of departure is the dimensionless Reynolds equation in cartesian coordinates, a nonlinear differential operator. Since velocity in one direction is assumed, this equation reads:

$$\frac{\partial}{\partial X} \frac{d}{2} \frac{\partial P^2}{\partial X} + \gamma \frac{\partial}{\partial Y} \frac{d}{2} \frac{\partial P^2}{\partial Y} - \Lambda \frac{\partial a P}{\partial X} - \sigma \frac{\partial a P}{\partial T} = 0. (4)$$

The variable  $P$  represents the dimensionless pressure and needs to be solved. The diffusion coefficient  $d$  and the advection coefficient  $a$  are known functions of the dimensionless bearing clearance  $H$  and the position in the bearing.  $\gamma$  is the squared aspect ratio.  $\Lambda$  and  $\sigma$  are the dimensionless velocity and the dimensionless squeeze number.

#### 4.1. Discretisation

The discretisation of the Reynolds equation is based on the filmthickness *between* two grid points ( $d_{i \pm \frac{1}{2}}$  and  $a_{i \pm \frac{1}{2}}$ ), instead of coefficients *in* the grid points. These two discretisations lead to different solutions when an internal boundary is crossed. The first discretisation needs only one relaxation point to cross a boundary, while the second one invariably needs a number of points. Therefore the position of the discontinuity is presented more accurately with the first method, resulting in a more accurate solution.

A first and a second order accurate discretised Reynolds equation (in stencil notation:  $L(P)_{i,j,k} = f_{i,j,k}$ ) are presented in appendix A.

#### 4.2. Multigrid

Multigrid has originally been introduced for an isotropic function  $P$ , with a smooth behaviour of  $\nabla P$ . The Reynolds equation for gas lubrication can be non-isotropic and shows strongly discontinuous coefficients across internal boundaries. This requires special measures for the solver.

A number of so-called black box multigrid methods have been proposed that overcome the difficulties just mentioned. Two basic methods of adaptation of the solver are available that regain the desired convergence rate.

Zeeuw (1990) has developed a multigrid solver based on matrix operations to obtain the coarse grid operator. Therefore this method can only be applied if the Reynolds equation has been linearised. It results in a nine-point relaxation stencil on coarse grids. The preliminary work needed for this method is quite extensive because matrices must be inverted.

An alternative method was proposed by Alcouffe, Brandt, Dendy and Painter (1981). A multigrid solver was derived for a Laplace equation with strongly discontinuous coefficients. The method did not include advection and a nonlinear equation. The advantage of the method is that it uses a five point relaxation stencil on coarse grids and does not need matrix inversions.

The algorithm presented is based on the work of Alcouffe et al. (1981). It is implemented in the Full MultiGrid, Full Approximation Scheme (Brandt, 1984) for a nonlinear equation.

#### 4.2.1. Relaxation

The operator in a multigrid solver must be such that the relaxation is stable and an effective smoother. "Stable" means that every frequency component is reduced by the relaxation process. For multigrid efficiency in addition, good smoothing properties are essential, i.e. all high frequency components need to be reduced fast.

The preferred discretisation for the operator is the one with second order accuracy. However due to stability and smoothing requirements, its applicability is limited to regions where the diffusion derivative is larger than the advection derivative. On the contrary, the relaxation of the first order accurate scheme is stable and a good smoother. Therefore, when the second order scheme is not stable or not a good smoother and if a second order solution is needed, the first order is used and the accuracy is increased from first to second by introducing: "defect correction" (Khosla and Rubin, 1974).

Caution is needed along and across internal boundaries. These discontinuities cause locally large pressure gradients, depending on the geometry of the bearing and the bearing velocity. The safest method is to use first order discretisation with, if necessary, defect correction.

The type of relaxation depends on the ratio of the derivatives in the  $X$ - and  $Y$ -direction. If it is isotropic, a one point Gauss-Seidel relaxation can be used. In non-isotropic regions, Gauss-Seidel line-relaxation should be used.

#### 4.2.2. Intergrid transfer

The differences are described between the constructed intergrid transfer procedures and the implementation of Alcouffe et al. (1981). The guiding principle is the smooth behaviour of:  $\frac{d}{2}\nabla P^2 - \Lambda aP$ , which represents the mass flow.

The interpolation and restriction operators must prevent that information is averaged when crossing internal boundaries. A common choice for the restriction operator is applying the inverse of the interpolation operator for internal boundary problems. This choice is very expensive. Whereas a coarse approximation also gives satisfying results. The latter is based on a weighting with the reciprocal of the diffusion coefficients.

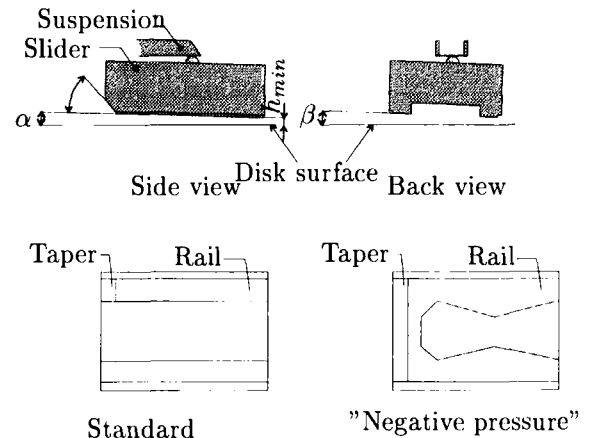


Figure 2. Slider geometry

The interpolation is based on the discretised operator.

The coarse grid operator is based on the discretisation of the fine grid operator. The method for calculating the advection and diffusion coefficients  $a$  and  $d$  was based on Alcouffe et al. (1981).

## 5. Applications

Two applications will be presented which are usually solved with different methods, namely a hard disk slider and a herringbone grooved journal bearing.

### 5.1. Hard disk sliders

The study of hard disk sliders has been stimulated by the minimisation of the hard disk dimensions. Several slider designs have been proposed, like the standard two rail slider (for example the IBM 3370) and the so-called "negative pressure slider". Sliders are often judged by their equilibrium position. Three degrees of freedom must be solved to find the equilibrium position, namely the minimal filmthickness ( $h_{min}$ ), the pitch angle ( $\alpha$ ) and the roll angle ( $\beta$ ) (Figure 2).

The numerical method solves the pressure distribution with the equilibrium position of the slider. The degrees of freedom are solved most efficiently on the coarsest grid of a multigrid cycle

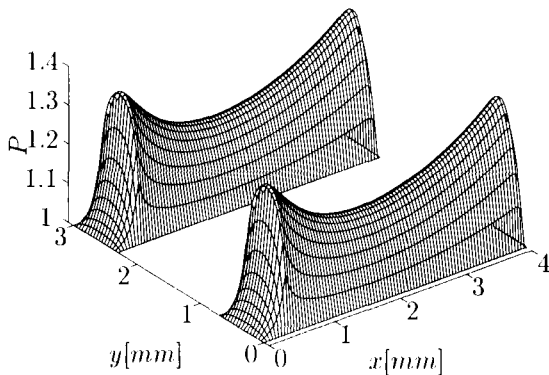


Figure 3. Pressure distribution under a IBM 3370 slider

(Venner, 1991). The equilibrium position is found in two steps. During the first step, the pressure distribution and the load balance are matched, when the finest level is level two. If the multigrid process contains three or more levels, the load and momentum are balanced.

The efficiency of the numerical procedure is demonstrated for an IBM 3370 slider, as well as for a negative pressure slider.

#### 5.1.1. IBM 3370 slider

The IBM 3370 slider is a standard two rail slider, with flat tapers. The area between the rails does not contribute to the lifting capacity.

Choi and Yoon (1994) developed a method for the prediction of the equilibrium position of a hard disk slider by using an optimization technique. Three standard sliders are discussed in their article, the results for the IBM 3370 will be compared with the present results. The notation and the equations of Choi are employed.

The method of Choi solves first the static pressure distribution. It needs 4 till 8 times more iterations to solve the pressure distribution with the equilibrium position.

The present method solves the standard slider on 7 succeeding levels. The coarsest grid has per rail  $1 \times 10$  nodes, the finest has  $127 \times 703$  nodes. The area between the rails is not disre-

| level | $\alpha[\mu\text{rad}]$ | $\beta[\mu\text{rad}]$ | $h_{min}[\mu\text{m}]$ |
|-------|-------------------------|------------------------|------------------------|
| 1     | 300.0                   | 0.00                   | 0.100                  |
| 2     | 300.0                   | 0.00                   | 0.500                  |
| 3     | 146.5                   | 8.67                   | 0.566                  |
| 4     | 144.8                   | 7.93                   | 0.568                  |
| 5     | 144.2                   | 7.49                   | 0.569                  |
| 6     | 146.1                   | 7.30                   | 0.571                  |
| 7     | 146.0                   | 7.19                   | 0.571                  |
| Ruiz  | 143.                    | 7.1                    | 0.55                   |
| Choi  | 145.                    | 7.2                    | 0.56                   |

Table 1

Results for a IBM 3370 slider on 7 levels.

tised. The multigrid method needs two V-cycles with two pre and two post relaxations per level to solve the pressure distribution. Four cycles in total are needed to find the equilibrium position. This means that 16 relaxation of the finest grid are needed. However, on levels two and three, more cycles are needed, depending on the initial condition. The computational costs are very low for the low level cycles. Therefore these can be neglected when more than three levels are involved. The pressure distribution is given in Figure 3. Only one out of 64 gridpoints is shown.

The solution of the proposed method and the results of Choi and Yoon (1994) are listed in table 1. They compared their results with Ruiz and Bogy (1990). Excellent agreement of the minimal film thickness  $h_{min}$ , the pitch angle  $\alpha$  and the roll angle  $\beta$ , is seen between the three methods. On the finest level, level seven, the most accurate results are obtained. It is obvious that the differences between the solutions on succeeding levels become less when the level is finer. However the convergence of the solution is not exactly second order. This is caused by the switch from taper to rail, which in general does not coincide with a gridline. This reduces the convergence rate.

#### 5.1.2. Negative pressure slider

The so-called "negative pressure slider" consists of two rails with a threshold in between. Behind the threshold is a recessed area with a sub ambient pressure. This sucks the slider to the disk.

The negative pressure slider can be solved

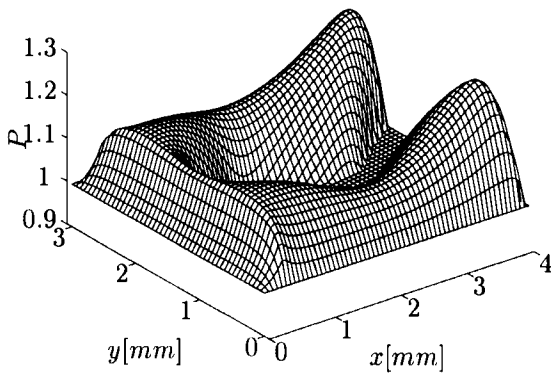


Figure 4. Pressure distribution under a negative pressure slider

| level | $\alpha$ [ $\mu\text{rad}$ ] | $\beta$ [ $\mu\text{rad}$ ] | $h_{min}$ [ $\mu\text{m}$ ] |
|-------|------------------------------|-----------------------------|-----------------------------|
| 1     | 145.0                        | 7.20                        | 0.560                       |
| 2     | 145.0                        | 7.20                        | 1.176                       |
| 3     | 298.5                        | 11.80                       | 1.117                       |
| 4     | 308.3                        | 11.91                       | 1.133                       |
| 5     | 304.6                        | 11.96                       | 1.141                       |
| 6     | 304.7                        | 11.99                       | 1.146                       |

Table 2

Results for negative pressure slider on 6 levels.

with the same efficient method. The number of operations is a bit larger because multigrid W-cycles are needed instead of V-cycles. The complete slider is discretised, i.e. also the area between the rails. The coarsest level has 11 x 14 nodes, the finest 383 x 479 nodes. The pressure distribution is presented in Figure 4. Only one out of 64 points is plotted.

Geometries have not been published and therefore the results can not be compared. Table 2 presents the results on the six levels. The convergence of the solution is first order because the inaccurate description of the internal boundaries dominates the error in the solution.

| level | $F_x$ [N] | $F_y$ [N] |
|-------|-----------|-----------|
| 1     | -109.9    | 56.5      |
| 2     | -147.3    | 56.7      |
| 3     | -165.7    | 52.7      |
| 4     | -174.9    | 49.0      |
| 5     | -178.3    | 47.2      |
| 6     | -180.6    | 46.0      |
| 7     | -181.5    | 45.6      |

Table 3

Static results of a herringbone bearing.

## 5.2. Herringbone grooved journal bearing

Herringbone grooved journal bearings are applied in rotating machinery such as audio and video equipment. For gas bearings in particular, uncontrolled whirl can cause fatal damage to the bearing. Therefore the prediction of whirl is important for the designer. The stability of a bearing is simulated by solving the Reynolds equation and the equations of motion. The result is a transient prediction of the journal centre locus.

In a transient analysis, the previous solution is applied as an estimation for the next time step by the numerical method. The multigrid method is called "F-cycle". On the coarsest level 16 x 3 nodes are used, on the finest level (level 7) 1024 x 255 nodes. Three V-cycles, each with four relaxations at the finest level, are needed for the static solution. During the begin of the transient analysis, just two V-cycles within a F-cycle suffice; and when the high frequency oscillations have disappeared one V-cycle suffices.

The herringbone bearing under consideration has 8 grooves with a groove angle of 30 degrees and a land-groove ratio of 1. The groove depth is 1 [ $\mu\text{m}$ ] and the maximum eccentricity is 5 [ $\mu\text{m}$ ]. The grooved bearing is stationary and the smooth journal rotates with 100 [rps]. The attached rotor mass is 0.5 [kg]. The dimensions of the bearing are a diameter of 4 [cm] and a length of 3 [cm].

First, the static solution is solved for the dimensionless eccentricity  $(\epsilon_x, \epsilon_y) = (0.75, 0)$  of the herringbone bearing. The resulting forces  $F$  on the journal are given in table 3 for the seven levels. The convergence is reduced by the inaccurate description of the internal boundaries. This static

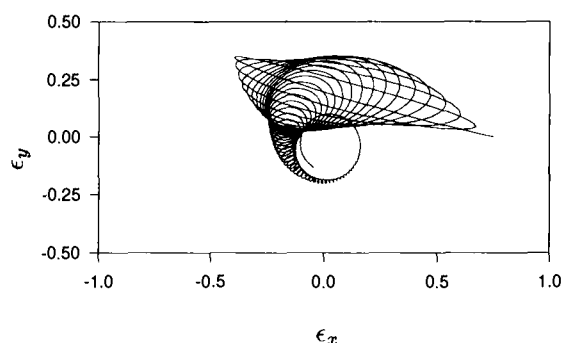


Figure 5. Journal centre path

solution is the departure point for the transient simulation of the loaded journal. Its centre path is given in figure 5.  $\Delta T$  is equal to  $\Delta X$ . In order to arrive at the limit cycle, thousands of time steps are needed, which is no problem for this efficient algorithm.

## 6. Conclusion

An efficient numerical method is derived for the static, equilibrium, and time dependent solution of a gas lubricated bearing. The method is based on a second order finite difference discretisation scheme and a multigrid solver. The efficiency of the method is demonstrated by the fact that the number of operations and the memory capacity needed are almost proportional to the number of gridpoints involved.

The method has been shown to be well suited for taking into account compressibility and complex geometries. The gridpoints are equally spaced on the domain. A geometry that is not smooth is therefore represented with first order accuracy because the exact location of the discontinuity can not be represented by the discretisations.

The method is applied to two examples, namely a hard disk slider and a herringbone grooved journal bearing. The equilibrium position of the slider is obtained with the same efficiency, independent of the geometry. The equilibrium of a slider requires the double amount of work of the static

solution. In a transient simulation of a herringbone bearing, the previous pressure distribution is applied as an estimation for the next distribution. In combination with a multigrid "F-cycle", this reduces substantially the number of operations per timestep as compared to a static solution.

## Acknowledgement

The authors would like to thank their colleagues of the Tribology Group and A. Reusken of the Eindhoven University of Technology in the Netherlands for their contributions, discussions and suggestions.

## Nomenclature

|                      |  |
|----------------------|--|
| $a$                  | advection coefficient  |
| $d$                  | diffusion coefficient  |
| $f$                  | right hand side term   |
| $F$                  | force  |
| FDM                  | finite difference method   |
| FEM                  | finite element method  |
| $h(H)$               | clearance( $h = h_0 H$ )   |
| $Kn$                 | Knudsen number   |
| $l$                  | length   |
| $L$                  | relaxation operator  |
| $n$                  | number of gridpoints   |
| $p(P)$               | pressure( $p = p_0 P$ )  |
| $R_g$                | gas constant   |
| $t(T)$               | time ( $t = \frac{T l_x}{u}$ )                                   |
| $\underline{u}$      | sumvelocity  |
| $x, y(X, Y)$         | cartesian coordinates<br>( $x = l_x X, y = l_y Y$ )              |
| $\Delta X, \Delta T$ | stepsizes  |
| $\alpha$             | pitch angle  |
| $\beta$              | roll angle   |
| $\epsilon$           | eccentricity   |
| $\gamma$             | squared aspect ratio ( $= \frac{l_x^2}{l_y^2}$ )                 |
| $\eta$               | viscosity  |
| $\lambda$            | molecular mean free path   |
| $\Lambda$            | bearing velocity number<br>( $= \frac{6\eta u l_x}{p_0 h_0^2}$ ) |
| $\rho$               | density  |
| $\vartheta$          | temperature  |
| $\sigma$             | squeeze number ( $= \frac{12\eta u l_x}{p_0 h_0^2}$ )            |

**Sub- and superscripts**

|            |                             |
|------------|-----------------------------|
| <i>min</i> | minimum value               |
| <i>x</i>   | index in <i>x</i> direction |
| <i>y</i>   | index in <i>y</i> direction |
| <i>i</i>   | index in <i>X</i> direction |
| <i>j</i>   | index in <i>Y</i> direction |
| <i>k</i>   | index in <i>T</i> direction |
| 0          | reference value             |
| 1          | first order accurate        |
| 2          | second order accurate       |

**A. Discretisation**

The discretisation of the operators  ${}^2L(P)_{i,j,k}$  and  ${}^1L(P)_{i,j,k}$  is given only in *X*- and *T*-direction, with  $X = i\Delta X$ , and  $T = k\Delta T$ . The second order accurate operator is:  ${}^2L^h(P)_{i,k} =$

$$\begin{aligned} & \left. \frac{d_{i+\frac{1}{2}}(P_{i+1}^2 - P_i^2) - d_{i-\frac{1}{2}}(P_i^2 - P_{i-1}^2)}{2(\Delta X)^2} \right|_k \\ & - \Lambda \left. \frac{a_{i+\frac{1}{2}}(P_{i+1} + P_i) - a_{i-\frac{1}{2}}(P_i + P_{i-1})}{2\Delta X} \right|_k \\ & - \sigma \left. \frac{3a_k P_k - 4a_{k-1} P_{k-1} + a_{k-2} P_{k-2}}{2\Delta T} \right|_i. \end{aligned} \quad (5)$$

Alternatively the operator  ${}^1L^h(P)_{i,k}$  is used:

$$\begin{aligned} & \left. \frac{d_{i+\frac{1}{2}}(P_{i+1}^2 - P_i^2) - d_{i-\frac{1}{2}}(P_i^2 - P_{i-1}^2)}{2(\Delta X)^2} \right|_k \\ & - \Lambda \left. \frac{a_{i+\frac{1}{2}} P_i - a_{i-\frac{1}{2}} P_{i-1}}{\Delta X} \right|_k \\ & - \sigma \left. \frac{3a_k P_k - 4a_{k-1} P_{k-1} + a_{k-2} P_{k-2}}{2\Delta T} \right|_i. \end{aligned} \quad (6)$$

The advection and diffusion coefficients *a* and *d* are functions of the dimensionless bearing clearance:

$$d_{i+\frac{1}{2},j} = \frac{1}{2}(H_{i+\frac{1}{2},j-\frac{1}{2}}^3 + H_{i+\frac{1}{2},j+\frac{1}{2}}^3), \quad (7)$$

$$a_{i+\frac{1}{2},j} = H_{i+\frac{1}{2},j}. \quad (8)$$

**REFERENCES**

Alcouffe, R. E., Brandt, A., Dendy, J. E. and Painter, J. W. (1981). The multi-grid method for the diffusion equation with strongly discontinuous coefficients, *SIAM J. Sci. Stat. Comput.* **2**(4): 430-454.

Bonneau, D., Huitric, J. and Tournerie, B. (1993). Finite Element Analysis of Grooved Gas Thrust Bearings and Grooved Gas Face Seals, *Journal of Tribology* **115**: 348-354.

Brandt, A. (1984). *Multigrid Techniques: 1984 Guide with Applications to Fluid Dynamics*, Gesellschaft fuer Mathematik und Datenverarbeitung MBH, Bonn.

Burgdorfer, A. (1959). The Influence of the Molecular Mean Free Path on the Performance of Hydrodynamic Gas Lubricated Bearings, *Journal of Basic Engineering* **81**: 94-100.

Castelli, V. and Pirvics, J. (1968). Review of Numerical Methods in Gas Bearing Film Analysis, *Journal of Lubrication Technology* **90**: 777-792.

Choi, D.-H. and Yoon, S.-J. (1994). Static Analysis of Flying Characteristics of the Head Slider by Using an Optimazation Technique, *Journal of Tribology* **116**: 90-94.

Fukui, S. and Kaneko, R. (1988). Analysis of Ultra-Thin Gas Film Lubrication Based on Linearized Boltzmann Equation: First Report - Derivation of a Generalized Lubrication Equation Including Thermal Creep Flow, *Journal of Tribology* **110**: 253-261.

Hsia, Y. T. and Domoto, G. A. (1983). An Experimental Investigation of Molecular Rarefaction Effects in Gas Lubricated Bearings at Ultra-Low Clearances, *Journal of Lubrication Technology* **105**: 120-130.

Khosla, P. K. and Rubin, S. G. (1974). A Diagonally Dominant Second-Order Accurate Implicit Scheme, *Computers and Fluids* **2**: 207-209.

Lipschitz, A., Basu, P. and Johnson, R. P. (1991). A Bi-Directional Gas Thrust Bearing, *Tribology Transactions* **34**(1): 9-16.

Mitsuya, Y. (1993). Modified Reynolds Equation for Ultra-Thin Film Gas Lubrication Using

- 1.5-Order Slip-Flow Model and Considering Surface Accommodation Coefficient, *Journal of Tribology* **115**: 289–294.
- Nguyen, S. H. (1991). p-Version Finite Element Analysis of Gas Bearings of Finite Width, *Journal of Tribology* **113**: 417–420.
- Pinkus, O. and Lund, J. W. (1981). Centrifugal Effects in Thrust Bearings and Seals Under Laminar Conditions, *Journal of Lubrication Technology* **103**: 126–136.
- Ruiz, O. J. and Bogy, D. B. (1990). A Numerical Simulation of the Head-Disk Assembly in Magnetic Hard Disk Files: part 1 - Component Models, *Journal of Tribology* **112**: 593–602.
- Taylor, C. M. and Dowson, D. (1974). Turbulent Lubrication Theory - Application to Design, *Journal of Lubrication Technology* pp. 36–47.
- Venner, C. H. (1991). *Multilevel Solution of the EHL Line and Point Contact Problems*, PhD thesis, University of Twente, The Netherlands.
- Zeeuw, P. M. D. (1990). Matrix-dependent prolongations and restrictions in a blackbox multigrid solver, *Journal of Computational and Applied Mathematics* **33**: 1–27.

## Decrease in friction coefficient under extremely low load

Yasuhisa Ando

Mechanical Engineering Laboratory, AIST, MITI  
Namiki 1-2, Tsukuba, Ibaraki, Japan

When a copper and a silicon test specimen were rubbed against each other under a very low contact pressure, with a load applied in the direction to pull apart the test specimens (negative normal load) to offset the attraction active between them, the friction coefficient decreased. The decrease of friction coefficient was considered to be due to the lubricating effect of a liquid film formed between the solid surfaces, and friction tests were carried out with variable sliding speeds to test this hypothesis. The result showed two cases: one of friction coefficient increasing and the other decreasing with sliding speed. This can be explained by the decreased surface area of direct contact between the two solids, and the viscous resistance of fluids, respectively.

### 1. INTRODUCTION

Using contact areas of several tens to several hundred  $\mu\text{m}^2$  subjected to normal loads of several  $\mu\text{N}$  to several mN, the author studies tribological phenomena occurring on a very small area under a very small contact load. Such conditions are found in micromachines [1, 2].

The study of tribological phenomena under these conditions assists in the development of lubricating methods for micromachines. It is also possible to relate the tribological phenomena of the nanometer order, currently studied using atomic force microscopes (AFM), to the tribological phenomena of normal size.

In a previous test carried out by the author, a steel ball and a block gauge were rubbed against each other on a reciprocating friction tester to study the relation among normal load, friction force, and adhesion force (pull-off force) which was measured when the surfaces were pulled off [3]. The test results showed that the friction coefficient tends to increase with decreasing load, and that the friction force is proportional to the sum of the normal load and pull-off force. Also, when the normal load was gradually decreased the test specimens did not

separate but friction remained even when the applied load became negative. This indicates that the adhesion force acts between the surfaces in the friction state, just like in the static state.

In another test, the author studied the relation among friction force, normal load and pull-off force using two types of copper specimens and silicon wafers with a different contact surface profile [4]. The normal load was varied from positive to negative. A copper specimen and a silicon wafer, both with a flat contact surface, were rubbed against each other while decreasing the normal load. The friction force decreased linearly with the normal load, while the friction coefficient (calculated assuming that the pull-off force was equivalent to normal load) was generally constant and changed only very little with the load. When the normal load, applied to the copper specimen and silicon wafer rubbing against each other with Hertzian contact, was decreased, the rate of decrease of friction force increased as the normal load approached the pull-off force. Also, the friction coefficient, where pull-off force was considered, increased at low loads. The relation between normal load and friction force measured with decreasing load coincided very well with the equation of Hertzian contact where adhesion force



was considered, indicating that the friction force was proportional to the apparent Hertz load discussed by Johnson, et al [5].

When a copper and a silicon specimen with a flat contact surface were rubbed against each other under a certain very low (negative) normal load, the friction coefficient with pull-off force considered decreased just slightly with the load. Two mechanisms explain this decrease. One is that the measured pull-off force is different from the adhesion force actually acting on the friction surface. Pull-off force, which was used in defining the friction coefficient, was measured in the static state before and after the measurement of friction force. Accordingly, if the pull-off force is greater than the actual adhesion force during friction, the effect of the pull-off force becomes conspicuous under low load conditions, resulting in the decreased friction coefficient. The second reason for the decrease is that a friction mechanism, which is different from that which is effective under a high contact pressure, plays a major role when the contact pressure is extremely low. For instance, the friction coefficient decreases when a fluid film is formed on the contact surface, preventing direct contact between solids.

In the present test, a copper specimen and a silicon wafer both with a flat contact surface were rubbed against each other to measure and evaluate the change in friction coefficient relative to a variable applied normal loads. Also, the effect of sliding speed on the friction coefficient was studied using the normal load as a parameter. This paper reports the results of the tests. The effect of ambient humidity on the friction force and pull-off force was also measured to study the reason why the friction coefficient decreases when the load is very low.

## 2. EXPERIMENTAL METHODS

Figure 1 shows a schematic drawing of the reciprocating friction apparatus. A copper test specimen is fixed to parallel leaf spring A, a silicon plate is attached to parallel leaf spring B, and the test specimens face each other.

Parallel leaf spring A consists of four leaf

springs. The copper test specimen is installed on the center block between the upper two leaf springs, which moves vertically by the deformation of the leaf springs. The center part of the lower leaf springs is fixed to the stacked PZT actuator. Capacitance sensor A and parallel leaf spring A are moved vertically together along the silicon plate by the PZT actuator with a magnification mechanism. When the copper test specimen is in contact with the silicon plate and a friction force acts between the test specimens, the center block moves relatively and sensor A measures the relative displacement of the block.

The copper test specimen can be also moved perpendicular to the silicon plate by the stacked PZT actuator and the table with a stepping motor. Parallel leaf spring B is displaced perpendicular to the copper test specimen, and the displacement is measured by optical sensor B. The outputs of sensors A and B are A/D converted, then the friction force is calculated from the relative displacement of parallel leaf spring A, while the normal load and the pull-off force are calculated from the displacement of parallel leaf spring B.

The friction force was measured under both constant load and gradually decreasing load. The procedure is outlined below. The detailed experiment procedure is almost the same as that reported in a previous paper [3].

In the constant-load friction measurement, we reciprocated a copper test specimen once on a silicon plate under a constant positive-to-negative load while measuring the normal load during friction. We also measured the force required to separate the copper test specimen from the plate before and after the measuring the friction force. We examined the relationship among friction force, normal load, and pull-off force by repeating the measurements under different normal loads.

In the friction measurement under a gradually decreasing load, we started friction by pressing the test specimen against the plate, and moved the test specimen in the direction away from the plate during friction while gradually decreasing the normal load. If the adhesion force acts between the two test

specimens, friction continues to exist even when the normal load has become negative, and a force is applied to separate the test specimens, which separate at the moment when the pull-off force exceeds the adhesion force. We examined the relationship among the friction force, normal load, and pull-off force.

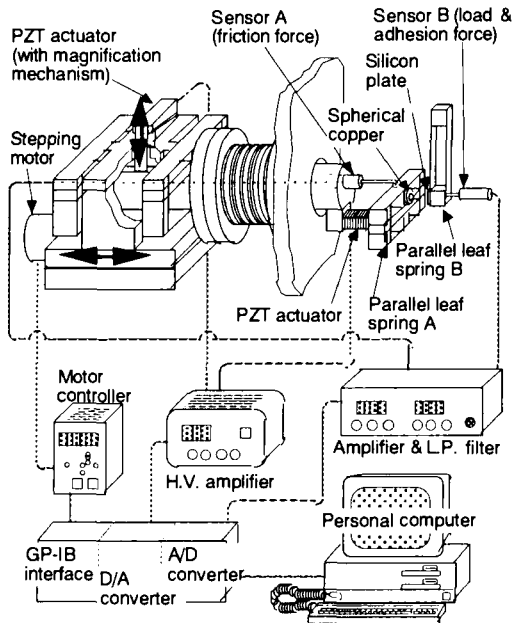


Figure 1. Schematic drawing of experimental apparatus

The effect of sliding speed was investigated as described below. First, the pull-off force was measured in the static state. Second, to measure the friction force, the two test specimens were brought into contact under a certain load, and rubbed against each other for one stroke at the speed of  $1.6 \mu\text{m/s}$ . Third, while keeping the test specimens in contact, the sliding speed was increased in steps up to 48 or  $64 \mu\text{m/s}$  and then again decreased in steps down to  $1.6 \mu\text{m/s}$  to measure the friction force at each sliding speed in the same way as in the initial measurement of the friction force. Last, the test specimens were pulled off to measure the pull-off force.

This test procedure was repeated by varying the contact load in steps to assess the relation

between sliding speed and friction coefficient at differing loads. The sliding distance and the location of friction on the silicon wafer were the same for all the sliding speeds tested.

The effect of relative humidity on friction force and friction coefficient was also studied by supplying dry air to the measurement vessel to vary the relative humidity. The test specimens were ultrasonic-cleaned with ethanol and then cleaned with pure water before the measurements. The test conditions are summarized in Table 1.

Table 1 Experimental conditions

| Test pieces  | Copper/Silicon |          |         |
|--|----------------|----------|---------|
| (1) Effect of normal load (Constant load friction) |                |          |         |
| Relative humidity (%)                              | 1.1~1.5        | 18       |         |
| Normal load ( $\mu\text{N}$ )                      | -61~327        | -90~316  |         |
| Sliding speed ( $\mu\text{m/s}$ )                  | 1.6            |          |         |
| Sliding distance ( $\mu\text{m}$ )                 | 25.6           |          |         |
| (2) Reducing load friction                         |                |          |         |
| Relative humidity (%)                              | 53             | 1.1      |         |
| Normal load  | 0 ~ -119       | 0 ~ -106 |         |
| Sliding speed ( $\mu\text{m/s}$ )                  | 1.6, 8.0, 16.0 |          |         |
| (3) Effect of sliding speed (Constant load)        |                |          |         |
| Relative humidity (%)                              | 0.4~2.3        | 17~21    | 52      |
| Normal load ( $\mu\text{N}$ )                      | -73~284        | -93~207  | -63~235 |
| Sliding speed ( $\mu\text{m/s}$ )                  | 1.6~64         |          |         |
| Sliding distance ( $\mu\text{m}$ )                 | 76.9           |          |         |

### 3. EXPERIMENTAL RESULTS AND DISCUSSIONS

Figure 2 shows an SEM image of the copper specimen observed at the end of the experiments. The contact surface is almost flat. The apparent contact area as measured in this figure is approximately  $370 \mu\text{m}^2$ . Surface roughness ( $R_{\text{rms}}$ ) of the flat area is approximately 8 nm as measured by an atomic force microscope.

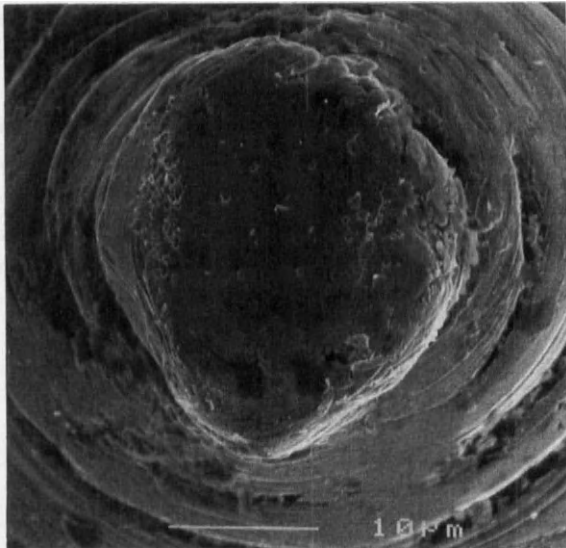
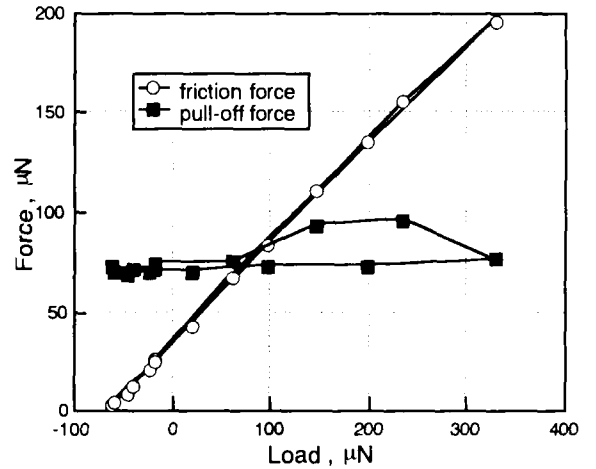


Figure 2. SEM image of copper test specimen

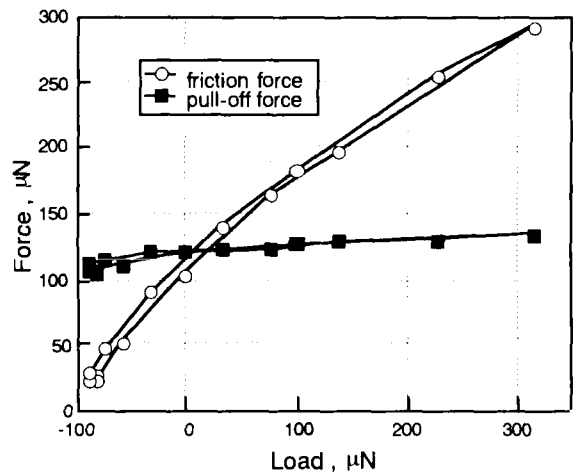
Figure 3 shows the relation between normal load and friction force when the test specimens were rubbed under a certain load. The figure also shows the relation between the normal load and the average of the pull-off forces measured before and after the measurement of friction force. These measurements were conducted in air of relative humidity of about 1% and 18% respectively. The measurement started with the normal load set at a negative value. The normal load was increased to more than 300  $\mu\text{N}$  in steps, and then decreased. Under a relative humidity of 1%, the pull-off force varies with the load, while for a relative humidity of 18%, the pull-off force is almost constant while the friction force in the load increasing process varies slightly from that in the load decreasing process.

The behavior of friction force relative to normal load was as described below. At 1% relative humidity, friction force varies linearly with normal load. At 18% relative humidity, friction force decreases more rapidly when the load gets smaller. Also at 18% relative humidity, the test specimens were pulled off during friction when the normal load was decreased to -90  $\mu\text{N}$  or below and thus no measurements were taken for smaller loads than this. The lowest friction force measured was 23  $\mu\text{N}$ ,

which is considerably larger than 2  $\mu\text{N}$  measured at the 1% relative humidity.



(a) Relative humidity 1.1 ~ 1.5%



(b) Relative humidity 18%

Figure 3. Friction and pull-off force versus normal load

Figure 4(a) shows the relation between friction coefficient and normal load defined by the data shown in Figure 3(a). Symbols  $\circ$  represent friction coefficients of the ordinary definition while symbols  $\bullet$  represent friction coefficients which are equivalent to the friction force divided by the sum of the normal load and the average of the pull-off forces measured before and after friction measurement. For

negative normal loads, the friction coefficients that do not consider pull-off force are a negative value, and thus are not shown. When pull-off force is considered, the friction coefficients approach a constant value. Figure 4(b) shows only those friction coefficients in which pull-off force is considered. The friction coefficients decrease sharply with decreasing load when the surface separating force increases and the sum of (negative) normal load and the pull-off force approaches zero.

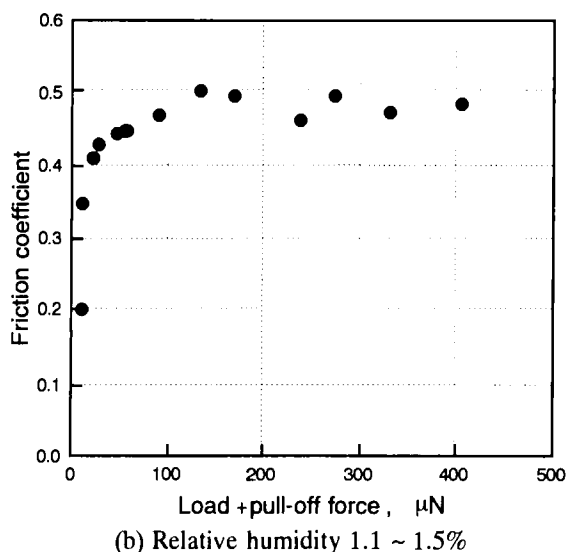
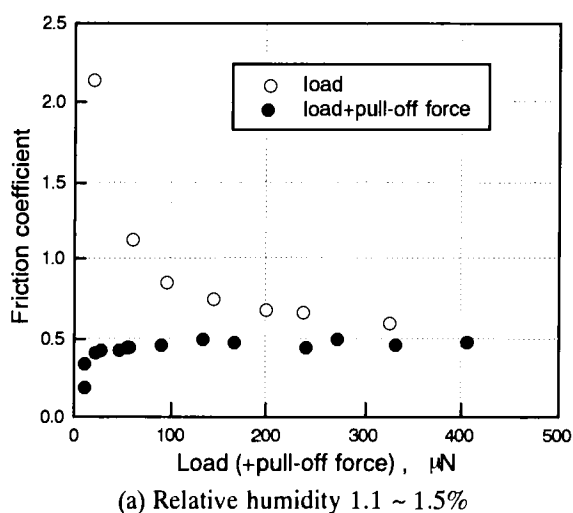


Figure 4. Relationship between friction coefficient and sum of normal load and pull-off force.

Figure 5 shows the behavior of two kinds of friction coefficients at 18% relative humidity. Friction coefficients approach a certain value when pull-off force is considered, yet continue to rise in the low load area and do not decrease as they did in Figure 4. This is because the measured pull-off force is smaller than the actual adhesion force acting on the surfaces or there exists a load-independent friction force that is effective when the contact load is extremely small.

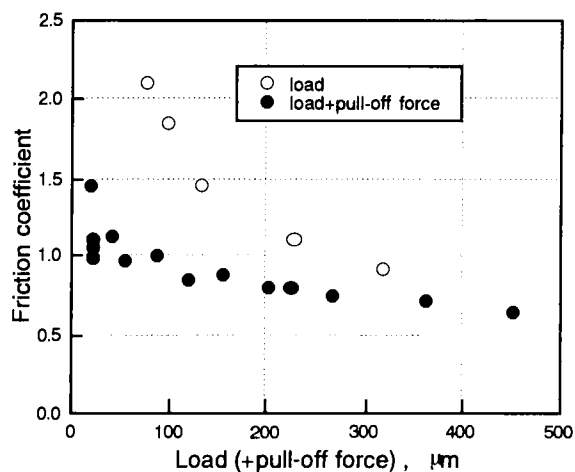
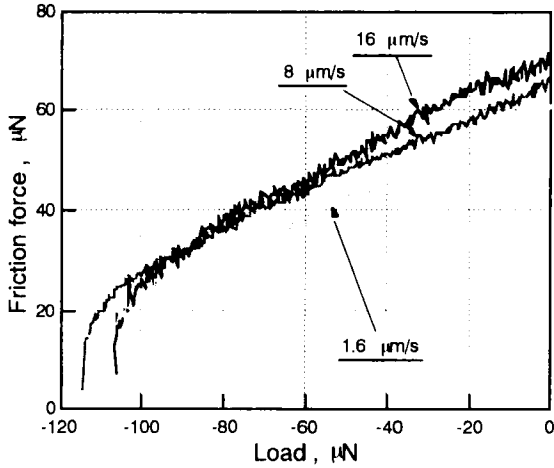
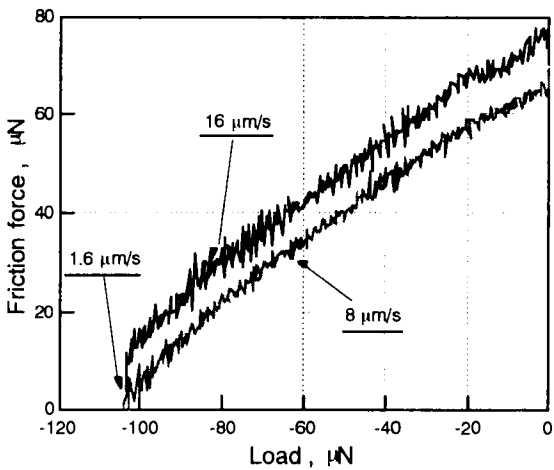


Figure 5. Relationship between friction coefficient and normal load (+ pull-off force). (Relative humidity 18%)

Figure 6 shows the behavior of friction force between the two specimens at sliding speeds of 1.6, 8.0 and 16  $\mu\text{m/s}$ , under steadily decreasing normal load. The tests were carried out under two different relative humidity conditions. At 53% relative humidity, the friction force changes almost linearly when the speed is low. When the speed increases, the friction force suddenly decreases immediately before the test specimens are separated and the pull-off force becomes smaller. At 1.1% relative humidity, the friction force varies more linearly with normal load than at 53% relative humidity. For speeds of 1.6 and 8.0  $\mu\text{m/s}$ , friction continues until the friction force reaches almost zero.



(a) Relative humidity 53%



(b) Relative humidity 1.1%

Figure 6. Friction force under reducing normal load measured at different sliding speeds

The reasons why the friction force decreases immediately before the test specimens are separated in the 53% relative humidity atmosphere are because the adhesion force acting on the contact surface decreases sharply, and because the friction force itself decreases. Assuming that the friction force is proportional to the sum of the adhesion force acting on the contact surface and the normal load, the friction force decreases when the adhesion force decreases because of a partial loss of adhesion energy

as the contact surface is separated as the normal load is gradually decreased. This phenomenon is actually observed on the contact surface between a sphere and a plane. Even when the size of the area on which adhesion energy acts remains unchanged, the friction force may decrease when water in the atmosphere condenses in the space between the contact surfaces and a liquid film is formed, because this film sharply reduces the direct contact between solids. The existence of such a liquid film is also verified by the fact that the change immediately before the separation of the test specimens is greater at the higher relative humidity and the faster sliding speed. The behavior of pull-off force relative to sliding speed can be explained by the increased clearance between the surfaces of two solids due to the existence of such a liquid film.

As discussed above, there are two possible explanations for the friction coefficient decreasing at low loads: one, pull-off force and adhesion force, which is active during friction, are different from each other, and the other, a liquid film with a lubricating effect is formed. It is difficult, however, to determine which of these two factors is dominant even when measurements are taken by varying the applied load. If a liquid film is present between the surfaces during friction, the friction coefficient is also likely to vary with sliding speed.

Figures 7 to 9 show the relation between friction coefficient and sliding speed at relative humidities of 0.4 to 2.3%, 17 to 21%, and 52%, respectively. The values in inset boxes in the respective figures represent the sum of the average of the pull-off forces measured before and after friction measurement at each setting load and the normal load, or are equivalent to the effective normal load. The friction coefficient is calculated assuming that these values are constant during friction. For effective load 68 μN in Figure 7, the friction coefficient behaves differently between the speed increasing and decreasing process. This is because the adhesion force or the normal load changed during measurement.

Under all conditions except the case of effective load 68 μN at relative humidity 0.4 to

2.3%, the friction coefficient increases with decreasing sliding speed. This is because a liquid film is present between the surfaces (due to water condensation or contamination), with the result that the higher the sliding speed, the smaller the area of direct contact between solids, thus decreasing the friction coefficient. Yet why does the friction coefficient decrease with increasing sliding speed

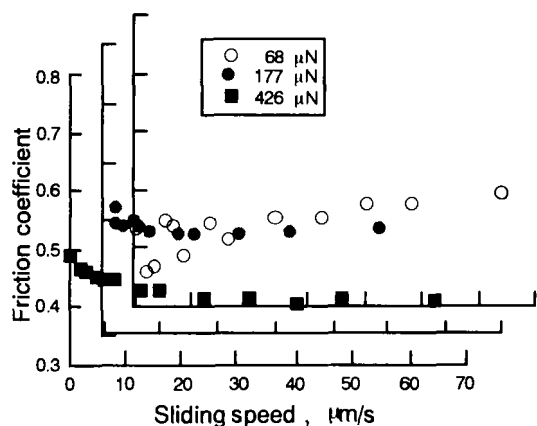


Figure 7. Relationship between friction coefficient and sliding speed. (Relative humidity 0.4 ~ 2.3%)

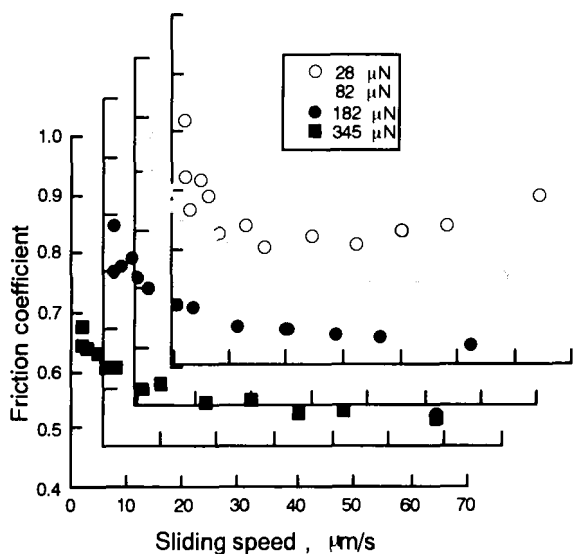


Figure 8. Relationship between friction coefficient and sliding speed. (Relative humidity 17 ~ 21%)

even when the relative humidity is extremely low? It may be that water is condensed in a narrow space of approximately Kelvin radius [6] (approximately 0.3 nm with 1%) between the contact surfaces even when the relative humidity is as low as 1%. Since all direct contact between the solids occurs within this area, any small quantity of liquids present on the surface could get into the contact area and thus decrease the friction force.

For the effective load of 68  $\mu\text{N}$  in Figure 7, the friction coefficient increases with increasing sliding speed. For effective load 28  $\mu\text{N}$  in Figure 8, the friction coefficient decreases in the lower speed range, but increases with sliding speed when the speed is 30  $\mu\text{m/s}$  and above. The friction coefficient becomes a minimum at about 20  $\mu\text{m/s}$ . The increase in friction coefficient with increasing speed can also be explained by the presence of a liquid film. When the sliding speed is high or the contact surface pressure is very low, the area of direct contact between solids is negligible due to the liquid film. In this case, the viscous resistance of the liquid film becomes more dominant than the frictional resistance due to contact between the solids.

The area in which viscous resistance is effective may increase with increasing relative humidity and film thickness when the distance between the solid surfaces is constant (Figure 10).

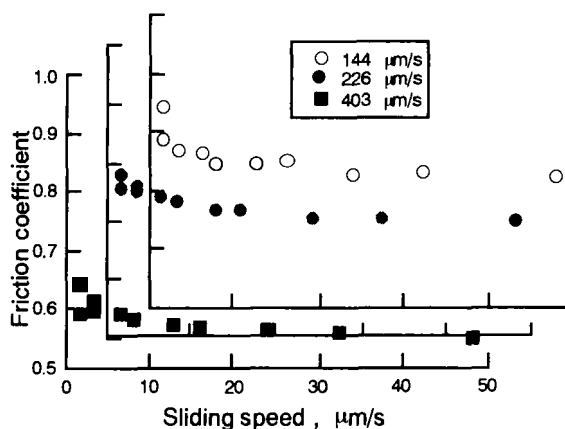


Figure 9. Relationship between friction coefficient and sliding speed. (Relative humidity 51%)

Since this type of resistance is nearly independent of normal load, the total friction force is small and the effect of viscous resistance becomes conspicuous when the load is small. In Figure 5, for example, the increase of friction coefficient considering pull-off force may be explained by viscous resistance. In Figures 7 to 9, friction coefficient increases even when the relative humidity is so high that one should expect decreased, rather than increased, friction through fluid lubrication. This can also be explained by the existence and effect of viscous resistance.

The complex behavior of friction coefficient relative to variable loads and sliding speeds was qualitatively explained in this paper by assuming the existence of a liquid film between contact surfaces. Quantitative studies are needed to clarify if a fluid film is indeed formed at such very low sliding speeds as tested in the present experiments. We shall conduct such quantitative studies in the future together with studies using various sizes of contact areas and over a wider range of sliding speeds.

#### 4. CONCLUSIONS

To study the relation among friction force, normal load and pull-off force through measurement,

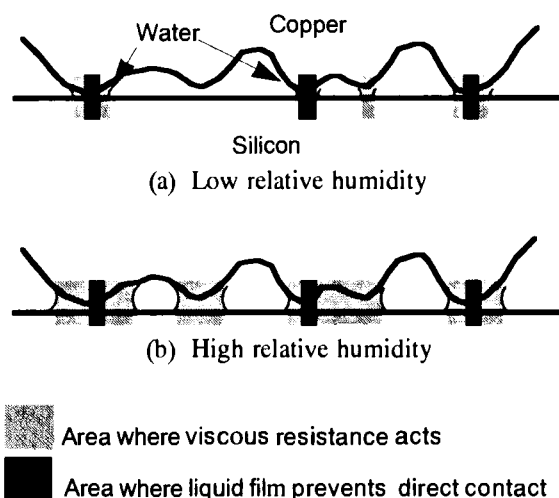


Figure 10. Effect of relative humidity on area where viscous resistance acts

a copper specimen and a silicon wafer both with a flat contact surface were rubbed against each other at a relative humidity of 1 to 53%, sliding speed of 1.6 to 64  $\mu\text{m/s}$ , and normal load of -93 to 327  $\mu\text{N}$ . The following conclusions were obtained.

- (1) In the atmosphere of approximately 1% relative humidity, the friction coefficient considering pull-off force decreased with decreasing load.
- (2) In the atmosphere of 18% relative humidity, the friction coefficient increased at low loads even when the pull-off force was considered.
- (3) When the sum of the normal load and pull-off force (effective load) was 82  $\mu\text{N}$  and above, the friction coefficient increased with decreasing sliding speed when measured under a constant load and variable sliding speeds.
- (4) For an effective load of 82  $\mu\text{N}$  and below, the friction coefficient increased with increasing sliding speed.
- (5) In the measurement of friction force under decreasing loads, the greater the sliding speed, the greater the change in the friction force immediately before the test specimens separated, and the pull-off force also decreased.
- (6) The above conclusions (1), (3) and (5) can be qualitatively explained by decreased direct contact between the solids due to the formation of a liquid film. Conclusions (2) and (4) can be qualitatively explained by the viscous resistance of liquids.

#### REFERENCES

1. Y. Tai, L. Fan & R. S. Muller : Proc. IEEE Micro Electro Mechanical Systems (1988) 1.
2. H. Ota, T. Oda & M. Kobayashi : Proc. IEEE Micro Electro Mechanical Systems (1995) 197.
3. Y. Ando, Y. Ishikawa and T. Kitahara, Trans. ASME. J. Tribology, 117 (1995) 569.
4. Y. Ando, Y. Ishikawa and T. Kitahara, Japanese J. Tribology, 40 (1995) in printing.
5. K. L. Johnson, K. Kendall and A. D. Roberts, 324 (1971) 301.
6. J. N. Israelachvili, "Intermolecular and Surface Forces," Academic Press Ltd., London (1985).

## Modelling friction in the analysis of metal forming and machining processes

P.L.B. Oxley

School of Mechanical and Manufacturing Engineering,  
University of New South Wales, Sydney 2052, Australia

Asperity interaction slipline field models are given to explain the role of tool surface roughness, lubrication condition and apparent contact pressure on the tool-work interface frictional conditions in metal forming and machining processes. It is shown how the slipline fields used to model asperity deformation can be joined in a consistent manner with the slipline field representing the bulk deformation for the process considered. In the case of machining, consideration is given to the influence of strain-rate and temperature on the chip material flow stress and hence on the frictional condition at the tool-chip interface. Evidence is given that the lubrication at the tool-work interface in some forming processes can be elastohydrodynamic in nature even for conditions where asperity interactions are taking place.

### 1. INTRODUCTION

This paper is mainly concerned with conditions where the lubricant film at the tool-work interface is thin (or virtually non-existent) compared with the height of asperities on the contacting surfaces, which is the case in many forming and machining processes. For such conditions the frictional force at the interface results from the interaction of asperities on the surfaces. Only brief consideration is given to conditions where the lubricant film thickness is greater than the asperity height and the frictional force results purely from the shearing of the film.

In considering the friction at tool-work interfaces and between metallic surfaces in sliding contact in general the most widely used asperity interaction model is the adhesion model of Bowden and Tabor [1]. With this model the frictional force is assumed to be the force needed to shear the welded junctions formed by adhesion at the tips of contacting asperities. Tabor [2] has shown that if account is taken of the plastic deformation of asperities under the combined action of the normal and shear stresses acting on them then the model can account for lubrication effects and explain, for example, the very high values of friction coefficient observed in experiments carried out in vacuum. In order to allow for the influence of the surface roughness of the contacting surfaces on friction it is necessary with the adhesion model to introduce a separate and

independent ploughing term. This is usually neglected on the grounds that its contribution to friction will be much smaller than that of the adhesion term. There is now strong evidence to suggest that sliding friction can be represented more realistically by an alternative model - the so-called wave model. With this, the frictional force is assumed to result from the pushing of waves of plastically deformed material across the softer surface ahead of asperities on the harder surface. This model effectively combines the adhesion and ploughing processes in the single model and allows for their interaction. The present paper describes the application of the wave model to modelling tool-work interface friction in the analysis of forming and machining processes.

Experiments show that the surface roughness of both the tool and work surfaces can affect the friction between these surfaces. The most important role of the workpiece surface roughness appears to be to facilitate the entrapment of lubricant in the surface valleys which then comes into play in the contacting regions during working. This mechanism of lubrication is perhaps most relevant to forging type processes where the tool approaches the workpiece in a direction normal to the workpiece surface. In what follows account is not taken of the influence of workpiece surface roughness and attention is concentrated on the part played by the tool surface roughness in determining the frictional

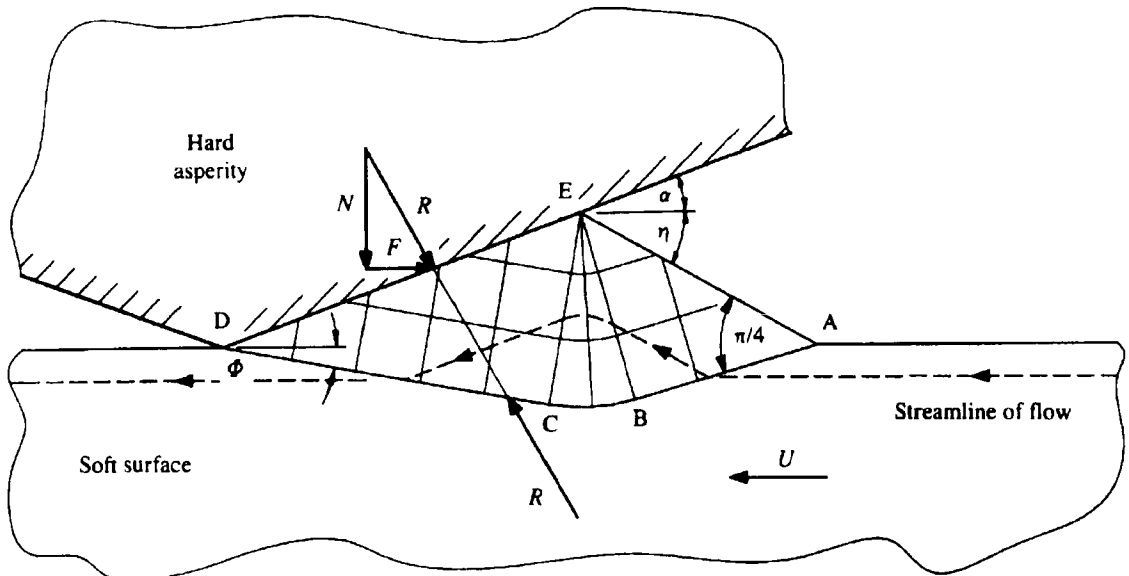


conditions at the tool-work interface. It is this latter roughness together with the lubrication condition which plays the dominant role in determining the interface frictional conditions in processes such as extrusion, rolling, machining and the like.

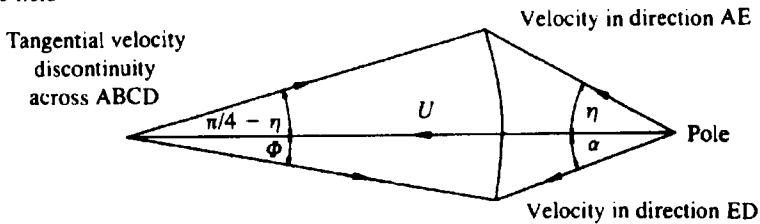
2. WAVE MODEL

The plane strain, steady state slipline field introduced by Challen and Oxley [3] to represent the wave model of friction is given in Figure 1. The hard asperities are assumed to be rigid and the deforming material to be rigid-perfectly plastic (non-hardening). In constructing the field the independent variables are taken to be the slope of the hard

asperity  $\alpha$  and the normalized strength of the interfacial film  $f$  along DE, where  $f = \tau/k$  with  $\tau$  the shear strength of the interfacial film and  $k$  the shear flow stress of the deforming material. It can be seen that  $\alpha$  and  $f$  are in effect surface roughness and lubrication parameters respectively. With this model the straight line joining A and D must be parallel to the sliding velocity  $U$  to satisfy volume constancy. Also, the shear force on the soft asperity (wave) must act in the direction DE to oppose motion, with the value of  $f$  determining the inclination of the sliplines to DE. These conditions together with the condition that the sliplines must be inclined at  $\pi/4$  to the stress-free surface EA to satisfy equilibrium define the slipline field. It follows that



(a) Slipline field



(b) Hodograph

Figure 1. Wave model of friction.

$$\alpha + \Phi = \frac{1}{2} \cos^{-1} f \quad (1)$$

and

$$\eta = \sin^{-1} \left\{ (1-f)^{-1/2} \sin \alpha \right\} \quad (2)$$

where  $\Phi$  is the angle between U and CD and  $\eta$  is the slope of EA. The hodograph in Figure 1 shows that there is a discontinuity in the tangential component of velocity across the boundary slipline ABCD so that material that enters and leaves the field with a velocity U flows in the directions AE and ED in the regions ABE and CDE and along a curved path in the centred fan region BCE.

An expression for the coefficient of friction for this model is found by working along sliplines such as ABCD from the free surface EA, where the hydrostatic stress  $p$  is equal to  $k$  and compressive, using the relevant Hencky equation to determine the stresses at the interface DE. In this way it can be shown that

$$\mu = \frac{A \sin \alpha + \cos(\cos^{-1} f - \alpha)}{A \cos \alpha + \sin(\cos^{-1} f - \alpha)} \quad (3)$$

where

$$A = 1 + \frac{1}{2}\pi + \cos^{-1} f - 2\alpha - 2 \sin^{-1} \left\{ (1-f)^{-1/2} \sin \alpha \right\}.$$

Equation (3) predicts in agreement with experience that an increase in surface roughness (increase in  $\alpha$ ) or a decrease in the effectiveness of the lubrication (increase in  $f$ ) will both increase  $\mu$ . Challen et al. [4] have made experiments in which a hardened steel wedge representing a model asperity was indented vertically into the horizontal surface of an aluminium alloy specimen with subsequent low speed ( $\approx 0.3 \text{ mm s}^{-1}$ ) movement of the specimen in a direction normal to the edge of the wedge with the vertical force held constant. Measured values of  $\mu$  were found to be in good agreement with values given by equation (3) for a wide range of  $\alpha$  and  $f$  values. Black et al. [5] have confirmed this good agreement for an even wider range of conditions. Moalic et al. [6] have shown that equation (3) predicts  $\mu$  accurately for actual (multi-asperity) surfaces so long as  $\alpha$  is measured from those parts of the asperities which are in contact during sliding.

The asperity deformation model given in

Figure 1 is suitable for modelling friction in metal working processes in the sense that it considers the interaction of a hard surface with a relatively soft one. It does however represent those cases where the contact is at the tip of asperities with the real area of contact much less than the apparent area of contact. Such cases correspond to values of apparent contact pressure (normal force between contacting surfaces divided by the apparent area of contact) which are much smaller than those normally encountered in metal working processes. Consideration is now given to the influence of apparent contact pressure on the asperity interactions taking place.

The plane strain, steady state slipline fields introduced by Challen and Oxley [7] to take account of the influence of apparent contact pressure on asperity deformation are given in Figure 2. The asperities on the harder surface are represented by a regular symmetrical sawtooth form made up of straight-sided teeth (wedges). The slope of the hard asperities is again taken as  $\alpha$  and the normalized interfacial film strength as  $f$ . It is easily shown that the angles  $\Phi$  and  $\eta$  in Figure 2 can be determined from equations (1) and (2) as before. The progression from Figures 2(a) to 2(c) represents the increase in the ratio of the real to apparent area of contact  $A_r/A_a$  which occurs with increase in the apparent contact pressure. The fields in Figures 2(a) and 2(b) will be referred to as the single fan and double fan fields and apply in the ranges  $0 < A_r/A_a \leq 0.5$  and  $0.5 < A_r/A_a < 1.0$  respectively. The field in Figure 2(c) for which  $A_r/A_a = 1.0$  will be referred to as the full contact field. The flow of material through the fields is indicated in each case by the typical streamlines given in Figure 2. It should be noted from the hodographs that material which passes through the wave is retarded relative to the rest of the flow. Expressions for the coefficient of friction, ratio of real to apparent area of contact etc. in terms of apparent contact pressure were obtained by Challen and Oxley [7] from stress analyses similar to that referred to for the single fan field. Examples of results calculated from these expressions are given in Figure 3 for  $\alpha = 5^\circ$  and a range of  $f$  values. Results were also obtained by Challen and Oxley [7] for  $\alpha = 15^\circ$  and  $\alpha \rightarrow 0^\circ$ . The results show that for lower values of the normalized apparent contact pressure  $P_a/k$  where the single fan field applies,  $\mu$  for a given  $\alpha$  and  $f$  is independent of

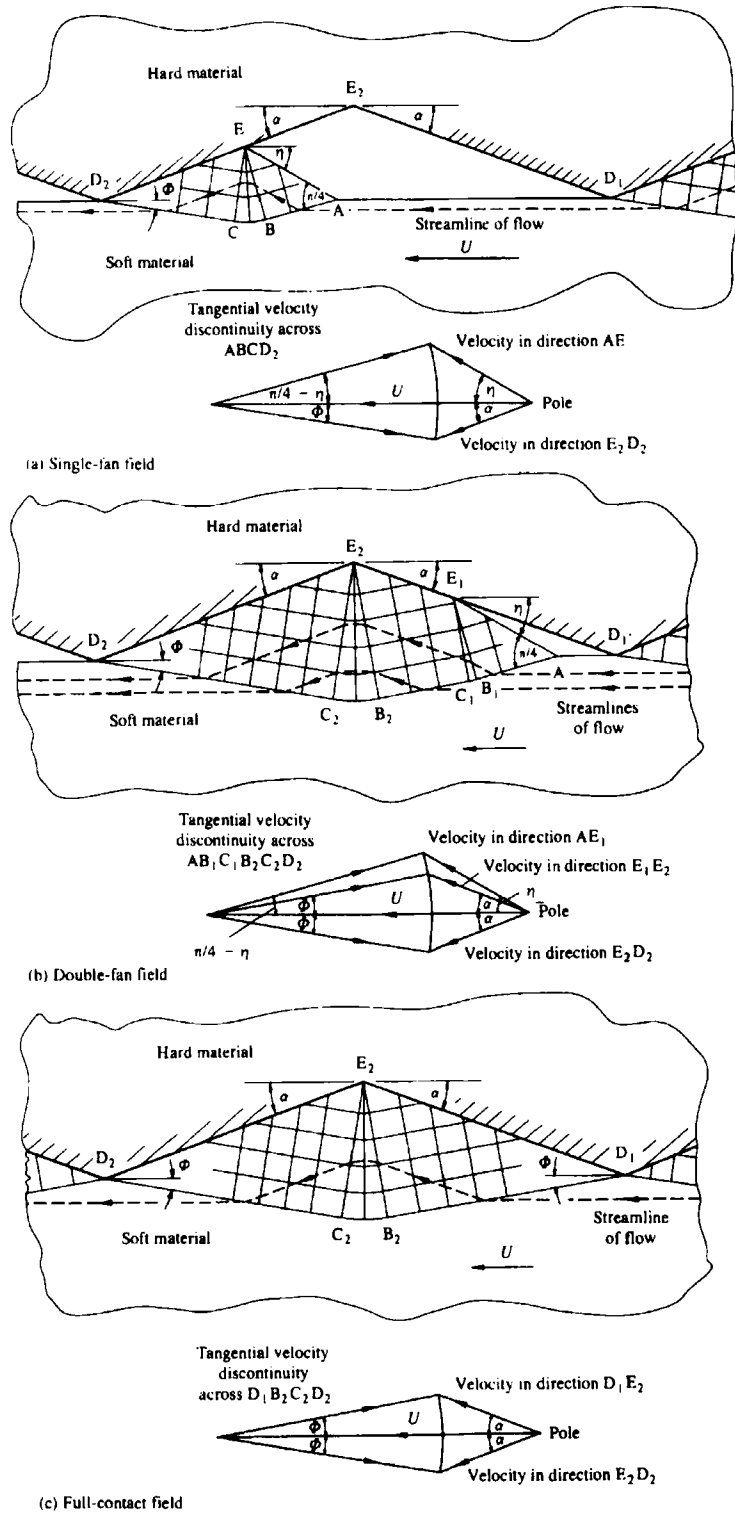


Figure 2. Slipline fields and hodographs showing influence of apparent contact pressure.

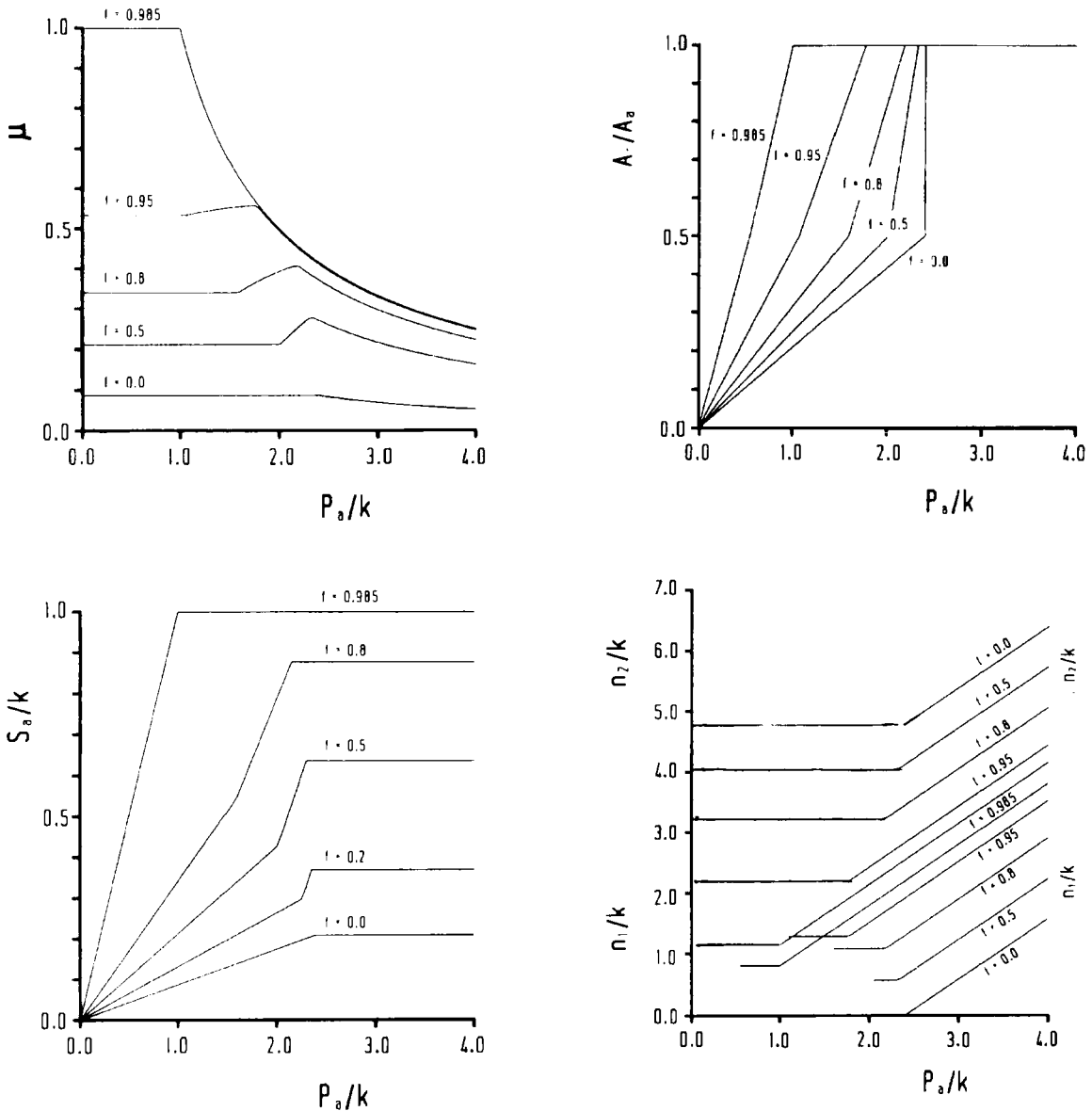


Figure 3. Calculated results for  $\alpha = 5^\circ$  showing the influence of  $P_a/k$  on  $\mu$ ,  $A_r/A_a$ ,  $S_a/k$  and  $n_1/k$  and  $n_2/k$ .

the value of  $P_a/k$  thus obeying the basic laws of friction. From the point where the double fan field takes over to full contact conditions  $\mu$  is predicted to increase with increase in  $P_a/k$  for most values of  $f$ . Once the full contact field is established then  $\mu$  decreases hyperbolically with increase in  $P_a/k$ . The results show that the value of  $P_a/k$  required to give  $A_r/A_a = 1$  increases with decrease in  $f$  and with decrease in  $\alpha$ . For the full contact field the results

show that the apparent shear stress  $S_a/k$  for a given  $\alpha$  and  $f$  is independent of  $P_a/k$  with its value decreasing with decrease in  $f$  and decrease in  $\alpha$ . The results for the interface normal stresses  $n_1/k$  and  $n_2/k$  (where  $n_1$  acts on  $E_2D_1$  and  $n_2$  acts on  $E_2D_2$ ) show that their values are independent of loading for the single and double fan fields but are directly proportional to loading for the full contact field.

Detailed experimental investigations of the single

fan field have been made and good agreement shown between predicted and experimental results as mentioned above. Far less experimental work has been done on the double fan and full contact fields. Possibly the most important question with the full contact model is whether steady state conditions as postulated in the model can exist once the real and apparent areas of contact are equal. Strong evidence which says they can has been provided by Doyle et al. [8]. In their experiments these researchers used a transparent sapphire cutting tool to observe the frictional interactions occurring at the tool-chip interface directly during metal cutting experiments. Their results show that although in the immediate vicinity of the cutting edge there was intimate contact ( $A_r/A_a \approx 1.0$ ), as would have been expected considering the high normal pressure at the interface and the chemically clean contacting surfaces, relative movement was observed at the interface in this region. To explain this movement for such extreme conditions, Doyle et al. have likened the process to the translation of elastic buckles in the chip surface along the interface in a manner resembling the movement of a ruck in a carpet. In support of this they have pointed out the observation of such an effect by Schallamach [9] when highly elastic rubbers slide against smooth surfaces. However, they considered this mechanism doubtful for metals where the elastic strains that can be sustained are several orders of magnitude smaller than for rubbers. Agreeing with this Oxley [10] proposed that the full contact field (Figure 2(c)) gave a far better explanation of their observations. The demonstration that steady state flow can occur when the real and apparent areas of contact are equal does not rule out the possibility of seizure which has been proposed by Trent [11] and others as the most common condition encountered at the tool-chip interface in machining. For the models given in Figure 2 steady state conditions theoretically apply as long as  $\Phi > 0$ . Once  $\Phi = 0$  then material can no longer flow into, or out of the field and seizure might be said to have occurred. In their experiments for the single fan field (Figure 2(a)) Challen et al. [4] found that steady state conditions ceased well before  $\Phi = 0$  as the material fractured because of the high strains involved in wave formation. Therefore, in considering the transition from steady state to seizure conditions, the ductility of the deforming material is a significant property. Oxley [10] has concluded

that for most practical machining conditions the flow at the interface is steady state and is best modelled by the full contact field given in Figure 2(c). He has pointed out that by indicating retardation of the flow at the interface this field can explain the swept-back layer usually observed adjacent to the chip surface which has been in contact with the tool cutting face.

An important feature of the analysis based on the slipline field models given in Figure 2 is that it allows the values of contact pressure at which full contact occurs to be predicted as a function of the surface roughness of the harder surface and of the lubrication condition. Some idea of the accuracy of these predictions can be obtained from tool-work interface stresses determined from experimental investigations of plane strain extrusion and machining. Metallographic examinations of the tool-work interface for both these processes suggest that full contact conditions exist. By analysing experimental flow fields for plane strain extrusion through wedge-shaped dies Conning et al. [12] were able to determine the apparent contact pressures at the die-work interface for various die angles. The lubrication in these experiments was so effective that  $f$  had extremely low values approaching zero at the interface. The results showed that  $P_a/k$  varied from approximately 3 for a die half-angle of  $30^\circ$  to 4 for a die half-angle of  $60^\circ$ . From an analysis of machining results, Oxley and Hastings [13] found that values of  $P_a/k$  at the tool-chip interface, where  $f$  was large and approached unity, were of the order of 1.2. For typical die and tool surfaces it might be expected that the average asperity slope  $\alpha$  would fall in the range  $0^\circ$  to  $5^\circ$ . From the results in Figure 3 ( $\alpha = 5^\circ$ ) the transition to full contact is predicted to take place at  $P_a/k$  values of approximately 2.4 and 1 for  $f$  values of 0 and 1, while the corresponding values for  $\alpha \rightarrow 0^\circ$  are [7] 2.6 and 1. The experimental values of  $P_a/k$  (3-4 for extrusion and 1.2 for machining) are therefore somewhat greater than the corresponding predicted transition values (2.4-2.6 for extrusion and 1 for machining). Therefore, for the examples considered the theory predicts full contact conditions as observed in the experiments.

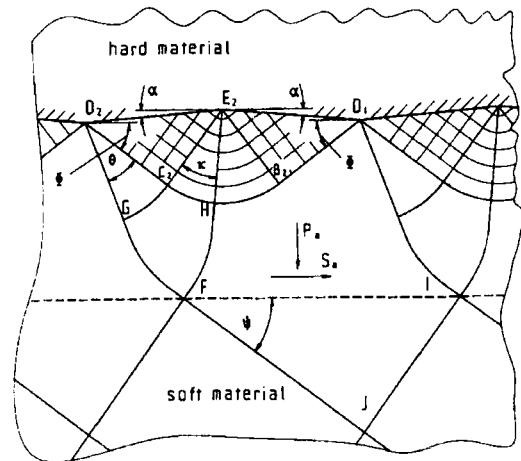
Some support for the shape of the curves of  $S_a/k$  against  $P_a/k$  and hence for the shape of the  $\mu$  curves in Figure 3 has been given by Shaw et al. [14]. They measured the friction between heavily plastically deformed sliding surfaces under various conditions of lubrication and found a smooth transition from the

proportionality region at low loads to a rather flat curve at high loads. In Figure 3 the slope of the  $S_a/k$  against  $P_a/k$  lines is greatest when the double fan field is being considered but it should be noted that these figures apply to an ideal surface made up of symmetrical asperities all having the same slope. For a real surface it would not be unreasonable to expect that as load increased through its intermediate range the steeply increasing  $S_a/k$  values associated with the double fan fields of some asperities would be compensated by the constant  $S_a/k$  values attributable to those asperities already in full contact. Hence there would be a smooth transition from the single fan model to the full contact model, thus yielding friction force versus load curves of similar shape to those observed by Shaw et al. [14].

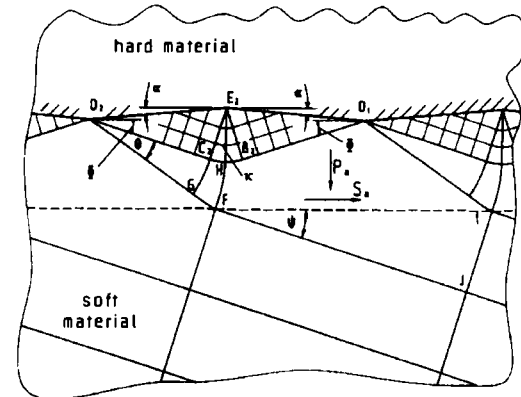
### 3. COMBINED FRICTION AND BULK DEFORMATION SLIPLINE FIELD

Consideration is now given to how the slipline fields representing asperity interactions (Figure 2) can be joined to the slipline field representing the bulk deformation process under consideration. To simplify matters attention will be limited at this stage to those processes where the work material in the bulk field adjacent to the tool face, although in a plastic stress state, can be assumed to be moving as a rigid body. There are many examples of such cases given in the literature. In these the bulk slipline field adjacent to the die interface consists of straight sliplines indicating that the hydrostatic stress and velocity are constant throughout this region. It is shown in Figure 4 how this type of field can be joined to the asperity interaction field for the full contact field (Figure 2(c)) which appears to be the applicable field for many processes. The approach used is similar to that described by Sutcliffe [15] in considering the indentation by flat punches of a specimen undergoing bulk plastic deformation.

To join the two fields a fan of angle  $\theta$  centred at  $D_2$  is constructed as shown in Figure 4. Slipline  $D_2G$  is then extended to the point F where it meets the straight slipline FJ of the bulk field tangentially. The field is completed by constructing the slipline FH to meet the appropriate radial line of the fan centred at  $E_2$ . With this combined field plastic deformation only occurs as material flows through the region  $D_1B_2C_2D_2E_2$ . The region  $D_1IJFH$  is assumed to be



(a)



(b)

Figure 4. Combined asperity interaction and bulk deformation slipline fields; (a)  $\alpha = 5^\circ$ ,  $f = 0.1$ , (b)  $\alpha = 5^\circ$ ,  $f = 0.7$ .

rigid and to be stressed below the yield point while the remainder of the field is rigid but in a plastic stress state. The horizontal line drawn through point F can be conveniently looked upon as the boundary between the asperity interaction and bulk fields. The thickness of the boundary layer will be of the same order of magnitude as the asperity depth and will therefore for most processes be minute compared to the size of the bulk field. To construct the field for given values of  $\alpha$  and  $f$  it is necessary to determine  $\theta$  in terms of these parameters. This is achieved in the following way. Assume that the value of the hydrostatic stress at F is known then the contact

pressure  $P_a$  on the boundary can be expressed in terms of  $p_F$  as

$$P_a = p_F + k \sin 2\Psi \quad (4)$$

where  $\Psi$  is the angle made by the slipline FJ with the boundary with  $\Psi$  given by

$$\Psi = \frac{1}{2} \cos^{-1} \frac{S_a}{k} \quad (5)$$

where  $S_a$  is the shear stress (frictional shear stress) on the boundary determined from the expressions given by Challen and Oxley [7] for the given values of  $\alpha$  and  $f$ .  $P_a$  can also be obtained in terms of  $p_F$  by working along sliplines from F using the Hencky equations to determine the hydrostatic stresses  $p_1$  and  $p_2$  in the regions  $D_1B_2E_2$  and  $C_2D_2E_2$  respectively. Thus working from F to G and G to  $C_2$

$$p_2 = p_F + 2k(\theta + \Phi - \Psi) + 2k\theta \quad (6)$$

and then from  $C_2$  to  $B_2$

$$p_1 = p_2 - 2k(2\Phi) \quad (7)$$

The normal stresses  $n_1$  and  $n_2$  on the interfaces  $E_2D_1$  and  $E_2D_2$  are now given by

$$n_1 = p_1 - k \sin(\Phi + \alpha) \quad (8)$$

and

$$n_2 = p_2 + k \sin(\Phi + \alpha) \quad (9)$$

and in terms of these stresses it is easily shown that

$$P_a = \frac{n_1 + n_2}{2} \quad (10)$$

or combining equations (6) to (10) that

$$P_a = p_F + 4k\theta - 2k\Psi \quad (11)$$

Equating equations (11) and (4) then gives

$$\theta = \frac{2\Psi + \sin 2\Psi}{4} \quad (12)$$

To complete the field the angle  $\kappa$  made by  $E_2H$  with  $E_2C_2$  is found by selecting its value to make the change in hydrostatic stress around the slipline loop  $C_2HFGC_2$  zero as required. This gives

$$\kappa = \theta + \Phi - \Psi \quad (13)$$

For given values of  $\alpha$  and  $f$ ,  $\theta$  and  $\kappa$  can now be calculated from equations (12) and (13) using values of  $\Psi$  and  $\Phi$  determined from equations (5) and (1) and the appropriate slipline field constructed. Two examples are given in Figures 4(a) and 4(b). In both cases  $\alpha = 5^\circ$  while in Figure 4(a)  $f = 0.1$  and in Figure 4(b)  $f = 0.7$ . In order to check the validity of such fields it is necessary to show that the rigid region  $D_1IJFH$  is not overstressed. So far no complete stress solution has been found for this region. However, a partial check can be made in the way suggested by Hill [16] by considering the stresses at critical corners of the region. Hill's analysis shows that except for very small values of  $\alpha$  and  $f$  ( $\alpha < 2^\circ$ ,  $f < 0.1$ ) the assumed rigid corner at  $D_1$  is overstressed. This problem can be overcome by replacing the sharp corner in the hard surface at  $D_1$  by a small flat surface parallel to the sliding direction. Alternatively the sharp corner in the slipline field at  $D_1$  can be eliminated by assuming that a small free surface exists to the left of  $D_1$  as with the double fan field.

So far only full contact conditions in which  $A_r = A_a$  have been considered in constructing the combined field. In this case the frictional shear stress  $S_a$  is independent of the apparent contact pressure  $P_a$  and it is only necessary to show that the value of  $P_a$  calculated from the bulk deformation field is sufficiently large for the full contact field to apply. When  $P_a$  is such that  $A_r/A_a < 1$  and the single fan or double fan fields apply than  $S_a$  is a function of  $P_a$  as well as of  $\alpha$  and  $f$  as shown by the results in Figure 3. Interestingly for such cases the normalized frictional shear stress boundary condition ( $S_a/k$ ) which determines through equation (5) the inclination of the bulk field sliplines to the tool face can not be specified independently of the bulk process taking place, i.e. independently of  $P_a$ . An iterative procedure will therefore be necessary in obtaining solutions for problems of this nature. Combined fields for these cases have been considered by Li [17]. Future work will need to investigate the combination of asperity interaction

and bulk fields for those processes such as rolling where plastic deformation is occurring in the bulk material adjacent to the tool face.

#### 4. NATURE OF LUBRICATION

It has been shown above how the frictional condition at the tool-work interface in metal working processes can be described in terms of a surface roughness parameter  $\alpha$  and a lubrication parameter  $f$  where  $f = \tau/k$  with  $\tau$  the shear strength of the lubricant film. Consideration is now given to the mechanism of lubrication which applies in the case of the wave model of friction and how the shear strength of the lubricant film might be measured. It is appropriate to start by considering some of the background work on the strength of lubricant films.

Shear tests on thin organic films such as those of Briscoe and Tabor [18] have shown that at constant values of shear strain-rate (defined as shear velocity applied to film divided by film thickness) and temperature their shear strength is related to the normal pressure acting on the film by the relation

$$\tau = b + cn \quad (14)$$

where  $\tau$  is the shear strength,  $n$  is the normal pressure and  $b$  and  $c$  are constants. According to Johnson [19] and Tabor [20] this equation applies under vastly different testing conditions. It applies under elastohydrodynamic lubrication (EHL) conditions such as those encountered when the tests are made on a disc machine using combined rolling and sliding with comparatively thick films of the order of  $1 \mu\text{m}$  thickness. It also applies in slow-speed sliding experiments made on extremely smooth surfaces in which the film may be only a few tens of ångströms thick. For normal liquid lubricants  $b$  is generally very small compared with  $cn$  and can be ignored. In this case equation (14) reduces to

$$\tau = cn \quad (15)$$

Experiments such as those of Evans and Johnson [21] on a disc machine show that above a certain strain-rate the shear strength, for a given normal pressure and temperature, assumes a more or less constant value known as the limiting shear strength. Equation (15) then applies irrespective of the value

of strain-rate.

Black *et al.* [22] made wedge experiments similar to those described by Challen *et al.* [4] using a liquid lubricant to determine the relationship between the shear strength of the film and the normal stress at the wedge-wave interface. The lubricant used in the tests was Shell Vitrea 100. A main requirement of the tests was to vary the normal stress  $n$  at the interface over a range which was sufficient to check the  $\tau$  -  $n$  relationship. This was achieved by using specimen materials of different hardnesses so that  $n$  varied by over an order of magnitude. The materials used for this purpose were in ascending order of hardness: Woods alloy, 99% commercially pure aluminium, cold-rolled 5083-H321 aluminium-magnesium alloy and cold-rolled brass. The experimental results obtained showed that once steady-state conditions had been achieved in a test there was little variation in the measured forces acting at the interface which indicated a film of fairly uniform properties at the interface. Black *et al.* [22] calculated the average values of  $\tau$  and  $n$  by resolving the measured forces parallel and normal to the interface and then dividing the relevant component by the geometric area of the interface measured from experimental waves. This presupposed that the real and apparent areas of contact at the interface were equal. Black *et al.* [22] showed this to be a reasonable assumption by demonstrating that for the measured wedge surface roughness and apparent contact pressure the full contact field (Figure 2(c)) would have applied at the interface. After making a small correction for the surface roughness of the wedge at the wedge-wave interface it was shown that the values of  $\tau$  and  $n$  determined in this way could be accurately represented by the relation

$$\tau \approx 0.11n \quad (16)$$

That is, the relationship given in equation (15) applied and the value of the constant  $c$  was similar to the value reported by Johnson [19] and others. Black *et al.* [22] also made tests using Molykote 321 R Bonded Lubricant which is a solid lubricant in an inorganic binder which they did not publish. These results, although more scattered than the oil results, still showed a good fit with equation (15) but with  $c$  having a much lower value, namely  $c \approx 0.03$ .

Black *et al.* [22] compared their oil results with the limiting shear strength results obtained by Evans



and Johnson [21]. The values of  $n$  in the two types of tests fell in the same range (0.2 to 1.8 GPa in the wedge tests) with the oil-film temperature only slightly higher in the disc machine tests than in the wedge tests. The results for the Shell Vitrea 100 were found to be very close to the results of Evans and Johnson [21] for Santotrac 50 traction fluid. On this basis Black *et al.* [22] suggested that the lubrication mechanism at the wedge-wave interface was the same as with the disc machine, namely EHL, and that the measured shear stress in their tests was the limiting shear strength.

Ford [23] has calculated the film thickness  $h$  at the wedge-wave interface assuming EHL conditions and using a Grubin style analysis. For a simple wedge shaped inlet geometry he obtained the relation

$$h = \frac{6\eta_0 u \delta}{\tan \beta} \quad (17)$$

where  $\eta_0$  is the viscosity of the lubricant at entry,  $\delta$  is the pressure viscosity exponent,  $\beta$  is the angle between the contacting surfaces at entry and  $u$  is the entraining velocity. Bloor *et al.* [24] have derived a similar relation in their EHL analysis for the plane strain drawing process. For the wave model in Figure 1 it can be seen that  $\beta = \alpha + \eta$ . However, the tracing of the profile of an experimental wave given in Figure 5 shows that the corner corresponding to the corner at E in Figure 1 is not sharp, as with the theoretical model, but rounded. This rounding results from the wedge tests having been made on a real (hardening) material while in the theoretical solutions in Figure 1 a rigid-perfectly plastic (non-hardening) material is assumed. For more details see Conning *et al.* [12]. By drawing a tangent to the wave profile in Figure 5,  $\beta$  is estimated to be about  $0.2^\circ$ . However, it could be considerably less, especially if the elastic deformation of this region which would have occurred during a test is taken into account. Taking  $\beta = 0.2^\circ$  together with



Figure 5. Tracing of profile of experimental wave.

$\eta_0 = 0.26 \text{ Pa s}$ ,  $\delta = 2 \times 10^{-8} \text{ Pa}^{-1}$  and  $u = v_{ED} = 2.2 \times 10^{-4} \text{ ms}^{-1}$  as determined from the hodograph then it is found from equation (17) that  $h \approx 1 \text{ nm}$ . If  $\beta$  is taken as  $0.02^\circ$  then  $h \approx 10 \text{ nm}$ . Surface roughness measurements showed that the asperities on the wedge face were of the order of  $60 \text{ nm}$  high and it is clear that a film thickness of  $1 \text{ nm}$  or even  $10 \text{ nm}$  is insufficient to separate the surfaces in the conventional sense. However, if, as pointed out by Black *et al.* [22], the flow along the wedge face is represented by the full contact field, then metal-to-metal contact can be avoided by a film along the wedge-wave interface which is much thinner than the asperity height. With this model the soft material flows into and out of the valleys on the hard surface and it would not seem unreasonable to look upon the lubricant film as progressing along the interface by a snaking action.

The experimental results of Evans and Johnson [21] show that the minimum shear strain-rate for which the measured shear strength is equal to the limiting shear strength for Santotrac 50 is  $10^4 \text{ s}^{-1}$  for a film temperature of  $40^\circ\text{C}$  and a mean pressure of  $1.57 \text{ GPa}$ . For the wedge tests the velocity at the wedge-wave interface was approximately  $2 \times 10^{-4} \text{ ms}^{-1}$ . Therefore, for a film thickness of  $1 \text{ nm}$  the shear strain-rate is  $2 \times 10^5 \text{ s}^{-1}$  which, considering the results of Evans and Johnson [21], would not be inconsistent with the contention that EHL conditions exist at the interface with the film shear strength equal to the limiting shear strength. It is of interest that in recent times a number of workers have made direct measurements of EHL film thicknesses of the order of  $1 \text{ nm}$  (see Dowson [25]).

Black *et al.* [26] have used the wedge test to measure the shear strength of the lubricant film at the wedge-wave interface for a range of lubricants. Considering the similarities of the conditions at this interface and those at tool-work interfaces in many metal working processes it might well be expected that the values of shear strength measured in this way would be applicable in the analysis of processes. In their tests Black *et al.* [26] used a half wedge so that the forces on the wedge face could be measured at all stages of the test, including the start when the wedge was indented vertically into the specimen. The specimen material used was cold-rolled 5083-H321 aluminium-magnesium alloy. The wedge was machined from Bohler Vew K460 Amutits tool steel, hardened and tempered to RC55, ground and then

polished on its leading face with 1200 grade paper in a direction normal to the edge. It was then washed in acetone and dried in a hot stream of air. The surface roughness obtained on the wedge leading face, measured normal to the edge was approximately  $0.04 \mu\text{m}$  (CLA). Three tests were carried out for each lubricant with one dry test made. The wedge was carefully checked and cleaned between each test. As in previous wedge tests one slow sliding speed ( $\approx 0.3 \text{ mm s}^{-1}$ ) was used.

Results obtained for some of the lubricants tested are given in Table 1. The shear and normal stresses  $\tau$  and  $n$  at the interface were determined by the same method as in the earlier investigation of Black *et al.* [22]. The values of interface friction coefficient  $\mu_i$  given in the table were found from the ratio of the

shear and normal forces acting at the interface during steady-state wave formation and initial indentation. It can be seen from Table 1 that the lubricants exhibit a range of  $\tau$  values with the solid lubricant Molykote, giving by far the lowest value of  $\tau$ .

If the shear strength of the lubricant film is determined by equation (15), then an interesting problem arises in connection with the results for the full contact field given in Figure 3. With the single and double fan fields the normal stresses  $n_1$  and  $n_2$  at the interfaces  $E_2D_1$  and  $E_2D_2$  (Figure 2) are independent of the apparent contact pressure. Therefore, in these cases it is acceptable to characterise the influence of different lubricants on the frictional conditions in terms of the value of  $f$  associated with each lubricant. However, for the full

Table 1  
Measured shear strength values for different lubricants

| Lubricant          | $\mu_i$        |             | Steady state stresses     |                        |
|--------------------|----------------|-------------|---------------------------|------------------------|
|                    | Wave formation | Indentation | $\frac{\tau}{\text{MPa}}$ | $\frac{n}{\text{MPa}}$ |
| Vitrea 100         | 0.074          | 0.192       | 70.94                     | 961.32                 |
| Vitrea 100         | 0.103          | 0.204       | 88.06                     | 859.15                 |
| Vitrea 100         | 0.092          | 0.206       | 86.02                     | 938.47                 |
| Average            | 0.089          | 0.201       | 81.68                     | 919.65                 |
| Standard deviation | 0.014          | 0.008       | 9.35                      | 53.62                  |
| Motor oil          | 0.058          | 0.209       | 56.85                     | 983.48                 |
| Motor oil          | 0.060          | 0.207       | 58.33                     | 979.74                 |
| Motor oil          | 0.065          | 0.213       | 60.17                     | 928.73                 |
| Average            | 0.061          | 0.209       | 58.45                     | 963.98                 |
| Standard deviation | 0.004          | 0.003       | 1.67                      | 30.59                  |
| HVI 650            | 0.124          | 0.189       | 104.41                    | 843.52                 |
| HVI 650            | 0.128          | 0.208       | 116.80                    | 911.46                 |
| HVI 650            | 0.111          | 0.211       | 103.20                    | 926.54                 |
| Average            | 0.121          | 0.202       | 108.14                    | 893.84                 |
| Standard deviation | 0.009          | 0.012       | 7.53                      | 44.22                  |
| Molykote           | 0.025          | 0.188       | 31.33                     | 1255.92                |
| Molykote           | 0.024          | 0.204       | 26.27                     | 1092.08                |
| Molykote           | 0.026          | 0.207       | 26.20                     | 1018.57                |
| Average            | 0.025          | 0.200       | 27.94                     | 1122.19                |
| Standard deviation | 0.001          | 0.010       | 2.94                      | 121.50                 |
| Dry                | —              | 0.201       | —                         | —                      |

contact model  $n_1$  and  $n_2$  increase as  $P_a$  is increased and hence according to equation (15) so does  $\tau$  and as a consequence  $f$ . The apparent shear stress  $S_a/k$  will therefore no longer be independent of loading in this range as it is shown to be in Figure 3 but will increase as  $P_a/k$  increases. A further problem is to do with the change in normal stress from one side of the asperity valley to the other - note from the results in Figure 3 that  $n_2 > n_1$ . Therefore, although the film thickness might be determined by the conditions at entry to the interface the question arises as to whether or not  $\tau$  varies along the interface as a result of the normal stress varying. Further work will be needed to resolve these problems.

## 5. PROCESS FRICTION MODELLING

### 5.1. Forming

In making their wedge tests with liquid lubricants Black *et al.* [26] noted that the test surface of the specimen acquired a mirror-like finish after the passage of the wave across it. Based on this observation these authors [27] have recently proposed that the wedge test could be adapted as a burnishing process. This would differ from conventional burnishing processes in that the force applied normal to the surface being burnished would deliberately be held constant. This ensures that under plane strain conditions the plastic wave will be pushed along the surface with the wedge edge on the surface. In this way no material is removed (torn) during the process and as a consequence the quality of the surface obtained can be greatly enhanced. In considering friction modelling in forming processes this novel burnishing process provides a good starting point.

To determine the level of surface finish which might be achieved with the proposed burnishing process Black *et al.* [27] made a series of wedge tests in which the surface roughness of the test surface was measured before and after each test. The specimen material was again cold-rolled 5083-H321 aluminium-magnesium alloy with Shell Vitrea 100 used as the lubricant. Tests were made with both a tool steel wedge as before and with a sapphire wedge. Surface roughness measurements on the wedge contact faces and the specimen test surface prior to the tests gave the following values in what would be the sliding direction and normal to this

direction in a test respectively (all measurements in  $\mu\text{m Ra}$ ): 0.05 and 0.07 for the steel wedge; 0.02 and 0.02 for the sapphire wedge; and 0.14 and 0.12 for the specimen. The surface roughness values achieved on the test surface after it had been burnished are given in Table 2. It can be seen that in all cases an excellent surface finish has been achieved with the wedge face surface roughness more or less replicated on the burnished surface. This gives strong support to the suggestion by Black *et al.* [22] that the full contact field applies at the interface with metal to metal contact avoided by a thin ( $\approx 1\text{ nm}$ ) but highly effective EHL film. Equation (17) shows that as speed is increased the film thickness increases and as a consequence the role of surface roughness in determining the frictional shear stress decreases. Once the film thickness exceeds the height of asperities then the frictional shear stress will be determined only by the properties of the lubricant. The definition of the frictional boundary condition is then somewhat simpler than when the full contact field applies and both surface roughness and lubricant film strength contribute to the frictional shear stress.

Table 2  
Surface roughness values measured on test surface after burnishing

| Wedge material | Surface roughness ( $\mu\text{m Ra}$ ) |                    |
|----------------|--|--------------------|
|                | Parallel to U                          | Perpendicular to U |
| Sapphire       | 0.02                                   | 0.03               |
|                | 0.02                                   | 0.02               |
|                | 0.02                                   | 0.02               |
|                | 0.02                                   | 0.03               |
| Tool steel     | 0.02                                   | 0.04               |
|                | 0.03                                   | 0.04               |
|                | 0.03                                   | 0.05               |
|                | 0.02                                   | 0.05               |

When the film thickness in the above process exceeds the height of asperities then asperity interactions will not take place and burnishing will no longer occur. In reviewing metal working processes where the speeds are sufficiently high to promote hydrodynamic lubrication at the tool-work

interface, Bloor *et al.* [24] have noted that one of the first indications of a significant film thickness is the appearance of a matt-finish on the produced component. Parsons *et al.* [28] have reported on this effect for a wide range of lubricants in high speed (up to  $45 \text{ ms}^{-1}$ ) drawing experiments. In designing processes to work under hydrodynamic lubrication conditions it is important to have the means of calculating the film thickness from the process parameters. It should then be possible to select parameters to minimize friction and wear or alternatively, if a polished surface finish is required, to ensure that the film is thin enough to allow some asperity interactions to take place. To determine the film thickness in plane strain drawing Bloor *et al.* [24] have made an EHL analysis in which account was taken of the elastic deformation of the drawn strip at entry and exit to the die and of the plastic deformation of the strip within the die. The lubricant was assumed to be an incompressible Newtonian fluid. It was shown that, for given conditions, an equation similar to equation (17) gave a good estimate of average film thickness for the results obtained from the analysis.

Thick lubricant films can be provided even in slow speed processes by coating the workpiece with suitable low shear strength materials. An example is the phosphate coating technique for lubricating billets of steel which are to be cold extruded. The effectiveness of coatings from the viewpoint of giving low friction and a thick film can be judged from the results of some slow speed ( $\approx 1 \text{ mm s}^{-1}$ ) plane strain extrusion experiments made by Farmer and Oxley [29] and Conning *et al.* [12]. In these either alodine (a dichromate conversion coating) or phosphate coatings were applied together with sodium stearate to lubricate the aluminium-magnesium alloy specimen used in the experiments. The objective of the experiments was to obtain flow patterns (deformed grids) for the process taking place which were then used to construct slipline fields representing the flow. In their construction Conning *et al.* [12] made no attempt to force the sliplines to meet the die face at a predetermined angle. Therefore, their results can be used to give an estimate of the frictional shear stress acting at the die face. For all of the cases considered (die half angles  $30^\circ$ ,  $45^\circ$  and  $60^\circ$ ) the slipline fields show that the sliplines meet the die face at an angle close to  $\frac{1}{4}\pi$ . This indicates (see equation (1)) that the shear

strength of the film was very small compared with the shear flow stress of the deforming material. That the film was thick compared to the height of asperities on the die face was shown by the matt-finish on the extruded surface which showed no indication of burnishing. An interesting feature of the flow patterns obtained in these extrusion experiments was that the specimen corner at die entry was always rounded in a similar manner to that for the wave in Figure 5. The space between the specimen surface and die/container surface in this corner was found to be packed tight with lubricant. It can be concluded that as with the wave the shape of the specimen surface at die entry played an important part in determining the lubrication condition at the die face.

In ending this section it is of interest to return to the results in Table 1. These show that once steady state sliding conditions are established the values of shear strength  $\tau$  and interface friction coefficient  $\mu_i$  (note that for a perfectly smooth wedge  $\mu_i$  is equal to  $c$  in equation (15)) vary markedly from lubricant to lubricant. However, for the indentation part of the tests the results show that  $\mu_i$  had approximately the same value  $\approx 0.2$  for all of the tests including the dry test. Noting that in each test the contacting surfaces were the same during indentation and sliding it can be concluded that the difference in the  $\mu_i$  values resulted from differences in lubrication conditions in the two cases. Black *et al.* [26] have attempted to explain this difference by noting that while in wave formation the conditions are such as to establish an EHL film at the interface the conditions at the interface during indentation are such as to inhibit EHL. In this connection it is sufficient to note that the entraining velocity measured down the wedge face from the specimen surface (lubrication source) was negative during indentation. Therefore, during indentation no lubricant was drawn into the interface and the indentation values of  $\mu_i$  are representative of dry conditions. Interestingly, the results indicate that even with Molykote positive entrainment is needed for effective lubrication of the interface. If it is accepted that lubrication in metal working processes is essentially EHL then it can be seen that to be effective lubricant must be provided in regions where there is positive entrainment into the tool-work interface. An example is to be found in machining where attempts have been made to lubricate the tool-chip interface by applying liquid

lubricants under pressure along the gap between the tool clearance face and workpiece. Little success has been achieved so far with this method and machining remains one of the classical problems of unlubricated sliding.

## 5.2 Machining

Most practical machining operations are made using a plentiful flow of cutting fluid. In many processes including turning and milling the fluid acts as a coolant and plays little if any role as a lubricant at the tool-chip interface. In slow speed processes such as tapping, broaching and gear cutting on the other hand the cutting fluid can, as pointed out by Wakabayashi *et al.* [30], act as an efficient boundary lubricant. These authors have investigated the kinetics of lubrication in this context when using carbon tetrachloride as a model gas-phase lubricant. In what follows attention is limited to unlubricated machining which is the condition most commonly met in practice.

The orthogonal (plane strain) chip formation model used by Hastings *et al.* [31] in developing a predictive machining theory is given in Figure 6. It can be seen that the geometry of chip formation for a given tool rake angle  $\alpha$  and undeformed chip thickness  $t_1$  is not complete unless either  $\phi$ , the so-called shear angle, or the chip thickness  $t_2$  is known. In order to define the geometry it is usual to derive equations for predicting  $\phi$ . In early attempts to do this the frictional condition at the tool-chip interface was represented by an average coefficient or, more

usually, angle of friction  $\lambda$ . If  $\lambda$  could be measured by some independent friction test or if its value did not vary greatly with cutting conditions this would be an acceptable approach. However, it has only been found possible to measure  $\lambda$  by machining tests and the variations in  $\lambda$  with  $\alpha$ ,  $t_1$  and cutting speed  $U$  even for a given work material-tool material combination are too great to allow the use of an average value. This has led Oxley [32] and others including Rowe and Spink [33] to suggest that the shear strength of the interface might be a more effective friction parameter. This approach is now considered.

It is generally accepted that for most cutting conditions the real and apparent areas of contact are equal over much of the tool-chip contact region with plastic deformation occurring in a thin boundary layer of chip material adjacent to the tool-chip interface. As the normal pressure between chip and tool decreases towards the end of the tool-chip contact then the ratio of real to apparent areas reduces and approaches a value appropriate to normal sliding conditions. Hastings *et al.* [31] have neglected this latter region in their analysis on the grounds that it is relatively small and transmits only a small part of the resultant cutting force. As with earlier theories the first step in predicting cutting forces etc. is to determine the shear angle  $\phi$ . The outline of the method, which is described in detail by Hastings *et al.* [31], is as follows. For a range of values of  $\phi$  the resultant force  $R$  (Figure 6) transmitted across the shear zone in which the chip is formed is calculated from an analysis of the stresses along the plane AB. In making the stress analysis account is taken of the variations in flow stress with strain, strain-rate and temperature. Once  $R$  is known it is resolved along the tool-chip interface (assumed to be a direction of maximum shear stress) to give the frictional force  $F$ . By dividing  $F$  by the interface area (which is obtained from the analysis) the average value of the interface shear stress  $\tau_{int}$  is determined. For the same range of  $\phi$  values the temperatures and strain-rates in the boundary layer at the interface are calculated and used to determine the average shear flow stress in the chip along the interface  $k_{chip}$ . The solution for  $\phi$  is taken as the value which makes  $\tau_{int} = k_{chip}$  as the assumed model of chip formation is then in equilibrium. In making these calculations it is necessary to know the thickness of the boundary layer. This was

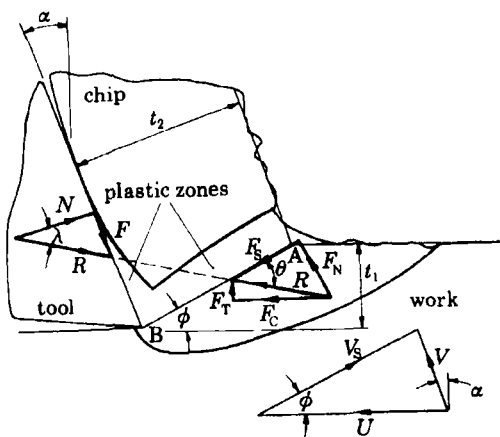


Figure 6. Chip formation model used in developing predictive machining theory.

determined in the following way.

The photomicrograph of a typical chip section given in Figure 7 shows that a severely deformed layer of material exists adjacent to the chip surface which has been in contact with the tool cutting face. This consists of material which has passed through the tool-chip interface boundary layer. As mentioned earlier in the paper, Trent [11] has associated this deformation with seizure at the tool-chip interface while Oxley [10] has concluded that it results from the flow at the interface being retarded by the mechanism indicated by the slipline field given in Figure 2(c). Irrespective of the actual asperity interactions taking place it is clear that the velocity changes from near zero at the cutting face to the full chip velocity over a boundary layer which is thin compared with the chip thickness. Estimates show that for normal cutting conditions, on say a

lathe, the average strain-rate in the boundary layer is in the range  $10^4$  to  $10^6 \text{ s}^{-1}$ , the corresponding temperature range is 800 to 1000°C and the strain occurring as material flows through the interface region is exceedingly high (5 to much higher values). All of these factors depend upon the thickness of the boundary layer and it is not obvious what mechanism determines this thickness. Oxley and Hastings [34] have proposed that the actual value taken up for given cutting conditions will be that which minimizes the rate of frictional work at the interface. They determined this value as follows. For the conditions at the interface (high strains, strain-rates and temperatures) it was assumed that the strain-hardening taking place would be negligible and that the flow stress in the boundary layer and hence  $k_{\text{chip}}$  would only vary with strain-rate and temperature. Their equations, derived from the analysis of the

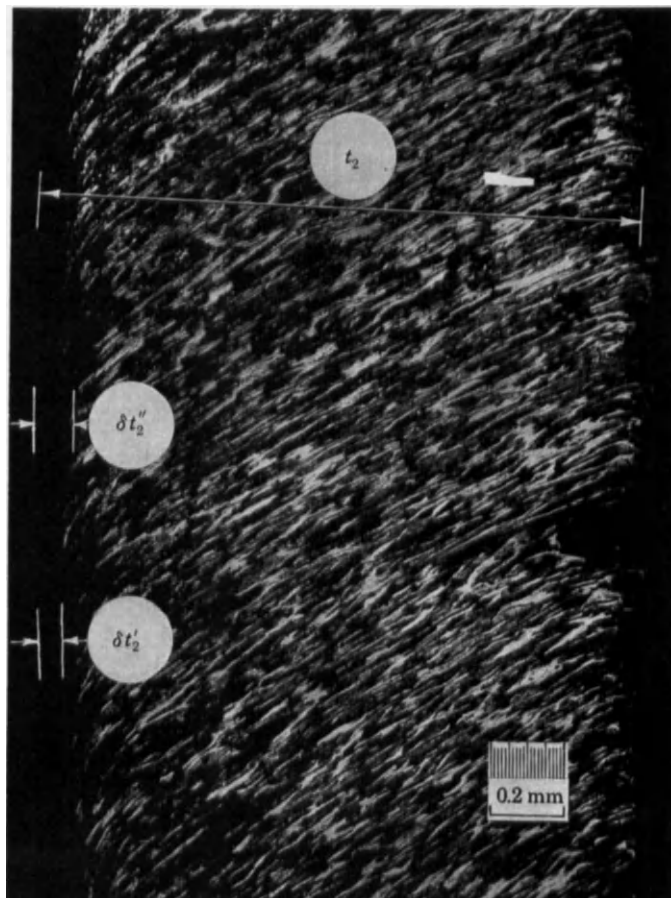


Figure 7. Photomicrograph of chip section.

orthogonal machining process, showed that a decrease in boundary layer thickness increased the strain-rate and the temperature. Noting that for the work material considered (plain carbon steel) the flow stress normally increases with increase in strain-rate and decrease in temperature they showed that a certain value of thickness could always be found which gave strain-rate and temperature combinations which minimized  $k_{chip}$ . This in turn minimized the frictional and total work rates. Predicted boundary layer thicknesses satisfying this minimum energy condition have been found to agree closely with experimental values measured from chip sections for very wide ranges of cutting conditions [31][34]. In particular it is predicted that the thickness decreases rapidly with increase in cutting speed and experimental results confirm this [31]. Predicted values of shear angle  $\phi$ , cutting forces etc. determined in this way have also been shown to be in close agreement with experimental values.

## 6. CONCLUDING REMARKS

By using the wave model to represent asperity interactions along the tool-work interface it has been shown how the interface frictional condition can be defined in terms of surface roughness and lubrication parameters. The asperity deformation models used in this paper are for plane strain conditions and it will be necessary to seek their three-dimensional counterparts if due consideration is to be given to the three-dimensional nature of the surface roughness of actual surfaces. Future work should also give wider consideration to the influence of strain-rate and temperature on frictional conditions.

## REFERENCES

1. F.P. Bowden and D. Tabor, *Nature*, 150 (1942) 197.
2. D. Tabor, *Proc. R. Soc. Lond.*, A251 (1959) 378.
3. J.M. Challen and P.L.B. Oxley, *Wear*, 53 (1979) 229.
4. J.M. Challen, L.J. McLean and P.L.B. Oxley, *Proc. R. Soc. Lond.*, A394 (1984) 161.
5. A.J. Black, E.M. Kopalinsky and P.L.B. Oxley, *Wear*, 123 (1988) 97.
6. H. Moalic, J.A. Fitzpatrick and A.A. Torrance, *Proc. Instn Mech. Engrs*, 201 (1987) 321.
7. J.M. Challen and P.L.B. Oxley, *Wear*, 100 (1984) 171.
8. E.D. Doyle, J.G. Horne and D. Tabor, *Proc. R. Soc. Lond.*, A366 (1979) 173.
9. A. Schallamach, *Wear*, 17 (1971) 301.
10. P.L.B. Oxley, *Wear*, 65 (1980) 227.
11. E.M. Trent, *Metal Cutting*, Butterworths, London, 1977.
12. S.W. Conning, L.E. Farmer and P.L.B. Oxley, *Phil. Trans. R. Soc. Lond.*, A311 (1984) 495.
13. P.L.B. Oxley and W.F. Hastings, *Proc. R. Soc. Lond.*, A356 (1977) 395.
14. M.C. Shaw, A. Ber and P.A. Mamin, *Trans. A.S.M.E., J. Basic Eng.*, 82 (1960) 342.
15. M.P.F. Sutcliffe, *Int. J. Mech. Sci.*, 30 (1988) 847.
16. R. Hill, *J. Mech. Phys. Solids*, 2 (1954) 278.
17. X. Li, A computer-based numerical study of the role of cooling in machining, PhD thesis, University of New South Wales, 1991.
18. B.J. Briscoe and D. Tabor, *J. Adhesion*, 9 (1978) 145.
19. K.L. Johnson, *Proc. 7th Leeds-Lyon Symp. on Tribology*, Westbury House, 1980, p3.
20. D. Tabor, in J.M. George (ed), *Microscopic aspects of adhesion and lubrication*, Elsevier, Amsterdam, 1982, p651.
21. C.R. Evans and K.L. Johnson, *Proc. Instn Mech. Engrs*, 200 (1986) 303.
22. A.J. Black, E.M. Kopalinsky and P.L.B. Oxley, *Wear*, 137 (1990) 161.
23. R.A.J. Ford, Private communication.
24. S.M. Bloor, D. Dowson and B. Parsons, *J. Mech. Eng. Sci.*, 12 (1970) 178.
25. D. Dowson, *J. Phys. D., Appl. Phys.* 25 (1992) A334.
26. A.J. Black, E.M. Kopalinsky and P.L.B. Oxley, *Proc. Instn Mech. Engrs*, 208 (1994) 281.
27. A.J. Black, E.M. Kopalinsky and P.L.B. Oxley, *Int. J. Mech. Sci.*, in press.
28. B. Parsons, R. Taylor and B.N. Cole, *Appl. Mech. Conf. Proc. Instn Mech. Engrs*, 180 (1965-66) 230.
29. L.E. Farmer and P.L.B. Oxley, *J. Mech. Phys. Solids*, 19 (1971) 369.
30. T. Wakabayashi, J.A. Williams and I.M. Hutchings, *Proc. Instn Mech. Engrs*, 209 (1995) 131.
31. W.F. Hastings, P. Mathew and P.L.B. Oxley, *Proc. R. Soc. Lond.*, A371 (1980) 569.
32. P.L.B. Oxley, *CIRP Annals*, 13 (1966) 127.
33. G.W. Rowe and P.T. Spink, *Trans. A.S.M.E., J. Eng. Ind.*, 89 (1967) 530.
34. P.L.B. Oxley and W.F. Hastings, *Phil. Trans. R. Soc. Lond.*, A282 (1976) 565.

## Friction characteristics at tool-chip interface in steel machining

K. Maekawa<sup>a</sup>, T. Kitagawa<sup>b</sup> and T.H.C. Childs<sup>c</sup>

<sup>a</sup>Department of Mechanical Engineering, Ibaraki University,  
4-12-1 Nakanarusawa, Hitachi 316, Japan

<sup>b</sup>Department of Mechanical Engineering, Kitami Institute of Technology,  
165 Koen-cho, Kitami 090, Japan

<sup>c</sup>Department of Mechanical Engineering, University of Leeds,  
Leeds LS2 9JT, United Kingdom

The split-tool method is extensively employed to evaluate friction characteristics at the tool-chip interface in steel machining. In this investigation medium plain carbon structural steels with different hardnesses are turned using TiN cermet, P20 and K20 carbide tools. Based on the measured stress distributions on the rake face, friction characteristics are discussed from the viewpoint of the mechanical and thermal properties of work and tool materials. Hardness and thermal conductivity affect the chip contact length as well as the coefficient of friction at the lightly loaded sliding zone near the chip leaving point. Friction becomes severe as the hardness of the workpiece is low and/or the thermal conductivity of the tool or its affinity with the workpiece is high. Discussion is extended to an investigation into the friction characteristics of high manganese steel and low-carbon free-cutting steel. Friction characteristics of a cut-away tool are found to be the same as those of a natural contact length tool, when an 18%Mn-18%Cr steel is turned using a P20 tool. A high friction condition close to the chip leaving point is also cut away by the restriction of contact length. When a low-carbon leaded resulphurized steel is turned using a P20 tool, both chip contact length and friction coefficient decrease markedly compared with the machining of an equivalent plain carbon steel. This is due to the lubrication effect of the free-cutting additives. The finite-element machining simulation in conjunction with the friction characteristic equation thus determined is applied to the illustration of machinability improvement through the use of free-cutting steel.

### 1. INTRODUCTION

The modification and control of frictional behaviour on the tool face are the central concern in metal machining, leading to the use of lubricants or the development of various free-cutting steels. It has generally been recognized that the Coulomb-Amonton laws of sliding friction do not hold on the chip contact area, but the contact normal and friction stresses have unique distributions [1, 2]: the normal stress increases monotonically from the chip leaving point to the cutting edge, whereas the friction stress remains constant over the half of the tool-chip contact area nearest the cutting edge but decreases to zero over the other half. A photoelastic tool [3], a sapphire tool [4] and a special tool dynamometer with di-

vided rake face [5] were used to verify these results. As far as the more general combination of steel workpieces and carbide tools is concerned, however, few quantitative investigations into the stress distributions have been made.

As for friction characteristics at the tool-chip interface, it is likely that adhesion is predominant over abrasion, where the friction force stems from shear fracture of the bonded materials. A newly generated chip, having a highly chemically activated surface, slides over the rake face. Temperature and pressure at the interface lead to an extreme friction condition: a peak temperature of 800 °C and a maximum normal stress of 3 GPa are observed when steel is machined at a cutting speed of 100 m/min [6]. According to the adhesion theory of dry friction [7], the friction force



$F_t$  and the normal force  $N_t$  are given as

$$F_t = \tau_t A_p = \tau A_r, \quad N_t = \sigma_t A_p = H A_r \quad (1)$$

where  $A_p$  and  $A_r$  respectively are the apparent and real areas of contact, and  $\tau$  and  $H$  are the shear stress and micro-hardness at the bonded asperities. In a lightly loaded condition where  $A_r/A_p$  is very small the Coulomb-Amonton laws of friction hold. The coefficient of friction  $\mu$  is constant, being independent of  $A_p$  and  $A_r$ . When  $\sigma_t$  becomes extremely large and  $A_r/A_p$  approaches 1,  $\tau_t$  equals the shear flow stress  $k$  of the chip material. The following empirical equation satisfies these conditions [8, 9]:

$$\tau_t = k[1 - \exp\{-(\mu\sigma_t/k)^n\}]^{1/n} \quad (2)$$

where  $\mu$  is here regarded as a friction coefficient and  $n$  is a constant.

The purpose of the present study is twofold: to measure stress distributions at the tool-chip interface using a split-tool dynamometer, and to discuss friction characteristics based on the measured stress and Eq. (2) when machining various steels using carbide tools in dry conditions. Investigation is extended to the frictional behaviour of a cut-way or restricted contact tool and computer simulation of the role of friction in steel machining.

## 2. SPLIT-TOOL DYNAMOMETRY

Figure 1 shows the principle of a split tool dynamometer [5, 9]. Two parts of a tool with a divided rake face are supported independently with a small gap ( $< 5 \mu\text{m}$ ) between them. The friction force  $F_t$  and the normal force  $N_t$  are measured by strain gauges mounted on each tool body. By changing the split position or the distance  $\ell$  from the cutting edge, the friction stress  $\tau_t$  and the normal stress  $\sigma_t$  on the tool rake face are given by

$$\tau_t = \frac{1}{w} \frac{dF_{t1}}{d\ell}, \quad \sigma_t = \frac{1}{w} \frac{dN_{t1}}{d\ell} \quad (3)$$

where  $w$  is the width of cut, and the subscript 1 denotes the divided tool containing the cutting edge portion. The measurement for the other half

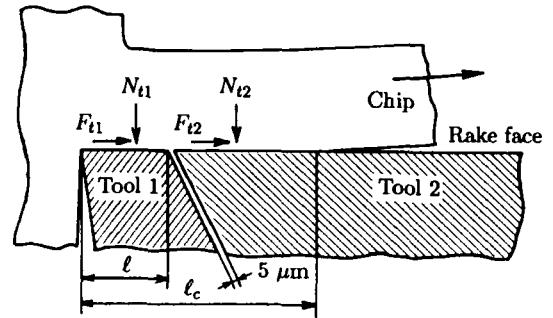


Fig. 1 Principle of split-tool dynamometry.

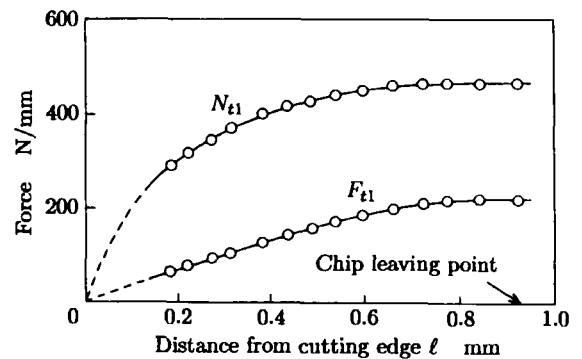


Fig. 2 Change of cutting force with varying distance from cutting edge: 0.45% C plain carbon steel, TiN cermet with  $0^\circ$  rake angle,  $V=200$  m/min,  $f=0.2$  mm/rev,  $w=2.5$  mm, dry.

is necessary to ascertain that the total cutting force is unchanged with the variation of the split position.

Figure 2 shows an example of the measured  $F_{t1}$  and  $N_{t1}$  as a function of the distance from the cutting edge. The cutting conditions are listed in the figure, in which a disc of 2.5 mm width was turned radially in air. Both forces gradually increase with increasing distance, though measurements at less than 0.18 mm were not carried out owing to the reduction of edge strength.

Unless otherwise specified, a disc of 2-2.5 mm width was turned radially in air using a  $0^\circ$  rake-angle tool at a cutting speed of 100 or 200 m/min and a feed of 0.2 mm/rev in the following experiments.

## 3. FRICTION CHARACTERISTICS AT THE TOOL-CHIP INTERFACE

### 3.1. Machining of medium carbon steels

To make a comparison with the machining of a 0.45%C carbon steel (S45C, HV=177) using a P20 grade carbide tool, 0.25%C (S25C, 140) and quenched 0.55%C (S55C, 275) steels, having different hardnesses, were turned using the same tool. In addition, a straight tungsten carbide (K20) and a TiN cermet tool were employed for S45C steel machining. The following are the distributions of  $\sigma_t$  and  $\tau_t$  given by Eq. (3) in conjunction with the measurement of the variation of force over the rake face using the split tool dynamometer.

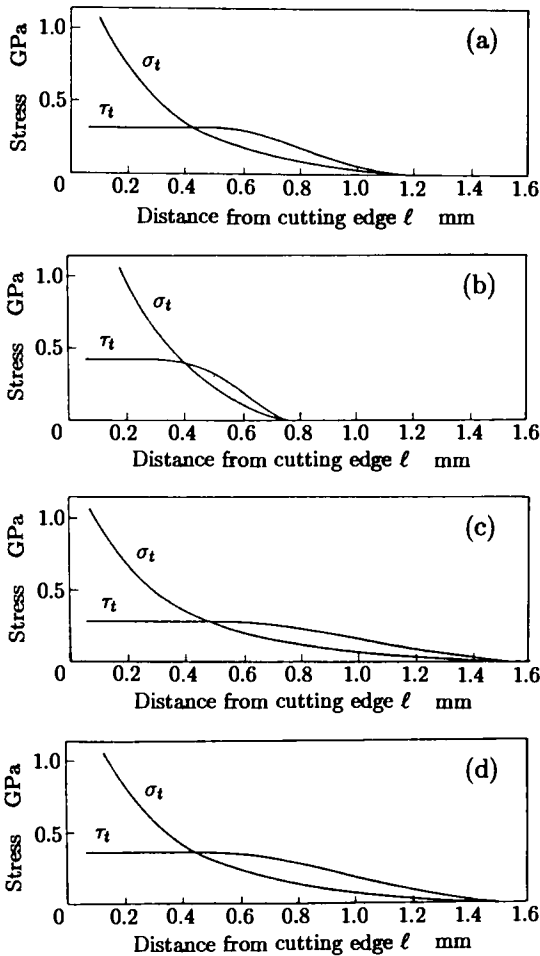


Fig. 3 Distributions of normal stress  $\sigma_t$  and friction stress  $\tau_t$  on tool rake face against P20 tool: (a) S45C at  $V=200$  m/min, (b) S55C at  $V=200$  m/min, (c) S25C at  $V=200$  m/min and (d) S45C at  $V=100$  m/min.

Figure 3 shows the effect of the work materials against a P20 tool: (a) S45C, (b) S55C, (c) S25C, all at a cutting speed of 200 m/min, and (d) S45C at a cutting speed of 100m/min. The results verify that  $\sigma_t$  increases exponentially towards the cutting edge whereas  $\tau_t$  has a trapezoidal distribution saturated close to the cutting edge. With increasing workpiece-hardness both chip contact length and width with a constant  $\tau_t$  become short. The magnitude of this  $\tau_t$  is proportional to the hardness at room temperature. When the cutting speed is decreased from 200 m/min (Fig.3 (a)) to 100 m/min (Fig.3 (d)), the saturated length of  $\tau_t$  rises and the chip contact length increases.

Figure 4 represents the effect of the tool materials against S45C steel: (a) TiN cermet and (b) K20 carbide. Comparing Fig.4 with Fig.3 (a), the saturated  $\tau_t$  is unchanged at 315 MPa, and the distance between the cutting edge and  $\sigma_t=\tau_t$  is the same, being independent of the tool materials. Besides, the length of the saturated  $\tau_t$  as well as the chip contact length increases in order of TiN, P20 and K20. This order reflects thermal conductivity: TiN has the smallest. It also reflects the chemical affinity between the tool and workpiece.

Figure 5 (a) and (b) show the relationship between  $\sigma_t$  and  $\tau_t$  based on the data of Figs. 3 and 4 respectively, where the curves were fitted

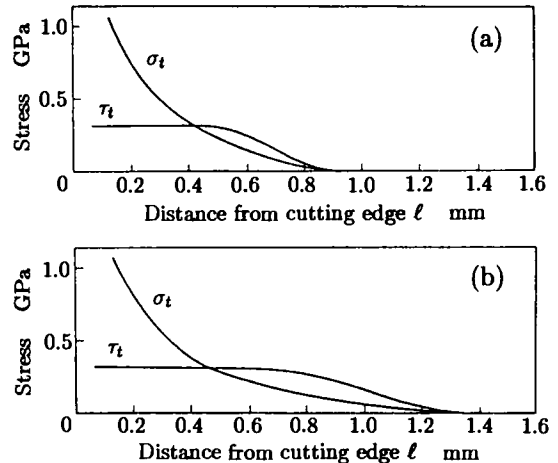
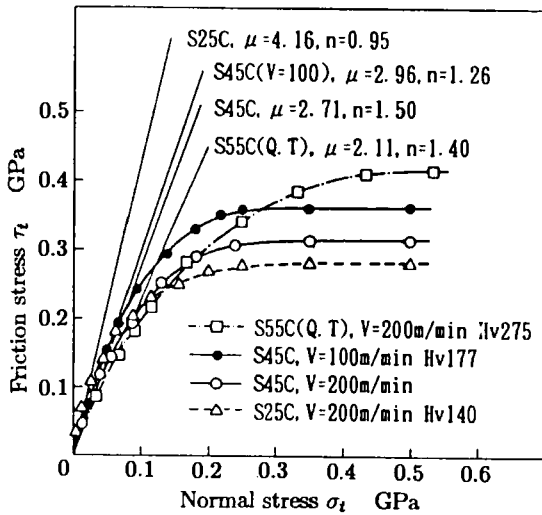
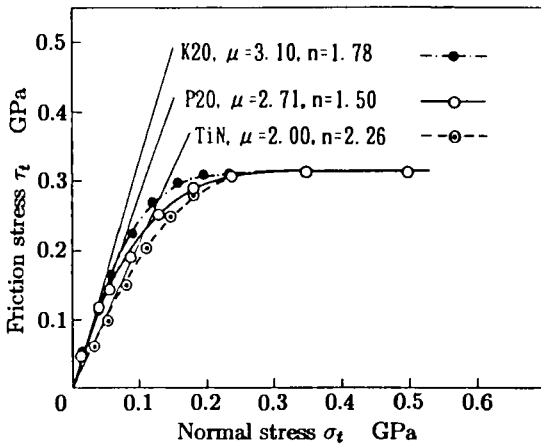


Fig. 4 Distributions of  $\sigma_t$  and  $\tau_t$  against 0.45%C steel: (a) TiN at  $V=200$  m/min and (b) K20 at  $V=200$  m/min.



(a)



(b)

Fig. 5 Relationship between normal and friction stresses on tool rake face: (a) effect of tool materials against 0.45%C steel and (b) effect of work materials against P200 tool.

by using Eq. (2) with the values of  $\mu$  and  $n$  listed in the figures. The approximation by Eq. (2) is found to be perfect: as  $\sigma_t$  tends to zero,  $\tau_t/\sigma_t$  tends to  $\mu$ , but as  $\sigma_t$  increases  $\tau_t$  saturates. The hardness of work materials and the thermal conductivity or perhaps the chemical composition of tools affect the coefficient of friction at the lightly loaded sliding zone near the chip leaving point. The characteristic value  $\mu$  becomes high as the hardness and/or the thermal conductivity of the tool or the affinity of the tool with the workpiece is low.

### 3.2. Machining of low-carbon free-cutting steel

Friction characteristics of a leaded resulphurised low-carbon steel (Steel L, 0.08%C-1.3%Mn-0.07%P-0.323%S-0.25%Pb) are compared with those of an equivalent plain carbon steel (Steel P, 0.1%C-0.4%Mn-0.025%P-0.019%S). Figure 6 shows the distributions of  $\sigma_t$  and  $\tau_t$  on the rake face as a function of the distance from the cutting edge, when the steels were turned using a P20 tool at a cutting speed of 100 m/min. Again, it is confirmed that for both steels  $\tau_t$  shows a trapezoidal profile that increases from the chip leaving point to the cutting edge and saturates at the shear flow stress of the chip, whereas  $\sigma_t$  has an exponential form that increases rapidly towards the cutting edge. The maximum value of  $\sigma_t$  exceeds 1 GPa, where the hydrostatic component is much larger than the deviatoric stress. Compared with  $\tau_t$  of Steel P,  $\tau_t$  of Steel L is decreased near the end of the contact, resulting in  $\tau_t < \sigma_t$  and much shorter chip contact length.

Figure 7 compares the  $\sigma_t - \tau_t$  relationship for the steels. Compared with Steel P, Steel L yields a smaller  $\mu$  and lower saturation stress. For both steels, a similar expression to Eq. (2) can be fit-

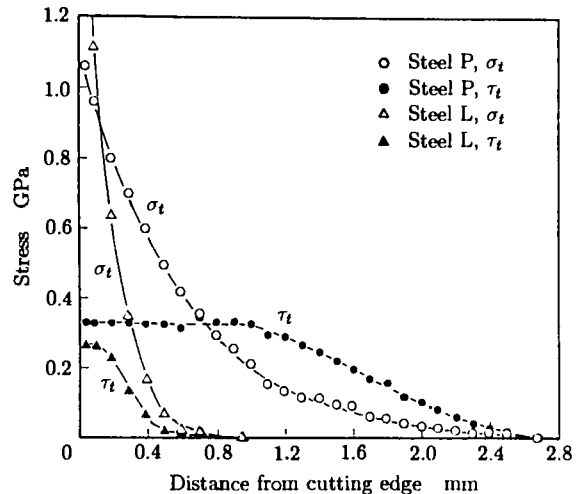


Fig. 6 Distributions of  $\sigma_t$  and  $\tau_t$  measured by split-tool dynamometry: plain carbon steel (Steel P) and leaded-resulphurized carbon steel (Steel L) (see Table 1), P20 with  $0^\circ$  rake angle,  $V=100$  m/min,  $f=0.2$  mm/rev,  $w=2$  mm, dry.

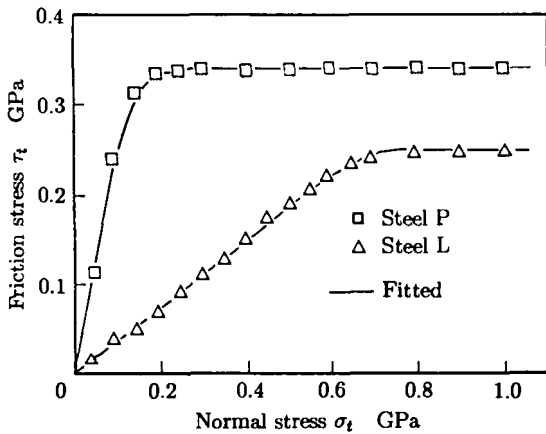


Fig. 7 Relationship between  $\sigma_t$  and  $\tau_t$  on tool rake face: cutting conditions are the same as Fig.6.

ted, where the values of  $\mu$  and  $n$  are listed in Table 1 (to appear in Section 4.2). The R value in the table means that the saturated friction stress of Steel L is 0.737 times that of Steel P. Since both steels have similar flow characteristics [8], the difference between the characteristic values represents an effect of lubrication by MnS and lead.

### 3.3. Machining using cut-away tool

Spit-tool dynamometry can be applied to the investigation into the friction characteristics of a cut-away tool whose chip contact length is restricted to be shorter than that of a natural one by setting the secondary rake face. Figure 8 shows the distributions of  $\sigma_t$  and  $\tau_t$  on the primary rake face when an 18%Mn-18%Cr steel (HV=282) is turned radially using a P20 cut-away tool, whose restricted length is set at 0.25 mm, at a cutting speed of 60 m/min. The symbols  $\odot$  denote this case, whereas the solid lines show the results obtained using a conventional or natural contact length tool. Compared with the machining of the plain carbon steels (Fig.3) the chip contact length is shorter and both stresses are larger close to the cutting edge; a saturated  $\tau_t$  of 600 MPa and a peak  $\sigma_t$  of more than 3GPa. The cut-away tool yields the same stress distributions as the conventional tool, though no stress exists beyond the restriction length of 0.25 mm.

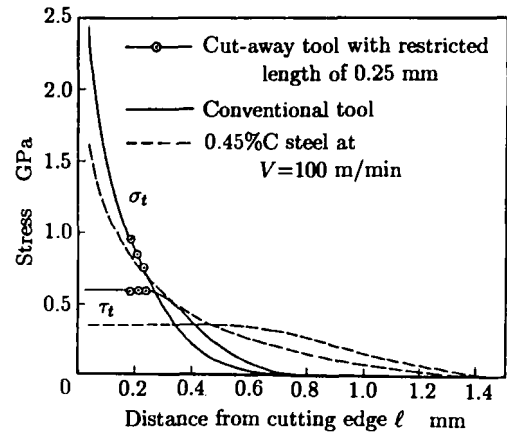


Fig. 8 Distributions of  $\sigma_t$  and  $\tau_t$  on tool rake face of cut-away and conventional tools: 18%Mn-18%Cr steel, P20 with  $0^\circ$  angle,  $V=60$  m/min,  $f=0.2$  mm/rev,  $w=2$  mm, dry.

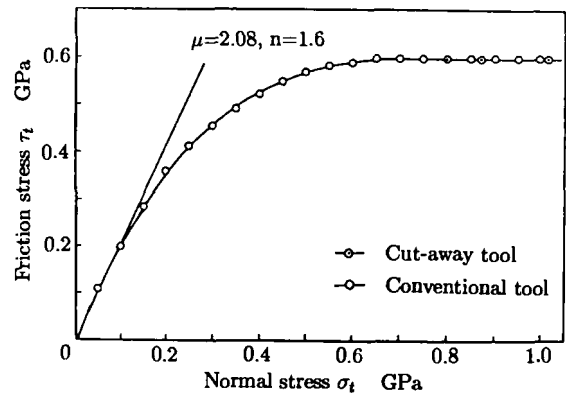


Fig. 9 Relationship between  $\sigma_t$  and  $\tau_t$  on tool rake face: cutting conditions are the same as Fig.8.

Figure 9 shows the relationship between  $\sigma_t$  and  $\tau_t$ , where the solid line denotes the approximation by Eq. (2) with the characteristic constants of  $\mu=2.08$  and  $n=1.6$ . Both cut-away and conventional tools obey the same friction characteristics. Compared with the plain carbon steels (Fig.5), the value of  $\mu$  is the smallest.  $\mu$  tends to become small where the saturated friction stress or the shear flow stress of the chip increases.

## 4. DISCUSSION

#### 4.1. Friction characteristics vs work and tool materials

It is found from Figs. 5 and 9 that the coefficient of friction at a lightly loaded sliding zone close to the chip leaving point, as well as the chip contact length, is affected by the hardness of work materials and the thermal conductivity or type of tools. The characteristic value of  $\mu$  of Eq. (2) becomes small when the hardness of the workpiece is high and/or the thermal conductivity or affinity with work of the tool is low. Based on the adhesion theory of dry sliding friction [7], the friction stress  $\tau_t$  is proportional to the ratio  $A_r/A_p$  which depends on the normal stress  $\sigma_t$  acting at the interface. It is likely that junction growth is reduced by the increase of strength of the chip. If this is the case for S55C steel, a smaller  $\mu$  will be understood.

On the other hand, the effect of the thermal conductivity or work affinity of a tool on frictional behaviour is not clear. Figure 10 shows the local rake temperature measured using a micro thermocouple which was embedded within the tool [6]. The edge of a 20  $\mu\text{m}$ -diameter tungsten wire, coated with alumina for insulation, is exposed on the rake face to create a hot junction with the chip. A disc of S45C steel is turned

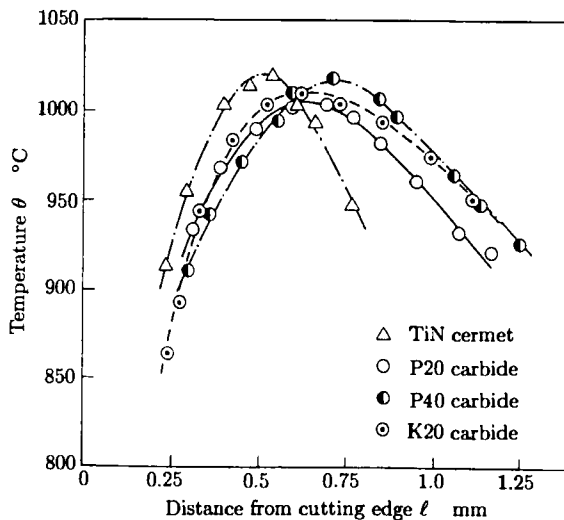


Fig. 10 Temperature distributions on tool rake face for different tool materials: 0.45% C steel,  $0^\circ$  rake angle,  $V=200$  m/min,  $f=0.2$  mm/rev,  $w=2$  mm, dry.

at a cutting speed of 200 m/min and a feed of 0.2 mm/rev. Although the temperature profile largely depends on the chip contact length, the peak temperature decreases in order of TiN, K20 and P20. This does not correspond to the increasing thermal conductivity of the tools. A similar tendency can be seen in the temperature at the lightly loaded sliding zone close to the end of contact. On the other hand the order TiN, P20, K20 is known to reflect the order of chemical affinity between the tools and steel workpieces at high temperature. It seems that the influence of chemical affinity is greater than that of temperature. This frictional behaviour is different from conventional friction at elevated temperatures, in which the coefficient of sliding friction increases with increasing temperature [10]. The relative effects of chemical affinity of the work and tool materials [11] and temperature should be investigated further.

#### 4.2. Computer simulation of the role of friction

Recent developments in computational mechanics enable us to simulate a cutting process [12]. The role of friction in metal machining can be analysed based on the friction characteristics thus determined. It is worth making a brief review of a computer simulation approach using the finite element method.

In principle, the following elastic-plastic constitutive equation and energy equation are solved simultaneously:

$$\dot{\sigma}_{ij} = \left[ \frac{E}{1+\nu} \left( \delta_{ik}\delta_{jl} + \frac{\nu}{1-2\nu} \delta_{ij}\delta_{kl} \right) - \alpha^* \frac{9G^2}{\bar{\sigma}^2(3G+H')} \sigma'_{ij}\sigma'_{ij} \right] \dot{\epsilon}_{kl} \quad (4)$$

$$\dot{\theta} + v_j \theta_{,j} - K \theta_{,kk} = Q/\rho C \quad (5)$$

Equation (4) is the tensor expression for isotropic hardening materials obeying the Mises yield criterion and the Prandtl-Reuss flow rule, where  $\dot{\sigma}_{ij}$  is the Jaumann rate of Euler stress,  $\dot{\epsilon}_{kl}$  is the velocity strain,  $\sigma'_{ij}$  is the deviatoric component of Euler stress,  $\bar{\sigma}$  is the equivalent stress;  $E, G, H'$  and  $\nu$  are Young's modulus, the shear modulus,

Table 1 Chemical composition and material properties of plain and leaded-resulphurized steels

|                       | Steel P  | Steel L  |
|-----------------------|--|--|
| Chemical composition  | 0.1%C, 0.4%Mn, 0.025%P, 0.019%S  | 0.08%C, 1.3%Mn, 0.07%P, 0.323%S, 0.025%Pb  |
| Friction constants    | R=1.0, $\mu=2.31$ , n=3.89   | R=0.737, $\mu=0.38$ , n=8.78   |
| Flow stress constants | A=883 exp(-0.0011 $\theta$ )<br>+167 exp{-0.00007( $\theta$ -150) <sup>2</sup> }<br>+108 exp{-0.00002( $\theta$ -350) <sup>2</sup> }<br>+78 exp{-0.0001( $\theta$ -650) <sup>2</sup> }<br>M=0.0323+0.000014 $\theta$<br>N=0.185 exp(-0.0007 $\theta$ )<br>+0.055 exp{-0.000015( $\theta$ -370) <sup>2</sup> }<br>k=0.00024, m=0.0019 | A=893 exp(-0.0011 $\theta$ )<br>+186 exp{-0.00011( $\theta$ -135) <sup>2</sup> }<br>+147 exp{-0.00002( $\theta$ -330) <sup>2</sup> }<br>+98 exp{-0.0001( $\theta$ -650) <sup>2</sup> }<br>M=0.0325+0.000008 $\theta$<br>N=0.180 exp(-0.0007 $\theta$ )<br>+0.055 exp{-0.000015( $\theta$ -370) <sup>2</sup> }<br>k=0.00028, m=0.0016 |
| Other constants       | E=206 GPa, $\nu=0.33$<br>K=36.0 Wm <sup>-1</sup> K <sup>-1</sup><br>$\rho=7950$ kg m <sup>-3</sup><br>C=461 J kg <sup>-1</sup> K <sup>-1</sup>   | E=206 GPa, $\nu=0.33$<br>K=36.0 Wm <sup>-1</sup> K <sup>-1</sup><br>$\rho=7950$ kg m <sup>-3</sup><br>C=461 J kg <sup>-1</sup> K <sup>-1</sup>   |

the work hardening rate and Poisson's ratio, respectively;  $\delta_{ij}$  is the Kronecker delta;  $\alpha^* = 0$  for elastic deformation and  $\alpha^* = 1$  for the plastic state. In Eq. (5)  $\theta$  is the temperature,  $\dot{\theta}$  is the time derivative of temperature,  $v_j$  is the velocity,  $K$  is the thermal conductivity,  $Q$  is the internal heat generation,  $\rho$  is the density and  $C$  is the specific heat.

The finite element method could be employed to solve Eq. (4) and Eq. (5) under the appropriate cutting geometry, material property and friction (Eq. (2)) boundary conditions. A review can be seen elsewhere [12]. The analysis applies to two-dimensional steady-state machining for which the iterative convergence method [9, 12] is proposed. An initial assumption is required as to the shape of the chip, which is supposed to be preformed on the surface of the workpiece and to be stress free. Calculation proceeds by incrementally displacing the workpiece towards the tool so that a load develops between chip and tool. A plastic state develops in the chip formation zone and checks are made to see whether the consequent plastic flow is consistent with the assumed chip shape. If it is not, the assumed shape is systematically and automatically altered and the calculation is repeated. The cycle continues until the assumed and calculated flows converge. Temperature rise and the change of flow properties are also incorporated in the analysis.

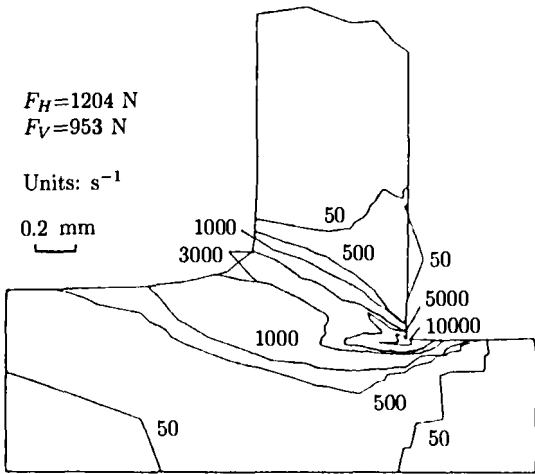
It should be noted that good material prop-

erty data are essential inputs to the analysis. In particular, flow-stress characteristics of the workpiece should cover a wide range of conditions across temperatures of R.T. - 1000 K, strain rates of  $10^{-3}$  - 5000 s<sup>-1</sup> and strains of 0 - 2. The Hopkinson-bar compression tests give reliable data for steels and other metals and alloys [13]. The uniaxial flow stress  $\bar{\sigma}$  (MPa) is empirically expressed as a function of the strain  $\bar{\epsilon}$ , strain rate  $\dot{\bar{\epsilon}}$  and temperature  $\theta$  (°C) according to

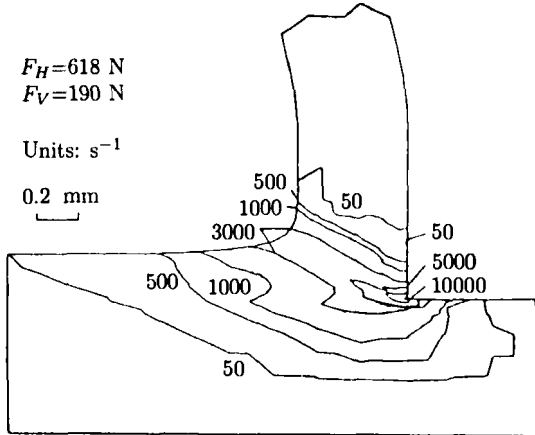
$$\bar{\sigma} = A(10^{-3}\dot{\bar{\epsilon}})^M e^{k\theta} (10^{-3}\bar{\epsilon})^m \times \left[ \int_{\theta, \dot{\bar{\epsilon}}=h(\bar{\epsilon})} e^{-k\theta/N} (10^{-3}\bar{\epsilon})^{-m/N} d\bar{\epsilon} \right]^N \quad (6)$$

where the coefficients A, M and N vary with temperature, and k and m are constants.

It may be demonstrated by means of the finite-element machining simulation how friction at the tool-chip interface interacts with a cutting process. As mentioned in Section 3.2, free-cutting additives, such as MnS and lead, modify friction characteristics on the rake face. The two-dimensional simulation method is employed for the machining of Steel P and Steel L. Table 1 shows the specification and properties of the workpieces used in the simulation. Cutting conditions are set at a cutting speed of 100 m/min, and an undeformed chip thickness or feed of 0.2



(a) Steel P

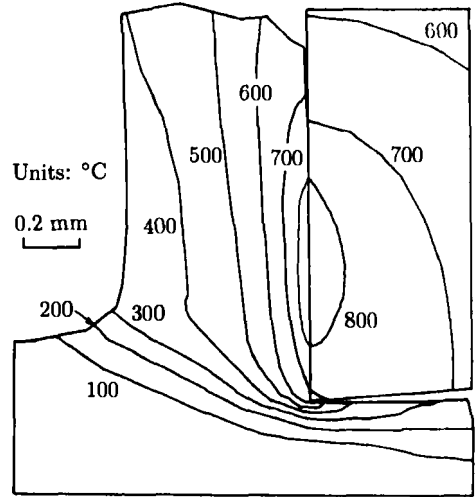


(b) Steel L

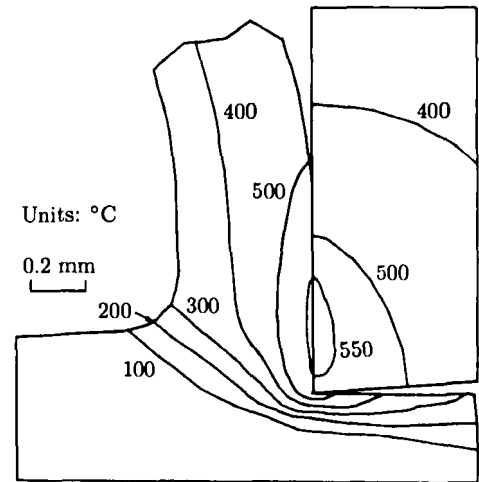
Fig. 11 Comparison of predicted chip shape and equivalent plastic strain rate between plain (Steel P) and leaded-resulphurized (Steel L) low-carbon steels: cutting conditions are the same as Fig.6.

mm. A P20 grade carbide tool with a  $0^\circ$  rake angle is assumed to have a thermal conductivity of  $67 \text{ Wm}^{-1}\text{K}^{-1}$ . No coolant is used, but a coefficient of  $1 \text{ Wm}^{-2}\text{K}^{-1}$  is postulated to yield heat transfer into air.

Figure 11 shows the chip shape and the distribution of equivalent plastic strain rates for (a) Steel P and (b) Steel L. Although the steels have a similar flow property (see Table 1), a comparison of the figures clearly demonstrates that the difference in the friction characteristics is the primary cause of large changes in the cutting mechanism:



(a) Steel P



(b) Steel L

Fig. 12 Comparison of isotherms close to tool tip showing effect of free-cutting additives: cutting conditions are the same as Fig.6.

as the friction becomes severe the chip thickens, curls less and increases its contact length. Plastic deformation within the workpiece broadens ahead of and below the cutting edge, which may result in a large accumulated plastic strain occurring near the tool face as well as larger secondary flow due to friction. The cutting forces markedly decrease in the machining of Steel L, as shown in the figure.

Figure 12 shows the isotherms near the cutting edge. The peak temperature drops by nearly 300

K in Steel L. Its position, however, appears closer to the cutting edge. The temperature of the machined surface is almost the same in both steels, since heat generation by the plastic deformation within the workpiece is not so large, and the heat mostly flows into the chip and tool.

## 5. CONCLUSIONS

Split-tool dynamometry has been extensively employed to evaluate frictional behaviour at the tool-chip interface in steel machining. The measured normal stress increases monotonically from the chip leaving point to the cutting edge, whereas the friction stress remains constant over the half of the tool-chip contact nearest the cutting edge but decreases to zero over the other half. Discussion of friction characteristics has been based on the adhesion model, in which the friction can be expressed not by the Coulomb-Amontons laws of sliding friction but by a characteristic equation depending on the normal stress and the shear flow stress of the chip. The major results obtained from various combinations of work and tool materials are summarised as follows:

- (1) When medium plain carbon steels with different hardness are turned by a P20 carbide tool, the coefficient of friction at the lightly loaded sliding zone near the chip leaving point becomes low as the hardness of the workpiece increases.
- (2) When a 0.45%C steel is turned using TiN, P20 or K20 tools the coefficient of friction rises in the order TiN, P20, K20 which reflects increasing chemical affinity between tool and workpiece. However, the coefficient of friction may also depend on temperature. These tools have different thermal conductivities which lead to different peak temperatures. The relative effects of composition and temperature should be studied further.
- (3) When a low-carbon leaded resulphurized steel is turned using a P20 tool, both chip contact length and friction coefficient decrease markedly compared with the machining of an equivalent plain carbon steel. This is due to the lubrication effect of the free-cutting additives.
- (4) When an 18%Mn-18%Cr steel is turned using a cut-away P20 tool friction characteristics are found to be the same as those of a natural contact length tool. A high friction condition close to the chip leaving point is also cut away by the restriction of contact length.
- (5) The finite-element machining simulation in conjunction with the friction characteristic equation thus determined has been applied to the illustration of machinability improvement through the use of free-cutting steel.

## REFERENCES

1. M.C. Shaw, *Metal Cutting Principles*, Clarendon Press, Oxford (1984) Chap. 10.
2. N.N. Zorev, *Proc. Int. Product Eng. Research Conf.*, Pittsburgh, Pa. (1963) 42.
3. E. Usui and H. Takeyama, *J. Eng. Ind., Trans. ASME, B82* (1960) 303.
4. P.K. Wright, *J. Metals Technol.*, 8 (1981) 150.
5. S. Kato and K. Yamaguchi, *J. Eng. Ind., Trans. ASME, B94* (1972) 683.
6. E. Usui, T. Shirakashi and T. Kitagawa, *J. Eng. Ind., Trans. ASME, B100*, May (1978) 236.
7. F.P. Bowden and D. Taybor, *Friction and Lubrication of Solids*, Oxford Univ. Press, London (1954).
8. K. Maekawa, T. Kitagawa and T.H.C. Childs, *Proc. 2nd Int. Conf. on Behaviour of Materials in Machining*, York, Nov. (1991) 132.
9. E. Usui and T. Shirakashi, *On the Art of Cutting Metals - 75 Years Later*, ASME Publ., PED-7 (1982) 13.
10. I.M. Hutchings, *Tribology - Friction and Wear of Engineering Materials*, Arnold, London (1992) Chap. 3.
11. Y. Yamane, H. Usuki and N. Narutaki, *Wear*, 139 (1990) 195.
12. K. Maekawa, T. Shirakashi and T. Obikawa, *Proc. Instn Mech. Engrs, Part B*, 210 (1996) 233.
13. T. Shirakashi, K. Maekawa and E. Usui, *Bull. Japan Soc. Prec. Eng.*, 17, 3 (1983) 161.



## Wear characteristics of various cutting tools in steel machining

T. Kitagawa<sup>a</sup>, A. Kubo<sup>a</sup> and K. Maekawa<sup>b</sup>

<sup>a</sup>Department of Mechanical Engineering, Kitami Institute of Technology,  
165 Koen-cho, Kitami 090, Japan

<sup>b</sup>Department of Mechanical Engineering, Ibaraki University,  
4-12-1 Nakanarusawa, Hitachi 316, Japan

The present paper describes tool wear characteristics of various cutting tools in steel machining. Tool wear tests are extensively conducted in which plain carbon steels, high manganese steel and austenitic stainless steel are turned using various tungsten carbides and alumina tools. Not only wear rates but also distributions of temperature and stresses on the tool face are measured, for which the embedded thermocouple method and split-tool dynamometry are employed. Tool wear characteristics are discussed on the basis of the experimental data thus obtained. A wear model based on thermally-activated adhesion is found to be applicable to the description of crater wear which mainly depends on tool temperature and contact normal stress; however, a simulation experiment reveals that in steel machining a temperature-dependent abrasion model predominates over the adhesion model for the representation of flank wear in which temperature drops below 1,175 K for a P20 tool. Consequently the mechanism of crater and flank wear consists of both adhesion and abrasion, and a combined wear characteristic equation is proposed. Finally, an analytical prediction method combining the energy method with the estimation of the wear characteristic constants is proposed, its suitability being demonstrated when an 18%Mn-5%Cr alloy steel is turned using a P20 single point tool.

### 1. INTRODUCTION

Tool wear is of particular importance in metal machining since tool life is largely determined by how fast the wear develops. Tool life influences machining economics and product quality. Taylor's tool-life equation [1] has been used to estimate the cutting performance of a tool; however it requires wear tests which involve changing cutting speed, feed and tool geometry against various work materials, which is time-consuming, wasteful of materials and rather expensive. A comprehensive, scientifically-based approach should be adopted to overcome these disadvantages; it is desirable to derive a wear characteristic equation based on physical quantities including contact stress, sliding distance and temperature at the tool-chip and tool-workpiece interfaces.

Many factors are incorporated in tool wear including abrasion, adhesion, diffusion, solution, corrosion, oxidation, fatigue, superficial plastic deformation, plastic collapse, erosion and brittle

fracture. For steel machining using a carbide tool at medium to high speeds, adhesion dominates tool wear, since high temperature and high pressure are influential factors. The principal mechanism of friction on the rake face has been described on the basis of the adhesion theory [2, 3]. Accordingly, the tool wear mechanism can also be explained as follows: as the real area of contact increases, the volume rate of wear increases. It is empirically found that the following relationship holds:

$$\frac{dW}{dL} = z \frac{A_r}{A_p} = z \frac{\sigma_t}{H} \quad (1)$$

where  $dW/dL$  is the volume worn away both per unit sliding length and unit apparent area of contact,  $A_p$  and  $A_r$  respectively are the apparent and real areas of contact,  $z$  is the probability that a real contact will result in a wear particle,  $\sigma_t$  is the normal contact stress, and  $H$  is the microhardness at the bonded asperities. The second

part of Eq. (1) is obtained on the basis of the adhesion theory of dry sliding friction: the friction force  $F_t$  and the normal force  $N_t$  are given as

$$F_t = \tau_t A_p = \tau A_r, \quad N_t = \sigma_t A_p = H A_r \quad (2)$$

where  $\tau_t$  is the friction stress and  $\tau$  is the shear stress at the bonded asperities. Assuming that a temperature rise largely influences  $H$  and  $z$ , which may have forms of

$$H \propto \exp\left(\frac{\alpha_1}{\theta}\right) \quad \text{and} \quad z \propto \exp\left(\frac{-\Delta E}{k\theta}\right), \quad (3)$$

the following equation will be derived [4]:

$$\frac{1}{\sigma_t} \frac{dW}{dL} = C_1 \exp\left(\frac{-C_2}{\theta}\right) \quad (4)$$

where  $\alpha_1$  is a constant,  $\Delta E$  is the activation energy,  $k$  is the Boltzmann constant,  $\theta$  is the absolute temperature here, and  $C_1$  and  $C_2$  are constants to be determined by wear tests. Since the Maxwell-Boltzmann canonical distribution is postulated, the model may be called the thermally-activated adhesion wear model. Mechanical factors such as  $\sigma_t$  and  $dL$  distinguish Eq. (4) from similar wear equations derived by other researchers [5, 6].

The present study deals with wear characteristics of various cutting tools, mainly carbide tools, when machining plain carbon steels, high manganese steels and stainless steel. The main purpose is to investigate the applicability of Eq. (4) to tool wear, for which wear tests together with the measurements of stress and temperature at the contact interfaces are carried out. Attention is given to the limitation of the thermally-activated adhesion wear model, being modified to include an abrasive effect on tool wear. Finally, analytical prediction of tool wear based on the characteristic equation is demonstrated when an 18%Mn-5%Cr steel is turned using a P20 carbide tool.

## 2. EXPERIMENTAL PROCEDURE

Figure 1 shows a schematic diagram of the definition of wear, temperature and stress on the tool face of a turning tool. The determination of the

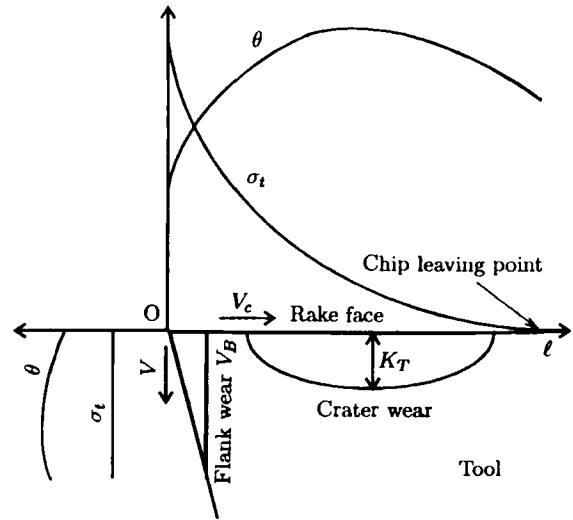


Fig. 1 Schematic of definitions of wear, temperature and stress on tool face.

wear rate  $dW/dL$  per unit area included in Eq. (4) is twofold: for crater wear the depth, measured by a stylus profilometer at a specified cutting time,  $dK_\ell/dT$ , may be translated by

$$\frac{dW}{dL} = \frac{1}{V_c} \frac{dK_\ell}{dT} \quad (5)$$

where  $V_c$  is the chip velocity, and  $K_\ell$  is the wear depth at the distance  $\ell$  from the cutting edge, and  $T$  is the cut time. The measurement is carried out in the direction of chip flow at the centre of the depth of cut. For flank wear the wear rate  $dW/dL$  per unit area may be given by

$$\frac{dW}{dL} = \frac{\tan \gamma}{V} \frac{dV_B}{dT} \quad (6)$$

where  $\gamma$  is the clearance angle,  $V$  is the cutting velocity, and  $V_B$  is the width of the flank wear land.  $V_B$  is measured by an optical microscope after sufficient pre-machining using a tool having an artificial wear land of 0.4 mm initially ground to  $-0.5^\circ$  on the side clearance face. A similar technique is used for the measurements of stress and temperature on the flank wear land.

As for the measurement of a stress distribution on the rake face, split-tool dynamometry [3, 7] is employed, ie two parts of a tool with divided rake face are supported independently with

a small gap ( $< 5 \mu\text{m}$ ) between the parts. Cutting force is measured by strain gauges mounted on each tool body. By changing the split position or the distance  $\ell$  from the cutting edge, the friction stress  $\tau_t$  and the normal stress  $\sigma_t$  on the tool rake face are given by

$$\sigma_t = \frac{1}{w} \frac{dN_{t1}}{d\ell}, \quad \tau_t = \frac{1}{w} \frac{dF_{t1}}{d\ell} \quad (7)$$

where  $w$  is the width of cut, and the subscript '1' denotes the divided tool containing the cutting edge portion. A disc of 2.5 mm width is turned radially in air. It is difficult to apply a similar method to the determination of stress on a flank wear land of less than 0.6 mm in width. Since the normal and friction stresses are considered to be almost uniformly distributed on the wear land, except in the vicinity of the cutting edge [4], the mean stress is assumed; the difference of the cutting force between a worn and a sharp tool may yield the force acting on the wear land, and the mean stress is obtained by dividing the force by the area of the wear land.

Temperature is measured using a micro-thermocouple embedded within the tool [4]. The edge of an insulated narrow wire is exposed on the tool face to create a hot junction with the chip or the workpiece. Figure 2 shows a special ceramic tool for the measurement of flank temperature, in which a Pt-wire of 20  $\mu\text{m}$  diameter is embedded and sintered with alumina powder. Figure 3 represents the measured distributions of tool temperatures when machining a 0.46%C car-

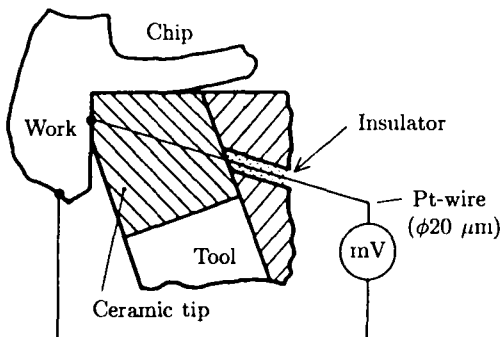


Fig. 2 Measurement of flank temperature using embedded micro thermocouple.

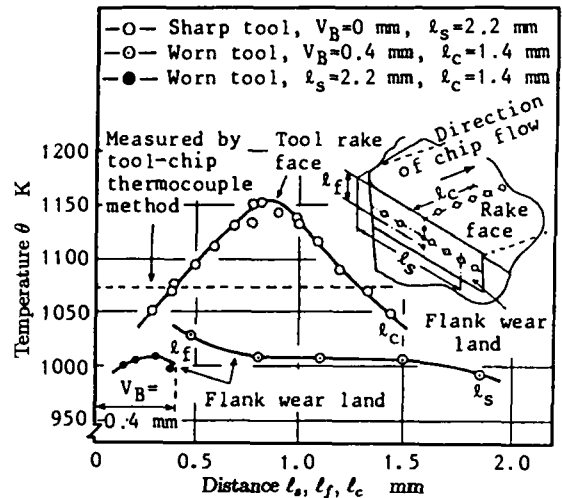


Fig. 3 Measured temperature distributions on tool face: 0.46%C steel, P20 (0,0,6,6,15,15,0.5),  $V=100 \text{ m/min}$ ,  $f=0.26 \text{ mm/rev}$ ,  $d=2 \text{ mm}$ , dry.

bon steel in air using a P20 carbide tool with a wear land of  $V_B=0.4 \text{ mm}$ . The attached figure denotes the measured positions. The rake temperature markedly changes with the distance from the cutting edge, whereas the flank temperature is distributed almost uniformly. For comparison, the dashed line shows the mean rake temperature measured by the tool-chip thermocouple method [8]. It is inappropriate to use the mean temperature for the evaluation of crater wear characteristics, which largely depend on a temperature profile.

### 3. TOOL WEAR CHARACTERISTICS

#### 3.1. Crater wear of carbide tools

Using the  $dW/dL$ ,  $\sigma_t$  and  $\theta$  thus obtained, the suitability of Eq. (4) can be investigated. Figure 4 shows crater wear characteristics of tungsten carbide tools in machining steels, including a 0.45%C plain carbon steel, high manganese steels and a stainless steel. The cutting conditions and tool geometry are listed in the figure. A stable cutting state without tool vibration is attained using a high-rigidity tool; tool shank dimensions are  $30 \times 30 \text{ mm}$  with an overhang of 30 mm. No cutting fluid is used.

For every combination of the tool and work

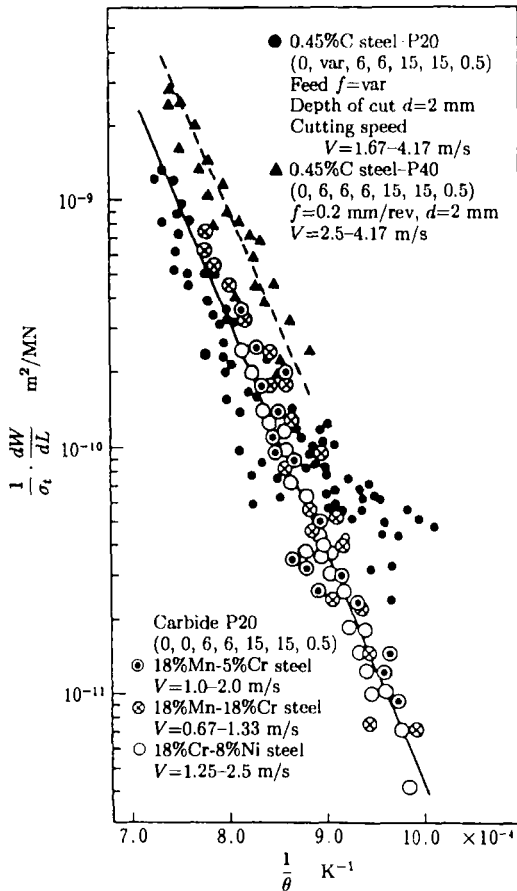


Fig. 4 Crater wear characteristics of tungsten carbide tools in machining steels.

materials, a linear relationship holds between  $(1/\sigma_t)(dW/dL)$  and  $1/\theta$  on a semi-logarithmic scale. When using a P20 tool the characteristic constants  $C_1$  and  $C_2$  have the same values for these steels. When machining the 0.45% C steel P20 and P40 tools give different  $C_1$  values, and the experimental points scatter significantly in the temperature range below  $8.5 \times 10^{-4} \text{ K}^{-1}$  or 1,175 K.

The derivation of Eq. (4) suggests that the  $C_1$  value mainly depends on the mechanical strength of the tool subsurface at the interface (the constituent of a subsurface is a diffused layer, as will be discussed later). The difference in wear characteristics between P20 and P40 lies in their cobalt content: P40, containing more cobalt and smaller TiC+TaC, is softer than P20. This causes a large  $C_2$  of Eq. (4) for the P40 steel. The  $C_2$  value

consisting of  $(-\alpha_1 + \Delta E/k)$  also has relation to a subsurface state in which diffusion between iron and cobalt plays a substantial role. According to a static diffusion experiment [9], a fragile Fe-W-Co carbide compound starts to form at temperatures above 1,200 K; as a result, hard WC grains disappear at the interface. This layer is removed as soon as it is formed during machining. The rate of the compound generation depends mainly on temperature, but is considered to be independent of the work materials because the steels have similar activation energy for diffusion and similar thermal softening with temperature. This is the reason for giving the same  $C_1$  and  $C_2$  values for any combination of the steels and the P20 tool.

The scatter of the experimental points in the lower temperature range becomes apparent when machining the 0.45% C steel. It is possible that another wear mechanism such as abrasion by hard particles dispersed in the steel plays a part. This point will be discussed further in Section 4.1.

For crater wear of a TiC-coated P20 tool [10], similar characteristics to Eq. (4) holds in 0.45% C steel machining. Both of the characteristic constants differ from those of the P20 tool, giving a low wear rate.

### 3.2. Flank wear of carbide tools

Figure 5 represents flank wear characteristics when machining a 0.46% C steel using a P20 carbide tool. The dashed line denotes the crater wear characteristic line approximated by Eq. (4) for the same combination. For comparison, the result for a 0.25% C steel is shown by the symbol  $\bigcirc$ . The numbers in the figure denote the cutting speed. It is found that both flank wear and crater wear obey the same mechanism in the temperature range above 1,175 K. Since the flank temperature is lower by more than 100 K compared with the rake temperature (see Fig.3), the experimental points require higher cutting speeds (above 200 m/min). In the lower temperature range, an equation similar to Eq. (4) can describe the wear characteristics, but the constants  $C_1$  and  $C_2$  are different from those in the higher range. Besides, a distinct difference appears in the flank wear rates of the two steels at the same temperatures: the  $C_1$  value increases with carbon content. This suggests that abrasion is intimately related to the variation of the  $C_1$  and  $C_2$  values,

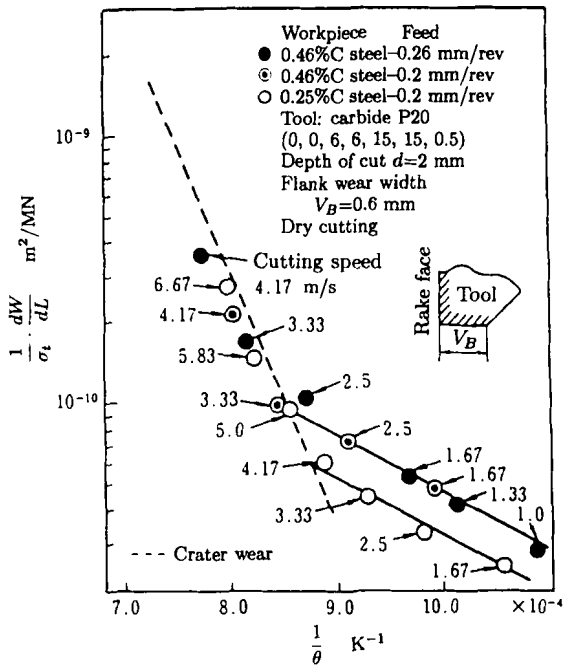


Fig. 5 Flank wear characteristics when machining steels using P20 carbide tool.

which will be discussed further in Section 4.1.

### 3.3. Wear of alumina tool

Figure 6 shows wear characteristics of an alumina ceramic tool when machining a 0.45% C steel; the small symbols denote crater wear and the large ones flank wear. It is likely that a wear characteristic equation similar to (4) holds in the higher temperature range. In the lower range, however, wear rates are not affected by temperature but remain almost constant, being much lower than those of the carbide tool shown in Figs. 4 and 5. This agrees with the results of an electron microprobe and cathode-luminescence study [11] which concludes that neither diffusion nor solution occurs at the alumina-steel interface. Subsurface damage of the tool through plastic deformation and/or micro cracks dominates the thermally-insensitive wear. In the higher temperature range an intermediate spinel phase, which has the chemical formula  $FeO-Al_2O_3$ , may start to form [11]. This must cause wear of the alumina tool to increase, since the mechanical strength of the compound is lower than that of alumina.

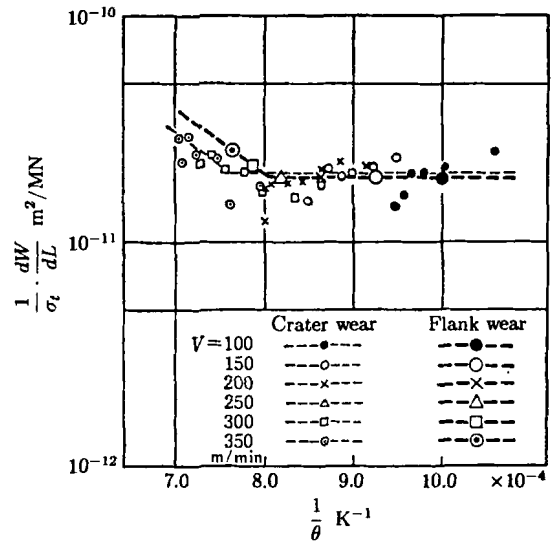


Fig. 6 Wear characteristics of alumina tool in steel machining.

## 4. DISCUSSION

### 4.1. Wear characteristic equation including abrasion effect

As shown in Figs. 4 and 5, the thermally-activated adhesion wear model can be applied to both crater wear and flank wear of carbide tools in steel machining. Not only temperature and normal stress at the contact interface, but also metallographic changes such as the generation of complex carbide compounds and the dissolution of WC grains, play a part in the adhesion wear. In addition, the influence of abrasive particles dispersed within the steels becomes apparent in the temperature range below 1,175 K. Figure 7 shows further crater wear characteristics of a P20 tool when machining various plain carbon steels. Again, Eq. (4) sufficiently describes the crater wear, although the experimental points scatter around the characteristic line. It is obvious that as the percentage of carbon content is high, the wear rates increase throughout the whole temperature range. In general, a hard cementite  $Fe_3C$  dispersed within pearlite increases with carbon content, which has an abrasion effect on tool wear [12]. The addition of deoxidation elements such as aluminium and silicon produce hard inclusions such as  $Al_2O_3$  and  $SiO_2$ . To in-

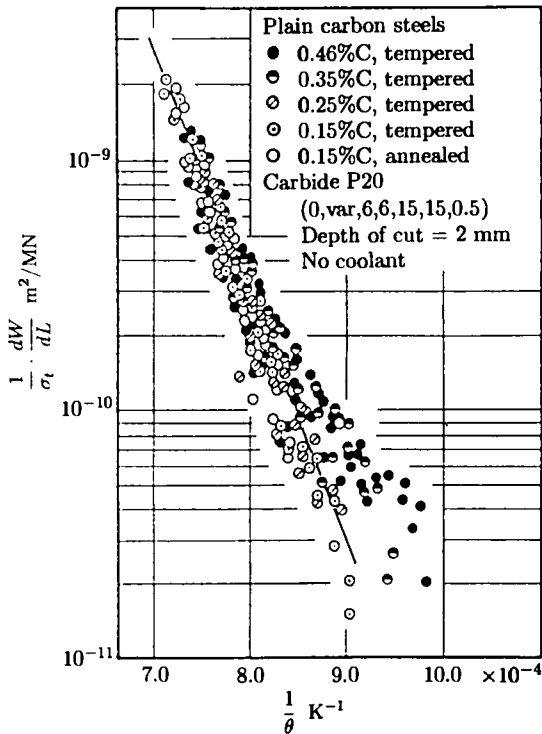


Fig. 7 Crater wear characteristics of P20 carbide tool in machining various plain carbon steels.

investigate how these hard particles influence the wear characteristic equation, the following simulation test is carried out [13].

Since it is difficult to mix and melt a large quantity of  $Al_2O_3$  particles within a steel matrix without changing its mechanical properties, a 0.47% C carbon steel ( $\phi 200$  mm) with a unique V-shaped groove (the surface width is 5 mm) is turned as shown in Fig. 8. The groove is filled with a mixture of bond containing plastic glue (20%), iron powder (80%) and  $Al_2O_3$  powder (1,000 wt.ppm for the whole steel rod,  $\phi 53-74 \mu m$  and  $\phi 105-149 \mu m$ ) as an abrasive. The compressive fracture strength of the mixture after solidification is 120 MPa. Since the cut distance of the groove is 1/126 of the periphery of the bar, many  $Al_2O_3$  particles within the groove instantaneously scratch the tool face with every revolution.

Assuming that contact stress and tool temperature during machining is almost the same as those of the conventional work material, Fig. 9 shows the influence of the abrasive particles on

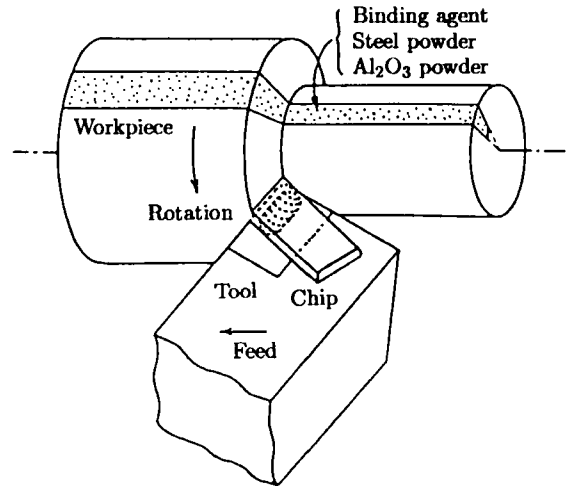


Fig. 8 Setup for simulation experiment of abrasion effect.

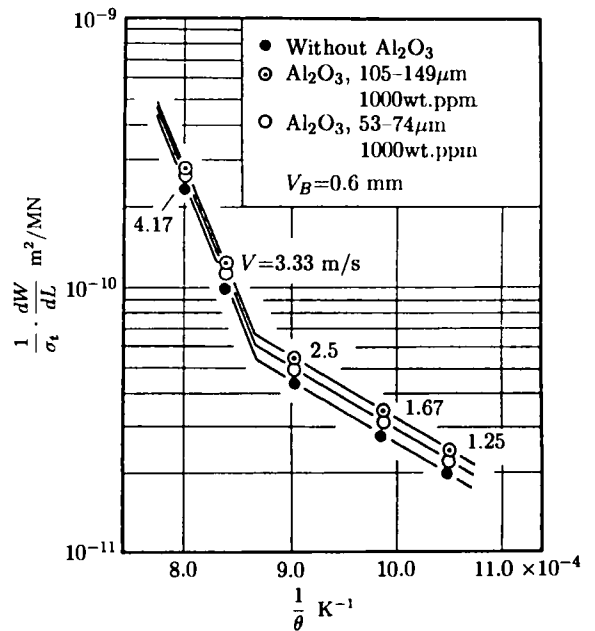


Fig. 9 Influence of abrasive particles on flank wear characteristics: 0.47% C steel, P20 (-5,-6,5,6,15,15,0.4),  $f=0.2$  mm/rev,  $d=2$  mm, dry.

the flank wear characteristics. The characteristic lines are translated almost parallel to the axes: the large particle size gives higher wear rates at the same temperatures. A similar tendency takes place for crater wear. The characteristic lines

without  $\text{Al}_2\text{O}_3$  in Fig. 9 do not coincide with those in Figs. 4, 5 and 7. This is due to different chemical composition and mechanical properties of the latest P20 tool.

The experimental results and discussion so far make it clear that throughout the whole temperature range, abrasion as well as adhesion appears in the tool wear characteristics. According to the abrasion theory [14], the wear rate  $dW/dL$  per unit area is given by

$$\frac{dW}{dL} = \kappa \frac{\sigma_t}{H'} \quad (8)$$

where  $\kappa$  is a constant depending on the shape and amount of abrasive particles and  $H'$  is the hardness of a harder material (a cutting tool here). When introducing a temperature effect similar to the relationship (3), ie

$$H' \propto \exp\left(\frac{\alpha_2}{\theta}\right) \quad \text{and} \quad \kappa \propto \exp\left(\frac{\alpha_3}{\theta}\right) \quad (9)$$

into Eq. (8), we obtain

$$\frac{1}{\sigma_t} \frac{dW}{dL} = C'_1 \exp\left(\frac{-C'_2}{\theta}\right) \quad (10)$$

The abrasives are distributed within the steel matrix, including ferrite, austenite, pearlite and grain boundaries. As the interface temperature between the matrix sustaining the abrasives and the tool rises, the matrix softens and therefore its rigidity decreases. This is the reason why the constant  $\kappa$  has the temperature dependency given by the relationship (9). When Eq. (10) is combined with Eq. (4), the total wear rate may be given as

$$\frac{1}{\sigma_t} \frac{dW}{dL} = C_1 \exp\left(\frac{-C_2}{\theta}\right) + C'_1 \exp\left(\frac{-C'_2}{\theta}\right) \quad (11)$$

Since the constants in the right-hand terms have different specific values ( $C_1 \gg C'_1$  and  $C_2 > C'_2$  as shown in Figs. 4 and 5), Eq. (11) can describe the wear characteristics that have a folded characteristic line. Consequently the mechanism of the tool wear consists of both adhesion and abrasion which largely depends on temperature at the interface. There is a critical temperature of 1,175 K for the P20 carbide tool at which abrasion ceases to be the predominant factor and above which

adhesion predominates. Moreover, in the higher temperature range the wear equation (4) based on the thermally-activated adhesion model describes tool wear in which the characteristic constants  $C_1$  and  $C_2$  are not affected by the variation of steels. This may be attributed to the formation of a Fe-W-Co carbide compound at the interface. In the lower temperature range a similar wear equation (10) holds, based on the temperature-dependent abrasive model in which the constants are obviously dependent on the carbon content of the steels.

#### 4.2. Analytical prediction of tool wear

Once the constants involved in Eq. (11) are thus determined, tool wear can be predicted, together with estimations of temperature and normal stress on the tool face. The energy method [15] or the finite element machining simulation [16] can be employed for the prediction of tool wear; however, the determination of the wear characteristic constants needs sophisticated experimental techniques and is time-consuming. In this paper a prediction method that combines the energy method with the evaluation of the wear constants is newly proposed.

Figure 10 shows this proposed method. Based on orthogonal cutting data, the chip shape, cutting force and tool-face stress in three-dimensional machining can be determined so as to minimize the total cutting energy [15]. Tool-face temperature is analysed numerically using the obtained cutting model, heat source and thermophysical properties. Although for a specified combination of tool and work materials wear data on  $dW/dL$  under several cutting conditions are required, the characteristic constants can be determined, assuming that Eq. (11) holds. As a result, the wear rate  $dW/dL$  on the tool face is evaluated under a wide range of cutting conditions, excepting initial breakdown of the cutting edge and deep groove or notch wear.

Figure 11 demonstrates the predictions of crater wear, rake temperature and normal stress when an 18%Mn-5%Cr alloy steel is turned using a P20 tool at a cutting speed of 120 m/min, a feed of 0.2 mm/rev, a depth of cut of 2 mm and without coolant. The tool geometry is (0,0,6,6,15,15,0.5) and the cutting time is 40

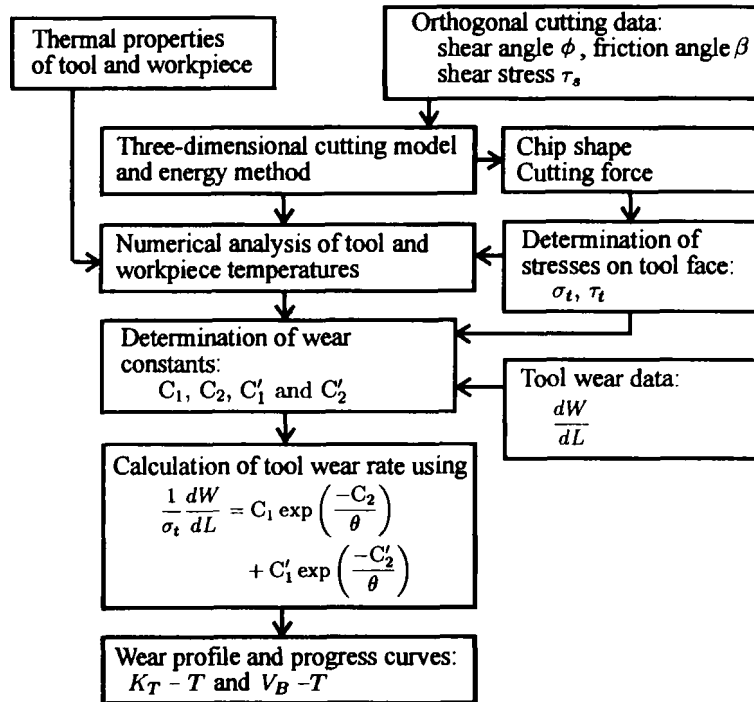


Fig. 10 Prediction system for tool wear based on the energy method and wear characteristic equation.

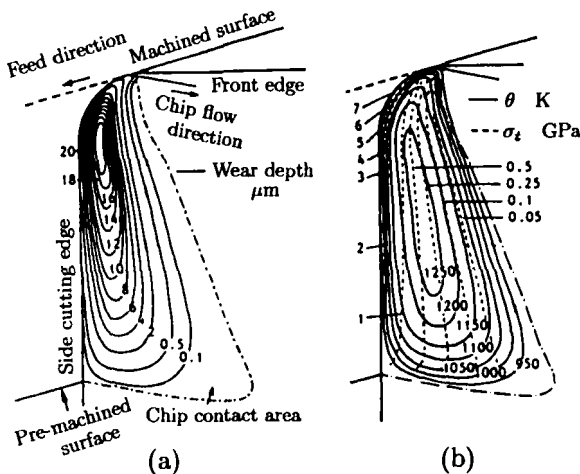


Fig. 11 Predicted (a) crater wear, and (b) temperature and normal stress at cutting time of 40 s: 18%Mn-5%Cr steel, P20 (0,0,6,6,15,15,0.5),  $V=120$  m/min,  $f=0.2$  mm/rev,  $d=2$  mm, dry.

s. The finite difference method [4] is employed for the temperature calculation. The details of the energy method are shown elsewhere [15, 17].

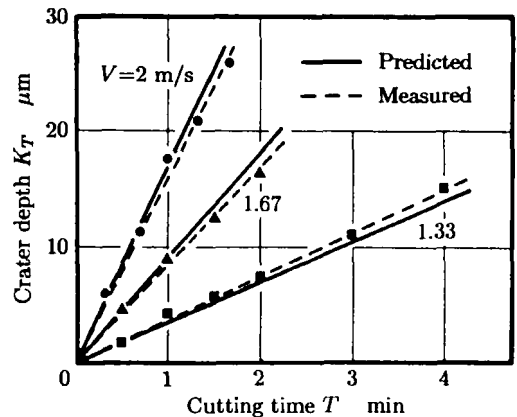


Fig. 12 Comparison of predicted crater wear progress curves with experiment: cutting conditions are the same as Fig.11.

Figure 12 shows the progress of the maximum crater depth  $K_T$  with time for the P20 tool with wear characteristic constants of  $C_1=22.45$   $m^2/MN$ ,  $C_2= 21,770$  K and  $C'_1=C'_2=0$ . Good agreement between the prediction (solid lines)



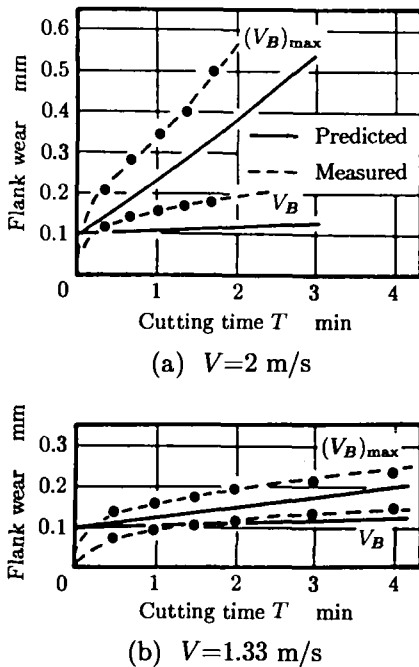


Fig. 13 Comparison of predicted flank wear progress curves with experiment: cutting conditions are the same as Fig.11.

and the experiment (dashed lines) can be seen at every cutting speed.

Figure 13 shows the flank progress curves with time (a) at a cutting speed of 120 m/min and (b) 80 m/min, where an initial wear width of 0.1 mm is postulated. Both predicted maximum wear and mean wear width  $(V_B)_{\max}$  and  $V_B$  respectively do not agree well with experiment (dashed lines), but the wear rates  $d(V_B)_{\max}/dT$  and  $dV_B/dT$  show good agreement. Deep groove or notch wear at the major cutting edge is not predicted by the present method. Further investigation into evaluations of initial breakdown and notch wear is needed to enhance the suitability of the present prediction system shown in Fig.10.

## 5. CONCLUSIONS

Wear characteristics of various, mainly carbide, cutting tools in steel machining has been investigated experimentally. Using the measured wear rate, contact stress and tool temperature, the suitability of a wear characteristic equation based

on the thermally-activated adhesion wear model has been discussed. The major results obtained are summarised as follows:

- (1) For crater wear of carbide tools, the thermally-activated adhesion wear model holds for the machining of plain carbon steels, high manganese steels and austenitic stainless steel using a P20 carbide tool, in which the characteristic constants involved in the wear equation are independent of the work materials.
- (2) A P40 carbide tool including a higher percentage of cobalt than its P20 counterpart yields higher wear rates at the corresponding interface temperatures.
- (3) For flank wear of the P20 tool a similar wear characteristic equation to crater wear holds in the temperature range above 1,175 K, but in the lower temperature range the constants involved in the wear equation are largely different from those for crater wear, being dependent on the carbon content of the plain carbon steels.
- (4) Although an alumina ceramic tool shows a temperature-insensitive nature, a critical temperature distinguishing adhesion from abrasion also appears around 1,175 K.
- (5) A simulation experiment for the verification of an abrasion effect by hard particles dispersed within steels results in the coexistence of adhesion and abrasion throughout the whole temperature range.
- (6) A wear characteristic equation given as

$$\frac{1}{\sigma_t} \frac{dW}{dL} = C_1 \exp\left(\frac{-C_2}{\theta}\right) + C'_1 \exp\left(\frac{-C'_2}{\theta}\right)$$

is proposed to describe both crater and flank wear, where  $dW/dL$  is the wear rate per unit area,  $\sigma_t$  is the contact normal stress,  $\theta$  is the tool temperature at the interface; and  $C_1$ ,  $C_2$ ,  $C'_1$  and  $C'_2$  are constants to be determined for a combination of tool and work materials. The equation combines the thermally-activated adhesion model with a temperature-dependent abrasion model.

- (7) An analytical prediction method combining the energy method with the estimation of the wear characteristic constants is proposed, its suitability being demonstrated when an

18%Mn-5%Cr alloy steel is turned using a P20 single point tool.

## REFERENCES

1. F.W. Taylor, *Trans. ASME*, 28 (1906) 31.
2. F.P. Bowden and D. Tabor, *Friction and Lubrication of Solids*, Oxford Univ. Press, London (1954).
3. E. Usui and T. Shirakashi, *On the Art of Cutting Metals - 75 Years Later*, ASME Publ., PED-7 (1982) 13.
4. E. Usui, T. Shirakashi and T. Kitagawa, *Trans. ASME, J. Eng. Ind.*, 100, May (1978) 236.
5. K.J. Trigger and B.T. Chao, *Trans. ASME*, 78, July (1956) 1119.
6. H. Takeyama and R. Murata, *J. Jap. Soc. Prec. Eng.*, 27, 1 (1961) 33. (in Japanese)
7. S. Kato and K. Yamaguchi, *J. Eng. Ind., Trans. ASME*, B94 (1972) 683.
8. G. Boothroyd and W.A. Knight, *Fundamentals of Machining and Machine Tools*, 2nd ed., Marcel Dekker, New York (1989) Chap. 3.
9. N. Narutaki and Y. Yamane, *Proc. 2nd ICPE*, Tokyo (1976) 190.
10. E.Usui, *Contemporary Metal Cutting Theory*, Kyoritu-shuppan, Tokyo (1990) Chap. 4. (in Japanese)
11. G. Brandt and M. Mikus, *Wear*, 115, 3 (1987) 243.
12. S. Ramalingam, *Mat. Sci. Engg.*, 43 (1980) 101.
13. K. Maekawa, A. Kubo and T. Kitagawa, *Bull. Jap. Soc. Prec. Eng.*, 22, 3 (1988) 183.
14. E. Rabinowicz, L.A. Dunn and P.G. Russel, *Wear*, 4 (1961) 345.
15. E. Usui, A. Hirota and M. Mashiko, *J. Eng. Ind., Trans. ASME*, B100, May (1978) 222.
16. K. Maekawa, T. Shirakashi and T. Obikawa, *Proc. Instn Mech. Engrs, Part B*, 210 (1996) 233.
17. K. Maekawa and T. Kitagawa, *Bull. Jap. Soc. Prec. Eng.*, 19, 4 (1985) 254.

## Fundamental study of nano-scale machining using bubble raft model

K. Maekawa, Y. Hojo and I. Ohshima

Department of Mechanical Engineering, Ibaraki University,  
4-12-1 Nakanarusawa, Hitachi 316, Japan

The bubble raft model has been employed to investigate the cutting mechanism in nano-scale machining. The present paper first describes the instrumentation and measurement, then examines the influence of cutting conditions and tool geometry on chip formation and subsurface damage. Damage caused by edge dislocations increases with increasing depth of cut, or tool edge radius, or both. Atomistic defects, including vacancies and grain boundaries initially induced into the model, cause the damage to develop. These phenomena have been successfully visualized by means of the behaviour of soap bubbles. The experimental results are compared with those obtained by the molecular dynamics simulation of orthogonal machining of a copper single crystal. Qualitative agreement between the bubble raft model and the MD simulation can be seen with respect to basic cutting phenomena including chip formation and subsurface damage, in which a similar deformation mechanism through dislocations plays a primary role. Interaction between tool and workpiece is also a key factor in nano-scale machining.

### 1. INTRODUCTION

Recent developments in the precision machining of X-ray mirrors and magnetic memory discs, by means of the diamond turning of copper and aluminium alloys using high-rigidity machine tools, generate surface accuracy of sub-micrometre order [1]. There is a growing demand for developing more precise or ultra-precision machining in which a removal at an atomistic level is an ultimate goal. To establish nano-scale machining technologies including developments in micro-machine devices, monitoring and machine control, and the optimisation of cutting conditions, it is vital to clarify cutting phenomena such as chip formation, cutting force, surface roughness and sub-surface damage at feeds of a few atomistic layers.

Molecular dynamics (MD) simulations have been employed for this purpose, and the physical aspects are partially understood with respect to: the dependence of the specific energy on the depth of cut [2], the role of dislocations on chip formation [3], the minimum depth of cut for producing chips [4], tribological phenomena [5] and three-dimensional chip formation [6]. However, there remain problems of uncertainty of the po-

tentials used and spatial/time limitations in these computer experiments.

MD simulations involve tracking the motion of atoms and molecules as a function of time. Typically, this motion is described by Newton's equations of motion and yields a set of  $3N$  second-order differential equations, where  $N$  is the number of particles. These can be solved with finite-timestep integration methods, typically tenths to a few femtoseconds [7]. Most current simulations then integrate for up to a total time from picoseconds to only a few nanoseconds for a system of  $N=1000-10000$ , despite the advent of much faster computers. The classical equations of motion require a method for calculating the forces between atoms. Currently there are two approaches: the first assumes that the potential energy of the system as a function of the relative atomic positions of the atoms can be represented in a mathematical form that contains some free parameters. The parameters are then chosen to describe some set of physical properties of the system of interest, and forces are obtained by taking the gradient of the potential energy with respect to atomic positions. The second approach involves the calculation of interatomic forces directly from an *ab initio* electronic structure calculation [8]. However,

there is no guarantee of the accuracy of either approach in obtaining the forces from a potential or a semiempirical electronic structure calculation; poorly chosen parameterisations and functional forms can yield nonphysical forces. It is clear that uncertainty of the calculation of forces as well as spatial/time limitations in current MD simulations necessitate an experimental verification of the simulation models.

In the present study the bubble raft model [9] is employed to investigate nano-scale cutting mechanisms as well as to make a comparison with the MD simulation [5]. Describing the experimentation, we demonstrate the influence of tool edge radius, depth of cut and crystal imperfection on chip formation and subsurface damage. The simulation experiments using soap bubbles assume that a (111) plane of an *fcc* crystal is cut using a rigid tool in a  $[10\bar{1}]$  direction. The experimental results are compared with those obtained by the MD calculation [5], where orthogonal machining of a (111) plane of a copper single crystal using a diamond-like tool at a cutting speed of 20 m/s is simulated, postulating the Morse potentials and a system of 2496 copper atoms and 120 carbon atoms.

## 2. EXPERIMENTATION

According to Bragg's instrumentation [9], a large population of soap bubbles can be formed on the surface of a soap solution by blowing compressed air into it through a narrow orifice of 0.05 mm diameter. The soap solution consists of 15.2 ml of oleic acid diluted by 50 ml of distilled water, 73 ml of 10% solution of tri-ethanolamine and 164 ml of pure glycerine. This is diluted in three times its volume of water to reduce viscosity. The orifice is set about 5 mm below the surface, and the air pressure, supplied by a small compressor, is controlled by a water manometer. Figure 1 shows a schematic diagram of the experimental apparatus. A cutting tool made of an acrylic board is driven by a step motor to yield a cutting action against the bubbles in a container. Cutting force is measured using two force sensors with a four-gauge measurement of the deflection of double cantilever springs positioned at the bottom and the front of the soap assemblage. The bottom of the container is blackened to show up

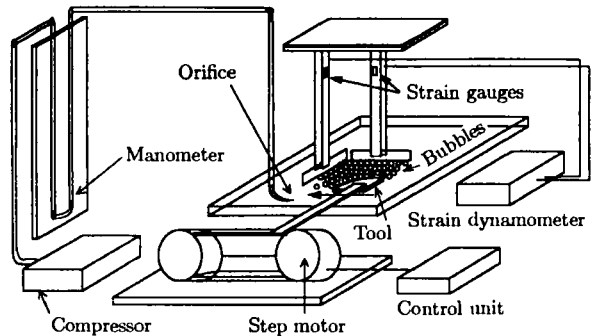


Fig. 1 Nano-scale machining simulation apparatus using bubble raft model.

each bubble more clearly. During machining the behaviour of the bubbles is recorded by a 35 mm camera or an 8 mm videotape recorder.

Assuming that a (111) close packed plane of an *fcc* copper single crystal whose lattice constant is 3.61 Å is cut in a  $[10\bar{1}]$  direction, a bubble diameter of 1.2 mm is correspondent to a nearest-neighbour distance of 2.55 Å on the plane. This scale transformation is applied to the determination of tool edge radius. The cutting speed is set at 1.1 mm/s, whereas the MD simulation [5] assumes 20 m/s which corresponds to a speed of  $6.65 \times 10^6$  m/s in the bubble model. The equivalent tool edge radius is set at 0, 3 and 5 nm, and the depth of cut at 1 and 2 nm. The influence of these parameters on chip formation and subsurface damage will be investigated for both perfect and imperfect crystals including vacancies and grain boundaries.

## 3. CHIP FORMATION AND SUBSURFACE DAMAGE

### 3.1. Influence of depth of cut and tool edge radius

Figure 2 represents a snapshot of the behaviour of bubbles at a depth of cut of  $t=1$  nm with varying tool edge radius: (a)  $r=3$  nm, (b) 5 nm and (c) 0. When the edge radius is small ((c) and (a)), disorder of the bubble structure in the vicinity of the tool tip is light. In addition, the bubbles above an extension line of the bottom of the tool edge are removed as a chip by the cutting action. As a result, disorder of the machined surface and

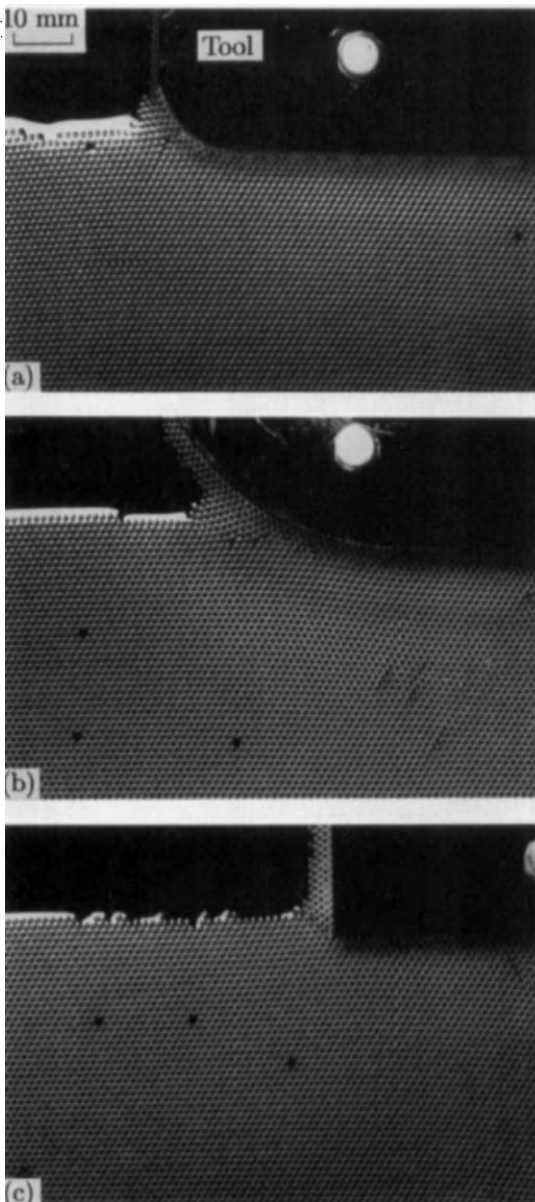


Fig. 2 Behaviour of soap bubbles, showing the influence of depth of cut ( $t=1$  nm after scaling) on chip flow and subsurface damage: (a) tool edge radius  $r=3$  nm, (b) 5 nm and (c) 0, when using acrylic tool at cutting speed of 1.1 mm/s.

subsurface damage are negligibly small. In the case of (b)  $r=5$  nm, on the contrary, the bubbles expected to be removed are indented below the bottom of the tool edge, edge dislocations propagating from the tool tip several depths of cut into

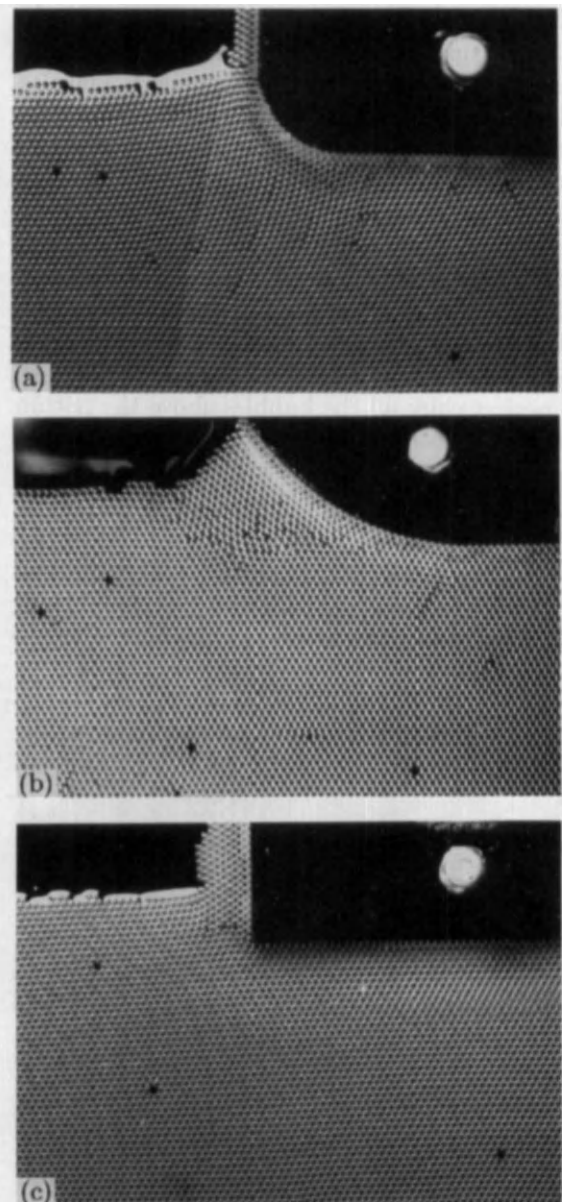


Fig. 3 Behaviour of soap bubbles, showing the influence of depth of cut ( $t=2$  nm after scaling) on chip flow and subsurface damage: (a) tool edge radius  $r=3$  nm, (b) 5 nm and (c) 0, when using acrylic tool at cutting speed of 1.1 mm/s.

the workpiece.

Figure 3 depicts a similar snapshot to Fig. 2 but with the depth of cut doubled,  $t=2$  nm. Compared with Fig. 2, the indentation phenomenon becomes more apparent at  $r=3$  nm and 5 nm.

Edge dislocations are frequently generated from the tool tip and propagate in the directions of  $60^\circ$  and  $120^\circ$  against the cutting direction. Thus lattice strain in the bubble structure caused by machining is not released by the elastic indentation of the layers but relieved by the rearrangement of bubbles through dislocations. Disorder of the bubbles is extended in front of the tool tip as the tool edge radius increases: in particular, an arch-shaped grain boundary can be seen at  $r=5$  nm. An ideal tool of  $r=0$ , on the other hand, does not show such structural disorder, but generates a perfect chip; all the bubbles above the bottom of the tool edge are removed as a chip.

### 3.2. Influence of vacancies and grain boundaries

Figure 4 represents a snapshot of the behaviour of bubbles at  $t=2$  nm and  $r=3$  nm where many vacancies and dislocations are introduced in the

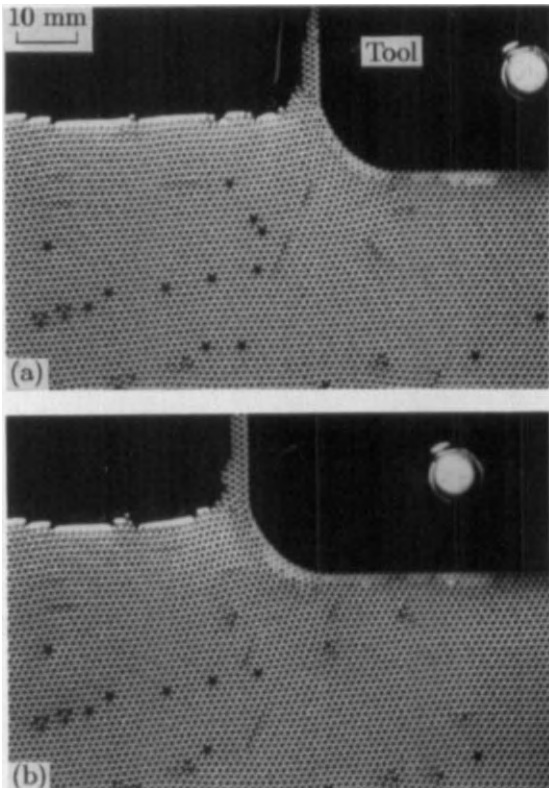


Fig. 4 Behaviour of soap bubbles with existing vacancies, where the difference of cut distance between (a) and (b) is 12 mm.

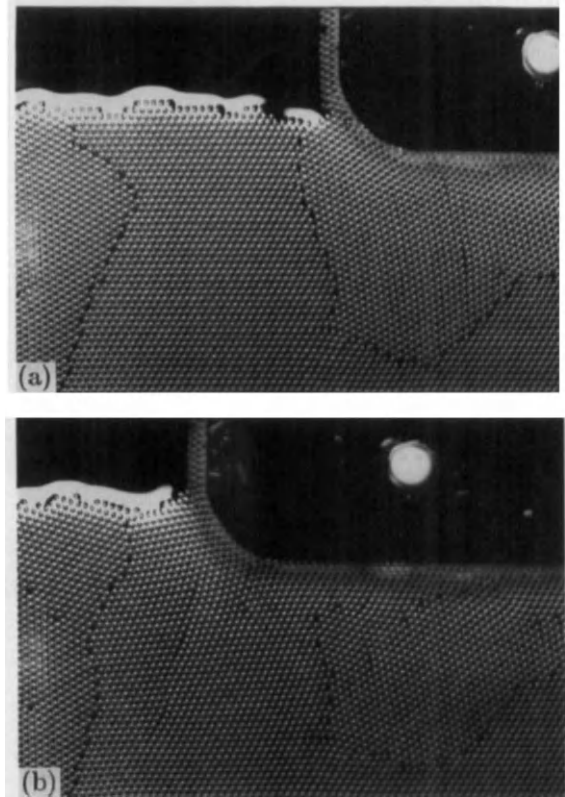


Fig. 5 Behaviour of soap bubbles with existing grain boundaries, where the difference of cut distance between (a) and (b) is 24 mm.

workpiece before machining. The dark spots in the figure denote vacancies, and the grey line segments edge dislocations. With the tool movement, (a) to (b), edge dislocations frequently nucleate from the tool tip and penetrate into a deep portion within the workpiece via vacancies. Some vacancies close to the tool tip disappear to serve as the rearrangement of the bubble structure. As a result, deeper subsurface damage than in Fig.3 (a) can be seen.

Figure 5 shows the influence of interfacial defects or grain boundaries on chip flow and subsurface damage at  $t=2$  nm and  $r=3$  nm. Although edge dislocations generated at the tool tip penetrate the workpiece, the grain boundary prevents them from propagating outside the grain; subsequent subsurface damage caused by machining is confined within the grain. In addition, another grain starts forming below the tool flank. Figure 5 (b) shows that the grain boundary ahead

of the tool edge as shown in Fig.5 (a) disappears after machining. With the advancement of the tool the other grain boundary ahead of the tool edge as shown in Fig.5 (b) changes its shape and a sub-grain starts to generate by means of a rotation of the existing grain. There is deeper subsurface damage than in the cutting of a single crystal (Fig.3 (a)), though the chip shape is almost the same.

## 4. DISCUSSION

### 4.1. Cutting mechanism of soap bubbles

The metal cutting mechanism at feeds in the nanometre range is largely affected by an atomistic interaction between tool and work atoms [5, 10]. In the cutting simulation using the soap bubbles, an acrylic board was used as the tool. Since it has a high affinity for soap bubbles, it is observed that the bubbles removed as a chip or those generated as a machined surface adsorb on the tool rake face or the tool flank. The cutting experiment is therefore carried out using a tool made of Teflon whose affinity for soap bubbles is much lower.

Figure 6 shows the chip formation and subsurface damage obtained using the Teflon tool at  $t=2$  nm with various tool geometries: (a)  $r=3$  nm,  $\alpha=0^\circ$ ,  $\gamma=30^\circ$ , (b)  $r=0$ ,  $\alpha=0^\circ$ ,  $\gamma=30^\circ$ , and (c)  $r=0$ ,  $\alpha=10^\circ$ ,  $\gamma=20^\circ$ , where  $\alpha$  is the rake angle and  $\gamma$  is the clearance angle. In the comparisons of Fig.6 (a) with Fig.3 (a) and Fig.6 (b) with Fig.3 (c), the bubbles still adsorb on the tool faces, but the cutting action is enhanced; the Teflon tool produces more work bubbles as a chip. By setting a larger clearance angle, the machined surface is generated closer to the tool tip, leading to less subsurface damage. The level of the machined surface, however, is below the bottom of the tool edge due to the adsorbate on the tool flank. The increase of the rake angle (Fig.6 (c)) produces a thinner chip as compared with the zero rake-angle tool (Fig.6 (a)). Thus, chemical affinity as well as tool geometry influences the cutting mechanism of the soap bubbles.

The generation and propagation of edge dislocations in the vicinity of the tool edge play a major role in nano-scale machining. It is interesting to note that the deformation pattern resembles a slip line field for the deformation of a perfect

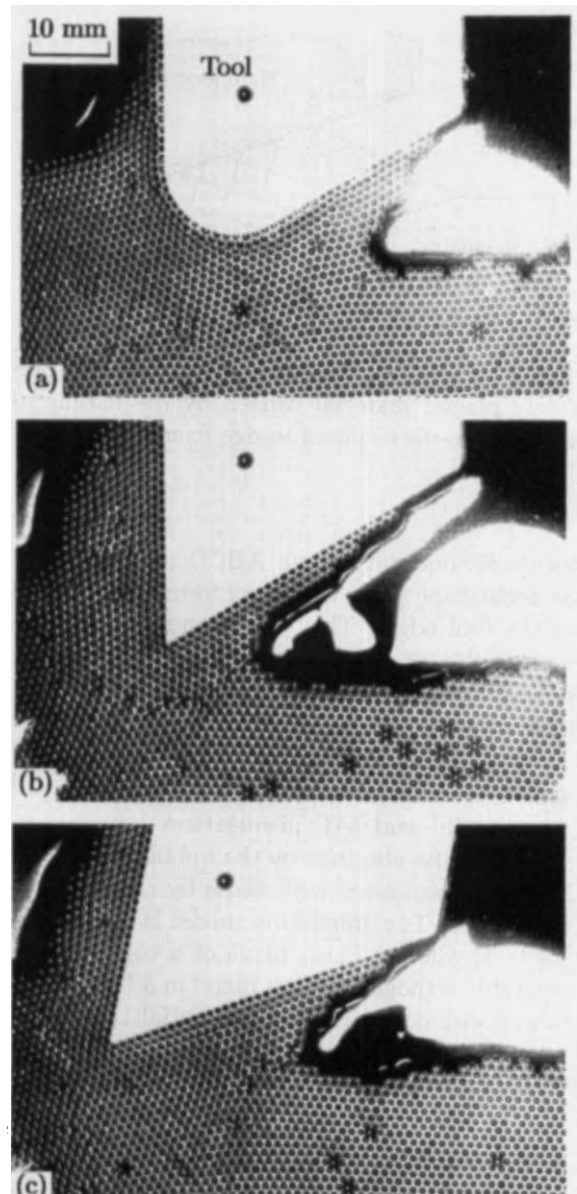


Fig. 6 Behaviour of soap bubbles when using Teflon tool with various geometry: (a) tool edge radius  $r=3$  nm, rake angle  $\alpha=0^\circ$ , clearance angle  $\gamma=30^\circ$ , (b)  $r=0$ ,  $\alpha=0^\circ$ ,  $\gamma=30^\circ$ , and (c)  $r=0$ ,  $\alpha=10^\circ$ ,  $\gamma=20^\circ$ .

plastic material caused by the sliding of a rigid two-dimensional wedge. Figure 7 shows a steady state slip line field for the plastic deformation of a soft asperity by a hard asperity [11], where no adhesion between the wedge and the substrate is postulated. As compared with Fig.3 (b), the ve-

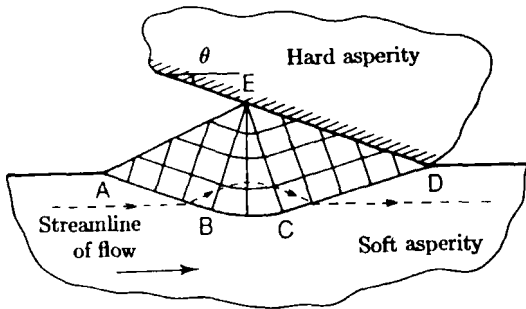


Fig. 7 Slip line field for the deformation of a perfectly plastic material caused by the sliding of a rigid two-dimensional wedge from right to left [11].

locity discontinuity along ABCD coincides with an arch-shape grain boundary formed just ahead of the tool edge. This correspondence suggests a similarity in deformation mechanism between nano- (soap bubbles in a strict sense) and macro-scale machining.

#### 4.2. Correlation between bubble raft model and MD simulation

The results obtained by the bubble raft experiment are compared with those by the MD simulation [5]. The simulation model is outlined in Table 1, where a (111) plane of a copper single crystal is orthogonally machined in a  $[10\bar{1}]$  direction, postulating the Morse potentials:

$$\phi(r_{ij}) = D[\exp\{-2\alpha(r_{ij}-r_0)\}-2\exp\{\alpha(r_{ij}-r_0)\}] \quad (1)$$

where  $\phi$  is a pair potential energy function,  $r_{ij}$  is the relative distance between two atoms and  $D$ ,  $\alpha$  and  $r_0$  correspond to the cohesion energy, the elastic modulus and the atomistic distance at equilibrium respectively. Table 2 lists the parameters of Morse type potentials. The cutting conditions, except cutting speed, correspond to those in Fig. 2.

Figure 8 represents a snapshot of the work atoms at a total time step of 60,000, ie a cut distance of 12 nm, in the cases of (a)  $r=3$  nm, (b) 5 nm and (c) 0. The symbols  $\circ$  and  $\bullet$  indicate respectively the instantaneous temperatures below and above 1,000 K which are simply converted from the kinetic energy of the atoms. Figure 9

Table 1 MD simulation model and cutting conditions

|                      |                                      |
|----------------------|--------------------------------------|
| Work material        | Cu single crystal                    |
| Tool                 | Diamond (111) plane                  |
| Number of atoms      | 2498 Cu, 120 C                       |
| Governing equations  | Newton's equation<br>Morse potential |
| Numerical procedures | Verlet's method                      |
| Initial temperature  | 300 K                                |
| Time step            | 10 fs                                |
| Cutting speed        | 20 m/s                               |
| Depth of cut         | 1 nm                                 |
| Rake angle           | 0°                                   |
| Edge radius          | 3 nm                                 |
| Cut plane            | (111)                                |
| Cut direction        | $[10\bar{1}]$                        |

Table 2 Parameters of Morse type potentials

|                              | Cu-Cu  | Cu-C  | C-C   |
|------------------------------|--------|-------|-------|
| $D$ , eV                     | 0.3429 | 0.100 | 2.423 |
| $\alpha$ , $\text{\AA}^{-1}$ | 1.3588 | 1.700 | 2.555 |
| $r_0$ , $\text{\AA}$         | 2.6260 | 2.200 | 2.522 |

shows the trajectories of the work atoms corresponding to Fig. 8, where the translation of the straight parallel lines by one layer denotes the occurrence of shear deformation due to the propagation of edge dislocations. A similarity in the structural disorder caused by machining can be seen between the bubble experiment (Fig. 2) and the MD simulation (Figs. 8 and 9). As the tool edge radius increases, the material removed as a chip decreases and subsurface damage becomes more severe; in particular, the indentation behaviour and an arch-shaped deformation boundary ahead of the tool tip can be also seen in Fig. 9 (b). However, the movement of the work atoms in the deformation zone is more active in the MD simulation. This difference stems from the cutting speed used between the two models: 20 m/s vs 1.1 mm/s.

Figure 10 compares the change of cutting force with time in the cases of (a) the bubble raft model (Fig. 2 (a)) and (b) the MD simulation (Fig. 8 (a)), where  $F_H$  is the horizontal component and  $F_V$



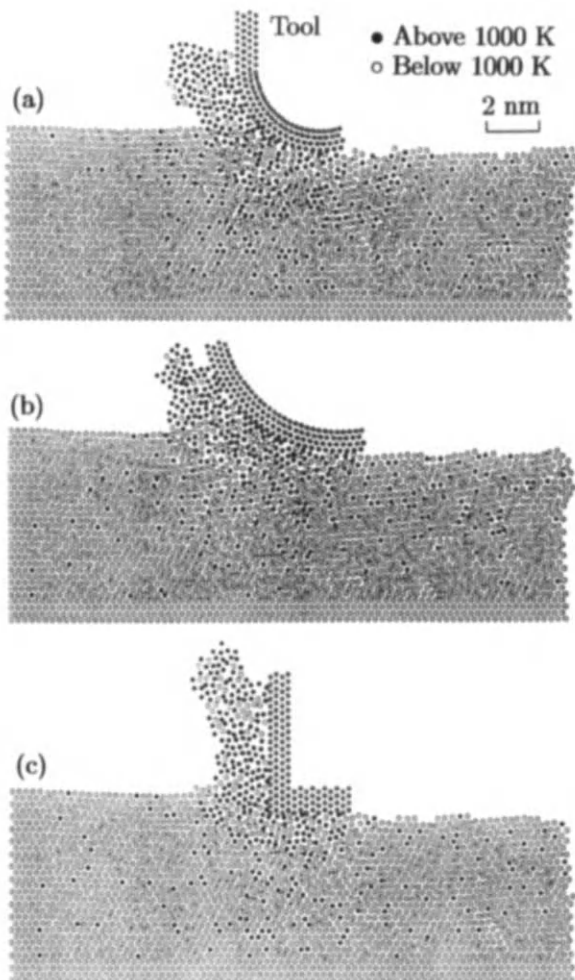


Fig. 8 Behaviour of work atoms and the distribution of temperature in machining (111) plane of perfect copper crystal with various tool edge radius: (a)  $r=3$  nm, (b) 5 nm and (c) 0.

the vertical one. The time step in the MD simulation is 10 fs, and the force is monitored at every 50 steps. The bubble experiment gives a higher  $F_H$  than  $F_V$  with fewer fluctuations, which arises from the adsorption of soap bubbles onto the tool flank and a quasi-static deformation at a cutting speed of 1.1 mm/s. In both models macroscopic shear in the workpiece caused by the movement of edge dislocations results in peaks in the cutting force.

The role of atomistic defects introduced in the bubble raft model, such as the formation of subgrains and enhancement of structural disorder, is

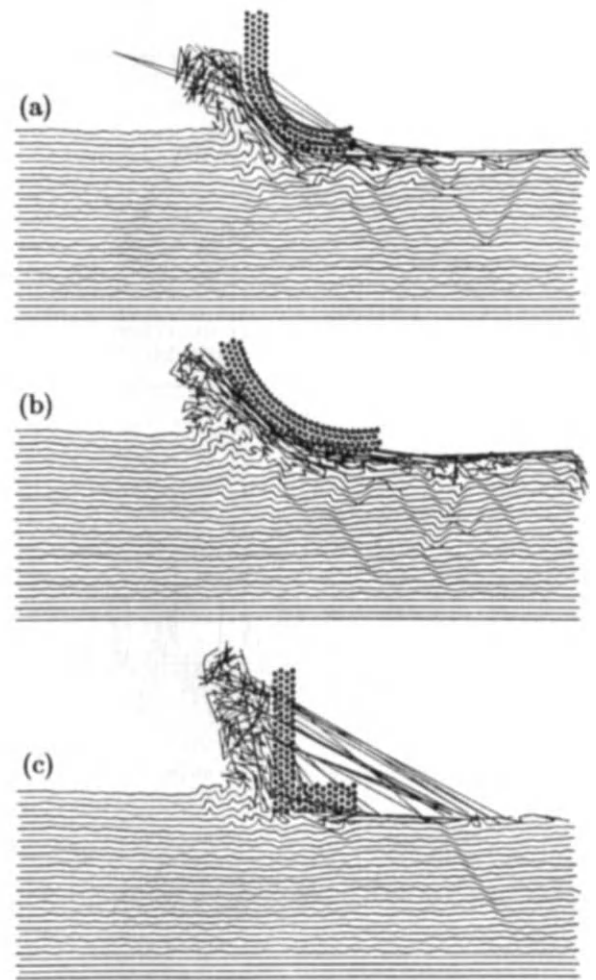


Fig. 9 Changes of atomic layers in  $[10\bar{1}]$  direction in machining (111) plane of perfect copper crystal with various tool edge radius: (a)  $r=3$  nm, (b) 5 nm and (c) 0.

also simulated in the MD calculations [4, 12].

To make a quantitative comparison between the two models it is vital to determine the parameters in pair potentials of the soap bubbles, and of the soap bubbles and the tool. This will not be straightforward and needs sophisticated techniques undeveloped at present. Even though the potential shape may be identified, the difference in time-scale or cutting speed in both models is inevitable due to lack of computational power. These are the present limitations of the comparative approach.

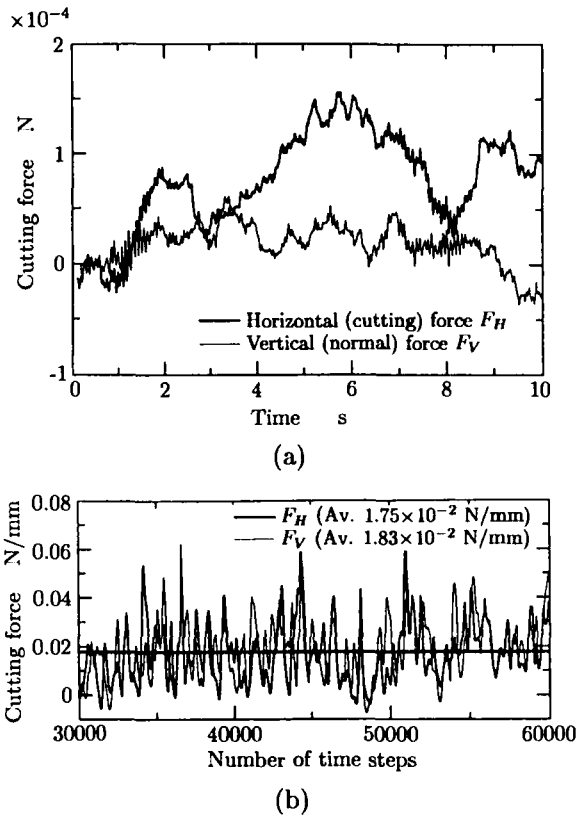


Fig. 10 Variation of cutting force at  $t=1$  nm and  $r=3$  nm: (a) bubble raft model and (b) MD simulation.

## 5. CONCLUSIONS

In the present study the bubble raft method according to Bragg and Nye [9] has been employed to investigate the nano-scale cutting mechanisms of soap bubbles as well as to make a comparison with molecular dynamics simulations of a copper single crystal. The major results obtained are summarised as follows:

- (1) Assuming that a (111) plane of an *fcc* crystal is machined using a rigid tool in a  $[10\bar{1}]$  direction, cutting conditions and tool geometry substantially affect chip formation and subsurface damage of the bubble workpiece. When the tool edge radius is small and/or the depth of cut is small, displacement of the bubbles is limited to be at or just below the machined surface, and more work bubbles are removed as a chip.
- (2) Existing vacancies and edge dislocations in the soap bubbles result in further disorder of the bubble structure owing to the interaction between the defects and the dislocations propagated from the tool tip.
- (3) Qualitative agreement between the bubble raft model and the MD simulation can be seen with respect to basic cutting phenomena, including chip formation and subsurface damage in which a similar deformation mechanism through dislocations plays a primary role. The interaction between tool and workpiece is also a key factor in nano-scale machining.
- (4) To make a quantitative comparison between the two models it is vital to determine a pair potential between soap bubbles. The introduction of appropriate interaction between the bubbles and the cutting tool is also essential. The advent of much faster computers is required for this comparative approach.

## REFERENCES

1. N. Ikawa, R.R. Donaldson, R. Komanduri, W. König, P.A. McKeown, T. Moriwaki and I.F. Stowers, *Ann. CIRP*, **40**, 2 (1991) 587.
2. J. Belak and I.F. Stowers, *Proc. Am. Soc. Prec. Eng.* (1990) 76.
3. S. Shimada, N. Ikawa, G. Ohmori and H. Tanaka, *Ann. CIRP*, **41**, 1 (1992) 117.
4. S. Shimada, N. Ikawa, H. Tanaka, G. Ohmori and J. Uchikoshi, *Ann. CIRP*, **42**, 1 (1993) 91.
5. K. Maekawa and A. Itoh, *Wear*, **188** (1995) 115.
6. R. Rentsch and I. Inasaki, *Ann. CIRP*, **44**, 1 (1995) 295.
7. D.W. Heermann, *Computer Simulation Method, 2nd edn*, Springer, Heidelberg (1990) 13-103.
8. R. Car and M. Parrinello, *Phys. Rev. Lett*, **55** (1985) 2471.
9. W.L. Bragg and J.F. Nye, *Proc. Roy. Soc. London, A190* (1949) 474.
10. K. Maekawa and Y. Hojo, *Proc. 8th ICPE*, Compiègne, France (1995) 319.
11. J.M. Challen and P.L.B. Oxley, *Wear*, **53** (1979) 229.
12. K. Maekawa, *J. Soc. Mat. Sci., Japan*, **46** (1997) to appear. (in Japanese)

## EHL TRACTION IN TRACTION DRIVES WITH HIGH CONTACT PRESSURE

S. AIHARA, S. NATSUMEDA and H. ACHIHA

Research and Development Center, NSK Ltd.  
1-5-50 Kugenuma-Shinmei, Fujisawa, Kanagawa, JAPAN

Traction Drives have been considered as smooth and efficient power transmitters and much effort has been carried out to investigate traction. Traction theories proposed by Johnson and Tevaarwerk and by Bair and Winer seem to satisfy many tribologists and engineers. However, recent experimental results show some discrepancy from those previously reported. In this paper traction theories and experiments are briefly discussed and compared with the authors' traction results under high contact pressure, high speed and high temperature.

### 1. INTRODUCTION

Traction was once a vibrant and active research topic in EHL, however, recently such enthusiasm seems to have waned as far as published papers are concerned. This decline in interest may be attributable to several reasons including the following: researchers are impatient with the rate of progress in achieving practical traction drives (especially automotive CVT), and the traction mechanism is considered to be explained by the Johnson-Tevaarwerk theory or the Bair-Winer theory.

However, the attempt to apply traction drives to CVT (Continuously Variable Transmission) for automobiles has been carried out steadily and without ceasing, so the technological possibility of practical realization is much closer at hand today than ever before. Practical CVT is subject to extremely severe operating conditions including high contact pressure, high speed and high temperature. For practical applications, a variety of special traction oils have been developed, though only a few kinds have proved to be successful.

Oils with high traction coefficient were investigated and found to have some properties that are different from ordinary lubricants<sup>1)</sup>. We measured traction properties by means of a four-disc machine and a two-disc machine with a special traction oil and examined their traction properties. Some unusual properties were noted when compared with conventional theories.

### 2. Traction Theory

Evans and Johnson made full discussion on rheological properties and traction regimes ten years ago<sup>2,3)</sup>. Since those review papers, the situation of traction has not changed much. Next the history is described briefly.

Traction estimation based on the assumption of Newtonian fluid was abandoned soon, as the estimated traction was too large at high contact pressure, particularly when pressure coefficients of viscosity were based on Barus relation.

In the 1960s and 70s non-Newtonian effects of fluid on traction were investigated widely<sup>4)</sup>. With a few lubricant rheological properties considered, traction characteristics were formulated. Hirst and Moore<sup>5)</sup> revealed that lubricant rheology became intrinsically non-linear under conditions that were very close to isothermal. And viscosity was found to be a function of shear stress rather than shear rate, in accordance with the Eyring model of viscous flow<sup>6)</sup>. Moore recently made a detailed review on lubricant rheology in EHL contacts<sup>7)</sup>.

Two models were widely regarded to be the most reliable models, and both are based on the visco-elastic model. Johnson and Tevaarwerk<sup>8)</sup> analyzed and measured traction curves taken by means of a two disc machine and proposed a non-linear visco-elastic model with Eyring stress. The formula is shown in equation (1). It is a three-parameter model which, for uni-directional shear, relates the shear stress  $\tau$  to the shear rate  $\dot{\gamma}$  by

$$\dot{\gamma} = \frac{\tau}{G} + \frac{\tau_0}{\eta} \sinh\left(\frac{\tau}{\tau_0}\right) \quad (1)$$

where  $G$  and  $\eta$  are the elastic shear modulus and viscosity of the lubricant;  $\tau_0$  is a reference stress which is called the 'Eyring stress'. All three properties of the lubricant vary with pressure  $p$  and temperature  $\theta$ .

Though equation (1) predicts that the shear stress increases without limit for a fluid with a constant viscosity, whenever the shear rate is increased. But in fact, a limit exists for the shear stress. Temperature of fluid rises by shear of the contact, hence the viscosity of fluid decreases and the shear stress decreases too.

From experiments performed by researchers in other fields, evidence indicates the existence of a glass transition of lubricating fluids at high pressure. Barrow et al<sup>9)</sup> described that any fluid acts as an amorphous solid, that is, glass transition, around the viscosity of  $10^{12}$  Pa·s. However, the glass transition is influenced by the time as shown in Fig.1<sup>10)</sup>. Namely, as time shortens (frequency increases) the glass transition pressure decreases so the transition viscosity decreases.

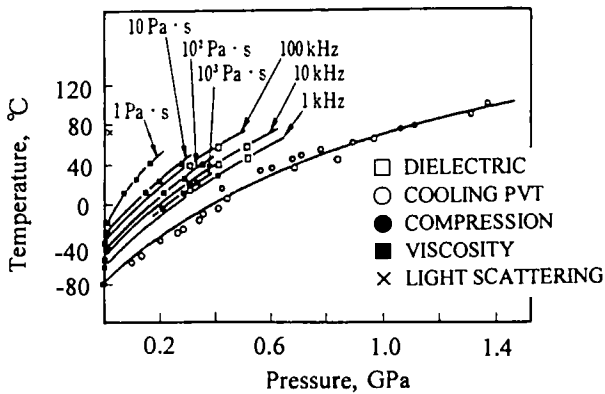


Fig.1 Glass Transition Diagram (Naphtenic Oils)

Maximum traction coefficient was regarded as the cause of solidification of lubricant, regardless whether it is glass or plastic. Thereafter, the existence of a limiting shear stress as a property of fluid was proved by the experiments of Bair and Winer<sup>11,12)</sup>. Bair made an in-depth review relating to high pressure rheology of lubricants in 1994<sup>13)</sup>.

Bair and Winer's formula for traction was expressed as equation (2).

$$\dot{\gamma} = \frac{\dot{\tau}}{G} + \frac{\tau_L}{\eta} \ln \left[ 1 / \left( 1 - \frac{\tau}{\tau_L} \right) \right] \quad (2)$$

where  $\tau_L$  is a limiting shear stress.

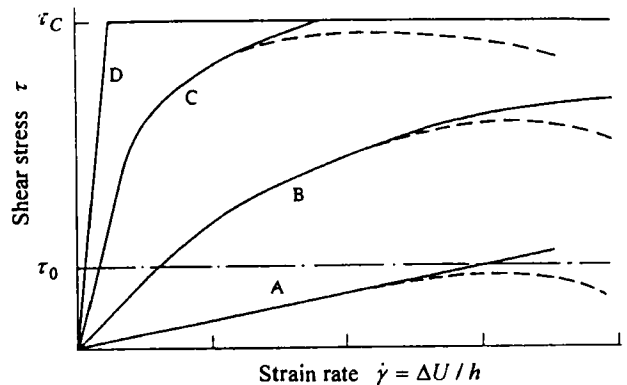
To investigate the behaviour of lubricant, Bair and Winer<sup>14)</sup> and Bair et al<sup>15)</sup> conducted flow visualization experiments for thin oil films to demonstrate the presence of localized shear bands. Solidification of lubricant was confirmed by other researchers but the experimental conditions were usually long time-scale and rather static. Hoglund and Jacobson<sup>16)</sup> measured the limiting shear stress according to the following formula.

$$\tau_L = \tau_0 + \gamma \cdot p \quad (3)$$

where  $\gamma$  is the slope of the limiting shear stress-pressure relationship.

However, in EHL contact the pressure impulse is around a millisecond. The rheological behaviour may be non-equilibrium. To cope with such a difficult timespan Wikstrom and Hoglund<sup>17)</sup> used a jumping ball method and measured limiting shear stress. Measured  $\gamma$  was on the same order as those by Hoglund and Jacobson<sup>16)</sup> whose range was 0.02-0.15.

Equations (1) and (2) are formulated from different rheological viewpoints, but actual conditions of EHL traction cannot be clearly separated like that. The shear stress-shear rate relationship is divided into four regimes as shown in Fig.2. Namely, A) Newtonian viscous behaviour where the lubricant behaves as a Newtonian liquid and shear stress rises in proportion to shear rate. B) Non-Newtonian (Eyring) viscous behaviour; C) both linear elastic and non-linear viscous behaviour, and D) linear elasticity and a limiting shear stress.



A: Newtonian B: Eyring C: viscoelastic D: elastic-plastic  
 — isothermal      - - - shear heating

Fig.2 Traction curves with different models<sup>2)</sup>

It is not easy to separate the regime IV from the regime III. A similar curve in regime IV can be derived by the visco-elastic model with consideration of thermal effect as mentioned above.

Two types of traction drives are used in industry, one type is to transmit rotation. In this case, contact pressure and speed are not high. The other type of traction drive is used to transmit power with high efficiency, and in this case, contact pressure is usually high and traction regime corresponds to regime IV or III in Fig. 2. Traction drives for automobile application are subjected to very high contact pressure, high speed and high temperature. Traction analysis of such application, therefore, can be treated in two ways as mentioned above.

**3. Traction Measurements since Johnson-Tevaarwerk Analysis**

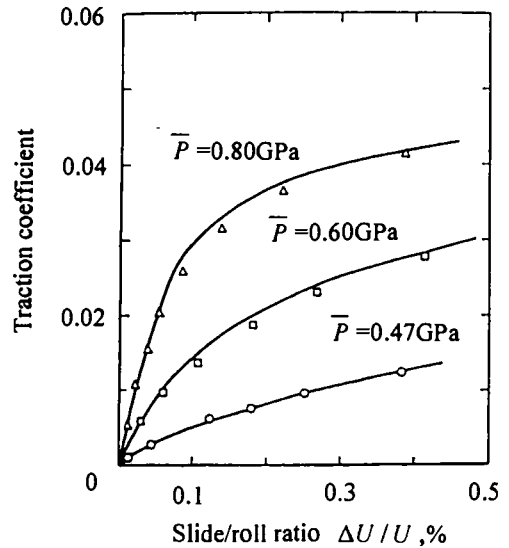
**3.1 Muraki-Kimura's work**

A four-disc machine is capable of obtaining very low slide/roll ratio and is useful for traction research. Muraki and Kimura<sup>18-22)</sup> carried out extensive work on traction and made analytical examination based on Johnson and Tevaarwerk's visco-elastic model with some modifications. Basically their method involves curve fitting, which the authors will use in the analysis of this paper too, in order to derive rheological parameters,  $\bar{\alpha}, G, \tau_0$ , and further temperature rise are considered. They used central film thickness as an average film thickness, considering compressibility of lubricant. An approximate formula is as follows<sup>23)</sup>.

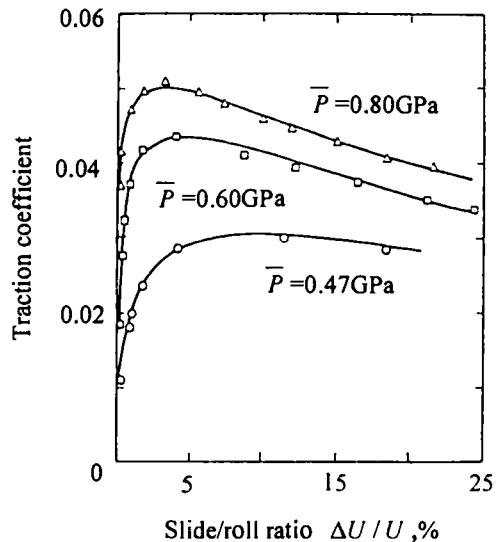
$$h = 1.33 \frac{\rho_0}{\rho_p} h_{\min} \tag{4}$$

where  $h_{\min}$  is derived by Dowson-Higginson's formula.  $\rho_0$  is fluid density at inlet and  $\rho_p$  is the density at max. pressure.

The temperature rise of lubricant only influences the viscosity, namely causes a reduction in viscosity.



a) low slide/roll ratio region



b) high slide/roll ratio region

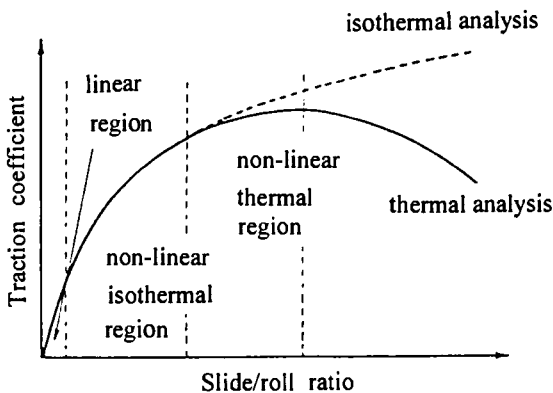


Fig.3 Traction curve and its regime

Fig. 4 Comparison between analysis (Muraki-Kimura) and Measurement (Johnson-Cameron)

The reduction of the lubricant viscosity induces a reduction of traction in the region of high slide/roll ratio as shown in Fig. 3. Their prediction agreed well with existing traction curves and their own traction curves. Comparisons with Johnson and Cameron<sup>24)</sup> are shown in Fig. 4.

Fig. 4 a) shows the results for the low slide/roll ratio region and b) shows the results for the high slide/roll ratio region where the effect of temperature rise is significant. Their predictions correspond well with experimental tractions, though some physical properties had to be assumed.

As Fig. 4 indicates, traction can be expressed by visco-elastic properties of lubricant only with the consideration of temperature rise. They also found the calculated  $\bar{\alpha}$ , pressure-viscosity coefficient of lubricant, corresponded well with those obtained by independent measurements.

They also proposed a simplified formula to predict maximum traction coefficient with sufficient precision as shown in equation (5).

$$\mu_{max} = \frac{\bar{P}}{\bar{P} + 13.3\tau_0} \left( \bar{\alpha}\tau_0 + \frac{\tau_0}{\bar{P}} \ln \frac{26.7\eta_{N0}}{\beta\zeta\tau_0 h\bar{P}} \right) \quad (5)$$

For the definition of the symbols, the original paper should be consulted.

**3.2 Kato et al's work**

Interest in traction has been shown by the researchers of gears, as the ultimate gear with an infinite number of gear teeth. M. Kato et al have carried out extensive experimental and analytical work on traction<sup>24)</sup>. They have examined the effect of spin and skew and the effect of skew was found to be more significant.

As a model of traction, they used the limiting shear stress model by Bair and Winer. Their main interest is the maximum traction coefficient which is controlled by limiting shear stress. The most interesting feature of their experimental results is the relationship between contact pressure and maximum traction coefficient. They measured traction with traction oils, Santotrac oil and specially formulated traction oils, for a wide range of contact pressures, with different disc curvature but with a constant load, thus eliminating the effect of temperature rise. They also used ceramic discs in addition to steel discs.

Typical results are shown in Fig. 5. In the region of low contact pressure, max. traction coefficient increases with increasing pressure as revealed by

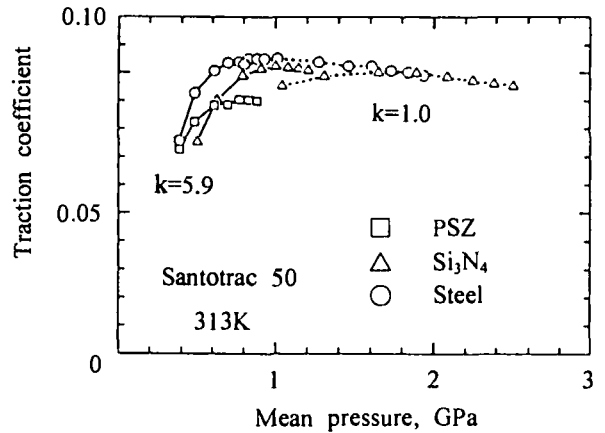


Fig.5 Maximum traction coeff. vs mean pressure

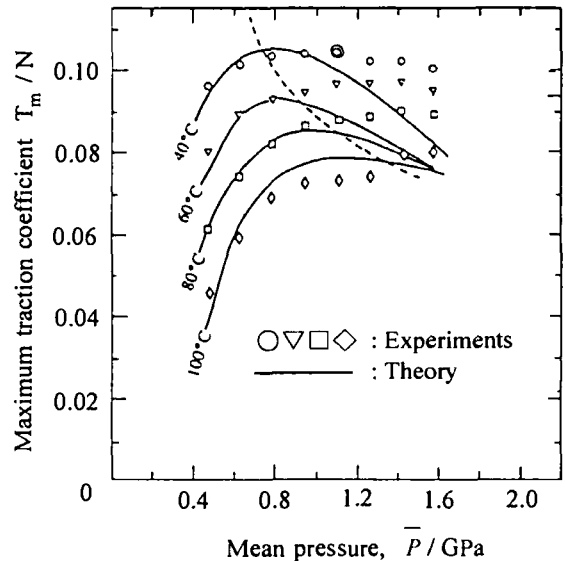


Fig. 6 Maximum shear stress for Santotrac 50<sup>3)</sup>

many experiments by other researchers. But max. traction soon reaches maximum value around at 1GPa and ends to decrease with increasing pressure. However, they regard the max. traction coefficient as a constant above the threshold pressure in their later analysis.

Kato et al's results are compared with Evans and Johnson's results<sup>2)</sup>. Evans and Johnson predicted a more drastic decrease in the maximum traction coefficient for Santotrac 50 as shown in Fig. 6. Measured traction coefficient, in fact, did decrease a little for low temperature condition but still increased with increasing pressure for over 60 degC.

Evans and Johnson proposed a simplified equation for maximum traction coefficient [see equation (6)].

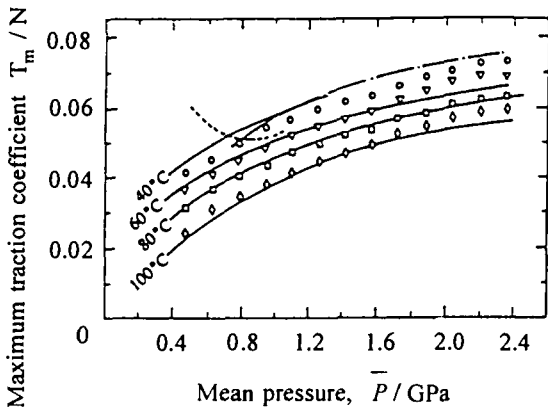


Fig.7 Maximum traction coefficient for HVI650<sup>31</sup>

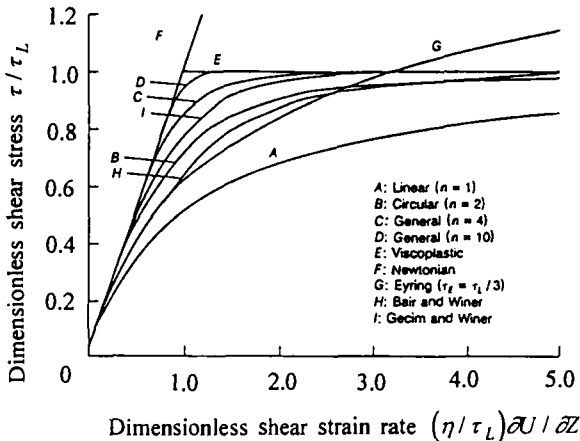


Fig.8 Rheological & mathematical models <sup>25)</sup>

$$\mu_{max} \cong 0.87 \bar{\alpha} \tau_0 + 1.74 \frac{\tau_0}{\bar{p}} \ln \left\{ \frac{12}{\tau_0 h} \left( \frac{2K\eta_0}{1+9.6\zeta} \right)^{1/2} \right\} \quad (6)$$

Though equation (6) predicts a drastic reduction in traction with increasing pressure for Santotrac 50, the equation still predicts a further increase for a mineral oil HVI 650 and corresponds well to measured values as shown in Fig. 7. Kato et al's results may be specific to traction oils.

**3.3 Prediction of traction curve**

Though the visco-elastic model and the limiting shear stress model are related to lubricant rheology, there is another way to express traction curve which may be convenient for design calculations. Hamrock <sup>25)</sup> proposed the following equation.

$$\dot{\gamma} = (\tau / \eta) \left[ 1 - (\tau / \tau_L)^n \right]^{-1/n} \quad (7)$$

When n=1.8, equation(7) becomes Bair-Winer model, Gecim-Winer model <sup>26)</sup> for n=2.8 and Hamrock's circular model for n=2. Basically the curves are based on the limiting shear stress model.

**4.Traction measurement at high pressure and high speed, and its analysis <sup>1),27),28)</sup>**

**4.1 Experimental results**

A four-disc machine is capable of being set precisely at a very small slide/roll ratio and is a very useful device to investigate traction properties under conditions such as low slip. However, the condition is limited to no-spin contact. A two-disc machine can be used to measure traction for the case of contact with spin, which is common in an actual CVT. In Fig. 9, the structure of a four-disc machine is shown. Central disc and outer discs are driven independently.

In the case of traction drive applied to CVTs for automobiles, operating conditions are often very severe. Namely, maximum contact pressure is very high at 3 GPa or higher, rolling speed exceeds over 30 m/s and lubricant temperature goes up over 120 deg C. Furthermore, only traction oils can be used in such CVT since high traction is essential. CVTs for automobiles were discussed at Leeds several years ago <sup>29)</sup> and the recent situation is summarized<sup>30)</sup> elsewhere.

To cope with such required conditions, a specially designed four-disc machine and a two-disc machine were built and traction measurement was carried out. Considering automotive CVT, test conditions were

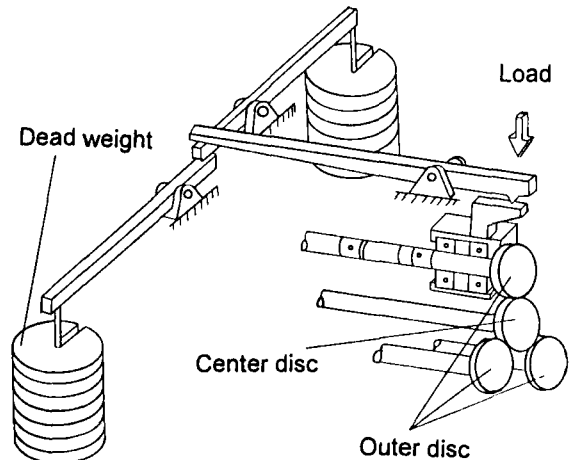


Fig.9 Schematic diagram of a four disc machine

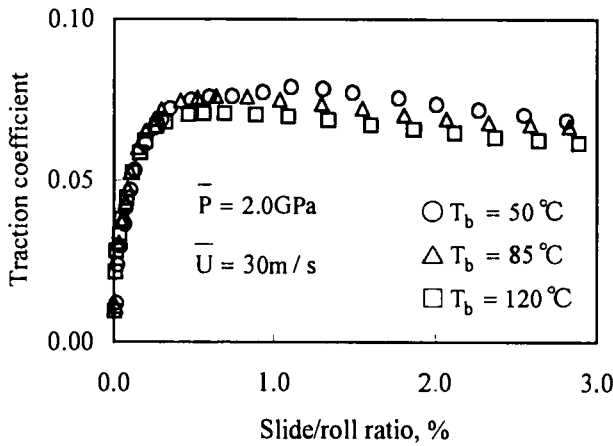


Fig.10 Effect of lubricant temperature on traction curve

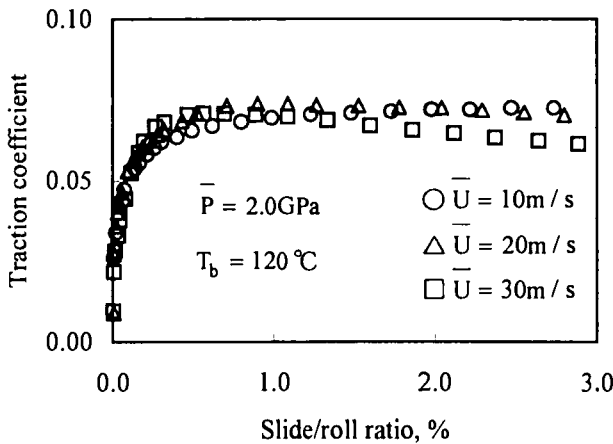


Fig. 11 Effect of rolling speed on traction curve

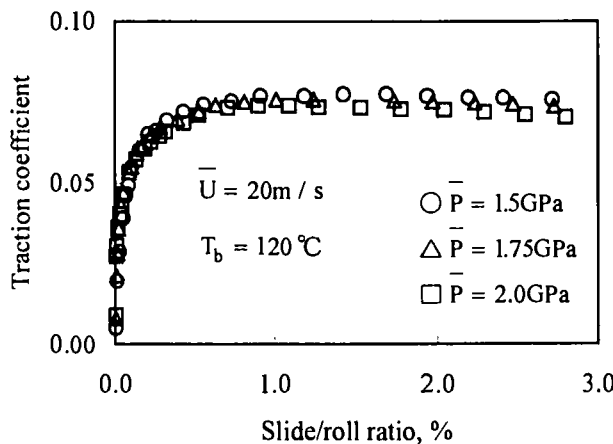


Fig.12 Effect of contact pressure on traction curve

fixed as follows: the highest mean Hertzian pressure 2.0 GPa (maximum pressure 3 GPa), the highest rolling speed 30 m/s, the highest temperature 140

degC. Traction oils used in this study were specially formulated by Idemitsu Kosan Co. Ltd. and Santotrac 50. The former's traction characteristics are similar to Santotrac 50, but it has a higher traction coefficient at high temperature over 100 deg C. Also, its pressure coefficient of viscosity is similar to that of Santotrac 50. Therefore, the measured traction data can be related to the results obtained with Santotrac 50 by other researchers.

Examples of test results are presented. The effect of lubricant temperature is shown in Fig. 10, the effect of rolling speed in Fig 11, and the effect of contact pressure in Fig. 12. As expected, temperature affects Maximum traction coefficient ( $\mu_{max}$ ) considerably. Even at 120 degC  $\mu_{max}$  is goes up to over 0.07. Traction curves are almost identical regardless of speed. In high slide/roll ratio region, higher speed and higher temperature reduce the traction force.

$\mu_{max}$  decreases with increase in contact pressure at such high pressure, though the degree is not big. A similar tendency was observed by Kato et al under a lower speed condition as shown in Fig.5. But previous experiments had always shown increase in traction coefficient with increasing pressure. It should be noted, however, traction force still increases with increase of pressure (load).

4.2 Analysis of Rheological Parameters

Experimental results were compared with the rheological traction models. To evaluate rheological properties alone the lateral elastic deformation of the discs was adjusted. Figs. 10 to 12 are the adjusted curves.

There are two aspects in the design of CVT: one is the maximum traction coefficient which determines the transmittable power, and the other is the traction property in the small slide/roll ratio, which is related to efficiency of CVT, or loss of speed, loss of torque, loss of power. The former simply depends on the development of traction oils with high traction coefficient. The efficiency varies not only with the lubricant but also with the shape of contacts and material too.

Therefore, description of this region in mathematical terms is an essential step for optimum design. The Bair-Winer model and the Johnson-Tevaarwerk model are the models under consideration. The most probable rheological values were chosen to fit the traction curve in the small



slide/roll ratio region.

1) elastic model

In this case, the only parameter is the shear modulus G.

$$\dot{\gamma} = \frac{1}{G} \dot{\tau} \tag{8}$$

G is actually derived from equation (9).

$$G = \frac{n \cdot \bar{U} \cdot h_{cen}}{b} \tag{9}$$

here, n: slope of traction curve, h<sub>cen</sub>: central film thickness, b: semi-width of Hertzian contact. To calculate the film thickness, the inlet-shear heating was considered, but the compressibility of lubricant was not.

2) non-linear viscous model

Rheological parameters are  $\bar{\alpha}$  and reference stress or Eyring stress  $\tau_0$ . Curve was fitted to the Eyring equation.

$$\dot{\gamma} = \frac{\tau_0}{\eta_N} \sinh \frac{\tau}{\tau_0} \tag{10}$$

and

$$\eta_N = \eta_0 \cdot \exp(\bar{\alpha} \cdot p) \tag{11}$$

$\tau_0$  is assumed to satisfy equation (12) and  $\tau_{00}$  and m are derived.

$$\tau_0 = \tau_{00} + m \cdot p \tag{12}$$

As is usual in traction calculations, mean Hertzian pressure and parallel film were assumed.

Fig.13 shows the comparison between the aforementioned models and measured traction. The visco-elastic model exhibits better curve-fitting for a wider range of slide/roll ratios, as expected, than the

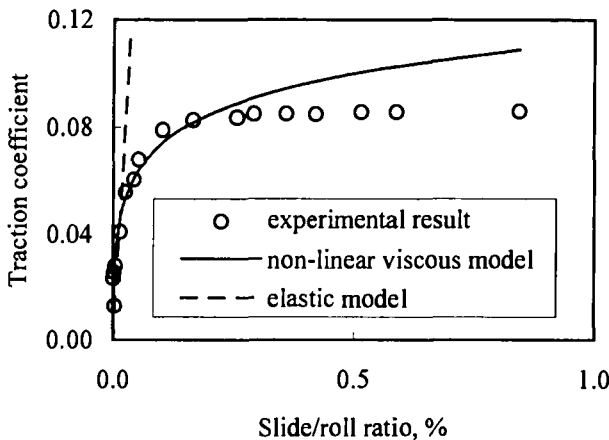


Fig.13 Comparison of models and measured traction

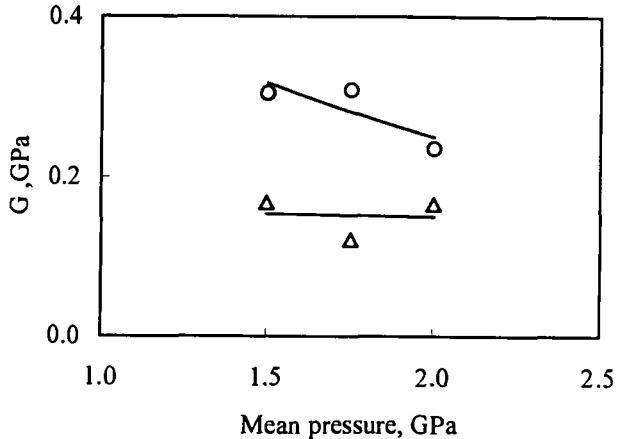


Fig. 14 Shear modulus G to contact pressure

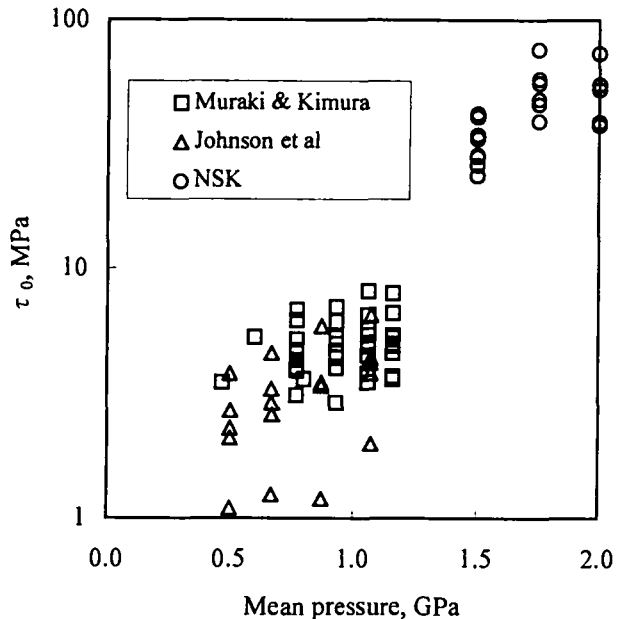


Fig. 15 Comparison of Eyring stress

derived parameters for both models.

Fig.14 shows the derived shear modulus of lubricant G. G depends on contact pressure and increases with increasing pressure, but the obtained G value is independent of contact pressure, or shows some decrease. Also G is very small when compared with those derived from traction curves for low and medium pressure. Moore mentioned that the G obtained are always much lower than those indicated by independent forms of measurement<sup>7)</sup>. As an example the values in Fig.14 are too small when the limiting shear stress ( $\tau_L$ ) is calculated from the

relationship of equation (13).

$$\tau_L = G/30 \tag{13}$$

When G is derived from a traction curve, then G should be around 5 GPa. The difference is nearly order of magnitude.

Then Eyring model was applied to the measured traction curves, and Eyring stress ( $\tau_0$ ) and pressure coefficient of viscosity ( $\bar{\alpha}$ ) were derived. Present data were compared with the results obtained by others with Santotrac oil and other oils as shown in Fig.15. The comparison shows considerable discrepancies from those reported so far.

As may be clearly seen from Fig. 14,  $\tau_0$  of present analysis is very large and much higher than the extrapolated values from the previous data.

$\bar{\alpha}$  was said to correspond well to the  $\alpha$  when measured under static condition.  $\alpha$  was measured with present traction oils by means of falling ball method<sup>1)</sup> but over 1 GPa the ball did not fall, and there was a glass transition, even at the temperature of 120 deg C. Test pressure of 2 GPa (or maximum pressure 3 GPa) is much higher than glass transition pressure and a large difference between  $\alpha$  and  $\bar{\alpha}$  was expected. The obtained  $\bar{\alpha}$  was almost 1/3 of  $\alpha$ .

**5. Rheological properties in traction**

Ohno et al<sup>31)</sup> measured fluid compressibility up to 1.5 GPa and found the discrepancy from the relationship Dowson et al used<sup>32)</sup> for their EHL calculation, as shown in equation (14).

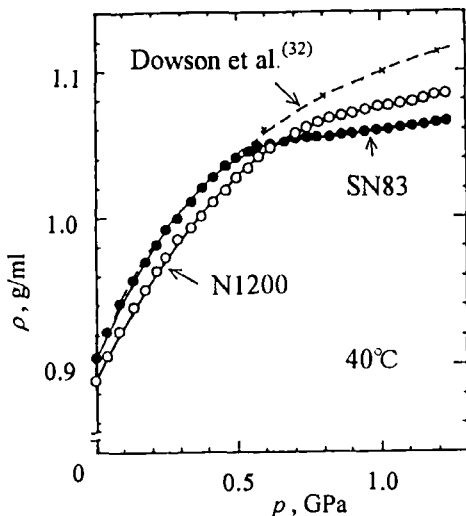


Fig. 16 Change of density with pressure

$$\frac{\rho}{\rho_0} = 1 + \frac{0.58p}{1+1.68p} \tag{14}$$

where  $p$  : GPa. The result is shown in Fig. 16. From the density curve, they derived the bulk modulus.

When the bulk modulus was correlated with  $\alpha p$ , each oil showed a similar tendency as shown in Fig.17<sup>33)</sup>. The curves are divided into three sections, namely, for  $\alpha p > 25$  fluid is an elastic-plastic solid, for  $25 > \alpha p > 13$  fluid is a visco-elastic solid and for  $13 > \alpha p$  fluid is a liquid. They also found a good correlation between “plateau” K (over  $\alpha p$  25) and maximum traction coefficient<sup>32)</sup>.

Evans and Johnson’s traction map for Santotrac 50 is shown in Fig.18<sup>3)</sup>. The boundary of the elastic-plastic regime is around  $\alpha p = 25$  and corresponds well to Ohno et al’s results. But for mineral oil HVI650, the boundary is different.

The conditions of the authors’ traction experiments are plotted in Fig. 18. When  $\alpha$  is used, it refers to conditions relating to the elastic-plastic regime, on the other hand, when  $\bar{\alpha}$  is used, it refers to conditions relating to the Eyring regime.

**6. Proposals and Conclusion**

The findings in the final part of the last section was the starting point of the author’s analysis. The authors are prepared to accept either model if it fits to the measured traction curves reasonably well but as

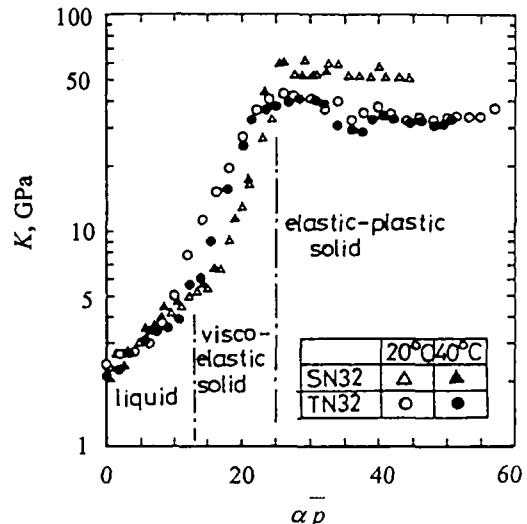


Fig 17 Relationship between bulk modulus and  $\alpha p$

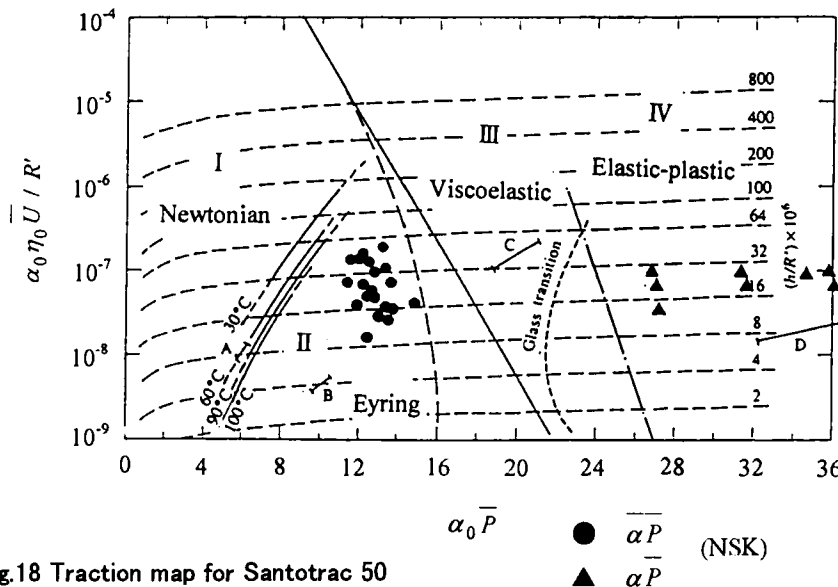


Fig.18 Traction map for Santotrac 50

mentioned above the derived values were rather contradictory. The analysis was limited to the small slide/roll ratio region, because we are interested in this region to examine the efficiency of CVT. But, at the same time, the derived  $\bar{\alpha}$  (or viscosity  $\eta_N$ ) was too small to obtain relevant results from thermal analysis.

Much traction research has been done with mineral oils and di-ester oils, but for actual CVT only traction oils are used and they are still under development. The difference between the authors' results and previous results may be induced by the difference in lubricant or by the substantial difference in experimental conditions.

Traction is usually analyzed with mean pressure and parallel film. However, at high pressure the difference between maximum pressure and mean pressure exceeds 1GPa. In such a situation, the assumption of average pressure may not be valid. Particularly, when spin and solidification are concerned, higher spin occurs in the region of low pressure, where the lubricant may still be a liquid. Analysis of spin was more easily handled with the visco-elastic model.

This may indicate what is required of future traction research as the next stage on the path toward a new traction theory.

For designers and engineers, who are actively working to develop practical CVT, an approximate equation might be sufficient. Having said that, the

development of CVT is under way and even though it is approaching a final stage, we believe that it is still premature to offer an approximate equation, since further fundamental research is still needed to clarify certain aspects of the traction mechanism.

#### REFERENCES

- 1) Achiha, H., Natsumeda, S., Nakamura, Y. and Fujishiro, I. "Traction Characteristics under High Contact Pressure, High Rolling Speed and High Temperature", Proc. ITC Yokohama, 1995 (JAST) to be published.
- 2) Evans, C.R. and Johnson, K.L., "The Rheological Properties of Elastohydrodynamic Lubricants", Proc. IME, Vol.200, C5 (1986) 303-312
- 3) Evans, C.R. and Johnson, K.L., "Regimes of Traction in Elastohydrodynamic Lubrication", Proc. IME, Vol.200, C5 (1986) 313-324.
- 4) Crook, A.W., "The Lubrication of Roller, Part III. A Theoretical Discussion of Friction and the Temperatures in the Oil Film", Phil. Trans. Roy. Soc. Lond., Ser A, Vol.254 (1961) 237-258.
- 5) Hirst, W. and Moore, A.J., "Non-Newtonian behaviour in Elasto-hydrodynamic Lubrication", Proc. Roy. Soc. Lond., Ser A, Vol.337 (1974) 101-121.
- 6) Eyring, H., "Viscosity, Plasticity and Diffusion as Examples of Reaction Rates", J. Chem. Phys., Vol.4 (1936) 283.
- 7) Moore, A.J., "The Behaviour of Lubricants in Elasto-hydrodynamic Contacts", An Invited Lecture at the Annual House Meeting of the IME Tribology Group, (1995-12).
- 8) Johnson, K.L. and Tevaarwerk, J.L., "Shear Behaviour Ser A, Vol.356 (1977) 215-236.

Relaxation in Liquid Mixture”, Proc. Roy. Soc. Lond., Ser. A, Vol.309 (1969) 473-496.

10) Bair, S. and Winer, W.O., “Some Observations on the Relationship Between Lubricated Mechanical and Dielectric Transitions Under Pressure”, Trans. ASME, JoLT, Vol.102 (1980) 229-234.

11) Bair, S. and Winer, W.O., “Shear Strength Measurements of Lubricants at High Pressure”, Trans. ASME, JoLT, Vol.101 (1979) 251-257.

12) Bair, S. and Winer, W.O., “Some Observations in High Pressure Rheology of Lubricants”, Trans. ASME, JoLT, Vol.104 (1982) 357-364.

13) Bair, S., “Recent Developments in High-Pressure Rheology of Lubricants”, Proc. 21st Leeds-Lyon Symp. (1994) 169-187.

14) Bair, S. and Winer, W.O., “The High Pressure High Shear Stress Rheology of Liquid Lubricants”, Trans. ASME, JoT, Vol.114 (1992) 1-13.

15) Bair, S. Winer, W.O. and Distin, K.W., “Experimental Investigation into Shear Localization in an Operating EHD Contact”, Proc. 19th Leeds-Lyon Symp., (1993) 383-388.

16) Hoglund, E. and Jacobson, B., “Experimental Investigation of the Shear Strength of Lubricants Subjected to High Pressure and Temperature”, Trans. ASME, JoT, Vol.108 (1986) 571-578.

17) Wilkstrom, V. and Hoglund, E., “Investigation of Parameters Affecting the Limiting Shear Stress-Pressure Coefficient: A New Model Incorporating Temperature”, Trans. ASME, JoT, Vol. 116 (1994) 612-620.

18) Muraki, M. and Kimura, Y., “Traction Characteristics of Lubricating Oils: 1st Report (Transition from Full to Partial EHL)”, J. of JSLE, Vol.28 (1983) 67-74. (in Japanese)

19) Muraki, M. and Kimura, Y., “Traction Characteristics of Lubricating Oils: 2nd Report (A Simplified Thermal Theory of Traction with a Nonlinear Viscoelastic Model)”, J. of JSLE, Vol.28 (1983) 753-760. (in Japanese)

20) Muraki, M. and Kimura, Y., “Traction Characteristics of Lubricating Oils: 3rd Report (Application and Verification of the Thermal Theory)”, J. of JSLE, Vol.29 (1984) 216-223. (in Japanese)

21) Muraki, M. and Kimura, Y., “Traction Characteristics of Lubricating Oils: 4th Report (Transition Characteristics of Mineral Base Oils)”, J. of JSLE, Vol.30 (1985) 45-52. (in Japanese)

22) Muraki, M. and Kimura, Y., “Traction Characteristics of Lubricating Oils: 5th Report (Transition Characteristics of Synthetic Hydrocarbon Oils)”, J. of JSLE, Vol.30 (1985) 767-774. (in Japanese)

English Version of refs 18) to 22) can be found in J. JSLE International Edition: formerly JSLE, now JAST

23) Hirst, W and Moore, A.J., “Elastohydrodynamic Lubrication at High Pressures”, Proc. Roy. Soc. Lond., Ser. A, Vol.360 (1978) 403-425.

24) Kato, K., Iwasaki, T., Kato, M and Inoue, K., “Evaluation of Limiting Shear Stress of Lubricants by Roller Test”, JSME Intl. J., Ser C, Vol.36 (1993) 515-522.

A series of traction works have been published in Japanese, in Proc. JSME.

25) Hamrock, B.J., “Fundamentals of Fluid Film Lubrication”, McGraw Hill (1994) p614.

26) Gecim, B. and Winer, W.O., “Lubricant Limiting Shear Stress Effect on EHD Film Thickness”, Trans. ASME, JoLT, Vol.102 (1980) 213-220,

27) Achiha, H., Natsumeda, S, and Aihara, S, “Evaluation of Traction Characteristics at High Pressure and High Speed”, Preprints of Tribology Conference, JAST 96-Autumn, (1996) to be published.

28) Achiha, H., Natsumeda, S, and Aihara, S, “Traction Characteristics of Traction Oils at High Hertzian Pressure”, Trans. ASME (To be submitted).

29) Machida, H. and Aihara, S., “State of the Art of the Traction Drive CVT Applied to Automobiles” Proc. 17th Leeds-Lyon Symp. (1990) 267-275.

30) Imanishi, T., Machida, H. and Tanaka, H., “Life, Efficiency and Design of Large Capacity Half Toroidal CVT for Passenger Car”, Proc. FISITA '96 (Prague) P1638.

31) Ohno, N., Kuwano, N. and Hirano, F., “Effect of Bulk Modulus of Solidified Oils under High Pressure on Traction Behaviour”, J. JAST (Tribologist), Vol. 38 (1993) 927-934. <In Japanese>

English Version of ref 31) can be found in J. JAST International Edition: formerly JSLE, now JAST

32) Dowson, D. Higginson, G.R. and Whitaker, A.V., “Elasto-hydrodynamic Lubrication-a survey of isothermal solutions”, JMES, Vol.4 (1962) 121.

33) Ohno, N., Kuwano, N. and Hirano, F., “Bulk Modulus of Solidified Oil at High Pressure as Predominant Factor Affecting Life of Thrust Bearings”, Tribology Trans., Vol. 38 (1995) 285-292.

## The effect of spin motion upon elastohydrodynamic elliptical contacts

M. Taniguchi <sup>a</sup>, D. Dowson <sup>b</sup> and C. M. Taylor <sup>b</sup>

<sup>a</sup>Research and Development Centre, NSK Ltd.,  
1-5-50 Kugenuma-Shinmei, Fujisawa, Kanagawa 251, Japan

<sup>b</sup>Department of Mechanical Engineering, The University of Leeds,  
Leeds LS2 9JT, United Kingdom

In some highly stressed, lubricated machine elements like toroidal-type continuously variable transmissions (CVTs) and angular contact ball bearings, the elastohydrodynamic conjunctions experience some spin as well as rolling motion. In this study, isothermal elliptical elastohydrodynamic lubrication (EHL) problems have been solved numerically with various spin angular velocities incorporated with rolling motion, for a Newtonian lubricant, assuming smooth surfaces on the pair of contacting bodies. A computational programme was developed to solve the elliptical EHL problem with spin motion by using the forward-inverse combined technique.

### 1. INTRODUCTION

#### 1.1. Elliptical EHL problems with spin

Heavily-loaded lubricated contacts in machine elements, such as rolling bearings and gears, have been analysed using elastohydrodynamic lubrication (EHL) theory. The high pressure of the lubricant film, which supports the load, causes elastic deformation of the contacting surfaces. It also gives rise to an enhancement of the viscosity of the lubricant. The relation between the thickness and the pressure of the lubricant film is governed by the Reynolds equation. In 1959, Dowson and Higginson [1] presented a fully comprehensive numerical solution to a line contact lubrication problem. The Reynolds equation for the hydrodynamics and the elasticity equation for deformation were satisfied simultaneously.

Since then, strongly supported by the development of computing facilities, extensive numerical analyses of EHL have been carried out [2–5]. The studies have ranged from line contact problems to point contact problems. Solutions have been obtained for high pressure up to a few GPa, this being representative of the real contact in rolling bearings and between gear teeth.

Apart from a simple rolling contact, a spin motion at the contact gives a kinematic variation to the EHL problems. In some machine elements, the spin motion plays a significant role in lubricated contacts. The spin motion in an angular contact ball bearing, at each contact between a ball and the outer or inner race, was well described in [6].

A continuously variable transmission (CVT) with rolling elements is another application in which the spin motion has often been discussed. For example, Figure 1 shows the schematic geometry of a half toroidal CVT. The power is transmitted from the input disk to the output disk via a pair of power rollers. At the contacts ( $O$  and  $O'$ ) between the power roller and disks, an EHL film is produced by the rolling motion, and in fact, the power is transmitted by the shear action of the lubricant film, so called traction drive. A few percent of sliding is essential to yield a sufficient shear stress at the contact, as suggested in [7]. The geometry of the half toroidal CVT also gives a spin motion to the contacts.

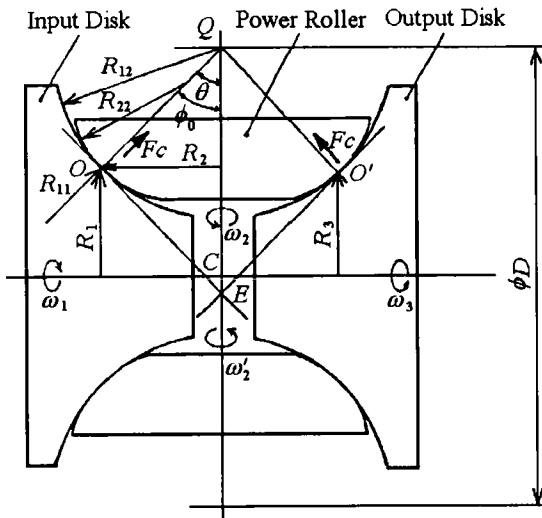


Figure 1 Geometry of half toroidal CVT [7]

The half toroidal CVT is being developed as an automatic transmission for automobiles. A range of successful applications has been reported [8–11].

A few contributions have been made to investigate spin motion in lubricated contacts, with or without a rolling motion. Mostofi and Gohar [12] solved the point contact EHL problems with and without spin by a straightforward relaxation technique. All conditions were chosen to match an interferometry experiment. Problems with quite high spin and very low rolling speed could be solved.

Xu's study [13], a part of which was published separately in [14], was another work which focussed on spin motion in a contact. After examining cavitation in the contact with pure spin motion and the pure spin problem, an isothermal elliptical contact problem with spin and rolling was solved by the Gauss-Seidel iterative method.

In this study, the problem of isothermal, elliptical EHL contacts with smooth surfaces and kinematic conditions including spin motion was investigated numerically.

## 1.2. Notation

- $a$  semi-major axis of Hertzian contact ellipse  
 $B$  spin to roll ratio,  $2\Omega/U$   
 $b$  semi-minor axis of Hertzian contact ellipse

- $C_{sp}$  coefficient of minimum film reduction  
 $E'$  equivalent elastic modulus  
 $F_c$  normal load  
 $G$  non-dimensional materials parameter,  $\alpha E'$   
 $H$  non-dimensional film thickness,  $h/R_x$   
 $h$  film thickness  
 $h_0$  nominal distance of two bodies  
 $h_{cenHD}$  central film thickness prediction by Hamrock and Dowson [2]  
 $h_{minHD}$  minimum film thickness prediction by Hamrock and Dowson [2]  
 $h_{minN}$  minimum film thickness prediction from present study  
 $k$  ellipticity ratio of the contact,  $a/b$   
 $P$  non-dimensional pressure,  $p/E'$   
 $p$  pressure in lubricant film (gauge pressure)  
 $p_{iv,as}$  asymptotic isoviscous pressure  
 $p_{maxHz}$  maximum Hertzian pressure  
 $R_x, R_y$  principal radii of curvature of equivalent ellipsoid  
 $s(x,y)$  separation between two bodies  
 $U$  non-dimensional speed parameter,  $\eta_0 u_0/E'R_x$   
 $u$  mean velocity component in the  $x$  direction  
 $v$  mean velocity component in the  $y$  direction  
 $W$  non-dimensional load parameter,  $F_c/E'R_x^2$   
 $w(x,y)$  elastic deformation  
 $X$  non-dimensional Cartesian coordinate,  $x/b$   
 $x$  Cartesian coordinate (rolling direction, minor axis of contact ellipse)  
 $Y$  non-dimensional Cartesian coordinate,  $y/a$   
 $y$  Cartesian coordinate  
 $\alpha$   $1/p_{iv,as}$   
 $\gamma$  relaxation factor for SOR method  
 $\eta$  viscosity  
 $\bar{\eta}$   $\eta/\eta_0$   
 $\eta_0$  viscosity at atmospheric pressure  
 $\rho$  fluid density  
 $\bar{\rho}$   $\rho/\rho_0$   
 $\rho_0$  fluid density at atmospheric pressure  
 $\Omega$  non-dimensional spin angular velocity,  $\omega\eta_0/E'$   
 $\omega$  (mean) angular velocity of spin

## 2. GOVERNING EQUATIONS

### 2.1. Geometry

The contact between an equivalent ellipsoid and a plane shown in Figure 2 was studied, where the equivalent ellipsoid has a pair of principal radii of curvature ( $R_x, R_y$ ).

Both surfaces were assumed to be smooth, so that the effect of surface asperities was neglected.

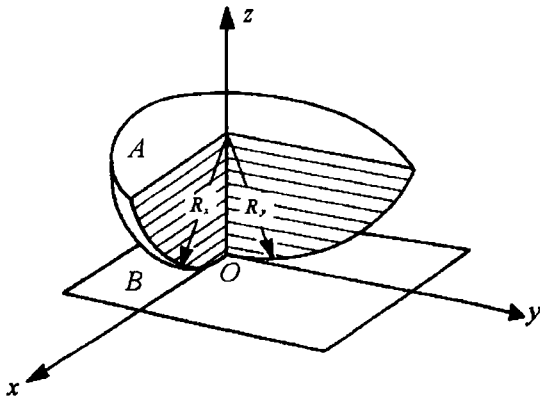


Figure 2 Equivalent geometry [3]

The separation in the  $z$  direction between two rigid bodies which contact at the origin  $O$  can be expressed, with paraboloidal approximation, as;

$$s(x,y) = \frac{x^2}{2R_x} + \frac{y^2}{2R_y} \tag{1}$$

Many machine elements, such as a ball bearing, have elastic contacts in which the direction of rolling or sliding motion coincides with the minor axis ( $b$ ) of the Hertzian ellipse. Thus, hereafter, the  $x$ -axis is chosen to be in this direction.

2.2. Elastic deformation

The pressure of the lubricant film becomes extremely high, such that local elastic deformation results. The elastic deformation ( $w$ ) of a semi-infinite body by a distributed pressure is expressed as follows;

$$w(x,y) = \frac{2}{\pi E'} \iint \frac{p(x_1,y_1)}{\sqrt{(x-x_1)^2 + (y-y_1)^2}} dx_1 dy_1 \tag{2}$$

In this study, the nine-point bi-quadratic approximation developed by Lin and Chu [15] was used to calculate the elastic deformation at each nodal point on the mesh appropriated

for numerical analysis.

In EHL problems, two elastic bodies are separated by a lubricant film. The normal load applied to the contact is supported by the EHL film. The double integration of the lubricant film pressure ( $p(x,y)$ ) will be equal to the applied load ( $F_c$ ).

$$F_c = \iint p(x,y) dx dy \tag{3}$$

2.3. Film thickness

The film thickness in an EHL contact can be written as;

$$h(x,y) = h_0 + s(x,y) + w(x,y) \tag{4}$$

where  $h_0$  represents the nominal distance of a rigid ellipsoid and a plane on the  $z$ -axis. In EHL problems the value of  $h_0$  is generally negative, due to the large elastic deformation compared with the film thickness.

2.4. Kinematics

Once a spin motion exists on the contact surface, the velocity distribution is a function of the position in the field.

Suppose that an ellipsoid  $A$  and a plane  $B$  come into contact as shown in Figure 3. There is a rolling/sliding motion in the  $x$  direction, but none in the  $y$  direction (no side slip). Spin motion exists as well. The motion of the contacting surfaces is defined as shown in Figure 3, i.e., on body  $A$  and  $B$  respectively;

1. The velocities of the surfaces parallel to the axis are  $u_{0A}$  and  $u_{0B}$  in the  $x$  direction and zero in the  $y$  direction.
2. The angular velocities of the spin motion are  $\omega_A$  and  $\omega_B$ .

Counterclockwise spin motion is determined to have a positive value of  $\omega$ , from a view point of  $z = +\infty$ . The mean velocities can be defined as follows;

$$u_0 = \frac{u_{0A} + u_{0B}}{2} \tag{5}$$

$$\omega = \frac{\omega_A + \omega_B}{2} \tag{6}$$

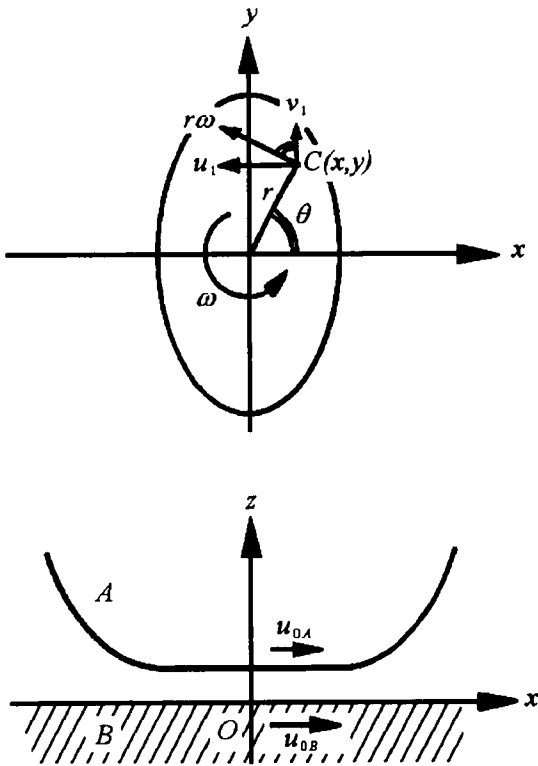


Figure 3 Motion of surfaces

At a point  $C(x,y)$ , the spin motion gives rise to velocity components in the  $x$  and  $y$  directions. These are, on the surface of body  $A$ ;

$$u_{1A} = -r\omega_A \sin\theta = -y\omega_A$$

$$v_{1A} = r\omega_A \cos\theta = x\omega_A$$

and for body  $B$ ;

$$u_{1B} = -y\omega_B$$

$$v_{1B} = x\omega_B$$

To combine the translation and spin gives the total expression for velocities at a point  $C(x,y)$ .

$$u_A = u_{0A} + u_{1A} = u_{0A} - y\omega_A \tag{7}$$

$$u_B = u_{0B} + u_{1B} = u_{0B} - y\omega_B \tag{8}$$

$$v_A = v_{1A} = x\omega_A \tag{9}$$

$$v_B = v_{1B} = x\omega_B \tag{10}$$

Now, the mean velocities between the two surfaces at point  $C$  are, in the  $x$  and  $y$  directions respectively;

$$u = \frac{u_A + u_B}{2} = u_0 - y\omega \tag{11}$$

$$v = \frac{v_A + v_B}{2} = x\omega \tag{12}$$

### 2.5. Reynolds equation

Assuming a Newtonian lubricant, the two dimensional Reynolds equation (in pressure) can be written as;

$$\frac{\partial}{\partial x} \left[ \frac{\rho h^3}{12\eta} \cdot \frac{\partial p}{\partial x} \right] + \frac{\partial}{\partial y} \left[ \frac{\rho h^3}{12\eta} \cdot \frac{\partial p}{\partial y} \right] = \frac{\partial}{\partial x} (\rho u h) + \frac{\partial}{\partial y} (\rho v h) \tag{13}$$

Substitution of equations (11) and (12) into equation (13) gives the Reynolds equation for a rolling/sliding motion coupled with spin.

$$\frac{\partial}{\partial x} \left[ \frac{\rho h^3}{12\eta} \cdot \frac{\partial p}{\partial x} \right] + \frac{\partial}{\partial y} \left[ \frac{\rho h^3}{12\eta} \cdot \frac{\partial p}{\partial y} \right] = \frac{\partial}{\partial x} [\rho(u_0 - y\omega)h] + \frac{\partial}{\partial y} (\rho x\omega h) \tag{14}$$

### 2.6. Lubricant properties

The Roelands formula for the pressure-viscosity relationship can cover a wide range of pressure [16]. That is, for the isothermal condition;

$$\eta = \eta_0 \exp \{ \{ \ln(\eta_0) + 9.67 \} \times \{ -1 + (1 + 5.1 \times 10^{-9} p)^2 \} \} \tag{15}$$

where the dynamic viscosity ( $\eta$ ) and the viscosity at ambient pressure ( $\eta_0$ ) are in [Pas]. Pressure ( $p$ ) is in [Pa]. The Roelands parameter ( $Z$ ) is considered to be constant at any pressure.

Compressibility of the lubricant was taken into account by using the following expression for the variation of density with pressure,



after Dowson and Higginson [17];

$$\rho = \rho_0 \left( 1 + \frac{0.58 \times 10^{-9} p}{1 + 1.68 \times 10^{-9} p} \right) \quad (16)$$

where pressure ( $p$ ) is in [Pa].

### 3. NUMERICAL ANALYSIS

#### 3.1. Non-dimensional Reynolds equation

For convenience, EHL problems have often been solved by numerical procedures in terms of non-dimensional parameters. The Reynolds equation (equation (14)) can be normalised and written as;

$$\begin{aligned} & \frac{\partial}{\partial X} \left[ \frac{\bar{\rho} H^3}{12 \bar{\eta}} \cdot \frac{\partial \mathcal{P}}{\partial X} \right] + \frac{1}{k^2} \frac{\partial}{\partial Y} \left[ \frac{\bar{\rho} H^3}{12 \bar{\eta}} \cdot \frac{\partial \mathcal{P}}{\partial Y} \right] \\ & = \frac{b}{R_x} \left( U - \frac{a\Omega}{R_x} Y \right) \frac{\partial}{\partial X} [\bar{\rho} H] + \frac{b^2 \Omega}{k R_x^2} X \frac{\partial}{\partial Y} [\bar{\rho} H] \end{aligned} \quad (17)$$

For the details of the non-dimensional parameters, see notation.

#### 3.2. A forward-inverse combined technique

The Reynolds equation for an EHL problem has widely been solved by the forward iterative method. The pressure distribution can be numerically determined over a field where the oil film thickness is specified. The forward method, however, presents difficulties in obtaining converged results under heavily loaded conditions.

The reason for the difficulty is due to the nature of concentrated EHL contacts. The oil film pressure is very high at the contact centre and the pressure gradient is steep around the edges of the heavily loaded contact. Also, the film thickness is almost constant near the centre of the contact due to the elastic deformation of the contacting bodies. In the forward solution, small errors or differences in the film thickness must give large differences in the pressure distribution under such conditions. This may well cause large error in pressure, causing the analysis not to converge.

Dowson and Higginson [1] first introduced an inverse technique to solve the Reynolds

equation for the line contact EHL problem. Using this technique, the film thickness can be obtained over a field where the pressure distribution is assumed, with certain boundary conditions. Thus, the defect of the forward method is no longer a problem. The technique was applied to a point contact problem by Evans and Snidle [18]. They needed, however, a complicated analytical procedure seeking for a range of film thicknesses as a boundary condition.

The forward iterative approach can thus solve the low pressure problem without difficulty, while the inverse method can be applied to the high pressure region. To combine both methods offers a great advantage, as shown in [19–22].

In this study, a numerical technique, in which the forward iterative method and the inverse technique are combined together, was used to solve the elliptical contact EHL problem with/without spin motion.

#### 3.2.1. Forward solution

In the region where the film pressure was relatively low, a forward iterative method was applied to solve the Reynolds equation. Vogelpohl's PHI ( $\phi$ ) substitution has often been used in the forward numerical solution of EHL problems. The parameter ( $\phi$ ) is defined as;

$$\phi = PH^{\frac{3}{2}} \quad (18)$$

This parameter makes the non-dimensional Reynolds equation (equation(17)) into a more appropriate form for numerical analysis, as follows;

$$\begin{aligned} & \bar{H} \left( \frac{\partial}{\partial X} \left[ \frac{\bar{\rho}}{\bar{\eta}} \frac{\partial \phi}{\partial X} \right] + \frac{1}{k^2} \frac{\partial}{\partial Y} \left[ \frac{\bar{\rho}}{\bar{\eta}} \frac{\partial \phi}{\partial Y} \right] \right) \\ & - \phi \left( \frac{\partial}{\partial X} \left[ \frac{\bar{\rho}}{\bar{\eta}} \frac{\partial \bar{H}}{\partial X} \right] + \frac{1}{k^2} \frac{\partial}{\partial Y} \left[ \frac{\bar{\rho}}{\bar{\eta}} \frac{\partial \bar{H}}{\partial Y} \right] \right) \\ & = \frac{12b}{R_x} \left( U - \frac{a\Omega}{R_x} Y \right) \frac{\partial}{\partial X} [\bar{\rho} H] + \frac{12b^2 \Omega}{k R_x^2} X \frac{\partial}{\partial Y} [\bar{\rho} H] \end{aligned} \quad (19)$$

where  $\bar{H} = H^3$ .

The Reynolds equation with the  $\phi$  parameter (equation (19)) can be discretized for computation by using a standard finite difference method over non-uniform mesh grids on a non-dimensional  $X$ - $Y$  field. For the point  $(i,j)$ , equation (19) can be interpreted as a linear function of  $\phi$  as follows;

$$A_{ij}\phi_{i-1,j} + B_{ij}\phi_{i+1,j} + C_{ij}\phi_{i,j-1} + D_{ij}\phi_{i,j+1} - L_{ij}\phi_{i,j} - M_{ij} = 0 \tag{20}$$

where  $\phi_{i,j}$  implies the value of  $\phi$  at the point  $(i,j)$ .  $A_{ij}$ ,  $B_{ij}$ , ...,  $M_{ij}$  in equation (20) are the coefficients which are determined by the values of  $H$ ,  $\bar{\eta}$  and  $\bar{\rho}$  at each nodal point, the mesh structure and the location of the point  $(i,j)$  on the  $X$ - $Y$  field. The derivation and expression of the coefficients are described in Taniguchi [23].

A successive over-relaxation (SOR) method, based on the Gauss-Seidel method, is an iterative numerical technique to solve simultaneous linear equations. With given boundary conditions, equation (20) can be solved by the SOR method using the following generalised form, at the  $(m)$ th iteration;

$$\begin{aligned} \phi_{i,j}^{(m)} = & \phi_{i,j}^{(m-1)} - \frac{\gamma}{L_{ij}} (M_{ij} - A_{ij}\phi_{i-1,j}^{(m)} - B_{ij}\phi_{i+1,j}^{(m-1)} \\ & - C_{ij}\phi_{i,j-1}^{(m)} - D_{ij}\phi_{i,j+1}^{(m-1)} + L_{ij}\phi_{i,j}^{(m-1)}) \end{aligned} \tag{21}$$

The relaxation parameter ( $\gamma$ ) has the value of  $1 < \gamma < 2$  in the over-relaxation technique.

### 3.2.2. Inverse method

In order to apply the inverse method in the high pressure region, the non-dimensional Reynolds equation (equation (17)) was transformed into the following form;

$$\begin{aligned} & \frac{\partial}{\partial X} \left[ \frac{\hat{H}^3}{12} \frac{\partial \hat{Q}}{\partial X} \right] + \frac{1}{k^2} \frac{\partial}{\partial Y} \left[ \frac{\hat{H}^3}{12} \frac{\partial \hat{Q}}{\partial Y} \right] \\ & = \frac{b}{R_r} \left[ U - \frac{a\Omega}{R_r} Y \right] \frac{\partial \hat{H}}{\partial X} + \frac{b^2 \Omega}{kR_r^2} X \frac{\partial \hat{H}}{\partial Y} \end{aligned} \tag{22}$$

where  $\hat{H}$  (non-dimensional modified film thickness),  $\hat{\eta}$  and  $\hat{Q}$  (non-dimensional equivalent reduced pressure) are respectively given by;

$$\hat{H} = \bar{\rho}H, \quad \hat{\eta} = \bar{\rho}^2\bar{\eta}, \quad \hat{Q} = \int_0^P \frac{1}{\hat{\eta}(P_1)} dP_1$$

Rewriting equation (22) in terms of  $\hat{H}$  gives;

$$(A\hat{H}^2 + BY + C) \frac{\partial \hat{H}}{\partial X} + (D\hat{H}^2 + EX) \frac{\partial \hat{H}}{\partial Y} + F\hat{H}^3 = 0 \tag{23}$$

Equation (23) can be solved by using a marching technique in a region where;

1. The pressure distribution is given all over the region, so that the coefficients ( $A_{ij}$ ,  $D_{ij}$  and  $F_{i,j}$ ) of the equation can be calculated.
2. The film thickness is known along the boundary of the region.

A finite difference approximation and an iterative technique, described in [19] and [21], enabled equation (23) to turn into a cubic equation of  $\hat{H}_{i,j}$  and to be solved numerically.

### 3.3. Mesh structure

In order to save computational memory, several non-uniform meshes with various degrees of grid refinement were applied onto the  $X$ - $Y$  field, which had the boundary;

$$-5.2 \leq X \leq 2.0, \quad -2.0 \leq Y \leq 2.0$$

Coarse grids were adopted in the low pressure region near the boundary of the field. Fine grids were used in the high pressure region, especially in the rear half (in the main flow direction) and to the sides of the Hertzian contact region, where a significant change in pressure might be expected.

### 3.4. Zone splitting in the $X$ - $Y$ field

The forward iteration is suitable for a solution with a low pressure region, while the inverse technique can be applied for a high pressure region. These two regions can be

overlapped so as to connect the results from each method smoothly. Then, the result of the inverse solution at a location just outside of the forward iteration region is used as the boundary condition for the forward calculation and vice versa.

The  $X$ - $Y$  field was split into five zones in the present analysis, with reference to a limiting pressure ( $p_{lim}$ ).

Zone 1. Where  $p \leq p_{lim}$ , excluding Zone 2.

The lowest pressure zone.

Zone 2. A thin ring-shaped zone where  $p \leq p_{lim}$  which surrounded Zone 3.

Zone 3. The pressure was larger than the limiting pressure ( $p > p_{lim}$ ). A ring-shaped zone consisting of every nodal point which was within 2 grid points distance (in either the  $X$  or  $Y$  directions) from any point in Zone 2.

Zone 4. Also a ring-shaped zone neighbouring to Zone 3,  $p > p_{lim}$ .

Zone 5. The rest. The highest pressure zone.

The Reynolds equation was solved by the forward iterative method in Zones 1, 2 and 3, with the boundary pressure of Zone 4. Meanwhile, in Zones 3, 4 and 5 the inverse technique was used, Zone 2 providing the boundary film thickness.

The limiting pressure ( $p_{lim}$ ) was chosen to be in the range from 50 to 200 [MPa] according to the conditions.

### 3.5. Programme flow

The general structure of the numerical procedure was based on that reported by Seabra and Berthe [21]. Figure 4 is the flow chart. The programme was written in FORTRAN 77 programming language.

## 4. RESULTS AND DISCUSSIONS

### 4.1. Common conditions

The characteristic parameters of the materials were fixed at the values shown in Table 1 throughout the present study. A steel-to-steel contact was considered and a mineral-based oil, HVI650, at 90[°C] was chosen for the analyses.

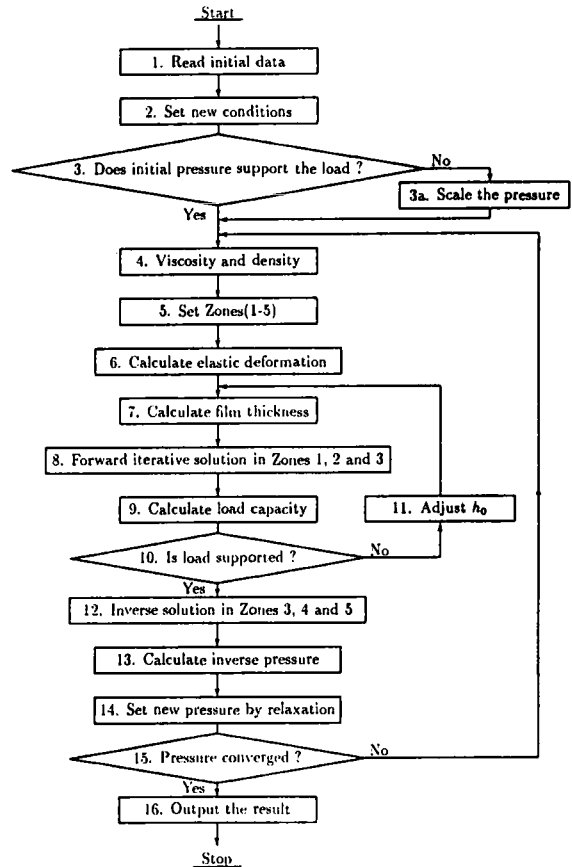


Figure 4 Programme flow

Table 1 Material parameters

|            |                     |                       |
|------------|---------------------|-----------------------|
| $E'$       | [GPa]               | 219.7                 |
| $\eta_0$   | [Pas]               | 0.037                 |
| $\alpha_0$ | [Pa <sup>-1</sup> ] | $1.84 \times 10^{-8}$ |
| $Z$        |                     | 0.57                  |

### 4.2. Analysis without spin

A series of analyses were carried out for the conditions without spin motion. The results were also used as initial data for the spin analysis.

The load ( $F_c$ ), rolling velocity ( $u_0$ ) and ellipticity ( $k$ ) were treated as variables in this series. The range of each variable is shown in Table 2. It should be noted here that the influence of ellipticity upon the pressure and the film thickness was examined by changing the equivalent principal radius of

Table 2 Conditions for analyses without spin

|       |         |                              |
|-------|---------|------------------------------|
| $F_c$ | [N]     | 200 – 4000                   |
| $u_0$ | [m/sec] | 5.0 – 20.0                   |
| $k$   |         | 2.6 – 4.1                    |
| $U$   |         | $3.6 - 20.9 \times 10^{-11}$ |
| $G$   |         | 3650                         |
| $W$   |         | $1.7 - 33.8 \times 10^{-6}$  |

curvature ( $R_x$ ) in the rolling direction ( $x$ ), while the other equivalent principal radius ( $R_y$ ) was kept constant. This situation is commonly seen in a toroidal-type continuously variable transmission (CVT) as it changes the reduction ratio.

Converged solutions were obtained for the conditions with the maximum Hertzian pressure being from 0.57 to 1.55 [GPa]. The distinctive characteristics of EHL were obtained from the solution, such as the central pressure close to the maximum Hertzian pressure, pressure spikes, and an almost flat lubricant film around the centre followed by a thinner film area in a horseshoe outline in the  $X$ - $Y$  field.

The computed data for the minimum and central film thicknesses were compared with the formulae established by Hamrock and Dowson [2]. Agreement of the central film thickness between computed values and those predicted by the formula was excellent. The error between them never exceeded  $\pm 3.1\%$ . However, the predicted values for the minimum film thickness according to the Hamrock and Dowson's formula were sometimes over 10% less than the numerically computed values.

Following Hamrock and Dowson's

procedure [2], a least square power fit was applied to the present results for  $h_{\min}$  to make a new formula for the minimum film thickness ( $h_{\min N}$ ). The power factor for the non-dimensional materials parameter ( $G$ ), 0.49, was appropriated from the H-D formula. The influence of ellipticity in the formula, ( $1 - e^{-0.68k}$ ) was also adopted from the H-D formula. Using a least square power fit to the results for the minimum film thickness, a new formula for the minimum film thickness in this study was completed as follows;

$$H_{\min N} = 5.68U^{0.69}G^{0.49}W^{-0.062}(1 - e^{-0.68k}) \quad (24)$$

The power factor for  $U$  in this study, 0.69, was very close to that of the H-D formula of 0.68. However, the power factor for  $W$ ,  $-0.062$ , was different from that of the H-D formula,  $-0.073$ . The computed results of minimum film thickness and the prediction by  $H_{\min N}$  agreed very well. The error between them was within  $\pm 2.7\%$ .

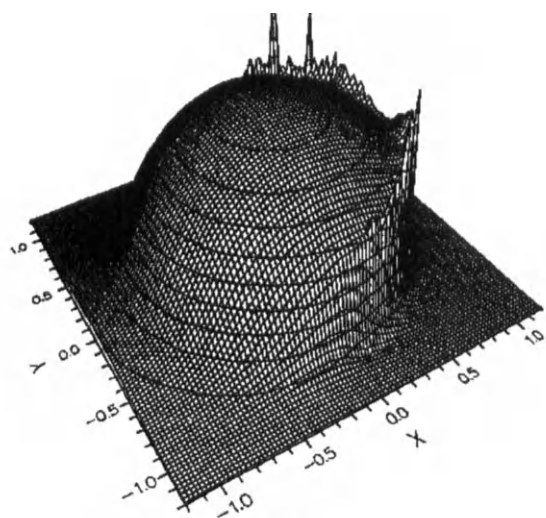
#### 4.3. Pressure distribution with spin motion

The effect of spin motion upon the EHL of the elliptical contact was examined. Table 3 shows the conditions for spin analysis.

The pressure distribution obtained for Case A is shown in Figure 5. The pressure maps have been presented in 3-D style on a non-dimensional  $X$ - $Y$  field. Pressure contours are shown in units of 0.1 [GPa], with the lowest one being 0.1 [GPa]. The symmetry with respect to the  $X$ -axis in pressure distribution without spin (1) was lost by the spin motion as shown in (2).

Table 3. Conditions for spin analysis

|               |           | Case A                     | Case B                     | Case C                     | Case D                     | Case E                     |
|---------------|-----------|----------------------------|----------------------------|----------------------------|----------------------------|----------------------------|
| $F_c$         | [N]       | 1100                       | 500                        | 500                        | 500                        | 500                        |
| $u_0$         | [m/sec]   | 14.5                       | 14.5                       | 10.0                       | 14.5                       | 14.5                       |
| $\omega$      | [rad/sec] | 0 – 2500                   | 0 – 5000                   | 0 – 2500                   | 0 – 2500                   | 0 – 2500                   |
| $U$           |           | $1.05 \times 10^{-10}$     | $1.05 \times 10^{-10}$     | $7.26 \times 10^{-11}$     | $7.58 \times 10^{-11}$     | $1.52 \times 10^{-10}$     |
| $G$           |           | 3650                       | 3650                       | 3650                       | 3650                       | 3650                       |
| $W$           |           | $9.30 \times 10^{-6}$      | $4.23 \times 10^{-6}$      | $4.23 \times 10^{-6}$      | $2.20 \times 10^{-6}$      | $8.78 \times 10^{-6}$      |
| $k$           |           | 3.2                        | 3.2                        | 3.2                        | 2.6                        | 4.1                        |
| $\Omega$      |           | $0 - 4.21 \times 10^{-10}$ | $0 - 8.42 \times 10^{-10}$ | $0 - 4.21 \times 10^{-10}$ | $0 - 4.21 \times 10^{-10}$ | $0 - 4.21 \times 10^{-10}$ |
| $p_{\max Hz}$ | [GPa]     | 1.01                       | 0.77                       | 0.77                       | 0.68                       | 0.90                       |



(1) No Spin

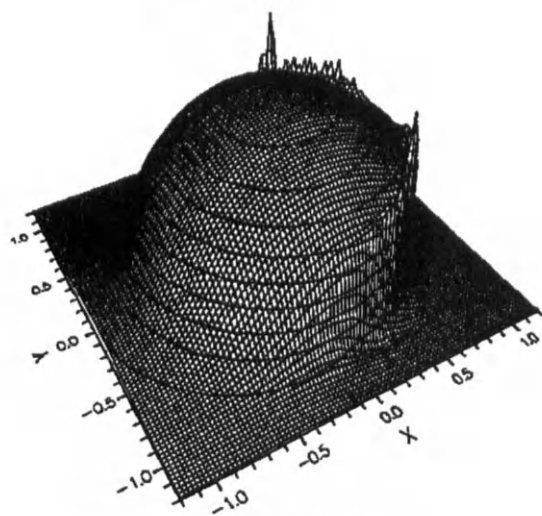
(2)  $\omega = 2500$  [rad/sec]

Figure 5 Pressure distribution  
without/with spin

A slightly higher pressure was generally observed in  $Y < 0$  than  $Y > 0$  when spin motion was introduced. Nevertheless these two pressure distributions look very similar.

At each level of spin rate, the pressures at the centre of the contact were almost constant, being slightly smaller than the maximum Hertzian pressure. The pressure spikes varied, but no clear tendency was found for those

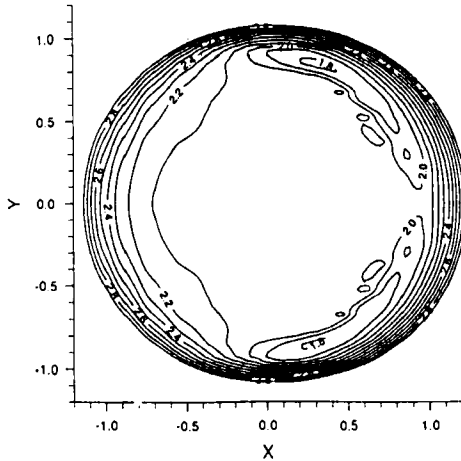
variation against the increase of spin.

The spin motion was found to make little influence upon the pressure distribution throughout the study.

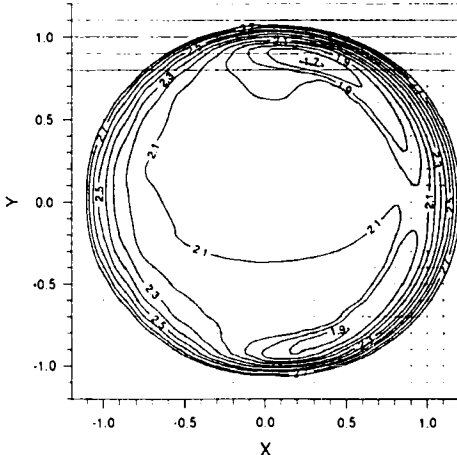
#### 4.4. Film thickness with spin motion

Figure 6 shows the results of film thickness for Case A with increasing spin rate, displayed as 2-D contour maps on non-dimensional  $X$ - $Y$  field. Twelve levels of film thickness contours are drawn in steps of  $0.1 \mu\text{m}$ . The numbers inserted into the contours show the film thickness in  $\mu\text{m}$ . It is clearly shown that the symmetry of the contours with respect to the  $X$ -axis in the analysis without spin was gradually lost as the rate of spin increased. The point of minimum film thickness was located on the upper side of the contact in the contour map, just downstream from the centre of the contact in the  $X$ -direction, near the edge of the Hertzian ellipse. The positive spin applied here, which has been defined to be counterclockwise, decreased the entraining velocity in this half ( $Y > 0$ ) of the lubricated region. In the other half of the region, the spin motion acted as to increase the entraining velocity in the  $X$ -direction. The film thickness contours in this part of the conjunction exhibited an increase in the film thickness with increasing spin.

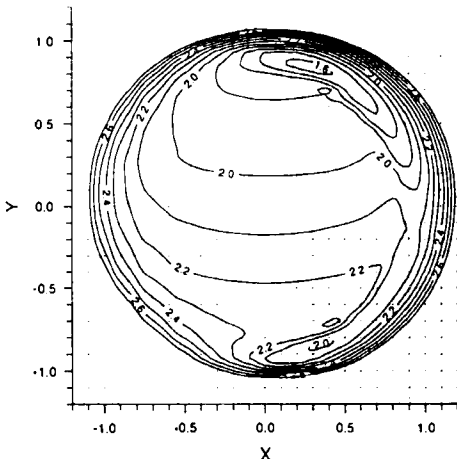
The minimum and central film thicknesses are plotted against spin in Figure 7 for Case A. It again shows that the minimum film thickness gradually reduces as spin increases. The curve for minimum film thickness was almost linear in Figure 7. On the other hand, the results of the central film thickness remained constant against the variation in spin. This can be reflected by the fact that the spin has no effect upon the motion at the very centre of the contact. The graph also shows an excellent agreement of the central film thickness with the value predicted by the Hamrock and Dowson's formula. The errors between the computed central film thicknesses and the predicted ones were less than 1.0 % for this condition. Similar results were obtained for other conditions in Table 3, the reducing  $h_{\min}$  and almost constant  $h_{\text{cen}}$  with spin increase.



(1) No Spin



(2)  $\omega = 1000$  [rad/sec]



(3)  $\omega = 2500$  [rad/sec]

Figure 6 Influence of spin upon film thickness

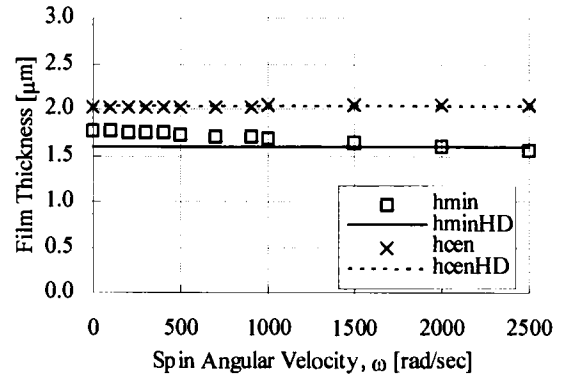


Figure 7 Minimum and central film thickness against spin

4.5. Reduction in minimum film thickness

Spin has been found to have little influence upon the central film thickness. However, it certainly reduces the minimum film thickness, which was located on the side region of the contact where the spin motion worked to reduce the entraining velocity. Thus, it might be meaningful to discuss the effect of spin motion by taking account of the rolling motion. From this point of view, Xu [13] introduced the non-dimensional spin to roll ratio determined as follows;

$$B = \frac{2\omega R_x}{u} = \frac{2\Omega}{U} \tag{25}$$

Figure 8 shows the effect of spin to roll ratio upon the minimum film thickness. The ordinate ( $C_{sp}$ ) is the coefficient of reduction in minimum film thickness by spin determined by the following formula;

$$C_{sp} = 1 - \frac{H_{min}}{H_{min(B=0)}} \tag{26}$$

where  $H_{min(B=0)}$  is the minimum film thickness calculated without spin while other conditions remain constant. Two sets of results from Xu's study [14], Xu-A and Xu-B, and the results from the present study with the different values of parameters ( $U$ ,  $W$  and  $k$ ) are also plotted in the graph.

It is clear from Figure 8 that the operating conditions have a significant effect upon the relationship between  $C_{sp}$  and  $B$ . The coefficient of minimum film thickness reduction ( $C_{sp}$ ) was found to be almost linear with  $B$ , where  $B \leq 25$ . It should be noted here that there is little difference between the curves for Case B and Case C in the plots for small  $B$ . This implies that the influence of rolling speed ( $U$  in non-dimensional term) upon the coefficient of minimum film reduction is no longer significant when  $C_{sp}$  is compared with the spin to roll ratio ( $B$ ).

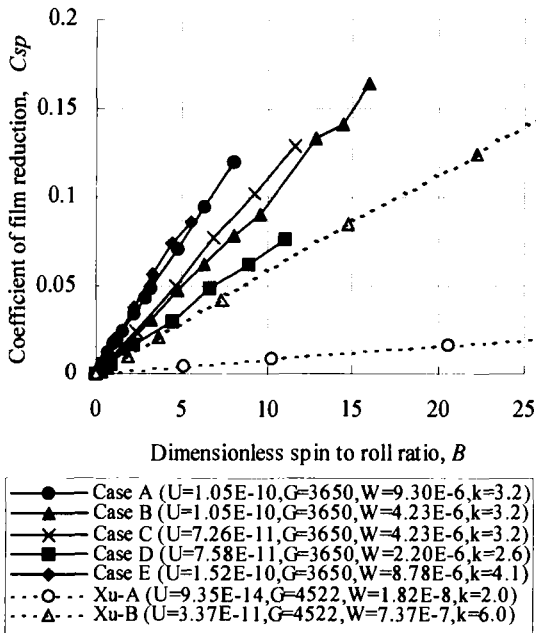


Figure 8 Effect of spin to roll ratio upon minimum film thickness

Also the plot tells us that the slope of these curves is closely related to the load condition ( $W$  in non-dimensional term), though other factors, such as  $G$  and  $k$ , may have some influence. At light load, like Xu-A, the spin to roll ratio had a small influence upon the minimum film thickness. The minimum film thickness fell sharply against the increase of spin to roll ratio when heavy load was applied, as seen in the result of the present analysis.

Thus, the reduction rate of minimum film thickness against spin to roll ratio can be

formulated with the following assumptions;

1.  $C_{sp}$  is effectively a linear function of  $B$ , when  $B$  is small enough.
2. Rolling speed ( $U$ ) has a negligible effect upon this function.
3. The gradient of the linear function is solely determined by load ( $W$ ), neglecting the effect of other parameters, such as  $G$  and  $k$ .

Using curve fit procedures to the plots, the minimum film thickness with spin motion was predicted by the following formula;

$$H_{\min} = (1 - 3.47W^{0.47}B)H_{\min(B=0)} \quad (27)$$

The error between the minimum film thicknesses obtained by the numerical analysis and those from equation (27) was within  $\pm 1\%$  at  $B < 25$ , except for Case Xu-B.

It is very likely that the minimum film thickness reduced by spin is affected by load. The spin motion at the contact causes a reverse motion to the rolling in half of the lubricated region. This has been considered to be the cause of reduction in minimum film thickness when spin is applied. In most EHL cases, the minimum film thickness is located near to the side edge of the parallel film region, that is almost equivalent to the Hertzian contact ellipse. Meanwhile the reverse motion caused by spin at a point is determined by the product of the angular velocity of spin and the distance between the point and the centre of the contact. A heavy load case gives a large contact ellipse which may result in a large reverse velocity to rolling at the side of the contact, where the minimum film thickness is located. Thus, under a heavy load, the minimum film thickness is more likely to be affected by spin than under light load conditions.

In case of the lubricated contact in the half toroidal CVT discussed in [7], the non-dimensional spin to roll ratio ( $B$ ) was around 1. As far as the isothermal analysis is concerned, it is possible that the spin motion reduces the minimum film thickness of the contact in the CVT by a few percent, when compared with the film prediction for no spin condition.

## 5. CONCLUSION

Isothermal elliptical elastohydrodynamic lubrication (EHL) problems have been solved numerically with various spin angular velocities ( $\omega$ ) incorporated with rolling motion, for a Newtonian lubricant, assuming smooth surfaces on the pair of contacting bodies. A computational programme was developed to solve the elliptical EHL problem with spin motion by using the forward-inverse combined technique. Pressure distributions and film thicknesses were initially obtained by numerical analyses for Newtonian EHL problems without spin motion, for maximum Hertzian pressures up to 1.55 [GPa].

As for the effect of spin upon the lubrication, the followings were found;

- The spin motion did not have any significant effect upon the magnitude of the pressure and the central film thickness, although the distribution of pressure changed.
- The minimum film thickness was reduced by spin, and it was located in the side of the contact where spin motion worked against the rolling velocity.
- At small spin rates, the load parameter, as well as the speed parameter, was found to have a strong relation to the reduction in the minimum film thickness due to spin.

## REFERENCES

1. D. Dowson and G.R. Higginson, *J. Mech. Eng. Sci.*, 1-1 (1959) 6.
2. B.J. Hamrock and D. Dowson, *Trans. ASME, J. of Lub. Tech.*, 99-2 (1977) 264.
3. R.J. Chittenden, D. Dowson, J.F. Dunn and C.M. Taylor, *Proc. of the R. Soc. of London*, A397 (1985) 245.
4. L.G. Houperit and B.J. Hamrock, *Trans. ASME, J. of Tribol.*, 108-3 (1986) 411.
5. A.A. Lubrecht, W.E. ten Napel and R. Bosma, *Trans. ASME, J. of Tribol.*, 109-3 (1987) 437.
6. T.A. Harris, *Rolling Bearing Analysis* (3rd edition), John Wiley & Sons, New York (1991).
7. M. Taniguchi, H. Machida and S. Aihara, *Vehicle Tribology, Proc. of the 17th Leeds-Lyon Symposium on Tribology*, Elsevier, Amsterdam (1991) 287.
8. H. Machida and Y. Ichihara, *Proc. of the 23rd FISITA*, Paper 905086 (1990).
9. M. Nakano, T. Hibi and K. Kobayashi, *SAE Technical Paper 922105* (1992).
10. H. Machida, H. Itoh, T. Imanishi and H. Tanaka, *SAE Technical Paper 950675* (1995).
11. T. Imanishi, H. Machida and H. Tanaka, *Proc. of FISITA 96*, Paper 1638 (1996).
12. A. Mostofi and R. Gohar, *J. Mech. Eng. Sci.*, 24-3 (1982) 173.
13. H. Xu, PhD Thesis, The University of Leeds (1988).
14. D. Dowson, C.M. Taylor and H. Xu, *Proc. Instn. Mech. Engrs.*, 205-C3 (1991) 165.
15. J.F. Lin and H.Y. Chu, *Trans. ASME, J. of Tribol.*, 113-1 (1991) 12.
16. C.J.A. Roelands, PhD Thesis, Delft University of Technology (1966).
17. D. Dowson and G.R. Higginson, *Elastohydrodynamic Lubrication*, Pergamon Press, Oxford (1966).
18. H.P. Evans and R.W. Snidle, *Trans. ASME, J. of Lub. Tech.*, 103-4 (1981) 539.
19. H.P. Evans and R.W. Snidle, *Proc. of the R. Soc. of London*, A382 (1982) 183.
20. K.P. Hou, D. Zhu and S.Z. Wen, *Trans. ASME, J. of Tribol.*, 109-3 (1987) 432.
21. J. Seabra and D. Berthe, *Wear*, 130-2 (1989) 301.
22. C.C. Kweh, H.P. Evans and R.W. Snidle, *Proc. Instn. Mech. Engrs.*, 203-C2 (1989) 133.
23. M. Taniguchi, PhD thesis, The University of Leeds (1995).



## Non-steady state effects on oil film thickness and traction forces

Yasuyoshi Tozaki, Kazuhiro Yamamoto, Noriyuki Hayashi and Susumu Matsumoto

Nagasaki Research and Development Center, Mitsubishi Heavy Industries, Ltd.,  
1-1 Akunoura-machi, Nagasaki, Japan

The purpose of this study is to know the change of oil film thickness and traction forces, when the difference of rotational speed of two traction drive rollers becomes unsteadily large by torsional vibration or machine trouble. The simultaneous measurements of optical film thickness and traction forces are performed to investigate the elastohydrodynamic lubrication (EHL) film formation under flooded conditions, on the crowned roller and glass disc interferometry apparatus. The measured profile and thickness of film are compared to the theoretical values given by the two dimensional non-steady thermal EHL calculation. The traction forces measured simultaneously on the crowned roller in the rolling direction are compared to one calculated by two dimensional non-steady thermal non-Newtonian model.

### 1. INTRODUCTION

If torsional vibration or machine trouble takes place on a traction drive, the EHL films in contacts would have to survive and transmit power even in the rapid change of surface speed. Because of the squeeze action produced by the change of speed, the behaviour of such films can deviate by the non-Newtonian effects or thermal effects from that of the corresponding steady state films. Though Oh[1] presented an isothermal solution to this kind of problem, it was inadequate to explain the behaviour of such films because the thermal and non-Newtonian effects are not taken into account. From the point of view of the thermal effects on EHL contacts, a number of papers have been published [2, 3, 4] but almost all investigations were restricted to the time independent condition. But recently, progress in solving a non-steady one dimensional thermal EHL problem with a non-Newtonian fluid has been made by Yang[5].

However, no work has yet been done in treating two-dimensional and in being confirmed by experiment. In this paper, a non-steady thermal EHL model is proposed and

traction forces are calculated under non-steady state conditions. These are compared with the experimental data.

### 2. EXPERIMENTAL PROCEDURES

To investigate the change of the oil film thickness and the traction forces, simultaneous measurements of the oil film thickness and the traction forces are performed.

#### 2.1 Experimental apparatus

The optical three-dimensional contact apparatus is shown schematically on Fig. 1.

By optical interference of the glass disc and the roller, the oil film thickness between them is measured. The glass disc can be driven at a desired speed by AC servo-motor. The roller is pressed up on the glass disc by the dead weight and driven passively by the glass disc.

The flywheel is attached to the roller, and so when the rotational speed of the glass disc is changed rapidly, the difference of rotational speeds between the glass disc and the roller can be produced. The change of the interference fringe is recorded by the video

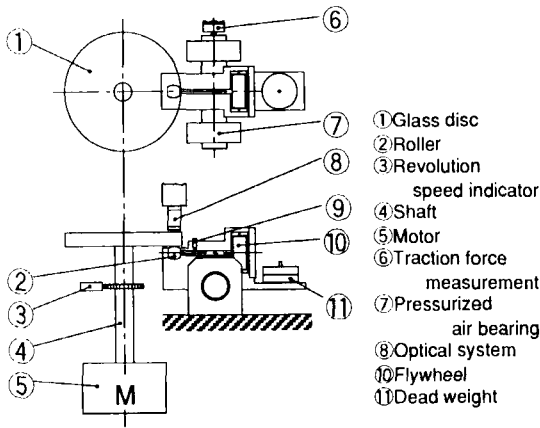


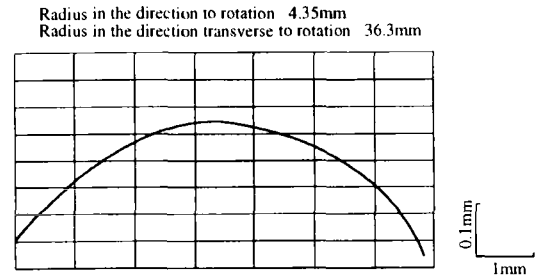
Fig. 1 Schematic of apparatus

Table 1 Properties of glass disc

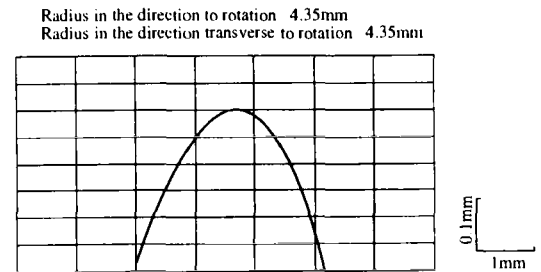
|                     |                                      |
|---------------------|--------------------------------------|
| Material            | Glass disc                           |
| Elastic modulus     | 75 GPa                               |
| Dimension           | Diameter ; 100 mm, Thickness ; 10 mm |
| Parallel error      | 10 μm                                |
| Accuracy of surface | λ / 2                                |
| Coating             | Chromium layer                       |

Table 2 Properties of lubricant

| Temperature [°C] | Viscosity [Pa·s] | Pressure-viscosity coefficient |
|------------------|------------------|--------------------------------|
| 24               | 0.52             | 42                             |
| 45               | 0.054            | 33                             |
| 100              | 0.0055           | 16                             |



(a) Barrel-shaped



(b) Ball-shaped

Fig. 2 Shape of roller

Table 3 Test conditions

|        | Shape of roller | Load [N] | Acceleration of rotating speed | Temperature of lubricant [°C] | Note                                       |
|--------|-----------------|----------|--------------------------------|-------------------------------|--|
| Case 1 | Ball-shaped     | 30       | 100 to 500 rpm/sec             | 24                            | Effect of shape of roller                  |
| Case 2 | Barrel-shaped   | 30       | 100 to 500 rpm/sec             | 24                            |  |
| Case 3 | Barrel-shaped   | 15       | 100 to 300 rpm/sec             | 24                            | Effect of acceleration of rotational speed |

tape recording during testing.

The roller, the flywheel and the dead weight are supported by the pressurized air bearings to detect traction force on the roller in the rolling direction accurately.

2. 2 Test pieces

The properties of glass disc are shown in Table 1 and the shapes of the roller are shown in Fig. 2. Also the properties of lubricant are shown in Table 2.

2. 3 Test conditions

Table 3 shows the test conditions. To investigate the influence of thermal, non-Newtonian and squeeze action, the tests were performed under the different load and the change of speed conditions and using different shape of rollers.

3. MATHEMATICAL BACKGROUND

3. 1 Basic equations

The rheological model proposed by Eyring[6] is adopted to describe the non-Newtonian properties of lubricant. For simplicity, the visco-elastic effects in compression and in shear are neglected. The constitutive equation of lubricant is then expressed as

$$\partial u / \partial z = (\tau_0 / \tau) \sinh(\tau_0 / \tau) \tag{1}$$

where  $u$ ,  $\tau$ , and  $\eta$  are the velocity, the shear stress and the viscosity of lubricant, all are functions of  $x$ ,  $z$ , and  $t$ ;  $\tau_0$  is the characteristic shear stress of Eyring fluid, which is assumed to be constant in the present analysis.

Then the equivalent viscosity of the lubri-

cant,  $\eta^*$  [7] is introduced by

$$1/\eta^* = (1/\eta) \sinh(\tau/\tau_0)/(\tau/\tau_0) \quad (2)$$

The Reynolds equation governing the pressure distribution has been derived as

$$\frac{\partial}{\partial x} \left( \frac{h^3}{\eta^*} \frac{\partial p}{\partial x} \right) + \frac{\partial}{\partial y} \left( \frac{h^3}{\eta^*} \frac{\partial p}{\partial y} \right) = 12 \frac{U_1 + U_2}{2} \frac{\partial h}{\partial x} + 12 \frac{\partial h}{\partial t} \quad (3)$$

The boundary conditions of Eq. (3) are taken as

$$\left. \begin{aligned} p &= 0 \quad \text{at inlet} \\ p &= \frac{dP}{dx} = 0 \quad \text{at outlet} \end{aligned} \right\} \quad (4)$$

The film shape between an elastic roller and a glass disc is given by

$$h(x, t) = h_0(t) + \frac{x^2}{2R_1} + \frac{y^2}{2R_2} - \frac{2}{\pi E'} \iint \frac{\rho(x, y)}{\sqrt{(x - \bar{x})^2 + (y - \bar{y})^2}} d\bar{x} d\bar{y} \quad (5)$$

Neglecting the heat conduction along  $x$ -direction and the heat convection along  $z$ -direction, the energy equation governing the temperature distribution in the film is given by

$$k_f \frac{\partial^2 T}{\partial z^2} + q = \rho c \frac{\partial T}{\partial t} \quad (6)$$

$$q = \tau \frac{\partial u}{\partial z} \quad (7)$$

In addition, the numerical procedure of the calculation is shown in Fig. 3.

#### 4. COMPARISON OF EXPERIMENTAL RESULTS WITH CALCULATION

##### 4.1 Experimental results

Fig. 4 is the experimental results of the slip ratio, the traction coefficient and the oil film thickness under the conditions of case 1 which is shown in Table 3.

The slip ratio is defined as

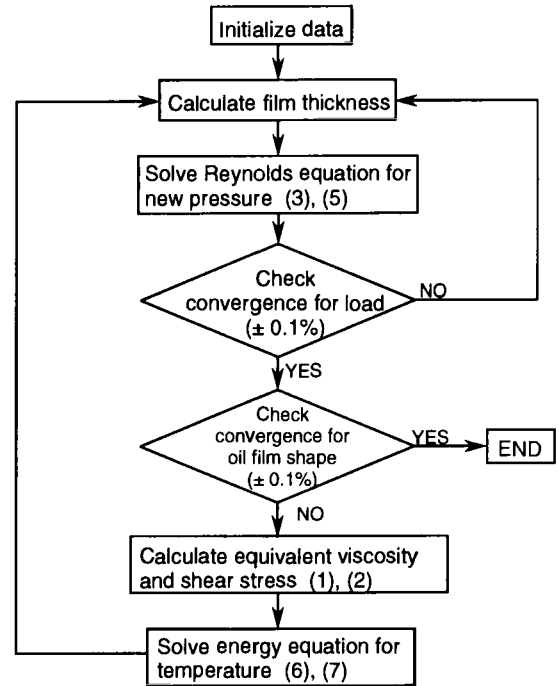


Fig. 3 Flowchart of computational scheme

$$s = (U_1 - U_2)/U_1 \quad (8)$$

where,  $U_1$ ; velocity of the glass disc  
 $U_2$ ; velocity of the roller

In this experimental test, triangular-shaped alteration of velocity is given to the glass disc when it is rotating steadily at a constant speed. The velocity of the roller can not catch up with the velocity of the glass disc which drives the roller, because of mass inertia of the flywheel attached to the roller. So the slip ratio changes largely by dependence on the difference of the velocity between the glass disc and the roller. At first, the traction coefficient tends to increase as the slip ratio increase. While the slip ratio continues to increase further, the traction coefficient suddenly begins to decrease. After the velocity of the glass disc reaches the maximum speed or the slip ratio becomes the maximum value, the traction coefficient has decreased until the slip ratio recovers to a certain level. Then the traction coefficient

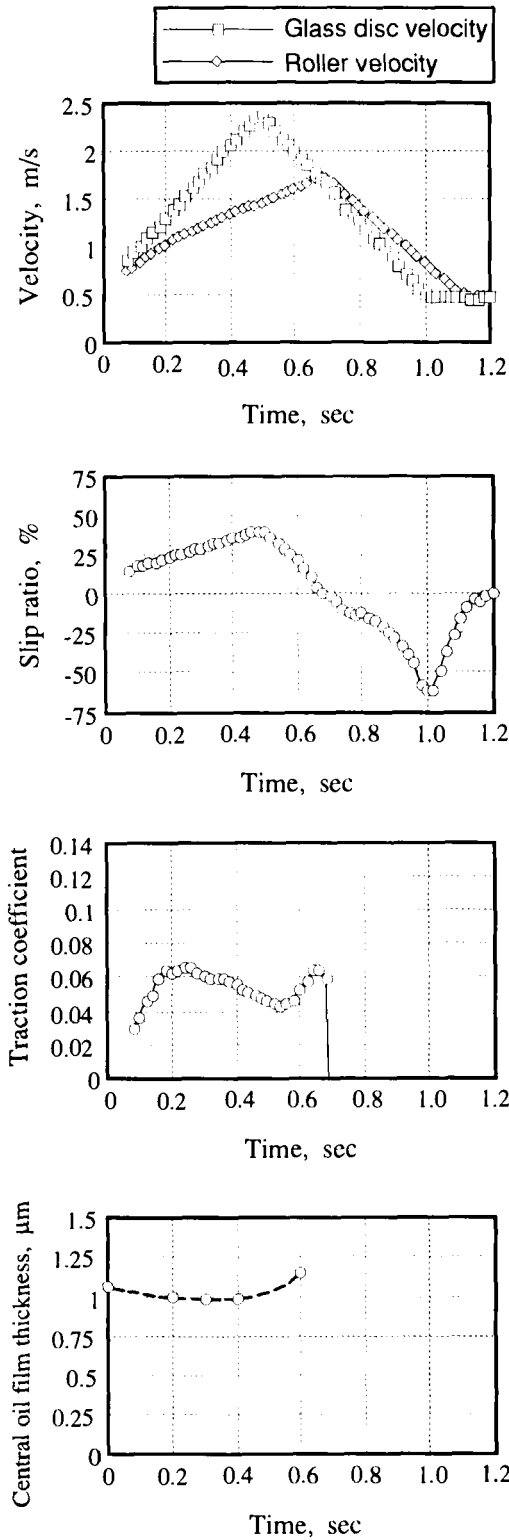


Fig. 4 Experimental results

begins to increase again as the slip ratio decreases, but soon the plot of the traction coefficient disappears since slip direction between the glass disc and the roller is reversed by mass inertia of the flywheel.

Usually, in case velocities of both the glass disc and the roller increase with no slip, the oil film thickness should increase. But, in this test condition, the slip ratio becomes so large that the influence of temperature rise due to shear of the oil film becomes major in comparison with the influence of velocity.

#### 4.2 Effects of the slip ratio

Fig. 4 is arranged according to time history, while Fig. 5 is arranged by slip ratio. We calculated the traction coefficient and the oil film thickness by the isothermal calculation according to the conditions of case 1 which was shown in Table 3. The results, calculated in isothermal condition, of the

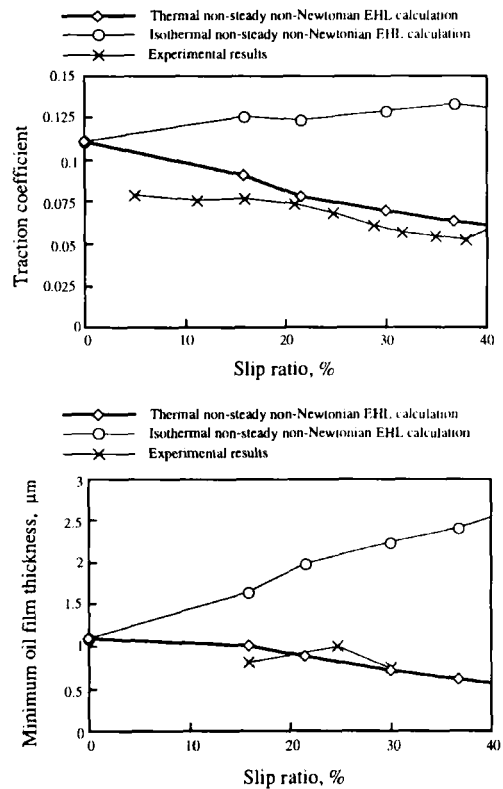


Fig. 5 Slip ratio vs Traction coefficient and minimum oil film thickness

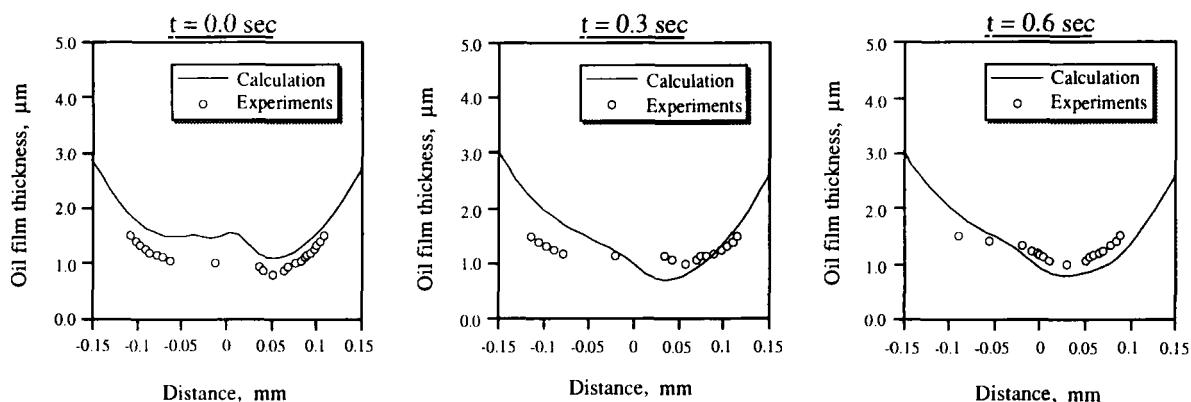


Fig. 6 Comparison of oil film shape

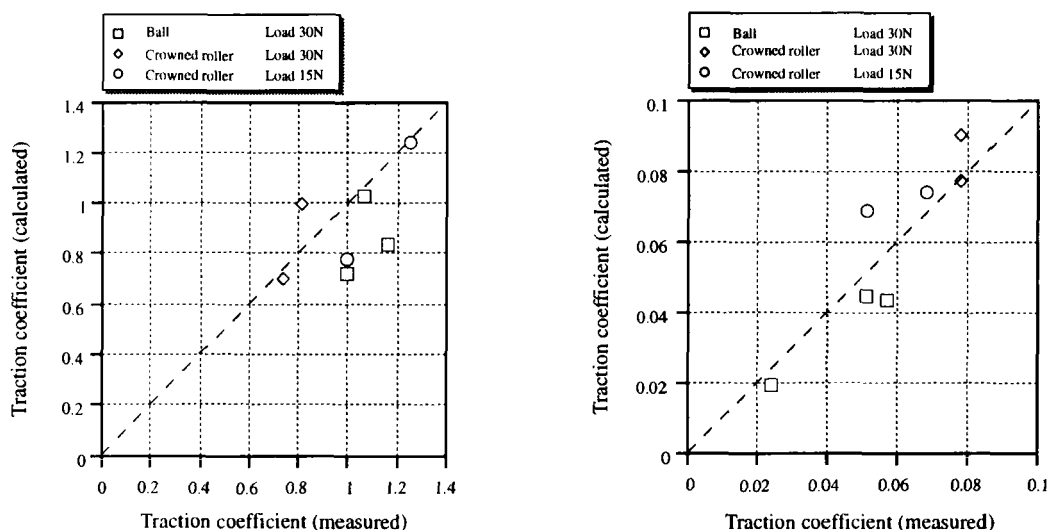


Fig. 7 Comparison between measured and calculated results

traction coefficient and the oil film thickness increase according to increase of the slip ratio, but the experimental results show that both the oil film thickness and the traction coefficient decrease in the same condition. The results, calculated by thermal EHL, of the oil film thickness and the traction force are reasonably close to the measured results. Thus, it was confirmed that the temperature rises due to shear affects oil film thickness and traction forces.

#### 4.3 Comparison of the oil film shape

Fig. 6 shows the oil film shape and the calculated oil film shape is compared with

measured one. Calculated results of the oil film shape agree reasonably well with the experimental results.

Thinner part of the oil film shape, which is peculiar to EHL film, is confirmed at the outlet position.

#### 4.4 Confirmation of accuracy

Comparison between the measured and calculated oil film thickness and traction force for various conditions is shown in Fig. 7.

For a perfect agreement, all points should fall on the indicated 45° straight line.

Calculated results of oil film thickness and

traction force are reasonably close to the measured results.

## 5. CONCLUSION

In the present paper, the simultaneous measurements of the oil film thickness and the traction forces are performed to investigate the EHL film formation on the crowned roller and the glass disc with the optical interferometry apparatus.

The measured film shape and the oil film thickness are compared to the calculated values given by the two-dimensional non-steady thermal EHL analysis.

The obtained results are summarized as follows;

1. The measurements of the oil film thickness and the traction forces were successfully carried out under non-steady condition.

Oil film thickness decreased when the difference of rotational speed becomes unsteadily large and traction forces changed according to slip ratio of the glass disc and the roller.

2. Calculated results of the oil film thickness and the traction forces were reasonably close to the measured results. It was confirmed that the calculation method is practical and useful.

The change of the oil film thickness and the traction coefficient is known by the experiment and the calculation, when vibration or machine trouble takes place at two rollers.

Traction drives which are used under non-steady condition could be designed using this method.

## Nomenclature

- $E'$  equivalent Young's modulus of solids, Pa  
 $h$  film thickness, m  
 $k_f$  thermal conductivities of lubricant, W/(m<sup>2</sup>K)  
 $P$  hydrodynamic pressure, Pa  
 $t$  time, s  
 $u$  fluid velocity in  $x$ -direction, m/s  
 $U_1, U_2$  tangential velocities of solid surfaces, m/s  
 $x$  spatial coordinate along the film, m  
 $z$  spatial coordinate perpendicular to  $x$ , m  
 $T$  temperature, °K  
 $\tau$  shear stress in  $x$ -direction, Pa  
 $\tau_0$  characteristic shear stress of Eyring fluid, Pa  
 $R_x, R_y$  effective radius, m

## REFERENCES

- [1] K. P. Oh, ASME Journal of Tribology, vol.106 (1984)
- [2] H. S. Cheng and S. Sternlicht, ASME Journal of Basic Engineering, vol.87 (1965)
- [3] D. Dowson and A. V. Whitaker, Proc. of the Institution of Mechanical Engineers, vol.180, Part 3B (1965)
- [4] D. Zhu and S. Wen, ASME Journal of Tribology, vol.106 (1984)
- [5] P. Yang and S. Wen, ASME Journal of Tribology, vol.114 (1992)
- [6] H. Eyring, Journal of Chemical Physics, Vol.4 (1936)
- [7] P. Yang and S. Wen, ASME Journal of Tribology, vol.112 (1990)

## An Analysis of Elastohydrodynamic Film Thickness in Tapered Roller Bearings

R Yamashita \* D Dowson † and C M Taylor ‡

Institute of Tribology, Department of Mechanical Engineering,  
 The University of Leeds, Leeds LS2 9JT, UK

An approximate fluid film lubrication model based upon the application of elastohydrodynamic film thickness formulae to the roller and raceway contacts is introduced to the kinematics and static loading analysis of tapered roller bearings. The analysis has been carried out under the condition of given radial and axial loads without misalignment. The load distributions, the film thicknesses and the deflections of the inner raceway are presented.

Also, the full elastohydrodynamic analysis of barrelled isosceles trapezium conjunctions which can be reduced from the tapered roller and raceway contacts has been carried out. The appearance of pressure and film thickness distributions are very different (asymmetrical) from those in elliptical conjunctions because of the geometry of the conjunction. The minimum and central film thicknesses and the pressure distributions are shown.

### 1. Nomenclature

|               |  |
|---------------|--|
| $\bar{a}$     | mesh size in the $y$ direction   |
| $\bar{b}$     | mesh size in the $x$ direction   |
| $c_p$         | constant for Roelands equation,<br>$= 1.96 \times 10^8 \text{ N/m}^2$                                      |
| $D$           | influence coefficient of<br>elastic deformation  |
| $Diff_H$      | difference in film thickness,<br>$=  H - H^{(HD)} /H$  |
| $Diff_P$      | difference in pressure,<br>$=  P - P_h /P$   |
| $E$           | modulus of elasticity, Pa  |
| $E'$          | effective elastic modulus, Pa<br>$= 2 \left\{ \frac{1-\nu_a^2}{E_a} + \frac{1-\nu_b^2}{E_b} \right\}^{-1}$ |
| $F$           | applied load, N  |
| $F_{EHD}$     | load calculated from $P$ , N   |
| $F_c$         | centrifugal force, N   |
| $\mathcal{F}$ | left hand side of Equation 15  |
| $G$           | dimensionless materials<br>parameter, $= \alpha E'$  |
| $h$           | film thickness, m  |

|          |   |
|----------|---|
| $H$      | dimensionless film thickness,<br>$= h/R_{ae}$   |
| $i^*$    | $=  (X + \bar{m})/(2\bar{b}) - i  + 1$  |
| $j^*$    | $=  (Y + \bar{l})/(2\bar{a}) - j  + 1$  |
| $k$      | ellipticity parameter   |
| $K$      | load-elastic deformation<br>coefficient   |
| $l$      | nominal roller length, m  |
| $l_a$    | effective roller length, m  |
| $l_h$    | half of roller effective length, m  |
| $M$      | moment, Nm  |
| $M_c$    | gyroscopic couple, Nm   |
| $p$      | pressure, Pa  |
| $P$      | dimensionless pressure, $= p/E'$  |
| $P_h$    | nondimensional Hertzian central<br>pressure   |
| $q$      | load per unit length, N/m   |
| $r$      | position vector   |
| $R_a$    | mean radius of tapered roller, m  |
| $R_{ae}$ | mean radius of equivalent<br>tapered roller, m  |
| $R_r$    | crowning radius of roller, m  |
| $R_s$    | radius of roller large end, m   |
| $S$      | geometrical separation of un-<br>deformed bodies in $x - y - S$<br>coordinate system, m |

\*Present contact address is Research and Development Center, Koyo Seiko Co. Ltd., 24-1 Kokubuhiganjyo-cyo, Kashiwara-shi, Osaka 582, Japan.

E-mail address : ryamashita@tec.koyo-seiko.co.jp

†Research Professor

‡E-mail address : C.M.Taylor@leeds.ac.uk

|                   |   |                      |  |
|-------------------|---|----------------------|--|
| $s'$              | geometrical separation of undeformed bodies in $x' - y' - s'$ coordinate system, m                          | $\nu$                | roller large end, radians<br>flange angle, radians<br>or Poisson's ratio |
| $S'$              | geometrical separation of undeformed bodies in $x' - y' - S'$ coordinate system, m                          | $\rho$               | density of lubricant, $\text{N}\cdot\text{s}^2/\text{m}^4$               |
| $\bar{S}_{(X,Y)}$ | nondimensional geometrical separation of undeformed bodies in $X - Y - S$ coordinate system, m              | $\bar{\rho}$         | dimensionless density, $= \rho/\rho_0$                                   |
| $U$               | dimensionless speed parameter, $= \eta_0 u / E' R_{ae}$   | $\psi$               | position angle of roller, radian   |
| $u$               | mean surface velocity in $x$ direction, m/s or deflection of inner raceway, m                               | $\omega$             | relaxation coefficient   |
| $v$               | mean surface velocity in $y$ direction, m/s   | $\omega_a$           | angular velocity of roller, radian/s                                     |
| $W$               | dimensionless load parameter, $= q / (R_{ae} E')$ for line contact, $= F / (R_{ae}^2 E')$ for point contact | $\bar{\zeta}_c x$    | $\zeta$ coordinate of the centre of gravity of roller                    |
| $x, y, z$         | Cartesian coordinate system   | $\xi, \eta, \zeta$   | Cartesian coordinates  |
| $X, Y, Z$         | Cartesian coordinate system   | $\Gamma, \Phi, \Psi$ | coefficient matrices of translations                                     |
| $z$               | number of rollers   |                      |  |
| $Z_1$             | viscosity-pressure index  |                      |  |
| $\alpha$          | taper angle of outer raceway, radian, or pressure-viscosity coefficient, $\text{Pa}^{-1}$                   |                      |  |
| $\alpha_t$        | angle of tangent line of elliptical function and $x$ axis   |                      |  |
| $\beta$           | taper angle of inner raceway, radian  |                      |  |
| $\gamma$          | misalignment or angle of roller centre line, radian   |                      |  |
| $\delta$          | elastic deformation, m  |                      |  |
| $\bar{\delta}$    | dimensionless elastic deformation   |                      |  |
| $\Delta_r$        | crown drop, m   |                      |  |
| $\epsilon$        | taper angle of roller, radian, or coefficient of Reynolds equation  |                      |  |
| $\eta$            | viscosity of lubricant, Pa·s  |                      |  |
| $\eta_\infty$     | constant for Roelands equation, $6.31 \times 10^{-5} \text{N}\cdot\text{s}/\text{m}^2$                      |                      |  |
| $\bar{\eta}$      | dimensionless viscosity, $= \eta/\eta_0$  |                      |  |
| $\theta$          | taper angle of equivalent roller, radian  |                      |  |
| $\kappa$          | taper angle of raceway, radian  |                      |  |
| $\lambda$         | angle of position of  |                      |  |

### Subscripts

|                    |                                     |
|--------------------|-------------------------------------|
| $i$                | inner raceway                       |
| $o$                | outer raceway                       |
| $r$                | roller                              |
| $f$                | flange                              |
| $min$              | minimum                             |
| $cen$              | central                             |
| $a, b$             | bodies                              |
| $x, y, z$          | in $x, y$ or $z$ direction          |
| $l$                | line contacts                       |
| $n$                | point contacts                      |
| $0$                | $P = 0$                             |
| $H00$              | $H_{00}$                            |
| $ehd$              | EHD                                 |
| $\xi, \eta, \zeta$ | in $\xi, \eta$ or $\zeta$ direction |

### Superscripts

|        |                    |
|--------|--------------------|
| $(HD)$ | Hamrock Dowson     |
| $(n)$  | $n$ -th iterations |

## 2. Introduction

The performances of rolling bearings, gears and traction drives strongly depend on lubrication. Elastohydrodynamic (EHD) lubrication analysis has been applied to the lubrication of heavily loaded contacts which can be found in these applications. The predictions of the overall performance of these bearings are very difficult, even though EHD theory gives some indications of lubricant film thickness, pressure distributions and traction forces.



Applying EHD theory to a tapered roller bearing is a very complicated task, as the kinematics and static loading analysis itself is very difficult. Even in dry conditions, the numerical computations for the loading analysis do not always give results, as they diverge under high speed conditions which produce high centrifugal forces and gyroscopic couples.

At the present time a combined analysis of the loading and elastohydrodynamic lubrication of a complete tapered roller bearing has not been reported. Further EHD analysis of such bearings needs extension to incorporate the realistic footprint geometry.

In this paper, a numerical solution to the kinematics and static loading problem in tapered roller bearings considering EHD film thickness, with an approximate fluid film model, is presented.

The results of the comparisons between dry conditions and the approximate fluid film lubrication model of the contact loads of inner raceway, outer raceway and flange is presented. The effects upon film thicknesses and inner raceway deflections are also shown.

It is demonstrated that tapered roller and raceway contacts can be reduced to tapered roller and plane contacts. In addition, basic equations for a full EHD analysis of the tapered roller and plane contacts with an iteration formula are presented.

The results of the full EHD analyses with varying speed or applied load are presented and compared with those predicted by standard EHD film thickness formulae and Hertzian analysis.

### 3. Geometry of tapered roller bearings

The geometry of a tapered roller bearing is shown in Figure 1.

As rollers contact to an inner raceway, an outer raceway and the flange of the inner raceway, the geometry of tapered roller bearings is more complicated than ball or cylindrical roller bearings.

While the roller large end and flange contact can be considered as an elliptical conjunction, the roller and raceway contacts can be described as isosceles trapezium conjunctions from the footprint of the contacts as shown Figure 2 (a).

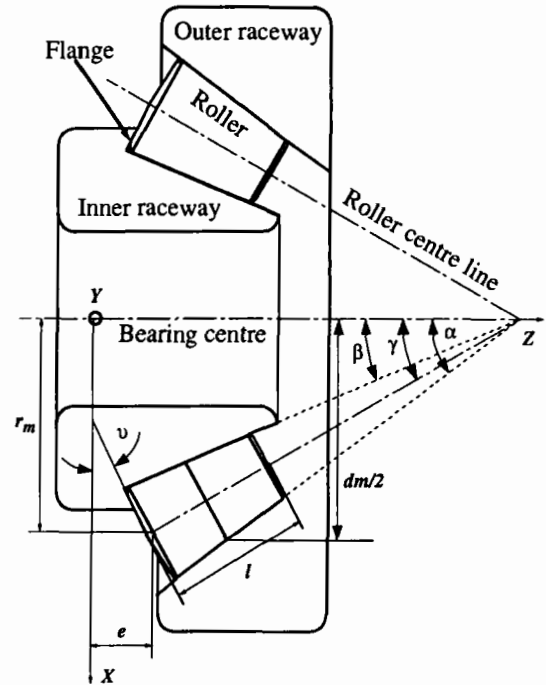


Figure 1. Tapered roller bearing with characteristic geometrical dimensions

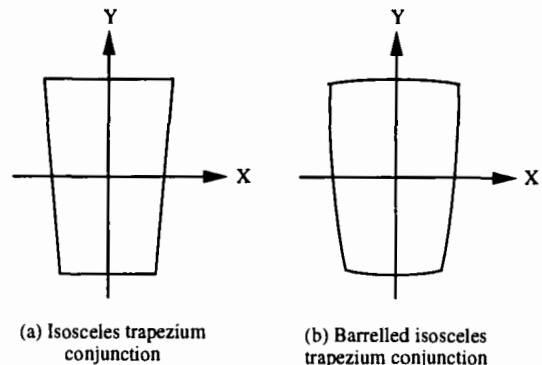


Figure 2. The footprints of isosceles trapezium conjunctions

Usually, rollers are crowned to prevent the edge loads as shown in Figure 3. Therefore, the foot print of crowned roller and raceway contacts can be described as barrelled isosceles trapezium conjunctions as shown in Figure 2 (b).

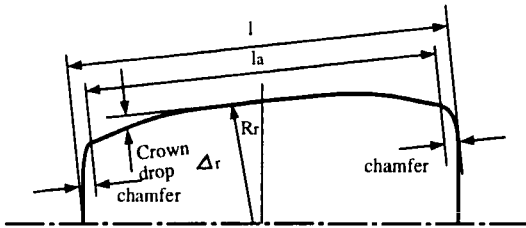


Figure 3. Roller profile of full crowning

As it is reasonable to assume that rollers are crowned, the contact conjunctions for the loading and full EHD analyses are assumed to be the barrelled isosceles trapezium conjunctions in this paper.

#### 4. Approximate fluid film model

##### 4.1. Contact model considering EHD

An approximate fluid film lubrication model based upon the application of EHD film thickness formulae to the roller and raceway contacts is introduced to the kinematics and static loading analysis of tapered roller bearings.

As the rollers and raceways can be represented as a set of very thin disk-shaped slices along the longitudinal direction, the contact model for the kinematics and static loading analysis of tapered roller bearings in dry conditions is usually considered to be the contact of two slices of the roller and raceway, as rectangular conjunctions.

When two slices contact under dry conditions under a load per unit length  $q$ , an elastic deformation  $\delta$  occurs as shown in Figure 4.

The relationship between  $q$  and  $\delta$  for dry con-

tact is given by (see reference [5])

$$q = K_l \delta^{1.11} \tag{1}$$

where  $K_l$  is the load-elastic deformation coefficient for a line contact.

If the distance between the centre of the two slices is constant and an EHD film is produced, the total elastic deformation of the slices becomes equivalent to the sum of  $\delta$  and the EHD central film thickness  $h_{cen}$  as shown in Figure 5.

Therefore, an load per unit length considering EHD,  $q_{ehd}$ , can be given as

$$q_{ehd} = K_l (\delta + h_{cen})^{1.11} \tag{2}$$

where  $h_{cen}$  is obtained from the EHD film thickness formula by Dowson and Toyoda [3].

Applying Equation 2 for the roller and the raceway contact, the load per unit length of the inner raceway side  $q_{i,ehd}$  and the outer ring side  $q_{o,ehd}$  can be re-written as

$$q_{i,ehd} = K_l (\delta_i + h_{cen,i})^{1.11} \tag{3}$$

$$q_{o,ehd} = K_l (\delta_o + h_{cen,o})^{1.11} \tag{4}$$

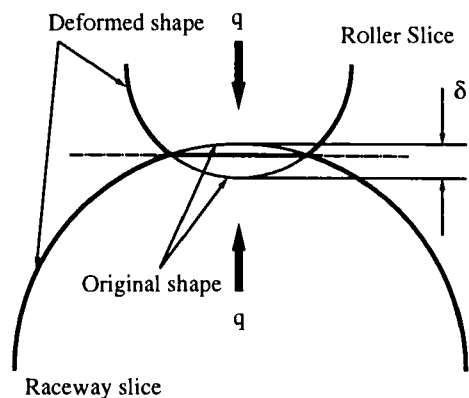


Figure 4. Contact of two slices in dry contact

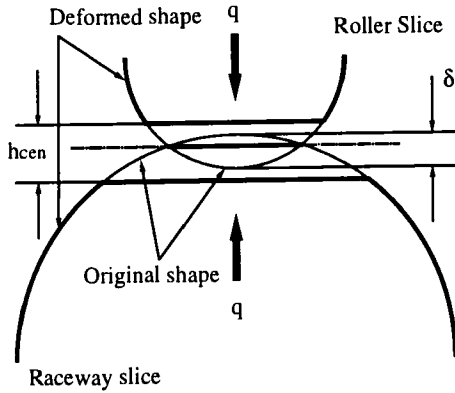


Figure 5. Contact of two slices considering EHD film

The roller end and flange contact is normally considered to be a point contact as shown in Figure 6. The model for a point contact can be obtained in the same way for the roller and raceway contact, as shown in Figure 7.

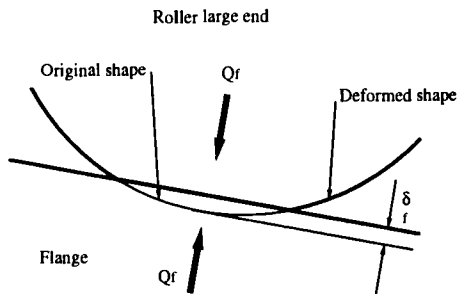


Figure 6. The roller end and flange contact in dry contact

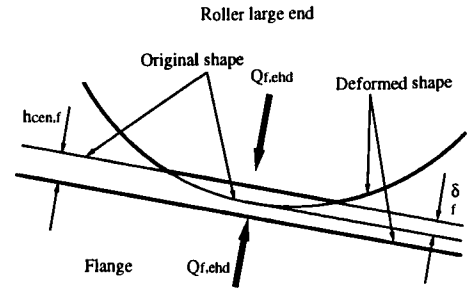


Figure 7. The roller end and flange contact considering EHD film

The normal load considering the pressure of an EHD film,  $Q_{f,ehd}$ , applied to the roller end can be written as

$$Q_{f,ehd} = K_n(\delta_f + h_{cen,f})^{1.5} \quad (5)$$

where  $K_n$  is the load-elastic deformation coefficient for a point contact and  $h_{cen,f}$  is obtained from the EHD film thickness formula by Hamrock and Dowson [4].

#### 4.2. Equilibrium equations

To evaluate roller displacements ( $u_\xi, \varphi_\eta, u_\zeta$ ) and inner ring displacements ( $\delta_x, \delta_y, \delta_z, \gamma_x, \gamma_y$ ) the following equilibrium equations are needed.

Roller equilibrium equations under EHD contacts are as follows (see Figure 8)

$$\left( \int_0^{l_a} q_{i,ehd} d\zeta_i - \int_0^{l_a} q_{o,ehd} d\zeta_o \right) \cos \epsilon + Q_{f,ehd} \sin \nu_f + F_c \cos(\gamma - \varphi_\eta) = 0 \quad (6)$$

$$- \left( \int_0^{l_a} q_{i,ehd} d\zeta_i - \int_0^{l_a} q_{o,ehd} d\zeta_o \right) \sin \epsilon + Q_{f,ehd} \cos \nu_f + F_c \sin(\gamma - \varphi_\eta) = 0 \quad (7)$$

$$\int_0^{l_a} q_{o,ehd} [(\bar{\zeta}_c - \bar{\zeta}) \cos \epsilon + \rho_r \sin \epsilon] d\zeta_o$$

$$\begin{aligned}
 & - \int_0^{l_a} q_{i,ehd} [(\bar{\zeta}_c - \bar{\zeta}) \cos \epsilon + \rho_r \sin \epsilon] d\zeta_i \\
 & + Q_{f,ehd} (R_s \cos \lambda - \bar{\zeta}_c) \sin \nu_f - M_c = 0 \quad (8)
 \end{aligned}$$

$$+ \begin{bmatrix} M_x \\ M_y \\ M_z \end{bmatrix} = \begin{bmatrix} 0 \\ 0 \\ 0 \end{bmatrix} \quad (10)$$

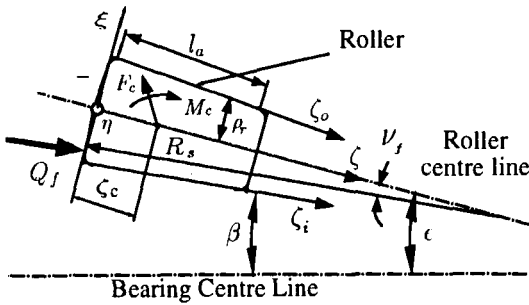


Figure 8. A roller in a tapered roller bearing

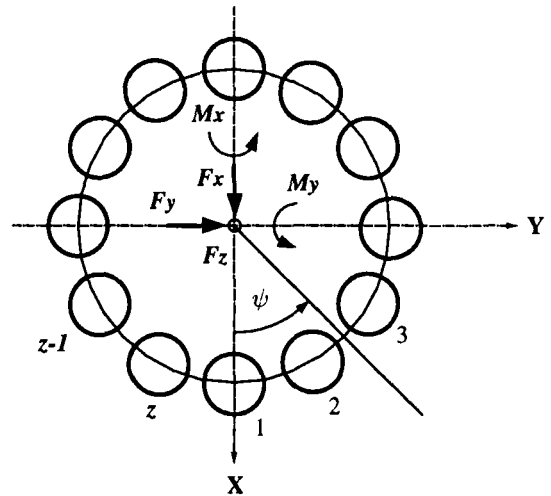


Figure 9. Angular position of roller and bearing loads

Bearing equilibrium equations under EHD contacts can be obtained by summation of the forces on all the rollers as

$$\begin{aligned}
 & \begin{bmatrix} F_x \\ F_y \\ F_z \end{bmatrix} - \sum_{j=1}^z \left\{ [\Psi][\Phi] \times \right. \\
 & \left. \begin{bmatrix} \cos \epsilon \int_0^{l_a} q_{i,ehd} d\zeta_i + Q_{f,ehd} \sin \nu_f \\ 0 \\ -\sin \epsilon \int_0^{l_a} q_{i,ehd} d\zeta_i + Q_{f,ehd} \cos \nu_f \end{bmatrix} \right\}_j \\
 & = \begin{bmatrix} 0 \\ 0 \\ 0 \end{bmatrix} \quad (9)
 \end{aligned}$$

where  $F_x$ ,  $F_y$  and  $F_z$  are the applied loads as shown in Figure 9.

The equilibrium conditions for the moments can be expressed in a similar way

$$\begin{aligned}
 & \sum_{j=1}^z \left\{ \int_0^{l_a} (r''_i)[\Psi][\Phi] \begin{bmatrix} q_{i,ehd} \cos \epsilon \\ 0 \\ -q_{i,ehd} \sin \epsilon \end{bmatrix} d\zeta_i \right. \\
 & \left. - (r''_f)[\Psi][\Phi] \begin{bmatrix} Q_{f,ehd} \sin \nu_f \\ 0 \\ Q_{f,ehd} \cos \nu_f \end{bmatrix} \right\}_j
 \end{aligned}$$

where  $M_x$  and  $M_y$  are the moments as shown in Figure 9 and  $M_z$  is the bearing driving torque when friction forces are considered. Therefore,  $M_z$  is not needed for solving the unknown bearing displacements.

These Equilibrium equations are solved with the EHD film thickness formulae by the Newton method.

### 5. Full EHD analysis of barrelled isosceles trapezium conjunctions

#### 5.1. Basic equations

The tapered roller and raceway contacts can be reduced to equivalent tapered roller and plane contacts as explained in Appendix A. Figure 10 shows the geometry of the equivalent roller and plane contact. When the taper angles of the roller

and raceway and the mean radius of the roller,  $\epsilon$ ,  $\kappa$  and  $R_a$ , are given, the taper angle and mean radius of the equivalent tapered roller can be expressed as

$$\tan \theta = \frac{\tan \epsilon \tan \kappa}{\tan \epsilon + \tan \kappa} \quad (11)$$

$$R_{ae} = \frac{\sin \theta}{\sin \epsilon} R_a \quad (12)$$

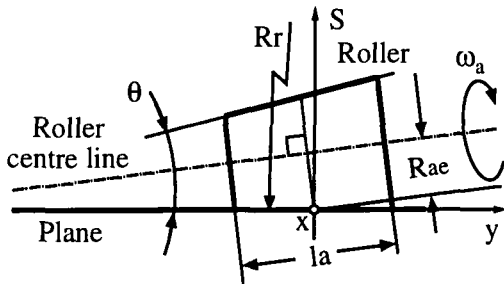


Figure 10. Equivalent tapered roller and plane

The Reynolds equation appropriate for time-invariant conditions can be expressed as follows.

$$\frac{\partial}{\partial x} \left( \frac{\rho h^3}{\eta} \frac{\partial p}{\partial x} \right) + \frac{\partial}{\partial y} \left( \frac{\rho h^3}{\eta} \frac{\partial p}{\partial y} \right) = 12 \frac{\partial(\rho h u)}{\partial x} \quad (13)$$

Substituting for  $\epsilon = \bar{\rho} H^3 / (12 \bar{\eta} U)$ , Equation 13 in non-dimensional terms becomes

$$\frac{\partial}{\partial X} \left( \epsilon \frac{\partial P}{\partial X} \right) + \frac{\partial}{\partial Y} \left( \epsilon \frac{\partial P}{\partial Y} \right) - \frac{\partial(\bar{\rho} H)}{\partial X} = 0 \quad (14)$$

The finite difference approximation is;

$$\begin{aligned} & \epsilon_{i+1/2,j} (P_{i+1,j} - P_{i,j}) / \bar{b}^2 \\ & + \epsilon_{i-1/2,j} (P_{i-1,j} - P_{i,j}) / \bar{b}^2 \\ & + \epsilon_{i,j+1/2} (P_{i,j+1} - P_{i,j}) / \bar{a}^2 \\ & + \epsilon_{i,j-1/2} (P_{i,j-1} - P_{i,j}) / \bar{a}^2 \\ & - (\bar{\rho}_{i,j} H_{i,j} - \bar{\rho}_{i-1,j} H_{i-1,j}) / \bar{b} = 0 \end{aligned} \quad (15)$$

where

$$\begin{aligned} \epsilon_{i+1/2,j} &= (\epsilon_{i+1,j} + \epsilon_{i,j}) / 2 \\ \epsilon_{i-1/2,j} &= (\epsilon_{i-1,j} + \epsilon_{i,j}) / 2 \\ \epsilon_{i,j+1/2} &= (\epsilon_{i,j+1} + \epsilon_{i,j}) / 2 \\ \epsilon_{i,j-1/2} &= (\epsilon_{i,j-1} + \epsilon_{i,j}) / 2 \end{aligned}$$

The boundary conditions for this problem are as follows.

$$\begin{aligned} P &= 0 \quad \text{at } X = -\bar{m}, -\bar{l} \leq Y \leq \bar{l} \\ P &= 0 \quad \text{at } X = \bar{n}, -\bar{l} \leq Y \leq \bar{l} \\ P &= 0 \quad \text{at } -\bar{m} \leq X \leq \bar{n}, Y = \bar{l} \\ P &= 0 \quad \text{at } -\bar{m} \leq X \leq \bar{n}, Y = -\bar{l} \\ P &= \frac{\partial P}{\partial X} = \frac{\partial P}{\partial Y} = 0 \\ &\text{at the cavitation boundary.} \end{aligned}$$

The dimensionless film thickness  $H(X, Y)$  at the point  $(X, Y)$  can be given as

$$H(X, Y) = H_{00} + \bar{\delta}(X, Y) + \bar{S}(X, Y) \quad (16)$$

The elastic deformation in a contact area is calculated as described by Hamrock and Dowson [4]. The elastic deformation can be written as

$$\bar{\delta}(i, j) = \frac{2}{\pi R_{ae}} \sum_{k=-\bar{m}}^{\bar{n}} \sum_{l=-\bar{l}}^{\bar{l}} P_{k,l} D_{i,j} \quad (17)$$

See Appendix B for  $D_{i,j}$ .

The dimensionless geometrical separation can be obtained from Equation A2 as

$$\bar{S}(X, Y) = \frac{1}{2} \cdot \frac{\cos \theta}{l_h Y \sin \theta / R_{ae} + 1} X^2 \quad (18)$$

The force equilibrium equation in dimensionless form can be expressed as

$$4 \bar{a} \bar{b} E' \sum_i \sum_j P_{i,j} - F = 0 \quad (19)$$

The mean surface velocities,  $u$  in  $x$  direction and  $v$  in the  $y$  direction, can be written as

$$u = \{u_{xy} \cos \alpha_t + (R_{ae} + y \sin \theta) \cdot \omega_a\} / 2 \quad (20)$$

$$v = (-u_{xy} \sin \alpha_t - x \sin \theta \cdot \omega_a) / 2 \quad (21)$$

where

$$u_{xy} = \frac{y_c \sin \theta + R_{ae}}{\cos \theta} \omega_a \quad (22)$$

$$\alpha_t = \tan^{-1} \left[ x \left\{ x^2 / \tan^2 \theta - (y_c + R_{ae} / \sin \theta)^2 \right\}^{1/2} \right] \quad (23)$$

$$y_c = \frac{y}{1 - \tan^4 \theta} + \frac{R_{ae} \tan^4 \theta}{\sin \theta (1 - \tan^4 \theta)} - \left\{ \frac{\tan^4 \theta (y + R_{ae} / \sin \theta)^2}{(1 - \tan^4 \theta)^2} - \frac{x^2 \tan^2 \theta}{1 - \tan^4 \theta} \right\}^{1/2} \quad (24)$$

As  $v$  is very small with small  $\sin \alpha_t$  and  $\sin \theta$ , it is assumed that  $v = 0$  in this paper. See reference [9] for more details.

The variation of density with pressure is given by Dowson and Higginson's formula [2] as follows.

$$\bar{\rho} = 1 + \frac{0.6 p_g}{1 + 1.7 p_g} \quad (25)$$

The variation of viscosity with pressure is obtained from the Roelands equation [8] and can be written as

$$\bar{\eta} = \frac{\eta}{\eta_0} = \left( \frac{\eta_\infty}{\eta_0} \right)^{1 - (1 + p/c_p)^{2.1}} \quad (26)$$

## 5.2. Iterative formula

By defining the left hand side of Equation 15 as  $\mathcal{F}_{(i,j)}$ , the iterative formula in the  $n$ -th iterations to solve  $P_{i,j}$  can be obtained as follows.

$$P_{i,j}^{(n)} = P_{i,j}^{(n-1)} - \omega \frac{\mathcal{F}_{(i,j)}^{(n-1)}}{(\partial \mathcal{F}_{(i,j)} / \partial P_{i,j})^{(n-1)}} \quad (27)$$

See Appendix C for  $\partial \mathcal{F}_{(i,j)} / \partial P_{i,j}$ .

The solutions of all  $P_{i,j}$  can be obtained by applying Equation 27 at each  $i$  and  $j$  until errors become less than specified tolerances. This iterative formula has been used with multigrid method [1,7].

During the iterations,  $H_{00}$  has to be renewed to satisfy the force equilibrium equation, but the modification should be small enough to ensure

that  $H_{(X,Y)}$  does not fall below zero. The prediction of  $H_{00}$  at the  $n$ -th iterations is given as

$$H_{00}^{(n)} = H_{00}^{(n-1)} - \omega_{H00} \frac{F - F_{EHD}}{F_{EHD}} \quad (28)$$

## 6. Results

### 6.1. Approximate fluid film model

#### 6.1.1. Calculation details

The geometrical dimensions of sample bearing and the properties of sample oil (VG 32) are shown in Tables and 1 2, respectively.

The analyses have been carried out by changing the rotational frequency of the inner raceway with other conditions fixed. The conditions for comparisons between a dry contact model and the approximate fluid film lubrication model are shown in Table 3. Also, the conditions to calculate the effect of the rotational frequency are shown in Table 4

Table 1  
Dimensions of sample bearing

|                                       |         |    |
|---------------------------------------|---------|----|
| Nominal bore diameter                 | 34.295  | mm |
| Nominal outside diameter              | 65.087  | mm |
| Nominal width                         | 18.034  | mm |
| Roller large end diameter             | 7.506   | mm |
| Nominal roller length ( $l$ )         | 12.61   | mm |
| Roller chamfer                        | 1.22    | mm |
| Roller effective length ( $l_a$ )     | 10.17   | mm |
| Crown radius of roller ( $R_r$ )      | 2680    | mm |
| Radius of roller end ( $R_s$ )        | 98.31   | mm |
| Outer raceway half angle ( $\alpha$ ) | 14.0833 | °  |
| Inner raceway half angle ( $\beta$ )  | 10.5833 | °  |
| Flange angle ( $\nu$ )                | 11.0333 | °  |
| Number of roller ( $z$ )              | 19      |    |

Type:LM48548/LM48510

Table 2  
Properties of the sample lubricant, turbine oil VG32 at 313.5 K (40°C)

|                                |       |                     |          |
|--------------------------------|-------|---------------------|----------|
| Kinematic viscosity            | 36.30 | mm <sup>2</sup> /s  | $\nu_0$  |
| Density                        | 0.851 | g/cm <sup>3</sup>   | $\rho$   |
| Viscosity                      | 30.89 | mPa·s               | $\eta_0$ |
| Pressure-viscosity coefficient | 20.0  | (GPa) <sup>-1</sup> | $\alpha$ |

Table 3  
Conditions to calculate comparisons between the dry and EHD models

|                                    |                       |            |
|------------------------------------|-----------------------|------------|
| Radial load                        | 4.5 kN                | $F_x$      |
| Axial load                         | 4.5 kN                | $F_z$      |
| Misalignment around the X axis     | 0°                    | $\gamma_x$ |
| Misalignment around the Y axis     | 0°                    | $\gamma_y$ |
| Inner raceway rotational frequency | 0 : 10000 : 24000 rpm | $N_i$      |

Table 4  
Conditions for analyses with varying rotational frequency

|                                    |  |            |
|------------------------------------|--|------------|
| Radial load                        | 4.5 kN                                   | $F_x$      |
| Axial load                         | 4.5 kN                                   | $F_z$      |
| Misalignment around the X axis     | 0°                                       | $\gamma_x$ |
| Misalignment around the Y axis     | 0°                                       | $\gamma_y$ |
| Inner raceway rotational frequency | 2000 : 4000 : 6000 :<br>8000 : 10000 rpm | $N_i$      |

6.1.2. Comparison with a dry contact model

The results for the inner, outer and flange contact loads are shown in Figures 11, 12 and 13 as a function of the roller positions respectively. The differences of these contact loads between the EHD and dry contact analyses are very small.

Therefore, the fatigue life predictions of tapered roller bearings may not be affected by considering EHD film thicknesses under those conditions as the fatigue life is calculated from the distributions of the roller loads.

The roller end and flange contact angles  $\nu_f$  shown in Figure 14 also show no difference under these conditions.

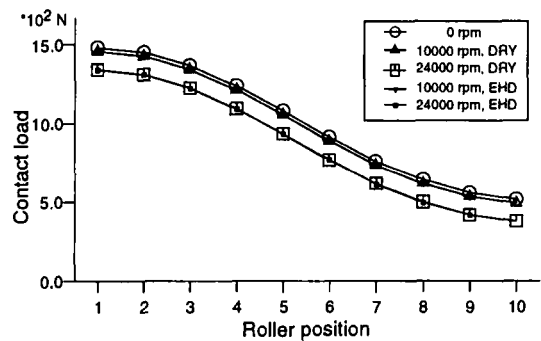


Figure 11. Inner raceway contact loads

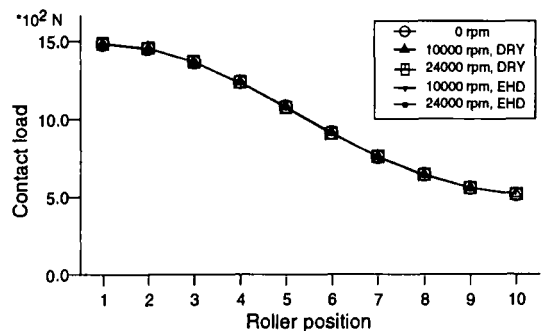


Figure 12. Outer raceway contact loads

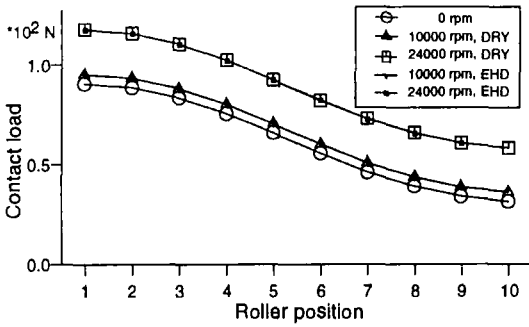


Figure 13. Flange contact loads

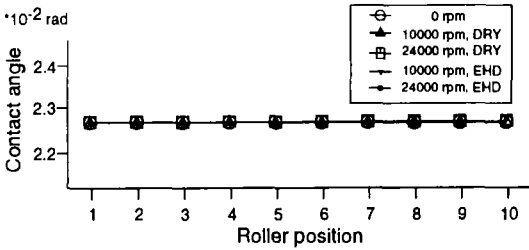


Figure 14. Roller end and flange contact angle

6.1.3. Effect of rotational frequency

The minimum film thicknesses at the inner and outer raceways and the flange are increased with increasing rotational frequency, as shown in Figures 15, 16 and 17, as expected from the EHD film thickness formulae.

The central film thicknesses at the inner and outer raceways and the flange are also increased with increasing rotational frequency, as shown in Figures 18, 19 and 20.

Figures 21 and 22 show the effects of rotational frequency on the deflections of the inner raceway. The formation of the oil film does not affect the radial deflection but the axial deflection is decreased with increases the rotational frequency.

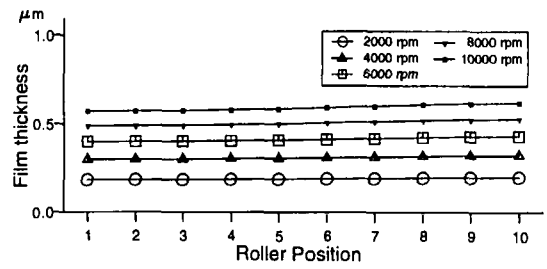


Figure 15. Effect of rotational frequency on minimum film thickness at the inner raceway

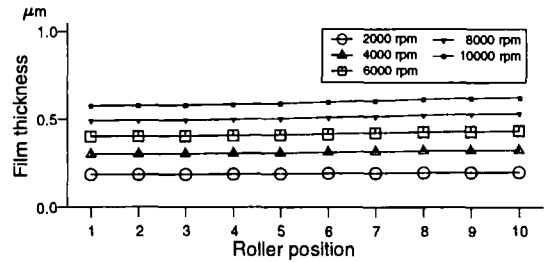


Figure 16. Effect of rotational frequency on minimum film thickness at the outer raceway

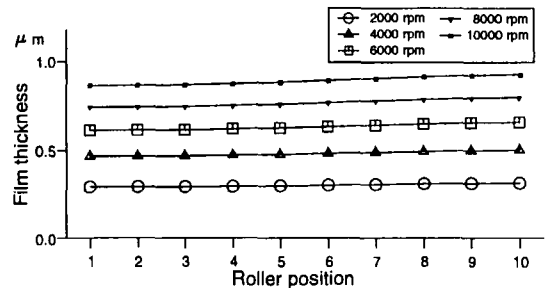


Figure 17. Effect of rotational frequency on minimum film thicknesses at the flange



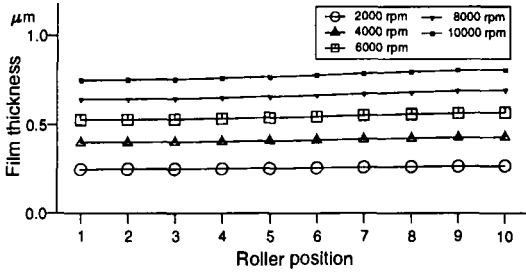


Figure 18. Effect of rotational frequency on central film thickness at the inner raceway

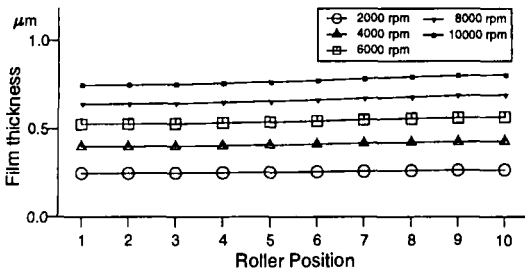


Figure 19. Effect of rotational frequency on central film thickness at the outer raceway

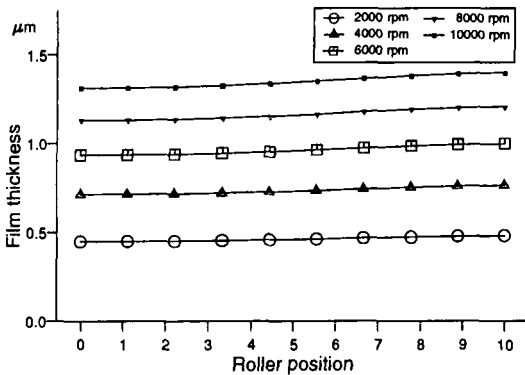


Figure 20. Effect of rotational frequency on central film thicknesses at the flange

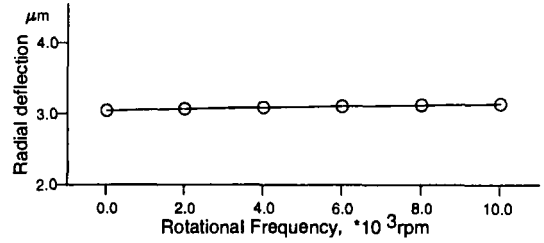


Figure 21. Effect of rotational frequency on radial deflection of the inner raceway on the EHD model

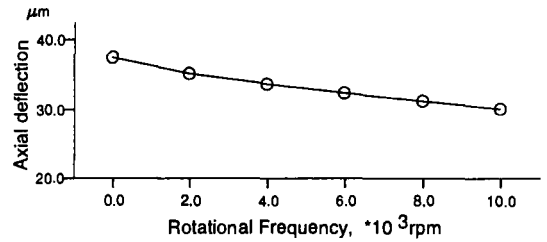


Figure 22. Effect of rotational frequency on axial deflection of the inner raceway on the EHD model

6.2. Full EHD analysis

6.2.1. Calculation details

The geometrical dimensions of a sample tapered roller are given in Table 5 and the properties of the lubricant, turbine oil VG 32, have been shown in Table 2.

Table 5  
Dimensions of sample tapered roller

|                           |       |                                     |
|---------------------------|-------|-------------------------------------|
| Centre radius             | 10.0  | mm ( $R_{ae}$ )                     |
| Half length               | 25.0  | mm ( $l_h$ )                        |
| Crown radius              | 3000  | mm ( $R_r$ )                        |
| Taper angle               | 0.349 | radians ( $\theta$ ) ( $20^\circ$ ) |
| Modulus of elasticity     | 208.0 | GPa ( $E_{a,b}$ )                   |
| Poisson's ratio           | 0.3   | ( $\nu_{a,b}$ )                     |
| Effective elastic modulus | 228.6 | GPa ( $E'$ )                        |

All results were calculated by a V-cycle full multigrid, with the coarsest grid and the finest grid of  $17 \times 17$  and  $65 \times 65$ , respectively. Domains for calculations were taken as  $-0.05 \cdot R_{ae} < X < 0.025 \cdot R_{ae}$  and  $-0.5 \cdot l_h < Y < 0.5 \cdot l_h$ .

The coefficient  $\omega$  was set to 0.1-0.8 and  $\omega_{H00}$  was fixed as  $1.0 \times 10^{-5}$ . The tolerance of the pressures and the force equilibrium equation were set to  $1.0 \times 10^{-4}$  and  $1.0 \times 10^{-2}$ , respectively. The initial values of  $P$  were all set to zero and, therefore, the initial values of  $\delta$  were all zero.

### 6.2.2. Effect of speeds

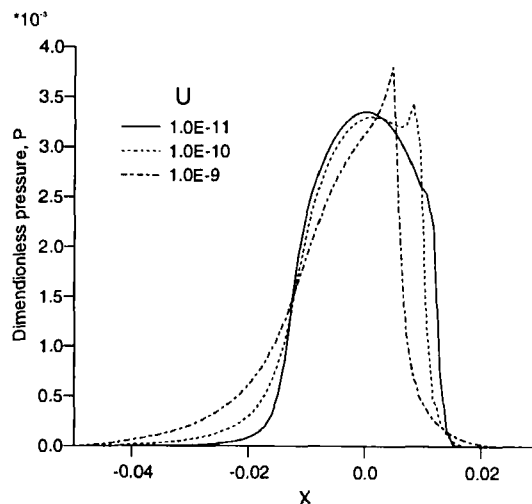
Calculations have been carried out for various  $U = 1.0 \times 10^{-11}$ ,  $1.0 \times 10^{-10}$  and  $1.0 \times 10^{-9}$  with  $W = 1.0 \times 10^{-5}$  and  $G = 4571$ .

The variations of  $P$  and  $H$  along the X-axis are shown in Figure 23. The pressure spike is clearly visible and the restriction at the outlet and the flat area at the centre are clearly seen. With increasing  $U$ , the pressure spike is appeared and the position moves toward the inlet. The film thickness is increased with increasing  $U$ , as expected.

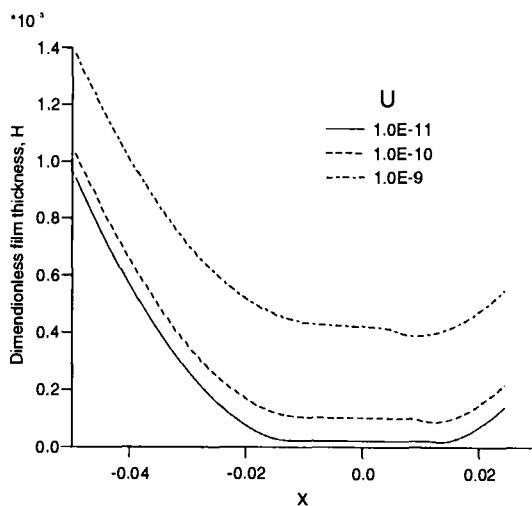
The contour plots of  $P$  and  $H$  for  $U$  are shown in Figures 24 and 25. These figures are transformed into a square, but the actual size is  $X : Y = 1 : 12$ .

With  $U$  increasing, the gradient of the inlet and outlet pressure becomes smaller and larger, respectively. At low speed, the pressure profiles are very similar to those of a Hertzian contact but they are asymmetrical due to the geometry. The asymmetry of the profiles increases with increasing of  $U$ . Although a pressure spike occurs at these conditions, it is not very clear.

The film thicknesses in the central area for various  $U$  are flat, which corresponds to the feature of the pressure distributions. The restriction appears in the flat area near the outlet and there is no horseshoe feature which would have been expected in elliptical conjunctions.

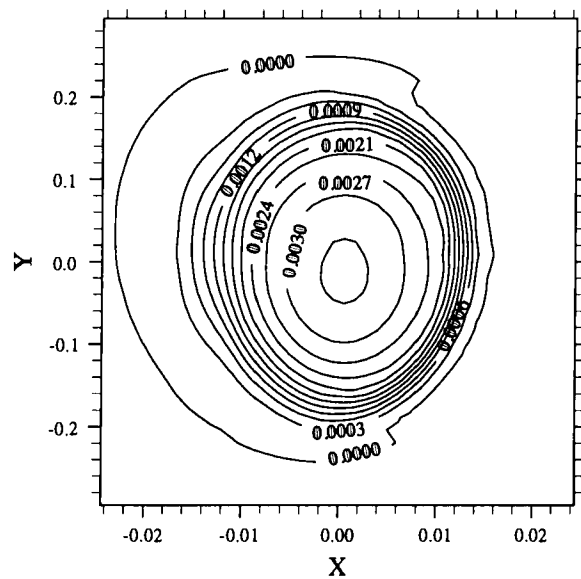
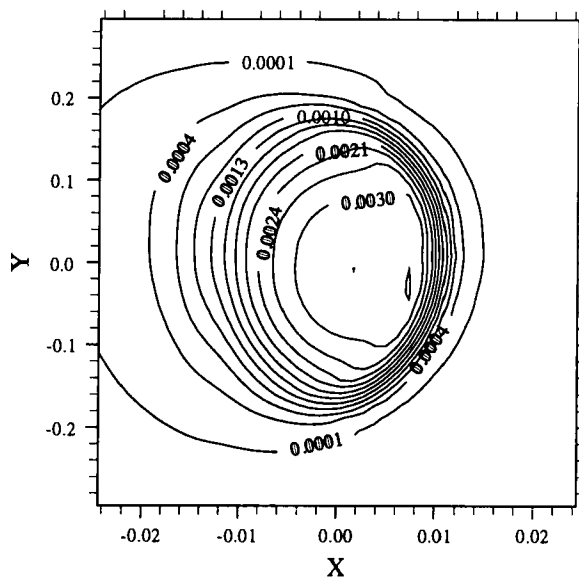
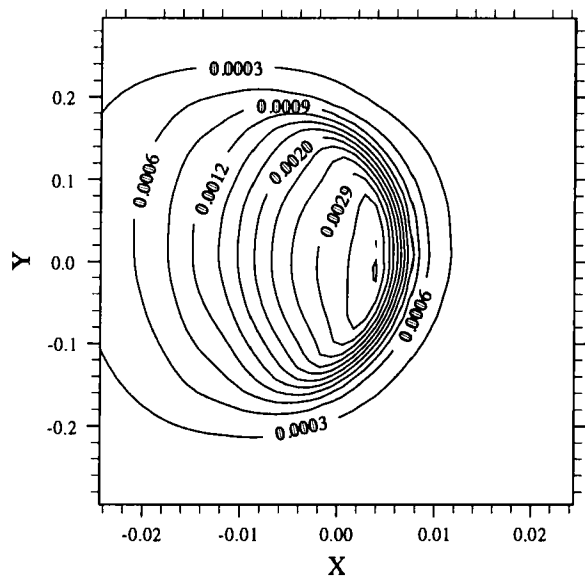
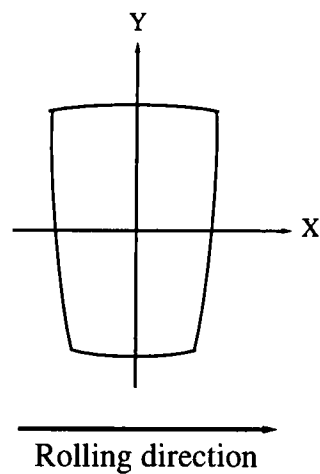


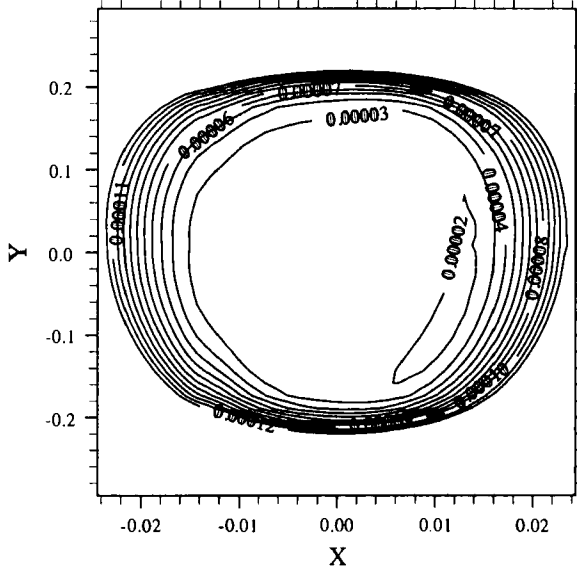
(a) dimensionless pressure



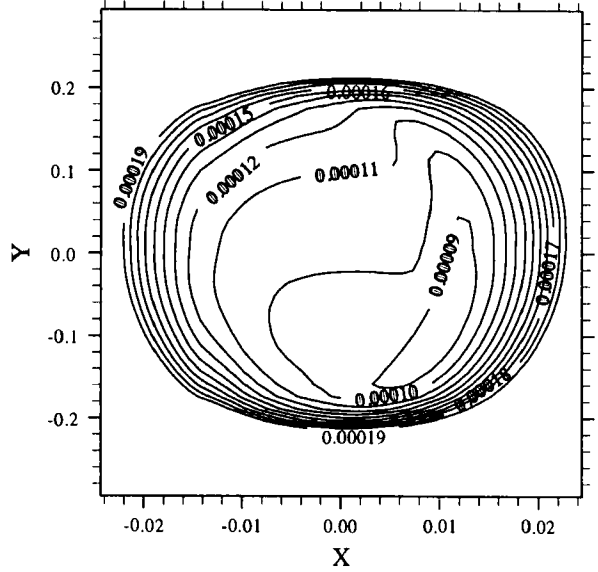
(b) dimensionless film thickness

Figure 23. Variation of pressure and film thickness for dimensionless speeds along the X-axis at  $G = 4571$  and  $W = 1.0 \times 10^{-5}$

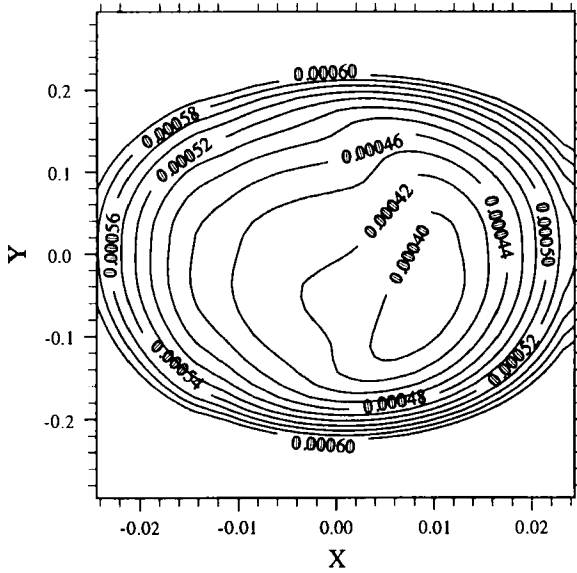
(a)  $U = 1.0 \times 10^{-11}$ (b)  $U = 1.0 \times 10^{-10}$ (c)  $U = 1.0 \times 10^{-9}$ Figure 24. Contour plots of dimensionless pressure for various  $U$  at  $G = 4571$  and  $W = 1.0 \times 10^{-5}$



(a)  $U = 1.0 \times 10^{-11}$



(b)  $U = 1.0 \times 10^{-10}$



(c)  $U = 1.0 \times 10^{-9}$

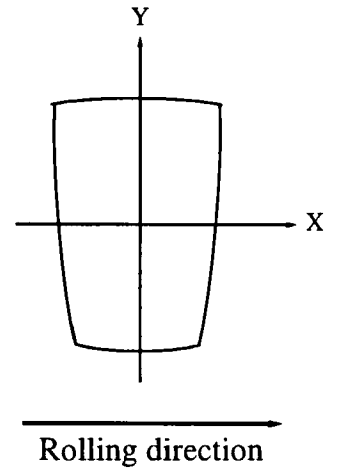


Figure 25. Contour plots of dimensionless film thickness for various  $U$  at  $G = 4571$  and  $W = 1.0 \times 10^{-5}$

### 6.2.3. Effect of loads

Calculations were also carried out for  $W = 5.0 \times 10^{-6}$ ,  $1.0 \times 10^{-5}$  and  $5.0 \times 10^{-5}$  with  $U = 1.0 \times 10^{-10}$  and  $G=4571$ .

The variation of  $P$  and  $H$  along the  $X$ -axis for each  $W$  is shown in Figure 26.

The pressurised area increases with increasing  $W$ . Also,  $P_{cen}$  is rapidly increased with increasing  $W$ . The pressure at the spike is higher than  $P_{cen}$  at lighter load but  $P_{cen}$  becomes greater than the pressure at the spike with increasing  $W$ .

The central area of the film thicknesses is flat and the flat area increases with increasing  $W$ .  $H_{cen}$  decreases very slowly with increasing  $W$  and  $H_{min}$  also behaves in a similar way.

The restriction in the film thickness moves towards the outlet with increasing  $W$  as the pressurised area is increased.

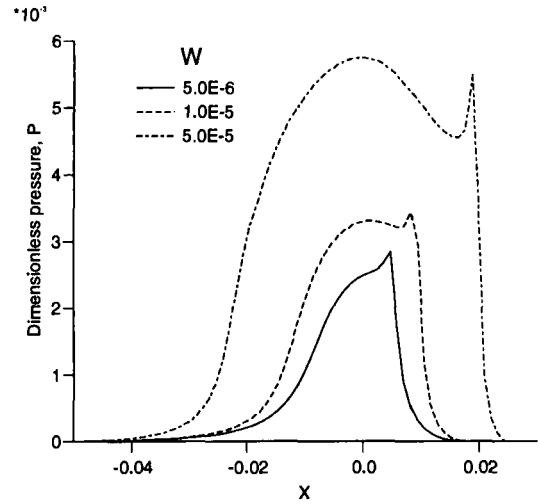
The contour plots of  $P$  and  $H$  for each condition are shown in Figures 27 and 28.

It is clear that the pressurised area increases with  $W$  as a natural result. The pressure spike occurs under all these conditions but it is only clearly visible at  $W=5.0 \times 10^{-5}$ .

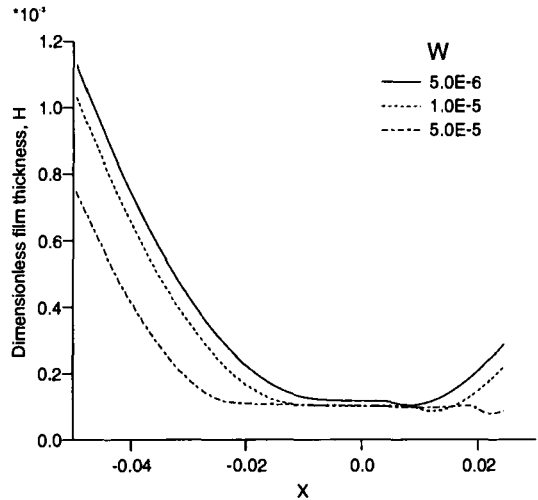
The asymmetry of the profiles, due to the geometry and heavier loads, makes them noticeable.

The central flat area, the restriction at the outlet and the asymmetry of film thickness can be recognised. The central flat area increases and the restriction at the outlet moves the outlet with increasing  $W$  as the wider area is needed to support heavier load.

Again the asymmetry of the profiles increases as  $W$  increases.

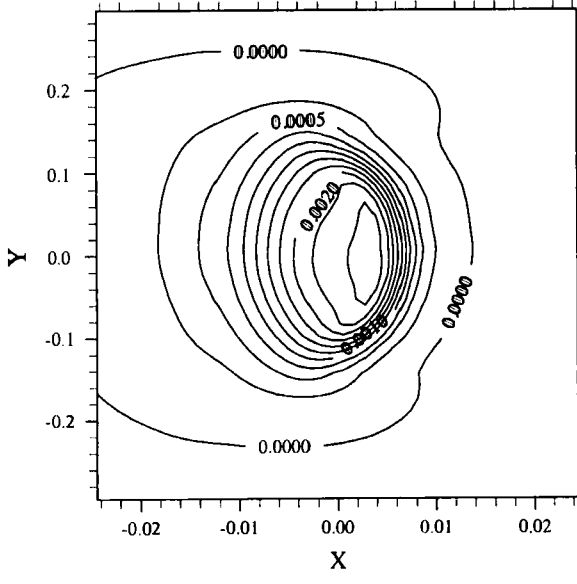


(a) dimensionless pressure

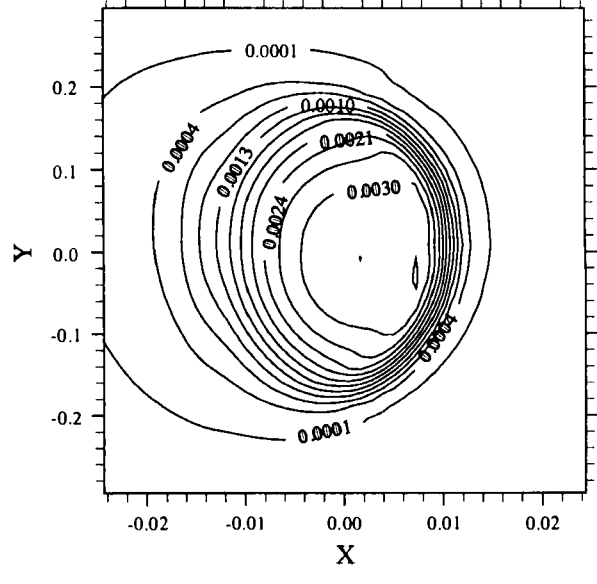


(b) dimensionless film thickness

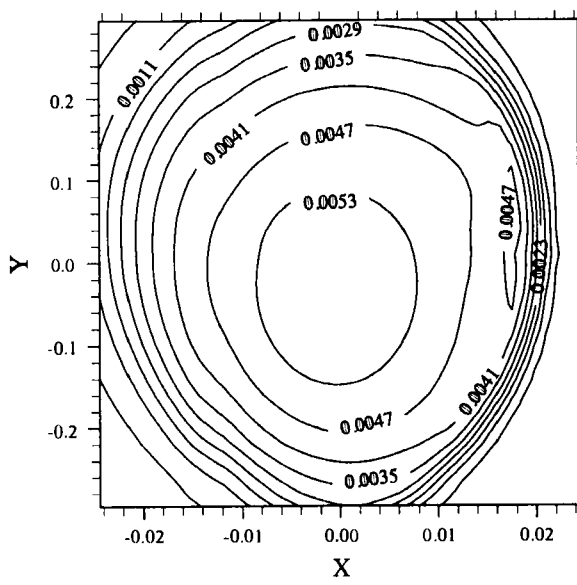
Figure 26. Variation of pressure and film thickness for dimensionless loads along the  $X$ -axis at  $G = 4571$  and  $U = 1.0 \times 10^{-10}$



(a)  $W = 5.0 \times 10^{-6}$



(b)  $W = 1.0 \times 10^{-5}$



(c)  $W = 5.0 \times 10^{-5}$

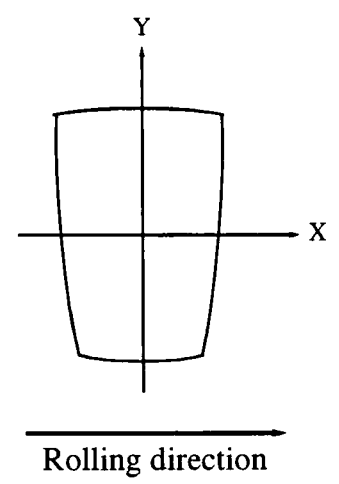
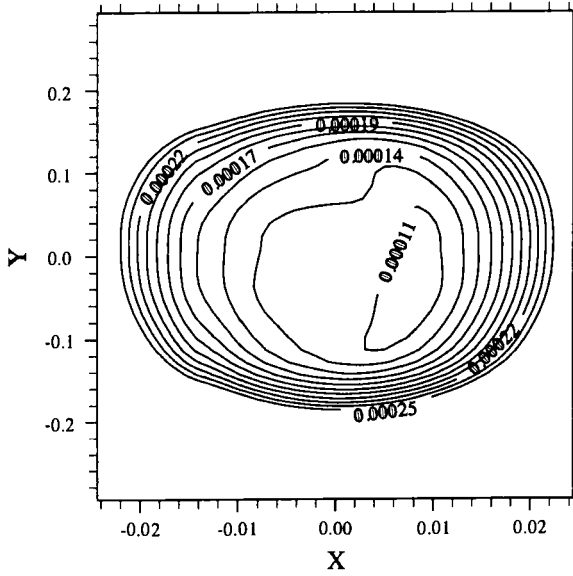
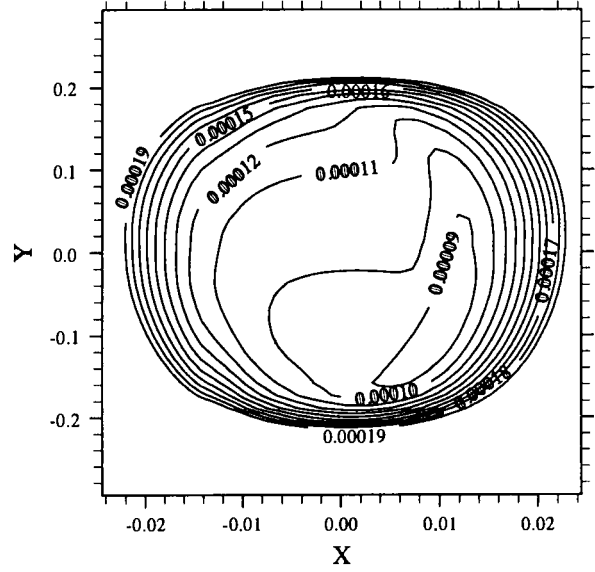


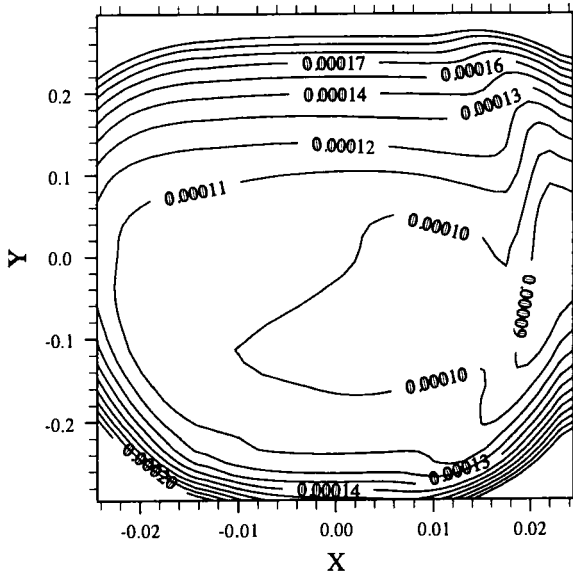
Figure 27. Contour plots of dimensionless pressure for various  $W$  at  $G = 4571$  and  $U = 1.0 \times 10^{-10}$



(a)  $W = 5.0 \times 10^{-6}$



(b)  $W = 1.0 \times 10^{-5}$



(c)  $W = 5.0 \times 10^{-5}$

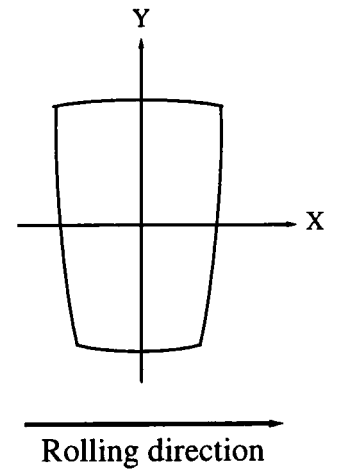


Figure 28. Contour plots of dimensionless film thickness for various  $W$  at  $G = 4571$  and  $U = 1.0 \times 10^{-10}$

### 7. Comparisons of computed film thicknesses and pressures with those predicted by simple analyses

The film thicknesses and pressures shown in the previous sections were compared with those predicted by EHD film thickness formulae (Hamrock and Dowson's formulae [4]) and by the Hertzian analysis on the assumption that the conjunction was elliptical. The values of  $U$  for the prediction were taken those at the centre of the roller.

The results of the calculations are shown in Table 6.

Table 6  
Comparisons of dimensionless film thicknesses and pressures

| $U$                             | $1.0 \times 10^{-11}$ | $1.0 \times 10^{-10}$ | $1.0 \times 10^{-9}$ |
|---------------------------------|-----------------------|-----------------------|----------------------|
| $W$                             | $1.0 \times 10^{-5}$  | $1.0 \times 10^{-5}$  | $1.0 \times 10^{-5}$ |
| $H_{min} \times 10^{-5}$        | 1.686                 | 8.199                 | 38.490               |
| $H_{min}^{(HD)} \times 10^{-5}$ | 1.731                 | 8.286                 | 39.658               |
| $H_{cen} \times 10^{-5}$        | 2.186                 | 10.134                | 42.063               |
| $H_{cen}^{(HD)} \times 10^{-5}$ | 1.940                 | 9.073                 | 49.519               |
| $P_{cen} \times 10^{-2}$        | 0.3363                | 0.3305                | 0.3196               |
| $P_h \times 10^{-2}$            | 0.3409                | 0.3409                | 0.3409               |
| $Dif_{H_{min}}$ [%]             | 4.5                   | 1.1                   | 3.0                  |
| $Dif_{H_{cen}}$ [%]             | 11.3                  | 10.5                  | 17.7                 |
| $Dif_{P_{cen}}$ [%]             | 1.4                   | 3.2                   | 6.7                  |

Table 6  
Comparisons of dimensionless film thicknesses and pressures (cont.)

| $W$                             | $5.0 \times 10^{-6}$  | $1.0 \times 10^{-5}$  | $5.0 \times 10^{-5}$  |
|---------------------------------|-----------------------|-----------------------|-----------------------|
| $U$                             | $1.0 \times 10^{-10}$ | $1.0 \times 10^{-10}$ | $1.0 \times 10^{-10}$ |
| $H_{min} \times 10^{-5}$        | 10.052                | 8.199                 | 7.881                 |
| $H_{min}^{(HD)} \times 10^{-5}$ | 8.716                 | 8.286                 | 7.367                 |
| $H_{cen} \times 10^{-5}$        | 11.727                | 10.134                | 10.223                |
| $H_{cen}^{(HD)} \times 10^{-5}$ | 9.505                 | 9.073                 | 8.146                 |
| $P_{cen} \times 10^{-2}$        | 0.2499                | 0.3305                | 0.5552                |
| $P_h \times 10^{-2}$            | 0.2706                | 0.3409                | 0.5830                |
| $Dif_{H_{min}}$ [%]             | 13.3                  | 1.1                   | 6.5                   |
| $Dif_{H_{cen}}$ [%]             | 19.0                  | 10.5                  | 20.3                  |
| $Dif_{P_{cen}}$ [%]             | 8.3                   | 3.2                   | 1.4                   |

The differences  $Dif_{H_{min}}$  at the lowest loaded condition,  $W = 5.0 \times 10^{-6}$ , is 13.3%. Other differences  $Dif_{H_{min}}$  are within the range 1.1% and 6.5%. Therefore, the agreements on  $H_{min}$  are very good except for the lowest loaded condition.

By contrast,  $Dif_{H_{cen}}$  ranges from 10.5% to 20.3%. These differences are caused by the geometry of the conjunction which causes the asymmetry of the film profiles and the pressure distributions.

The agreements of  $P_{cen}$  are very good as  $Dif_{P_{cen}}$  values are within the range 1.4% and 8.3%.

### 8. Conclusions

An approximate fluid film lubrication model based upon the application of elastohydrodynamic (EHD) film thickness formulae has been introduced to the kinematics and static loading analysis of tapered roller bearings.

Calculations to compare a dry contact model and the approximate fluid film lubrication model and to investigate the effect of rotational frequency have been carried out. As a result, it can be concluded that;

1. It has been clearly demonstrated that the EHD effect upon the load distributions, the contact angles of the roller end and flange, the contact load distributions and the radial deflections of the inner raceway for various values of rotational frequency and misalignment are very small. On the other hand, the axial deflection of the inner raceway decreases with increasing rotational frequency.
2. The minimum and central film thicknesses in all contact areas increase with increasing rotational frequency, as expected from EHD film thickness formulae.

Also, a full EHD analyses of barrelled isosceles trapezium conjunctions to simulate tapered roller and raceway contacts has been carried out. By varying the speed parameter and/or the load parameter, the distributions of pressure and film thickness have been obtained. These results can give the following conclusions.



1. Pressure and film thickness profiles are asymmetrical due to the geometry of the barrelled isosceles trapezium conjunction and the asymmetry increase with speed and load.
2. The film thickness in the central area is essentially flat and the restriction in the film thickness occurs at the outlet, but there is no horseshoe shape. Pressure spikes occur near the outlet, except at the lowest speed, as expected. The position of the restriction shifts toward the outlet with increasing load.
3. Minimum and central film thicknesses increase with speed but decrease very slowly with increasing load.
4. The minimum film thicknesses agree quite well with those predicted by the EHD film thickness formula, except at the lowest loaded condition, since the differences between those are 13.3% under the lowest loaded condition and 1.1% to 6.5% under other conditions. By contrast, the differences in the central film thickness from those predicted by the EHD film thickness formula are large (10.5% ~ 20.3%).
5. The central pressures agree very well with the Hertzian maximum pressure with differences of only 1.4% to 8.3%. Therefore, central pressures in the range of these conditions can be predicted well by the Hertzian analysis.

## REFERENCES

1. Brandt, A., "Multi-level Adapted Solutions to Boundary-Value Problems", *Math. of Comp.*, Vol.31 No.138 (1977) pp.333-390.
2. Dowson, D., and Higginson, G. R., *Elastohydrodynamic Lubrication: The Fundamentals of Roller and Gear Lubrication*, Pergamon, Oxford (1966).
3. Dowson, D., and Toyoda, S., "A Central Film Thickness Formula for Elastohydrodynamic Line Contacts", *Proc. 5th Leeds-Lyon Symp.*, (1978) pp.60-65.
4. Hamrock, B. J., and Dowson, D., "Isothermal Elastohydrodynamic Lubrication of Point Contacts, Part III - Fully Flooded Results", *Trans. ASME, Journal of Lubrication Technology*, Vol.99 (1976) pp.264-276.
5. Harris, T.A., *Rolling Bearing Analysis*, Wiley (1966).
6. Liu, J. Y., "Analysis of Tapered Roller Bearings Considering High Speed and Combined Loading", *Trans. ASME, Journal of Lubrication Technology*, Oct., Vol.98 (1976) pp.564-574.
7. Lubrecht, A. A., Venner, C. H., ten Napel, W. E. and Bosma, R., "Film Thickness Calculating in Elastohydrodynamically Lubricated Circular Contacts, Using a Multigrid Method", *Trans. ASME, Journal of Tribology*, Jul., Vol.110 (1988) pp.503-507.
8. Roelands, C. J. A., Vlugter, J. C. and Waterman, H. I., "The Viscosity - Temperature - Pressure Relationship of Lubricating Oils and Its Correlation with Chemical Constitution", *Trans. ASME, J. Basic Eng.* (1963) pp.601-610.
9. Yamashita, R., "A Study of the Elastohydrodynamic Lubrication of Tapered Roller Bearings", PhD Thesis, The University of Leeds (1996).

## Appendix A. Equivalent Tapered roller

The geometry of a tapered roller adjacent to a tapered raceway can be effectively redefined in terms of an equivalent tapered roller approaching a plane.

Consider a rigid tapered roller which just touches a rigid inner or outer raceway as shown in Figures A1 and A2. The total separation of the roller and the raceway can be given by using the parabolic approximation as

$$s'_{(x',y')} \approx \frac{1}{2y'} \left( \frac{1}{\tan \epsilon} + \frac{1}{\tan \kappa} \right) x'^2 \quad (A1)$$

where  $\epsilon$  is the taper angle of the roller and  $\kappa$  is the taper angle of the raceway,  $-\alpha$  for the outer raceway and  $\beta$  for the inner raceway as indicated in Figures A1 and A2.

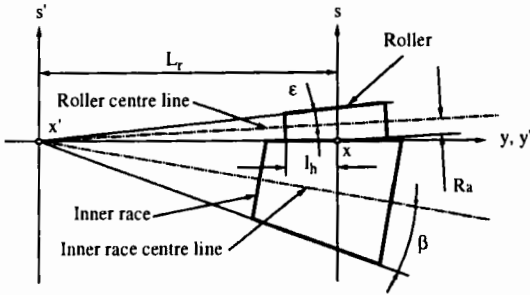


Figure A1. Tapered roller and inner raceway contact

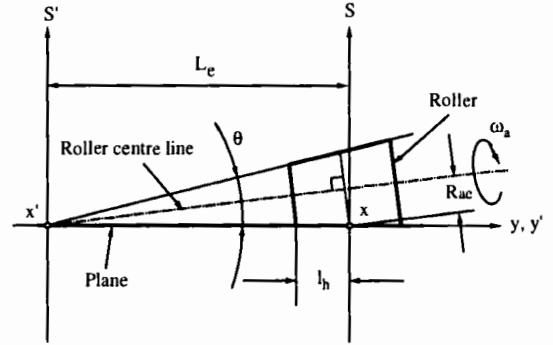


Figure A3. Equivalent tapered roller and plane

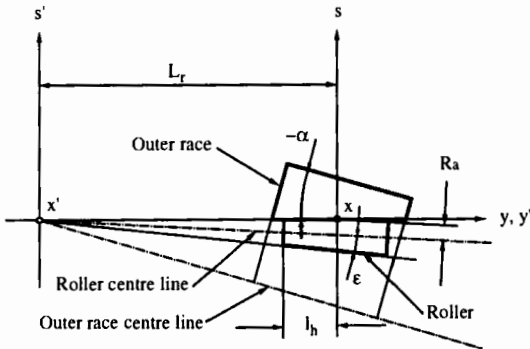


Figure A2. Tapered roller and outer raceway contact

Figure A3 shows the geometry of the tapered roller and plane contact. The geometrical separation of the equivalent tapered roller and the plane in the  $x' - y' - S'$  coordinate system with the parabolic approximation can be written as,

$$S'_{(x',y')} \approx \frac{1}{2y'} \frac{1}{\tan \theta} x'^2 \tag{A2}$$

where  $\theta$  is the taper angle of the equivalent roller as indicated in Figure A3.

The two separations,  $s'_{(x',y')}$  and  $S'_{(x',y')}$ , should be the same for a given pair of  $x'$  and  $y'$ . Therefore,  $\theta$  can be defined by using  $\epsilon$  and  $\kappa$  as follows by comparing Equations A1 and A2.

$$\tan \theta = \frac{\tan \epsilon \tan \kappa}{\tan \epsilon + \tan \kappa} \tag{A3}$$

Thus, the mean radius of the equivalent tapered roller can be expressed as

$$R_{ae} = \frac{\sin \theta}{\sin \epsilon} R_a \tag{A4}$$

**Appendix B. Influence coefficient**

The influence coefficient of elastic deformation as defined in Equation 17 is as follows.

$$\begin{aligned} D_{i^*,j^*} &= 2\bar{b}(i^* - 1) \\ &\times \ln \left[ \frac{\bar{a}(j^* - 1) + \sqrt{\bar{a}^2(j^* - 1)^2 + \bar{b}^2(i^* - 1)^2}}{\bar{a}j^* + \sqrt{\bar{a}^2j^{*2} + \bar{b}^2(i^* - 1)^2}} \right] \\ &+ 2\bar{a}(j^* - 1) \\ &\times \ln \left[ \frac{\bar{b}(i^* - 1) + \sqrt{\bar{a}^2(j^* - 1)^2 + \bar{b}^2(i^* - 1)^2}}{\bar{b}i^* + \sqrt{\bar{a}^2(j^* - 1)^2 + \bar{b}^2i^{*2}}} \right] \\ &+ 2\bar{b}i^* \ln \left[ \frac{\bar{a}j^* + \sqrt{\bar{a}^2j^{*2} + \bar{b}^2i^{*2}}}{\bar{a}(j^* - 1) + \sqrt{\bar{a}^2(j^* - 1)^2 + \bar{b}^2i^{*2}}} \right] \end{aligned}$$

$$+2\bar{a}j^* \ln \left[ \frac{\bar{b}i^* + \sqrt{\bar{a}^2 j^{*2} + \bar{b}^2 i^{*2}}}{\bar{b}(i^* - 1) + \sqrt{\bar{a}^2 j^{*2} + \bar{b}^2 (i^* - 1)^2}} \right] \quad (\text{B1})$$

### Appendix C. Partial derivative

The left hand side of Equation 15 is

$$\begin{aligned} \mathcal{F}_{(i,j)} &= \epsilon_{i+1/2,j}(P_{i+1,j} - P_{i,j})/\bar{b}^2 \\ &+ \epsilon_{i-1/2,j}(P_{i-1,j} - P_{i,j})/\bar{b}^2 \\ &+ \epsilon_{i,j+1/2}(P_{i,j+1} - P_{i,j})/\bar{a}^2 \\ &+ \epsilon_{i,j-1/2}(P_{i,j-1} - P_{i,j})/\bar{a}^2 \\ &- (\bar{\rho}_{i,j}H_{i,j} - \bar{\rho}_{i-1,j}H_{i-1,j})/\bar{b} \end{aligned} \quad (\text{C1})$$

Therefore, the partial derivative in the iterative formula, Equation 27, is as follows.

$$\begin{aligned} \frac{\partial \mathcal{F}_{(i,j)}}{\partial P_{i,j}} &= \frac{\partial \epsilon_{i+1/2,j}}{\partial P_{i,j}} \frac{P_{i+1,j}}{\bar{b}^2} - \frac{\epsilon_{i+1/2,j}}{\bar{b}^2} \\ &+ \frac{\partial \epsilon_{i-1/2,j}}{\partial P_{i,j}} \frac{P_{i-1,j}}{\bar{b}^2} - \frac{\epsilon_{i-1/2,j}}{\bar{b}^2} \\ &+ \frac{\partial \epsilon_{i,j+1/2}}{\partial P_{i,j}} \frac{P_{i,j+1}}{\bar{b}^2} - \frac{\epsilon_{i,j+1/2}}{\bar{b}^2} \\ &+ \frac{\partial \epsilon_{i,j-1/2}}{\partial P_{i,j}} \frac{P_{i,j-1}}{\bar{b}^2} - \frac{\epsilon_{i,j-1/2}}{\bar{b}^2} \\ &- \frac{\bar{\rho}_{i,j}}{\partial P_{i,j}} \frac{H_{i,j}}{\bar{b}} - \frac{H_{i,j}}{\partial P_{i,j}} \frac{\bar{\rho}_{i,j}}{\bar{b}} \\ &- \frac{H_{i-1,j}}{\partial P_{i,j}} \frac{\bar{\rho}_{i-1,j}}{\bar{b}} \end{aligned} \quad (\text{C2})$$

## ELASTOHYDRODYNAMIC LUBRICATION IN PLAIN BEARINGS

H. XU

Dept. of Advanced Engineering Analysis  
T&N Technology Ltd  
Rugby, CV22 7SA, U.K.

The development of predictive technique based upon the theory of elastohydrodynamic lubrication (EHL) has made a powerful tool available to bearing researchers and application engineers. Its application has subsequently assisted to understand many aspects of engine bearing behaviour, and effects of the interaction between a bearing and its supporting housing. The paper describes some recent work carried out in the field. Efforts are made to relate solutions from EHL analyses to the practical experiences encountered in the field. It reveals an excellent agreement between some of the experienced problems and the predictions. It shows that the structural stiffness of the bearing and housing can have a significant influence upon bearing performance. The use of the EHL predictive tool is also extended to investigate the stress state of the bearing and housing system. Results correlate qualitatively well with damage in the bearing used in a test rig.

### 1. INTRODUCTION

The progress in engine technology has led to the new generation of engines which operate at higher speeds and produce greater power output. On the other hand, the consistent drive for lighter components makes the inertial loading and substantial elastic deflection become the dominant features associated with many engine components. In particular, a connecting-rod bearing experiences a complex sequence of severe structural distortion through an engine cycle. Under such conditions, the lubrication of the crankpin and connecting rod bearing is significantly affected. In order to effectively understand the operational behaviour of the bearing, it is essential that the elastohydrodynamic lubrication (EHL) theory is adopted. An tool based on such a theory enables us to achieve much more realistic predictions of the performance of engine bearings, particularly in the case of connecting rod big ends<sup>[1,2]</sup>. As demonstrated by many researchers, the adoption of such a tool can greatly enhance our understanding of how engine bearings operate<sup>[3]</sup>.

The development of the numerical simulation tool for the elastohydrodynamic lubrication of dynamically loaded bearings has proved difficult. A significant break through was only achieved with the help of the improved computing power and the adoption of the

Newton-Raphson technique<sup>[4-10]</sup>. The methods employed an compliance matrix of the bearing surface in the analysis. Due to the non-linear nature of the problem, an iterative scheme was used to achieve converged solutions. The method developed were either finite difference or finite element based techniques. Departing from this, Kumar et al developed a modal approach to the problem<sup>[11]</sup>. By selecting a number of basic modes of the bearing surface distortion, this method used a linear combination of them to approximate the actual deformed bearing shape. By skilfully restricting the number of the modes to be used in analysis, it was possible to achieve reasonably accurate solution efficiently.

The realistic predictions of oil film pressures can be also employed in FE analyses of the bearing/housing structure. Such an analysis can provide us with more relevant information which is essential for the understanding the working mechanism of a bearing in terms of not only lubrication parameters but also its stress state and interaction with the housing. It can be expected that the use of EHL solutions will inevitable make the results of such analyses more credible.

This paper starts with a brief review of the work in the development of elastohydrodynamic lubrication of plain bearings. The progress and approaches

employed by different researchers are then summarised. This is followed by the subject of the application of the EHL tools for enhancing our understanding of the engine journal bearings. The general characteristics of EHL in engine crankpin bearings are examined. Efforts are then made to relate predictions from EHL analyses to the practical experiences associated with bearings used in both car engines and a bearing test rig. Finally the influence of structural designs of a connecting rod upon the bearing performance is studied. A comparison of solutions from two rod designs reveals exciting differences.

## 2. DEVELOPMENT IN EHL TECHNIQUES

Elastohydrodynamic lubrication is a phenomenon when the generated hydrodynamic pressure in a lubricated conjunction is so high that it causes significant elastic deformation to the bounding surfaces. This leads to a modification to the shape of the fluid film in the lubricated conjunction, which in turn modifies hydrodynamic pressure. In the case of a plain bearing, the deformation of the bearing surface

is controlled by the structure of the bearing and housing. When a plain bearing is used in an IC engine, it is subjected to a dynamic load, which repeats through each engine cycle. The understanding of such a lubrication process becomes overwhelmingly complex matter.

The development of predictive tools for the analysis of the elastohydrodynamic lubrication of dynamically loaded plain bearings had a difficult start. It was not until the middle of 80s when some successful computational packages were developed. The dramatic enhancement in the computing power and the introduction of some robust numerical algorithms contributed much to the progress. The numerical methods employed in the analysis were mainly based upon either a finite difference or a finite element approximation, with an exception of the deflection modes based method developed by Kumar et al. At an early stage of the development, short bearing and 2D structural assumptions were adopted by some group of researchers in order to derive at more rapid solutions. As faster and faster computers emerged, this concern became a less important issue. On the contrary,

Table 1.  
Brief review of the development of EHL tools

| PROGRAM SOURCE                                  | LUBRICATION THEORY | ELASTIC MODEL | INERTIAL EFFECTS | SOLUTION TECHNIQUE**                   |
|---|--------------------|---------------|------------------|--|
| Fantina, Godet & Frene, (1983)                  | Short              | 2D            | No               | Forward Iterative, FD                  |
| Oh & Goenka, (1985)                             | Finite             | 3D            | No               | Newton-Raphson, FE                     |
| Goenka & Oh, (1986)                             | Short*             | 3D            | No               | Newton-Raphson, FE                     |
| McIvor & Fenner, (1989)                         | Finite             | 3D            | No               | Newton-Raphson, FE                     |
| Xu & Smith, (1990)                              | Finite             | 2D            | No               | Newton-Raphson, FD                     |
| van der Tempel, Moes & Bosma, (1985)            | Short              | 2D            | No               | Newton-Raphson, FD                     |
| Aithen & McCallion, (1991)                      | Short*             | 2D            | Yes              | Newton-Raphson, FE                     |
| Kumar, Goenka & Booker, (1990)                  | Finite             | Modeshapes    | No               | -                                      |
| Bonneau, Guines, Frene & Toplosky, (1995)       | Finite             | 3D            | Yes              | Newton-Raphson, FE                     |
| Krasser, Laback, Loibnegger & Priebisch, (1994) | Finite             | 3D            | No               | Forward Iterative & Newton-Raphson, FD |

\*: Parabolic pressure distribution along bearing width

\*\* : FD for finite difference and FE for finite element approximations

attempts were made by some researchers to include more parameters in the study. Recently, the effects of the bearing and housing body force have been included. Table 1 gives a summary of the development work carried out by different researchers.

**3. EHL OF ENGINE PLAIN BEARINGS**

As mentioned in the introduction, an engine connecting rod bearing typically operates in an elastohydrodynamic lubrication regime. The compliance of the bearing surface around the crankpin can significantly modify the distribution of the hydrodynamic pressure. This effect is particularly pronounced when the cap half of a connecting rod bearing is loaded against the journal. Figures 1 and 2 give a comparison of the bearing clearance shape and the pressure profile along the centre line of the connecting rod bearing of a modern passenger car engine. Comparisons of solutions from EHL and rigid analyses are made in these diagrams. The inner circle represents the crankpin while the out line is a plot of the bearing surface profile along the centre line position. For EHL results, effects of the elastic deflection is also included. The dashed lines between the crankpin circle and the bearing profile line represent oil film thicknesses, while the arrowed solid lines indicate the locations and magnitudes of hydrodynamic pressures. The con-rod axis is vertical and the lower half of the plot corresponds to the cap half of the bearing.

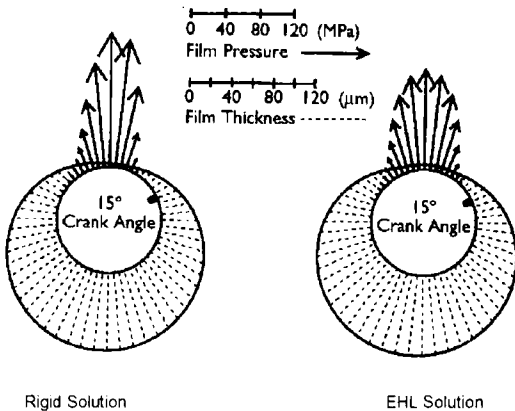


Figure 1. Oil Film pressures and Film thickness for a Connecting Rod Bearing at 4500 rev/min

In Figure 1, the results are taken from 15 degree crank angle at the maximum torque condition (4500 rev/min). The EHL effect has led to the reduction of the maximum hydrodynamic pressure from just under 200 MPa to about 135 MPa. This means that the rigid analysis overestimates the peak pressure by near 50%. When the bearing is loaded on the more flexible part of the structure, the high pressure zone spreads widely in the circumferential direction, which is in sharp contrast to the rigid solution, as shown in Figure 2. Results presented in this diagram are taken from the engine top dead centre non-firing position, which leads to the maximum loading against the cap of the connecting rod. The engine speed used in this analysis is 6500 rev/min. It is clear that the EHL effect causes the production of two high pressure peaks at the two ends of the lubrication conjunction. The actual peak hydrodynamic pressure is significantly lower than what is predicted by the rigid theory. This agrees with the general nature of EHL: the softer the materials of the bounding surfaces are, the greater reduction in the peak hydrodynamic pressure is.

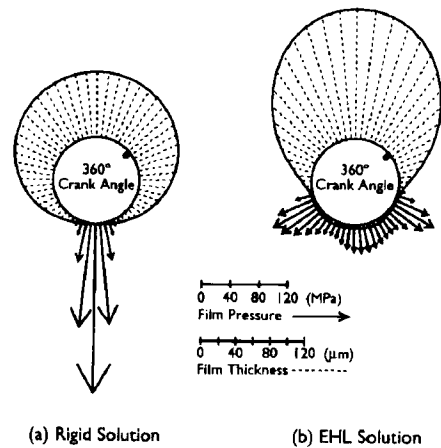


Figure 2. Oil Film Pressure and Film thickness for a Connecting rod Bearing at 6500 rev/min

The two high pressure zones can be attributed to the pinch effect when the applied load acts to stretch the bearing and housing structure. This effect is unique to the elastohydrodynamic lubrication of the cap half of connecting rod bearings. It is of interest to note that these footprints of two peak pressure regions correspond well with positions of bearing damage in some high speed engines, which include hard rubs and

fatigue cracks. Such damage has been reported on cap bearings at positions nearer to the split line than to the crown of the bearing.

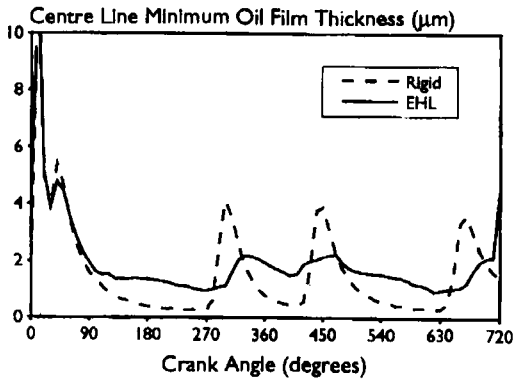


Figure 3. Minimum Oil Film Thickness for Connecting Rod Crankpin Bearing at 6500 rev/min - Rigid vs EHL

The presence of bearing surface flexibility has generally an adverse effect upon the minimum value of oil film thickness. This occurs normally at the very edge of the bearing. Indeed, this prediction is verified by the measurement of some tested bearings, which demonstrate changes in the profile of the bearing surfaces. These changes may be attributed to the wear of the bearing surface or plastic displacement of the bearing material. The maximum changes of profile are measured at the bearing edge. However, along the bearing centre line, the minimum oil film thickness is significantly increased. Figure 3 gives a comparison of the through cycle variation of the minimum oil film thicknesses along the centre line of the bearing as predicted by the EHL and rigid theories. With elastic deflection of the bearing surface, the minimum oil film thickness experiences considerably less variation.

#### 4. EHL FOR PRACTICAL PROBLEMS.

##### 4.1 High speed con-rod bearings

In figures 4 and 5, photographs of the cap bearings from two different engines are shown. Both of the bearings were damaged after running at high speed. The bearing in Figure 4 was for a passenger car engine. The problem was reported to occur when the engine was operated at over 6000 rev/min. The severe fatigue and other damage was unusual and raised concerns that the overall rigidity and the

relative differences of the rigidity at different locations may have caused adverse effects upon the hydrodynamic performance of the bearing. This led to more severe stressing of the bearing lining and resulting in premature fatigue. The bearing given in Figure 5 was from a high performance engine. Severe wear was reported when the engine speed was increased beyond 15000 rev/min. For both bearings, the damage is shown to be near to the split lines of the bearings. They are located at the leading sides of the bearings as observed from the rotating journal. Interestingly, the higher the engine speed is, the nearer the location of the damage is to the split line.

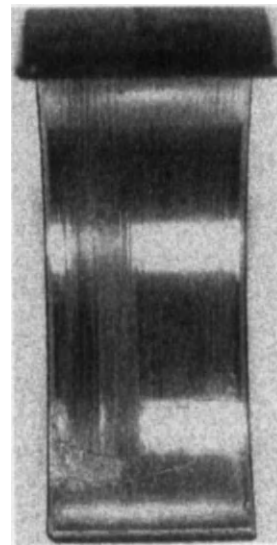


Figure 4. Fatigue/wear mark of the cap half of a con-rod bearing of a passenger car engine, after running at 6000 rpm

It is obvious that the conventional rigid bearing theories are deficient in tackling these problems. However, the pinch effect discussed in the foregoing section is able to provide us with some insight of the problem. EHL simulations were thus carried out to understand the problems.

The isometric pressure distribution of the passenger car engine connecting rod bearing is shown in Figure 6. This is at 360 degree crank angle, when the maximum inertial loading is produced. It can be seen that the two hydrodynamic pressure peaks are

generated in the regions about 20-30 degrees from the split lines. The location of the leading pressure peak correlates well with the observed position of damage in the bearing (figure 4).

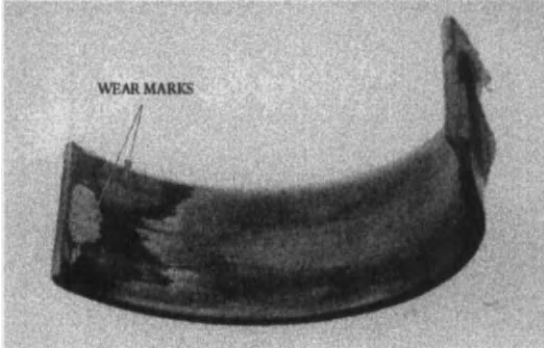


Figure 5. Wear at the leading split line area of the cap half of a high speed racing car con-rod bearing

with the peak pressure at about 10 degrees from the split. More interestingly, the pressures also vary markedly in the axial direction, with high values occur very near to the bearing edge. In the central part, the pressures are significantly lower. This effect is confirmed by the practical observation. As shown in Figure 5, the severe wear marks appear at the bearing edge, starting from the split line of the cap bearing. A careful examination of the predicted results also shows that the pressure peak on the leading side of the cap bearing is higher that on the trailing side. For the oil film, a thinner film is associated with the leading peak. This is of interest since the wear marks are located on the leading side of the bearing.

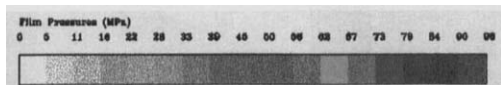
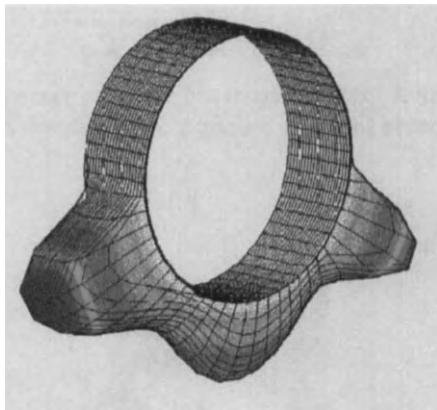


Figure 6. Isometric pressure distribution of the con-rod bearing of a passenger car engine (360 degree crank angle, 7000 rev/min)

In Figure 7, the pressure profile of a high performance engine connecting rod bearing is presented. The diagram is at 359 degree crank angle position. This is the time when the bearing experiences its maximum peak oil film pressure, and nearly the maximum inertial load. The pressure distribution is quite different from the one produced at lower engine speed (Figure 6). The peak pressure regions have shifted right to the bearing split line,

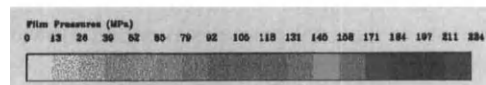
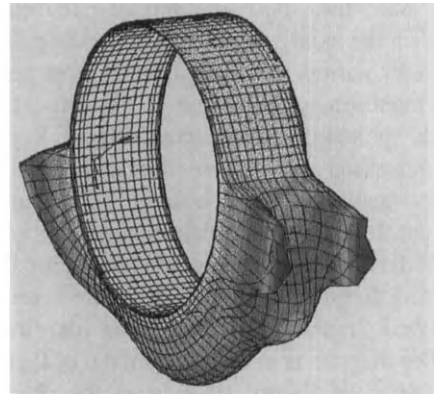


Figure 7. Isometric view of oil film pressure on the con-rod bearing of a high performance engine (Engine peed: 16000 rev/min; 359 degree crank angle)

**4.2. Sapphire seizure test**

The Sapphire bearing test rig is widely used by bearing manufacturers for bearing material development and production quality assurance. It is also used for tests for other purposes. One of them is to test the seizure resistance of bearing materials. In the test, an axial groove is machined on the lining close to the bearing crown in order to disrupt the formation of oil film and thus induce the occurrence of bearing seizure.



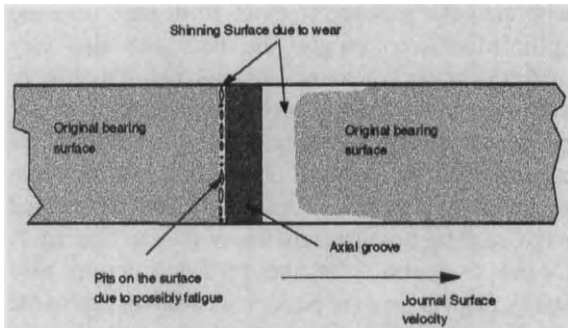


Figure 8. Surface Condition of a tested Sapphire seizure test bearing

The optical examination of the tested bearing shows that the bearing surface immediately downstream the axial groove is significantly polished. So is a very narrow band immediately upstream the groove. Interestingly, a column of pits also appears inside the polished narrow band. Figure 8 give a simple illustration of these observed features.

EHL analysis of the bearing behaviour was carried out. In Figure 9, the clearance shape and the profile of the oil film pressures along the centre line of the bearing is presented. The results are taken at 3 degree crank angle, when the peak oil film pressure peaks. The diagram is in the same format of Figures 1 and 2, with the journal rotating in the clockwise direction. The upward slot of the surface at the upper left corner of the bearing represents the axial groove. It is obvious that the oil film thickness in the region downstream to the axial groove is very thin. However, the peak oil film pressure occurs on the other side of the groove. More importantly, its magnitude is significantly higher than that produced from an ungrooved bearing. On the upstream side of the groove, the bearing surface also forms a sharp intrusion into the oil film.

All this information provides an excellent explanation of the observations. The very thin oil film thickness in the region downstream of the groove leads to severe local wear. As this happens, the bearing surface drop down and reduces the oil film thickness at the extruded tip on the upstream side of the groove, which then produce the narrow band of the polished surface (wear mark). In Figure 10, an isometric view of the pressure profile is provided in order to understand the mechanism of the pits generation. It is shown that the oil film pressure peak

is also very narrow and located right at the position where pitting occurs. Since the value of the pressure is over 500 MPa and varies through each test cycle, it can be concluded that this damage is due to the material failing under fatigue.

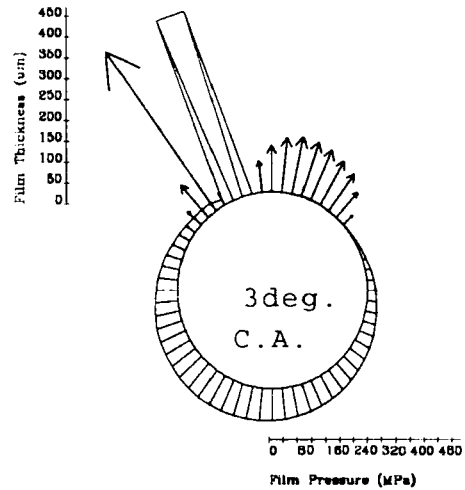


Figure 9. Oil ilm pressure and clearance shape along the centre line of the bearing at 3 degree crank angle

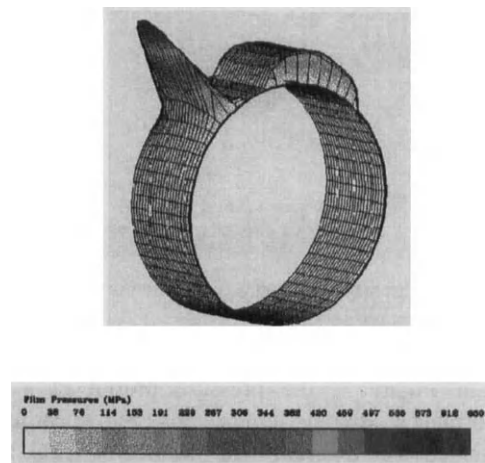


Figure 10. Isometric view of pressure profile generated on a bearing for Sapphire seizure test, (at 3 degree crank angle, 3000 rev/min)

**5. EHL RESULTS FOR STRESS ANALYSIS**

The bearing and connecting rod from the Sapphire bearing test rig has been selected for the EHL and stress analysis. In this study, efforts were made to understand the fatigue cracks generated in the tested bearings. Postmortem examination of the Sapphire tested bearings reveal generally two types of cracks: one type is a cracking face going vertically from the surface of the bearing down to the bonding layer between the bearing lining and the steel backing, the other type is along the lining/steel bonding layer, as illustrated in Figure 11. This diagram is reproduced from the measurement data. The first type of the crack does not always come to the bearing edge. These cracks are generated in the rod bearing at the location of the maximum peak pressure, in areas near to the bearing edges. In the diagram, the area enclosed by the dotted line is the cracking area in the bonding layer, while the solid line represent the vertical cracks.

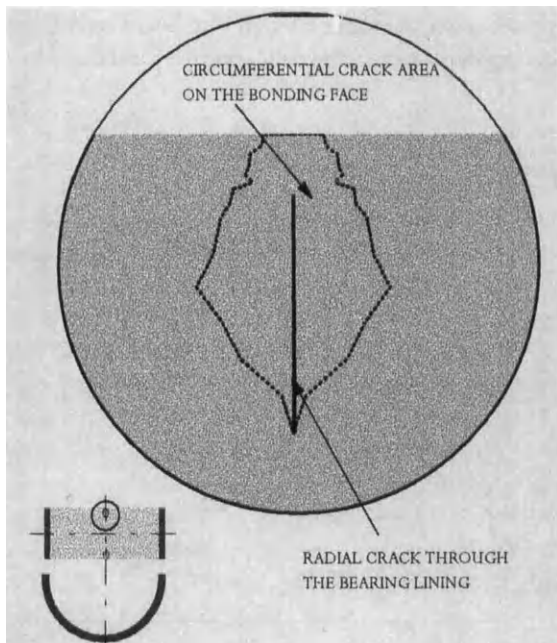


Figure 11. Cracks observed from the Sapphire tested bearings, reproduced from measured data

In a previous paper<sup>[2]</sup>, It was shown that the rigid lubrication theory can lead to the overestimation of the peak value of the hydrodynamic pressure by a factor of 5. It is therefore essential to use the realistic pressure distribution as the boundary condition for the stress analysis in order to understand the mechanism of the cracks.

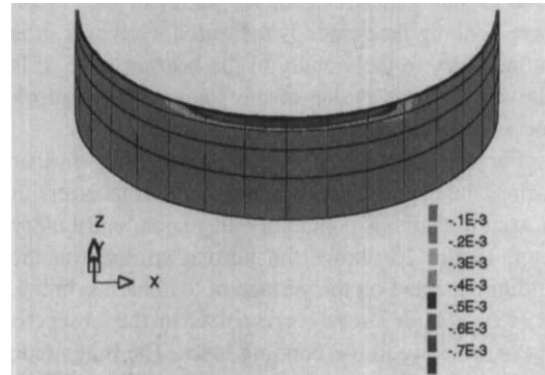


Figure 12. Contour of the shear strain on the bonding face in the axial direction.

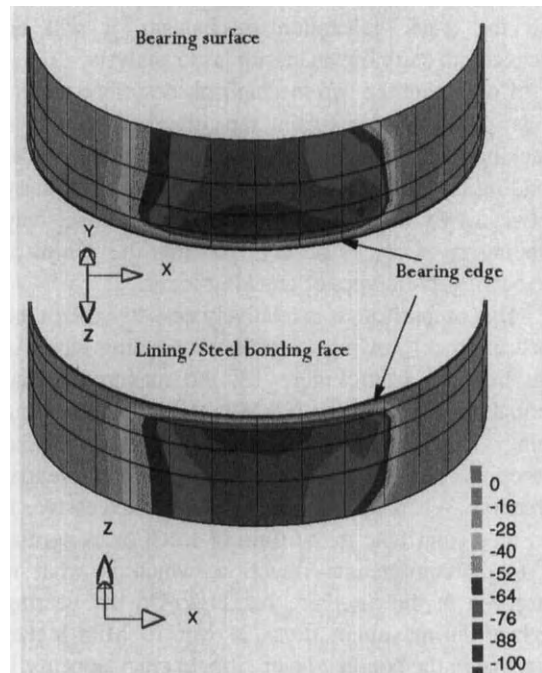


Figure 13. Contours of the normal stresses in the axial direction on the inner and bonding faces of the bearing aluminium lining

In figure 12, the shear strain contours are presented. Only the body of the bearing lining is shown in the diagram. The face exposed to the reader is the bonding face between the lining and steel. The upper side is the bearing edge while the bottom end is on the bearing centre plane. The shear component is in the axial direction on the circumferential plane. It shows a significant level of the strain in the region where bonding face crack is measured. However, it is confined only to the vicinity of the bearing edge. It is believed that this is one of the sources of the crack generation in the bonding layer.

For the cracking in the bonding layer further towards the centre of the bearing, the normal stress in the axial direction is potentially the major contributory factor. Figure 13 shows the normal stresses on the bonding face and on the surface of the bearing lining. The area of high stress corresponds to the observed area of cracking in the bonding layer. The magnitude of these stress is also much higher than the yield limit of the bearing lining material. Should the stresses induce plastic deformation of the bearing, then this may be resisted by the more rigid steel of the backing. To fully understand the resulting complex stress state and the crack generation mechanism, it will be necessary to carry out an elastoplastic analysis.

Combining the two mechanisms described above, it is possible to explain the observed areas of cracking. The kinks in the measured outline of the bonding layer cracking appears to mark the boundary between two areas. Towards the bearing edge, only bonding layer cracks occurs. Towards the centre of the bearing, both types of cracking occur.

By comparison, it is relatively easy to explain the vertical crack growing towards the bonding face. As can be seen from Figure 13, the maximum axial normal stresses are over 100 MPa through the bearing lining. This can cause compression strain in axial direction, but tensile strain in the circumferential direction. When such a strain becomes excessive, it can then contribute to the form of crack faces normal to the circumferential direction, which is what is observed in the Sapphire bearings. On the bearing surface the maximum stress is over 10 MPa higher than that in the bonding layer. Should crack appears, it is reasonable therefore to expected that it will start from the bearing surface and grow downward into the bearing lining, which is what was observed in the tested bearing.

## 6. EFFECTS OF STRUCTURAL DESIGNS

Elastohydrodynamic lubrication takes into account the influence of the compliance of bounding surfaces of the lubricated conjunction. In the case of engine bearing lubrication, the compliance of the bounding surfaces are controlled by the bearing and housing designs. We thus can employ the EHL predictive tool to enhance our knowledge of the engine bearing operating mechanism as a part of a crankshaft/connecting-rod system.

To assess the influence of the big end housing structure of a connecting rod upon the bearing performance, the high performance engine reported earlier was selected. Two different rod designs were used in the analyses: one has the shape of the "I" section rod as widely used in the industry and another has the "I" section of the rod turned by 90 degree, namely the Carillo rod. The structures of the big-end housings were designed accordingly, with a more flexible material used for the second rod. The structural compliance of the two rods are therefore significantly different. For the convenience of presentation, the former design is to be denoted as the conventional rod and the latter one the Carillo rod.

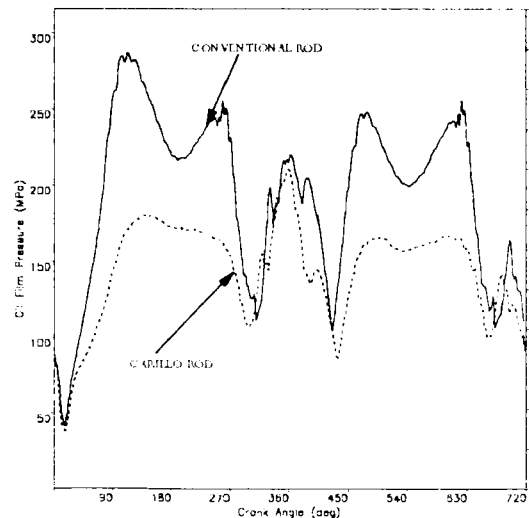


Figure 14. Effects of con-rod designs upon the through cycle oil film pressures  
(Con-rod bearing of a high speed engine, 16000 rpm,  
In the analysis, conv-rod 48x3, carillo rod 48x4)

Simulations of the elastohydrodynamic lubrication of the bearing with the two rod designs were carried out. A brief comparison has been made of some of the key performance parameters. The results are based on the engine running condition of 16000 rev/min at full load.

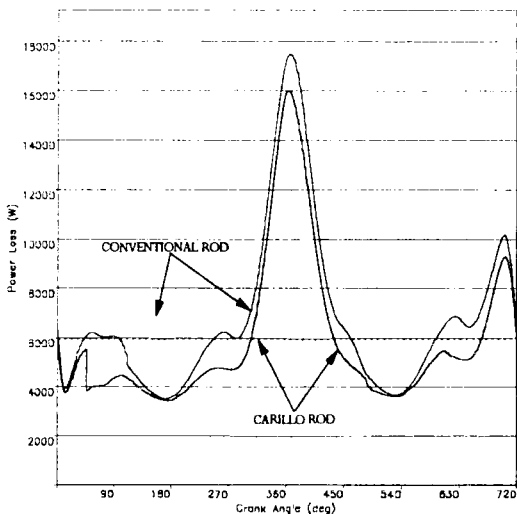


Figure 15. Effects of con-rod designs upon the through cycle bearing power losses (bearing of a high speed engine, 16000 rpm, In the analysis, conv-rod 48x3, carillo rod 48x4)

The influence of the structural compliance of the bearing housing upon the bearing performance is shown to be pronounced. In Figure 14, the through cycle variation of the peak pressures are presented. The bearing fitted into the conventional rod is shown to endure much higher hydrodynamic pressures. The difference is particularly significant when the bearing load is perpendicular to the rod axis. Through most of the engine cycle, the pressure peak is shown to be about 50% higher. This is also reflected in the minimum oil film thickness values. As mentioned earlier, the minimum oil film thickness is generally located at the bearing edge. When the bearing is loaded in the lateral direction, the Carillo rod gives rise to a substantial reduction in the minimum film thickness. This effect is also contributed by the fact that the big-end housing of the Carillo rod has a stiffer support at the edge. Interestingly, this stiffness profile makes the variation of the oil film into a more concave shape. In terms of the frictional power loss, the bearing backed by the conventional rod is predicted to

induce consistently high values, as shown in Figure 15. The through cycle average of the power loss from the bearing is about 15% higher than that from the bearing supported by the Carillo rod.

## 7. CONCLUSIONS

In this keynote paper, I have attempted to highlight some of the development in the area of elastohydrodynamic lubrication in plain bearings, in particular, in the areas associated with the application of EHL analyses to problems encountered in engineering practice. The results have clearly demonstrated the power of such a tool for providing an insight of bearing behaviour and influence of bearing and housing structure designs upon the bearing performance.

Many components of the modern engines are designed to operate under severe elastic deformation. In the case of engine bearings, this can have a significant influence upon their operational performance. EHL effects can generally lead to a reduction in the maximum oil film pressure. Although it also gives rise to an increase in the minimum oil film thickness along the centre line of the bearing, the abrupt drop of oil pressure to the ambient at the bearing edge lead to a reduction in the local oil film thickness. Bearing surfaces in the axial direction become concave.

When a bearing is loaded on the cap half, a pinch effect is observed, which is characterised by two pressure peaks near to the split line of the bearing. The location of the pressure peaks move further apart as the engine speed is increased. The oil films at the location of these peaks are thin, which are in good agreement with the bearing damage observed in some engines.

The use of EHL solutions enables us to carry out more meaningful stress analyses, and thus better understanding of the bearing behaviour and life in its working environment. Such an analysis of a Sapphire tested bearing provided much insight into the fatigue cracking in the bearing lining.

The structural compliance of the connecting rod has a significant impact upon the performance of the bearing it supports. The bearing supported by the Carillo format of rod design with a more flexible structure performs much better than that supported by a conventional connecting rod.

## REFERENCES:

1. Goenka, P K and Oh, K P, 'An Optimum Connecting Rod Design Study - A Lubrication Viewpoint', Trans ASME, J. Tribology, Vol 108, 1986, p487.
2. Fenner, D N, McIvor, Conway-Jones J D C, J M and Xu, H, 'The Effect of Compliance of Peak Oil Film Pressure in Connecting Rod Bearings', Proceedings for 19th Leeds-Lyon Symposium on Tribology, Leeds, 1992, p149.
3. Xu, H, 'Effects of EHD Contacts Upon the Bearing and Housing Behaviour', SAE Technical Paper 960987. 1996.
4. Oh, K.P. and Goenka, P.K., 'The Elastohydrodynamic Solution of Journal Bearings under Dynamic Loading', ASME J. Tribology, Vol. 107, 1985, p389.
5. McIvor, J.D.C. and Fenner, D.N., 'Finite Element Analysis of Dynamically Loaded Flexible Journal Bearings: A Fast Newton-Raphson Method', ASME J. Tribology, Vol. 111, 1989 p597.
6. Xu, H. and Smith, E.H., 'A New Approach to the Solution of Elastohydrodynamic Lubrication of Crankshaft Bearings', Proc. ImechE., Vol. 204, 1990, p187.
7. van der Tempel, L., Moes, H. and Bosma, R., 'Numerical Simulation of Dynamically Loaded Flexible Short Journal Bearings', ASME J. Tribology, Vol. 107, 1985, p396.
8. Aithen, M.B. and McCallion, H., 'Elastohydrodynamic Lubrication of Big-End Bearings, Part 1: Theory', Proc. ImechE., Part C, Vol. 205, 1991, p99.
9. Bonneau, D., Guines, D., Frene, J. and Toplosky, J. 'EHD Analysis, Including Structural Inertia Effects and a Mass Conserving Cavitation Model', ASME J. Tribology, vol. 117, 1995, p540.
10. Krasser, J., Laback, O., Loibnegger, B. and Pribsch, H.H., 'Anwendung eines elastohydrodynamischen Verfahrens zur Berechnung von Kurbeltriebslagern', MTZ Motorentechnische Zeitschrift, 55. Jhg (1994), pp. 656-663.
11. Kumar, A., Goenka, P.K. and Booker, J.F., 'Modal Analysis of Elastohydrodynamic Lubrication: A Connecting rod Application', ASME J. Tribology, Vol. 112, 1990, p524

## Simulation of the Oil Film Behaviour in Elastic Engine Bearings Considering Pressure and Temperature Dependent Oil Viscosity

H.H. Priebsch and J. Krasser

AVL List GmbH,  
Kleiststraße 48, A-8020 Graz, Austria

Design analyses of crank train bearings of reciprocating engines are strongly influenced by the oil parameters considered in the simulation models. Therefore, an in-depth study of the combined effects of pressure and temperature impacts on the viscosity of the oil appears to be vital to the validation of traditional elastohydrodynamic (EHD) slider bearing analyses.

For this purpose a comprehensive thermo-elastohydrodynamic (TEHD) calculation method was developed and implemented into a computer code.

The presented results show the quantitative effects of pressure and temperature dependent oil viscosity and density on both the oil film thickness and the oil film pressure. Furthermore, results of the heat flow, shell and oil film temperatures of typical crankshaft bearings under loading conditions in fired Diesel and gasoline engines are discussed.

### 1. INTRODUCTION

Among engine parts, the reliability of crank train bearings has always been of central importance. Nowadays refined simulation tools for the analysis of engine parts are increasingly requested by the design engineers for two reasons:

- In order to reduce development times of new engines by extended prediction and optimization in the design stage.
- Traditional calculation methods show increasingly unrealistic results for bearing parameters on one hand (e.g. minimum oil film thickness) and often can not explain bearing failures on the other.

The reason is that because of the optimization strategies (e.g. low friction, low noise) and because of increased specific loads additional physical effects have become important for the simulation of the bearing behaviour in the running engine. The most important additional effects to be considered by an extended bearing simulation tool are: Structural elasticity and dynamics, energy

flow and influence of temperature and pressure upon oil viscosity.

Latest publications show, that the complex effect of the interaction of structure elasticity and oil film pressure build up can be analyzed by efficient software already [e.g. 1].

Basic analyses for a thermo-elastohydrodynamic (TEHD) theory were carried out in [2] for an idealized 2-D problem. In [3] an extended model for the cavitation region is introduced and comparisons to measured results are discussed. Many other authors discuss methods and solutions for the TEHD problem but do not consider the unsteady load situation of an engine bearing. Although, the unsteady loading is taken into account in [4] and [5], the authors assume major simplifications for the pressure and temperature distributions in [4] whereas the authors in [5] use rigid structures in their analyses. As the need for the consideration of the interactions between dynamic bearing loads, heat flow and structure deformations are evident from literature, AVL have carried

out the development of a respective simulation software. In [6] first results of the application of this software are shown for a Diesel engine bearing. The theoretical background and further application of the AVL simulation tool CBTEHD for Diesel and gasoline engine bearings are described in this paper. The results quantify the effects of pressure and temperature influences upon the viscosity of the bearing oil film.

## 2. GOVERNING EQUATIONS

### 2.1. Generalized Reynolds equation

The Reynolds equation has to be generalized in order to consider variable oil viscosity and density in the bearing. The most general case, which is treated here, allows for viscosity and density varying in all three dimensions of space and in time. Such variations may be caused e.g. by a 3-D temperature distribution in combination with a 2-D pressure distribution or by non-Newtonian effects in the oil film. This work focuses on the temperature effects while the discussion of non-Newtonian behaviour in crank train bearings is left to future investigations.

For main bearings (i.e. fixed shell) the generalized Reynolds equations reads

$$-\frac{\partial}{\partial x} \left( \theta \alpha^2 \frac{\partial p}{\partial x} \right) - \frac{\partial}{\partial z} \left( \theta \alpha^2 \frac{\partial p}{\partial z} \right) + \frac{\partial}{\partial x} (\theta \beta) + \frac{\partial}{\partial z} (\theta \gamma) = 0$$

where

$$-\alpha^2 := h^3 \int_0^1 \bar{\rho} \cdot \left( \int_0^1 \frac{y'}{\bar{\eta}'} dy' - \frac{\int_0^1 \frac{y'}{\bar{\eta}'} dy'}{\int_0^1 \frac{1}{\bar{\eta}'} dy'} \cdot \int_0^1 \frac{1}{\bar{\eta}'} dy' \right) d\bar{y}$$

$$\beta := h \cdot U \int_0^1 \bar{\rho} \cdot \left( 1 - \frac{\int_0^1 \frac{1}{\bar{\eta}'} dy'}{\int_0^1 \frac{1}{\bar{\eta}'} dy'} \right) d\bar{y}$$

$$\gamma := h \cdot \int_0^1 \bar{\rho} d\bar{y}$$

Together with the conditions for the lubrication (L) and cavitation (C) regions,

$$p > p_c \wedge \theta = 1 \Leftrightarrow (x, z) \in L$$

$$p = p_c \wedge \theta \leq 1 \Leftrightarrow (x, z) \in C,$$

this equation determines the pressure  $p$  and the fill factor  $\theta$ . The latter serves to model cavitation effects and is defined as the fraction of volume filled with oil at each location in the bearing [7].

The numerical solution of the Reynolds equation is based on the finite volume method [6,8].

### 2.2. Energy equation of the oil film

The energy equation of the oil film,

$$\begin{aligned} & \rho^c p \left\{ \frac{\partial \bar{T}}{\partial t} + \bar{u} \frac{\partial \bar{T}}{\partial x} + \bar{w} \frac{\partial \bar{T}}{\partial z} \right. \\ & \left. + \frac{1}{h} \left[ \bar{v} - \bar{y} \cdot \left( \frac{\partial h}{\partial x} + \bar{u} \frac{\partial h}{\partial x} + \bar{w} \frac{\partial h}{\partial z} \right) \right] \frac{\partial \bar{T}}{\partial y} \right\} \\ & + \frac{\bar{T}}{\bar{\rho}} \frac{\partial \bar{\rho}}{\partial T} \left( \frac{\partial p}{\partial x} + \bar{u} \frac{\partial p}{\partial x} + \bar{w} \frac{\partial p}{\partial z} \right) - \frac{\kappa}{h^2} \frac{\partial^2 \bar{T}}{\partial y^2} \\ & = \frac{\bar{\eta}}{h^2} \left[ \left( \frac{\partial \bar{u}}{\partial y} \right)^2 + \left( \frac{\partial \bar{w}}{\partial y} \right)^2 \right] \end{aligned}$$

considers heat convection in all three dimensions, heat conduction in radial direction, compression and viscous heating. The introduction of the relative clearance

height  $\bar{y} := \frac{y}{h}$  as independent variable in radial direction facilitates the numerical solution. In the cavitation region (C) the thermal conductivity ( $\kappa$ ) and the viscosity ( $\eta$ ) are assumed to scale with the fill factor ( $\theta$ ), which results in an unchanged energy equation. In fact, due to the rather large clearance in the cavitation region there will

be little conduction and viscous heating, anyway.

The numerical solution of this equation is based on finite differences.

### 2.3. Energy equation of the shell

For the thermal analysis the actual geometry of the shell is neglected. The shell is modeled as a cylinder. The boundary conditions for the heat equation

$$\rho_B c_B \cdot \frac{\partial T_B}{\partial t} - \kappa_B \cdot \Delta T_B = 0$$

are the continuity of temperature and heat flow at the inner surface (heading to the oil film) and Biot boundary conditions

$$\frac{\partial T_B}{\partial n} + Bi \cdot (T_B - T_a) = 0$$

at the outer surfaces.

Discretization is done by means of finite differences.

Theoretical investigations [5,8] as well as numerical simulations show, that the shell temperature exhibits only slight variations in time. Therefore, a transient calculation, as indicated by the heat equation, requires a rather long simulation time (e.g. 50 engine cycles in [5]) if the estimates for the shell temperature distribution is poor at the beginning of the calculation.

To reduce the amount of simulation time the following procedure was developed: During the first cycle the specific heat of the shell is multiplied with a factor of  $10^{-4}$  to  $10^{-3}$ . After each cycle the shell temperature is set to its average over the preceding cycle and the factor for the specific heat is increased until, after 2-3 cycles, it has been set to 1. After about 5 cycles the shell temperature will reach its almost steady state.

### 2.4. Energy equation of the oil groove

As the Reynolds equation does not provide any information about the oil flow within the oil groove, a spatially constant oil

temperature in the groove is assumed. It is determined by use of the heat balance [6,8]

$$\begin{aligned} \rho c_p V_S \frac{\partial T_S}{\partial t} = \\ = \int_S \left( \kappa_B \frac{\partial T_B}{\partial r} - \kappa \frac{\partial T}{\partial y} \right) dS + \rho c_p \Phi_i (T_{S,0} - T_S) \end{aligned}$$

### 2.5. Journal temperature

The journal temperature is assumed constant and has to be supplied to the calculation procedure. If an estimation is used for the calculation, it can be checked by evaluating the amount of dissipation energy leaving the bearing through the journal. Because of symmetry considerations only a small fraction of up to 10% of the total heat generated is expected to be conducted through the journal (and the whole crankshaft).

### 2.6. Elasticity equation

The consideration of the deformation of the bearing shell due to the oil film pressure requires a Finite Element model of the bearing shell (Fig. 1).

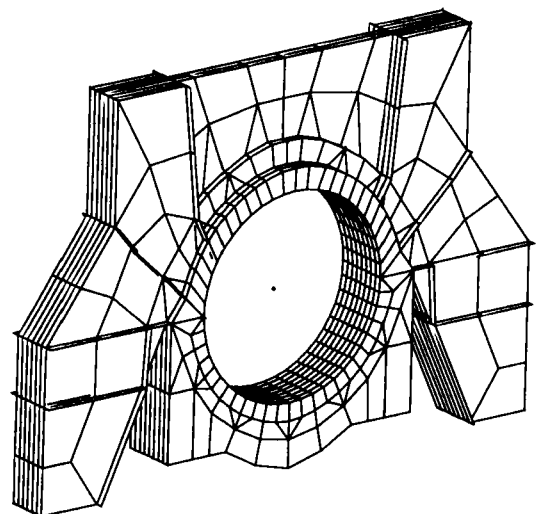


Fig. 1 Finite Element model of a main bearing



This model is reduced to the radial degrees of freedom of the nodes lying at the inner surface by static condensation. With the resulting mass, damping and stiffness matrices the elasticity equation for the bearing shell is

$$\mathbf{M} \ddot{\mathbf{u}}_B + \mathbf{D} \dot{\mathbf{u}}_B + \mathbf{K} \mathbf{u}_B = \mathbf{f}.$$

This equation is solved by means of an implicit time integration method.

**2.7. Equation of motion of the journal**

The journal is modeled as a single mass yielding as equation of motion

$$m \ddot{\mathbf{x}}_J = \mathbf{f}_J + \mathbf{f}_A,$$

the equilibrium of inertia, oil film and outer forces. The latter are an input to the calculation procedure.

**2.8. Viscosity**

Oil viscosity is regarded as a function of both local oil pressure and local oil temperature following Rodermund's formula

$$\eta(p, T) = A \cdot \exp \left[ \frac{B}{C + T} \left( 1 + \frac{p}{F} \right)^{D+E} \frac{B}{C+T} \right].$$

For the parameters A through F of an SAE 10W-40 oil see Table 1.

**2.9. Density**

For the dependence of oil density on pressure and temperature the Dowson-Higginson formula,

$$\rho(p, T) = \rho_0 \cdot \left( 1 + \frac{f_1 \cdot p}{1 + f_2 \cdot p} \right) \cdot [1 - f_3 \cdot (T - T_0)]$$

with  $f_1 = 0.6E-9 \text{ Pa}^{-1}$ ,  $f_2 = 1.7E-9 \text{ Pa}^{-1}$ ,  $f_3 = 6.5E-4 \text{ deg-C}^{-1}$ , is used.

**2.10. Mesh densities**

Different mesh densities are applied for the oil film, the thermal analysis of the

bearing shell and the calculation of the elastic deformations. Typically, 120 to 180 nodes in circumferential direction and about 25 nodes in axial direction are employed for the discretization of the Reynolds equation and the energy equations. Radially 7 to 14 nodes are used for the energy equation of the oil film and 7 for the energy equation of the shell. In the finite element meshes of the shell surface there are at least 40 nodes circumferentially and 3 nodes axially. The model depicted in Fig. 1 possesses  $48 \times 9$  nodes.

For details about the solution process refer to [6,8].

**Table 1 Calculation parameters**

|   | Diesel                      | Gasoline              |
|---|-----------------------------|-----------------------|
| Main bearing no.                                    | 2                           | 2                     |
| Bearing diameter                                    | 44 mm                       | 70 mm                 |
| Bearing width                                       | 18 mm                       | 20 mm                 |
| Relative clearance                                  | 0.001                       | 0.000714              |
| Speed   | 4000 rpm                    | 5000 rpm              |
| Oil groove extension                                | 270-90 deg                  | 270-90 deg            |
| Oil groove width                                    | 4.5 mm                      | 6 mm                  |
| Journal temperature                                 | 121 deg-C                   | 133 deg-C             |
| Inlet oil temperature                               | 90 deg-C                    |                       |
| Ambient temperature                                 | 90 deg-C                    |                       |
| Heat transfer coefficient between shell and ambient | 500 W/m <sup>2</sup> .deg-C |                       |
| Oil type  | SAE 10W-40                  |                       |
| Rodermund coefficients                              | A                           | 0.1331635E-3          |
|   | B                           | 969.140625            |
| (Pa.s, Pa, deg-C)                                   | C                           | 107.8995              |
|   | D                           | 0.6018862             |
|   | E                           | -5.477296E-3          |
|   | F                           | 1668.604E5            |
| Dowson-Higginson coefficients                       | $\rho_0$                    | 864 kg/m <sup>3</sup> |
|   | $T_0$                       | 50 deg-C              |
| Heat conductivity/oil                               | 0.14 W/m.deg-C              |                       |
| Specific heat/oil                                   | 2083 J/kg.deg-C             |                       |
| Heat conductivity/shell                             | 50 W/m.deg-C                |                       |
| Specific heat/shell                                 | 400 J/kg.deg-C              |                       |
| Density/shell                                       | 7800 kg/m <sup>3</sup>      |                       |

### 3. RESULTS

The calculation method has been implemented in the program CBTEHD. By means of this program the following bearings have been analyzed:

- Main bearing no. 2 of a 2 stroke 3 cylinder Diesel engine at 4000 rpm.
- Main bearing no. 2 of a 4 stroke 4 cylinder gasoline engine at 5000 rpm.

The parameters for the calculations are listed in Table 1. The loads on the journal have been calculated by means of the AVL software for nonlinear dynamics, NIDYN. They are depicted in Fig. 2 and Fig. 3, respectively.

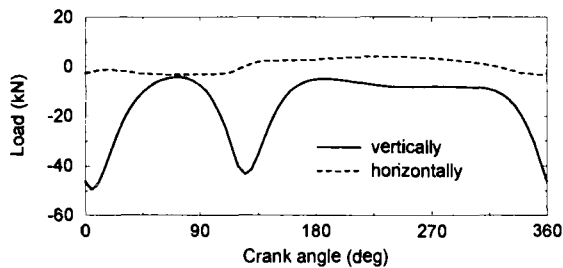


Fig. 2 Load on the journal for main bearing no. 2 of a 2 stroke Diesel engine.

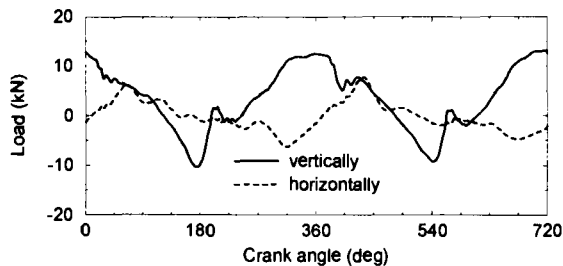


Fig. 3 Load on the journal for main bearing no. 2 of a 4 stroke gasoline engine.

#### 3.1. Main bearing of a Diesel engine

*Peak oil film pressure.* Fig. 4 shows the calculated peak oil film pressure for the variants:

- Pressure and temperature dependent oil viscosity and density ( $\eta = \eta(p, T)$ )
- Constant oil viscosity and density ( $\eta = \eta_{p=1 \text{ bar}, T=105 \text{ deg-C}}$ )

- Pressure and temperature dependent oil viscosity, only. ( $\eta = \eta(p, T), \rho = \text{const.}$ )

By comparing the first two variants one can see that the consideration of the pressure and temperature dependence of the oil viscosity and density leads to an increase in peak oil film pressure of about 11%. If only the oil viscosity is assumed variable, while the oil density is kept constant, there is an additional increase in peak oil film pressure of 6%.

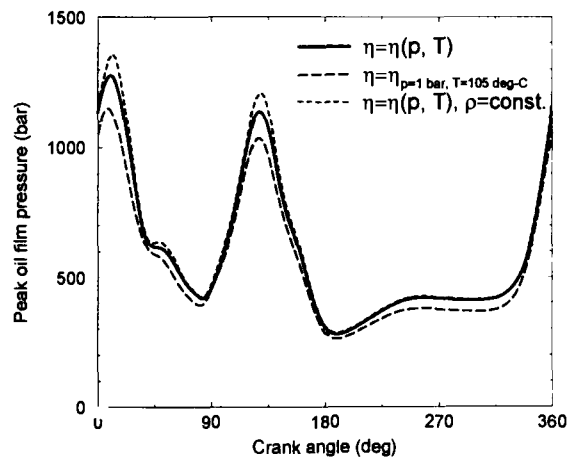


Fig. 4 Peak oil film pressure. Diesel engine.

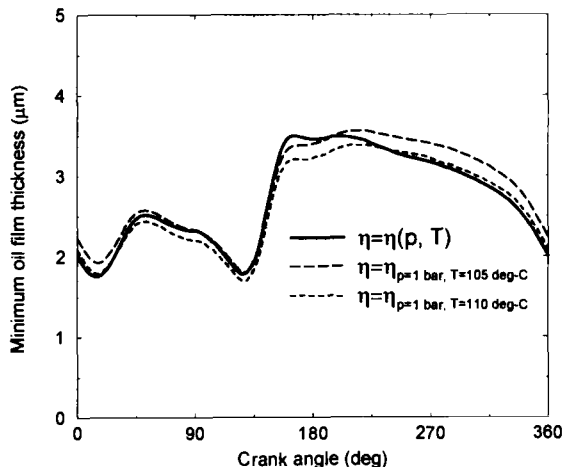


Fig. 5 Minimum oil film thickness. Diesel engine.

*Minimum oil film thickness.* In Fig. 5 the calculated minimum oil film thickness is shown for the TEHD case with variable viscosity and density and two EHD cases with

constant viscosity and density. In contrast to the peak oil film pressure, the results for the minimum oil film thickness are not changed significantly, whether a constant or a variable density is assumed. It has to be stressed that the difference between TEHD and EHD results depends strongly on the (constant) bearing temperature which must be assumed for the estimation of the viscosity in the EHD calculation.

Therefore, on the transition from EHD to TEHD one may observe an increase of 3.6% in the minimum oil film thickness in one case (if 110 deg-C are assumed as constant temperature) and a decrease of (2.8%) in another (for 105 deg-C).

For this bearing the qualitative differences in the results are more important than the quantitative ones. Particularly, there is a temporal (and spatial) shift of the absolute minimum of the oil film thickness. As further investigations have shown [6,8] these qualitative differences are mostly due to the pressure dependence of the viscosity.

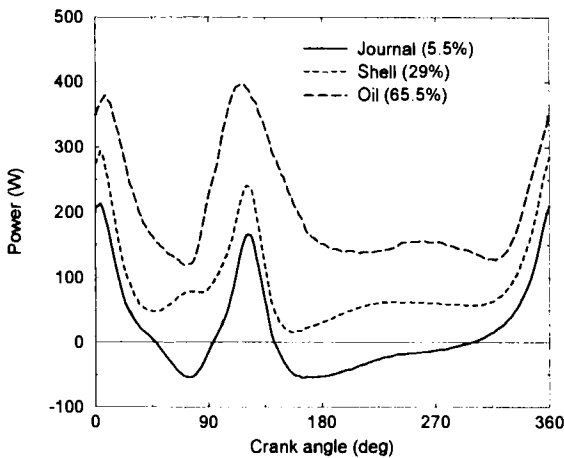


Fig. 6 Heat flow. Diesel engine.

*Heat flow* (Fig. 6). About two thirds of the heat generated by viscous dissipation in the oil are carried out of the bearing by convection.

The journal acts as heat buffer. Most of the heat received at high loads is returned to the oil at low loads.

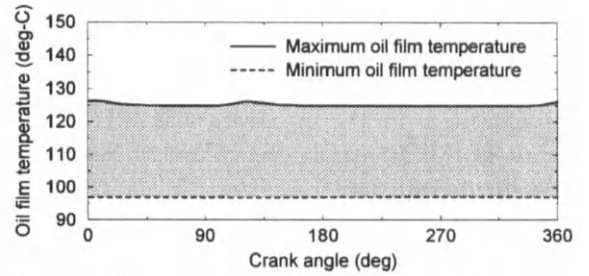


Fig. 7 Minimum and maximum oil film temperatures. Diesel engine.

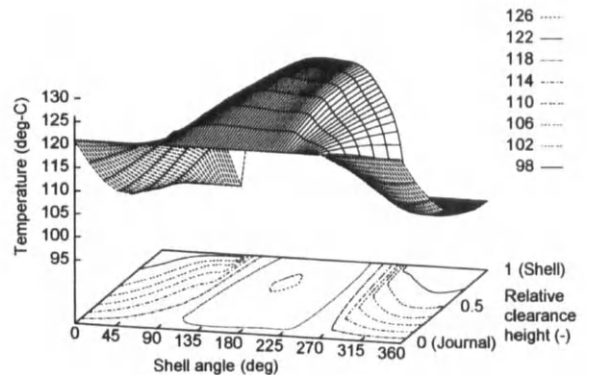


Fig. 8 Oil film temperature in the plane of symmetry of the bearing at 120 deg-CA. Diesel engine.

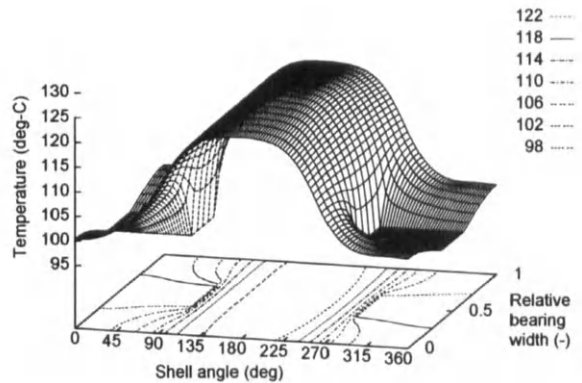


Fig. 9 Shell surface temperature. Diesel engine.

*Temperatures.* The maximum oil film temperature is equal to the maximum shell temperature almost throughout the whole cycle. Only at the pressure peaks the oil film temperature rises to a maximum of 126.5 deg-C. The minimum oil temperature is

always the temperature of the oil in the oil groove (97-deg-C). This results in a maximum difference of oil temperatures in the bearing of 29.5 deg-C (Fig. 7, Fig. 8). The maximum temperature rise from the inlet temperature of 90 deg-C is 36.5 deg-C. On the shell surface there is a temperature variation of 28 deg-C, with the minimum again at the oil groove, Fig. 9.

### 3.2. Main bearing of a gasoline engine

The Finite Element structure of this bearing is depicted in Fig. 1.

*Peak oil film pressure.* (Fig. 10) Comparing the peak oil film pressure for pressure and temperature dependent viscosity and density ( $\eta = \eta(p, T)$ ) with the pressure for constant viscosity and density ( $\eta = \eta_{p=1 \text{ bar}, T=120 \text{ deg-C}}$ ) one can see that the absolute maximum over the engine cycle hardly changes for the two variants. Nevertheless, significant differences in the peak oil film pressure at 700-60, 165-180, 310-385 and 500-550 deg-CA can be observed. The maximum relative difference is almost 100% at 20 deg-CA.

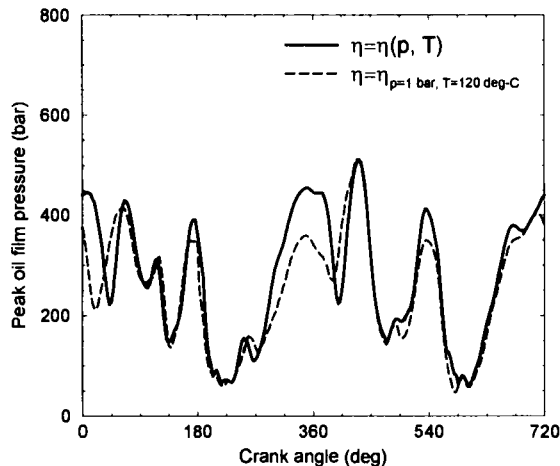


Fig. 10 Peak oil film pressure. Gasoline engine.

*Minimum oil film thickness.* Similar to the main bearing of the Diesel engine, the absolute minimum of the minimum oil film thickness is almost the same for all three calculations in Fig. 11, the first being a

thermoelastohydrodynamic one, the two others being elastohydrodynamic. But again, the (temporal) location is completely different for the two types of calculation. While for the TEHD calculation the minimum appears at 120 deg-CA, the minimum for the EHD calculations is at 441 deg-C. Particularly at 120 deg-CA, the deviation of the EHD calculations is rather high (0.65  $\mu\text{m}$  or 35%).

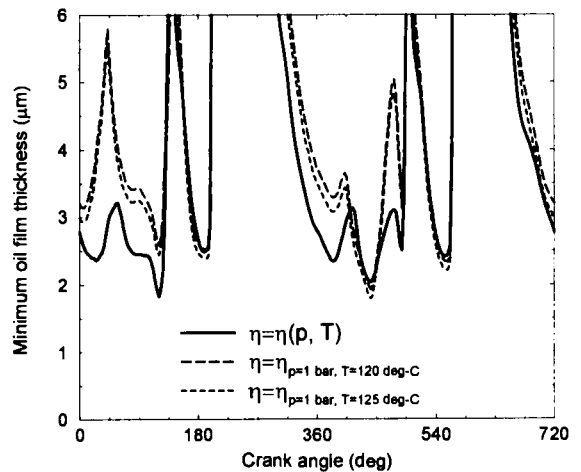


Fig. 11 Minimum oil film thickness. Gasoline engine.

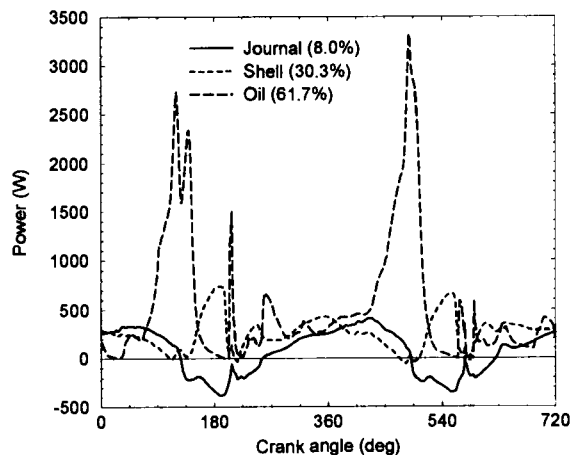


Fig. 12 Heat flow. Gasoline engine.

*Heat flow.* For the bearings studied here the portions of the heat transported out of the bearing over the journal, the shell and the oil, respectively, are approximately the same. However, there is a difference in the timing of

the heat transport: In the Diesel engine bearing (Fig. 6) all three portions exhibit the same qualitative behaviour and most of the heat leaves the bearing at high loads (i.e. when most of the heat is generated). In the gasoline engine bearing (Fig. 12) the three portions do not have this similarity and most of the heat leaves the bearing by convection at rather low loads, when the journal approaches the bearing center.

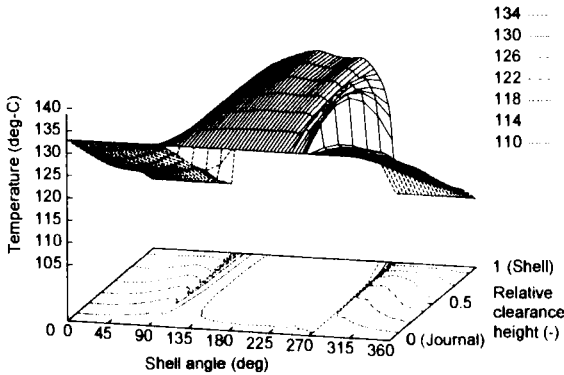


Fig. 13 Oil film temperature in the plane of symmetry of the bearing at 120 deg-CA. Gasoline engine.

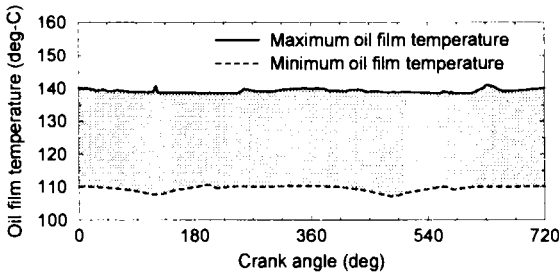


Fig. 14 Maximum and minimum oil film temperatures. Gasoline engine.

*Temperatures.* The maximum oil film temperature rise (to 141 deg-C) with respect to the oil inlet temperature of 90 deg-C is 51 deg-C, Fig. 14, which is – as expected – substantially higher than for the Diesel engine bearing. Again the minimum oil film temperature is equal to the oil temperature in the oil groove (109.5 deg-C on the average). The oil film temperature (Fig. 13) and shell surface temperature (Fig. 15) distributions

are qualitatively the same as for the Diesel engine bearing.

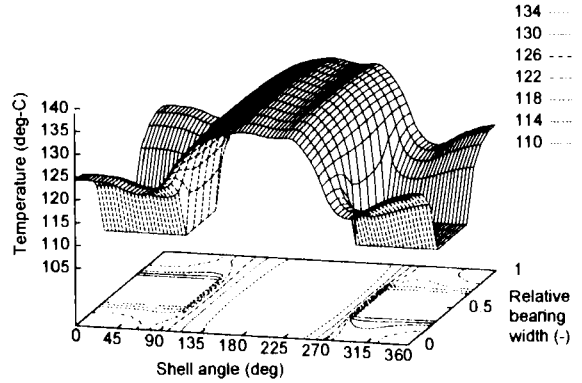


Fig. 15 Shell surface temperature. Gasoline engine.

#### 4. CONCLUSIONS

The mathematical model of a thermo-elastohydrodynamic calculation method for crank train bearings has been described. The method has been used for the analysis of main bearings of both Diesel and gasoline engines. The following conclusions can be drawn from the results:

- The consideration of the pressure and temperature dependence of the oil viscosity and density (TEHD) may lead to a temporal (an consequently spatial) shift of the absolute minimum of the oil film thickness compared with EHD results.
- Significant differences in peak oil film pressure can be observed between TEHD and EHD calculations.
- Nearly two thirds of the frictional heat leave the bearing by convection (oil flow).
- The journal acts as heat buffer. Most of the heat received under high loads is returned to the oil at low loads.
- The temperature rise in the oil film from the oil inlet temperature is 36.5 deg-C for the Diesel engine bearing and 51 deg-C for the gasoline engine bearing.

## GLOSSARY

|              |  |
|--------------|--|
| —            | function in $(x, \bar{y}, z, t)$                               |
| ...'         | function in $(x, y', z, t)$ (only for integration)             |
| Bi           | Biot number (heat transfer coefficient / thermal conductivity) |
| $c_B$        | specific heat of the shell                                     |
| $c_p$        | specific heat of the oil                                       |
| C            | cavitation region  |
| CA           | crank angle  |
| D            | damping matrix of shell  |
| f            | nodal forces acting from the oil film on the shell             |
| $f_A$        | applied (outer) force on the journal                           |
| $f_J$        | oil film forces acting on the journal                          |
| h            | clearance height   |
| K            | stiffness matrix of shell                                      |
| L            | lubrication region   |
| m            | journal mass   |
| M            | mass matrix of the shell                                       |
| p            | oil film pressure  |
| $p_c$        | cavitation pressure  |
| r            | radial co-ordinate in the shell                                |
| S            | oil supply region (oil groove)                                 |
| t            | time   |
| T            | oil temperature  |
| $T_a$        | ambient temperature  |
| $T_B$        | shell temperature  |
| $T_S$        | oil temperature in the oil supply                              |
| $T_{S,0}$    | oil inlet temperature  |
| u            | circumferential velocity of the oil film                       |
| $u_B$        | shell deformations   |
| U            | circumferential velocity of the journal                        |
| v            | cross-film velocity of the oil film                            |
| $V_S$        | volume of the oil supply                                       |
| w            | axial velocity of the oil film                                 |
| x            | circumferential co-ordinate in the oil film                    |
| $x_J$        | journal position   |
| $y, \bar{y}$ | cross-film (radial) co-ordinate in the oil film                |
| z            | axial co-ordinate in the oil film                              |
| $\eta$       | oil viscosity  |
| $\theta$     | fill factor, fraction of volume filled with oil                |
| $\kappa$     | thermal conductivity of the oil                                |
| $\kappa_B$   | thermal conductivity of the shell                              |
| $\rho$       | oil density  |
| $\rho_B$     | density of the shell   |

$\Phi_i$  ..... oil flow from the oil supply into the clearance

$\Delta$  ..... Laplace operator

$\frac{\partial}{\partial n}$  ..... normal derivative

## REFERENCES

1. J. Krasser, O. Laback, B. Loibnegger and H.H. Priebsch, Anwendung eines elastohydrodynamischen Verfahrens zur Berechnung von Kurbeltriebslagern (Application of an elastohydrodynamic calculation method for the analysis of crank train bearings), MTZ Motorentechnische Zeitschrift, 55.Jhg (1994) 656-663.
2. L.J. Rohde and K.P. Oh, A Thermoelastohydrodynamic Analysis of a Finite Slider Bearing, J.Lubr. Techn., 1975, 451-459.
3. R. Boncompain, M. Fillon and J. Frène, Analysis of Thermal Effects in Hydrodynamic Bearings, J.Tribol., Vol. 108 (1986) 219-224.
4. H. Moes, P.B.Y. Ten Hoeve and J. Van der Helm, Thermal Effects in Dynamically Loaded Flexible Journal Bearings, J.Tribol., Vol. 111 (1989) 49-55.
5. R.S. Paranjpe and T. Han, A Transient Thermohydrodynamic Analysis Including Mass Conserving Cavitation for Dynamically Loaded Journal Bearings, J.Tribol., Vol. 117 (1995) 369-378.
6. H.H. Priebsch, B. Loibnegger, J. Krasser and O. Laback, A calculation method for crank train bearings considering pressure and temperature dependent oil viscosity, SIA 3<sup>rd</sup> International Congress, Paris, May 1996.
7. B. Jacobson and L. Floberg, The Finite Journal Bearing Considering Vaporization, Chalmers Tekniska Hoegskolas Handlingar, Vol. 199 (1957) 1-116.
8. J. Krasser, Thermoelastohydrodynamische Analyse dynamisch belasteter Radialgleitlager (Thermoelastohydrodynamic analysis of dynamically loaded journal bearings), Dissertation, Graz University of Technology, 1996.

## HYDRODYNAMIC ANALYSIS OF JOURNAL BEARINGS WITH STRUCTURAL INERTIA AND ELASTICITY BY A MODAL FINITE ELEMENT METHOD

E.G. Olson<sup>a</sup> and J.F. Booker<sup>a</sup>

<sup>a</sup>Sibley School of Mechanical and Aerospace Engineering, Cornell University, Ithaca, New York, 14853, U.S.A.

An elastohydrodynamic lubrication model is presented for the coupled problem of a hydrodynamic lubricating fluid in an elastic structure that includes structural inertia. The problem is formulated and the governing equations solved with the finite element method for a realistic journal bearing subject to dynamic loading.

Comparisons with an existing model that neglects structural inertia agree excellently for the realistic bearing considered, showing that structural inertia can often be neglected without significant loss of accuracy. However, the new model presented can capture important effects of structural inertia for special problems, is conceptually simple, and exhibits significant improvements over existing methods with respect to numerical stability and speed.

### 1. INTRODUCTION

#### 1.1. Background

The finite element approach to hydrodynamic lubrication has gained popularity since its early uses in the late 1960's by Wada and Hayaishi [1], Reddi [2] and others. The finite element method continues to be attractive because it offers conceptual ease in coupling together hydrodynamic and elastic properties and also flexibility in handling complex geometry and boundary conditions. For example, Oh and Huebner [3] provide a finite element formulation where journal bearing elastic distortions are computed with a simple iterative technique for steady-state cases. The straightforward *direct iteration method* (as it is called in this work) is presented by LaBouff and Booker [4] for dynamically loaded journal bearings. However, cumbersome modifications to this algorithm are required to allow for adequate stability across a sufficiently large class of problems.

The *quasi-static modal method* (as it is called in this work) of Booker [5] supposes that the relative displacement of the lubricated surfaces is a linear combination of certain mode shapes. The quasi-static modal method is implemented for dynamically loaded journal bearing applications by Kumar, Booker, Goenka, Boedo and Wilkie [6, 7] and proves itself more stable than the direct iteration method. Still, all

the computational analyses that use the quasi-static modal method in existing publications are limited to small sets of elastic mode shapes (not always enough to adequately capture all the important effects of elasticity).

Oh [8] provides yet another formulation that incorporates the Newton-Raphson approach to solving nonlinear problems and originally applied it to the elastohydrodynamic contact problem. Oh and Goenka [9] also apply the Newton-Raphson approach to dynamically loaded journal bearings and a "fast" version of the method is presented by McIvor and Fenner [10]. The Newton-Raphson approach is reportedly stable and convergent across a range of problems, but is described by Yang and Wen [11] as "perhaps the most complicated" of the currently available methods.

A large body of literature exists that addresses existing finite element treatments of the elastohydrodynamic problem, and the works cited here are meant only to highlight some important developments in a context that applies to the present work, but not to serve as a comprehensive survey of previous research.

One shortcoming of the aforementioned finite element treatments of the elastohydrodynamic lubrication problem, additional to complexity and numerical instability, is the omission of structural inertia. Without including structural inertia, the occurrence of self-excited oscillations (instability) in high speed bearings is

precluded and (obviously) any other effects of structural inertia cannot be captured. Still, ignorable effects of structural inertia are often assumed because the structural displacements in hydrodynamic problems limit themselves to small values (on order of the clearance space).

Despite the frequently applied assumption of negligible structural inertia, some studies look into its effect on bearing systems. Boedo [12] investigates the dynamics of engine bearing systems with rigid body assumptions. Recently, Bonneau, Guines, Frene and Toplosky [13] proposed a method of incorporating inertia forces due to structural kinematics in connecting-rod bearings. However, in that study the inertia due to "bearing clearance motions" is ignored since it is small compared to that from "crank-throw motion." That study also cites earlier attempts to model the effects of inertia due to crank-throw motion in connecting-rod bearings.

## 1.2. The Present Study

Effects of structural inertia from "bearing clearance motions" are expected to be most significant for bearings with low lubricant viscosity, large clearances, rapidly varying applied loads, high structural mass, low stiffness and minimal cavitation. The *dynamic modal method* presented in this study models and captures significant effects of structural inertia in certain problems where such effects are important. Further, the dynamic modal method is conceptually simple, can be computationally faster than some existing methods and is numerically stable for a very broad range of journal bearing applications, while some existing methods are not. One limitation of the current formulation is the assumption of negligible effects from fluid inertia, which is treated by Elrod, Anwar and Colsher [14] among others. Still, this assumption holds true for the bearing in the present study.

This paper first derives the general equations that govern the coupled problem of a lubricating fluid bounded by a flexible journal bearing sleeve and a rigid journal, where both structures include inertia. This derivation is the basis of the dynamic modal method, which is validated through an analysis of a dynamically loaded journal bearing using EHLFE

(Elasto-Hydrodynamic Lubrication with Finite Elements); a FORTRAN computer program. A more comprehensive version of the same derivation, along with additional validating studies and investigations is provided by Olson [15]. EHLFE implements not only the new dynamic modal method but also the (previous) quasi-static modal method and the (previous) direct iteration method, so that the dynamic modal method can be compared, contrasted and validated against two other (previously developed) methods.

EHLFE's implementation of the quasi-static modal method has been compared extensively to the previously developed computer code FEMEHL, alias MODEHD, of Booker, Kumar and Goenka [5, 6, 16, 17, 18] and the computer code of Boedo, Booker and Wilkie [7]. EHLFE was the only code of the three that could accommodate more than just a few elastic modes, but agreement was excellent for all the cases that were compared (rigid, elastic, non-mass conserving cavitation, mass conserving cavitation).

By using the variable time step, stiff system numerical integration method of backward difference formulae with the full Jacobian matrix being approximated by the method of difference quotients, a method explained by Shampine and Gordon [19], EHLFE can accommodate virtually any number of elastic modes in an elasto-hydrodynamic journal bearing analysis. This capability allows for investigations into elastic modal convergence that were simply not possible in previous works and eliminates the need for involved arguments and comparisons to other results (from Newton-Raphson or direct iteration methods) to establish the minimum number of required modes for a given analysis. Studies in this work indicate that the quasi-static modal method exhibits peculiar numerical instabilities that can be overcome, in many cases, by prescribing special initial conditions and very small integration time steps. The quasi-static modal method can also become less stable as more modes are added to an analysis. In contrast, the dynamic modal method is consistently stable, avoids the need for very small integration time steps, and can be computationally faster as a consequence. The dynamic modal method is also computationally faster than the



quasi-static modal method in numerical simulations that use large numbers of modes.

Upon interpreting the results from the studies presented here, it is evident that the dynamic modal method and the quasi-static modal method yield similar results for certain realistic problems. Thus, for many practical problems the dynamic modal method merely has the advantage of simple numerical implementation, and numerical stability and speed, while the assumption of negligible structural inertia (that is widely used) holds true.

Other simulations are presented by Olson [15] where effects from structural inertia are important, such as in a bearing with a rapidly varying load, an uncavitated bearing, bearing derivatives of a gas engine main bearing and rigid bearing stability analyses that identify operating regimes where self-excited oscillations (instabilities) occur.

### 1.3. Notation

#### 1.3.1. scalars (integer)

|     |                               |
|-----|-------------------------------|
| $k$ | rigid body freedom order      |
| $m$ | modal (elastic) order         |
| $n$ | nodal (fluid mesh) order      |
| $l$ | nodal (structural mesh) order |

#### 1.3.2. scalars (real)

|           |                                     |
|-----------|-------------------------------------|
| $t$       | time                                |
| $\rho$    | local fluid density                 |
| $\mu$     | local fluid viscosity               |
| $E$       | Young's modulus                     |
| $\nu$     | Poisson's ratio                     |
| $h$       | local film thickness                |
| $p$       | local film pressure                 |
| $e$       | journal displacement (eccentricity) |
| $\omega$  | journal angular velocity            |
| $p_{cav}$ | cavitation pressure                 |
| $m^j$     | mass of journal                     |

#### 1.3.3. vectors (real)

|                 |                           |         |
|-----------------|---------------------------|---------|
| $\{\hat{n}_z\}$ | unit normal               | (1x1)   |
| $\{\hat{n}\}$   | unit normal               | (2x1)   |
| $\{U\}$         | average velocity          | (2x1)   |
| $\{e\}$         | journal displacement      | (kx1)   |
| $\{f_{ext}\}$   | external force            | (kx1)   |
| $\{f_{fluid}\}$ | resultant fluid force     | (kx1)   |
| $\{\delta^s\}$  | displacement of $\square$ | various |
| $\{r^s\}$       | forces on $\square$       | various |

|         |                    |             |
|---------|--------------------|-------------|
| $\{h\}$ | film thickness     | (nx1)       |
| $\{p\}$ | film pressure      | (nx1)       |
| $\{q\}$ | flow               | (nx1)       |
| $\{c\}$ | clearance (radial) | (nx1)       |
| $\{X\}$ | state              | (2m+2k x 1) |

#### 1.3.4. matrices (real)

|          |                    |       |
|----------|--------------------|-------|
| $[G]$    | static equilibrium | (nxk) |
| $[A]$    | area (fluid mesh)  | (nxn) |
| $[\Psi]$ | elastic mode shape | (nxm) |
| $[K^s]$  | nodal stiffness    | (lxl) |
| $[K^s]$  | condensed $[K^s]$  | (nxn) |
| $[M^s]$  | nodal mass         | (lxl) |
| $[M^s]$  | condensed $[M^s]$  | (nxn) |
| $[K^p]$  | pressure fluidity  | (nxn) |

#### 1.3.5. miscellaneous

|         |                                       |
|---------|---------------------------------------|
| $( )$   | total derivative with respect to time |
| $( )^S$ | reference to full elastic structure   |
| $( )^s$ | reference to condensation of $( )^S$  |
| $( )^j$ | reference to journal                  |
| $( )_e$ | reference to one element              |
| x, y, z | fluid film coordinates                |
| X, Y, Z | global (system) coordinates           |

## 2. BEARING STRUCTURAL MODEL

The physical journal bearing model is illustrated in Figure 1, where all nodal quantities, except for  $\{\delta^s\}$ , are depicted in their positive sense.

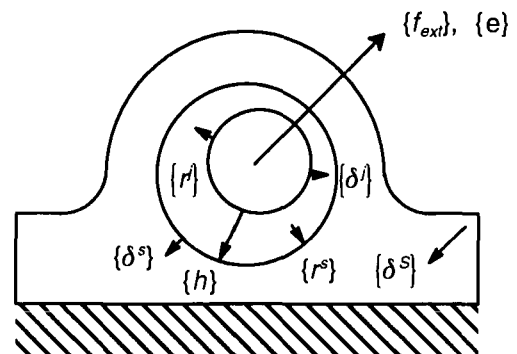


Figure 1. Journal Bearing Physical Model

and the appropriate inertial Cartesian coordinate system is given in Figure 2.

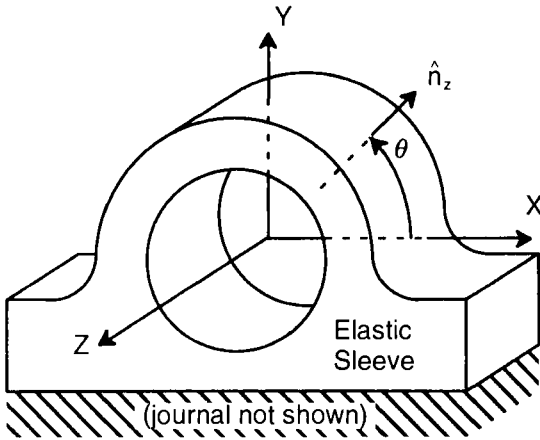


Figure 2. Inertial Coordinate System

**2.1. Equation of Motion for Elastic Sleeve**

The finite element form of the equation of motion that applies to the linearly elastic sleeve is well known, and its full derivation can be found in most classical finite element texts that address structural elasticity. Cook [20] derives the general equation for an undamped, discretized elastic solid using potential and kinetic energy expressions together with Lagrange’s equations. His derivation gives the equation that governs the journal bearing elastic sleeve as

$$[M^s]\{\ddot{\delta}^s\} + [K^s]\{\delta^s\} = \{r^s\} \quad 1.$$

An important assumption made is that transverse (x and y directions in Figure 3) tractions on the fluid surface can be ignored. Consequently, all equations (degrees of freedom) in 1 that are not directly associated with the cross-film direction (z direction in Figure 3) on the fluid surface can be condensed-out through static condensation (for  $[K^s]$ ) and dynamic (Guyan) reduction (for  $[M^s]$ ), leaving a much smaller set of coupled equations.

**2.1.1. The Condensed Form**

After condensation/reduction, the only degrees of freedom left from equation 1 are those associated with the nodes on the surface contacting the fluid in the cross-film direction. The condensed form is

$$[M^s]\{\ddot{\delta}^s\} + [K^s]\{\delta^s\} = \{r^s\} \quad 2.$$

**2.1.2. The Modal Form**

The number of equations can be further reduced by introducing the modal approximation

$$\{\delta^s\} \approx [\Psi]\{\delta^s\}' \quad 3.$$

where the  $n$  physical (nodal) displacements are constructed from  $m \ll n$  modal (generalized) displacements through the  $n$  transformation relations  $[\Psi]$ .

Substitution of equation 3 into equation 2 yields the equation of motion for the elastic sleeve in terms of modal displacements.

$$\{r^s\}' - [K^s]'\{\delta^s\}' = [M^s]'\{\delta^s\}' \quad 4.$$

where  $\{r^s\}' = [\Psi]^T\{r^s\}$

$$[K^s]' = [\Psi]^T[K^s][\Psi]$$

$$[M^s]' = [\Psi]^T[M^s][\Psi]$$

**2.1.3. Mode Generation**

Although the transformation matrix  $[\Psi]$  could be arrived at in any fashion (such as by evaluating analytic functions), it is currently most useful to use mode shapes that are specific to individual elastic structures. Since the algorithm being presented is based on a formulation that uses absolute displacements (relative to an inertial coordinate system), the modes can be generated by the classical method of modal decomposition from structural dynamics. That is, they come from solving

$$[K^s][\Psi] = [M^s][\Psi][\Omega^2]$$

for  $[\Psi]$  and  $[\Omega^2]$  so that the columns of  $[\Psi]$  contain the eigenvectors (mode shapes) of  $[K^s]$  taken with respect to  $[M^s]$ , and the diagonal matrix  $[\Omega^2]$  contains (as diagonal entries arranged in ascending order) the eigenvalues (natural frequency squares) of the system. Neither the lower natural frequencies in  $[\Omega^2]$  nor the shapes of the corresponding modes in  $[\Psi]$  are expected to

change significantly for different mesh densities, so mode shapes can be easily converted from any structural mesh to a different fluid mesh by straightforward interpolation. Finally, appropriate scaling of  $[\Psi]$  gives

$$[\Psi]^T [K^s] [\Psi] = [\Omega^2] \quad \text{if} \quad [\Psi]^T [M^s] [\Psi] = [I]$$

so that  $[K^s]'$  and  $[M^s]'$  can be conveniently diagonal.

Experience shows that the modes corresponding to the lowest eigenvalues are the most influential ones for nearly all elastic analyses. Consequently, the modes to include come from the first several columns of  $[\Psi]$ , while the last columns of  $[\Psi]$  can usually be discarded. Also, certain modes can often be discarded by taking advantage of geometric symmetries particular to some problems.

**2.2. Equation of Motion for Rigid Journal**

The basic assumptions used to derive this equation of motion include

- no axial (Z direction) journal translation
- no journal misalignment

The more comprehensive version of this derivation [15] includes misalignment with gyroscopic forces. Since the journal is rigid, the equations of motion come from the generalized form of Newton's second law of motion for a rigid body. The general forms of the equations are formulated in many dynamics texts, such as Goldstein [21]. When applied to the journal, these equations are

$$\begin{Bmatrix} F_{x_{ext}} + F_{x_{fluid}} \\ F_{y_{ext}} + F_{y_{fluid}} \end{Bmatrix} = \begin{bmatrix} m^i & 0 \\ 0 & m^j \end{bmatrix} \begin{Bmatrix} \ddot{e}_x \\ \ddot{e}_y \end{Bmatrix}$$

which can be written in generalized form

$$\{f_{ext}\} + \{f_{fluid}\} = [M^j]\{\ddot{e}\} \tag{5}$$

The hydrodynamic solution (discussed next) requires that the z displacements be known for the journal at every node of the fluid mesh, so the relationship between the generalized rigid journal displacements  $\{e\}$  and the corresponding displacements at the fluid film nodes  $\{\delta^j\}$  must be known and are related through the static

equilibrium matrix  $[G]$  such that

$$\{\delta^j\} \equiv [G]\{e\}$$

where  $[G]$  is comprised simply of  $\cos(\theta)$  and  $\sin(\theta)$  terms (re Figure 2 defining  $\theta$ ) in the absence of journal misalignment. Thus, the resultant generalized forces of the fluid on the journal are

$$\{f_{fluid}\} \equiv [G]^T \{r^j\}$$

**3. FLUID MODEL FORMULATION**

The finite element form of the fluid model (used in this formulation) is well developed and its full derivation is given by Booker and Huebner [22] for 3-noded triangular elements. The appropriate fluid film coordinate system for the current application to journal bearings is pictured in Figure 3.

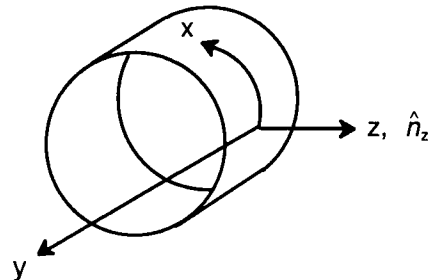


Figure 3. Fluid Film Coordinate System

The formulation employs the usual assumptions that reduce the Navier–Stokes equations to the Reynolds equation

$$\nabla \cdot \left( \frac{\rho h^3}{12\mu} \nabla p \right) = \nabla \cdot (\rho h \bar{U}) + \frac{\partial}{\partial t} (\rho h)$$

with appropriate boundary conditions. In its finite element, discretized form the solution to the Reynold's equation comes from the  $n$  coupled equations

$$\{q\} = [K^p]\{p\} + \{Q\} \tag{6}$$

With  $[K^p]$  and  $\{Q\}$  specified for a complete oil film, equation 6 can be solved as a standard finite element problem with mixed boundary conditions (essential boundary conditions

within  $\{p\}$  and natural boundary conditions within  $\{q\}$ .

### 3.1. Cavitation Modeling

The solution to equation 6 can yield negative pressures because the fluid boundaries are likely to be composed of converging/diverging surfaces. Since lubricants cannot support significant negative pressures, a linear complementarity problem is employed to model film cavitation and reformation. The problem requires a

$$\left( \{p\}, \{Q^e\} \right)$$

satisfying

$$[K^p]\{p\} = \{q\} - \{Q\}$$

$$\{p\} \geq \{p_{cav}\}$$

$$\{Q^e\} \geq \{0\}$$

$$(p_i - p_{cav}) Q_i^e = 0 \text{ for } i = 1, \dots, n$$

on every node with a natural boundary condition, so that in the solution at least one variable in each pair of

$$\left( (p_i - p_{cav}), Q_i^e \right)$$

must be zero for each  $i$ . Such a pair is a *complementary pair* and the approach is termed a *linear complementarity problem*. The solution to this problem is found numerically by the Murty [23] iteration algorithm.

Existing film cavitation models are numerous and vary in their complexity. Kumar, Booker, Boedo and Wilkie [7, 16, 17] and Bonneau, Guines, Frene and Toplosky [13] explore cavitation algorithms that conserve mass (or flow) while Kumar and Booker [18] extend the theory to account for energy conservation. Brewe [24] introduces a model for vapor cavitation, and the list goes on. Any cavitation model (in its finite element form) can be applied to the dynamic modal method in the current discussion, and numerical studies are provided that implement the mass conserving cavitation algorithm of Kumar and Booker [16, 17].

### 3.2. Nodal Fluid Forces

Once found via equation 6, the nodal pressures are related to the nodal fluid forces by the hydrostatic relation

$$\{r^s\} = [A]\{p\}$$

where  $[A]$  is the consistent system area matrix whose derivation is supplied by Olson [15].

$$\{r^s\} = \left\{ r^s(\{h\}, \{\dot{h}\}, t) \right\} \tag{7}$$

The film thickness  $\{h\}$  is a function of the absolute displacements  $\{\delta^s\}$  and  $\{\delta^j\}$  along with the journal bearing radial clearance  $\{c\}$ , so that the nodal film thickness vector is computed from the  $n$  kinematic relations

$$\{h\} = \{c\} + \{\delta^s\} - \{\delta^j\} = \{c\} + \{\delta^s\} - [G]\{e\}$$

Time  $t$  is included in relation 7 because nodal film thickness and squeeze rate can change with time so that the fluid forces can also vary over time.

Since fluid inertia is neglected in this model, it is important to note that the nodal forces from the fluid acting on the elastic journal bearing sleeve are equal and opposite to the nodal forces from the fluid acting on the journal so that equilibrium considerations give the constitutive relation

$$\{r\} \equiv \{r^s\} = -\{r^j\}$$

### 4. COUPLED INITIAL VALUE PROBLEM

The governing equations of this elastohydrodynamically lubricated journal bearing system are given by equations 2 and 5 together with the fluid film relation of 6. After applying the modal transformation approximation of equation 3, equation 2 is approximated by equation 4. The equations are summarized below in a convenient form.

$$\begin{aligned} \{\ddot{e}\} &= [M^j]^{-1} \{ \{f_{ext}\} - [G]^T \{r\} \} \\ \{\delta^s\}' &= [M^s]^{-1} \{ \{r\}' - [K^s] \{\delta^s\}' \} \end{aligned} \tag{8}$$

where

$$\{r\} = \left\{ r(\{h\}, \{\dot{h}\}, t) \right\}, \{f_{ext}\} = \{f_{ext}(t)\}$$

These equations pose an initial value problem whose state and state rate are written

$$\{X\} \equiv \begin{Bmatrix} \{e\} \\ \{\dot{e}\} \\ \{\delta^s\}' \\ \{\delta^s\}' \end{Bmatrix}, \{\dot{X}\} = \begin{Bmatrix} \{\dot{e}\} \\ \{\ddot{e}\} \\ \{\delta^s\}'' \\ \{\delta^s\}'' \end{Bmatrix}$$

with initial conditions given by

$$\{X\}_{t=t_0}$$

This initial value problem easily lends itself to numerical integration where the modal elastic sleeve displacements, the rigid body journal displacements and their rates of change comprise the state at any given time. During integration, the nodal forces  $\{r\}$  arising from the fluid can be determined from the current time and state. Externally applied forces  $\{f_{ext}\}$  are determined from the current time. All other arrays in equation 8 remain fixed during numerical integration.

## 5. NUMERICAL STUDIES WITH EHLFE

The EHLFE computer program consists of a pre-preprocessor for handling elasticity input data prior to a main analysis, a preprocessor for handling all other input data prior to a main analysis, the main analysis program and a post-processor for viewing data after a main analysis. The main program performs the general analysis of a dynamically or steadily loaded journal bearing and has numerous options, some of which include

- three analysis types (dynamic/quasi-static/static methods)
- three elastic models (rigid/modal elastic/fully elastic)
- two cavitation models (mass conserving/non-mass conserving)
- two thermal models (thermal gradients/isothermal)

The numerical studies that comprise the remaining part of this work were generated with EHLFE, and it is instructive to highlight some

important information regarding the studies.

- Mode shape generation for the quasi-static modal method is accomplished in a fashion identical to the method presented by Boedo, Booker and Wilkie [7]. That is, eigenvectors of a *relative* stiffness matrix are taken with respect to the area matrix  $[A]$ .
- The 3-dimensional model of the bearing sleeve structure was created with the PATRAN 3 finite element modeler and the 3-dimensional mesh utilizes HEX8 elements. Stiffness and mass matrices were created and reduced with the MSC/NASTRAN 67 finite element analysis computer program. Details of the theory behind the MSC/NASTRAN analysis program are documented by MacNeal [25].
- Results were generated using a Sun Microsystems Sparc 10 workstation.
- EHLFE uses the linear 3 noded triangular elements described by Booker and Huebner [22].

### 5.1. Procedural Outline

```

generate/choose/convert mode shapes
compute fixed, primed matrices in 8
set fixed & moving boundary conditions
set initial time & state
set integration error & time step limits
set integration finish time
initialize set of cavitated nodes to null
until finish time
  for current time & state
    locate moving boundary conditions
    find time-dependent external loads
    find film thickness & squeeze rate
    until cavitation closure complete
      determine system equation
      apply pressure constraints
      solve for unknown pressures
      check cavitation closure
      update set of cavitated nodes
    find nodal & resultant fluid force
    find modal fluid force
    find rigid body & modal accelerations
  find new state
  increment time
  output results
end

```

### 6. GAS ENGINE MAIN BEARING STUDY

This bearing is from the Dresser–Rand Company’s reciprocating, 4–stroke gas–compressor engine, model KVSR 12–4 that has eight main bearings supporting a crankshaft, each being split into two bearings that share a common sleeve by a full circumferential oil supply groove. Owing to the symmetry of the two split bearings, only half of the sleeve structure is used and only one of the two halves of main bearing #4 is analyzed. Here, the term “main bearing” will refer to only one of the two split halves. This dynamically loaded numerical study uses the realistic duty cycle from the engines #4 main bearing. Analyses of all 8 main bearings and further studies of the #4 bearing are given by Olson [15]. The engine main bearing geometry is shown in Figure 4.

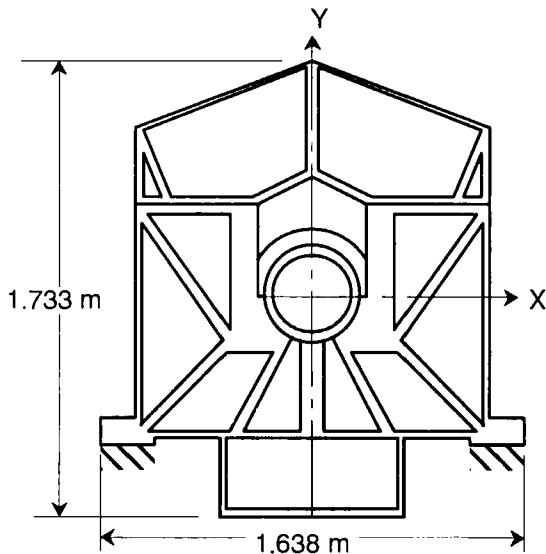


Figure 4. Bearing Geometry

and all other bearing properties are given in tables 1 and 2.

Table 1. Bearing Sleeve Material Properties

|                                 |  |
|---------------------------------|--|
| <u>Gray Cast Iron (frame)</u>   |  |
| $E = 70.0 \text{ GPa}$          |  |
| $\nu = 0.250$                   |  |
| $\rho = 7200.0 \text{ kg/m}^3$  |  |
| <u>Aluminum (bearing shell)</u> |  |
| $E = 70.0 \text{ GPa}$          |  |
| $\nu = 0.346$                   |  |
| $\rho = 2710.0 \text{ kg/m}^3$  |  |

Table 2. Bearing Defining Parameters

|  |  |
|--|--|
| <u>Bearing Specifications</u>                  |  |
| length   | = 0.07938 m                            |
| diameter                                       | = 0.2795 m                             |
| clearance (radial)                             | = $1.075 \times 10^{-4} \text{ m}$     |
| angular velocity                               | = 360.0 rev/min ccw                    |
| journal mass                                   | = 335.9 kg                             |
| external feed pressure                         | = $101.3 \times 10^3 \text{ Pa (abs)}$ |
| symmetry feed (groove) pressure                | = $446.1 \times 10^3 \text{ Pa (abs)}$ |
| <u>Lubricant Properties (SAE–30 at 62.8°C)</u> |  |
| viscosity                                      | = 0.04058 Pa–s                         |
| cavitation pressure                            | = 0.0 Pa (absolute)                    |

The duty cycle associated with this bearing is shown in Figure 5.

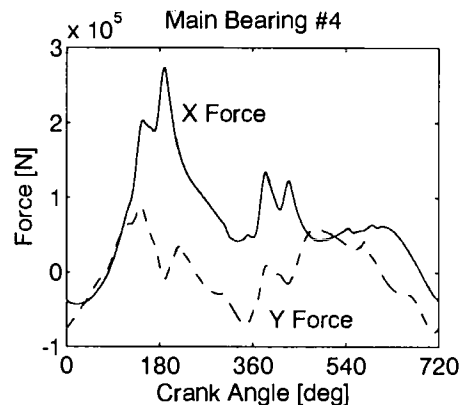


Figure 5. Bearing Duty Cycle

The finite element mesh descriptions are given in Table 3, with the solid model mesh shown in Figure 6 and the fluid mesh shown in Figure 7.

Table 3. Bearing Mesh Descriptions

| <u>Number of Nodes or Elements</u>      |       |
|---|-------|
| (3-Dimensional Sleeve Mesh)             |       |
| circumferential nodes on fluid surface: | 48    |
| axial nodes on fluid surface:           | 11    |
| total nodes in solid mesh:              | 16640 |
| (2-Dimensional Fluid Mesh)              |       |
| circumferential nodes (wrapped):        | 80    |
| axial nodes:                            | 11    |

The effects of the mass conserving cavitation algorithm of Kumar and Booker [16, 17] are investigated in these simulations. Both rigid and elastic results are presented with and without using the mass conserving cavitation model. Results are provided for the dynamic modal method (the dynamic modal method and the quasi-static modal method give virtually identical results in every case) and the elastic cases use 20 elastic modes (the first 6 elastic modes are shown in Figure 8).

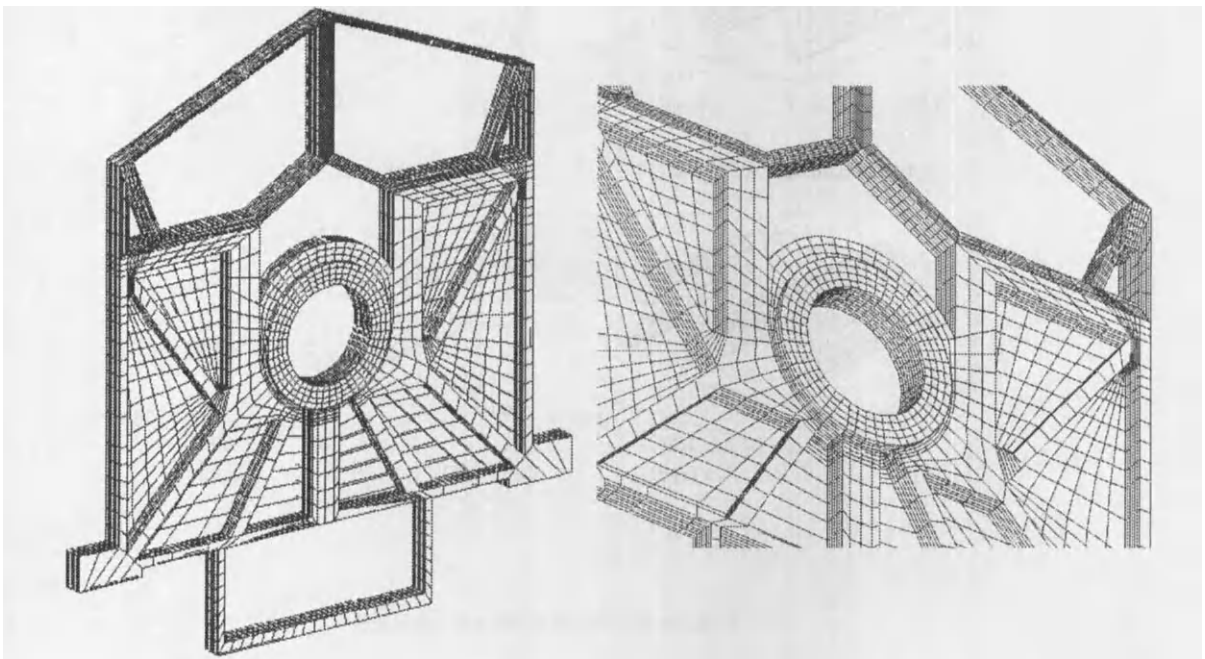


Figure 6. Bearing Solid Model Mesh

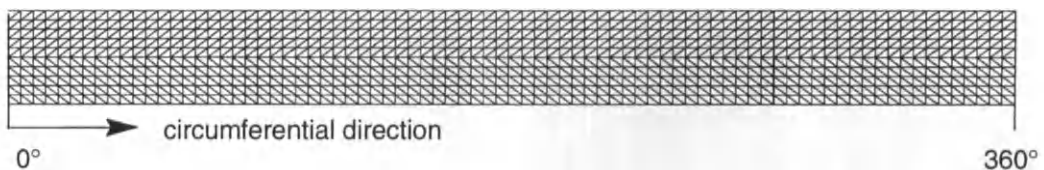


Figure 7. Bearing Finite Element Fluid Mesh

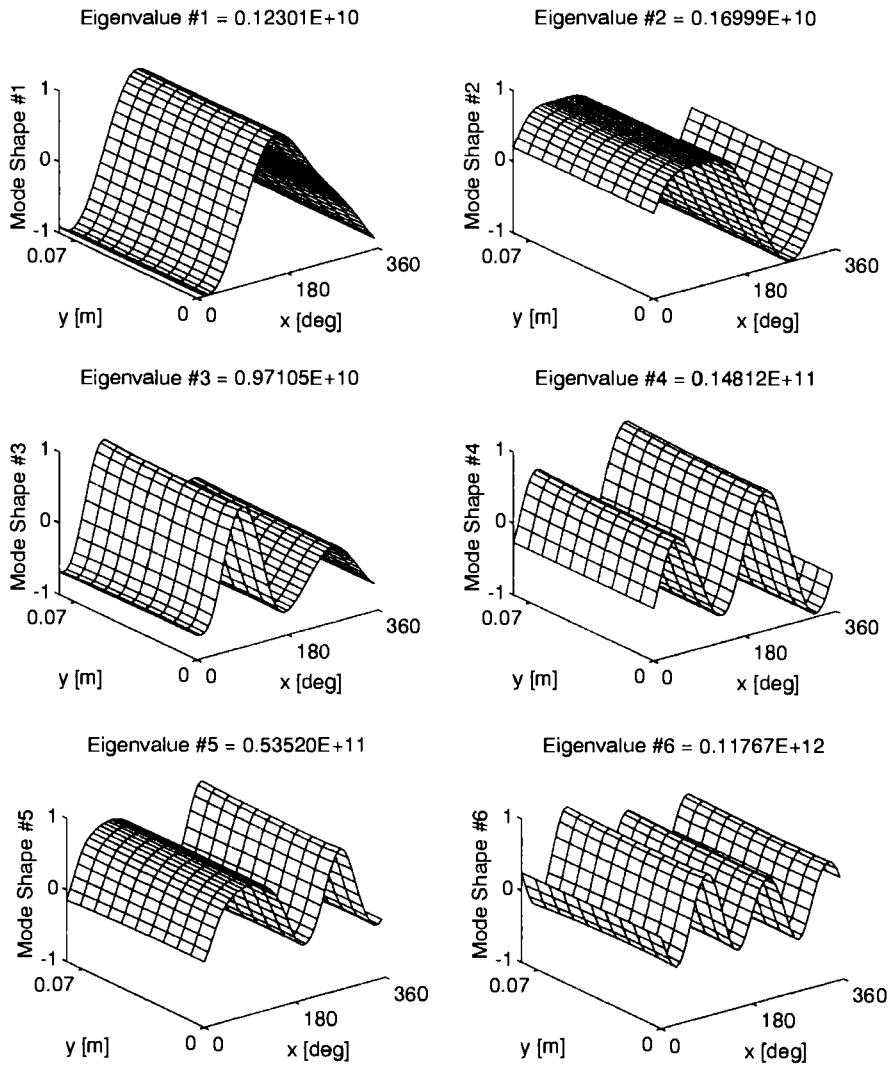


Figure 8. Bearing Mode Shapes



### 6.1. Minimum Film Thickness

Figure 9 shows minimum film thickness varying with crank angle, where the effects from elasticity are minimal. It is interesting to observe that the mass conserving cavitation

algorithm serves to significantly decrease the largest value of minimum film thickness for both the rigid and elastic simulations. Furthermore, the effects that arise from accounting for mass conservation are small in regions where minimum film thickness takes on small values.

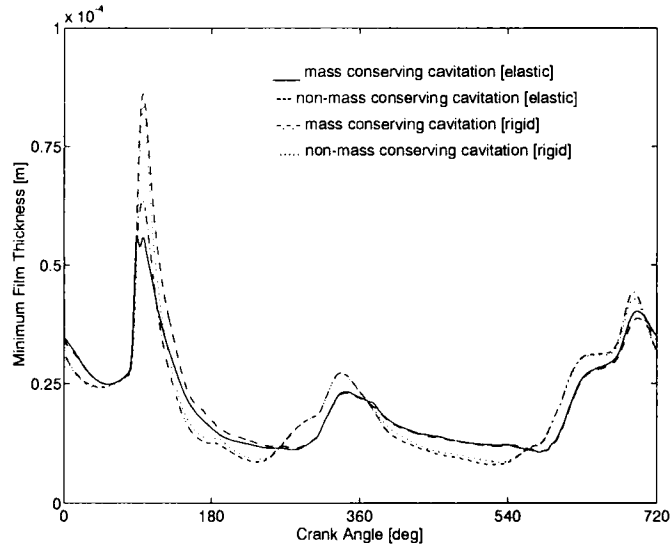


Figure 9. Bearing Min Film Thickness vs Crank Angle

### 6.2. Maximum Film Pressure

Figure 10 shows maximum film pressure varying with crank angle, where the effects from elasticity are substantial. Interestingly,

simulations that use the mass conserving cavitation algorithm do not yield appreciably different results from those that use the non-mass conserving cavitation algorithm.

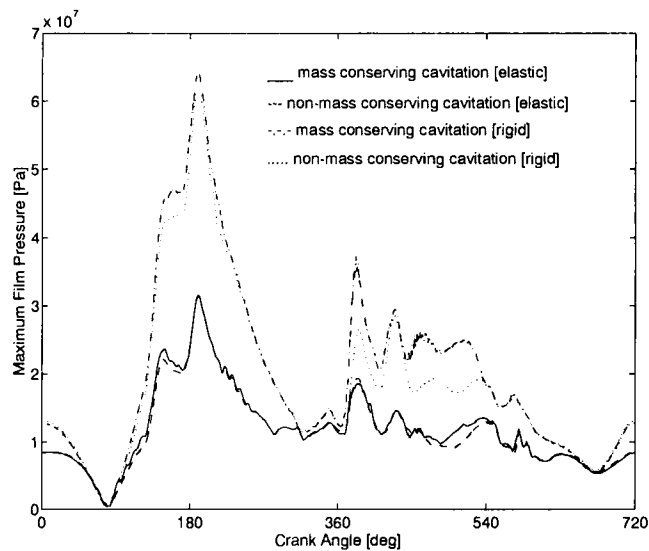


Figure 10. Bearing Max Film Pressure vs Crank Angle

## 7. CLOSURE

The dynamic modal method demonstrates some practical improvements over previously formulated methods; namely computational stability. The pre-existing quasi-static modal method of Booker [5] that is explored by Kumar, Booker, Goenka, Boedo and Wilkie [6, 7] and the direct iteration method of LaBouff and Booker [4] both gave instances of numerical instability that necessitated special, problem dependent adjustments to allowable errors, integration time steps and initial conditions. The quasi-static and direct iteration methods even proved unable to generate any solutions whatsoever in at least a few cases where the new dynamic modal method showed no sign of numerical instability at all.

At the present time it is unclear which modal method (dynamic or quasi-static) is computationally faster, since relative speed has been qualitatively found to be problem dependent, and each method has unique advantages when applied to practical problems. Still, the dynamic modal method is clearly faster than the quasi-static modal method in cases where very small integration time steps are required to overcome instability (with the quasi-static modal method), as well as in numerical simulations that use large numbers of elastic modes.

The formulation provided in this work also applies to a general class of problems (additional to journal bearings) that can include spherical and planar bearings.

As computational speed is enhanced and more elastic mode shapes can be routinely included in simulations, it is likely that numerical stability will play an increasingly important role in the implementation of the methods that are compared and contrasted in this work.

## 8. ACKNOWLEDGMENTS

Funding contributions for this research were made by Pratt & Whitney, a division of United Technologies Corporation. This research also used some resources of the Integrated Mechanical Analysis Project at Cornell University.

## 9. REFERENCES

1. Wada, S., and Hayashi, H., *Conference of Japanese Society of Lubrication Engineers* (in Japanese), Hiroshima, Oct., 1968.
2. Reddi, M.M., *Finite-Element Solution of the Incompressible Lubrication Problem*, ASME Journal of Lubrication Technology, Vol. 91, No. 3, 1969, pp. 524-533.
3. Oh, K.P., and Huebner, K.H., *Solution of the Elastohydrodynamic Finite Journal Bearing Problem*, ASME Journal of Lubrication Technology, Vol. 95, No. 3, 1973, pp. 342-352.
4. LaBouff, G.A., and Booker, J.F., *Dynamically Loaded Journal Bearings: A Finite Element Treatment for Rigid and Elastic Surfaces*, ASME Journal of Tribology, Vol. 107, No. 4, 1985, pp. 505-515.
5. Booker, J.F., *Program FEMEHL: Theoretical Guide*, Report No. MSD-87-14, Sibley School of Mechanical and Aerospace Engineering, Cornell University, Ithaca, New York, April, 1987.
6. Kumar, A., P.K. Goenka, and J.F. Booker, *Modal Analysis of Elastohydrodynamic Lubrication: A Connecting Rod Application*, ASME Journal of Tribology, Vol. 112, No. 3, 1990, pp. 524-534.
7. Boedo, S., Booker, J.F., and Wilkie, M.J., *A Mass Conserving Modal Analysis for Elastohydrodynamic Lubrication*, Lubricants and Lubrication, Proc. 21<sup>st</sup> Leeds-Lyon Symposium on Tribology, Elsevier, Amsterdam, 1995, pp. 513-523.
8. Oh, K.P., *The Numerical Solution of Dynamically Loaded Elastohydrodynamic Contact as a Nonlinear Complementarity Problem*, ASME Journal of Tribology, Vol. 106, No. 1, 1984, pp. 88-95.
9. Oh, K.P., and Goenka, P.K., *The Elastohydrodynamic Solution of Journal Bearings Under Dynamic Loading*, ASME Journal of Tribology, Vol. 107, No. 3, 1985, pp. 389-395.

10. McIvor, J.D.C, and Fenner, D.N., *Finite Element Analysis of Dynamically Loaded Flexible Journal Bearings: A Fast Newton-Raphson Method*, ASME Journal of Tribology, Vol. 111, No. 4, 1989, pp. 597-604.
11. Yang, P., and Wen, S., *A Fast, Robust, Straightforward Algorithm for Thermal Elastohydrodynamic Lubrication*, Tribology International, Vol. 26, No. 1, 1993, pp. 17-23.
12. Boedo, S., *Dynamics of Engine Bearing Systems: Rigid Body Analysis*, M.S. Thesis, Cornell University, Ithaca, New York, 1986.
13. Bonneau, D., Guines, D., Frene, J., and Toplosky, J., *EHD Analysis, Including Structural Inertia Effects and a Mass-Conserving Cavitation Model*, ASME Journal of Tribology, Vol. 117, No. 3, 1995, pp. 540-547.
14. Elrod, H.G., Anwar, I., and Colsher, R., *Transient Lubricating Films with Inertia-Turbulent Flow*, ASME Journal of Tribology, Vol. 106, No. 1, 1984, pp. 134-139.
15. Olson, E.G., *A Finite Element Treatment of Hydrodynamic Lubrication with Structural Inertia and Elasticity*, Ph.D. Dissertation, Cornell University, Ithaca, New York, 1995.
16. Kumar, A., and Booker, J.F., *A Finite Element Cavitation Algorithm*, ASME Journal of Tribology, Vol. 113, No. 2, 1991, pp. 276-286.
17. Kumar, A., and Booker, J.F., *A Finite Element Cavitation Algorithm: Application/Validation*, ASME Journal of Tribology, Vol. 113, No. 2, 1991, pp. 255-261.
18. Kumar, A., and Booker, J.F., *A Mass and Energy Conserving Finite Element Lubrication Algorithm*, ASME Journal of Tribology, Vol. 116, No. 4, 1994, pp. 667-671.
19. Shampine, F., and Gordon, M.K., *Computer Solution of Ordinary Differential Equations: The Initial Value Problem*, W.H. Freeman, San Francisco, California, 1975.
20. Cook, R.D., *Concepts and Applications of Finite Element Analysis*, John Wiley and Sons, Inc., New York, 1974.
21. Goldstein, H., *Classical Mechanics, 2<sup>nd</sup> Ed.*, Addison-Wesley Publishing Co., Reading, Massachusetts, 1981.
22. Booker, J.F., and Huebner, K.H., *Application of Finite Element Methods to Lubrication: An Engineering Approach*, ASME Journal of Lubrication Technology, Vol. 94, No. 4, 1972, pp. 313-323.
23. Murty, K.G., *Note on a Bard-Type Scheme for Solving the Complementarity Problems*, Opsearch, Vol. 11, 1984, pp. 123-130.
24. Brewster, D.E., *Theoretical Modeling of the Vapor Cavitation in Dynamically Loaded Journal Bearings*, ASME Journal of Tribology, Vol. 108, No. 4, 1986, pp. 628-638.
25. MacNeal, R.H., *The Nastran Theoretical Manual*, The MacNeal-Schwindler Corp., 1972.

## The elastohydrodynamic lubrication of heavily loaded journal bearing having non-cylindrical axial geometry

Hassan E. Rasheed  
 Arab Academy for Science & Technology, Alexandria, Egypt

The elastohydrodynamic analysis of bearings having non-cylindrical geometrical configurations in the axial direction is presented in this paper. Several geometrical configurations having concave, convex and wedge-shaped surfaces are examined. The effects of changing the shape and radius to length ratio of the journal are investigated. The results show a marked increase in the load carrying capacity over that of the plain cylindrical bearing. A decrease in the friction variable is also found. These effects become pronounced for relatively long bearings. Among the geometries selected the concave shaped bearing is found superior to all other geometries.

### 1. INTRODUCTION

The analysis of bearings having elastic liners and of several geometrical configurations have been reported in different ways in the literatures [1-5]. Some investigators treated the elastohydrodynamic lubrication of non-circular geometrical shapes of the bearing liner especially those having elliptical and multiple lobes configurations [6-7]. Others examined the effect of geometrical changes caused by either the deflection of the journal or the angular misalignment together with the elastic deformation of the liner [8-9]. On the other hand the recent advancement in numerically controlled machine tools has made the accurate machining of rather complex shapes a feasible task. This has encouraged some researchers to attempt to study the performance of bearings having non-cylindrical axial configurations and running under normal loading conditions considering the journal and the liner as rigid elements [10-12]. Fortunately improved performance characteristics over the plain cylindrical bearings are reported. However to the author's knowledge nothing has been reported concerning the elastohydrodynamic analysis of those types of bearings. It is the aim of this paper to fill this gap.

### 2. ANALYSIS

To obtain the performance characteristics of a bearing of arbitrary axial shape a curvilinear system of coordinates is adopted. The analysis proposed by El-Gamal [12] is extended in the present work to include the deformation of the bearing liner and the variation of the lubricant viscosity with film

pressure. The system of coordinates used is shown in Fig. 1. The fluid inertia forces are considered negligible compared to viscous forces. The lubricant flow in the bearing is assumed laminar, incompressible and the viscosity of the lubricant is assumed to vary along the fluid film depending solely on the film pressure as is always the case for heavily loaded bearings.

The equations governing the lubricant flow in a dimensionless form may be written as,

$$\frac{\partial^2 \mu^*}{\partial \eta^2} = \frac{\lambda^2}{\mu^*} \frac{\partial p^*}{\partial \theta}$$

$$0 = \frac{\partial p^*}{\partial \eta}$$

$$\frac{\partial^2 w^*}{\partial \eta^2} = \left(\frac{R}{L}\right) \frac{1}{\mu^*} \frac{\partial p^*}{\partial \zeta}$$

$$\frac{\partial u^*}{\partial \theta} + \left(\frac{R}{c}\right) \frac{\partial v^*}{\partial \eta} + \left(\frac{R}{L}\right) \left( \frac{\partial w^*}{\partial \zeta} + \frac{1}{\lambda} \frac{d\lambda}{d\zeta} w^* \right) = 0$$

$\lambda(\zeta)$  is a geometry variable defined as

$$\lambda(\zeta) = \left[ 1 - \left( \frac{dH^*(\zeta)}{d\zeta} \right)^2 \right]^{1/2}$$

and  $H^*(\zeta)$  is an arbitrary function describing the bearing geometrical configuration. The *a priori* selection of the geometrical shape of the bearing dictates the form of the function  $H^*$  and

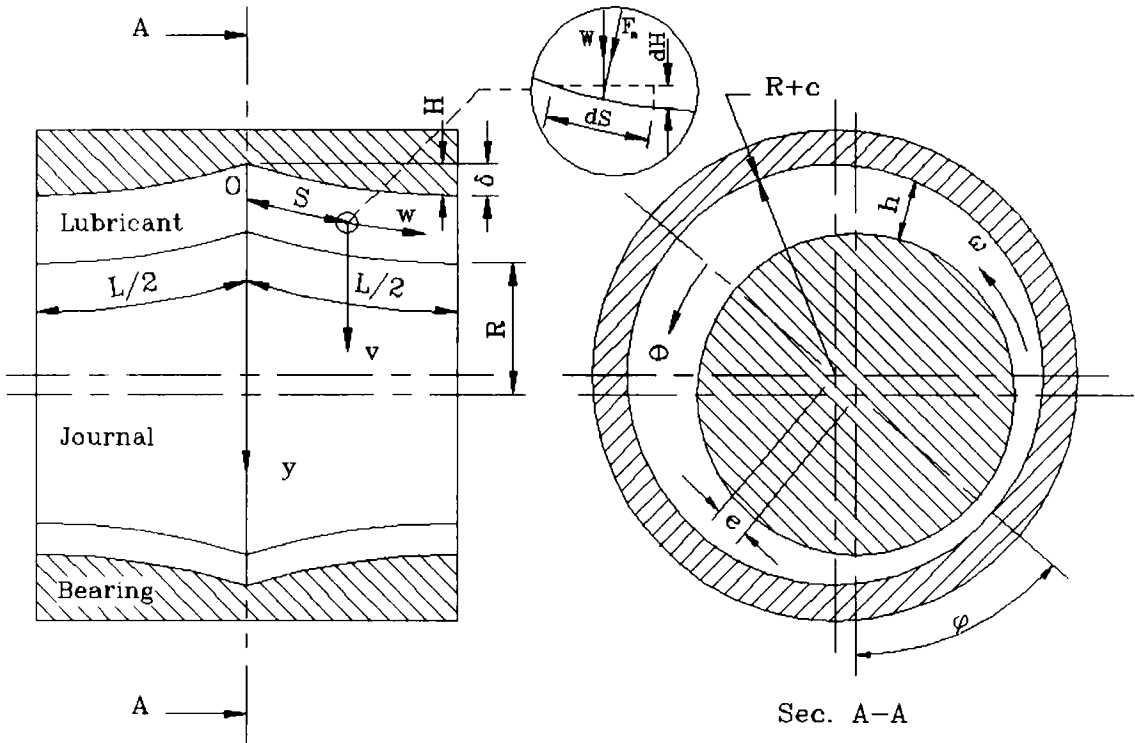


Fig. 1 The curvilinear coordinate system.

consequently the variable  $\lambda$ . Three geometrical configurations are selected for the analysis, namely the concave, convex and wedge shapes (see Fig. 2). These geometrical configurations can simply be described by a single function  $H^*$  which may be written as :

$$H^* = a_1\zeta + a_2\zeta^2$$

in which  $a_1$  and  $a_2$  are constants, their values depend on bearing geometry, as follows:

$a_1=0, a_2 = 4\delta^*$  for bearing of concave geometry

$a_1=4\delta^*, a_2 = -4\delta^*$  for bearing of convex geometry

$a_1=2\delta^*, a_2 = 0$  for wedge shaped geometry

For completion ;

$a_1 = a_2 = 0$  for bearing of plain cylindrical shape.

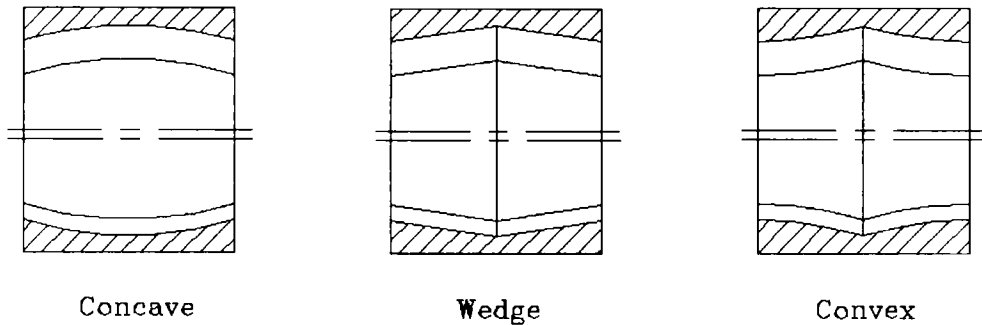


Fig. 2 The bearing geometrical configurations.

The integration of Eqns. 1 with respect to  $\eta$  twice and making spatial averaging across the film thickness lead to a Reynolds - like equation of the following form,

$$\frac{\partial}{\partial \theta} \left( \frac{\lambda h^{*3}}{\mu^*} \frac{\partial p^*}{\partial \theta} \right) + \left( \frac{R}{L} \right)^2 \frac{1}{\lambda^2} \frac{\partial}{\partial \zeta} \left( \frac{\lambda h^{*3}}{\mu^*} \frac{\partial p^*}{\partial \zeta} \right) = \frac{6}{\lambda} \left[ 1 + (\delta^* - H^*) \left( \frac{L}{R} \right) \right] \frac{\partial h^*}{\partial \theta} \quad (2)$$

The boundary conditions are,

$$\theta = 0, \quad p^* = 0, \quad \theta = \theta_{\text{eff}}, \quad p^* = \frac{\partial p^*}{\partial \theta} = 0$$

$$\zeta = 0, \quad \frac{\partial p^*}{\partial \zeta} = 0, \quad \zeta = 1/2, \quad p^* = 0$$

with  $h^* = 1 + \varepsilon \cos \theta + h_e^*$

where  $h_e^*$  is the change in the lubricant film thickness due to elastic deformation of the bearing liner under fluid pressure.

In the present analysis it is assumed that the journal is rigid and experience no elastic deformation under pressure. In general the determination of  $h_e^*$  requires the solution of the three - dimensional elasticity equations of equilibrium and compatibility. However, when the ratio of the thickness of the bearing bush to the radius of the bearing is small ( $t/R_b \leq 0.1$ ) and Poisson's ratio ranging between 0.3 and 0.4, it is shown by Hooke et al [1] and Jain and Sinhasan [5] that a simple plane stress model may approximate satisfactorily the complex three - dimensional model. The model is based on the assumption that a plane stress condition exists and the tangential strains are considered negligible. The same models results from the assumption of plane strain condition and the neglect of tangential stresses. Using this model the resulting deformation may be written as,

$$h_e^* = C_v p^* = \frac{\mu_o \omega R R_b t (1 - \nu^2) p^*}{c^3 E} \quad (3)$$

It remains here to consider the viscosity variation with pressure. As for heavily loaded bearings, the viscosity varies along the film depending very much

on the value of the local pressure. Many investigators dealing with bearings having elastic bushings considered the viscosity to be pressure dependent only, see [3] and [4]. However a simple viscosity pressure relation is used in the present analysis and is in the form,

$$\mu^* = \text{EXP}(\alpha^* p^*) \quad (4)$$

The radial and tangential load components are,

$$W_r^* = -2 \int_0^{1/2} \int_0^{\theta_{\text{eff}}} \lambda \left[ 1 + (\delta^* - H^*) \left( \frac{L}{R} \right) \right] p^* \cos \theta \, d\theta \, d\zeta$$

$$W_t^* = 2 \int_0^{1/2} \int_0^{\theta_{\text{eff}}} \lambda \left[ 1 + (\delta^* - H^*) \left( \frac{L}{R} \right) \right] p^* \sin \theta \, d\theta \, d\zeta$$

The resultant load and the attitude angle are,

$$W^* = \left( W_r^{*2} + W_t^{*2} \right)^{1/2}$$

$$\text{and } \phi = \tan^{-1} \left( W_t^* / W_r^* \right)$$

The frictional force and the normal force acting on the journal surface are given by,

$$F^* = 2 \int_0^{1/2} \int_0^{2\pi} \frac{1}{\lambda} \mu^* \left( \frac{\partial u^*}{\partial \eta} \right)_{\eta=h^*} \left[ 1 + (\delta^* - H^*) \left( \frac{L}{R} \right) \right] d\theta \, d\zeta$$

$$F_n^* = \left( F_{n_r}^{*2} + F_{n_t}^{*2} \right)^{1/2}, \quad \text{where}$$

$$F_{n_r}^* = -2 \int_0^{1/2} \int_0^{\theta_{\text{eff}}} \left[ 1 + (\delta^* - H^*) \left( \frac{L}{R} \right) \right] p^* \cos \theta \, d\theta \, d\zeta$$

$$F_{n_t}^* = 2 \int_0^{1/2} \int_0^{\theta_{\text{eff}}} \left[ 1 + (\delta^* - H^*) \left( \frac{L}{R} \right) \right] p^* \sin \theta \, d\theta \, d\zeta$$

and the friction variable may be calculated from,

$$fR/c = F^* / F_n^*$$

**3. RESULTS AND DISCUSSION**

It is expected, as is always the case in elasto-hydrodynamic problems, that a decrease in the load carrying capacity  $W^*$  due to elastic deformation of the liner will take place for any geometrical shape (see Figs. 3a and b). But it is to be noted that the decrease in  $W^*$  is overwhelmed by the marked increase in  $W^*$  due to changing the geometrical shape from cylindrical to any of the geometries considered. This is clearly demonstrated from Fig. 3 when compared to Fig. 4 respectively. The percentage changes in the load carrying capacity for the shapes considered relative to the plain cylindrical case are given in Figs. 4a, b, c and d versus  $R/L$  for different values of  $\epsilon$ . They all show an increase in the load carrying capacity ranging from about 5% to surprisingly 80%. The longer the bearing the larger the percentage increase in  $W^*$  especially at low eccentricity ratios. The figures show that the concave geometry is superior to all other geometries over the entire range of  $R/L$  and  $\epsilon$ . And this is pronounced for relatively long bearings and lower values of  $\epsilon$ . The percentage change in the friction variable is also plotted (see Figs. 5a, b, c and d). The concave and wedge - shaped geometries show a decrease in  $fR/c$  especially for long bearings and at low eccentricity ratios. The convex geometry gives a decrease in  $fR/c$  for longer bearings and an increase in  $fR/c$  for  $R/L$  approximately over 0.6. The largest decrease in  $fR/c$  is always given by the concave geometry especially for long bearings.

The percentage change in the attitude angle  $\phi$  is also given in Figs. 6a, b, c and d. A decrease in the attitude angle relative to that of the plain cylindrical bearing is obtained for all geometries considered ranging from practically zero to approximately 15%. The percentage decrease in  $\phi$  is practically of the same order for all geometries especially at larger values of  $\epsilon$ . The maximum decrease in  $\phi$  is found to be approximately at  $R/L = 0.5$  for all geometries and any value of  $\epsilon$ .

**4. CONCLUSIONS**

It is concluded here that the new geometrical bearing configurations considered, all give considerable increase in the load carrying capacity over the plain cylindrical bearing. This is pronounced most for relatively long bearings and low eccentricity ratios. A decrease in the friction

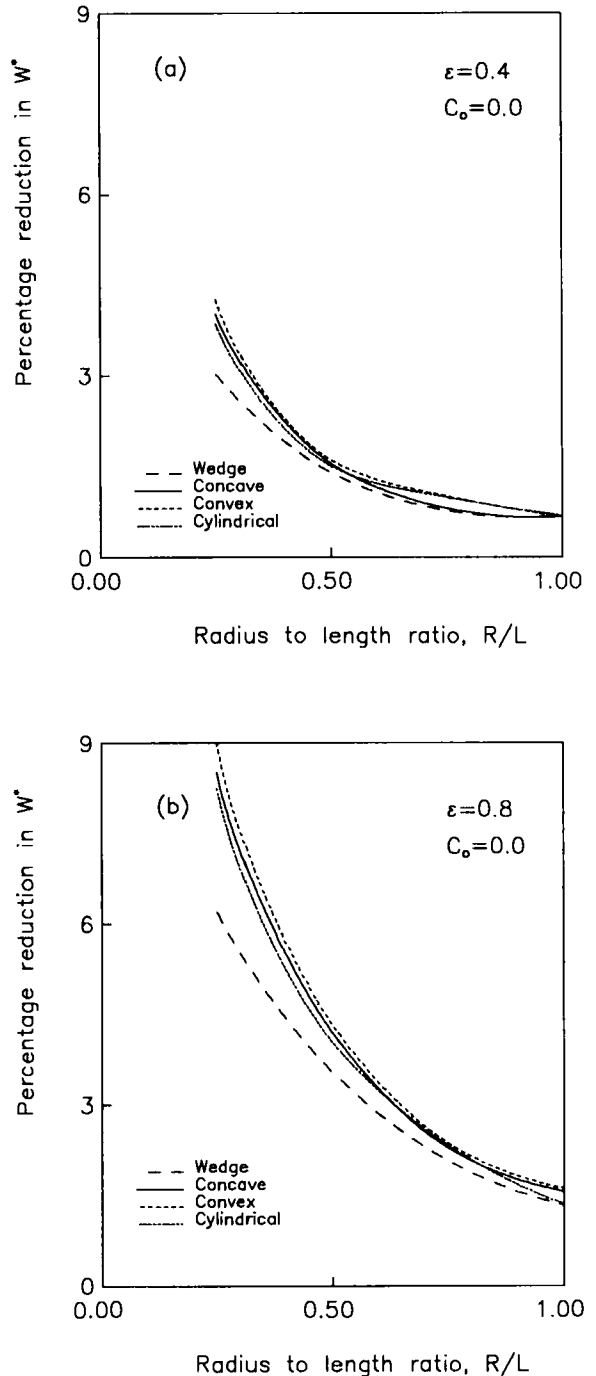


Fig.3 The percentage reduction in  $W^*$  due to the deformation of the bearing liner for different geometries.

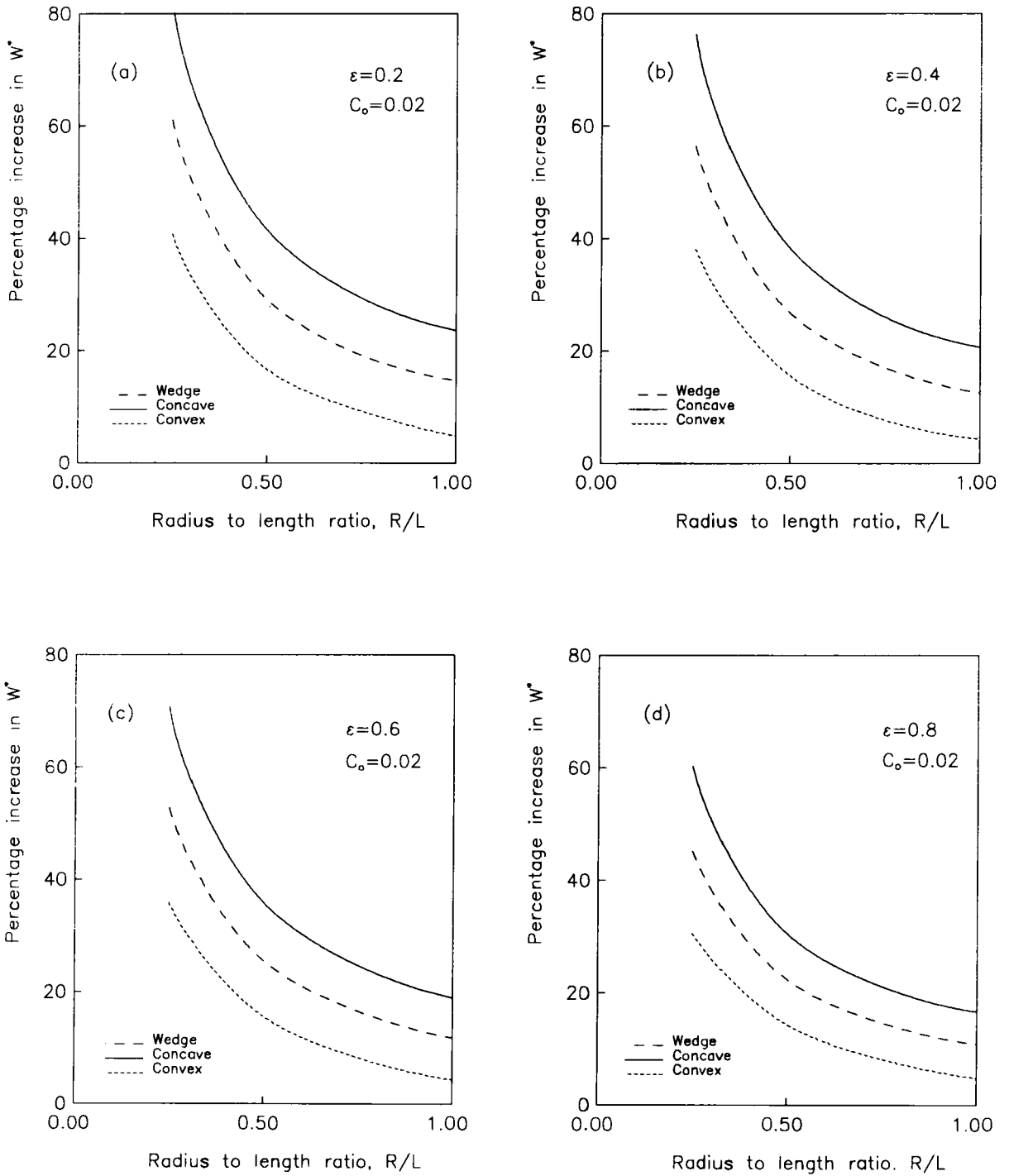


Fig. 4 The percentage increase in the dimensionless load carrying capacity,  $W^*$ , for different bearing geometries relative to that of the plain cylindrical bearing, versus  $R/L$  for different eccentricity ratios  $\epsilon$ .



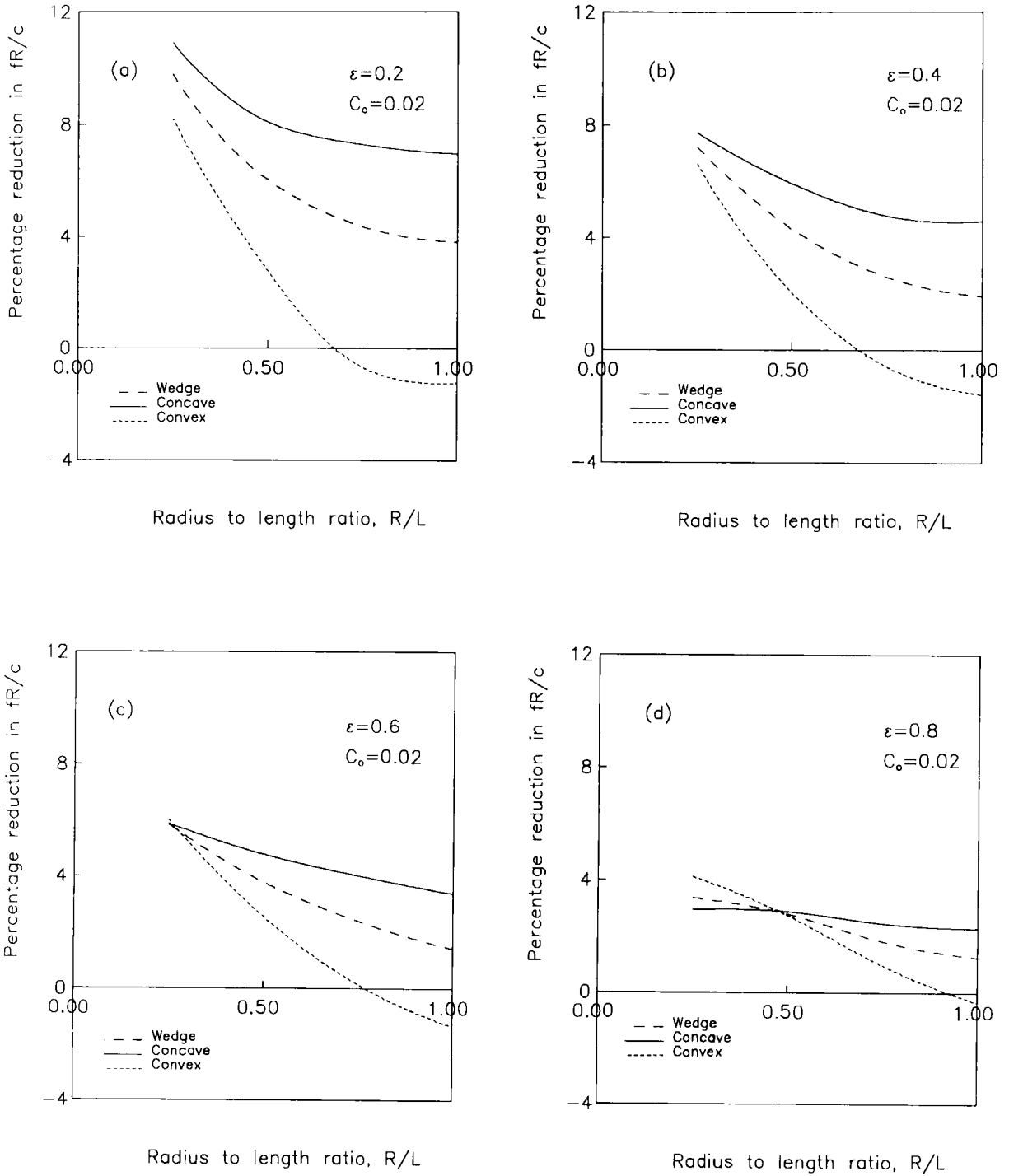


Fig.5 The percentage reduction in the friction variable,  $fR/c$ , for different geometries relative to the plain cylindrical journal bearing, versus  $R/L$  for different eccentricity ratios  $\epsilon$ .

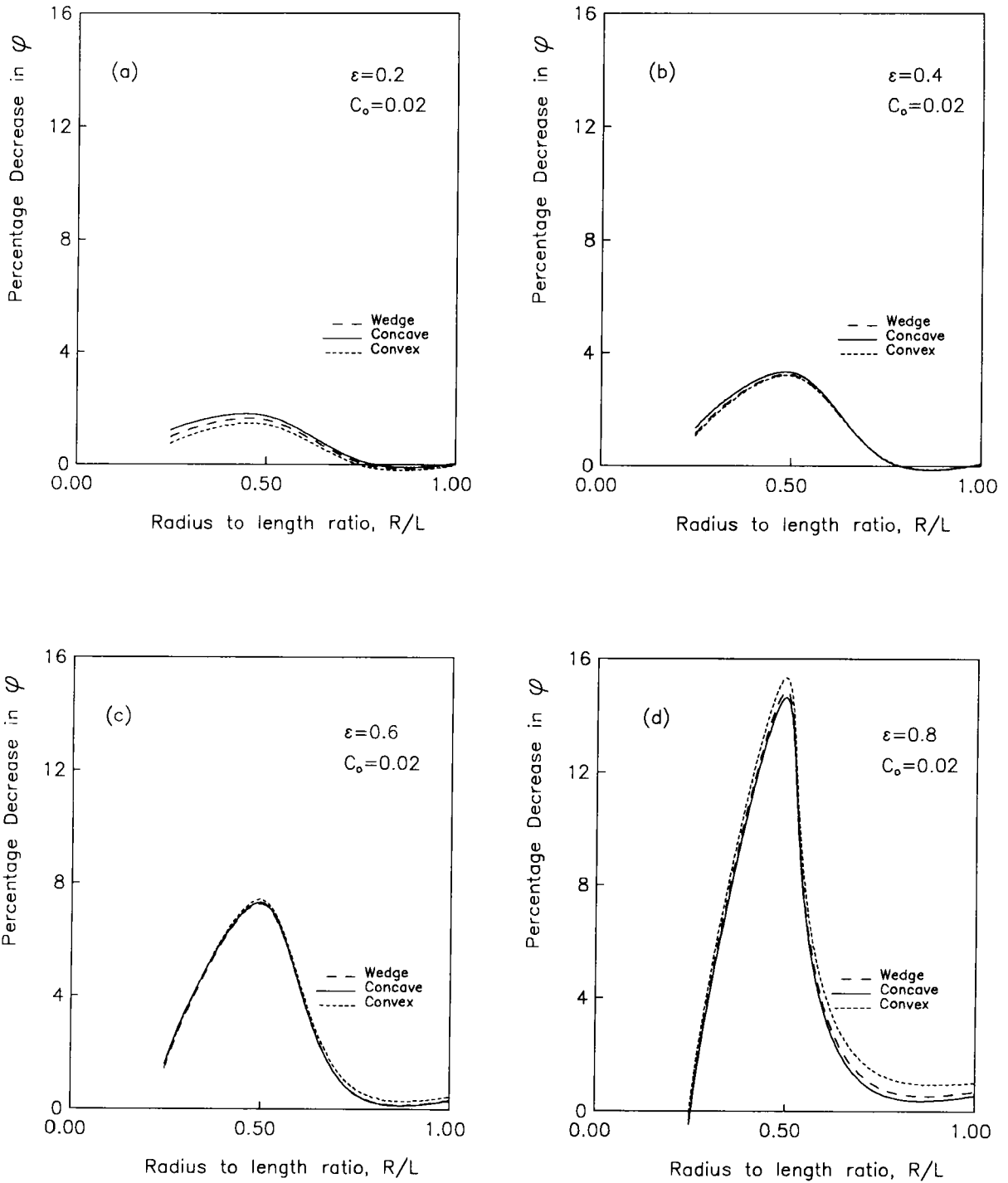


Fig.6 The percentage decrease in the attitude angle,  $\phi$ , for different bearing geometries relative to that of the plain cylindrical bearing, versus  $R/L$  for different eccentricity ratios  $\epsilon$ .

variable is also found for the concave and wedge shaped geometries. A similar decrease in the friction variable is present for relatively long bearings having convex geometry. The concave geometry is found superior to all other geometries and is best recommended for the design of heavily loaded journal bearings.

## NOMENCLATURE

- $c$  radial clearance (m)  
 $C_0$  Elasticity coefficient  
 $E$  Young's modulus (Pa)  
 $h^*$  dimensionless film thickness ( $h^* = h/c$ )  
 $L$  axial length along bearing surface (m)  
 $p^*$  dimensionless fluid pressure  
 $p^* = p / (\omega \mu_0 R^2 / c^2)$   
 $R$  minimum shaft radius (m)  
 $R_b$  minimum bearing liner radius (m)  
 $t$  bearing liner thickness (m)  
 $u^*$ ,  $v^*$ ,  $w^*$  dimensionless velocity components in directions  $\theta$ ,  $\eta$ ,  $\zeta$  respectively ( $u^* = u / \omega R$ ,  $v^* = v / \omega R$ ,  $w^* = w / \omega R$ )

## Greek symbols

- $\alpha^*$  lubricant dimensionless viscosity index  
 $\alpha^* = \alpha (\omega \mu_0 R^2 / c^2)$   
 $\delta^*$  dimensionless maximum axial variation of bearing geometry ( $\delta^* = \delta / L$ )  
 $\varepsilon$  eccentricity ratio  
 $\zeta$ ,  $\eta$  dimensionless coordinates along and normal to one side of the bearing surface respectively ( $\zeta = S / L$ ,  $\eta = y / c$ )  
 $\theta$  coordinate in tangential direction (rad)  
 $\mu^*$  dimensionless fluid viscosity ( $\mu^* = \mu / \mu_0$ )  
 $\mu_0$  inlet fluid viscosity (Pa s)  
 $\nu$  Poisson's ratio  
 $\omega$  journal angular velocity (rad/s)

## DATA FOR THE LUBRICANT AND OPERATING CONDITIONS

Bearing radial clearance,  $c = 100 \mu\text{m}$   
 Journal minimum radius,  $R = 25 \text{ mm}$   
 Rotational speed,  $N = 25 \text{ rev/s}$   
 Maximum axial variations of geometrical shape;  
 $\delta = 2.5 \text{ mm}$ ,  $5 \text{ mm}$  and  $10 \text{ mm}$

Bearing surface axial lengths:

$L = 25 \text{ mm}$ ,  $50 \text{ mm}$  and  $100 \text{ mm}$

Lubricant dimensionless viscosity index :

$\alpha^* = 0.006843$

Lubricant inlet temperature,  $T_0 = 60 \text{ }^\circ\text{C}$

Bearing liner thickness,  $t = 2.5 \text{ mm}$

## REFERENCES

1. Hooke C.J., Brighton D.K. and O'Donoghue J.P. The effect of elastic distortions on the performance of thin shell bearings. Proc. Inst. Mech. Eng., vol. 181 (Part 3D), 1966-7, pp 63 - 69.
2. Benjamin M.K. and Castelli V.A. Theoretical investigation of compliant surface journal bearings. ASME Trans., Journal of lubrication technology, vol. 93, No 1, 1971, pp. 191 - 201.
3. Conway H.D. and Lee H.C. The analysis of the lubrication of a flexible journal bearing. ASME Trans., Journal of lubrication technology, vol. 97, No 4, 1975, pp. 599 - 604.
4. Jain S.C., Sinhasan R. and Singh D.V. Elastohydrodynamic analysis of a cylindrical journal bearings shell. Wear, vol. 78, 1982, pp 325 - 335.
5. Jain S.C. and Sinhasan R. Performance of flexible shell journal bearings with variable viscosity lubricants. Tribology Int., vol. 16, No 6, 1983, pp. 331 - 339.
6. Prabhakaran Nair K., Sinhasan R. and Singh D.V. EHD effects in elliptical journal bearings. Wear, 118 (2), 1987, pp 120 - 146.
7. Prabhakaran Nair K., Sinhasan R. and Singh D.V. A study of EHD effects in the three - lobe journal bearings. Tribology Int., 20 (3), 1987, pp. 125 - 132.
8. Pinkers O. and Bupara S.S. Analysis of misaligned groove journal bearings. ASME, Journal of Lubr. Tech., vol. 101, 1979, pp. 503 - 509.
9. El-Gamal H.A., Awad T., Helmy A. and El-Fahham I.M. Effect of shaft misalignment of the performance of heavily loaded journal bearings. Fourth Int. Conf. of Fluid Mechanics (ICFM4) April, 28-30, vol III, 1992, pp 569 - 582.
10. Leung P.S., Graighed I.A. and Wilkinson T.S. An analysis of the steady and dynamic characteristics of a spherical hydrodynamic

- journal bearing. *Journal of Tribology*, vol. 111, 1989 , pp. 459 - 467.
11. El-Gamal H.A. Analysis of the steady state performance of a wedge - shaped hydrodynamic journal bearing. *Wear*, 184 , 1995 .
  12. El-Gamal H.A. The effect of axial geometrical variations on sliding element bearing characteristics. XI National Conference on Industrial Tribology, Jan 22 - 25 , 1995 , New Delhi, India.

## Mode Stiffness Variation in Elastohydrodynamic Bearing Design

S. Boedo<sup>a</sup> and J.F. Booker<sup>b</sup>

<sup>a</sup>Borg-Warner Automotive, Inc., Ithaca, New York, 14850 USA

<sup>b</sup>Cornell University, Ithaca, New York, 14853 USA

A mode-based mass-conserving formulation for transient elastohydrodynamic lubrication (described elsewhere) has been shown to be an attractive analysis method for “global” bearing structures where only a few mode shapes are required to capture the essential features of deformation. The modal analysis method further suggests a novel means of implementing structural design changes by selective stiffening or softening of one or more mode shapes, the physical means of which is left as an inverse engineering problem. The design methodology is applied to an ungrooved connecting rod bearing lubricated through a crankpin feed hole.

### PRINCIPAL NOMENCLATURE

|       |                               |
|-------|-------------------------------|
| a     | residual density rate         |
| b     | residual force                |
| c     | clearance                     |
| d     | relative displacement         |
| e     | journal absolute displacement |
| f     | journal external force        |
| g     | body force                    |
| h     | film thickness                |
| n     | normal                        |
| p     | pressure                      |
| q     | mass flow                     |
| r     | surface force                 |
| x,y,z | film coordinates              |
| A     | area                          |
| B     | elastic equilibrium           |
| C     | damping                       |
| G     | static equilibrium            |
| H     | density rate damping          |
| I     | identity                      |
| K     | stiffness                     |
| Q     | transformation                |

|           |                       |
|-----------|-----------------------|
| T         | transformation        |
| X,Y,Z     | system coordinates    |
| $\delta$  | absolute displacement |
| $\rho$    | mixture density       |
| $\Lambda$ | eigenvalue            |
| $\Psi$    | eigenvector           |

### 1. INTRODUCTION

The mode-based method of elastohydrodynamic (EHD) lubrication has been shown to be a suitable analysis alternative for “globally” elastic bearing structures where the essential features of elastic deformation are captured by a linear combination of a small set of mode shapes [1-4]. Although initially developed to improve computational speed over conventional node-based methods [5] while maintaining acceptable accuracy, the mode-based approach also offers a possible alternative toward EHD structural design methodology.

We suggest a novel means of implementing and evaluating design changes to a lubricated structure by selective stiffening or softening one or more of its elastic mode shapes. The result is a modified absolute structural stiffness matrix which represents some unspecified physical geometry. Our point here is to ascertain the EHD characteristics of this mode-altered stiffness matrix *a priori* and independently from the task of creating the corresponding physical structure.

We apply the methodology to a finite element representation of an ungrooved connecting rod bearing which is lubricated by a single crankpin feed hole. Minimum film thickness, maximum film pressure, and oil flow are employed as measures of bearing performance.

**2. MODAL EHD FORMULATION**

Much of what follows is described in detail elsewhere [1-4]. Figure 1 shows a bearing system (with its fixed rectilinear coordinates X,Y,Z) comprised of a restrained elastic sleeve structure A and a free rigid circumferentially symmetric journal B with smooth surfaces  $S^a$  and  $S^b$  which interact through a thin lubricant film (with its curvilinear coordinates x,y,z). Although cylindrical geometry is represented here, the analysis which follows has been applied to spherical configurations found in such applications as piston bearings and artificial hip joints [6].

**2.1 Structural Relations**

Sleeve structure A is represented by a contiguous set of finite elements, from which one can define a set of master degrees of freedom along inward and outward normals to surfaces  $S^a$  and  $S^b$ , respectively. That is,

for this problem, normal  $\bar{n}$  is radially-outward from the bearing center.

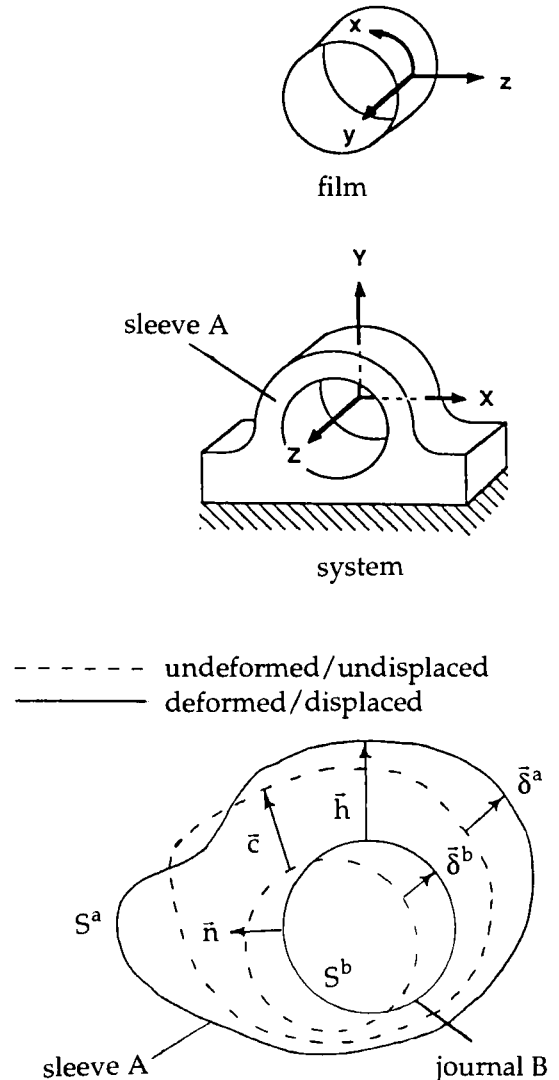


Figure 1. Bearing system schematic

Following the usual condensation procedure for finite elements, equilibrium of sleeve structure A can be represented by  $n^s$  relations

$$\underline{\underline{\tilde{K}}} \underline{\underline{\delta}}^a = \underline{\underline{r}}^a + \underline{\underline{g}}^a \quad (1)$$

where the absolute stiffness matrix  $\tilde{K}$  relates  $n^s$  master absolute displacements  $\delta^a$  with  $n^s$  master force components  $r^a, g^a$  derived from work-equivalent surface tractions and body forces, respectively.

Application of static equilibrium and virtual work principles to rigid journal B results in  $k + n^s$  relations

$$\underline{\underline{G}}^T \underline{\underline{r}}^b = \underline{\underline{f}} \quad (2a)$$

$$\underline{\underline{\delta}}^b = -\underline{\underline{G}} \underline{\underline{e}} \quad (2b)$$

where the static equilibrium matrix  $G$  relates nodal master forces  $r^b$  and absolute nodal displacements  $\delta^b$  with  $k$  system components of journal absolute displacement  $e$  and journal external load  $f$ .

Combining equations (1) and (2) gives  $n^s$  elastostatic relations

$$\underline{\underline{K}} \underline{\underline{d}}^s - \underline{\underline{B}} \underline{\underline{f}} + (\underline{\underline{B}} \underline{\underline{G}}^T - \underline{\underline{I}}) \underline{\underline{g}}^a = \underline{\underline{r}}^s$$

in terms of  $n^s$  relative nodal displacements

$$\underline{\underline{d}}^s = \underline{\underline{\delta}}^a - \underline{\underline{\delta}}^b$$

so

$$\underline{\underline{h}} = \underline{\underline{c}} + \underline{\underline{d}}^s$$

where relative stiffness and elastic equilibrium matrix

$$\underline{\underline{K}} = \underline{\underline{\tilde{K}}} - \underline{\underline{\tilde{K}}} \underline{\underline{G}} (\underline{\underline{G}}^T \underline{\underline{\tilde{K}}} \underline{\underline{G}})^{-1} \underline{\underline{G}}^T \underline{\underline{\tilde{K}}}$$

$$\underline{\underline{B}} = \underline{\underline{\tilde{K}}} \underline{\underline{G}} (\underline{\underline{G}}^T \underline{\underline{\tilde{K}}} \underline{\underline{G}})^{-1}$$

depend on system elasticity and bearing geometry.

## 2.2 Hydrodynamic Relations

Representing the 2-dimensional lubricant film as a set of finite elements connected at  $n^f$  nodes, a mass-conserving formulation for generic lubrication problems gives the  $2n^f$  hydrodynamic relations [3,4]

$$\underline{\underline{C}} \underline{\underline{\dot{d}}}^f + \underline{\underline{b}} = \underline{\underline{r}}^f$$

$$\underline{\underline{H}} \underline{\underline{\dot{d}}}^f + \underline{\underline{a}} = \underline{\underline{\dot{\rho}}}$$

where damping matrices  $C, H$  and residual vectors  $a, b$  depend on nodal density  $\rho$ , nodal film thickness  $h$ , specified nodal pressure and flow  $\{p^*, q^*\}$ , and which relate relative nodal displacement rates  $\dot{d}^f$  with nodal forces  $r^f$  and nodal density rates  $\dot{\rho}$ . Note that the fluid film mesh and the structural surface mesh (on surface  $S^a$ ) need not be identical.

## 2.3 Modal EHD Equations of Motion

The essential approximation in the modal EHD analysis is the replacement of  $n^s$  structure-based displacements  $d^s$  and  $n^f$  film-based displacements  $d^f$  with  $m \ll n^s$  (and  $m \ll n^f$ ) modal displacements  $d'$  through the use of transformation relations

$$\underline{\underline{d}}^s = \underline{\underline{T}}^s \underline{\underline{d}}'$$

$$\underline{\underline{d}}^f = \underline{\underline{Q}}^{fs} \underline{\underline{T}}^s \underline{\underline{d}}'$$

where  $T^s$  has been chosen from a set of eigenvectors or mode shapes  $\Psi$  which satisfy the area-based eigenvalue problem

$$\underline{\underline{K}} \underline{\underline{\Psi}} = \underline{\underline{\Lambda}}^s \underline{\underline{\Psi}} \underline{\underline{\Lambda}}$$

and where  $Q^{fs}$  maps mode shapes from the structure mesh onto the fluid film mesh. Structure-based area matrix  $A^s$  is assembled from the corresponding structural finite element representation of surface  $S^a$ . The validity of such mappings is suggested for global structures through the observed insensitivity of the lowest-ordered area-based mode shapes to changes in mesh density, coupled with the additional assumption that the lowest-ordered mode shapes are sufficient to capture essential features of bearing deformation [2].

Transforming and combining elastostatic and hydrodynamic relations results in a set of  $m + n^f$  modal EHD relations

$$\underline{\underline{C'}} \underline{\underline{d'}} + \underline{\underline{b'}} = \underline{\underline{K'}} \underline{\underline{d'}} - \underline{\underline{B'}} \underline{\underline{f}} + \underline{\underline{g'}}$$

$$\underline{\underline{HQ}}^{fs} \underline{\underline{T}}^s \underline{\underline{d'}} + \underline{\underline{a}} = \underline{\underline{\rho}}$$

whereupon specification of  $m$  modal displacements and  $n^f$  initial nodal densities completes problem specification of an initial value problem. Special forms of the modal EHD relations for quasi-static lubrication and bearing rigidity are discussed elsewhere [3,4].

### 3. MODAL DESIGN METHODOLOGY

Geometric and material variation to the elastic structure shown in Figure 1 are reflected through changes in its absolute stiffness matrix  $\tilde{K}$  and body force vector  $g^a$ . As the deformation of global structures are essentially captured by a small set of mode shapes, we propose a novel means of assessing design modification for global structures through selective modification of the lowest-ordered eigenvalues  $\tilde{\Lambda}$  which satisfy the related area-based eigenvalue problem

$$\underline{\underline{\tilde{K}}} \underline{\underline{\tilde{\Psi}}} = \underline{\underline{A}}^s \underline{\underline{\tilde{\Psi}}} \underline{\underline{\tilde{\Lambda}}}$$

where  $\tilde{\Psi}$  are now the mode shapes of the absolute stiffness matrix. Assuming structural modifications leave mode shapes  $\tilde{\Psi}$ , area matrix  $A^s$ , and body forces  $g^a$  essentially unaltered, a new set of eigenvalues  $\tilde{\Lambda}^*$  result in a modified absolute stiffness matrix

$$\underline{\underline{\tilde{K}}}^* = \underline{\underline{A}}^s \underline{\underline{\tilde{\Psi}}} \underline{\underline{\tilde{\Lambda}}}^* \underline{\underline{\tilde{\Psi}}}^{-1}$$

representing some unspecified physical geometry. The determination of the actual physical structure corresponding to  $\tilde{K}^*$  (and  $g^a$ ) will be left as an unsolved inverse-engineering problem. Given  $\tilde{K}^*$  (and  $g^a$ ), formation of the modal EHD equations of motion proceeds as before.

### 4. APPLICATION

Figure 2 shows a half-model finite element representation of a sample ungrooved big-end connecting rod studied previously [2-4]. Fixed ambient-pressure and liquid-density boundary conditions

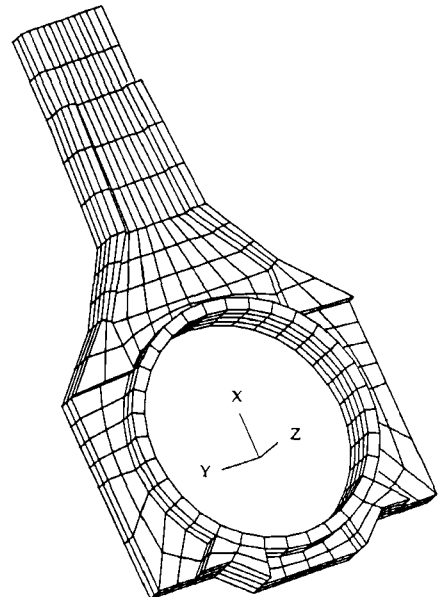


Figure 2. Connecting rod FEM model



(representing conditions at the bearing ends) and moving feed-pressure and liquid-density boundary conditions (representing a single crankpin feed hole) are applied to the finite element lubricant film model. Bearing specifications, modeling details, and bearing duty are discussed elsewhere [2-4].

Figure 3 shows the first eleven members of a set of area-based mode shapes taken from the absolute stiffness matrix representing the original connecting rod model. Table 1 shows that modes 1 and 2 have significantly lower eigenvalues compared to the rest. Mode 1 represents near rigid body translation of the conrod big-end normal to the conrod centerline, while mode 2 represents big-end translation and deformation parallel to the conrod centerline. As previous studies [1-4] have shown that bearing elongation in the direction of the conrod centerline influences bearing behavior, let us assume that structural modifications can be made to the original conrod design which produces variation only in the mode 2 eigenvalue, leaving the others essentially unchanged.

Hypothetical mode-softened and mode-stiffened structures are created through a reduction and increase, respectively, of the original mode 2 eigenvalue of the absolute stiffness matrix, as given in Table 1. Figures 4-6 and Table 2 shows that this design process alters only one eigenvalue of the corresponding relative stiffness matrix and leaves mode shapes essentially unchanged.

Figure 7 shows the effects of structural modification on time histories of minimum film thickness and maximum film pressure over the engine cycle. In each case, the first seven modes are found to be adequate in capturing the essential features of bearing deformation. It is observed that both mode-softened and mode-stiffened structures

generally reduce film thickness throughout the engine cycle; a significant drop in film thickness is observed for the mode-softened structure during engine firing. However, mode-stiffening reduces film pressure during those parts of the engine cycle when the load resides in the cap region. Assuming film thickness history to be acceptable, it can be concluded that the mode-stiffened structure offers an improvement over the original structure by reducing film pressure in the cap region.

Figure 8 shows spatial distributions of film thickness, film pressure, and mixture density at 360 degree crankangle, where mode-stiffening is observed to reduce effects of bearing sleeve wrap while maintaining a small fluid pocket in the cap region. Mode-softening, on the other hand, increases bearing wrap which produces a significant pressure spike where the sleeve "pinches" against the rigid journal.

Table 3 shows that cycle-averaged flow increases for the mode-softened structure while remaining essentially unchanged for the mode-stiffened structure.

**Table 3**  
**Cycle-averaged outlet oil flow ( $10^{-6} \text{ m}^3/\text{s}$ )**  
**7 modes, 4000 rpm**

|                          |        |
|--------------------------|--------|
| mode-softened structure  | 1.9167 |
| original structure       | 1.7128 |
| mode-stiffened structure | 1.6773 |

## 5. SUMMARY

This paper illustrates the use of a mode-based EHD lubrication model to evaluate design changes for global structures through

**Table 1**  
**Area-based eigenvalues for absolute stiffness matrix modes**

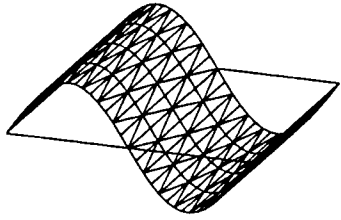
---

| <u>Mode</u> | Eigenvalue (TN/m <sup>3</sup> ) |                                |                                 |
|-------------|---------------------------------|--------------------------------|---------------------------------|
|             | <u>Original Structure</u>       | <u>Mode-Softened Structure</u> | <u>Mode-Stiffened Structure</u> |
| 1           | 0.004                           | 0.004                          | 0.004                           |
| 2           | 0.133                           | 0.013                          | 1.332                           |
| 3           | 0.226                           | 0.226                          | 0.226                           |
| 4           | 0.638                           | 0.638                          | 0.638                           |
| 5           | 1.166                           | 1.166                          | 1.166                           |
| 6           | 1.355                           | 1.355                          | 1.355                           |
| 7           | 1.976                           | 1.976                          | 1.976                           |
| 8           | 3.116                           | 3.116                          | 3.116                           |
| 9           | 3.128                           | 3.128                          | 3.128                           |
| 10          | 5.092                           | 5.092                          | 5.092                           |
| 11          | 5.368                           | 5.368                          | 5.368                           |

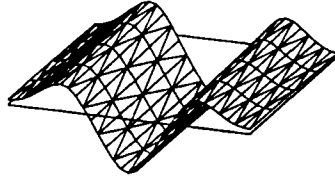
**Table 2**  
**Area-based eigenvalues for relative stiffness matrix modes**

---

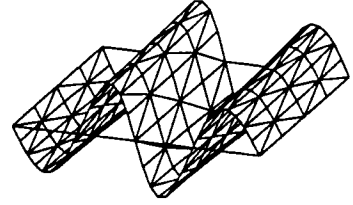
| <u>Mode</u> | Eigenvalue (TN/m <sup>3</sup> ) |                                |                                 |
|-------------|---------------------------------|--------------------------------|---------------------------------|
|             | <u>Original Structure</u>       | <u>Mode-Softened Structure</u> | <u>Mode-Stiffened Structure</u> |
| 1           | 0                               | 0                              | 0                               |
| 2           | 0                               | 0                              | 0                               |
| 3           | 0.218                           | 0.028                          | 0.218                           |
| 4           | 0.235                           | 0.218                          | 0.814                           |
| 5           | 1.151                           | 1.151                          | 1.151                           |
| 6           | 1.329                           | 1.324                          | 1.355                           |
| 7           | 1.723                           | 1.692                          | 1.923                           |
| 8           | 3.084                           | 3.080                          | 3.105                           |
| 9           | 3.122                           | 3.122                          | 3.122                           |
| 10          | 5.091                           | 5.091                          | 5.092                           |
| 11          | 5.368                           | 5.368                          | 5.368                           |



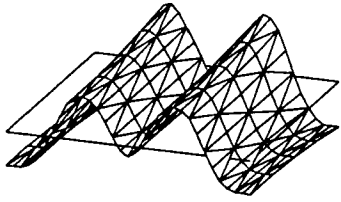
Modeshape 1



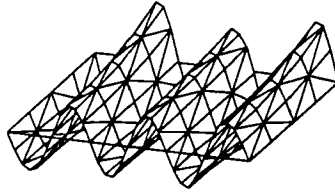
Modeshape 2



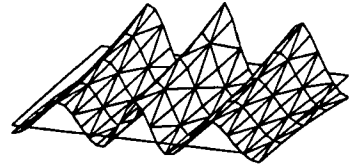
Modeshape 3



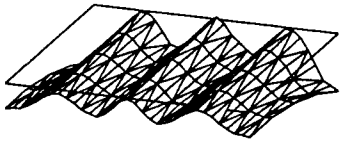
Modeshape 4



Modeshape 5



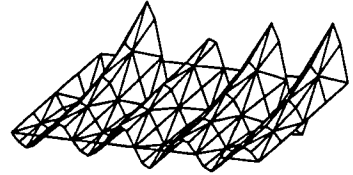
Modeshape 6



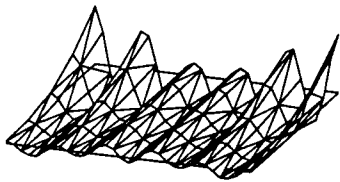
Modeshape 7



Modeshape 8



Modeshape 9



Modeshape 10



Modeshape 11

Figure 3. Area-based eigenvectors of absolute stiffness matrix: original and mode-modified structures

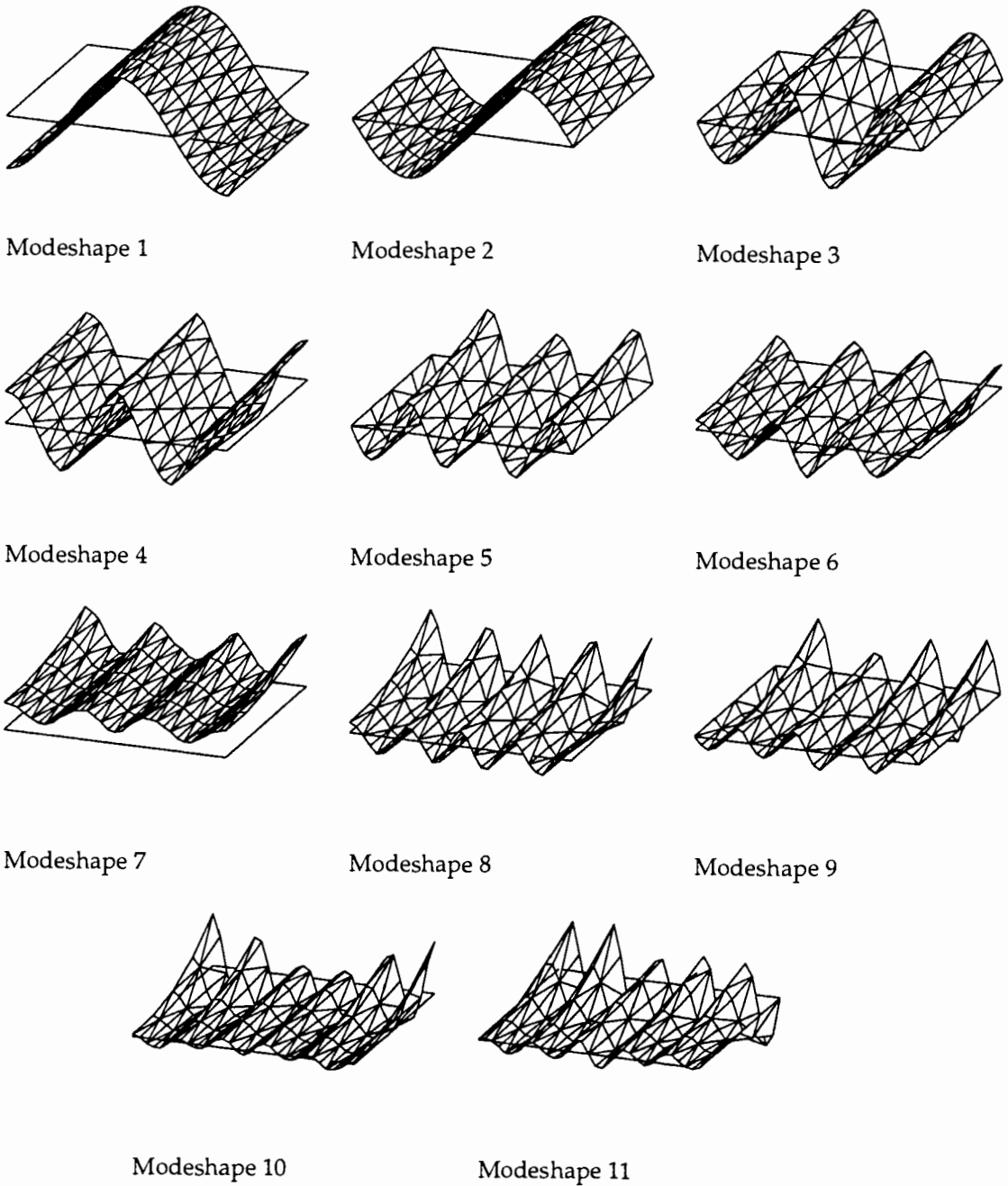
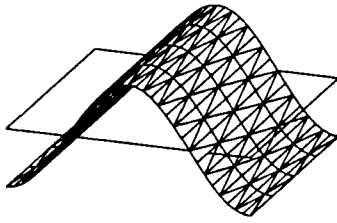
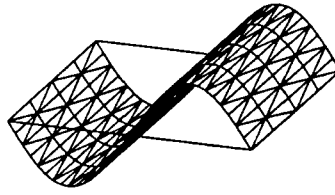


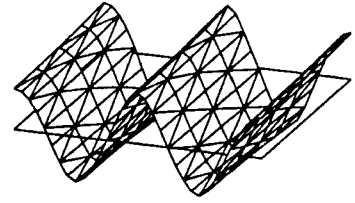
Figure 4. Area-based eigenvectors of relative stiffness matrix:  
original structure



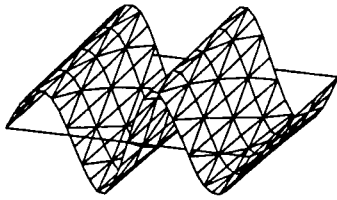
Modeshape 1



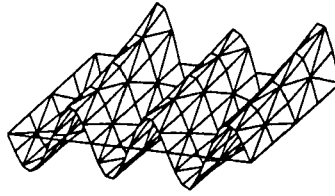
Modeshape 2



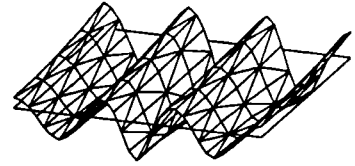
Modeshape 3



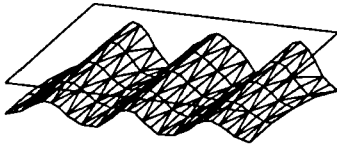
Modeshape 4



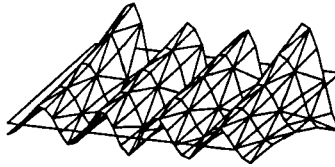
Modeshape 5



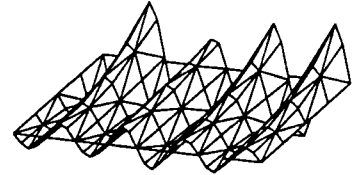
Modeshape 6



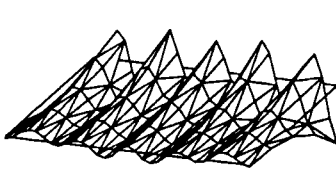
Modeshape 7



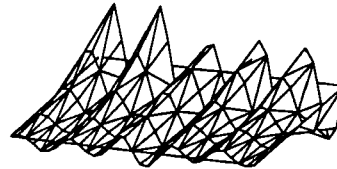
Modeshape 8



Modeshape 9

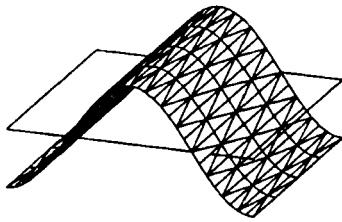


Modeshape 10

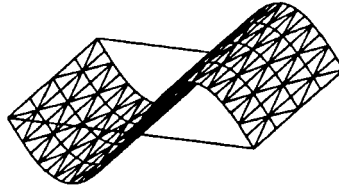


Modeshape 11

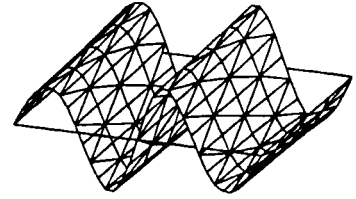
Figure 5. Area-based eigenvectors of relative stiffness matrix:  
mode-softened structure



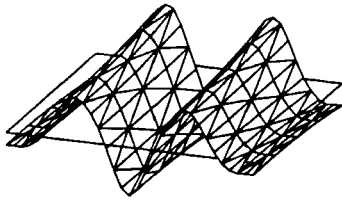
Modeshape 1



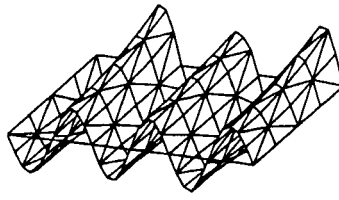
Modeshape 2



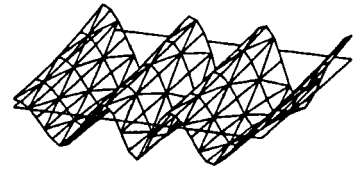
Modeshape 3



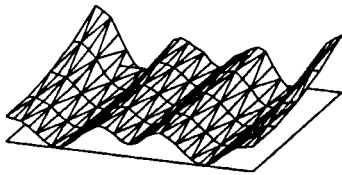
Modeshape 4



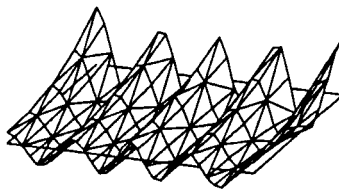
Modeshape 5



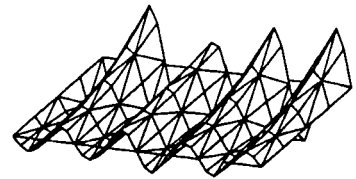
Modeshape 6



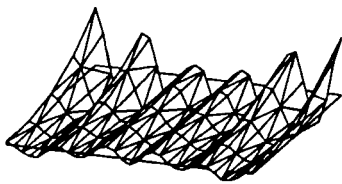
Modeshape 7



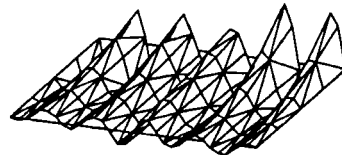
Modeshape 8



Modeshape 9



Modeshape 10



Modeshape 11

Figure 6. Area-based eigenvectors of relative stiffness matrix: mode-stiffened structure

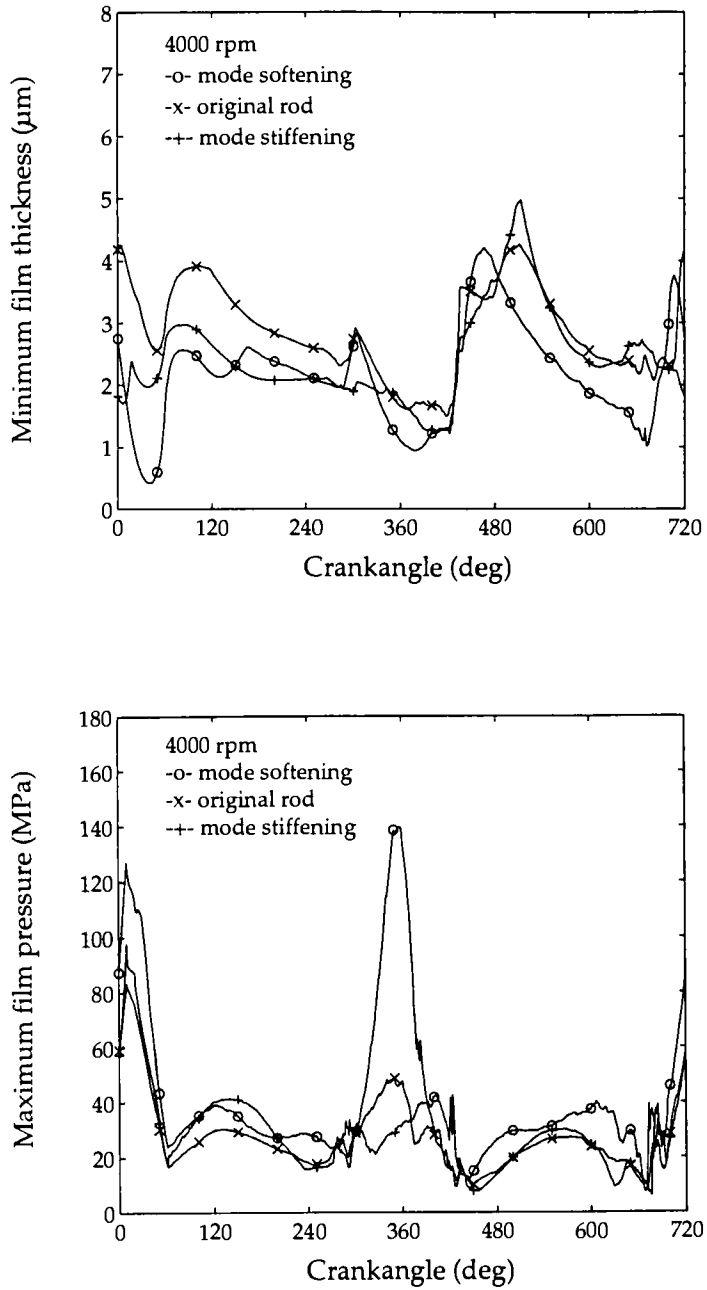


Figure 7. Film thickness and film pressure comparison

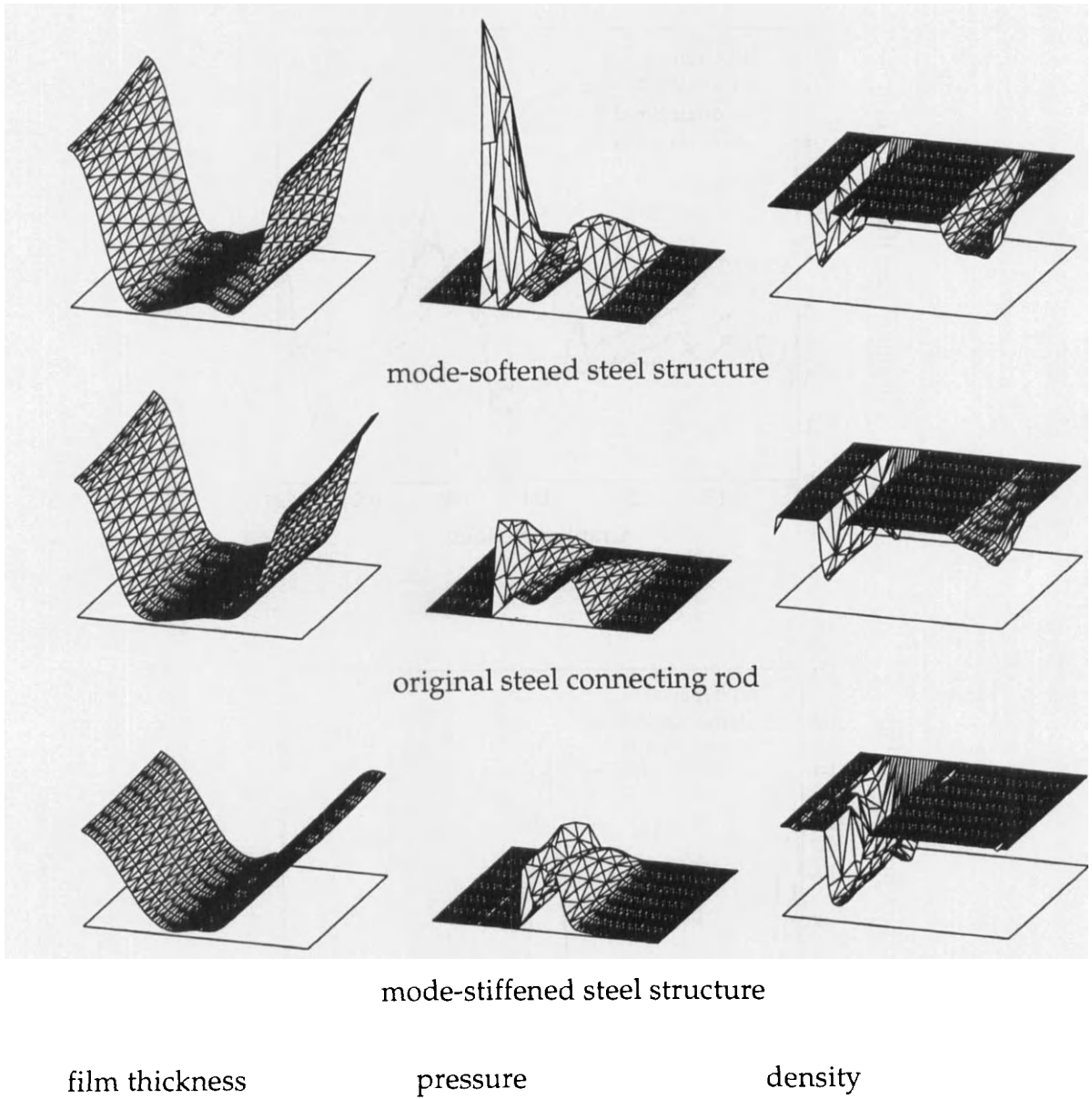


Figure 8. Distributions at 360 deg crankangle



selective stiffening or softening of low-order mode shapes. The method allows the designer to evaluate EHD performance comparisons without the explicit need to construct the corresponding physical structure. Application to a connecting rod bearing indicates that selective stiffening of the lowest ordered mode representing deformation along the conrod centerline can improve bearing performance through a reduction in film pressure when the bearing load resides in the cap region.

## REFERENCES

1. A. Kumar, P.K. Goenka and J.F. Booker, "Modal Analysis of Elastohydrodynamic Lubrication: A Connecting Rod Application," ASME J. Trib., vol. 112, 1990, p. 524.
2. S. Boedo, J.F. Booker and M.J. Wilkie, "A Mass Conserving Modal Analysis for Elasto-hydrodynamic Lubrication," Proc. 21<sup>st</sup> Leeds-Lyon Symposium on Tribology, Lubricants and Lubrication, Elsevier, 1995, pp. 513-523.
3. S. Boedo and J.F. Booker, "Surface Roughness and Structural Inertia in a Mode-Based Mass-Conserving Elasto-hydrodynamic Lubrication Model," ASME Paper 96-Trib-36.
4. S. Boedo, "A Mass-Conserving, Modal-Based Elastohydrodynamic Lubrication Model: Effects of Structural Body Forces, Surface Roughness, and Mode Stiffness Variation," Ph.D. thesis, Cornell University, 1995.
5. K.P. Oh and P.K. Goenka, "The Elastohydrodynamic Solution of a Journal Bearing under Dynamic Loading," ASME J. Trib., vol. 107, 1985, pp. 389-395.
6. M. Kothari, "Elastohydrodynamic Lubrication of Metal-on-Metal Hip Joints," Ph.D. thesis, Cornell University, 1996.

## Written Discussion - Contributions

### DISCUSSION

#### SESSION II - ANALYTICAL/ NUMERICAL STUDIES (1)

**Paper II (i) 'Influence of Local and Global Features in EHL Contacts'** by Professor A A Lubrecht (INSA, Lyon, France).

**Dr J A Greenwood**, (Cambridge University, UK). You showed that the EHL pressure distribution around a dent was almost the same as the dry contact pressure distribution, with almost equal peaks on each side of the dent. But you then showed a picture of the subsurface shear stresses which are extremely un-symmetrical. Since the sub-surface stresses are entirely determined by the surface tractions, how can this be?

**Reply by Professor A A Lubrecht**, (INSA, Lyon, France). The stationary dry contact and EHL pressure distributions are very similar as is shown in Figure 1. Figure 3 shows that for the transient case of pure rolling, the pressure over the trailing edge is consistently larger than the pressure over the leading edge of the dent.

the stress distribution shown in Figure 4 represents the maximum of the stress at each location over time. Because of this representation of the maximum values only, a small but persistent difference in pressure gives rise to a rather marked difference in the maximum stress pattern.

**Paper II (ii) 'Fully Coupled Elasto-hydrodynamic Solution Techniques for the Analysis of Real Rough Line Contacts Using Finite Element and Finite Difference Models'** by C D Elcoate, H P Evans and T G Hughes (University of Wales, Cardiff, UK)

**Dr J B Medley**, (University of Waterloo, Canada). The authors are to be congratulated for a concise, well organised presentation of their model development. Can they comment on the additional features that would be required to study fluid film breakdown.

**Reply by Dr H P Evans** (University of Wales, Cardiff, UK). The question of fluid film breakdown is an interesting one. A failure mechanism based on the transverse leakage of lubricant from within the contact area along the valley features of the ground gear surfaces has been proposed by one of the authors\*, and a further paper on that mechanism is in preparation. The mechanism depends on transverse flow and will not emerge in a line contact approach as described in the current paper.

\* Evans, H P & Snidle, R W. "A Model for Elastohydrodynamic Film Failure in Contacts between Surfaces having Transverse Finish", Trans ASME Jn. of Tribology (in press).

**Professor A A Lubrecht** (INSA, Lyon, France). The authors are to be complemented for having studied such an important but difficult problem. The coupling of real geometry and rheology is indeed very promising. However, the film thickness is influenced by the slide-to-roll ratio, whenever the surfaces are non-smooth.

The authors calculate the film thickness for the (stationary) case of pure sliding, but then couple it to a calculation under rolling-sliding conditions. Could the authors please comment on this?

**Reply by Dr H P Evans** (University of Wales, Cardiff, UK). The question is correct in its inference that the speed conditions adopted are not consistent with the stationary roughness case. The purpose of the paper is to draw attention to the capability of the method described to deal with the low lambda values that occur in gear contacts. The conditions adopted for analysis correspond to those actually occurring in scuffing disk experiments carried out at Cardiff. The model will be fully consistent with this experimental program when time dependence has been incorporated, but the essential robustness of the method is demonstrated by the results presented in this paper.

**Dr C J Hooke** (University of Birmingham, UK). Could the authors indicate the speed of their solution process and how it varies with the number of nodal points in their mesh?

**Reply by Dr H P Evans** (University of Wales, Cardiff, UK). At present the models incorporate a Gaussian elimination solution routine to solve the resultant fully populated matrices. The solution time per cycle for this solution routine is proportional to the number of mesh points to the power 3. The solution time per cycle for the original measured data, equivalent to 96 points in a half Hertzian contact width (b) and 408 points in total, is 22 seconds. The solution time per cycle for the interpolated data, equivalent to 288 points in (b) and 1224 points in total, is 650 seconds. These figures result from running the model on a DEC alpha 255/300 workstation. The interpolated data for which the solution time is stated represents the finest mesh spacing adopted and is finer than is necessary to establish the essential features of the solution. It is recognised that the Gaussian elimination solver adopted, which has been used throughout the model development due to its reliability and for the sake of continuity is not the most efficient solver available. A program of work is now in place to upgrade the solution method used to increase the efficiency of the models presented.

**Dr. Guangteng Gao** (Imperial College, London, UK). I would like to congratulate the authors for making such an important contribution to rough surface EHL. It is remarkable to see that the numerical analysis is able to cope with EHL problems with such thin films. For conditions in which film thicknesses are much smaller than the surface roughness, there will be some occasional asperity contacts between the two surfaces, especially when the film thickness is only 0.007  $\mu\text{m}$ , which is much smaller than the out-of-contact roughness. I would like to know whether such asperity contacts are allowed in the computation process and how the authors address such issues.

**Reply by Dr H P Evans** (University of Wales, Cardiff, UK). The model presented in the paper does not have a mechanism for asperity collision. Such an effect could only be seen in a time dependent solution and does not emerge from the numerical solution at this stage in its development. However the extreme pressure deviations suggested at the asperities under low lambda conditions could

be expected to lead to surface modification, if not to surface failure.

**Paper II (iii) 'Fatigue and Brittle Fracture Analysis of Surface Engineered Materials in Rolling Contact'** by T.H. Kim and A.V. Olver (Imperial College, London, UK).

**Dr P A Dearnley** (University of Leeds, UK).

1. The initial surface roughness of bearings and gears is considerably modified during the running-in-phase - are the roughness values considered here relatable to real surfaces after running-in, or are they based on 'as manufactured' surface roughness values?
2. The creation of residual compressive stress following nitriding is essential to the successful improvement in rolling contact fatigue duration and pitting resistance. Can your gear model predict what level of residual stress is required for "acceptable" life in gears or bearings?
3. Your considerations appear focused on events some 2-3 $\mu\text{m}$  below the surface. Simple Hertzian analysis shows that the maximum shear stress, in many bearing situations, is some tens of micrometers below the surface; accordingly 'deep' nitriding cases of 80-150 $\mu\text{m}$  are commonly specified. In the light of these comments how can you justify focusing on a region some 2-3 $\mu\text{m}$  below the surface? (Incidentally, many nitrided surfaces in the outer 2-3 $\mu\text{m}$  contain pores and are enriched in the brittle  $\gamma'$  and  $\epsilon$  nitride phases; these have no beneficial residual compressive stress).

**Reply by Mr T H Kim and Dr A V Olver** (Imperial College, London, UK).

1. We have used artificially generated surface profiles to simulate the contact of rough surfaces and the parameters were chosen so as to generate a typical ground finish with a rms value of about 0.18 $\mu\text{m}$ . No yield occurred with these surfaces for the conditions in the analysis and, as the material is a hard bearing

steel (M50), the roughness tends to persist. In the paper, we aimed to demonstrate the detrimental effect of roughness during sliding - rolling contact in relation to the smooth contact. The effect of the degree of roughness due to different manufacturing methods, finishes applied and running-in of the components, can be incorporated as the model is capable of using real measured surfaces.

2. Yes. The model determines the stress generated for given contact conditions and accounts for the hardness and residual stress variation that results from surface treatments, such as nitriding, in determining the fatigue life. These variations are accommodated in the analysis to account for different characteristics of various surface treatments available. It is also possible to use the model to predict the required minimum, or ideal distribution of hardness and residual stresses, in order to achieve acceptable life for a particular contact condition.
3. Attention is concentrated on the first few microns in depth because:
  - (a) this is where fatigue is usually observed to initiate.
  - (b) this is where the model predicts the greatest probability of failure.

This shallow region very close to the surface is subjected to very high stresses due to the roughness and the dominance of these stresses in determining the fatigue life is discussed in the paper. However, the stress distribution reverts to that of the Hertzian solution a few tens of microns below the surface and these stresses are also included in the analysis to determine the fatigue life of the component. The model solves for stresses in the region large enough to assess the stresses induced by the contacts (typically 200 microns wide and 400 microns deep). In the analysis of the nitrided material, we assumed no brittle nitride phase is left on the surface. Removal of these layers is carried out in practice as they serve no beneficial purpose in terms of the fatigue resistance.

**Dr J A Williams** (Cambridge University, UK). In your presentation you demonstrated the initiation of sub-surface plasticity: if this occurs in the first few cycles of operation the surfaces may presumably in the long term be left with additional protective residual stresses. Is your analysis compatible with shakedown and how this might influence the number of cycles to failure.

**Reply by Mr T H Kim and Dr A V Olver** (Imperial College, London, UK). Our analysis assumes elastic contact and no plastic effect is taken into account at present. This was considered sufficient as the stresses generated were below the yield stress for the conditions analysed. However, if the plasticity is to be included in the analysis for more severe contact conditions, it is necessary to understand exactly how the onset of yield would alter the material's response. When two rough surfaces roll and slide together, both the stresses due to the friction and the local effect of the roughness, tend to cause the point of first yield to occur close to the (softer) surface. Any resulting plastic deformation would be expected to lead to modified residual stresses, but it is not clear that these would necessarily be protective. In our analysis, we have taken into account the residual stresses that result from the surface treatment processes and these stresses were high enough in the case of the nitriding treatment studied here to reduce greatly the effect of the applied shear stresses, affecting both yield and fatigue damage.

**Paper II (iv) "Elastohydrodynamic Effects in Piston Ring Lubrication in Modern Gasoline and Diesel Engines"** by Dr J E Rycroft, Dr R I Taylor and Dr L E Scales (Shell Research Ltd., Chester, UK).

**Mr Y Tozaki** (Mitsubishi Heavy Industries, Nagasaki, Japan).

1. Can your program calculate at starved conditions?
2. Do you have the intention or experience to calculate the marine diesel engines?

**Reply by Dr R I Taylor** (Shell Research Ltd., Chester, UK). The hydrodynamic lubrication software that has been developed for piston analysis within Shell can take oil starvation of the upper rings (due to the scraping action of the lower rings) into account. Details may be found in the SAE paper (SAE 941981). However, it was found that around dead centre positions, fully flooded conditions applied. Therefore in the elasto-hydrodynamic analysis described in this paper, fully flooded conditions were assumed as only piston dead centre positions were considered. We have not yet used the software to analyse marine diesel engines.

**Ir. Ysbrand Wijnant** (University of Twente, The Netherlands). Has any dimensionless analysis been performed so as to see if elastic deformations should be taken into account? (Doing so would give you an answer whether to include elasticity).

**Reply by Dr R I Taylor** (Shell Research Ltd, Chester, UK). As described in the paper a hydrodynamic lubrication analysis of the piston assembly, including the squeeze effect, was initially carried out in order to estimate the minimum oil film thickness and the peak pressure under the contact for top and bottom dead centre positions. If the Barus equation for the viscosity pressure variation of a lubricant is assumed, then viscosity varies as  $\exp(\alpha P)$ , where  $\alpha$  is the pressure viscosity coefficient of the lubricant. Broadly speaking, if  $(\alpha P)$  is greater than one, then EHD effects are likely to become important. For the gasoline engine the peak pressure at top dead centre was estimated to be 124 bars, whereas for the diesel engine the peak pressure at top dead centre was estimated to be 2950 bars. For most lubricants  $\alpha$  is approximately  $1/5000 \text{ bars}^{-1}$ . Therefore, we would expect EHD effects to be important for the diesel engine, but not for the gasoline engine.

**Dr M-T Ma** (University of Central Lancashire, Preston, UK). It appears that the authors have not shown the effects of the elastic deformation of piston rings on the tribological performance of the rings (e.g. film thickness and friction). Therefore, it is not convincing to conclude that the EHD analysis is worthwhile to undertake in piston-ring

lubrication situations (diesel engines). Could the authors comment on this?

**Reply by R I Taylor** (Shell Research Ltd., Chester, U.K.). The significant elastic deformations of the top piston ring in the diesel engine do indeed alter the oil film thickness around top dead centre firing. The minimum oil film thickness calculated hydrodynamically (which occurred just after top dead centre firing) was estimated at 0.006 microns, whereas when EHD lubrication was taken into account, the minimum oil film thickness increased to 0.16 microns. For the gasoline engine, the minimum oil film thickness (close to top dead centre firing) was estimated at 0.13 microns, whereas the EHD estimate was 0.31 microns. Although there may not be a major effect on friction around dead centre positions (since the piston ring is low), for the diesel engine the change in shape of the top ring, and the corresponding change in oil film thickness, could have a large influence on top ring wear rate estimates.

### **SESSION III - EXPERIMENTAL (1)**

**Paper III (i). "Nanometre Elasto-hydrodynamic Lubrication"** by Dr A J Moore, (BP Oil Technology Centre, Sunbury-on-Thames, UK).

**Dr J B Medley** (University of Waterloo, Ontario, Canada). Did you impose any sliding velocity in the thin lubricant films and did you use the Barus equation to represent pressure-viscosity behaviour?

**Reply by Dr A J Moore** (BP Oil Technology Centre, Sunbury-on-Thames, UK). No sliding was imposed, but since the ball specimen was driven by the disc the condition was not quite one of pure rolling. Yes, the Barus equation was used to represent the variation in viscosity with pressure.

**Paper III (ii) "Optical Interferometric Observations of the Effects of a Moving Dent on Point Contact EHL"**, by Professor M Kaneta, Dr

T Kanada and Mr N Nishikawa (Kyushu Institute of Technology, Japan).

**Dr S A Johnson** (Unilever Research, Port Sunlight, UK). Would Professor Kaneta please explain the influence of the radius of curvature on the dent on the observed behaviour? The dent used has a relatively large radius of curvature compared to that produced, for example, by a small, hard, contaminating particle. Would Professor Kaneta also like to comment on what sort of flow his dent is supposed to mimic?

**Reply by Professor M Kaneta** (Kyushu Institute of Technology, Japan). This is a very fundamental study to understand the effects of moving defects on point EHL contacts. The radius of curvature of the dent used depends on the depth of the dent and ranges from 0.4 mm to 0.8 mm. We have not investigated the effects of the radius of curvature of the dent on EHL film behaviour. However, we suppose that the dent having a very small radius of curvature does not exert substantial effects on the EHL film, because such a dent seems not to bring about a large amount of side-leakage.

**Paper III (iv) “Technique for Measuring EHD Film Thickness in Non-Steady State Contact Conditions”**, by Dr J Sugimura and Professor H A Spikes, (Imperial College, London, UK).

**Dr J B Medley** (University of Waterloo, Ontario, Canada). What do you think was causing the rapid “apparent” fluctuations in film thickness when the velocity was first applied?

**Reply by Dr J Sugimura and Professor H A Spikes** (Imperial College, London, UK). The fluctuations were probably due to changes in disc speed, which were caused by a rotational oscillation of the driveline including the DC motor. Since the frequency of the oscillation is about 12 Hz, which is far smaller than the natural frequency of the shaft supporting the disc, (and that of the horizontal shaft transmitting torque from the gear box to this shaft), the primary suspect may be the DC motor. (Gear contacts may also have higher frequency. The oscillation occurred with either the reduction gears connected or not).

**Dr C J Hooke** (University of Birmingham, UK). The authors show the variation of film thickness with time for step changes in velocity. Clearly, a step change is impossible and there will actually be a finite period of acceleration or deceleration. Could the authors indicate the time involved and could they say how far the ball and disc moved during this period?

**Reply by Dr J Sugimura and Professor H A Spikes** (Imperial College, London, UK). The authors agree that the rapid on/off motions are actually acceleration and deceleration with very high rate of change of velocity. In abrupt halting, the time involved is between 0.02 and 0.04 seconds. Hence, when the disc speed is 78.8 mm/s, as shown in Figure 9, the disc would travel for 1.6 to 3.2 mm before it stops. It would imply that there is a substantial oil flow under rapidly-changing speed. The level to which the thickness first drops may therefore depend on the rate of deceleration and the response of the oil film to that change. This is in the process of being investigated further. As to the ball, we have not yet made speed measurements on this, but it may have moved a similar distance as the disc. A simple calculation of motion of a free ball rotated by a traction between the ball and the disc has shown that the ball attains the speed of the disc as quickly as one thousandth of a second when the disc undergoes the ideal step change, which suggests little effect of the ball inertia. Nonetheless, there may be some skidding which may have caused the slower thickness drop found within 0.1 seconds after the first drop, when the disc has been stopped.

**Dr Victoria Wikström** (SKF, ERC BV, The Netherlands). The paper is addressing a very important subject, hitherto not treated within experimental/optical EHD. However, in the test set-up, the ball is driven only by the traction between ball and disc. When assuming pure rolling even during the acceleration, which from Figure 2 in the Synopsis is seen to be very high, the authors seem to make a mistake. From the pictures shown at the presentation, there was a substantial drop in film thickness from the first picture to the second, which the authors could not explain. Is it not possible that a rather high sliding

(caused by slip in the ball-disc contact) can cause this drop? Would the authors also please comment on why they did not use a higher sampling rate for the images? (50 Hz is not high, and improvement and better understanding of the up/down phase could have been obtained).

**Reply by Dr Sugimura and Professor H A Spikes** (Imperial College, London, UK). The authors used a normal video recorder simply on the basis of availability and convenience in what was the first application of the ultrathin interferometry to non-steady state conditions. The study has demonstrated that, so far as the resolution and the confidence of measurement are concerned, the ultrathin method is suitable for time-varying systems and the authors now intend to employ a faster video recorder as soon as they can get hold of one.

#### **SESSION IV - ANALYTICAL/NUMERICAL** (2)

**Paper IV(i) "Amplitude Reduction of Waviness in Transient EHL Line Contacts"** by Dr C H Venner\*, Mr F Couhler\*\*, Professor A A Lubrecht\*\* and Dr J A Greenwood\*\*\* (\*University of Twente, The Netherlands), \*\* INSA Lyon, France, \*\*\* University of Cambridge, UK).

**Dr C J Hooke** (University of Birmingham, UK). The authors show a most interesting relationship between amplitude reduction and roughness wavelength for metallic contacts where piezo-viscous effects are significant. It is possible to obtain a similar relationship for soft contacts [1] but here the amplitude reduction can be related to the ratio of roughness wavelength to the length of the entrainment zone. Have the authors considered this possibility in hard contacts?

[1] See Paper VI(i) of the present volume.

**Reply by Dr C H Venner** (University of Twente, The Netherlands). In our paper we have found that

the amplitude reduction is a function of one parameter only:

$$\nabla = \frac{\lambda M^{3/4}}{bL^{1/2}} \propto \lambda W^{1/4} E^{-1/4} R^{-3/4} \left( \eta_0 \alpha u \right)^{-1/2} \quad (1)$$

The question now is if we can relate this expression to a ratio between wavelength and an "entrainment length". In Hooke (1996) the discussor defined entrainment length as the distance from the dry contact end to the point where the maximum pressure gradient occurs. For isoviscous contacts this point can indeed be determined, i.e. it is located at  $h = 1.5 h_c$  where  $h_c$  is the film thickness at  $dp/dx = 0$ . An approximation for the location of this point can then be found from assuming the gap to have the Hertzian shape. Using only the first term of a series expansion we have:

$$h = h_c + \frac{8}{3} K^{1/2} x^{3/2}, \quad (2)$$

where  $x$  is the distance from the dry contact end, and:

$$K = \frac{1}{\sqrt{8\pi}} \frac{1}{R} \left( \frac{W}{E'R} \right)^{1/2} \quad (3)$$

see Hooke (1977). Let  $e$  stand for the  $x$  at which  $h = 1.5 h_c$  then:

$$e \propto K^{-1/3} h_c^{2/3} \quad (4)$$

Subsequently, with an expression for  $h_c$ , the entrainment length can be given in terms of the different parameters. Unfortunately for a piezo-viscous contact the point of maximum pressure gradient can not so easily be found. However, we can find a generalization of the definition of this point which for isoviscous contacts indeed reduces to the point of maximum pressure gradient. Reynolds' equation expresses conservation of mass.

$$\frac{d\phi}{dx} = 0 \quad (5)$$

$$\text{where } \phi = \phi_p + \phi_s \quad (6)$$

is the total mass flow with  $\phi_p$  its pressure flow component and  $\phi_s$  its shear flow component:

$$\phi_p = -\frac{\rho h^3}{12\eta} \frac{dp}{dx} \quad \phi_s = \rho u h \quad (7)$$

If we denote by  $\phi_{so}$  the shear flow component at the point where  $dp/dx = 0$  equation (5) can be integrated:

$$\phi_p + \phi_s = \phi_{so} \quad (8)$$

where

$$\phi_{so} = \rho_c u h_c \quad (9)$$

From (6) with (7), (8) and (9) we obtain that  $\partial\phi/\partial h = 0$  at  $\rho h = 1.5 \rho_c h_c$  and for the case of an incompressible lubricant  $h = 1.5 h_c$ . If the lubricant is isoviscous this is indeed the point where also the pressure gradient attains its maximum. However, in general it can be characterised by the fact that it is the point where a change in the film thickness (keeping all other variables fixed) would not change the mass flow, i.e. would have an equal but opposite effect on the shear and pressure flow components.

From Hooke (1977) (Appendix C) we can derive that for piezoviscous contacts:

$$h_c \propto k^{-1/4} (\alpha \eta_o u)^{3/4} \quad (10)$$

As (2) still holds,  $h = 1.5 h_c$  is obtained at a distance:

$$e \propto K^{-1/2} (\alpha \eta_o u)^{1/2} \quad (11)$$

from the dry contact end. Substitution of K from (3) then gives:

$$e \propto R^{3/4} W^{-1/4} E^{1/4} (\alpha \eta_o u)^{1/2} \quad (12)$$

and we see that:

$$\nabla = (\lambda/b) M^{3/4} L^{-1/2} \propto \frac{\lambda}{e} \quad (13)$$

Hence, the parameter we found can indeed be seen as the ratio between the wavelength of the waviness and the entrainment length, provided the definition of entrainment length is generalised to the distance between the dry contact end and the point in solution where  $\theta\phi/\partial h = 0$ , i.e. the point in the solution characterised by the fact that a film thickness change would have an equal but opposite effect on the poisseuille flow and shear flow components.

Hooke, C J, 1977, "The elastohydrodynamic lubrication of heavily loaded contacts", J of Mechanical Engineering Science, Proc. IMechE, 19, 4, 149-156.

Hooke, C J. 1996, "Elastohydrodynamic lubrication of soft solids", Presented at the 1996 Leeds-Lyon Symposium on Tribology, Leeds, September 1996.

**Paper IV (ii) "Effect of Micro-Cavitation on Oil Film Thickness and Pressure Distributions in Micro-EHL Line Contact"** by S Kamamoto\*, M Sakuragi\*, K Fujimoto\*\* and T Yamamoto\*\*\* (\*Koyo Seiko Co. Ltd., Osaka, Japan, \*\* University of Tokyo, Japan, \*\*\* Tokyo University of Agriculture and Technology, Japan).

**Dr J A Greenwood** (University of Cambridge, UK). You showed us a graph of how the onset of micro-cavitation varied with the operating parameters. According to our linearised theory of the behaviour of waviness, the amplitude of the pressure fluctuations due to a waviness of amplitude ( $z_1$ ) is given by;

$$\frac{P_1}{\bar{p}} = -\frac{z_1}{h} \frac{1}{(A+C)}$$

$$\text{where, } A = \frac{2\lambda \bar{p}}{\pi h E'} \quad \text{and } C = \frac{(\gamma - \beta) \bar{p}}{\left(1 + \gamma \bar{p}\right) \left(1 + \beta \bar{p}\right)}$$



- and there is good evidence that the response in full computations is linear for very much larger waviness amplitudes than one might expect.

Accordingly, by taking  $\left(\frac{-}{p}\right)$  as the mean Hertzian pressure, we can predict that micro-cavitation will begin when  $\left(\frac{p_1}{p}\right) = -1$ , so that the pressure minima are just zero (on the scale of EHL pressures, with  $\bar{p} \approx 1$  GPa, it does not seem to matter whether cavitation takes place at  $p = 0$  or at  $p = -p_v$ ).

$$\text{- i.e. when } \frac{z_1}{h} = A + C$$

How well, if at all, does this agree with your graph?

**Reply by S. Kamamoto** (Koyo Seiko Co. Ltd., Japan). If the pressure fluctuation in an EHL contact due to wavy surfaces is larger than the maximum Hertzian contact pressure, the micro-cavities may be formed after all bumps in the Hertzian contact area. The linearised theory for the behaviour of waviness introduced by Greenwood [1,2] can predict the surface waviness amplitude  $z_1$  to form the micro-cavitation as follows:

$$z_1 = h (A + C) \quad (1)$$

$$A = \frac{2\lambda p_h}{\pi h E'} \quad (2)$$

$$C = \frac{(y - \beta p_h)}{(1 + y p_h)(1 + \beta p_h)} \quad (3)$$

where,  $y, \beta$  are given from the Dowson-Higginson formula for pressure-density relationship ( $y = 2.266 \times 10^{-9} \text{ Pa}^{-1}$ ,  $\beta = 1.683 \times 10^{-9} \text{ Pa}^{-1}$ ),  $p_h$  is the

maximum Hertzian contact pressure and  $z_1$  is the amplitude defined by  $z = z_1 \sin(2\pi x/\lambda)$ .

When comparing our results with the linearized theory, the equation (1) and (2) can be rewritten as:

$$\Sigma_{\cos} = 2H (A + C) \quad (4)$$

$$A = \frac{\Lambda_{\cos}}{2\pi H} \quad (5)$$

where the dimensionless parameters are given as:

$$b = R \sqrt{\frac{8W}{\pi}}, \frac{8W}{\pi}, \frac{hR}{b^2}, \Lambda_{\cos} = \frac{\lambda}{b}, \Sigma_{\cos} = \frac{2z_1 R}{b^2}$$

and  $h$  is given by the central film thickness in smooth surface instead of the mean film thickness in the contact region.

In Figure 1, the linearized theory is compared with the results given by the micro-EHL analyses taking into account the micro-cavitation (Figure 13). It is found that the linearized theory agrees very well with our results when the materials parameter  $G$  and the velocity parameter  $U$  are small. It is noted that the linearized theory agrees with the detailed micro-EHL analysis in spite of such a simple analysis.

However, when the materials parameter  $G$  or the velocity parameter  $U$  is large, the linearized theory underestimates the surface waviness amplitude to form the micro-cavitation.

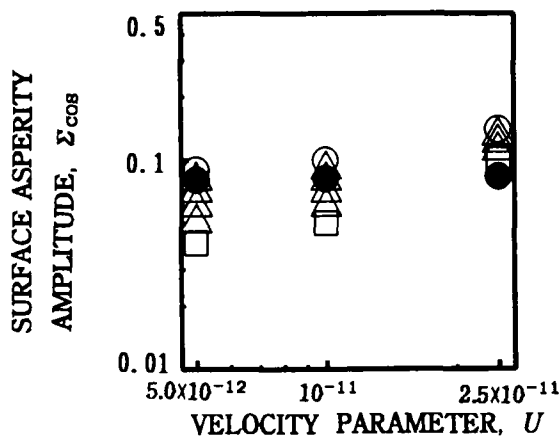
Since the edge effects at the top of each bump increase with the dimensionless parameter  $G$  or  $U$  increasing the surface waviness amplitude to form the micro-cavitation given by the linearized theory may be underestimated.

#### Additional References

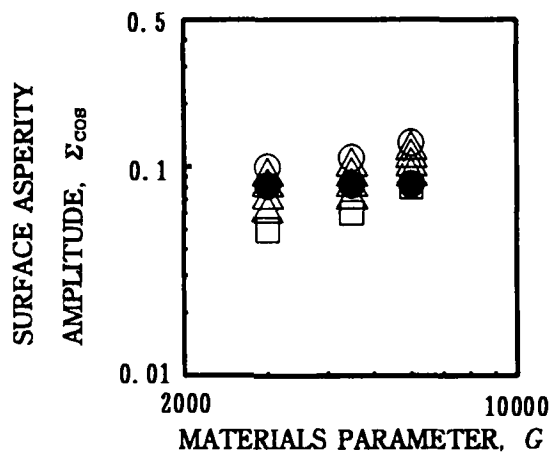
1. J. A. Greenwood and G. E. Morales-Espejel, Proc. IMechE, Part J, (1996), in print.

2.J A Greenwood and G E Morales-Espejel, Proceedings of the 23rd Leeds-Lyon Symposium on Tribology, (1996), in print.

- : The micro-cavities are formed after all bumps in the Hertzian contact area.
- △ : Some micro-cavities are formed.
- : The micro-cavity is not formed
- : The linearised theory (Greenwood)



(a) The effect of velocity parameter  $U$   
 ( $G=3000, P_h=1.5\text{GPa}, W=2.71\times 10^{-4}, \Lambda=0.25$ )



(b) The effect of materials parameter  $G$   
 ( $P_h=1.5\text{GPa}, U=10^{-11}, W=2.71\times 10^{-4}, \Lambda=0.25$ )

**Paper IV(3) “A New Relaxation Scheme for Solving EHL problems”**, by Mr E Nurgat and Dr M Berzins (School of Computer Studies, The University of Leeds, UK).

**Dr J A Greenwood** (University of Cambridge, UK). You have specified your lubrication conditions by giving us (L) and (M); and in addition by giving us (G, U and W). But the one parameter that really matters, the one that determines whether the contact is “heavily loaded” or not - in the sense that the viscosity becomes high enough to eliminate Poiseuille flow - is  $\bar{\alpha} \equiv (\alpha P_o)$ .

Of course  $P = \frac{1}{\sqrt{2\pi}} G \sqrt{W} = \frac{1}{\sqrt{2\pi}} L \sqrt{M}$ , so we can work it out : but please will you tell us its value?

**Reply by Mr Nurgat and Dr M Berzins** (School of Computer Studies, The University of Leeds, UK). For the test problems presented in our paper,

the values of  $\bar{\alpha} = \alpha P_h$ , which determines whether the contact is heavily loaded or not ranged from 10 to 60. The exact values for each test problem are as follows:

For the case  $L=10$ , the value of  $\bar{\alpha}$  was between 10 for  $M=20$  and 21 for  $M=200$ .

For the case  $L=14$ , the value of  $\bar{\alpha}$  was between 14 for  $M=20$  and 30 for  $M=200$ .

For the case  $L=28$ , the value of  $\bar{\alpha}$  was between 28 for  $M=20$  and 60 for  $M=200$ .

These values may be calculated using the values of maximum Hertzian pressure,  $P_h$ , presented in the paper and multiply by  $\alpha$ . Alternatively, we can use the following relationship:

$$\bar{\alpha} = \frac{L}{\pi} \left( \frac{3M}{2} \right)^{1/3}$$

Figure 1 Criterion of micro-cavity formation

**Dr C H Venner** (University of Twente, Enschede, The Netherlands).

The authors present Gauss-Seidel Line relaxation with a truncated system as a “New relaxation scheme” for EHL point contact problem. This discussor would like to contribute the following points. Firstly, Gauss-Seidel line relaxation was already described in detail in Chapter 4 of reference [2]. It was not adopted as a suitable relaxation scheme for the full problem because by means of local mode analysis (Fourier analysis) on a model problem characteristic for the EHL problem it can be shown that the scheme is indeed very good for large  $\varepsilon/h^2$  but not stable for small  $\varepsilon/h^2$ . The cause of the instability is the accumulation of changes in the discrete film thickness integrals. As a result low frequency components will be amplified. This effect can be partly counteracted by the use of damping. However, the stability is then obtained at the price of a significant reduction of the smoothing properties. In fact for damping values of 0.1 the error amplification factor for high frequency components will be close to unity, and as a result the error reduction that can be obtained with a multigrid cycle will be very poor. The stability problem due to the accumulation can be overcome by updating all film thicknesses for each pressure change that has been computed, i.e. to make it full Gauss-Seidel, also in the discrete integrals. However, that option is far too expensive to be realistic. A much better way to avoid the accumulation is by some sort of distributive relaxation, which led to the Jacobi Distributive relaxation.

Now for actual implications one should not look at the two schemes as competing alternatives for the full problem. One can easily combine the best behaviour of both schemes in a single line relaxation procedure. At the price of a few conditional statements, in the procedure that constructs the system of equations to be solved for a given line the coefficients of the (band) matrix for the given value of  $i$  can simply be chosen locally based on the value of  $\varepsilon/h^2$ . The entire scheme then automatically will behave as a Gauss-Seidel line relaxation, or as a distributive Jacobi relaxation, either globally (low loads) or locally

(inside the contact region versus outside the contact region).

Secondly, the authors conclude that their scheme appears to work as well as DRS, by comparing the film thickness result obtained with results obtained with the solver of their colleagues from the engineering department. However, by definition such a comparison can only say something about the discretization that is used, e.g. if the same discretization is used one should obtain the same value, the use of multi-integration can account for differences within the accuracy of the multi-integration algorithm, and if a different discretization is used for sufficiently small mesh sizes one should converge to the same value. Such a comparison is by no means a proof of efficiency. The authors should have compared the error reduction per multigrid cycle, given the exact same values of the cycle parameters for both solvers. In this respect this discussor would like to know what values for cycle convergence the authors obtained. In section 5 the authors state “Hardly any change in normo was observed after a number of iterations”. This strongly suggests that asymptotically the scheme stalls or that it has poor smoothing properties.

**Reply by Mr E Nurgat and Dr M Berzins** (School of Computer Studies, The University of Leeds, UK). The first issue addressed in this discussion makes the assumption that we have presented Gauss-Seidel Line relaxation scheme with a truncated system as a ‘New relaxation scheme’ for solving Elasto-Hydrodynamic Lubrication (EHL) point contact problems. This is not the case as the scheme described in the paper is a new combination of the two existing Gauss-Seidel and Jacobi Line relaxation schemes with a different updating procedure for each scheme. In particular the ‘block up-dating’ procedure or the Jacobi part of the iteration seems to be important with regard to the success of the method. Dr Venner points out in his thesis and in the discussion that Gauss-Seidel Line relaxation scheme is very good for large values of  $\varepsilon/h^2$  but it is not stable for small values of  $\varepsilon/h^2$ . It is for this reason that we have developed a scheme where Gauss-Seidel Line relaxation is only used in the regions of the computational domain where  $\varepsilon/h^2$  is

large and Jacobi Line relaxation scheme is employed in the remaining parts of the domain where  $\varepsilon/h^2$  is small. We fully agree with Dr Venner's comments regarding the use of a Gauss-Seidel scheme and the desirability of using something like the Jacobi Distributive scheme. The present paper is an attempt to use an alternative to the Jacobi Distributive scheme and to try to see experimentally whether or not it works.

On the second issue, we have pointed out in our paper that from the results obtained so far, it is too early to draw any conclusions as we are still in the process of analysing the accuracy of our solutions and we are conducting a stability analysis. However, it is very encouraging at this stage that the solutions obtained using a relatively very simple scheme are in line with those obtained using other well known schemes. The error reduction of both NORMO and Root Mean Square Residual per multigrid cycle are as follows:

Cycle 1 : 11,  
 Cycle 2 : 2,  
 Cycle 3 : 1

We have mentioned in our paper that hardly any change in NORMO and Root Mean Square Residual is observed after a number of iterations. We have not come across EHL papers that use NORMO and Root Mean Square Residual as a means for testing the accuracy of the solution. Hence, it is difficult to make any comparisons or draw any conclusions. It is not very clear as to which is the best method to use in order to check the accuracy of the solutions, but from a mathematics point of view, NORMO and Root Mean Square Residual are appropriate. However, convergence problems do arise due to the cavitation region and this may be the cause of the problem. In any case, we feel that this needs further study.

## **SESSION V - EXPERIMENTAL (2)**

### **Paper V(i) "Film Thickness Anomalies in Very Thin Elastohydrodynamic Oil Films" by F M**

Baskerville and Dr A J Moore (BP Oil Technology Centre, Sunbury-on-Thames, UK).

**Mr M Smeeth** (Imperial College, London, UK). Could you tell us what was the composition of the DI package used? - and which particular element of this you believe is responsible for the observed increase in boundary friction at 100°C?

**Reply by Dr A J Moore** (BP Oil Technology Centre, Sunbury-on-Thames, UK).

The DI package used was a commercial material consisting of a secondary alkyl C<sub>3</sub>/C<sub>6</sub> zinc dialkyldithiophosphate (ZDDP) anti-wear/anti-oxidant additive, a phenate detergent and a succinimide dispersant in a mineral oil solvent. The observed rise in boundary friction is due to the influence of the ZDDP. In some types of DI package, e.g. those containing a surface active detergent such as a sulphonate or a salicylate, the influence of the ZDDP may be countered by that of the detergent. Phenates, though do not have a comparable effect.

**Professor J M Georges** (Ecole Centrale de Lyon, France). The results obtained with DOCP VI improver are interesting. The behaviour of the film changes with temperature. Have you considered the temperature of such polymer solution?

**Reply by Dr A J Moore** (BP Oil Technology Centre, Sunbury-on-Thames, UK).

We think it is probably unwise to attempt too detailed an interpretation of our results for polymer solutions at very low values of film thickness; as we have already observed, behaviour was not highly repeatable in this regime. In addition, the appearance of the relationship between film thickness and speed is affected by the fact that film thickness moves to a progressively lower range of values as temperature rises because of the changes in viscous properties.

**Dr R I Taylor** (Shell Research & Technology Centre, Thornton, Chester, UK). Is it possible that the discrepancy in  $\alpha$ -values you report is due to the

inadequacies of the Barus equation? Would the Roelands' equation be better?

**Reply by Dr A J Moore** (BP Oil Technology Centre, Sunbury-on-Thames, UK).

We do not believe that the use of the Barus equation is responsible for anomalies in the values of  $\alpha$ . Although the fluids examined varied in their closeness of fit to the Barus equation, the proportional disparity in  $\alpha$  observed remained unaltered.

**Paper V(ii) "An Experimental Study of Film Thickness in the Mixed Lubrication Regime"** by Dr G Guangteng and Professor H A Spikes (Imperial College, London, UK).

**Dr S Johnson** (Unilever Research, Port Sunlight Laboratory, UK). Would Dr Guangteng like to comment on the usefulness of his technique for quantifying the surface roughness of 'rough' metal balls when under load? It would appear that the shape of the reflected intensity v wavelength 'histogram' could be used to give a distribution of surface heights relative to the top surface of the disc's spacer layer, rather than just the mean separation quoted thus far.

**Reply by Dr G Guangteng and Professor H A Spikes** (Imperial College, London, UK). In principle the method could be used to produce a distribution of separations between the spacer layer and the steel surface. There are two reasons why this was not done. Firstly the authors are not yet sufficiently confident of the accuracy of the separation profiles obtained to do this; each measure depends upon just one or two rows of screen pixels and there might be spurious results from, for example, dust in the optical path. Secondly, in this work images were obtained from a TV camera operating at 50 Hz and no attempt was made to gate the input. Thus each image is probably an average over about 20 ms. The authors are not sure of the validity of such an effect on any separation profile obtained. It is possible to capture an image over a much shorter time period and this may be done in future work.

**Mr Y Tozaki** (Mitsubishi Heavy Industries, Japan). Did you measure the surface roughness after the test?

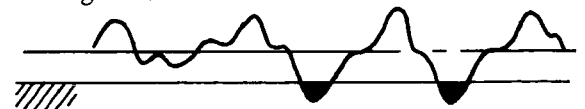
**Reply by Dr G Guangteng and Professor H A Spikes** (Imperial College, London, UK). The undeformed surface roughness of each steel, test ball was measured before each test to characterise surface finish. However we did not measure the surface after testing. This would be useful but would have to be done with proper relocation of the contact. Such work is currently being undertaken.

**Mr G McClure** (University of Leeds, UK). Optical interferometry techniques have been used previously, to measure ultra-thin film thicknesses with super finished ball bearings and optical glass discs. How have measurable interference fringes been produced with these relatively rough surfaces?

**Reply by Dr G Guangteng and Professor H A Spikes** (Imperial College, London, UK). The surfaces studied were rough by ball bearing standards but still not very rough with a mean undeformed slope of less than  $3.5^\circ$ . Also the spacer layer may have helped since although the film thickness varied by tens of nanometers from position to position within the contact, this variation was still a small proportion of the total of separation plus spacer layer thickness. Certainly it proved experimentally possible to obtain interference images.

**Dr J A Greenwood** (University of Cambridge, UK). I would be grateful if you could explain again what the experimental measurement of film thickness consists of. I understand that you measure the difference between the static position and the lubricated position; and if you were doing this "externally" by a direct measurement of the lift of the centre of the ball, I should understand.

But how by measuring light intensities do you distinguish between:



and,



**Reply by Dr G Guangteng and Professor H A Spikes** (Imperial College, London, UK). We are measuring the optical separation between a steel ball surface and the chromium semi-reflecting layer on a smooth glass disc. Because the semi-reflecting layer is coated on top with a layer of transparent silica spacer layer, our measurements are always the sum of this spacer layer thickness and also the thickness of any oil or air gap separating the spacer layer and the steel ball surface.

Initially we measure the average separation over the central region of the contact in the static, dry, loaded contact. This measurement represents spacer layer + any residual air gap due to full conformity not being attained between the solid surfaces. We then let oil seep into the still static contact. Because oil has a larger refractive index than air, the optical thickness of the residual gap changes, enabling us to calculate its true spatial value ( $h_o$ ) and distinguish this from the true spacer layer thickness ( $h_{sp}$ ) which is invariant. We then start rolling and what we now measure is the average optical spacer layer thickness + average optical oil film separation, i.e.  $n_{sp}h_{sp} + n_{oil}h_{oil}$ .

The semantic problem highlighted in the paper is whether to think in terms of the mean oil film separation (which is the difference between the measured value and the spacer layer thickness)  $h_{oil}$  and the hydrodynamic component of this separation which could be taken to be  $h_{oil} - h_s$  since  $h_s$  is present even in the static contact and is thus not generated by hydrodynamic entrainment.

**Paper V(iii) 'Surface Elastic Deformation by Solvent Structural Force in Very Thin Film Lubrication'** by Professor T Kato and H Matsuoka (University of Tokyo, Japan).

**Dr J A Williams** (University of Cambridge, UK). In your analysis you call upon the familiar Hertz equations to describe your contact between crossed cylinders. However, Hertzian contact is strictly between two homogeneous elements, while your specimens are clearly layered solids - a thin layer of mica supported by a soft layer of glue over a still glass substrate - so that the contact is certainly not Hertzian.

**Paper V(iv) 'Failure of Very High Speed Elastohydrodynamic Contacts'** by Mr D J Hirst and Dr A V Olver (Imperial College, London, UK)

**Dr J A Greenwood** (University of Cambridge, UK). If your parameter ( $\Omega$ ) is consistently less than theory, then you are not only generating heat by spin, but also by slipping and at your speeds this must be enormous. Where does it go to? I wonder if quoting (PV) as Watts/m<sup>2</sup> might be more meaningful; than GPa m/s?

**Reply by Mr J D Hirst and Dr A V Olver** (Imperial College, London, UK). Professor Greenwood is quite correct: the heat input is very high from both the spin and the sliding of both contacts. (Throughout the paper we have tended to refer to total relative contact motion as 'slip', which has rotational and linear components, referred to as 'spinning' and 'sliding' respectively). It is estimated that the total heat from the two test contacts amounts to between 1 and 2 kW at maximum conditions. A further source of heat is provided by viscous shear of the lubricant within the 'biro'.

The majority of the heat is removed by conduction into the ball and the raceways. This is then carried into the lubricant and the surroundings, by convection whereby it is removed from the test station. At this point, any further convection from the lubricant serves simply to heat up the laboratory!

## **SESSION VI - 'SOFT' EHL**

**Paper VI(i) 'Elastohydrodynamic Lubrication of Soft Solids'** by Dr C J Hooke (University of Birmingham, UK).

**Professor T Yamamoto** (Tokyo University of Agriculture and Technology, Japan). This paper summarized very well the properties concerning 'soft' EHL. The feature "simplified effect of roughness" which the author indicated in the paper can be effective for the tribology of wet friction material which is porous and composed of dents, with the majority of the contact area being flat. Would you give us your comments on applying your concept of EHL to this material?

**Reply by Dr CJ Hooke** (University of Birmingham). It is almost impossible to answer your question fully without having more information about the way in which the friction material is being used.

If the system consists of a pad of material rubbing on a surface then fluid will be entrained at the front of the pad and, under steady state conditions, conditions there will largely control the film thicknesses under the whole conjunction. There will of course, be local variations around each dent. The downstream edge of each dent will act as a local inlet to an EHL contact and will, in theory, control the clearance downstream of it. However, if the clearance generated at the dent is greater than that produced at the pad inlet, then the dent will eventually become starved and the clearance drop to that generated at the pad inlet. If it is lower, then the dent will eventually become fully flooded and pressurised, thus increasing the downstream clearance. In either event it is the contact inlet rather than the dents that will eventually control the clearances. There will of course be considerable time delay and redistributional effects at each dent that will complicate this somewhat simplified analysis.

In estimating the clearances produced at the pad inlet and at the rear of each dent, the dry contact pressure distribution must be estimated. This will, necessarily have a parabolic form of the type given in equation 5. Then equation 6 can be used to estimate the entrained clearance. It is, of course, necessary to use the component of entraining velocity normal to the boundary in this calculation,

Flow under the remainder of the pad, and any spreading of locally high clearances can then be found using Hirano's analysis.

Under transient conditions it is likely that each dent will act as a local source or sink of fluid and, initially, it is probable that each dent will produce a downstream clearance that reflects the EHL inlet characteristic of the downstream side of the dent.

Frictional behaviour will be complex but for elastomeric materials seems to be related to the visco-elastic response of the elastomer to the surface roughnesses of the counterface. This is, of course related to the ratio of roughness to film thickness and to the roughness wavelength. Asperities on the elastomer appear simply to be partially flattened as suggested in the paper and to have little effect on frictional performance.

**Dr H van Leeuwen** (Eindhoven University, The Netherlands). I want to congratulate the author on a good overview of the subject, which includes non-steady state EHL. Also the author's approximate equations for the film thickness are appreciated. I have two questions on the time dependent entraining velocity;

- (1) Is the "wave" of the minimum film thickness in phase with the entraining velocity?
- (2) Is it possible to estimate the speed of propagation of ( $h_{min}$ ) through the contact?

**Reply by Dr. C.J. Hooke** (University of Birmingham, U.K.)

The actual behaviour of the minimum film thickness in soft contacts under dynamic conditions is complex. However, a reasonable picture of the behaviour can be obtained on the following basis.

Clearances are generated at the inlet to the conjunction with values determined, approximately, by the instantaneous entrainment conditions there. There is one critical exception to this and that is where the entrainment velocity falls to zero. In that case the clearance is determined by the rate of change of entraining velocity.

These clearances are convected through the contact, with little change, at a speed close to the entrainment velocity. This velocity clearly may change from the velocity at which the clearance was generated and may even reverse. The actual magnitude of the changes during transition are governed by Hirano's equations and are easy to calculate.

When the clearance passes through the exit region it undergoes a final, short duration reduction before increasing again. The magnitude of this reduction depends on the relationship between the conditions under which the clearance was generated and those obtaining as it passes through the exit.

Dealing with the specific questions :

- (1) If the amplitude of motion is large compared with the contact width, the 'wave' of minimum film thickness will be largely in phase with the entrainment velocity. There will, however, be a time delay equal to the duration of transit of the clearance across the conjunction. In addition complex effects can be expected near the point where the entrainment velocity reverses.
- (2) After entrainment reversal the old exit restriction will propagate through the contact at a velocity closely equal to the entrainment velocity. There will be some complications during the initial movement of  $h_{\min}$  into the contact but once inside the clearance is unlikely to change significantly.

**Paper VI(ii) 'Film Thickness Measurements in Elastohydrodynamically Lubricated Elastomeric Contacts'** by Dr S A Johnson\*, Dr M J Adams\*, Mr A Arvanitoki\*\* and Professor B J Briscoe\*\* (\*Unilever Research, Port Sunlight Laboratory, UK. \*\*Imperial College, London, UK (University of Birmingham, UK).

**Professor Dr Ing G Poll** (University of Hannover, Germany). In the graph showing the friction coefficient versus speed there is a distinction between a "boundary/mixed" and "IEHL" region. Both in the boundary and IEHL region there is a

tendency of increasing friction with speed. Is it possible that in the "boundary" region, in reality, there is a micro-EHL action induced by the micro-geometry (roughness), whereas the IEHL region is dominated by a hydrodynamic mechanism related to the macroscopic shape of the specimen?

**Mr H van Leeuwen** (Eindhoven University, The Netherlands). It is nice to see that the investigations of Visscher find acclaim in the measurement of film thickness in elastomeric contacts. I have the following question.

The behaviour of the coefficient of friction vs a speed number does not look like the boundary lubrication characteristic normally looks like. What is the film thickness in this area? And if it should be full film lubrication, what is then causing the transitions in this coefficient of friction?

**Reply by Dr S A Johnson** (Imperial College, London, UK). These questions relate to the physical mechanisms responsible for the three traction regimes observed by the authors in an oil-lubricated contact between a smooth glass hemisphere and a soft, and relatively rough, elastomeric flat. These traction regimes occurred at small, medium and large values of dimensionless velocity parameter,  $M$ , and were ascribed to resulting from boundary, 'mixed', and 'full' IEHL lubrication respectively. As will be discussed below, this is not supposed to imply that micro-IEHL is not important in reducing the traction in the 'full' IEHL regime. It is the purpose of the rest of this answer to clarify what I believe is meant by boundary, mixed, and full IEHL lubrication in the context of rough elastomeric contacts, and where I believe that micro-EHL is important in determining the traction.

This discussion was prompted by some data, supplementary to the paper, that was presented at the Symposium. The main purpose of this was to illustrate a practical example where the sliding velocity and viscosity dependence of the traction were adequately predicted by macro-EHL theories; as represented by eqns. 20 and 21. These data were for an optically-smooth glass probe ( $R = 8$



mm) sliding across a human inner forearm ( $W = 0.2N$ ). The relevant experiments were performed in a manner described previously [18], with the traction being measured as a function of velocity ( $V = 1 - 50$  mm/s) using a wide range of Newtonian silicone fluids ( $\eta = 0.8 - 58000$  mPas) as lubricants. The data were presented graphically as a log-log 'master' curve in such a way to illustrate the validity of eqn. 20. At relatively large values of the dimensionless velocity parameter,  $M$ , the traction did indeed behave in a manner expected from a consideration of IEHL of the macroscopic contact geometry alone.

The two questions are not primarily directed at the high  $M$  part of the master curve (i.e. the full IEHL regime - which is further defined below), but rather at that part of the curve corresponding to relatively small  $M$  values. This is the regime where we qualitatively interpret the data as implying that the fluid films between each asperity tip and the glass are sufficiently thin, or even non-existent, such that the contact as a whole can be considered as operating in a boundary or even in a 'dry', unlubricated, regime (the traction was only slightly lower than that measured for the unlubricated contact). In this region of the master curve, for the lowest viscosity fluid (0.8 mPas), the traction only doubled for a factor of fifty increase in sliding velocity. I consider that such a small dependence of traction on velocity is not inconsistent with a boundary lubrication mechanism - I suspect that the choice of a magnified log axis for the friction coefficient led to the questioner incorrectly deducing the magnitude of the effect.

At the small  $M$  values, our phenomenological traction data suggest that a significant proportion of the fluid films at asperity tips must be considerably below 100 nm in thickness. The evidence for this comes from measurements in water, where both stick-slip motion and large pH and surfactant effects are evident [18]. 'Stick' requires some proportion of 'dry' contact, where the fluid is excluded from at least some asperity tips in order to provide contact regions that have a finite yield stress. A dependence of the traction on either solution pH or the presence of small amounts of surfactants indicates that the separation distance between the deformed skin asperities and

glass must be within a range where interfacial forces can operate; namely below ca. 20 nm. Also, the traction in water is very much greater than that measured in dilute surfactants, particularly at relatively low sliding velocities. This is evidence that the efficiency with which micro-EHL can generate fluid films at asperity tip contacts, and so effectively reduce the overall traction, must be lower (high traction in pure water) than that associated with repulsive interfacial forces (low traction in dilute aqueous surfactants).

It is difficult to make a direct comparison between the traction data obtained in water with that in 0.8 mPas silicone oil because, although the two fluids have similar viscosities, water plasticises the surface of human skin whereas silicone fluids do not [18]. Nevertheless, for the same  $\Lambda$ -ratios ( $\Lambda = h_{\min}/R_q$ , where  $h_{\min}$  is the film thickness calculated from macro-EHL and  $R_q$  is the root-mean-square roughness of the undeformed skin surface), it is likely that micro-EHL will be even less effective in reducing the traction in 0.8 mPas silicone oil than in water because the asperities will be less compliant. The reason why the traction is so much higher for water [18] than for the dry contact, or, indeed, for low viscosity silicone oil, is due to a larger real area of contact in the plasticised system between the more compliant asperities and the glass. Thus, relative to the dry contact, I propose that any slight reductions in the traction observed at low  $M$  values in silicone fluids are most likely due to some measure of boundary lubrication.

It is certainly true that there will be considerable asperity flattening within the contact circle, and Professor Poll's suggestion that micro-IEHL should be important in some region of the master curve is certainly true. At medium values of  $M$ , the traction falls as  $M$  increases until a minimum in the traction is reached - we identify this minimum point with the onset of full IEHL and the region of falling traction values with the mixed lubrication regime. Using a smooth contact approximation, the macro-IEHL film thickness under the conditions of lowest traction is calculated (see ref. [18] for a description of the contact geometry and relevant materials' parameters) to be ca.  $7\mu\text{m}$ . This is significantly less than the typical  $R_q$  of undeformed forearm skin which we have measured

to be ca. 20  $\mu\text{m}$ . I think that micro-IEHL is responsible for the persistence of low traction values in that part of the full IEHL regimes where the  $\Lambda$ -ratios are considerably less than unity. However, the film thickness predicted by the macro-IEHL equations at the onset of the mixed regime is ca. 2  $\mu\text{m}$ . Therefore, it would appear that micro IEHL is incapable of reducing the traction in this particular contact pair once the  $\Lambda$ -ratio is below about 0.1, and any lubrication observed in this region is likely to be boundary in nature.

In summary, I would suggest that the three lubrication regimes that the contact passes through as the product of  $\eta$  and  $V$  increases are boundary (where the traction increases in the manner predicted by eqns. 20 or 21). Micro-IEHL is responsible for shifting the position of minimum traction (i.e. the onset of full IEHL) to smaller values of  $M$  than would be predicted on the basis of the  $\Lambda$ -ratio alone, and therefore must be important in both the mixed lubrication regime and the initial (low  $\Lambda$ ) part of the full IEHL regime. The full IEHL regime can be divided into two parts, in both of which there is a negligible contribution to the traction from shear of boundary films - this being the connotation of the term 'full'. I suggest that the lower  $M$  and  $\Lambda$  part of the full IEHL regime is dominated by micro-IEHL, and the higher  $M$  and  $\Lambda$  part by macro-IEHL-although it should be emphasised that there appears to be little distinction between the two in our traction data obtained so far.

**Mr H van Leeuwen** (Eindhoven University, The Netherlands). In which mode has the optical system been used, closed loop or focus error signal measurement?

**Reply by Dr S A Johnson** (Imperial College, London, UK). The optical follower was used in a closed-loop mode in order to maximise the range with which displacement measurements could be made without having to move it.

**Dr M Visscher** (The University of Leeds, UK). The authors presented a nice paper on film thickness measurements based on Compact Disc technology. I would like to make some additional

comments which may be useful to the authors and to others.

- (1) The authors mentioned a focus spot of about 1.5  $\mu\text{m}$  in diameter. This is true in air, where the focus spot is diffraction limited. The 6 mm thick glass disc, however, introduces spherical aberration, causing the spot to be much larger. Its diameter can be estimated from geometrical optics, and is about 40  $\mu\text{m}$ .
- (2) The authors mention that the calibration factor, needed to overcome the difference between the "optical" and the real film thickness, was much larger than expected from the lubricant's refractive index. They suggest that diffuse scattering from within the bulk of their white elastomeric specimen might be the cause. Have the authors considered to mix a colour filler into the material which would adsorb the laser light? In my experiments at Eindhoven University, we always used coloured polyurethane, either green or black, and the refractive index could be used as a calibration factor.

**Reply by Dr S A Johnson** (Imperial College, London, UK).

- (1) Dr Visscher's comment is an important one. The optical followers optics have a relatively large numerical aperture so that the focal spot diameter is diffraction-limited in air. In order to minimise the spherical aberration normally associated with such large numerical aperture optics, the lens combinations inside the transducer are chosen to be self-compensating. However, placement of the spinning disc between the optical follower and its focal point has the effect of re-introducing spherical aberration and this will, indeed, cause a loss in lateral resolution. Fortunately this will have only a very minor effect on the accuracy of the reported central film thickness data. This is because the diameter of the contact between the elastomer and the glass disc was always considerably greater than the diameter of the aberrated laser spot. Nevertheless, in future work, correcting this aberration will be necessary if we wish to profile the film

thickness across the width of the contact with the full potential lateral resolution of the current method. We thank Dr. Visscher for his cautionary comment.

- (2) The commercial optical follower we use ceases to operate once the reflected intensity is below a certain value (approximately 2%). This was found to be the case when we attempted to make film thickness measurements between the glass disc and a clear elastomer. It has been our experience that white elastomers have a higher reflectivity in air than black, red or green elastomers, and all our film thickness studies have been done using the white *Silflo* material. If elastomers of different colours are sufficiently reflective in silicone fluids for our particular optical follower to operate effectively, then Dr. Visscher's suggestion could prove valuable.

**Paper VI (iii) 'Some Aspects of the Contact Mechanics and Lubrication of Low Modulus Materials in Rough Interfaces'** by Professor R.S. Sayles, Mr I Lee-Pradoe and Mr C Bouvet (Imperial College, London, U.K.).

**Dr J A Williams** (Cambridge University, UK). In support of your demonstration of a soft body sliding on a comparatively rough surface you showed the results of some calculations of the loaded profile of the homogeneous compliant body. Have you completed similar calculations for the rigid body covered by a thin elastomeric compliant film?

**Reply by Dr R S Sayles, Mr I Lee-Prudhoe and Mr C Bouvet** (Imperial College, London, UK). We have not yet performed this calculation, but the program developed by James Cole (1) allows this to be achieved and we are grateful to Dr Williams for reminding us that this is possible - and we will do it.

- (i) Cole, S J and Sayles, R S. "A Numerical Model for the Contact of Layered Elastic Bodies with Real Rough Surfaces" Trans. ASME, J. Tribology, 1991, V114, 334.

**Mr D J Hirst** (Imperial College, London, UK). I appreciate that you probably have no direct measurement of this, but if someone had suffered an accident, say, and had badly burnt their fingers, would you expect;

- (a) the fingerprint - and its natural fractal to be removed by the burn? - and that therefore;
- (b) the person would then have much greater difficulty in picking up objects?

**Reply by Dr R S Sayles, Mr I Lee-Prudhoe and Mr C Bouvet** (Imperial College, London, UK). As you suspect, we have no real evidence on what would happen in the case of finger burns, but would hazard a guess that the finger print would be modified, and in severe cases, perhaps removed, at least in the short term. The effects of this would probably result in a non-fractal geometry with a greater potential for elastic conformity, which in turn would increase the ease in which hydrodynamic films might form with wetted objects, and hence represent an increased difficulty in handling wet objects. But on the other hand (no pun intended), when dry, the increased real contact area, offered by this greater elastic conformity, would probably produce an increase in the overall shear force that could be applied for gripping objects.

**Paper VI(iv) 'The Sealing and Lubrication Principles of Radial Lip Seals: Measurement of Local Tangential Deformations and Film Thicknesses in the Contact Between Shaft and Seal'** by H van Leeuwen and Mr M Wolfert (Eindhoven University of Technology, The Netherlands).

**Professor Dr.-Ing. G Poll** (University of Hannover, German). How do you explain the difference between the area of contact (0.08 mm wide) and the wear path width (up to ) 0.5 mm wide) in your experiments?

**Dr C J Hooke** (University of Birmingham, UK). The authors examine the pumping of seals assuming the asperities are organised into neat axial rows. With this arrangement, local

tangential deformations produce substantial pumping. They then find tangential displacements in actual seals and infer that these deformations must, therefore, be responsible for the seals pumping.

However, in practice the asperities are likely to be randomly oriented. If this is the case then any distortion of the seal will still leave a random asperity pattern that will lack the directional features required to cause the pumping action.

It might be argued that an aligned asperity pattern would be produced by the seals motion with ridges being formed that lie normal to the direction of sliding. However, it is difficult to accept this since they would then form normal to the distorted seal and again, in operation, the seal would lack the required directional surface features.

**Professor Dr.-Ing, G Poll** (Hannover University, Germany). When trying to correlate the measured film thickness and the friction torque, did you assume that the friction was entirely due to shear of the fluid, or did you consider a contribution due to boundary friction in asperity contacts?

## **SESSION VII - LUBRICANT PROPERTIES**

**Paper VII(i) 'A Simple Formula for EHD Film Thickness of Non-Newtonian Liquids'** by Dr S Bair and Professor W O Winer (Georgia Tech., USA).

**Professor R Coy** (Shell Research Ltd, Chester, UK). In many lubricants containing polymers the limiting shear stress ( $m = -\infty$ ) may be related to the permanent shear degradation of the polymer. Will this have an effect on the film thickness as predicted by your model?

**Reply by Dr S Bair and Professor W O Winer** (Georgia Tech, USA). The physical origin of the shear thinning should have no effect on the film thickness prediction. Permanent shear degradation

can be observed in an operating concentrated contact by extracting and analysing liquid from the exit. However, the addition of small concentrations of polymer has little effect on the measured limiting stress of a base oil. If permanent shear degradation occurred in a rheometer when limiting shear was obtained, then it would not be possible to recover the original low shear viscosity on succeeding measurements without reloading the rheometer. This difficulty has not been observed. We may then rule out significant permanent degradation as a source of a limiting stress.

**Mr M Workel** (University of Leeds, UK). Figure (1) from the Synopsis shows the curve of ( $\eta$ ) versus ( $\tau$ ) on a double logarithmic scale. At  $\tau \approx 10^2$  Pa both curves have only one measurement point. At  $\tau \approx 10^6$  Pa both curves have about 5 measurement points. From these very few points, the 'critical stress' ( $\tau_c$ ) is deduced as the intersection point of the horizontal line and the (linear) decreasing one. Do the authors think that finding ( $\tau_c$ ) from these measurements is highly prone to measurement errors (especially because  $\tau_c \approx 10^4$  Pa) and  $10^4$  Pa  $\ll 10^6$  Pa, where most points lie).

Do the authors think that these few measurements justify the formula assumed?

**Reply by Dr S Bair and Professor W O Winer** (Georgia Institute of Technology, USA).

The reader might note that the data points for the power law regime of Figure 2 were obtained with a High-Pressure Rheogoniometer by the measurement technique described in Ref. [7] of the original paper. This instrument provides measurements of normal stress difference as well as shear stress. The slope of the power law regime shown in Figure 2 can be related to the normal stress difference [7]. If the slope were very much different from that shown in Figure 2, then the normal stresses measured in Ref [7] could not be explained by existing models. Measurements of viscosity at shear stresses of  $10^2$  Pa and  $10^6$  Pa, together with the power law slope, uniquely define the critical stress,  $\tau_c$ .

To illustrate the effectiveness of our approach see the attached Figure 2a. The data points were recently obtained with a commercial rheometer which only operates at atmospheric pressure. The solid curve is equation (2) of the paper with  $\tau_c \equiv 5400$  Pa. The broken curve is also equation (2) but with  $\tau_c$  varying weakly with pressure as specified in Ref. [4]. The agreement is good. In this numerical prediction it was convenient to fix  $\tau_c$ . The resulting film thickness is not affected by the alternate approaches to specifying  $\tau_c$ .

Regarding the film thickness solution, it is the rheological response of the liquid at a shear stress around  $10^6$  Pa which controls film forming for thicknesses of about 100nm\*. Other curves drawn through the high shear stress data of Figure 2 and obeying equation (2) would give similar film thicknesses - for instance  $\tau_c$  of  $5 \times 10^4$  Pa combined with  $m = 0$ . Of course, this would not agree with rheological measurements. It is for this reason that the EHD contact is a poor rheometer.

The constitutive equation (2) is justified by the enormous quantity of rheological evidence which shows that a non-Newtonian liquid displays both a terminal regime and a power-law regime (and possibly, a second Newtonian regime). While it has become fashionable in the tribology community to utilize constitutive equations which compute easily, we feel that it is not helpful to the field in general to promote these, if they cannot be supported by rheological measurement.

\* Bair, S. (1996), "Elastohydrodynamic Film Forming with Shear Thinning Liquids", Accepted Trans. ASME J. Tribology.

**Professor A Cameron** (Great Wilbraham, Cambridge, UK). The authors refer to a solution "as originally suggested by Grubin".

In 1985 I reported on the 1984 meeting of the German Society of Tribology (1) where the Vogelpohl medal was given to A M Ertel "the true author of 'Grubin's ehl solution'".

I described how Ertel, when working in Berlin, had faked a suicide in 1945 and defected to the West. The Russian authorities saw through his deception

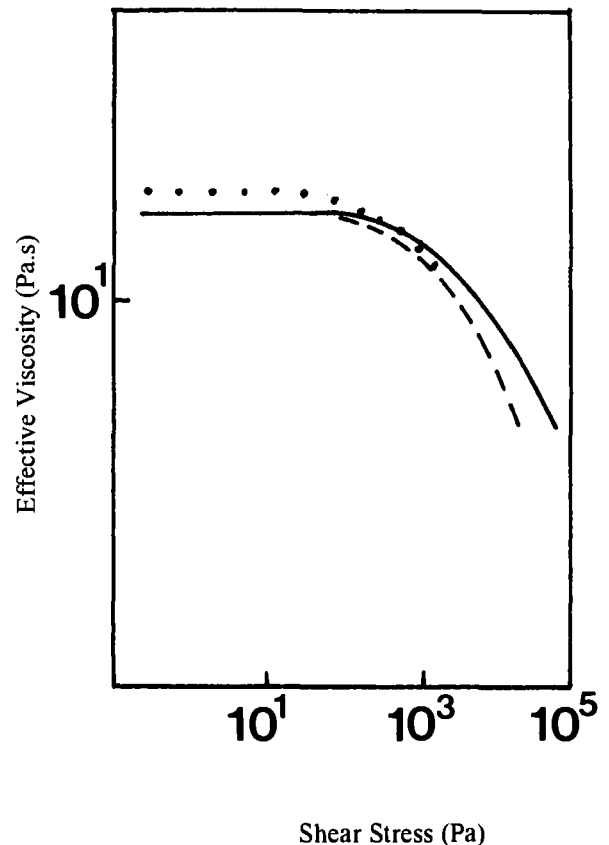


Figure 2(a) LF 5346 at Ambient Pressure

and so Ertel became a "no-person". Now Grubin was an examiner for his Kandidat Nauk (PhD) and had written "the value of the work is extraordinarily high and should bring the author world acclaim". Grubin then published it, with no mention of Ertel. This has always seemed a rather unusual procedure.

Professor Blok has told me that he heard from a Leningrad professor that Grubin realised that this most impressive work would never see the light of day, Ertel now being a 'no-person'. He therefore decided to publish it under his own name, even though he risked the accusation of plagiarism.

This postscript to the drama I described in 1985 casts quite a different and very favourable light on Grubin.

(1) A Cameron (1985) Righting a 40-year-old wrong. A M Ertel - the true author of

'Grubin's ehl' solution. Tribology International, Vol. 18(2), p. 82.

**Paper VII(ii) 'Behaviour of Some Vegetable Oils in EHL Contacts'** by Dr N Ohno\*, Mr A Shiratake\*, Mr N Kuwano\* and Professor F Hirano\*\* (\*Saga University, Japan, \*\* Kyushu University, Japan).

**Dr P Cann** (Imperial College, London, UK). How did you measure the reflow time of the wake?

Did you see any evidence of starvation of the inlet in your EHD tests?

**Reply by Dr N Ohno** (Saga University, Japan). The author would like to thank Dr Cann for the interest she showed in this paper. Concerning the measurement of reflow time, we measured the disappearance time of the wake after the sudden stop of rolling motion by the usual interferometric method. Concerning the evidence of starvation, for measurement of EHD film thickness we used the usual interferometric method. So we can see the evidence of starvation of the inlet side of EHD contacts. However, we could not observe the oil starvation of the inlet on the tested lubricants.

**Paper VII(iii) 'Estimation of Pressure Viscosity Coefficient by High-Speed and High-Pressure Traction Drive Test'** by T Nakamura, F Itoigawa and T Matsubara (Nagoya Institute of Technology, Japan).

**Dr A J Moore** (BP Oil Technology Centre, Sunbury-on-Thames, UK). Is 30°C a realistic operating temperature in the turbocharger application which inspired this study?

**Reply by T Nakamura, F Itoigawa and T Matsubara**, (Nagoya Institute of Technology, Japan). In practical use of the supercharger (not a turbocharger), the operating temperature of the traction fluid may be higher than 30 °C. From the point of view of high maximum traction and efficiency, however, a low fluid temperature will be desirable. A realistic supercharger system which is applied with the traction drive has an oil recirculation and cooling device. So, 30 °C is not an impractical temperature as the test condition.

**Dr J B Medley** (University of Waterloo, Ontario, Canada). Why did you choose the Ree-Eyring model to represent your traction curve rather than a limiting shear model and, perhaps, the approach taken by Wu and Cheng (Tribology Transactions 37, 1, 138-146 (1994))?

**Reply by Dr T Nakamura, Mr F Itoigawa and Dr T Matsubara** (Nagoya Institute of Technology, Japan). According to the traction map which is proposed by Evans and Johnson, our test conditions are assumed to be in the non-linear viscoelastic regime.

Even if the limiting shear model proposed by Bair and Winer or by Gecim and Winer is assumed, similar calculations to the case that the Ree-Eyring Model is assumed can be performed by regarding the limiting shear stress  $\tau_L$  as an unknown parameter measured by fitting instead of Eyring stress  $\tau_o$ . However, we choose the Ree-Eyring model to present the traction curves which are obtained in our tests because it seems to be physically well-grounded rather than the limiting shear stress.

**Professor R C Coy** (Shell Research Ltd, Chester, UK). What is the sensitivity of the pressure viscosity coefficient ( $\alpha$ ) to the value of ( $\tau_o$ )? Does your conclusion on the constancy of ( $\alpha$ ) with surface velocity hold for other values of ( $\tau_o$ )?

**Reply by Dr T Nakamura, Mr F Itoigawa and Mr T Matsubara** (Nagoya Institute of Technology, Japan). The value of maximum traction is associated with both mean film temperature and a value of  $\alpha\tau_o$ . Calculation results show that a variation of fluid film temperature (from 63°C) with surface velocity (from 15 m/s to 44 m/s) in our test conditions is relatively small in comparison with the magnitude of temperature rises. In addition, a variation in the value of a maximum traction obtained in our experiments is also small. These facts show that the value of  $\alpha\tau_o$  varies only a little with the surface velocity. Since  $\tau_o$  is not so influenced by the film temperature in comparison with  $\alpha$ , it is assumed that  $\tau_o$  has a constant value. Consequently, the small variation of film temperature gives rise to the small variation

of  $\alpha$ . Even if the magnitude of the value of  $\tau_0$  varies, the tendency of the variation of the value of  $\alpha$  is not changed because of the small variation of the value of  $\alpha\tau_0$ , mentioned above.

**Paper VII(iv) 'Simulated Lubricant non-Newtonian Behaviour under Elastohydrodynamic Conditions'** by Mr S Chynoweth, Professor R C Coy and Dr L E Scales (Shell Research Ltd, Chester, UK).

**Dr A J Moore** (BP Oil Technology Centre, Sunbury-on-Thames, UK). In view of the very high shear rates quoted in the NEMD simulations, can the authors say whether "realistic" traction coefficients can be determined at shear rates of practical relevance?

**Reply by Mr S Chynoweth, Professor R C Coy and Dr L E Scales** (Shell Research Ltd, Chester, UK). The NEMD simulations are carried out at very high shear rates to obtain the "constitutive" equation for the lubricants investigated in the EHD models. However, once the shear thinning region has been simulated at the pressures, temperatures and shear rates amenable to NEMD simulation, the effect of temperature and pressure on the non-Newtonian region is generally applicable across the  $(P, T, \gamma)$  parameter space. For example, in Figures 2 and 3 it is clear that at the highest pressures plotted (around a Giga Pascal) shear thinning occurs at relatively low shear rates. Indeed for heptamethylnonane shear thinning occurs as low as  $10^2 \text{ s}^{-1}$  shear rates. Thus realistic traction coefficients can be obtained in the realm of practical shear rates for the isothermal systems modelled in this paper.

## SESSION IX ANALYTICAL/NUMERICAL (3)

**Paper IX(ii) "Time Dependent Solutions with Waviness and Asperities in EHL Point Contacts"** by P Ehret, D Dowson and C M Taylor (Institute of Tribology, Department of Mechanical Engineering, The University of Leeds, UK).

**Mr Y Tozaki** (Mitsubishi Heavy Industries, Japan). When the oil film profiles for  $t = 0$  and  $t = 0.78$  are compared, the flat part of the oil film thickness is seen to decrease. What is the reason for this?

**Dr C H Venner and Mr Y H Wignand** (University of Twente, Enschede, The Netherlands). In the limit of vanishing pressure flow the Reynolds equation reduces to  $(\bar{\rho} H)_x + \left(\bar{\rho} H\right)_t = 0$ , with the solution  $(\bar{\rho} H) = (\bar{\rho} H)_{(X-t)}$ .

Hence, if the conditions in the contact region are such that density variations can be neglected, film changes will move through the contact region unchanged, and, in the case of waviness, no amplitude reduction should be observed. The authors argue that this provides a "simple test" for accuracy, and that amplitude reduction inhibited in the solutions presented by Venner and Lubrecht must be artificial and thus should disappear with decreasing time step. They then choose to perform their simulations using the same mesh size as Venner and Lubrecht, but with half the timestep. The discussors would like to contribute the following points.

Firstly, the conditions considered by the authors are such that  $\alpha\phi_h \approx 10$ . This is till a relatively low value. Moreover, as the Roelands' pressure viscosity equation is used (with  $z = 0.44$ ) it appears to the discussors that for these conditions the authors' claim that there should be no viscous effects whatsoever is too strong. For example, for the solutions presented by the authors  $0.02 \leq \epsilon \leq 4 \cdot 10^{-6}$  in the region  $-1 \leq X \leq 0$ . Now at  $\epsilon = 0(0.01)$  viscous effects are not negligible and can show in the solution. Consequently, certainly in the first part of the Hertzian contact region some amplitude reduction should be observed, and this is indeed

the case; see Figure 3 ( $t = 1.56$ ). This effect will be stronger if  $\epsilon$  is larger, as is for example likely to be the case for the waviness results presented by Venner and Lubrecht where the value of the  $\epsilon$  is

roughly between 2 and 10 times larger than for the case considered here by the authors (Venner and Lubrecht have the same  $\alpha p_n$ , but  $2 \cdot 10^{-11} \leq U \leq 8 \cdot 10^{-11}$ ).

Secondly we would like to comment on the choice of a timestep that is half the spatial mesh size, in comparison with a timestep that is equal to the spatial mesh size. Consider the advection equation:

$$Lu = a \frac{\partial u}{\partial x} + b \frac{\partial u}{\partial y} = 0 \quad (1)$$

Let this equation be discretized on a grid with a mesh size ( $h$ ) in the  $x$  direction and ( $k$ ) in the  $y$  direction. The discrete operator satisfies:

$$L^{hk} u^{hk} = a \frac{\partial u}{\partial x} + 6 \frac{\partial u}{\partial y} + \tau^{hk} = 0 \quad (2)$$

with the truncation error  $\tau^{hk}$  being a function of higher derivatives of  $u$  multiplied with powers of the mesh sizes  $h$  and  $k$ . In particular using the second order "upstream" discretization for each of the derivatives we have:

$$\tau^{hk} = -\frac{1}{3} h^2 \left( a \frac{\partial^3 u}{\partial x^3} + b \frac{k^2}{h^2} \frac{\partial^3 u}{\partial y^3} \right) \quad (3)$$

As a measure for the truncation error we can look at its absolute value for an oscillatory characteristic component.

$$u = e^{i\omega(ay-bx)} \quad (4)$$

For such a component we obtain:

$$\left| \tau^{hk} \right| = h^2 \omega^3 \frac{b}{a} \left( \frac{b^2}{a^2} - \frac{h^2}{k^2} \right) \quad (5)$$

Hence, given  $h$ , to minimise the truncation error, the optimal choice for  $k$  is such that  $h/k = b/a$ . Applying this analysis to the advective part of the Reynolds equation, (with  $x$  and  $t$  instead of  $x$  and  $y$ ), we have  $a = b = 1$  and the optimal timestep (for the given discretization, i.e. second order upstream

/uptime) equals the mesh size in space. Any other choice, e.g.  $k = h/2$ , increases the truncation error for the characteristic component. Therefore, it is not likely that a solution obtained on a grid  $h, k/2$ , is really more accurate than a solution obtained on a grid  $h, k$  in spite of twice the amount of work being invested.

**Reply by Dr P Ehret, Professor D Dowson and Professor C M Taylor** (Institute of Tribology, Department of Mechanical Engineering, The University of Leeds). The authors would like to thank Dr C H Venner and Mr Y H Wijnant for their instructive comments. We would like to focus our response on the second part of their contribution, since the choice of the time step represents the essence of this discussion. The discussors have objected that the time step we have chosen, although twice smaller than theirs, leads to higher truncation errors. According to the discussors, this aspect is explained by a more appropriate choice of the time step and the spatial discretization which results in a vanishing truncation error. Unfortunately, we will see that the argument proposed to justify the choice of this time step is flawed.

We agree that the truncation error can be expressed by the equation (3), and we will base our development on this relation. However, by using the function (4), the discussors have stipulated that the solution, i.e. the film thickness, depends on the research of the oscillating components alone. This approach is incomplete. In fact, the solution depends on two different time scales; a short time scale given by the fluctuations of the solution depends on two different time scales; a short time scale given by the fluctuations of the solution at one point and a long time scale which represents the central value of this solution at this same point. Numerical artifacts, and damping effects results from the research of these two time scales simultaneously (Let us note that the multigrid technique is only applied spatially and we do not yet use the multigrid approach with the time component, which should make the time scheme more effective [1].

Following this remark, a function characteristic of the solution can be represented by:



$$u = u_s + u_1 \tag{1}$$

- where  $u_s$  represents a short time scale function, which can be expressed by an oscillatory function. The fluctuations of the solution are caused by the propagation of the surface features in the contact. This can be defined in the same manner as the function proposed by the discussors;

$$u_s = A_s e^{i\omega_s(at-bx)} \tag{2}$$

- and where  $u_1$  is a long time scale function, which provides the central value of the oscillatory function. The changes in function are dictated by the macro aspects of the contact (load, starved or flooded condition at the entrance of the contact, surface velocities etc). In the present case,  $u_1$  can be considered constant with time (the parameters previously cited are independent of time);

$$u_1 = A_1 E^{i\omega_1 t} \tag{3}$$

For such a function, the truncation error is expressed as;

$$\tau^{hk} = -\frac{1}{3} \left( h^2 \omega_s^3 \frac{b}{a} \left( \frac{b^2}{a^2} - \frac{k^2}{h^2} \right) A_s e^{i\omega_s(at-bx)} + h^2 \omega_1^3 a A_1 e^{i\omega_1 t} \right) \tag{4}$$

Since we do not know the values of  $A_s$  and  $A_1$ , it becomes difficult to find the optimum choice for and  $k$ . But first and foremost, the choice of the time step recommended by the discussors does not hold. It is therefore very likely that computations present numerical damping and large truncation errors, even if the time step equals the spatial discretization. This is the reason why we have proposed a simple test to check the quality of the solution, and to be sure that neither the time step or the spatial discretization entrain some numerical artifacts.

[1] from a discussion with Dr C H Venner.

**Paper IX(iv) ‘Thermal and Non-Newtonian Effects on Traction in an Elliptical EHD Contact Under High Loads and Sliding Speeds’**, by Dr M-T Ma (University of Central Lancashire, Preston, UK).

**Dr J A Greenwood** (University of Cambridge, UK). I am surprised at the difference between the results for an Eyring fluid and those for the Bair & Winer fluid. I believe you used an Eyring stress of  $0.15 p_o \sim 15$  MPa: my impression is that the more usual value is only 5 MPa, which may be responsible.

More generally I wonder what you gain by solving the problem for an elliptical contact which necessitates integration across the film as well as over the contact: a full 3 dimensional solution - compared with the solution for a roller contact, where only a 1 dimensional solution is needed: an enormous saving in computational effort.

**Reply by Dr M-T Ma**, (University of Central Lancashire, Preston, UK). Concerning the first part of the comment, Dr Greenwood is right. The large difference between the traction coefficients for the two fluid models results from the value of Eyring stress adopted:  $\tau_o = 0.015 p_o$ . The difference will be diminished if a smaller value of Eyring stress (e.g.  $\tau_o = 0.008 p_o$ ) is used.

With regard to the second part of the comment, the authors are not certain from what perspective (angle) they should respond to the question. The authors understand that an elliptical contact of larger ellipticity can be approximately treated as a roller to roller contact problem; and this will not make a significant difference as far as the evaluation of traction is concerned. However, effects across the film should be modelled in order to accurately predict the traction in the contact. In addition, by solving the problem in its three-dimensional form, the authors obtain the detailed variations of the shear stress in the contact which are of great importance in the understanding of traction mechanisms in EHD contacts and are of great interests to traction drive designers.

## **SESSION X      BIO-TRIBOLOGY**

**Paper X(i) “Influence of Geometry of Conjunction on Elastohydrodynamic Film Formation in Knee Prostheses with Compliant Layer”** Dr Ohtsuki, Professor T Murakami, Dr S Moriyama and Professor H Higahi (Kyushu University, Japan).

**Dr H P Evans** (University of Wales, Cardiff, UK). Can you explain what is meant by ‘degree of separation’ and how is it measured experimentally?

**Reply by Dr N Ohtsuki** (Kyushu University, Fukuoka, Japan). As explained in the account of the electric resistance method in this paper (2.5 Data processing), a degree of separation is defined as the ratio of measured voltage to applied voltage of 100 mV between femoral and tibial components. When the degree of separation is 1, it means full separation and when the degree of separation is 0, it means intimate contact.

**Professor J F Booker** (Cornell University, USA). In the experimental apparatus, was the tibial component free to align itself along the axis of rotation of the femoral component?

**Reply by Dr N Ohtsuki** (Kyushu University, Fukuoka, Japan). On the occasion of the installation of the tibial component, it moves freely to align itself because it is only put on the plane of the setting tray. But it does not move in the experiment under walking conditions due to the contact friction.

**Paper X(ii) “Micro-Elastohydrodynamic Squeeze-Film Lubrication of Compliant Layered Surfaces”** by Dr Z M Jin (University of Bradford, UK) and Professor D Dowson (University of Leeds, UK).

**Dr H P Evans** (University of Wales, Cardiff, UK). How was the deflection calculated?

**Reply by Dr Z M Jin** (University of Bradford, UK) and Professor D Dowson (University of Leeds). The deflection was calculated from the integral form of the elasticity equation for layered surfaces by means of the finite difference method (Meijers

1968). The solution domain was subdivided into a number of uniform meshes and the pressure distribution was assumed to be constant within each sub-division. The details can be found in a previous publication by Dowson and Jin (1990).

**Dr H P Evans** (University of Wales, Cardiff, UK). Where the pressure deviations in phase with the geometric waves, and if so were the pressure peaks at the tips or the depths of the waviness?

**Reply by Dr Z M Jin** (University of Bradford, UK) **and Professor D Dowson** (University of Leeds, UK). The pressure deviations were not in phase with the geometry’s waves. It appears from the results presented in Figures 2, 3 and 4 that positive pressure is built up from the valleys to the peaks of the waviness in the outward direction.

**Professor J F Booker** (Cornell University, USA). What are the specific geometric and material properties of the compliant layers for which the reported results apply?

**Reply by Dr Z M Jin** (University of Bradford, UK) **and Professor D Dowson** (University of Leeds, UK). Only the general solutions were presented in this paper. A specific case was solved by the authors in 1987, considering both the entraining velocity and the squeeze-film velocity due to the variation of the load and the speed in the normal human ankle joint during steady-state walking (Dowson and Jin 1987). It is anticipated that a relatively large deformation of asperities would be predicted under more realistic conditions in natural synovial joints, particularly towards the edge of the contact conjunction. However, the effect of asperity flattening under squeeze-film action is significantly less pronounced than that under sliding action.

**Dr K Vaidyanathan** (Federal Mogul Technical Center, Ann Arbor, Michigan, USA).

1. Why wasn’t the porosity effect incorporated in the model?
2. Was an attempt made to solve an inverse problem i.e. with the history of load as an input to the problem?

**Reply by Dr Z M Jin** (University of Bradford, UK) **and Professor D Dowson** (University of Leeds, UK).

1. The effect of porosity was investigated by the authors in 1992 (Jin et al 1992). It was found that under normal walking conditions, the effect of porosity had a negligible effect on the deformation of the articular cartilage during any one cycle. There is, however, a gradual change in the effective mechanical properties with time under load. Furthermore, it was shown that the effect of porosity on the lubricant flow could also be neglected when the lubricating film thickness was significantly large.
2. No attempt was made to solve the time history of the lubricating film thickness during squeeze-film motion in this paper. The transient variation of load as well as speed during walking was investigated in 1987 by the authors (Dowson and Jin 1987). The main purpose of the present investigation was to examine the effect of asperities under squeeze-film action.

#### Additional Referees

Dowson, D and Jin, Z M (1987), An analysis of micro-elastohydrodynamic lubrication in synovial joints considering cyclic loading and entraining velocities, in Fluid Film Lubrication - Osborne Reynolds Centenary, eds. by D Dowson et al, Elsevier Science Publishers BV, Amsterdam, pp 375-386.

Jin, Z M, Dowson, D and Fisher, J. (1992), The effect of porosity of articular cartilage on the lubrication of a normal human hip joint. Journal of Engineering in Medicine, Proc. IMechE, 206, pp 117-124.

**Paper X (iv) "Effects of Electric Field on Lubricating Ability of Synovial Constituents"** by Dr Y Nakanishi, Dr T Murakami and Mr H Higaki (Kyushu University, Fukuka, Japan).

**Professor J F Booker** (Cornell University, USA). The paper explores the effect of an electric field in a laboratory setting: are there also potential applications?

**Reply by Dr Y Nakanishi** (Kyushu University, Fukuoka, Japan). The effect of an electric field presented in this paper will apply to artificial joints by easy stages.

In the first place, we will propose the tribo-coating of synovial constituents by means of an electric field before implantation, which protects the sliding surfaces to prevent wear. For example, in the Metal-on-Metal lubrication, adsorbed proteins on sliding materials may act as the sacrificial film to keep the stability of frictional characteristics and the low wear rate. Therefore, we attempt to form the thick film of synovial constituents on sliding materials by means of an electric field.

The second or ultimate application is the active control of tribological characteristics by means of an electric field after implantation. However, we have to solve some difficulties; excess electric power for the human body, electrical erosion in the long term and so on.

## **SESSION XI ROLLING ELEMENT BEARINGS**

**Paper XI(ii) "Track Depletion and Replenishment in a Grease Lubricated Point Contact: A Quantitative Analysis"** by Dr P M E Cann (Imperial College, London, UK), Mr F Chevalier and Professor A A Lubrecht (INSA de Lyon France).

**Mr Y Greskenberger** (University of Hanover, Germany). You talked about stabilisation of the film thickness between 1200 and 1600 revolutions.

1. Did you keep the temperature constant all the time? or -

2. Did the temperature increase because of more friction after 1200 revolutions? Is there an important influence of the temperature around the contact zone? (e.g. on bleeding out of the base oil?)

**Reply by Dr P M E Cann** (Imperial College, London, UK).

1. Yes. There was a negligible change of  $\pm 1^\circ\text{C}$  during the test.
2. The test was carried out under nominal pure rolling at low speed so local temperature generation was very low.

A dramatic increase in replenishment levels is not seen at higher bulk temperatures. The effect of local temperature increases due to contact heating has not been studied.

**Paper XI(iv) "A Theoretical Analysis of Shear Stresses and Roller Slip in Rolling Bearings During Low-temperature Starting"** by Dr V Wikstrom, Dr R Larsson and Professor E Höglund (Lulea University of Technology, Sweden).

**Mr Y Tozaki** (Mitsubishi Heavy Industries, Japan).

1. Which case is more dangerous for skidding (a) outer ring rotation or (b) Inner ring rotation?
2. In the case of bad lubrication (not hydrodynamic condition), how do you calculate (predict) skidding?

**Reply by Dr V Wikström** (Lulea University of Technology, Sweden).

1. It is believed that outer ring rotation is a more difficult case, but that is then due to the inefficient distribution of lubricant that can be the consequence of no centrifugal force from the shaft acting to move lubricant outwards. As excess of lubricant, and often also high  $\lambda$  ratio (film thickness to surface roughness), are factors increasing the risk of skidding, it is

important not to have too large reservoirs of grease/oil present in the bearing. To the authors' knowledge, however, there is no work published showing that outer ring rotation may increase skidding.

2. This is a very interesting question, which could well be the subject of yet another investigation. In the present paper, full film lubrication is assumed everywhere: hydrodynamic in the unloaded zone and EHD in the loaded zone and no starvation is assumed everywhere: hydrodynamic in the unloaded zone and EHD in the loaded zone and no starvation is accounted for. It would however be possible to include partial surface contact depending on the amount of lubricant present, an approach which will include the problem of predicting lubricant replenishment in a full bearing. Another difficulty is to choose the dry friction coefficient properly for the spots that are totally starved.

**Dr J A Greenwood** (University of Cambridge, UK). In a tapered roller bearing, the rib thrust is an integral part of the operation: but in a cylindrical roller bearing it is "optional". You find that the biggest effect of parameter variation is the height of the rib: so what rib-force are you using?

**Reply by Dr V Wikstrom** (Luleå University of Technology, Sweden). The rib-roller contact is assumed to be a gap of fixed geometry completely filled with lubricant. The roller speed relative to the rib is calculated for every increment in roller angular velocity, and a purely viscous force is then calculated using a gap height measured on a NU 1024. The pressure is ambient, and the roller is assumed not to skew. The authors are aware that this is a simplification compared to a real bearing, but it may be closer to reality at low temperatures with highly viscous lubricant which is not easily squeezed out of the rib-roller contact. Also, in grease lubricated bearings, it is not unreasonable to believe that bulk grease present between rollers and ribs can cause rather large forces restraining or driving the rollers. Bulk grease has an apparent viscosity close to infinity when the shear rates are low, and since grease is a Bingham-plastic material, a threshold shear stress exists that needs

to be overcome before the roller can have any relative motion to the rib.

## **SESSION XII BOUNDARY LUBRICATION**

**Paper XII(i) "Direct Measurement of Boundary Lubricating Films"** by Mr V Anghel, Dr P M Cann and Professor H A Spikes (Imperial College, London, UK).

**Dr J B Medley** (University of Waterloo, Ontario, Canada). Do you think sliding velocity would influence this phenomenon? Can you give the range of "nominal" lambda ratios for your experiments?

**Reply by Professor H A Spikes** (Imperial College, London, UK). Sliding may influence the extent of thick film formation and this will be investigated in further work. The composite surface roughness was about 12 nm. This means that the results spanned a range from about  $\lambda = 0.1$  to 4.

**Professor A Cameron** (Anglia Polytechnic University, UK). It is indeed impressive to see how the spacer layer technique has been developed. It would be interesting to see how plating a non-reactive metal on the steel ball changes the results. Before we used the silica spacer, gold was found to be a useful replacement for the semi-reflecting chrome layer. It also conducts electricity. What are the authors' thoughts?

**Dr J A Williams** (University of Cambridge, England, UK). Is it possible using your technique to distinguish between films on the plate and on the ball? Clearly you are limited to the surface treatment that can be given to the plate, but presumably the ball could have films of other metals both more and less reactive evaporated on to its surface.

**Reply by Professor H A Spikes** (Imperial College, London, UK). In this study, no attempt

was made to disentangle the contribution of film formation on the steel ball and that on the silica spacer layer. In previous work looking at film formation by polymer solutions, the steel ball was replaced by a tungsten carbide one and this was found to greatly reduce boundary effects; implying that film formation on steel was important. Certainly a useful approach would be to coat the steel ball with a reflective, inert layer such as gold. It would not be helpful to replace the semi-reflective layer by gold since this does not come into contact with the lubricant since the spacer layer is in the way. It is difficult to see how the adsorption properties of the spacer layer can be significantly modified except by perhaps forming a monolayer coating of a strongly organic film.

**Paper XII(ii) "Performance of Environmentally Adapted Hydraulic Fluids at Boundary Lubrication"** by Mr J Rieglert and Dr E Kassfeldt (Luleå University of Technology, Sweden).

**Dr J A Williams** (University of Cambridge, UK). You show wear as a volumetric loss from your specimens. Could you express this as an actual rate and do you have any indication of the mechanism of wear loss? Presumably as there is no catastrophic increase in ( $\mu$ ) the failure is not one of scuffing.

**Reply by Mr J Rieglert and Dr E Kassfeldt** (Luleå University of Technology, Sweden). Even though the environmentally adapted oils give higher wear, their coefficient of friction is lower than for the mineral oil. This points to a conclusion that scuffing is not the primary wear mechanism in this case, as you pointed out. Oxidative wear is often related to a low coefficient of friction, due to the low shear strength of the oxide layer. Oxidative wear can be a possible explanation but is not yet further investigated.

The wear coefficients were calculated according to Archard's equation.

The wear coefficient for respective oil is shown in the Table.

### **Wear Coefficients according to Archard**

| <u>Oil</u> | <u>K</u>               | <u>k</u> (mm <sup>3</sup> /Nm) |
|------------|------------------------|--------------------------------|
| A          | 2.5 x 10 <sup>-9</sup> | 2.9 x 10 <sup>-9</sup>         |
| B          | 1.6 x 10 <sup>-8</sup> | 1.9 x 10 <sup>-8</sup>         |
| C          | 1.9 x 10 <sup>-8</sup> | 2.3 x 10 <sup>-8</sup>         |
| D          | 1.1 x 10 <sup>-8</sup> | 1.3 x 10 <sup>-8</sup>         |

where;

$$K = \frac{QH}{W}$$

$$k = \frac{Q}{W}$$

K = wear coefficient [dimensionless]

$$k = \text{dimensional wear coefficient} \left[ \frac{\text{mm}^3}{\text{Nm}} \right]$$

W = normal load [N]

$$Q = \frac{\text{wear volume}}{\text{distance slid}} \left[ \frac{\text{mm}^3}{\text{m}} \right]$$

H = indentation hardness [N/m<sup>2</sup>]

**Paper XII(iii) "Influence of Lubricant Additives on Friction in a Disc Machine"** by H Xu and Professor J B Medley (University of Waterloo, Ontario, Canada).

**Dr J A Williams** (University of Cambridge, UK). You demonstrated the importance of the ( $\lambda$ ) ratio on the overall friction coefficient of your rough surface experiments for which you assumed, I think, a Greenwood and Williamson form of topography. This requires that the surface can be ascribed a single, characteristic value of asperity curvature. How did you assess its value from your topographical measurements and could you indicate the sorts of values you have used.

**Dr M Visscher** (The University of Leeds, UK). The authors derived average pressure and average shear stress values for the "real contacts". To this end they used the Greenwood and Williamson

contact model to calculate the real area of contact. This and other contact models make use, however, of parameters which are not intrinsic properties of the surface, but depend on the measurement parameters (see Refs. 1,2). The mean peak radius, for example, varies significantly with the sampling interval. Hence by manipulating the roughness measurement, one can get any value one likes. My question, therefore, is; have the authors considered this fact, and how have they overcome the problem?

Ref. 1. Greenwood, J A (1992), 'Fundamentals of Friction: Macroscopic and Microscopic Processes' (Proc. NATO Advanced Study Institute on Fundamentals of Friction), NATO, ASI Series E, Vol. 220, 57-76.

Ref. 2. Visscher, M, Dowson, D and Taylor, C M. (1996), 'Surface Roughness Modelling for Piston Ring Lubrication: Solving the Problems', Proceedings of the 22nd Leeds-Lyon Symposium on Tribology, 'The Third Body Concept: Interpretation of Tribological Phenomena', 527-537.

**Dr J C Bell** (Shell Research Ltd, Thornton, UK). The authors have estimated the contribution to friction of lubricant additives by the use of the limiting shear stress ( $\tau_L$ ) model of Wu and Cheng. The mechanism by which additives affect ( $\tau_L$ ) is far from clear. Would the authors please clarify this mechanism and how it is reflected in the Wu and Cheng model?

**Reply by Ms H Yu and Professor J B Medley** (University of Waterloo, Ontario, Canada). Drs Williams and Visscher seem to be asking essentially the same question. In our presentation, we did not elaborate on our "Greenwood and Williamson" type model but in our paper details are provided in Section 4.3 and Appendices B, C and D. The influence of Greenwood and Williamson led us to assume that asperities had spherical tips, deformed independently and that Gaussian distributions could be applied to surface and asperity height distributions. However, using the relationship for contact spot density, derived by Cooper et al (1969) and also in Appendix B of our paper in a somewhat different manner, we assumed

that all contacting asperities at a particular separation  $x$  (Figure B1) had spherical tips of about the same radius of curvature (but various heights) which could be represented adequately by an average value ( $\beta$ ). The method of obtaining the separation  $z$  and corresponding  $\beta$  for a given load can be found in De Vaal (1983) and also in Appendix D of our paper, and the numerical values for our two rough surfaces (discs R1 and R2) are listed in Table 4. By determining a separation  $z$  and an average  $\beta$ , both related to the applied load, we allowed small surface ripples and/or noise which might be part of the trace of the surface heights (Figure 6), details of which would be sensitive to sampling interval, to merge when the surfaces are at separation  $z$  and thus not influenced by the calculated real area of contact significantly. In this manner, our calculated  $\beta$  was not a single constant value for the surface but a function of the applied load which, in turn, set the separation  $z$ . For our surface topography and loads, the  $\beta$  value was not likely to change much unless the load was reduced significantly.

This approach differs from that of Visscher et al [D2] but it seems to achieve a somewhat similar result in that it eliminates smaller scale "asperities" from consideration. Since our surfaces were run-in before testing so that virtually all asperities would be deforming elastically under load, plasticity index could not have been used to determine a sampling interval. However, our approach might provide a versatile alternative which would be useful in the modelling of Visscher et al.

If a Greenwood and Williamson model requires a "mean peak radius" as stated by Dr Visscher or a "single characteristic value of asperity curvature" as stated by Dr Williams, then perhaps we should not have associated Greenwood and Williamson so directly with our model. Since the calculation of real areas of contact was only a means to an end in our paper, we make no claims to have a universal model based on "intrinsic" surface properties. However, we do feel that the adopted approach gives a unique prediction of real area of contact which is reasonably accurate for the run-in surfaces in our study.

In response to the question of Dr Bell we have found that under our conditions of high pressure and low temperature, the friction can be controlled by the limiting shear stress and the additives cause a decrease in the limiting shear stress as predicted by Equation 4 of our paper by reducing the value of ( $m$ ) which is the index number from the model of Wu and Cheng (1994). The determination of ( $m$ ) is described in detail in Appendix A of our paper. One can speculate that the additives influence the formation of the shear bands, described by Bair et al. (1993) by allowing the lubricant to "slide over itself" more readily. However, Dr Bell may be seeking a specific and verified mechanism related to the lubricant chemistry and including the influence of temperature. It was beyond the scope of the present study to determine these important aspects of the mechanism, but nevertheless we do feel that some experimental evidence of its existence has been obtained.

#### Additional Reference

De Vaal, J W (1983), 'Thermal contact conductance of rough surface', MSc Thesis, University of Waterloo, 76-80.

**Paper XII(v) 'The Role of Boundary Lubrication in Scuffing Reactions'**, by Dr R Smalley (SKF ERC, Nieuwegein, The Netherlands) and Professor A Cameron (Anglia Polytechnic University, UK).

**Dr J C Bell** (Shell Research Ltd, Thornton, UK). Variations in the contact resistance behaviour are explained in terms of hydrodynamic effects at low temperatures and chemical film formation at the higher temperatures. The influence of orientation of roughness of the rougher specimen surfaces was most marked in the "chemical reaction film" regime. Would the authors care to comment on the mechanisms that may be responsible for this difference, in view of their observation that the behaviour of both orientations was very similar in the "hydrodynamic film" regime.

**Reply by Dr R Smalley** (SKF ERC, Nieuwegein, The Netherlands) **and Professor A Cameron** (Anglia Polytechnic University, UK). The reply is quite difficult but the surface roughness and its orientation to the sliding direction has a strong

effect upon the thermodynamics of the complete system under boundary lubrication and has been shown in the following papers: J P Sharma and A Cameron, "Surface Roughness and Load in Boundary Lubrication", ASLE Trans. 1973 Vol. 16, 258-266 also A Cameron, R S Day et al. "Interaction of Additive and Base Stock", ASLE Trans. 1976, Vol. 19, 195-200.

**Dr.-Ing. G Poll** (University of Hanover, German). Can the difference in boundary layer stability between brass and steel be explained by the lower hardness (yield limit) of brass? If so, did you find difference between brass grades containing more or less tin which can be related to the mechanical stability of the bulk material supporting the boundary layers?

**Reply by Dr R Smalley** (SKF ERC, Nieuwegein, The Netherlands) and **Professor A Cameron** (Anglia Polytechnic University, UK). The stability of the chemical reacted boundary layer will be mainly influenced by the thermodynamics of the two contacting surfaces and only indirectly by the mechanical properties of the "contacting" asperities. The strength of the material will be influenced in part by the metallurgical phase distribution of the brass and the steel which in turn will affect the thermodynamics of the polar reacting groups. This interesting aspect as pointed out by Dr Poll will be the focus of further investigations.

### **SESSION XIII      FRICTION,** **TRACTION AND WEAR**

**Keynote Paper XIII(i) 'Modelling Non-Steady Elastohydrodynamic Lubrication with Focus on Lubricant Rheology'**, by Professor E Hoglund and Dr R Larsson (Luleå University of Technology, Sweden).

**Dr R I Taylor** (Shell Research Ltd, Thornton, UK). You mentioned that to minimise surface shear stresses it is better to use a more compressible lubricant. However, another school

of thought is to choose oils with high pressure coefficients, to maximise the oil film thickness. The molecular structure needed to get high pressure coefficients generally gives relatively incompressible oils, and vice versa. Could the authors comment?

**Reply by Professor E Hoglund and Dr R Larsson** (Luleå University of Technology, Sweden). First of all it is not the surface shear stress that is minimised if compressibility is high, it is the sub-surface stresses. It is true that a high pressure coefficient will give thicker films. High pressure coefficient will also give larger pressure spike amplitude. Pressure peaks caused by asperity interaction will also be higher if the pressure coefficient is high. High pressure peaks are bad since the sub-surface stresses will increase and it is thus desirable to combine low pressure coefficient and high compressibility to minimise the rise of surface fatigue.

**Dr P L Wong** (City University of Hong Kong). For non-steady situations there is an important parameter: time. My first question is: have the authors studied the time effect on the density measurements. Two graphs of density - pressure results of two oils were shown. The authors' density results are derived from the results obtained by other investigators (Feng and Ramesh). Would the difference be explained by the time effect? If so, and the authors believe that the time effect of density-pressure measurements is true, the authors' proposed density-pressure model should be modified such that the time effect can be incorporated. At least in the conclusion of Feng and Ramesh's paper, they mentioned that there is no time effect based on a comparison with measurements obtained by the much slower measuring technique of Bair and Winer. Could the authors comment on this?

**Reply by Professor E Hoglund and Dr R Larsson** (Luleå University of Technology, Sweden). The time effect on lubricant compressibility is not explicitly studied in the experiments by Lindqvist et al, but a comparison is made with the results by Ramesh [1]. In that paper there is also a discussion written by S Bair and W O Winer. The latter authors draw attention to the



similarity between their static measurement of compressibility and Ramesh's highly transient measurement. The results by Lindqvist et al are also obtained under transient conditions but at a lower loading speed than used by Ramesh' highly transient measurement. The results by Lindqvist et al are also obtained under transient conditions but at a lower loading speed than used by Ramesh. All three measurements correspond well to each other at low pressure. But the compressibility results presented here diverge much from Ramesh' results at high pressure ( $p > 0.8$  GPa). This may be explained by the different loading times. The results from Lindqvist et al are obtained at realistic loading times, comparable to those found in chl.

[1] K T Ramesh, "The short-time compressibility of elasto-hydrodynamic lubricants", ASME Journal of Tribology, 1991, 113, pp 361-371.

**Paper XIII(iii) "Decrease of Friction Coefficient Under Extremely Low Normal Load"** by T Ando (AIST, MIYI, Ibaraki, Japan).

**Dr F Ji.** Have you considered time effect on the friction coefficient?

**Reply by Dr Y Ando** (AIST, MIYI, Ibaraki, Japan). No. The friction coefficient was just measured under touch and then separate. The time effect might have significant influence on the friction coefficient, because surface topography and surface films might affect the friction coefficient.

## **SESSION XIV METAL FORMING**

**Paper XIV(i) Keynote Paper "Modelling Friction in the Analysis of Metal Forming and Machining Process"** by Professor P L B Oxley (University of New South Wales, Australia).

**Professor D Dowson** (Institute of Tribology, Department of Mechanical Engineering, The University of Leeds, UK). I congratulate the author on a tour de force. It is good to see plasticity and lubrication studies integrated in this way.

Your experiments were carried out at very low speeds, but the shear rates in the film are of order  $10^6$  (1/s). Have you measured or calculated the temperatures in the contact? If so, how do they vary in the various test conditions considered?

You refer to 'EHL' films, but it might be helpful to use the term adopted in drawing processes of 'plasto-hydrodynamic lubrication' or 'PHL'. If both 'elastic' and 'plastic' deformations are considered, we adopted the term 'elasto-plasto-hydrodynamic lubrication' (EPHL).

**Reply by Professor P L B Oxley** (University of New South Wales, Australia). I thank Professor Dowson for his kind comments on the paper. I agree with him that for the wave formation process PHL would be a more appropriate description than EHL and that once account is taken of the elastic deformation at entry we should use the term EPHL. So far we have not determined the temperature in the contact zone but are intending to do this in future work - we are now doing tests at much higher speeds than that reported in the paper.

**Dr P A Dearnley** (Institute of Tribology, Department of Mechanical Engineering, The University of Leeds, UK). In your paper you mention the possibility of a 'Solid Lubricant' near the interfaces in metal cutting. Are you aware of some work carried out at Birmingham University by Dr. Chambers (c. 1981) who postulated the possibility of super-plastic behaviour of metal in the secondary shear zone? Might their idea modify or help interpretations? Such mechanisms may be possible because of the very fine grain sizes ( $< 1\mu$  m) that enable superplasticity mechanisms to operate.

**Reply by Professor P B L Oxley** (University of New South Wales, Australia). I am grateful to Dr Dearnley for pointing out the work of Dr Chambers. I did not know of this work and will look into the possibility of superplastic behaviour occurring in the shear zone at the tool-chip interface.

**Dr K Maekawa** (Ibaraki University, Japan).

1. According to recent observations using AFM and MD simulations, liquid lubricant shows solid-like behaviour. In your slip line field model for EHL with a nanometre-thick film, how does the above behaviour correlate with your model? I just wonder if the model is applicable to the cases with changing lubricant thickness.
2. Your slip line analysis treats only two-dimensional plane strain conditions. How does the influence of three dimensional wedge shapes take place?
3. In your cutting model, you use the shear plane model, despite the fact that it includes a plastic deformation zone around the plane. What is the limitation to your slip line model?

**Reply by Professor P L B Oxley** (University of New South Wales, Australia).

I have little experience of using AFM and MD situations and therefore find it difficult to answer Dr. Maekawa's first question. I have always thought that the lubricant film at the wedge-wave interface will show solid-like behaviour in line with the work of others but have no direct evidence if this. Referring to the second question, a similar steady-state process to the wave formation process can occur with a three-dimensional wedge. However, with this process the apex of the wedge travels below the deformed surface and produces a ploughed track with material displaced to both sides. Williams and Xie (Williams, J A and Xie, J. Phys. D., Appl. Phys., 1992, 25, A158-A164) have considered the analysis of this process using the upper bound method. Regarding our cutting model, I think that it is better described as a shear zone model rather than a shear plane model. The main limitation of the model I described is that it assumes plane strain conditions. In recent years we have used this model as a basis to make predictions for oblique (three-dimensional tool) cutting conditions using a semi-empirical approach. We have shown good agreement between predicted and experimental results.

**Paper XIV(ii) 'Friction Characteristics of Tool-Chip Interface in Steel Machining'** by Dr K

Maekawa (Ibaraki University, Japan), T Kitagawa (Kitami Institute of Technology, Japan) and Professor T H C Childs (Institute of Tribology, Department of Mechanical Engineering, The University of Leeds, UK).

**Dr P A Dearnley** (Institute of Tribology, Department of Mechanical Engineering, The University of Leeds, UK). In discussion the topic of chip-tool contact length was raised. Many other workers have also observed a variance in chip/tool contact length (for a given steel workpiece material being machined at the same cutting conditions) for different tool materials. Cermet (TiC-Ni), ceramics ( $Al_2O_3 + ZrO_2$ ) and carbides coated with TiC, TiN or  $Al_2O_3$  produce shorter contact lengths than those observed for uncoated WC-Co cemented carbides. The explanation suggested by Professor Childs was that there was a change in the shear strength in the flow zone (or secondary shear zone) produced by using different cutting tool materials.

It is my view that the chip-tool length, when cutting steels, is strongly influenced by the chemistry between the tool surface and the chip underside. In particular, there appears to be a relationship between the contact length and the wetting of carbides, oxides and nitrides by molten iron - wetting angles for oxides, TiC and TiN are several degrees, whereas for tungsten carbide the wetting angle is zero/perfect wetting). In crude terms there is a greater driving force for the chip to remain in contact with WC-Co tools than is the case for the coated, cermet or ceramic tools. This will result in a practical difference in the work done in the secondary shear zone (or flow zone) and accordingly the size of the heat affected zone and the magnitude of the maximum rake face temperature will be greater for the uncoated WC-Co based tools (with long contact lengths) than for the coated, cermet and ceramic tools. Direct evidence of these temperature differences are given in one of my earlier papers\*

\* P A Dearnley, Metals Technology, 10, (6), 205-211 (1983).

**Reply by Professor T H C Childs** (Institute of Tribology, Department of Mechanical Engineering, The University of Leeds, UK). Dr Dearnley

misunderstands what I said. I meant there is a change in shear stress between the chip and the tool, not within the chip near the tool. This area will be influenced by chemistry as Dr Dearnley suggests. As a matter of fact, we also believe that the tool thermal conductivity also plays a subtle role through influencing rake temperatures and hence the rake interactions.

**Dr J A Williams** (Engineering Department, University of Cambridge, UK). In dividing  $\tau$  by  $\sigma$  along the rake face of the tool you obtain curves of the form of eqn 1 which contains two disposable constants. One  $\mu$  is the coefficient of friction between chip and tool in that region of the contact which is relatively lightly loaded towards the point at which it loses contact with the tool. Can any physical significance be ascribed to the other? In treating the data in this way one loses the numerical value of one of the measured quantities viz the rake face contact length. I am not clear why this is a wise thing to do. The values of  $\mu$  obtained are very high certainly greater than unity and so there is clearly a good deal of adhesion occurring in this region. Under such circumstances, not dissimilar to the old idea of junction growth, the derived coefficient of friction is very sensitive to the degree of contamination of the conjunction. This suggests that the form of the  $\tau/\sigma$  curve will not be independent of the scale, i.e. the feed, of the experiment.

**Reply by Professor T H C Childs** (Institute of Tribology, Department of Mechanical Engineering, The University of Leeds, UK). Dr Williams asks a good question. There are difficulties in describing the friction law between the chip and the tool with sufficient detail to be useful. One issue is the very clean (and high friction) conditions he refers to; another is that in these conditions chip formation is very sensitive to small changes in friction, or to small errors in describing the friction. However, I am sure that the boundary condition on the rake face should be a condition on the stresses and not on the contact length. The whole difficulty of predicting flow in machining is that geometry (of which contact length is a part) is not constrained by the tooling. The fact that it can be argued that the stress condition has not been properly researched is another matter.

**Professor R C Coy** (Shell Research Ltd., Chester, UK). For tool materials with lead and manganese sulphide additives, is there evidence of surface films (i.e. solid lubricants) on the chip and tool surfaces?

**Reply by Professor T H C Childs** (Institute of Tribology, Department of Mechanical Engineering, The University of Leeds, UK). It is very common to observe deposits of lead and manganese sulphide (and other solid lubricants such as silicates) on the rake face of cutting tools. The book by E M Trent (Metal Cutting, 3rd Edition, Butterworths 1991) shows a number of examples. It is rarer to find traces on the back of the chips. In fact, very few people look there as the observations on the tool are so much easier.

**Paper XIV(iii) 'Wear Characteristics of Various Cutting Tools in Steel Machining'** by Dr T. Kitagawa (Kitami Institute of Technology, Japan), Mr A. Kubo (Kitami Institute of Technology, Japan) and Dr. K Maekawa (Ibaraki University, Japan).

**Dr P A Dearnley** (Institute of Tribology, Department of Mechanical Engineering, The University of Leeds, UK). Do you consider that diffusion wear is also an important factor in the development of crater wear?

I think there is some confusion in the terminology used in this paper in relation to 'adhesion wear' in that the authors appear to imply that the temperature sensitive 'adhesion wear' contains a component of diffusion wear.

**Reply by Dr T Kitagawa**, Kitagawa (Kitami Institute of Technology, Japan), Mr A. Kubo (Kitami Institute of Technology, Japan) and Dr. K Maekawa (Ibaraki University, Japan). As you pointed out, a diffusion process is also an important factor in the development of crater wear. In the wear characteristic equation we derived from an adhesion wear model,  $z$  is the probability that a real contact will result in a wear particle, in which the Maxwell-Boltzmann canonical distribution is postulated. The diffusion is indirectly considered in this assumption. A rough

estimation using a characteristic constant of  $C_2 = 21,770\text{K}$  yields an activation energy of  $180\text{ kJ mol}^{-1}$  ( $43\text{ kcal mol}^{-1}$ ), which is nearly equal to the activation energy for the diffusion of Co within Fe. In the end the wear equation has a similar form to a diffusion type equation, but is distinguished from it so far as mechanical factors such as normal stress and sliding distance are taken into account. Thus, our wear model is based on adhesion wear which has the factor ( $z$ ) mentioned above, so that we call it the thermally-activated adhesion wear model.

## **SESSION XV TRANSMISSIONS** **(2) - C.V.T.'s**

**Paper XV(i) "EHL Traction in Traction Drives with High Contact Pressure"** by Dr S Aihara, Dr S Natsumeda and Mr H Achiha (NSK Ltd, Japan).

**Professor R C Coy** (Shell Research Ltd, Chester, UK). Density measurements are done under steady state hydrostatic conditions and the fluid can be considered isotropic. In a dynamic traction drive the fluid is subject to high shear stresses at high pressures and may no longer be isotropic. What do you think the effect of anisotropy in the fluid will have on density and could this effect help to explain the difference between theory and experiment in traction?

**Reply by Dr S Aihara, Dr S Natsumeda and Mr H Achiha** (NSK Ltd, Japan). Density measurement results by Ohno et al was referenced, as they found three different regimes between bulk modulus and ( $\alpha p$ ) as shown in Fig. 17 from these measurements. Their measurements were done under static condition and their prediction does not explain our traction results. Höglund showed a different curve of density change with pressure during very short period, or dynamic condition, at the conference and found no discontinuity in the curve. As the lubricant passes through the contact in about one millisecond, we need more research of lubricant rheology under dynamic condition.

We think the effect of anisotropy will be considered after that. In fact molecular dynamics analysis is being carried out to investigate such effects and I hope it works well to explain traction.

**Dr V Wikström** (SKF ERC BV, The Netherlands) and **Professor E Höglund** (Luleå University of Technology, Sweden). The authors have presented a most welcome experimental investigation into high-pressure traction. However, the results need to be discussed further, since it is most surprising to see a maximum traction level which decreases with pressure. Prior traction measurements by e.g. Johnson and Tevaarwerk (1) or Bair and Winer (2) have shown a maximum traction coefficient which increases with pressure.

The maximum traction coefficient will be decided by the limiting shear strength of the lubricant, and contrary to the findings of the authors, the limiting shear stress has been found to increase with pressure. Measurements at 0.6 - 2 GPa by Höglund and Jacobson (3) show that it increases approximately linearly with pressure, following the equation

$$\tau_L = \tau_o + \gamma p$$

The same has been seen by Ramesh and Clifton (4) at pressures of the same magnitude as in the paper (1-4 GPa).

In EHD contacts, the inlet and contact temperature may change even though the lubricant bath temperature is held constant, especially when the degree of slide-to-roll ratio increases, see e.g. Ausherman et al (5), who recorded a temperature rise at the inlet of up to  $120^\circ$ . They also show that the in-contact temperature rise is highly dependent on the maximum Hertzian pressure. Since only the bulk temperature was monitored in the present paper, it might be reasonable to believe that with increasing pressure, inlet and contact temperature have increased and hence that the traction coefficient has decreased due to the temperature increase and not due to the higher pressure. It is well documented that increased temperature will decrease both the limiting shear stress (6) and the maximum traction coefficient (7). Could the

authors please comment on what the temperature rise might be in their apparatus, and how large the influence on their measured traction a different temperature would have?

It would be interesting to make the same type of experiments with a low-traction oil (PAO or similar) where the temperature rise, if present, should be somewhat lower.

#### References

1. Johnson, K L, Tevaarwerk, J. "Shear behaviour of EHD Oil Film", Proc. Roy. Soc. of London, A 256, pp 215-236, (1977).
2. Bair, S, Winer, W O. "Some Observations in High Pressure Rheology of Lubricant". ASME J. of Lubrication Technology, July, Vol. 104, pp 357-364, (1982).
3. Höglund, E, Jacobson, B. "Experimental Investigation of the Shear Strength of Lubricants Subjected to High Pressure and Temperature", ASME J. of Tribology, October, Vol. 108, pp 571-578, (1986).
4. Ramesh, K T, Clifton, R J. "A Pressure-Shear Plate Impact Experiment for Studying the Rheology of Lubricants at High Pressures and High Searing Rates", ASME J of Tribology, April, Vol. 109, pp 215-222, (1987).
5. Ausherman, V K, Nagaraj, H S, Sanborn, D M, Winer, W O. "Infrared Temperature Mapping in EHL", ASME J of Lubrication Technology, April, pp 236-243, (1976).
6. Wikström, V, Höglund, E. "Investigation of Parameters Affecting The Limiting Shear Stress-Pressure Coefficient A New Model Incorporating Temperature", ASME J of Tribology, No. 3, Vol. 113, pp 612-620 (1994).
7. Houpert, L, Flamand, L, Berthe, D. "Rheological and Thermal Effects in Lubricated EHD Contacts", ASME J. of Lubrication Technology, October, Vol. 103, pp 526-532, (12981).

#### Reply by Dr S Aihara, Dr S Natsumada and Mr H Achiha (NSK Ltd, Japan).

We considered the temperature increase due to inlet shear heating in order to do traction calculations based on a non-Newtonian model with Eyring stress. We limited our calculation in the small slide-roll ratio region because thermal effects by shear should be excluded. Namely the region of 0 to 0.2 (or 0.3) % was considered. Sliding velocity is 0 to 0.06 m/s (0.1 m/s at maximum). Furthermore, as the rolling speed is very high (20-30 m/s), the film is thick. It should be noted that the reduced radius of CVT is much greater than that of rolling bearings.

The situation is quite different from the measurement by Ausherman et al, but rather resembles the measurement of Dow and Kannel (1), though their pressure is very low. Their results show that temperature increase in the contact is determined by the temperature increase at pure rolling as long as the slide-roll ratio is small. Therefore, as to our concern, temperature increase by the shear can be dismissed. But I agree with the discussor that the temperature rise is essential in traction, but if we enter such region we cannot use average properties (average pressure, average temperature, average traction).

In our measurement contact pressure was increased with increasing load. But the comparison with the results by Kato et al (Fig. 5) with constant load but with different pressure and at low speed is remarkably consistent. We think the coincidence is too great to attribute it only to the temperature rise in the contact. That is why we proposed more research in lubricant rheology under more extreme conditions.

With regard to the observation that maximum traction coefficient is almost constant with increasing contact pressure at such high pressure. This means that traction force increases almost linearly with applied load. Even if the traction coefficient decreases a little, the traction force increases and this is essential in practical traction drives.

As to a final question, Evans and Johnson showed a difference in pressure-traction relationship

between a mineral oil and Santotrac oil (traction oil) as in Figs. 6 and 7, but at least disc temperature was controlled to reduce the effect of temperature.

#### References

- (1) Dow, T A and Kannel, J W "Evaluation of Rolling/Sliding EHD Temperature", Proc. 6th Leeds-Lyon Symposium on Tribology (1979), 228-240.

**Paper XV(ii) "The Effect of Spin Motion Upon Elastohydrodynamic Elliptical Contacts"** by Dr M Taniguchi (NSK Ltd, Japan), Professor D Dowson and Professor C M Taylor (The University of Leeds, UK).

**Dr J Kannel** (Battelle, Ohio, USA). Have you evaluated the effects of non-Newtonian or thermal action on film thickness? It seems that spin would be more important when these effects are considered.

**Reply by Dr M Taniguchi** (NSK Ltd, Japan), **Professor D Dowson and Professor C M Taylor** (The University of Leeds, UK). The authors have not calculated a thermal ehd problem with spin motion. However, the effects of the non-Newtonian behaviour of the lubricant have been studied with/without sliding and spin motion, based upon Eyring's theory.

The pressure spike was found to be diminished by either sliding or spin motion. A large slip gave a reduction in the minimum and central film thicknesses. An increase in spin motion on one surface of the contacting bodies also caused a reduction in minimum film thickness. However, this is considered to be due mainly to the reduction in film entraining velocity introduced by spin motion. The details will be published in a further paper.

**Dr X Ai** (The Timken Company, Oh, USA). Spin motion commonly exists in machine elements such as continuously variable transmission (CVT), angular ball bearings and tapered roller bearings. Incorporating spin motion in EHL contact modelling adds an additional degree of difficulty to the already complex problem. The discussor would

like to congratulate the authors for their contribution to this interesting and important topic.

Spin motion causes film thickness reduction due to the counter action to rolling at one side of the contact. The film thickness reduction increases linearly with spin to roll ratio, B. The slope of this linear relationship is, according to the authors, solely determined by the load parameter, W, e.g.

$$\frac{H_{\min}}{H_{\min(B=0)}} = 1 - 3.47 W^{0.47} B$$

The counter velocity to rolling, at a point in the contact, is the product of angular speed and the distance from the point to the center line of contact. Increasing load produces a larger contact ellipse which increases the counter velocity to rolling. This certainly in part explains the dependence of film thickness reduction on load parameter. However, what concerns us is the possible effect of contact ellipticity ratio on film thickness reduction since this was left out by the authors. Since contact ellipse and thus counter velocity to rolling can also be changed independently through contact ellipticity ratio, k (contact geometry), dependence of film thickens reduction on ellipticity ratio was expected. Would the authors shed light on this issue?

**Reply by Dr M Taniguchi** (NSK Ltd, Japan), **Professor D Dowson and Professor C M Taylor** (University of Leeds, UK).

The authors would like to thank Dr Ai for his thoughtful remarks.

The formula of the minimum film thickness reduced by spin motion was derived from the (EHL) calculation with the contact ellipticity ratio (k) varying from 2 to 6. The conditions were mainly based upon the experimental conditions of a half toroidal CVT. In this range of ellipticity ratio, the film reduction formula agreed well with the computed results and the effect of (k) was relatively small.

However, as Dr Ai mentioned, it would be necessary to consider the effect of ellipticity ratio

upon the minimum film thickness in cases of a long elliptical contact as seen in rolling bearings.

In this study, the contributions of the ellipticity ratio of the contact ellipse ( $k$ ) and the non-dimensional materials parameter ( $G$ ) to the film reduction caused by spin motion were not fully explored, although some results suggest that a large ( $k$ ) reduces the minimum film thickness more significantly than a small ( $k$ ), with the presence of spin motion in the contact region. A further study is required in this area.

**Dr J Greenwood** (University of Cambridge, UK). The effect of spin, as you say, is to speed up one side of the contact and to slow down the other. Can you tell us what range of spin you are considering? - does the "slow" side move backwards, or is its speed much the same?

If your factor ( $W^{0.47}B$ ) giving the reduction in film thickness is small is it possible (you have not given us the full definition of  $B$  in the presentation) that it is really just an expression for the relative speed reduction at the contact edge and that what we really have is a factor  $(1 - \mu_{\min}/\bar{u}^{0.70})$ . In other words, that ( $h_{\min}$ ) depends not on ( $u$ ) but on ( $u_{\min}$ )?

**Reply by Dr M Taniguchi** (NSK Ltd, Japan), **Professor D Dowson and Professor C M Taylor** (The University of Leeds, UK). The spin angular velocity given to the lubricated contact is too small to reverse the rolling motion in the contact ellipse in this study. For example, in the largest spin case in Figure 6 (2500 [rad/sec]), the spin motion yielded the velocity component in the rolling direction, being approximately 20% of the translational rolling velocity on the side of the contact ellipse.

The authors could not find any direct relationship between the minimum film thickness and the minimum velocity in the ehd elliptical contact with spin motion.

**Paper XV(iv) "An Analysis of Elastohydrodynamic Film Thickness in Tapered Roller Bearings"** by Dr R Yamashita (Koyo Bearings

Ltd, Japan), Professor C M Taylor and Professor D Dowson (The University of Leeds, UK).

**Ir Y H Wynant** (University of Twente, the Netherlands). Could the authors comment on the situation should the model presented by extended to a full transient analysis for the determination of film thickness.

**Reply by Dr R Yamashita, Professor C M Taylor and Professor D Dowson** (The University of Leeds, UK). The primary objective of the research described in our paper has concentrated upon the static loading analysis and kinematics associated with tapered roller bearings. In particular load distributions and deflections of components have been determined and details presented. An initial assessment of pressure and film thickness distributions in the unusual contact geometry of the tapered roller bearing has been undertaken. Such analysis has also been quasi-static in nature. The extension of the work for transient situations would be highly demanding in terms of computational effort and time and the authors are not contemplating this in the immediate future.

**Professor A A Lubrect** (INSA de Lyon, France). The authors are to be complimented for having treated such an important problem, however, in view of the complex geometry, and considering the coarse discretization, some doubts concerning the precision of the results seems appropriate. Could the authors state the precision of their result.

**Reply by Dr R Yamashita**, (Koyo Bearings Ltd, Japan) **Professor C M Taylor and Professor D Dowson** (The University of Leeds, UK). The caution expressed by Professor Lubrect is appropriate. The major thrust of the work, as indicated in the response to the previous question, related to the establishment of the static loading analysis of the tapered roller bearing. The elastohydrodynamic analysis undertaken for the contact between a tapered roller and raceway was only a preliminary steady state analysis undertaken to obtain a feel for the likely implications of the realistic contact geometry as compared to the more conventional treatments. The coarseness of the mesh utilised in the analysis would indeed bring

into question the precision of pressure and film thickness calculation determinations in detail, and the authors will be examining this issue in the future.

## **SESSION XVI PLAIN BEARINGS**

**Paper XIV(ii) "Simulation of the Oil Film Behaviour in Elastic Engine Bearings Considering Pressure and Temperature Dependent Oil Viscosity" Dr H H Pribsch and Mr J Krasser (A.V.L. List GmbH, Australia).**

**Dr H Xu** (T. & N. Technology Ltd., Cawston House, Rugby, UK). Can the authors give their view on the fact that the bearing surface temperatures are higher than the oil film temperature? For if that is the case, no heat will flow into the bearing/housing. What is then the heat source to increase the temperature in the bearing body?

**Reply by Dr H H Pribsch and Mr J Krasser** (A.V.L. List GmbH, Australia). We regret that Dr Xu seems to be misled by the perspective of the Figs. 8 and 13. In fact, there is a negative temperature gradient in the oil film towards the bearing surface everywhere in the bearing. This is illustrated in Fig. 16 where the temperature gradient, calculated as:

$$\frac{T_{\text{bearing surface}} - T_{\text{first point in oil film next to bearing surface}}}{\Delta \bar{y} \cdot h}$$

is shown for the plane of symmetry of the bearing of the gasoline engine (compare with Fig. 13).

**Paper XVI(iv) "The Elastohydrodynamic Lubrication of Heavily Loaded Journal Bearing having non-Cylindrical Axial Geometry" by Dr H. El-Sayed Rasheed** (Arab Academy of Sciences & Technology, Alexandria, Egypt).

**Dr J B Medley** (Department of Mechanical Engineering, University of Waterloo, Ontario,

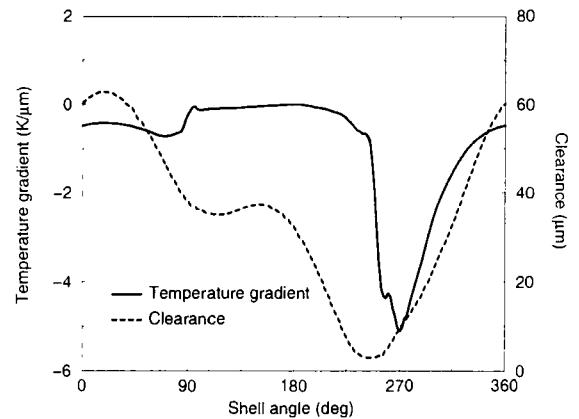


Fig.16 Temperature gradient in the plane of symmetry of the bearing at 120 CA gasoline engine

Canada). Do you have some physical explanations for the improved performance of your non-cylindrical journal bearings?

As a general comment, I think such physical explanations are important in determining optimisation strategies and investigating the possibility that some important physical phenomena have not been neglected.

**Reply by Dr H El-Sayed Rasheed** (Arab Academy for Sciences & Technology, Alexandria, Egypt).

The increase in the load carrying capacity is attributed to the increased wedging action resulting from increased tangential velocity due to axial variation of the bearing geometry. This can be visualized from the Reynolds-like equation derived in the paper (Eqn. 2). Inspection of this equation especially in the neighbourhood of the plane of symmetry of the bearing ( $\zeta \cong 0$ ) may clarify matters. Eqn. 2 when applied close to  $\zeta = 0$ , the parameters  $\lambda$  and  $H^*$  will be approximately  $\lambda \cong 1$  and  $H^* \cong 1$ . Eqn. 2 can therefore be rewritten in approximate form close to the plane  $\zeta = 0$  as,



$$\frac{\partial}{\partial \theta} \left[ \frac{h^{*3}}{\mu^*} \frac{\partial \rho}{\partial \theta} \right] + \left( \frac{R}{L} \right)^2 \frac{\partial}{\partial \zeta} \left[ \frac{h^{*3}}{\mu^*} \frac{\partial \rho}{\partial \zeta} \right]$$

$$= 6 \left[ 1 + \delta^* \left( \frac{L}{R} \right) \right] \frac{\partial h^*}{\partial \theta}$$

In comparison the familiar Reynolds equation for plain journal bearings may be written as,

$$\frac{\partial}{\partial \theta} \left[ \frac{h^{*3}}{\mu^*} \frac{\partial \rho}{\partial \theta} \right] + \left( \frac{R}{L} \right)^2 \frac{\partial}{\partial \zeta} \left[ \frac{h^{*3}}{\mu^*} \frac{\partial \rho}{\partial \zeta} \right] = 6 \frac{\partial h^*}{\partial \theta}$$

It can easily be seen that the dimensionless forcing velocity of the rotating solid boundary which is unity in the case of a plain journal bearing has effectively become  $\left[ 1 + \delta^* \left( \frac{L}{R} \right) \right]$ , that it has

increased by an amount proportional to the maximum dimensionless axial variation of the geometry  $\delta^*$  and this proportionality constant is the ratio  $L/R$ . That is the increase in film pressure due to the increase in this velocity is more pronounced, as stated in the paper, for a long bearing.

**Paper XVI (v) "Mode Stiffness Variation in EHD Bearing Design"** by Dr S Boedo and Professor J F Booker (Cornell University, USA).

**Mr Marco Workel** (The University of Leeds, UK). What is the (physical) explanation for the film thickness increase (instead of film decrease) at zero degree crank angle for the stiffer mode?

**Reply by Dr S Boedo** (Borg Warner Automotive, New York, USA) and **Professor J F Booker** (Cornell University, USA). The authors assume Mr Workel's comments refer to the firing-exhaust portion of the engine cycle (zero to 150 degrees crank angle), where it is indeed true that the mode-softened structure produces thinner films than those obtained with either the original or the mode-stiffened structure (see Figure 7). The physical explanation for this drop in bearing performance may be partly addressed through comparison of mode eigenvalues 3 and 4 of the relative stiffness matrix listed in Table 2. Mode-softening results in

a relatively large drop in mode 3 stiffness when compared with the original structure. The subsequent reliance on mode 4 stiffness alone is apparently inadequate as the load moves into the stem region and high film pressures are generated from engine firing. A better design strategy suggests evaluation of bearing performance over a two-parameter design space represented by both mode 3 and 4 eigenvalues. The cusp found in the mode-stiffened time history is most likely due to a discrete spatial jump in the nodal location of minimum film thickness.

**Dr Kumar Vaidanathan** (Federal-Mogul Corporation, USA). Is any work planned in taking modal analysis and extending it to the bearing noise issue?

**Reply by Dr S Boedo** (Borg Warner Automotive, New York, USA) and **Professor J F Booker** (Cornell University, USA).

The effects of nonuniform clearance coupled with bearing elasticity would provide an interesting computational study, the results of which could lead to a link between mode shape contribution and bearing noise. Experimental clearance studies are commonly employed in field testing as a means to evaluate wrist-pin bearing noise. The reader is also directed to the companion Leeds/Lyon 1996 paper by Olson and Booker, who present a modified modal analysis scheme including inertia effects attributed to clearance-scale structural motion.

**Dr C J Hooke** (University of Birmingham, UK).

The authors use modes defined by an existing structure and consider the effect of varying the flexibility of these modes. This possibly limits the analysis since variations in the mode shape cannot be examined. Have the authors considered using a generalised non-orthogonal modal system? This would allow greater flexibility in optimising the system although it would somewhat complicate the analysis process.

**Reply by Dr S Boedo** (Borg Warner Automotive, New York, USA) and **Professor J F Booker** (Cornell University, USA).

The authors believe that the modal method of analysis in its present form allows for the use of non-orthogonal transformations of structure-based relative (not absolute) displacements. At this juncture in EHD analysis, however, we suggest a more comprehensive comparison of orthogonal mode shape and modal body forces for global structures currently in practice before contemplation of more complicated analysis procedures.

**23rd Leeds-Lyon Symposium on Tribology**

***'Elastohydrodynamics '96'  
Fundamentals and Applications in Lubrication and Traction'***

**Leeds - 10th-13th September 1996**

**List of Delegates**

| <b><u>Title</u></b> | <b><u>Name</u></b> | <b><u>Address</u></b>   | <b><u>Title</u></b> | <b><u>Name</u></b> | <b><u>Address</u></b>  |
|---------------------|--------------------|---|---------------------|--------------------|--|
| <b>Dr S</b>         | <b>Aihara</b>      | NSK Ltd<br>R & D Centre<br>1-5-50 Kugenuma-<br>Shinmei, Fujisawa,<br>Kanagawa 251<br>Japan                  | <b>Dr Y</b>         | <b>Berthier</b>    | INSA de Lyon,<br>Laboratoire de<br>Mecanique des<br>Contacts, Batiment<br>113, 20 Avenue<br>Albert Einstein<br>69621 Villeurbanne<br>Lyon France |
| <b>Mr M P</b>       | <b>Alanou</b>      | Cardiff School of<br>Eng. Mechanical<br>Eng. Division<br>P O Box 917<br>Cardiff<br>CF2 1XH                  | <b>Dr S</b>         | <b>Bogdanski</b>   | Warsaw University<br>of Technology<br>Institute of<br>Aeronautics and<br>Applied Mechanics<br>Nowowiejska 24,<br>00-665 Warsaw,<br>Poland        |
| <b>Mr Y</b>         | <b>Ando</b>        | Micro-Mechanisms<br>Division, Mech.<br>Eng. Lab. AIST.<br>MITI, Namiki 1-2<br>Tsukaba, Ibaraki<br>305 Japan | <b>Prof J F</b>     | <b>Booker</b>      | Cornell University<br>School of<br>Mechanical &<br>Aerospace Eng.<br>Upson Hall<br>Ithaca New York<br>14853 USA                                  |
| <b>Ms V</b>         | <b>Anghel</b>      | Imperial College<br>Tribology Section<br>Dept. of<br>Mechanical Eng.<br>Exhibition Road<br>London SW7 2BX   | <b>Mrs M</b>        | <b>Bourgeat</b>    | INSA de Lyon,<br>Laboratoire de<br>Mecanique des<br>Contacts, Batiment<br>113, 20 Avenue<br>Albert Einstein<br>69621 Villeurbanne<br>Lyon France |
| <b>Dr J C</b>       | <b>Bell</b>        | ORTRL/5 Shell<br>Research Limited<br>P O Box 1<br>Chester<br>CH1 3SH  |                     |                    |  |

| <u>Title</u>    | <u>Name</u>        | <u>Address</u>  | <u>Title</u>    | <u>Name</u>       | <u>Address</u>  |
|-----------------|--------------------|---|-----------------|-------------------|---|
| <b>Dr J L</b>   | <b>Bozet</b>       | Universite de Liege<br>Service de<br>Tribologie Bat. C3,<br>rue E Solvay 21<br>B-4000 Liege<br>Belgium  | <b>Dr X Y</b>   | <b>Chen</b>       | Shanghai<br>University<br>Research Institute<br>of Bearings<br>P O Box 224<br>149 Yangchang<br>Road<br>Shanghai 200072,<br>PR China |
| <b>Prof B J</b> | <b>Briscoe</b>     | Imperial College of<br>Science,<br>Technology and<br>Medicine, Dept. of<br>Chemical Eng. &<br>Technology<br>Prince Consort Road<br>London SW7 2BY | <b>Prof THC</b> | <b>Childs</b>     | The University of<br>Leeds, Dept. of<br>Mechanical Eng.<br>Leeds<br>LS2 9JT   |
| <b>Mr K R</b>   | <b>Brockwell</b>   | National Research<br>Council/CSTT<br>U-89, Alert Road,<br>Uplands, Ottawa<br>Ontario K1A 0R6<br>Canada  | <b>Dr R J</b>   | <b>Chittenden</b> | The University of<br>Leeds<br>Industrial Unit of<br>Tribology<br>Dept. of<br>Mechanical Engrg<br>Leeds LS2 9JT                      |
| <b>Prof A</b>   | <b>Cameron</b>     | Anglia Polytechnic<br>University, Rookery<br>Farm House, Frog<br>End<br>Gt. Wilbraham<br>Cambridge CB1<br>5JB                                     | <b>Mr S</b>     | <b>Choi</b>       | LG Electronics<br>Senior Research<br>Engineer<br>327-23 Gasan-<br>Dong<br>Keum Chun-Gu<br>Seoul 153-023<br>Korea                    |
| <b>Dr P M</b>   | <b>Cann</b>        | Imperial College<br>Tribology Section<br>Dept. of<br>Mechanical Engrg.<br>Exhibition Road<br>London SW7 2BX                                       | <b>Dr E</b>     | <b>Ciulli</b>     | University of Pisa<br>Dipartimento di<br>Costruzioni<br>Meccaniche &<br>Nucleari<br>Via Diotalvi 2<br>56126 Pisa<br>Italy           |
| <b>Mr N</b>     | <b>Chamberlain</b> | T & N Technology<br>Ltd, Cawston<br>House, Cawston<br>Rugby CV22 7SA  |                 |                   |   |

| <u>Title</u>    | <u>Name</u>      | <u>Address</u>   | <u>Title</u>         | <u>Name</u>                 | <u>Address</u>   |
|-----------------|------------------|--|----------------------|-----------------------------|--|
| <b>Prof R C</b> | <b>Coy</b>       | Shell Research<br>Limited<br>Thornton Research<br>Centre, P O Box 1<br>Chester CH1 1SH   | <b>Dr.Eng.<br/>H</b> | <b>El-Sayed<br/>Rasheed</b> | Arab Academy for<br>Sci & Tech,<br>College of Eng. &<br>Tech. Dept. of<br>Mechanical Eng.<br>Alexandria<br>Egypt   |
| <b>Prof G</b>   | <b>Dalmaz</b>    | INSA de Lyon,<br>Laboratoire de<br>Mecanique des<br>Contacts, Batiment<br>113, 20 Avenue<br>Albert Einstein<br>69621 Villeurbanne<br>Lyon France | <b>Mr C D</b>        | <b>Elcoate</b>              | University of Wales<br>Cardiff, Division of<br>Mechanical Engrg,<br>School of Eng.,<br>Queen's Building,<br>The Parade<br>P O Box 917<br>Cardiff CF2 1XH         |
| <b>Dr P A</b>   | <b>Dearnley</b>  | The University of<br>Leeds, Dept. of<br>Mechanical Eng.<br>Leeds LS2 9JT UK  | <b>Dr D M</b>        | <b>Elliott</b>              | The University of<br>Leeds Dept. of<br>Mechanical Eng.<br>Leeds<br>LS2 9JT UK  |
| <b>Mr A N</b>   | <b>Dickensen</b> | The University of<br>Leeds, Dept. of<br>Mechanical Eng.<br>Leeds LS2 9JT UK  | <b>Dr H P</b>        | <b>Evans</b>                | University of Wales<br>Cardiff School of<br>Eng. Division of<br>Mechanical Eng.<br>and Energy<br>Studies, Queen's<br>Buildings, The<br>Parade<br>Cardiff CF2 1XH |
| <b>Dr A</b>     | <b>Dodd</b>      | NSK-RHP Eur.<br>Technology Centre<br>Mere Way,<br>Ruddington Fields<br>Business Park<br>Ruddington<br>Nottingham NG11<br>6JZ                     | <b>Dr L</b>          | <b>Flabbi</b>               | Ausimont s.p.A.<br>Via S. Pietro 50/a<br>20021 Bollate (MI)<br>Italy   |
| <b>Prof D</b>   | <b>Dowson</b>    | The University of<br>Leeds, Dept. of<br>Mechanical Eng.<br>Leeds<br>LS2 9JT UK   |                      |                             |  |
| <b>Dr P</b>     | <b>Ehret</b>     | The University of<br>Leeds, Dept. of<br>Mechanical Eng.<br>Leeds LS2 9JT UK  |                      |                             |  |

| <u>Title</u>      | <u>Name</u>          | <u>Address</u>   | <u>Title</u>  | <u>Name</u>      | <u>Address</u>   |
|-------------------|----------------------|--|---------------|------------------|--|
| <b>Prof L</b>     | <b>Flamand</b>       | INSA de Lyon,<br>Laboratoire de<br>Mecanique des<br>Contacts, Batiment<br>113, 20 Avenue<br>Albert Einstein<br>69621 Villeurbanne<br>Lyon France         | <b>Mr K S</b> | <b>Goh</b>       | The University of<br>Leeds Dept. of<br>Mechanical Eng.<br>Leeds<br>LS2 9JT UK  |
| <b>Dr G</b>       | <b>Gao</b>           | Imperial College<br>Tribology Section<br>Dept. of<br>Mechanical Engrg.<br>Exhibition Road<br>London SW7 2BX  | <b>Dr J A</b> | <b>Greenwood</b> | The University of<br>Cambridge<br>University Eng.<br>Dept. Trumpington<br>Street Cambridge<br>CB2 1PZ                      |
| <b>Mr E R M</b>   | <b>Gelinck</b>       | University of<br>Twente, Faculty of<br>Mechanical Eng.<br>Tribology Section,<br>P O Box 217<br>7500 AE Enschede<br>The Netherlands                       | <b>Mr R T</b> | <b>Harding</b>   | The University of<br>Leeds Dept. of<br>Mechanical Eng.<br>Leeds LS2 9JT UK   |
| <b>Prof J-M</b>   | <b>Georges</b>       | Ecole Centrale de<br>Lyon, Laboratoire<br>de Tribologie et<br>Dynamique des<br>Systems UMR<br>CNRS, BP 163<br>Ecully, France                             | <b>Mr D</b>   | <b>Hirst</b>     | Imperial College<br>Tribology Section<br>Dept. of<br>Mechanical Engrg.<br>Exhibition Road<br>London SW7 2BX                |
| <b>Prof J-M</b>   | <b>Georges</b>       | Ecole Centrale de<br>Lyon, Laboratoire<br>de Tribologie et<br>Dynamique des<br>Systems UMR<br>CNRS, BP 163<br>Ecully, France                             | <b>Prof E</b> | <b>Höglund</b>   | Luleå University of<br>Technology,<br>Division of<br>Machine Elements<br>S-971 87<br>Luleå Sweden                          |
| <b>Dipl-Ing J</b> | <b>Gerstenberger</b> | Institut für<br>Maschinenelemente<br>Konstruktionstechnik<br>und Tribologie -<br>Universität<br>Hannover<br>Welfengarten 1A<br>30167 Hannover<br>Germany | <b>Dr C J</b> | <b>Hooke</b>     | The University of<br>Birmingham<br>School of<br>Manufacturing and<br>Mechanical Eng.<br>Edgbaston<br>Birmingham<br>B15 2TT |

| <u>Title</u>  | <u>Name</u>      | <u>Address</u>   | <u>Title</u>  | <u>Name</u>      | <u>Address</u>  |
|---------------|------------------|--|---------------|------------------|---|
| <b>Dr L</b>   | <b>Houpert</b>   | Timken France<br>BP 89<br>68002 Colmar<br>Cedex<br>France  | <b>Dr G J</b> | <b>Johnston</b>  | Mobil Technology<br>Company<br>P O Box 480<br>Paulsboro<br>NJ 08066-0480<br>USA   |
| <b>Prof S</b> | <b>Ioannides</b> | SKF Eng. and<br>Research Centre,<br>Postbus 2350<br>3430 DT<br>Nieuwegein<br>The Netherlands                       | <b>Mr D A</b> | <b>Jones</b>     | The University of<br>Leeds Dept. of<br>Mechanical Eng.<br>Leeds LS2 9JT UK  |
| <b>Dr F</b>   | <b>Itoigawa</b>  | Nagoya Institute of<br>Technology<br>Dept. of Mechanica<br>Engrg.<br>Gokiso-ch, Showa-<br>Nu, Nagoya<br>466 Japan  | <b>Dr S</b>   | <b>Kamamoto</b>  | Koyo Seiko Co. Ltd<br>Research &<br>Development<br>Centre 24-1<br>Kokubuhiganjyo-<br>cho Kashiwara-shi,<br>Osaka 582, Japan |
| <b>Dr F</b>   | <b>Ji</b>        | The University of<br>Leed, Dept. of<br>Mechanical Eng.<br>Leeds LS2 9JT UK   | <b>Prof M</b> | <b>Kaneta</b>    | Kyushu Institute of<br>Technology<br>Dept. of<br>Mechanical Engrg<br>1-1 Sensui-cho,<br>Tobata Kitakyushu<br>804 Japan      |
| <b>Dr Z M</b> | <b>Jin</b>       | The University of<br>Bradford, Dept. of<br>Mech. and<br>Manufacturing<br>Eng. Bradford<br>BD7 1DP                  | <b>Dr J W</b> | <b>Kannel</b>    | Battelle<br>505 King Avenue<br>Columbus<br>Ohio 43201-2693<br>USA   |
| <b>Mr B</b>   | <b>Jobbins</b>   | The University of<br>Leeds Dept. of<br>Mechanical Eng.<br>Leeds LS2 9JT UK   | <b>Mr N</b>   | <b>Kapur</b>     | The University of<br>Leeds Dept. of<br>Mechanical Eng.<br>Leeds LS2 9JT UK  |
| <b>Dr S A</b> | <b>Johnson</b>   | Unilever Research<br>Port Sunlight<br>Laboratory<br>Quarry Road East<br>Bebington, Wirral<br>Merseyside<br>L63 3JW | <b>Mrs E</b>  | <b>Kassfeldt</b> | Luleå University of<br>Technology, Dept.<br>of Mechanical Eng.<br>S-971 87<br>Luleå Sweden                                  |

| <u>Title</u>  | <u>Name</u>        | <u>Address</u>  | <u>Title</u>  | <u>Name</u>             | <u>Address</u>   |
|---------------|--------------------|---|---------------|-------------------------|--|
| <b>Prof T</b> | <b>Kato</b>        | The University of<br>Tokyo<br>Dept. of<br>Mechanical Eng.<br>7-3-1 Hongo,<br>Bunkyo-ku<br>Tokyo 113, Japan  | <b>Mr L</b>   | <b>Lafarge</b>          | INSA de Lyon,<br>Laboratoire de<br>Mecanique des<br>Contacts, Batiment<br>113, 20 Avenue<br>Albert Einstein<br>69621 Villeurbanne<br>Lyon France |
| <b>Mr H J</b> | <b>Kim</b>         | The University of<br>Leeds Dept. of<br>Mechanical Eng.<br>Leeds LS2 9JT UK                                  | <b>Mr I</b>   | <b>Lee-<br/>Prudhoe</b> | Imperial College<br>Tribology Section<br>Dept. of<br>Mechanical Engrg.<br>Exhibition Road<br>London SW7 2BX                                      |
| <b>Mr T H</b> | <b>Kim</b>         | Imperial College<br>Tribology Section<br>Dept. of<br>Mechanical Engrg.<br>Exhibition Road<br>London SW7 2BX | <b>Dr A J</b> | <b>Lehtovaara</b>       | Tampere University<br>of Technology<br>Machine Design<br>P O Box 589<br>Fin-33101 Tampere<br>Finland   |
| <b>Dr T</b>   | <b>Koga</b>        | Oita University<br>Faculty of Eng.<br>Dan Noharu<br>Oita-City<br>Japan 870-11                               | <b>Prof A</b> | <b>Lubrecht</b>         | INSA de Lyon,<br>Laboratoire de<br>Mecanique des<br>Contacts, Batiment<br>113, 20 Avenue<br>Albert Einstein<br>69621 Villeurbanne<br>Lyon France |
| <b>Mr J</b>   | <b>Krasser</b>     | AVL List GmbH<br>KleistraBe 48<br>8020 Graz<br>Austria  |               |                         |  |
| <b>Mr A R</b> | <b>La Fountain</b> | Imperial College<br>Tribology Section<br>Dept. of<br>Mechanical Engrg.<br>Exhibition Road<br>London SW7 2BX | <b>Dr M-T</b> | <b>Ma</b>               | The University of<br>Central Lancashire<br>Dept. of Eng. and<br>Product Design<br>Preston PR1 2HE  |
|               |                    |   | <b>Dr K</b>   | <b>Maekawa</b>          | The University of<br>Leeds, Dept. of<br>Mechanical Engrg.<br>The University of<br>Leeds LS2 9JT UK   |



| <u>Title</u>  | <u>Name</u>    | <u>Address</u>  | <u>Title</u>  | <u>Name</u>                 | <u>Address</u>   |
|---------------|----------------|---|---------------|-----------------------------|--|
| <b>Dr C N</b> | <b>March</b>   | The University of<br>Leeds, Industrial<br>Unit of Tribology<br>Dept. of<br>Mechanical Eng.<br>Leeds LS2 9JT UK  | <b>Mr J</b>   | <b>Molimard</b>             | INSA de Lyon,<br>Laboratoire de<br>Mecanique des<br>Contacts, Batiment<br>113, 20 Avenue<br>Albert Einstein<br>69621 Villeurbanne<br>Lyon France       |
| <b>Mr H</b>   | <b>Marie</b>   | Mobil Oil<br>Francasse<br>Research Centre<br>BP 37<br>76 330 ND de<br>Gravenchon<br>France  | <b>Dr A J</b> | <b>Moore</b>                | BP Oil Technology<br>Centre<br>Chertsey Road<br>Sunbury-on-<br>Thames<br>Middlesex<br>TW16 7LN, UK   |
| <b>Mr M J</b> | <b>Martin</b>  | University of Wales<br>College of Cardiff,<br>School of Eng.<br>Division of<br>Mechanical Eng.<br>and Energy<br>Studies, P O Box<br>925, Cardiff CF2<br>1YF | <b>Dr G E</b> | <b>Morales-<br/>Espejel</b> | ITESM, Centro de<br>Sistemas de<br>Manufactura<br>E. Gorza Sada<br>2501 Sur<br>64849 Monterrey<br>NL, Mexico   |
| <b>Mr G</b>   | <b>McClure</b> | The University of<br>Leeds, Dept. of<br>Mechanical Eng.<br>Leeds LS2 9JT UK   | <b>Prof T</b> | <b>Murakami</b>             | Kyushu University<br>Dept. of Intelligent<br>Machinery and<br>Systems<br>Faculty of Eng.<br>6-10-1 Hakozaki,<br>Higashi-ku,<br>Fukuoka 812-81<br>Japan |
| <b>Dr J B</b> | <b>Medley</b>  | University of<br>Waterloo<br>Dept. of Mech Eng.<br>Waterloo, Ontario<br>N2L 3G1 Canada  | <b>Prof T</b> | <b>Nakamura</b>             | Nagoya Institute of<br>Technology<br>Dept. of<br>Mechanical Engrg.<br>Gokiso-cho.,<br>Shoowa-ku<br>Nagoya<br>466 Japan                                 |
| <b>Mr D</b>   | <b>Mehenny</b> | The University of<br>Leeds, Dept. of<br>Mechanical Eng.<br>Leeds LS2 9JT UK   |               |                             |  |

| <u>Title</u>  | <u>Name</u>      | <u>Address</u>   | <u>Title</u>  | <u>Name</u>    | <u>Address</u>   |
|---------------|------------------|--|---------------|----------------|--|
| <b>Mr Y</b>   | <b>Nakanishi</b> | Kyushu University<br>Dept. of Intelligent<br>Machinery and<br>Systems, Hakozaki,<br>Higashi-ku,<br>Fukuoka 812-81,<br>Japan                      | <b>Mr S</b>   | <b>Ogano</b>   | Imperial College<br>Tribology Section<br>Dept. of<br>Mechanical Engrg.<br>Exhibition Road<br>London SW7 2BX                                      |
| <b>Mr H</b>   | <b>Narai</b>     | NSK-RHP<br>European<br>Technology Centre<br>Mere Way,<br>Ruddington Fields<br>Business Park<br>Ruddington<br>Nottingham NG11<br>6JZ              | <b>Dr N</b>   | <b>Ohno</b>    | c/o Dr D J Schipper<br>Tribology Section<br>Dept. of MechEng.<br>University of<br>Twente<br>P O Box 217<br>7500 AE Enschede<br>The Netherlands   |
| <b>Dr D</b>   | <b>Nelias</b>    | INSA de Lyon,<br>Laboratoire de<br>Mecanique des<br>Contacts, Batiment<br>113, 20 Avenue<br>Albert Einstein<br>69621 Villeurbanne<br>Lyon France | <b>Prof N</b> | <b>Ohtsuki</b> | Kyushu University<br>Faculty of Eng.,<br>Graphic Science<br>4-2-1 Ropponmatsu<br>Chuo-ku, Fukuoka<br>City, Fukuoka<br>810 Japan                  |
| <b>Mr H P</b> | <b>Nixon</b>     | Manager - Mech/<br>Tribochemical Sci<br>The Timken Co.<br>P O Box 6930<br>Canton<br>Oh 44706-0930<br>USA   | <b>Dr H</b>   | <b>Okamura</b> | Toyota Motor<br>Corporation<br>Higashi Fuji<br>Technical Center<br>Drivetrain Eng.<br>Division<br>1200 Mishuku,<br>Susono, Shizuoka<br>Japan 411 |
| <b>Mr E</b>   | <b>Nurgat</b>    | The University of<br>Leeds, School of<br>Computer Studies<br>Leeds LS2 9JT UK  | <b>Dr A</b>   | <b>Olver</b>   | Imperial College<br>Tribology Section<br>Dept. of<br>Mechanical Engrg.<br>Exhibition Road<br>London SW7 2BX                                      |

| <u>Title</u>      | <u>Name</u>    | <u>Address</u>   | <u>Title</u>         | <u>Name</u>     | <u>Address</u>  |
|-------------------|----------------|--|----------------------|-----------------|---|
| <b>Prof P L B</b> | <b>Oxley</b>   | The University of New South Wales<br>School of Mechanical and Manufacturing Engrg., P O Box 1, Kensington<br>NSW Australia<br>2033 | <b>Prof Dr-Ing G</b> | <b>Poll</b>     | Institut für Maschinenelemente<br>Konstruktionstechnik und Tribologie -<br>Universität Hannover<br>Welfengarten 1A<br>30167 Hannover<br>Germany |
| <b>Mr F</b>       | <b>Palomba</b> | Elasis ScpA - SIAT<br>G, Fiat Group<br>v. Impero<br>Pomiguano<br>D'Aus(NA)<br>Italy  | <b>Mr M</b>          | <b>Priest</b>   | The University of Leeds, Dept. of Mechanical Eng.<br>The University of Leeds LS2 9JT UK   |
| <b>Dr M Ya</b>    | <b>Panovko</b> | Mechanical Eng.<br>Research Institute<br>Academy of Sciences<br>Griboyedova Str. 4<br>101830 Moscow<br>Russia                      | <b>Mrs M</b>         | <b>Ratoi</b>    | Imperial College<br>Tribology Section<br>Dept. of Mech Engrg.<br>Exhibition Road<br>London SW7 2BX  |
| <b>Mr T</b>       | <b>Paquet</b>  | Toyota Motor Europe (TMME)<br>Technical Centre-<br>Bedrijfspark<br>Weyveld, Hoge Wei<br>33A-B1930<br>Zaventem, Belgium             | <b>Mr J</b>          | <b>Rieglert</b> | Luleå University of Technology<br>Division of Machine Elements<br>S-97187 Luleå<br>Sweden   |
| <b>Mr T A</b>     | <b>Polak</b>   | Neale Consulting Engineers Ltd<br>43 Downing Street<br>Farnham<br>Surrey GU9 7PH   | <b>Mr L M</b>        | <b>Rudd</b>     | Tribology, FL Centre<br>Bld. 415<br>DRA Pyestock<br>Farnborough<br>Hants GU14 0LS   |
|                   |                |  | <b>Dr J E</b>        | <b>Rycroft</b>  | Shell Research Limited<br>Shell Research & Technology Centre,<br>Thornton<br>P O Box 1<br>Chester CH1 3SH                                       |

| <u>Title</u>  | <u>Name</u>    | <u>Address</u>   | <u>Title</u>   | <u>Name</u>    | <u>Address</u>  |
|---------------|----------------|--|----------------|----------------|---|
| <b>Dr Ph</b>  | <b>Sainsot</b> | INSA de Lyon,<br>Laboratoire de<br>Mecanique des<br>Contacts, Batiment<br>113, 20 Avenue<br>Albert Einstein<br>69621 Villeurbanne<br>Lyon France | <b>Mr A J</b>  | <b>Smith</b>   | NSK-RHP<br>European<br>Technology Centre,<br>Mere Way<br>Ruddington Fields<br>Business Park<br>Ruddington<br>Nottingham NG11<br>6JZ                         |
| <b>Dr R</b>   | <b>Sayles</b>  | Imperial College<br>Tribology Section<br>Dept. of<br>Mechanical Eng.<br>London SW7 2BX   | <b>Dr R W</b>  | <b>Snidle</b>  | University of Wales<br>College of Cardiff,<br>School of Eng.<br>Division of<br>Mechanical Eng.<br>and Energy<br>Studies, P O Box<br>925, Cardiff CF2<br>1YF |
| <b>Mr C T</b> | <b>Schäfer</b> | INA Wälzlager<br>Schaeffler KG<br>Dept TB;<br>Industriestrasse 1-3<br>91074<br>Herzogenaurach<br>Germany   | <b>Dr J</b>    | <b>Sorab</b>   | Ford Motor<br>Company<br>20000 Rotunda<br>Drive, MD 2629<br>SRL, Dearborn<br>MI 48121-2053<br>USA   |
| <b>Dr R J</b> | <b>Smalley</b> | SKF Eng. and<br>Research Centre<br>Postbus 2350<br>3430 DT<br>Nieuwegein<br>The Netherlands  | <b>Prof H</b>  | <b>Spikes</b>  | Imperial College<br>Tribology Section<br>Dept. of<br>Mechanical Engrg.<br>Exhibition Road<br>London SW7 2BX   |
| <b>Mr M</b>   | <b>Smeeth</b>  | Imperial College<br>Tribology Section<br>Dept. of<br>Mechanical Engrg.<br>Exhibition Road<br>London SW7 2BX                                      | <b>Mrs M S</b> | <b>Starkey</b> | GKN Technology<br>Ltd, Birmingham<br>New Road<br>Wolverhampton<br>WV4 6BW   |

| <u>Title</u>    | <u>Name</u>      | <u>Address</u>   | <u>Title</u>  | <u>Name</u>           | <u>Address</u>   |
|-----------------|------------------|--|---------------|-----------------------|--|
| <b>Dr J</b>     | <b>Sugimura</b>  | Kyushu University<br>Dept. of Energy<br>and Mechanical<br>Eng. 6-10-1<br>Hakozaki, Higashi-<br>ku, Fukuoka 812-<br>81Japan                   | <b>Mr K</b>   | <b>Vaidyanathan</b>   | Federal Mogul<br>Corporation<br>Senior Technical<br>Analyst<br>3990 Research Park<br>Drive, Ann Arbor<br>MI 48108 USA                            |
| <b>Dr M</b>     | <b>Taniguchi</b> | NSK Ltd<br>R & D Centre<br>1-5-50 Kugenuma-<br>Shinmei Fujisawa,<br>Kanagawa 251<br>Japan  | <b>Mr R H</b> | <b>van der Stegen</b> | University of<br>Twente, Dept. of<br>Mechanical Eng.<br>Tribology Group<br>P O Box 217, 7500<br>AE, Enschede The<br>Netherlands                  |
| <b>Dr R I</b>   | <b>Taylor</b>    | Shell Research &<br>Technology Centre,<br>Thornton<br>P O Box 1<br>Chester CH1 3SH   | <b>Mr H J</b> | <b>van Leeuwen</b>    | Eindhoven<br>University of Tech.<br>Dept. of Mech Eng.<br>WH 04-111, P O<br>Box 513<br>NL-5600 M B<br>Eindhoven<br>The Netherlands               |
| <b>Prof C M</b> | <b>Taylor</b>    | The University of<br>Leeds, Dept. of<br>Mechanical Eng.<br>Leeds LS2 9JT UK  | <b>Dr C H</b> | <b>Venner</b>         | University of<br>Twente, Faculty of<br>Mechanical Eng.<br>P O Box 217<br>7500 AE Enshede<br>Holland  |
| <b>Mr Y</b>     | <b>Tozaki</b>    | Mitsubishi Heavy<br>Industries Ltd<br>Tribology<br>Laboratory<br>Nagasaki R & D<br>Center<br>Akunoura-machi<br>Nagasaki-city<br>Japan 850-91 | <b>Mr F</b>   | <b>Ville</b>          | INSA de Lyon,<br>Laboratoire de<br>Mecanique des<br>Contacts, Batiment<br>113, 20 Avenue<br>Albert Einstein<br>69621 Villeurbanne<br>Lyon France |
| <b>Mr G</b>     | <b>Tripaldi</b>  | Eniricerche SpA<br>Via Maritano 26<br>20097 San Donato<br>Milanese, Milano<br>Italy  | <b>Dr M</b>   | <b>Visscher</b>       | The University of<br>Leeds, Dept. of<br>Mechanical Eng.<br>Leeds LS2 9JT UK  |

| <u>Title</u>  | <u>Name</u>     | <u>Address</u>  | <u>Title</u>    | <u>Name</u>     | <u>Address</u>   |
|---------------|-----------------|---|-----------------|-----------------|--|
| <b>Mr J M</b> | <b>Vree</b>     | SKF Eng. &<br>Research Centre<br>BV, Mailbox 2350<br>3430 DT<br>Nieuwegein<br>The Netherlands               | <b>Prof W O</b> | <b>Winer</b>    | Georgia Institute of<br>Technology<br>Woodruff School of<br>Mechanical Eng.<br>Atlanta, GA<br>30332-0405 USA   |
| <b>Mr D</b>   | <b>Wei</b>      | Imperial College<br>Tribology Section<br>Dept. of<br>Mechanical Engrg.<br>Exhibition Road<br>London SW7 2BX | <b>Dr P L</b>   | <b>Wong</b>     | City University of<br>Hong Kong<br>Dept. of<br>Manufacturing<br>Engrg., Kowloon<br>Hong Kong   |
| <b>Ir Y H</b> | <b>Wijnant</b>  | University of<br>Twente, Faculty of<br>Mechanical Eng.<br>P O Box 217<br>7500 AE Enschede<br>Holland        | <b>Mr M F</b>   | <b>Workel</b>   | The University of<br>Leeds, Dept. of<br>Mechanical Eng.<br>Leeds LS2 9JT UK  |
| <b>Dr I V</b> | <b>Wikström</b> | SKF Eng. &<br>Research Centre<br>BV, Postbus 2350<br>3430 DT<br>Nieuwegein<br>The Netherlands               | <b>Dr A</b>     | <b>Xiaolan</b>  | Principal Research<br>Engineer,<br>The Timken<br>Company<br>P O Box 6930<br>Canton, Oh 44706-<br>0930 USA  |
| <b>Dr J A</b> | <b>Williams</b> | Cambridge<br>University<br>Eng. Dept.<br>Trumpington Street<br>Cambridge<br>CB2 1PZ                         | <b>Dr H</b>     | <b>Xu</b>       | T & N Technology<br>Ltd, Cawston<br>House, Rugby<br>Warwickshire<br>CV22 7SA   |
| <b>Mr W H</b> | <b>Wilson</b>   | Editor - Industrial<br>Lubrication<br>Tribology, 18 Adel<br>Park Gardens<br>Leeds 16                        | <b>Prof T</b>   | <b>Yamamoto</b> | Tokyo University of<br>Agriculture and<br>Technology, Dept.<br>of Mechanical<br>Systems Eng.<br>2-24-16 Naka-cho,<br>Koganei-shi<br>Tokyo 184, Japan |

| <b><u>Title</u></b> | <b><u>Name</u></b> | <b><u>Address</u></b>   |
|---------------------|--------------------|---|
| <b>Dr R</b>         | <b>Yamashita</b>   | The University of<br>Leeds, Dept. of<br>Mechanical Engrg.<br>Leeds LS2 9JT UK                   |
| <b>Mr A E</b>       | <b>Young</b>       | The University of<br>Leeds, Dept. of<br>Mechanical Eng.<br>Leeds LS2 9JT UK                     |
| <b>Ms H</b>         | <b>Yu</b>          | University of<br>Waterloo<br>Dept. of<br>Mechanical Eng.<br>Waterloo, Ontario<br>N2L 3G1 Canada |